

**ELEVENTH INTERNATIONAL CONFERENCE
ON COMPOSITE MATERIALS**

**Gold Coast, Queensland, Australia
14th - 18th July 1997**

PROCEEDINGS

VOLUME VI

COMPOSITE STRUCTURES

**Editor
Murray L. Scott**

**AUSTRALIAN COMPOSITE STRUCTURES SOCIETY
WOODHEAD PUBLISHING LIMITED**

TABLE OF CONTENTS

Joints

How Relevant Are Load Rate Effects to Realistic Bonded Joints?	1
<i>M.J. Davis</i>	
Strength of Adhesively Bonded Composite Tubular Lap Joints	8
<i>L. Tong, S. Alexiadis, G.P. Steven</i>	
Experimental Characterization of Reinforcing Effects of FRP Sheets Bonded on Mortar and Concrete Beams	16
<i>Isao Kimpara, Kazuro Kageyama, Toshio Suzuki, Isamu Ohsawa, Koji Yamaguchi</i>	
Prediction of Tensile Fatigue Life for GFRP Adhesive Joint	26
<i>Yasushi Miyano, Stephen W. Tsai, Masayuki Nakada, Sangwook Sihn, Tomoya Imai</i>	
Resistance Welding of Carbon Fibre Fabric Reinforced Polyetherimide (CF fabric/PEI) Composite Material	36
<i>M. Hou, L. Ye, Y.-W. Mai</i>	
Residual Stresses in Thermoplastic Bonding to Metals: Experiments and Modeling	46
<i>Karthik Ramani, Wenping Zhao</i>	
Weldability and Heat Affected Zone (HAZ) Evaluation for High Energy Rate Joining of Thermoplastic Composites Using Microwaves	55
<i>H.S. Ku, E. Siores, J.A.R. Ball</i>	
Joining of Thermoplastic Composites by Bolts and Microwave Welding	65
<i>M. Jauss, R. Emmerich, P. Eyerer</i>	
Energy Absorbing Composite Joints and their Application to Noise Reduced Sonar Domes	74
<i>J.R. House</i>	
The Design and Manufacture of High Performance Unidirectional Composite Tubular Joints	84
<i>A.B. Clarke, R.G.H. Davies, K.D. Potter, M.R. Wisnom, R.D. Adams</i>	
A Novel Comb Joint Concept for High Strength Unidirectional Carbon Fibre Bonded Joints	95
<i>A. Towse, K.D. Potter, M.R. Wisnom, R.D. Adams</i>	
Bolt Bearing Behavior of Highly Loaded Composite Joints at Elevated Temperatures with and without Clamp-up	102
<i>Richard J. Wright, W. Steven Johnson, Hafiz Ahmad</i>	
Fracture of Composite-Metal Adhesive Joints under Thermo-Mechanical Loading	111
<i>Sharath P. Shetty, S. Mark Spearing</i>	
The Analysis of Bonded Lap Joints	119
<i>M. Chao, W.K. Chiu, R. Jones, J. Wang, D. Kelly</i>	
A Simple Unified Approach for the Analysis and Design of Adhesive Bonded Composite Laminates	129
<i>Flemming Mortensen, Ole Thybo Thomsen</i>	
Finite Element Analysis of Mechanically Fastened Joints in CFRP	139
<i>P.P. Camanho, F.L. Matthews</i>	

An Experimental Investigation into the Use of Inserts to Enhance the Static Performance of Thin Composite Bolted Lap Joints	148
<i>L. Mirabella, S.C. Galea</i>	
Design and Testing of an Aircraft Composite Hinge	158
<i>A.R. Rispler, M. Hou, L. Tong, G.P. Steven, L. Ye, Y.W. Mai</i>	
Study on the Bending Behavior of Laminates Connected by Rivets	167
<i>Ya-Jung Lee, Yau Shyu, Tung-Chien He</i>	
Thermoplastic Bonding to Metals via Injection Molding for Macro-Composite Manufacture	175
<i>Karthik Ramani, Brendan Moriarty</i>	

Non-Destructive Evaluation

Characterization of Impact Damage in CFRPs Using a Scanning Acoustic Microscope	185
<i>Shang-Lin Gao, Jang-Kyo Kim, Xing-Juan Xian</i>	
Response of Fibre Composite Laminates to Acoustic Emission Line Sources	193
<i>E. Rhian Green</i>	
A Nondestructive Approach to Evaluating Impact Damaged Composite Structures	203
<i>Hyonny Kim, Keith T. Kedward</i>	
Acousto-Ultrasonic Characteristics for Contact-Type Transducers Coupled to a Composite Beam	213
<i>S. Kitpornchai, T. Liu, K.M. Liew</i>	
Nondestructive Evaluation of Impact-Damaged CFRP Laminates by Acoustic Emission During Flexural Loading	223
<i>Oh-Yang Kwon, Doo-Hyun Hong</i>	
In-Situ Neutron Diffraction Characterisation of a NiTi-Fibre Reinforced Shape Active Composite	230
<i>T. Lorentzen, W.D. Armstrong</i>	
Interphase Characterisation of Composite Systems Using Intelligent Signal Processing of Ultrasonic Data	237
<i>D. Van Hemelrijck, A. Anastasopoulos, L. Tirry, A. Cardon, W.P. De Wilde</i>	
A Procedure for Studying Delamination in Complex Structures	246
<i>José Sancho</i>	
Calibration of Infrared Stress Measurement Technique for CFRP Composites and its Application	258
<i>Sunao Sugimoto, Takashi Ishikawa</i>	
Continuous Monitoring of Resin Content in Composite Prepreg Narrow Tapes	271
<i>Huang Yudong, Liu Li, Zhang Zhiqian, Liu Lixun</i>	

Repair

Thermal Residual Strain Measurement in a Composite Repair on a Cracked Aluminium Structure	279
<i>A.M. Albat, D.P. Romilly, M.D. Raizenne</i>	
Coherent Simulation and Testing for Composite Blade Repair	289
<i>O.O. Ochoa, B. McNichols, C. Oztelcan, J. Martin, K. Sem</i>	

Failure Mechanisms in Bonded Patch Repaired Structures	296
<i>Naveen Rastogi, B.P. Deepak, Som R. Soni, Arvind Nagar</i>	
Monitoring Damage in Bonded Composite Repairs of Cracked Metallic Components Using Surface Strain Measurements	306
<i>Stephen C. Galea</i>	
Shear Stresses in a Stepped Bonded Repair of a Laminate	317
<i>Holm Altenbach, Hanno Haars</i>	
Composite Bonded Repair of Cracked Panels Subject to Acoustic Fatigue	327
<i>R.J. Callinan, S.C. Galea, S. Sanderson</i>	
Temperature Effects on a Composite Repair	337
<i>R. Boykett, K. Walker</i>	
On the Design of Bonded Patches for One-Sided Repair	347
<i>C.H. Wang, L.R.F. Rose</i>	
Load History Dependence of Graphite Epoxy Joints/Repairs: an Experimental Study	357
<i>W.K. Chiu, S. Galea, R. Jones, S. Pitt</i>	
Observation of Static Strength and Fatigue Life of Repaired Graphite/Epoxy Using Tensile Coupon	365
<i>J.W. Choi, W. Hwang, H.C. Park, K.S. Han</i>	
Bonded Repairs in Composite Structures - a Finite Element Approach	374
<i>Randolph A. Odi, Clifford M. Friend</i>	
Influence of Impact Damage and Repair Schemes on the Strength of Foam-Cored Sandwich Beams	385
<i>S.D. Clark, R.A. Shenoi, H.G. Allen</i>	
Repair Design of Composites and Efficiency of Scarf Patch Repairs	395
<i>C. Soutis, F. Z. Hu</i>	
Epoxy Film Adhesive for Aluminum and Composite Repairing	405
<i>Bin Liang, Qingfang Liu, Linan Liu</i>	
Repair of Type B Damage to Marine Sandwich Structures	412
<i>Rodney S. Thomson, Raoul E. Luescher, Ivan Grabovac</i>	

Smart Materials

Use of Optical Fibre Sensors to Detect and Monitor Damage in Bonded Composite Repairs of Cracked Metallic Components	421
<i>Edward Tapanes, Stephen C. Galea</i>	
Elasticity Solution of Polymeric Piezoelectric C-Block Composite Actuator	432
<i>Haozhong Gu, Aditi Chattopadhyay</i>	
Anisotropic Piezo-Electro-Thermo-Viscoelasticity Theory with Applications to Composites	444
<i>H.H. Hilton, J. R. Vinson, S. Yi</i>	
Spatial Design of Piezoelectric Sensors and Actuators for Vibration Control of Laminated Composite Plates	454
<i>Seung-Jo Kim, Ji Hwan Kim, Keun-Young Park, Jung-Kyu Ryou</i>	
Prediction of Magnetoelectric Coupling and Effective Properties of Intelligent Materials: Piezoelectric / Piezomagnetic Composites	464
<i>Jin H. Huang, Ya-Hui Chiu, Jui-Che Hsu</i>	
Material Characterization of Thin Film Piezoelectric Polymers	474
<i>Frank Holloway, Aleksandra M. Vinogradov</i>	

Improvement of Damping Property of CFRP Composite Beam Interleaved with Shape Memory Polymer by Using CFRP Laminate as a Heater	483
<i>Nobuo Oshima, Takehito Fukuda, Daisuke Inui</i>	
Active Control of Crack-tip Stress Intensity by Contraction of Shape Memory TiNi Fibers Embedded in Epoxy Matrix Composite - Dependency of Stress Intensity Factor on Crack-tip Domain Size	493
<i>Akira Shimamoto, Yasubumi Furuya, Minoru Taya</i>	
A Two-Dimensional Shape Memory Alloy Actuator	500
<i>Weida Wu, Faramarz Gordaninejad</i>	
Fabrication and Characterization of Squeeze Cast AC4A Al/TiNi Shape Memory Composites	510
<i>Youngsu Cho, Ildong Choi, Ik-Min Park, Kyungmox Cho, Busob Kim, Deukman An</i>	
Vibration Control of Active Structures with Piezoelectric Modal Sensors and Actuators	519
<i>Changqing Chen, Yapeng Shen</i>	
Design of the Smart Components Based on Shape Memory Effect	528
<i>D.J. Lee, T.H. Jeong</i>	
Finite Element Analysis of Mechanical Properties of Shape Memory Alloys	540
<i>Yen Jinliang, Shen Yapeng, Chen Ru</i>	

Smart Structures

Integrated Finite Element Modelling of Smart Composite Structures	551
<i>Tamunoiyala S. Koko, Irewole R. Orisamolu, Malcolm J. Smith</i>	
Active Shape Control of Shape Memory Alloy Composite Structures	561
<i>M.W.M. van der Wijst, J. Zuidervaart, T. Peijs, P.J.G. Schreurs</i>	
Fabrication and Testing of Smart FRP Reinforcements	571
<i>Alexander L. Kalamkarov, Douglas O. MacDonald</i>	
Fatigue Behavior of Optical Fiber Sensor Embedded in Smart Composite Structures	582
<i>Tae Seong Jang, Jung Ju Lee, Dong Chun Lee, Dae Cheol Seo, Ho Kim</i>	
Efficient Parallel Design/Placement Optimization Methodology of Large Smart Structures	591
<i>Rong C. Shieh</i>	

Structures

Sensitivity Analysis of Composite Beam Structural Response Due to Defects	601
<i>K.L. Springer, W.S. Chan</i>	
A Model for the Behaviour of Thick Composite Laminates in Hydrocarbon Fibres	611
<i>N. Dodds, A.G. Gibson</i>	
Experimental and Numerical Method for Large Transformations of Reinforced Composite Structures	622
<i>A. Ben Dhia</i>	
The Effect of an Elastic Core on the Stability of Composite Circular Cylindrical Shells	632
<i>Yin Yunyu</i>	

Hole Identification in Composite Structures Using Boundary Data from Multiple Loading Modes	639
<i>Chyanbin Hwu, Yan-Chu Liang</i>	
Free-Edge Interlaminar Stress Analysis in Composite Laminates by the Extended Kantorovich Method	648
<i>Maenghyo Cho, Jin-Young Yoon</i>	
Buckling Analysis of Skew Composite Laminate Plates	658
<i>Hsuan-Teh Hu, Wen-Long Tzeng</i>	
Buckling of Delaminated Beam-Plates with Repairing Fasteners	668
<i>Chien-Chang Lin, Shou-Hsiung Cheng</i>	
Durability of Postbuckling Fibre Composite Shear Panels	677
<i>Rodney S. Thomson, Murray L. Scott</i>	
Postbuckling and Failure of Stiffened Composite Plates	687
<i>Chang-Sun Hong, Cheol-Won Kong, In-Cheol Lee</i>	
Postbuckling Failure of Carbon-Epoxy Compression Panels	695
<i>K.A. Stevens, S. Specht, G.A.O. Davies</i>	
Postbuckling Failure Analysis of Carbon/Epoxy Compression Panel	707
<i>H. Alesi, V.M. Nguyen, R. Jones, N. Mileshekin, D. Kelly</i>	
Fiber Architecture Based Design of Ductile Composite Rebar for Concrete Structures	723
<i>Frank K. Ko, Win Somboonsong, Harry G. Harris</i>	
Experimental and Numerical Evaluation of Bond Stress of Concrete Beams Reinforced by GFRP Bars	731
<i>Luis Calado, Carlo A. Castiglioni, Maria Rosario Agatino</i>	
Compression Failure of Laminated Composite Cylindrical Shells Under Axial Loading	742
<i>M.A. Battley, G.R. Dromgoole</i>	
Applied Theory of Sandwich Panels Allowing for Local Effects	753
<i>V.A. Polyakov</i>	
Accurate Prediction of Thermal Deformation of Sandwich Panels Considering the Effect of Adhesive	762
<i>Shigenori Kabashima</i>	
Free Vibration of Composite Shells	770
<i>S. Mirza, N. Li</i>	
Analysis of Anisotropic Multilayered Plates and Shells Based on a New Higher-Order Theory	779
<i>V.E. Verijenko, S. Adali, P.Y. Tabakov, C. Shaikh</i>	
Computational Model for Doubly Curved Laminated Shells Based on a Refined Asymptotic Theory	789
<i>Chih-Ping Wu, Jiann-Quo Tarn, Kai-Lin Yang</i>	
Problems in Modelling the Detail Geometry of a Composite Ship Structure, Fluid and Explosive in an Underwater Explosion Scenario	799
<i>John Marco, Jeff Lingard</i>	
Non-Linear Finite Element Analysis of Thin Composite Structures	808
<i>José Simões Moita, Cristóvão M. Mota Soares, Carlos A. Mota Soares</i>	
The Behaviors of Strengthened Concrete Girders with GFRP Laminates	819
<i>Dujun Yang, Shijie Wang</i>	
Hazards of Local Failure in Bending of Composite Sandwich Panels From Point Forces	826
<i>I.G. Zhigun, R.P. Shlitsa, V.V. Khitrov</i>	

HOW RELEVANT ARE LOAD RATE EFFECTS TO REALISTIC BONDED JOINTS?

M.J. Davis

*Directorate of Technical Airworthiness
Royal Australian Air Force*

SUMMARY: Adhesive bonded repairs have been a feature of RAAF maintenance practice since the first bonded composite patch was applied to C-130-A in May 1975. The Royal Australian Air Force has recently issued RAAF Engineering Standard C5033, on Bonded and Composite Repairs, with the design procedures for bonded repairs based largely on modeling the repair as a bonded joint. Efforts to obtain international acceptance of the fundamental elements of the Standard have been highly successful.

Analytical techniques have advanced significantly since the first practical repair, leading to a plethora of studies into a range of phenomenological issues of relevance to the performance of bonded repairs. Some of these studies have advocated that load rate effects result in significant changes to the stress-strain behaviour of adhesive systems, and have even suggested that these effects are of fundamental importance to repair design methodology. This paper will show that although the phenomena reported does indeed occur under specific conditions, its relevance to practical repair designs is limited.

KEYWORDS: adhesive bonding, bonded joint design, load rate, strain hold, strength of bonded joints, bonded repair

INTRODUCTION

Adhesive bonded joints are playing an increasing role in construction of aircraft structures. Bonded repairs are also being used in an increasing number of applications for repair of metallic structure on both defence [1 to 5] and civil aircraft [1, 6]. Australia has pioneered the use of adhesive bonded repair for metallic structures with applications of bonded repairs to cracks, reinforcements and repairs to corrosion and lightning damage on a wide range of aircraft. Of interest, the Royal Australian Air Force (RAAF) will be the only operator to fly C-130E aircraft to life of type without changing wing skins, due to the judicious use of bonded patches to repair wide-spread stress corrosion cracking. This repair alone has been estimated to have saved \$66 million (1990 value).

The RAAF is now planning the adoption of bonded repairs as a standard repair process, to be used as an alternative to conventional mechanically fastened repairs. To ensure that the technology is correctly managed, RAAF has developed RAAF Engineering Standard C5033 which provides overall control of the use of bonded repair technology. Two handbooks addressing repair design and application technology are currently in final draft form, and training courses in repair familiarisation and repair design have been established to ensure that only appropriate adhesive bonding technology is applied to RAAF assets.

The RAAF ENG STD, the design handbook and the repair design course rely on simple analytical techniques to develop repairs with a high level of structural integrity. A simple calculation is used to differentiate between those repairs which can be repaired using simple methods and those requiring a higher level analysis. The approach used relies on analytical equations applicable to bonded joints [7]. Recent published work [8] questions the validity of the analytical methods on which RAAF ENG STD C5033 is based. This paper will show that the conclusions of the previous work are not valid, and that, even if they were valid, the approach used in ENG STD C5033 has sufficient conservatism to ensure that structural integrity for repairs is maintained.

SHEAR STRESSES IN A BONDED JOINT

Adhesive shear stresses in bonded joints result from the relative displacement of the members being joined (adherends). As a joint is loaded, the adherends move apart, causing shear strains. If the adherends are very stiff and inextensible, the shear strains (and hence the shear stresses) are uniform along the length of the joint, (see Fig. 1)

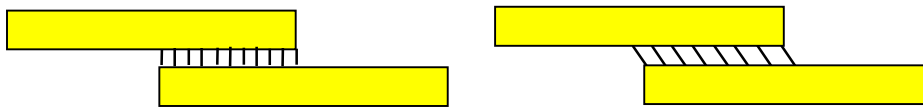


Figure 1. Shear in a bonded joint between inextensible adherends.

If such a joint is subject to increasing load, the adhesive will eventually pass its elastic limit, and plastic behaviour will occur. A typical shear stress-shear strain curve is shown in Fig. 2. This form of behaviour occurs in a Thick Adherend Test, used to characterise adhesive properties for joint design, (see ASTM D 3983-93). While this test is widely used for establishment of design values for adhesives, the stress-strain behaviour of all adhesives depends strongly on a range of factors, such as the test temperature [9]. At low temperatures, adhesives have a high shear modulus and a high shear strength, but are relatively brittle with minimal plastic behaviour. As the test temperature is increased, the shear strength and shear modulus decrease, and the plastic strain capacity increases.

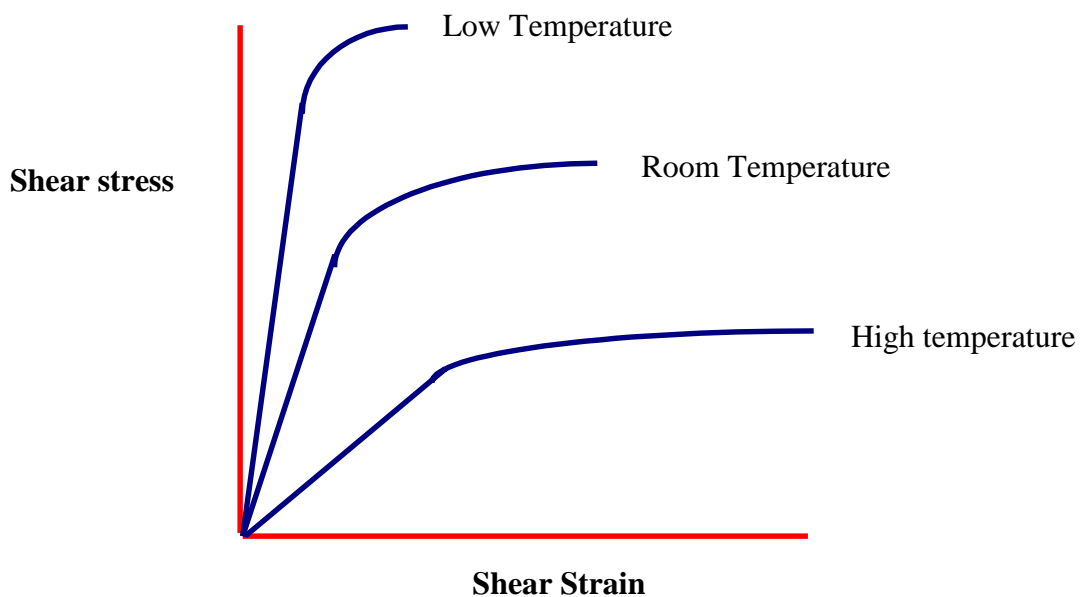


Figure 2. Typical shear stress-shear strain curve for an adhesive, showing typical effects due to test temperature.

A similar change in adhesive properties for different test loading rates has been reported [10], and the test data supplied shows that load rates *do* change the stress strain behaviour of the adhesive in the particular test specimens used in the work. This paper intends to show that it is possible to design real bonded joints such that load rate effects are irrelevant.

SHEAR STRESSES IN REAL JOINTS

For realistic joints between adherends which are extensible, the displacements due to shear are increased by the displacements due to the strains generated in the adherends themselves [7] (see Fig. 3). The resulting shear stresses and strains are non-uniform, with high stresses occurring at each end of the joint. If the overlap length is large enough, the shear stresses will decay from the maximum at the ends to zero in the middle of the joint. As the joint load is increased, the adhesive at the ends of the joint is plastically deformed, and plastic zones will form at the ends of the joint. Again, provided the overlap length is large enough, the elastic trough will still exist. If the adhesive shear strain at the end of the joint exceeds the maximum shear strain capacity of the adhesive, then the adhesive will fail.

JOINT LOAD CAPACITY

Hart-Smith gives the *potential load capacity* of an adhesive in a bonded joint as:

$$P = \sqrt{4\eta\tau_p\left(\frac{1}{2}\gamma_e + \gamma_p\right)Et} \text{ ignoring bending and thermal stress effects.} \quad (1)$$

The variable η is the adhesive thickness, γ_e is the elastic strain limit, γ_p is the plastic strain capacity of the adhesive, τ_p is the plastic stress limit for the adhesive, E is the elastic modulus of the adherends and t is the thickness of the adherend. The adhesive variables are determined by the thick adherend test as discussed before. Note that this calculation addresses the potential load capacity, because for thin adherends, it is the adherend which may limit the strength of the joint, and not the adhesive. If the adhesive has a load capacity greater than the parent material, then it will not fail.

The term $\tau_p\left(\frac{1}{2}\gamma_e + \gamma_p\right)$ is the strain energy associated with joint failure.

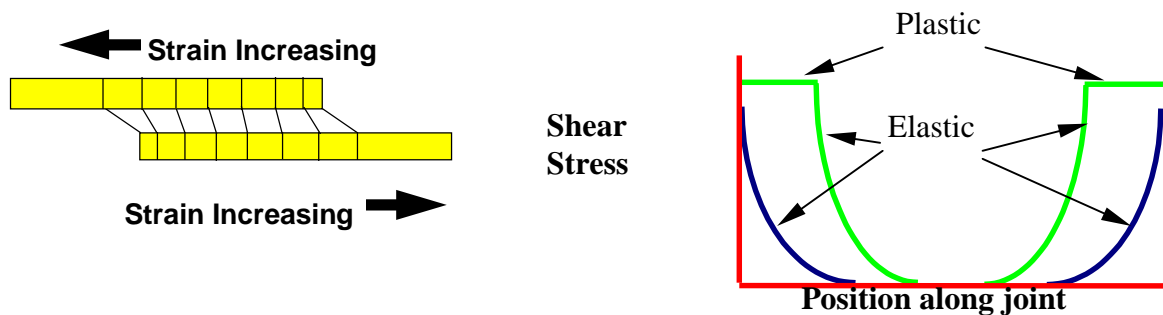


Figure 3. Shear stresses in bonded joints between thin adherends.

As described in reference [8] the adhesive properties *will* change with different load rates. However, even though it noted the influence of the strain energy term in the load capacity of an adhesive bond, the work at reference [8] did not test the specimens to failure, because to do so would have damaged the extensometer used to measure shear strain. Thus the plastic shear

strain at failure γ_p was not measured, and no conclusion could be drawn in respect of the total strain energy.

Because the changes in shear stress-shear strain behaviour are similar to the changes caused by different test temperatures, it is very probable that changes would also occur in plastic shear strain at failure. One could easily expect that a response similar to that of a change in temperature could occur for load rate effects, where changes in plastic shear limit stresses and strains would be matched by a corresponding change in ultimate plastic shear strain. Because the reference data did not measure failure shear strain, no clear conclusion can be drawn with regard to the effect on joint strength caused by load rates, and the statement that load rate independent analysis “cannot be said to be generally conservative” is not proven. While the shear stresses and strains may change with load rate effects, there is no evidence that those changes relate to the overall *load capacity* of the joint. The conclusions in [8] that the above analytical approach is unconservative would only be true if the changes in elastic limits for shear stress and shear strain τ_p and γ_e were not associated with a concurrent change in maximum strain capacity of the adhesive.

If one were to *assume* that the maximum shear strain capacity was not changed, the effect on the joint load capacity on the basis of the data points shown in reference [8] is about 5% for the worst case.

BONDED JOINT FAILURE MECHANISMS

Bonded joints may fail by a number of mechanisms. As shown above, if the adhesive shear strain at the end of the joint exceeds the maximum shear strain capacity (as determined by a thick adherend test), the failure will occur through the adhesive layer. This type of failure is termed cohesion failure. If the joint is subjected to out-of-plane tensile stresses, the joint will fail in peel. Both of these cases can be analysed using relatively simple models, [7, 11]. If the joint surface has not been adequately prepared, or if the preparation process is susceptible to in-service interfacial hydration, then the failure will occur at the interface, which is known as adhesion failure. This failure method can not be predicted, and must be stringently avoided by use of surface preparation processes which have been correctly validated, [12,13].

DESIGNING BONDED JOINTS WITHOUT LOAD RATE EFFECTS

For thin adherends (typically less than 3.8 mm (0.15 in.) for aluminium alloys) there is a fourth failure mode which is frequently overlooked in structural design. If the material being joined is thin and the overlap length is large enough to ensure generation of the complete elastic trough, the failure may be forced to occur in the adherends, and not in the adhesive, (see Fig. 4) [14]. This approach is the basis for repair design in RAAF ENG STD C5033.

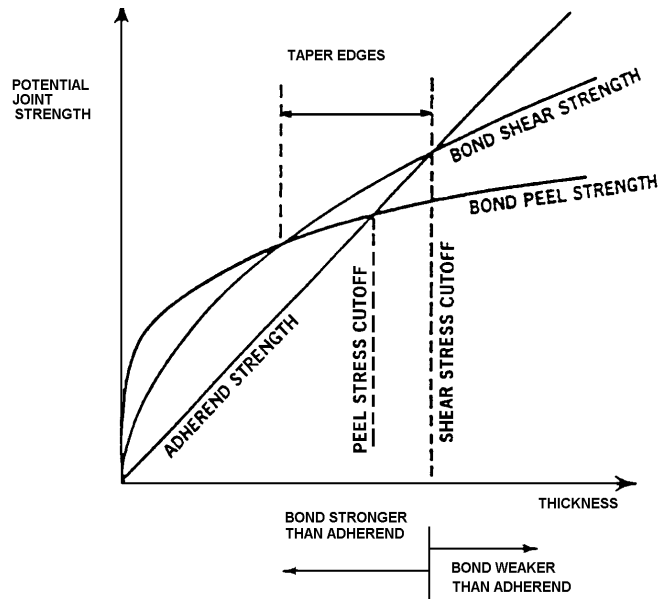


Figure 4. Potential joint strength for adhesive bonds between adherends of varying thickness (from [14]). For thin adherends, the joint strength is limited by the strength of the adherends. For these conditions, the adhesive is not the critical element, and minor variations in adhesive properties will not be relevant to the overall strength of the joint.

To achieve the required load capacity, a bonded joint must have sufficient overlap length. To guarantee that the required overlap is achieved, ENG STD C5033 calls for the plastic zone overlap length to be sufficient to carry ALL load at unnotched material ultimate strength of the parent material (see Fig. 5). The elastic zone then provides a margin of safety and also acts to minimise creep effects. A further check is made by calculation of the load capacity of the joint. If the load capacity of the adhesive is greater than the load capacity of the parent material, and the overlap length is sufficient to ensure that the elastic trough approaches zero away from the ends of the joint, then the structure will fail before the adhesive, and therefore *the adhesive will never be the critical element in the joint*. RAAF ENG STD C5033 uses a factor of 1.2 times the unnotched strength of the parent material to ensure that the adhesive is not critical. If the adhesive is never the critical element in the joint, then the minimal changes in adhesive properties due to loading rate effects are irrelevant. Similar arguments can be advanced concerning the relevance of failure theories for adhesive bonded joints.

WHERE ARE LOAD RATES IMPORTANT?

From the above discussions, it may be concluded that the strain rate effects described (in Reference [8]) are not significant in repairs and bonded joints if the adhesive is designed such that its load capacity is greater than the parent material. For typical aluminium alloys, if sufficient overlap exists, joints between adherends up to about 3.75 mm (0.15 inches) can be designed such that the adhesive is not critical. Thus, load rate effects are irrelevant to joints in most common structural bonds in aircraft. For joints where the adhesive is the critical element, load rate effects may be relevant, if testing to failure actually showed that the load capacity of the adhesive was effected.

However, there is one aspect of the work in reference [8] which is of relevance to joint analysis. The work shows that a standard loading rate may be required to minimise errors for tests to generate design data for adhesives. Once that data is generated, load rate effects may be ignored.

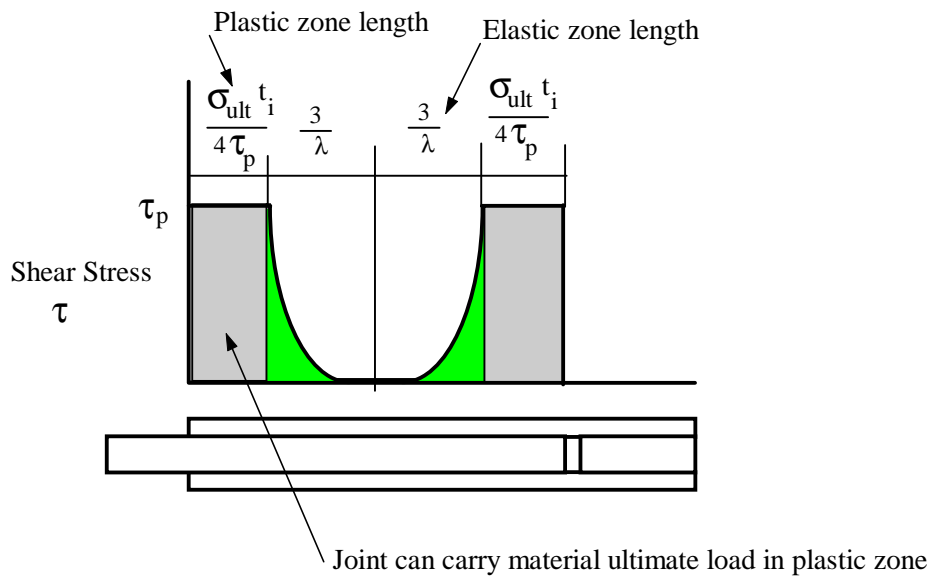


Figure 5. Methodology for determination of overlap length such that the adhesive is never critical under any load condition.

CONCLUSIONS

The assertion [8] that load rate independent analyses are unconservative has not been proven, because the test method used in the original work did not measure all relevant parameters required to ascertain the load capacity of the adhesive. While the elastic properties have been shown to change, without proper experimental procedure to measure the effects on plastic behaviour, no conclusion can be drawn. From the explanation of the differences between real bonded joints and the artificial conditions which exist in thick adherend specimens, together with the design methodology outlined for assuring that the adhesive is never the critical element in the joint, it may be concluded that loading rate effects have little relevance to bonded joint and repair designs. There may be a requirement to use a standard loading rate for tests to generate adhesive design data.

REFERENCES

1. Baker, A.A., *Bonded Composite Repair of Metallic Aircraft Components - Overview of Australian Activities*, AGARD SMP Meeting on Composite Repair of Military Aircraft structures, Seville, 3-5 Oct. 94.
2. Davis, M.J., FLTLT Kearns, K.J., and FLTLT Wilkins, M.O., *Bonded Repair to Cracking in Primary Structure: A Case Study*, PICAST2- AAC6, Melbourne 20-23 Mar 1995.
3. Druet, M., *Réparations Composites de Structures Métalliques - vingt ans d'Expérience*, AGARD SMP Meeting on Composite Repair of Military Aircraft structures, Seville, 3-5 Oct. 94.
4. Grosko, J., *Structural Modification and Repair of C-130 Wing Structure Using Bonded Composites*, AGARD SMP Meeting on Composite Repair of Military Aircraft structures, Seville, 3-5 Oct. 94.

5. Soo Yong Oh, *B/Ep Strap Repair of 25° Shoulder Longeron*, Proceedings of the Third Workshop on "Composite Repair of Metallic Aircraft Structures", Ottawa, 14-15 Sep 93.
6. Belason, E.B., *Status of Bonded Boron/Epoxy Doublers for Military and Commercial Aircraft Structures*, AGARD SMP Meeting on Composite Repair of Military Aircraft structures, Seville, 3-5 Oct. 94.
7. Hart-Smith, L.J., *Design and Analysis of Adhesive-Bonded Joints*, Air Force Conf. on Fibre Composites in Flight Vehicle Design, Dayton OH, Sep. 26-28, 1972.
8. Jones, R., Trippit, B., Chiu, W.K., and Thomas, J., *The Stress Analysis of Symmetric Lap Joints Revisited*, PICAST2- AAC6, Melbourne 20-23 Mar 1995.
9. Data sheets, FM73 adhesive, Cytec Corporation.
10. Chiu, W.K., Chalkley, P.D., and Jones, R. *Characterisation of FM73 Film Adhesive*, Proc. 5th Australian Aeronautical Conference, pp 409-414, 13-15 Sep. 1993.
11. Hart-Smith, L.J., *Designing to Minimise Peel Stresses in Adhesive Bonded Joints*, Delamination and Debonding of Materials, ASTM STP 876, W.S. Johnson, Ed., ASTM, pp 238-266, Philadelphia, 1985.
12. Davis, M.J., *A Call for Minimum Standards in Design and Application Technology for Bonded Structural Repairs*, Proc. Symp. on Composite Repair of Aircraft Structures, pp4-1, 4-15, Vancouver, Aug. 1995.
13. Davis, M.J., *The Role of Materials and Processes in Defective Aircraft Bonded Structural Repairs*, Proc. 41st SAMPE Int. Symp. and Exhib., pp 936-1950, Anaheim, 24-28 Mar. 1996.
14. Hart-Smith, L.J., *The Design of Repairable Advanced Composite Structures*, Douglas Paper 7550, presented to SAE Aerospace Tech. Conf. Long Beach CA., 14-17 Oct. 1985.

STRENGTH OF ADHESIVELY BONDED COMPOSITE TUBULAR LAP JOINTS

L. Tong, S. Alexiadis and G. P. Steven

Department of Aeronautical Engineering, University of Sydney, NSW 2006 Australia

SUMMARY: An experimental investigation is presented to show effect of the sleeve geometry and material on the strength of adhesively bonded tube-in-sleeve joints. Both mild steel and carbon fibre composite material were used to manufacture the sleeves. FM300 film adhesive was used for all specimens. The influences of the sleeve length, sleeve thickness and the gap distance between the two tubes were investigated. Test results showed that (a) specimens with long and thin sleeves seemed to have higher failure loads and to be more flexible, (b) specimens with thick sleeves tended to have lower failure loads than those with thin sleeves, and (c) specimens with composite sleeves appeared to have lower failure loads and less flexibility than those with metal sleeves.

KEYWORDS: tube-in-sleeve, adhesively bonded, static strength, stresses, finite element analysis

INTRODUCTION

Metal and composite tubes have been widely used in many industrial sectors, for example, pipelines and tension legs in the offshore oil exploitation engineering. Joining of these tubes becomes critical in the design stage for an efficient load-carrying structure. Adhesively bonding is one of the typical tubular joining configurations, and it comprises two tubes of different diameters joined by applying a thin layer of adhesive. Similar to adhesively bonded lap joints, adhesive layer is the load transfer medium between the two tubes for adhesively bonded tubular lap joints. Research works have been done for adhesive-bonded tubular joints subjected to axial loads and/or pure torques.

Lubkin and Reissner [1] investigated the distribution of stress in the adhesive lap joints between thin circular cylindrical tubes which are subjected to axially distributed loads. For these tubular joints subjected to torsional loads, Volkersen [2] gave a closed form solution for the shear stress in the adhesive layer. Alwar and Nagaraja [3] considered the adhesive as a viscoelastic material and found the stress distribution in the adhesive layer for an adhesively bonded tubular joint in tension. Shi and Cheng [4] presented an analytical analysis of adhesive-bonded cylindrical lap joints subjected to an axial load.

Adams and Peppiatt [5] analysed the stresses in adhesive bonded tubular lap joints subjected to axial and torsion loads, using axi-symmetric quadratic isoparametric finite elements. In the axial loading case, the stress concentrations arose by three mechanisms: differential straining, bending introduced by the non-co-linearity of the overlapping tubes and end effects.

Ikegami et al [6] examined the method of tapering the adhesive coupling at the boundary of the cylinder joint (fillet) as compared to a straight edge cylinder coupling at the boundary of the lap joint. Matsui [7] studied the size effects on the average ultimate shear stress of an adhesively bonded rectangular and tubular lap joint, measured by an applied ultimate load required to produce; cohesive failure in the adherends, interfacial failure, cohesive failure in the adhesive layers or adhesive failure. As well as this, the effects of geometric size and mechanical properties of both the adherend and adhesive were also considered.

Chon [8] analysed composite tubular lap joint in torsion and developed a closed form solution for the stress distribution. More comprehensive viscoelastic analyses of adhesive bonded tubular joints under torsion were given by Medri [9] and Zhou and Rao [10].

In this investigation, simple tensile tests were carried out for adhesively bonded composite tubes-in-metal sleeve joints and composite tube-in-composite sleeve joints. The ultimate failure loads and the axial extension were measured for the joints with different sleeve lengths, sleeve thicknesses and different gap distances. The effects of these geometric parameters were identified and discussed.

EXPERIMENTAL

Specimen Preparation

Figure 1 depicts a typical composite tube-in-sleeve joint which comprises two composite tubes joined together by bonding the two half sleeves. Composite tubes were manufactured by rolling up a T300/934 plain weave prepreg sheet on an appropriately chosen cylindrical mandrel, and then cured in an autoclave following the manufacturer's recommended process. Care needs to be taken to maintain an appropriate tension in the prepreg sheet in the tube rolling process. The sleeves were either made of mild steel or from the same composite plain weave. The nominal thickness of T300/934 plain weave is 0.25 mm. Four plies were carefully rolled up to form a composite tube that has a wall thickness of 1 mm. Film adhesive FM300-M was used to secondarily bond the tubes and the sleeves. The nominal thickness of the adhesive layer was 0.1 mm.

All specimens have the same inner diameter of 31 mm. The composite tubes have an identical wall thickness of 1 mm. In this study, two types of materials were selected to make the sleeves, one is mild steel, and the other is the same carbon fibre reinforced composite materials. The effects of some geometrical parameters of the sleeves were investigated by changing the following parameters: the sleeve thickness t_s and the sleeve length L as shown in Fig. 1. In addition, the gap distance was also selected as a variable in order to study its effect on the failure loads of the joints. Table 1 lists the material and geometrical parameters of the sleeves for all specimens. As given in Table 1, there are three sleeve lengths (ie 20, 25 and 30 mm), three gap distances (ie, 0, 5 and 10 mm), and two sleeve thicknesses (1 and 2 mm). There are three specimens for specimen group S30-2-0, S25-2-0, S20-2-0, S30-1-5 and S30-1-10, and there is only one specimen for the remaining specimen groups.

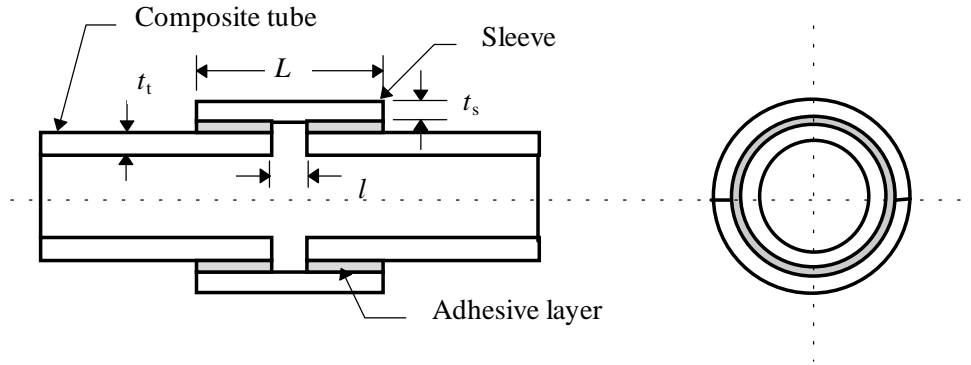


Fig. 1: A typical configuration of an adhesively bonded tube-in-sleeve joint

Table 1: Specimen geometrical parameters for adhesively bonded composite tube-in-metal/composite sleeve joints (composite tube thickness 1 mm)

Specimen group	No. of specimen	Sleeve material	Sleeve length L (mm)	Sleeve thickness t_s (mm)	Gap distance l (mm)
S30-2-0	3	Mild steel	30	2	0
S25-2-0	3	Mild steel	25	2	0
S20-2-0	3	Mild steel	20	2	0
S30-1-0	1	Mild steel	30	1	0
S25-1-0	1	Mild steel	25	1	0
S20-1-0	1	Mild steel	20	1	0
S30-1-5	3	Mild steel	30	1	5
S30-1-10	3	Mild steel	30	1	10
C30-1-0	1	Composite	30	1	0
C25-1-0	1	Composite	25	1	0
C20-1-0	1	Composite	20	1	0

The mechanical properties for a plain weave lamina are given in Table 2. The mechanical properties of FM300-M film adhesive and mild steel are given in Table 3.

Table 2: Mechanical properties for a plain weave lamina

Longitudinal and transverse modulus E_1 and E_2 (GPa)	57.23
Modulus in the through-thickness direction E_3 (GPa)	4.80
In-plane shear modulus G_{12} (GPa)	4.48
Out-of-plane shear modulus G_{13} and G_{23} (GPa)	4.4
In-plane Poisson ratio μ_{12}	0.05
Out-of-plane Poisson ratio μ_{13} and μ_{23}	0.28

Table 3: Mechanical properties for FM300-M film adhesive and mild steel

Material	FM300-M	Mild steel
Modulus E (GPa)	2.4	200
Poisson ratio μ	0.3	0.3

Test Set-up and Procedure

All composite tube-in-sleeve joints were loaded in axial tension on an Instron machine. To ensure that premature failure doesn't occur outside the tube-in-sleeve zone, end reinforcements were designed to hold the composite tube and to apply axial loads. This was achieved by first bonding metal sleeves at the end of the composite tube and then drilling a pin-load hole through both metal sleeves and the composite tube. All specimens were tested at a room temperature by applying an axial displacement or extension at a constant rate of 0.2 mm per minute. The applied displacements and the axial forces were recorded for all specimens.

Results and Discussions

Figures 2, 3 and 4 depict the typical graphs of the applied axial forces versus the axial extensions for specimen S20-1-0, S30-1-5 and C25-1-0 respectively. As shown in Figs 2 and 4, at the initial loading stage the load and extension graphs exhibit a nonlinear behaviour, and then the applied load increases almost linearly with the axial extension until a dramatically load drop occurred. This load drop was accompanied by a big bang that represented the ultimate failure of the joint specimens. For specimen group S30-1-5, prior to the final fracture of the joint, there exists a nonlinear variation segment in which the applied load oscillated at a very small amplitude. In fact, some specimens experienced a few noticeable load drops before the tube-in-sleeve joints completely lost its load transferring capacity.

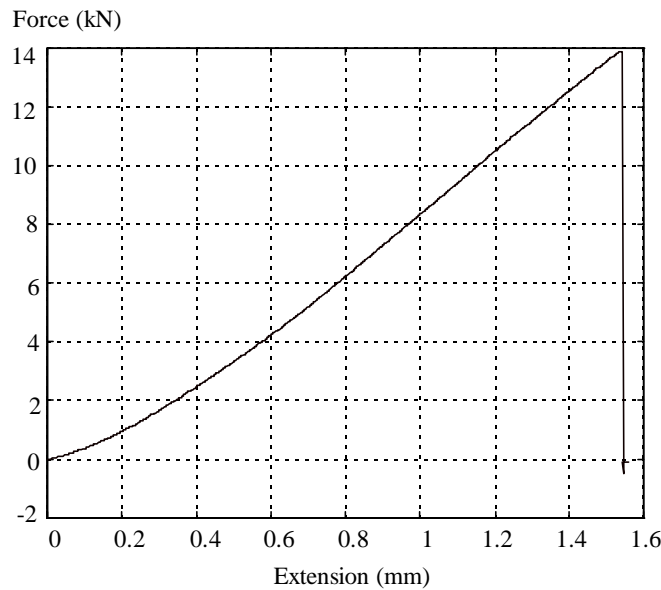


Fig. 2: Axially applied tensile force vs the axial extension for specimen S20-1-0

Careful Inspection revealed that there existed two typical failure surfaces. For the first case, adhesive was seen on the outer surfaces of the composite tubes and on the inner surfaces of the sleeves, which indicates adhesive failure. For the second case, some fibres were noticed on the inner surfaces of the metal sleeves, and this observation may suggest a delamination failure in the composite tubes. It should be pointed out that for most specimens both failure surfaces were observed at different locations for a single specimen because of the nonuniform thickness of the adhesive layer. It was noted that adhesive failure tends to take place in an area close to the joining lines of the two half sleeves where the adhesive layer was noticed to be very thin. The contributing factors may include: geometric difference between the tube and sleeves due to manufacturing tolerances, difference in the coefficients of thermal expansion between the metal and the composite material used.

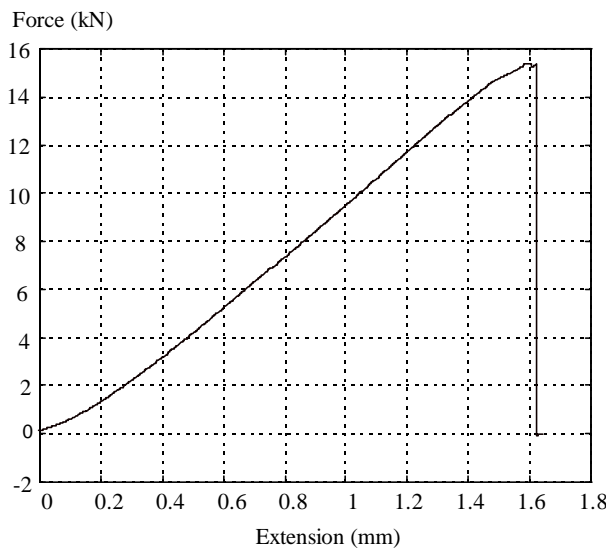


Fig. 3: Axially applied tensile force vs the axial extension for specimen S30-1-5

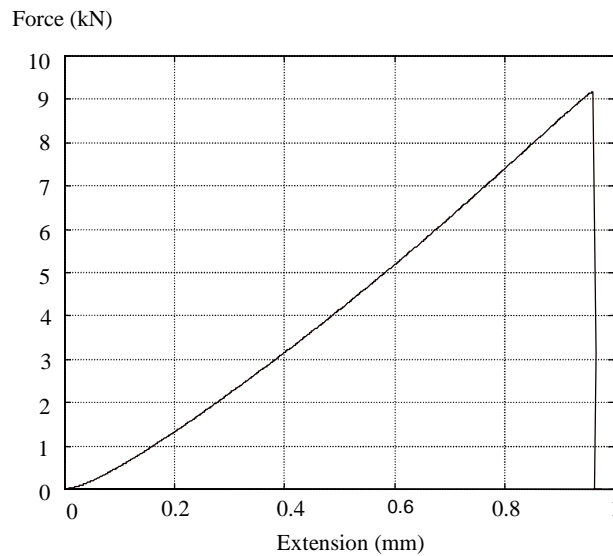


Fig. 4: Axially applied tensile force vs the axial extension for specimen C25-1-0

Table 4 summarises the failure loads and the failure extensions for all specimens. The standard deviations for these specimen groups with 3 specimens are also listed in Table 4 to indicate the range of the failure loads. For these specimens which have the same sleeve thickness and no gap between the two composite tubes, both the failure loads and the failure extensions become larger as the sleeve length increases from 20 mm to 30 mm. This indicates that when the sleeve length is the only varying parameter in the range of 20 mm and 30 mm, the joints with long sleeves fail at higher load and become more flexible. Figure 5 plots the measured failure loads versus the sleeve overlap length to sleeve thickness ratio $L/2t_s$. These curves present the same trends as that predicted by Lubkin and Reissner [1], namely, as the ratio $L/2t_s$ increases the failure loads increase. However, it is noted that Lubkin and Reissner [1] predicted a plateau after the ratio $L/2t_s$ becomes large enough for adhesive bonded tubular lap joints. Further test results need to be obtained to validate this predicted relationship between the failure load and the sleeve overlap length to thickness ratio. It is believed that the failure of the tube-in-sleeves joints transits from a peel dominated failure to a shear dominated failure when the ratio $L/2t_s$ increases. When the ratio $L/2t_s$ is low, increase in its value can reduce the peel stress in the adhesive layer and thus leads to the rising failure loads.

Table 4: Failure loads (kN) and extensions (mm) for the bonded composite tube-in-metal/composite sleeve joints

Specimen group	Failure load	Failure elongation
S30-2-0	7.33±0.359	1.40±0.262
S25-2-0	4.75±0.030	0.75±0.126
S20-2-0	2.60±0.747	0.49±0.061
S30-1-0	25.21	3.11
S25-1-0	21.08	1.88
S20-1-0	13.91	1.54
S30-1-5	16.86±1.779	1.76±0.191
S30-1-10	20.38±6.67	1.98±0.561
C30-1-0	16.77*	2.45
C25-1-0	9.19	0.96
C20-1-0	6.84	0.79

* Premature failure at one end reinforcement

For these specimens only having different sleeve thickness, the specimens with a sleeve thickness of 1 mm tend to have much higher average failure loads and larger average extensions than those with a sleeve thickness of 2 mm, for example, specimen S30-1-0 has an average failure load of 25.21 kN which is much larger than the average failure load 7.33 kN for specimen S30-2-0.

By comparing the average failure loads and extensions for specimen S30-1-0, S30-1-5, and S30-1-10, it is noted that specimen S30-1-0 tends to be the strongest one while specimen S30-1-5 tends to be the weakest one. Increasing the gap distance from 5 mm to 10 mm does increase the failure loads slightly. However, a relative large standard deviation was noted for specimen S30-1-10 which indicates a large scatter in the failure loads.

Another interesting result worth noting is that those joints having composite sleeves tend to fail at lower failure loads and less extensions than those having metal sleeves. By comparing the material properties for the mild steel and the composite materials listed in Tables 2 and 3, it is found that the mild steel has a much higher modulus, and thus a larger membrane and bending stiffness, than the plain weave composite material. Preliminary numerical results indicate that metal sleeves produce negative peel stress in the adhesive layer when subjected to a tensile load. Another contributing factor can be the residual stress that was created during the curing process due to the difference in the coefficient of thermal expansion between the metal and composite material for these joints with metal sleeves.

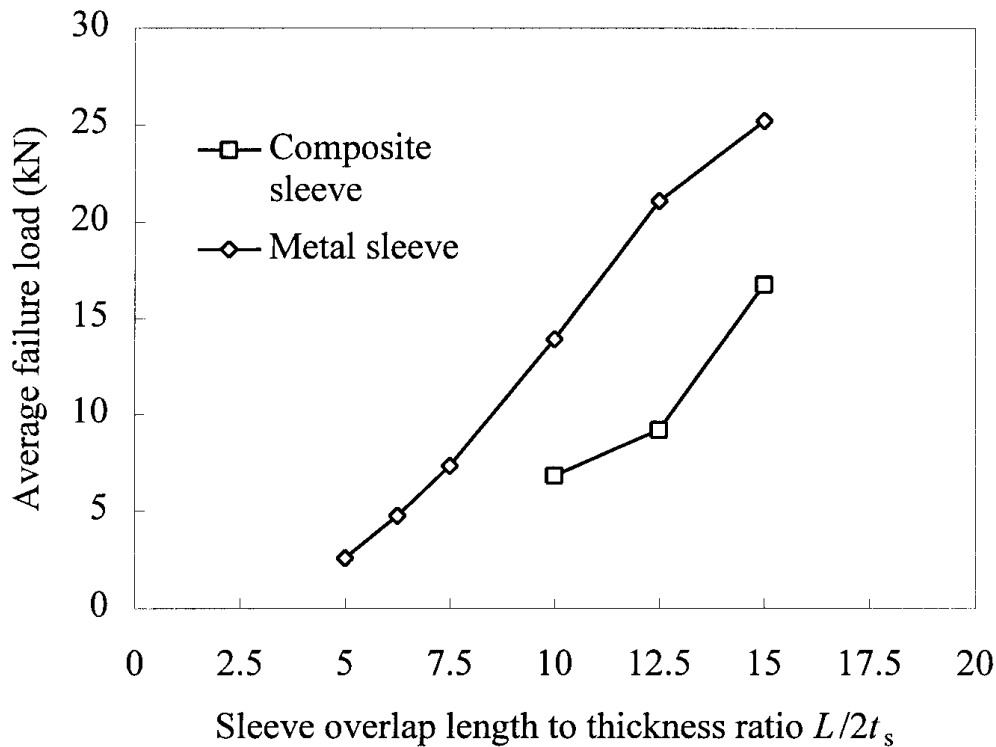


Fig. 5: Measured failure loads versus the sleeve overlap length to thickness ratio $L/2t_s$.

CONCLUSIONS

An experimental investigation was carried out to study the effects of the sleeve geometry and material on the strength of adhesively bonded tube-in-sleeve joints. Two types of materials were used to make the sleeves: mild steel and carbon fibre composite mater. FM300 film adhesive was used to adhesively bonded the tubes and the sleeves for all specimens. It was shown that the composite tube-in-metal sleeves joints with long and thin sleeves tend to have higher failure loads and to be more flexible than those with short and thick sleeves. The composite tube-in-composite sleeves joints appeared to have lower failure loads and less axial flexibility than the composite tube-in-metal sleeves joints. Increasing the gap distance from 5 to 10 mm between the composite tubes seemed to yield an increase in both failure loads and axial extensions.

REFERENCES

1. Lubkin, J. L. And Reissner, E., "Stress distribution and design data for adhesive lap joints between circular tubes", *Trans. ASME*, Vol. 78, 1956, pp 1213-1221
2. Volkersen, O., "Recherches sur la Theorie des Assemblages Colles", *Construction Metallique*, Vol. 4, 1965, pp 3-13
3. Alwar, R.S. and Nagaraja, Y. R., "Viscoelastic analysis of an adhesive tubular joints", *J. Adhesion*, Vol. 8, 1976, pp 79-92
4. Shi, Y.P. and Cheng, S., "Analysis of Adhesive-Bonded Cylindrical Lap Joints Subjected to Axial Load", *ASCE J. Engineering Mechanics*, Vol. 119, No. 3, 1993, pp 584-602
5. Adams, A.D. and Peppiatt, N.A., "Stress Analysis of Adhesive Bonded Tubular Lap Joints", *J. Adhesions*, Vol. 9, No. 1, 1977, pp. 1-18
6. Ikegami, K., Sugibayashi, T. and Matsui, K., "Strength of Cylinder Joint Adhesively Bonded by Coupling", *Archive of Applied Mechanics*, Vol. 65, 1995, pp 44-53
7. Matsui, K., "Size-Effects on Average Ultimate Shear Stresses of Adhesive-Bonded Rectangular or Tubular Lap Joints Under Tension-Shear", *J. Adhesion*, Vol. 10, No. 2, 1990, pp. 81-89
8. Chon, C.T., "Analysis of tubular joint in torsion", *J. Composite Materials*, Vol. 16, 1982, pp. 268-284
9. Medri, G., "Viscoelastic analysis of adhesive bonded lap joints between tubes under torsion", *J. Vibr. Acoust. Stress Reliability Des.* Vol. 110, 1988, pp. 384-388
10. Zhou, M. and Rao, M. D., "Viscoelastic analysis of bonded tubular joints under torsion", *Int. J. Solids Structures*, Vol. 30, 1993, pp. 2199-2211

EXPERIMENTAL CHARACTERIZATION OF REINFORCING EFFECTS OF FRP SHEETS BONDED ON MORTAR AND CONCRETE BEAMS

Isao Kimpara¹, Kazuro Kageyama¹, Toshio Suzuki¹, Isamu Ohsawa¹,
Koji Yamaguchi²

¹ *Department of Naval Architecture and Ocean Engineering,
Graduate School of Engineering, The University of Tokyo*

² *Division of Engineering, Graduate School, The University of Tokyo, 7-3-1 Hongo,
Bunkyo-ku, Tokyo 113, Japan*

SUMMARY: Much attention has recently been paid in recent years to rehabilitation such as repair and preservation of infrastructure using fiber reinforced plastics (FRP) sheets. This study is aimed at establishing some theoretical basis and guidelines for such applications by examining the failure process and the increased fracture toughness of mortar and concrete beams reinforced with carbon and glass fiber reinforced plastic (CFRP, GFRP) sheets. Two kinds of beam specimens with and without a center notch were prepared and subjected to three-point flexure: large specimen of concrete reinforced with GFRP or CFRP sheets and small specimen of mortar reinforced with GFRP sheets. The failure process as well as load, strain and crack opening displacement behavior were monitored by acoustic emission (AE) activity. The relation between reinforcing effect and fracture toughness at the initiation of AE activity is discussed based on these results.

KEYWORDS: rehabilitation of infrastructure, GFRP sheets, CFRP sheets, reinforcing effects, mortar and concrete beams, failure process, fracture toughness, acoustic emission

INTRODUCTION

Infrastructure might be damaged by earthquake, fatigue, overload or severe and long term environmental attacks during service. So rehabilitation of infrastructure is an obviously necessity. Bonding thin steel plates to critical areas of concrete subjected to tensile loading has been shown to be an effective strengthening method [1]. Over the past decade, high strength, light weight fiber reinforced plastics (FRP), primarily developed for aerospace and other industrial applications, have been successfully used in concrete structural members [2-4].

The bonding of thin FRP laminates exhibits an effective strengthening in tension in the critical tensile zone of concrete structures. The advantage of this system is much more easiness of application in service than the bonding of steel plates. Widespread use of carbon fiber sheets has already been observed in Japan with hundreds of field applications that include repairs of bridge beams, retaining walls, utility poles, slabs, chimneys, tunnels and other structures requiring strengthening, stabilization or seismic upgrade. Several reinforcing systems with carbon fibers have already been developed and evaluated by the research association of "CCA (Carbonfiber for Civil Application)", "CF Renaissance" and "CRS" (Carbonfiber Retrofitting System) in

Japan. In the present paper, the focus is on the experimental characterization of reinforcing effects of FRP sheets externally bonded to the bottom tensile zone of mortar and concrete specimens in terms of failure process and increased fracture toughness.

EXPERIMENTAL PROCEDURE

Large Concrete Specimen

The reinforcing material "FORCA Tow sheet" as shown in Fig. 1 was utilized and the bonding of glass-fiber or carbon-fiber Tow sheets to the concrete was similar to the actual spot process [6] as described in Fig. 2, where epoxy resin is used as primer for excellent bonding characteristics. Two kinds of specimens of concrete with and without center notch were prepared for the experiment. The size of the specimen was 18kg in weight, 710mm in length, 150mm in height and 75 mm in width as shown in Fig. 3, which was based on the test method of RILEM [5]. Figure 4 shows the experimental set up for three-point-flexure with a specimen and six acoustic emission (AE) transducers for moment tensor analysis [7] and two for conventional AE measurement. AE measurement was detected by 150kHz resonant-type piezo-electric transducers (PAC, R-15), stuck at suitable locations of the specimen. MISTRAS 2001 system of Physical Acoustic Corporation was utilized as AE measurement.

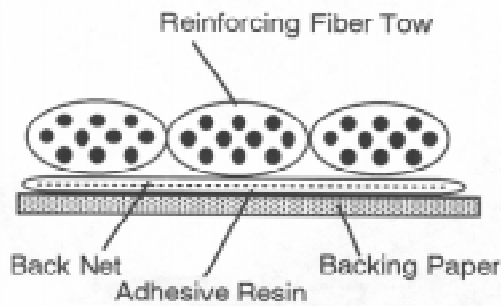


Fig.1: Cross-section of "FORCA Tow sheet".

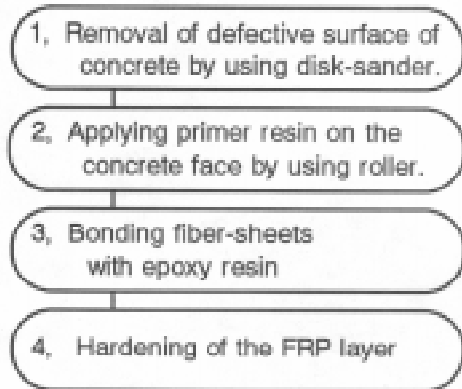


Fig. 2 : Process work of bonding of fiber- sheets on the concrete.

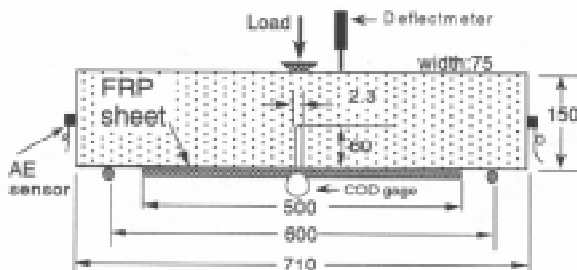


Fig. 3 : Details of large concrete specimen with center notch.

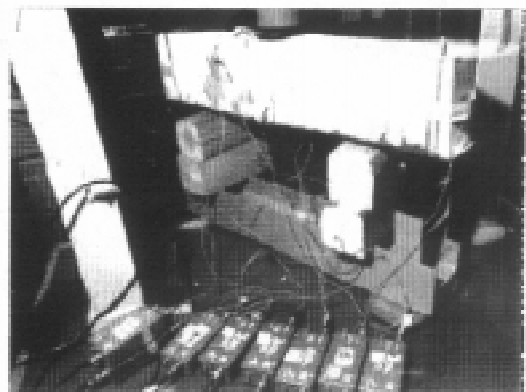


Fig. 4 : Experimental setup of three-point-flexure test and AE transducers for large concrete specimen.

Small Mortar Specimen

Figure 5 shows the size of the small specimen of mortar, which was based on the test method of JSME S 001 for fracture toughness; the specimen weighted 450 grams and included sand of maximum diameter 2.5mm. These small specimens were used for examining the effect of delamination between FRP layer and mortar by means of AE source location. Figure 6 shows experimental set up of three-point-flexure test of the small specimen. Conventional vinyl-ester resin was used for bonding fiber sheets without using primer resin and a 80 mm length plastic film was inserted between mortar and GFRP layer as pre-delamination.

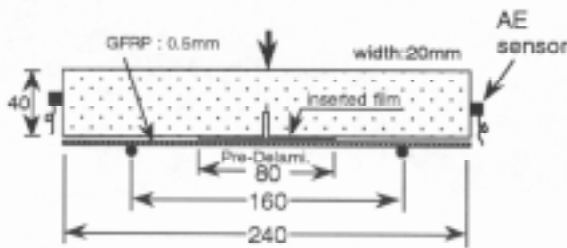


Fig. 5 : Details of small mortar specimen with center notch.

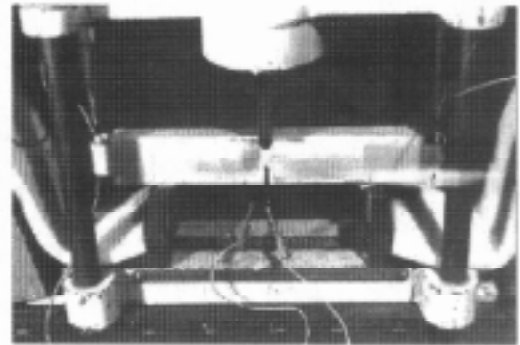


Fig. 6 : Experimental setup of three-point-flexure test and AE transducers for small mortar specimen.

RESULTS AND DISCUSSIONS

Large Concrete Specimen without a Center Notch

Figure 7 shows the relation between load versus deflection curves of concrete specimen without center notch. There was no appreciable difference in the initial stiffness, which means the slope does not depend on the type of reinforcement up to 0.5 mm deflection. The experimental result, however, indicated that the theory of composite beam can be applied. There was no appreciable difference also at the initiation of non-linearity and the initiation point did not depend on the

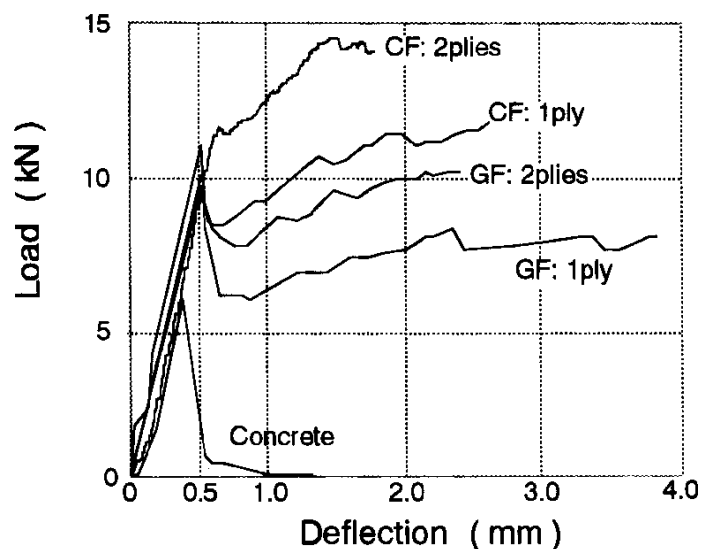


Fig. 7 : Relation between load vs. deflection curves of concrete specimen without center notch.

type of the reinforcement. The non-linear point, naturally, was higher than for the non-reinforced specimen and was defined as the initial failure point. The initial failure point can be estimated by applying the theory of composite beam expressed by Eqn. 1, using 4.6MPa as the flexural strength of concrete without reinforcement.

$$P_{init.} = \frac{4\sigma_c \sum (E_i I_i)}{\ell E_c I_c} \quad (1)$$

After the initial failure point, the difference in the load-deflection behavior evidently shows the dependence on the reinforcement. At the final failure, the reinforcement FRP layer did not show any sign of damage, and shear failure occurred in the concrete close to the reinforcement layer as shown in Fig. 8 . By assuming that the tensile failure of the FRP layer and compressive failure of the concrete occur at the same time, the final failure load can be calculated. Figure 9

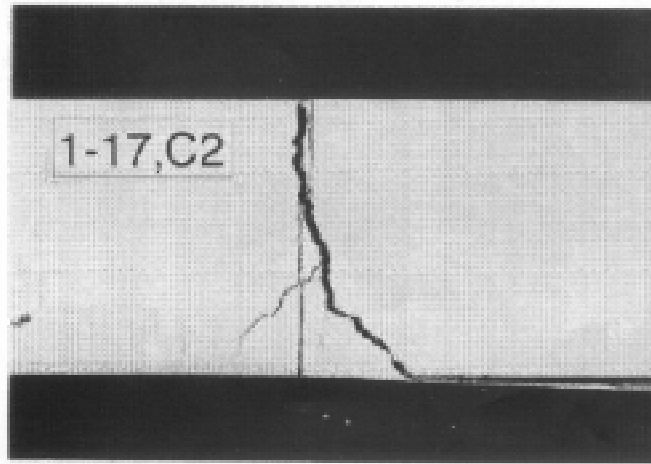


Fig 8: Typical failure mode including interfacial delamination of concrete specimen without center notch reinforced with carbonfiber sheet of two plies.

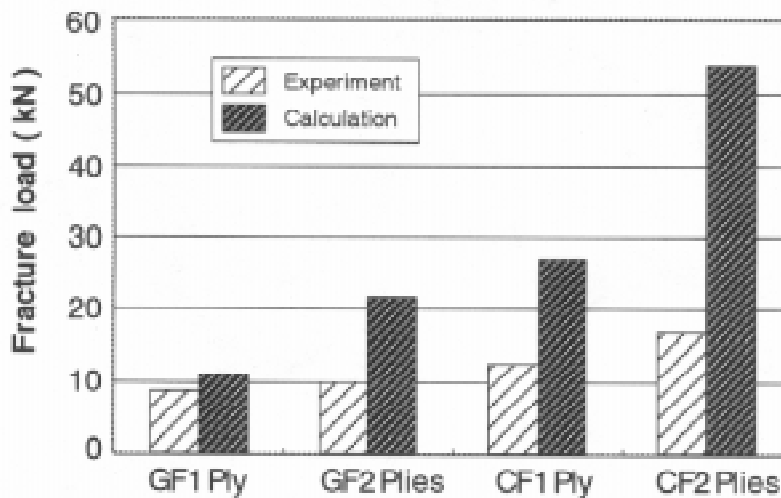


Fig 9 : Comparison of experimental and calculated final failure load for concrete specimen without center notch.

shows the comparison between experimental and calculated data. The result shows that experimental failure strength does not increase appreciably. This is because of the difference in the failure mode at final failure.

Large Concrete Specimen with a Center Notch

Figure 10 shows the typical failure mode of a reinforced specimen. Crack ① initiates and propagates vertically from the tip of the notch at first. Next, 45-degree cracks ② occur from the bottom to the center of the specimen. Finally, crack ③ at the bottom of the specimen extend from initiation point of the 45-degree crack to the direction of support of the flexural jig. The interface of the bottom crack was in the concrete and not between concrete and reinforcement

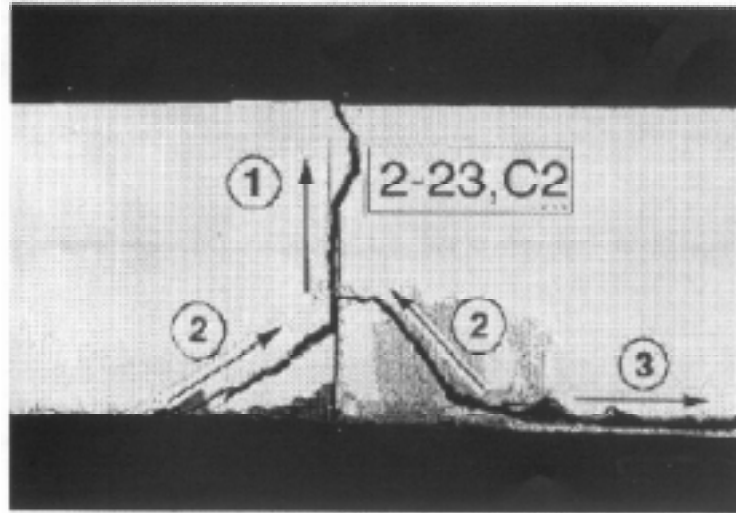


Fig. 10: Typical failure mode including notch extension, 45-degree crack and interfacial delamination of center notched concrete specimen reinforced with carbonfiber sheet of two plies.

layer, which verified the excellent bonding. Figure 11 shows the relation between load and crack opening displacement (COD). After 45-degree cracks are formed, measurement of COD became irrelevant, therefore only initial stage of the curves is displayed. To evaluate the critical load, the 5% offset procedure by the RELEM test method and the method for metallic material were used. However, stable values could not be obtained, therefore the AE technique was applied. When acoustic emissions initiated, the corresponding load was defined as " P_{AE} " as shown in Fig. 12. By using finite element analysis based on the condition of two dimensional plane strain and assuming perfect bonding of the interface between concrete and reinforcement layer, the stress intensity factor "K-value" of the notch tip was calculated based on the crack extension method by using P_{AE} as shown in Table 1. The mesh division of the FEM analysis is shown in Fig. 13. Most of the K_{IC} values were about $0.5 \text{ MPa m}^{1/2}$, and the difference in value was small compared to the non-reinforced specimen. Therefore the results showed that crack initiation does not depend on the reinforcement. That is to say, the crack initiation depends on the fracture toughness of concrete itself. Thus it was verified that the AE technique detects crack initiation effectively.

In the case of reinforced specimen without center notch, the FRP layer is expected to have reinforcing action. On the other hand, for specimens with center notch the FRP layer is expected to have a repair action. Figure 14 shows relation of maximum failure load for specimens without center notch and specimens with a center notch. The result indicated that is good corre-

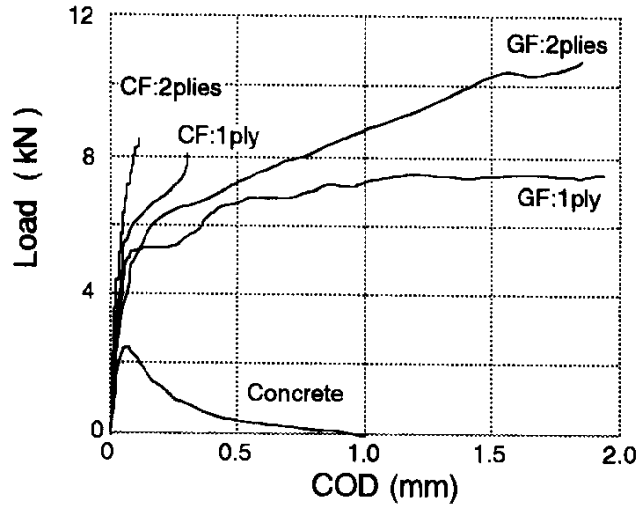


Fig. 11 : Relation between load vs. COD curves of reinforced concrete specimen with center notch.

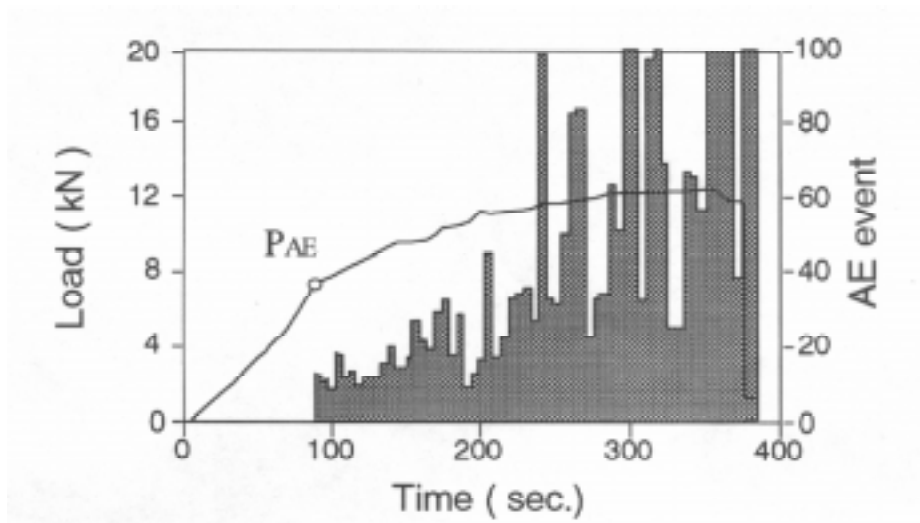


Fig. 12 : Typical diagram of load , AE hits activity vs. time of concrete specimen with center notch.

Table 1 : Comparison of experimental P_{AE} and stress intensity factor K_{IC} calculated by FEM.

	GF: 1ply	GF: 2plies	CF: 1ply	CF: 2plies	Concrete
P_{AE} (N)	3860	6260	6220	8090	2350
K_{IC} (MPa $m^{1/2}$)	0.424	0.561	0.499	0.518	0.595



Fig. 13 : Mesh division of the FEM analysis for the specimen.

lation between the reinforcing effect and the repairing effect.

For specimens with a center notch reinforced by FRP layer, K_{IC} is defined as inherent fracture toughness of concrete alone, K_{IM} is defined as the apparent fracture toughness of the reinforced specimen, and K_{IP} is the apparently increases in fracture toughness induced by the reinforcement. So the relation between K_{IC} , K_{IM} and K_{IP} can be expressed as Eqn.2. The effect of reinforcing " K_{IP}/K_{IC} " was calculated as shown in Table 2. The results indicate that the effect of reinforcement improves according to the increase in stiffness of the reinforcement.

$$K_{IC} = K_{IM} - K_{IP} \quad (2)$$

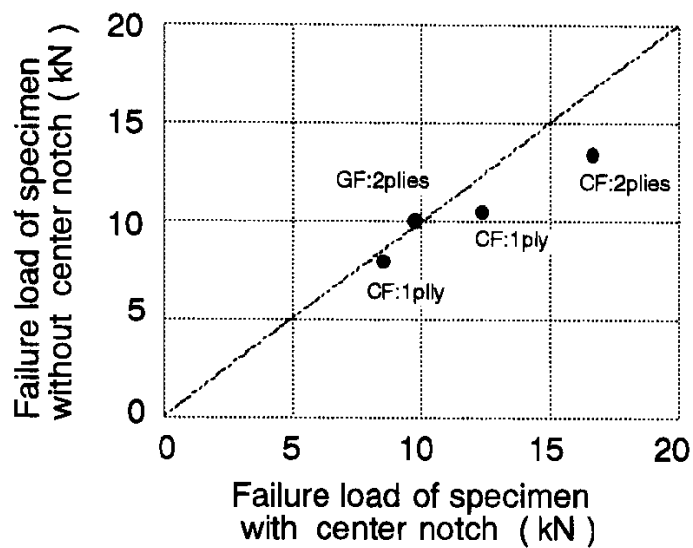


Fig. 14 : Relation of maximum failure load between specimen without center notch versus specimen with a center notch.

Table 2 : Reinforcing effect " K_{IP}/K_{IC} ".

	GF: 1ply	GF: 2plies	CF: 1ply	CF: 2plies
K_{IP}/K_{IC}	1.30	1.82	2.15	2.95

To classify crack type and to determine crack orientation in the concrete specimen, the moment tensor analysis is an effective method [7], which is a quantitative AE waveform analysis based on the moment tensor modeling of cracks. This analysis was applied here. Computer programs called MI-TRA and SIGMA were used to analyze the sets of AE waveforms recorded during the test. The results are plotted in Fig. 15 a,b. Orientations of tensile crack are shown by arrows, and shear cracks are given by crosses. One of the two orientations of the crosses corresponds to the direction of shear crack motion. Although composition of the concrete is non-homogeneous as shown in Fig. 16, the result of the analysis are apparently in good accordance with the failure mode. The arrows (tensile) mainly exist near the tip of the center notch, and the crosses (shear) exist in the lower part of the specimen.

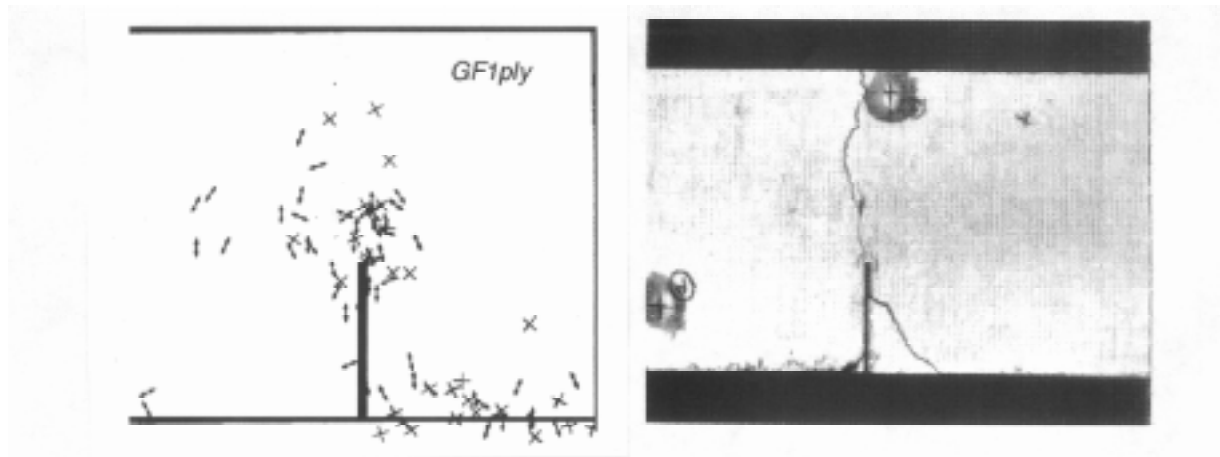


Fig. 15a : Crack type and orientation in the glassfiber 1-ply reinforced concrete specimen analyzed by the moment tensor method (left) and the failed specimen (right).

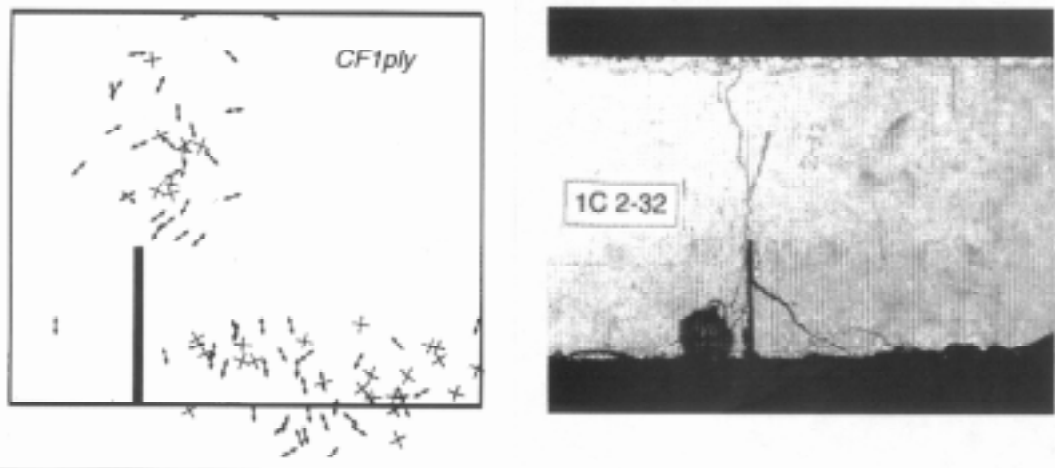


Fig. 15b Crack type and orientation in the carbonfiber 1-ply reinforced concrete specimen analyzed by the moment tensor method (left) and the failed specimen (right).

Small Mortar Specimen with a Center Notch

The small specimen of mortar was used to characterize a delamination failure process using the Acoustic Emission technique. Since primer resin was not used for bonding of FRP layer, the interfacial strength was lower compared to that of the large concrete specimen. Therefore delamination at the interface occurred easily. Figure 17(a)(b) shows the time history of AE hits and applied flexural load. The first AE peak “regions ① to ②” corresponds to extension of the center notch. The second AE peak “regions ③ to ④” corresponds to extension of interfacial delamination between the two supports of the flexural jig. After the second peak of AE activity, the activity decreased, which means that the interface between the sup-

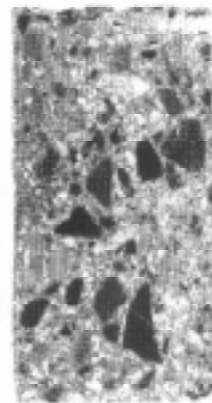


Fig. 16 Non-homogeneous cross section of a concrete specimen.

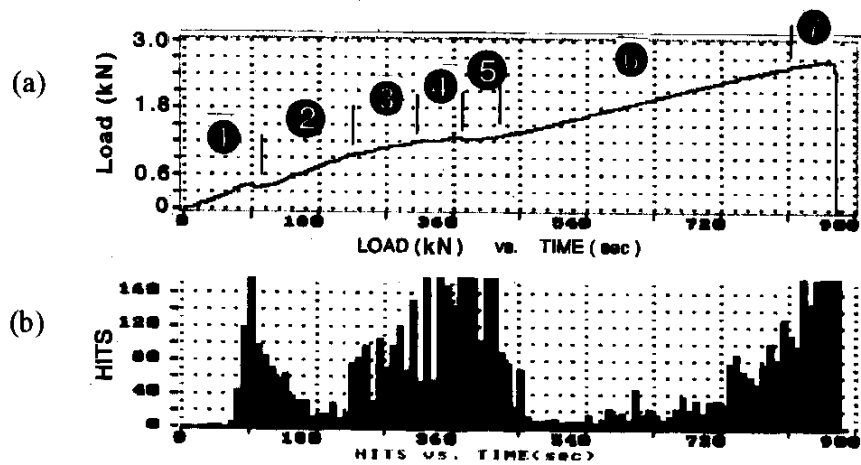


Fig. 17 Diagram of load (a), AE activity (b) vs. time for center-notched reinforced mortar specimen.

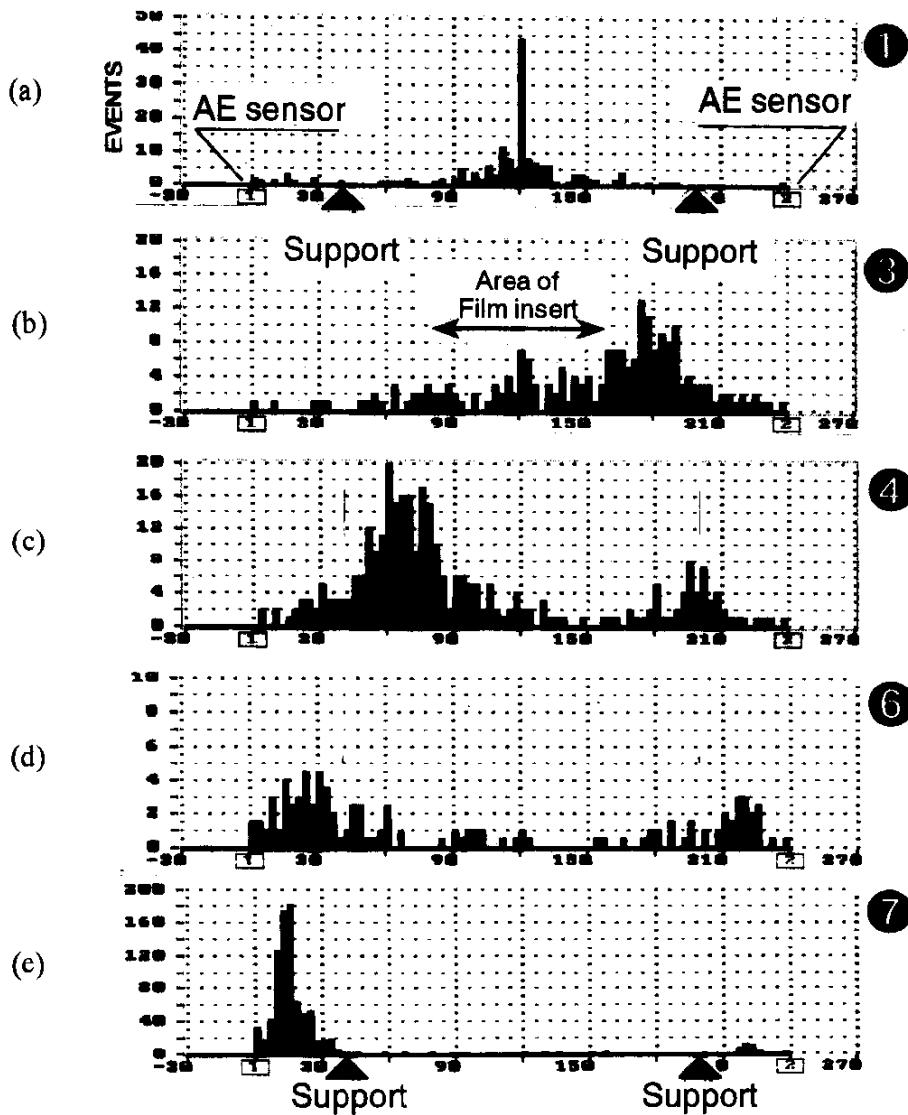


Fig. 18 : Change of AE source location by one-dimensional, two-sensor measuring method for center-notched reinforced mortar specimen.

ports had delaminated completely. The final AE peak "region ●" corresponds to extension of delamination at the interface of the overhang of the specimen. Figure 18 (a) (b)(c)(d)(e) indicates the AE source location on the specimen. By extracting the events and analyzing them at the AE source locations for specific period, the crack extension at the center notch and even the extension of interfacial delamination could be detected effectively.

CONCLUSIONS

The failure process and reinforcing effects of concrete and mortar specimens strengthened externally by bonding FRP sheets to the bottom tensile zone were characterized experimentally. The experimental results indicated that the reinforcing effects by FRP sheets improved with the increase in stiffness of the reinforcement. It was verified that AE technique detects crack initiation, source location and can be used to classify crack type and orientation effectively.

ACKNOWLEDGEMENT

The authors wish to acknowledge the partial support of Ministry of Education, Science and Culture of Japan under the Grant-in-Aid for Fundamental Scientific Research (A 07555316) and the CCA (Carbonfiber for Civil Application) Association. The authors are also grateful to Shimizu Corporation, the Chichibu Onoda Cement Corporation and the Tonen Corporation for providing the specimens and the reinforcing materials, and the Japan Physical Acoustic Corporation for the AE moment tensor analysis.

REFERENCES

1. R. Jones, R. N. Swamy and A. Charif, *Structural Engineer*, (London), 1988, 66(5), pp.85-94.
2. U.Meier and H.Kaiser," Strengthening of structures with CFRP laminates", *Proc. ASCE Specialty Conference on Advanced Composites Materials in Civil Engineering Structures*, ASCE, NY, 1991, pp.224-232.
3. M. A. Shahawy, M. Arockiasmy, T. Beitelman and R. Sowrirajan, "Reinforced concrete rectangular beams strengthened with CFRP laminates", *Composite: Part B* 27B(1996)pp.225-233.
4. K. Kageyama, I. Kimpara and K. Esaki," Fracture mechanics study on rehabilitation of damaged infrastructures by using composite wraps", *Proc.10th Intern. Conf. on Composite Materials (ICCM-10)* Whistler, B.C., Canada, Aug. 1995, pp.III-597-604.
5. S.P.Shah and A. Carpinteri,"Fracture Mechanics Test Method for Concrete", *RILEM Committee89-FMT(International Union of Testing and Research Laboratories for Materials and Structures)*, CHAPMAN AND HALL.
6. Tonen Corp." Process work of repair and reinforcement for concrete by using Tow-sheets" 1995.
7. S. Yuyama, T.Okamoto, M. Shigeishi and M.Ohtu, "Acoustic emission generated in corners of reinforced concrete rigid frame under cyclic loading",*Materials Evaluation*, Vol.53, No.3, pp.409-412, 1994.

PREDICTION OF TENSILE FATIGUE LIFE FOR GFRP ADHESIVE JOINT

Yasushi Miyano¹, Stephen W. Tsai², Masayuki Nakada¹, Sangwook Sihm² and Tomoya Imai¹

¹ *Materials System Research Laboratory, Kanazawa Institute of Technology, Ohgigaoka Nonoichi, Ishikawa 921, Japan*

² *Department of Aeronautics & Astronautics, Stanford University, Stanford, California 94305-4035, U.S.A.*

SUMMARY : A prediction method of fatigue failure load of GFRP adhesive joint under arbitrary frequency, load ratio and temperature was proposed. The method is based upon the four hypotheses, (A) same failure mechanism for static, creep and fatigue failure, (B) same time-temperature superposition principle for all failure load, (C) the linear cumulative damage law for monotone loading and (D) linear dependence of fatigue failure load upon load ratio. Tensile tests of GFRP adhesive joint for static, creep and fatigue loadings were conducted for various temperatures. The test results indicated the validity of the proposed method and the applicability of the hypotheses for GFRP adhesive joint.

KEYWORDS: GFRP, joint, static strength, creep strength, fatigue strength, time-temperature superposition principle

INTRODUCTION

It is well known that the mechanical behavior of polymer resins exhibits time and temperature dependence, called viscoelastic behavior, not only above the glass transition temperature T_g but also below T_g . Thus, it can be presumed that the mechanical behavior of polymer composites also significantly depends on time and temperature. It has been confirmed that the viscoelastic behavior of polymer resins as matrices is a major influence on the time and temperature dependence of the mechanical behavior of FRP [1-8].

In previous papers, we proposed a prediction method for the fatigue strength of polymer composites for an arbitrary frequency, stress ratio and temperature from the data measured by static tests at several constant loading-rates and various temperatures, and fatigue tests at a single frequency and various temperatures. The validity of this method was proven for the cases of the flexural behavior of satin-woven CFRP laminates and the tensile behavior of conical shaped GFRP joint using a bonding resin [9, 10].

In this paper, the validity of the prediction method is discussed for the case of the tensile behavior of GFRP adhesive joint.

PREDICTION PROCEDURE

We proposed a prediction method for fatigue failure load of composite structures for an arbitrary frequency, load ratio and temperature from the data measured by static tests at several constant loading-rates and various temperatures, and fatigue tests at a single frequency and various temperatures. The method rests on the four hypotheses, (A) same failure mechanism for static, creep and fatigue failure, (B) same time-temperature superposition principle for all

failure loads, (C) linear cumulative damage law for monotone loading and (D) linear dependence of fatigue failure load upon load ratio.

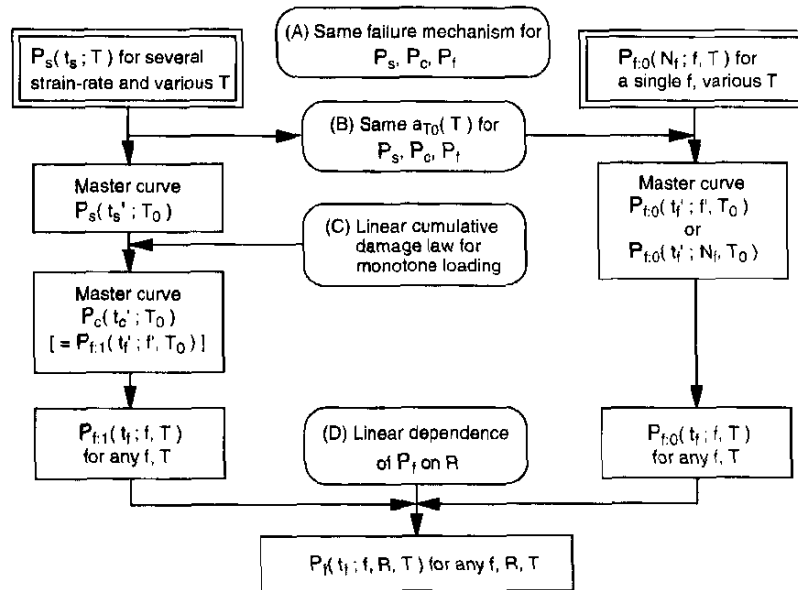
When these hypotheses are met, the fatigue failure load for an arbitrary combination of frequency, load ratio and temperature can be determined based on the following test results: (a) master curve of static failure load and (b) master curve of fatigue failure load for load ratio of zero. The master curve of static failure load is constructed from the test results at several constant loading-rates for various temperatures. On the other hand, the master curve of fatigue failure load for zero load ratio can be constructed from tests at a single frequency for various temperatures using the time-temperature superposition principle for the static failure load.

The outline of this method is shown schematically in Fig.1 together with definitions of some notations. The detail of the method will be presented with experimental results.

EXPERIMENTAL PROCEDURE

Preparation of FRP Joint

The GFRP adhesive joint (FRP joint) was made from a GFRP pipe, ductile cast iron rod and bonding resin as shown in Fig.2. The bonding resin consists of epoxy resin Mavidon MA1790-1 A/B (Mavidon Corp.) and glass fillers. The weight content of glass fillers is approximately 40.5%. Ductile cast iron rod is made from ductile iron castings Grade 80-55-06 (ASTM A 536-84). The bonding resin thickness and the bonding length of the FRP joint are respectively 4mm



- T, T₀ : temperature, reference temperature
- f, f' : frequency, reduced frequency
- t_s, t_c, t_f : time to failure under constant strain-rate, creep and fatigue loadings
- t_s', t_c', t_f' : reduced time to failure
- a_{T₀}(T) : time-temperature shift factor (a_{T₀}(T) = t_s/t_s' = t_c/t_c' = t_f/t_f' = f/f')
- R : load ratio (R = P_{min}/P_{max})
- N_f : number of cycles to failure (N_f = f t_f)
- P_s, P_c, P_f : static, creep, and fatigue failure loads
- P_{f,0}, P_{f,1} : P_f for R=0 and R=1

Fig.1 Prediction procedure of fatigue of FRP joint

and 28mm.

Test Procedure

The tensile tests for static and fatigue loadings were conducted for various temperatures. The test conditions are shown in Table 1. The tensile static tests were conducted at 5 testing temperatures between 40 and 80°C by using an Instron type testing machine. The tensile load was applied at both end screws of the FRP joint. The loading-rates (cross-head speeds) were 0.01, 1 and 100mm/min. The tensile fatigue tests were conducted at 5 testing temperatures between 40 and 80°C at a frequency $f=5\text{Hz}$, and at $T=61.9^\circ\text{C}$ and $f=0.05\text{Hz}$, by using an electro-hydraulic servo testing machine. Load ratio R (minimum load/maximum load) was 0.05. Additionally, the fatigue tests were also conducted at $T=40, 70^\circ\text{C}$, $f=5\text{Hz}$ and $R=0.5, 0.95$.

RESULTS AND DISCUSSION

Fractographs

Fractographs taken after static and fatigue failure are shown in Fig.3. The failure mode changed with temperature and the number of cycles to failure N_f . In the region of low temperature and small N_f the FRP joint mainly fails at the interface between the cast iron rod and bonding resin. In the region of high temperature and large N_f the FRP joint mainly fails in the bonding resin. The former is called fracture (B) and the latter is called fracture (A). All these failed specimens in Fig.3 and those observed in the other tests are similar regardless to loading patterns. We consider, therefore, that the failure mechanisms are the same for static and fatigue loadings.

Master Curve of Static Failure Load

Fig.4 shows the tensile static failure load P_s versus temperature T of the FRP joint at three loading-rates. From this graph, P_s depends on loading-rate and temperature. The left side of Fig.5 shows P_s versus time to failure t_s of the FRP joint at various temperatures T , where the t_s is defined as the time period from initial loading to P_s in constant loading-rate test. The master curve of P_s versus reduced failure time t_s' at a reference temperature $T_0=40^\circ\text{C}$ as shown in the right side of Fig.5 was constructed by shifting P_s at various temperatures along the log scale of t_s using the time-temperature superposition principle which holds for the creep compliance of bonding resin. The time-temperature shift factor $a_{T_0}(T)$ defined by

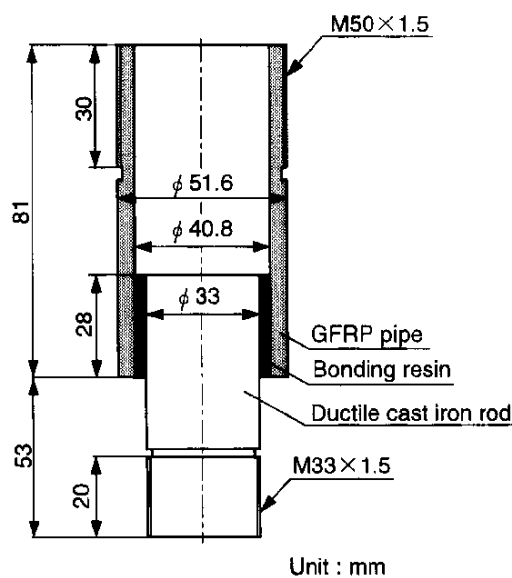


Fig.2 Configuration of FRP joint

Table 1 Testing conditions for FRP joint

Loading type	Loading rate [mm/min]	Frequency [Hz]	Load ratio P_{min}/P_{max}	Temperature [$^\circ\text{C}$]
Static	0.01	-	-	40,50,80, 70,80
	1			
	100			
Fatigue I	-	5	0.05	40,50,60, 70,80, 61.9
		0.05		
Fatigue II	-	5	0.5	40,70
			0.95	

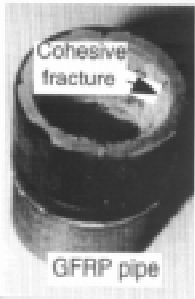

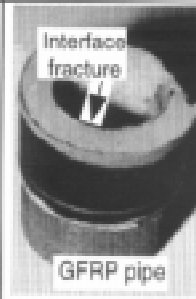

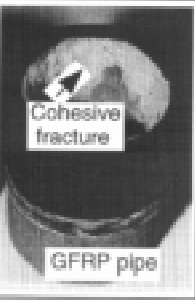
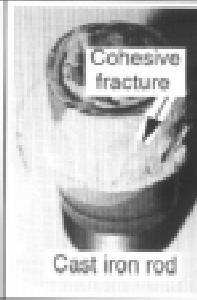
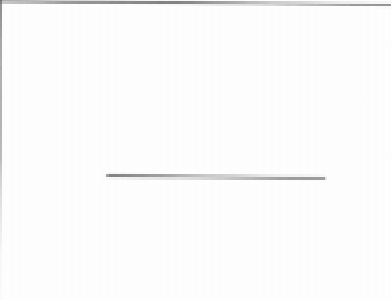
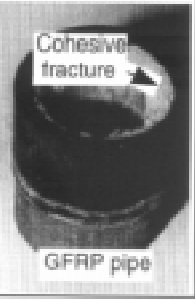
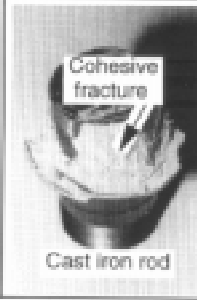
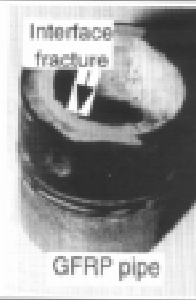

	Fracture(A)		Fracture(B)	
<p>Static V = 1mm/min</p>	 <p>Cohesive fracture GFRP pipe</p>	 <p>Cohesive fracture Cast iron rod</p>	 <p>Interface fracture GFRP pipe</p>	 <p>Interface fracture Cast iron rod</p>
	$P_s = 37.44\text{kN}, T = 70^\circ\text{C}$		$P_s = 51.84\text{kN}, T = 40^\circ\text{C}$	
<p>Fatigue f = 5Hz T = 70°C R = 0.95</p>	 <p>Cohesive fracture GFRP pipe</p>	 <p>Cohesive fracture Cast iron rod</p>		
	$P_f = 26.41\text{kN}, N_f = 143660$			
<p>Fatigue f = 5Hz R = 0.05</p>	 <p>Cohesive fracture GFRP pipe</p>	 <p>Cohesive fracture Cast iron rod</p>	 <p>Interface fracture GFRP pipe</p>	 <p>Interface fracture Cast iron rod</p>
	$P_f = 22.34\text{kN}, N_f = 84440, T = 70^\circ\text{C}$		$P_f = 32.93\text{kN}, N_f = 2160, T = 70^\circ\text{C}$	

Fig.3 Fracture appearances for FRP joint under static and fatigue loadings

$$a_{T_0}(T) = \frac{t_s}{t_s'} \quad (1)$$

Since P_s at various temperatures can be superimposed smoothly, the time-temperature superposition principle is applicable for P_s .

Fig.6 shows the time-temperature shift factors $a_{T_0}(T)$ for the master curve of P_s of FRP joint. The $a_{T_0}(T)$ are quantitatively in good agreement with Arrhenius' equation by using two different activation energies.

$$\log a_{T_0}(T) = \frac{\Delta H}{2.303R} \left(\frac{1}{T} - \frac{1}{T_0} \right) \quad (2)$$

Where, ΔH is activation energy [kJ/mol], R is gas constant 8.314×10^{-3} [kJ/(Kmol)].

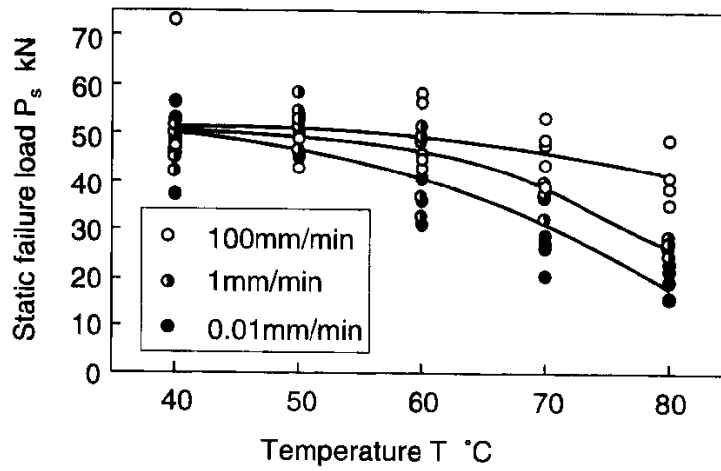


Fig.4 Static failure load P_s versus temperature for three loading rates

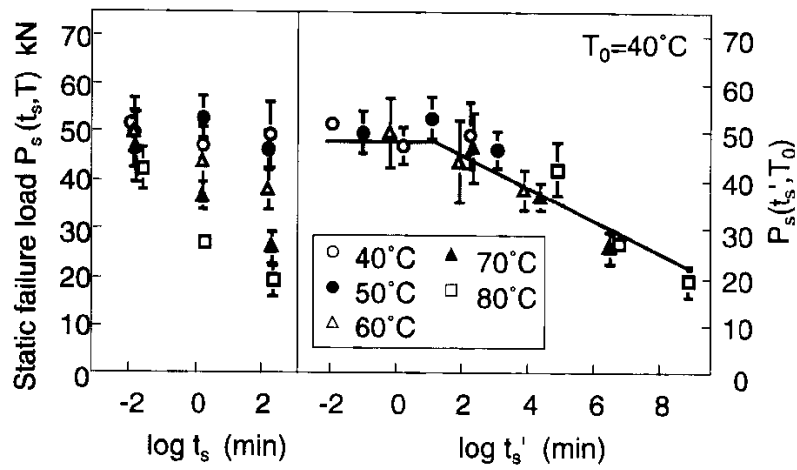


Fig.5 Master curve of static failure load P_s for FRP joint

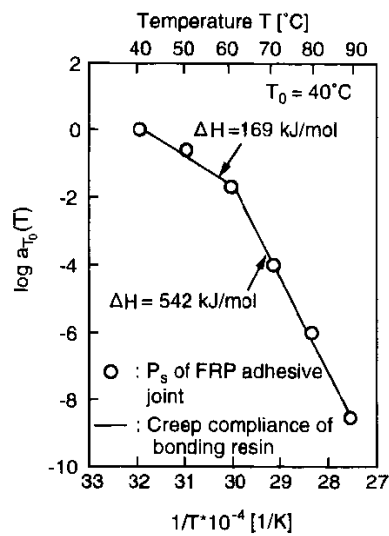


Fig.6 Time-temperature shift factors for FRP joint

Solid lines in this figure show $a_{T_0}(T)$ obtained experimentally for the creep compliance of the bonding resin.

Fig.7 shows the master curve of static failure load represented by the classification of fracture mode. The failure mode of FRP joint is classified into two mode. In the region of short time to failure and low temperature, the failure mode is fracture (B) where the static failure load scarcely changed with time to failure and temperature. In the region of long time to failure and high temperature, the failure mode is fracture (A) where the static failure load remarkably changed with time to failure and temperature.

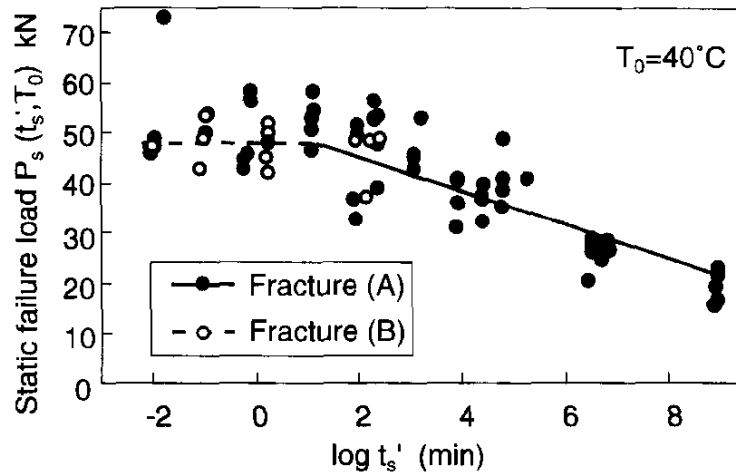


Fig.7 Classification of the fracture mode on the master curve of static failure load

Mater Curve of Creep Failure Load

We propose here a prediction method of creep failure load P_c from the master curve of static failure load using the linear cumulative damage law. Let $t_s(P)$ and $t_c(P)$ be the static and creep failure time for the load P . Suppose that the material experiences a monotone load history $P(t)$ for $0 \leq t \leq t^*$ where t^* is the failure time under this load history. The linear cumulative damage law states

$$\int_0^{t^*} \frac{dt}{t_c[P(t)]} = 1 \quad (3)$$

When $P(t)$ is equal to constant load P_0 , the above formula implies $t^* = t_c(P_0)$.

Fig.8 displays the creep failure load P_c versus time to failure t_c , where P_c is the fatigue failure load at load ratio 0.95. The left side shows the experimental data, while right side exhibits the data shifted to the reference temperature $T_0=40^\circ\text{C}$ using the shift factors for the static failure load. Since P_c at various temperatures can be superimposed smoothly, the time-temperature superposition principle is also applicable for P_c .

The right side of this figure also displays the master curve for the static failure load in the curve of thin line and that for the predicted creep failure load in the curve of thick line which is calculated by equation (3) using the master curve for the static failure load. The P_c can be predicted using the master curve of static failure load based on the linear cumulative damage law because the predicted P_c agrees well with the experimental data.

Master Curve of Fatigue Failure Load

We regard the fatigue failure load P_f either as a function of the number of cycles to failure N_f or

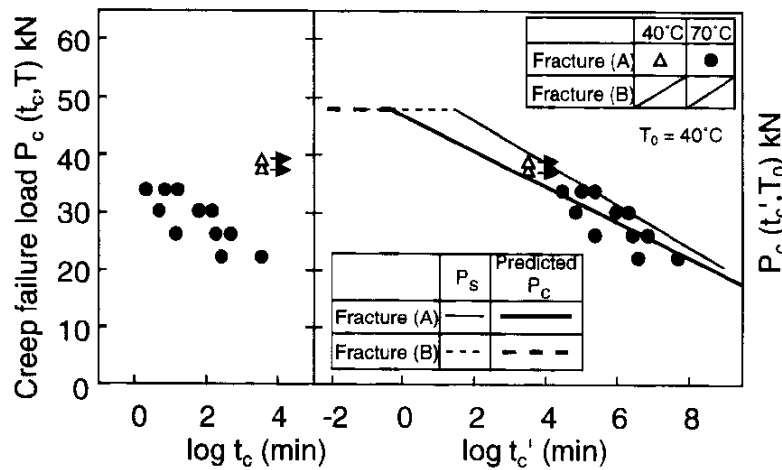


Fig.8 Master curve of creep failure load P_c for FRP joint and its prediction using linear cumulative damage law

of the time to failure $t_f = N_f/f$ for a combination of f , R , T and denote them by $P_f(N_f; f, R, T)$ or $P_f(t_f; f, R, T)$. Further, we consider that the static failure load $P_s(t_f; T)$ is equal to the fatigue failure load at $N_f=1/2$ and $R=0$ by choosing $t_f=1/(2f)$. At this point, we introduce special symbols for fatigue failure load at zero and unit load ratios by $P_{f;0}$ and $P_{f;1}$ where the latter corresponds to creep failure load.

To describe the master curve of $P_{f;0}$, we need the reduced frequency f' in addition to the reduced time t_f' , each defined by

$$t_f' = \frac{t_f}{a_{T_0}(T)} = \frac{N_f}{f'} \quad , \quad f' = f \cdot a_{T_0}(T) \quad (4)$$

Thus, the master curve has the form, $P_{f;0}(t_f'; f', T_0)$. An alternative form of the master curve is possible by suppressing the explicit dependence on frequency in favor of N_f as $P_{f;0}(t_f'; N_f, T_0)$. Recall that the master curve of fatigue failure load at $N_f=1/2$ reduces to the master curve of static failure load.

The fatigue failure load P_f versus the number of cycles to failure N_f (P_f - N_f curve) for FRP joint at 2 frequencies $f=5$ and 0.05Hz are shown in Fig.9. The P_f depends remarkably on temperature and frequency as well as N_f . The temperature condition of $T=70^\circ\text{C}$ at $f=5\text{Hz}$ can be converted into the condition of $T=61.9^\circ\text{C}$ at $f=0.05\text{Hz}$ for FRP joint by using the time-temperature superposition principle which holds for the static failure load. The P_f - N_f curve at $T=61.9^\circ\text{C}$, $f=0.05\text{Hz}$ agrees well with that at $T=70^\circ\text{C}$, $f=5\text{Hz}$. Therefore, the time-temperature superposition principle for the static failure load also holds for the fatigue failure load, and the hypothesis (B) is valid for fatigue failure load.

The upper portion of Fig.10 shows P_f versus the reduced time to failure t_f' . On the other hand, each point on the master curves of constant reduced frequency represents a number of cycles to failure. Connecting the points of the same N_f with these curves, the master curves of P_f for constant N_f are constructed as shown in the lower side of Fig.10. The P_f for a given number of cycles to failure at an arbitrary temperature and frequency can be determined by using the master curves of P_f as shown in this figure.

Fig.11 shows classification of the fracture mode on the master curve of fatigue failure load. In the region of small N_f , the failure mode is fracture (B) where the P_f decreases scarcely as N_f increases. In the region of large N_f , the failure mode is fracture (A) where the P_f decreases remarkably as N_f increases.

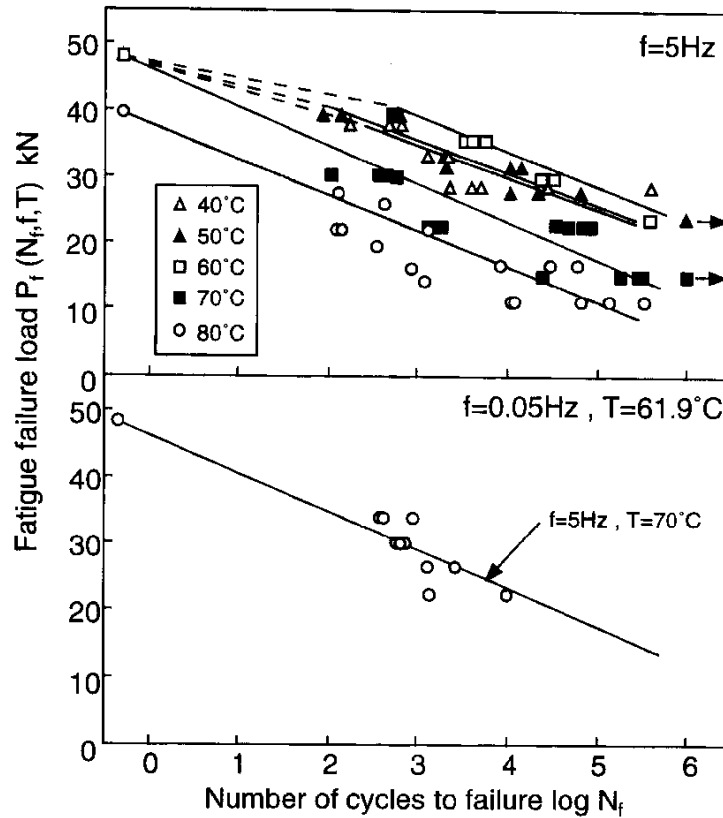


Fig.9 Fatigue failure load vs. number of cycles to failure at various temperatures and frequencies

Prediction of Fatigue Failure Load for Arbitrary Frequency, Load Ratio and Temperature

We have the master curve for creep failure load $P_c(t_c'; T_0)$ from which follows the creep failure load at any temperature T . The creep failure load, in turn, may be regarded the fatigue failure load $P_{f,1}(t_f; f, T)$ at unit load ratio $R=1$ and arbitrary frequency f with $t_c = t_f$. Further, from the master curve for fatigue failure load at zero load ratio, we can deduce the fatigue failure load $P_{f,0}(t_f; f, T)$ at zero load ratio for any frequency f and temperature T .

Invoking the hypothesis (D), we propose a formula to estimate the fatigue failure load $P_f(t_f; f, R, T)$ at an arbitrary combination of f, R, T by

$$P_f(t_f; f, R, T) = P_{f,1}(t_f; f, T)R + P_{f,0}(t_f; f, T)(1 - R) \tag{5}$$

Fig.12 shows experimental data of P_f-t_f for $f=5\text{Hz}$, $R=0.5$ and $T=40, 70^\circ\text{C}$. The curves of $R=0.05$ and $R=0.95$ respectively represent the least squares fit for experimental data of fatigue test of $R=0.05$ and predicted creep failure load. The curve of $R=0.5$ is calculated from equation (5) on the basis of the curves for $R=0.05$ and $R=0.95$. As can be seen, the predictions correspond well with the experimental data. We can predict P_f-t_f relation for given R, f and T from equation (5) if $P_{f,1}(t_f; f, T)$ and $P_{f,0}(t_f; f, T)$ are known.

CONCLUSION

We had proposed a prediction method of fatigue failure load of FRP joint under arbitrary fre-

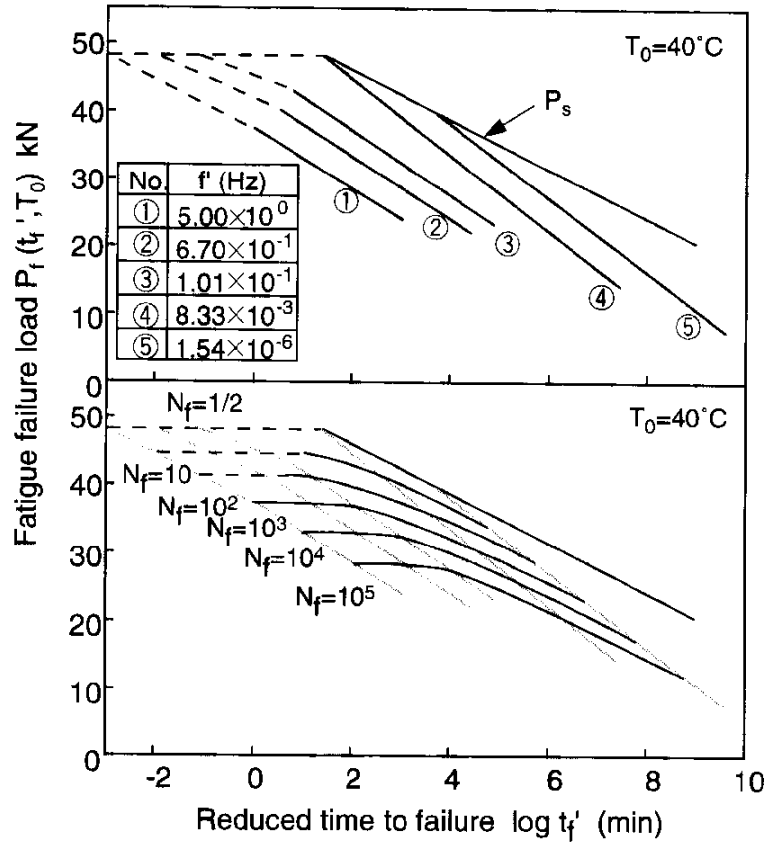


Fig.10 Master curve of fatigue failure load P_f for FRP joint

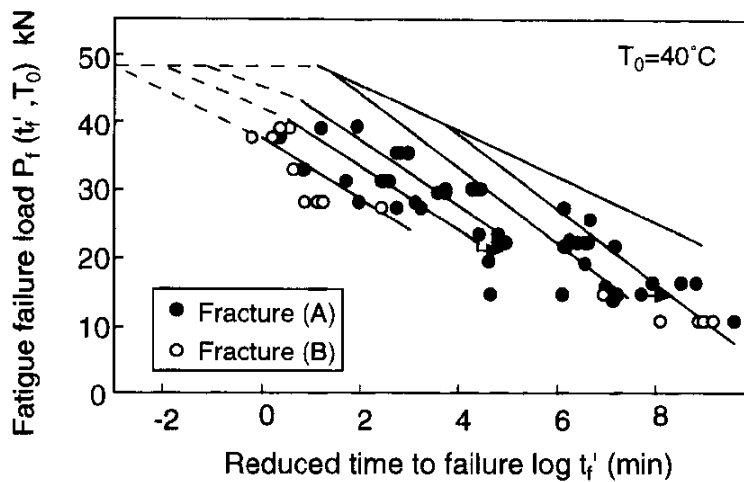


Fig.11 Classification of the fracture mode on the master curve of fatigue failure load

quency, load ratio and temperature. The method is based upon the four hypotheses, (A) same failure mechanism for static, creep and fatigue failure, (B) same time-temperature superposition principle for all failure loads, (C) the linear cumulative damage law for monotone loading and (D) linear dependence of fatigue failure load upon load ratio. Tensile tests of FRP joint for static, creep and fatigue loadings were conducted for various temperatures. The test results indicated the validity of the proposed method and the applicability of the hypotheses for this FRP joint.

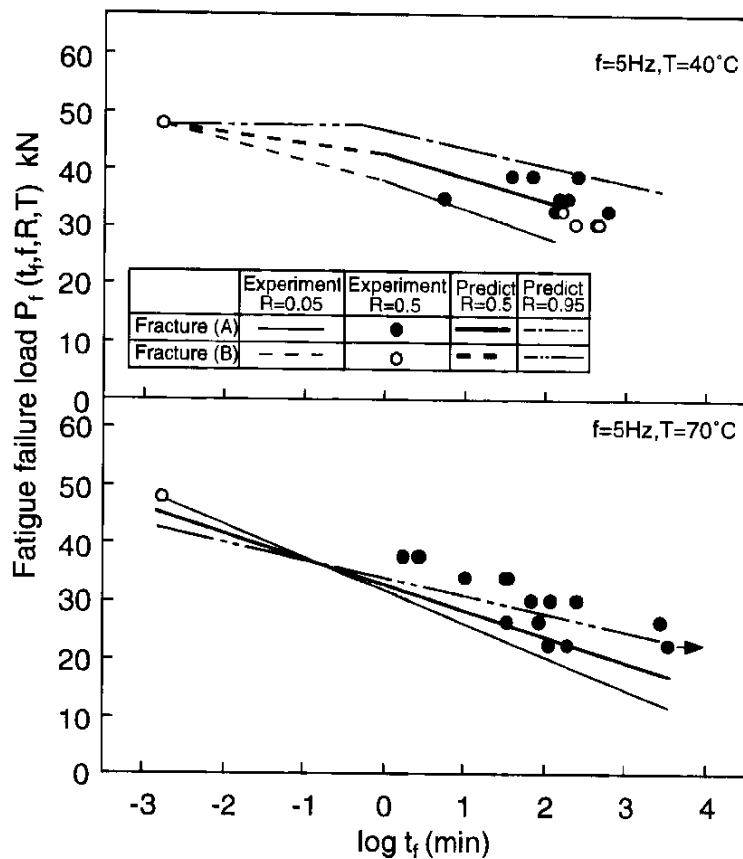


Fig.12 Prediction of fatigue failure load at R=0.5 for FRP joint

REFERENCES

1. Aboudi, J. and Cederbaum G., Composite Structures, 12, 243 (1989).
2. Ha, S.K. and Springer, G.S., J. Composite Materials, 23, 1159 (1989).
3. Sullivan, J.L., Composite Science and Technology, 39, 207 (1990).
4. Gates, T.S., Experimental Mechanics, 68 (1992).
5. Miyano, Y., Kanemitsu, M., Kunio, T. and Kuhn, H., J. Composite Materials, 20, 520 (1986).
6. Miyano, Y., McMurray, M.K., Enyama, J. and Nakada, M., J. Composite Materials, 28, 1250 (1994).
7. Miyano, Y., McMurray, M.K., Kitade, N., Nakada, M. and Mohri, M., Advanced Composite Materials, 4, 87 (1994).
8. Miyano, Y., Nakada, M. and McMurray, M.K., J. Composite Materials, 29, 1808 (1995).
9. Miyano, Y., McMurray, M.K. and Muki, R., Numerical Methods in Structural Mechanics, ASME AMD-204, 69 (1995).
10. Nakada, M., Miyano, Y., and Kadotani, K., Proc. of Asian Pacific Conference for Fracture and Strength '96, 309 (1996).

RESISTANCE WELDING OF CARBON FIBRE FABRIC REINFORCED POLYETHERIMIDE (CF FABRIC/PEI) COMPOSITE MATERIAL

M. Hou¹, L. Ye² and Y.-W. Mai²

¹ *Cooperative Research Centre for Advanced Composite Structures Ltd., 361 Milperra Road, Bankstown, NSW 2200, AUSTRALIA*

² *Centre for Advanced Materials Technology, Department of Mechanical and Mechatronic Engineering, The University of Sydney, NSW 2006, AUSTRALIA*

SUMMARY : This paper presents an experimental investigation of resistance welding of carbon fibre fabric reinforced polyetherimide composites (CF fabric/PEI) by resistance welding. An experiment apparatus was developed to carry out experiments which yield information on the processing parameters, such as current intensity, input energy, power, welding time and consolidation pressure. All of them can govern more or less the efficiency of the welding process. The heating element consisted of a single ply of CF fabric/PEI fabric prepreg. Experiments were conducted under displacement control. The quality of the welded samples was studied by using an ultrasonic, non-destructive evaluation technique (C-scan) as well as mechanical test (lap shear) program. Experimental results indicated that sufficient joining was obtained at power levels from 80 to 160 kW/m², under initial welding pressures varying from 0.15 to 0.40 MPa. The maximum lap shear strength achieved through resistance welding were equivalent to those of compression molded samples. The fracture surfaces of welded samples showed mostly cohesive failure or intralaminar failure. An optimum processing window was finally determined for the resistance welding of CF fabric/PEI composite system.

KEYWORDS: joining, composites, resistance welding, thermoplastic, carbon fibre, Polyetherimide

INTRODUCTION

Continuous fibre reinforced thermoplastic composites have been introduced as structural materials for high performance aerospace and industrial applications. High strain to failure, increased fracture toughness, better impact tolerance, short processing cycle time, infinite shelf life of prepreg, recyclability and reparability are some of the reasons cited for their growing popularity. The most important advantage of thermoplastics may lie in their potential for rapid, low-cost, mass production of reinforced composites. However, due to the deformation restriction of continuous fibre reinforcements, composite components with only relative simple geometry can be effectively produced from these materials. To make large and complex structures, several components must be jointed together. For this to happen it is very important to develop fast and reliable joining methods in the manufacturing and repairing of thermoplastic composites. The traditional joining methods are adhesive bonding and mechanical fastening. Adhesive joining is difficult for composites with thermoplastic matrix because of the difficulty of chemically bonding to the matrix. On the other hand, mechanically fastened joints are subjected to problems of stress concentration and damage of

the reinforcing fibres, especially for unidirectional fibre reinforced composites. Thermally welding may offer a solution to the problem of joining thermoplastic composite materials [1]. It eliminates problems of introducing another material into the bonding surface and the stress raising factors associated with mechanical fasteners [2].

This paper presents an experimental investigation of resistance welding of carbon fibre (CF) fabric reinforced polyetherimide (PEI) composites. The special interest is to develop a clear understanding of the effects of processing conditions on the structural and mechanical properties of the joint product. Resistance welding is a method for quickly heating and melting composites at the bond surface by passing electric current through a resistive element which is placed at the bond line and remains permanently there [3,4]. In the present study, an experimental apparatus was developed to carry out resistance welding. Processing parameters, such as welding pressure, input power level and welding time have been investigated. The heating element is a single ply of CF fabric/PEI prepreg. The graphite fibres in the heating element produce Joule heating when an electric current is passed through the element. The quality of welded surface was examined by non-destructive evaluation technique (C-Scan) and lap shear test. Experimental results indicated that sufficient bonding was obtained at power levels from 80 to 160 kW/m², under initial welding pressures varying from 0.15 to 0.40 MPa. The maximum lap shear strength achieved through resistance welding were equivalent to those of compression molded samples. The fracture surfaces of welded samples showed mostly cohesive failure or intralaminar failure. An optimum processing window was finally determined for the resistance welding of CF fabric/PEI composite system.

EXPERIMENTAL

Material

The material used in this study was solvent impregnated carbon fibre fabric reinforced polyetherimide (Ultem 1000) prepreg supplied by Ten Cate Advanced Composites, the Netherlands. The carbon fabric has a 5H satin woven construction. The prepreg has a resin content of 44.1 wt %. PEI is an amorphous polymer and has a glass transition temperature of about 217°C. During the solvent impregnation process some air was entrapped by the PEI polymer, which formed many tiny air bubbles on the surface of the prepreg. The cross-section micrograph of the CF/PEI prepreg shows that most of the PEI matrix (about 60%) remains outside the warp/weft fibre bundles and there exist a lot of voids in the middle of the fibre bundle, especially at the contact area between the warp and weft fibre bundles. Consolidation of the laminates was performed using a small steel mold with a rectangular cavity (250 mm x 150 mm) and a laboratory hot press. The following conditions were used in the preparation of pre-consolidated laminate: molding temperature 320°C, pressure 2.0 MPa and holding time of 15 min [5]. Each laminate contained 10 layers of the CF/PEI prepreg; this led to a thickness of about 2.6 mm for a fully consolidated laminate. Specimen with a dimension of 100 mm long and 25 mm wide were then machined from the panel with a diamond saw. All bond surfaces were polished slightly with sand paper and cleaned with acetone prior to welding. In addition, compression molded lap shear samples were also prepared to provide a basis for comparison.

Heating Element

Since the heating element remains embedded at the interface in this process, it is important that it is compatible with the composites to be jointed. Therefore a single CF fabric/PEI prepreg was used as the resistive element, taking advantage of the semi-conducting nature of the graphite fibres. To make heating element with good impregnation/consolidation quality, single CF fabric/PEI prepreg was also compression moulded according to the above mentioned conditions. To introduce rich matrix layer in the heating element, single CF fabric/PEI prepreg sandwiched between two PEI film (with a thickness of 0.076 mm) was also prepared. The heating element was then cut from the pre-consolidated single prepreg with a dimension of 120 mm long in the warp fibre direction and 12.5 mm wide in the weft fibre direction. To introduce current to the warp carbon fibre, the matrix was burnt from both ends of the prepreg (approximately 40 mm at each end).

Experimental Set-up

The experimental set-up used for the resistance welding is shown in Figure 1. It consists of a stack of material to be welded, the electrical components and an universal testing machine. Direct current used for welding is supplied by a power transformer with a maximum current output of 30 A and a maximum voltage output of 30 V. The stack of material to be welded consisted of two 10 ply pre-consolidated laminate and a heating element. Two couples of brass blocks bolted together to provide contact pressure were selected as clamp connectors for the heating element. It was found that the maximum contact resistance between the brass clamps and the fibres is only 8% of the total resistance of the heating element, when the clamped fibre length is more than 20 mm. Under this condition it gets a more homogeneous heating of the heating element. Two blocks of spruce wood were chosen as insulators, helping to reduce heat losses and to provide alignment of the samples to be welded.

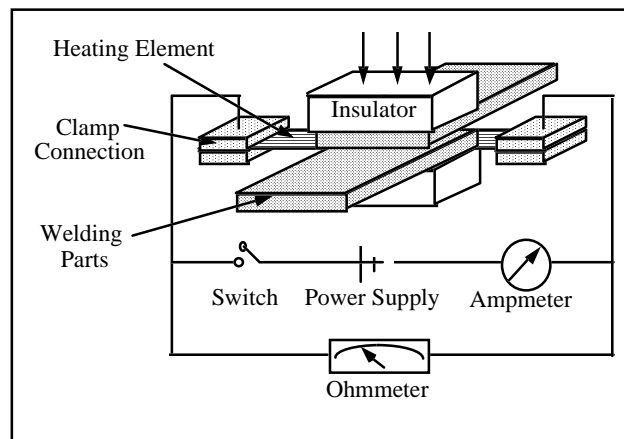


Figure 1. Experimental set-up

The important parameters for the welding process are the power P (in kW/m^2) and the input energy E (in kJ/m^2), which are supplied at the welding interface per unit area [3]:

$$P = I^2 R / LW \quad (1)$$

$$E = P t \quad (2)$$

where R is the resistance of the heating element (in Ohm), I the electrical current put into the system (in Ampere), P the power (in kW/m^2) and t the electrified time (in second); L and W are the length and width (both in meter) of the welding area.

Mechanical Testing

Lap shear tensile test (ASTM D1002) was performed at room temperature for both resistance welded and compression moulded specimens. The test specimen was 200 mm in length and 25 mm in width with a overlap length of 12 mm. Three or two replicates were tested for each set of process parameters. Before testing the welded samples were polished by 0.5 mm on each side so that the edge irregularities obtained during the welding process due to transverse matrix flow and squeeze effects could be removed.

RESULTS AND DISCUSSION

Demarcation of Heating Element

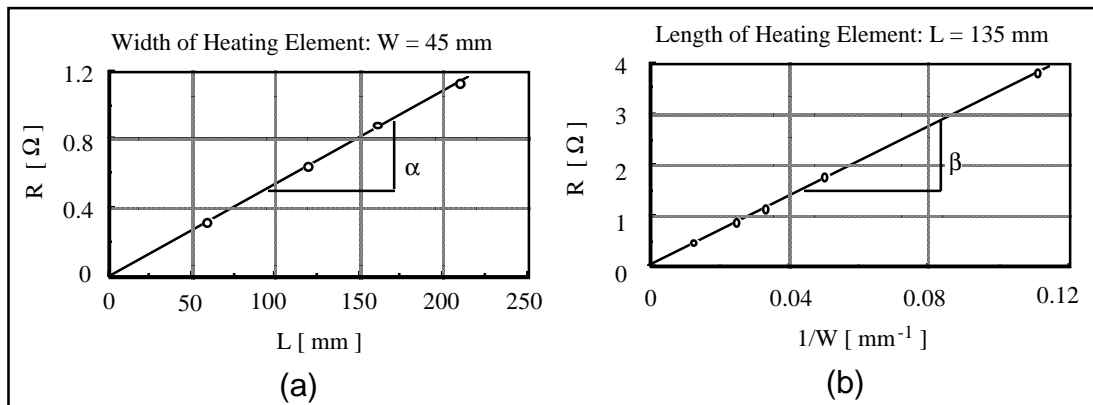


Figure 2. Resistance of CF fabric/PEI in relation to its dimension

The resistance of a material is directly proportional to its length and inversely proportional to its cross section. It is assumed that the CF fabric/PEI prepreg has a constant fibre volume fraction in the warp fibre direction, a constant thickness and the fibres are homogeneously distributed across the width, so that the resistance R of the prepreg should be calculated as follows:

$$R = r L/W \quad (3)$$

where L is the length of the prepreg, W its width, and r the specific resistance of the material (at constant thickness of the heating element). To obtain the value of r , the resistance of single CF fabric/PEI prepreps of various length, but a constant width of 45 mm, and of prepreps having various width, but a constant length of 135 mm have been measured. Both sets of data result in linear curves when plotting the R values vs. L and $1/W$, respectively (Figure 2). Note that the resistance of the connection between clamps and fibres is already removed by

extrapolation! From the slope of both curves, a mean value of 0.242 for the coefficient r can be obtained. By using this value, the resistance of any CF/PP heating element with known length and width can be calculated.

Effect of Power Level on Welding Process

Preliminary experiments were performed in order to determine the maximum and minimum input power levels necessary to carry out resistance welding economically. The conditions required for the minimum power level were that 100% of the welding region be melted within a time of 120 seconds. This was tested by examining fractured welding surface. According to the results of some trial and error experiments, the minimum accepted power level was found to be 80 kW/m^2 . It was noted that at a power level of as low as 60 kW/m^2 , it took a too long time (about 3-4 min) until the whole surface could be melted, and at the same time the samples became very soft and flexible, and could not maintain their original geometry. It implied that most of the energy got lost by heating up the bulk samples and the surroundings. It is known that besides heating and melting the matrix at the interface, the quantity of heat produced by the heating element gets partially lost into the bulk interior of the samples to be welded and into the environment as a result of convection, radiation and conduction. The longer the welding time is, the greater is the heat loss. At high power levels, on the other hand, the melting time can be kept short, because the heating rate is rather high. If, however, the power level is too high (200 kW/m^2), the matrix can be burnt away resulting in fibre oxidation, which reduces the joining efficiency and increases the resistance of the heating element. For this reason, the following experiments were carried out between the two power limits, i.e. 80 to 160 kW/m^2 .

Effect of Welding Pressure

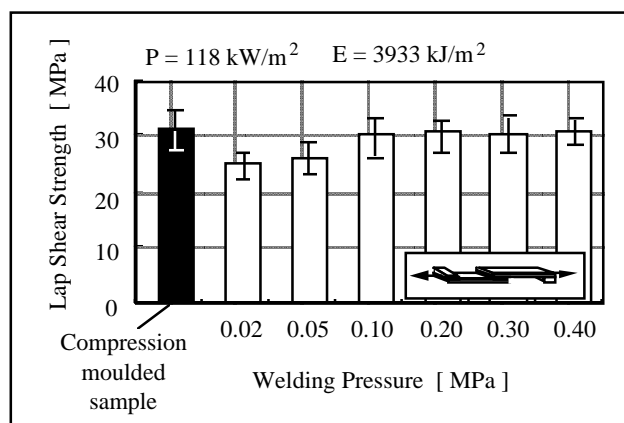


Figure 3. Effect of welding pressure on lap shear strength

When the thermoplastic matrix melts, stored elastic energy in the fibres is released which can lead to warpage and deconsolidation [6]. Therefore, parts to be welded must be properly supported by external pressure during the welding process. The effect of initial welding pressure on lap shear strength of welded sample is shown in Figure 3, in which the lap strength of compression molded sample is also shown as a bench-mark. All samples were welded at the same power level of 118 kW/m^2 and an input energy of 3933 kJ/m^2 . The experimental results show that low initial welding pressures (0.02-0.05 MPa) resulted in weak joints. The reason is as follows: if the initial welding pressure is low, then the consolidation

pressure is not high enough to suppress the elastic deformation of the fibres and to remove air voids at the interface. The results of ultrasonic investigation (C-scan) of these samples welded at different pressures verified the assumption. The initial welding pressure suitable for the experiments in this study was found to be in the range of 0.15 - 0.40 MPa.

Effect of PEI Film

The mechanism governing the formation of interply bonds has been established as autohesion or selfdiffusion [7] and the bond line thickness has a significant effect on the final mechanical property of the welded sample [4]. Figure 4 shows the lap shear strength of samples welded with two kind of heating elements, i.e. heating element with PEI film and without PEI film. It can be seen that the lap shear strength of samples welded with PEI film heating element are about 20 to 30% higher than that of samples manufactured with heating element without PEI film. The PEI film can produce a thin layer of PEI, about 0.05 mm, on both side of the heating element. The softening and deformation of these thin PEI layers can effectively promote the intimate contact between the welding surface, which is of benefit to the diffusion of macromolecules across the interface. Therefore, the welding experiments were carried out using heating element with PEI film.

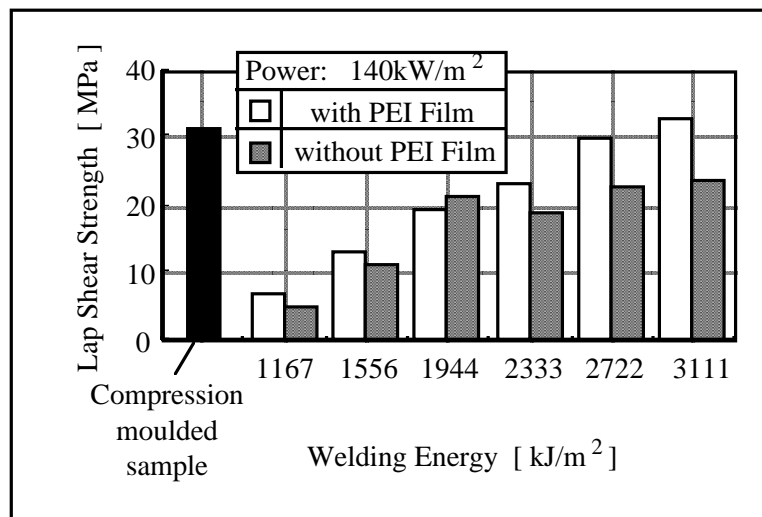


Figure 4. Lap shear strength of CF fabric/PEI samples welded with/without PEI (input power 140 kW/m²)

Input Energy in Relationship to Power Level

From the results of section 3.2 input power levels of 80, 118, 140 and 160 kW/m², respectively, were chosen for the resistance welding. The other parameter varied in these experiments was the electrified time, which controls the amount of thermal energy supplied to the welding interface by the heating element. The lap shear strengths of samples welded at these four power levels are plotted in Figures 4 to 7 as a function of the thermal energy released by the heating element. The value in the black box represents the lap shear strength of a compression molded specimen. From these figures the following general trends can be seen: (1) the lap shear strength of the welded specimens approaches a peak level with increasing welding energy and then decreases slightly for each power level; (2) the energy needed for the peak value of lap shear strength decreases dramatically with increasing power

level. (3) except for the power level of 160 kW/m^2 , the maximum lap shear strengths achieved at the other three power levels approached up to 95% of the lap shear strength value of the compression molded specimen.

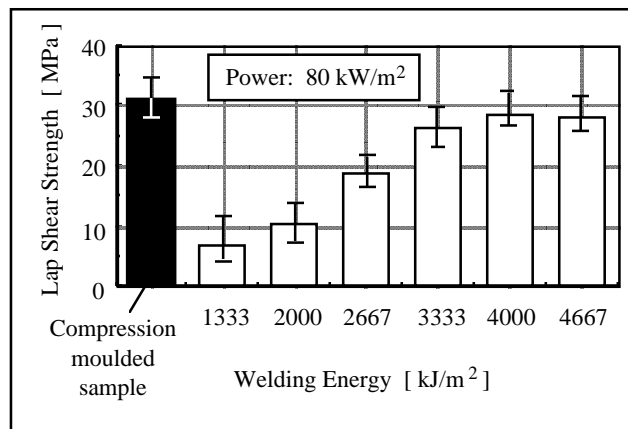


Figure 5. Lap shear strength of CF fabric/PEI composite welded at power level of 80 kW/m^2

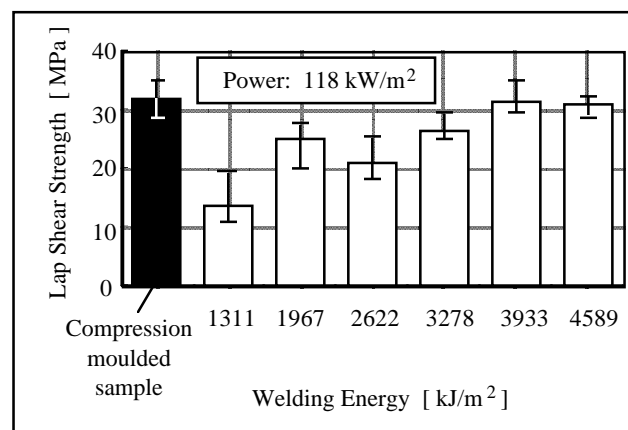


Figure 6. Lap shear strength of CF fabric/PEI composite welded at power level of 118 kW/m^2

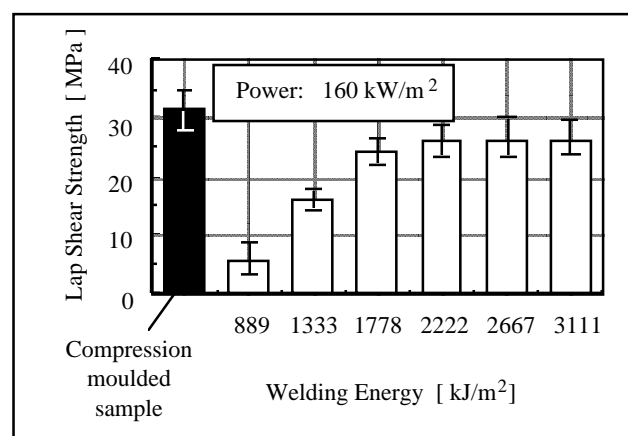


Figure 7. Lap shear strength of CF fabric/PEI composite welded at power level of 160 kW/m^2

The welded regions were examined by both an ultrasonic technique and fracture surface analysis. The latter could be made after the lap shear test. The fracture surfaces of welded parts show that the portion of fractured area increased clearly with increasing welding energy, and this is in agreement with the observation made by the ultrasonic technique. Each specimen was examined optically to determine the mode of failure. It was found that there were two distinct modes of failure, i.e. intralaminar and interfacial failure. Intralaminar failure, as shown in Figure 8 (a), was considered to occur when fracture occurred either within the bulk structure of the composites, within the heating element or within both of them. Interfacial failure (Figure 8 b) resulted in the fracture at the interface the between heating element and the composite. All samples shown in Figure 4-7 show a change in failure mode from interfacial to intralaminar failure with increasing welding energy. At low input power level, a greater amount of energy produced by the heating element gets lost into both bulk specimen and environment, because the heating rate of the interface at low power level is much lower than that at high power level [8]. Therefore, a longer electrified time or more energy will be needed at lower power level than at higher power level for melting the same amount of matrix at the interface. If the electrified time at a given power level is too short, the thermal energy released by the heating element is not enough to melt the polymer matrix at the bonding surfaces, thus leading to weak or no joint. A situation like this can be seen from the low lap shear strength achieved with low input welding energy in these figures, which shows that the failure occurs at the interface between the laminate and the heating element because of incomplete bonding; this resulted in a lap shear strength of only 10 to 30% of that of compression molded sample. With increasing welding time, more polymer matrix of the contacting surfaces will be molten; this increases the welding area and leads to a change of failure mode from interfacial to intralaminar failure. This is associated with a higher lap shear strength, for example, at an input energy of 3933 kJ/m² and an input power level of 118 kW/m² (Figure 6), the lap shear strength is 30 MPa, which is close to the value of compression molded sample.

The maximum lap shear strength achieved with power level of 160 kW/m² is 86% of that of benchmark. The reasons are to be believed due to (a) the interface and/or interphase between matrix and fibre has been damaged to some extent by passing electric current through fibres [8] and (b) a relatively short period of dwell time of polymer matrix at its molten state. The latter factor prevents the polymer chains to penetrate and entangle sufficiently into the adjacent interface, which results in a partially diffused interface.

CONCLUSIONS

An experimental study on the subject of resistance welding of pre-consolidated, carbon fibre fabric reinforced polyetherimide (CF fabric/PEI) was successfully performed. An optimum initial welding pressure was found to be in the range of 0.15 - 0.40 MPa.

As a conclusion, the optimum processing window for resistance welding of CF fabric /PEI composite based on a critical level of lap shear strength can be evaluated from the experimental results. Assuming 86% lap shear strength of the benchmark (compression

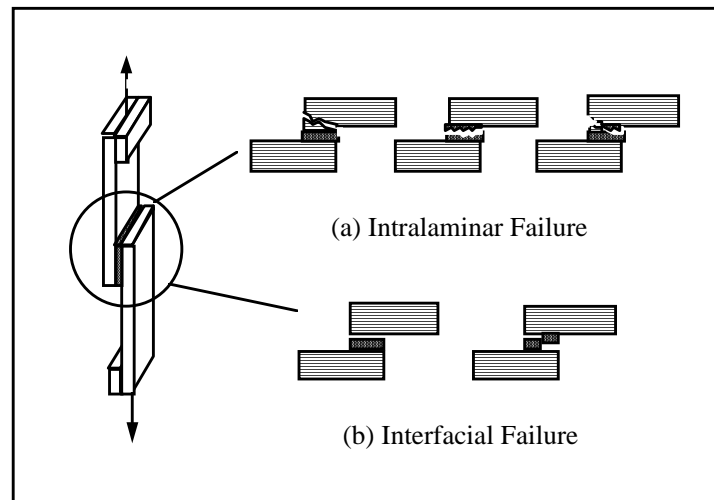


Figure 8. Failure types of lap shear test

molded sample) is the critical mechanical property of the joint. The relationship between processing conditions required to reach this desired level of strength can be illustrated as a form of a processing window in Figure 9. The points in this diagram represent the welding conditions used in this experiment. The ordinate represents the input power (in kW/m^2), the abscissa the welding time (or electrified time), and the product of both of them results in the input energy (in kJ/m^2), illustrated in form of equivalent energy lines. The entire figure is divided into five sections. Section II and section III represent the limits for the input power. If the power is too high the matrix can be burnt away and decomposed. Owing to the low heating rate at the interface and great loss of thermal energy into the bulk specimen and the surroundings, on the other hand, low power causes too much energy loss or insufficient joining quality. Area (I) is the processing window, in which good bonding can be achieved at a power level range from 80 kJ/m^2 to 160 kJ/m^2 . The mechanical properties of these joints (lap shear strength) are equivalent to 86% of that of the compression molded base line. Inside this area the input energy needed for sufficient welding decreases with increasing power level. Too much thermal energy (or too long electrified time) results in a great movement of fibres at the interface and unsteady geometry of the welded specimens because of their softening (area V). If the input thermal energy is not sufficient enough (e.g. due to a too short electrified time) in order to melt the matrix at the interface, it produces only weak or even no bonding at all (area IV).

ACKNOWLEDGMENTS

This work was carried out as part of the Cooperative Research Centre for Advanced Composite Structures (CRC-ACS) Research Program (Task 1.6.1 Thermoplastic Composites). Thanks are due to West Lake Plastics Company (USA), who kindly supplied the PEI film (Ultem 1000) material. Also thanks to Mr. L. Flood and the technicians in the Materials Laboratory of the CAMT of the University of Sydney for their assistance in the experiments.

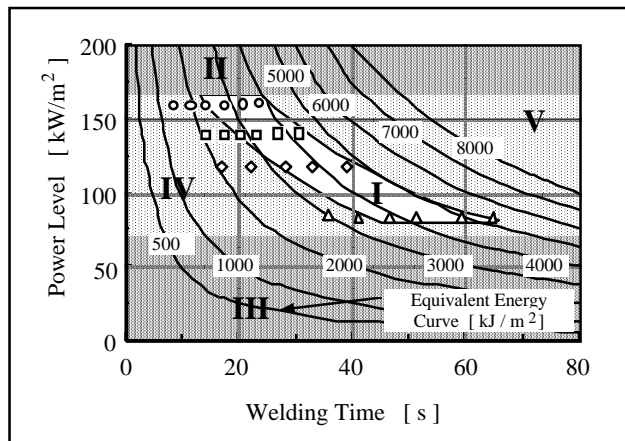


Figure 9. Processing window for resistance welding of CF fabric/PEI composites

REFERENCES

1. D. M. Maguire, "Joining Thermoplastic Composites", SAMPE Journal, Vol. 25, No. 1, Jan. / Feb. 1989, p. 11-14
2. A. B. Strong, D. P. Johnson and B. A. Johnson, "Variables Interactions in Ultrasonic Welding of Thermoplastic Composites", SAMPE Quarterly, Jan. 1990, p. 36-41
3. Hou, M. and Friedrich K., "Resistance welding of continuous glass fibre-reinforced polypropylene composites", Composites Manufacturing, Vol. 3, No. 3 (1992) p. 153-163
4. Howie, I., Gillespie, J. W. and Smiley, A. J., "Resistance welding of graphite-polyarylsulfone/polysulfone dual-polymer composites", J. of Thermoplastic Composite Materials, Vol. 6-July 1993, p. 205-225
5. Hou, M., Ye, L., Lee, H. J. and Mai, Y W., "Manufacture of carbon fibre fabric reinforced polyetherimide (CF/PEI) composite material", submitted to J. of Composites Science and Technology, February 1996
6. Voyutskii, S. S., "Autohesion and adhesion of high polymers", Polymer Reviews, Vol. 4, New York, Interscience Publishers, 1963
7. Gutowski, "A Resin Flow/Fibre Deformation Model for Composites", SAMPE Quarterly, July 1985, p. 58-64
8. Hou, M. and Friedrich, K., "Resistance Welding of Continuous Carbon Fibre/Polypropylene Composites", Plastics, Rubber and Composites-Processing and Application, 18 (1992) p. 205-213

RESIDUAL STRESSES IN THERMOPLASTIC BONDING TO METALS: EXPERIMENTS AND MODELING

Karthik Ramani and Wenping Zhao

School of Mechanical Engineering, Purdue University, West Lafayette, IN 47907-1288, USA

SUMMARY: The ability to create strong joints between thermoplastics and metals offers many advantages. Differential properties between the polymer and metal generate residual stresses during cooling. In our study, both amorphous thermoplastic thin films and semi-crystalline thermoplastic thin films are joined to metal strips and the curvature is measured during controlled cooling. A series of five designed experiments uses a fast cooling (~ 30 °C/second) and slow cooling ($\sim 4.5 - 10$ °C/minute) to create different residual stresses. Experimental evidence shows that the residual stresses begin to develop at ~ 190 °C for amorphous *Poly Ether Imide* (PEI, $T_g = 210$ °C), but at ~ 255 °C for semi-crystalline *Poly Ether Ether Ketone* (PEEK, $T_g = 143$ °C). A mechanics based curvature model, combined with the elasticity and viscoelasticity of thermoplastics, successfully predicts the residual stress development. An elastic behavior is exhibited during the fast cooling (~ 30 °C/second), whereas a viscoelastic behavior occurs during slow cooling (~ 4.5 °C/minute).

KEYWORDS: residual stress; thermoplastic adhesive bonding; elastic/viscoelastic

INTRODUCTION

Hot-melt thermoplastic adhesives are finding more applications in bonding various materials. One of the most important applications is to create structural joints between thermoplastics and metals. Thermoplastic joining to metals can also be extended to create joints in-situ in manufacture of a thermoplastic part such as during injection molding. In addition, the potential for fast joining together with significantly better durability than thermoset based joints makes the thermoplastic bonding approach an attractive option for future manufacturing [1]. In our earlier studies, a thin-film thermoplastic-metal joining process was investigated extensively [1-4]. The surface preparation, contact pressure during consolidation, heating and cooling rates, hold times at melt and recrystallization temperature, effect of bond line thickness and uniformity, and anodization to increase durability were included in the process development. This study is intended to investigate the residual stress development associated with thin-film thermoplastic-metal bonding.

Residual stresses generated at the polymer-metal interface during bonding can influence joint strength and durability significantly. The presence of high internal stresses at the interface can cause loss of adhesion and/or cracking. For thermoplastic adhesive bonding to metals, differential properties between polymer and metal generate residual stresses during the cooling process. A sound experimental and theoretical understanding of the relationship

between residual stress development and the bonding process will contribute to reducing the processing time, improving the processing and resulting joint performance.

The role of residual stresses in polymers has been recognized as an important issue in several related areas, such as coatings, adhesive bonding, and polymeric composites. Moran *et al.* [5] investigated the residual stress in thermoplastic coating films. Chapman *et al.* [6] developed a model to predict residual stresses in thermoplastic composites. However, no model has been developed to describe the residual stress development in thermoplastic polymer-metal bonding during processing. This study develops and experimentally validates a model for predicting the residual stress evolution during processing.

EXPERIMENTAL

Design of Experiment

In this study, a beam curvature method was employed to investigate the residual stress development at the polymer-metal interface. A thermoplastic thin-film was heated to melt and bonded to a metal strip. During the subsequent cooling process, a curvature developed because of the differential properties of the polymer and metal.

The polymers used in this study are semi-crystalline *Poly Ether Ether Ketone* (Westlake Plastic company, PEEK 450G, 0.127 mm thick) and amorphous *Poly Ether Imide* (PEI, GE, Ultem 1000, 0.127 mm thick). Both of them exhibit excellent physical properties compared to most other engineering polymers, such as higher strength and rigidity at room and elevated temperature. The superior properties make them ideal polymers for use in various applications, including adhesive bonding.

In this study, a thin steel strip (Precision Brand, 0.102 mm thick) is used as the substrate for bonding the polymers.

The experiments were performed in a computer controlled press. The polymer-metal beam sample (50 x 5mm) was placed in between the two relatively large hot platens (228 x 228mm) of the press. Figure 1 shows a schematic diagram of the experimental set-up. The two hot platens were brought very close to each other (~12mm) to provide a uniform temperature field. Two thermocouples located at different positions gave very close temperature measurements (Figure 2). The temperature difference between the two thermocouples was ~10 °C above 240 °C and ~20 °C below 240 °C. The curvature was monitored along with the temperature using a high resolution camera and data acquisition system during the cooling process.

Based on the bonding processes developed in our laboratory, three typical process cycles of PEEK/steel bonding and two typical process cycles of PEI/steel bonding were investigated, and were identified as cycle #1 through #5. Table 1 shows the basic processing parameters. For PEEK, its crystallinity and the process cooling rate were considered as important factors in designing the process cycles. The purpose of the process cycle #1 was to investigate a fast cooling process which resulted in very low crystallinity. The process cycle #3 was to simulate the residual stress effects of a slow cooling process which produced ~35% crystallinity by weight determined using differential scanning calorimetry (DSC) [2]. The process cycle #2 would produce approximately the same crystallinity as the cycle #3 but included a fast

cooling process from 210 °C to room temperature. The process cycles #4 and #5 are for amorphous PEI.

Using the experimental setup (Figure 1) and process cycles #1 through #5, the evolution of curvature with temperature produced in the steel substrate was measured. The curvatures with the elastic properties of the steel are used to calculate the residual stress in the film using [7]

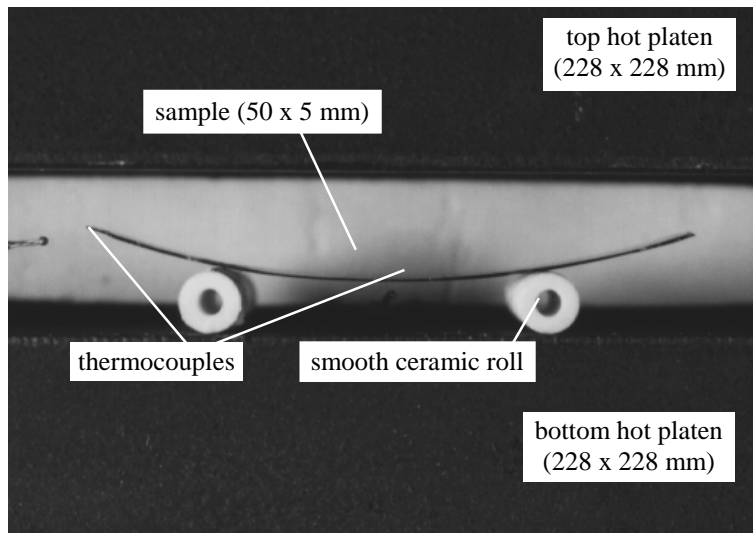


Figure 1 Experimental setup

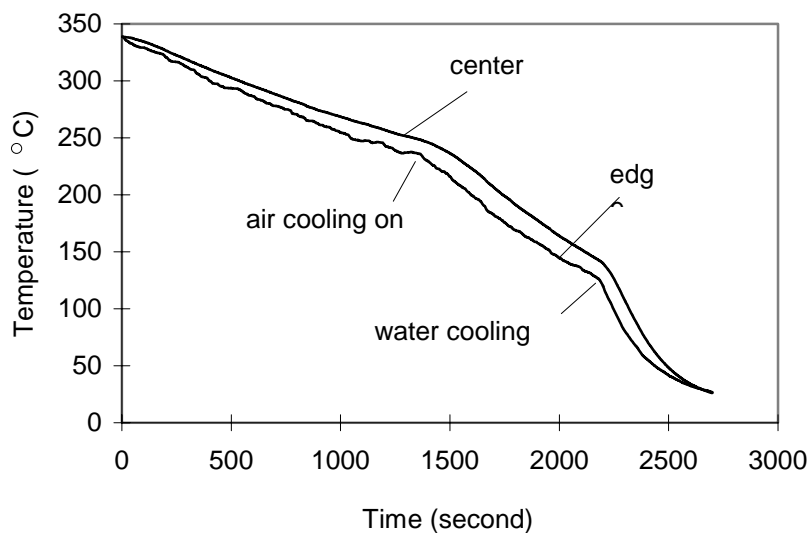


Figure 2 Temperature profile during cooling

Table 1 Polymer film-steel strip bonding process

Process cycle	Polymer	Bonding Processing parameters
#1	PEEK	heat to 370 °C, hold for 20 minutes, fast cooling (~30 °C/second) to room temperature
#2	PEEK	heat to 370 °C, hold for 20 minutes, slow cooling (~4.5 °C/minute) to 210 °C, fast cooling (~30 °C/second) to room temperature
#3	PEEK	heat to 370 °C, hold for 20 minutes, slow cooling (~4.5 - 10 °C/minute) to room temperature
#4	PEI	heat to 370 °C, hold for 15 minutes, fast cooling (~30 °C/second) to room temperature
#5	PEI	heat to 370 °C, hold for 15 minutes, slow cooling (~4.5-10 °C/minute) to room temperature

$$\sigma_i = \frac{E_m h^3}{6c(h+c)(1-\gamma_m)} \frac{1}{r(T_i)} \quad (1)$$

where σ_i : residual stress

T_i : temperature

E_m : elastic modulus of the steel strip

h : the thickness of the steel strip

c : the thickness of the polymer

$r(T_i)$: radius of the curvature

γ_m : Poisson's ratio of the steel strip

Obviously the curvature and residual stress will change during the cooling process. It will be shown in the modeling section that the curvature and residual stress development is not completely described by equation (1) alone.

Experimental Results

The residual stresses in the film calculated using equation (1) with measured curvatures are presented in Figure 3 for experimental process cycles #1 through #5 for PEEK and PEI. In Figure 3, the small standard deviations of the average residual stress results demonstrate the repeatability of the experiments. Errors in the experiments introduced by the measurements of temperature and curvatures were estimated below 15 percent. Comparing the experimental results of process cycle #1, #2 and #3 for PEEK, we can conclude that high crystallinity (corresponding to high elastic modulus) resulting from the initial slow cooling to 210 °C results in high residual stresses. Process cycle #2 produce higher residual stress than process cycle #3. For PEI, the residual stress difference between slow cooling and fast cooling is smaller compared to the corresponding difference in residual stresses for PEEK.

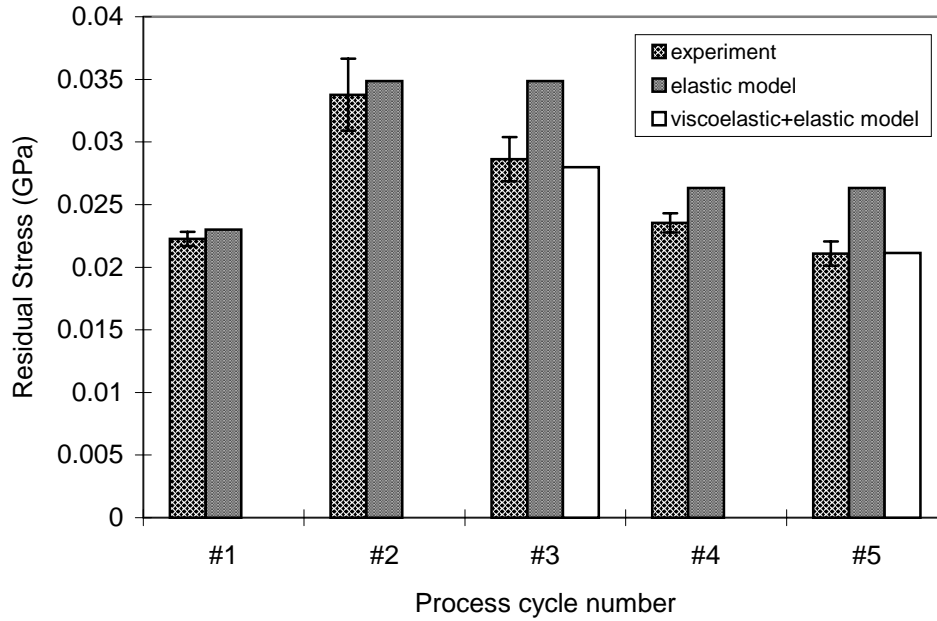


Figure 3 Residual stress comparison of experiments with model

The curvature change with temperature is shown in Figure 4 for PEI film-steel strip bonding and in Figure 5 for PEEK film-steel strip bonding. Both of them are obtained from slow cooling experiments (process cycle #3 and #5). The curvature as a result of residual stresses begins to develop at ~ 190 °C for amorphous PEI ($T_g = 210$ °C), but at ~ 255 °C for semi-crystalline PEEK ($T_g = 143$ °C).

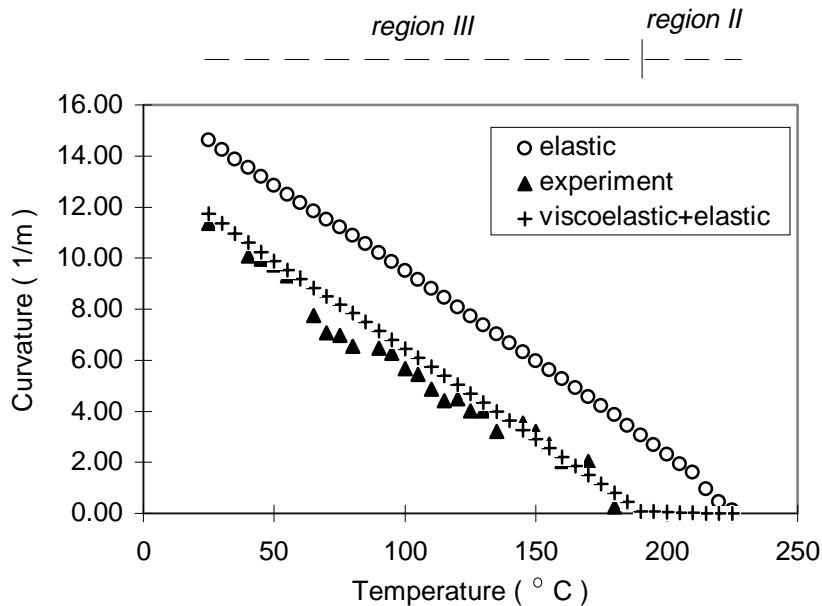


Figure 4 Curvature development of PEI film-steel strip bonding during slow cooling (process cycle #5)

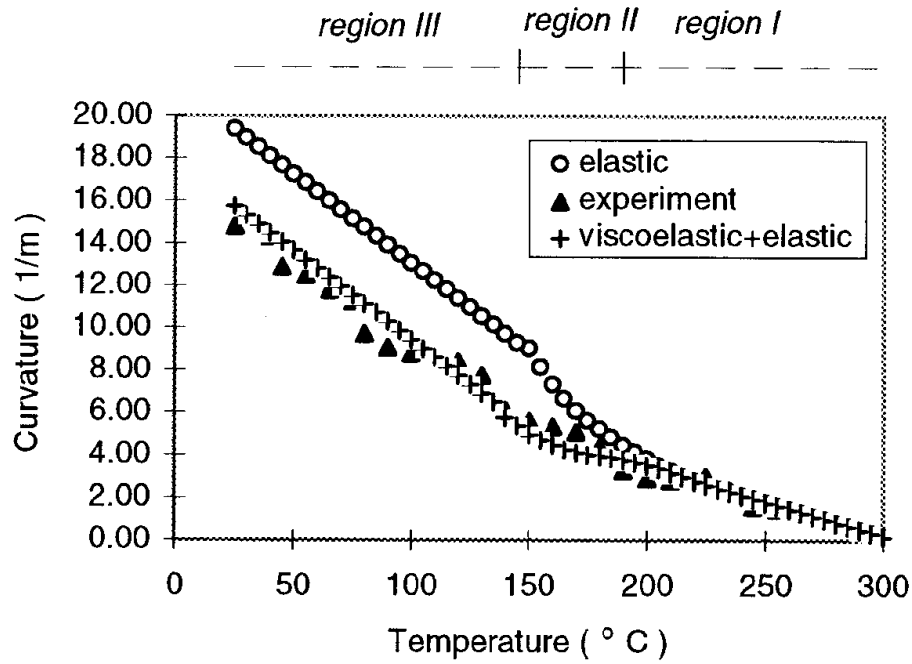


Figure 5 Curvature development of PEEK film-steel strip bonding during slow cooling (process cycle #3)

MODELING AND ANALYSIS

The residual stress is initiated by the differential thermal shrinkage between the polymer and metal. In the melt region, the polymer behaves as a viscous liquid and is considered to be in a stress-free state. As it is cooled down to its rubbery region, a curvature begins to develop. The development of the residual stresses during cooling is closely related to the elastic and viscoelastic properties of the polymer and the cooling rate. In this section, an elastic model is developed with potential applicability for a fast cooling process that allows little stress relaxation. For the slow cooling process, a Maxwell stress relaxation model was used to explain the residual stress development in the glass transition region. In addition, the shrinkage due to crystallization of PEEK was relatively small and neglected. The residual stress is assumed to be uniform along the whole length of the sample.

Elastic Model

An incremental elastic model is described below. At a temperature step T_i , the incremental stress $\Delta\sigma_i$ is generated by the incremental thermal strain $\Delta\varepsilon_i$

$$\Delta\varepsilon_i = (\alpha_p - \alpha_m)\Delta T_i \quad (2)$$

$$\Delta\sigma_i = -\frac{E_p(T_i)\Delta\varepsilon_i}{(1 - \gamma_p)} \quad (3)$$

where α_p : thermal expansion coefficient of the polymer

α_m : thermal expansion coefficient of the metal

$E_p(T_i)$: elastic modulus of the polymer at temperature T_i

γ_p : Poisson's ratio of the polymer

Adding this incremental stress to the previous stress σ_{i-1} , the present stress σ_i will be

$$\sigma_i = \sigma_{i-1} + \Delta\sigma_i \quad (4)$$

Considering the curvature-introduced contraction in the polymer [7], the present curvature will be

$$\frac{1}{r(T_i)} = \frac{\sigma_i}{\frac{E_m h^3}{6c(h+c)(1-\gamma_m)} + \frac{(h+c)E_p(T_i)}{2(1-\gamma_p)}} \quad (5)$$

The residual stress and curvature at each temperature step are calculated using equation (4) and (5). The actual residual stress at a temperature step is a little lower than the above calculated stress because of the curvature-introduced contraction in the polymer. The residual stresses are recalculated using equation (1) with the calculated curvatures from equation (5).

This elastic model is employed to calculate the curvature and residual stresses for all of our five process cycles. In Figure 3, it is shown that the elastic model matches the experimental results for process cycle #1, #2 and #4. However, the elastic model predicts higher residual stresses for process cycle #3 and #5 than the experiments. It is also noticed in Figure 4 and 5 that the calculated curvature using this elastic model begins to be higher than the experimental results in the glass transition region of the slow cooling process cycle #3 and #5.

Viscoelastic Model and Analysis

During a slow cooling process, three temperature regions are analyzed. *Region I* is above glass transition temperature of the polymer. The residual stress level is relatively low in region I because the thermal shrinkage results in a small strain and the elastic modulus of the polymer is also very low. Therefore, an elastic model successfully explains the curvature development in this range (see region I of Figure 5). However, in *region II*, the glass transition region, a rapid increase of the elastic modulus of the polymer can cause a large increase of the residual stress level. The residual stress level is close to the yield strength of the polymer in this region. A stress relaxation can be noticed in region II of Figure 4 and 5. In *region III*, below glass transition temperature, the elastic modulus of the polymer will not change significantly with temperature, but its yield strength will increase rapidly with temperature. The elastic model is satisfactory in region III. Figure 6 shows the comparison of the calculated elastic residual stress and the yield strength of the polymer during cooling.

The stress relaxation in *region II* depends upon the cooling rate. That is why a fast cooling in this region allows very little relaxation and the elastic model successfully predicts the corresponding residual stresses. Process cycle #2 of Figure 3 shows a comparison of the elastic model and experiments.

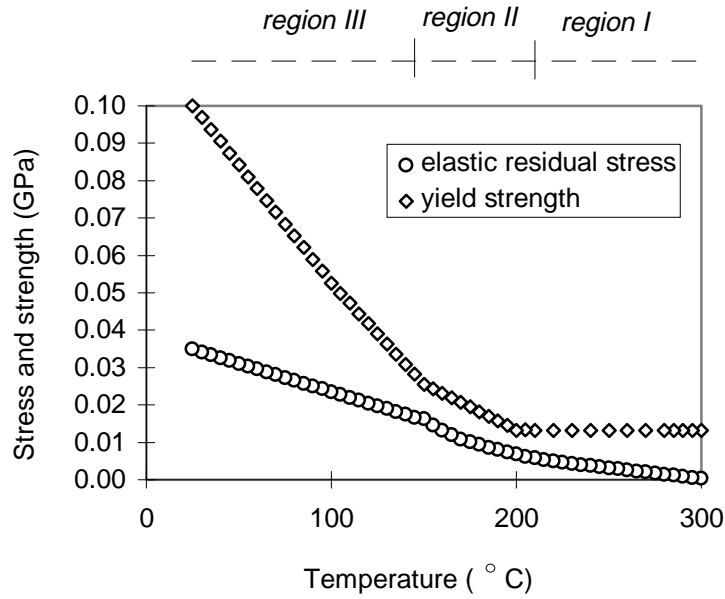


Figure 6 Comparison of calculated elastic residual stress with the yield strength of PEEK

The Maxwell model is combined with the Boltzmann superposition principle to analyze the stress relaxation in the glass transition region (*region II*). The stress relaxation begins at temperature T_b and ends at temperature T_e . For PEEK, $T_b = 210$ °C and $T_e = 140$ °C were determined through comparing the experimental curvature results with the calculated results using the elastic model. The residual stress σ_i at temperature T_i is

$$\sigma_i = \sigma_e + \Delta\sigma_I e^{-t_i/\tau_i} \quad (6)$$

$$\Delta\sigma_I = \Delta\sigma_i + \Delta\sigma_{I-1} e^{-t_{i-1}/\tau_{i-1}} \quad (7)$$

The σ_e is the residual stress at T_b and will not undergo relaxation. $\Delta\sigma_i$ is the residual stress increase from the previous temperature T_{i-1} to the present temperature T_i . The total stress $\Delta\sigma_I$ without σ_e will relax. t_i is the elapsed time at the present temperature step. τ_i is the relaxation time associated to the present temperature, which can be determined using the dynamic mechanical analysis (DMA) experiments.

$$\tan \delta_i = \frac{E''(T_i)}{E'(T_i)} = \frac{1}{\tau_i \omega} \quad (8)$$

where E'' : loss modulus

E' : storage modulus

$\tan \delta_i$: tangent of the phase angle

ω : measurement frequency

Biddlestone *et al.* [8] investigated the dynamic mechanical property of PEI. The dynamic mechanical properties of PEEK were obtained from Krishnaswamy *et al.* [9]. The parameters

for our models listed in Table 2 were obtained using ASTM standards by the polymer manufacturers.

Table 2 Materials' data

material	elastic modulus (GPa)	Poisson's ratio	thermal expansion coefficient ($10^{-5} / ^\circ \text{C}$)
PEEK (450G)	4.05 (~35 %) 2.70 (~0 %)	0.4	4.68 ($T < T_g$) 10.8 ($T > T_g$)
PEI (Ultem 1000)	3.30	0.36	5.58 ($T < T_g$) ~10. ($T > T_g$)
Steel	190	0.30	1.5

The elastic modulus of polymer is measured at room temperature.

(%) = crystallinity

Figures 4 and 5 compare the viscoelastic+elastic model, the elastic model and the experimental curvatures for PEI and PEEK in a slow cooling process. The viscoelastic+elastic model correctly explains the curvature development during the slow cooling process.

CONCLUSIONS

Based on development of beam curvature during cooling for an amorphous thermoplastic (PEI) and a semi-crystalline thermoplastic (PEEK), the experimental study combined with the model and analysis has resulted in the following key conclusions. First, the curvature experiments successfully reveal the residual stress development during thermoplastic bonding to metals. Second, the elastic model can be used to correctly predict the residual stresses for fast cooling processes (~30 °C/second). Finally, the viscoelastic+elastic model correctly predicts the curvature change and the residual stress development with temperature for slow cooling process (~4.5 - 10 °C /minute). The model developed and the results can be used in residual stress analysis and optimization of thermoplastic-metal bonding.

ACKNOWLEDGMENTS

The authors would like to acknowledge the NSF CAREER Award (DMI 9501646) and NSF Equipment Grant (DMI 9500232).

REFERENCES

- Ingram, C. and K. Ramani, *Int. J. Adhesion and Adhesives*, **17**(1), 39,1997.
- Ramani, K., J. Tagle, D. Devanathan, A. Nazre, D. Swarts, and S. Lin, *Polymer. Eng. Sci.*, **35**, 1972, 1995.
- Ramani, K., J. Tagle, D. Devanathan, A. Nazre, D. Swarts, and S. Lin., *ICCM-10*, **3**, 309, 1995.
- Ramani, K. and J. Tagle, *Polym. Compos.*, **17**(6), 879,1996.
- Moran, D. and P. Whitmore, *Mat. Res. Soc. Symp. Proc.* **52**, 293, 1995.
- Chapman, T., J. W. Gillespie, JR. and R. B. Pipes, *J. Compos. Mat.*, **24**, 616, 1990.
- Corcoran, E., *J. Paint Tech.* **41**, 635, 1969.
- Biddlestone, F., A. A. Goodwin, J. N. Hay and G. A. C. Mouledous, *Polymer*, **32**, 3119, 1991.
- Krishnaswamy, R. and D. S. Kalika, *Polymer*, **35**, 1157, 1994.

WELDABILITY AND HEAT AFFECTED ZONE (HAZ) EVALUATION FOR HIGH ENERGY RATE JOINING OF THERMOPLASTIC COMPOSITES USING MICROWAVES

H S Ku ¹, E. Siores ² and J.A.R. Ball ³

^{1,3} *Faculty of Engineering and Surveying,
University of Southern Queensland,
West Street, Toowoomba, 4350, Australia,*

² *School of Mechanical and Manufacturing Engineering,
Swinburn University of Technology,
PO Box 218, Hawthorn, Melbourne, 3122, Australia*

SUMMARY: Industrial microwave technology for processing polymers and polymer based composites is currently in a state of considerable flux. This paper extends the applications horizon of microwaves in the area of reinforced thermoplastic composites joining, and places emphasis on the development of equipment and facilities aiming at maximising bond quality. It discusses the microwave facility used, including a 0.8 kW variable control power generator operating at 2.45 GHz, waveguide and a tuning piston designed for obtaining a standing wave at the seam of the butted and lapped test pieces. The effect of power input and cycle time on the heat affected zone is detailed together with the underlying principles of test piece material interactions with electromagnetic field. The process of autogenous joining of 33% by weight of random glass fibre reinforced nylon 66, polystyrene (PS) and low density polyethylene (LDPE) as well as 23.3 % by weight of carbon fibre reinforced PS thermoplastic composites is mentioned together with developments using filler materials, or primers in the heterogenous joining mode. The weldability dependence on the dielectric loss tangent of these materials is also described.

KEYWORDS: complex relative permittivity, loss tangent, fibre-reinforced thermoplastic composites, microwave and peripheral facilities, short-circuit plunger, butted test pieces

INTRODUCTION

The general mechanisms [1] that govern the energy dissipation process and the microwave/material interaction include dipole friction, current loss and ion jump relaxation. The growth in using thermoplastic composites in structural materials remains very strong [2] and welding technology development fuels that growth. The advantages [3][4] of using thermoplastic composites over the frequently used thermosetting composites include their capability to be formed into complex shapes at lower costs and high productivity rates. Most

thermoplastic composites are joined by fusion bonding and the processes employed consist of resistance welding, ultrasonic bonding, vibrational bonding, high frequency welding, traditional infrared heated air, hot plate, hot melt and room-cure adhesives. The pros and cons of the above processes [2] were fully discussed and the frequency range [5] used in the high-frequency welding was 3 to 40 MHz which is in the radio frequency range. However, three papers on microwaves joining of thermoplastic composites [3][6][7] have appeared. The merits [3] of employing microwaves in joining thermoplastics composites include having a clean and reliable interface at the joints and fast joining time with minimum destruction of the properties of the bulk materials. Limitations encountered in other processes are avoided.

The prototype equipment used for the study is shown in figure 1. The microwaves generated from the magnetron are guided through WR340 waveguide to the test pieces. Avoiding radiation leakage is of primary concern and the welding process is enclosed within a microwave oven cavity so that microwaves will not radiate to the environment. Other possible risks of using the test rig and the materials are studied as well.

MICROWAVE AND PERIPHERAL FACILITIES

Equipment is built around a modified commercial microwave oven. The two magnetrons were removed from the original locations and one of them (0.8 kW) is relocated onto the top of the oven cavity via a piece of WR340 waveguide. Another piece of waveguide with slits opened for positioning the test pieces is placed upright in the oven cavity so as to avoid hazardous radiation. The upper end was fitted with a flange connected to the magnetron mounted on top of the oven. The lower end is similarly attached to an additional length of waveguide containing a shorting plunger.

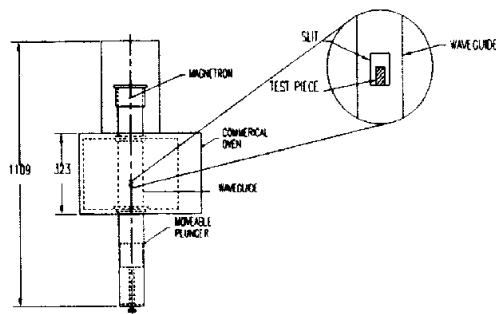


Figure 1: Microwave Facilities Configuration

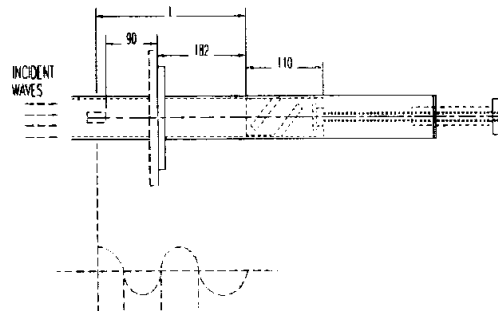


Figure 2: Stationary Wave in Waveguide

With reference to figure 1, the incident waves are generated by the magnetron. They travel downwards through three sections of WR340 waveguide and interact with the test pieces located in the second section before being reflected back by the top face of the adjustable plunger. The plunger was designed and manufactured to have a sliding fit contact with the waveguide. The interaction between the incident and the reflected waves sets up a standing wave [8] and it is desirable that the maximum electric field occurs at the seam of the butted and lapped test pieces. This was achieved by adjusting the moveable piston so that its top face is an odd multiple of $\lambda_g/4$ from the centre of the slit; where λ_g is the wavelength within the waveguide.

SHORT-CIRCUIT PLUNGER AND ITS DIMENSIONS

The relationship between the wavelength within the guide, λ_g and the free space wavelength, λ_o is as follows [8] :

$$1/\lambda_g^2 = 1/\lambda_o^2 - (1/2a)^2 \tag{1}$$

where a is the larger of the internal dimension of the waveguide and is in mm.

Using, the relationship $v = f\lambda_o$ (2)

$$\lambda_o = (3 \times 10^{11}) / (2.45 \times 10^9) = 122.45 \text{ mm}$$

For the waveguide used, WR340, a = 86.36 mm and b = 43.18 mm,

therefore, $\lambda_g = 173.63 \text{ mm}$ and $\lambda_g/4 = 43.408 \text{ mm}$.

Referring to figure 2, the distance between the centre of the slit and the top face of the plunger, l , was initially 286 mm. To create maximum electric field l has to be varied so that $l = n \times \lambda_g/4$ and n is an odd integer. If $n = 7$ is chosen then $l = 7 \times \lambda_g/4 = 7 \times 43.408 \text{ mm} = 303.9 \text{ mm}$. The distance, l , can be varied by adjusting the plunger up and down by rotating the knob at the bottom of the plunger. Hence, in order to have a maximum of electric field at the specimen, the plunger is adjusted by $303.9 \text{ mm} - 286 \text{ mm} = 17.9 \text{ mm}$ in the downward direction. This is the maximum electric field when the test pieces are at room temperature and this setting formed part of the initial set-up.

Leakage of power past the plunger is expected because of the sliding fit, and measures must be taken to prevent it. Any leakage is minimised by using a non-contact method to produce an apparent short circuit at the front face of the plunger. The actual point of contact is arranged to be at a point where the current is effectively zero. This is accomplished as shown in figure 3. At a distance of $\lambda_g/4$ from the top face of the piston [8], the traverse electric field, E has a maximum value and the traverse magnetic field H is zero. Thus the ratio of traverse components E/H is infinite at this point and hence the input wave impedance of a $\lambda_g/4$ length of waveguide closed at its far end is infinite. Similarly, the input impedance of a $\lambda_g/2$ length is zero. In practice, neither the infinite nor the zero values can be attained but it is convenient to assume so in practice.

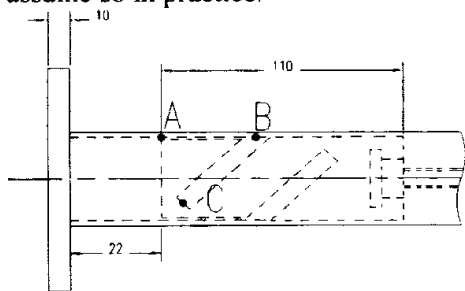


Figure 3: Moveable Plunger

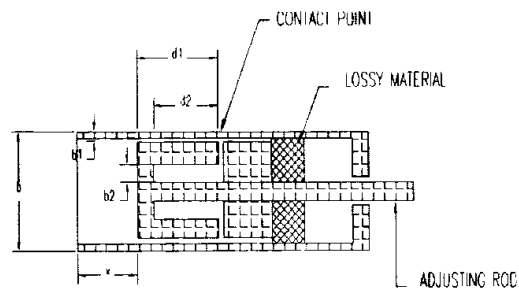


Figure 4: Non-contact Type Adjustable Short Circuit in Waveguide

In figure 3, the part ABC is regarded as a narrow waveguide of length $\lambda_g/2$ short-circuited at C and folded at its centre, B. Thus its input impedance at A is zero, and there is an equivalent short-circuit at the other side of the sliding fit. The piston therefore appears as a continuous short-circuit across the waveguide. The sliding contact occurs at B which is $\lambda_g/4$ from the end, point C. At point B, the impedance is high with small magnetic field [8] and the current is therefore small and radiation leakage through the sliding contact is therefore extremely small.

Variations in contact resistance with movement of piston are of little importance. Here actual physical short-circuits are replaced by virtual short-circuits and the physical contact made at a place where poor contact is not critical.

An example [9] for the dimensions of the moveable plunger is shown in figure 4, in which, $b = 20$ mm, $b_1 = 0.6$ mm $b_2 = 4.0$ mm.

Therefore in WR340, when $b = 43.18$ mm,

b_1 , by proportion, $= 0.6/20 \times 43.18$ mm $= 1.30$ mm and $b_2 = 4.0/0.6 \times 1.30$ mm $= 8.636$ mm.

Since the plunger has a sliding contact with the waveguide, the clearance between the two is made to be 0.5 mm. The angle of 45° was chosen for convenience of manufacture. The dimensions of the plunger are shown in figure 5.

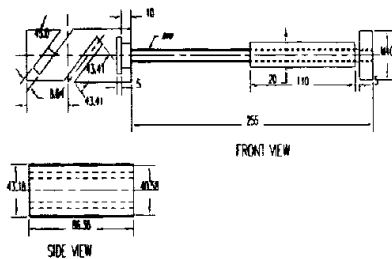


Figure 5: Dimensions of the Moveable Plunger

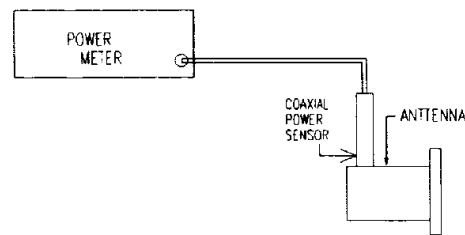


Figure 6: Set-up for Measuring Leakage

RISK ASSESSMENT

Of the risks involved in this research, radiation leakage from the equipment may be by far the most worrying to people nearby. Careful measures have been taken to cope with the problem. First, the magnetron is enclosed in a metal case on top of the microwave oven cavity enclosure so that microwaves can only travel downwards to and through the three sections of the waveguide to the top face (reflector) of the plunger. Virtually no radiation can leak through the case to the surroundings. Power leakage is expected and will be most serious through the slits into which the test pieces are inserted, but it does not propagate to the environment because it is contained inside the enclosure of the microwave oven cavity. Another possible leakage point may be the sliding fit between the moveable plunger and its sleeve as shown in figure 3, but the problem has been minimised by the non-contacting short circuit technique described previously. The end of the plunger waveguide is also covered up by a metal plate and radiation leakage to the surrounding is virtually zero. However, in order to check that the equipment complies with the recommended exposure limit [10] of 10 mW/cm², measurements of radiation leakage were made using power meter, power sensor and an antenna. A coaxial to waveguide (WR 340) adaptor was used as the antenna. The set-up is shown in figure 6. Measurements were taken at a distance of one (1) metre radius around the equipment, where an operator usually stands and that distance also satisfies the far-field distance [11] requirement of the antenna of 120 mm. In all positions, the power leakage was much less than 10 mW/cm².

The graphite fibre (GF) and carbon fibre (CF) filaments are embedded in the polymers and hence all the possible risks [12][13][14] associated with them do not apply in this case.

The next item to be considered was the graphite powder. Graphite powder can emit some dust when sprayed onto the test pieces. The powder may cause irritation to the eyes and when

inhaled it may lead to respiratory irritation. Goggle, disposable protective gloves and masks must therefore be worn when spraying is carried out. As the quantity used is very small, the problem is not serious. It can, however, flash when exposed to microwave energy and this in turn may set some types of polymer alight. A powder foam fire extinguisher is therefore installed in the nearby area for use in an outbreak of fire. The five minute two part adhesive [15] is poisonous and its contact with skin and eyes have to be avoided. Its vapour should not be breathed in. Protective gloves and goggles are to be worn while mixing and using it. The one part adhesive [16] should not come into contact with skin and eyes. It will bond on contact. Breathing in its vapour has to be avoided. Goggles and protective gloves have to be worn when using.

The next item to be discussed is the GF reinforced (33%) nylon 66; no adverse health effects should occur [17] if the product is handled in accordance with the product label. The test pieces are injection-moulded products and are not granules so they carry none of the risks [17] associated with granules. The material is combustible but has certain self-extinguishing properties [17]. The decomposed products include ammonia and carbon monoxide, so exposure to it must be in accordance with the National Occupational Health and Safety Commission [17]. The study was therefore carried out in a ventilated area. The next material to be mentioned is polystyrene (PS). The test pieces are moulded products and the risks [18] inherited by the granules do not apply here. The polymer will burn [18] when supplied with sufficient heat and oxygen and will emit toxic fumes when being burned with insufficient oxygen. The test area was therefore well ventilated. The last item to be discussed is low density polyethylene (LDPE), which will burn [19] in the presence of extreme heat and oxygen. A powder foam fire extinguisher is readily available for use if it catches fire.

MATERIALS MICROWAVES INTERACTION CONSIDERATIONS

High energy rate welding of thermoplastic composites using microwave was studied because it was believed that the microwave/materials interactions of some of thermoplastic composites with and without fillers will favour the process. The material properties of greatest importance [20] in microwave processing of a dielectric are the complex relative permittivity $\epsilon = \epsilon' - j\epsilon''$, and the loss tangent, $\tan\delta = \epsilon''/\epsilon'$. The real part of the permittivity, ϵ' , sometimes called the dielectric constant, mostly determine how much of the incident energy is reflected at the air-sample interface, and how much is absorbed. The most important property in microwave processing is the loss tangent, $\tan\delta$ which predicts the ability of the material to convert the absorbed energy into heat. For optimum microwave energy coupling, a moderate value of ϵ' , to enable adequate penetration, should be combined with high values of ϵ'' and $\tan\delta$, to convert microwave energy into thermal energy. In a material with a very high loss tangent, the microwave energy density will reduce with distance of penetration into the material. This phenomenon is known as the skin effect. For a material having a polar molecule eg water, the real and imaginary parts of the permittivity vary with frequency as shown in figure 7. Because of the skin effect, it may not be possible to work at the relaxation frequency. The 2.45 GHz frequency was chosen because it seems [21] that it has been the most popular choice for property measurement and the magnetrons for that frequency are most readily available.

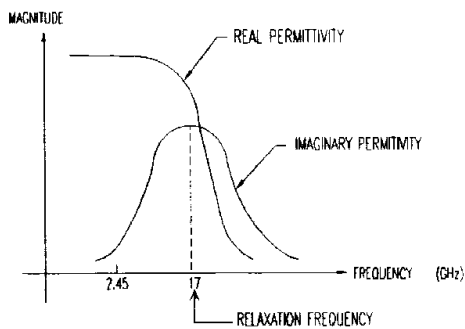


Figure 7: Dielectric Relaxation of Typical Polar Dielectric

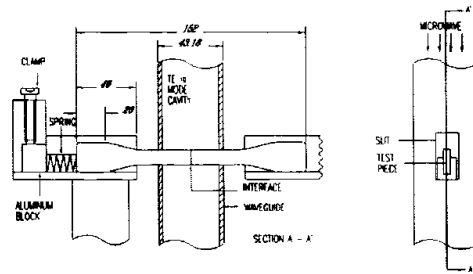


Figure 8: Test Pieces in Position

Random GF reinforced (33%) nylon 66 was chosen for the study because the loss tangent [22] of nylon 66 is high as compared with other commonly used thermoplastic materials. The composite is commercially available in Australia. Random GF reinforced (33%) LDPE was selected because there was a successful case [7] of welding the composite with HDPE as matrix using microwave energy and it was believed that LDPE will couple better to microwaves [20] as its crystallinity is lower than the HPDE. The composite is not readily available in the market and it was specially manufactured in Plastic and Rubber Technical Education Centre (PARTEC) in Brisbane, Australia. Polystyrene (PS) matrix was chosen because first, it is a common thermoplastic polymer matrix [23] and second, its loss tangent [22] is very near to that of LDPE and a comparison could be made later on. The random CF (23.3%) reinforced PS and the random GF (33%) reinforced PS were manufactured in PARTEC. In all cases, the length of the reinforcing fibre was 6 mm or less and the test pieces were injection-moulded to shape. However, typical lengths [24] of fibres used in reinforced injection moulding materials were 0.8 to 25 mm.

TEST PIECE MICROWAVE INTERACTION RESULTS

The two mirror image test pieces were cut using a band saw from a standard tensile test piece for composite materials. They were then located, spring loaded and clamped as shown in figure 8. The spring was made to push the two pieces when the interface was melted by microwave energy and weld them together. The spring force was kept to be about 10 N. With the exception of the CF reinforced PS, the test pieces gave no reaction to microwaves without filler. Graphite powder was then sprayed onto the interface of the test pieces of composites other than CF reinforced PS. The powder was made to stick to the interface by first smearing the latter with very small amount of one part adhesive. To enhance microwave absorption, the side faces of the test pieces, up to 20 mm from the interface were also sprayed with graphite powder. The power used was 240 W and the duration of exposure was 4 seconds for test pieces for all composites. During the first few welding trials, welding sometimes took place between the test pieces but at most of the time, the spring forced the test pieces to slip over each other due to the small interface area ($3 \times 10 \text{ mm}^2$). Even if they did weld, the bond strength obtained was very weak relative to the strength of the parent material.

To overcome the problem, the interface was roughened by rubbing it against a piece of coarse, grade 80, emery paper. The test pieces of all kinds of composites were then joined together by a small amount of one part adhesive. Graphite powder was again sprayed onto the side faces of the three types of materials as in the previous case. The composite test pieces were welded with 240 W power and 4 seconds of exposure time. The heat affected zone

(HAZ) for the CF reinforced PS was the part of the test pieces contained in the waveguide ie 21.5 mm from both sides of the interface and was on the upper part of them as shown in figure 9. When the exposure time was increased to 5 seconds, the spring forced the two pieces to bend to a vee- shape with the lower part of the joint being broken.

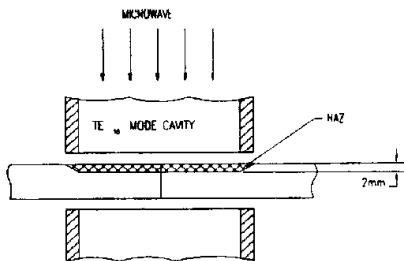


Figure 9: HAZ for GF/PS

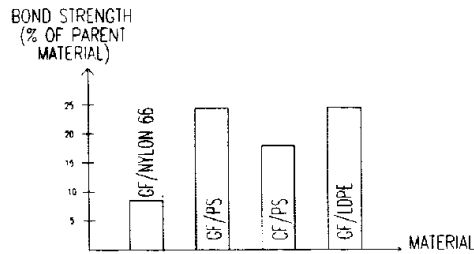


Figure 10: Bond Strength of the Weld

The test pieces of other materials had 20 mm from both sides of the interface as their HAZs and this was totally due to the amount of graphite powder sprayed. When the exposure time was increased to 5 seconds, the graphite powder flashed and burnt the test pieces. The graphite powder was over-heated and glowed as a result of ‘thermal runaway’ due to localised heating of the test pieces. Tensile tests were carried out with the successfully welded test pieces and it was found that the bond strengths of all materials ranged from 8.5 % to 24.3% of those of the parent materials. The results are shown in figure 10.

Shimadzu tensile testing machine was used for the test. A load range of 2000 N and a load rate of 600 N per minute were selected for the test. After being tensile-tested, the interfaces of the broken test pieces were investigated and the adhesive on the interface was ground away by a tool grinder. In PS/GF test pieces, black marks were observed on the grey interface and were estimated to occupy up to 45% of the interface area. The marks might be burning marks and looked similar to those found on the interface of the same material after the material was sawn using a metallic bandsaw. After removing several thin layers of the interface, the marks still appeared and might be as thick as 2 mm and it was deduced that the marks were left behind after the burning and melting of the composite and that welding of the material did happen but only up to 45% of the interface area. If this were taken into account, it could be argued that the bond strength of the welded part was up to 54% of the parent material. However, it was difficult to locate similar black marks on the same position in the case of welded nylon 66/GF test pieces because the base material was black. Similar black marks could also be traced with LDPE/GF test pieces and the corrected bond strength of the weld would be up to 48% of the parent material.

Another primer used was five minute two part adhesive containing 100% liquid epoxy and 8% amine, which was microwave reactive [20]. Butt joint was initially chosen for the welded connection between the two tensile test pieces. Bond strength measurements were not taken. Thermal runaway gave rise to slippage between the butted interfaces and the partially bonded test pieces were discarded. Lap joint was then selected for the connection of the two tensile test pieces. GF/PS was first selected for the study. The lapped area was made to be 20 mm x 10 mm. The lapped areas were first roughened by rubbing them against coarse, grade 80, emery paper. They were then cleaned by immersing them in methanol and allow to dry in air before applying primer onto them. After applying the filler, the two pieces were tightened by a rubber band, which encircled the lapped areas four times as depicted in figure 11. This is to fix the relative position between the two test pieces and to apply pressure onto the lap joint.

The pressure on the lap joint was estimated to be 4 N and it was critical as the bond strengths of the test pieces cured by leaving them in ambient conditions for 16 hours [15] with and without the rubber band pressure were 611 N and 335 N respectively.

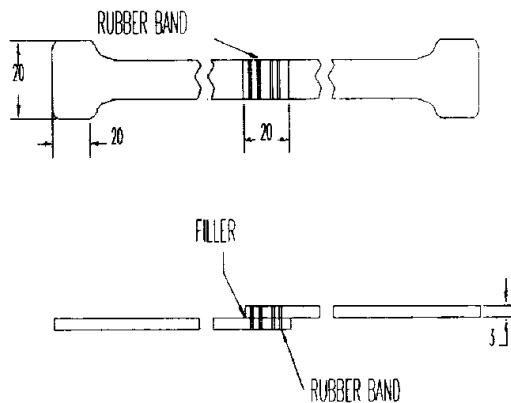


Figure 11: Test Pieces with Lap Joints

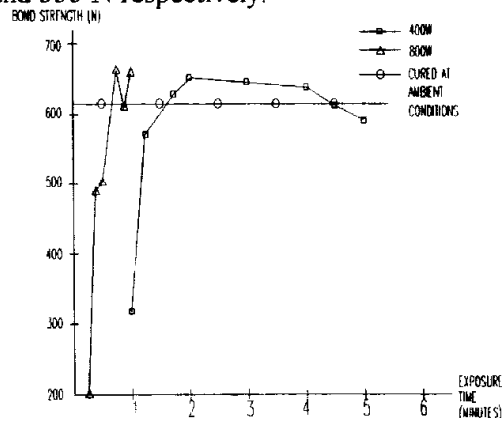


Figure 12: Bond Strength of GF/PS and Five Minute Two Part Adhesives

After tightening with rubber band, the two halves of the test pieces were positioned in the slot across the waveguide similar to the situation illustrated in figure 8 except they stood there themselves with no clamping. The test pieces were then exposed to two different power levels of 400W and 800W with varying time of microwave exposure. In all cases, only the parts smeared with filler were warmed or heated depending on the power level used and the time of microwave exposure. The test pieces were allowed to cool to room temperature or below 60°C [15] before being tensile tested to obtain maximum bond strength. The results are summarised in figure 12.

With reference to figure 12, it was found that with 400 W power level, peak bond strength was achieved by exposing the test pieces to microwave for 2 minutes; the bond strength at this exposure duration exceeded that obtained by ambient conditions (conventional) curing by 7% but the time required was a mere 0.2% of its counterpart. Between the duration of one and a half to four and a half minutes, the bond strengths of microwave cured filler were higher than those obtained by allowing the adhesive to set under ambient conditions. With a power level of 800 W, maximum bond strength was achieved when the exposure time was 45 seconds and it exceeded the still air cured bond strength by 8%, but the time required was only 0.08% of its counterpart. The lower bond strengths obtained, for test pieces exposed to microwaves for over 2 minutes and over 45 seconds for power levels of 400 W and 800 W respectively, may be due to over-cured of the adhesive.

With some exposure durations, the bond strengths were higher than those cured conventionally because the parent material might have melted and diffused into the primer or interface and this was reflected in the softening of the lapped area after it was just removed from the applicator and examined using low power microscope. The HAZ seemed to be confined to the lapped area, which could be bent by hand easily and outside which the warming and heating effect of microwave energy could not be felt. The tensile tests revealed that sixty percent of the failures were due to the adhesive and took place at the joints. The remaining failures took place at the original materials (GF/PS), which had an average strength of 1423 N. With a power level of 400 W and exposure time of 2 minutes, the highest bond strength achieved was 720 N; while with a power level of 800 W and exposure time of 45 seconds, the peak bond strength obtained was 905 N and they were 18% and 48% respectively stronger than the test pieces cured in ambient conditions. The values of '18%' and '48%' reveal the importance of power

level used and it can be argued that the higher the power level used, the more efficient is the processing method.

CONCLUSIONS

From the pilot study, it seems that graphite powder was not a suitable filler because it flashes too easily. It also tended to contaminate and discolour the test pieces. Carbon fibres, however, can still be used as reinforcing agents because most of the unwanted HAZs in the test pieces can be masked by microwave reflective materials, leaving only the parts that need to be exposed to microwave energy. The current 5 minute two part adhesive would be used as primer for welding other composites. Other two part adhesive that contain epoxy and polyamide, and epoxy constituents and nonyl phenol plus 2-piperazin-1-yl-ethylamine, all of which [20] are microwave energy reactive, have been identified and will be used in the future research studies as filler material to enhance the microwave/material coupling potential.

The equipment will be further developed to accommodate a directional coupler and adaptors for measuring the power consumed in joining the composite test pieces, thermopiles for monitoring the temperature at the interface during welding, two electric field probes, and two electric motors to drive the piston continuously so that maximum electric field can always be maintained at the point where the interface of the butted test pieces is, as the temperature of test pieces varies during welding. The shape of the test pieces will also be modified so that the areas of the interface will be larger to prevent slipping. This consists of using specially designed lap joint for tensile test piece. Impact tests will also be incorporated to the study. The number of types of materials to be tested will be increased to include CF and GF reinforced thermoplastic polyurethane (TPUR) as the plastic contains hydroxyl and cyanate groups [20] which are reactive to microwave energy.

The potential benefits of the technology will be to speed up the replacement of thermosetting resins by advanced thermoplastic composites in the structural parts of aeronautical, military and recreational industries

REFERENCES

1. Siores, E., "Microwave Technology for Welding and Joining", *Materials World*, Vol. 2, No. 10, 1994, p.526.
2. Schwartz, M.M., *Composite Materials Handbook*, McGraw-Hill, 2nd edition, 1992, pp.6.55-6.
3. Varadan, V.K. and Varadan, V.V., "Microwave Joining and Repair of Composite Materials", *Polymer Engineering and Science*, Mid-April, Vol. 31, No. 7, 1991, pp. 470 - 486.
4. Partridge, I.K., *Advanced Composites*, Elsevier Applied Science, 1989, pp. 44-6.
5. Schwartz, M.M., *Joining of Composite-matrix materials*, ASM International, 1995, p. 64.
6. Stokes, V.K., "Joining Methods for Plastics and Plastic Composites : An Overview", *Polymer Engineering and Science*, Mid-October, Vol. 29, No. 19, 1989, pp.1310-24.

7. Wu, C.Y. and Benatar, A., "Microwave Joining of HDPE Using Conductive Polyaniline Composites", Proceedings of Society of Plastics Engineers. 50th Annual Technical Conference, 1992, pp. 1771-4.
8. Glazier, E.V.D. and Lamont, H.R.L., Transmission and Propagation, The Services' Textbook of Radio, Volume 5, London, Her Majesty's Stationery Office, 1958, pp. 151-7, 174-7, 197 - 9.
9. Rizzi, P.A., Microwave Engineering Passive Circuits, Prentice Hall, 1988, pp. 320-1.
10. Jacques, T., Microwaves: Industrial, Scientific and Medical Applications, Artech House Inc., 1992, pp. 503, 558.
11. Balanis, C.A., Antenna Theory, Analysis and Design, John Wiley & Sons Inc., 2nd ed., 1992, pp. 32-4, 58-9.
12. Luce, S, Introduction to Composites Technology, SME, 1988, pp. 35-7.
13. ACI Fibreglass, Material Safety Data Sheet (MSDS) for fibreglass, 1987, pp. 1-2.
14. Gougeon Brothers, Inc., MSDS for graphite fibres, undated, pp. 1-5.
15. Selleys Araldite, five minute epoxy adhesive user instructions, Selleys Chemical Company Pty. Limited.
16. Selleys Fix 'n' Go, Supa Glue user instructions, Selleys Chemical Company Pty. Limited.
17. ICI Plastics, MSDS for GF reinforced (33%) nylon 66, undated, pp. 1 -5.
18. Dow Chemical (Australia) Ltd., MSDS for polystyrene, 1994, pp. 1-4.
19. Kemcor, Australia, MSDS for LDPE, Kemcor Australia, 1995, pp.1 -4.
20. National Research Council, Microwave Processing of Materials , National Advisory Board Commission on Engineering and Technical Systems, National Research Council, 1994, p.7, 100, 105.
21. Metaxas, A.C. and Meredith, R.J., Industrial Microwave Heating, Peter Peregrinus Ltd., 1983, pp.43, 278.
22. Michaeli, W., Plastics Processing, Carl Hanser Verlag, Munich Vienna New York, 1995, pp. 189-90.
23. Shackelford, J.F., Introduction to Material Science for Engineers, 3rd., Macmillan, 1994, p.486.
24. Strong, A.B., Fundamentals of Composite Manufacturing : Materials, Methods and Applications, Society of Manufacturing Engineers, 1989, p.143.

JOINING OF THERMOPLASTIC COMPOSITES BY BOLTS AND MICROWAVE WELDING

M. Jauss¹, R. Emmerich², P. Eyerer^{1,2}

¹*Institute for Polymer Testing and Polymer Science, University of Stuttgart, Pfaffenwaldring 32, D-70569 Stuttgart, Germany.*

²*Fraunhofer Institute for Chemical Technology, Joseph-von-Fraunhofer-Str. 7, D-76327 Pfinztal (Berghausen), Germany.*

SUMMARY: The paper gives a contribution to the joining of thermoplastic composites by bolts and by microwave welding. It is based on two studies dealing with tests of bolted joints and the development of a new microwave welding process. Dimensioning of bolted joints and tests to examine the behavior of bolted joints for three thermoplastic composite materials with different matrices and configurations are discussed in the first section. Especially the influence of clamping by washers on the transferable loads is examined. The second section gives an overview to the microwave welding process. The potential of the microwave welding process is shown in order to get a further welding technology for plastics and their composites.

KEYWORDS: thermoplastic composites, joining, bolt, welding, microwaves

INTRODUCTION

High performance composites based on thermoplastic matrices are a well-suited alternative to steel or aluminum sheets for the high volume production of structural lightweight parts. Compared to metals they offer good weight specific properties. A one-step high speed processing technology leads to very short cycle times (less than 1 minute). Processing pressures are much lower than those to form metal sheets. This reduces investment costs for the production equipment distinctly. The efficient use of thermoplastic composites for structural applications requires reliable joining technologies to assemble parts of identical and different materials. One possibility is to adapt technologies from thermoset composites. But low-cost requirements and specific properties of thermoplastic composites require to adjust established or develop new technologies, respectively.

Joining methods for plastics and their composites can broadly be classified into mechanical fastening, adhesive bonding and welding [1]. Mechanical fastening is the most commonly used method to assemble structural parts of different materials. Like adhesive bonding it is used for joining all materials including metals. Parts joined by mechanical fastening and adhesive bonding need not to be of the same material. Welding is limited to thermoplastics and takes advantage of their ability to be reprocessed.

Basic material properties for thermoplastic composites have already been established but data related to specific applications and secondary technologies like joining by bolts are not available [2]. Load introduction into composites by bolted joints causes high stress concentrations. The manufacturing of the holes weakens the material. However, compared to adhesive bonded and welded joints they offer low cost, ease of manufacture and reliability [3]. Bolted joints can easily be disassembled but decrease weight-specific efficiency of structural parts. Large area joints like adhesion bonding or welding have a more uniform load introduction and add less weight to the structure. Concerning to costs and ease of manufacturing welded joints favor thermoplastic composites. Microwave welding is a new process and has the potential to get a further technology for joining plastics and their composites. In the first section of the paper the behavior of bolted joints in glass fabric reinforced thermoplastic composites with and without axial clamping for selected joint geometries and laminate configurations is examined. The second section gives an overview to first tests of joining thermoplastic composites by microwave welding.

JOINING BY BOLTS

Dimensioning

The design of bolted joints is based on four parts: joint geometry, fastener placement, stresses and failure modes. Typical joint geometries are single or double lap shear joints. Single lap joints bend under tensile loading [3]. For this study a bolted joint testing device in double lap shear geometry was constructed to prevent bending of the samples as source for failure. The device allows for bolt diameters between 5 and 10 mm and tests with and without axial clamping (Fig. 1). In this study only bolts with 8 mm diameter were examined.

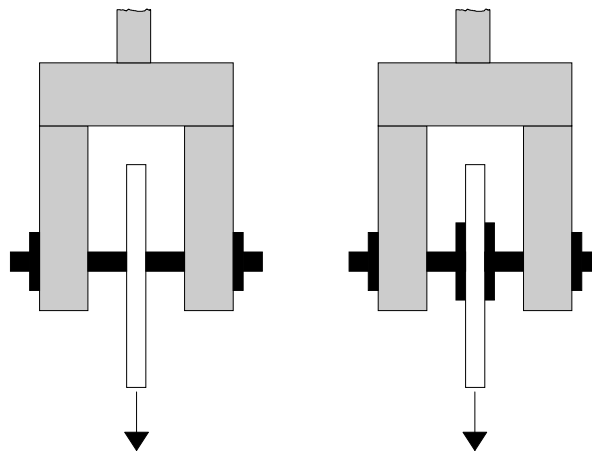


Fig. 1: Bolted joint testing device with and without axial clamping

Axial clamping with washers improves load transfer significantly. STOCKDALE assumes a sturdy tightened preload on the washers to double the transferable load. A maximum preload increases it four times [4]. This is caused by two effects: clamping affects as delamination protection, and load introduction is changed from single form lock to a combination of form and friction lock caused by the axial compression. For the distinct creep behavior of thermoplastics the maximum preload is limited for longtime applications.

Fastener placement is critical to the load transfer into the composite part. It influences stress distributions and the occurring of failure modes. Geometric parameters for design and placement of bolted joints are the bolt diameter d , the specimen width w , distance e of the bolt center from the free end and the laminate thickness t (Fig. 2). P is the load attained during the test. These parameters in combination with the fiber orientation determine the dominating failure mode.

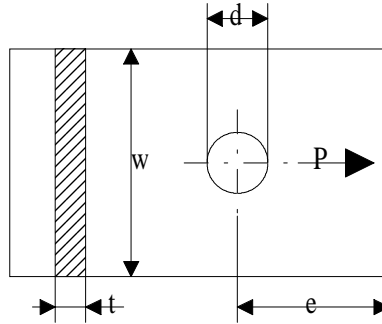


Fig. 2: Geometric parameters of bolted joints

A basic rule for the design bolted joints in composites says that the specimen has to fail by bearing to have well defined structural and geometric conditions. Load transfer results from the pressure on the bearing. Criteria for the design are bearing strength and notch toughness of the laminate. Bearing strength depends on fiber orientation, shear strength of the matrix and the delamination protection. 0° fibers increase bearing strength but decrease notch toughness, $\pm 45^\circ$ fibers increase notch toughness but decrease bearing strength. A combination of this is expected to reach optimum load transmission [5]. General guidelines recommend a ratio $e/d \geq 3$ and $w/2d \geq 3$ for the proper design of bolted joints [6].

Common properties determined by tests of bolted joints are bearing strength σ_b , tensile strength σ_t in the reduced cross-section and shear strength τ given by Eqn 1 to 3 [2]:

$$\sigma_b = \frac{P}{td} \quad (1)$$

$$\sigma_t = \frac{P}{(w-d)t} \quad (2)$$

$$\tau = \frac{P}{2et} \quad (3)$$

Four possible failure modes appear for bolted joints in composites: bearing, tension, shear-out and cleavage (Fig. 3). Bearing failure occurs when the composite fails in compression and the bolt hole elongates. Shear-out and cleavage failures are due to shear and transverse tensile failure of the composite laminate. Tensile failure occurs when the material around the hole can not support the applied tensile loading due to its reduced cross section and stress

concentrations [3]. In general, a combination of these failure modes occurs dependent on the design of the geometric parameters.

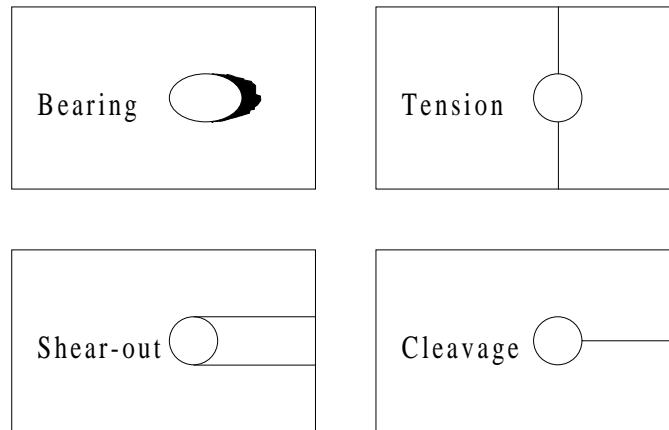


Fig. 3: Failure modes of bolted joints in composites

Experimental

Three woven glass fabric reinforced thermoplastic composite materials with different matrices were tested: Polypropylene (PP), Nylon 6 (PA6) and Nylon 12 (PA12). For the Nylon 12 structure two configurations were available: a homogeneous laminate layer structure which was used for the other matrix materials, too, and a sandwich structure with woven glass fabric reinforced facings and a glass mat reinforced core. The materials were processed either by double belt press or by hot pressing. The bolt holes in the specimens were manufactured by a standard twist drill. Plastic washers have been used to prevent delamination caused by the twist drill.

The bolted joint testing device was installed on a universal testing machine. The free end of the specimen was fixed by hydraulic clamps. The tests were performed by a deformation speed of 3 mm/min to measure load versus deformation. The specimens are tested either without clamping or with sturdy tightened clamping. The washer diameter was three times the bolt diameter. For these test methods two typical load-deformation curves occur (Fig. 4 and 5).

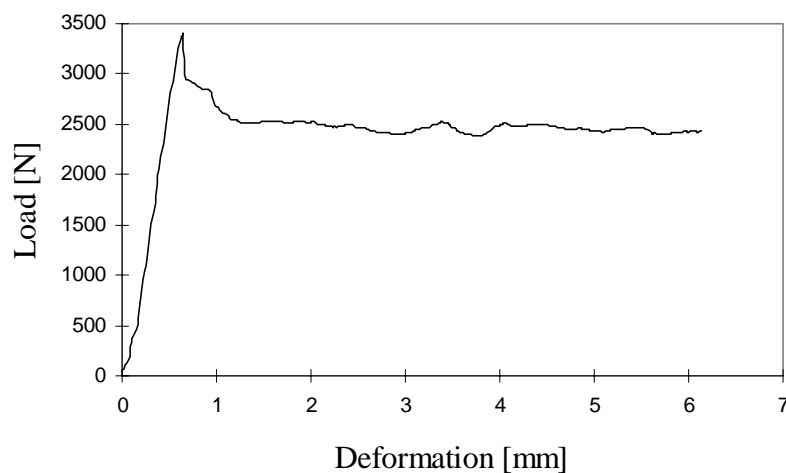


Fig. 4: Typical load-deformation diagram for bolt tests without clamping

Based on recommended dimensioning ($e/d = 5$; $w/2d \geq 3$) bearing occurs as typical failure mode for tests without clamping. For lower distances w tension failure mode was also observed. The bearing and tensile stresses as well as the shear stress are easily to determine. The first peak gives the load P for Eqn (1) to (3). For some specimens the load to failure increased over the first peak load.

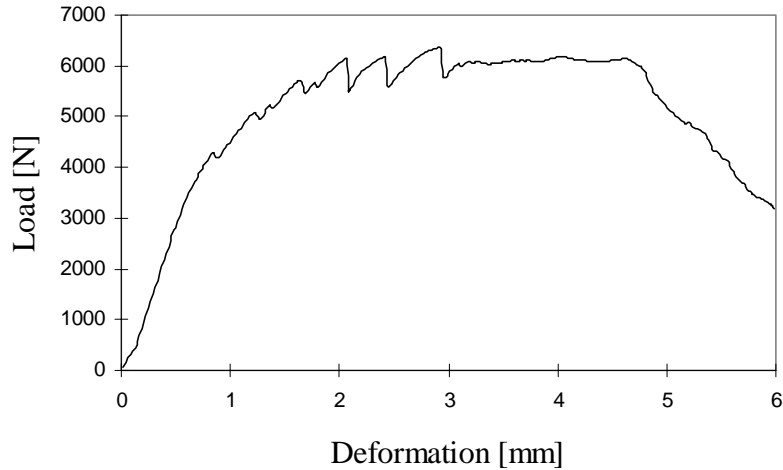


Fig. 5: Typical load-deformation diagram for bolt tests with sturdy tightened clamping

The specimens tested with sturdy tightened clamping failed in a combination of failure modes resulting from the complex three dimensional stress distribution in a wide area of the specimen. The load-deformation diagram shows many peaks due to the stepwise failing of the material (Fig. 5). Therefore the evaluation is more complex and needs to be done referring to a standardized method. The standard DIN 65562 evaluates as follows: the first peak yields the load of the bearing strength of the first hole elongation. The maximum peak represents the maximum bearing stress, the maximum tensile and shear stress. For the inaccuracy of this method the resulting maximum loads of the tests are compared instead of the bearing strengths (Table 1). The transferable load for sturdy tightened clamping is about twice the load without clamping due to delamination protection and additional friction locked load transfer.

Table 1: Maximum loads, [N] (8 mm bolt diameter; $0^\circ/90^\circ$ fiber orientation)

Testing Parameters	PP-Laminate	PA6-Laminate	PA12-Laminate	PA12-Sandwich
No Clamping	3180	3810	3210	2350
Sturdy Clamping	7000	6880	6530	4900

Evaluating bearing stresses following the above mentioned guidelines yields same results (Table 2). The clamped specimens exhibit the double bearing strength as non-clamped specimens.

Transferable loads do not differ much between laminates with different matrix materials. The sandwich material withstands lower loads and bearing stresses than homogeneous laminates. This results from the high content of weaker glass mat reinforced core material. Lower stress concentrations because of random orientated fibers in the core are dominated by higher stress concentrations in the glass fabric reinforced facings. Failure occurs in the facings by tension mode, delamination of facing and core layer, and by bearing.

Table 2: Bearing strength, [Mpa] (8 mm bolt diameter; 0°/90° fiber orientation)

Testing Parameters	PP-Laminate	PA6-Laminate	PA12-Laminate	PA12-Sandwich
No Clamping	198	238	200	147
Sturdy Clamping	438	430	408	306

The influence of geometric parameters and fiber orientation on transferable loads is shown in Table 3. Variation of width w does scarcely influence bearing strength but failure modes. Specimens with low ratio $w/2d$ fail by tension mode, that with higher ratio by bearing mode. Specimens having a $\pm 45^\circ$ fiber orientation reach higher stresses than those having $0^\circ/90^\circ$. The $\pm 45^\circ$ fiber orientation decreases stress concentration peaks in the hole areas. Failure sources are reduced. This emphasizes the critical stress concentrations as failure sources especially for 0° fiber orientations.

Table 3: Bearing strength for variations of testing parameters, [Mpa] (8 mm bolt diameter, no clamping)

Testing Parameters	PA12-Laminate	PA12-Sandwich
$w/2d = 1.5; e/d = 5; 0^\circ/90^\circ$	215	131
$w/2d = 3; e/d = 5; 0^\circ/90^\circ$	209	161
$w/2d = 5; e/d = 5; 0^\circ/90^\circ$	200	147
$w/2d = 5; e/d = 5; \pm 45^\circ$	230	166

MICROWAVE WELDING

Basics

Meltability of thermoplastic composite matrices allows for a variety of joining methods based on welding, e.g. ultrasonic welding, vibration welding or high frequency welding. A new innovative method is welding by microwaves. Microwaves are expression for electromagnetic waves with frequencies between 300 Mhz and 300 GHz. The microwave welding process is based on two mechanisms: polar friction and eddy current heating. Polar molecules are excited by an alternating electromagnetic field and dissipate energy by internal friction. Free charge carriers in conductive materials are accelerated and generate eddy currents in alternating electromagnetic fields dissipating energy. Microwaves heat volumetric and uniform throughout the material [7]. The interaction of a material in a microwave field is

governed by the dielectric loss property. The temperature rise ΔT of materials in a microwave field is given by [8]:

$$\Delta T = \frac{\omega t F^2 \epsilon_0 \epsilon''}{\rho c_p} \quad (4)$$

ω is the angular frequency of the field, t the time of exposure, F the intensity of the electric field, ϵ_0 the electric field constant, ϵ'' the dielectric loss factor of the material, ρ the density and c_p the heat capacity. Typical microwave generators have a frequency of 2.45 GHz. Dielectric loss factor and heat capacity are material properties and depend on temperature and frequency, respectively.

Welding Tests

Heating of pure polymers by microwaves requires a polar molecular structure which may vary in a wide range. Some polymers are microwave transparent, some absorb energy very well. In order to control the heat dissipation in the welding zone, a welding agent with well defined dielectric properties is recommended. A polar modification of the welding agent based on compatibility to the welded polymers is difficult. Possible polar additives may function as separation agents, too. Therefore, it is more advantageously to modify the agent with respect to a certain conductivity. The welding agent used for this study was modified with respect to conductivity using carbon black.

Thermoplastic composites have a low matrix content in the surface and the fibers are not weldable. To receive good welding results it is important to have enough matrix material in the welding zone. Therefore, the use of a welding agent is not only for heating control but also for the supply of matrix material in the welding zone. The welding process of thermoplastics itself is based on temperature and pressure. Pressure causes a flow of the melt for good contact.

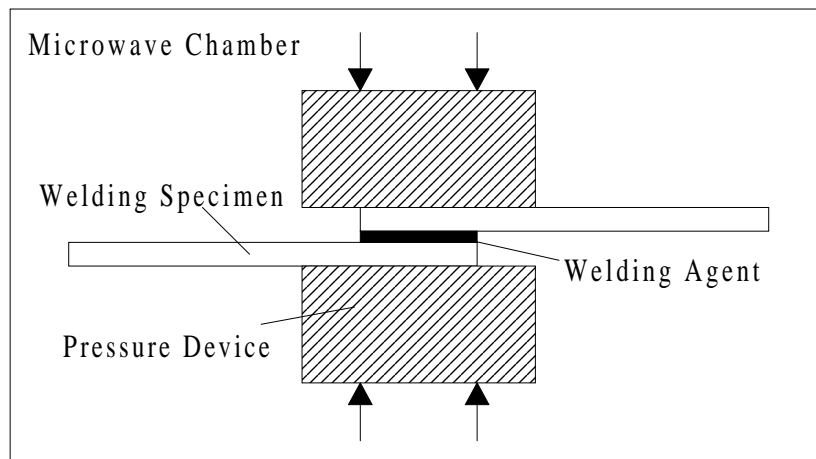


Fig. 6: Principle arrangement of microwave welding

The welding tests were performed in a standard microwave chamber constructed for cooking. The power is adjustable between 0.34 kW and 1.7 kW. A pressure device of microwave transparent material fixes and compresses the specimens with a load of about 400 N. The device allows for an elastic compensation of reduced material thickness when molten. Three woven glass fabric reinforced thermoplastic composite materials with different matrices

(Polypropylene, Nylon 6, Polyethyleneterephthalate) were used for the examinations. The test specimens were taken out of sheets having the dimension 140 to 110 mm². The sheets were welded in single lap geometry with 20 mm overlap. The principle experimental arrangement of the microwave welding device is shown in Fig. 6.

The welded specimens were cut into stripes of 15 mm width. The lap shear strength was determined in a modified tensile test using a universal testing machine with hydraulic clamps (Table 4). Deformation speed was 2 mm/min. The Polypropylene composites show the best shear strength. Polypropylene is microwave transparent and the modification of the welding agent results in a homogeneously dissipating material. Nylon 6 and Polyethyleneterephthalat have a certain polarity disturbing the welding process. The welding agent is difficult to modify in order to achieve homogeneous energy dissipation. This is to be optimized in future.

Table 4: Average lap shear strength for microwave welded specimens, [MPa]

Material	Lap Shear Strength
Polypropylene (PP)	16.8
Nylon 6 (PA6)	12.8
Polyethyleneterephthalate (PET)	10.2

Vibration welding of the Polypropylene composite material yields an average lap shear strength of about 10 MPa. This demonstrates the potential of microwave welding for plastics and their composites.

CONCLUSIONS

Thermoplastic composites joined by bolts and tested for double lap geometry show typical load-deformation behavior and failure modes dependent on the applied geometric parameters. Clamping affects significantly the transferable loads. Sturdy tightened clamping by washers doubles the transferable loads compared to specimens without clamping. This is due to delamination protection and additional load transfer by friction. The same occurs for bearing stresses evaluated for first peak loads. Typical failure mode for tests without clamping are bearing, with clamping a combination of various failure modes. Different matrix materials have not much influence but the orientation of the fiber reinforcement. Samples having +/- 45° fiber orientation withstand higher bearing stresses than those having 0°/90° orientation. This results from lower stress concentrations as sources for failure. Additional work is to be done to get further understanding on the influence of all parameters.

Meltability of thermoplastic composites allows for joining methods based on welding. Microwave welding is a process based on either dissipating energy by internal friction of polar molecules moving in the alternating electromagnetic field or dissipating energy by generating eddy currents. A welding agent is necessary for good welding results because of heat control and adding matrix polymer to compensate the low matrix content in the surface of the composite sheets. Welding tests with a welding agent modified for conductivity showed good results especially for Polypropylene. Compared to vibration welded specimens the microwave specimens reach nearly the double lap shear strength. This demonstrates the potential of microwave welding for plastics and their composites.

REFERENCES

1. Stokes, V. K., "Joining Methods for Plastics and Plastic Composites: An Overview", *Polymer Engineering and Science*, Vol. 29, No. 19, 1989, pp.1310-1324.
2. Walsh, R., Vedula, M. and Koczak, M. J., "A Comparative Assessment of Bolted Joints in a Graphite Reinforced Thermoset vs. Thermoplastic", *Sampe Quarterly*, July 1989, pp. 15-19.
3. Benatar, A., "Joining of Polymeric Composites", *Proceedings of Manufacturing International*, Publ. by ASME, NY, USA, Vol. IV, 1988, pp. 141-153.
4. Stockdale, L. H. and Matthews, F. L., "The effect of clamping pressure on bolt bearing loads in glass fibre reinforced plastics", *Composites* 7, No. 1, 1976, p.34.
5. Bergmann, H. W., *Konstruktionsgrundlagen für Faserverbundbauteile*, Springer-Verlag, Berlin, New York, Tokyo, 1992.
6. Michaeli, W. and Wegener, M., *Einführung in die Technologie der Faserverbundwerkstoffe*, Hanser-Verlag, München, Wien, 1989.
7. Siores, E., Do Rego, D., "Microwave Applications in Materials Joining", *Journal of Materials Processing Technology* 48, 1995, pp. 619-625.
8. Metaxas, R. C. and Meredith, R. J., *Industrial Microwave Heating*, IEEE Power Engineering Series 4, Peter Peregrinus Ltd., London, 1983.

ENERGY ABSORBING COMPOSITE JOINTS AND THEIR APPLICATION TO NOISE REDUCED SONAR DOMES.

J R House

*Structural Materials Centre, Defence and Evaluation Research Agency
Holton Heath, Poole, Dorset, BH16 6JU, United Kingdom.*

SUMMARY: This paper concerns the noise and vibration advantages of an energy absorbing composite joint and its relevance to noise reduced glass reinforced polyester (GRP) sonar domes. Once installed on an operational boat, hydrodynamic flow and supporting structural induced vibrations cause the dome to vibrate thus radiating noise and interfering with sonar sensor response. The results of a vibration transmissibility study on a glass reinforced polyester/steel interface are discussed as the first step in designing a composite viscoelastic joint that can act as a vibration sink to absorb flow generated and structureborne noise within GRP sonar domes. Preliminary investigations concerning the absorption of compressional waves by use of a tapered viscoelastic interlayer are discussed. It is shown that a tapered viscoelastic interlayer placed between a GRP beam and steel supporting substrate can produce a significant absorption of vibrational energy, reducing waterborne radiated noise and providing a significantly quieter noise platform than conventional sonar jointing technology.

KEYWORDS: composite joints, energy absorption, noise reduction, damage tolerance, fatigue resistance.

INTRODUCTION

Sonar systems are now used for a variety of applications whether it be for the detection of enemy ships in naval applications, sub bottom profiling in oceanographic surveys or for fish location and identification. Those sonar systems are invariably enclosed within a dome fabricated in Glass Reinforced Polyester (GRP) composite.

For effective operation it is essential that the sonar platform be as free from noise and vibration as possible. However, one potential source of sonar platform noise is the dome itself. Flow induced noise and that generated within the supporting structure can cause the dome itself to generate waterborne sound and interfere with the sonar sensors. It is suggested that one way of reducing this interference may be by the incorporation of a viscoelastic interlayer between the dome and supporting structure to act as an acoustic sink to all structureborne vibrations in this area.

The purpose of this paper is to present some preliminary laboratory findings obtained from the use of tapered viscoelastic interlayers between GRP/steel interfaces. It is known that for typical sonar dome thicknesses and sonar operational frequencies it is the compressional waves and not the flexural waves that are the dominant source of noise. Thus as a first stage this investigation the concerns compressional waves only.

BACKGROUND

Essentially the problem of acoustic interaction at the joint between a GRP sonar dome and its (often) steel supporting structure can be outlined as follows. Turbulent-flow induced energy can couple into the GRP dome. That vibrational energy will propagate along the GRP until the steel joint interface is reached where one or a combination of effects occur:

- (a) vibrational energy is reflected back along the GRP, mode conversion possibly taking place, the compressional waves in particular being free to radiate as waterborne sound into the sonar sensor space.
- (b) energy is transmitted through the joint into the steel supporting structure. However, more importantly energy in the form of compressional and/or flexural waves from the steel support side can propagate into the GRP where once again the compressional waves are free to radiate into the sensor site and acoustic energy will be emitted at the impedance discontinuity caused by the dissimilar materials of the GRP/steel interface.

The acoustic interaction at a simple joint between dissimilar materials has been studied in [1-3] so it is not intended to discuss this in detail here. Briefly, the references show that high vibrational reflection losses* can be obtained at a GRP/steel interface provided the joint input impedance is matched. This is generally coupled with a low transmission loss*. Conversely, it is possible to obtain a high transmission loss but at the expense of a good reflection loss. In all these cases vibrational energy is not lost or absorbed but merely redirected or altered by mode conversion. An alternative approach is to provide a joint that actually absorbs the energy. It is suggested that this may best be achieved by use of a viscoelastic polymeric interlayer between the GRP and steel to act as an acoustic sink .

THE VISCOELASTIC JOINT

It can be shown theoretically [2] that the reflection and transmission loss for compressional waves at or across a two layer interface is dependant on the input impedance of the second layer, this is given by the following transmission line equation:

$$Z_{in} = Z [(Z_1 \cosh(\alpha+jk)x + Z \sinh(\alpha+jk)x) / (Z \cosh(\alpha+jk)x + Z_1 \sinh(\alpha+jk)x)] \quad (1)$$

where Z_{in} = the input impedance at the joint interface

Z_1 = the characteristic impedance of the termination

Z = the complex characteristic impedance of the layer (joint)

x = the thickness of the layer α = the attenuation constant of the layer

k = the wave number ($2\pi f/c$) c = the complex wave velocity

f = the frequency

This has been incorporated into a computer program which will model single and multilayer laminar structure.

Use of the multilayer programme demonstrated that a simple solid viscoelastic polymeric interlayer does not have the ideal characteristic impedance for a vibration sink. This is because the polymer is not being allowed to deform or worked upon in such a way as to make

maximun use of its viscoelastic nature. The polymer needed to be more compliant and this was best achieved by the inclusion of air into the polymer thus making it in the form of a closed cell foam. A subprogram was used to allow the incorporation of compliant inclusions such air bubbles to modify the wave velocity and density and hence its characteristic impedance. Kerners theory ^[4] has been used to calculate the effective wave velocity of the polymer assuming prior knowledge of the bulk modulus, dynamic shear modulus, poissons ratio and volume fraction of air.

Thus:

$$c_{eff} = \sqrt{[(K_{eff} + 4\mu_{eff}/3)/((1-\phi)\rho)]} \tag{2}$$

$$\text{where } K_{eff} = [(K(1-\phi)/(1+3k\phi/4\mu)] \tag{3}$$

$$\mu_{eff} = [\mu/1+(\phi/15(1-\sigma)/((1-\phi)(7-\sigma)))] \tag{4}$$

where: K = polymer bulk modulus K_{eff} = effective bulk modulus of the layer

μ_{eff} = effective shear modulus of the layer ϕ = volume fraction of air

σ = Poisson's ratio of polymer ρ = polymer density

μ = polymer shear modulus

The values of μ and K are of course complex but for simplicities sake K has been taken as real for all frequencies. The Poisson's ratio is assumed to be 0.4996 (i.e. a typical value for unfilled rubbers).

A prediction using this model is shown in figure 1, illustrating reflection and transmission loss as a function of frequency for a simple polymeric laminar interlayer.

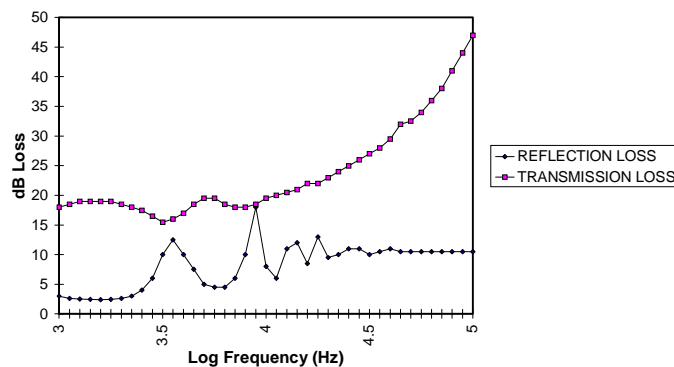


Fig. 1: Reflection and transmission loss at GRP/Steel Interface with interlayer.

The interlayer between the steel and GRP is a nitrile rubber layer (AML3186) 250mm thick. The predictions assume the rubber has a 0.02 volume fraction of air typical for most rubber mouldings. This material has been selected deliberately as it is known to be in the middle of its molecular mainchain transition region (i.e. highly viscoelastic) over the temperature range 0 to 15C at frequencies between 1 to 20kHz (3 to 4.3 on log scale). Its dynamic physical properties of the polymer are shown in figures 2 and 3.

Clearly illustrated in figure 1 are the reflection loss peaks which occur at multiples of half wavelengths and are indicative of layer with a wave velocity of 1700m/s. These peaks are seen to be narrow band below 12kHz (4.08 on log scale) with low reflection loss minima of only 4dB at ~6kHz. Broadband reflection loss of 10dB is only achieved above 20kHz. This layer may only be useful in the high frequency range where the layer contains many multiples of half wavelengths. The transmission loss, never falls below 17dB above 1kHz (3 on log scale). It would be possible to improve the low frequency performance of this layer by making it thicker, thus inducing the halfwave resonances at lower frequencies. However, this may be impractical and the best compromise may be to make the layer three half wavelengths thick as per the prediction in figure 1

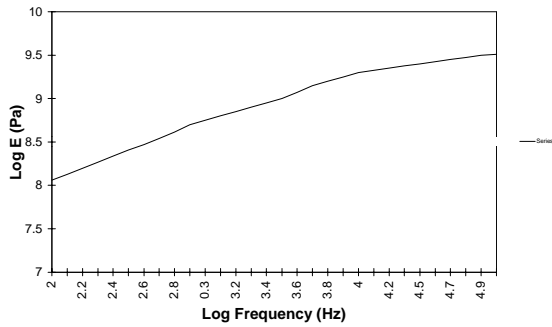


Fig. 2: Dynamic Youngs Modulus

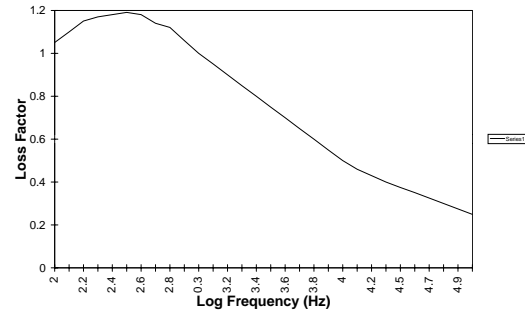


Fig. 3: Loss Factor

where it has been set for 12kHz. One technique for overcoming the narrowband reflection loss at low frequencies is that of geometric impedance matching. This is a popular technique used in the design of anechoic linings for non-reverberant acoustic chambers. It involves the shaping of the layer in the form of a wedge such that the compressional waves in the GRP enter the viscoelastic layer gradually. Theoretical treatment of wedges is not trivial but a simple approximation may be made by assuming the 250mm layer to be divided into 16 layers as shown in figure 4.

Each layer is assumed to be 10mm thick consisting of part GRP and part viscoelastic polymer, the ratio of GRP to viscoelastic polymer gradually decreasing until it is entirely polymer. The all polymer layer (layer No 1) is 100mm thick. A linear law of mixtures can then be applied to calculate the characteristic impedance of each layer thus:

$$Z_L = Z_{GRP}\phi_{GRP} + Z\phi \tag{5}$$

where Z_L = characteristic impedance of the composite layer

Z_{GRP} = characteristic impedance of the GRP.

Z = characteristic impedance of the viscoelastic polymer.

ϕ_{GRP} = volume fraction of GRP in the layer.

ϕ = volume fraction of viscoelastic polymer in the layer.

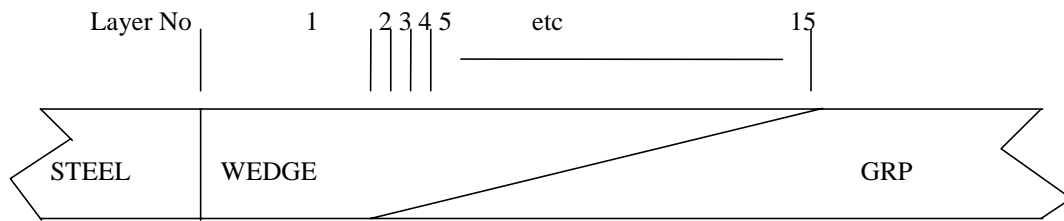


Fig. 4: Composite viscoelastic wedge as modelled

Tapering the joint in this way not only improves the impedance matching of the layer but also provides a more structurally sound joint by allowing a larger surface area for bonding. Results for this form of joint are shown in figure 5.

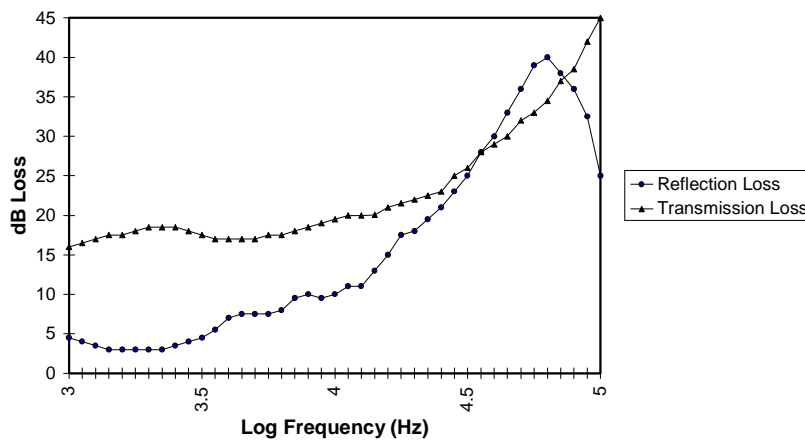


Fig. 5: Transmission and reflection loss for viscoelastic wedge joint.

The reflection loss is now 10dB from 8kHz and above and the dips have now been eliminated. The transmission loss is still good with less evidence of the thicknesswise resonances. In fact tapering the joint layer in this way has resulted in a shift of the halfwave resonances to higher frequencies in this case from 3.4kHz to 4.4kHz. These results looked sufficiently encouraging to investigate a practical version of the joint.

A Practical Joint

For this exercise investigations were carried out on simple GRP beams 70mm wide by 25mm thick. The joint as constructed, consisted of a wedge of a high density (density - 1700kgm^{-3}), 80 IRHD nitrile rubber. The tapered part was 150mm long backed by a layer 100mm long and 50mm thick as shown in figure 6. To improve the joint structural integrity, a groove 6mm wide and 135mm deep was cut into the base of the wedge. The wedge was then bonded to a corresponding steel tongue which is in turn bolted to a steel beam.

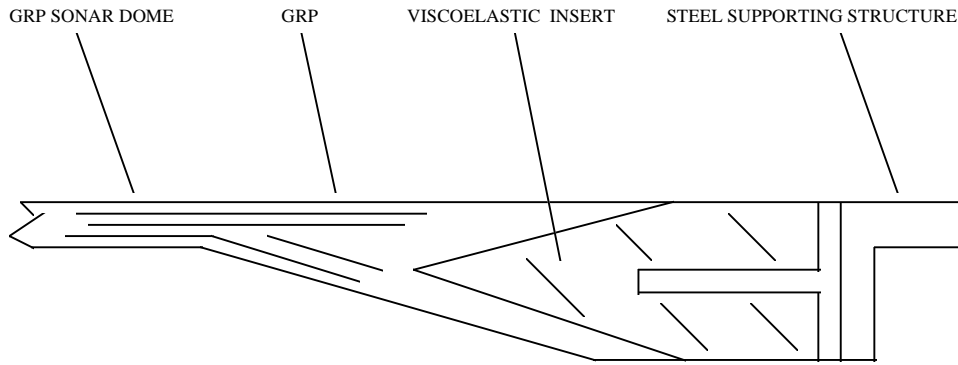


Fig. 6: The composite viscoelastic wedge as tested.

Experimental Assessment

The experimental tests have divided into two parts:

- (a) Assessment of structureborne compressional waves.
- Waterborne noise radiation assessment.

Structureborne Assessment

This was intended to confirm, at least in trend, the predictions made above. The assessment was carried out at a temperature of 10C (bearing in mind the temperature sensitivity of the dynamic physical characteristics of the polymer) using the instrumentation illustrated in fig.7. A small transducer was attached end on to the GRP beam (in such a way as to excite compressional waves) with a lightweight accelerometer attached alongside. The transducer was excited with tone bursts where the tone frequency was varied between 5 to 12kHz. The accelerometer was used to monitor the burst after it had reflected from the far end of the beam with the joint attached. The reflection loss was established by comparing the returned signal with that from a similar sized GRP beam with no viscoelastic joint (assuming that to be perfectly reflecting).

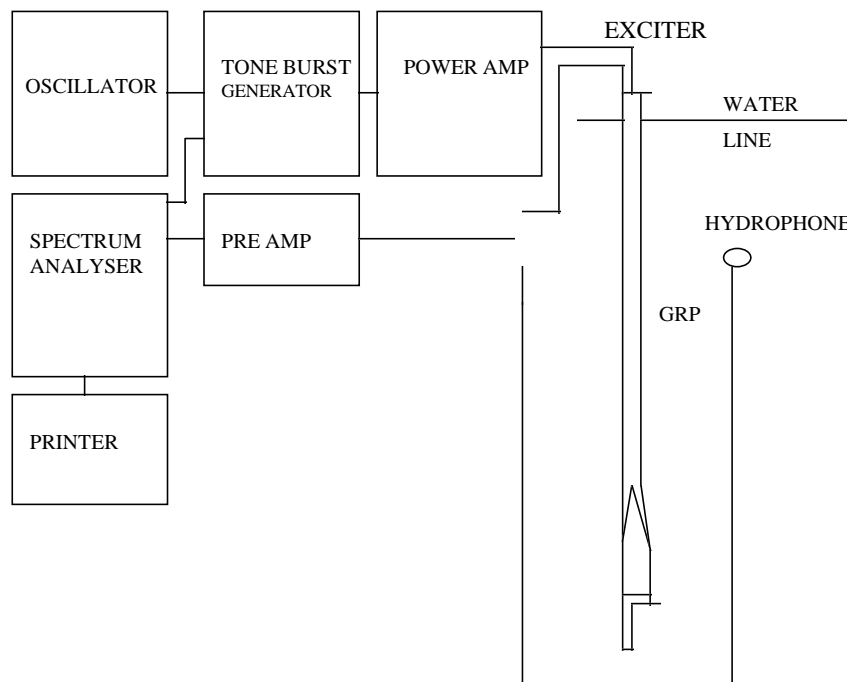


Fig. 7. Instrumentation used for investigating joint noise radiation characteristics

The transmission loss was established by comparing the acceleration levels at the far end of the plain GRP beam to that across the joint at the end of the steel beam (the actual attenuation loss along the steel was measured to be much less than 0.25dB).

Waterborne Measurements

These measurements were intended to provide a qualitative assessment of the noise radiation characteristics of various joint configurations. In this case the same instrumentation was used as before, except the accelerometer was replaced by a small probe hydrophone. This was mounted on a traversing mechanism that allowed it to scan the length of the beam and joint 150mm from the face of the beam. The complete GRP beam, joint and steel substructure were then suspended vertically in an acoustic water tank facility until the top of the GRP beam with transducer were just proud of the water surface. The transducer was then excited with 10kHz tone bursts and the hydrophone used to monitor the signal radiated from various positions along the beam and joint. This test was carried out for waves travelling from both the GRP to Steel and Steel to GRP, the latter case being carried out by inverting the configuration and bonding the transducer to the end of the steel beam.

RESULTS AND DISCUSSION

Reflection loss for the wedge joint is shown in figure 8. The results indicate a loss of more than 10dB above 6kHz rising to around 16.5dB at 12kHz. This is slightly higher than predicted and probably due to the forementioned inaccuracies of the predictive model and the fact that for practical reasons the wedge as constructed is not identical to that theoretically modelled. However, the general trend is comparable. Also shown for comparison purposes are the measured results for a straight forward GRP/steel butt joint and a joint where the GRP/steel interface has been tapered at an angle of 10degrees. As seen the GRP/steel butt joint is the worst case; the impedance mismatch between the GRP and steel is large hence the majority of the compressional wave energy is reflected back up the GRP. This joint provided a reflection loss of only 2dB at all frequencies tested. The tapered GRP/steel interface provided an improvement in reflection loss of typically 3 to 5.5dB over the frequency range 5 to 12kHz. The reason for this is that the tapering provided a gradual transition of the input impedance allowing more compressional wave energy to be transferred to the steel beam.

Measured transmission loss results are shown in figure 9. Once again the best performance was obtained from the viscoelastic joint which provided a transmission loss of more than 18dB from 6kHz upwards. This was again similar in trend at least to that predicted. The GRP/steel butt joint provided transmission loss of around 7dB due purely to impedance mismatch at the joint interface. The GRP/steel tapered joint interface has the worst transmission loss and indicated that although it provided a high reflection loss, it was at the expense of transmission loss, there was no actual absorption of compressional waves.

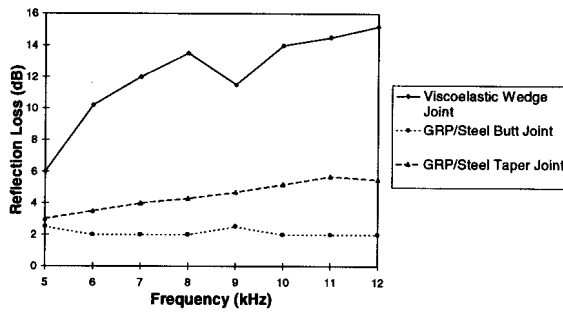


Fig. 8: Reflection loss

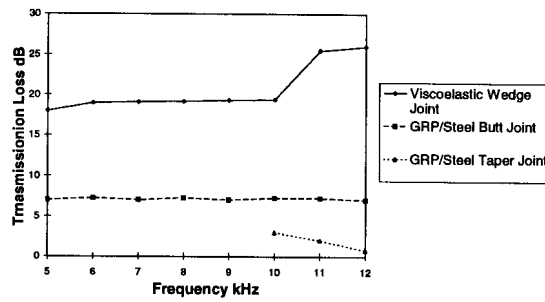


Fig. 9: Transmission loss

Waterborne Noise Radiation Characteristics

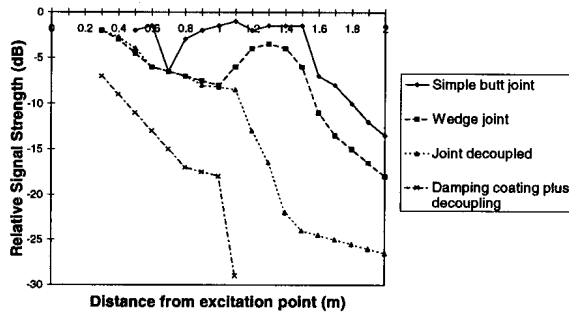


Fig. 10: Noise transmission GRP/steel

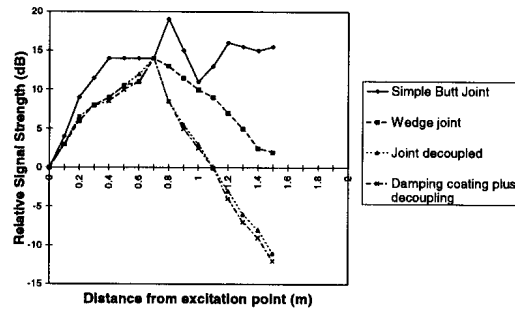


Fig. 11: Noise transmission Steel/GRP

The waterborne noise radiation characteristics are illustrated in figure 10 for the case where the compressional wave is propagating from GRP to steel. This would simulate the compressional waves generated by turbulent flow energy around a GRP sonar dome. The Y axis represents the radiated signal strength (as sensed by the hydrophone) at a point along side the GRP beam. The GRP/steel interface is ~1.40m from where the beam is being excited. The X axis represents the hydrophone position from the the excitation point alongside the beam. Also illustrated for comparison purposes are the noise radiation characteristics for a GRP/steel butt joint. As anticipated the butt joint is the worst case. The noise signal levels radiated from the GRP are typically ~-2dB except around the position 0.7m from the excitation point. Here there there is some constructive interference of the incoming tone burst and with that reflected at the GRP/Steel interface. Beyond the GRP/steel interface the radiated noise levels are reduced. This is because not all the compressional wave energy has been transmitted across the joint into the steel beam. With the viscoelastic wedge insert there is little constructive interference. As might be expected, close to the excitation point the radiated signal levels are about the same but further along the GRP beam at 1.0m from the excitation point, the radiated noise levels are some 8dB lower. However, at the joint itself there is an increase in the joint noise radiation characteristics again due to the impedance discontinuity at the joint interface. It is nevertheless some 3dB lower than the butt joint in this area. The noise

radiating from the joint can be isolated by application of an acoustic decoupling layer in the form of a thin layer of closed cell foam across the joint area. Further improvements to the reduction of radiated noise was achieved by application of a compressional wave damping material to the GRP.

The results for the compressional waves propagating from steel to GRP (this would be equivalent to ship structure-borne noise) are shown in figure 11. In all four cases the a high noise radiation hot spot is identified immediately behind the joint. The worst case is the butt joint where noise levels on the GRP side are high and dominated by that radiated by the joint itself. The inclusion of the viscoelastic wedge reduced the noise levels by up to 10dB on the GRP side compared to the butt joint. However, further improvements were obtained with the application the decoupling material and compressional wave damping material.

CONCLUSIONS

A simple study has been made into the use of a viscoelastic joint to reduce potential noise sources in GRP sonar domes. The study concerned the reduction of noise emitted by compressional waves, generated by (a) turbulent energy around the GRP dome and (b) structureborne vibrations from steel supporting structure. A simple predictive model and experimental measurements have confirmed the effectiveness of a viscoelastic interlayer in reducing compressional waves noise problems in the GRP when placed between the GRP and steel. The tests show that if the layer is tapered to the GRP in the form of a wedge 150mm long backed by a layer of the same material 100mm thick, the following results are obtained:

- (a) compressional waves propagating along the GRP are effectively terminated by the viscoelastic wedge, thereby reducing reflection of compressional waves back up the GRP; noise radiation from this source will therefore be reduced.
- (b) the viscoelastic wedge presents a considerable transmission loss to compressional waves travelling fro the steel supporting structure to the GRP once again providing a much quieter GRP structure than one incorporating a simple butt joint.
- (c) the noise reduction capabilities of a viscoelastic joint can be further enhanced by application of a decoupling layer to the joint and a compressional wave damping material to the GRP.

Together conclusions (a) and (b) indicate that as result of the use of the viscoelastic wedge insert compressional wave energy was effectively absorbed, i.e. little energy was reflected at the joint interface and little was transmitted across. The radiated noise characteristics were much lower than those of conventional butt joint technology. However, from the point of view of providing a quiet sonar dome, additional benefits were obtained by application of an acoustic decoupling coating to the joint area and compressional wave damping material to the GRP itself.

Although this work was carried out specifically to improve sonar performance and only compressional wave excitation has been considered, there are many implications for an energy absorbing joint of this nature. Its use in composite construction of mass transport vehicles could provide a much quieter environment for passengers. Furthermore, by considering shock and impact as dynamic events in the frequency domain and tuning the viscoelastic characteristic accordingly it may be possible to provide more damage tolerant composite structures.

GLOSSARY OF TERMS

Transmission Loss	$20\log$ (input acceleration/transmitted acceleration)
Reflection Loss	$20\log$ (input acceleration/reflected acceleration)

REFERENCES

1. Power J. "Energy Transmissibility Aspects of Joint Designs" Plessey Marine Company Ltd. Technical Note No. 69/80/353.
2. Cremer L, Heckl M. and Ungar E. "Structureborne Sound". Springer-Verlag, Berlin, Heidelberg, New York.
3. Hibbert J H. "Consultancy Investigation in Relation to Admiralty Marine Technology Establishment" Salford University, United Kingdom.
4. Kerner E. "The Elastic and Thermoplastic Properties of Composite Media", Proc Phys Soc LXIX, 8-13, pages 808 - 813.
5. Brehovskikh L. "Waves in Layered Media", Academic Press, 1960.

THE DESIGN AND MANUFACTURE OF HIGH PERFORMANCE UNIDIRECTIONAL COMPOSITE TUBULAR JOINTS

A.B. Clarke¹, R.G.H. Davies², K.D. Potter¹, M.R. Wisnom¹, R.D. Adams².

¹ *Department of Aerospace Engineering, University of Bristol. Queen's Building, University Walk, Bristol, BS81TR. England*

² *Department of Mechanical Engineering, University of Bristol. Queen's Building, University Walk, Bristol, BS81TR. England*

SUMMARY: This paper considers some of the issues raised in the design and manufacture of truss structures based on the use of unidirectional CFRP tubes. One critical factor in the minimisation of weight is the maximisation of operating strains in the tubular members. To achieve high strain levels without an excessive increment in manufacturing cost requires careful design of the jointing system. Two approaches are reported here, the first relies on a bonded joint, using a constant thickness tube with minimal preparation. The second uses a tapered seat mechanical joint, which adds some cost and complexity to the tube and weight and complexity to the end joint. Results are presented for both types of joint and possibilities for improvement are discussed.

KEYWORDS: tubular joints, bonded joints, mechanical joints, unidirectional materials

INTRODUCTION

In principle, the use of unidirectional carbon fibre composites permits the design and manufacture of components and structures of outstanding performance and minimum weight. One way of achieving this performance in practical applications is via the use of a truss structure and such structures have been widely used in the design and manufacture of satellite and other space structures, (Refs 1,2,3). Many such structures are deflection limited and as such operate at relatively low strains, being primarily driven by stiffness and thermal stability. For these structures the performance of end connections may not be a critical issue. For structures that are not deflection limited, the performance will depend to a large extent on the allowable strains in the truss members, which depends in turn on the strength of the end connections. High levels of operating strain remote from the end connections can simply be achieved by tapering off the thickness of the tube at some distance from the joint. This practice adds weight to both the tubes and the end fittings, (as the end fittings must become larger to accommodate the greater outside diameter of the tube). In addition the costs of the tubular elements will be increased, and the complexity of the assembly is increased as each tube must be manufactured to the specific length required, rather than being cut to length from a standard tube. If the increases in tube allowable strain due to tapering the tube remote from the end joints are sufficient this option may be the most weight effective, but this will not always be the case. The work reported here was aimed at developing end joint geometries that permitted the maximum working strains to be achieved. The baseline chosen was the use of a bonded joint of double lap shear geometry. This option was explored analytically and

practically and the results compared to an approach based on moulding in a tapered root geometry into which loads can be transferred via a mechanical joint type.

THE DOUBLE LAP SHEAR JOINT

The design of double lap shear tubular joints was based on an understanding of flat laminate joints developed in another part of the overall programme. The critical features of this understanding are noted below.

For a joint involving composite adherends a critical factor in maximising joint strength is the avoidance of interlaminar failure in the composite induced by peel forces. To ensure that this failure mode is suppressed a long adhesive chamfer beyond the end of the outer adherend is introduced into the design and the outer adherend is also chamfered back to minimise stiffness mismatch stresses at the end of the joint, fig 1, ref 4. The initiation of failure in the adhesive then appears to be in the region of the tip of the chamfer in the outer adherend (point X in fig 1). The tensile strain in the adhesive rises from the end of the fillet, at which point it must match the strain in the centre adherend, until it reaches the tip of the chamfer on the outer adherend. This rise is associated with load transfer across the joint and is non-linear in form. In principle, the tensile strain reaches infinity at the geometrical singularity at the tip of the outer adherend chamfer. In the FE modelling, the value of the predicted tensile strain at this point is mesh dependent and rises rapidly as the mesh size is reduced, as would be expected for a geometrical singularity. The geometry that is being modelled is idealised with sharp edges. In the real case there will be some level of rounding that serves to avoid the infinity suggested by the geometrical singularity.

Despite this, there will be an extremely large strain concentration at the tip of the adherend which would be expected to lead to adhesive failure at an end load much less than that experienced. Equally, if the precise level of geometrical rounding was the only relevant factor, a high level of sample to sample variability in end load carrying capacity would be expected. This is not seen in practice, with specimens that are quite different in terms of very detailed geometry at the tip of the outer adherend having very similar strengths. There are, perhaps, three factors that serve to ameliorate the effects of this extreme stress concentration.

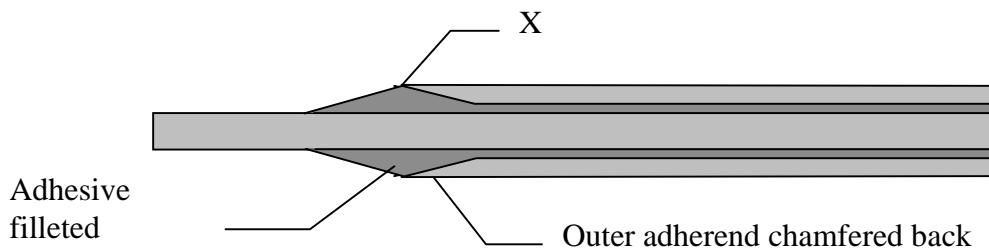


Fig 1. Geometry of the flat double lap shear joint

The first is that the peak strains are localised into a very small volume such that the fracture toughness of the adhesive is sufficient to prevent propagation of damage on energetic grounds. The second is that the volume of the region immediately surrounding this zero failure probability zone is still very small. It is in this region, where stresses and strains are still very high, that nucleation and propagation of failure is expected. In such small volumes

of highly stressed material, it is to be expected that statistical effects will be of great importance in determining the probability of failure, via a strength/volume relationship. The third factor is that the high peak strains experienced can be equated to high local strain rates, even when the specimen as a whole is experiencing moderate strain rates. The adhesives used are strain rate sensitive materials, being both stronger and exhibiting higher moduli at high strain rates. It seems most likely that the first two effects are more important than the third, but all three may influence the strengths experienced in practice. The use of these geometrical features has been seen to lead to flat double lap shear joints of very high performance with operating strains over 0.8% at failure, with failure occurring outside the joint region, this work is reported in ref 5.

The work on tubular joints built upon the understanding of the features that lead to good performance in laminar joints (ref 6) by a consideration of how the change in geometry changes the stress state in the joints. The principal difference between flat and tubular joints is that there is a higher degree of constraint in the tubular case, especially when metallic and composite adherends are used together. This shows up most when the influence of thermally induced stresses is considered. The adhesive performance required for the targets of this programme is only available from systems that are cured at high temperature. On cooling down from cure to room temperature, substantial strains can be induced. In the flat laminate case the strain in the through thickness direction can be completely relieved, in the tubular case this is locked in, resulting in higher strains in the adhesive. Predicted joint strengths are therefore lower than for flat double lap shear joints, and are lower for titanium end pieces than for CFRP end pieces, reflecting the differences in coefficient of thermal expansion. The selection procedure for the adhesives to be used in the bonded tubular joints was based on the factors noted below.

- High lap shear strength
- High strain to failure
- Lap shear strength > 20MPa between -50 & 100⁰C
- Good hot/wet properties
- Adhesive must be readily filletable
- Low coefficient of thermal expansion
- Cure T compatible with rest of structure: < 180⁰C
- Low Poisson's ratio
- Good bonding to CFRP & titanium
- Low viscoelasticity
- Minimal moisture pickup
- Minimal effect from immersion in water or other fluids such as fuel.

On the basis of manufacturer's data and in-house testing adhesive grade 3448 from 3M was selected for trials. The 3448 material is a paste development of an aerospace grade film adhesive.

The unidirectional tubes were of two designs. The first was a conventional tubular prepreg lay-up of Toray T800 fibres in an Hexcel 924 matrix (specimen A). The second utilised a novel reinforcement form consisting of precured rods of IM7 fibre in an epoxy matrix. This reinforcement is manufactured by Neptco Inc under the name of Graphlite[®] (specimen B).

® Graphlite is a registered trademark of Neptco Inc.

The reinforcement is claimed to lead to superior product performance by ensuring that fibres are straight and that this straightness is maintained throughout lay-up and cure. For conversion into tubular form 0.74mm rods were used and set into film adhesive with surface plies of T800/924 prepreg to ensure a good bonding surface. The end fitting was manufactured from titanium alloy, to the design shown in fig 2.

The design and manufacture of efficient double lap shear tubular joints is much more complex than for flat laminate double lap shear joints. Issues such as how to prepare the inside surface of a tube for bonding and how to ensure that the necessary fillets and chamfers are achieved on the inside of a tube have to be tackled prior to any manufacture and test of joints. The use of a pressure fed grit blasting machine was used to prepare both inside and outside surfaces of the tube and end fitting.

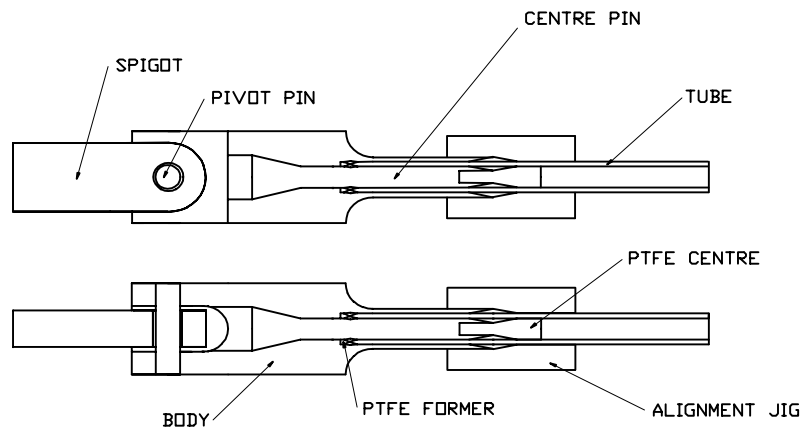


Fig 2. Schematic design of tubular double lap shear joint

The necessity to have a double lap shear joint is met by the use of a centre pin with a flared end for load transfer into the joint body.

Small machined PTFE spacers are used to generate the required fillet geometries and an alignment jig is used to form the outer fillet and hold all parts in register. A small rebate has been machined into both centre pin and body to increase the available size of adhesive fillet at the back of the joint. Despite this the absolute size of the rear fillet is considerably less than that of the front fillet. However, the increase in diameter of the body prior to the start of the rear fillet should tend to de-stress this region such that the small fillet volume does not lead to premature failure. Joint overlap length is set at 50mm. Minor misalignments with respect to the test machine will be taken out via the pinned spigots. A taper is created on the CFRP tube using high speed rotary burrs. Tube ID is 10mm and OD is 13mm. Bond line thickness is 0.7mm.

Tube Joint Test Results

Double lap shear tube joints have been tested. The first was made up from 0.74mm carbon fibre rods as described earlier. A small hole was drilled in the titanium joint body to permit adhesive to be injected into the joint. This proved to be very difficult due to the extreme viscosity and viscoelasticity of the 3M3448 adhesive used. These properties of the uncured

adhesive give it excellent gap filling and non-slump characteristics, and are thus ideal for flat double lap shear joints, but make it more difficult to utilise in the tubular joint case.

The assembled tube and end joints was tested in an Instron servohydraulic tensile testing machine under position control.

Specimen A was tested with failure occurring at 32kN

Failure occurred by a partial failure of the bond line at each end, allowing the tube to split into two parts longitudinally, as shown in fig 3. An examination of the failed joints showed that the adhesive had not penetrated between the tube and the centre pin so that the tube was, in effect, bonded as a single lap joint rather than a double lap joint.

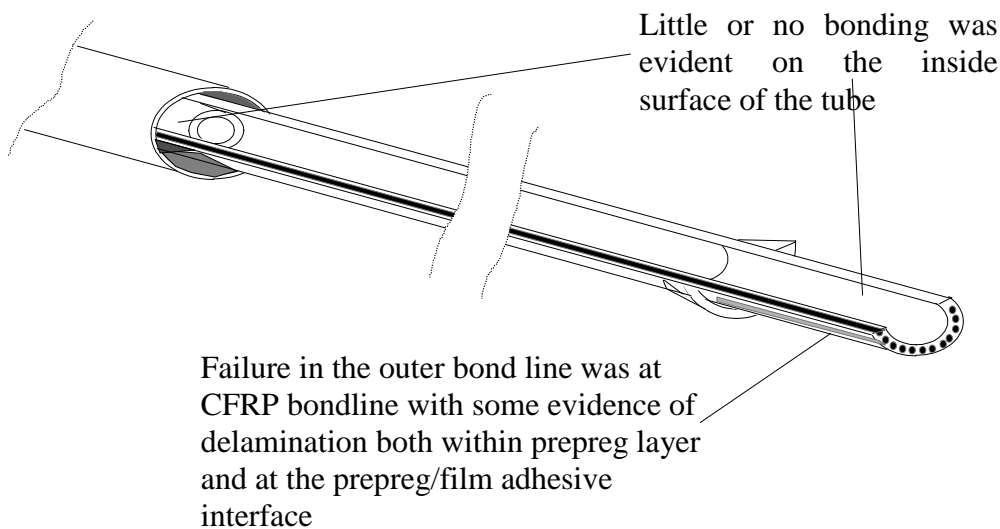


Fig 3. General features of failed tube test specimen

Specimen B utilised a T800/924 prepreg tube and 3M3448 adhesive. In this case, excess adhesive was introduced into the end fittings and the tube was driven into place whilst being revolved, driving out excess adhesive. This meant that the PTFE centre piece shown in fig 2 could not be employed. Failure in this joint occurred at 56kN; failure occurred primarily at the bond line between the outer Ti element of the fitting and the adhesive. The adhesive thickness in the joint was rather variable with some voidage visible, although not in regions of peak stresses. The adhesive thickness variation is caused by a slight misalignment between the tube and end fitting of about 0.6° (0.5mm in 50mm). As designed the inner Ti pin should end at the same position as the outer Ti tube. In this test specimen the inner pin has not been seated fully home and the end of the inner pin is about 7mm short of the end of the outer tube. See fig 4.

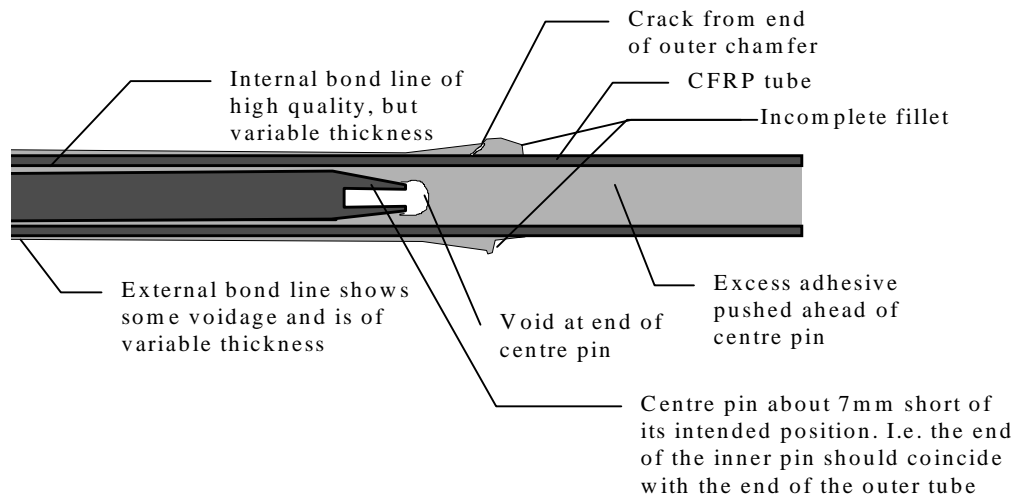


Fig 4. Cross section through failed joint. (Outer adherend not shown).

The inner bond line appears to be completely intact and the titanium pin has failed at its minimum cross section, see fig 2. This is assumed to be as a result of the outer bond line failure, rather than vice versa. Taking an average circumference of 11.5mm for the tube (10mm ID, 13mm OD) the load carrying capacity at failure was 1.55kN/mm. This equates to 1036MPa stress in the tube, or 0.67% strain. It should be noted that, as a result of the offset between inner and outer Ti adherends, the stresses in the outer fillet will be higher than expected, which will result in a reduction in the strength of the joint. We would expect to see a lower strength in tubular joints than in flat joints, as noted earlier. Using non-linear finite element analysis we can predict a strength of 57.4kN for the tubular double lap shear joint with 3M3448 adhesive. Thus the achieved joint strength is within 3% of the expected strength despite the deviations from ideal geometry. The exact mode of failure is hard to detect, as it is difficult to separate effects that initiated failure from those that occurred as a result of failure. For approximately 15mm around the circumference, there is a visible crack at the tip of the outer adherend. It may be that cracking in this region was the initiating factor and that the growing crack diverted into the titanium/adhesive interface, leading to total separation.

MECHANICAL JOINTS

The mechanical joint design was based on the same tube dimensions as the bonded joint, but instead of having a constant diameter tube a flare is introduced into the ends of the tube. The basic geometry analysed is as shown in fig 5.

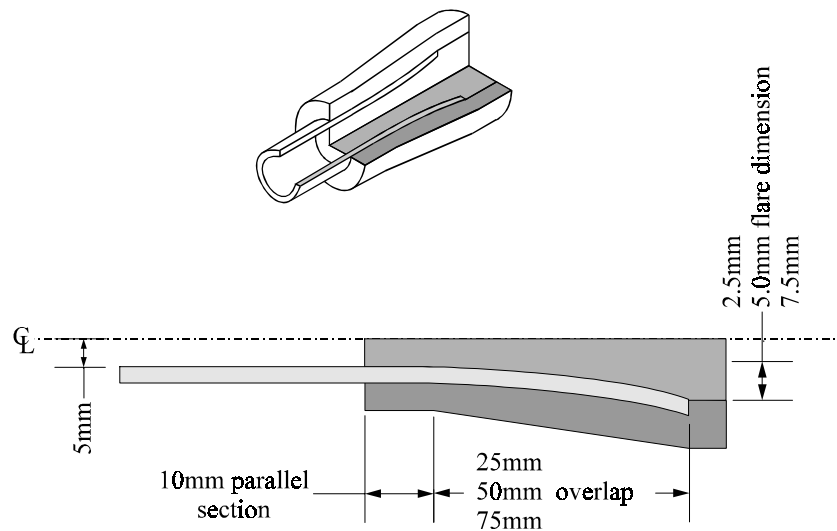


Fig 5. Geometry of the mechanical joint.

The variables taken in the design and optimisation of this joint were the length and depth of the flared region, assuming a smooth flaring out from the parallel sided tube without any step or discontinuity at the interface between flared and parallel sections.

The conclusions of this analytical work were that the smallest flare generally gave the lowest stresses and that the effective stress concentration in the axial direction reduces as the joint length increases, see fig 6. The stresses were predicted using non-linear axisymmetric finite element methods. The very clear message from the analytical work is that, in contrast to bonded joints, the stress concentration at the end of the joint can be very greatly reduced, see also ref 7. This feature makes such a joint scaleable. That is to say that doubling the dimensions should give rise to a doubling of end load carrying capacity per unit joint width. This is not true for adhesive bonding and represents a severe limitation on the use of such joints at very high load intensities. On the negative side the weight of a mechanical joint will be greater than that of a bonded joint, at least for relatively low absolute levels of end load. As absolute end load increases the weight, expressed as grams per kN of end load will reduce for the mechanical joint, and this may become the lighter solution at very heavy end loads.

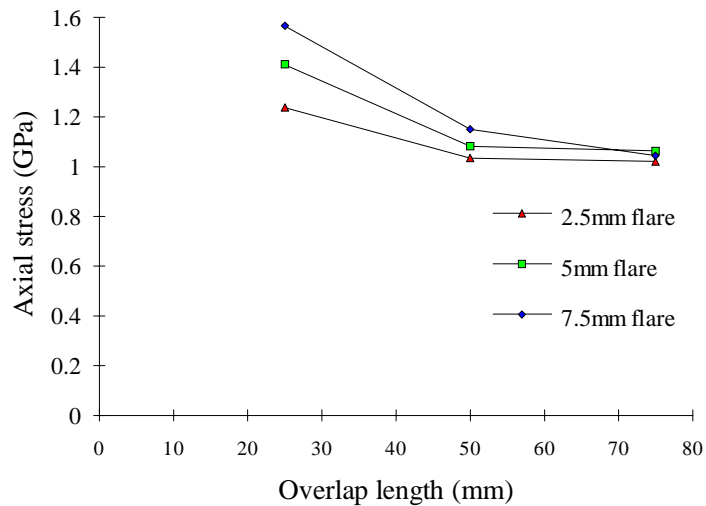


Fig 6. Peak axial stress for an applied load equivalent to an average axial stress of 1GPa, with respect to the geometry of the joint.

Whilst the mechanical end joint design described above should give the best performance the manufacture of such a flared tube would be expected to be very difficult. With this in mind a simplified version of the joint has been designed for initial manufacture and test trials. Instead of a constant thickness flared region, this joint has been designed as a moulded in taper based on thickening up a tube with a parallel sided bore, see fig 7.

The test piece was manufactured from T800/924 prepreg with all plies being unidirectional and aligned to the tube axis. The taper was created in the simplest way possible, by laying up additional layers of prepreg over the basic parallel lay-up prior to consolidation and autoclave cure. This approach was taken rather than that of interleaving the additional plies within the tube lay-up to minimise production costs and avoid as far as possible the formation of consolidation induced defects in the lay-up.

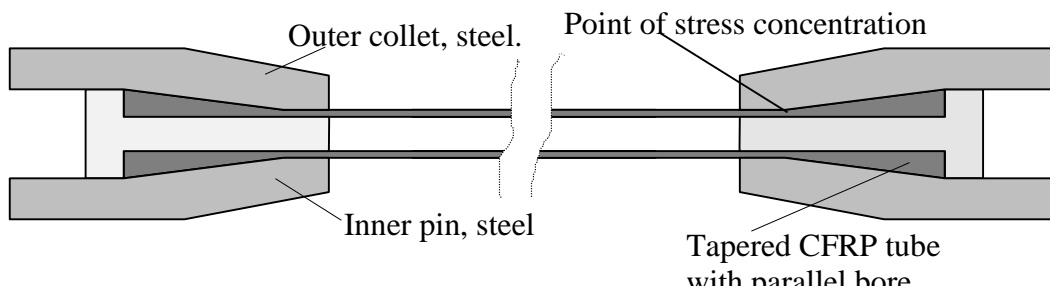
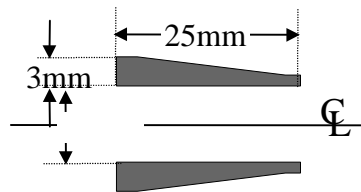


Fig 7. Schematic of tapered tube mechanical joint

When tested this tube gave a load at failure of 77kN. The failure mode picture was complex with failures in the composite tube at both ends, plus a smaller area of failed fibres at the middle of the tube. The failure process is believed to be as follows. Primary failure occurred at the stress concentration at the end of the taper as shown in fig 7. This failure is clearly tensile. Secondary failure is then believed to have occurred at the other end of the tube at the

end of the metallic joint piece. This failure is clearly compressive and probably arose as a consequence of sudden relaxation of the test machine. The last failure is believed to be at the centre of the tube where, either sudden bending applied as a result of test machine relaxation or stress wave reflection caused a very localised failure. No evidence can be seen of any delamination from the ends of the additional plies used to build up the external taper up to a magnification of $\times 100$. The failure load equates to 2120N/mm or 1413MPa (0.92% strain, requiring a stress concentration of ~ 1.7 to induce failure). This is the highest stress we have achieved to date in any joint style. It should be possible to improve on the design of this joint by modification of the geometry to reduce the stress concentration at the end of the taper. Fig 8. shows the load transfer region of this joint at actual size to give an impression of how little composite material is needed to transfer a load of 7.8 tonnes.



*Fig 8. Load transfer region of joint. Scale 1:1.
Weight of load transfer zone less than 5gr*

This simpler, but easily achievable, design shows a much more sudden change of geometry at the end of the load transfer region than the baseline flared geometry and, as expected, this results in a higher effective stress concentration in this case; $\times 1.7$ compared to $\times 1.2$ for the smoothly flared design.

DISCUSSION

A very good understanding of the factors leading to high strength in tubular double lap shear joints has been developed. The critical features are achieving a tapered adhesive fillet beyond the end of the adherends to minimise peel stresses within the laminate and tapering of the adherend tips to minimise the stresses within the adhesive layer. Together these features lead to a failure mode that makes the maximum use of the available adhesive tensile strength and strain capability. More effort is required to develop the capability of accurately predicting tubular double lap shear strength. Titanium end fittings have been developed for tubular double lap shear joints. Further effort is required in the development of assembly methods for tubular double lap shear joints. It is much more difficult to achieve the necessary features in the adhesive layer in the tubular format, compared to the flat format, as access is not available to the inside of the joint. The rheological and application properties of the adhesive that lead to good performance in flat format lead to difficulties in the manufacture of tubular double lap shear joints. Future efforts will be concentrated on how we can achieve the correct geometry with the currently selected adhesive as this is capable of giving exceptional strength. However, in parallel we will continue to seek adhesives with improved application properties for the tubular joints. Despite the difficulties with manufacture of the more complex tubular joints and the expectation of lower strengths due to an increased constraint and increased thermal stresses we have achieved a high working strain at failure in the tubular bonded joints. The maximum strain at failure achieved to date is 0.67% for a joint of imperfect geometry. This compares favourably with the maximum working strain achieved in flat double lap shear joints, being about 80% of that value, despite additional constraints and imperfect geometry. The unresolved difficulties with respect to achievement of a perfect

geometry will have to be overcome before we can identify the maximum working strains and hence load carrying capacity in a tubular joint.

A very good understanding of the factors leading to high strength in tubular mechanical joints has been developed. The elements of a practical tubular mechanical joint have been designed and acquired. Preliminary results from tubular mechanical joints show the highest end load carrying capacity of any joint style tested to date. Failure in the tube at a stress of 1413MPa was achieved, demonstrating that very high loads can be transferred into tubular UD members. This stress equates to 0.92% strain, a value 10% above the best flat double lap shear joint value achieved to date and 37% above the best tubular double lap shear joint value achieved to date. Further optimisation of these mechanical joints should be possible, permitting even higher end loads to be carried.

A realistic comparison between the bonded and mechanically jointed tubular members depends on more than a simple consideration of relative working strains, we need to look at the potential applications to put the two designs into focus. The single greatest advantage of the bonded solution is probably that joints can be made at any point. This means that we can procure tubing in long lengths, cut these to size and bond them together without having to make a different tube for each length. Thus the tooling bill for any particular assembly is kept to a minimum. Equally, the length tolerance on each tube can be relatively relaxed, especially if the joint is designed so as to destress the rear of the joint. Thus potential problems of tolerance build up during the assembly of a truss can be avoided. One disadvantage is that, as we have seen, assembly can present problems and only an external inspection of the joint is possible, although some internal defects may be detectable by NDT. Perhaps the greatest disadvantage is that absolute levels of end load are limited. Whilst it is true that high levels of working strain can be achieved, this is only possible in relatively thin walled tubing so that for a high end loading a large number of tubes and end fittings are required. Even this "disadvantage" may sometimes have positive implications as a large number of tubes has benefits with respect to structural redundancy. The actual end fittings are fairly straightforward to manufacture by normal metalworking techniques, either by turning or potentially by casting.

For the mechanically jointed option the actual end fittings are harder to manufacture. When a tube is flared out at both ends the element of the end fitting that directly interacts with the tube must be split to permit assembly and a separate external collar must be used to react the loads imposed by the tension in the tube. This means that the joints can be assembled and disassembled, which in turn gives the potential for proof testing of each and every tube and joint prior to assembly into a structure. Because these joints lack the stress and strain singularities that bedevil the analysis of bonded joints, and make strength predictions so difficult, they should be scalable to thicker tubes without leading to the reduction in composite adherend working strains that is associated with bonded joints. This means that the number of both tubes and joints can be below that required for bonded tube structures, if the structures must be designed to carry high loads. Of course, if less elements are used to carry a given load the level of redundancy is also declining. The considerable benefits of the mechanical end joints are not without costs; these include a requirement to make a different moulding for each tube length required, with tooling and manufacturing scheduling implications. In addition the tolerancing requirements on tube length can become very tight when the tubes are required to interact with rigid and fixed end pieces.

For any particular structure one may be able to define which approach is optimal in terms of weight, cost, complexity, redundancy, inspectability etc. In the general case, no specific conclusion can be reached as to which design is to be preferred, what can be said is that both designs are capable of further development beyond the state presented here and that improvements should be possible on the 0.67% and 0.92% strains at failure reported here. Both these strain values are well beyond those currently used for design purposes in most applications of CFRP. The future developments of improved jointing techniques can make a major impact on the weight, manufacturability and costs of composite structures, the work presented here is only a first step in the right direction.

ACKNOWLEDGEMENT

The authors would like to acknowledge the support of the UK Engineering and Physical Sciences Research Council, via contract number GRK66833

REFERENCES

1. Pickett, A.K. & Hollaway, L. The analysis of elastic-plastic adhesive stress in bonded lap joints in FRP structures. *Composite Structures*, 4, (1985) p135-60
2. Green, A.K. & Phillips, L.N. Crimp bonded end fittings for use on pultruded composite sections. *Composites*, (1982) p219-24
3. Franz, J. & Laube, H. Strength of carbon fibre composite/titanium bonded joints as used for SPAS-type structures. *Proceedings of workshop "Composites Design for Space Applications"*. ESTEC. Oct 1985 (ESA SP-243) p301-8.
4. Adams, R.D. Atkins, R.W. Harris, J.A. & Kinloch, A.J. Stress analysis and failure properties of carbon fibre reinforced plastic/steel double lap joints. *J. Adhesion* (1986) 20. p29-53
5. Towse, A. Mechanical and thermal analysis of double-lap tubular joints. IACS Report 10, iss 1, University of Bristol (March 1996)
6. Adams, R.D. & Harris, J.A. The influence of local geometry on the strength of adhesive joints. *Int. J. Adhesion and Adhesives*. Vol 7, no 2. 1987
7. Sonius, M.N. & Tew, B.W. Parametric design optimisation of an entrapped fibre connection. *Composite Structures*, 35. 1996

A NOVEL COMB JOINT CONCEPT FOR HIGH STRENGTH UNIDIRECTIONAL CARBON FIBRE BONDED JOINTS

A.Towse¹, KD Potter¹, MR Wisnom¹ and RD Adams²

¹ *Department of Aerospace Engineering, University of Bristol, Queen's Building, University Walk, Bristol, BS8 1TR, UK.*

² *Department of Mechanical Engineering, University of Bristol, Queen's Building, University Walk, Bristol, BS8 1TR, UK*

SUMMARY: This paper describes a novel concept for achieving high joint strengths at low cost by a comb joint approach. An advantage of the joint is scalability, where a number of these joints can be stacked to meet the requirements at much lower weight, cost and risk than a single very long and heavy joint. An analysis was carried out where mechanical loads were applied to a generic fully restrained element of a comb stack, and the resulting strains were superimposed on the residual strain state resulting from thermal cooldown from cure temperature. The technique was then extended to a three comb stack (3x1mm carbon strips), where it was seen that the joint strength would be expected to be 3.2kN/mm. A full-size demonstrator was built utilising the same design philosophy as presented above, the resulting failure gave a joint strength of 6.64kN/mm, a failure load in excess of any previously seen adhesive joint.

KEYWORDS: adhesive joints, high load intensity, comb joint, finite element analysis, thermal stresses.

INTRODUCTION

The theoretical performance advantage of using high strength carbon fibre in unidirectional form has been well known and accepted for many years. However, the problems begin when attempting to utilise such materials in structures due to the difficulty of jointing. The preferred solution is to utilise adhesive bonding in a number of different geometries, such as single lap, double lap, stepped or scarf joints. The first suffers from low joint strengths measured in terms of N/mm of joint width, whilst the latter pair are stronger but at much greater cost and process risk. Even the strongest double-lap joints peak at around 3kN/mm.[1] It would be possible to design a long shallow scarf joint to take out large loads, but the cost and weight of such a joint would become prohibitive for large loads. An alternative approach is presented here, in that multiple strong and simple double lap joints are stacked to form a compact weight efficient joint, capable of carrying the high loads by splitting the load through the members in the comb. In this fashion, the joint need now only be marginally longer than the overlap of each joint. Furthermore, the comb joint solution has inherently greater redundancy and resistance to damage, as the central comb members are protected by the outer members, in every case but an edge-wise impact.

GENERIC COMB GEOMETRY

Previous work [1,2] has been focused on pushing the limits of performance from double and single lap joints. For well known reasons, this has concentrated primarily on designing the end 10% of the overlap well, and ensuring they are manufactured to high quality to ensure good strength values. This has been very successful, although it has been acknowledged throughout that these joints may involve difficulty to manufacture. This is especially true at the rear, or blind, end of the joint where it is initially difficult to produce a spew fillet, and secondly it is very difficult to gain access to this point to inspect the resultant geometry. For this reason, this paper has used a realistic rear geometry that is simple to manufacture and requires no rear spew fillets. The manufacturing procedure would be to trim to size, surface treat (grit blast) and assemble before adhesive injection. The geometry is as shown schematically in Fig. 1.

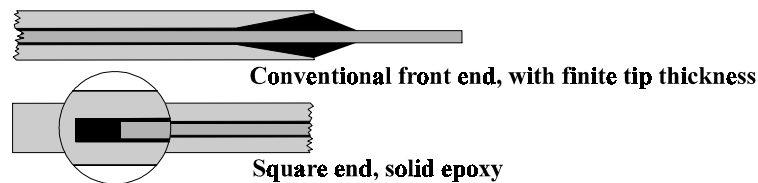


Fig. 1: Front and rear comb joint geometry

It should be noted that although spew fillets and reverse tapers have been seen to be beneficial [1], the best results would come from an extremely sharp adherend tip. This would be expensive to machine as well as being sensitive to damage during manufacture or repair. The joints in this report deal with finite tip thicknesses of 0.2mm which is castable (HP turbine blades are routinely cast to this thickness in Ti) and practical.

FINITE ELEMENT MODELLING

To gain an understanding of the failure load and mode of the comb joints in question, a non-linear analysis was carried out using the ABAQUS FEA suite of software, including the effects of material non-linearity and residual thermal strains from cure. To that end, an adhesive stress-strain curve was gained from previous work [3] for the Permabond ESP110 two-part Aluminium filled adhesive (RT properties).

Quadratic quadrilaterals using the plane strain assumption were used throughout the model, with quadratic triangles where necessary. The yield criterion used was von Mises, in preference to the more rigorous Raghava criterion. It was found that the difference in failure load prediction for the joints between the two criteria was within the scatter one could expect in experimental tests, and therefore the more robust von Mises was chosen. The unidirectional CFRP was modelled as 924C-T800, with $E_x=170\text{GPa}$, $E_y=10\text{GPa}$, $\nu_{xy}=0.27$ and $G_{xy}=7\text{GPa}$. The epoxy modulus to yield was linear and with a value of 3.83GPa with $\nu=0.38$. The post-yield behaviour was modelled as in Fig. 2. The titanium properties were $E_{Ti}=110\text{GPa}$ and $\nu_{Ti}=0.3$.

Stress - Strain curve for ESP110

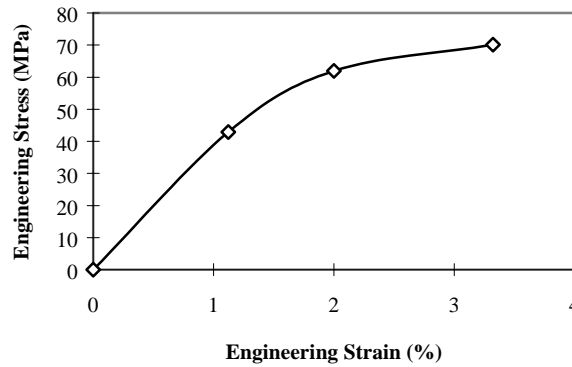


Fig. 2: ESP110 stress-strain curve

The failure criterion that was applied was the critical strain at a distance criterion. The distance chosen was 0.19mm, which was calibrated from previous tests using this adhesive system on end-tab specimens. The experimental failure load was observed, and the required distance for the prediction to match the experiment was determined. However, there is an added complication with this joint, in that at the rear of the joint there is no clear indication in which direction to apply the criterion. Ideally, it should be critical strain at a distance in any direction, as the nature of the strain distribution around the singularity was not circular. Therefore, a criterion of critical strain at a radius was chosen, with the same distance as before. Consequently, it is accepted that this strain at a distance may not be applicable to strain at a radius, and therefore the predictions may be inaccurate. The FEA will, however, also give qualitative information on the likely failure mode and location of the joint. The final geometry of the comb models is as shown in Fig 3.

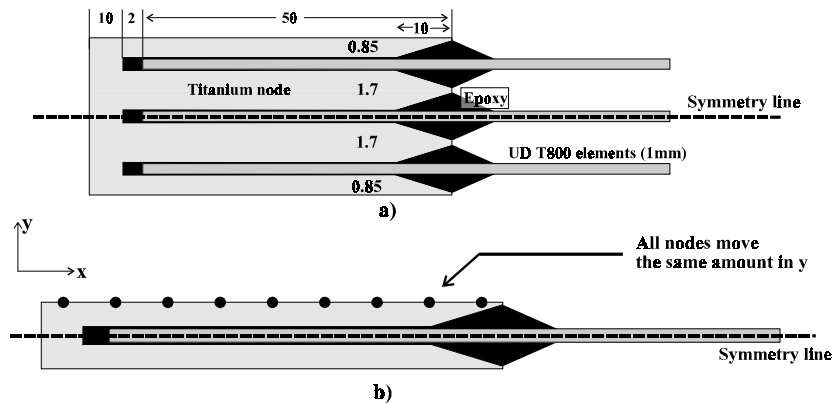


Fig. 3: Single and three comb stack, showing plane of symmetry

SINGLE COMB ELEMENT

To gain an understanding of the performance of a comb element which is deep within a large stack (utilising a monolithic metallic node), it was decided to analyse a single comb element, as shown schematically in Fig. 3b). The loads and boundary conditions that were applied to this model are as shown below in Fig. 4. A symmetric boundary condition was applied to the bottom edge of the model, with the nodes along the top edge coupled to move by the same

distance in 'y' due to thermal or mechanical loading. A face pressure, incrementally stepping up to 1.5GPa tension was applied at the free end of the carbon. For the thermal loading, all the nodes were given an initial temperature of 120°C (T_g of the adhesive), and allowed to cool with the same boundary conditions as the mechanical load to 20°C, giving a total δT of 100°C.

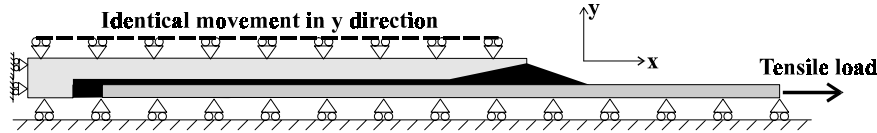


Fig. 4: Single comb element boundary conditions, with constraint equation

By repeating linear runs, with and without the constraint along the top edge, it was seen that differing levels of hydrostatic stress were induced in the epoxy, resulting in lower von Mises stress (higher hydrostatic) for the constrained model than for the unconstrained model. It was apparent, therefore, that more yielding would occur on the outer elements of a large stack of elements due to the lower hydrostatic constraint, hence failure could reasonably be expected to occur from the outer elements first.

The single comb element model was then subjected to a full non-linear analysis, including the effect of residual thermal stresses set up by cooling from cure. The criterion of strain at a radius was applied, both at the front and the rear, including the constraint equation. The results are summarised in Table 1.

Table 1: Strength predictions for single comb element

Adhesive failure strain	Stress in T800 at failure (GPa)	Failure location	Joint strength (N/mm)
3.3%	1.20GPa (0.69% ϵ)	Top of front fillet	1200

It can be seen that the joint strength (in N/mm terms) is not high, although considering the nature of the geometry at the rear end, and the requirement for manufacturability at the front (finite tip thicknesses), the strengths are reasonable. The failure mode was by epoxy cracking from the tip of the Titanium adherend at the front of the joint.

The biggest advantage of the comb joint is its stacking ability. For example, if the requirement was for a 5kN/mm joint, we would need to stack up at least 4 elements to achieve this. As will be seen later, this stacking does not follow such a linear relationship. A further point of note is the effect of the hydrostatic stress state close to failure of the joint. By definition, this will induce a high through-thickness tensile stress (peel) on the unidirectional CFRP, which could induce a second failure mode of peel in the central combs of a large stack if epoxy cracking did not occur first.

THREE COMB STACK

These models are more indicative of a real joint, as no assumed constraint needs to be applied to model the joint deformation. The loads and boundary conditions are as shown in Fig. 5. The method of thermal and mechanical load application is the same as that described previously.

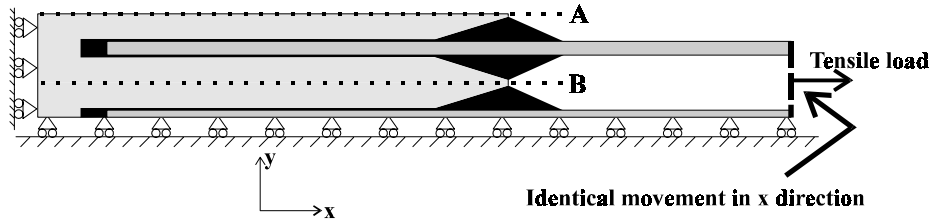


Fig. 5: Three comb stack boundary condition showing mechanical load

The thermal load resulted in an overall deformation and shrinkage of the joints, with the resultant stresses and strains driven primarily by the high CTE of the epoxy. This resulted in some localised yielding of the adhesive around the sharp edges of the model, both at the rear and in the front spew fillet. However, the situation is somewhat different to the single comb element analysed previously in that no assumed displacement profile has been applied, i.e. no constraint equation is used. By comparison of the deformations present in the three comb stack with those forced by the constraint equation in the constrained single comb element, it was seen that the deformations in the three comb stack were different than the constrained model, resulting in lower hydrostatic stress and therefore more yielding and lower failure loads than would have been achieved with three fully constrained single comb elements.

Therefore the single comb model is the strongest, and will probably be indicative of the centre comb element(s) in a large stack of, say, 10 or more elements. However, the outer elements are not subject to the same constraint from their neighbours, and we can expect failure to occur from the outermost elements in the stack, assuming no differences in assembly. The primary reason for this extra constraint in the centre is due to the 1.7mm thick Ti strip that separates the inner and outer comb elements. Under thermal or mechanical tensile/ loading compressive, forces act on this strip in an attempt to bend it due to thermal or Poisson contraction. However, the thickness of this strip in comparison to the thickness of the outermost strip of Ti means they have greatly differing bending stiffness. The cube law of bending means that this centre thick strip has 8x the stiffness of the outer one, and therefore deforms less and shields the inner epoxy layer from large deformation. This increases the σ_y component, although not to the levels seen in the single comb model with applied constraint, and results in greater hydrostatic and lower von Mises stress. This is backed up by the failure load predictions for the three comb stack, as presented in Table 2.

Table 2: Strength predictions for three comb stack

Adhesive failure strain	Stress in T800 at joint failure (GPa)	Failure location	Joint strength (N/mm)
3.3%	1.066GPa (0.61% ϵ)	Outer comb element, front adhesive fillet, exposed tip	3198

The governing failure location is the front of the joint, at the outside comb element at the enclosed corner giving a total joint strength of 3198 N/mm, although failure is almost equally likely from the front or rear of the joint, the front being only marginally worse. It is likely, therefore, that for a more ductile adhesive capable of more than 3.3%, the failure would be controlled by the geometry at the rear of the joint, and measures such as altering the stiffness blend between inner and outer adherends would seem appropriate. It is also clear that the model analysed here does not behave in the same way as three single comb elements. For

three fully constrained single comb elements, the strength would be 3600N/mm, versus 3198N/mm for the three comb stack. This is due to the constraint factors mentioned earlier. For comparison, a prediction for a double lap joint with 3mm central CFRP adherend and 1.5mm CFRP outer adherends using the same load, adhesive and similar geometry was found to be 2200N/mm, including thermal effects. This joint used the reverse taper and spew fillet at both ends, and would therefore be more complex to manufacture, as well as being 31% weaker than the three comb stack joint, using the same amount of carbon. The double lap joint is, however, a much lighter joint than the Titanium three comb stack (approx. 4.8g for T800 double lap joint, neglecting adhesive compared to c.19.4g for Titanium 3 comb stack, also neglecting adhesive). The trade-off between material cost, assembly cost, process risk, weight and load carrying capacity between the carbon double lap joint and the three comb stack is beyond the scope of this paper. What is clear, however, is that by splitting the single 3mm thick carbon adherend into three parts, the operating strain can be increased from 0.42% for the double lap joint to 0.61% for the three comb stack, with the corresponding increase in load.

PRACTICAL TEST

After the completion of the above analysis, a test on a 5 comb stack joint of similar dimensions to the analysed geometry was undertaken. The adhesive used was not ESP110, as parallel work on double lap joints suggested that the 3M 3448 paste adhesive is superior in RT and hot/wet performance to ESP110. Furthermore, 3448 does not present the problems associated with bonded carbon to Aluminium-filled epoxy.

A five comb stack was tested under tensile load, the failure occurring at 6.64kN/mm by cohesive failure in the adhesive from the tip of the Titanium adherend, as predicted. It is not possible to state from which element of the stack the failure originated, as the post-failure load redistribution and energy release caused damage and failure to all the fillets throughout the stack.

DISCUSSION

It is clear from the results that the fully constrained single comb model represents a very idealised element, and will only be indicative of a comb element which is at or close to the centre of a large stack of elements. How deep this stack must be to mimic this constrained condition has not been investigated. It is also apparent, that this centre comb (and indeed all the elements not at the outside edges) have lower principal strains due to their higher constraint. Therefore, the two outer comb elements are the most likely to initiate failure and are the most likely to sustain in-service damage. It would be prudent to devote more time to NDT and inspection of these outermost elements as they represent the weakest link in the joint. This is a fortunate situation, as detailed inspection of central elements will present many problems in practice.

The single comb element, with full constraint, generates large through-thickness (peel) stresses in the carbon due the presence of a significant hydrostatic stress state. Therefore, although the central comb elements have a lower chance of failure from epoxy cracking, for very deeply embedded comb elements there is an increased chance of this second failure mode causing delamination deep within the joint. If this presents itself to be a problem with large stack joints, then it would be required to split the joint into two (say from one 14 comb

stack to two seven comb stacks). This would reduce the constraint at the centre and reduce the chance of delamination.

It is apparent then, that a method for carrying large loads through the use of a relatively simple adhesively bonded joint has been proven. However, the practical use of such an arrangement still requires some thought. For example, the stability of such a stack of thin laminate sheet under compressive loads is likely to be very poor indeed. Consequently, some linkage between the elements will be required, a light foam or honeycomb would seem the most likely candidate. The baseline for this analysis has concentrated on the Titanium adherend being a monolithic block, from which the required shapes are removed, probably via the use of a tapered mill and slotting saw. It is possible, however, to stack up multiple double lap joints to achieve a similar result.

CONCLUSIONS

Both single comb elements and three comb stacks have been analysed, and it has been shown that, for these geometries, failure is expected to be initiated from the outermost elements at the front of the joint. The strength prediction for the three comb stack in comparison to a prediction for a single CFRP double lap joint with a 3mm central adherend and 1.5mm carbon outer adherends can be seen to be higher, 3.198kN/mm for the three comb stack cf. 2.2kN/mm for the double lap joint. The practical test of a five comb stack has demonstrated the capability of carrying 6.64kN/mm (16.9 tons/inch) with a purely adhesively bonded joint. It also demonstrates the ability of utilising high-strength unidirectional material to carry high loads at moderate strains without the normal problems associated with the jointing.

In conclusion, the comb joint concept is a good candidate where high load transfer is required, such as a highly loaded anchorage or tether. It also has the ability for easy scaling up to meet the required load, simply by adding more elements, although the relationship between number of elements and final joint strength is not linear. Care must be taken with large stacks as delamination could be seen in the central elements.

ACKNOWLEDGEMENT

The authors would like to acknowledge the support of the UK Engineering and Physical Sciences Research Council, via contract number GRK66833.

REFERENCES

1. Adams R.D., Atkins R.W., Harris J.A. & Kinloch A.J. "Stress analysis and failure properties of carbon-fibre reinforced plastic/steel double lap joints", *J. Adhesion* **20** 1986, 29-53
2. Tsai M.Y. & Morton J. "The effect of a spew fillet on adhesive stress distributions in laminated composite single-lap joints", *Composite Structures* **32** (1995) 123-131
3. Grant L.D.R., "The characterisation of adhesive joints found typically in the automotive industry" PhD thesis, University of Bristol, (1994)

BOLT BEARING BEHAVIOR OF HIGHLY LOADED COMPOSITE JOINTS AT ELEVATED TEMPERATURES WITH AND WITHOUT CLAMP-UP

Richard J. Wright¹, W. Steven Johnson², and Hafiz Ahmad³

*¹Mechanical Engineering, Georgia Institute of Technology,
Atlanta, Georgia 30332-0405, USA*

*²Materials Science and Engineering, Georgia Institute of Technology,
Atlanta, Georgia 30332-0245, USA*

*³Lockheed Martin Aeronautical Systems, 86 South Cobb Drive, Zone 0648, Dept. 73-C2,
Marietta, GA 30063, USA*

SUMMARY: In this paper, data on time dependent behavior of bolted joints made from 64 ply IM7 carbon fiber/ K3B thermoplastic polyimide quasi-isotropic layup tested in pure bolt bearing and in bearing bypass is presented. Composite panels were aged at temperatures of 177°C (350°F) and 204°C (400°F) for 5000 and 10,000 hours to simulate cumulative effects of supersonic flight conditions on a bolted composite joint. Change in joint bearing capacity and determination of time dependent behavior have been covered in this study. For testing, coupons sized and drilled to correspond to the ratios found in actual joints were loaded to a wide range of loads both with and without clamp-up forces. Testing was done at a temperature of 177°C (350°F), to simulate supersonic cruise temperature. Bearing creep testing revealed time dependent behavior only in a very narrow loading region, above which bearing failure occurred almost instantaneously, and below which no damage occurred. Testing of aged material has shown degradation in material aged at 177°C (350°F) for 5000 hours, however, material aged at 177°C (350°F) for 10,000 hours demonstrated a recovery in bearing capacity while comparison with material aged at 204°C (400°F) for 5000 and 10,000 hours showed neither equivalent nor increased performance degradation.

KEYWORDS: bolt, bearing, joints, creep, aging, bypass

INTRODUCTION

Aircraft traveling at supersonic speeds encounter increased skin temperatures as a result of aerodynamic friction. Future advanced high speed aircraft will be expected to sustain high speeds for longer periods of time than current aircraft can. At the same time, material advances have made composites very attractive for such an aircraft. Fatigue resistance and high strength to weight ratios suggest graphite fiber/thermoplastic composite systems as an alternative to metallic systems for primary structures in an advanced supersonic aircraft. Highly loaded bolted joints will be required in such structures. Since supersonic composite aircraft containing highly loaded bolted joints have never been produced, there is no existing database on how a composite system would perform over the life of a such an aircraft. Key issues about how such a joint would perform include actual strength of the joint under different loading conditions, effects of prolonged loading at cruise temperature, and degradation effects of long-term exposure to high temperatures.

The objective of this paper is to present data on the behavior of highly loaded bolted composite joints at elevated temperatures over long periods of time. The results of this research include data on observed bearing behavior and evaluation of thermal aging effects.

MATERIAL

The composite material being used for these tests is IM7 carbon fibers with K3B thermoplastic polyimide (manufactured by DuPont). Sixty- four ply quasi-isotropic ($[\pm 45^\circ/90^\circ/0^\circ]_4$) lay-up panels of material were fabricated by DuPont. Besides the panels left unaged for testing original properties, other panels were put into forced air aging ovens for aging at 177°C (350°F) and at 204°C (400°F). The aged panels were wrapped in fiberglass cloth to provide separation and cushioning without sacrificing surface exposure to airflow.

Coupons of material for testing were cut from the panels to correspond with an optimal bolt spacing as determined by experimental testing [1]. The ratio of coupon width to bolt hole diameter is six, and the ratio of edge distance to hole diameter is four as shown in Fig. 1. A slot for inserting a hole edge reference wire is cut into the bottom of the hole (on the grip side). The slot is sized to closely fit the measurement wire. The thickness of the coupon is the thickness of the panel. On average, specimens are .89cm (.35") thick.

EXPERIMENTAL SETUP

Configuration

The specific tests done in this program replicate the loading situation for a panel in pure bolt bearing. Pure bolt bearing as described here is a loading situation where 100% of the load in a panel is transmitted at the bolt hole. In a multi-row bolted joint, bolts along the edge of the panel are loaded in this condition. Single bolt holes at the edge of the panel in pure bolt bearing are modeled by a coupon with a bolt hole drilled through it. Bearing- bypass tests, where there is a load in the panel crossing the bolt hole as well as at the bolt hole were performed at Lockheed Martin.

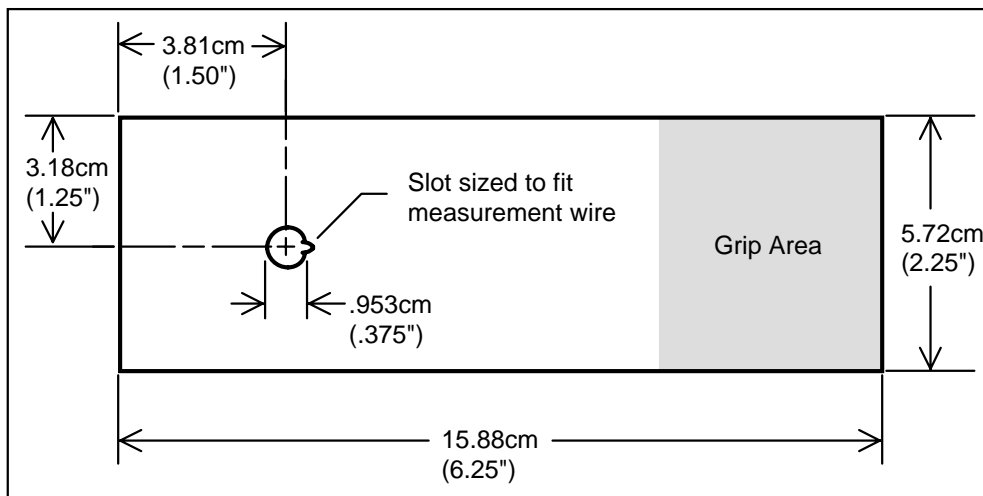


Figure 1: Bolt bearing testing coupon geometry

The basic experimental test setup for the bolt bearing tests in Fig. 2 is similar to that used in past research [1] and consists of a clevis with a bushing in it to apply clamp-up force to the

coupon. A .95 cm (.374") diameter high strength steel aircraft bolt is put through the clevis and the coupon with the measurement wire hanging in the slot below the bolt hole.

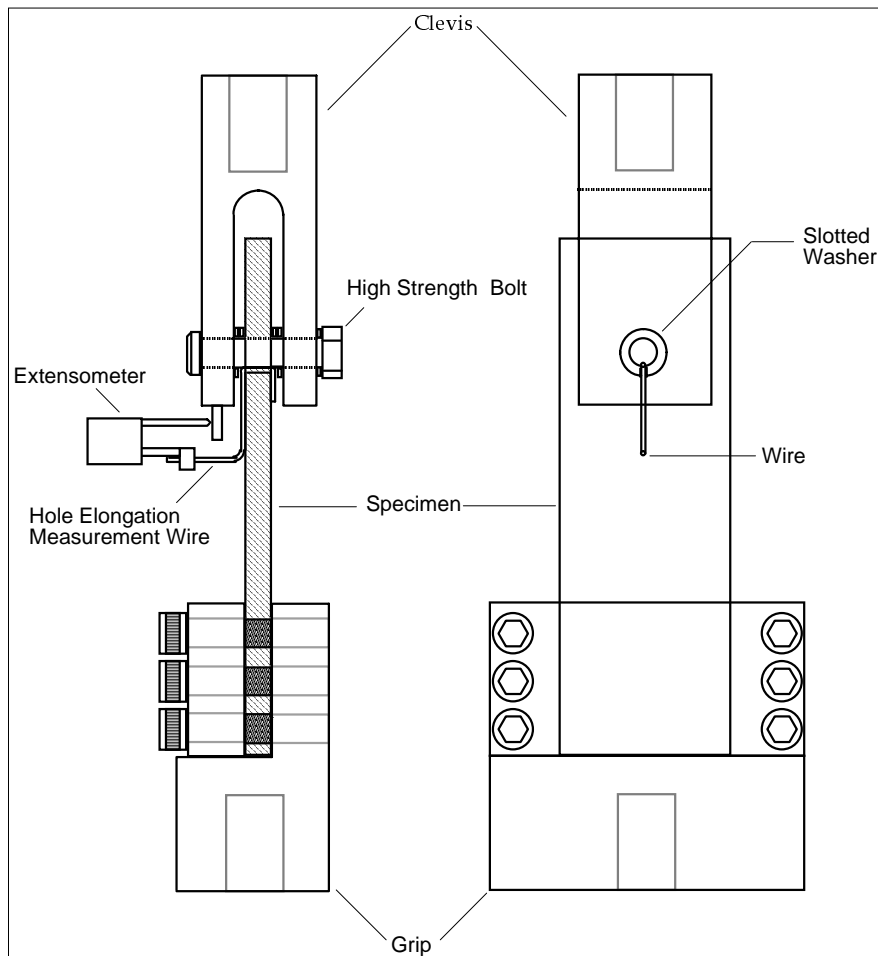


Figure 2: Testing setup with clevis, specimen, extensometer, measurement wire, and grip.

On either side of the specimen, (in contact with its surface) are two 1.59cm (.625") diameter corrosion resistant steel aircraft washers .159cm (.0625i) thick, which are slotted to allow space for the measurement wire to pass. The coupon is held at the other end by a bolted grip with fine tungsten carbide teeth. Bolt hole elongation is measured with an MTS 2.54cm (1") gauge length clip-on extensometer mounted on the .16cm (.063") stainless steel wire with its free blade clip attached to a post on the clevis.

Testing

In bearing creep testing, the fixture is placed in an oven (temperature range for the ovens built for this testing is room temperature to 220°C (428°F)) with the coupon in place. A 20:1 lever arm creep machine supplies a static load for the duration of each test bearing creep test (250 hours). Output from the extensometer is routed through an analog amplifier and sent to a pen chart recorder so that hole displacement data is plotted as a function of time. One duplicate of each test was conducted.

EXPERIMENTAL RESULTS AND DISCUSSION

Bearing Creep

Bearing creep tests have all been run at 177°C (350°F). All specimens are dried for 62 days at 116°C (250°F) to remove any volatile content before being put in the creep frames for testing. Each test runs for a continuous 250 hours under load at temperature. Four basic series of bearing creep tests have been run: First, testing joints clamped up to 5.65 N·m (50 in-lb) torque with unaged coupons. Second, testing of unclamped bearing on unaged coupons where no washers or other constraint was present to prevent deformation of the specimens (washers were absent, but measurement wire was present). Third, testing of unclamped bearing on specimens aged at 177°C (350°F) for 5,000 and 10,000 hrs. Fourth, unclamped bearing testing on material aged at 204°C (400°F) for 5000 and 10,000 hrs. Loads for bearing creep are defined here in two ways: 1. Total load applied to the specimen (given in kN and lbs.). 2. Bearing load stress, which is defined by Eqn. (1) and is given in MPa and ksi. Data from these experiments given in Figures 3, 4, 5, and 6 is the average from each test and its duplicate. The very good reproducibility of the tests has put the runs very close to their duplicates.

$$\{\sigma_b\} = P/(t \cdot D) \quad (1)$$

Failure Criterion

Failure is defined as any permanent deformation of the bolt hole of 4% of its diameter or more (MIL-HDBK-5G, 1994), which is .038cm (.015”) in this instance. This failure criterion is illustrated here (as in Figure 4) as being the largest elastic deformation seen (immediately after loading in the 31.1 kN or 365.4 MPa (7000lbs. or 53ksi) test shown in Fig. 5) with the 4% of the diameter added to it.

Clamped-up Tests

These tests were done on unaged specimens with standard aircraft washers providing clamp up force on either side of the specimens. As seen in Fig. 3, the presence of clamp-up appears to have prevented bearing creep at loads up to 40 kN or 473 MPa (9000lbs. or 68.6 ksi), or 150% of the baseline load for the joint, 26.7kN or 315 MPa (6000 lbs. or 45.7 ksi). During testing, the washers on either side left marks on the specimens; these were found to be smoothed areas and not measurable indentions. The bolt holes in all of the test coupons recovered elastically to the original bolt hole diameter of .953cm (.375”).

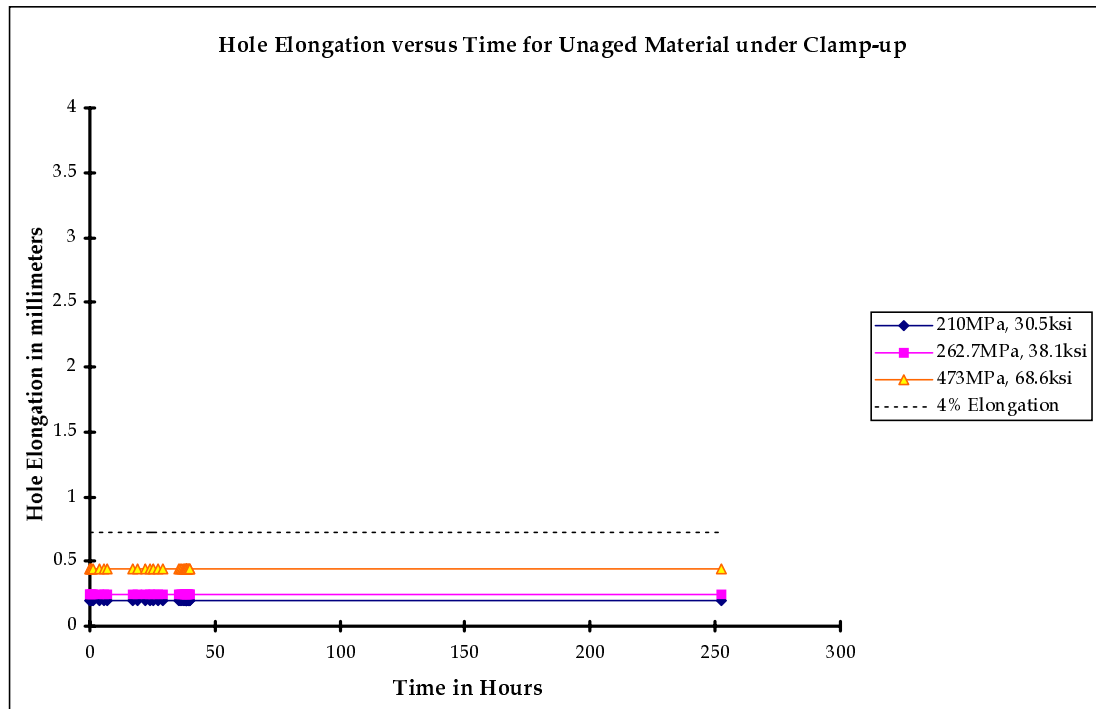


Figure 3: Clamped-up Bolt Bearing Behavior of Unaged Material

Unclamped Bolt Bearing Tests

Based on the results of the clamped up specimens, the researchers decided to look at the worst case scenario for this joint system: Unclamped bearing, where the washers are removed from the bolt so that there is no constraining clamp-up to prevent spreading out of the material and failure of the laminate. In these tests, it was revealed that the laminate had sustained loads with clamp-up that would result in nearly instantaneous bearing failure without the constraining clamp-up force.

Unclamped Bolt Bearing In Unaged Material

The first series of unclamped bearing tests was carried out in unaged material. The coupons were dried before testing and slotted. The testing started at a load of 40kN or 473MPa (9000lbs. or 68.6ksi). This load produced rapid bearing failure, as can be seen in Figure 4. It appears that the critical value for sustaining loads is somewhere around 31.1 kN or 365.4 MPa (7000lbs. or 53ksi). At this load, the joint showed a creep-like failure pattern which moved until the material spread out enough to fill the clevis, thus producing the “Knee” visible in Figure 4. The damage to the specimen, however, appeared to be identical to the crushing and intralaminar cracking produced by outright bearing failure. Given the known properties of the matrix material in regard to brittleness increasing with temperature [3], this result is consistent. Note the absence of time dependent behavior in material at a slightly lower load of 28.9 kN or 341.5MPa (6500lbs. or 49.5ksi). Specimens tested at loads below 31.1 kN or 365.4 MPa (7000lbs. or 53ksi) recovered elastically to its original dimensions.

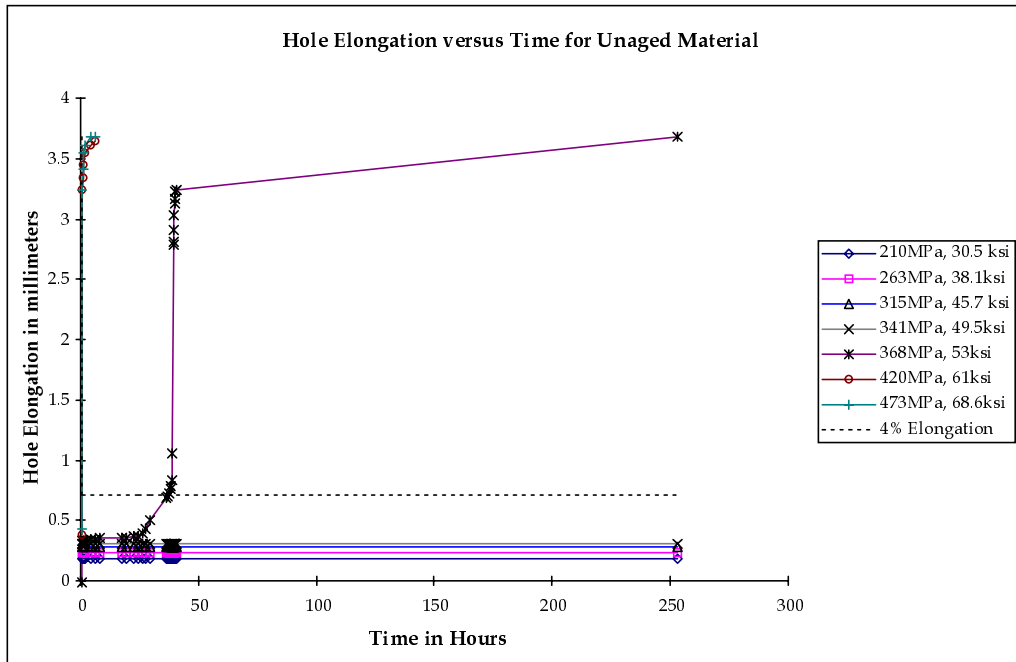


Figure 4: Unclamped Bearing Behavior of unaged material

Unclamped Bearing In Material Aged 5,000 and 10,000 Hours At 177°C (350°F)

The second series of unclamped bearing tests was performed with material which had been aged at 177°C (350°F) for 5,000 and 10,000 hours. In these tests, the target loads were the highest loads the unaged material had survived. As seen in Fig. 5, the material aged at 177°C (350°F) for 5000 hours showed immediate bearing failure at 28.9 kN or 341MPa (6500 lbs. or 49.5 ksi). More interestingly, the material showed time dependent deformation that arrested itself at 26.7kN or 315 MPa (6000 lbs or 46.2 ksi). The specimens in the latter case had clear delaminations on either side above the bolt hole with the outer 45° plies pushed out from the specimen, creating bulges or ‘ears’. From these tests it is clear that there has been loss of unclamped bearing strength after aging at 177°C (350°F). At the same time, the damage remained bearing failure with delamination, crushing under the bolt, and outer ply separation. However, material aged at 177°C (350°F) for 10,000 hours appears to have shown a recovery in properties by sustaining a load of at 28.9 kN or 341MPa (6500 lbs. or 49.5 ksi) without damage and sustaining a load of 31.1 kN or 365.4 MPa (7000lbs. or 53ksi) for 2.3 hours before failure.

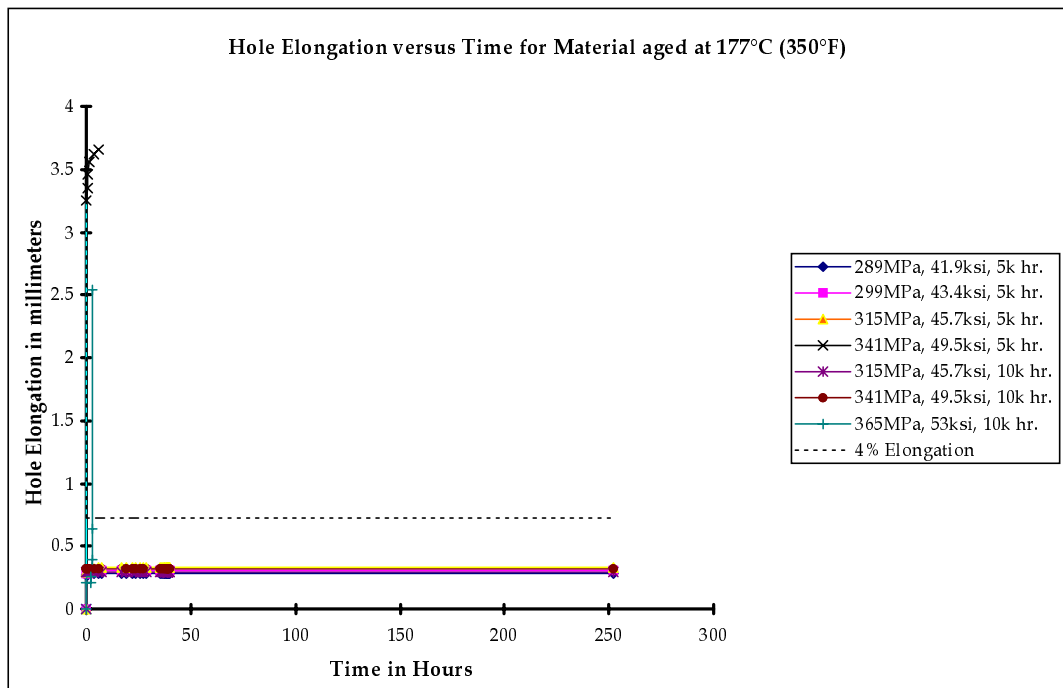


Figure 5: Unclamped Bearing Behavior of Material Age at 177°C (350°F)

Unclamped Bearing In Material Aged At 204°C (400°F)

Unclamped bearing tests were conducted with material aged for 5000 and 10,000 hours at 204°C (400°F). As in the last test, the strategy was to use the highest load the previous test had survived. For this test, the load was 26.7kN or 315 MPa (6000lbs. or 45.7ksi). The

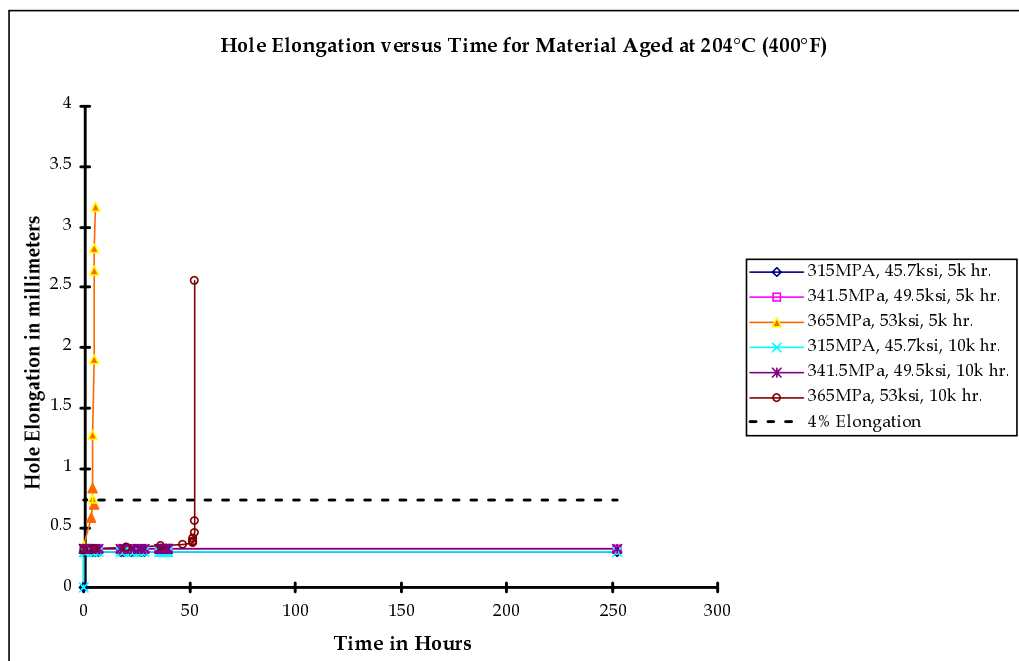


Figure 6: Unclamped Bearing Behavior of Material Aged at 204°C (400°F)

unexpected result was that the material apparently was less affected by exposure to temperatures of 204°C (400°F) than it was when aged at 177°C (350°F). As can be seen in Figure 6, the material aged at this temperature did not show deformation at 26.7kN or 315 MPa (6000lbs. or 45.7ksi) the way material aged at 177°C (350°F) for 5000 hours had. The specimen aged at 204°C (400°F) recovered elastically to its original dimensions. In comparison, the coupons aged at 177°C (350°F) tested at this same load both showed significant “Ears” on either side above the bolt hole where delamination had begun and apparently arrested when enough crushed material gathered to distribute the load. More importantly, material aged at 204°C (400°F) survived loading to 28.9 kN or 341MPa (6500 lbs. or 49.5 ksi) while material aged at 177°C (350°F) for 5000 hours suffered instantaneous bearing failure at this load. At 10,000 hours, the material aged at 204°C (400°F) actually showed time dependent failure resistance superior to the unaged material by surviving 53 hours before failure at 31.1 kN or 365.4 MPa (7000lbs. or 53ksi) while unaged material only survived 38 hours.

Bearing/Bypass Interaction Test Results

The bearing/bypass interaction static tests were conducted using the 64-ply quasi-isotropic IM7/K3B specimens. Test results showed that under the tensile loading conditions, IM7/K3B specimens have higher bearing strengths both at room temperature and at elevated temperature compared to the minimum design allowable strengths. At elevated temperature 177°C (350°F), the IM7/K3B specimens under compression loadings showed significant reduction in strengths. However, compared to the required minimum allowable design bearing

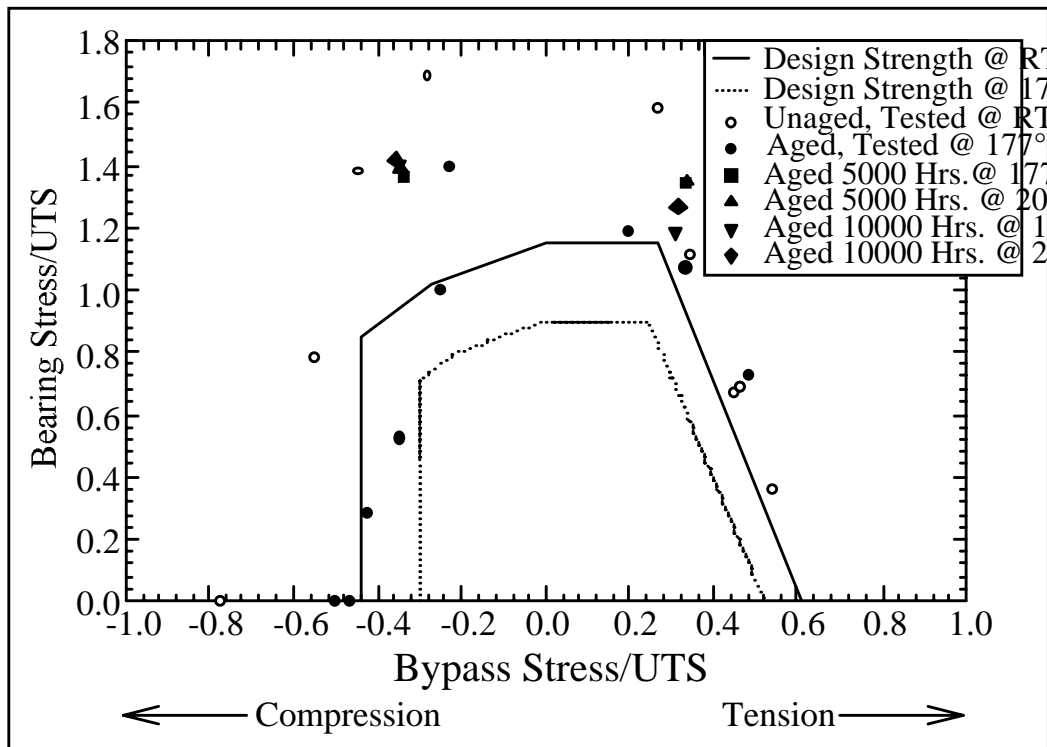


Figure 7: Bearing/Bypass Static Test Results for 64-Ply IM7/K3B Laminates (Note: All Aged Specimens were Tested at RTA and UTS= Ult. Tensile Strength of Laminate)

strength at 350°F, these test values were still better. These results are shown in Fig. 7. A set of test specimens were aged for 5000 and 10000 hours at 350°F and 400°F respectively. The bearing/bypass interaction test results of these specimens have been superimposed on the bearing/bypass interaction plot, shown in Fig. 7. The aged specimens were tested only at room temperature. This was necessitated by the limited number test specimens available for testing. The test results indicate that the aging conditions used for these specimens have little or no impact on the bearing/bypass residual strength of 64-ply, quasi-isotropic IM7/K3B laminates.

CONCLUSIONS

IM7/K3B has shown itself to be insensitive to time dependent deformation. It is apparent from testing that time dependent behaviors can be expected to only show up in a very narrow band of loadings. Testing has pointed to clamp-up force as the source of the most obvious change in coupon bearing strength at temperature. Unclamped bearing testing has shown these materials can withstand their ultimate design loads at temperature, even without clamp-up force to prevent delamination.

As can be seen in the data, the material has lost bearing strength as an apparent consequence of being aged at the supersonic cruise temperature regime being explored. It should be noted that the material still withstood the ultimate design load for the joint under all tested circumstances. However, material aged at the temperature of 204°C (400°F) showed neither the same degree nor enhancement of the aging process which apparently reduced the strength of the material aged at 177°C (350°F) for 5,000 hours and 10,000 hours.

ACKNOWLEDGMENTS

This work has been supported by Lockheed Martin Aeronautical Systems under NASA HSR contract NAS1-20220 Task 24- Wing Structures. The authors extend their thanks to Mr. Ed Ingram and Mr. Brian Cornell at Lockheed Martin for their support in this effort.

REFERENCES

1. Crews, J. H., jr. and R. V. A. Naik. 1986. "Failure Analysis of a Graphite/Epoxy Laminate Subjected to Bolt Bearing Loads", *Composite Materials: Fatigue and Failure*, ASTM STP 907,; 115-133, H. T. Hahn, Ed., American Society for Testing and Materials, Philadelphia.
2. MIL-HDBK-5G. 1994. *Military Handbook: Metallic Materials and Elements for Aerospace Vehicle Structures*.
3. Sacks, S. and W. S. Johnson. 1996. "Effects of Thermal Aging on the Mechanical Behavior of K3B Matrix Material", *Proceedings of the 11th American Society for Composites Technical Conference*, Johnson, W. S. Ed. Technomic Publishing, Lancaster, Pennsylvania, 1996, pp. 666-674.

FRACTURE OF COMPOSITE-METAL ADHESIVE JOINTS UNDER THERMO-MECHANICAL LOADING

Sharath P. Shetty and S. Mark Spearing

*Department of Aeronautics and Astronautics, Massachusetts Institute of Technology,
Cambridge, Massachusetts 02139, U. S. A.*

SUMMARY: This paper deals with the problem of the fracture of composite to metal adhesive joints subject to thermo-mechanical loading. The problem is analyzed using a fracture mechanics model, which predicts the critical temperature change at which fracture occurs for a given pair of materials as a function of their thickness ratio. The experimental program carried out to verify the analytical results is described. Thermal tests were conducted on single and double lap joints of metal adhesively bonded to composite. The fracture resistance of the adhesive joint was measured by mechanical testing. It was observed that the steady-state fracture mechanics analysis correctly predicted trends in the critical temperature drop to cause failure as a function of adherend properties. The mechanical tests revealed that scrim-reinforced film adhesives can exhibit resistance curve behavior. It was also noted that a single value of adhesive toughness is not sufficient to characterize fracture data.

KEYWORDS: thermomechanical loading, steady state fracture, adhesive joining, strain energy release rate.

INTRODUCTION

The problem of joining metals to composite materials is increasingly encountered in structural design. Designers in the aerospace industry, for example, have to deal with this issue in various applications ranging from metal facings on composite substructures for increased erosion resistance, through foam-insulated cryogenic tanks, to bonded composite repair of metallic structures. These joints may consist of multiple layers, and ideally are made by adhesive bonding. The reliability of such a joint can often be a major concern, by virtue of the stresses that arise when these dissimilar materials are subjected to thermomechanical loading. Under these conditions, the mismatch in elastic and thermal properties, combined with material interfaces, can result in the fracture of one or more layers, or the interface between them.

In this paper, experimental results are presented for a representative problem of technological interest: single and double lap joints between graphite-epoxy composite and metal adherends subject to purely thermal loading. These data are compared with predictions of a fracture mechanics model [1]. The toughness parameters required to fit the thermal testing data are obtained by mechanical fracture tests. The intention is to provide a conservative lower bound to data, which can be useful for design purposes.

The structure of the paper is as follows: the mechanics of an elastic, brittle, composite-metal lap joint are briefly presented first. Then the thermal testing procedure is described,

along with results and discussion. This is followed by a description of mode I and mode II fracture testing. Finally, the correlation between the theoretical model and the thermal and mechanical test data is discussed.

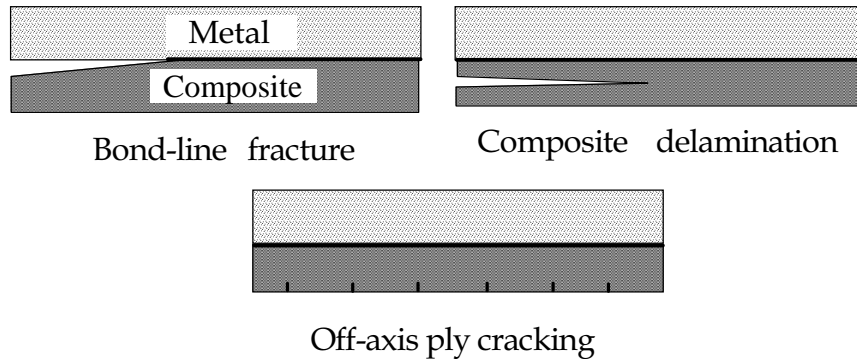


Fig. 1: Failure modes of a composite-metal single lap joint.

ANALYTICAL MODEL

The mechanics of composite-metal joints can be illustrated by considering single and double lap joints between dissimilar adherends. The problem is simplified by considering the deformations of both layers to be linear elastic and brittle and by ignoring the role of the adhesive. This assumption gives conservative lower bounds for fracture, as in practice, non-linear effects such as plasticity, viscoelasticity or creep of the adherends or adhesive may serve to limit the stress levels in the two materials. Experimental observations of such lap joints under thermal loading show that there are three possible failure modes: debonding of the interface, composite delamination, and matrix cracking [2-4]. These modes are illustrated in figure 1.

The stress and strain distributions on application of a uniform temperature change are obtained using simple beam theory, together with assumptions of equilibrium and the compatibility of curvatures and strains of the two materials [5,6]. They are represented in terms of the following non-dimensional parameters [7-9]

the ratio of layer thicknesses:	$\xi = t_1 / t_2$
the elastic mismatch parameter:	$A = (\bar{E}_1 - \bar{E}_2) / (\bar{E}_1 + \bar{E}_2)$
the ratio of the elastic moduli :	$\lambda = \bar{E}_1 / \bar{E}_2 = (1 + A) / (1 - A)$
and the free thermal strain:	$\varepsilon_t = (\alpha_1 - \alpha_2) \Delta T$

where $t_{1,2}$ are the thicknesses of the layers, $\bar{E}_{1,2}$ are the effective Young's moduli, $\alpha_{1,2}$ are the coefficients of thermal expansion and ΔT the temperature change. In the case of the composite, the material properties in the longitudinal direction are considered.

Interfacial fracture and delamination are modeled as steady-state fracture problems in which the strain energy released as the crack propagates is independent of the crack length. This provides a lower-bound estimate of the thermomechanical loading required for fracture [1,2].

The difference between the strain energies stored in control volumes far ahead and behind the crack tip is equated to the fracture resistance of the bond line. This enables prediction of the critical temperature change for interfacial fracture. For a single lap joint, which is modeled as a bimaterial beam, the strain energy stored (per unit length) ahead of the crack tip is given by the following expression [1,4]:

$$U_{el} = \frac{\beta^2 t_1}{2\bar{E}_1} [3\lambda\xi^3 (\xi + 1)^2 (1 + \lambda\xi^3) + \xi^2 (1 + \lambda\xi)(\lambda\xi^3 + 1)^2] \quad (1)$$

where

$$\beta = \frac{\varepsilon_1 \bar{E}_1}{[\xi(\lambda\xi^3 + 1)(1 + \lambda\xi) + 3\lambda\xi^2 (1 + \xi)^2]}$$

This is the energy released as the joint undergoes interfacial fracture, since the region far behind the crack tip is stress-free. The expression is plotted in figure 2. For a double lap joint undergoing simultaneous debonding of both interfaces, the corresponding expression is:

$$U_d = \frac{\varepsilon_1^2 t_1 \bar{E}_1}{1 + \lambda\xi'} \quad (2)$$

Here, t_2 refers to twice the thickness of the center layer, t_1 the thickness of either of the other layers, and ξ' denotes the ratio of the two. For the case of single interfacial fracture, the strain energy released is the difference of equations (2) and (1), i.e.

$$U_s = U_d - U_{el} \quad (3)$$

This is plotted in figure 3. The strain energy stored in the double lap joint is higher due to the inherent symmetry constraint. This is true for the range of thickness ratios where thin film effects are not prominent.

A similar approach is used to model delamination. The critical temperature drop for matrix cracking, the third failure mode, can be predicted by comparing the maximum transverse stresses in the composite ply groups with its strength in the transverse direction.

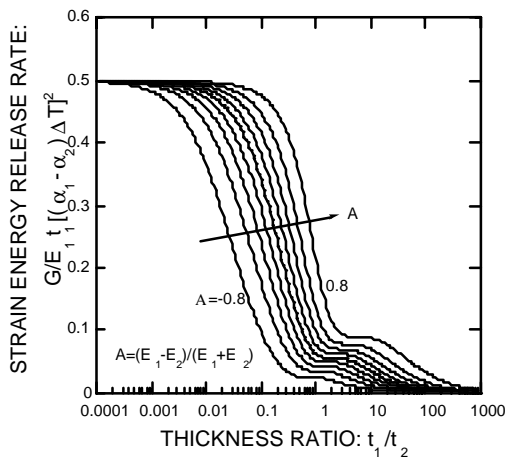


Fig. 2: Single lap joint strain energy release rate

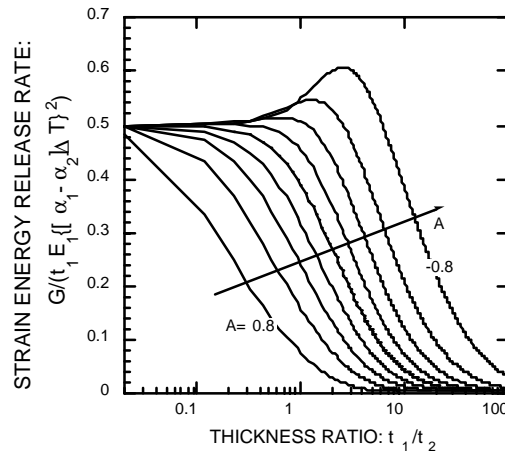


Fig. 3: Double lap joint strain energy release rate

EXPERIMENTAL PROCEDURE

Specimen Fabrication and Materials

To verify the analytical results, thermal loading tests were conducted on metal-composite single and double lap joints. This testing was performed in two stages. In the first stage, 117 mm x 30 mm strips of 6061-T6 aluminum alloy were bonded to strips of 16-ply unidirectional AS4/3501-6 graphite/epoxy composite with the same planform. Single and symmetric double-sided specimens were manufactured with the same composite thickness (2 mm), but varying aluminum thicknesses, such that thickness ratios were between 0.42 and 3.16. These materials and thickness ratios were expected to debond at the interface over a range of temperatures. The specimens were manufactured following a standard procedure [10]. Surface preparation of the metal consisted of light abrasion with garnet paper and subsequent cleaning using a cheesecloth soaked with methyl ethyl ketone. FM 123-2 film adhesive (Cytec) was used for bonding, and the cure was performed at 380°C for 2 hours under 102 kPa chamber air pressure and vacuum.

The second stage consisted of experiments with similar specimens, but included a wider range of material properties and specimen thicknesses. An important difference from the first stage was that the specimens were precracked (to 25 mm from one end). This was done in order to ensure steady state fracture, which was an important assumption in the model. Aluminum or steel (AISI 01) adherends (140 mm x 25 mm) were bonded to AS4/3501-6 graphite/epoxy unidirectional and cross-ply composite laminates. The laminates consisted of 16 or 32 plies, giving a laminate thickness of 2 or 4 mm. The metal thickness was varied between 1.6 and 16.4 mm. The surface preparation of the metal was carried out as before. A mold release agent (MoldWiz™ F-57 NC) was sprayed on each piece of metal over the area to be pre-cracked. The bond cure was carried out as in the previous set of experiments. The thermomechanical properties of the materials used are listed in Table 1.

Table 1: Thermomechanical Properties Of Adherends

	Aluminum	Steel	UD CFRP
E_L (GPa)	70	200	141
E_T (GPa)	70	200	10
ν_{LT}	0.3	0.3	0.32
α_L (ppm/K)	24	11	-0.5
α_T (ppm/K)	24	11	30

In parallel, the fracture toughness of the adhesive was measured. Mechanical tests were conducted to obtain the mode I and mode II fracture resistance of the adhesive. The double cantilever beam (DCB) method was employed for mode I, following ASTM standard D3433-93 [11]. Aluminum adherends 152 mm in length, 25.4 mm wide and 12.7 mm thick were bonded together using FM 123-2 adhesive, with a precrack of 25 mm. The surface preparation used was consistent with that used in the thermal testing. The mode II test specimens were similar to those used for end-notch flexure (ENF) testing of polymer matrix composites [12]. These were identical to the mode I specimens, with the exception that the precrack length was 50 mm.

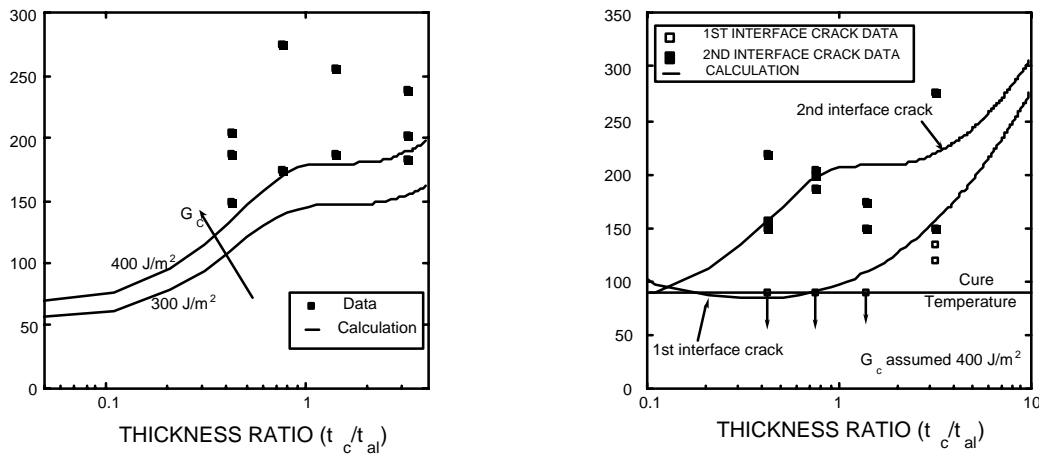
Test Procedure

The thermal test specimens were placed in a liquid nitrogen-cooled thermal cycling chamber which had a low temperature limit of 85 K. The specimens were cooled at a nominal rate of 7 K/min and brought back to room temperature, at which point they were examined for signs of fracture under an optical microscope. The minimum temperature after which fracture was first observed was noted as the critical temperature.

The mechanical tests were performed on a 100 kN capacity servohydraulic testing machine. Data were collected using commercially available data acquisition software. The tests were performed in displacement control at a rate of 0.01 mm/s throughout, which ensured fracture in approximately one minute. Data sampling was at a frequency of 2 Hz. A traveling optical microscope was used to monitor crack extension.

Results

In the first stage of thermal testing, all the specimens failed by interfacial debonding. Figures 4a and 4b show experimental data for the change in temperature to cause fracture as a function of composite-to-aluminum thickness ratio for single and double-sided specimens respectively. Curves of predicted fracture temperature for fixed values of adhesive fracture resistance are also plotted. In the case of the double lap joints, some of the specimens were observed to have undergone fracture at one interface when as they cooled from the cure temperature. This is indicated by arrows in figure 4b. Thus, the double lap joints are more prone to interfacial fracture than single lap joints, as was expected. It is seen that trends in critical temperature drop to cause fracture are correctly predicted, but the scatter in data is considerable. The scatter is attributed to the fact that all the specimens do not undergo steady state fracture; the initial flaw length apparently varied between specimens.



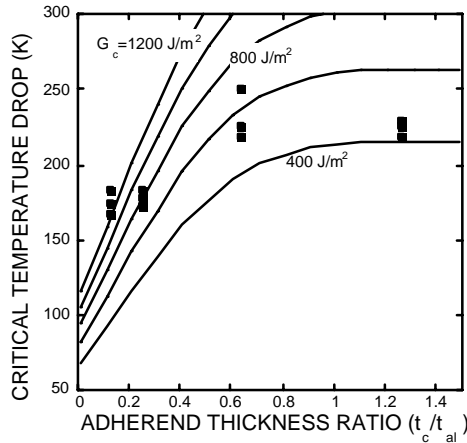
(a) $[0]_{16}$ Gr-Ep/Al single lap joint

(b) $[0]_{16}$ Gr-Ep/Al double lap joint

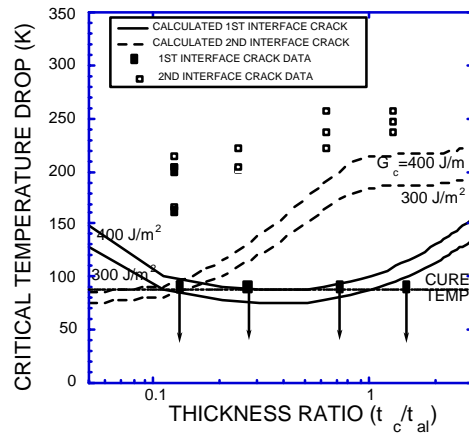
Fig. 4: Thermal fracture data for unprecracked specimens

In the second stage of thermal testing, the mode of fracture was again predominantly interfacial, except in the cross-ply specimens where there was a combination of delamination, matrix cracking and interfacial debonding. The pattern of interfacial debonding was identical in all cases; the fracture always initiated at the metal-adhesive interface and then shifted to the composite-adhesive interface. Figures 5(a-e) show results for each specimen configuration.

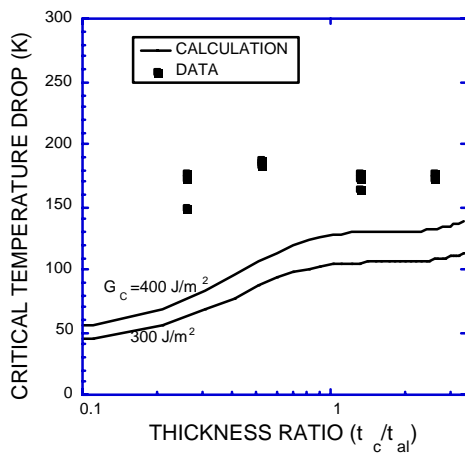
It is observed that the scatter in the data was reduced compared to the unprecracked specimens. The predicted fracture temperature drop curves act as lower bounds to the data, but no single value of adhesive toughness seems adequate to characterize the data. The effect of thickness is qualitatively correctly predicted; the critical temperature drop increases with thickness ratio for constant composite thickness, and decreases with increasing composite thickness for the same thickness ratio (see figures 5a and 5d).



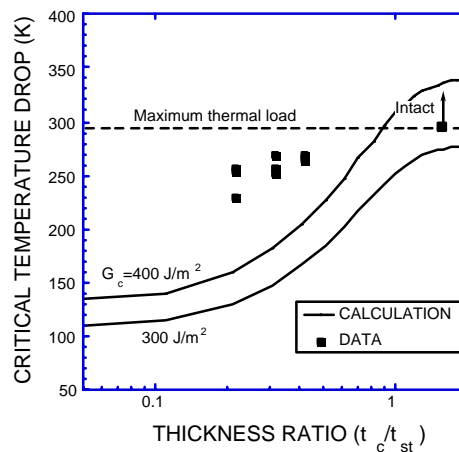
(a) $[0]_{16}$ Gr-Ep/Al single lap joint



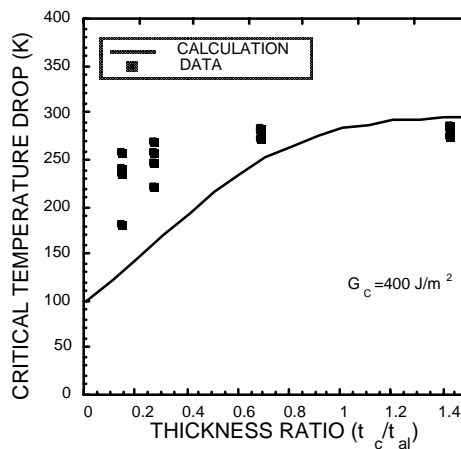
(b) $[0]_{16}$ Gr-Ep/Al double lap joint



(c) $[0]_{32}$ Gr-Ep/Al single lap joint



(d) $[0]_{16}$ Gr-Ep/Steel single lap joint



(e) $[0_4/90_4]$ Gr-Ep/Al single lap joint

Fig. 5: Thermal fracture data for precracked specimens

The fracture in the mechanical tests was found to be cohesive (i.e. the crack ran predominantly through the adhesive rather than at the interface between the adhesive and metal), and the crack growth was stable. It was observed that both the mode I and mode II toughness values were not unique, but increased with crack length, thus demonstrating resistance curve (R-curve) behavior. There was a marked difference between the initiation values of mode I and mode II fracture toughness (100 J/m^2 and 900 J/m^2 respectively). The mechanism responsible for the R-curve behavior was clearly apparent from inspection of the fracture surfaces using a scanning electron microscope (SEM) [13]. As the crack front advanced, the fibers were pulled out of the adhesive at oblique angles, thus dissipating energy and hence increasing the fracture energy required for crack propagation. The role of friction in the ENF tests was uncertain, and it is unclear as to how much this affected the mode II results.

Discussion

In order to compare the thermal test data with the steady state fracture model, values for adhesive fracture toughness were assumed. These were verified by the mechanical test results. The initiation values for the mode I and mode II toughness are approximately 100 J/m^2 and 900 J/m^2 respectively. The mixed mode fracture toughness is expected to lie between these two values [9], and this correlates well with the toughness values that can be extrapolated from the thermal test data. It should be noted that the fracture toughness is expected to be a strong function of the mode mixity. This was assumed to be constant at approximately 60° for the metal/[0]₁₆ composite specimens for the range of thickness ratios used, based on results from Suo and Hutchinson [2]. The effect of possible changes in mode mixity needs to be investigated in greater detail.

Additional factors that must be taken into account are the temperature dependence of the adhesive properties and the effect of large scale non-linearity of the adhesive and adherend properties. The cumulative effect of all the above factors needs to be considered to accurately predict the fracture behavior of the metal-composite lap joints.

CONCLUSIONS

The steady-state fracture mechanics analysis correctly predicts trends in the critical temperature drop to cause failure as a function of adherend properties (unidirectional vs. crossply, steel vs. aluminum), adherend thickness, and single vs. double lap joint. However, more detailed modeling is necessary to achieve more precise predictions.

It is apparent that in some circumstances, steady state fracture solutions can provide a useful lower bound to experimental results. This is potentially useful for preliminary design and material selection purposes. Failure mechanism maps can be constructed using these results, which are informative and act as convenient design tools [1].

REFERENCES

1. Spearing, S. M., "Design Diagrams for Reliable Layered Materials", *AIAA paper 96-1476, Proceedings 37th AIAA/ASME/ASCE/AMS/ASC Structures, Structural Dynamics and Materials Conference*, April 1996, pp 1458-1467.

2. Hutchinson, J. W. and Suo, Z., "Mixed Mode Cracking in Layered Materials", *Advances in Applied Mechanics*, Vol. 29, 1991, pp. 63–191.
3. Drory, M. D., Thouless, M. D. and Evans, A. G., "On the Decohesion of Residually Stressed Thin Films", *Acta Metallurgica et Materialia*, Vol. 36, 1986, pp. 2019–2028.
4. Spearing, S. M., Tenhover, M. A., Lukco, D. B., Viswanathan, L. and Hollen, D. K., "Models for the Thermomechanical Behavior of Metal/Ceramic Laminates", *Electronic Packaging Materials Science VII, Materials Research Society Symposium Proceedings*, 1994, pp. 323-331.
5. Timoshenko, S., *Journal of the Optical Society of America*, Vol. 11, 1925, pp. 233-255.
6. Boley, B. A. and Weiner, J. H., *Theory of Thermal Stresses*, Krieger, 1985.
7. Suo, Z. and Hutchinson, J. W., "Steady State Cracking in Brittle Substrates Beneath Adherent Films", *International Journal of Solids and Structures*, Vol. 25, 1989, pp. 1337-1353.
8. Dundurs, J. J., "Edge Bonded Dissimilar Orthogonal Elastic Wedges under Normal and Shear Loading", *Journal of Applied Mechanics*, Vol. 36, 1969, pp. 650-52.
9. Evans, A. G. and Hutchinson, J. W., "Thermomechanical Integrity of Thin Films and Multilayers", *Acta Metallurgica et Materialia*, Vol. 43, 1995, pp. 2507-2530.
10. Lagace, P. A., Brewer, J. C., and Varnerin, C., *TELAC Manufacturing Course Notes*, TELAC Report 88-4B, Massachusetts Institute of Technology, 1990.
11. ASTM Designation D 3433-93, *Annual Book of ASTM Standards*, Vol. 15.06, 1993, pp. 218-224.
12. Grady, J. E., "Review of Fracture in Adhesive Joints Considering Rocket Motor Application", *NASA-TP-3199*, 1992, pp. 39-43.
13. Shetty, S. P., and Spearing, S. M., "Fracture Resistance of a Fiber-Reinforced Film Adhesive", submitted to *Scripta Materialia*.

THE ANALYSIS OF BONDED LAP JOINTS

M. Chao^{1, 2}, W. K. Chiu², R. Jones², J. Wang³, and D. Kelly³

¹ Cooperative Research Centre for Advanced Composite Structures Limited, 506 Lorimer St, Fishermens Bend, Vic. 3207, Australia

² Department of Mechanical Engineering, Monash University, Clayton, Vic 3168, Australia

³ Department of Aerospace Engineering, The University of New South Wales, Sydney, Australia

SUMMARY: Structural adhesives are being increasingly used in the joining of both primary and secondary aircraft structures. However, the properties of film adhesives (eg. FM 73) have been shown to demonstrate significant time dependencies, even at room temperature. This paper investigates the impact of these time dependent properties on the structural behaviour of adhesively bonded joints. To this end a series of finite element analysis were conducted where the time dependent properties of the adhesive were modelled using a unified plasticity theory. This work shows that, when performing certification assessments which require statements on the integrity and the durability of adhesively bonded joints subjected to complex load spectra, it may be necessary to consider an analysis which accounts for both time and load history effects.

KEYWORDS: bonded joints, composite repairs, certification, stress analysis

INTRODUCTION

When designing bonded repairs, or adhesively bonded joints, the stress/strain response of the adhesive plays a central role in determining both the load carrying capacity and the fatigue performance of the repair or joint, see [1, 2]. In recent years Chiu et al. [3] have developed a variant of the thick-adherend short over-lap adherend test specimen for characterising the stress/shear behaviour of thin film adhesives. The results revealed that the properties of the film adhesive FM73 were strongly time-dependent, even at room temperature. Chiu et al. [3] also used a unified constitutive model to describe the time dependent behaviour of the adhesive.

This paper assesses the significance of this time-dependent behaviour, in a realistic symmetric double lap joint, via a detailed finite element analysis. This study reveals that the stress/strain behaviour of the adhesive in a double lap joint is dependent on both the loading rate and the load history. When, at room temperature, the joint is subjected to monotonic loading with a constant loading rate the energy density at the worst point in the joint is almost time independent. However, it will be shown that when the joint is loaded monotonically but in a complex manner then the load history dependent properties of the adhesive can become significant. This effect has implications for the fatigue assessment of bonded joints. It thus appears that, when performing a certification assessment which requires statements of the integrity and durability of adhesively bonded joints subjected to complex load spectra, it may be necessary to consider an analysis which accounts for both time and load history effects.

THEORETICAL BACKGROUND

In the past few years there has been an increasing interest in the use of unified constitutive models for predicting the non-linear response of structural materials. These models overcome many of the deficiencies of the classical approach to the inelastic behaviour of materials. They were originally developed to model the response of metals in the high temperature regime where creep and stress relaxation are particularly important [4]. Classical techniques of modelling plasticity have a high degree of accuracy provided the loading is monotonic. However, they become increasingly inaccurate when the material is subjected to cyclic loading. In order to overcome this shortcoming an extension of the unified constitutive model, originally developed by Ramaswamy [5], was used in this investigation. This model was an extension of the generic back stress (Ω_{ij}) and drag stress (Z) model proposed by Stouffer and Bodner [6]. The model was later shown to be applicable to a range of materials and has been extensively used within Australia, see Kuruppu, et al. [7] and Jones, et al. [2, 8, 9]. The Ramaswamy-Stouffer model has also been extended to describe the mechanical behaviour of thin film adhesives, see Chiu et al [3].

This formulation uses two internal state variables, back stress Ω_{ij} (deviatoric) tensor and drag stress Z to define the state of the material. Here the inelastic deformation is driven by the over stress which is defined as $(S_{ij} - \Omega_{ij})$. Similar types of theories have been widely used to describe the time dependent behaviour of thermoplastics. In this approach, the flow equation is defined as:

$$\dot{\epsilon}_{ij}^i = D \exp \left[\frac{-A}{2} \left(\frac{Z^2}{3K_2} \right)^n \right] \frac{(S_{ij} - \Omega_{ij})}{\sqrt{K_2}} \quad (1)$$

where $\dot{\epsilon}_{ij}^i$ is the inelastic strain rate tensor, S_{ij} is the deviatoric stress and $K_2 = \frac{1}{2} (S_{ij} - \Omega_{ij})(S_{ij} - \Omega_{ij})$. Here D , A and n are material constants. The term $(S_{ij} - \Omega_{ij}) / \sqrt{K_2}$ in equation (1) is the normalised overstress and defines the straining direction. The drag stress is history dependent and evolves with the effective inelastic strain ϵ^i . The initial drag stress is Z_0 , final Z_1 , and m_0 controls the rate of evolution. The ‘‘growth’’ of the drag stress is defined by equation (2).

$$Z = Z_1 + (Z_0 - Z_1) e^{-m_0 \epsilon^i} \quad (2)$$

The back stress is initially zero and its evolution is controlled by an evolution equation, viz:

$$\dot{\Omega}_{ij} = f_2 \dot{S}_{ij} + f_1 \dot{\epsilon}_{ij}^i - \frac{3}{2} f_1 \frac{\Omega_{ij}}{\Omega_{\max}} \dot{\epsilon}^i \quad (3)$$

where $\dot{\epsilon}^i = \sqrt{\frac{2}{3} \dot{\epsilon}_{ij}^i \dot{\epsilon}_{ij}^i}$ is the effective inelastic strain rate. Here, f_1 , f_2 and Ω_{\max} are material constants. The effective inelastic strain rate is defined in the normal fashion.

VALIDATION OF MODEL

Consider the symmetric double lap joint shown in Figure 1. This joint has an overlap length of 90 mm, and consists of two identical aluminium adherends with an elastic modulus $E = 70000$ MPa, and $t=1.5$ mm. The aluminium adherends and doublers were assumed to be bonded together using a FM73 film adhesive. The adhesive, FM73 film, was 0.2 mm thick and had a shear modulus of 750 MPa and its behaviour may be described using the state variable formulation described above. Some typical material parameters for the constitutive law for FM73 at room temperature are given in Table 1. This joint was analysed using both the 1 dimensional formulation, referred to as BJ4C and described in detail in [8], and a variant of the modified ABAQUS analysis program described in [9]. In each case a remote stress of 401 MPa was assumed to be monotonically applied to the ends of the inner adherend with the load increasing from 0 to its maximum load in either 0.1 sec, 1 sec, 10 sec or 100 sec. A comparison of the calculated maximum mean shear strains γ in the joint is shown in Table 2.

Table 1: Some typical material parameters for FM73 film at room temperature, see [3]

	A	D	f_1 (MPa)	f_2	n	m_0	Ω_{max}	Z_0 (MPa)	Z_1 (MPa)
Room temp.	1	10000	800	0.2	0.85	10	12.5	120	350

Table 2: Comparison of mean shear strain γ with 1D Visco-Plastic Formulation, $L/2t = 15$

Dimension	Loading Time (sec)			
	0.1	1	10	100
1D algorithm	0.143	0.152	0.163	0.177
Finite element 2D/3D	0.152	0.165	0.179	0.189
% Diff	5.9	7.9	8.9	6.3

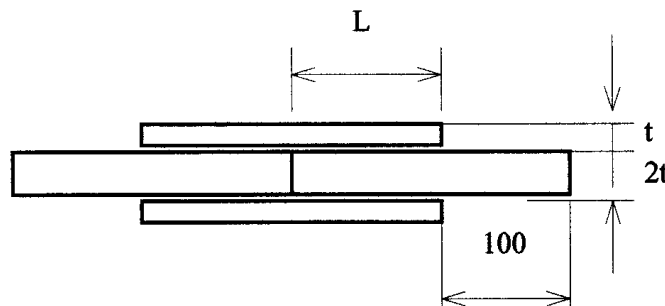


Figure 1: A schematic diagram of the symmetric double lap joint

ANALYSIS OF DOUBLE LAP JOINTS

Having thus validated the finite element implementation a further series of finite element analysis of various double lap joints (Figure 2) were then performed. The joints analysed in this paper had ($L/2t$) ratios of 7.5 and 15 and a range of load histories were evaluated. Due to symmetry, only a quarter of the double lap joint(s) needed to be modelled (Figure 2). These joints had overlap lengths of 90 mm (for $L/2t=15$), and 45 mm (for $L/2t=7.5$) respectively. The elastic modulus of the adherends was $E=70000$ MPa. The thicknesses were 3 mm (for the inner adherend) and 1.5 mm (for the doubler). The aluminium adherends and doublers were assumed to be bonded together using FM73. The FM73 adhesive was 0.2 mm thick and had a shear modulus of 750 MPa. These joints were loaded to a maximum remote stress of 401 MPa. with the load going from 0 load to its maximum value in either 0.1 sec, 1 sec, 10 sec or 100 sec. The stress/strain relationship at the worst (critical) point in the adhesive layer during these load up sequences is shown in Figures 3 ($L/2t=15$) and 4 ($L/2t=7.5$). These figures show that the stress/strain behaviour of the adhesive is dependent on the loading rate (the higher the loading rate, the higher is the apparent yield stress). The maximum stress level (apparent yield stress) in the adhesive is higher when the joint is loaded more rapidly. These figures also show that the strain level in the adhesive is dependent on the loading history. Here the higher loading rate resulted in lower adhesive strain levels. These results reveal the difficulties in assessing the conservativeness of any rate independent bonded joint analysis, or in determining the integrity of such a joint based on either the maximum stress or the maximum strain failure theories.

In contrast to the stress or strain based approaches, Hart-Smith's [4] analysis of a double lap joint, revealed that the load carrying capacity of the bond can be estimated from the energy density at the worst point in the adhesive. This design methodology was based on the assumption that the adhesive behaviour can be approximated with a single stress/strain curve. This simplification was not used in our analysis. Here, the adhesive was allowed to undergo both creep and visco-plastic behaviour. As shown in Figures 3 and 4 the stress/strain relationship at any location along the adhesive layer was governed by the local adhesive strain rate (ie. the higher the local adhesive strain rate, the larger will be the apparent yield stress of the adhesive).

To determine how the rate-dependent adhesive properties affect the overall conclusion presented by Hart-Smith [4], the energy density at the worst point in the adhesive layer was also calculated. The results are shown in Table 3. The first observation, apparent from this Table, is that the energy density at the worst point is slightly higher when the ($L/2t$ ratio) is 7.5. Hence one would expect the joint with a lower ($L/2t$) ratio to have a slightly lower load carrying capacity. This has been shown in the experimental studies conducted by Wang and Kelly [10]. More importantly we find that, whilst the local stress/strain behaviour of the adhesive are largely dependent on the loading rate, the energy density at the worst point of the adhesive is relatively independent of the loading rate. There is only approximately 8% variation (refer to Table 3) in the energy density from the slowest to the fastest loading rate. Thus the formulae presented by the Hart-Smith [4] for estimating the load carrying capacity of a double lap joint appears to be valid when the joint is loaded in a truly monotonic fashion and when failure occurs in the adhesive.

A separate set of analyses were performed using similar joint configurations (ie. $L/2t=7.5$ and $L/2t=15$) under a more complex two stage loading process. In the first analysis, the initial load up from 0 - 350 MPa was undertaken in 1 sec (phase 1) and the final load up from 350 MPa to 422 MPa was attained in 100 sec (phase 2). In the second analysis, the initial load up from 0 - 50 MPa was undertaken in 100 sec (phase 1) and the load up from 350 MPa to 422 MPa took 1 sec (phase 2). The stress/strain behaviour at the worst point in the adhesive layer are shown in Figures 5 and 7. For comparison purposes the stress/strain curves for the cases when the load was increased from 0 - 422 MPa in both 1 and 100 sec are also included. As expected, the stress/strain behaviour of the adhesive is dependent on the loading history. Figure 5 also shows that during phase 1 of the loading, the stress/strain curve of the adhesive is similar to that when the joint was loaded from 0 - 422 MPa in 1 second. When the specimen undergoes the second phase of loading (350 - 422 MPa), the stress/strain behaviour of the adhesive tends towards the stress/strain curve when the joint was loaded from 0 - 422 MPa in 100 sec. It should also be noted that the final strain level attained by the adhesive is also slightly larger than when it was loaded monotonically from 0 - 422 MPa in 100 sec. The energy density at the worst point in the adhesive was also calculated and, for the first load case, the results are shown in Figure 6. For comparison the energy density curves for monotonic loading from 0 - 422 MPa in both 1 and 100 sec are also included in Figure 6. In this case the energy density calculated when the joint was loaded in this complex loading procedure is approximately 16 % higher than that calculated when the joint was monotonically loaded.

Table 3: Effect of loading rate on energy density both $L/2t=7.5$ and 15 at room temp.

Energy Density (MPa)	L/2t	Loading Time (sec)	0.1	1	10	100	% Diff
.	7.5	Adhesive layer	42.6	44.4	46.1	47.1	9.5
	15	Adhesive layer	41.6	43.7	44.9	45.1	7.8

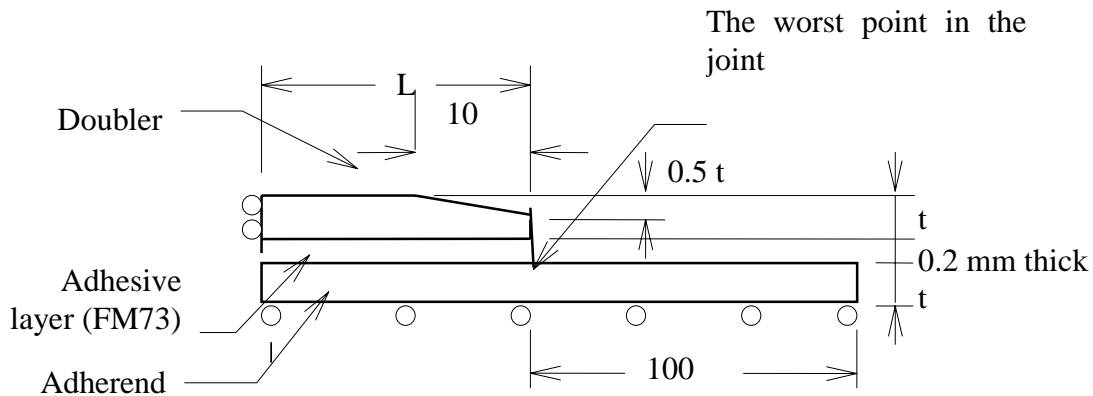


Figure 2: A quarter of a symmetric double lap joint

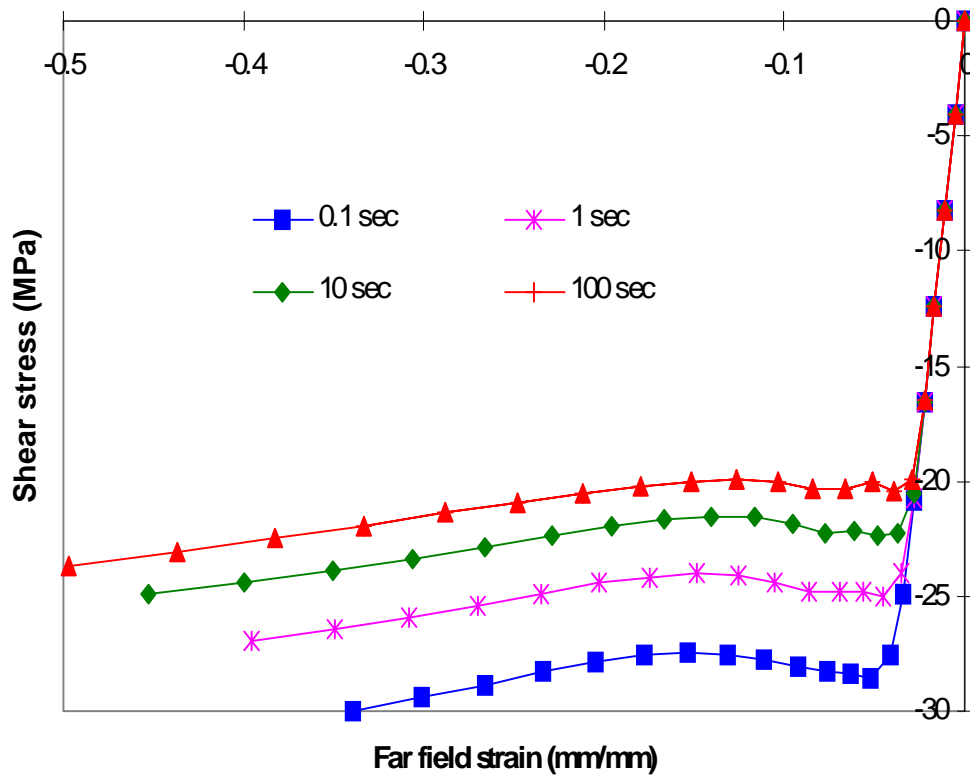


Figure 3: Adhesive shear stress-strain curves at a critical point in the joint, $L/2t=15$.

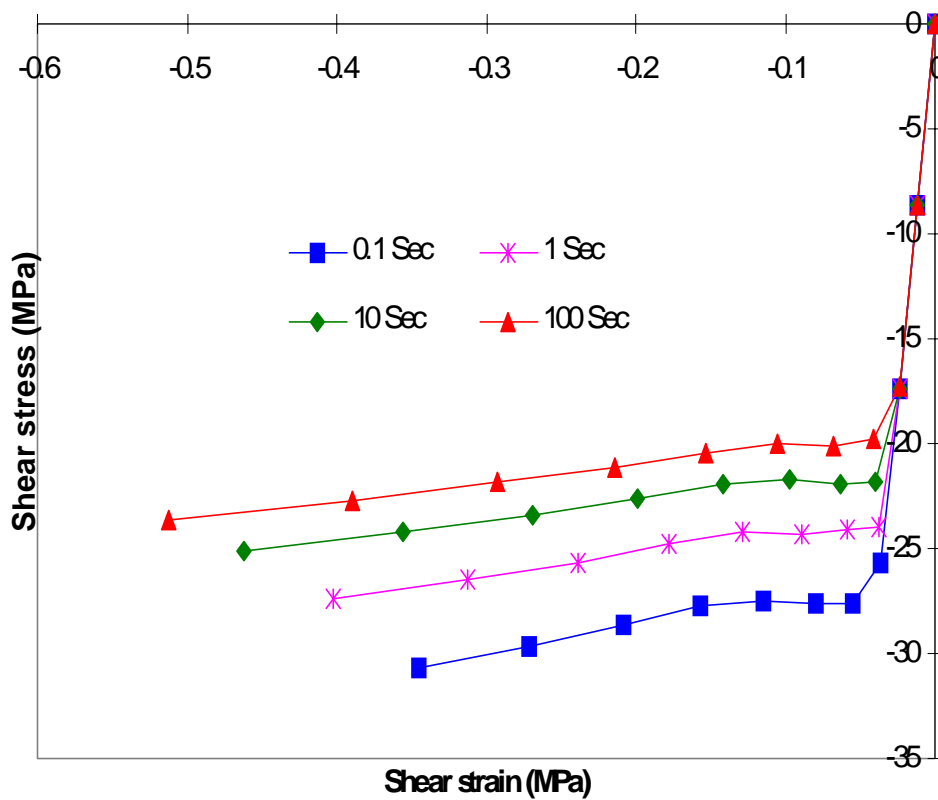


Figure 4: Adhesive shear stress-strain curves at a critical point in the joint, $L/2t=7.5$.

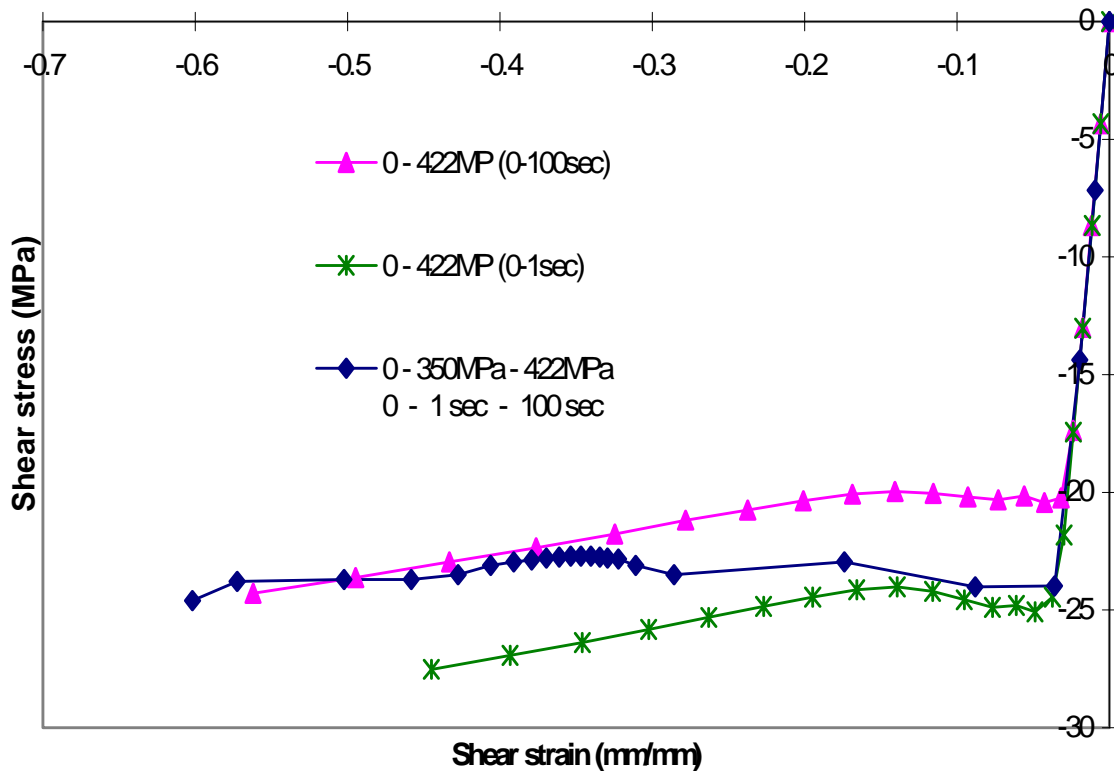


Figure 5: Adhesive shear stress-strain curves at the critical point, $L/2t=15$, complex loading

Figure 7 shows the stress/strain behaviour of the adhesive at the worst point in the joint when it was loaded initially from 0 to 350 MPa in 100 sec (phase 1) and subsequently loaded from 350 MPa to 422 MPa in 1 sec (phase 2). The typical stress/strain behaviours at the same point when the joint is loaded from 0 to 422 MPa in 1 sec and 100 sec are included for comparison. As expected, the initial portion of the stress/strain curves under the first phase of the complex loading was similar to that when the joint was loaded monotonically from 0 - 422 MPa in 100 sec. However, when the loading rate was increased (ie. from 350 - 422 MPa in 1 sec), the stress/strain behaviour changes accordingly, and the local apparent yield stress of the adhesive was observed to have increased. Here the stress/strain curve of the adhesive during the second phase of the loading approaches its stress/strain curve when the joint was loaded monotonically from 0 - 422 MPa in 1 second.

The energy density curve calculated at the worst point of the adhesive is shown in Figure 8. Here the energy density curves for the cases when the joint was loaded from 0 - 422 MPa in 1 and in 100 sec are also included. It can be seen that the energy density of adhesive in the joint subjected to the complex load history is approximately 9 % less than that calculated when the joint was loaded up monotonically from 0 - 422 MPa in 100 seconds.

These analyses show that, at room temperature, when the loading history is simply monotonic the rate dependent properties of the adhesive in the double lap joint have limited effects on the load carrying capacity of the adhesive bond. However, when the joint is subjected to a complex monotonic loading history the time dependent properties of the adhesive should not be ignored.

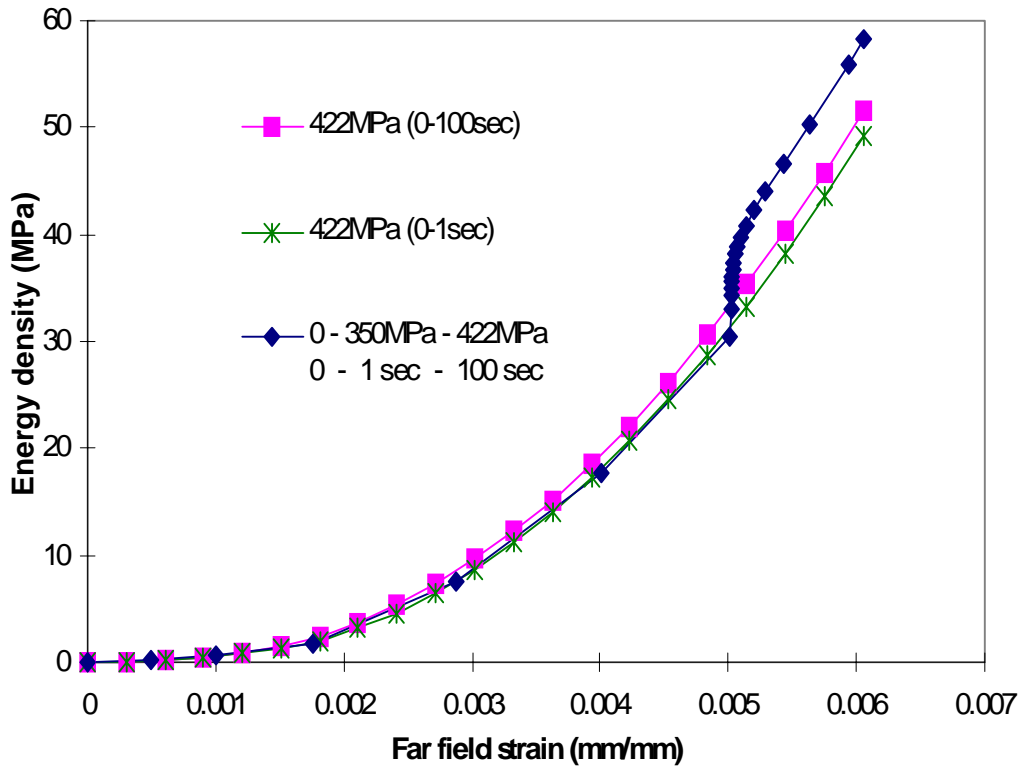


Figure 6: Strain energy density at a critical point in the adhesive, $L/2t=15$, complex loading

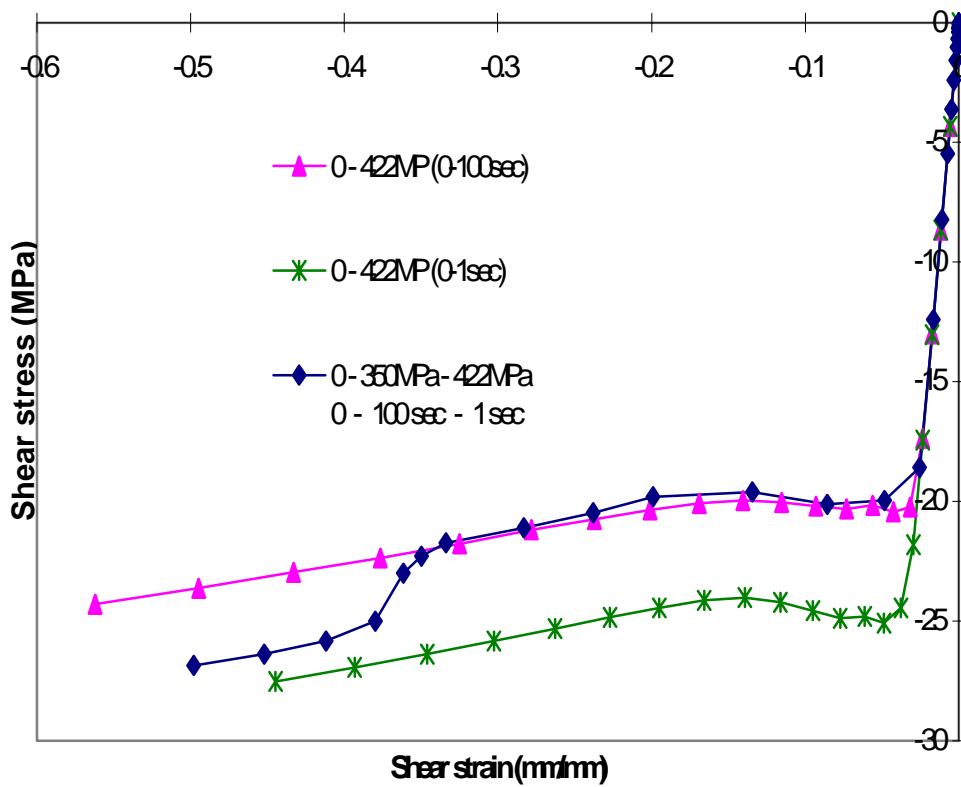


Figure 7: Adhesive shear stress-strain at critical point, complex loading

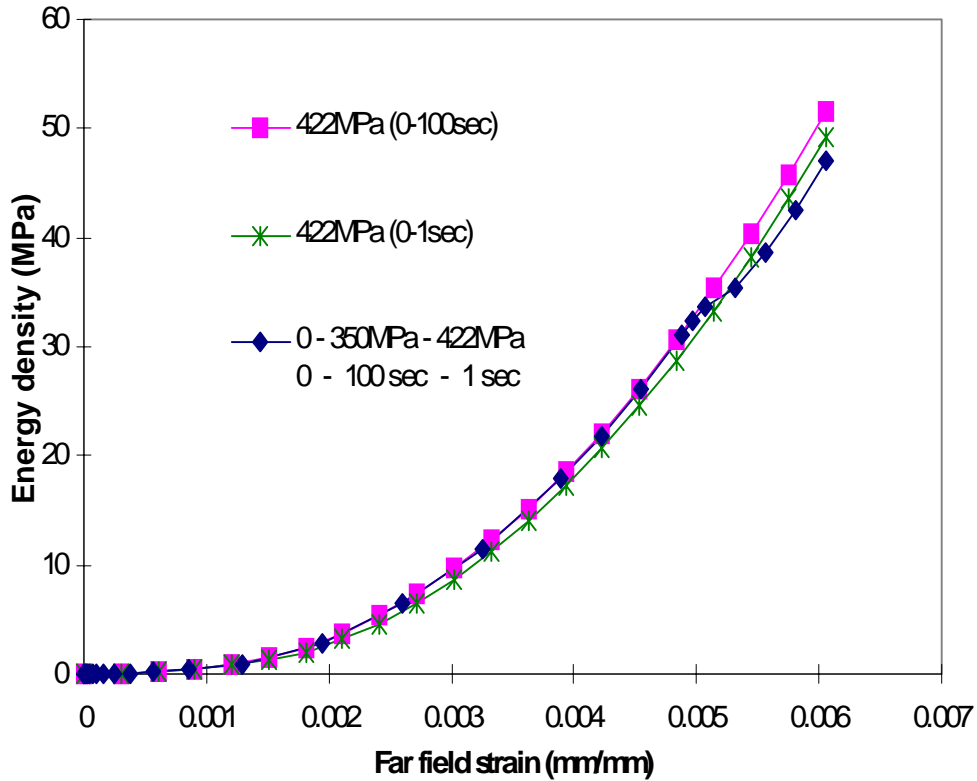


Figure 8: Strain energy density at a critical point in the adhesive, $L/2t=15$, complex loading

CONCLUSION

This paper has revealed that the stress/strain behaviour of the adhesive in a double lap joint can be dependent on both the loading rate and the load history. At room temperature when the load is monotonic and has a constant loading rate the energy density at the worst point in the joint is almost time independent. When the joint is still loaded monotonically but in a complex manner then the load history dependent properties of the adhesive can become significant. This effect has implications for the fatigue assessment of bonded joints. It thus appears that, when performing a certification assessment which requires statements of the integrity and durability of adhesively bonded joints subjected to complex load spectra, it may be necessary to consider an analysis which accounts for both time and load history effects.

ACKNOWLEDGMENT

Support for this project was provided by the Cooperative Research Centre - Aerospace Structures, Australia.

REFERENCES

1. Hart-Smith, L.J. (1988), "Design and analysis of bonded repairs for metal aircraft structures", Chapter 3, Bonded Repair of Aircraft Structures, Edited by Baker, A.A. and R. Jones, Martinus Nijhoff, The Netherlands.
2. Jones R., Molent L., Paul J. J. , Saunders T., Chiu W. K, "Development of a composite repair and the associated inspection intervals for the F111C stiffener runout region", In NASA Conference Publication 3274, pp.339-350, 1994.
3. W. K. Chiu, P. D. Chalkley and R. Jones, "Effects of Temperature on the Shear Stress-Strain behaviour of Structural Adhesives (FM73) ", Computers and Structures, 53, 3, pp 483-489, 1994.
4. Stouffer, D.C. and Dame L. T., "Inelastic deformation of metals", John Wiley and Sons, New York, 1996.
5. Ramaswamy, V.G. (1986), "A constitutive model for the inelastic multiaxial cyclic response of a nickel base superalloy Rene 80", NASA, CR-3998, 36.
6. Stouffer, D.C. and S.R. Bodner (1982), "A relationship between theory and experiment for a state variable constitutive equation", Mechanical Testing for Deformation Model Development, (Edited by R.W. Rhode and J.C. Swearingen), ASTM STP 765, 239-250.
7. Kuruppu, M.D., J.F. Williams, N. Bridgford, R. Jones, and D.C. Stouffer (1992), "Constitutive modelling of the elastic-plastic behaviour of 7050-T7451 aluminium alloy", Journal of Strain Analysis, 27, pp.85-92.
8. Jones, R., B. Trippit, W.K. Chiu, and J. Tomas (1995), "Lap joint theory revisited", Polymers and Polymer Composites, 3, pp.11-19.
9. Trippit, B. and R. Jones (1995), "Recent Australian developments in the engineering applications of constitutive modelling", Numerical Implementation and Application of Constitutive Models in the Finite Element Method, ASME, AMD-Vol. 213/MD-Vol.63, pp.15-20.
10. Wang, J. & D. Kelly (1996), "Experimental investigation on time-dependent behaviour of adhesively bonded joints", Proceedings of the 2nd International Symposium on Aeronautical Science and Technology, Indonesia, pp.630-645.

A SIMPLE UNIFIED APPROACH FOR THE ANALYSIS AND DESIGN OF ADHESIVE BONDED COMPOSITE LAMINATES

Flemming Mortensen and Ole Thybo Thomsen

*Institute of Mechanical Engineering, Aalborg University,
Pontoppidanstraede 101, DK-9220 Aalborg East, Denmark*

SUMMARY: This paper presents a newly developed unified approach for the analysis and design of adhesive bonded joints. The adherends are modelled as beams or wide plates in cylindrical bending, and are considered as generally orthotropic laminates using classical laminate theory. Consequently, adherends made as asymmetric and unbalanced composite laminates can be included in the analysis. The adhesive layer is modelled in two ways. The first approach assumes the adhesive layer to be a linear elastic material and the second approach takes into account the inelastic behaviour of many adhesives. The governing equations are formulated in terms of sets of first order ordinary differential equations, which are solved numerically using the so called 'multi-segment method' of integration.

KEYWORDS: adhesive bonded joints, laminates, cylindrical bending, linear/non-linear behaviour of adhesives, 'multi-segment method' of integration

INTRODUCTION

The use of polymeric fibre reinforced composite materials has gained widespread acceptance as an excellent way to obtain stiff, strong and very lightweight structural elements. However, load introduction into composite structural elements through joints, inserts and mechanical fasteners is associated with considerable difficulties. The primary reason for this is the layered structure of composite laminates, which results in poor strength properties with respect to loading by interlaminar shear and transverse normal stresses. Thus, the interaction between composite elements and adjoining parts often proves to be among the most critical areas of a structural assembly.

Joining of composite structures can be achieved through the use of bolted, riveted or adhesive bonded joints. The performances of the mentioned joint types are severely influenced by the characteristics of the layered composite materials, but adhesive bonded joints provide a much more efficient load transfer than mechanically fastened joint types. Accurate analysis of adhesive bonded joints, for instance using the finite element method, is an elaborate and computational demanding task [1, 2], and there is a specific need for analysis and design tools that can provide accurate results with little computational efforts involved. Such tools would be very useful for preliminary design purposes, i.e. in

the stages of design where fast estimates of stress and strain distributions as well as joint strengths are needed.

The main objective of the present paper is to consider a newly developed unified approach for the analysis of adhesive bonded joints. The approach can be used for the analysis of any of the following commonly used joint types: Single lap joints, scarfed single lap joints, bonded doubler lap joints, double lap joints, stepped lap joints (single and double sided) and scarfed lap joints (single and double sided).

In the analysis the adherends are modelled as beams or wide plates in cylindrical bending and are considered as generally orthotropic laminates using classical laminate theory. Consequently, adherends made as asymmetric and unbalanced composite laminates can be included in the analysis. The adhesive layer is modelled as continuously distributed linear tension/compression and shear springs. As non-linear effects in the form of adhesive plasticity play an important role in the load transfer, the analysis allows inclusion of nonlinear adhesive properties. The load and boundary conditions can be chosen arbitrarily.

Only the approach for analysis of single lap joints will be shown in this paper. However, the approach can be used for all the adhesive bonded joints mentioned above. Analysis procedures for these cases have been developed and are being implemented in the new composite analysis and design software package ESAComp [3]. ESAComp, which is being developed for the European Space Agency, provides an easy-to-use environment for preliminary evaluation and analysis of plies, laminates as well as structural composite components. The developed analysis tools for adhesive bonded joints are completely integrated in the ESAComp environment, which offers complete access to the ESAComp design system [3].

MATHEMATICAL FORMULATION

The single lap joint configuration composed of two similar or dissimilar generally orthotropic laminates subjected to general loading conditions is shown in Fig. 1.

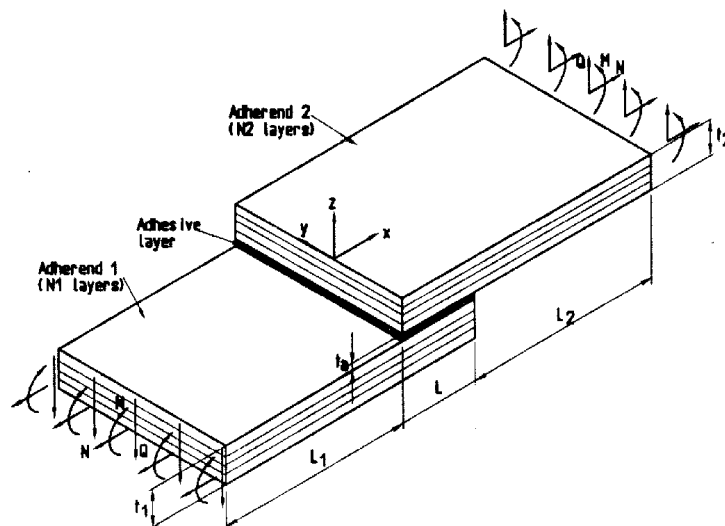


Fig. 1: Schematic illustration of adhesive single lap joint subjected to general loading conditions.

The adherend thicknesses are t_1 and t_2 and the thickness of the adhesive layer is t_a .

Basic Assumptions for the structural modelling

The basic assumptions adopted for the structural modelling are the following:

The adherends:

- Beams or wide plates in cylindrical bending, which are described by use of ordinary 'Kirchoff' plate theory.
- Generally orthotropic laminates using classical laminate theory (e.g. asymmetric and unbalanced composite laminates can be included in the analysis).
- The laminates are assumed to obey linear elastic constitutive laws.
- The strains are small, and the rotations are very small.

The adhesive layer:

- Modelled as continuously distributed linear tension/compression and shear springs.
- Inclusion of nonlinear adhesive properties, by using a tangent modulus approach for the nonlinear stress-strain relationship in conjunction with a modified von Mises yield criterion.

Load and Boundary Conditions:

- Can be chosen arbitrarily.

The system of governing equations is set up for two different cases; the adherends are modelled as wide plates in cylindrical bending or as narrow beams.

Modelling of adherends as plates in cylindrical bending

For the purposes of the present investigation, and with references to Fig. 1, cylindrical bending can be defined as a wide plate (in the y-direction), where the displacement field can be described as a function of the longitudinal coordinate only. As a consequence of this, the displacement in the width directions will be uniform. Thus, the displacement field can be described as:

$$u_0^i = u_0^i(x), \quad v_0^i = v_0^i(x), \quad w^i = w^i(x) \quad (1)$$

where u_0 is the displacement in the longitudinal direction, v_0 is the displacement in the width direction, and w is the displacement in the vertical direction (all with respect to the middle surfaces of the laminates), and where $i = 1, 2$ corresponds to the laminates 1 and 2, respectively (see Fig. 1). As a consequence of this, the following holds true:

$$u_{0,y}^i = v_{0,y}^i = w_{,y}^i = w_{,yy}^i = 0 \quad (2)$$

It should be noted that the concept of 'cylindrical bending' is not unique, and that other definitions than the one used in the present formulation can be adopted (see [4]).

Substitution of the quantities in Eqn 2 into the constitutive relations for a laminated composite material [4] gives the constitutive relations for a laminate in cylindrical bending:

$$\begin{aligned} N_{xx}^i &= A_{11}^i u_{0,x}^i + A_{16}^i v_{0,x}^i - B_{11}^i w_{,xx}^i, & M_{xx}^i &= B_{11}^i u_{0,x}^i + B_{16}^i v_{0,x}^i - D_{11}^i w_{,xx}^i \\ N_{yy}^i &= A_{12}^i u_{0,x}^i + A_{26}^i v_{0,x}^i - B_{12}^i w_{,xx}^i, & M_{yy}^i &= B_{12}^i u_{0,x}^i + B_{26}^i v_{0,x}^i - D_{12}^i w_{,xx}^i \\ N_{xy}^i &= A_{16}^i u_{0,x}^i + A_{66}^i v_{0,x}^i - B_{16}^i w_{,xx}^i, & M_{xy}^i &= B_{16}^i u_{0,x}^i + B_{66}^i v_{0,x}^i - D_{16}^i w_{,xx}^i \end{aligned} \quad (3)$$

where A_{jk}^i , B_{jk}^i and D_{jk}^i ($j,k = 1,2,6$) are the extensional, coupling and the flexural rigidities. N_{xx}^i , N_{yy}^i and N_{xy}^i are the stress resultants and M_{xx}^i , M_{yy}^i and M_{xy}^i are the moment resultants.

Based on the basic assumptions, the following kinematic relations for the laminates are derived:

$$u^i = u_0^i + z\beta_x^i, \quad \beta_x^i = -w_{,x}^i, \quad \beta_y^i = 0 \quad (4)$$

With reference to Fig. 1 the equilibrium equations are specified in three regions; $-L_1 \leq x \leq 0$, $0 \leq x \leq L$ and $L \leq x \leq L + L_2$.

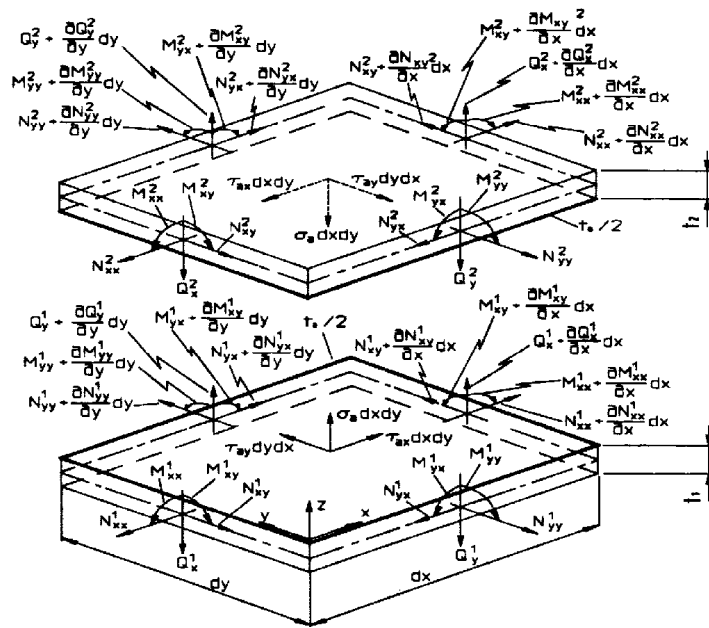


Fig. 2: Equilibrium elements in the overlap zone; $0 \leq x \leq L$.

Referring to Fig. 2, the equilibrium equations can be written as follows:

$$\left. \begin{aligned} N_{xx,x}^i &= 0 \\ N_{xy,x}^i &= 0 \\ Q_{x,x}^i &= 0 \\ M_{xx,x}^i &= Q_x^i \\ M_{xy,x}^i &= Q_y^i \end{aligned} \right\} \begin{aligned} i &= 1 \text{ for } -L_1 \leq x \leq 0, \\ i &= 2 \text{ for } L \leq x \leq L + L_2. \end{aligned} \quad (5)$$

$$\left. \begin{aligned} N_{xx,x}^1 &= -\tau_{ax}, & N_{xx,x}^2 &= \tau_{ax} \\ N_{xy,x}^1 &= -\tau_{ay}, & N_{xy,x}^2 &= \tau_{ay} \\ Q_{x,x}^1 &= -\sigma_a, & Q_{x,x}^2 &= \sigma_a \\ M_{xx,x}^1 &= Q_x^1 - \tau_{ax} \frac{t_1+t_a}{2}, & M_{xx,x}^2 &= Q_x^2 - \tau_{ax} \frac{t_2+t_a}{2} \\ M_{xy,x}^1 &= Q_y^1 - \tau_{ay} \frac{t_1+t_a}{2}, & M_{xy,x}^2 &= Q_y^2 - \tau_{ay} \frac{t_2+t_a}{2} \end{aligned} \right\} 0 \leq x \leq L.$$

The coupling between the two adherends is established through the constitutive relations for the adhesive layer, which as a first approximation is assumed to be homogeneous, isotropic and linear elastic. The constitutive equations for the adhesive layer are established by a spring model, where the adhesive layer is assumed to be composed of continuously distributed shear and tension/compression springs. The constitutive equations of

the adhesive layer are suggested in accordance with [5, 6, 7]:

$$\begin{aligned}\tau_{ax} &= \frac{G_a}{t_a}(u_2 - u_1) = \frac{G_a}{t_a}\left(u_0^2 - \frac{t_2}{2}\beta_x^2 - u_0^1 - \frac{t_1}{2}\beta_x^1\right) \\ \tau_{ay} &= \frac{G_a}{t_a}(v_2 - v_1) = \frac{G_a}{t_a}(v_0^2 - v_0^1) \\ \sigma_a &= \frac{E_a}{t_a}(w^2 - w^1)\end{aligned}\quad (6)$$

where G_a is the shear modulus and E_a is the elastic modulus of the adhesive layer. As a consequence of the modelling of the adhesive layer it is not possible to fulfil the condition of zero shear stresses at the free edges of the adhesive, see Fig. 1. However, in real adhesive joints no free edges at the ends of the overlap zone are present. Instead a fillet of surplus adhesive, a so called spew fillet, is formed at the ends of the overlap. This spew fillet allows the transfer of shear stresses at the overlap ends. Modelling the adhesive layer by spring models has been compared with other known analysis methods such as FEM [1] (including the spew fillet), and the results show that the overall stress distribution and the predicted values are in very good agreement.

From the equations derived it is possible to form the complete set of system equations for the problem. Thus combination Eqn 3, 4, 5 and 6 yields for laminate 1 and 2 in the areas $-L_1 \leq x \leq 0$ and $L \leq x \leq L + L_2$ (outside of overlap):

$$\left. \begin{aligned}u_{0,x}^i &= k_{1i}N_{xx}^i + k_{2i}N_{xy}^i + k_{3i}M_{xx}^i, & N_{xxx}^i &= 0 \\ w_{,x}^i &= -\beta_x^i, & Q_{x,x}^i &= 0 \\ \beta_{x,x}^i &= k_{4i}N_{xx}^i + k_{5i}N_{xy}^i + k_{6i}M_{xx}^i, & M_{xx,x}^i &= Q_x^i \\ v_{0,x}^i &= k_{7i}N_{xx}^i + k_{8i}N_{xy}^i + k_{9i}M_{xx}^i, & N_{xy,x}^i &= 0\end{aligned}\right\} \quad i = 1, 2. \quad (7)$$

The coefficients $k_{1i} - k_{9i}$ ($i = 1, 2$) contain laminate stiffness parameters and are a result of isolating $u_{0,x}^i, v_{0,x}^i$ and $w_{,xx}^i$ from N_{xx}^i, N_{xy}^i and M_{xx}^i in Eqn 3. Eqn 7 constitute a set of eight linear coupled first-order ordinary differential equations. Within the overlap zone, i.e. for $0 \leq x \leq L$, combination of Eqn 3, 4, 5 and 6 yields for laminate 1 and 2:

$$\begin{aligned}u_{0,x}^1 &= k_{11}N_{xx}^1 + k_{21}N_{xy}^1 + k_{31}M_{xx}^1, & u_{0,x}^2 &= k_{12}N_{xx}^2 + k_{22}N_{xy}^2 + k_{32}M_{xx}^2 \\ w_{,x}^1 &= -\beta_x^1, & w_{,x}^2 &= -\beta_x^2 \\ \beta_{x,x}^1 &= k_{41}N_{xx}^1 + k_{51}N_{xy}^1 + k_{61}M_{xx}^1, & \beta_{x,x}^2 &= k_{42}N_{xx}^2 + k_{52}N_{xy}^2 + k_{62}M_{xx}^2 \\ v_{0,x}^1 &= k_{71}N_{xx}^1 + k_{81}N_{xy}^1 + k_{91}M_{xx}^1, & v_{0,x}^2 &= k_{72}N_{xx}^2 + k_{82}N_{xy}^2 + k_{92}M_{xx}^2 \\ N_{xx,x}^1 &= \frac{G_a}{t_a}u_0^1 + \frac{G_a t_1}{2t_a}\beta_x^1 - \frac{G_a}{t_a}u_0^2 + \frac{G_a t_2}{2t_a}\beta_x^2, & N_{xx,x}^2 &= -\frac{G_a}{t_a}u_0^1 - \frac{G_a t_1}{2t_a}\beta_x^1 + \frac{G_a}{t_a}u_0^2 - \frac{G_a t_2}{2t_a}\beta_x^2 \\ N_{xy,x}^1 &= \frac{G_a}{t_a}v_0^1 - \frac{G_a}{t_a}v_0^2, & N_{xy,x}^2 &= -\frac{G_a}{t_a}v_0^1 + \frac{G_a}{t_a}v_0^2 \\ M_{xx,x}^1 &= Q_x^1 + \frac{G_a(t_1+t_a)}{2t_a}u_0^1 + \frac{G_a t_1(t_1+t_a)}{4t_a}\beta_x^1, & M_{xx,x}^2 &= Q_x^2 + \frac{G_a(t_2+t_a)}{2t_a}u_0^1 + \frac{G_a t_1(t_2+t_a)}{4t_a}\beta_x^1 \\ & - \frac{G_a(t_1+t_a)}{2t_a}u_0^2 + \frac{G_a t_2(t_1+t_a)}{4t_a}\beta_x^2, & & - \frac{G_a(t_2+t_a)}{2t_a}u_0^2 + \frac{G_a t_2(t_2+t_a)}{4t_a}\beta_x^2 \\ Q_{x,x}^1 &= \frac{E_a}{t_a}w^1 - \frac{E_a}{t_a}w^2, & Q_{x,x}^2 &= -\frac{E_a}{t_a}w^1 + \frac{E_a}{t_a}w^2\end{aligned}\quad (8)$$

Eqn 8 constitute a set of 16 linear coupled first-order ordinary differential equations. A solution vector containing the fundamental variables for each adherend can be defined such that:

$$\{y^i\} = \{u_0^i, w^i, \beta_x^i, v_0^i, N_{xx}^i, N_{xy}^i, M_{xx}^i, Q_x^i\} \quad i = 1, 2 \quad (9)$$

These variables will be determined through the analysis. In addition, the following quantities:

$$\{y_{res}^i\} = \{N_{yy}^i, M_{yy}^i, M_{xy}^i, Q_y^i\} \quad i = 1, 2 \quad (10)$$

can be determined from the equilibrium equations and the constitutive relations. To solve the problem the boundary conditions have to be stated:

$$\begin{aligned}
 x = -L_1, L + L_2 : \text{prescribed} : & \left. \begin{array}{l} u_0^i \text{ or } N_{xx}^i, w^i \text{ or } Q_x^i, \\ \beta_x^i \text{ or } M_{xx}^i, v_0^i \text{ or } N_{xy}^i \end{array} \right\} i = 1, 2 \\
 x = 0 : \text{adherend 1} : & \text{Continuity across junction} \\
 & \text{adherend 2} : N_{xx}^2 = N_{xy}^2 = M_{xx}^2 = Q_x^2 = 0 \\
 x = L : \text{adherend 1} : & N_{xx}^1 = N_{xy}^1 = M_{xx}^1 = Q_x^1 = 0 \\
 & \text{adherend 2} : \text{Continuity across junction}
 \end{aligned} \tag{11}$$

The boundary conditions for adherend 2 at $x = 0$ and for adherend 1 at $x = L$ are derived from the assumption that the adherend edges are free, see Fig. 1.

Modelling of adherends as beams

Modelling the adherends as narrow beams can be considered as a special case of cylindrical bending. When the adherends are modelled as beams the width direction displacements are not considered, and only the longitudinal and vertical displacements are included. Thus, the displacement field in Eqn 1 is reduced to:

$$u_0 = u_0(x), \quad w = w(x) \tag{12}$$

For this case the constitutive relations for a composite beam are reduced to:

$$N_{xx}^i = A_{11}^i u_{0,x}^i - B_{11}^i w_{,xx}^i, \quad M_{xx}^i = B_{11}^i u_{0,x}^i - D_{11}^i w_{,xx}^i \tag{13}$$

The kinematic relations (Eqn 4), the equilibrium equations (Eqn 5) and the constitutive relations for the adhesive layer (Eqn 6) are the same as for cylindrical bending case except that all variables associated with the width direction are null.

The problem is reduced to a set of six coupled first-order ordinary differential equations for each adherend outside the overlap zone and twelve inside the overlap zone. For this problem, the solution vector containing the fundamental variables for each adherend is defined by:

$$\{y^i\} = \{u_0^i, w^i, \beta_x^i, N_{xx}^i, M_{xx}^i, Q_x^i\} \quad i = 1, 2 \tag{14}$$

The boundary conditions can be stated as for the cylindrical bending case (Eqn 11) except that v_0 or N_{xy} do not have to be specified on the boundaries $x = \text{constant}$.

Multi-segment method of integration

The set of governing equations, i.e. Eqn 7, 8 for the cylindrical bending case and the reduced set of equations for the narrow beam case, together with the boundary conditions Eqn 11, constitute a multiple-point boundary value problem, which can be expressed in the following general form:

$$\begin{aligned}
 \{y^1(x)\}_{,x} &= [\mathbf{A}_{11}(x)] \{y^1(x)\} + \{\mathbf{B}_1(x)\} & -L_1 \leq x \leq 0 \\
 \left\{ \begin{array}{l} \{y^1(x)\} \\ \{y^2(x)\} \end{array} \right\}_{,x} &= \begin{bmatrix} [\mathbf{A}_{11}^*(x)] & [\mathbf{A}_{12}^*(x)] \\ [\mathbf{A}_{21}^*(x)] & [\mathbf{A}_{22}^*(x)] \end{bmatrix} \left\{ \begin{array}{l} \{y^1(x)\} \\ \{y^2(x)\} \end{array} \right\} + \left\{ \begin{array}{l} \{\mathbf{B}_1(x)\} \\ \{\mathbf{B}_2(x)\} \end{array} \right\} & 0 \leq x \leq L \\
 \{y^2(x)\}_{,x} &= [\mathbf{A}_{22}(x)] \{y^2(x)\} + \{\mathbf{B}_2(x)\} & L \leq x \leq L + L_2
 \end{aligned} \tag{15}$$

The boundary conditions at $x = -L_1$, $x = 0$, $x = L$, $x = L + L_2$ (see Fig. 1) are stated by specifying linear combinations of the fundamental variables:

$$\begin{aligned} x = -L_1 & : [\mathbf{T}_0] \{ y^1(-L_1) \} = \{ \mathbf{U}_0 \} & x = L & : [\mathbf{T}_2] \left\{ \begin{array}{l} \{ y^1(L) \} \\ \{ y^2(L) \} \end{array} \right\} = \{ \mathbf{U}_2 \} \\ x = 0 & : [\mathbf{T}_1] \left\{ \begin{array}{l} \{ y^1(0) \} \\ \{ y^2(0) \} \end{array} \right\} = \{ \mathbf{U}_1 \}, & x = L_2 & : [\mathbf{T}_3] \{ y^1(L_2) \} = \{ \mathbf{U}_3 \} \end{aligned} \quad (16)$$

It should be emphasised that the equations in Eqn 16 do not involve any restrictions on the boundary conditions, and that any natural boundary conditions may be stated in this form. The multiple-point boundary value problem constituted by Eqn 15 and Eqn 16 is solved using the 'multi-segment method of integration' [8]. This method is based on a transformation of the original 'multiple-point' boundary value problem into a series of initial value problems. The principle behind the method is to divide the original problem into a finite number of segments, where the solution within each segment can be accomplished by means of direct integration.

NON-LINEAR ADHESIVE FORMULATION

Most polymeric structural adhesives exhibit inelastic behaviour, in the sense that plastic residual strains are induced even at low levels of external loading. Thus, the assumption of linear elasticity of the adhesive is an approximation.

The concept of effective stress/strain is one way of approaching this problem, and it assumes, for a ductile material, that plastic residual strains are large compared with the creep strains at normal loading rates. Therefore a plastic yield hypothesis can be applied, and the multidirectional state of stress can be related to a simple unidirectional stress state through a function similar to that of von Mises.

However, it is widely accepted that the yield behaviour of polymeric structural adhesives is dependent on both deviatoric and hydrostatic stress components. A consequence of this phenomenon is a difference between the yield stresses in uniaxial tension and compression. This behaviour has been incorporated into the analysis by the application of a modified von Mises criterion suggested by [9]:

$$s = C_S (J_{2D})^{1/2} + C_V J_1, \quad C_S = \frac{\sqrt{3(1+\lambda)}}{2\lambda}, \quad C_V = \frac{\lambda-1}{2\lambda}, \quad \lambda = \frac{\sigma_c}{\sigma_t} \quad (17)$$

where s is the effective stress, J_{2D} is the second invariant of the deviatoric stress tensor, J_1 is the first invariant of the general stress tensor and λ is the ratio between compressive and tensile yield stress. For $\lambda = 1$, Eqn 17 is reduced to the ordinary von Mises criterion. At the failure load level, the first of Eqn 17 is transformed into the expression:

$$s = C_{S,ult} (J_{2D})_{ult}^{1/2} + C_{V,ult} (J_1)_{ult} \quad (18)$$

where the subscript 'ult' denotes 'ultimate'. Eqn 18 describes the failure envelope for the general case of a ductile material, and in three-dimensional stress space Eqn 18 represents a paraboloid with its axis coincident with the line $\sigma_1 = \sigma_2 = \sigma_3$.

The effective strain e is given by:

$$e = C_S \frac{1}{1+\nu} (I_{2D})^{1/2} + C_V \frac{1}{1-2\nu} (I_1) \quad (19)$$

where ν is Poisson's ratio. I_{2D} is the second invariant of the deviatoric strain tensor and I_1 is the first invariant of the general strain tensor.

The non-linear formulation can be solved together with an effective stress-strain relationship derived experimentally from tests on adhesive bulk specimens [5, 7]. Thus it is assumed that the bulk and ‘in-situ’ mechanical properties of the structural adhesive are closely correlated [9, 10].

The non-linear solution can be obtained based on a tangent modulus approach for the effective stress-strain relationship for the adhesive. For each adhesive point the effective strain ϵ and stress s are calculated using the elasto-static solution procedure, and if the stresses s are larger than some given proportional limit (s_{prop}) the elasticity modulus for this point is reduced. Convergence is usually achieved within a few iterations.

EXAMPLES AND DISCUSSION

To show the applicability of the developed linear and non-linear solution procedure two examples will be presented. One where the adhesive is assumed to be linear elastic and one where adhesive non-linearity is included. The adherends and adhesive properties assumed in the examples are given by (see Fig. 1 for reference):

Laminate 1 : graphite/epoxy $[0^\circ, 30^\circ, 60^\circ]_4$, $t_1 = 1.5$ mm, $l_1 = 50.0$ mm;

Laminate 2 : graphite/epoxy $[60^\circ, 30^\circ, 0^\circ]_4$, $t_2 = 1.5$ mm, $l_2 = 50.0$ mm;

Adhesive : epoxy AY103, $E_a = 2800$ MPa, $\nu_a = 0.4$, $t_a = 0.05$ mm;

Lengths : $L_1 = L_2 = 30.0$ mm, $L = 20.0$ mm;

Load & B.C. : $x = -L_1$: $u_0^1 = w = v_0^1 = M_{xx} = 0$,

$x = L + L_2$: $w = v_0^2 = M_{xx} = 0$, $N_{xx} = 0.1$ kN/mm;

Modelling : Wide plates in cylindrical bending.

The lay-up of the laminates is made such that the joint is symmetric seen from the adhesive layer midplane and such that the plies facing the adhesive layer are 0° plies.

The adhesive layer stresses are normalised with respect to the prescribed tension load on the loaded edge, which is given by:

$$\sigma_N = N/t_2b \quad (20)$$

where N is value of the axial tension load.

Example 1: Linear adhesive analysis

The vertical and the width direction displacements of the adherends are shown in Fig. 3.

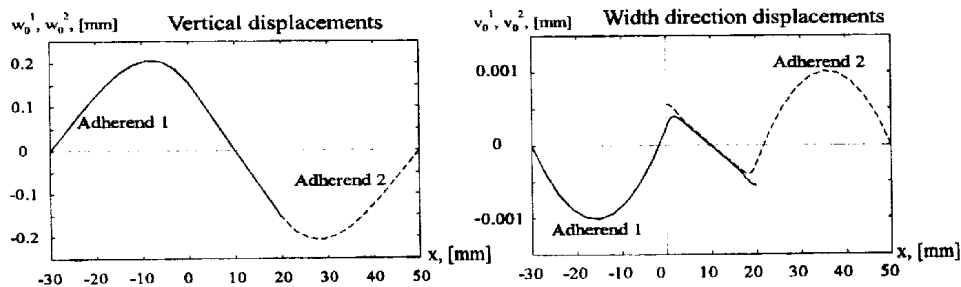


Fig. 3: Vertical displacements w^1, w^2 and width direction displacements v_0^1, v_0^2 .

The width direction displacements v_0^1, v_0^2 shown in Fig. 3 occur because of the inclusion of the coupling effects in the laminates. Fig. 4 shows the distribution of the adhesive layer stresses, and it is seen that the peak stresses are located close to the free ends of the overlap. As a consequence of the inclusion of the coupling effects in the laminates it is seen that width direction shear stresses (τ_{ay}) are induced.

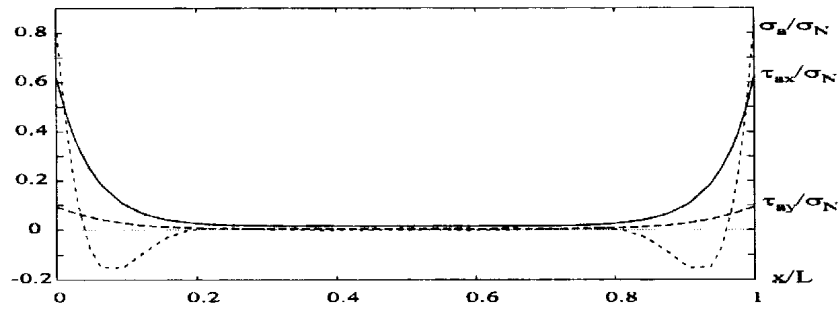


Fig. 4: Normalised adhesive layer stresses, τ_{ax}/σ_N , τ_{ay}/σ_N , σ_a/σ_N .

Example 2: Non-linear adhesive analysis

The stress/strain curve for the used adhesive AY103 from Ciba-Geigy is obtained from bulk specimens [2]. The non-linear material properties for this adhesive are given by:

$$\lambda = 1.3 \quad (\lambda = \sigma_c/\sigma_t), \quad s_{prop} = 27.0MPa, \quad s_{ult} = 71.5MPa, \quad e_{ult} = 0.049 \quad (21)$$

Using these properties together with the modified von Mises criterion results in the adhesive layer stress distribution shown in Fig. 5.

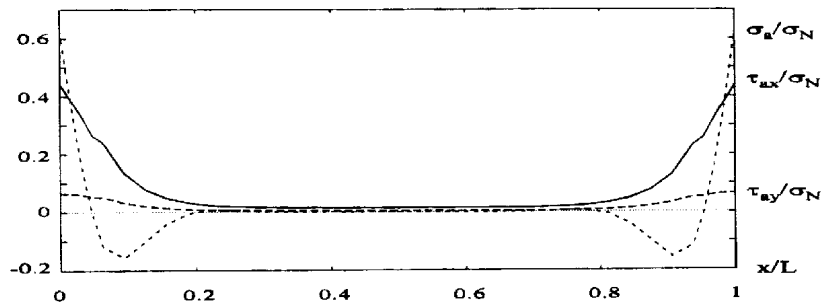


Fig. 5: Normalised adhesive layer stresses, τ_{ax}/σ_N , τ_{ay}/σ_N , σ_a/σ_N obtained by using the non-linear solution procedure.

Comparison of the adhesive stress distributions obtained for the linear case in Fig. 4 and for the non-linear case in Fig. 5 shows that inclusion of the non-linear effects reduce the maximum predicted stresses with about 25%. Based on these results it is concluded that inclusion of adhesive non-linearity is very important, as adhesive plasticity can occur even at low levels of external loading

CONCLUSION

A general method for analysis of adhesive bonded composite laminates has been presented. The analysis accounts for coupling effects induced by adherends made as asymmetric and unbalanced laminates. The analysis allows specification of any combination of boundary conditions and external loading, and it allows inclusion of the non-linear behaviour of many structural adhesives. The analysis can be carried out with the adherends modelled as narrow beams or wide plates in cylindrical bending.

The developed analysis procedures have proven to be robust, reliable and computationally effective, and the obtained results are very accurate. Thus the requirements specified with respect to the implementation in ESAComp are fulfilled.

REFERENCES

1. Crocombe, A.D. & Adams, R.D., "Influence of the Spew Fillet and other Parameters on the Stress Distribution in the Single Lap Joint", *Journal of Adhesion*, 13(2), 1981, pp. 141-155
2. Harris, J.A. & Adams, R.D., "Strength Prediction of Bonded Single Lap Joints by Non-Linear Finite Element Methods", *International Journal of Adhesion and Adhesives*, Vol.4, 1984, pp. 65-78.
3. Saarela, O., Palanter, M., Hberle, J. and Klein, M., "ESAComp: A Powerful Tool for Analysis and Design of Composite Materials", *Proc. of Int. Symp. on Advanced Materials for Lightweight Structures*, ESA-WPP-070, ESTEC, Noordwijk, The Netherlands, 1994, pp. 161-169.
4. Whitney, J.M., "Structural Analysis of Laminated Anisotropic Plates.", *Technomic Publishing Company. Inc., Lancaster*, 1987, pp. 24.
5. Thomsen, O.T., "Elasto-Static and Elasto-Plastic Stress Analysis of Adhesive Bonded Tubular Lap Joints". *Composite Structures*, 21, 1992. pp. 249-259.
6. Thomsen, O.T., Rits, W., Eaton, D.C.G. & Brown, S., "Ply Drop-off Effects in CFRP/Honeycomb Sandwich Panels-Theory", *Composite Science and Technology*, 56, 1996, pp. 407-422.
7. Tong, L., "Bond Strength for Adhesive-Bonded Single Lap Joints", *Acta Mechanica, Springer-Verlag*, 117, 1996, pp. 101-113.
8. Kalnins, A., "Analysis of Shell of Revolution Subjected to Symmetrical and Non-Symmetrical Loads", *Trans. ASME, J. Appl. Mech.*, 31, 1964, pp. 467-476.
9. Gali, S., Dolev, G. & Ishai, O., "An Effective Stress/Strain Concept in Mechanical Characterization of Structural Adhesive Bonding", *International Journal of Adhesion and Adhesives*, 1, 1981, pp. 135-140.
10. Lilleheden, L., "Properties of Adhesive In Situ and In Bulk", *International Journal of Adhesion and Adhesive*. Vol. 14, No. 1, 1994, pp. 31-37.

FINITE ELEMENT ANALYSIS OF MECHANICALLY FASTENED JOINTS IN CFRP

P. P. Camanho and F. L. Matthews

*Centre for Composite Materials, Imperial College of Science, Technology and Medicine,
London SW7 2BY, United Kingdom.*

SUMMARY: The effects of friction and clearance on the stress distribution around a hole in a mechanically fastened joint are investigated using a three-dimensional finite element model. The effects of these parameters are assessed by comparison with the perfect-fit, frictionless case. The influence of friction and clearance on the stress concentration factors related to bearing and tension failures, on the position of the maximum stresses and on the contact angle are investigated. It is concluded that with increasing friction, the maximum radial stress decreases whereas the maximum hoop stress increases. The locations where the maximum values occur are also influenced by the presence of friction. These effects may influence both strength and failure mode. The presence of clearance increases the maximum radial stress at the bearing plane and the maximum hoop stress at the end of the contact. It is concluded that a clearance fit reduces the joint strength.

KEYWORDS: joining, mechanical fastening, friction, clearance, finite element method

INTRODUCTION

Mechanically fastened joints have a wide range of applications in aeronautical industry. Typical applications in aircraft are the skin to spar connections in a wing, wing to fuselage connection and tail to fuselage connection. Although design procedures are well established to join metallic parts, the complex behavior of composite laminates and the possibility of choosing between several material combinations demands further research. As a joint is a critical component in a structure, improved designs are required to avoid a significant weight penalty. It was found [1-7] that factors like joint geometry, fibre orientation, stacking sequence and through-thickness pressure are important parameters on the joint strength. To include all these factors in a detailed stress analysis, required before predicting strength, numerical methods are adequate. In order to deal with the three-dimensional stress state at the hole boundary, the effects of stacking sequence and through-thickness pressure, three-dimensional models have been proposed [8], [9]. Such models are quite adequate when predicting bearing failure mode, where three-dimensional effects are extremely important [9], [10]. In this work, the effects of friction and clearance between the pin and the hole on the stress distributions around a pin-loaded hole in carbon-fibre reinforced plastics (CFRP) are investigated using a three-dimensional finite element model. The model is validated using an analytical solution derived for an infinite plate [11]. The stress distributions and stress concentration factors obtained for clearance fits and contacts with friction between the pin and the laminate are then compared with the frictionless, perfect-fit model. The present model will be developed in the future to include strength and failure mode prediction.

MODEL VALIDATION

In order to assess the accuracy of the finite element model, a comparison was made with the results obtained using de Jong's [11] analytical solution. A quasi-isotropic $(0^\circ/+45^\circ/-45^\circ/90^\circ)_s$ CFRP laminate is modelled using a three-dimensional finite element model. The material properties used are: $E_{11}=146.90$ GPa, $E_{22}=E_{33}=10.89$ GPa, $G_{12}=G_{13}=6.41$ GPa, $G_{23}=3.89$ GPa, $\nu_{12}=\nu_{13}=0.38$ and $\nu_{23}=0.78$. ABAQUS' [12] three-dimensional eight-node isoparametric laminated brick elements were used to model the laminate. Due to symmetry, only half of the laminate was modelled and the loading pin is assumed rigid. The laminate is clamped along one edge and a displacement is given to the rigid pin. A frictionless contact between the pin and the hole is assumed. The contact zone is calculated and a perfect-fit connection between the pin and the hole is modelled.

A FORTRAN program was created in order to process ABAQUS [12] results. The stresses at the hole boundary nodes are transformed from the material axes of each layer to a cylindrical coordinate system and the average stress at each position is calculated. These stresses are then normalized using the bearing stress, S_b , defined as:

$$S_b = \frac{P}{dt} \quad (1)$$

P being the load applied to the joint, t the laminate thickness and d the hole diameter.

The circumferential co-ordinate direction θ and the planes associated with the principal failure modes are defined in Fig. 1.

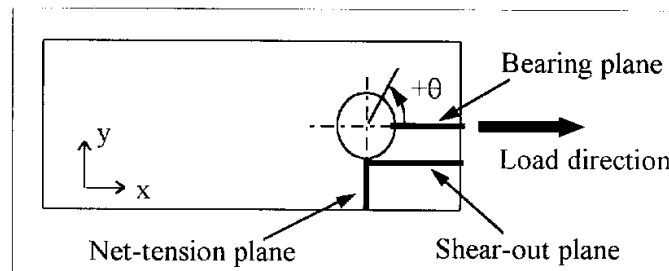


Fig. 1: Definition of planes and angle θ

The distribution of the normalized radial and hoop stresses along the hole boundary obtained by the current model and by the analytical solution [11] are shown in Fig. 2.

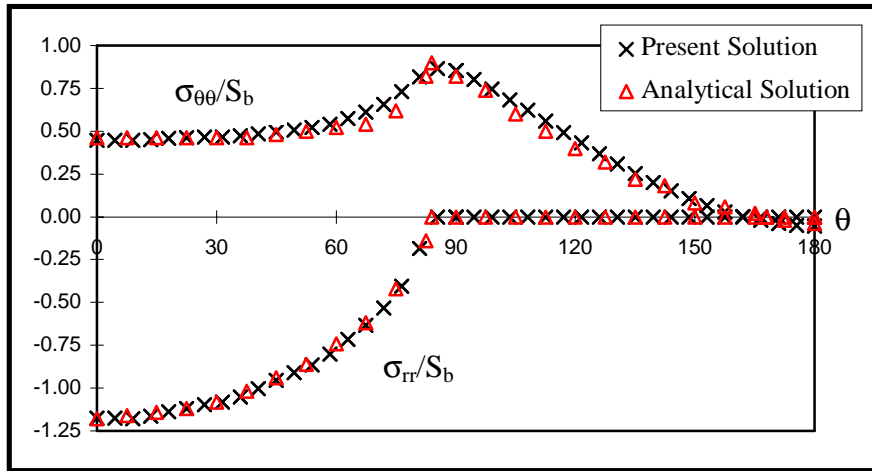


Fig. 2: Comparison of results

It can be seen that a good agreement between the finite element model and the analytical solution is achieved. Note that these distributions are independent of pin displacement.

EFFECT OF FRICTION

The same laminate configuration was used to verify the effect of friction on the stress distribution around pin-loaded holes. Three coefficients of friction, 0.2, 0.4 and 0.6, are used and the results are compared with the previous (frictionless) model.

The isotropic Coulomb friction model was used on the bolt-hole contact surface. The contact surfaces will slide when the following relation is satisfied:

$$\sigma_{r\theta} \geq \mu \sigma_{rr} \tag{2}$$

μ being the coefficient of friction between the pin and the laminate and σ_{rr} and $\sigma_{r\theta}$ the radial and shear stress respectively.

Small sliding between the pin and the hole is assumed. This means that a given node at the hole boundary will interact with the same local surface of the pin during the loading. Using this procedure, instead of verifying the contact between a node at the hole boundary and the entire surface of the rigid pin, the model is computationally more efficient and physically realistic.

The normalized radial, hoop and shear stress distributions along the hole boundary are shown in Fig. 3, Fig. 4 and Fig. 5 respectively.

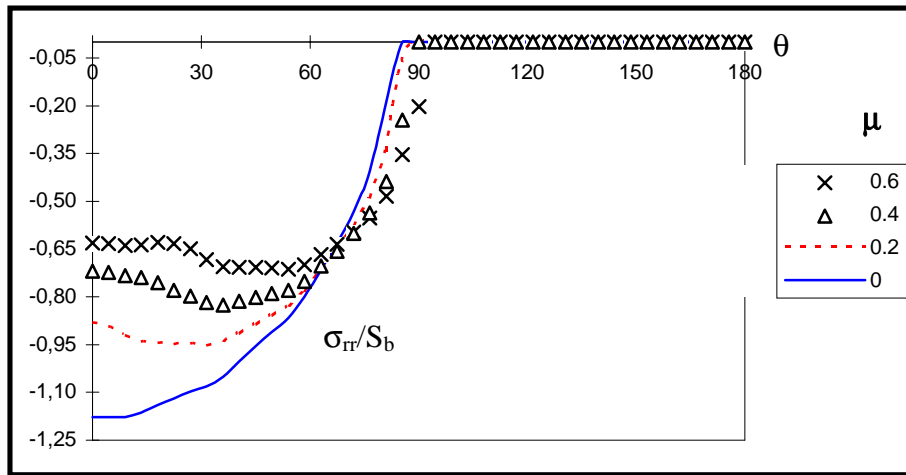


Fig. 3: Normalized radial stress distribution along the hole boundary

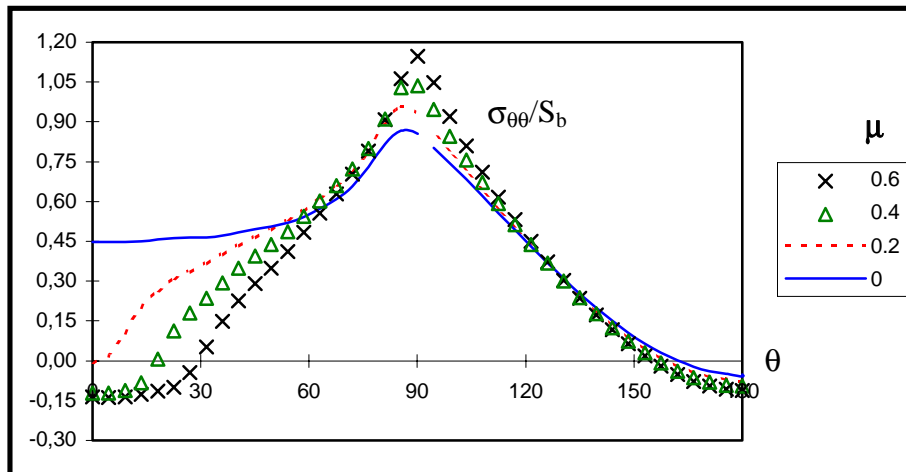


Fig. 4: Normalized hoop stress distribution along the hole boundary

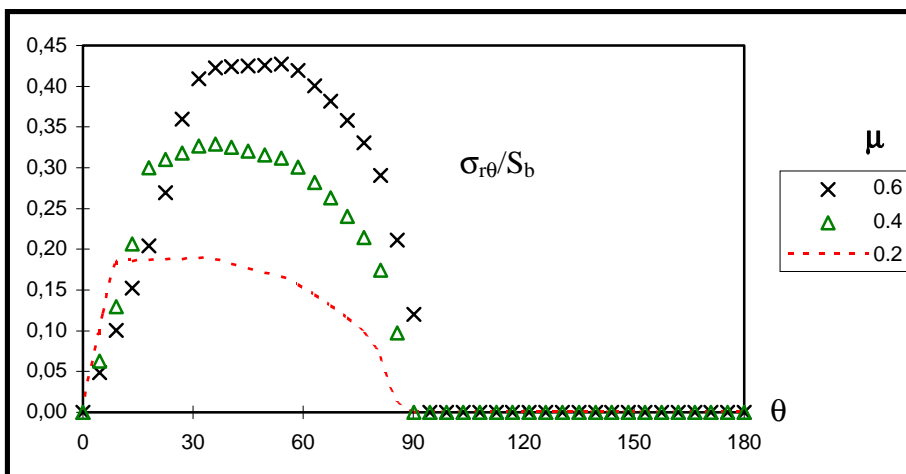


Fig. 5: Normalized shear stress distribution along the hole boundary

Increasing friction reduces the maximum radial stress and moves the location where the maximum occurs away from the bearing plane. The stress gradient along the hole boundary is also smaller when friction increases. The opposite effect occurs in the distribution of the hoop stress. It can be seen from Fig. 4 that the maximum hoop stress increases with increasing friction. The place where the maximum occurs is not significantly affected by the friction. The hoop stress near the bearing plane changes from tension to compression with increasing coefficient of friction. The angle where the compressive hoop stress occurs increases from 15° to 30° when the coefficient of friction increases from 0.4 to 0.6. As expected, the shear stress along the hole boundary increases with increasing coefficient of friction and the position of maximum shear stress moves away from the bearing plane (Fig. 5).

Stress concentration factors K_{bb} and K_{tb} are defined as:

$$K_{bb} = \frac{(\sigma_{rr})_{\max}}{S_b} \tag{3}$$

$$K_{tb} = \frac{(\sigma_{\theta\theta})_{\max}}{S_b} \tag{4}$$

The effects of friction on K_{bb} and K_{tb} and on the positions where these coefficients occur are shown in Fig. 6 and Fig. 7.

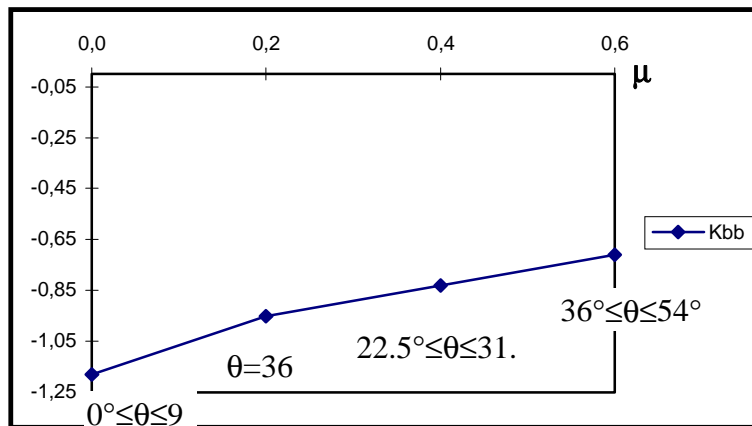


Fig. 6: Effect of μ on K_{bb}

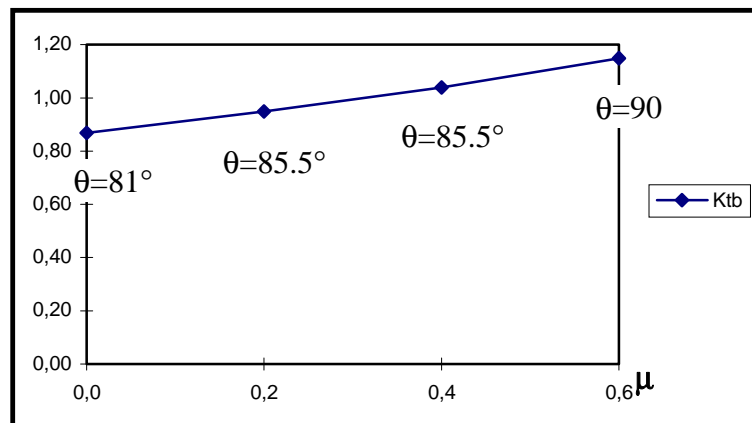


Fig. 7: Effect of μ on K_{tb}

The values of K_{bb} decrease in absolute value from -1.18 to -0.71, for coefficients of friction of 0 and 0.6 respectively. The position of maximum K_{bb} moves from $\theta=0^\circ$ to $\theta=54^\circ$. For the same coefficients of friction, K_{tb} increases from 0.87 to 1.15, but the position of the maximum value only changes by 4.5° , from 85.5° to 90° .

In Fig. 8, the sliding and non-sliding zones are shown for the several coefficients of friction.

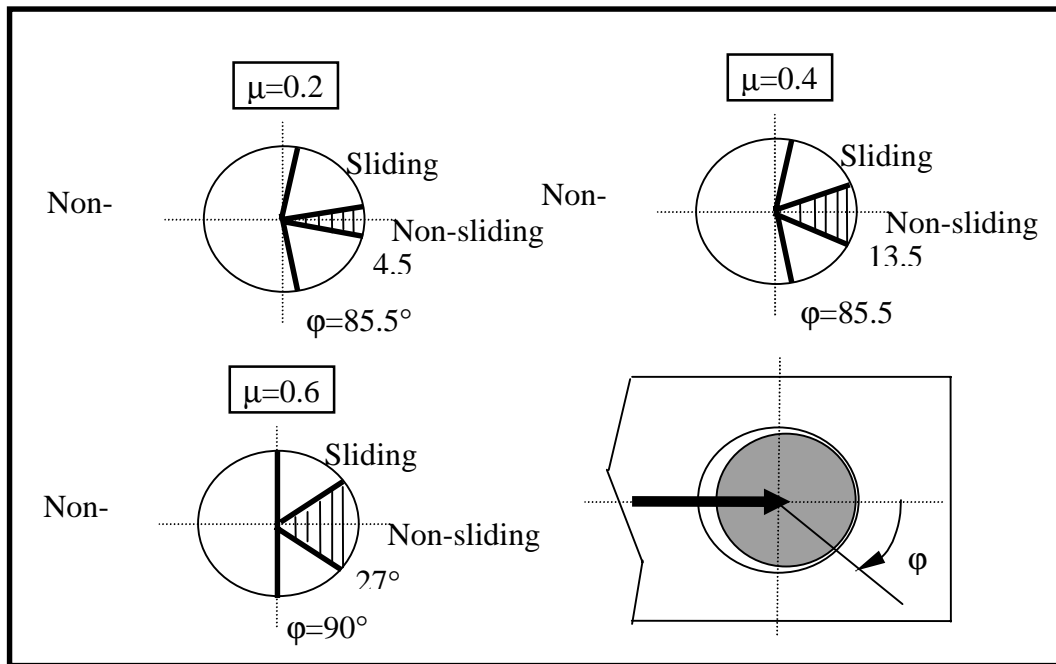


Fig. 8: Sliding zones and contact angles for several values of μ

As expected, the arc where sliding occurs decreases with increasing friction. The contact angle, ϕ , increases from 85° (frictionless situation and for $\mu=0.2$ and 0.4) to 90° ($\mu=0.6$).

EFFECT OF CLEARANCE

The effect of clearance was assessed by comparison of the results obtained from the perfect fit model with the results of a model including the minimum clearance value prescribed by prEN Aerospace 6037 standard (7/95 draft; clearance of 0.0127 mm) [13]. A rigid pin and a frictionless contact were assumed.

The normalized radial and hoop stresses around the hole boundary are shown in Fig. 9 for both configurations. For the model including clearance, the results are shown for several displacements of the pin: 2, 4 and 10% of the hole diameter.

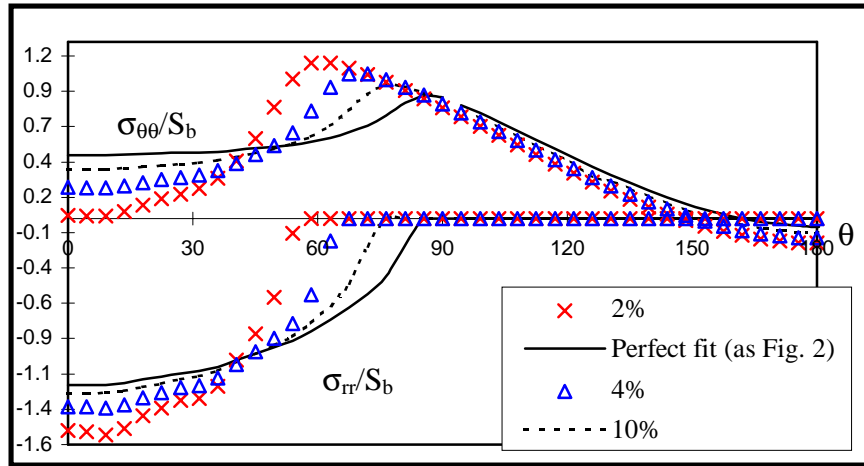


Fig. 9: Stress distributions for perfect-fit and clearance

The presence of clearance increases the normalized radial and normalized hoop stresses near the bearing plane and at the end of the contact arc respectively. At the bearing plane, the presence of clearance decreases the normalized hoop stress. These trends are reduced when the displacement of the pin is increased and, consequently, when the contact angle increases. This is further shown in Fig. 10 where the relation between K_{tb} , K_{bb} and the displacement of the pin is shown. The contact angles (ϕ) are also shown in Fig. 10 and defined in Fig. 8.

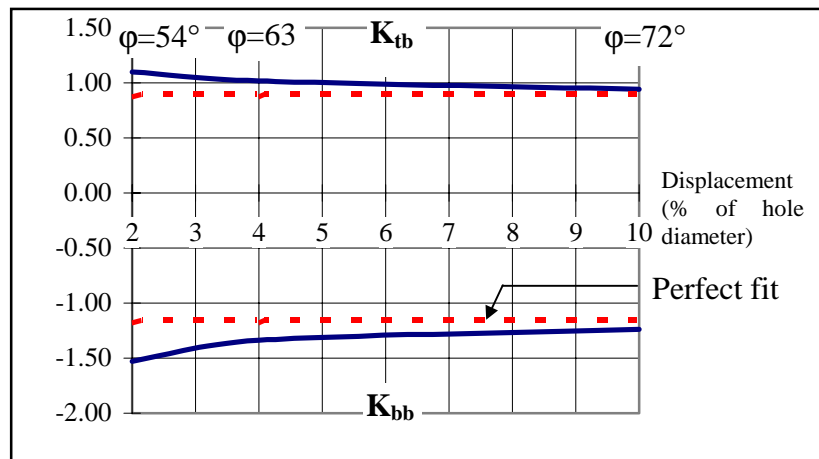


Fig. 10: Relation between displacement, K_{tb} and K_{bb}

The non-linear relation between the contact angle and applied load is shown in Fig. 11.

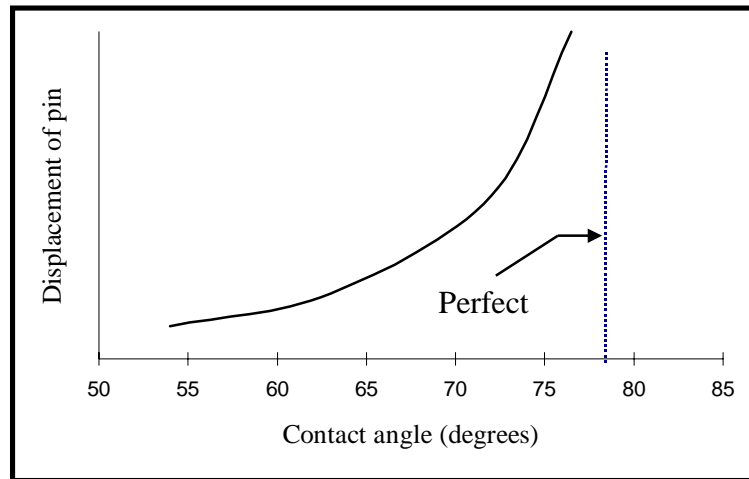


Fig. 11: Relation between displacement and contact angle

Both stress concentration factors K_{tb} and K_{bb} increase with the presence of clearance. These factors decrease for high pin displacements, but never reach the values obtained with a perfect-fit. Such results are related to the reduction of the contact angle shown in Fig. 11.

CONCLUSIONS

Based on the results obtained we can conclude that friction has a significant effect on the stress distribution around a pin-loaded hole, and consequently on the strength of a mechanically fastened joint. The most significant effect of friction is the reduction of the maximum radial stress and the change in location of the maximum away from the bearing plane. The reduction of the maximum radial stress can improve the bearing strength but the variation of position at the hole boundary where it occurs can change both damage mechanisms and bearing strength. The hoop stress near the bearing plane is reduced and becomes compressive for high coefficients of friction. This effect should not have significant influence on the bearing strength. The maximum hoop stress increases, but the position where it occurs is not significantly affected. Such effect is undesirable in joints prone to tensile failures. As expected, the shear stress increases with increasing friction, and friction increases the contact angle slightly. These effects may influence both strength and failure mode, so reliable methods to determine coefficient of friction between a metallic pin and a laminate are required, and a model to predict the strength of this type of joint should take into account the effect of friction.

The presence of clearance between the pin and the hole increases the maximum radial stress at the bearing plane and the maximum hoop stress at the end of the contact. Considering that these stresses are related to bearing and tension failures respectively, we can conclude that a clearance fit leads to a reduction of the joint strength. With this type of fit the relation between the contact angle and applied load is non-linear and the contact angle is less than the contact angle for a perfect fit. If we also consider that clearance reduces fatigue life of mechanically fastened joints in CFRP, we can conclude that such fits should be avoided.

Comprehensive information about effects on the load-carrying capability of the joint can be obtained if a strength prediction method is included in the present model. The current model will be developed in order to predict failure and failure mode using progressive damage laws based on experimental observations. As the stress concentration factors depend on the lay-up

used and joint geometry, the influence of friction and clearance will be assessed in laminates with other lay-ups and finite dimensions. In order to improve the predictions of the through-thickness stresses, new finite element models using three-dimensional elements in each layer of the laminate will be created.

ACKNOWLEDGMENTS

The first author wishes to acknowledge the support given by JNICT- Junta Nacional de Investigação Científica e Tecnológica, Sub-Programa Ciência e Tecnologia do 2º Quadro Comunitário de Apoio- Portugal.

REFERENCES

1. Hart-Smith, L.J., "Mechanically-Fastened Joints for Advanced Composites- Phenomological Considerations and Simple Analysis", *Douglas Paper 6748*, 1978, pp. 1-32.
2. Kretsis, G. and Matthews, F.L., "The Strength of Bolted Joints in Glass Fibre/Epoxy Laminates", *Composites*, Vol. 16, 1985, pp. 92-105.
3. Collings, T.A., "The Strength of Bolted Joints in Multi-Directional CFRP Laminates", *Composites*, Vol. 8, 1977, pp. 43-54.
4. Hart-Smith, L.J., "Design and Analysis of Bolted and Riveted Joints in Fibrous Composite Structures", *Douglas Paper 7739*, 1986, pp. 1-15.
5. Matthews, F.L., Kilty, P.F. and Godwin, E.W., "Load-Carring Joints in Fibre Reinforced Plastics", *Plastic and Rubber Process and Applications*, Vol. 2, 1982, pp. 19-25.
6. Hodgkinson, J.M., de Beer, D.L. and Matthews, F.L., "The Strength of Bolted Joints in Kevlar RP", *ESA SP-243*, 1986, pp. 53-61.
7. Collings, T.A., "On the Bearing Strengths of CFRP Laminates", *RAE Technical Report 82033*, 1982, pp. 1-23.
8. Matthews, F.L., Wong, C.M. and Chryssafitis, S., "Stress Distribution Around a Single Bolt in Fibre-Reinforced Plastic", *Composites*, Vol. 13, 1982, pp. 316-322.
9. Camanho, P.P. and Matthews, F.L., "Stress Analysis and Strength Prediction of Mechanically Fastened Joints in FRP: a Review", to be published in *Composites*.
10. Chang, F.K. and Chang, K.Y., "A Progressive Damage Model for Laminated Composites Containing Stress Concentrations", *Journal of Composite Materials*, Vol. 21, 1987, pp. 834-855.
11. de Jong, T., "Stresses Around Pin-Loaded Holes in Elastically Orthotropic or Isotropic Plates", *Journal of Composite Materials*, Vol. 11, 1977, pp. 313-331.
12. ABAQUS Users Manual, Hibbit, Karlsson and Sorensen Inc., Version 5.5, 1995.
13. Sims, G.D., Payne, D.R. and Ferriss, D.H., "Analysis and Experimental Validation of Structural Element Test Methods", *Proceedings Seventh European Conference on Composite Materials*, London, U.K., May 14-16, 1996, Vol. III: Composites Testing and Standardization, Woodhead Publishing Limited, pp. 73-78.

AN EXPERIMENTAL INVESTIGATION INTO THE USE OF INSERTS TO ENHANCE THE STATIC PERFORMANCE OF THIN COMPOSITE BOLTED LAP JOINTS

L. Mirabella and S.C. Galea

*Cooperative Research Centre for Advanced Composite Structures, 506 Lorimer Street,
Fishermens Bend, Victoria, 3207, Australia.
Airframes and Engines Division, DSTO Aeronautical and Maritime Research Laboratory,
Fishermens Bend, Victoria, 3207, Australia.*

SUMMARY: The aim of this program was to investigate the use of interference fit and bonded inserts in thin 8 ply quasi-isotropic, composite mechanically fastened single lap joints. The static behaviour of the joint was evaluated with various insert configurations. Bearing tests were also undertaken in order to evaluate the bearing behaviour of the laminate with the various insert configurations. Results from the bearing tests showed slight improvement in the bearing strength for press-fit straight inserts. A significant increase, up to 100%, in bearing strength was observed for the bonded top-hat insert compared to the no inserts case. The failure mode for the bolted joint specimens, without the inserts, appeared to be predominantly pull through of the fastener, even though the specimens were designed to fail in bearing. The pull-through type failure was caused by the secondary bending in the specimen which resulted in high severe pull-through stresses by the fastener head and collar. The top-hat inserts assisted in reducing the high pull-through stress exerted by the fastener head and collar and in some cases was so successful that the failure mode changed from pull-through to bearing with a corresponding 30% increase in the load carrying capacity of the joint.

KEYWORDS: inserts, bolted composite joints, g/e bolted joints.

INTRODUCTION

Lightweight, efficient, thin skinned composite laminates are experiencing increasing use in aerospace structures. In most applications thin laminates are bonded together, however mechanically fastened joints are also used extensively because of the requirements for inspection, manufacturing breaks, assembly and equipment access, and replacement/repair of damaged structures. However the strength of composite laminates are considerably weakened by the presence of fastener holes. For composites the maximum strength efficiency, ie [bolt joint strength] / [un-notched strength], of a single bolted joint in tension is only about 40% compared to 65% for metals. This is mainly due to the high stress concentrations, K_t from the high degree of brittleness, or lack of plasticity, and high degree of anisotropy of the material. In metallic structures yielding acts to relieve local high stresses and also to equalise uneven load distribution. Therefore a technique which will allow a more compliant response around a composite hole, in order to relieve stress concentrations, should result in an increase in composite bolted joint strength (ie promotes fastener load sharing.)

There are a variety of techniques available to increase the strength of mechanically fastened joints in composites. These include:

1. Softening around the hole to reduce the stress concentration at the hole by:
 - (a) installing softening strips, ie substituting 0° carbon fibres by strips of glass fibres about four diameters wide around the hole or
 - (b) incorporating additional $\pm 45^\circ$ plies.
2. Increasing the stiffness around the hole by introducing extra 0° fibres or by incorporating a thin titanium alloy sheet in the laminate around the hole. The latter is quite effective in increasing the bearing strength of the hole.
3. Bonding doublers over the hole.
4. Installing bonded inserts to reduce the stress concentration as well as increasing the bearing strength of the laminate. Inserts can be used to repair damaged bolted joints and are used to restore the bearing strength of the laminate.

Hart-Smith [1] postulates that, as long as no fibres are broken when the bolts are installed, interference-fit fasteners should cause a much larger softened area due to the development of a delamination zone which will provide stress concentration relief. However, forcing fasteners into composite holes to produce an interference-fit may cause undesirable/excessive matrix, fibre and delamination damage around the hole. However controlled expansion of a sleeve that remains statically in contact with the fibres, while a fastener is pressed in, can produce interferences of up to 0.178 mm.

In general the benefits of interference-fit fasteners are to [2] [3]

- i) reduce fastener rotation, which is more severe for thick composite laminates
- ii) lower joint deflection
- iii) reduced overall backlash,
- iv) equal fastener load sharing,
- v) reduction in relative fastener flexibility,
- vi) delayed or reduced hole elongation, especially in fatigue,
- vi) reduce water intrusion/reduce fuel leakage problems and
- vii) improve electrical conductivity and lightning strike protection,

Interference-fit fasteners show only slight improvements in initial static strength, however there is substantial evidence that interference (close-fits) will substantially improve the fatigue life of composite bolted joints. The life of composite joints with loose fitting holes is compromised, especially for reversed loading fatigue (i.e. compression-tension), due to back and forth rocking of the fastener. Unlike metallic structures, large interferences are of no real benefit in composite bolted joints since all that is desired is a "net" fit. However, a net fit is not practical therefore the interference limit need only be the accumulation of the tolerances with the net fit being the minimum [2].

The aim of this study [4] was to improve the static strength of thin composite mechanically fastened single lap joints by incorporating metallic inserts.

Three types of fasteners, viz. rivet, a swagged collar fastener and an interference fastener system were also evaluated, without the inclusion of the aluminium or steel inserts. The experimental study involved subjecting the specimens to increasing uniaxial load until the specimen failed. Strain measurements and high speed video images, obtained during the test, indicated the degree of secondary bending occurring in the specimen. Tests were also undertaken in order to evaluate the bearing behaviour of the laminate with the various insert configurations.

SPECIMEN

Lap Joint Specimens

Coupons

The material used in this experimental investigation was AS4/3501-6 carbon fibre/epoxy resin system. The 130 mm by 38 mm coupons were cut from 900 mm by 600 mm panels of layup $[\pm 45, 0, 90]_s$ and $[\pm 45, 90, 0]_s$, the long dimension being aligned parallel to the 0° fibres. In order to verify that there were no manufacturing defects, the panels were ultrasonically inspected before cutting

The specimens have been designed to fail in bearing only, hence the width-to-diameter (w/d) and edge distance-to-diameter (e/d) ratios varied between 5.7 - 9.2 and 2.8 - 4.6. Fig. 1a shows the tandem fastener lap-joint specimen used in this investigation. The joint manufacturing process were conducted in accordance with McDonnell Douglas process specifications [5].

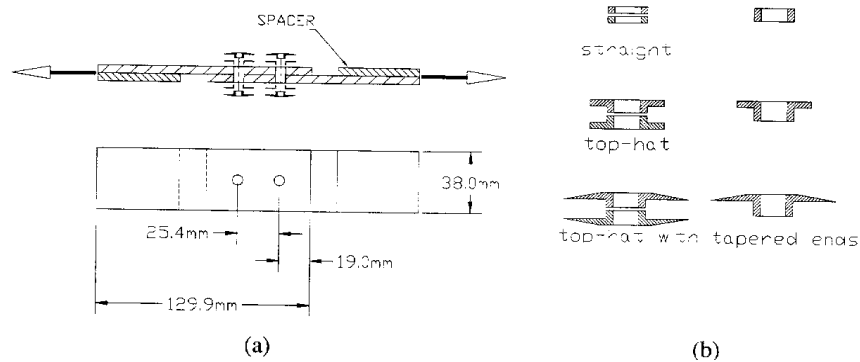


Fig. 1: (a) Tandem fastener single lap-joint specimen used in this investigation.
(b) Configurations of either press-fit or bonded aluminium and steel inserts.

Fasteners

The three types of fasteners evaluated were (1) NAS 1919M05 rivets, (2) NAS 2015 pin & NAS 2013 - 05 collar, and (3) CIL9SP-VC05-02 sleeved pin and CIFIC-MV05 collar. These types of fasteners have different fits, standard, close, and interference. They were the same type of fasteners used by Au-Yeung et al [6]. Fasteners were installed at HdH Victoria, using standard aerospace procedures. The fastener diameters were those recommended by the manufacturer for this particular laminate thickness. A fourth fastener, similar to type (2) was also evaluated. It comprised of a NAS2013-08 collar and NAS 2018H05 fasteners which had the same diameter as the outside diameter of the inserts, ie. 6.35mm.

Inserts

Three basic insert types were considered in this study, viz., (a) straight insert, (b) hat shaped inserts and (c) hat inserts with tapered top, these are depicted in Fig. 1b. The inserts were made from two different types of materials, aluminium or mild steel in order to study the effects of different insert compliances.

The inserts were installed with either a slight interference (press) fit or bonded into the hole. The interference-fit inserts were pressed into a hole of 6.35 mm nominal diameter, the level of interference was nominally 40 μm . The bonding installation procedure used an acrylic adhesive, Versilock 201/17, a room temperature curing adhesive which requires approximately 24 hours to cure. The adhesive thickness was allowed for in the design of the inserts which had "top-hats", a section of the bond line is depicted in Fig 1a. The bond thickness was set to approximately 0.18 mm, this was taken from experience gained at AMRL

in bonding inserts in metallic components [7]. Therefore in this case the nominal hole size for a 6.35 mm diameter insert was 6.71 mm.

Initially the jig used to install the inserts in the coupons only allowed one insert at any time to be installed. Whilst this technique has been used in other testing programs at AMRL with inserts in thick aluminium bolted joints it was unsuccessful in this testing program. The inaccurate tolerance of the concentricity of the insert in the coupon lead to inaccurate hole spacing, causing problems during the fastener installation stage. Consequently, a new more rigid jig which was designed to a tighter tolerance was manufactured. The new jig allowed the coupons to be clamped along their length enabling two inserts at a time to be installed, hence achieving the correct hole spacing. Nominally three specimens of each type were manufactured and tested.

After assembly the specimens were ultrasonically C-scanned and inspected for any manufacturing / assembly damage around the hole

A limited number of specimens were strain gauged in order to determine bending and in-plane strains during testing. Strain gauge locations are illustrated in Fig. 2.

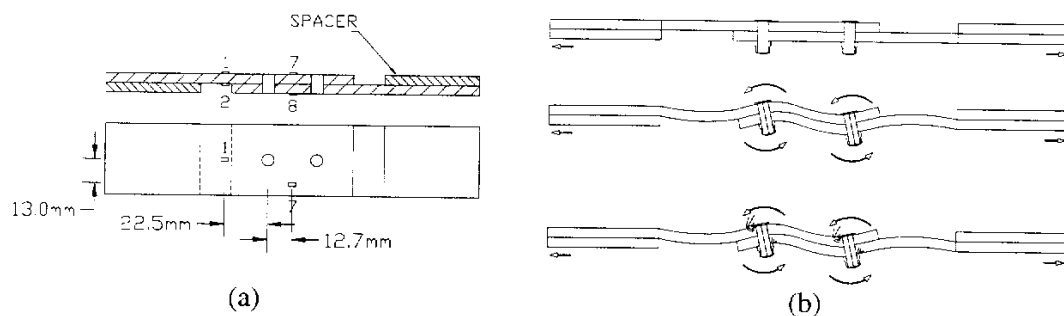


Fig. 2: (a) Strain gauge locations on specimen. (b) Deformed shape of two fastener single lap joint specimen due to uniaxial load.

Bearing Specimens

Two basic pin diameters were used, viz., 4.2 and 6.35 mm. The 4.2 mm diameter pin was used to load the coupons with no inserts, with interference-fit and bonded inserts. The 6.35 mm diameter pin was used to load a coupon with no inserts. The specimen and fixture used to undertake the bearing test is shown in Fig. 3a and 3b. This allowed the bearing specimen to be subjected to tensile or compressive loads.

TEST PROCEDURE

Lap Joint Tests

Mechanically fastened joint specimens were placed, with spacers, in the MTS 100 kN uniaxial testing machine as shown in Fig. 4. (The strain gauged specimens were subjected to an initial tensile ramp load up to approximately 2 kN, to ensure that the experimental set-up was correct and to check strain gauge readings). The specimens were then subjected to increasing uniaxial tensile load until failure occurred. In all cases the loading rate was 2 kN/min.

The strains, loads and displacements were acquired using a PC-based data acquisition systems. Data manipulation was undertaken after testing to determine in-plane and bending strains. Some of the tests undertaken were observed using a high speed video system.

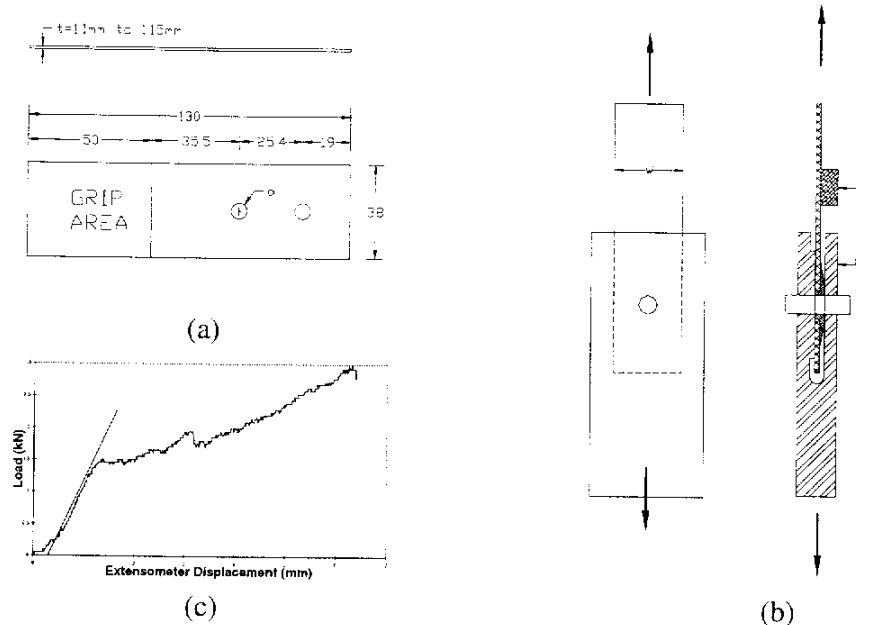


Fig. 3: (a) Typical bearing test specimen. (b) Bearing test arrangement. (c) Load vs deflection of a typical bearing test.

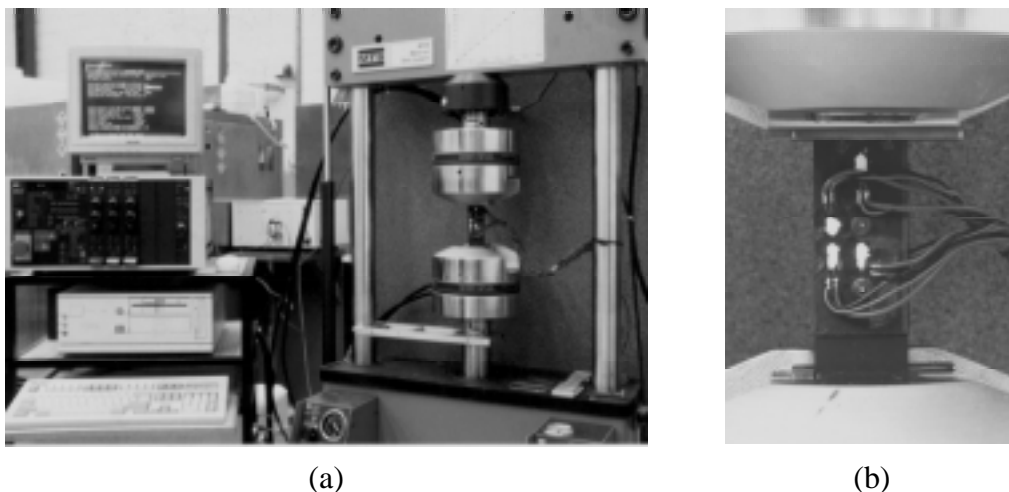


Fig. 4: (a) Specimens, with spacers, in the MTS 100 kN uni-axial testing machine. (b) Specimen mounted in hydraulic grips of servo hydraulic testing machine.

Bearing Tests

The bearing test arrangement is depicted in Fig. 3b and shows the location of a 25 mm gauge clip gauge positioned between points A and B. This allowed specimen deflection to be measured whilst the specimen was being loaded. Load and clip gauge readings were recorded while the specimens were tested to failure. All tests were performed at room temperature.

RESULTS and DISCUSSION

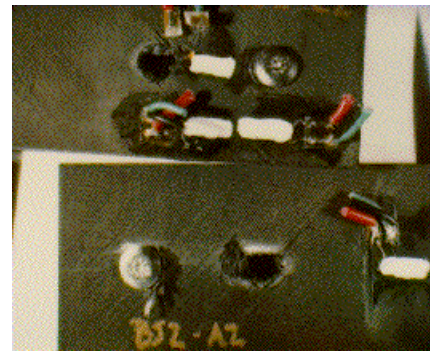
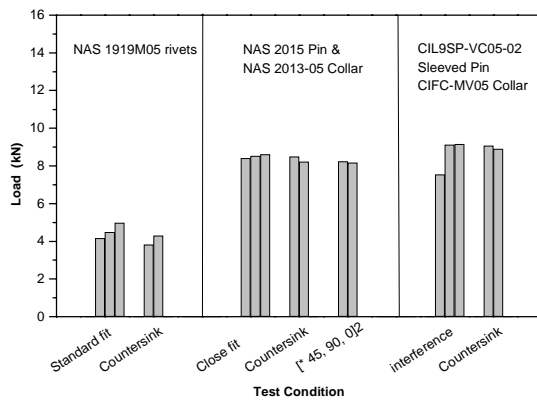
Fasteners

The results of the ultimate load test of the lap joint specimen with the various fastener types and without the inclusion of the aluminium or steel inserts are presented in Fig. 5a. Pull through of the fasteners was the failure mode in these specimens, as illustrated in Fig. 5b.

The interference fit specimens had the highest ultimate load, this was expected since the K_t decreases with reduction in the hole clearance. (ie bolt diameter increases). When a uniaxial load is applied to a plate containing a hole or a hole containing an unloaded fastener with a large radial clearance the hole will ovalise, in the direction of the applied load, causing a stress concentration at the side of the hole. Ovalisation of the hole can be restricted by reducing the radial clearance between the hole and the fastener, thus reducing the stress concentration. If interference is introduced the stress concentration is reduced further due to load transfer by friction from the plate to the fastener. It is postulated [8], that the introduction of interference-fit fasteners in composites could contribute to an increase in static strength.

The introduction of slight countersinks caused a slight decrease in the joint strength. The countersink was introduced to reduce the assembly damage between the edge of the fastener hole and the nominal radius under the head of the fasteners.

Of the two different layups ($[\pm 45, 0, 90]_s$ and $[\pm 45, 90, 0]_s$) the latter gave slightly lower results. The NAS2015 pin & NAS2013-05 had less scatter in the results.



(a)

(b)

Fig. 5: (a) Comparison of ultimate load for the three types of fasteners in a single lap joint arrangement. (b) Typical example of pull-through failure.

Bearing Tests

Load vs deflection of a typical bearing test is depicted in Fig. 3c. Initially there is “bedding in” of the pin followed by a linear region. The load where the deflection becomes non-linear indicates the initial failure load, and this point is defined as the bearing yield point. The maximum load carried by the hole was defined as the ultimate bearing load. The yield and ultimate bearing loads for each configuration are depicted in Fig. 6a and 6b.

The results show that the bonded tapered hat insert gave the highest bearing yield and ultimate loads. The interference tapered hat insert gave the lowest bearing yield and ultimate loads, due to the insert tilted out of the hole. This did not occur for the bonded case. The tilt of the inserts was caused by a localised bending moment. The length of bearing surface in the insert is twice as long as the bearing surface on the outside of the tapered hat insert, these two surface are eccentric to each other which produces a localised moment.

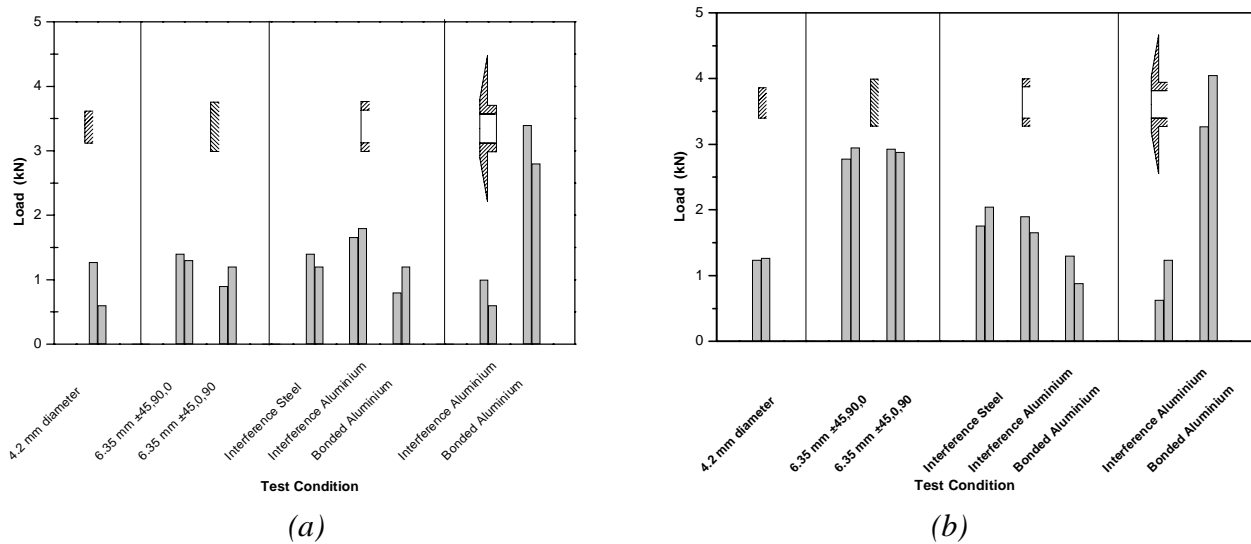


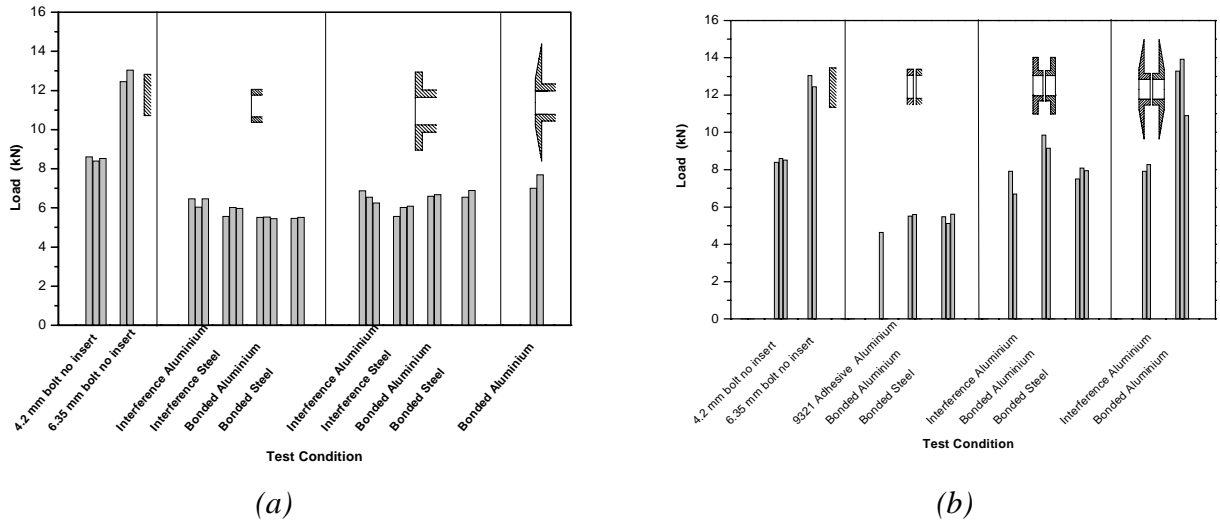
Fig. 6: (a) Yield and (b) ultimate bearing loads for various hole diameters and insert configurations .

The 6.35 mm pin and the interference fit straight steel insert case had similar bearing yield loads. The bearing yield load for the aluminium interference fit insert was nominally 33% to 50% higher than the steel insert and no insert case. The 6.35 mm pin used in the no insert case was made from the same material as the steel inserts. The aluminium has a similar stiffness as the composite material, whereas the stiffness of the steel is considerably higher than the composite, and would cause a higher bearing stress concentration than the aluminium. However the bonded aluminium tapered hat insert had the highest bearing yield load, thus it was expected that the aluminium tapered hat insert in a single lap joint would give the best performance.

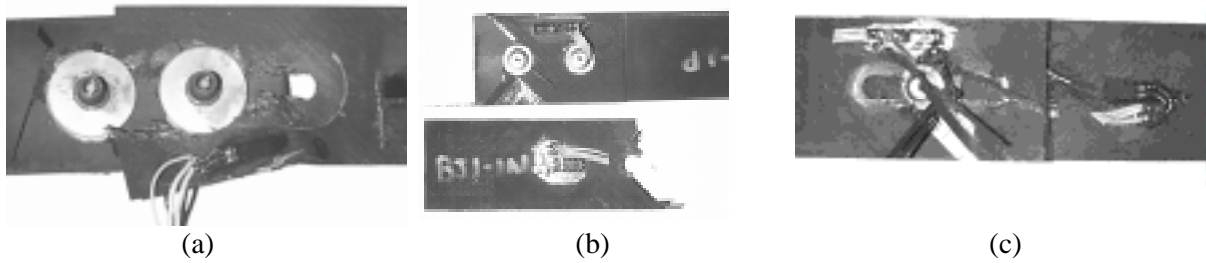
Lap joint tests

The results of the lap joint test are presented in Fig. 7. All the lap joints failed by pull through of the fastener head or collar, see Fig. 5b. with the exception of the bonded double hat inserts. Some of the fasteners failed in tension because the grip length was too short, i.e. the collars were pulled away. The bonded tapered hat inserts failed in bearing, whereas the bonded hat inserts failed in a combination of net tension and bearing. The failure modes are depicted in Fig. 8. The high speed video images obtained during the testing showed the fasteners “rocking” and digging into the composite material until it eventually pulled through. To quantify the secondary bending in these joints strain gauges were attached.

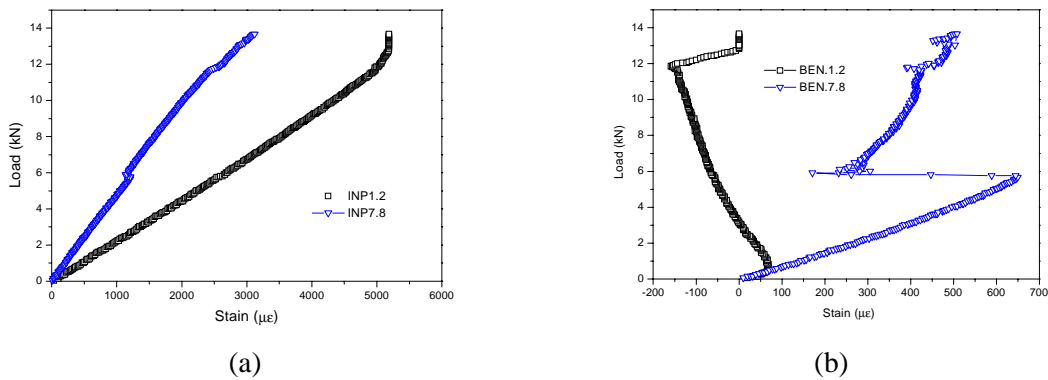
The in-plane and bending strains for the 6.35 mm diameter fastener are plotted in Fig. 9a and 9b respectively. Fig. 10a and 10b shows the bending strains for gauges 7 and 8 and 1 and 2 respectively. The strain gauges 7 and 8 are located on opposite faces between the two fasteners near the edge of the specimen, see Fig. 3. Similarly strain gauges 1 and 2 are the far field gauges on opposite faces located near the testing machine hydraulic grips. The results show in-plane strain between the two fasteners (gauges 7 and 8) are approximately half that of the far field gauges 1 and 2. Strain gauges 7 and 8 have more bending than the far field gauges 1 and 2 and at approximately 6 kN there was a sudden reduction in bending, the total in-plane load showed a slight drop off in load. The sudden reduction occurred with the similar type but smaller fastener (NAS2015). The other two fasteners NAS1919 rivets and CIL9SP interference rivet showed less secondary bending. The bonded tapered insert showed large secondary bending between the two fasteners as well as in the far field.



(a) (b)
 Fig. 7: Ultimate test of (a) single and (b) double inserts in lap joints with NAS2015 pins & NAS2013-05 collars.



(a) (b) (c)
 Fig. 8: Failure modes of bonded inserts: (a) Bonded tapered hat insert showing bearing failure. (b) Bonded hat insert with net-tension failure mode. (c) Bonded hat insert with combined pull-through, net-tension and bearing type failure.



(a) (b)
 Fig. 9: The (a) in-plane and (b) bending strains for the 6.35mm diameter fastener NAS2018.

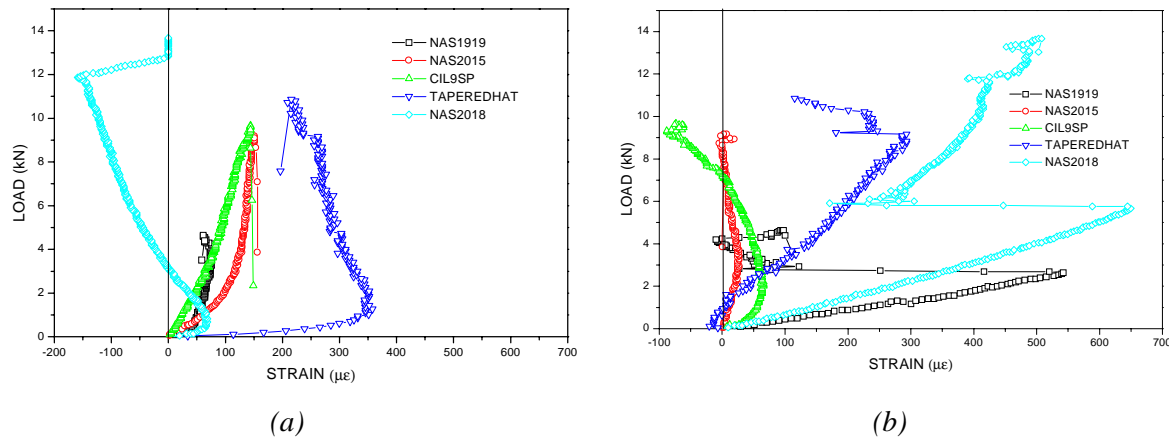


Fig. 10: A comparison of bending strains for gauges (a) 1 and 2 and (b) 7 and 8 for various fasteners / insert combinations.

Installing inserts generally means the overall diameter of the fastener has increased resulting in a reduction of the bearing stress for a given load and consequently an increase in joint strength. The inserts had the same outside diameter as the 6.35mm diameter fastener and the performance of the various insert / fastener configurations are also compared with the large diameter fastener. This can be seen in the bearing test results depicted in Fig. 6, where there is no bending, however if bending is present the insert may degrade the performance.

The mechanism which caused these joints to fail is due to the localised secondary bending, which causes the fasteners to rotate/rock, causing the fastener to pull through the composite material. This mechanism was clearly displayed in the high speed video images.

The bonded tapered hat insert increases the distance between the center line of the fastener and the reacting force between the insert and the composite material, since the localised moment remains constant, it implies that the reactive force must decrease. The reactive force is higher the closer to the center-line of the fastener, this force produced localised highly stressed region which eventually crushes/damages in the composite material and allows the fastener to rotate /rock. As the load is increased the fastener continues to bite into the composite material until the fastener pulls through.

The reactive force is lower for the bonded tapered hat insert, also there is a greater area which reduces the stresses at the edge of the insert and it does not damage the composite material. The bending moment between the two fasteners is it reduced with the tapered hat insert in comparison with the 6.35mm fastener, however it induces a greater far field bending.

Two of the three bonded aluminium tapered hat double insert lap joint specimens performed slightly better than the 6.35mm fasteners see Fig. 7b. The third specimen which was strain gauged, the result of which are presented in Fig 10 failed below 12kN

The bearing test showed that the bonded aluminium tapered hat insert gave the best performance, where as the interference fit aluminium tapered hat insert also rotated causing premature failure by fastener pull-through. A similar mechanism occurred for the interference fit tapered insert in the lap joint specimens.

Rocking/rotating of the fasteners appears to be restricted by bonding the tapered hat insert causing a change in failure mode to bearing and a corresponding increase in failure load. The load is similar to the 6.35mm diameter fastener which has a higher clamping force than the tapered hat insert. The 6.35mm diameter fastener single lap joint specimen failed in pull through mode, where as the tapered hat insert failed in bearing. The aluminium tapered hat arrangement is approximately 30% lighter than the 6.35mm diameter fastener.

Other factors which would have assisted the bonded tapered insert is the ability to transfer load through shear in the adhesive, under the hat, this enabling an additional load path besides bearing of the composite.

CONCLUSIONS

Results from the bearing tests showed slight improvement in the bearing strength for press-fit straight inserts. A significant increase, up to 100%, in bearing strength was observed for the bonded top-hat insert compared to the no insert case. The failure mode for the bolted joint specimens, without the inserts, appeared to be predominantly pull through of the fastener, even though the specimens were designed to fail in bearing. The pull-through type failure was caused by the secondary bending in the specimen which resulted in high shear pull-through stresses by the fastener head and collar. The top-hat inserts assisted in reducing the high pull-through stress exerted by the fastener head and collar and in some cases was so successful that the failure mode changed from pull-through to bearing with a corresponding 30% increase in the load carrying capacity of the joint.

ACKNOWLEDGEMENTS

The authors wish to acknowledge the assistance of Howard Morton and ASTA in the ultrasonic C-scanning, Mr Murray Scott and Mr Mark McVillie for the strain gauging, Dr J Finney, Mr J. Roberts and Ms Eva Kowval and Hon Martin for advice. Peter Pearce for supply of resin. HdH (Vic) for installing fasteners and Gary Coombes (HUCK Australia Pty Ltd) for providing the fasteners used in the testing program.

REFERENCES

1. Hart-Smith L.J. 1989 "The design of Efficient Bolted and Riveted Fibrous Composite Structures", Douglas Paper 8335.
2. Parker, R.T. 1989 "Mechanical Fastener Selection" Engineering Materials Handbook Vol 1 Composites, ASM International, Metals Park, Ohio 44073 USA.
3. Hart-Smith L.J. 1991 "An Engineer's Viewpoint on Design and Analysis of Aircraft Structural Joints", Proceedings of Int. Conf. on Aircraft Damage Assessment and Repair, Melbourne, Australia.
4. Mirabella, L and Galea, S.C. "The Static Strength of Mechanically Fastened Carbon-Epoxy Joint With Bending An Experimental Investigation" CRC-ACS report. (to be published)
5. McDonnell Douglas Company *Process Specification PS 14111* 'Machining and Drilling of Composites' 1979 and amendments.
6. Au-Yeung, H., Ellis, C.J. and Lee, C.C. "An Experimental Investigation of the Static Strength of Some Bolted and Bonded Lap Joints in Thin Composite Skins" CRC-AS TM93025.
7. Heller M., Hill T.G., Williams J.F. and Jones R. "Increasing the Fatigue Life of Cracked Fastener Holes Using Bonded Repairs" Theoretical and Applied Fracture Mechanics 11 (1989) 1-8.
8. Mann, J.Y. and Jost, G.S. 1983 "Stress Fields Associated with Interference Fitted and Cold Expansion Holes" Metals Forum V. 6 No 1.

DESIGN AND TESTING OF AN AIRCRAFT COMPOSITE HINGE

A.R. Rispler¹, M. Hou², L. Tong¹, G.P. Steven¹, L. Ye³, Y.W. Mai³

¹ *Department of Aeronautical Engineering, University of Sydney, NSW 2006, Australia*

² *Cooperative Research Centre for Advanced Composite Structures Ltd, 361 Milperra Rd, Bankstown, NSW 2200.*

³ *Department of Mechanical Engineering, University of Sydney, NSW 2006, Australia*

SUMMARY: A composite hinge has been designed to replace an existing metallic hinge on an aircraft aileron. The existing design consisted in a double webbed hinge which was then attached to the aileron by means of a fork fitting. The proposed single web hinge design aims at reducing the manufacturing cost. Two different composite material systems (thermoset and thermoplastic) were used to manufacture the single web hinges. The sizing of the hinge was performed by conducting a 3-D finite element analysis and using maximum allowable ply strain as the failure criteria. A special purpose test rig was employed to test all hinge specimens under the worst loading case. The initiation of failure in all hinges appeared to be delamination. The ultimate load expected during the operation of the hinge was met by the thermoplastic hinge. The initiation of failure on the thermoset hinge was just below the ultimate load.

KEYWORDS: composite hinge, testing and design, thermoplastics, RTM

INTRODUCTION

The metallic hinge of an aircraft aileron was used as the baseline design for a composite replacement part. A schematic drawing of the original design is shown in Fig. 1. The overall geometry of the new hinge was dictated by the aileron's front spar and also by the position of the fork fitting which connects the hinge to the wing. The composite hinge was designed as part of the Innovative Network Program from the Cooperative Research Centre for Advanced Composite Structures (CRC-ACS) and its principal objective was to reduce the manufacturing cost of the hinge while meeting the operational loads and conditions. Another main goal of the program was to compare the strength of thermoplastics vs thermoset composite materials when used in a highly loaded environment and validate the design cycle by testing the final components. The thermoset hinges were manufactured using liquid moulding technology (RTM) and non-crimp fabrics. The thermoplastic hinges were produced from carbon fiber fabric reinforced polyetherimide (CF/PEI) using compression moulding and co-consolidation procedures.

Four RTM hinges and five thermoplastic hinges were tested to failure. The initiation of failure in all hinges appeared to be delamination. The load at which delamination could be heard was lower for the RTM specimens. Once delamination was visible to the naked eye, fibre breakage occurred close to the web/flange intersection resulting in catastrophic failure. The thermoplastic hinges delaminated at a higher load and catastrophic failure was not observed

up to a tested load of 25 kN. No visible failure could be seen in the thermoplastic hinges while the extent of failure on the RTM hinges was very large once the load was removed. The ultimate load expected during the operation of the hinge was met by the thermoplastic hinge. The initiation of failure on the thermoset hinge was just below the ultimate load.

COMPOSITE HINGE DESIGN

Geometry

The overall geometry of the hinge was given by the front spar profile. The attachment method was to be chosen between mechanically fastening (original design), secondary bonding or a combination of the above methods. The positioning of the load pick-up point was also a fixed parameter. The above constraints left the following parameters as variables: number of webs, lay-up, flange and web thicknesses and number of parts in the hinge assembly.

To aid in deciding the more promising geometries, the actual aluminium hinge (Fig. 1, left) was analysed with finite element analysis so as to acquire an idea on load paths within the hinge. After comparing a number of concepts in terms of manufacturing cost it was decided to further develop the single web hinge concept (Fig. 1, right) which would reduce the number of parts on the hinge assembly from two to one. This would result in reduced manufacturing cost and weight.

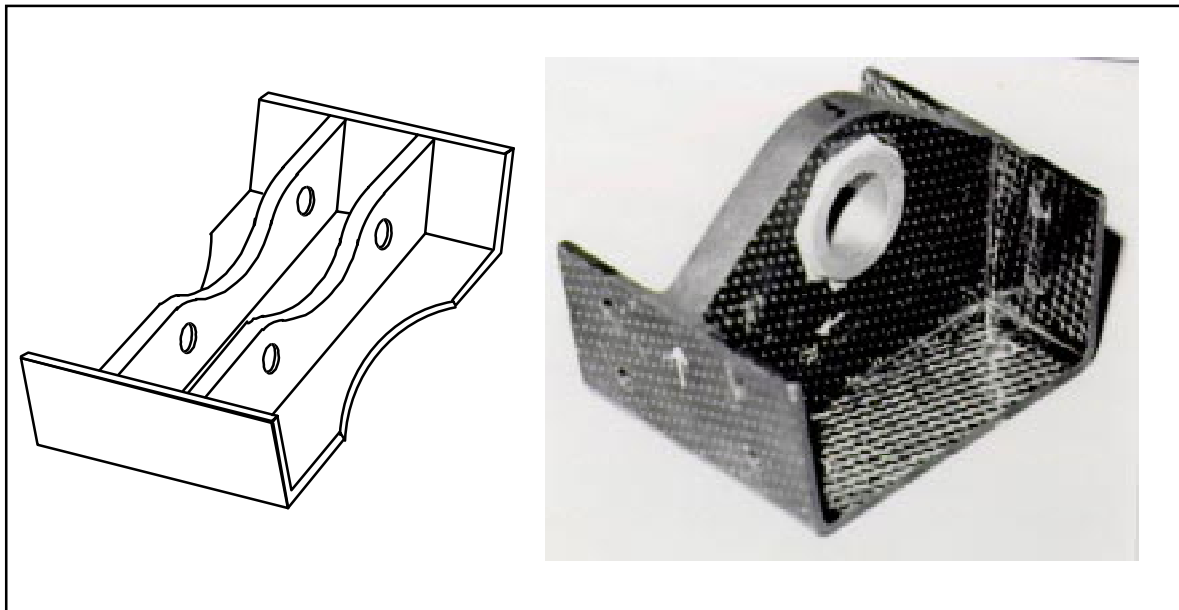


Fig. 1: Actual aluminium hinge schematic (left) and proposed composite hinge (right)

Loads

The load cases applied to the aileron were obtained from the aircraft manufacturer and were divided into four main cases as follows:

Rib Line Loads

Upper Surface Suction

Distributed Surface Pressures

Induced Bending-Deflected

These cases were combined to give worst loading conditions on the aileron. The critical case which was chosen for the hinge analysis was the combination of cases (3) + (4). The combination of the above load cases was then resolved into aileron hinge reactions by adding the reaction of the individual load cases. The largest of these reactions (10000 N) was employed for all finite element analysis performed on the hinge. This value includes a 1.5 ultimate factor. Single hinge failure conditions could not be investigated due to lack of data from the aircraft manufacturer. The additional data required to do such analysis would include new induced bending parameters for each of the assumed failed hinges.

Finite Element Analysis

The lay-up for the hinge was chosen to be quasi-isotropic as the efficiency of highly orthotropic laminates around bolt/pin loaded holes is known to be inadequate. Furthermore, Hart-Smith [1] showed that the farther a laminate pattern is outside a quasi-isotropic lay-up, the more likely it is to fail prematurely by through-the-thickness cracks parallel to the maximum concentration of fibres.

The thickness of the web was calculated using finite element analysis under the following assumptions:

Plane stress conditions on the web

Failure criteria employed to size the web was of maximum allowable ply strain

Material properties were taken from prepreg properties as RTM properties were not available for the chosen material

The resulting web thickness was 12 mm and the chosen material was non-crimp fabric (ie 28 plies of non-crimp fabric resulting in an assumed cured ply thickness of 0.43 mm). The lay-up consisted in 14 plies of ± 45 and 14 plies of 0/90's as follows (0/90/45/-45/0/90/-45/45/0/90/-45/45/0/90/-45/45/0/90/45/-45/45/-45/0/90/45/-45/0/90)_s. The five outer plies at either side of the web continued onto the flange while 18 plies were dropped-off at the web/flange intersection. Finally, the flange section had two wrap-around plies resulting in an average flange thickness of 3.0 mm.

A more complete 3D FEA was then carried out using plate shell elements with laminate properties to assess the fastening method to be employed and to verify maximum ply strains at critical regions. It was observed during this analysis that secondary bonding of the hinge would introduce large peel stresses on the adhesive due to the rotation of the hinge with respect to the front spar of the aileron. As the most critical stress in adhesive materials is the peel stress and since the hinge is a primary structure, it was decided to mechanically fasten the hinge to the front spar.

The critical region was identified as being the web/flange intersection at the tensile side of the hinge. A shaded deformed plot of the hinge indicating the highly strained area (darkest = highly strained) is shown on Fig. 2.

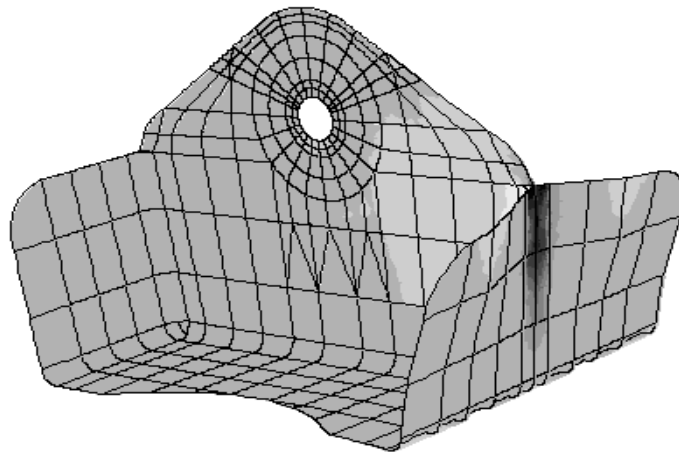


Fig. 2: Deformed FEA plot showing highly strained region (darkest area)

Manufacturing aspects

The thermoset hinges were manufactured using liquid moulding technology with carbon biaxial non-crimp fabrics (COTECH C-BX 440) and RTM6 resin. A summary of the manufacturing procedure for the RTM hinge is outlined below:

Firstly, the material was kitted and tackified with powdered 'B-staged' RTM6 resin. The plies were then assembled in order and heat set over wooden forming blocks under vacuum in an oven at 100⁰ C for 30 minutes. After trimming the plies and closing the steel moulds, the tool was subjected to full vacuum and the resin injected at 200 kPa. Prior to this, the resin and tool were preheated to 80⁰ C and 120⁰ C respectively.

The thermoplastic composite hinges were produced from solvent impregnated fibre fabric reinforced polyetherimide (Ultem 1000) prepreg supplied by Ten Cate Advanced Composites, the Netherlands. The carbon fabric has a 5H satin woven construction. The prepreg has a resin content of 44.1 wt.%. PEI is an amorphous polymer and has a glass transition temperature of 217 °C [2]. Because of the complex geometry of the hinge, co-consolidation (in a hot press) technique was used to manufacture the hinge, in which several components with simple geometry were first produced by compression moulding technique and then were co-consolidated in a specially designed forming mould [3]. To get fully consolidated thermoplastic composite parts with high quality, the optimum forming conditions for this material, eg. forming temperature, holding time and forming pressure, were determined by an impregnation model developed by Hou et al [4]. The final void content in the thermoplastic composite hinge was less than 0.2%.

Both thermoset and thermoplastic hinges were finally trimmed to their final dimension and the holes for the fastening bolts were hand drilled. The main bush hole (load pick-up point) was drilled with a hole saw. The bush was then bonded with BR95 paste adhesive and left to cure at room temperature for over 24 hours.

Test Set-up and Results

A special purpose test rig was designed to test the hinge specimens under the worst loading case expected during operating conditions. The tests were carried out in an INSTRON 1195 machine under displacement control at 0.2 mm/min. A load-displacement curve was obtained from the data acquisition system and the test was filmed with a SVHS video camera so as to be able to determine crack initiation/propagation. The test set-up consisted of a hollow steel beam with two machined steel plates matching the profile of the front spar. These parts were bolted together to a larger steel plate fitted to the INSTRON testing machine. A schematic of the test set-up and an actual photograph of the loaded hinge specimen is shown in Fig. 3.

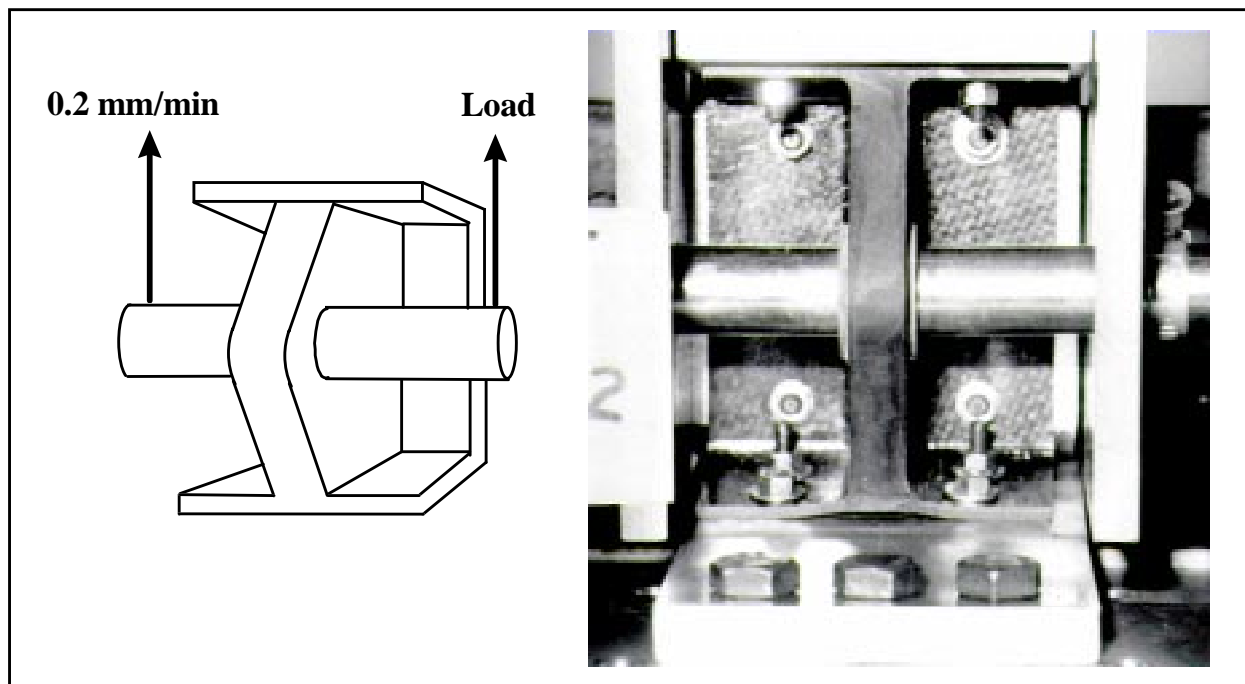


Fig. 3: Composite hinge test set-up

This load case was obtained from a full aileron model used during the INP. Four RTM hinges and five thermoplastic hinges were tested to failure. A typical load-displacement curve for both thermoplastics and thermoset composite hinges is shown in Fig. 4.

Both hinges behaved linearly up to the onset of the first crack growth in the tensile section, ie. in the bottom section the hinge being tested. After this event, non-linear behaviour was observed in both specimens. The main failure mode observed in all hinges appeared to be delamination in the tensile section (as shown in Fig. 5), while no failure indication was observed in the compression side. The load at which delamination started was much lower for the RTM specimens (from 9 up to 13.5 kN). Once delamination was visible to the naked eye, fibre breakage occurred close to the web/flange intersection resulting in catastrophic failure.

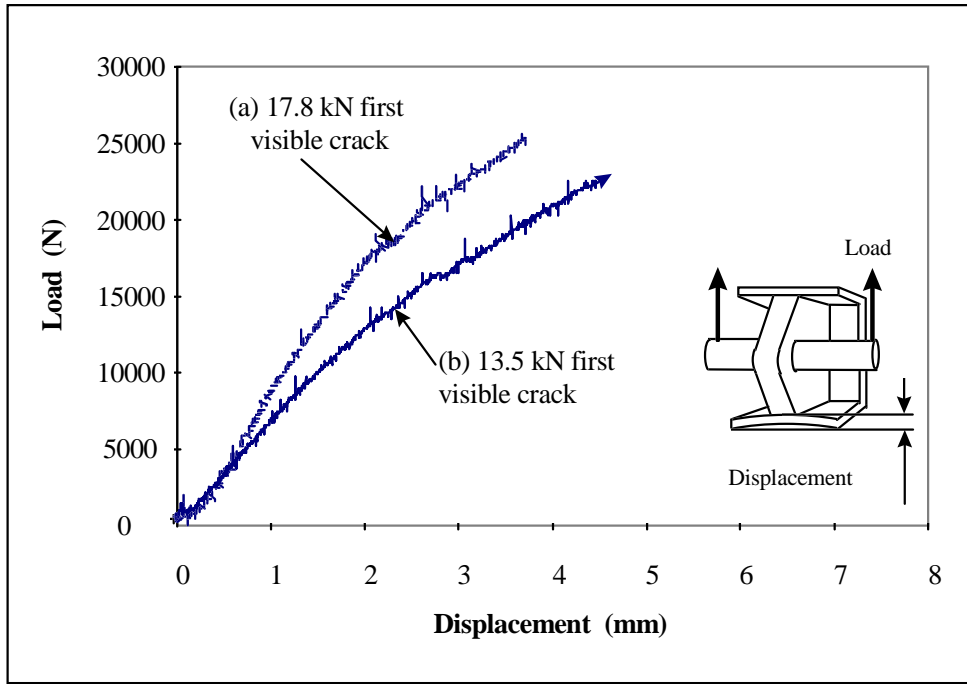


Fig. 4: Test results for highly loaded hinges made of (a) thermoplastic and (b) thermoset composite materials

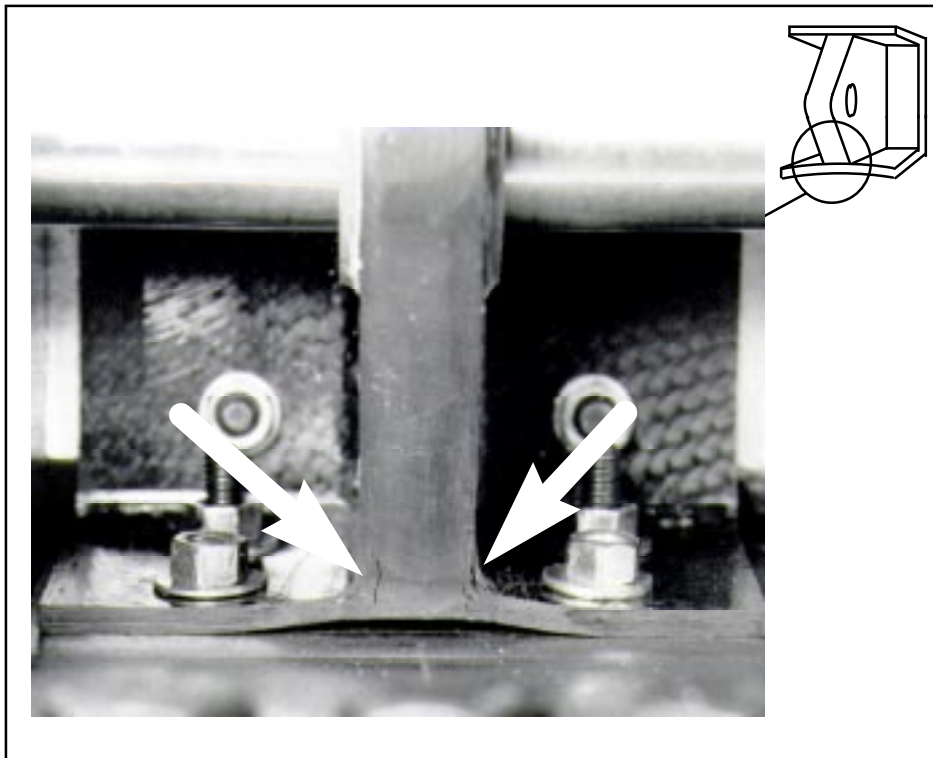


Fig.5: Delamination at tensile section of hinge being tested

The thermoplastic hinges delaminated at a higher load level (above 15 kN) and catastrophic failure was not observed up to the specified maximum test load of 25 kN. After the load was removed, only small delaminations could be seen in the thermoplastic hinges while the extent of failure on the RTM hinges was substantial. A schematic diagram of the failure mechanisms

observed during test is shown in Fig. 6. The primary cause for delamination is due to excessive stress in the transverse direction within the matrix of a composite material. These large stresses in the tensile section of the hinge are mainly due to the out-of-plane deformation of the web/flange intersection resulting in the plies tending to pull away from the center line of the web. The failure mode observed in all hinges can aid in explaining the largest strength of the thermoplastic hinge when compared to the RTM version. Because delamination is dominated mainly by the matrix property [5], it is not surprising to see that the composite hinge made from a more toughened matrix composite system (thermoplastic) could survive a higher load than that made from a brittle matrix composite system (thermoset). The ultimate load expected during the operation of the hinge was met by the thermoplastic hinge. The initiation of failure on the thermoset hinge was just below the ultimate design load.

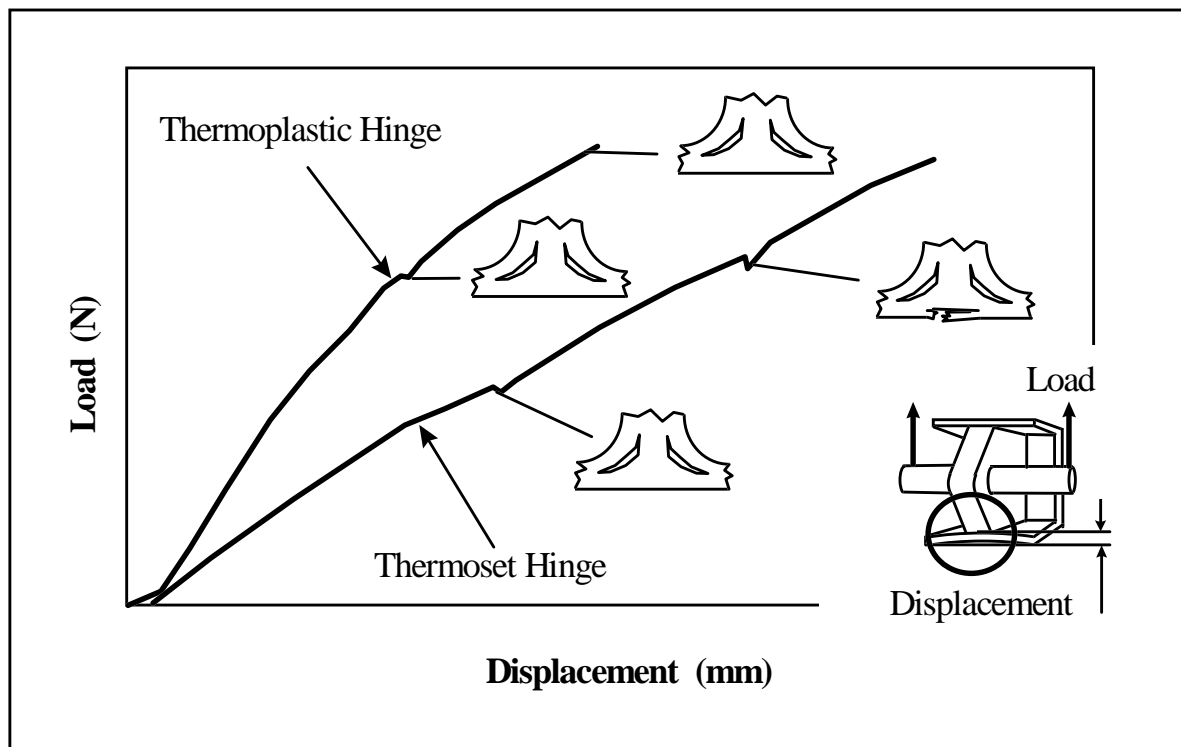


Fig. 6: Schematic diagram of failure mechanisms in tensile section of hinge

The effect of flange thickness distribution on the hinge strength was studied using thermoplastic composite hinges. The flange is made up of 10 layers of CF fabric/PEI prepregs and has a total thickness of 3 mm. To obtain continuous fibre orientation in the outer side of the hinge flange as well as in the web/flange intersection, these 10 layers of prepreg were divided into two groups, namely group a and group b (as indicated in Fig. 7). Group a corresponds to the build up around the web/flange intersection while group b forms the outer side of the flange. Two kinds of thermoplastic hinges with the same fibre orientation but with two different flange thickness distributions of $a/b = 7/3$ and $a/b = 5/5$ were tested. The results are shown in Fig. 7. As expected, hinge with $a/b = 7/3$ flange thickness distribution delaminated at a higher load level (17.8 kN) than that of $a/b = 5/5$ (15.5 kN). The reason is believed to be due to the fact that with more continuous fibre oriented in the load direction, the secondary tensile stresses within the matrix can be effectively reduced in the web/flange intersection.

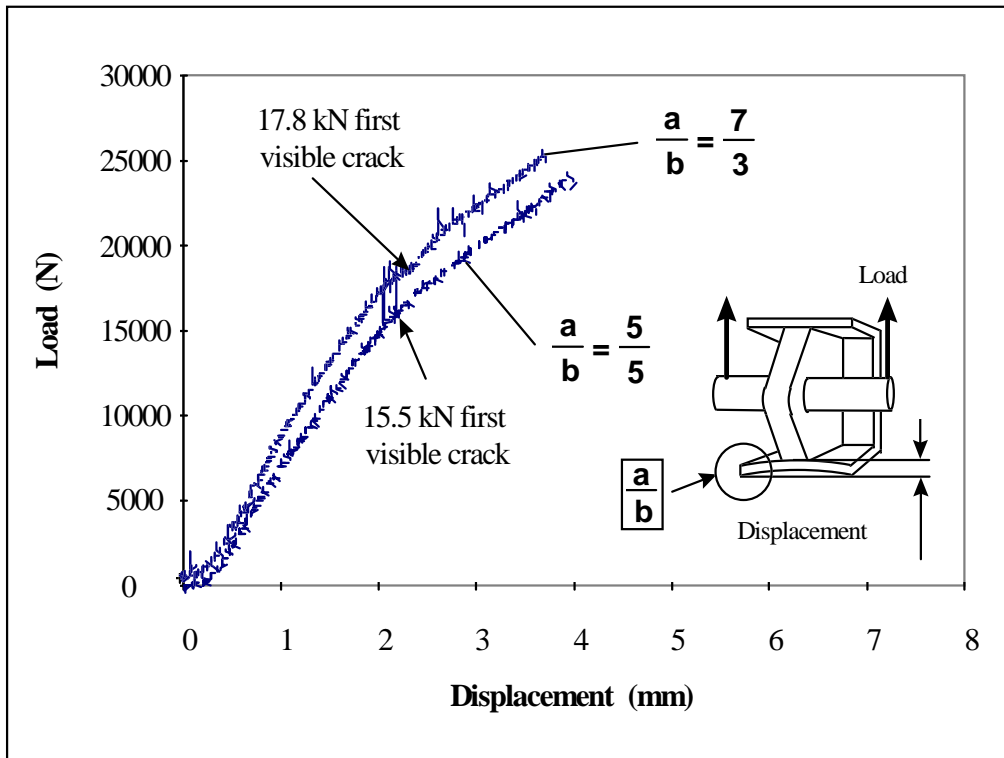


Fig. 7: Effect of flange thickness distribution on thermoplastic composite hinge strength

CONCLUSIONS

The manufacturing cost could significantly be reduced by adopting the single web hinge concept. The overall reduction in cost would depend on recurrent manufacturing cost and expected number of hinges to be produced. The largest cost in the development of the single web hinge concept was the RTM tooling for the thermoset components and the co-consolidation moulds required for the thermoplastic hinges. The strength comparison between thermoplastic and thermoset hinge coupons showed; as expected; that due to the failure mode being delamination, the thermoplastic hinges performed significantly better. Furthermore, if a hot-wet load enhancement factor was to be considered, the thermoplastic hinges would present a larger advantage due to the fact that their mechanical properties do not degrade as much as those of thermoset materials. A fatigue test program for the thermoplastic hinges is being considered at the moment.

ACKNOWLEDGMENTS

This work was carried out as part of the Cooperative Research Centre for Advanced Composite Structures (CRC-ACS) Research Programs. Thanks are due to Mr. M. Baker for the preparation of the thermoset hinges. We would also like to thank the technicians in the Materials Laboratory of CAMT at the University of Sydney, for their assistance in the experiments.

REFERENCES

1. L.J. Hart-Smith, "Joints", Engineered Materials Handbook on Composites, ASM International Vol1., pp. 479-495.
2. Fines, R. E. and Bartolomucci, J. P., "Polyether-imides (PEI)", Engineering Materials Handbooks, Volume 2, Engineering Plastics, edited by Epel, J. N. et al. Published by ASTM International, p. 156-158
3. Hou, M., Lin, Y. and Mai, Y. W., "Manufacturing process and mechanical properties of thermoplastic composite components", Journal of Materials Processing Technology, 63 (1997) p. 334-338
4. Hou, M., Lin, Y. and Mai, Y. W., "Optimisation of compression moulding conditions of carbon fibre fabric reinforced polyetherimide composite material", Proceedings of the international conference on advanced materials, Progress in Advanced Materials and Mechanics, August 12-15, 1996, Beijing, China, edited by Wang, T. C. and Chou, T. W., published by Peking University Press, 1996, p. 97-102
5. Avva, V. S., Allen, H. G., Shivakumar, K. N., "Through-the-thickness tension strength of 3-D braided composites", Proceedings of the American Society for Composites, ninth technical conference, sept. 20-22, 1994, Newark, Delaware, published by Technomic Publishing Co., p. 877-883

STUDY ON THE BENDING BEHAVIOR OF LAMINATES CONNECTED BY RIVETS

Ya-Jung Lee, Yau Shyu, Tung-Chien He

*Department of Naval Architecture and Ocean Engineering, National Taiwan University,
73 Chou-shan Street, Taipei, Taiwan, R.O.C.*

SUMMARY: A study with a numerical approach is conducted to investigate the post-buckling behavior of Laminates connected by rivets. However, the behavior of the laminate with a single rivet should be taken into consideration prior to solving the macro behavior of the laminate with several rivets. This study majorly focuses on the bending behavior and the interaction between the rivet and the laminate as the paperation. The finite element software ABAQUS is used to inspect the 3-D contact behavior between two contacting surface sets, the laminate and the rivet, and, the laminate and the stiffener. The user subroutine, UMAT is used to modify the engineering constants and the stresses when the elements are identified as failing. Several parameters are considered. As a result, it shows that the stacking sequence has great influence on the behavior.

KEYWORDS: post-buckling, contact behavior, failure criterion, rivets, laminates

INTRODUCTION

Due to the high specific strength, rigidity and corrosion resistance, composite materials have been widely utilized in airplanes, ships, automobiles and other respects. Among the various structures, laminates are a basic type. The flush-head rivets are frequently used on them for force transmission and the smoothness of the flowlines. When the laminates and the rivets act in union, and are subjected to various loadings, the behavior of the joint is rather complicated. The structure may buckle easily on the ground that the strength between the laminae is not high enough. While the deflection is increasing, local fracture is expanding around the rivets. Then, the efficiency will go downhill rapidly and cause the total failure of the structure. Therefore, the study on the behavior of the laminates connected by rivets should be practiced thoroughly.

There have been several research reports on this top since 1970. Most investigations restricted the analyses to 2D problem with a simple geometry, such as Ref. [1] to [2] and [4] to [5]. They determined the stress distribution and the failure strength of various modes. However, 3D analysis is imperative because the the interlaminar strength has great influence over the behavior. Few documents, Ref. [3], [6] and [7] had the analyses about structures of 3D geometries with in-plane deformations. However, these analyses treated the rivet or the bolt as a rigid body. The contact between the rivet and the laminate in radial direction was modified as constraints. In this way, the elastic characteristic of the rivet was not considered. Neither was buckling and post-buckling. Ref. [8]~[10] had the analyses on the buckling behavior of laminates jointed by several rivets. In these documents, the rivets are only modeled as elastic

nodes instead of an elastic body. Hence, it's obvious that the post-buckling behavior of laminates jointed by rivets still needs further research.

To this end, the present study uses the finite element software, ABAQUS, and models the rivet as an elastic body. The contact pressure and the stress distribution of the structure can be obtained. With user subroutine, UMAT, the engineering constants and stresses will be modified by proper failure criterion and the nonlinear behavior is understood.

PROBLEM DESCRIPTION

Composite laminated sheets are often jointed with metal stiffener by rivets as in Fig. 1. When the structure is subjected to in-plane loadings, the laminates may buckle and the area around the rivet will fail besides the fracture in the center of the laminate. To understand the local behavior, the area surround by dashed lines is extracted as the model to be analyzed. The loading changes to be out-of-plane to model the deformation and displacement in z -direction. The coordinate system and the geometry are shown in Fig. 2. The mesh, dimension and the dimension of the rivet are shown in Fig. 3. The prescribed displacement (h') is along side BC. Because of symmetry, face ABFE, HDCG and BCGF are symmetrical planes. D is the diameter of the rivet root. The length of the laminate is $L_t=15D$; the half length of the face plate of the stiffener is $L_b=5D$; e is the distance from the center of the rivet to the nearer edge and equals to $3D$; w is the width of the plate and also the rivet pitch. The laminate is made of the material T300/976. The rivet is aluminum alloy. The material constants are as table 1 and 2.

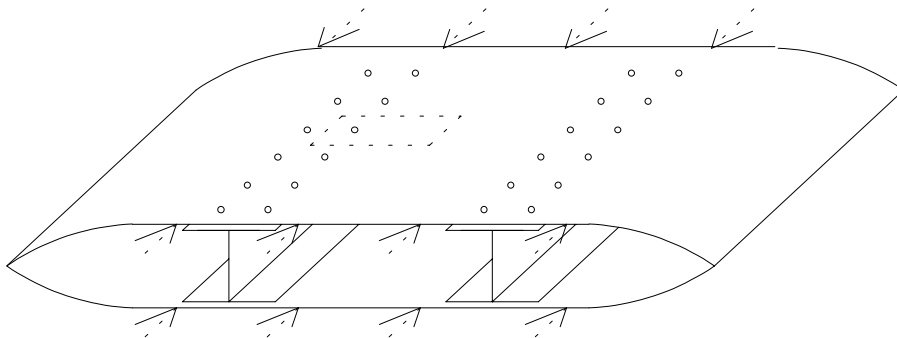


Fig. 1. laminate jointed with the stiffener by rivets under in-plane loadings

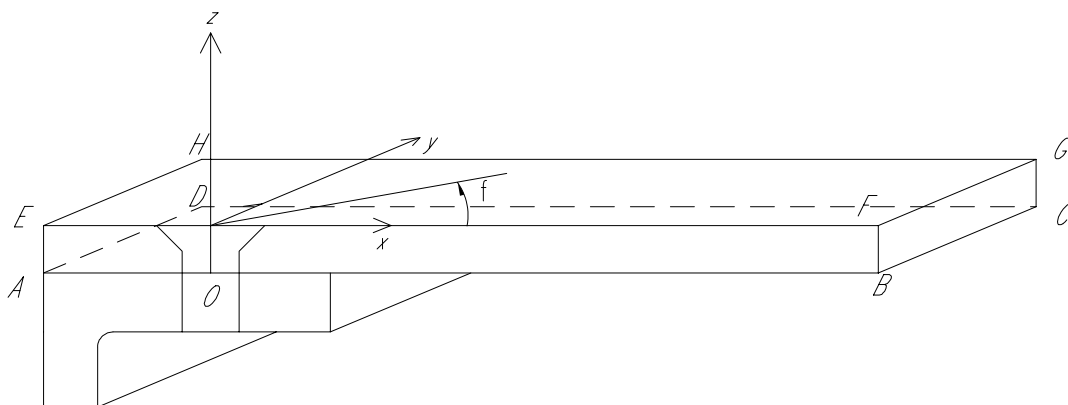


Fig. 2. the geometry of the structure

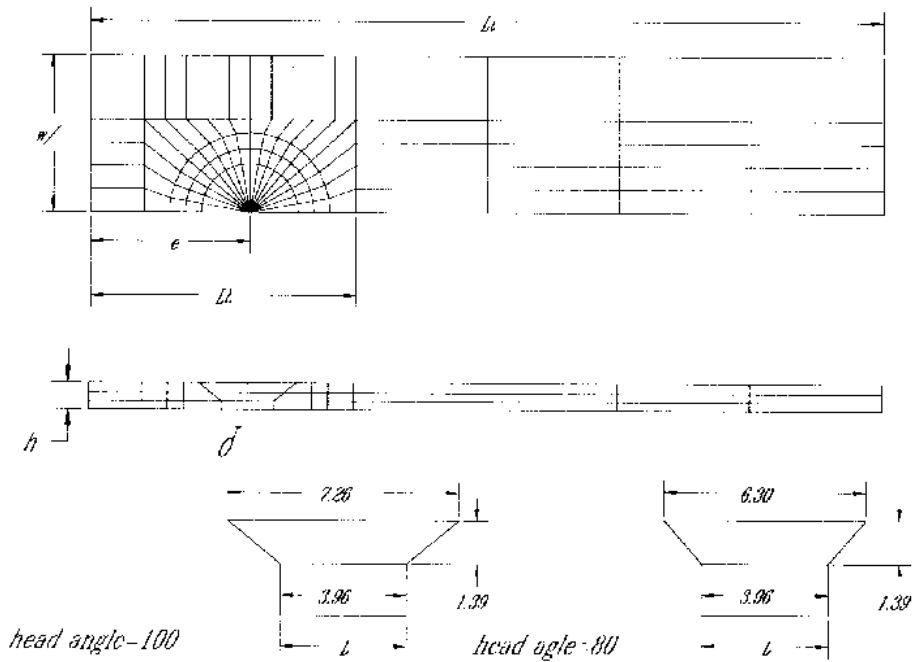


Fig. 3. finite element mesh and the dimension

Table 1: The material properties of the rivet and the stiffener

Aluminum Alloy	E(GPa) : 70	ν : 0.32
----------------	-------------	--------------

Table 2: The material properties of the composites

laminate : T300/976			
Engineering constants		strength	(MPa)
E_1 (GPa)	1.393E2	X_t	1.517E3
E_2 (GPa)	9.722	X_c	1.593xE3
E_3 (GPa)	9.722	Y_t	4.454E1
ν_{12}	0.29	Y_c	2.530E2
ν_{13}	0.29	Z_t	4.454E1
ν_{23}	0.29	S_{12}	1.069E2
G_{12} (GPa)	5.585	S_{13}	1.069E2
G_{13} (GPa)	5.585	S_{23}	1.069E2
G_{23} (GPa)	3.447		

CONTACT PROBLEM

Contact behavior is highly nonlinear. Here the contact includes the contact between the rivet and the laminate along the rivethole, and the laminate and the face plate of the stiffener. It is not modeled as prescribed constraints but 2 contact pairs in ABAQUS, meaning that the a contact set has 2 contact surfaces which belonged to separate contact elements. The contact behavior is confined to only small sliding. The originally matched contact nodes will stay close and won't contact with the nodes of the other elements. The friction is also neglected in this study.

FAILURE CRITERIA AND SIMULATIONS

In the present study, the 3D Hashin failure criterion and Ye delamination are adopted in the user subroutine, UMAT, as a supplement for ABAQUS and prediction of the failure of the elements . Let $X_t, X_c; Y_t, Y_c, Z_t, ; S_{12}, S_{23}, S_{13}$ denote the corresponding strengths. The failure criteria may be described as follows:

(a) Fiber Breakage

$$\left(\frac{\sigma_{11}}{X_t}\right)^2 + \left(\frac{\tau_{12}}{S_{12}}\right)^2 + \left(\frac{\tau_{13}}{S_{13}}\right)^2 \geq 1 \quad \sigma_{11} \geq 0 \quad (1)$$

$$|\sigma_{11}| \geq X_c \quad \sigma_{11} < 0 \quad (2)$$

The Young's modulus E_1 , Poisson ratio $\nu_{12}, \nu_{21}, \nu_{13}, \nu_{31}$, shear modulus G_{12}, G_{13} , stress components σ_{11}, σ_{12} and τ_{13} are all reduced to 0 within the damaged element of the layer for fiber failure.

(b) Matrix Failure

$$\left(\frac{\sigma_{22} + \sigma_{33}}{Y_t}\right)^2 + \left(\frac{1}{S_{23}^2}\right) \cdot (\tau_{23}^2 - \sigma_{22}\sigma_{33}) + \left(\frac{\tau_{12}}{S_{12}}\right)^2 + \left(\frac{\tau_{13}}{S_{13}}\right)^2 \geq 1 \quad \sigma_{22} + \sigma_{33} \geq 0 \quad (3)$$

$$\left(\frac{\sigma_{22} + \sigma_{33}}{2S_{12}}\right)^2 + \left(\frac{\sigma_{22} + \sigma_{33}}{Y_c}\right) \left[\left(\frac{Y_c}{2S_{12}}\right)^2 - 1 \right] + \frac{1}{S_{23}} (\tau_{23}^2 - \sigma_{22}\sigma_{33}) + \left(\frac{\tau_{12}}{S_{12}}\right)^2 + \left(\frac{\tau_{13}}{S_{13}}\right)^2 \geq 1 \quad \sigma_{22} + \sigma_{33} < 0 \quad (4)$$

The Young's modulus E_2 , Poisson ratio $\nu_{12}, \nu_{21}, \nu_{23}, \nu_{32}$, shear modulus G_{12}, G_{23} , stress components σ_{22}, τ_{12} and τ_{23} are all reduced to 0 within the damaged element of the layer for matrix failure.

(c) Delamination

$$\left(\frac{\sigma_{33}}{Z_t}\right)^2 + \left(\frac{\tau_{13}}{S_{13}}\right)^2 + \left(\frac{\tau_{23}}{S_{23}}\right)^2 \geq 1 \quad \sigma_{33} \geq 0 \quad (5)$$

$$\left(\frac{\sigma_{13}}{S_{13}}\right)^2 + \left(\frac{\sigma_{23}}{S_{23}}\right)^2 \geq 1 \quad \sigma_{33} < 0 \quad (6)$$

The Young's modulus E_3 , Poisson ratio ν_{23} , ν_{32} , ν_{13} , ν_{31} , shear modulus G_{23} , G_{13} , stress components σ_{33} , τ_{13} and τ_{23} are all reduced to 0 within the damaged element of the layer for delamination.

USER SUBROUTINE: UMAT

ABAQUS has provided a very complete material library. However, in the failure analysis, although ABAQUS has various kinds of criteria, the material properties and stresses cannot be modified within ABAQUS itself. Therefore, ABAQUS provides the flexibility for the users to write user subroutines to modify the materials. In the present study, UMAT is used to modify the values of the engineering constants and the stresses and calculate the stiffness matrix. Several verifications are needed to make sure it is available.

RESULTS

There are several parameters designed to evaluate the influence on the structure. They are the stacking sequence, the arrangement of the rivet, the stiffness of the stiffener, the head angle of the rivet and. In the present study, the prescribed displacement when failure happened is higher than the plate thickness. Therefore, the large deformation theory should be applied.

The Stacking Sequence

In the following study, the stacking sequence used is layer 4, the arrangement is taken as single line of rivet, the stiffener is elastic and the head angle of the rivet is 100. When one parameter is discussed, there will be 2 options for the parameter, but the others stay as above.

The relations between the reaction force (Rf) and h' are shown in the figures below. Fig. 4 shows the influence of the stacking sequence when the total number of layers is 24. Layup 4 is [(0/45/90/-45)₃]s while layup 5 is set-up as [(90/45/0/-45)₃]s. In Fig. 4, it's observed that the initial fracture starts when the prescribed displacement is raised to 1.2 to 1.4mm. The initial fracture of layup 4 begins later than layup 5. The slope of layup 4 is higher than layup 5, which means layup 4 has better strength. When final fracture happens, the load that the structure sustains goes down rapidly. In Fig. 4, it's also found that the final fracture of layup 4 happens earlier on the ground that layup 5 is easier to bend so that fractures later. From the computed results, the 0°, ±45° laminates are weaker and thus fracture earlier than the 90° laminate.

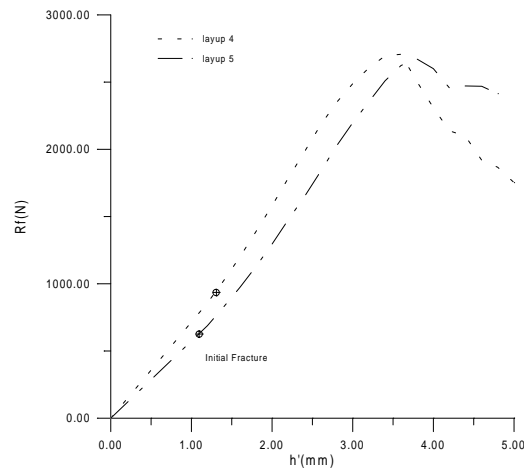


Fig. 4 The $Rf-h'$ relation under the parameter - stacking sequence

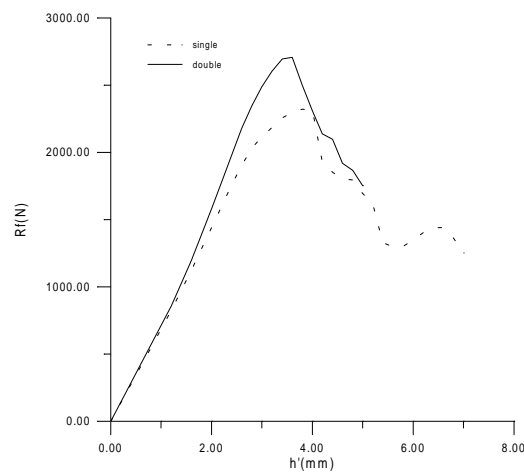


Fig. 5 The $Rf-h'$ relation under the parameter - arrangement of the rivets

The Arrangement of the Rivet

There are several arrangements in the real situation. Here, 2 types of arrangements are considered. The stacking sequence here is layup 4. When the constraint along the ADHG surface is symmetric to the $x-z$ surface, it's the double line case. When the boundary is free along ADHG, it's the single line case. From Fig. 5, we can see that the single line case has weaker strength and endures lower loading.

The Stiffness of the Stiffener

The material properties of the stiffener also effects the behavior of the structure. Therefore the stiffener is modeled as both rigid and elastic. When it's elastic, the material is taken as Aluminum alloy. In Fig. 6, it can be seen the structure with the elastic stiffener will have lower strength but sustain higher loading.

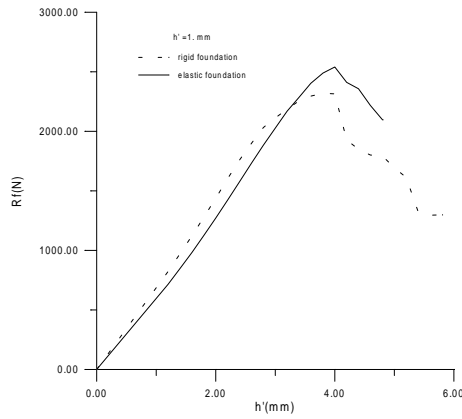


Fig. 6 The R_f - h' relation under the parameter - the material of the stiffener

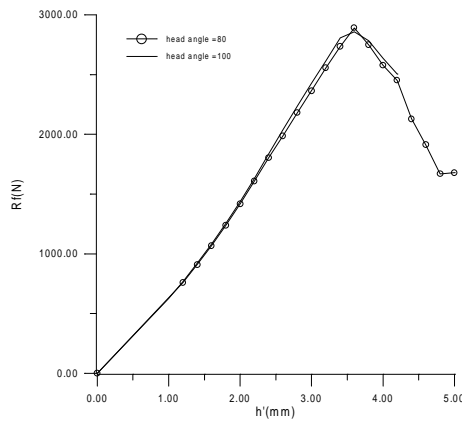


Fig. 7 The R_f - h' relation under the parameter - the head angle of the rivet

The Head Angle of the Stiffener

There are two frequently used head angles of rivets, 80° and 100° . The change of the head angle doesn't effect a lot according to Fig. 7. However, in the analysis, it's found that the fracture modes are quite different. The cases above and the structure with head angle of 100° mostly fracture around the hole, while with the rivet of head angle 80° , the structure fracture mostly near the area of prescribed displacement.

CONCLUSION

The stacking sequence is found to be very influential to the load sustaining ability of the laminate connected by the rivet. When the 0° lamina is placed closer to the surface instead of the 90° lamina, the high strength of the fiber will help the structure to have higer overall strength. The softer the stiffener is, the more flexible the structure is to deform. However, in the aspect of load sustaining ability and overall strength, the material of the structure and the head angle of the rivet don't influence the structure in great scale.

ACKNOWLEDGEMENT

This study is sponsored by the National Science Council, R.O.C.

REFERENCES

1. Theo De Jong, “Stresses Around Pin-Loaded Holes in Elastically Orthotropic or Isotropic Plates”, *J. Composite Material*, Vol. 11, pp. 313-330 (July 1977)
2. M. U. Raham, R. E. Rowlands and R. D. Cook ,“ An Iterative Procedure for Finite Element Stress Analysis of Frictional Contact Problems”, *Computers and Structures*, Vol. 18, No. 6, pp. 947 – 954 (1984)
3. I. H. Marshall, W. S. Arnold, J. Wood and R. R. Mousley, “ Observations on Bolted Connections in Composite Structures”, *Composite Structures*, Vol. 13, pp. 133-151 (1989)
4. B. L. Agarwal, “Static Strength Prediction of Bolted Joint in Composite Material”, *AIAA Journal*, Vol. 18, No. 11, pp. 1371-1375 (Nov. 1980)
5. Fu-Kuo Chang, R. A. Scott and G. S. Springer, “Strength of Mechanically Fastened Composite Joints”, *J. of Composite Materials*, Vol. 16, pp. 470-493 (1982)
6. Y. J. Lee, W. H. Chen, “Study On Mechanical Behavior of the Composite Laminates Connect by Bolts”, the Ph D. Thesis of National University of Taiwan (1991) (in Chinese)
7. Y. J. Lee and W. H. Chen, “Study on the Failure Behavior of Bolted Connections In Vessel made of GFRP Laminates”, *J. of the Society of Naval Architects of Japan*, Vol. 169, pp. 467 – 176 (1991)
8. Shoumei Wang and Yaoxin Han, “Finite Element Analysis for Load Distribution of Multi-Fastener Joints”, *J. of Composite Materials*, Vol. 22, pp.124-135 (Feb. 1988)
9. Y. J. Lee, H. J. Lin, J. J. Lin, “Numerical and Experimental Analysis on the Buckling Strength of Composit Materials Connected by Rivets (II)” the Technical Report of the Project of the Development of National Defense, CS 80-0210-D-002-33 (1991), (in Chinese)
10. Y. J. Lee, H. J. Lin, J. J. Lin, “Numerical and Experimental Analysis on the Buckling Strength of Composit Materials Connected by Rivets (III)” the Technical Report of the Project of the Development of National Defense, CS 81-0212-D-002-522 (1992), (in Chinese)

THERMOPLASTIC BONDING TO METALS VIA INJECTION MOLDING FOR MACRO-COMPOSITE MANUFACTURE

Karthik Ramani and Brendan Moriarty

*Composites and Polymer Processing Laboratory, School of Mechanical Engineering
1288 Mechanical Engineering Building, Purdue University, West Lafayette, IN 47907 USA*

SUMMARY: In this work, we explore a new method of in-situ joining of polymers to metals in injection molding to allow direct bonding between thermoplastic and metal parts. Such a method can integrate several down-stream steps in product manufacture, allow optimal design of products and joints, avoid adhesive application, assembly, and associated difficulties. A variety of process parameters and their effects upon the interface tensile strengths were examined. A full factorial experiment was conducted involving four of the critical process parameters identified. The effects upon tensile strength at break of the following process parameters were studied: 1) adherend surface temperature, 2) screw linear velocity, 3) bond-line thickness, and 4) pack and hold pressure. The fracture surfaces and the thermoplastic-metal interfaces were analyzed. The bonds fabricated with higher adherend surface temperatures had increased mean tensile strength and less adhesive failure. This increase in mean bond tensile strength and less adhesive failure was due to increased polymer penetration of the adherend surface roughness, at the μm level, as shown in the analysis of the polymer-metal interface.

KEYWORDS: bonding, thermoplastic, injection molding, tensile, fracture, polycarbonate, steel

INTRODUCTION

Thermoplastic adhesive bonding via injection molding is shown to be a cost effective method to create net shape polymer-metal macro-composites with interfaces of appreciable tensile strength. Traditionally, complex parts consisting of net shape plastic parts and metallic substrates are joined using thermoset adhesives or insert molding with special features. Thermoset adhesives use a separate assembly process and need time to cure. Joining in-situ in injection molding offers reduced times and steps to manufacture, is insensitive to tolerances required in assembly, and creates a stable interface. In this study, a thermoplastic was injection molded onto a grit blasted metal substrate to create tensile butt joints.

MOTIVATION

The primary objective of this research is to develop in-situ processes to join thermoplastics to metals in an injection molding process. In our earlier studies a hot-melt process was used as the model environment [1-3]. The surface preparation, contact pressure during consolidation,

heating and cooling rates, hold times at melt and recrystallization temperature, effect of bond line thickness and uniformity, and anodization to increase durability were included in the process development [4]. In a parallel study, the residual stresses between both amorphous and semi-crystalline thermoplastic polymers and metals are modeled and validated [5].

EXPERIMENTAL PROCEDURE

The objective of the experiments was to study the effects of injection molding process parameters upon the tensile strength of a butt joint. A butt joint eliminated the contribution of shrinkage stresses to bond strength which would occur in insert molded joints. The tensile test specimen consisted of 2 cylindrical rods (19.05 mm diameter) of 1018 low carbon steel. The bonding surfaces of the steel were grit blasted with 60 grit aluminum oxide. The bonding surfaces were scrubbed with a nylon brush and soaked in isopropyl alcohol to remove loose alumina grit. The steel inserts were then soaked in a bath of isopropyl alcohol and ultrasonically cleaned for 30 minutes. Reverse osmosis (RO) water was not used for cleaning because the steel inserts began to rust when soaked.

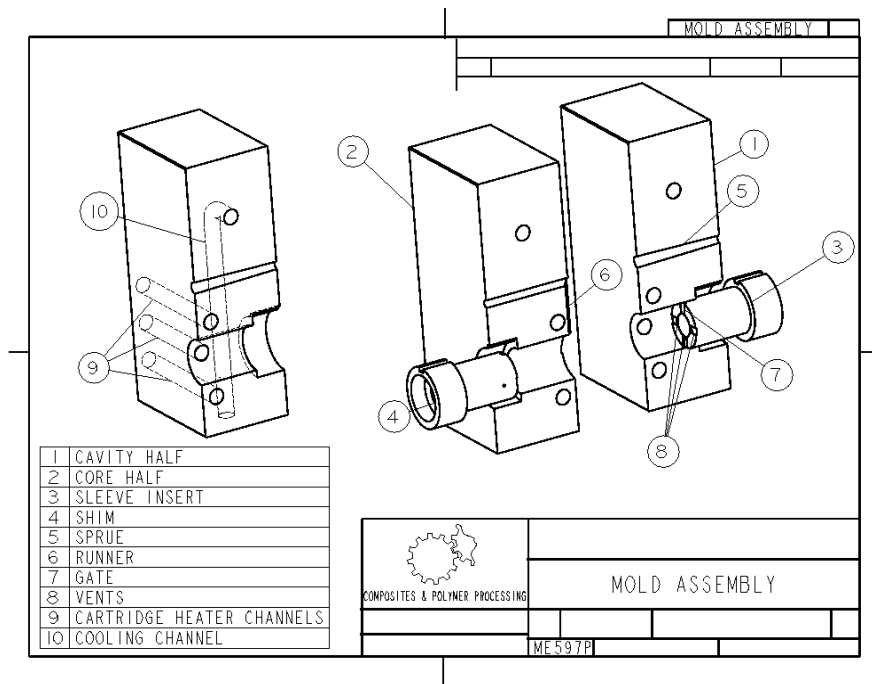


Figure 1: Mold Assembly Drawing

A special mold was designed to create tensile butt joint specimens of variable thickness (See Figure 1). The thickness of polymer between the two steel inserts was controlled with the use of shims of variable length. Additionally, a mold insert was designed to allow for variable gate dimensions. The injection molding was carried out on a 55 ton Cincinnati Milacron model VST 55 injection molding machine with a 32 mm diameter screw.

The limits of the ranges of several process parameters were explored in preliminary experiments. With a polymer cavity thickness of 0.3 mm, the mold filling was not consistent for every cycle due to variation in process parameters beyond the control of the operator. A polymer thickness of 0.5mm was used as a minimum since the resulting mold filling was consistent from cycle to cycle. Steel inserts without preheating were also used for creating

butt joints, however, the bond broke upon ejection from the mold. Several process parameters, such as length of ultrasonic cleaning time of the steel inserts were eliminated when it was determined that the parameter in question had no significant effect upon the bond tensile strength. As a result of these preliminary experiments, the following four process parameters were selected for a full factorial study: 1) adherend surface temperature, 2) injection screw linear velocity, 3) polymer thickness, and 4) pack and hold pressure.

Various methods of heating the rods in-situ were also investigated such as heating the adherend surface with a nitrogen hot gas torch. The hot gas torch effectively heated the adherend surface without heating the insert or mold below the surface. However, as soon as the torch was removed, the adherend surface rapidly cooled below the glass transition temperature resulting in very weak or no bonding. Therefore, the steel bars were heated in an oven prior to insertion into the mold. The oven temperature was set to either 316°C or 399°C to achieve the variations in the adherend surface temperatures. The steel samples remained in the oven for a period of 30 minutes to allow the entire insert to achieve thermal equilibrium with the oven.

After preheating, the steel rods were then inserted into the mold held at a constant temperature of 121°C. The adherend surface temperature was recorded using a Heimann model KT 15.82 infrared (IR) thermometer. Due to space constraints, the IR thermometer had to be placed at angle of approximately 40° below the horizontal plane. Due to this angle and the distance of the IR thermometer from the adherend surface, the actual area from which the IR thermometer collected data was ellipsoidal in shape with a major axis of 17mm and a minor axis of 13mm. The adherend surface temperature versus time was recorded using Labview data recording software. Mold filling occurred five seconds after the mold began to close, however the last adherend surface temperature data point was recorded just before mold closure began. Therefore, a decaying exponential curve fit was applied to the data and extrapolated for 5 seconds to estimate the adherend surface temperature at the time of mold filling. The molding machine filled the cavity between the two steel bars with GE Lexan polycarbonate in approximately 0.33 seconds.

After removal of the test specimens from the mold, the parts were allowed to cool to room temperature. The butt joint tensile specimens were then tested on a QTEST-VII testing machine with a constant crosshead speed of 5.08 mm per minute.

To study the bond interface region, several specimens were created using 6061-T6 aluminum alloy as opposed to 1018 steel. The aluminum adherends were grit blasted similar to the steel. Tensile bars were created using three different adherend preheating methods: high heat, low heat, and no heat. For the high heat and low heat, the oven was set to the same temperature as for the steel (i.e., 399°C and 316°C respectively). For all of the aluminum tests, an injection velocity of 10.668 cm/sec, bond thickness of 0.5 mm, and pack and hold pressure of 190 MPa were used. All other injection molding parameters remained the same. The bulk of the aluminum was removed from the bond area using a band saw, leaving approximately 2 mm of aluminum on both sides of the polycarbonate. During cutting on the band saw, the bond area was not heated significantly. The remaining aluminum was removed from the polycarbonate by soaking the pieces in a 15% solution of sodium hydroxide (NaOH) for approximately 24 hours. After 24 hours, the aluminum had completely dissolved away, exposing the polycarbonate bond interfacial surface. No visible deterioration of the polycarbonate due to the soak in the NaOH occurred. For the non-preheated aluminum, the polycarbonate did not bond to the aluminum. The polycarbonate discs were ultrasonically cleaned in isopropyl

alcohol for 10 minutes. The discs were then sputter coated with a thin layer (10-20nm) of gold/palladium (Au/Pd). The Au/Pd layer facilitates viewing the polycarbonate in the scanning electron microscope (SEM) by providing a conductive surface layer which prevents charging of the polymer surface. The polycarbonate bond interfacial surface was viewed on a JEOL 35CT SEM at an accelerating voltage of 15kV.

RESULTS AND ANALYSIS

Statistical Analysis

The tensile test data was statistically analyzed using the SAS statistical analysis software. A plot of the residuals versus normal quantiles yields a nearly linear relationship which is indicative of normally distributed data. The program computed the mean strength values for each parameter level setting (See Table 1).

Table 1: Statistical Analysis of Results

Parameter	Level Setting		Mean Bond Tensile Strength (MPa)	Statistical Confidence	Statistically Significant
Mean Adherend Surface Temperature (°C)	Hi	204	30.8	0.9999	YES
	Low	170	20.4		
Screw Linear Velocity (cm/sec)	Hi	10.668	26.4	0.3550	NO
	Low	5.080	25.3		
Polymer Thickness (mm)	Hi	1.0	23.9	0.6550	NO
	Low	0.5	27.6		
Pack and Hold Pressure (MPa)	Hi	190	24.8	0.9150	NO
	Low	129	26.9		

A Student-Newman-Keuls test was performed to analyze the statistical significance of the parameters' effects upon the mean bond tensile strength. The adherend surface temperature had the most significant effect upon the mean bond tensile strength. Changes in the injection screw linear velocity, polymer thickness, and pack and hold pressure did not have a significant effect upon the mean bond tensile strength.

The interaction among adherend surface temperature, screw linear velocity, and polymer cavity thickness proved to be the only interaction of significance (0.9996 statistical confidence). In Figure 2 for a constant pack and hold pressure of 190 MPa, the bond tensile strength for the optimum level settings for these three parameters is compared to the bond strength for the opposite level settings.

For the range of process parameters considered, the bond tensile strength is directly proportional to adherend surface temperature and screw linear velocity, and inversely proportional to polymer thickness. The bond strength is relatively insensitive to pack and hold pressures.

In the population of bonds created with a low injection screw linear velocity, bonds of negligible strength (< 5 MPa) occurred with a much higher frequency than in the population of bonds created with a higher injection screw linear velocity. This observation provides another reason to avoid low screw linear velocities.

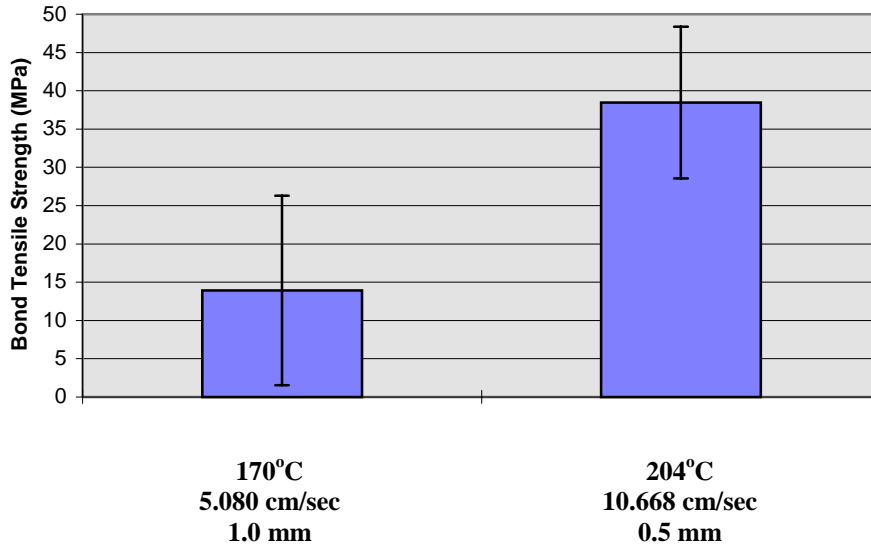
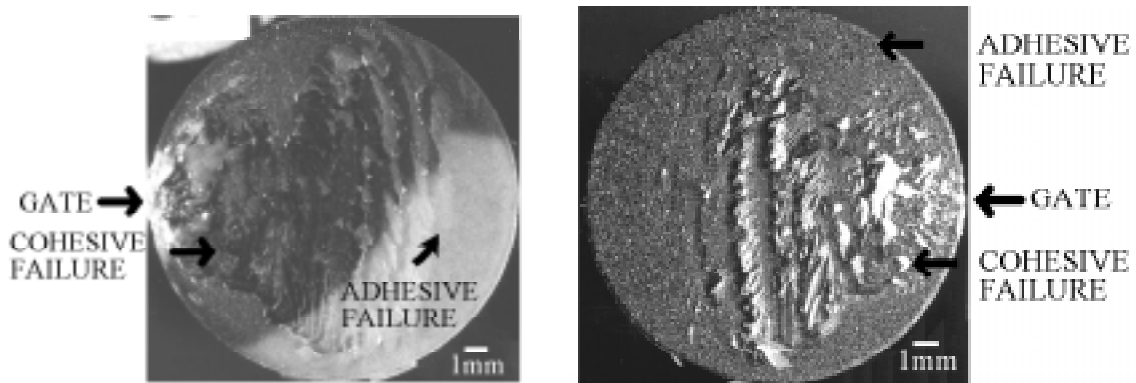


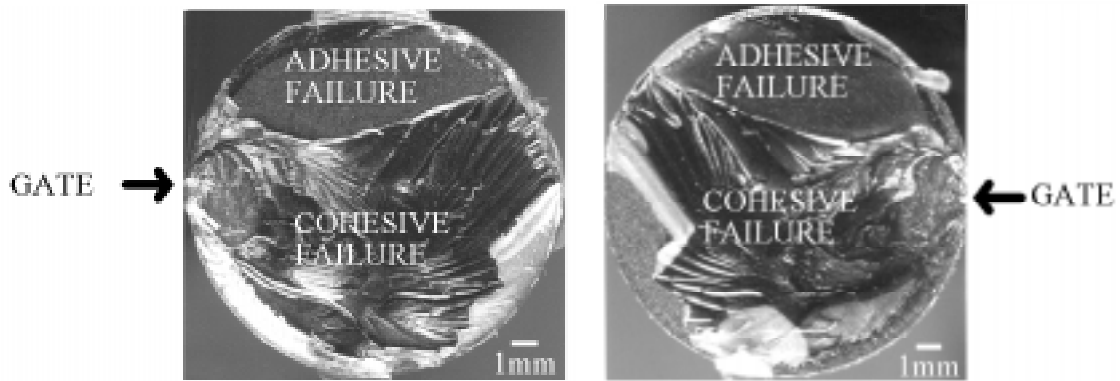
Figure 2: Comparison of Bond Strengths for Interaction of Adherend Surface Temperature, Screw Linear Velocity, and Polymer Thickness at Constant Pack and Hold Pressure of 190MPa

Fracture Surface Analysis

Observation of the fracture surfaces reveals that adhesive failure occurred on all of the specimens to varying degrees. A general trend was that the higher bond tensile strength pairs showed a lower area of adhesive failure. Comparing Figures 3a-b and 4a-b, it was observed that the failure surfaces for those bonds created with a low adherend surface temperature reveal more adhesive failure than bonds created with a higher adherend surface temperature.

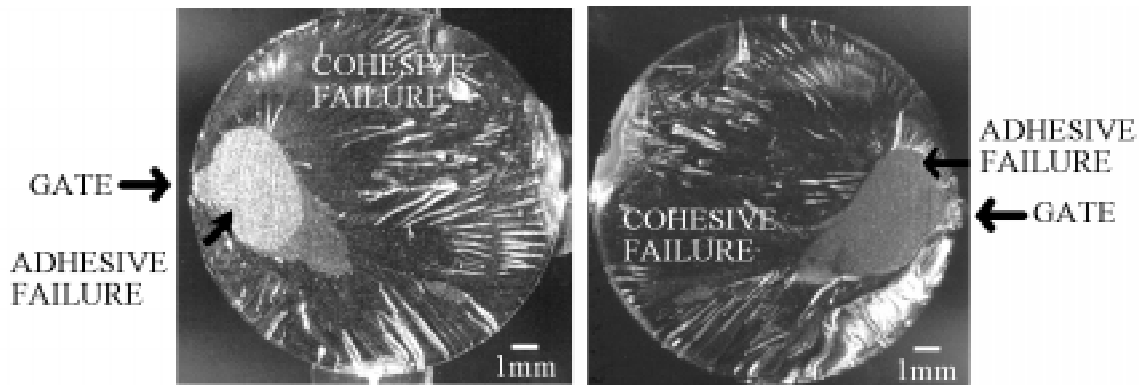


Figures 3a-b: Fracture Surface Pair from Bond Created with Low Adherend Surface Temperature



Figures 4a-b: Fracture Surface Pair from Bond Created with High Adherend Surface Temperature

Additionally, for some of the higher strength bonds, the adhesive failure tended to occur near the gate area (See Figures 5a-b).

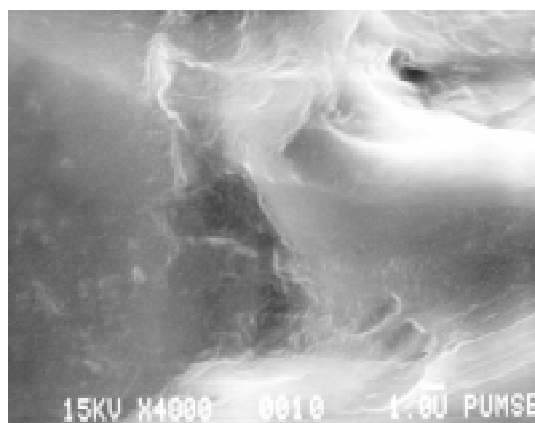


Figures 5a-b: Fracture Surface Pair from Bond Created with High Adhesive Surface Temperature Showing Adhesive Failure Near Gate

Bond Interface Microanalysis

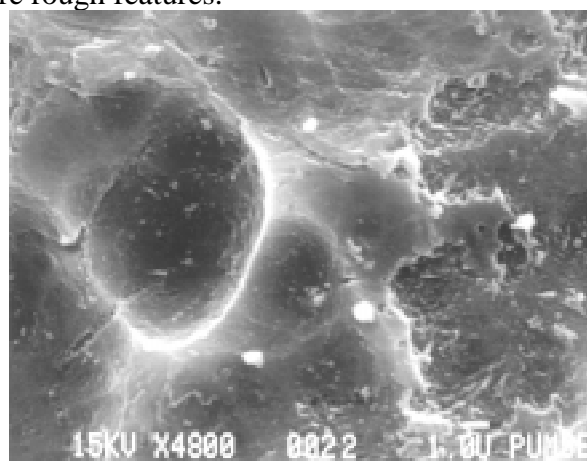
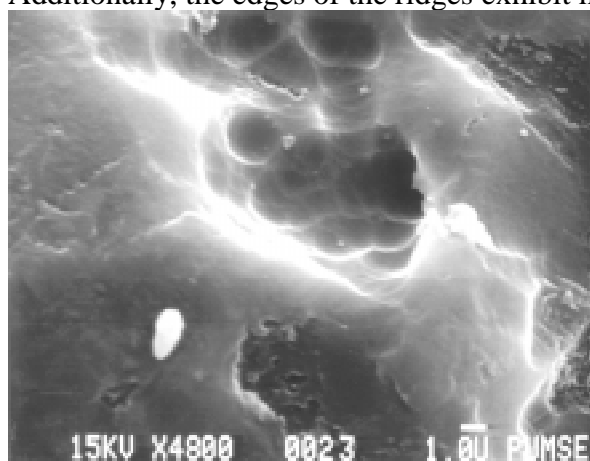
Surface profilometry measurements were taken of the grit blasted aluminum surface and the three polycarbonate surfaces (no preheat, low preheating, and high preheating). The radius of the profilometer stylus tip was $5\mu\text{m}$. The R_a values were approximately $3\mu\text{m}$ for all four surfaces.

Observing the polycarbonate surfaces in an SEM at 200X magnification revealed no apparent differences among the surfaces of grit blasted aluminum, and the polycarbonate surfaces for the three preheating conditions. However, at 4800X magnification the differences among the three preheating conditions are apparent. For the polycarbonate injection molded over the non-preheated aluminum surface, the polycarbonate is predominantly smooth. The few ridges that were observed exhibit smooth edges (See Figures 6a-b).



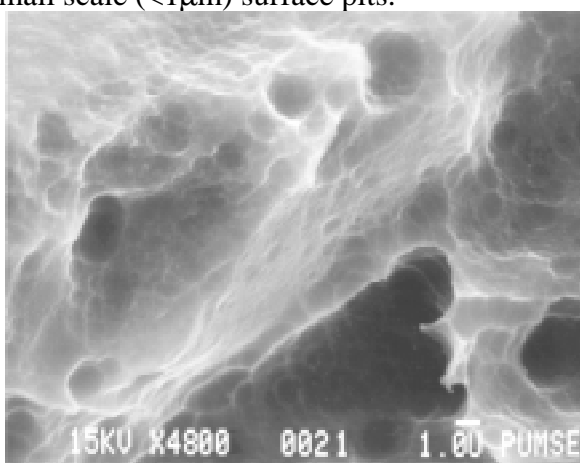
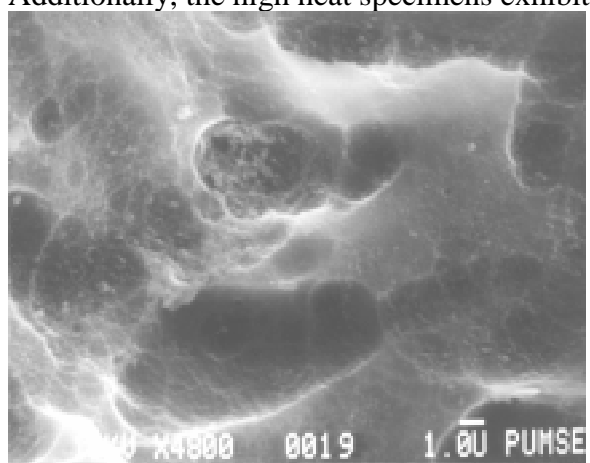
Figures 6a-b: SEM of Polycarbonate Surface with No Aluminum Preheating

SEM micrographs of the polycarbonate bonded to the aluminum preheated in the oven at 316°C show considerably more roughness than the unheated specimens (See Figures 7a-b). Additionally, the edges of the ridges exhibit more rough features.



Figures 7a-b: SEM of Polycarbonate Surface with Low Preheating

SEM micrographs of the polycarbonate bonded to the aluminum preheated in the oven at 399°C show similar medium (1-5µm) and large scale (>5µm) roughness (See Figures 8a-b). Additionally, the high heat specimens exhibit small scale (<1µm) surface pits.



Figures 8a-b: SEM of Polycarbonate Surface with High Preheating

An SEM micrograph of the grit blasted aluminum surface is shown for comparison (See Figure 12). Notice the small scale (<1 μ m) surface protrusions which are the cause for the pits on the polycarbonate bonded with high preheating of the aluminum.

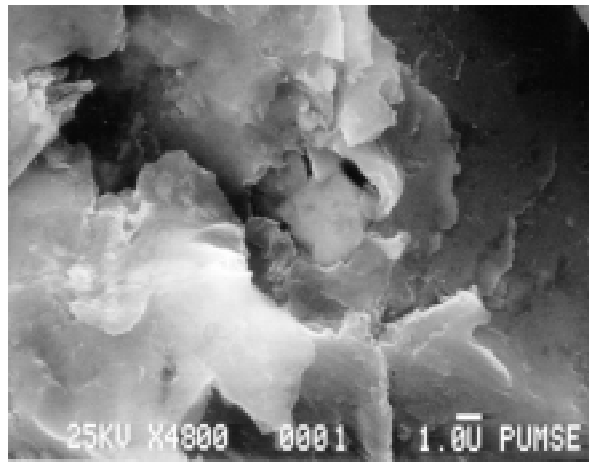


Figure 9: SEM of Aluminum Surface

While the large scale (>5 μ m) roughness of all four surfaces is approximately equivalent (See the profilometry results of the previous page), the small (<1 μ m) and medium scale (1-5 μ m) roughness differ significantly (as shown in Figures 6 through 9).

Bond Strength Variance Analysis

The variation in bond tensile strength is due to variations in several process parameters including adherend surface temperature and hydraulic transfer pressure. The mean adherend surface temperature of 204°C and a standard deviation of 14°C result in bonds with a strength of 30.8 MPa. The mean adherend surface temperature of 170°C and a standard deviation of 12 °C result in bonds with a mean bond strength of 20.4 MPa. If we assume, from the results of the full factorial study, that an increase in adherend surface temperature of 34°C (204°C - 170°C) results in an increase in bond strength of 10.4 MPa, then the variations in adherend surface temperature of 14°C and 12°C would contribute 4.3 MPa and 3.7 MPa to the variation in the mean bond tensile strength respectively.

The deviation in the bond tensile strength data is larger than the deviation attributed to variation in adherend surface temperature, suggesting that other factors or interactions are affecting the bond strength. Included among these noise factors is the hydraulic transfer pressure (the pressure at the screw tip when screw reaches the transfer position), which varied as much as 35 MPa from a nominal value of 138 MPa in a particular test group.

Viscosity Effects on Bond Strength

The increase in mean bond tensile strength with increased adherend surface temperature is due to increased penetration of surface roughness. Polymer viscosity is primarily a function of temperature and shear rate. For polycarbonate, the apparent viscosity is relatively insensitive to the shear rate [6]. The polymer viscosity is related to the polymer temperature by Equation 1.

$$\eta = A e^{E/RT} \quad (1)$$

where η is a defined shear viscosity, E is a viscous energy of activation for the polymer, R is the gas constant, T is absolute temperature, and A is a pre-exponential coefficient [6]. It was assumed that the polymer in contact with the adherend surface was at the same temperature as the adherend surface. For the high adherend surface temperature of 204°C, the melt viscosity of polycarbonate is 250,000 poise (g/cm-sec) at a shear rate of 10 radians per second [7]. For the low adherend temperature of 170°C, the melt viscosity for polycarbonate is over 1,500,000 poise (g/cm-sec) at a shear rate of 10 radians per second [7]. The significantly lower polymer viscosity at the higher adherend surface temperature allows the polycarbonate to penetrate the adherend surface micro-roughness to a greater degree. The scanning electron micrographs (Figures 6-8) confirm the fact that a greater amount of penetration of the small scale surface micro roughness (<1 μ m) is present in the bonds prepared with the higher adherend surface temperature.

CONCLUSIONS

A full factorial study of 1) adherend surface temperature, 2) screw linear velocity, 3) bond-line thickness, and 4) pack and hold pressure showed that adherend surface temperature was the most significant factor. The interaction among adherend surface temperature, screw linear velocity, and polymer cavity thickness proved to be the only interaction of significance. An increase in mean adherend surface temperature from 170°C to 204°C improved the bond strength from 20.4 MPa to 30.8 MPa on average. The increase in mean adherend surface temperature is due to increased polymer penetration of the adherend surface small scale (<1 μ m) roughness.

This study demonstrated in-situ joining of thermoplastics to metal in an injection molding process. Injection molding on a grit blasted surface proves to be a cost effective and eco-friendly method to manufacture macro-composites with polymer-metal interfaces of significant tensile strength.

ACKNOWLEDGMENTS

The authors would like to acknowledge the NSF CAREER Award (DMI 9501646) and NSF Equipment Grant (DMI 9500232). Additionally, the authors would like to thank Dr. Said Mansour of the Purdue Microstructural Analysis Facility.

REFERENCES

1. Ramani, K., J. Tagle, D. Devanathan, A. Nazre, D. Swarts, and S. Lin. "Thermoplastic Bonding for Structural Applications: The Role of Processing", Tenth International Conference on Composite Materials, August, 1995, Whistler, British Columbia, Canada.
2. Ramani, K., J. Tagle, D. Devanathan, A. Nazre, D. Swarts, and S. Lin, A Thin-film Bonding Process for Titanium to Polyetherketone (PEKEKK), Polymer Engineering and Science, 1995, **35**(24): p. 1972-1978.

3. Ramani, K. and J. Tagle, "Process Induced Effects in Thin-Film Bonding of PEKEKK in Metal-Polymer Joints", *Polymer Composites*, 1996, **17**(6): p. 879-886.
4. Ingram, C. and K. Ramani, "The Effect of Sodium Hydroxide Anodization on the Durability of Poly (ether ketone ether ketone ketone) Adhesive Bonding of Titanium", *Int. J. Adhesion and Adhesives*, 1997, **17**(1): p. 39-45.
5. Ramani, K. and W. Zhao., "The Role of Residual Stresses in Thermoplastic Bonding to Metals", in Eleventh International Conference on Composite Materials, July, 1997 submitted.
6. Progelhof, R.C. and J.L. Throne, "Polymer Engineering Principles: Properties, Processes, Tests for Design", 1993, New York: Hanser Publishers.
7. Lin, Y.-G., Lexan 123 Grade, "Viscosity vs. Shear Rate", GE Technical Literature. 1997, GE Plastics, Analytical Technology.

CHARACTERIZATION OF IMPACT DAMAGE IN CFRPS USING A SCANNING ACOUSTIC MICROSCOPE

Shang-Lin Gao, Jang-Kyo Kim* and Xing-Juan Xian⁺

*Department of Mechanical Engineering and Centre for Advanced Engineering Materials
Hong Kong University of Science and Technology, Clear Water Bay, Hong Kong.*

⁺Institute of Mechanics, Chinese Academy of Science, Beijing, China.

SUMMARY: This paper describes the quantitative technique using scanning acoustic microscopy (SAM) for characterizing the low energy impact delamination at individual laminar interfaces of carbon fibre/modified bismaleimide laminated composites. Accurate information on the damaged states, such as size and shape of delaminations through-the-thickness distribution, can be obtained using three kinds of ultrasonic techniques in reflection mode, namely ply-by-ply scanning, time-of-flight and B-scan analysis. Good correlation is found between the results obtained from fractography and SAM experiments. As a rapid, non-destructive inspection tool, SAM is also a powerful technique to characterize the micro-deformation and damage propagation mechanisms in the compression after impact (CAI) test specimens.

KEYWORDS: scanning acoustic microscopy (SAM), low-velocity impact, delamination, compression after impact (CAI), time-of-flight analysis

INTRODUCTION

During recent years the use of fiber reinforced laminated composites for primary and secondary aircraft structures has rapidly increased, mainly due to the need for reduced weight. One of the major concerns for a designer is the exact knowledge of the effect of impact damage on residual structural performance of these materials because the impact damage considerably reduces the stiffness and strength, particularly under compression [1]. However, the characterization of the damage tolerance is complicated by the fact that delaminations and cracks are often not on the impacted surface. Due to the lack of damage assessment capability and analytical models which can accurately predict the impact damage in laminated composites [2], composite parts are generally restricted to load or strain levels far below their potential.

Therefore, it is apparent that a reliable nondestructive evaluation (NDE) technique for assessing impact damage in composite structures is needed. X-ray radiography is often used to detect transverse cracking [3]. Conventional ultrasonic techniques are commonly used for characterization of delaminations with satisfactory results, but they often fail to detect micro-cracks and multiply-delaminations. Delamination is one of the most critical damage modes in laminated composites subjected to local bending and/or low-velocity impact [4].

An accurate description of delaminations and matrix cracking through the thickness is needed for better understanding of the damage process and their consequences. However, few ultrasonic methods have been reported on these subjects in the current literature [5]. Although some advanced ultrasonic set-ups can provide useful data, very complicated and expensive features such as multiple gates, multiple channels, multiple receivers, are necessary. They often fail to give good damage evaluations because of three dimensional images which are not appropriated [6]. As a consequence, current understanding of damage growth mechanisms due to impact is still limited.

The main purpose of the present study is to evaluate the multi-ply delaminations size and through-the-thickness damage distribution using advanced digital scanning acoustic microscopy (SAM). The details of three techniques, which are used to measure the ply-by-ply delamination shape, size and their distributions through the specimen thickness, are described. They are the C-scan based on the amplitude measurement in a thin time gate automatically shifted at each point along the time axis to cover the entire thickness of specimen; the time-of-flight (TOF) analysis, and the conventional B-scan imaging technique. Fractographic evaluation is also used to compare with the SAM results. Furthermore, the foregoing techniques are also used to study the damage propagation in composites containing different matrix materials.

EXPERIMENTAL PROCEDURES

The composite laminates studied were fabricated from Toray T300 carbon fibers and two different grades of modified bismaleimide (MBMI) : 2MBMI and 4MBMI which represent those designed for high temperature tolerance and low viscosity, respectively. The MBMI resins contained different amounts of polyethersulfone (PES) particles according to the supplier, Beijing Aeronautical Manufacturing Technology Research Institute (BAMTRI), China [8]. All laminate panels were made by hand lay-up of 16 layer prepregs with a lay-up sequence of $[(45/0/-45/90)_2]_s$. The nominal fiber volume fraction was 60%, and the thickness of the plate was 2.0 mm.

All impact tests were performed at room temperature with 100 mm × 100 mm square specimens on an instrumental impact tester, Dynatub 8250 Impact Test Machine. An impactor of weight 2.42 kg and with a hemispherical nose of 25.4 mm in diameter was impacted onto the centre of specimen whose edges were clamped between two circular rings. An energy of 5.3 J was applied to produce damage which could be only barely visible on the impacted surface. The load-displacement records were obtained directly from the data acquisition system.

The CAI tests were conducted on a Sintech 10/D Minnesota Testing Systems (MTS) using a Boeing Compression After Impact Test Fixture (BSS 7260).

The impact damage was evaluated by means of an advanced scanning acoustic microscope (SAM), Sonix Micro-Scan System. A focused acoustic beam was used to scan over the plane of the damaged laminate in a gated pulse-echo mode. The transducer with a 15 MHz probe was mounted on computer-controlled bridges, allowing a complete scan of test samples. Distilled water was used as the coupling medium between the transducer and test specimen. Measurements were made on a 90 mm × 90 mm area using a 250 × 250 point sampling grid which were processed using a software on a personal computer. Reflectograms of A-scan were recorded to show the amplitude/time response obtained on an undamaged area and areas

having delaminations at different interfaces. The amplitude of the echo reflected by a delamination is measured by placing the test gate on the representative region of the thickness of the structure to be tested, between the front surface echo and the back surface echo.

In addition to the ply-by-ply C-scan analysis which generates the images of gross damage through the whole laminate thickness, the time-of-flight (TOF) techniques were also applied to obtain the information about damage on individual plies. Because the flaw signals appeared in the gate placed on the time axis between the upper and lower sides of the specimen, quantitative calibration units could be performed in absolute to correlate the gray level with the depth of delaminations in the specimen. Having obtained the C-scan images, the cursor controlled x-y positions and amplitude-depth data were recorded.

After the SAM characterization, the specimen was examined destructively by cutting through the thickness and photographed using an optical stereo microscope to compare the damage detected by this method with that detected ultrasonically.

RESULTS AND DISCUSSION

Ultrasonic Pulse-Echo Scanning of the Impacted Composite Plates

Fig. 1 shows the whole accumulated damage area obtained from the C-scan image. The level of gray colour indicates the depth of the layer containing damages from the front surface. The total damage is in the form of a circle confirming the earlier finding [4] for a laminate composite with a similar lay-up sequence. Fig. 2(a) and (b) exhibit delaminations on the top eight layers of the laminate which were obtained from the ply-by-ply C-scan technique and the time-of-flight analysis, respectively. The ply-by-ply C-scanning allows imaging of damages accumulated ply-by-ply toward the bottom layer. Because of the duration of the ultrasonic echo, the measurements made in a given window for delamination on a layer may have also been influenced by delaminations above it. Even so, the distribution of delamination through-the-thickness can be evaluated. In the time of flight analysis, clearer individual delamination shape and through-the-thickness damage distribution can be obtained by controlling the cursor' gray level.

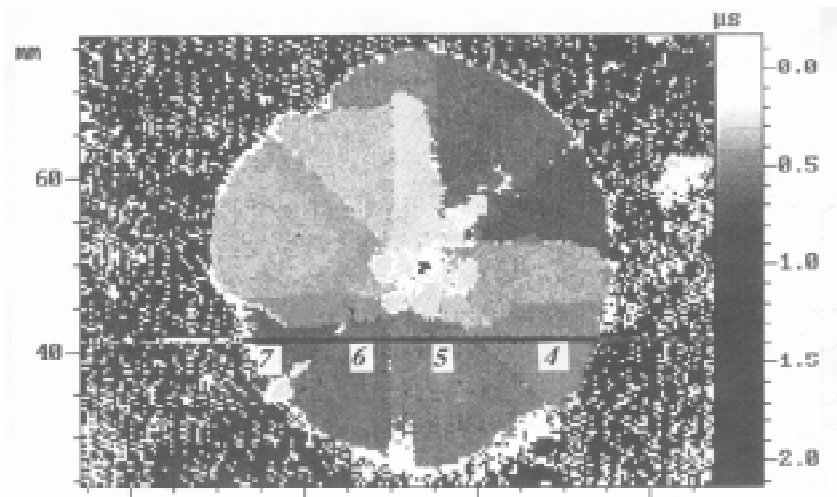


Fig. 1: A pulse-echo ultrasonic C-scan image of the impacted composite plate. The horizontal line, crossing delaminations in the fourth, fifth, sixth and seventh interface.

Table 1: The depth and size of delamination measured by time of flight analysis and fractography.

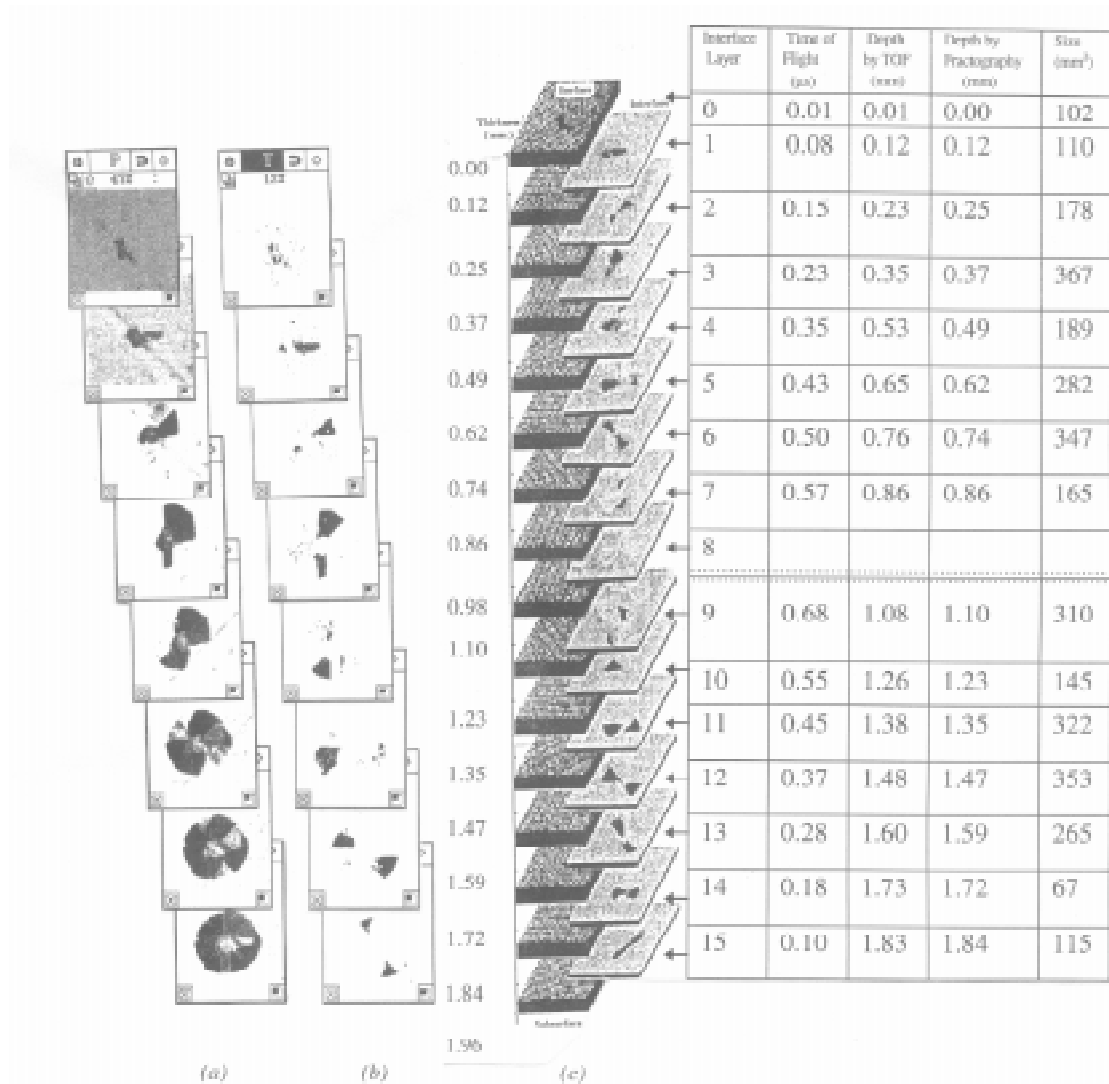


Fig. 2: The delamination patterns obtained from the front (impacted) surface up to the eighth ply (see table 1) by (a) ply-by-ply C-scanning, (b) time-of-flight analysis. (c) Schematic showing the distribution of delamination through-the-thickness of composite.

The delamination patterns on the eight layers of the laminate close to the bottom, which cannot be detected from front side due to shielding effect [7], were also produced in a similar way. As a consequence, an illustration of all the delaminations in an impacted composite plate is given in Fig. 2(c). It is noted that the delamination in a layer is “peanut shaped” with its major axis oriented in the direction of fiber of the lower ply and does not occur between two layers with the same orientation.

The quantitative results obtained for the same laminate are summarized in Table 1. The depths of delamination on individual plies were calculated by:

$$\text{Depth} = [\text{Plate thickness} / \text{Time of flight for plate}] \times \text{Time of flight for delamination.} \quad (1)$$

The depths of damage calculated in this way are in good agreement with those obtained from cross-sectional fractography. It is worth noting that all delamination propagated along the laminar interfaces owing to the inherent weakness of the interface. The sizes of delamination on each layer are also included in Table 1.

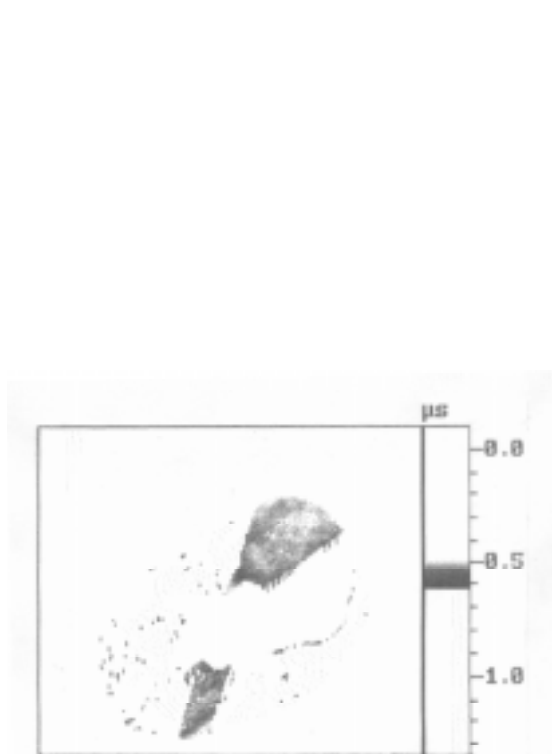


Fig. 3: The 3-D profile of time of flight image showing the delamination on the third interlayer; gray levels indicate the depth of delamination from the front surface.

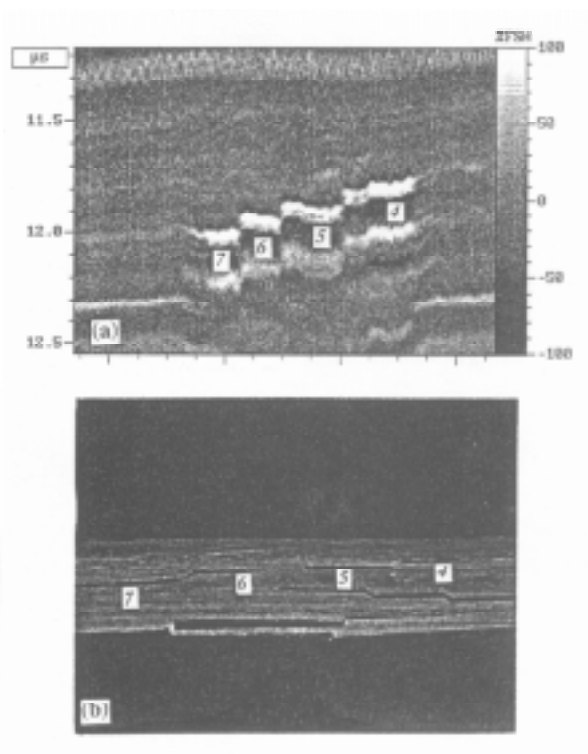


Fig.4: Cross-sectional view of delaminations in the fourth, fifth, sixth and seventh interface by (a) B-scan image, and (b) fractography along the line shown in Fig.1.

Furthermore, Fig. 3 shows a detailed three-dimensional time-of-flight image which suggests that the delamination on an interlaminar plane is not smooth, but microscopically rough, reflecting the toughness and impact resistance of the composite.

Fractography

To verify the above SAM result, the laminate whose damages are shown in Fig.1 was cut along the line 4-7. The polished cross-section was examined using an optical stereo microscope to compare the damage detected by B-scan, as shown in Fig. 4. The results clearly indicate that the number and through-the-thickness distribution of the delaminations measured by the two methods agree excellently.

Comparison of Damage Patterns of T300-2MBMI with that of T300-4MBMI

Because the T300-4MBMI system contained more thermoplastic particles, it has lower viscosity, significantly higher impact resistance and damage tolerance than the T300-2MBMI system at room temperature. Comparison of the SAM results showed considerable differences in the delamination size and the distribution through the specimen thickness: (i) As shown in Fig. 5, the relatively tougher T300-4MBMI composite has a smaller

damage area, with damage occurring on fewer layers than the brittle system (T300-2MBMI). (ii) The size of delamination on individual interface gradually increased though the thickness for the brittle system, while it decreases for tougher system (see Fig.5(b) and (c)). (iii) The most striking characteristic of the T300-4MBMI composite was that the front surface swelled after impact, an indication of plastic deformation being an important impact energy absorbing mechanism for this system at room temperature.

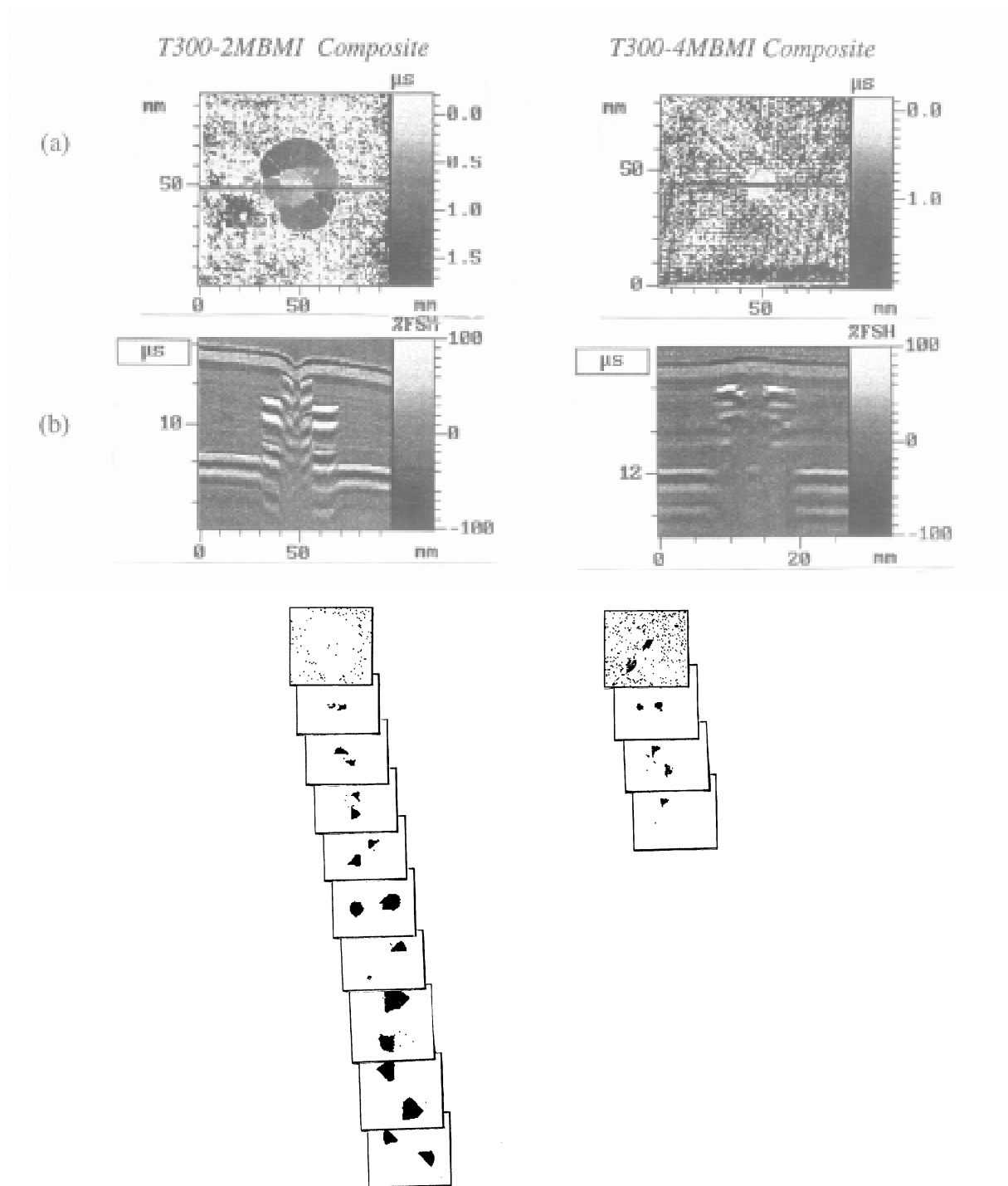


Fig. 5: Comparison of damage patterns of T300-2MBMI (left) and T300-4MBMI (right) composites by (a) C-scan images, (b) B-scan images (cross-section view along the lines in (a)) and (c) time of flight analysis (showing damage distribution through-the-thickness).

Damage Patterns of CAI Plate

When loaded in compression, impact damaged laminates experience significant strength reductions, due mostly to local instabilities [9]. Fig. 6 illustrated the C-scan images of the CAI test specimen. The laminate failed by buckling with significant delamination growth in the transverse direction. It suggests that buckling took place under compression from the impact damage present in the top several layers. The cracks extended along approximately 45° direction of compression, causing catastrophic fracture. The delamination extended completely across the specimen width but extended only a short distance in the loading direction. On the other hand, the delamination present on the other layers were not seriously affected by the CAI test.

Because the ability to predict the residual strength of a damaged structure is of major importance for an effective damage tolerant design, the SAM techniques described above can provide useful information for developing a quantitative analytical model.

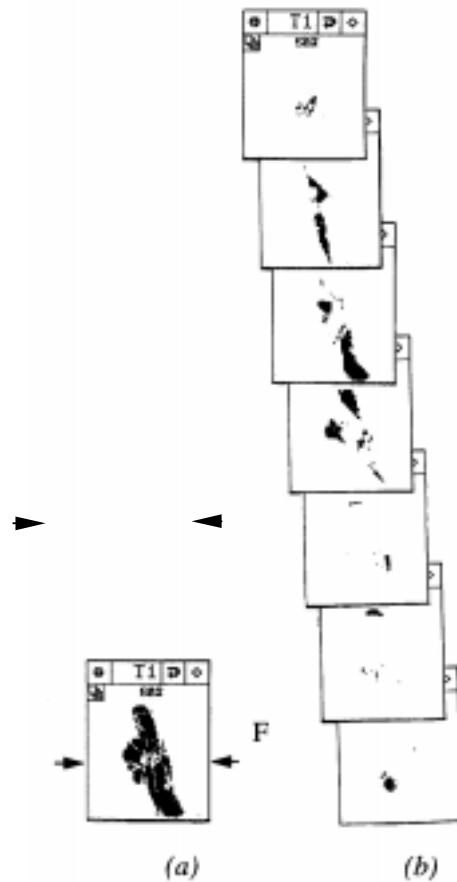


Fig. 6: C-scan images of the CAI plate showing the overall (a) and individual (b) delamination distribution through-the-thickness.

CONCLUSIONS

Accurate information on the damage states, such as three dimensional shape, size and distribution of multi-layer delaminations, is generated from the study of three different ultrasonic techniques based on SAM experiments. Excellent correlation is observed between the results obtained from these techniques and fractography.

There are considerable differences between CFRPs containing two different BMI matrix materials in terms of delamination size and distribution through the specimen thickness, which in turn reflect different micro-deformation and damage mechanisms.

As a rapid, non-destructive inspection tool, SAM is a powerful technique to characterize the delaminations and their propagation in CAI test specimens.

ACKNOWLEDGMENTS

The authors wish to thank the Research Grant Council (RGC) for continuing support of this project.

REFERENCES

1. Jang, B.P, Kowbel, W. and Jang, B.Z., "Impact Behavior and Impact-fatigue Testing of Polymer Composites", *Comp. Sci. & Technol.*, Vol. 44, 1992, pp.107-118.
2. Choi, H.Y. and Chang, F.K., "A Model for Predicting Damage in Graphite/epoxy Laminated Composites Resulting from Low-velocity Point Impact", *J. Comp. Mater.*, Vol. 26, 1992, pp. 2134-2140.
3. Wang, A.S.D., "Fracture Mechanics of Sublaminar Cracks in Composite Laminates", *AGARD 83, Conference Proceedings*, 1983, No.335.
4. Kaczmarek, H. and Maison, S., "Comparative Ultrasonic Analysis of Damage in CFRP under Static Indentation and Low-velocity Impact", *Comp. Sci. & Technol.*, Vol. 51, 1994, pp. 11-26.
5. Kaczmarek, H., "Ultrasonic Detection of Damage in CFRPs", *J. Comp. Mater.*, Vol. 29, 1995, pp. 59-95.
6. Wooh, S.C. and Daniel, I.M., "Three-dimensional Imaging of Impact Damage in Composite Laminates", *Revue of Progress in Quantitative Nondestructive Evaluation*, Vol. 9, pp. 1513-1520.
7. Buynak, C.F., Moran, T.J. and Martin, R.W., "Delamination and Crack Imaging in Graphite/epoxy Composites", *Mater. Evalu.*, Vol, 6B, 1987, pp. 1203-1211.
8. Zhao, Q.S., Li, Y.H., Gao, H. and Sun, D.S., *Proc. of SAMPE 34th*, Covina, Calif., 1989, pp. 27-32.
9. Abrate, S., "Impact on Laminated Composite Materials", *Appl. Mech Rev.*, Vol. 44, 1991, pp. 155-190.

RESPONSE OF FIBRE COMPOSITE LAMINATES TO ACOUSTIC EMISSION LINE SOURCES

E. Rhian Green

Department of Engineering, University of Leicester, Leicester, LE1 7RH, U.K.

SUMMARY: This paper employs a multiple transform method to predict the surface response of a cross-ply fibre composite laminate to line sources associated with the formation of dislocations. Each layer of fibre composite material is modelled as a transversely isotropic continuum and the laminate is constructed of four plies with the fibre direction in the two inner plies being parallel to each other and at right angles to that in the outer plies. Line sources give rise to straight crested waves travelling in the plane of the laminate at right angles to the direction of the line. Calculations are carried out for two different orientations of the line relative to the core fibre direction. Results are presented for crack opening and for shear dislocations lying in planes parallel to the plane of the laminate and located at the interfaces between each of the plies.

KEYWORDS: acoustic emission, Green's functions, dislocations

INTRODUCTION

The acoustic emission technique is one of the standard methods for the location of defects in monolithic engineering structures. In its simplest form, it consists of subjecting the structure to some external loads which give rise to the initiation of elastic waves from the defect, and of counting the arrivals at a specified surface location which exceed a given threshold in magnitude. In a monolithic material, this approach, coupled with a knowledge of the nature of stress wave propagation, serves to locate the defect and to provide an estimate of its size. Fibre composite laminates exhibit a wide variety of defects and fractures and it is necessary to derive additional information from the acoustic emission signal in order to classify the nature of the event and the location of the source. This inverse problem requires a detailed knowledge of the propagation of stress waves through the laminate (the laminate transfer functions) due to a range of sources with known characteristics, located at a specified internal position.

The response at any surface receiver arising from a known source event at a specified internal location is given in terms of the Green's function for the laminate and the time history of the source. The Green's function gives the response due to a source of known characteristics with a delta function time history, and the response to any other time dependence of the source is obtained by a convolution of the source time history with the Green's function solution. The inverse problem requires the determination of the source location and its extent, the character of the source event, and its time

history. If the location and character of the source can be determined and the Green's function evaluated, then the time history can be recovered from the receiver signal by deconvolution. An alternative approach, which avoids solving the difficult inverse problem, is to attempt to replicate the receiver signal by simulating the time history of sources of known characteristics and modifying the parameters of the source function in order to achieve good agreement with observed waveforms. This approach has been adopted in [1] and shown to be successful when applied to a number of different fracture events. In the work reported in [1], the source characteristics and the relative positions of source and receiver are taken as known, and the simulated signals are based on the earliest arrivals at the receiver, for which the Green's function is that associated with the surface response in a half space of isotropic elastic material. In order to employ this approach to the case of the fibre composite laminate it is necessary to determine the Green's functions associated with a range of initiating sources, located at various levels within the structure. In the practical situation neither the location nor the character of the initiating event is known and it is necessary to build up a library of solutions for comparison purposes. A number of solutions have been derived [2 - 6] for line sources located in a four-ply laminate and additional results are reported here.

ELASTIC WAVES

The study of wave propagation in fibrous laminates involves two main differences from that in monolithic isotropic materials. Firstly, the presence of long parallel fibres embedded in an isotropic matrix make the basic composite material both inhomogeneous and anisotropic, so that the waves undergo scattering and attenuation and their speeds vary with the direction of propagation. Secondly the presence of the interfaces between the layers of the laminate, give rise to multiple reflections and lead to a complex pattern of waves arriving at the surface. The problem of inhomogeneity can be overcome to a large extent by restricting consideration to disturbances whose wavelengths are large compared with a typical fibre diameter. In this circumstance, the scattering effect of the fibres will be small and the composite material forming each layer of the laminate may be modelled as a homogeneous, but anisotropic continuum. Typically, the fibres in a carbon fibre/epoxy resin prepreg have diameters of the order of $6\mu\text{m}$ whilst the prepreg has depth of the order of $125\mu\text{m}$. Disturbances with wavelengths of the order of some $30\mu\text{m}$ or greater, corresponding to frequencies of order 100MHz or less, will undergo little scattering from the fibres whilst still being small enough to be affected by the depth of the prepreg and to undergo reflection at the interfaces.

Whilst the restriction on wavelengths brings the simplification of homogeneity, the anisotropic nature of the composite makes the problem of elastic wave motion significantly more difficult than for isotropic materials. Thus, whereas waves travelling in isotropic materials move with one of two possible speeds in any direction of travel, for anisotropic materials in each direction there exist three possible wave speeds whose values are direction dependent. In consequence, the disturbance emanating from a point source is not radially symmetric as is the case for isotropic materials and, whereas for the isotropic material the equations governing the propagating signal involve only the radial space variable and the time, for the anisotropic material the signal is a function of all three space variables as well as the time. The determination of the Green's functions arising from point sources is consequently a computationally demanding task and a less demanding approach to understanding the effects of anisotropy can be obtained by examining the transmission of disturbances arising from line loads within or on the

surface of the laminate. Line loads of uniform strength will set up a motion in the form of straight crested waves, travelling in the plane of the laminate with speeds which vary with the orientation of the line relative to the preferred material directions. In this wave motion the spatial dimension of the problem is reduced by one, with the stress and displacement being functions of time and two space coordinates.

In addition to the complication of anisotropy, the presence of the layering gives rise to effects which do not appear in a single plate of monolithic material. As an example, consider the situation in which the source is located at an interface between the top two layers of the laminate and the elastic wave speeds in the lower layer are greater than those in the layer above. The situation can then arise in which the first arrival at the upper free surface of the laminate is not the signal which travels directly through the upper layer from the source but is the signal which starts travelling down from the source in the second layer, is reflected back at the interface between the second and third layer and subsequently travels up through the two top layers to reach the surface receiver. This is a situation which arises in fibre composite laminates for some angles of propagation but not for others.

In the numerical results which are reported here the fibre composite material is modelled as a transversely isotropic continuum for which the non-zero elements of the stiffness matrix are given in [7]. In this material, waves propagating in an arbitrary direction travel with one of three possible wave speeds denoted by c_L for the quasi-longitudinal speed, and by c_{T1} , c_{T2} for the fast and slow quasi-transverse speeds, respectively. These speeds vary with the direction of propagation but they have constant values for all propagation directions which lie along the generators of a cone whose axis is along the fibre direction. Table 1 gives the scaled values of these speeds on the cones with vertex semi-angle γ for $\gamma = 0^\circ, 30^\circ, 60^\circ, 90^\circ$. The entries give the values of the three speeds scaled by the speed c_1 of the longitudinal wave which travels in any direction at right angles to the fibre. The Table also includes scaled values of c_R , the Rayleigh surface wave speed in the direction γ .

Table 1: Scaled wave speeds at orientations γ relative to the fibres.

γ	0°	30°	60°	90°
c_L/c_1	4.782	4.159	2.480	1.000
c_{T1}/c_1	0.732	0.801	0.923	0.482
c_{T2}/c_1	0.732	0.678	0.555	0.482
c_R/c_1	0.732	0.673	0.535	0.451

The calculations reported here relate to a cross-ply laminate consisting of four layers, each of depth h , of a fibre composite material with the fibres in the two core layers being parallel to each other and at right angles to those in the outer layers. Attention is restricted to line sources which set up straight crested waves travelling at either an angle of 30° to the core fibre direction or at an angle of 60° to this direction. In the first of these two cases, the quasi-longitudinal and the slow quasi-shear wave speeds in the core layer, are greater than the corresponding speeds in the outer layers, whilst in the second case the situation is reversed. Consider a line source, situated at the interface between the top layer and the core, giving rise to signals which are monitored on the

upper surface at a distance of $8h$ from the plane of action of the source, such that the shortest distance from the source to the receiver is $\sqrt{65}h = 8.06h$. For the wave travelling at angle 30° to the core fibres, the direct quasi-longitudinal wave reaches the receiver at the non-dimensional time $T = c_1t/h = 3.25$, whilst the quasi-longitudinal wave which travels down through the core, is reflected as a quasi-longitudinal wave at the interface between the core and the bottom layer and travels back up through the core and the upper layer, reaches the receiver at the scaled time $T = 2.49$. The quasi-longitudinal wave which traverses the core four times before travelling through the upper layer to the receiver, reaches the receiver in the scaled time $T = 3.08$. In the case of the fast quasi-shear wave, the speed in the outer layer is greater than that in the core and the direct wave is the first arrival whereas for the slow quasi-shear wave the direct signal reaches the observation point at time $T = 14.53$, whilst the signal which traverses the core twice and then travels up through the top layer arrives at the earlier time of $T = 14.44$.

This approach of tracing the individual ray paths is formalised in the method of generalised rays [8] which has been employed to determine the signal in an isotropic plate exactly for a finite time. In the laminate, the reflection/transmission effects at the interfaces are considerably more complex than in the simple examples given here. Thus, a wave of any of the three types in general gives rise to three reflected and three transmitted waves and the process of tracing the individual ray paths becomes prohibitive. An alternative approach, based on the use of multiple transform techniques, leads to closed form solutions for the transformed components of stress and displacement at any location in the laminate surface. The response in the time domain at any specified location is then recovered by numerical inversion of the transform solutions. This paper reports the calculated surface displacements at a specified location, which result from internal line dislocation sources located either at the mid-plane or at one of the interfaces between the core and the outer layers. Earlier solutions relate to sources in the form of a line dislocation [2], line forces and double forces [3, 4], and line couples and double couples [5, 6]. Here these results are extended to include additional line dislocations and to compare the results with line double forces.

SOURCE CHARACTERISTICS

Acoustic emission sources are associated with discontinuities in traction components or in displacement components (dislocations) or both, acting across some finite area within the material. It is normally assumed that the area is sufficiently small compared with the dimensions of the structure that the source may be taken as acting at a point over an infinitesimal area. The parameters characterising the source consist of the location of this point, the direction \mathbf{n} of the normal to the area and the time histories of the discontinuity in each force component and in each displacement component. Discontinuities in force give rise to unequilibrated motions of the structure and must arise from some external cause. Their employment as internal sources, whilst not representing a physical internal event, serve to yield the Green's function solutions from which the response to more general discontinuities may be deduced. The Green's function solutions correspond to forces whose time histories are in the form of the Dirac delta function and the response to more general time histories may be recovered by convolution.

The nature of the response functions associated with different source events in an isotropic elastic medium has been examined in detail by Ohtsu and Ono [9, 10]. They

show that the crack opening dislocation can be modelled in terms of an orthogonal triad of double forces without moment (dipole forces), whilst a shear dislocation can be expressed in terms of a double couple without moment. By considering two equal and opposite forces of magnitude D/ϵ situated at a distance ϵ apart on their common line of action, and by proceeding to the limit as $\epsilon \rightarrow 0$ it is possible to determine the response to a discontinuity in the form of an equilibrated double force of magnitude D , such as can arise in the process of crack formation. Alternatively, taking two equal and opposite forces each of magnitude M/ϵ acting at a distance ϵ apart on the line normal to their directions, and proceeding to the limit as $\epsilon \rightarrow 0$ gives the solution due to a couple of magnitude M . This leads to an unequilibrated motion but the combination of two equal and opposite couples gives the double couple without moment which arises in association with a shearing dislocation. The transform method adopted here allows the response to both crack opening and shear dislocations, lying in any plane parallel to the plane of the laminate, to be evaluated directly.

RESULTS

The results presented here relate to line sources which act either in the mid-plane of the laminate or in one of the interfaces between the core and the outer layers and for which the line of action makes an angle γ with the fibre direction in the outer layers. These line sources generate straight crested waves travelling at an angle γ to the core fibres and the detailed calculations have been carried out for the two cases $\gamma = 30^\circ$ and $\gamma = 60^\circ$. Numerical results are based on a material for which the elastic constants have the values quoted above.

The graphs in Figs. 1 - 6 show the variation with time of the normal displacement at the upper surface of the laminate of overall depth $4h$, due to sources located at varying depths in the laminate. Each figure consists of three curves and in order to display these clearly the origins of two of the curves have been displaced downwards by different amounts. In each figure, the upper curve is the surface signal arising from a source at the upper interface (depth h below the surface), the middle curve shows the surface disturbance due to a source at the mid-plane (depth $2h$) and the bottom curve relates to a source at the lower interface (depth $3h$). In each case the time history of the source consists of a unit step function acting at $t = 0$. The graphs show the scaled normal displacement plotted against the non-dimensional time $T = c_1 t/h$, the time taken for the wave with speed c_1 to travel through the depth of one layer of the laminate.

Figs. 1 and 2 show the signals arriving at a point on the surface located a distance of $8h$ (two laminate depths) from the plane normal to the laminate through the line of action of a source corresponding to a crack dislocation. The line of action of the source in Fig. 1 is at angle $\gamma = 30^\circ$ and that in Fig. 2 is at $\gamma = 60^\circ$. The uppermost curve in Fig. 1 has a pronounced downward spike at a time $T = 15.6$, which is not evident in either of the other two curves nor in any of the curves in Fig. 2. This spike is associated with the arrival of the surface wave which is generated by the upper level disturbance at $\gamma = 30^\circ$ but not by the sources at the two lower levels. For the case $\gamma = 60^\circ$ the surface wave arrival time would be $T = 13.0$ and there is clearly no trace of this in Fig. 2, a result which is in accord with theoretical predictions. The other sharp peaks and troughs to be seen in these Figs. are associated with the arrivals of rays which have undergone multiple reflections at the various interfaces and the bottom free surface of the laminate.

It can be shown [10], that crack opening dislocation considered here is equivalent to the action of a combination of a double force in the direction normal to the plane of the laminate and a double force lying in the plane of the laminate with line of action in the direction of the propagating front. Results for these double forces acting at the top interface are presented in [4], from which it may be seen that the upper surface signal from the second of these double forces is substantially less than that from the first. In consequence, the signals shown here for the top curves in Figs. 1 and 2, are virtually identical with those for the double force acting normal to the plate, to within a scaling factor.

The signals displayed in Figs. 3 and 4 are for a shear dislocation source whose Burgers vector is in the direction of propagation of the straight crested wave, which in Fig. 3 makes an angle $\gamma = 30^\circ$ with the core fibre direction and in Fig. 4 is at angle $\gamma = 60^\circ$. Here, as in the previous two Figs., the receiver is located at a distance $8h$ along the surface from the plane normal to the plate through the line of action of the source. The downward spike associated with the arrival of the surface wave is again evident in the upper curve of Fig. 3, with no trace of a surface wave disturbance on the remaining two curves nor on any of the curves in Fig. 4. The signals emanating from this shear dislocation show fewer sharp peaks and troughs than are evident in the signals displayed in Figs. 1 and 2 and, with the exception of the surface wave disturbance, the motion is almost entirely of one sign in each curve.

The dislocation source for which the results are shown in Figs. 5 and 6, is a shear with Burgers vector parallel to its line of action, which is at orientation $\gamma = 30^\circ$ for Fig. 5 and at $\gamma = 60^\circ$ for Fig. 6. The receiver is located at the same position as for the previous Figs. The disturbance arising from this source is significantly less than is to be seen in the previous figures, there are very few sharp discontinuities and, in particular, there is no sharp peak associated with a surface wave to be seen in the top curve of Fig. 5.

All these results relate to a receiver placed at a distance $8h$ from the plane normal to the laminate through the line of action of the source. The transform method allows the response to be evaluated at any surface locations and plots have also been obtained showing the signals at distances $16h$ (four plate thicknesses) and $40h$ (ten plate thicknesses) from the plane of the source [11].

CONCLUSIONS

The results presented here are for waves propagating in perfectly elastic materials and arising from line sources in the form of a step function in time. In practice, most materials will exhibit some damping effects and real acoustic emission sources will be distributed over some finite area, with a finite rise time and having finite duration. These results are not therefore intended as predictions of the observed signals arising from acoustic emission but rather they serve to enhance the understanding of the effects of source characteristics, specimen geometry and of material parameters on the mode of propagation of the signal. Nevertheless, the technique adopted to derive these solutions can be readily modified to include material damping and to take account of differing time histories with little effect on the computational effort required. Similarly, extension of the results to sources acting over a strip rather than a line is also straightforward. It is the further extension to point sources and sources distributed over a finite area that

requires a significant increase in the computational effort. The technique for doing this has been developed by Lih and Mal [12], but to date the application of this technique has been limited to a few sources for which the spectra extend over a limited range of frequency.

ACKNOWLEDGEMENTS

This work was supported in part by the Engineering and Physical Sciences Research Council under research grant number GR/H90223.

REFERENCES

1. Suzuki, H., Takemoto, M. and Ono, K., "A Study of Fracture Dynamics in a Model Composite by Acoustic Emission Signal Processing", *J. of Acoustic Emission*, Vol 11, No 3, 1993, pp. 117-128.
2. Green, E. Rhian, "Green's Functions and their Reciprocal Relations in Layered Anisotropic Media", *Appl. Mech. Rev.*, Vol 137, 1995.
3. Green, E.R., "Acoustic Emission in a Fiber Composite Plate", *Review of Progress in Quantitative Nondestructive Evaluation*, Vol.14, Thompson, D.O. and Chimenti, D.E., Eds., Plenum Press, New York, 1995, pp. 1375-1382.
4. Green, E.R., "Acoustic Emission Sources in a Cross-ply Laminated Plate", *Composites Engineering*, Vol 5, No. 12, 1995, pp. 1453-1469.
5. Green, E.R., "Surface Response of a Cross-ply Fiber Composite Plate to Internal Acoustic Emission Line Sources", *Review of Progress in Quantitative Nondestructive Evaluation*, Vol.16, Thompson, D.O. and Chimenti, D.E., Eds., Plenum Press, New York, 1997, to appear.
6. Green, E.R., "Surface Response of Isotropic and Anisotropic Laminates to Acoustic Emission Sources", *Nondestructive Testing and Evaluation*, to appear.
7. Green, E.R., "Transient Impact Response of a Fibre Composite Laminate", *Acta Mechanica*, Vol 86, 1991, pp. 153-165.
8. Ceranoglu, A. N. and Pao, Y. H., "Propagation of Elastic Pulses and Acoustic Emission in a Plate", *ASME J. Appl. Mech.*, Vol 48, 1981, pp. 125-147.
9. Ohtsu, M. and Ono, K., "A Generalized Theory of Acoustic Emission and Green's Function in a Half Space", *J. Acoustic Emission*, Vol 3, No. 1, 1984, pp. 27-40 .
10. Ohtsu, M. and Ono, K., "The Generalized Theory and Source Representation of Acoustic Emission", *J. Acoustic Emission*, Vol 5, No. 4, 1986, pp. 124-133.
11. Green, E. R., "Dislocation Acoustic Emission sources in Cross-ply Laminates", *Leicester University Engineering Department Report No. 97-4*, , 1997.
12. Lih, S.-S. and Mal, A. K., "On the Accuracy of Approximate Plate Theories for Wave Field Calculations in Composite Laminates", *Wave Motion*, Vol 21, 1995, 17-34.

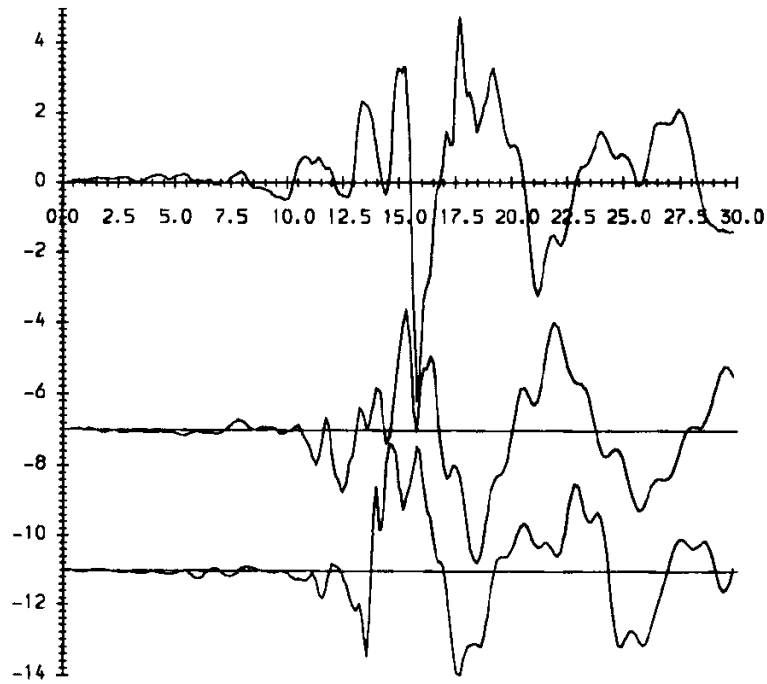


Fig. 1: Upper surface displacement at distance $8h$ from plane of source due to a crack opening dislocation at the upper interface (top curve); at the mid-plane (middle curve); and at the bottom interface (bottom curve). Line of action oriented at $\gamma = 30^\circ$.

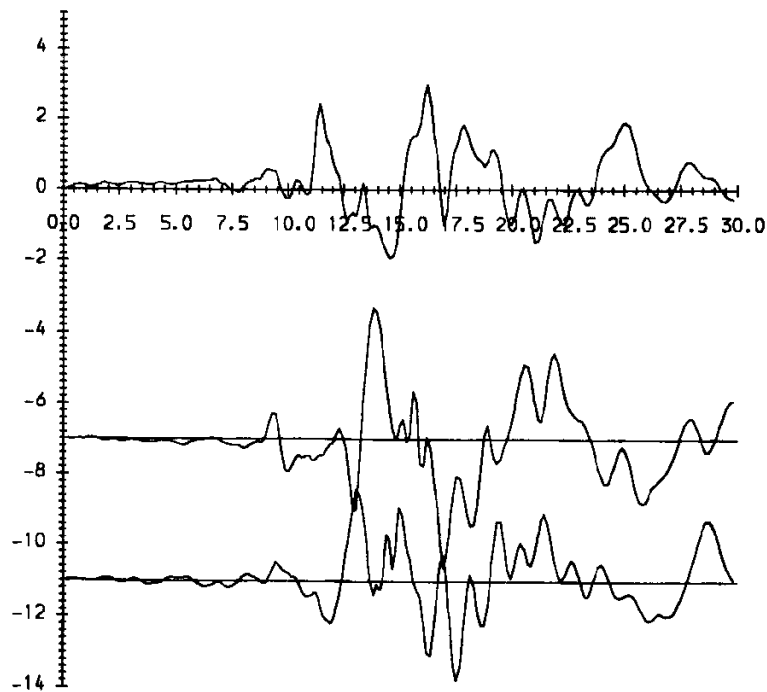


Fig. 2: Upper surface displacement at distance $8h$ from plane of source due to a crack opening dislocation at the upper interface (top curve); at the mid-plane (middle curve); and at the bottom interface (bottom curve). Line of action oriented at $\gamma = 60^\circ$.

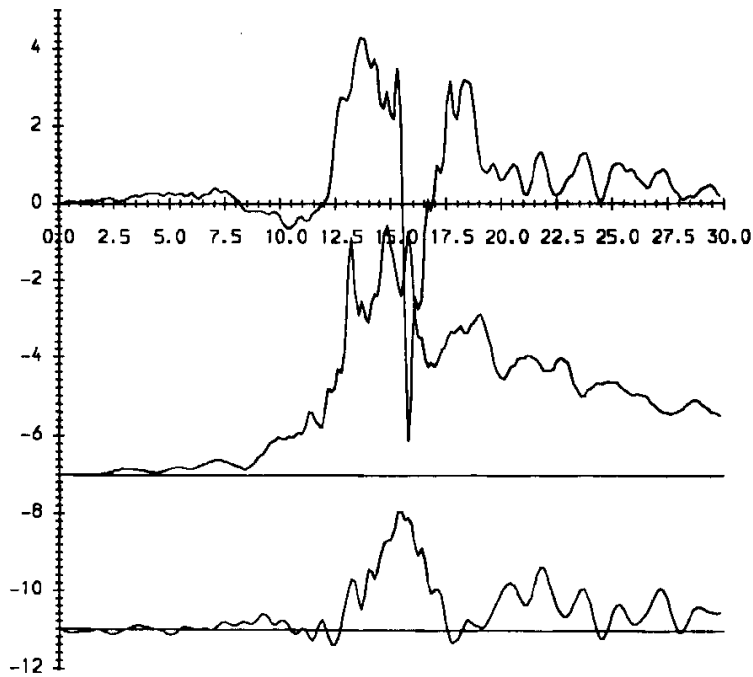


Fig. 3: Upper surface displacement at distance $8h$ from plane of source due to a shear dislocation in a plane parallel to the laminate and with Burger's vector normal to the line of action. Source acting at the upper interface (top curve); at the mid-plane (middle curve); and at the bottom interface (bottom curve). Line of action oriented at $\gamma = 30^\circ$.

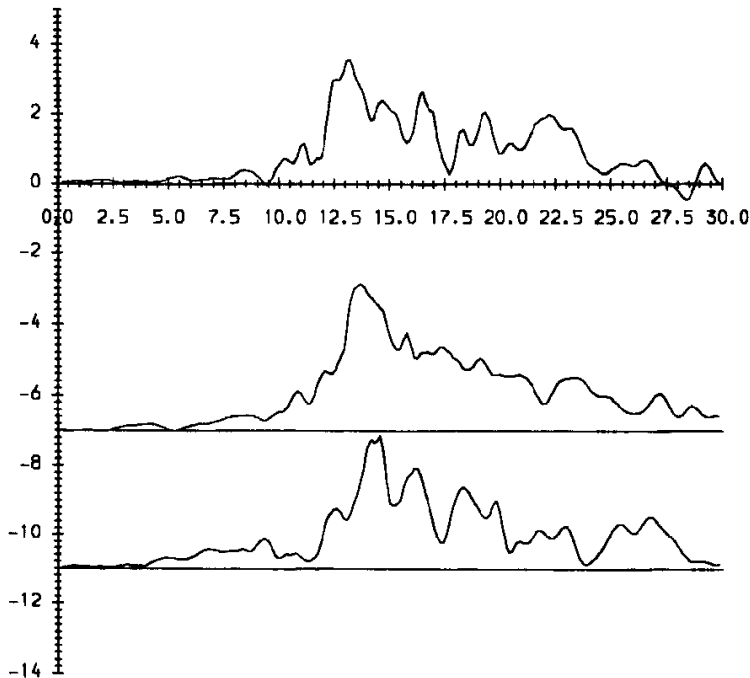


Fig. 4: Upper surface displacement at distance $8h$ from plane of source due to a shear dislocation in a plane parallel to the laminate and with Burger's vector normal to the line of action. Source acting at the upper interface (top curve); at the mid-plane (middle curve); and at the bottom interface (bottom curve). Line of action oriented at $\gamma = 60^\circ$.

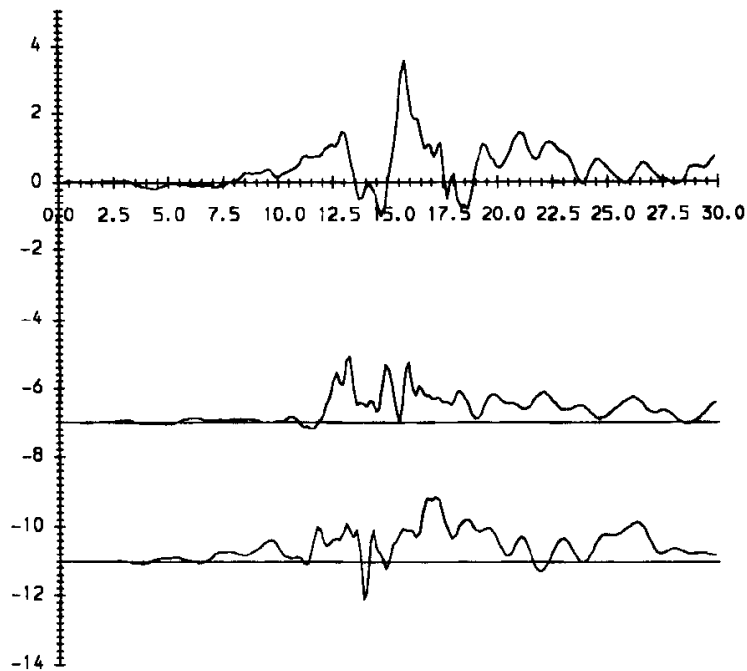


Fig. 5: Upper surface displacement at distance $8h$ from plane of source due to a shear dislocation in a plane parallel to the laminate and with Burger's vector parallel to the line of action. Source acting at the upper interface (top curve); at the mid-plane (middle curve); and at the bottom interface (bottom curve). Line of action oriented at $\gamma = 30^\circ$.

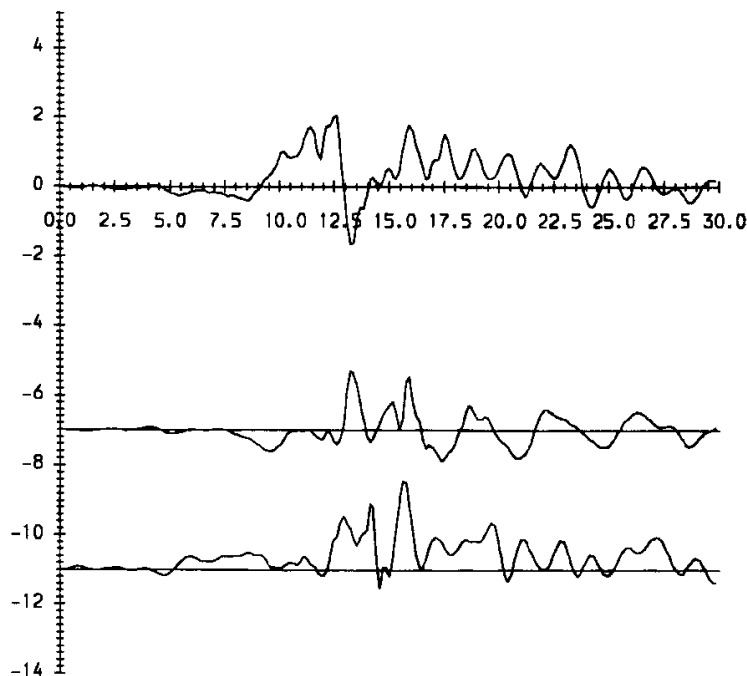


Fig. 6: Upper surface displacement at distance $8h$ from plane of source due to a shear dislocation in a plane parallel to the laminate and with Burger's vector parallel to the line of action. Source acting at the upper interface (top curve); at the mid-plane (middle curve); and at the bottom interface (bottom curve). Line of action oriented at $\gamma = 60^\circ$.

A NONDESTRUCTIVE APPROACH TO EVALUATING IMPACT DAMAGED COMPOSITE STRUCTURES

Hyonmy Kim, Keith T. Kedward

*Department of Mechanical and Environmental Engineering
University of California at Santa Barbara, Santa Barbara, California 93106, USA*

Summary: The challenge of assessing impact damage with regard to the global function of load bearing components represents a long standing issue for composite technologies. Four Point Bending stiffness tests are used to evaluate the effect of high velocity ice impact damage on the performance of minimum gauge structures. As the design of such structures is often driven by global buckling considerations, and since buckling is a stiffness dependent failure mode, knowledge of the reduction in bending stiffness due to impact damage and the ability to predict this reduction is of practical interest. A simple mechanics based methodology used for estimating reduction in bending stiffness is applied to predict critical buckling load for impact damaged plates. Results show a near 1:1 correlation between predicted reductions in bending stiffness and critical buckling load. This suggests that for initial assessments, four point bending tests may be performed instead of more complicated buckling tests.

KEYWORDS: post impact evaluation, nondestructive evaluation, damage tolerance, buckling prediction, composite structure design, strip methods

Introduction

In the evaluation of load bearing structures, one must consider strength as well as stiffness-influenced structural characteristics such as stability and vibration. Structures designed for minimum weight, thus often for minimum gauge thickness, are commonly found in the aerospace industry. When such structures are subjected to compressive loading, the stability of these structures must be assessed. Examples of such structures are stringer-stiffened fuselage airframes and fan cowls surrounding large modern gas turbine engines. Many of these thin gauge composite structures are situated such that they are susceptible to foreign object impact damage. While the design of a damage resistant structure is favorable for maintenance related and many other reasons (most all associated with costs), current certification methodology dictates the design of structures such that they tolerate an acceptable amount of impact damage while still meeting specific performance requirements (please note the difference between damage tolerant and damage resistant structures; Sjöblom [1]). In structures which are buckling critical design, the existence of impact damage can potentially result in a significant reduction in performance. Alternatively, the inclusion of

impact damage in a structure's design results in a structure of increased weight in order to satisfy damage tolerance requirements. The question of how much additional weight will the structure need to gain now arises. Thus the ability to predict the effect of impact damage on the performance of a structure is of significant interest.

Conventional two dimensional composite structures, while exhibiting potentially outstanding performance in the lamina plane, are vulnerable when subjected to modes of loading challenging the material in the out-of-plane direction. Foreign object impacts present a composite structure with an extremely complex loading state, especially in the case of high velocity impacts where dynamics need to be accounted for. Often impact damage creates what industry terms as Barely Visible Impact Damage (BVID). BVID comes in the form of intraply cracking, delaminations, and backside fiber failure.

The detection of BVID requires painstaking attention as it usually involves physical contact between a technician and the hardware. Due to the difficulty in detecting BVID, the designer must take into account the fact that the structure shall be expected to perform with BVID present. This account would be introduced at the design stage of the structure and shall ultimately be verified with a mechanical test of the entire structure. In order to assess whether a structure can functionally tolerate damage, simplified methods of analyses need to be available to the designer. These design methods, preferably based on fundamental mechanics, provide designers with a tool by which to scale specific structural parameters as well as take into account various damage zone sizes. This activity would be introduced at the design stage where decisions are much less costly than those made as one progresses towards the final completion of a product [2].

A method for predicting the reduction in bending stiffness and global buckling critical load has been developed. This method treats thin gauge plates with length to thickness ratios on the order of 100:1 and assumes global buckling as initial failure mode under in-plane compression. It is hypothesized that this mode of failure remains prevalent even for structures sustaining moderate forms of BVID, such as large delaminations.

While most aircraft structures contain some degree of curvature, the research presented here investigates flat plates. The treatment of flat plates is intended to serve as a foundation for which methods developed can be extended to curved shells. Several authors have performed meaningful investigations on the buckling of curved composite shells [3,4].

Impact Tests

High velocity impact tests have been performed on a series of flat 304.8 mm square composite plates [5]. The composite plates tested, summarized in Table 1, are AS4 fabric (5 and 8 harness satin weaves) with toughened 977 and 8552 resin systems. A progression of damage modes, illustrated in Figure 1, has been identified for each type of specimen with a clear distinction found between modes resulting in Visible Impact Damage (VID) and those resulting in BVID. All damage was produced by the high velocity impact of simulated hail ice spheres onto the targets which were held in a frame with rotationally (but not extensionally) fixed boundaries. The spheres constructed of multiple layers oriented in flat planes perpendicular to the direction of travel were 25.4 to 50.8 mm in diameter and were projected at speeds ranging from 30 to 200 m/sec. by a nitrogen gas cannon.

Of present interest are the BVID modes. Damage modes classified as Types I and II in Figure 1 are forms in which no target penetration occurred and BVID resulted. On pertinent panels, the delamination patterns have been mapped out by the ever-popular "quarter-tap" method as well as by hand held ultrasonic inspection methods.

Table 1. Carbon Fabric/Epoxy Composite Panel Test Matrix

Series ID	Material	Layup	Thk. (mm)	Qty.
ICE-01	AS4/977 5HS	[0/45/90] _s	1.42	3
ICE-02	AS4/977 5HS	[0/45/90/-45] _s	1.91	3
ICE-03	AS4/977 5HS	[0/45/90/-45/0/45] _s	2.62	2
ICE-04	AS4/8552 8HS	[0/45] _s	1.22	16
ICE-05	AS4/8552 8HS	[0/45/90] _s	1.83	6
ICE-06	AS4/8552 8HS	[0/45/90/-45] _s	2.44	6

Total: 36

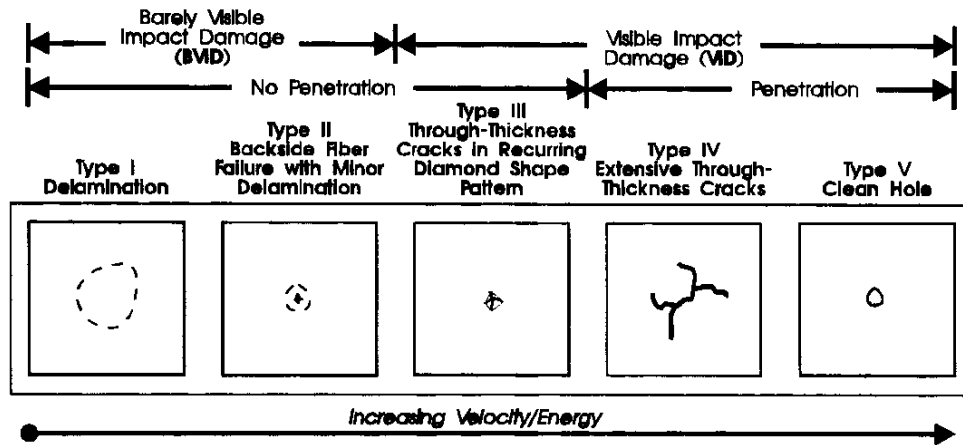


Figure 1. Failure Mode Progression Observed in Ice Impact Testing

Four Point Bending Tests

Four Point Bending (FPB) tests have been used to evaluate the effect of impact damage on thin gauge composite structures. The decision for using this test instead of the more popular Compression After Impact (CAI) test was made based on the nature of the structures being considered. As discussed, the global buckling of thin gauge structures is directly dependent on the plate bending stiffness. Thus, knowledge of the reduction in bending stiffness due to impact damage and the ability to predict this reduction is of significant interest when designing buckling critical structures.

The FPB geometry was selected due to one's ability to apply a field of constant moment and zero interlaminar shear force across a zone of damage on a composite panel. Many researchers have investigated the use of bending tests to evaluate the strength of composites. However, as pointed out by Wisnom [6] and Grédiac [7], there exists many inherent limitations when flexure tests are used to assess strength. Adler and Mihora [8] have used a related bending test (concentric ring-on-ring producing constant radial moment) to evaluate the effects of impact damage on circular ceramic plates.

A FPB test fixture for measuring stiffness has been configured such that load and support points do not interfere with zones of damage. For the 304.8 mm square panels, a support-span of $L = 279.4$ mm and a load-span to support-span ratio of 9:11 ($b = 25.4$ mm in Figure 3) was used. Polished stainless steel cylindrical bars were used for the support and loading noses. All ice impact test panels listed in Table 1 have been tested with this four point test fixture and the reduction in bending stiffness, albeit under this specific geometry, have

been measured. These measurements for the panels containing delamination damage shall be discussed further below and are presented in Table 2.

Predictive Methodology

A simple mechanics based method has been developed which accurately predicts the reduced bending stiffness for the delamination damaged panels under investigation. Detailed in Figure 2, this analysis consists of considering a delaminated plate which is theoretically decomposed into several strips. Pertinent strips contain sections along their length having different bending properties. An example of modeling a plate using eight strips to define a delamination zone is also shown in the figure. The stiffness under the applied FPB loading is determined for each strip separately using simple beam bending theory. As shown in Figure 2, strips which account for damage are modeled in three discrete sections, with the central section having a different plate bending stiffness D_2 (isotropic plate bending stiffness $D = \frac{Et^3}{12(1-\nu^2)}$) than the undamaged sections D_1 (with $D_2 < D_1$).

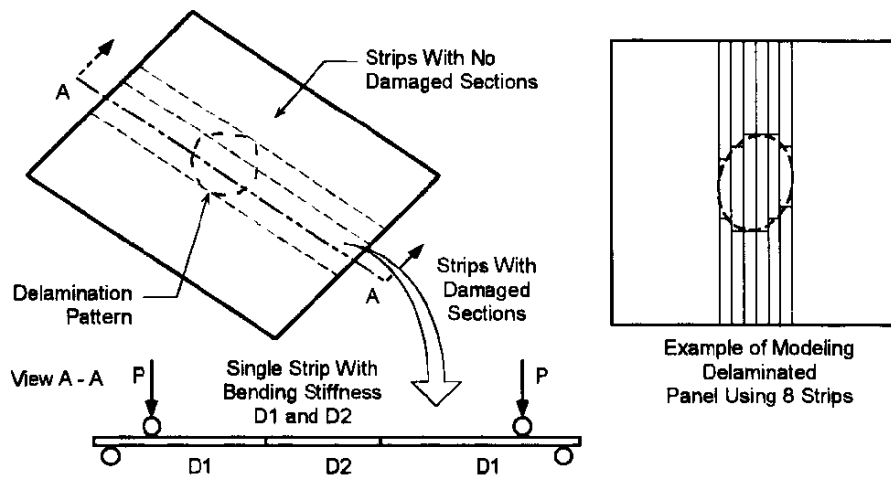


Figure 2. Strip Based Approach to Modeling Delaminated Panel

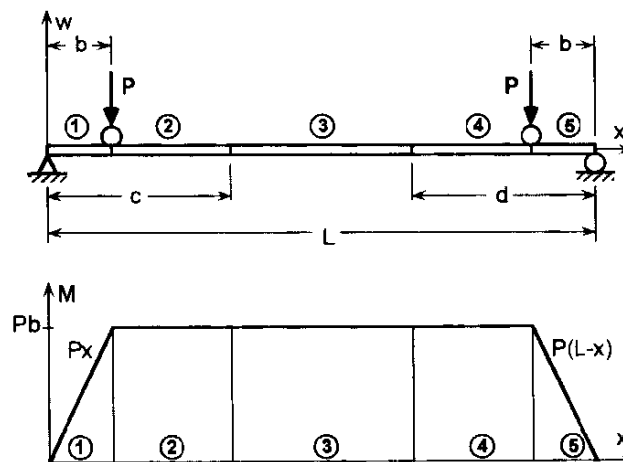


Figure 3. Simple Beam Model and Moment Diagram

The beam bending model of these multisectioned strips is detailed in Figure 3. For a general plate strip, we assume one-dimensional beam bending behavior:

$$\frac{d^2 w_i}{dx^2} = \frac{M_i}{D_i} \quad i=1, 2, \dots, 5 \quad (1-5)$$

Where i ranges from 1 to 5 to account for each beam section as shown in Figure 3. w_i are the transverse displacement functions with corresponding plate bending stiffness constants D_i for each section of the plate strip. In general, $D_1 = D_2 = D_4 = D_5$ and $D_3 < D_1$. In modeling the delaminated region, the assumption is made that a single delamination exists at the geometric midplane, yielding $D_3 = D_1/4$ (treat as split beam). As the beam is a one-dimensional problem, D_{11} from the Classical Lamination Plate Theory "D" matrix is used for values of D_i . The moments, as shown in Figure 3 are:

$$M_1 = Px \quad M_2 = M_3 = M_4 = Pb \quad M_5 = P(L-x) \quad (6)$$

Integration of Eqns 1 to 5 yield 10 unknown constants which are solved for by application of boundary and continuity conditions:

$$\text{Boundary Conditions:} \quad w_1(0) = w_5(L) = 0 \quad (7)$$

$$\begin{aligned} \text{Continuity:} \quad w_1(b) = w_2(b) \quad & \frac{dw_1(b)}{dx} = \frac{dw_2(b)}{dx} \\ w_2(c) = w_3(c) \quad & \frac{dw_2(c)}{dx} = \frac{dw_3(c)}{dx} \\ w_3(L-d) = w_4(L-d) \quad & \frac{dw_3(L-d)}{dx} = \frac{dw_4(L-d)}{dx} \\ w_4(L-b) = w_5(L-b) \quad & \frac{dw_4(L-b)}{dx} = \frac{dw_5(L-b)}{dx} \end{aligned} \quad (8-15)$$

The stiffness of a plate strip under this FPB configuration is defined as the total load $2P$ over the displacement at the loading points (note that $w_1(b) = w_2(b) = w_4(L-b) = w_5(L-b)$):

$$K = \frac{2P}{w_1(b)} \quad (16)$$

Finally, the total panel stiffness is simply the summation of all the individual strip stiffness contributions. While this analysis is specific to the four point bending test geometry, the methodology used in the analysis can be readily incorporated into buckling calculations due to its simplicity and mechanics based foundation.

Results

As shown in Table 2, the predictions of reduced bending stiffness (Predicted K) match fairly well with actual test measurements of bending stiffness (Measured K). The largest difference between Measured and Predicted K of 12% is found for specimen ICE-02B. Sources of error in predicting K lie in the mapping of the delamination zone and the assumptions made on the zone's reduced bending stiffness value. However, considering these sources of error, in addition to the great simplifications made by the predictive methodology used, the results are surprisingly accurate. Predictions on the order of 10% are considered quite adequate for most design purposes.

Table 2. Comparison of Predicted to Measured Bending Stiffness for Delaminated Panels

Panel ID	Layup	Material	Thickness	Undamaged K	Measured K	Predicted K
ICE-01C	[0/45/90] _s	AS4/977 5HS	1.42 mm	117.0 KN/m	104.4 KN/m	106.3 KN/m
ICE-02B	[0/45/90/-45] _s	AS4/977 5HS	1.91	273.2	219.6	245.5
ICE-02C	[0/45/90/-45] _s	AS4/977 5HS	1.91	273.0	232.9	245.9
ICE-04E	[0/45] _s	AS4/8552 8HS	1.22	79.0	67.8	73.9
ICE-05A	[0/45/90] _s	AS4/8552 8HS	1.83	251.0	213.1	220.5
ICE-06D	[0/45/90/-45] _s	AS4/8552 8HS	2.44	579.0	502.9	484.7
ICE-06F	[0/45/90/-45] _s	AS4/8552 8HS	2.44	579.0	547.9	535.7

Application: Buckling Prediction

Having first been validated for an analytically simple form of loading, that is four point bending, the predictive methodology previously developed is now applied towards predicting the reduction in buckling critical load for impact damaged composite structures.

For a structure composed of thin skins stiffened by stringers, individual bays (plate region between stringers) can potentially undergo local buckling relative to the whole structure. As shown in Figure 4, a flat plate with simply supported boundaries is customarily used to model a single bay [9] when predicting the local buckling critical load.

As a gross simplification, the plates listed in Table 1 are treated as isotropic plates with “D” matrix (from Classical Lamination Plate Theory) terms $D_{11} = D_{22}$ and $D_{16}, D_{26} \ll D_{11}$. This assumption is good for the eight ply Quasi-Isotropic fabric specimens tested (ICE-02 and ICE-06 panels listed in Tables 1 and 2). Following Szilard [9], the critical buckling load for an isotropic square plate under uniaxial compressive loading is:

$$N_{cr} = \lambda N_{x0} = 4N_{x0} \quad (17)$$

Where $N_{x0} = \frac{\pi^2 D}{a^2}$ is the Euler buckling load for a single simply supported plate strip. a is the square plate size dimension, and D is the plate bending stiffness. λ is the buckling load factor which equals 4 for the case of predicting critical buckling load for an undamaged square plate. For simply supported square plates which contain impact damage, λ shall be less than 4.

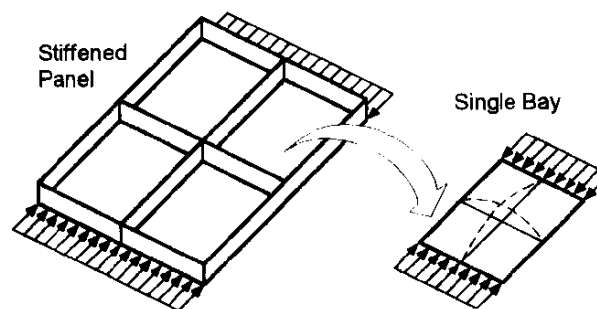


Figure 4. Single Bay Modeled From Stiffened Panel

A generic model of a plate with a rectangular zone of reduced bending stiffness is shown in Figure 5. The square zone of size a^* encompasses a region of damage such as the delamination shown here. For simplicity, the damage region is modeled with only a single rectangle. Further decomposition of the damage region into more strips is certainly possible, as well as implementable in the analytical methodology presented, for more accurate predictions.

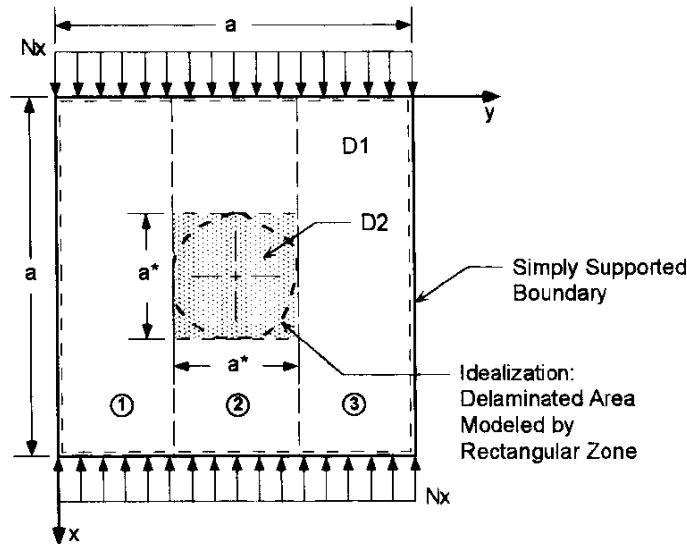


Figure 5. Model for Buckling Predictions

The model in Figure 5 is used to generate a simplified mechanics based prediction of the reduction in buckling load factor λ for impact delaminated structures. Two mechanics based models were developed. Both employ Rayleigh-Ritz's energy method for analysis which uses the total potential energy of a plate in the buckled state:

$$\Pi = \frac{1}{2} \iint_A D(x,y) \left\{ \left(\frac{\partial^2 w}{\partial x^2} \right)^2 + \left(\frac{\partial^2 w}{\partial y^2} \right)^2 - 2(1-\nu) \left[\frac{\partial^2 w}{\partial x^2} \frac{\partial^2 w}{\partial y^2} - \left(\frac{\partial^2 w}{\partial x \partial y} \right)^2 \right] \right\} dx dy - \frac{\lambda}{2} \iint_A N_{x0} \left(\frac{\partial w}{\partial x} \right)^2 dx dy \quad (18)$$

Note that the plate bending stiffness is a function of x and y . An assumed function for displacement:

$$w(x,y) = \sum_m \sum_n W_{mn} \sin \frac{m\pi x}{a} \sin \frac{n\pi y}{a} \quad (19)$$

is often used for a plate with simply supported boundaries. In the analyses, the simplest case of $m = 1, n = 1$ is used to model the first mode of plate buckling deformation. This simplifies Eqn 19 to:

$$w(x,y) = C \sin \frac{\pi x}{a} \sin \frac{\pi y}{a} \quad (20)$$

To determine the critical buckling load factor λ , Eqn 20 is substituted into Eqn 18, and the energy is minimized with respect to the single constant C .

Method 1. Rayleigh-Ritz Plate. Here Eqns 18 and 20 are directly applied to the model illustrated in Figure 5. The integrations are carried out piecewise over the domain:

$$\text{Let } U_i = D_i \left\{ \left(\frac{\partial^2 w}{\partial x^2} \right)^2 + \left(\frac{\partial^2 w}{\partial y^2} \right)^2 - 2(1-\nu) \left[\frac{\partial^2 w}{\partial x^2} \frac{\partial^2 w}{\partial y^2} - \left(\frac{\partial^2 w}{\partial x \partial y} \right)^2 \right] \right\}, \quad i=1,2 \quad (21)$$

$$\Pi = \frac{1}{2} \int_0^{\frac{1}{2}(a-a^*)} \int_0^a U_1 dx dy + \frac{1}{2} \int_{\frac{1}{2}(a-a^*)}^a \left(\int_0^{\frac{1}{2}(a-a^*)} U_1 dx + \int_{\frac{1}{2}(a-a^*)}^a U_2 dx + \int_{\frac{1}{2}(a+a^*)}^a U_1 dx \right) dy + \frac{1}{2} \int_{\frac{1}{2}(a+a^*)}^a \int_0^a U_1 dx dy - \frac{\lambda}{2} \iint_A N_{x0} \left(\frac{\partial w}{\partial x} \right)^2 dx dy \quad (22)$$

Eqn 20 is substituted into Eqn 22 and upon minimizing the energy with respect to the constant C , the critical buckling load factor can be determined.

Method 2. Rayleigh-Ritz Strip. Figure 5 shows the plate to be divided into three separate strips, two of which contain no damage. An Euler column buckling analysis is performed on each strip using the model illustrated in Figure 6; D_1 and D_2 are the plate bending stiffness. For each strip, the critical buckling load is determined. The undamaged strips (1) and (3) have $D_1 = D_3 = D$, thus $N_{x0,eff}^{(1,3)} = \frac{\pi^2 D}{a^2} = N_{x0}$. For strip (2), $D_2 = D_1/4$ (as before in the FPB analyses) and $N_{x0,eff}^{(2)}$ (which is $< N_{x0}$) is determined by employing the Rayleigh-Ritz method simplified for the one-dimensional strip problem of Figure 6.

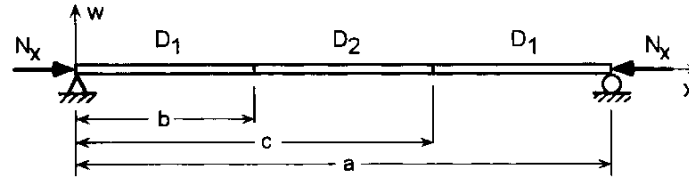


Figure 6. Rayleigh-Ritz Strip Model

Recalling Eqn 17, an assumption is made that the entire plate shall deform in the same manner as an undamaged simply supported plate. Furthermore, the reduction in total plate critical load shall be accounted for by modifying the strip critical load N_{x0} . The calculation of λ is as follows:

$$N_{cr} = \lambda_{tot} N_{x0} = 4 N_{x0, eff} \tag{23}$$

$$\text{where } N_{x0, eff} = \frac{N_{x0, eff}^{(2)} a^* + N_{x0, eff}^{(1,3)} (a - a^*)}{a} \tag{24}$$

$$\text{thus } \lambda_{tot} = 4 \frac{N_{x0, eff}}{N_{x0}} \tag{25}$$

Note that $N_{x0,eff}$ is determined by a simple “rule of mixtures” summation of the individual plate-strip Euler column buckling critical loads, scaled by the individual ratios of strip width to total width.

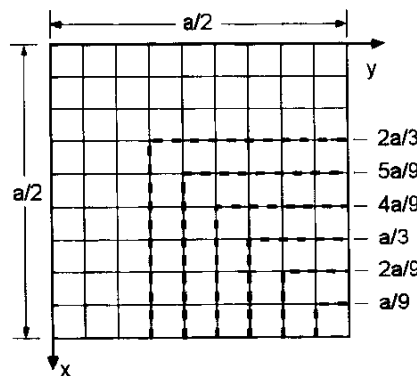


Figure 7. Finite Element Quarter Model

For validation of these predictive methods, a finite element model was created of a quarter plate with varying sized rectangular damage zones. Actual buckling tests of select panels are to be performed for more definite validation. The mesh and geometry of the finite element model is shown in Figure 7. Four node quadrilateral elements were used in the *ABAQUS* code to obtain eigenvalue buckling estimates.

The critical buckling load for damage zones of size $a^* = a/9$ to $2a/3$ were computed and comparisons made with the two analytical models. Figure 8 is a plot of the buckling load

factor reduction predictions made by the Rayleigh-Ritz Plate, Rayleigh-Ritz Strip, and the finite element models. The reduced load factor λ^* is reported relative to the undamaged load factor ($\lambda = 4$) as a function of the damage size ratio, a^*/a (see Figure 5). Surprisingly, the more simplistic Strip method predictions match more closely to the finite element. The Plate method predicts load factors which are consistently lower than the finite element and Strip methods.

Along side the buckling load factor reduction in Figure 8 are plotted the data points (reported in Table 2) for the predicted and measured reduced four point bending stiffness K^*/K . In addition to the reduced bending stiffness of actual damaged panels, predictions were made for panels with hypothetical square shaped damage zones identical in geometry to the buckling model in Figure 5. The analytical Strip method was used as well as finite element modeling to study the reduction in bending stiffness. The finite element model also serves as a comparison benchmark for the simplified methods used in predicting reduced bending stiffness. These results are plotted in Figure 8 as "FPB Hypothetical Strip" and "FPB Hypothetical FEM." The Strip method predictions were in general lower than the finite element (by max. 4%). It is of interest to note the near 1:1 correlation between the predicted reduction in FPB stiffness and the predicted reduction in buckling load factor. Another point of interest is the identical reduction ratios predicted by the FPB finite element and the buckling Rayleigh-Ritz Strip method. The same reductions are predicted for entirely different cases of loading configuration as well as analytical formulation.

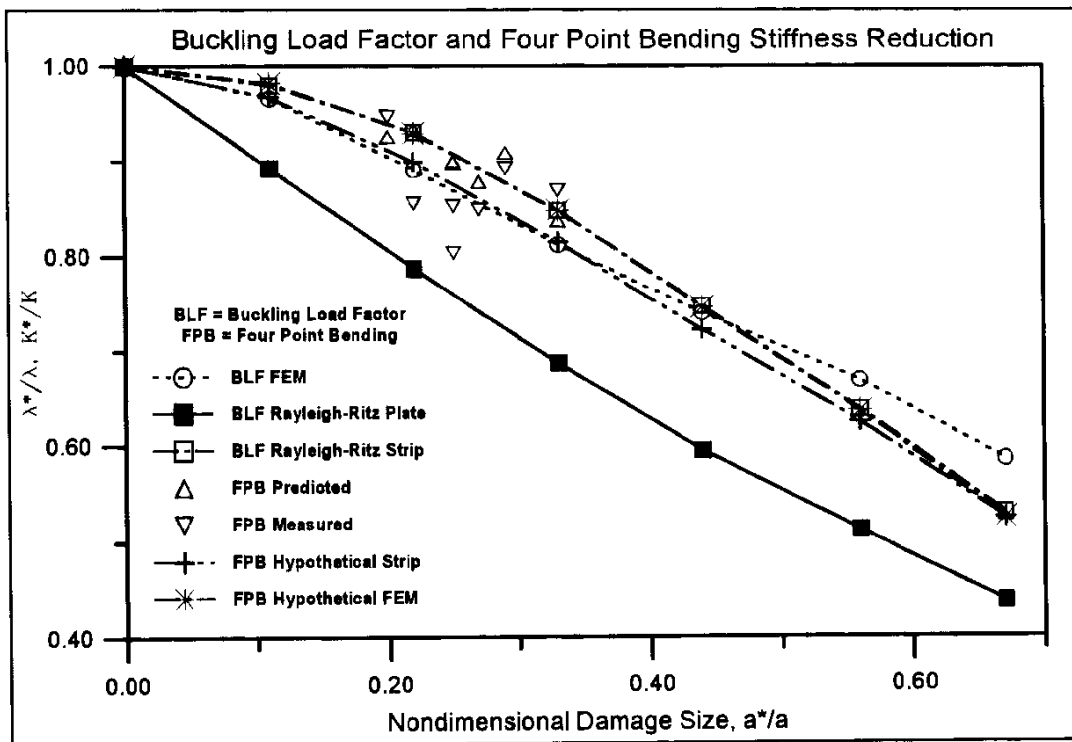


Figure 8. Comparison of Results for Buckling and Four Point Bending Reduction

Conclusions

A mechanics based predictive methodology has been developed to assess the effect of impact damage on composite structures. The method, although quite simplistic, accurately

predicted the reduction of four point bending stiffness for flat plates containing impact induced delamination damage. Applying the methodology to analytical buckling predictions, the method is found to predict the reduction in buckling critical load fairly well. Comparison of reduced buckling load and reduced bending stiffness, plotted versus damage size, shows a near 1:1 correlation between the two quantities. Reasons for the comparable trends are: the direct dependence of both the four point bending stiffness and the buckling critical load factor on the plate bending stiffness D , and the application of a bending moment field across the span of the plate; although moment varies along the length for the buckling problem. Additionally, functions used in describing the deformation shapes for first mode buckling and four point bending are identical.

While further investigation needs to be conducted into a broader set of buckling critical structures to investigate the range of applicability for the methodology developed herein, the results presented suggest that the use of four point bending tests are a simple means by which one can assess the reduction in buckling critical load for impact damaged composite plates. The methodology developed to predict the effects of impact damage on structural performance is applicable to many structures due to its mechanics based origins, thus facilitating the design of structures to be tolerant to known levels of impact damage.

Acknowledgments

The authors would like to acknowledge Douglas Welch, Gary Griesheim, Craig Musson, Chris Kogstrom, and Jeff Hill of United Technologies Pratt & Whitney for their assistance in the impact testing and their guidance towards maintaining the practical orientation of this research work.

References

1. Sjöblom, Peter. "Simple Design Approach Against Low Velocity Impact Damage," *International SAMPE Symposium and Exhibition*. Vol. 32. April 6-9, 1987.
2. Presentation by Philip Barkan, Professor of Mechanical Engineering, Stanford University.
3. Wilkins, D.J. "Compression Buckling Tests of Laminated Graphite-Epoxy Curved Panels," *AIAA Journal*, Vol. 13, No. 4, April 1975. pp. 465-470.
4. Chen, V.L., Wu X.X. and Sun C.T. "Prediction of Buckling Loads of Stiffened Composite Panels," Proceedings of ASME Winter Annual. Dallas, TX. Nov. 1990.
5. Kim, H., Welch, D.A. "Investigation of Hail Ice Impact on Composite Structures," *Pratt & Whitney Internal Report*. EII No. 95-200-0035-B. 1995.
6. Wisnom, Michael R. "Limitations of Linear Elastic Bending Theory Applied to Four Point Bending of Unidirectional Carbon Fibre-Epoxy," *AIAA-90-0960-CP*, 1990.
7. Grédiac, Michel. "Four-Point Bending Tests on Off-Axis Composites," *Composite Structures*, Vol. 24, 1993. pp. 89-98.
8. Adler, William F. and Mihora, Dennis J. "Biaxial Flexure Testing: Analysis and Experimental Results," *Fracture Mechanics of Composites*, Vol. 10. New York 1992. pp. 227-245.
9. Szilard, R. *Theory and Analysis of Plates, Classical and Numerical Methods*. Prentice-Hall, New Jersey, 1974.
10. ASTM Standards. "Standard Test Methods for Flexural Properties of Unreinforced and Reinforced Plastics and Electrical Insulating Materials," ASTM D790-92.

ACOUSTO-ULTRASONIC CHARACTERISTICS FOR CONTACT-TYPE TRANSDUCERS COUPLED TO A COMPOSITE BEAM

S. Kitipornchai¹, T. Liu², and K. M. Liew³

¹ *Department of Civil Engineering, The University of Queensland, Brisbane, Qld. 4072, Australia*

² *Department of Aircraft Engineering, Nanjing University of Aeronautics and Astronautics Nanjing, 210016, P. R. China*

³ *School of Mechanical and Production Engineering, Nanyang Technological University, Singapore*

SUMMARY: Acousto-ultrasonic technique is finding an increased usage among the nondestructive evaluation of composite materials. In this paper the acousto-ultrasonic characteristics for transmitting and receiving contact-type transducers coupled to a composite beam are considered. Through introducing some simplifying assumptions for the transducers, an analytical method which can deal with all wave processes involved with the system, i.e. wave generation, wave propagation and wave reception, is developed. Using this method, the spectral response of the normal contact stress sensed by the receiving transducer, due to an arbitrary input pulse excited by the transmitting transducer, is expressed in the form of explicit physical interpretations. The time history of the contact stress output for the receiver is obtained by using the Fast Fourier Transform (FFT) technique. Finally, from some numerical results the acousto-ultrasonic characteristics are discussed.

KEYWORDS: acousto-ultrasonic technique analysis, contact-type transducers, composite material evaluation, elastic wave propagation

INTRODUCTION

With the increasing use of advanced composites in many engineering structures, it is of growing importance to employ reliable and effective nondestructive evaluation (NDE) methods to determine the quality and mechanical serviceability of these materials. In recent years, an analytical ultrasonic NDE technique or stress wave factor (SWF) technique presented by Vary [1] has been receiving considerable attention. It has been found that this technique is especially useful for providing a measurable quantitative parameter which correlates well with mechanical properties of various composite materials such as stiffness, strength and fatigue life.

For the purposes of understanding this technique, the dispersion of the ultrasonic wave propagation in composite materials has been considered by many researchers; for instance Duke, Henneke et al.[2], Datta et al.[3], and Kim et al.[4]. Also, the quantitative features of the elastic wave field generated in composite laminates by surface pulses have been studied by Mal and Lih [5,6], Ditri and Rose [7] and etc. Furthermore, the problems of dynamic response of a transducer to waves, and wave propagation in a cracked composite plate have been recently investigated by the authors and other investigators [8,9]. It can be seen that

previous investigations relevant to the AU technique are all only concerned with one stage of the AU technique, since as is known, the AU technique consists of three basic physical stages: wave generation, wave propagation and wave reception. It is evident that in order to completely examine the AU results and hence study the stress wave factor the synthetical analysis of the three stages of the AU technique is further required.

Owing to the complexities involved, in the previous investigations, however, there seems to be only the work of Williams et al.[10] concerning this problem. The ultrasonic input-output model for transmitting and receiving transducers coupled to an isotropic elastic plate was investigated by tracing the multiple reflections of waves in the plate excited by a single tone burst input. Since it is based on the asymptotic solution for an isotropic half-space subjected to harmonic normal surface pulses, this model has many limitations, especially the difficulty in extending to the case of composite structures.

In this paper an analytical method for the investigation of the ultrasonic input-output characteristics of transmitting and receiving contact-type transducers coupled to a composite beam is developed. With the aid of some simplifying assumptions on transducers the governing equations for the AU system involved with wave emission, wave propagation and wave reception, are first established. Using a multiple integral transform method and contour integral technique, the spectral response of the normal contact stress between the receiving and the waveguide, due to an arbitrary input pulse excited by the transmitting transducer, is expressed in a form of explicit physical interpretations. The time histories of the response are then obtained through the inversion of the spectra by using the Fast Fourier Transform (FFT) method. Finally, some numerical results are presented to show the acousto-ultrasonic characteristics for transmitting and receiving contact-type transducers coupled to a composite beam.

MATHEMATICAL FORMULATION OF THE PROBLEM

The problem considered is depicted in Fig. 1. A transmitting and a receiving transducers are coupled to a beam reinforced with unidirectional fibers, and spaced apart by a distance x_0 . The input pulse in the form of a normal contact stress is first injected on the surface of the beam through the transmitting transducer to excited ultrasonic waves. As the first wave front arrives at the receiver, the output will be sensed in a form of normal contact stress. Here the electron-mechanic and the mechanic-electron transfer segments are not further considered.

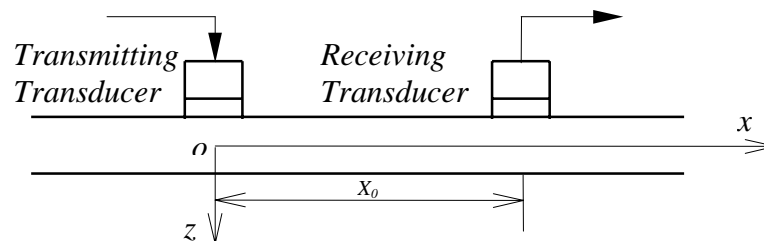


Fig. 1: Schematic of acousto-ultrasonic configuration

This does not affect the investigation in this paper, since the further consideration of these two segments only needs to introduce two transduction ratios [10].

Using the Timoshenko beam theory, the equations governing the motion of the beam considered can be shown as follows

$$G_{LT} Ak \left(\frac{\partial \varphi}{\partial x} - \frac{\partial^2 w}{\partial x^2} \right) + \rho A \frac{\partial^2 w}{\partial t^2} = q(x, t) \quad (1)$$

$$G_{LT} Ak \left(\frac{\partial w}{\partial x} - \varphi \right) + E_L I \frac{\partial^2 w}{\partial x^2} = \rho I \frac{\partial^2 \varphi}{\partial t^2} \quad (2)$$

where t is the time variable, x the space variable referring to the coordinate system with the x -axis parallel to the fibers as shown in Fig. 1, E_L, G_{LT} are the Young's moduli and the shear moduli, respectively, and the subscripts L and T denote the directions parallel and normal to the fibers, respectively, ρ, A, I are the mass density, cross sectional area and the cross sectional area inertia moment of the beam, respectively, and k is the shear coefficient with a fixed value of 0.833 for the case of rectangular cross-section under consideration. Here $w(x, t)$ denotes the transverse displacement of the beam, $\varphi(x, t)$ the slope of the cross section, and $q(x, t)$ the distributed force exerted on the surface of the beam by the transmitting and the receiving transducers.

To simplify the analysis of the problem it is assumed that: (1) the pressure distribution of the transducers is in a parabolic form⁷; (2) the contact area between the contact-type receiver and the beam is so small that the displacement of the receiver can be taken as that of the beam at the center of the contact area.

From the first assumption the term $q(x, t)$ in Eq. (1) can be expressed as

$$q(x, t) = [H(x + a_1) - H(x - a_1)] \left(1 - \frac{x^2}{a_1^2} \right) f(t) + [H(x - x_0 + a_2) - H(x - x_0 - a_2)] \left(1 - \frac{(x - x_0)^2}{a_2^2} \right) \sigma(t) \quad (3)$$

in which a_1 and a_2 are apertures of the transmitting and receiving transducers, respectively, $H(x)$ stands for the Heaviside function, $f(t)$ is the normal stress exerted on the beam by the transmitting transducer, and $\sigma(t)$ the normal stress sensed by the receiving transducer, which is the unknown function to be determined

Considering the motion of the receiving transducer and noting the second assumption above gives

$$M \frac{d^2 w(x, t)}{dt^2} = -a_2 \sigma(t) \quad (4)$$

in which M denotes the mass of the receiving transducer.

Applying Fourier time transform and spatial transform defined as

$$\bar{g}(x, \omega) = \int_0^{\infty} g(x, t) e^{-i\omega t} dt \quad (5)$$

$$\tilde{g}(\kappa, t) = \int_{-\infty}^{+\infty} g(x, t) e^{-i\kappa x} dx \quad (6)$$

to Eqs. (1-2) on t and x , respectively, and solving the resulting equations, the transformed solutions for $\tilde{w}(\kappa, \omega)$ and $\tilde{\varphi}(\kappa, \omega)$ are obtained as follows

$$\tilde{w}(\kappa, \omega) = (E_L I \kappa^2 + G_{LT} Ak - \rho I \omega^2) \tilde{q} / \Delta \quad (7)$$

$$\tilde{\varphi}(\kappa, \omega) = -i\kappa G_{LT} Ak \tilde{q} / \Delta \quad (8)$$

with

$$\Delta = \rho G_{LT} A^2 k \left[\frac{E_L I}{\rho A} \kappa^4 - \frac{I}{A} \left(1 + \frac{E_L}{G_{LT} k} \right) \kappa^2 \omega^2 - \omega^2 + \frac{\rho I}{G_{LT} A k} \omega^4 \right] \quad (9)$$

The spatial Fourier inverse transform corresponding to Eq. (6)

$$g(x, t) = \frac{1}{2\pi} \int_{-\infty}^{+\infty} \tilde{g}(\kappa, t) e^{i\kappa x} d\kappa \quad (10)$$

is applied to Eq. (7) to obtain

$$\begin{aligned} \bar{w}(x, \omega) = & \frac{\bar{f}(\omega)}{2\pi} \int_{-a_1}^{a_1} \int_{-\infty}^{+\infty} \left(1 - \frac{s^2}{a_1^2} \right) (E_L I \kappa^2 + G_{LT} A k - \rho I \omega^2) e^{i\kappa(x-s)} / \Delta ds d\kappa \\ & + \frac{\bar{\sigma}(\omega)}{2\pi} \int_{-a_2}^{a_2} \int_{-\infty}^{+\infty} \left(1 - \frac{\tau^2}{a_2^2} \right) (E_L I \kappa^2 + G_{LT} A k - \rho I \omega^2) e^{-i\kappa(\tau+x_0-x)} / \Delta d\tau d\kappa \end{aligned} \quad (11)$$

Additionally, applying the Fourier time transform Eq. (5) to the Eq. (4), we obtain

$$\bar{w}(x_0, \omega) = \frac{a_2 \bar{\sigma}(\omega)}{M \omega^2} \quad (12)$$

Setting $x = x_0$ in Eq. (11) and then comparing the resulting equation with Eq. (12), the unknown $\bar{\sigma}(\omega)$ can be finally expressed as follows

$$\bar{\sigma}(\omega) = \frac{M \omega^2 I_2 \bar{f}(\omega)}{2\pi a_2 - M \omega^2 I_1} \quad (13)$$

in which

$$I_1 = 2 \int_0^{a_2} \left(1 - \frac{\tau^2}{a_2^2} \right) I_1^* d\tau \quad (14)$$

$$I_2 = \int_{-a_1}^{a_1} \left(1 - \frac{s^2}{a_1^2} \right) I_2^* ds \quad (15)$$

with

$$I_1^* = \int_{-\infty}^{+\infty} (E_L I \kappa^2 + G_{LT} A k - \rho I \omega^2) e^{i\kappa \tau} / \Delta d\kappa \quad (16)$$

$$I_2^* = \int_{-\infty}^{+\infty} (E_L I \kappa^2 + G_{LT} A k - \rho I \omega^2) e^{i\kappa(x_0-s)} / \Delta d\kappa \quad (17)$$

For evaluating the integrals I_1^* and I_2^* , we now examine the roots of $\Delta=0$, i. e.

$$\frac{E_L I}{\rho A} \kappa^4 - \frac{I}{A} \left(1 + \frac{E_L}{G_{LT} k} \right) \kappa^2 \omega^2 - \omega^2 + \frac{\rho I}{G_{LT} A k} \omega^4 = 0 \quad (18)$$

Solving this equation for κ gives four possible roots. The first two roots are always of the following form for any frequency

$$\kappa_1, \kappa_2 = \pm \left[\frac{1}{2} \left(\frac{1}{c_0^2} + \frac{1}{c_s^2} \right) \omega^2 + \sqrt{\frac{1}{4} \left(\frac{1}{c_0^2} - \frac{1}{c_s^2} \right)^2 \omega^4 + \frac{1}{c_0^2 \alpha^2} \omega^2} \right]^{1/2} \quad (19)$$

with

$$c_0 = \sqrt{\frac{E_L}{\rho}}, \quad c_s = \sqrt{\frac{G_{LT}k}{\rho}}, \quad \alpha = \sqrt{\frac{I}{A}} \quad (20a,c)$$

while the forms of the other two roots are dependent on the magnitude of ω relative to a fixed value $\omega_c = \sqrt{G_{LT}k / \rho I}$, which can be expressed as:

when $|\omega| > \omega_c$,

$$\kappa_3, \kappa_4 = \pm \left[\frac{1}{2} \left(\frac{1}{c_0^2} + \frac{1}{c_s^2} \right) \omega^2 - \sqrt{\frac{1}{4} \left(\frac{1}{c_0^2} - \frac{1}{c_s^2} \right)^2 \omega^4 + \frac{1}{c_0^2 \alpha^2} \omega^2} \right]^{1/2}, \quad (21)$$

when $|\omega| \leq \omega_c$,

$$\kappa_3, \kappa_4 = \pm i\gamma, \quad (22)$$

with

$$\gamma = \pm \left[\sqrt{\frac{1}{4} \left(\frac{1}{c_0^2} - \frac{1}{c_s^2} \right)^2 \omega^4 + \frac{1}{c_0^2 \alpha^2} \omega^2} - \frac{1}{2} \left(\frac{1}{c_0^2} + \frac{1}{c_s^2} \right) \omega^2 \right]^{1/2} \quad (23)$$

From Eqs. (16,17) it is easily seen that these roots obtained are four simple poles of the integrands of I_1^* and I_2^* . With this knowledge, the evaluation of these two integrals can be carried out by the residue theory. Omitting the lengthy procedure, the final results are given as follows

$$I_1^* = -\frac{\pi}{EI} \left[\frac{\gamma e^{-\gamma\tau}}{(\gamma^2 + \omega^2 / c_s^2) \delta \omega} + \frac{\kappa_1 \sin \kappa_1 \tau}{(\kappa_1^2 - \omega^2 / c_s^2) \delta \omega} \right], \quad |\omega| \leq \omega_c \quad (24)$$

$$I_1^* = -\frac{\pi}{EI} \left[\frac{\kappa_1 \sin \kappa_1 \tau}{(\kappa_1^2 - \omega^2 / c_s^2) \delta \omega} - \frac{\kappa_3 \sin \kappa_3 \tau}{(\kappa_3^2 - \omega^2 / c_s^2) \delta \omega} \right], \quad |\omega| > \omega_c \quad (25)$$

$$I_2^* = -\frac{\pi}{EI} \left[\frac{\gamma e^{-\gamma(x_0-s)}}{(\gamma^2 + \omega^2 / c_s^2) \delta \omega} + \frac{\kappa_1 \sin[\kappa_1(x_0-s)]}{(\kappa_1^2 - \omega^2 / c_s^2) \delta \omega} \right], \quad |\omega| \leq \omega_c \quad (26)$$

$$I_2^* = -\frac{\pi}{EI} \left[\frac{\kappa_1 \sin[\kappa_1(x_0-s)]}{(\kappa_1^2 - \omega^2 / c_s^2) \delta \omega} - \frac{\kappa_3 \sin[\kappa_3(x_0-s)]}{(\kappa_3^2 - \omega^2 / c_s^2) \delta \omega} \right], \quad |\omega| > \omega_c \quad (27)$$

in which

$$\delta = \left[\left(\frac{1}{c_0^2} - \frac{1}{c_s^2} \right)^2 \omega^2 + \frac{4}{c_0^2 q^2} \right]^{1/2} \quad (28)$$

Substituting Eqs. (24-27) into Eqs. (14-15) and then integrating with respect to τ or s yields

$$I_1 = -\frac{2\pi}{EI a_2^2} \left[\frac{-2 + \gamma^2 a_2^2 + 2(\gamma a_2 + 1)e^{-\gamma a_2}}{\gamma^2 (\gamma^2 + \omega^2 / c_s^2) \delta \omega} + \frac{\kappa_1^2 a_2^2 - 2\kappa_1 a_2 \sin \kappa_1 a_2 - 2(\cos \kappa_1 a_2 - 1)}{\kappa_1^2 (\kappa_1^2 - \omega^2 / c_s^2) \delta \omega} \right], \quad |\omega| \leq \omega_c \quad (29)$$

$$I_1 = -\frac{2\pi}{EI a_2^2} \left[\frac{\kappa_1^2 a_2^2 - 2\kappa_1 a_2 \sin \kappa_1 a_2 - 2(\cos \kappa_1 a_2 - 1)}{\kappa_1^2 (\kappa_1^2 - \omega^2 / c_s^2) \delta \omega} - \frac{\kappa_3^2 a_2^2 - 2\kappa_3 a_2 \sin \kappa_3 a_2 - 2(\cos \kappa_3 a_2 - 1)}{\kappa_3^2 (\kappa_3^2 - \omega^2 / c_s^2) \delta \omega} \right], \quad |\omega| > \omega_c \quad (30)$$

$$I_2 = -\frac{2\pi}{Ela_2^2} \left\{ \frac{(\gamma a_1 + 1)e^{-\gamma(x_0 + a_1)} + (\gamma a_1 - 1)e^{-\gamma(x_0 - a_1)}}{\gamma^2(\gamma^2 + \omega^2/c_s^2)\delta\omega} + \frac{\{\cos[\kappa_1(x_0 - a_1)] - \cos[\kappa_1(x_0 + a_1)]\} - \kappa_1 a_1 \{\sin[\kappa_1(x_0 - a_1)] + \sin[\kappa_1(x_0 + a_1)]\}}{\kappa_1^2(\kappa_1^2 - \omega^2/c_s^2)\delta\omega} \right\},$$

$$|\omega| \leq \omega_c \quad (31)$$

$$I_2 = -\frac{2\pi}{Ela_2^2} \left\{ \frac{\{\cos[\kappa_1(x_0 - a_1)] - \cos[\kappa_1(x_0 + a_1)]\} - \kappa_1 a_1 \{\sin[\kappa_1(x_0 - a_1)] + \sin[\kappa_1(x_0 + a_1)]\}}{\kappa_1^2(\kappa_1^2 - \omega^2/c_s^2)\delta\omega} - \frac{\{\cos[\kappa_3(x_0 - a_1)] - \cos[\kappa_3(x_0 + a_1)]\} - \kappa_3 a_1 \{\sin[\kappa_3(x_0 - a_1)] + \sin[\kappa_3(x_0 + a_1)]\}}{\kappa_3^2(\kappa_3^2 - \omega^2/c_s^2)\delta\omega} \right\},$$

$$|\omega| > \omega_c \quad (32)$$

Having obtained the integrals I_1 and I_2 , from Eq. (13), the dynamic response of the contact stress between the receiving transducer and the beam waveguide in the frequency domain can be finally expressed as an explicit expression. From this expression it can be observed that: (1) the output of the system consists of two wave modes, with one being a traveling wave for any frequency, and the other when $|\omega| \leq |\omega_c|$ occurring in a form of an edge wave exponentially decaying in the x direction, and when $|\omega| > |\omega_c|$ a traveling wave; (2) each wave mode constitution has two wave fronts issued from two specific transmitting source points, respectively, one being the farthest with respect to the receiver and the other the nearest.

Using the fast Fourier Transform (FFT) technique, based on Eqs. (13, 29-32) the time domain response of the receiving transducer can be further obtained.

NUMERICAL RESULTS AND DISCUSSION

In this section, some numerical results are presented graphically to show the ultrasonic input-output characteristics for transmitting and receiving longitudinal transducers coupled to a composite beam.

For the numerical results given in this paper, the parameters for the composite beam and the mass of the transducers are chosen as: $h = 2 \text{ mm}$, $b = 20 \text{ mm}$, $E_L = 38.6 \text{ GPa}$, $G_{LT} = 4.14 \text{ GPa}$, $\rho = 1.8 \times 10^3 \text{ kg/m}^3$, $M = 0.01 \text{ kg}$, and the input is assumed to be the delayed sine pulse of time duration $f(t) = \sin(2\pi t/T)$ for $0 < t < T$; 0 for $t \geq 0$, where T is called as the input pulse width.

Fig. 2 shows a typical time history of the output of the receiving transducer, in which $T = 4 \mu\text{s}$. It can be observed that in this figure there exist three special instants: one is the beginning instant of the output response, which is denoted by S , and the other two are the instants at which the output response experience two peaks, which are denoted by M_1 and M_2 , respectively.

In order to analyze the physical interpretation of the above characteristic points, the group wave velocity c_{g1} and c_{g2} for the two wave modes involved in the output can be obtained by substituting Eqs. (19-21) into the relations

$$c_{g1} = d\omega / d\kappa_1, \quad c_{g2} = d\omega / d\kappa_3 \quad (33a,b)$$

Then the two maximum group velocities, denoted by $c_{g1\max}$ and $c_{g2\max}$ of the two wave modes, can be evaluated. Using these two maximums, the two earliest instants for the two wave mode excited by the transmitting transducer to arrive at the receiving transducer, are defined by the following equations

$$t_{s1} = (x_0 - a_1 - a_2) / c_{g1\max}, \quad t_{s2} = (x_0 - a_1 - a_2) / c_{g2\max} \quad (34a,b)$$

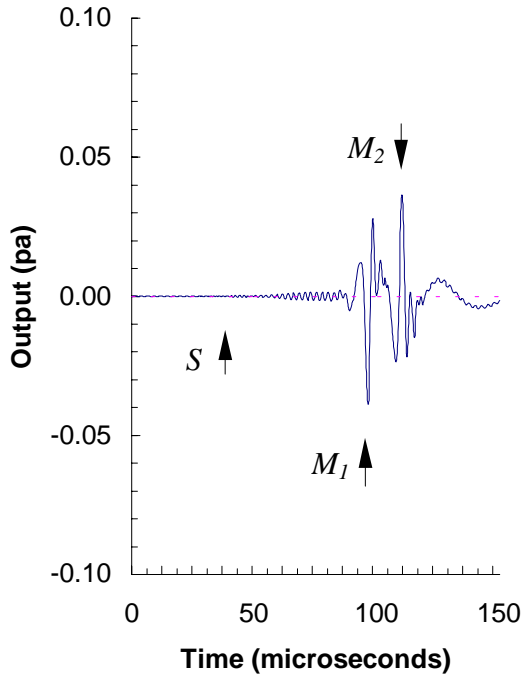


Fig. 2: Time history of the output $\sigma(t)$ for $x_0=150\text{mm}$, $a_1=a_2=10\text{mm}$, $T=4\mu\text{s}$

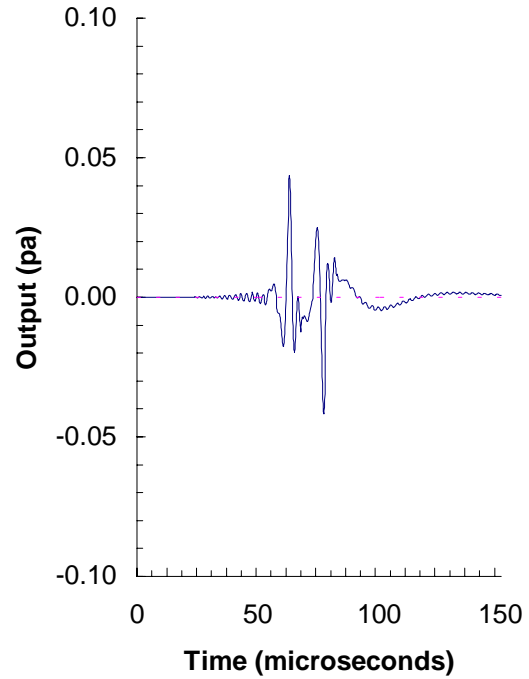


Fig. 3: Time history of the output $\sigma(t)$ for $x_0=100\text{mm}$, $a_1=a_2=10\text{mm}$, $T=4\mu\text{s}$

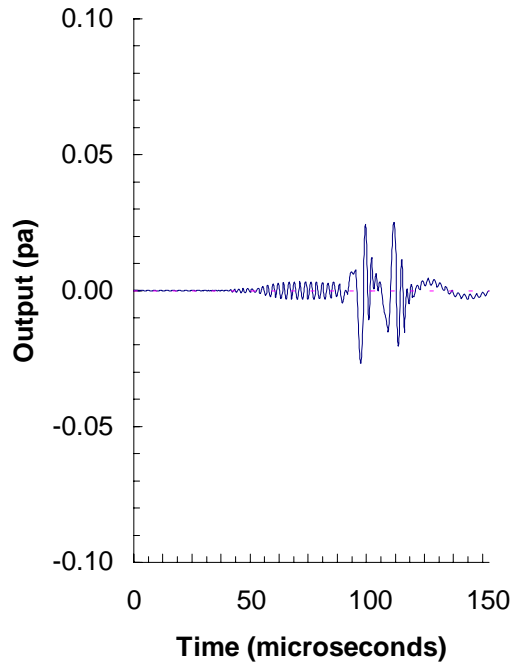


Fig. 4: Time history of the output $\sigma(t)$ for $x_0=150\text{mm}$, $a_1=a_2=10\text{mm}$, $T=3\mu\text{s}$

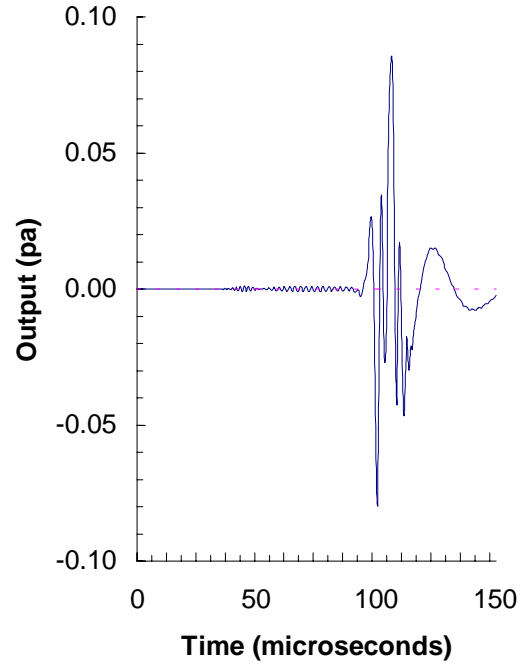


Fig. 5: Time history of the output $\sigma(t)$ for $x_0=150\text{mm}$, $a_1=a_2=5\text{mm}$, $T=3\mu\text{s}$

Through the above derivation and evaluation it is found that the instant obtained from Eq. (34b) is coincident with that marked by S in Fig. 2. This implies that the beginning point of the output response corresponds to the earliest arrival instant of the second mode components. It is evident that this conclusion is correct.

For examining the two peak instants, the instants when the components with maximum amplitude in frequency domain, respectively, issued from the two edges of the transmitting transducer, arrive at the center of the receiving transducer, are evaluated by

$$t_{M1} = (x_0 - a_1) / c^*, \quad t_{M2} = (x_0 + a_1) / c^* \quad (35a,b)$$

where c^* is the velocity of the component. It is found that the instants obtained from Eq. (35a,b) are in perfect agreement with those pinpointed by M_1 and M_2 in Fig. 2. This implies that the two maximum points of the output correspond to the two instants of the components of maximum amplitude issued from the two edges of the transmitting transducer arriving at the center of the receiving transducer.

To clarify the effects of the space between the transmitting and receiving transducers, the input pulse width and the aperture of the transducers on the output of the system, some numerical results for various values of such parameters are presented Figs. 3-5. Comparing Fig. 3 with Fig. 2, it can be observed that with an increase of the space between the transmitting and receiving transducers, the maximum output amplitude decreases. From Figs. 4 and 2, it can be seen that narrowing the input pulse width will lead to increase of high frequency components, but the maximum of the total output will decline. It is seen from the comparison of Fig. 5 with Fig. 2 that the smaller the aperture of the transducers is, the larger the amplitude of the output and the smaller the interval between its two maximum points. Obviously, these characteristics are all reasonable.

It should be noted that the numerical results given above are just the stress sensed by receiving transducers. For simulating the voltage output signals, it is required to incorporate the electron-mechanic transduction ratios of the transducers in the above analysis.

From the above numerical calculations and the features of the analytical method presented in the preceding sections it can be seen that although in this paper we only investigated the acousto-ultrasonic characteristics of a simple beam reinforced with unidirectional fibers paper, compared to the present wave path tracing method this investigation has provided a feasible approach for quantitatively analyzing the acousto-ultrasonic characteristics of complex structures. From this approach it may be possible to construct more reasonable and accurate stress wave factor definitions in which the influences of external testing conditions, such as the geometric characteristics of tested structures, transducers' spectral characteristics, mass or mounting pressure, aperture, spacing distance, coupling agent and so-on, can be eliminated or reduced as substantially as possible. This is of significance for improvement the current acousto-ultrasonic technique.

CONCLUDING REMARKS

In this paper, the acousto-ultrasonic input-output characteristics for transmitting and receiving contact-type transducers coupled to a composite beam have been investigated. An analytical method is developed. Some characteristic points arising in the output response are analyzed. The effects of the space between the transmitting and the receiving transducers, the input pulse width and the aperture of the transducers on the output of the AU system are examined. The results obtained in this paper can be used to make optimum design of the AU system, and the analysis method can be easily extend to some more complicated cases such as multiple transducers case.

ACKNOWLEDGMENTS

This research has been supported by grants from Australian Research Council and from China Jiangsu Provincial Natural Science Foundation.

REFERENCES

1. Vary, A., Bowles, K. J., "An Ultrasonic-Acoustic Technique for Nondestructive Evaluation of Fiber Composite Quality," *Polymer Engineering and Science*, Vol. 19, 1979, pp.373-376.
2. Duke, J. C., Henneke, E. G., Kiernan, M. T. and Grosskopf, P. P., "A Study of the Stress Wave Factor Technique for Evaluation of Composite Materials," *NASA CR 4195*, 1989
3. Datta, S.K., Shah, A.H., Bratton, R.L. and Chakraborty, T., "Wave Propagation in Laminated Composite Plates," *Journal of the Acoustical Society of America*, Vol. 83, No. 6, 1988, pp. 2020-2026.

4. Kim, I., Huang, H.A., Hahn, H.T. and Bakis, C.E., "Wave Dispersion in Thick Composite Laminates," in *Proceeding of Second International Symposium on Composite Materials and Structures*, Beijing, 1992, pp. 610-615.
5. Mal, A.K. and Lih, S.S., "Elastodynamic Response of a Unidirectional Composite Laminate to Concentrated Surface Loads: part I," *Journal of Applied Mechanics*, Vol. 59, No. 4, 1992, pp. 878-886.
6. Lih, S.S. and Mal, A.K., "Elastodynamic Response of a Unidirectional Composite Laminate to Concentrated Surface Loads: part II," *Journal of Applied Mechanics*, Vol. 59, No. 4, 1992, pp. 887-892.
7. Ditri, J.J. and Rose. J.L., "Excitation of Guided Waves in Generally Anisotropic Layers Using Finite Sources", *Journal of Applied Mechanics*, Vol. 61, No. 2, 1994, pp.330-338.
8. Liu, T. and Zhang, X., "Response of a Disk Mass on a Half-Space to Dilatational Waves," *Journal of Applied Mechanics*, Vol. 61, No. 3, 1994, pp. 722-724.
9. Karunasena, W.M., Liew, K.M. and Kitipornchai, S., "Hybrid Analysis of Lamb Wave Reflection by a Crack at the Fixed Edge of a Composite Plate," *Computer Methods in Applied Mechanics and Engineering*, Vol. 125, No. 1, 1995, pp. 221-233.
10. Williams, J.H., Karagulle, J.H. and Lee, S.S., "Ultrasonic Input-Output for Transmitting and Receiving Longitudinal Transducers Coupled to Same Face of Isotropic Elastic Plate," *Materials Evaluation*, Vol. 40, No. 6, 1982, pp. 655-662.

NON-DESTRUCTIVE EVALUATION OF IMPACT DAMAGED CFRP LAMINATES BY ACOUSTIC EMISSION DURING FLEXURAL LOADING

Oh-Yang Kwon and Doo-Hyun Hong

*Dept. of Mechanical Engineering, Inha University
253 Yonghyun-dong, Incheon 402-751, Korea*

SUMMARY: The degree of damage and the progressive failure of carbon-fiber reinforced epoxy(CFRP) laminates previously damaged by low velocity impact were characterized by acoustic emission(AE) and ultrasonic C-scan. Both the tensile and the compressive stresses were induced by flexural loading in the same specimen. With the increasing degree of impact damage, the stress level for the onset of AE activity was significantly reduced and therefore AE activity prior to the major ply failure was increased. It was also found that the severer the specimens were damaged by impact, the narrower the delamination was confined in the central region at the subsequent flexural loading. Both the degree of impact damage and the residual strength appeared to be very much dependent on the laminates structure. For a specific laminates structure, however, the degree of impact damage or the residual strength can be estimated by AE measurements during flexural loading.

KEYWORDS: nondestructive evaluation, CFRP laminates, impact-damage, acoustic emission, residual strength, ultrasonic C-scan

INTRODUCTION

Impact damage can be a serious problem in structures made of brittle materials such as composite laminates. CFRP laminates whose applications to aerospace structures are steadily increasing are likely to be damaged by low velocity impact of various moving objects such as tools, runway stones, ice balls, and even birds. For the damage assessment and residual strength prediction, various NDE techniques have been employed, either alone or in combination, such as ultrasonic C-scan, X-radiography, acousto-ultrasonics and acoustic emission.

Acoustic emission has been successfully applied to detect and locate the damaged area of impact-damaged composites during the subsequent quasi-static or low-cycle fatigue loading[1,2]. It was found that the severer the damage is, the more emission and the lower the stress level at which it initiates. It was also found that AE activity during the compression-after-impact(CAI) test of CFRP laminates was closely related to the degree of impact damage and the residual strength of laminates[3]. The CAI test has been widely adopted as the standardized method for evaluating the residual strength of impact-damaged composites[4]. The compression test, however, consists of complicated fixtures and procedures thus becomes an extremely expensive method[5]. On the other hand, the residual tensile strength of impact-damaged CFRP laminates did not show very good correlation with AE measurements since

tensile strength is virtually not affected by impact damage[6]. Since the flexural loading can induce both the tensile and the compressive stresses in the same specimen, we have tried to establish the relationship between AE activity and the degree of damage and the residual strength of low velocity impact-damaged CFRP laminates during flexural loading.

EXPERIMENT

Specimens were cut from fully cured, 16-ply autoclave-molded laminates made of high strength carbon/epoxy prepreg, which has elongation of 1.16%. Specimens have two stacking sequences of $[0_2/90_2]_{2S}$ (type-C) and of $[0_2/45_2/90_2]_S$ (type-Q). The test configuration and the dimension of specimen are shown in Fig. 1. The degree of impact damage was adjusted by changing the impact velocity from 0.94 to 1.48 m/s to be rated as 1J, 2J, 3J and 0J(undamaged) in terms of the absorbed energy at impact. Since specimens had the damaged area at the center, the four-point bending test with the span-to-depth ratio of 34 was employed.

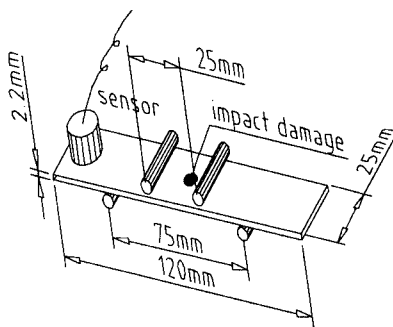


Fig. 1 Configuration and dimension of impact-damaged specimens

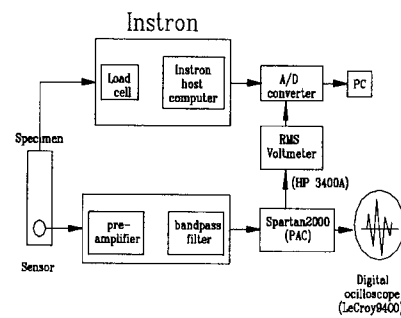


Fig. 2 A schematic diagram of AE data acquisition system

An electro-mechanical type testing machine (Model 8162, Instron) was used under displacement control for monotonic loading and under load control for loading-unloading-reloading tests. The latter ones were to measure the felicity ratio (FR). The crosshead speed was 0.5 mm/min for tests under displacement control whereas the loading rate was 0.27 kN/min for those under load control. The span-to-depth ratio was kept as 34 for all tests. The unloading points during the quasi-static loading-unloading tests were 30%, 50%, 70%, 80% and 90% of the ultimate flexural strength.

A schematic diagram of AE data acquisition system is shown in Fig. 2. A wideband AE sensor (WD, PAC) was attached at the end of the specimen. Detected signals were amplified by 40 dB at a preamp with 100 kHz to 1.2 MHz bandpass filtering then fed into the signal analyzer. A PC-based AE analyzer (Spartan2000, PAC) was employed to collect the events and to extract AE parameters. The intensity of AE activity was measured by a true RMS voltmeter (HP3400A) and recorded on a computer together with the load. Threshold was set at 56 μ V referred to the preamp input. A number of digital waveforms were recorded using a storage oscilloscope (LeCroy 9340).

RESULTS AND DISCUSSION

Residual Strength

The residual flexural strength measured and plotted with the degree of impact damage are shown in Fig. 3. One of the purpose of present study is to correlate the residual strength and the AE activity of low velocity impact-damaged CFRP laminates during flexural loading. In Fig. 3, the residual flexural strength of impact-damaged laminates is plotted as the function of nominal impact energy. Regardless of whether the damaged surface in tension or in compression, a monotonic decrease in residual strength with increasing impact-damage was observed for type-C specimens. The change became more significant for the damage level above some critical impact energy, for example, 2J. Type-Q specimens showed virtually no change in residual strength with the increasing degree of impact damage. The quasi-isotropic laminates were considered less vulnerable to impact damage.

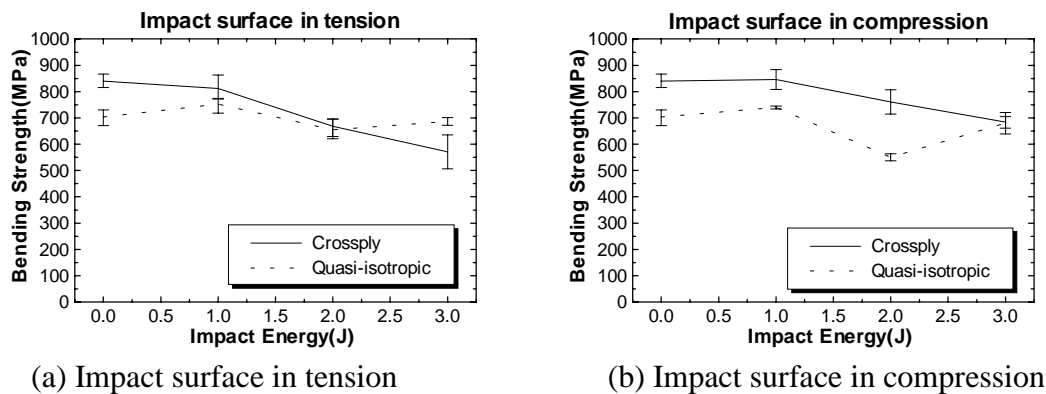


Fig. 3 Residual flexural strength with the degree of impact damage

AE RMS Voltage

The root-mean-square(RMS) voltage of AE signals is a typical parameter recorded during most of AE experiments for its simplicity and real time display. AE intensities in RMS voltage from type-C specimens together with load during the monotonic loading are shown in Fig. 4. With the increasing degree of impact damage, the activity during the initial stage prior to the major ply failure was increased and the time for the onset of AE activity was considerably shortened. The activity during this initial stage of loading has been known as the friction-generated acoustic emission[1], which is directly related to the presence or abundance of damaged area. Results from type-Q specimens showed similar but less significant trends than those from type-C specimens.

AE Events

Cumulative AE events with displacement or time from both types of specimens are shown in Fig. 5. It is likely to determine a critical impact energy for type-C specimens as some value between 1J and 2J from Fig. 5(a). For type-Q specimens, the same rule of thumb can be applied although the boundary is less distinct as shown in Fig. 5(b). This agrees well with the results of residual strength and AE RMS voltage measurements. Due to their laminates

structure, the type-C specimens appeared to be more vulnerable to impact damage than type-Q specimens.

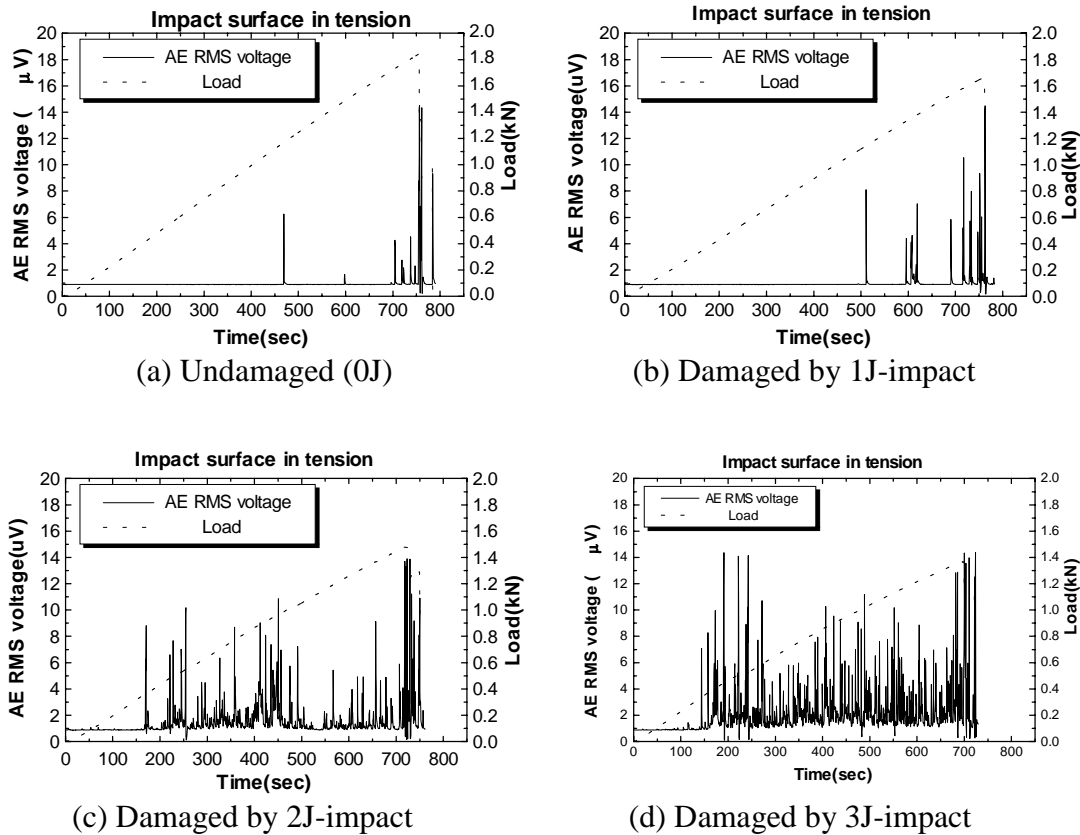


Fig. 4 AE intensity and load with displacement during flexural loading (type-C)

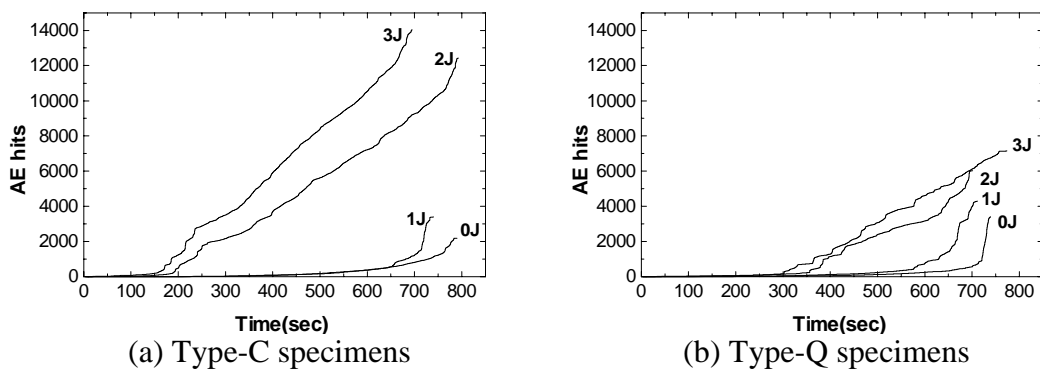


Fig. 5 Cumulative AE events vs. time during the monotonic flexural loading

Felicity Ratio and Integrity Ratio

Felicity ratio (FR) has been known as a useful index for the damage accumulation in composites, which is defined as the ratio of the load at which significant emission restarts to the previously applied maximum load. From the series of loading-unloading experiments, FR values were obtained for both types of specimens with different degree of damage. In Fig.

6(a), FR values from type-C specimens are shown as the function of the fraction of the ultimate flexural load. The specimen undamaged(0J) and that damaged by 1J-impact showed almost same values of FR, whereas those by 2J- and 3J-impact showed rapidly decreasing FR values with increasing load level. This also agrees well with the previous results by RMS voltage and cumulative events so that some value between 1J and 2J could be the critical impact energy for the laminates. Results from type-Q specimens showed similar but less significant trends than those from type-C specimens as shown in Fig. 6(b).

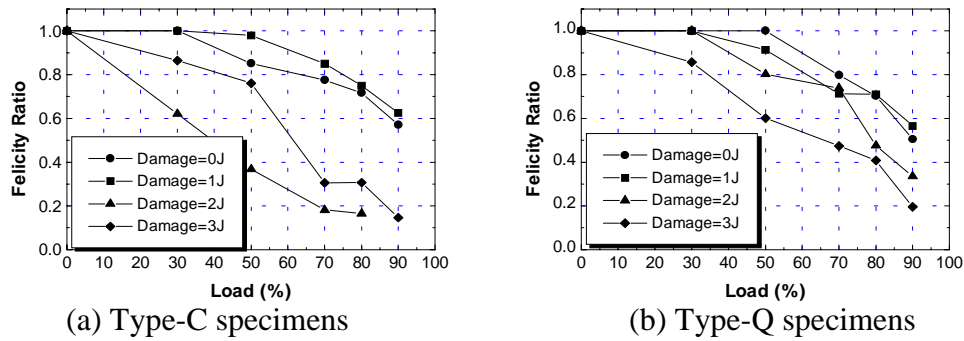


Fig. 6 Felicity ratio with the fraction of the ultimate flexural load

A newly proposed index named as integrity ratio (IR) was defined in the previous report[6] as the ratio of the load at which a significant increase in RMS voltage starts to the ultimate failure load. It was so named that the ratio rapidly decreases with the degree of damage as shown in Fig. 7. In this case IR has been redefined as follows based on the cumulative AE events and the concept of knee point[7].

$$IR = \frac{P_{knee}}{P_{max}} \tag{1}$$

where P_{knee} is the load corresponding to the knee point and P_{max} is the ultimate flexural load. IR can be obtained after the experiment and may be applicable only for the previously damaged laminates as in this study but it is easier to determine the integrity ratio than the felicity ratio.

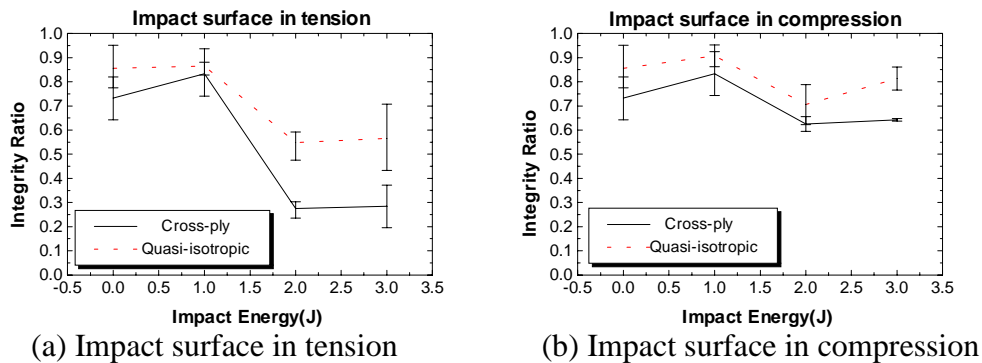


Fig. 7 Integrity ratio with the fraction of the ultimate flexural load

The ratio decreased with increasing impact energy more rapidly for type-C than for type-Q specimens as shown in Fig. 7. This is again due to the stacking sequence and type-C specimens are more vulnerable to impact damage. IR values also decreased abruptly as the impact energy increased from 1J to 2J. The condition applied to the specimens in Fig. 7(a) is considered severer than those in Fig. 7(b) since it has been known that the opposite side suffers more delamination due to low velocity impact than the impact surface does. The impact damage mainly consists of delamination which greatly affect the compressive property of laminates.

Ultrasonic C-scan Images of Damage

The central portion of specimens were also subjected to ultrasonic examination using an ultrasonic B/C-scan apparatus before and after the four-point bending tests. The ultrasonic images indicated delamination due to the impact-damage and the subsequent flexural loading as shown in Fig. 8 for type-C specimens. Fig. 8 (a) and (b) were taken before the flexural loading for type-C specimens damaged by 1J- and 2J-impact, respectively. Little damage was found in Fig. 8(a) whereas considerable delamination was observed in Fig. 8(b). This also agrees well with the result of AE measurements so that the critical impact energy for the laminates can be some value between 1J and 2J. Fig. 8 (c) and (d) were taken after the four-point bending tests for type-C specimens damaged by 1J- and 2J-impact, respectively. It was found that the severer the specimens were damaged by impact, the more the delamination was confined in the central region at the subsequent flexural loading. This can reduce the total area of delamination in highly damaged laminates such as the specimens damaged by 3-J impact, which often resulted in the less abundant AE activity especially the latter part of flexural loading.

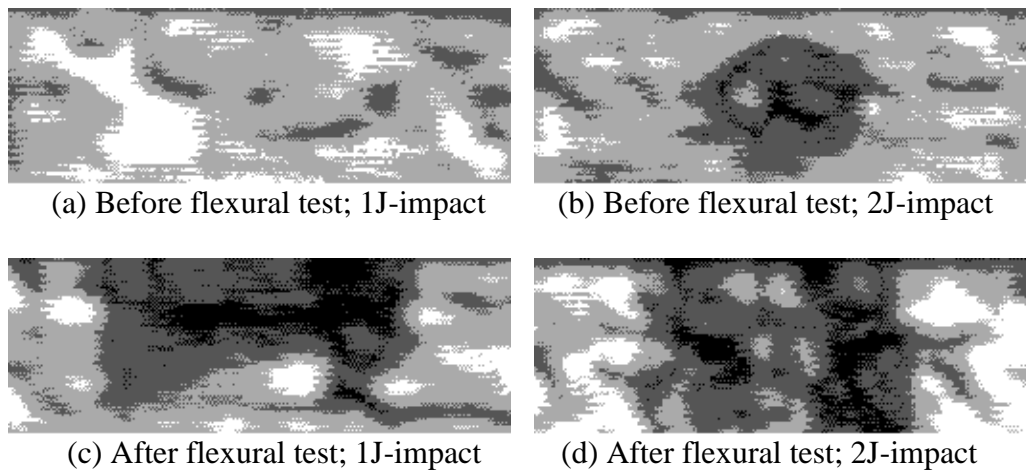


Fig. 8: Ultrasonic C-scan images of damaged area (type-C specimens)

CONCLUSIONS

Low velocity impact-damaged CFRP laminates specimens were tested under flexural loading and acoustic emission was monitored to correlate the residual strength and the degree of impact damage. With the increasing degree of impact damage, the stress level for starting AE activity was significantly reduced and the activity prior to the major ply failures was considerably increased. It was found that the severer the impact damage, the wider the delamination area before flexural loading but the narrower the delamination was confined in

the central region by the subsequent flexural loading. The opposite side suffers more delamination than the impact surface does, which is the major type of damage due to low velocity impact. The critical impact energy for the laminates used was found as some value between 1J and 2J. Both the degree of impact damage and the residual strength appeared to be very much dependent on the laminates structure.

ACKNOWLEDGEMENT

This work was supported by the Internal Research Fund, Inha University.

REFERENCES

1. Gorman, M.R., "Burst Prediction by Acoustic Emission in Filament Wound Pressure Vessels", *Journal of Acoustic Emission*, Vol. 9, 1990, pp. 131-139.
2. Ghaffari, S. and Awerbach, J., "Monitoring of Acoustic Emission in Impact-Damaged Composites", *Proceedings Second International Symposium on Acoustic Emission from Reinforced Plastics*, Montreal, Canada, July 21-25, 1986, Society for Plastics Industries, pp. 120-124.
3. Kimpara, I. et al., "A Proposal of Prediction Method of Compressive Residual Strength of Impact-Damaged CFRP Laminates", *Proceedings Tenth International Conference on Composite Materials*, Whistler, British Columbia, Canada, August 14-18, 1995, Vol. V: Structures, Poursartip, A. and Street, K.N., Eds, pp. 655-662.
4. NASA RP1092, "Specification for Compression-After-Impact Test: Standard Test for Toughened Resin Composites, ST-1", *NASA Reference Publication 1092*, 1982.
5. Sjoblom, P.O. and Hwang, B., "Compression After Impact: The \$5000 Data Point", *Proceedings 34th International SAMPE Symposium*, Reno, Nevada, May 8-11, 1989, pp. 1411-1421.
6. Kwon, O.Y., Lee, J.H. and Yoon, D.J., "Acoustic Emission Monitoring of Tensile Testing of Low Velocity Impact-Damaged CFRP Laminates", *Proceedings Tenth International Conference on Composite Materials*, Whistler, British Columbia, Canada, August 14-18, 1995, Vol. V: Structures, Poursartip, A. and Street, K.N., Eds, pp. 373-379.
7. Mitchell, J.R. and Newhouse, N., "Techniques for Using Acoustic Emission to Produce Smart Tanks for Natural Gas Vehicles", *Proceedings Fifth International Symposium on Acoustic Emission from Composite Materials*, Sundsvall, Sweden, July 10-14, 1995, pp. 273-278.

***IN-SITU* NEUTRON DIFFRACTION CHARACTERISATION OF A NITI-FIBRE REINFORCED SHAPE ACTIVE COMPOSITE**

T. Lorentzen and W.D. Armstrong

Materials Department, Risø National Laboratory, P.O. Box 49, Roskilde, Denmark

SUMMARY: This paper addresses the shape active smart composite system consisting of a NiTi continuous fibre reinforced composite based on an aluminium matrix. We have successfully manufactured a shape active composite system with quite unusual macroscopic properties. Through a thermomechanical process we induce both a forward and reverse phase transformation in the embedded fibres. We specifically focus on the utilisation of neutron diffraction for the monitoring of the on-going internal phase transformation in the composite, and successfully correlate the phase transformation with observable macroscopic measures of thermo mechanical deformation.

KEYWORDS: neutron diffraction, smart composites, shape active, continuous fibres, NiTi-reinforcement, phase transformation, internal stresses, in-situ

INTRODUCTION

Among the many candidates for smart materials or as elements of smart structures the characteristic shape memory capability of NiTi-alloys has drawn the attention of many researchers within the field of “Smart Materials and Structures”. The thermo mechanical behaviour does hold very interesting prospects for unusual and advantageous composite properties, when embedded in monolithic alloys.

Some of the first experimental investigations of this class of advanced materials [1-3] reported an increased elevated temperature flow strength in the NiTi shape memory reinforced composites relative to the unreinforced matrix alloys following a room temperature pre-strain. Armstrong and Kino [4] later subjected an experimental NiTi reinforced composite to a room temperature (RT) pre-strain process and observed unusual hardening behaviour. They subsequently exposed the composite to an unconstrained heating process and observed a spectacular non-linear thermal contraction. Similar to previously reported results they also observed a significant increase in the elevated temperature flow strength as compared to the unreinforced matrix alloy at elevated temperature as well as compared to the composite RT-behaviour.

It is well accepted that the properties of NiTi-alloys are very sensitive to the internal structure of the alloy. It has proven that the thermo mechanical process of elevated temperature consolidation of a composite material using such fibres, holds a high risk of reducing, if not eliminating, the phase transformation characteristics of the fibres. Process, temperature and time are critical and must be controlled within narrow limits.

Once produced successfully, a simple thermo mechanical test shows readily that the composite material behaves differently than a conventional metal/metal composite. However, in order to quantify that the macroscopic properties are indeed signs of an interior phase transformation in the embedded NiTi-fibres, experimental techniques other than traditional tensile testing are called for. In the present paper we particularly focus on the utilisation of neutron diffraction, whereby we selectively focus on either the embedded NiTi-fibres or on the aluminium matrix. The main aim is to demonstrate how the readily observable macroscopic effects of the phase transformation of the fibres can be directly correlated with the NiTi phase distribution by monitoring specific peak intensities and selected lattice parameters.

MATERIAL

The material under consideration is based on a 6082 aluminium alloy reinforced with continuous 50.7 at%Ni NiTi fibres of 190 μ m fibre thickness. The reinforcing fibres were laced onto 0.3mm thick end-notched sheets of the T6 heat treated matrix alloy. Sheets were stacked into a welded canister of the matrix alloy which was subsequently sealed and evacuated. The sealed can was heated to approximately 535 $^{\circ}$ C and consolidated using a maximum load of 25 metric ton. The consolidated can was water quenched, whereafter it remained at room temperature for five days before a T6 age treatment at 175 $^{\circ}$ C for 8 hours. Three test pieces of approximately 20.5vol% fibre content were subsequently machined from the can as well as a control specimen machined from an unreinforced part of the can. Fig.1 shows a micrograph of the central cross section of one of the composite specimens.

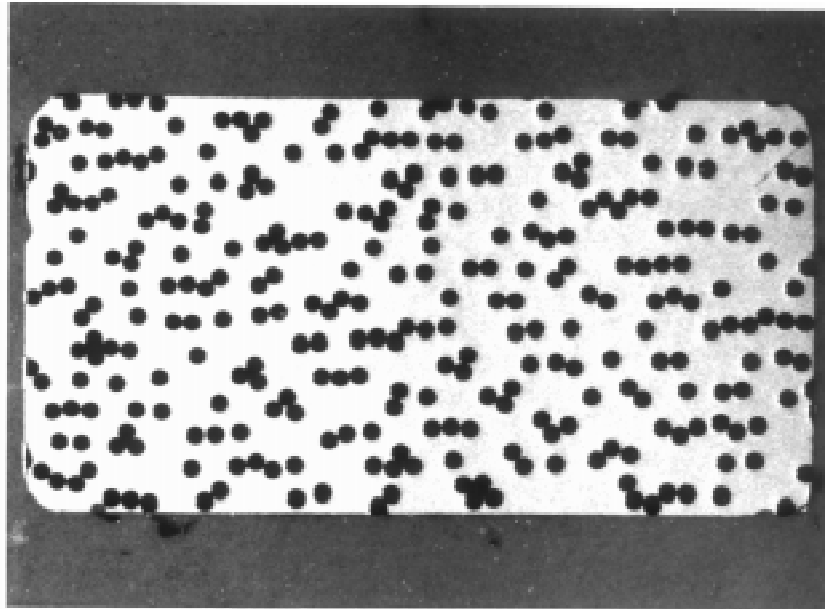


Fig. 1: Micrograph of the test specimen cross section.

NEUTRON DIFFRACTION

As mentioned we specifically focus on the utilisation of the neutron diffraction technique in the characterisation of the present materials. Using a dedicated thermo mechanical loading rig designed for in-situ diffraction experiments [5] and mounted on the TAS-8 diffractometer of the steady state DR-3 reactor at Risø, we monitor selected Bragg peak intensities and lattice parameters throughout the imposed thermo mechanical process.

Being a steady state source we are restricted to monitoring single peaks at a time, though peaks which are close together can be observed simultaneously by the installed position sensitive detector. Several peaks could be monitored by shifting the detector to a range of selected 2θ -settings though at the cost of deteriorated time resolution. In the present case we select an optimum time resolution to be the focus in the thermo mechanical processes where relaxation, creep etc. may result in a severe time dependency at specific temperatures.

We acknowledge that we get a rather limited monitoring of the complicated phase transformation process. A more complete picture would be obtained from a spallation source experiment, however, it appears unrealistic to perform an in-situ monitoring of the complete texture with the time resolution achieved in the present case where diffraction peaks are monitored at a rate ranging from one per 10 sec. to one per 90 sec.

EXPERIMENTAL

The outline of the experimental procedure is to perform an RT monitoring of the diffraction line spectre for the as-produced material in order to characterise the phase distribution of the NiTi fibres. We subsequently select a specific peak from the fibres to be our monitor of the progress in the phase transformation during the thermo mechanical process. The initial stage is an RT straining process to approximately 4% total strain, which is expected to induce an austenite-to-martensite phase transformation. Subsequently the now pre-strained test piece is subjected to an unconstrained heating process to 120°C during which the fibres are expected to recover some of the austenitic phase.

Room Temperature Characterisation

The line spectra for the as-produced test piece shown in Fig.2 clearly displays the two characteristic aluminium Bragg peaks as well as the austenite (110)-peak in-between the aluminium peaks. There is no sign of the martensitic phase in the fibre direction of the composite in the as-produced state. Following the subsequent RT straining process we repeat the diffraction line scan, and the result is superimposed on the as-produced line spectra in Fig.2. We now observe a Bragg peak at 4.6 angstrom, which was absent in the as-produced state. This peak, which is assumed to be from the martensitic phase, has been indexed in conflicting ways in a number of previous investigations [6-10] ; here it will be indexed as the martensite (001)-peak.

As the austenite (110)-peak is not well separated from the aluminium peaks, therefore we selected the martensite (001)-peak as our monitor of the progress of the phase transformation. The neutron detector was focused at this specific d-spacing range during the straining process, and the evolution of this specific Bragg peak as a function of strain is shown in Fig.3.

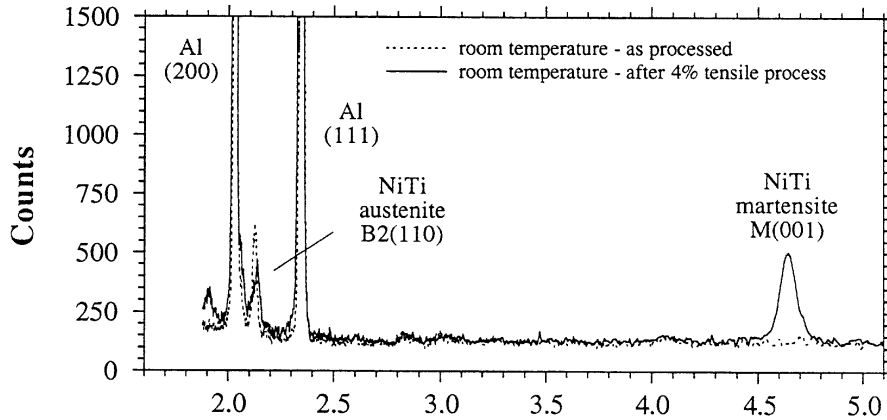


Fig. 2: RT diffraction line spectra for the as-produced specimen and following a 4% tensile straining process.

In Fig.3 we observe that the martensite (001)-peak intensity monotonically increases with strain; in the insert the specific strain levels at which the Bragg peaks were recorded are indicated by arrows. During the elastic part of the deformation there is no sign of the peak and then beginning at a total strain of 1.9% the peak intensity increases. A careful quantification of the peak intensity shows an increase in intensity which is approximately linear with strain and with a zero intensity intercept extrapolated to a total strain of 1%.

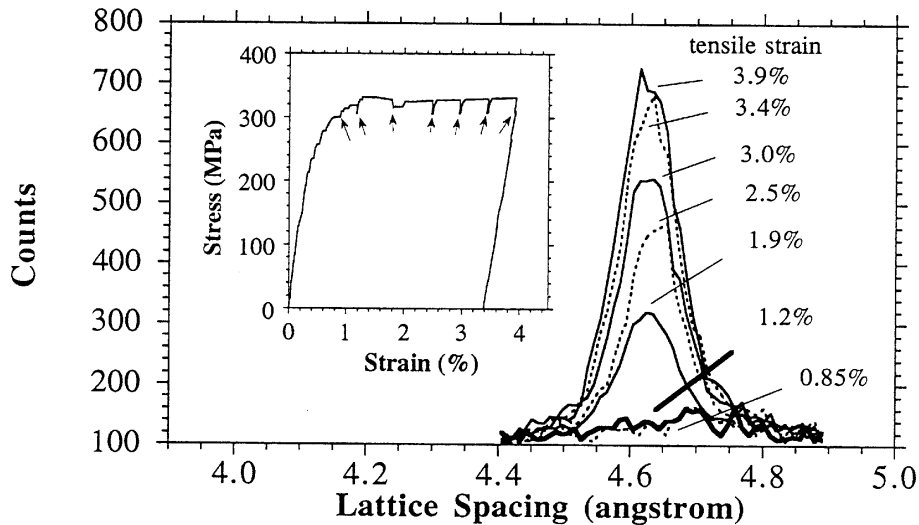


Fig. 3: Martensite (001)-peak intensity variation with straining.

Unconstrained Heating

The subsequent unconstrained heating process is expected to induce a recovery of some of the austenite at the cost of a reduction in content of martensite. The process is monitored by recording the macroscopic strain (or expansion) and again the neutron diffraction measurements are focused on the martensite (001)-peak. The macroscopic expansion is quite unusual as seen in Fig.4, which also displays the expected thermal expansion of the unreinforced alloy.

We note that the pre-strained composite sample displays a quite unusual non-linear thermal contraction in contrast to the normal thermal expansion of the monolithic alloy. This dramatic thermal contraction is a clear indication of the powerful shape memory response of the embedded fibres. Again these observations, based on macroscopic properties, can only qualitatively be assumed to be correlated with the internal phase transformation of the imbedded fibres, and more advanced techniques are called upon for a more direct correlation.

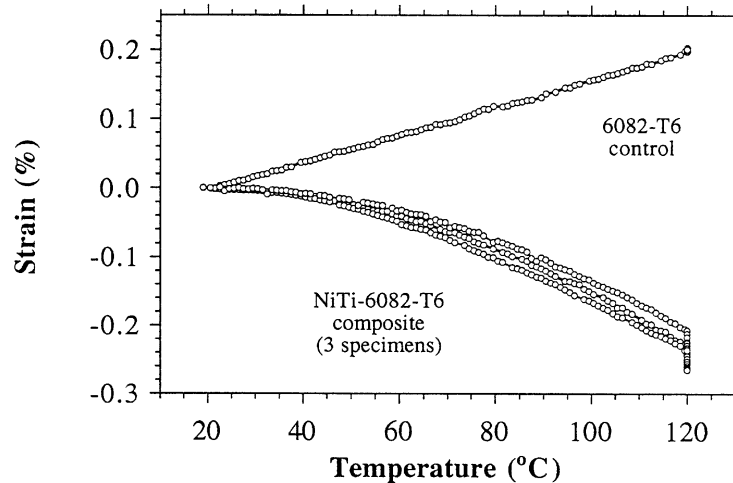


Fig. 4: Macroscopic expansion during unconstrained heating to 120°C for the unreinforced control specimen and for the NiTi-reinforced composite.

By using neutron diffraction we can take a step in this direction, and again we select to monitor the evolution in the martensite (001)-peak, and take the peak intensity as an indicator of the progress in the phase transformation. These results are shown in Fig.5.

From Fig.5 we clearly observe the progressive elimination of the martensite (001)-peak with temperature. In the superimposed insert of the macroscopic behaviour arrows indicate the level of thermal contraction at which the diffraction peaks were recorded. Again a careful examination shows the peak intensity to reduce essentially linearly with the macroscopic thermal contraction. The macroscopic thermal contraction can hence be directly correlated with the evolution in the phase transformation of the embedded fibres.

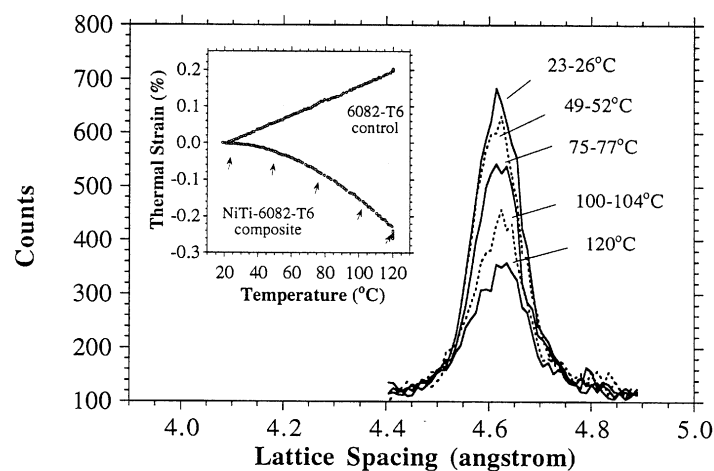


Fig. 5: Martensite (001)-peak intensity variation with temperature during unconstrained heating to 120°C.

As mentioned we obtain three specimens with identical process parameters from a specific can, which gives us the opportunity to repeat the test with a focus other than the martensite (001)-peak. A subsequent repetition of the entire thermo mechanical process was conducted, and for the unconstrained heating part of the process we changed the focus of the neutron diffraction experiment to the monitoring of the Al_{111} lattice expansion. This is shown in Fig.6 together with the lattice expansion of the unreinforced control specimen. Whereas the monitoring of the unreinforced lattice expansion nicely reflects the expected coefficient of thermal expansion of aluminium, the Al_{111} lattice parameter of the composite remains nearly constant until approximately 80°C, whereafter it starts to grow. The inclination is, however, smaller than for the unreinforced control specimen. The difference between the two curves is a measure of the longitudinal elastic internal strain in the aluminium matrix phase of the composite, and hence correlates the thermal contraction of the composite and the progressive reduction in the martensite content with the generation of a compressive internal strain in the matrix of the composite.

CONCLUSION

Shape active composites can be manufactured to have quite un-usual macroscopic properties which are readily monitored by traditional experimental techniques. However, in order to correlate these observations directly with the on-going phase transformation of the embedded fibres more advanced techniques are called for. We specifically focus on the utilisation of neutron diffraction, whereby we can follow the evolution of the internal phase transformation by continuously monitoring of the intensities of selected representative Bragg peaks. We have shown an essentially linear correlation between the applied strain and martensite content at room temperature.

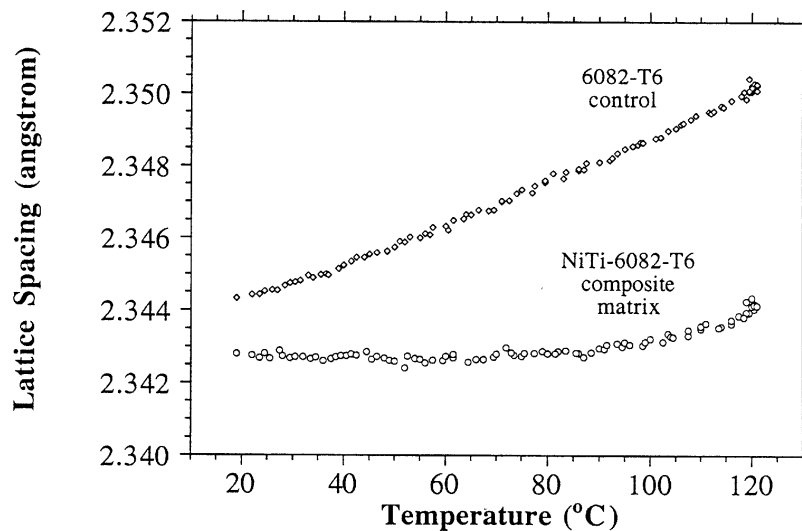


Fig. 6: Associated Al_{111} longitudinal lattice expansion for the unreinforced control specimen and for the NiTi-reinforced composite during unconstrained heating to 120°C.

A subsequent free thermal process to 120°C showed an un-usual and dramatic thermal contraction of the composite system. By monitoring the peak intensity of a selected martensite Bragg peak we again observed an essentially linear correlation between temperature and martensite content. Furthermore, by monitoring the lattice strain evolution in the aluminium matrix phase it is observed that this reverse phase transformation and macroscopic thermal

contraction results in the development of large compressive residual strains in the matrix of the composite.

ACKNOWLEDGEMENTS

The present investigation was conducted as part of the centre activities within the “Engineering Science Centre for Characterisation and Modelling of Materials” at Risø. We also acknowledge the support of the Danish Research Academy through the DANVIS program.

REFERENCES

1. Taya, M., Furuya, Y., Yamada, Y., Watanabe, R., Shibita, S. and Mori, T., “Strengthening Mechanisms of TiNi Shape Memory Fibre / Al Matrix Composite”, Proc. Smart Mater, edited by V. K. Varadan, SPIE, 1916, 1993, pp. 373-383.
2. Furuyada, Y., Sasaki, A. and Taya, M., “Enhanced Mechanical Properties of TiNi Shape Memory Fibre/Al Matrix Composite”, Materials Transactions JIM, 34, 1993, pp. 224-227.
3. Taya, M., Shimamoto, A. and Furuya, Y., “Design of Smart Composite Based on Shape Memory Effect”, Proceedings of the 10th International Conference on Composite Materials, ICCM-10, edited by A. Poursatip and K. Street, Woodhead Publishing Limited, Cambridge, England, vol.V, 1995, pp. 275-282.
4. Armstrong, W. D. and Kino, H., “Martensitic Transformations in a NiTi Fibre Reinforced 6061 Aluminium Matrix Composite”, Journal of Intelligent Materials Systems and Structures, vol. 6, 1995, pp. 809-816.
5. Lorentzen, T. and Sørensen, N., “A New Device for In-situ Loading of Samples during Neutron Diffraction Strain Measurements”, Proceedings of the 12th International Risø Symposium on Materials Science, edited by N. Hansen, D. Juul jensen, T. Leffers, H. Lilholt, T. Lorentzen, O. B. Pedersen and B. Ralph, Risø National Laboratory, Denmark, 1991, pp. 489-496.
6. Dautovich, D. P. and Purdy, G. R., “Phase Transformations in TiNi”, Canadian Metallurgical Quarterly, 4, 1965, pp. 129-143.
7. Lange, R. G. and Ziderweld, J. A., “Shape-Memory Effect and the Martensitic Transformation of TiNi”, Journal of Applied Physics, 39, 1068, pp. 2195-2200.
8. Wang, F. E., Pickart, S. J. and Alperin, H. A., “Mechanism of the TiNi Martensitic Transformation and the Crystal Structures of TiNi-II and TiNi-III Phases”, Journal of Applied Physics, 43, 1972, pp. 97-112.
9. Michal, G. M. and Sinclair, R., “The Structure of TiNi Martensite”, Acta Cryst. B., 37, 1981, pp. 1803-1807.
10. Bührer, W., Gotthardt, R., Kulik, A., Mercier, O. and Stab, F., “Powder Neutron Diffraction Study of Nickel Titanium Martensite”, Journal of Physics F., Metallurgical Physics, 13, 1983, pp. 77-81.

INTERPHASE CHARACTERISATION OF COMPOSITE SYSTEMS USING INDIRECT MECHANICAL TESTING AND ULTRASONIC SPECTROSCOPY

D. Van Hemelrijck¹, A. Anastasopoulos², L. Tirry¹, A. Cardon¹, W. P. De Wilde¹

¹ Free University Brussels, Faculty of Applied Sciences

Department of Mechanics of Materials and Constructions, building Kb, Pleinlaan 2, B-1050 Brussels, Belgium

² Envirocoustics A.B.E.E., Eleftheriou venizelou 7 & Delfon, 14452 Athens, Greece

SUMMARY: In the present study indirect measurement methods measuring the InterLaminar Shear Strength (ILSS), the shear modulus and the transverse tensile strength are used to assess the fiber-matrix interphase properties. Along with the mechanical destructive tests an ultrasonic nondestructive method was developed for the identification of the interphase properties. The analysis is based on advanced signal processing and supervised pattern recognition of the ultrasonic A-scan signals.

Different exemplary results show the suitability of this technique to determine characteristic values for different fiber/matrix combinations of glass and polypropylene (PP).

KEYWORDS: interphase, indirect measuring methods, ultrasonic, advanced signal process, supervised pattern recognition

INTRODUCTION

The Thermomechanical behaviour of fiber reinforced composite systems is influenced to a decisive extent by the quality of the bond between the reinforcing fiber and the plastic matrix. The fiber/matrix adhesion can frequently be improved by surface treatment of the fiber or by adding coupling agent to the matrix.

Different methods have been developed for measuring characteristic values to classify the bond quality between fiber and matrix. Micromechanical test techniques [1], as the fiber pull-out [2], the fragmentation or the micro-indentation test are well established methods to analyze the mechanical and physical properties of the fiber-matrix interphase.

Apart from these direct measuring methods, indirect measuring methods have also become established, such as the short beam bending test for determining the interlaminar shear strength (ILSS), the transverse tensile test and the inplane torsion test.

Along with the mechanical destructive tests, ultrasonic non-destructive testing was performed for the identification of different interphase properties as resulted from different fiber/matrix interphase combinations of glass and polypropylene (PP). The ultrasonic nondestructive evaluation method is based on signal processing and supervised pattern recognition analysis [3-7] of the A-scan signals. The A-scan signals were transformed to the frequency [8], auto and cross correlation domains [3,4]. A pattern vector is established for each A-scan signal, composing of descriptors calculated from all the previously mentioned domains. The most efficient descriptors were found by means of discriminant analysis and are used for the classification of the three different interfacial conditions, by means of the k-Nearest Neighbor Classifier.

MATERIAL SYSTEM AND SPECIMEN PREPARATION

The composite material system of which the interphase characteristics were studied, was Glass fiber with polypropylene (PP) matrix. Glass fiber (type E) roving of 480 Tex. were used and the fiber had a diameter of 20 μm . In order to obtain different interphase properties two types of sizing were used: (i) a sizing that was compatible with the PP-matrix, resulting in a good fiber-matrix adhesion; (ii) a incompatible sizing, resulting in a poor adhesion between fiber and matrix. Both sizings contained the same aminopropyl silane group, but different film formers (cf. [9]) were used to obtain different interphase properties. A high molecular mass acrylate latex yielded poor adhesion, whereas a PP-grafted with a maleic anhydride was used to obtain good adhesion. The sizing content on the glass-fibers varied between 0.5 and 1.0 % by weight. The (covalent) reaction between the silane and the glass surface on one hand and between the silane and the maleic anhydride groups in the other hand is extensively treated in [9-10]. Analysis of the surface of the sized glass-fiber by SEM and XPS showed that the surface is equally covered with a thin silane layer but that the maleic film former covers only 7 to 14% of the fiber surface (cf. figure 1). As the adhesion between PP and maleic film former is much better than the adhesion between PP and silane, only 7-14% of the fiber surface is responsible for the load carrying capacity of the composite laminate stressed in the perpendicular direction.

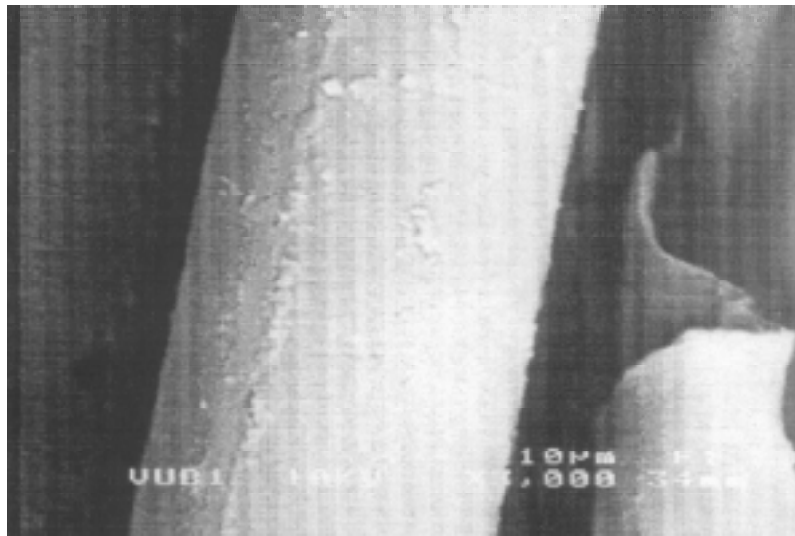


Figure 1: SEM photograph of a sized glass-fiber in the composite

To increase the surface of adhesion, a coupling agent (maleic anhydride modified PP, 1wt. %) is added to the PP-matrix. This coupling agent migrates towards the glass-surface [9] and bonds to the amino groups in the silane-layer.

Mechanical tests showed (cf. table 1) no significant differences between the bulk properties of the different pure matrix systems.

Table 1: Mechanical properties of the different matrix systems.

Property	Pure Matrix: (PP)	(PP) + 1 wt. % coupling agent	(PP) + 3 wt. % coupling agent
Strength	29.5 MPa	30 MPa	31 MPa
E-modulus	2.0 GPa	2.0 GPa	2.1 GPa

A pultrusion process was used to fabricate test plates of about 2mm thick. During this process the fiber bundle was pulled through a polypropylene bath at a constant rate of 6 m/min. and wound on a rectangular frame. The frame with the pultruded glass fibers were then dried for

one hour in an oven at 80°C. Before curing in a heated press, Teflon foil was wrapped around the frame. The applied cure cycle is shown in figure 2. After curing, the plates were cut with a water cooled diamond saw into nine 90°-specimens and stored at room temperature in a desiccator to dry. Of each plate the density and fiber volume fraction was measured and each plate was also microscopically investigated (SEM or optical microscope).

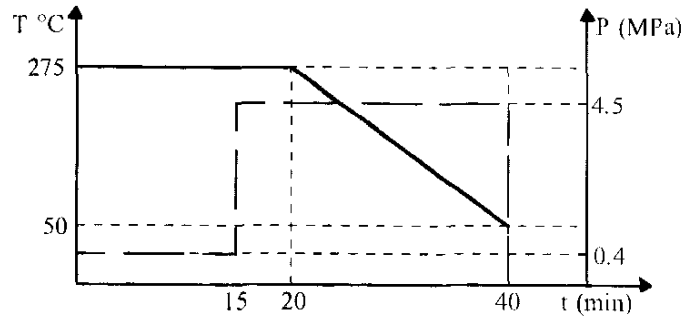


Fig. 2: Cure cycle

MECHANICAL TESTING.

In addition to the ILSS-tests done at DSM-research [9], the transversal tensile strength, Young's modulus perpendicular to the fiber direction and the inplane shear modulus was measured for the three different specimen types and for different fiber volume fractions. Before testing, the cut edges of the specimens were polished and end-tabs bonded on all specimens. The specimens of batch 1 had a good compatible sizing whereas the specimens from batch 2 had a poor incompatible sizing and those from batch 3 a good sizing and a coupling agent added to the matrix.

The transversal tensile strength was measured with an INSTRON 4505 test bench at a constant cross head speed of 1mm/min. From figure 3, we may observe a clear difference between the different batches. Each data point represents the mean value of 8 tested samples.

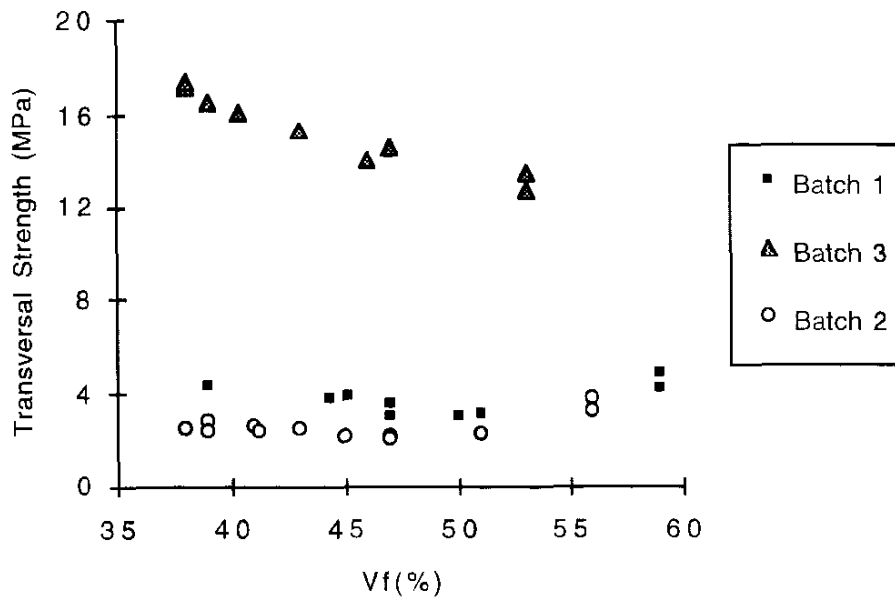


Figure 3: Variation of the transversal tensile strength as a function of the glass fiber fraction Vf for glass fiber/PP composites with a) an incompatible glass fiber sizing (Batch 2), b) a 'good' sizing (Batch 1) and c) a 'good' sizing and 1% of coupling agent (Batch 3).

The ILSS tests performed at DSM-research showed different results: for batch 2 the ILSS-value was 10 MPa, for batch 1 it was 22 MPa and for batch 3 28 MPa. However, here the difference between batch 1 and batch 2 is much more significant. On the other hand the difference between batch 3 and batch 1 is less than 25 %.

The results obtained for the transversal E-modulus are shown in figure 4. Using a different sizing of the fibers doesn't result in stiffness change, only a small increase of the transversal stiffness is observed when coupling agent is added to matrix (batch 3).

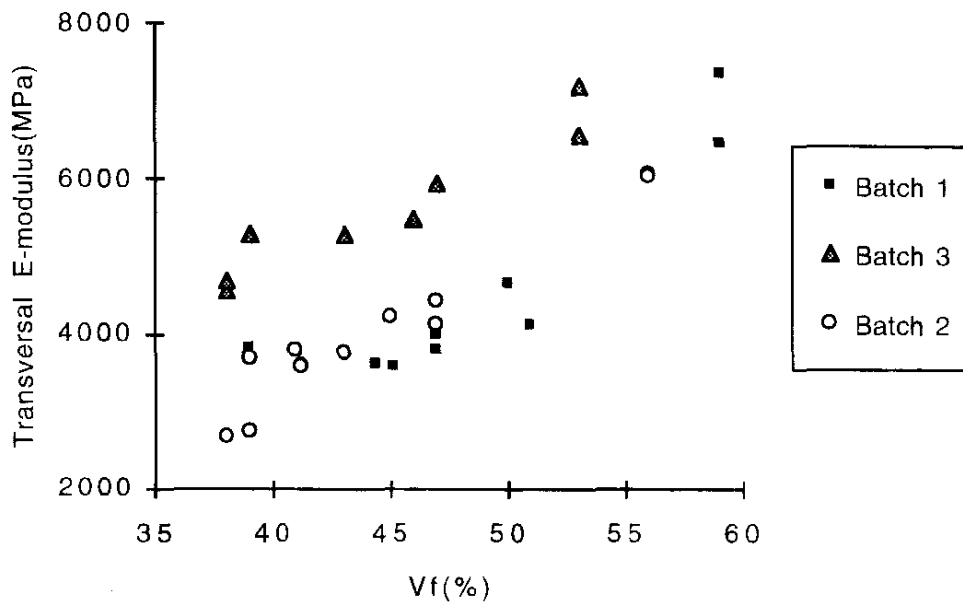


Figure 4: Variation of the transversal E-modulus as a function of the glass fiber volume fraction with a) an incompatible glass fiber sizing (Batch 2), b) a 'good' glass fiber sizing (Batch 1) and c) a 'good' glass fiber sizing and 1 mass percentage of coupling agent (Batch 3).

In order to obtain the inplane shear modulus an automated torsion test was used. Rectangular specimens with length l , width h and thickness d were twisted using a stepping motor (1 step = 0.036° angular rotation). The resulting torque was measured with a Lebow torque cell and the shear modulus was calculated with the following equation:

$$G = \frac{M_t \cdot L}{\beta \cdot \theta \cdot d^3 \cdot h}$$

where β is dependent on the ratio h/d .

It may be seen from figure 5, that the shear modulus of the systems with well sized glass fiber (batch 1 & batch 3) is approximately 50% higher than the shear modulus of the system with poor fiber-matrix adhesion (batch 2). The fact that the shear properties of batch 1 are nearly the same as those of batch 3 is probably due to mechanical locking of the film former in shear loading. Dependence of the fiber volume fraction is not observed.

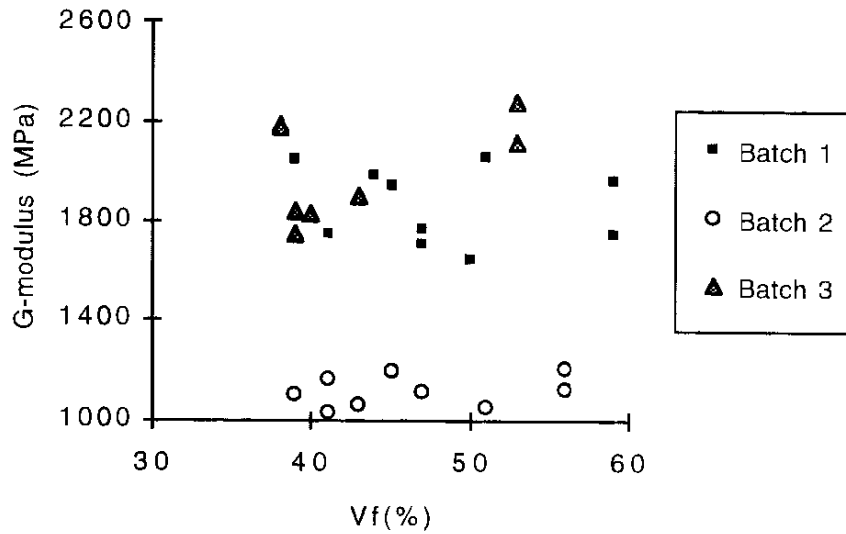


Figure 5: Variation of the G-modulus as a function of the glass fiber volume fraction with a) an incompatible glass fiber sizing (Batch 2), b) a 'good' glass fiber sizing (Batch 1) and c) a 'good' glass fiber sizing and 1 mass percentage of coupling agent (Batch 3).

NON DESTRUCTIVE TESTS

Ultrasonic pulse-echo immersion testing forms the basic of the experimental set-up, as described in detail elsewhere [11,12]. A full set of A-Scan signals, from each type of specimens, was digitised by using 1MHz, 5MHz, 10MHz and 15MHz transducers.

The results presented in the present paper were obtained with a 5 MHz focused transducer. The 1 MHz transducer did not exhibit the required resolution for the interphase/adhesion characterisation, while the 10 MHz and 15 MHz transducers induced problems of repeatability in terms of increased scattering of the calculated signal parameters/descriptors.

Typical A-scan signals from the three different types of specimens, previously denoted as batch 1, batch 2 and batch 3 are presented in figure 6a. The time domain signals are much alike, especially the signals from batch 1 and batch 3. The A-scan signals from the specimens of batch 2 are slightly different from those of batch 1 and batch 3, as can be realised by comparing the amplitude of the 2nd greatest positive peak.

Figure 6b shows the frequency response, in terms of Power Spectral Density (PSD), calculated by means of Fast Fourier Transform (FFT). Although the frequency domain contains the same information as the time domain, due to the existence of the inverse Fourier transform, it is helpful as a different point of view to highlight hidden information in the A-scan signal. This is evident in figure 6b, by comparing the differences between the PSD calculated for specimens of batch 1 and batch 3. The differences are more pronounced between the PSD of batch 2 and those of batch 1 and 3.

The signal processing stage was completed by calculating the Auto and Cross correlation transformation of the A-scan signals, although on first site they did not exhibit such high discrimination power as the frequency domain.

Based on the above mentioned observations a simple classification scheme was established for the discrimination of a two class problem defined by the two different adhesion cases i.e. poor fiber/matrix adhesion (batch 2) and good fiber/matrix adhesion (batch 1 and batch 3). In that case, by using a two dimensional pattern vector, with components/descriptors the number of peaks above 40% of the maximum amplitude in the frequency domain and the peak amplitude of the second greatest peak in the time domain, the K-Nearest Neighbor Classifier (K-NNC) resulted in a 100% recognition rate (error free classification).

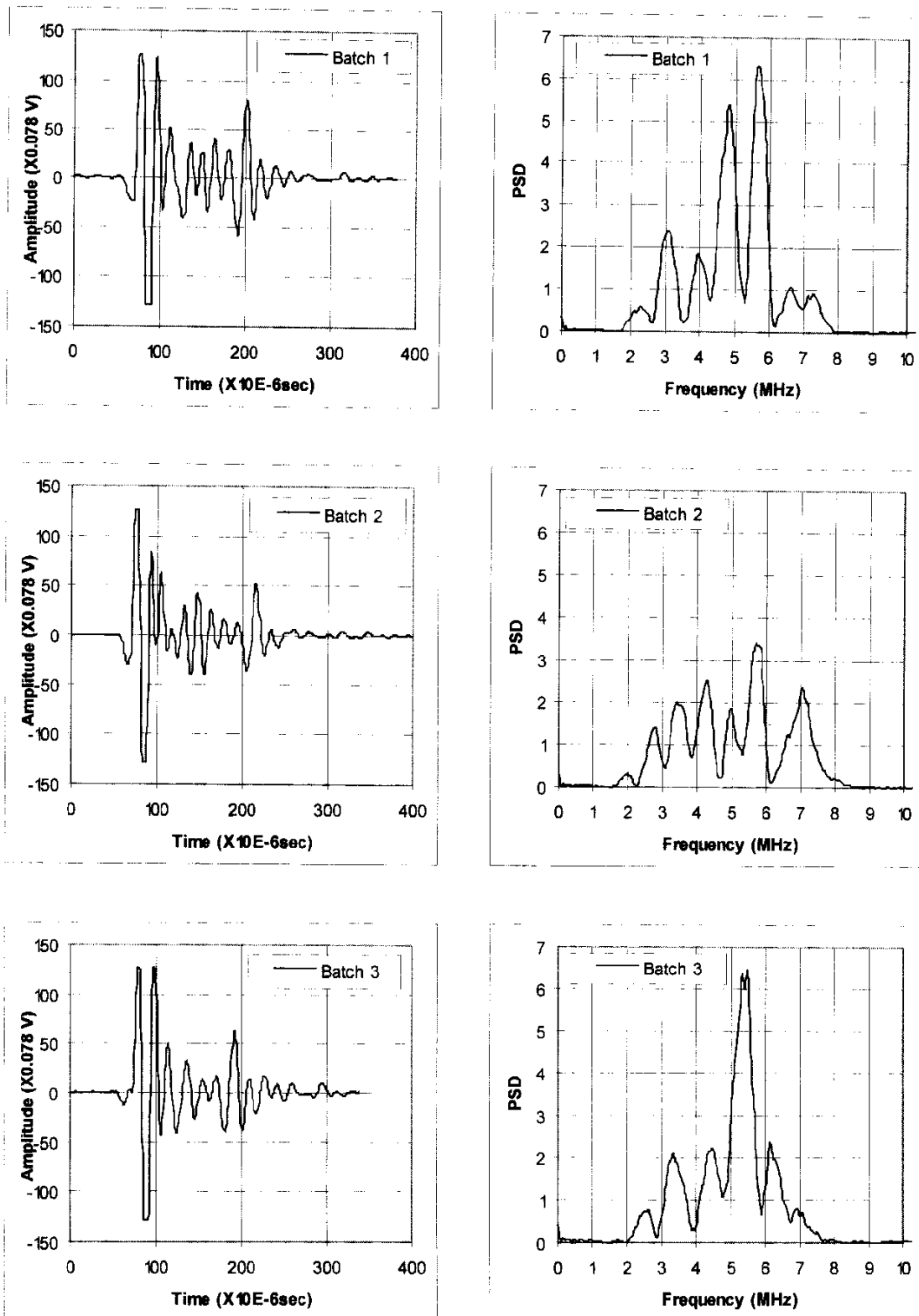


Figure 6:
a. Time domain (A-Scan signals)
b. Frequency domain (Power Spectral Density)

The decision process of the k-Nearest Classifier [3,6], is based on Euclidean distance calculations between the unknown pattern vector to all the previously known representative pattern vectors from each signal class, used as training set for the supervised pattern recognition system. Five pattern vectors from each type of specimens were used as training vectors for all the classification problems treated in the present study.

In order to proceed with automated pattern recognition characterisation of the interfacial properties and to discriminate the A-scan signals between the three different types of specimens, further development of the above mentioned methodology is required due to problems induced by the high similarity between signals of batch 1 and batch 3 specimens. Therefore, descriptors were calculated from time, frequency and autocorrelation domains and ranked according to their discrimination power as resulted by the calculation of Wilk's λ [3,4]. The Wilk's λ is defined as the ratio of the determinant of the within class scatter to the determinant of the total scatter. For the case of single signal parameter the Wilk's λ is equivalent to the ratio of the respective standard deviations. In any case, the lower the λ value, the higher the discrimination power of the descriptor set.

The ten (10) signal parameters listed in Table 2, were found to be the most useful for the discrimination of the interfacial properties, from the total set of 161 descriptors initially defined in a previous study[4].

Table 2 : Descriptors and their discrimination power for the three class problem

#	Descriptor	Domain	Description	Wilk's λ
1	FD1-2	Frequency	Bandwidth between 1 st and 2 nd greatest peak (Inter peak distance)	0.195
2	Askew	Auto Correlation	Signal Skewness	0.491
3	Akurt	Auto Correlation	Signal Kurtosis	0.506
4	F#P60%	Frequency	# of peaks above 60% of the base line.	0.530
5	D1-5	A-Scan	Time difference between 1 st and 5 th greatest peak (Inter peak distance)	0.541
6	F4GPA	Frequency	4 th greatest peak area	0.571
7	FD1-3	Frequency	Bandwidth between 1 st and 3 rd greatest peak (Inter peak distance)	0.582
8	APArca6	Auto Correlation	Partial area of band 6	0.642
9	D1-4	A-Scan	Time difference between 1 st and 4 th greatest peak (Inter peak distance)	0.686
10	F2GPP	Frequency	2 nd greatest peak position	0.688
11	FPArea3	Frequency	Partial area of band 3.	0.720
12	A#P70%	Auto Correlation	# of peaks above 70% of the base line.	0.726

The discrimination power of the above listed descriptors, as for instance the frequency band width defined by the first and second greatest peak of the frequency domain and the distance between the first and fifth peak in the time domain signal, cannot be easily identified by simple observation of the respective A-scans or frequency response graphs.

The correlation characteristics of the selected descriptors were examined by calculating the correlation matrix, which was further analyzed by means of hierarchical clustering [12,13], in order to define groups of uncorrelated signal parameters. The discrimination power of various combinations of the above listed descriptors was examined by means of the Wilk's λ and the final classification error.

The classification results for the three class problem, resulted in lower recognition rates compared to the two class problem, previously presented. The recognition rate varied between 70% and 85%, depending on the descriptors selection and the signals/patterns used for the training set. In all the cases, the classification error was due to confusion between signals of batch 1 with those of batch 3 and vice versa.

From the pattern recognition point of view, 15%-30% misclassification, is acceptable, considering the scattering of signals and the class overlapping. Furthermore the misclassification is observed between specimens categories with good fiber/matrix adhesion, which additionally exhibited minor differences on the mechanical tests.

CONCLUSIONS

The results obtained with the indirect measuring methods correlate well with the results obtained from direct measuring methods published in literature. Especially the transverse tensile test and the inplane torsion test yield acceptable results. Additionally these tests are standard available in most composite labs and are easy to conduct.

The method used for the non-destructive evaluation of the interphase properties is quite promising, since it is more sensitive compared to the standard mechanical destructive tests. By using signal processing and pattern recognition techniques it was possible to discriminate between batch 1 and batch 3, both exhibited comparable strength and stiffness properties. Although the preliminary results of experimentation in higher frequencies resulted in a different descriptor set mainly calculated from the autocorrelation domain, it is believed that such a frequency increase with the appropriate band pass filtering, assisted by an extensive discrimination study based on different classification schemes, will increase further the accuracy of the proposed method for the interphase characterization.

REFERENCES

1. Marotzke, C., Hampe, A., "Micromechanics of the Interface in Polymer Composites - Capabilities and Limitations of the Common Test Methods", *Proceedings of the Tenth International Conference on Composite Materials*, Whistler, British Columbia, Canada, August 14-18, 1995, Vol. VI: Microstructure, Degradation and Design, Poursartip, A. and Street, K.N., Eds, pp. 517-524
2. Michaeli, W., Kocker, K., "Fibre Bundle Pull-out Test for Thermoplastic Matrix Materials", *Proceedings of the Tenth International Conference on Composite Materials*, Whistler, British Columbia, Canada, August 14-18, 1995, Vol. VI: Microstructure, Degradation and Design, Poursartip, A. and Street, K.N., Eds, pp. 471-478
3. Schillemans, L., Van Hemelrijck, D., Anastassopoulos, A., et al., "Defect-identification in composite materials using pattern recognition techniques on ultrasonic data", *Advanced composite materials (Ed. H. Miyairi)*, VSP BV, Vol. 3, No. 3, 1993, pp. 51-57
4. Anastassopoulos, A., "Non Destructive characterisation of Damage in Composite Materials by Means of Pattern Recognition Techniques", Phd. thesis, Univ. of Patras, Mechanical engineering Dept., June 1995
5. Anastassopoulos, A., Van Hemelrijck, D., De Wilde, P., et al., "Defect Characterisation in Carbon-Epoxy Plates via Signal Processing and Pattern Recognition Analysis of Ultrasonic A-scan", *Ultrasonics International '93 conf.*, Vienna, Austria, July, 1993, pp. 835-838
6. Batchelor, B.G., "Practical Approach to Pattern Classification", 1974, Plenum Press.
7. Tou, J.T., Gonzalez, R.C., "Pattern Recognition Principles", 1974, Addison Wesley, Reading Massachusetts
8. Sinclair, A., "Analysis of the Ultrasonic Frequency Response for Flaw Detection: A technical Review", *Material Evaluation*, Vol. 43, 1985, pp. 105-107

9. Scholtens, B.J.R. and Brackman, J.C., "Influence of the Film Former on Fibre-Matrix Adhesion and Mechanical Properties of Glass-Fibre Reinforced Thermoplastics", *J. Adhesion*, Vol. 52, 1995, pp. 115-129
10. Rijdsdijk, H.A., Contant, M. and Peijs, A.A.J.M., "Continuous-Glass-Fiber-Reinforced Polypropylene Composites: Influence of Maleic-Anhydride-Modified Polypropylene on Mechanical Properties", *Composites Science and Technology*, Vol. 48, 1993, pp. 161-172
11. Van Hemelrijck, D., Sol, H., De Wilde, W.P., Cardon, A., et al., "Automatisation of C-scan data acquisition", *Proc. Cadcomp 90*, Computer aided design of composites, ed. W.P. De Wilde, W. Blain, C.A. Brebbia, Springer Verlag, April, 1990, pp. 315-324
12. De Roey, F., Van Hemelrijck, D., Schillemans, L., Daerden, I., Boulpaep, F., et al. "The application of automated ultrasonic inspection for damage detection and evaluation in composite materials", *Euromech 269*, Mechanical Identification of Composites (Ed. A. Vautrin, H. Sol), Elsevier Applied Science Publishers, Saint-Etienne, Dec. '90, pp. 415-423.
13. Anastassopoulos, A., Philippidis, T.P., Paipetis, S.A., "Failure Mechanism Identification in Composite Materials by Means of Acoustic Emission. Is it Possible?", *Proc. First Joint Belgian Hellenic Conference on Non Destructive Testing*, Eds. D. Van Hemelrijck and A. A. Anastassopoulos, A. A. Balkema, 1996, pp. 143-149.

A PROCEDURE FOR STUDYING DELAMINATION IN COMPLEX STRUCTURES

José Sancho

AIN. R&D Department. 31191 Cordovilla-Pamplona, Spain.

SUMMARY: When designing complex parts made out with laminated composites the problem of delamination is always present. Delamination studies are well known and today it is possible performing quite detailed analysis to obtain a full and accurate three dimensional stress field that lets the designer know about onset of delamination. Nevertheless, one of the most important problems to perform numerical analysis of the three dimensional stress field in composite materials, is the huge amount of computer resources required for these calculations. In most complex structures, this problem will make unfeasible performing these studies, being necessary performing destructive testing on prototypes to check the interlaminar shear strength of the structure.

To solve this problem, there are also some well known techniques as global-local approaches that can be used for designing with good results. From the engineer point of view, the problem that usually they are not implemented in commercial finite element codes so that engineers can not use them for everyday calculations.

KEYWORDS. delamination, finite element calculations, composite materials design, practical engineering design

INTRODUCTION

Composite laminated materials exhibit some particular behaviours that make them unique materials between all the used for engineering applications. From the very beginning of the development of these materials, mathematical theories to design structures were postulated, being one of the more classical ones the Classical Laminated Theory (CLT) [1, 2]. These initial theories were well fitted for most of the structures that were made with composite materials in those times. Nevertheless, with the popularisation of composites, new applications with higher stresses and much higher responsibility have been done up to now that primary structures in aircrafts, sportive cars, motorcycles, sporting equipment etc. are being made with composites [3-4].

Not only the responsibility of the structures has been incremented but also the complexity of the parts. In the beginning, most of the applications for composites were restricted to plates or quite simple parts platewise with very few problems for the nowadays designer. Usually the parts were not loaded to high so that some of the behaviours arising in structures highly loaded were not known.

It was in 1970 when Pipes & Pagano [5] solved a real three dimensional problem by means of finite differences and demonstrated the existence of interlaminar stresses in the vicinity of the free edges where equilibrium is not satisfied only by the stresses σ_x , σ_y , τ_{xy} appearing the so

called interlaminar stresses, namely interlaminar normal stress σ_z and interlaminar shear stresses τ_{xz} τ_{zy} . These stresses only appear (onset of delamination) when the structure is loaded so that the stress in some of the layers is close to the first ply failure strength for most of the materials and stacking sequences.

From that date, delamination has always been a subject of concern for the engineers dealing with composite design. Methods for solving the calculations are perfectly known as finite element analysis, nevertheless, to solve the three dimensional problem with finite element calculations is such a huge task that makes it unfeasible for most of the engineering problems. It is clear that new approaches for studying delamination should be developed to make these calculations affordable for the commercial finite element codes and computers currently available.

This paper presents two other possibilities, being the first one a technique of mesh transitions with couplings and constraining equations. In the areas where the mesh is not fully three-dimensional, simplifications on the material properties must be performed through the using of Classical Laminated Theory on equivalent groups of plies. These calculations can be performed in one or several shots depending on the knowledge that the designer has of the behaviour of the structure. A full three dimensional mesh with one element per layer in thickness can be made in the areas of interest while coarser meshes can be used in less loaded areas.

CLASSICAL LAMINATED THEORY AND EVOLUTION

The most known theory for calculating laminated composite structures is the CLT [6]. This theory is well established on the basis of both the hypothesis of plane stress in each one of the layers as in the Kirchoff one for thin plates, and it has been demonstrated to work perfectly with plates and platewise structures with a high length to thickness ratio. The basic set of equations for this theory is:

$$u(x,y,z) = u_0(x,y,z) - z \frac{\partial w_0}{\partial x}(x,y)$$

$$v(x,y,z) = v_0(x,y,z) - z \frac{\partial w_0}{\partial y}(x,y)$$

$$w(x,y,z) = w_0(x,y)$$

Being the coordinate system for the plate defined in the next figure:

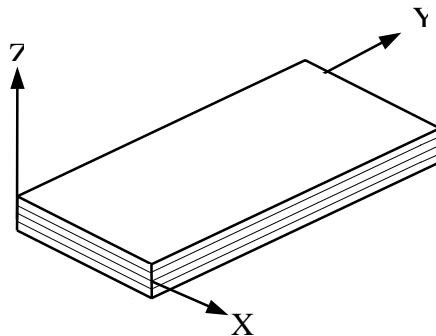


Fig.1 Model used in the Classical Laminated Theory

With CLT, in plane stresses σ_x , σ_y , τ_{xy} can be obtained but interlaminar stresses σ_z , τ_{xz} , τ_{zy} are not available as the assumption of keeping transverse cross sections perpendicular to the neutral axis of the plate has been made (Kirchoff hypothesis).

To solve this problem a number of higher order theories have been postulated. Most of them try to use the simplicity of the CLT while introducing more terms depending on the thickness, z , in a nonlinear way (exponents of z) to let the cross section of the laminate suffer deformations so that they do not need to finish perpendicular to the neutral axis in the deformed shape of the plate.

The general form of these higher order theories follow the next set of equations:

$$\begin{aligned} u(x,y,z) &= u_0(x,y,z) - z \frac{\partial w_0}{\partial x}(x,y) + u_3 z^3 + \dots + u_n z^n \\ v(x,y,z) &= v_0(x,y,z) - z \frac{\partial w_0}{\partial y}(x,y) + v_3 z^3 + \dots + v_n z^n \\ w(x,y,z) &= w_0(x,y) \end{aligned}$$

The more terms in z^n , the higher accuracy can be obtained in the interlaminar shear stresses τ_{xz} , τ_{zy} but the more degrees of freedom that are introduced in the set of equations. Many authors have presented their own theories that can be solved with expressions like the following one, presented by Murthy:

$$\begin{aligned} u &= u_0 + \left(\frac{5}{4}z - \frac{5}{3h^2}z^3 \right) \frac{12}{h^3} \int_{-h/2}^{h/2} uz dz + \left(\frac{1}{4}z - \frac{5}{3h^2}z^3 \right) \frac{\partial w_0}{\partial x} \\ v &= v_0 + \left(\frac{5}{4}z - \frac{5}{3h^2}z^3 \right) \frac{12}{h^3} \int_{-h/2}^{h/2} vz dz + \left(\frac{1}{4}z - \frac{5}{3h^2}z^3 \right) \frac{\partial w_0}{\partial y} \\ w &= w_0 \end{aligned}$$

Nevertheless, and although interlaminar stresses can be computed with good accuracy depending on the theory chosen, interlaminar normal stress σ_z is still out of the scope of the calculations. From experimentation and resolution of the true three dimensional state of stresses, it is known that interlaminar normal stress σ_z is responsible of most of the failures caused by interlaminar stresses so that it is very important including its calculation in the method used to design structures.

FINITE ELEMENT CALCULATIONS OF COMPOSITE MATERIALS

CLT is a very powerful tool for solving parts with a rather simple geometry. If the parts being designed are more complex or a higher precision is required in the analysis, Finite Element Method (FEM) should be used to perform the calculations. There are several steps increasing the complexity of the calculations to approach the real behaviour when designing composite structures with FEM.

Along the presentation of the different approaches for calculating composite structures, examples of results obtained using commercial codes MARC and ANSYS will be shown.

All the calculations are performed on a simple plate made out with T300/5208 carbon-epoxy with an stacking sequence of $[0/+45^\circ/-45^\circ/90]_s$ and a total thickness of 1 mm. The load

introduced is a deformation of 0.72% that will cause onset of delamination in the sample. Dimensions of the plate analysed are 120 mm. length and 30 mm. width [7].

Orthotropic material properties are included in the next table:

Table 1. Material properties used where all the values are expressed in GPa.

E_x	E_y	E_z	G_{xy}	G_{xz}	G_{yz}	μ_{xy}	μ_{xz}	μ_{yz}
181	10.3	10.3	7.17	7.17	4.13	0.28	0.28	0.51

Laminated Shell Approach

This is the simplest way of calculating composite structures by means of FEM. The structure must be modelled following its neutral axis to obtain a shell element model. Most of the software currently available allows the user to introduce offsets to simulate changes in the thickness of the laminate.

Basic theory to solve the problem is, again, the CLT although in most cases, a higher order theory is used so that normals to the centre plane in the undeformed configuration are supposed to remain straight although not necessarily normal to the centre plane in the deformed configuration.

ANSYS calculations are performed in this way so that interlaminar shear stresses τ_{xz} and τ_{zy} can be calculated. Besides that, an assumption to obtain a parabolic shear strain distribution is made. The basic matrix equations solved by this code are [8]:

$$\begin{Bmatrix} \{N\} \\ \{M\} \end{Bmatrix} = \begin{bmatrix} [E_0] & [E_1] \\ [E_1] & [E_2] \end{bmatrix} \begin{Bmatrix} \{\epsilon\} \\ \{\phi\} \end{Bmatrix}$$

In this expression, the submatrices $[E_0]$, $[E_1]$, and $[E_2]$ are computed as follows:

$$\begin{aligned} [E_0] &= \sum_{j=1}^{N_l} \int [T_m]_j^T [D]_j [T_m]_j \, dr \\ [E_1] &= \sum_{j=1}^{N_l} \int r [T_m]_j^T [D]_j [T_m]_j \, dr \\ [E_2] &= \sum_{j=1}^{N_l} \int r^2 [T_m]_j^T [D]_j [T_m]_j \, dr \end{aligned}$$

This equations are nothing else that the CLT but expresses in terms of FEM formulation in which the matrix $[T_m]$ is the layer to element transformation matrix and $[D]$ is the stress-strain law in each layer. All the integrals are performed between the lower dimension of each laminae and its upper dimension. The system of equations is formulated so at a global scale element by element not performing integration through thickness. This leads to a calculation of the interlaminar stresses based on the incremental form of the elasticity equations.

$$\begin{aligned} \frac{\partial \sigma_x}{\partial x} + \frac{\partial \tau_{xy}}{\partial y} + \frac{\partial \tau_{xz}}{\partial z} &= 0 \\ \frac{\partial \tau_{yx}}{\partial x} + \frac{\partial \sigma_y}{\partial y} + \frac{\partial \tau_{yz}}{\partial z} &= 0 \end{aligned}$$

Taking a look now to another commercial FEM code, MARC, it performs real integration through thickness, locating integration points inside each layer rather than on their interfaces. Number of integration points can be selected by the user [9].

Next figures show comparative results of interlaminar shear stress τ_{xz} between the interface of layer 2 and 3 from the calculations performed with ANSYS and MARC.

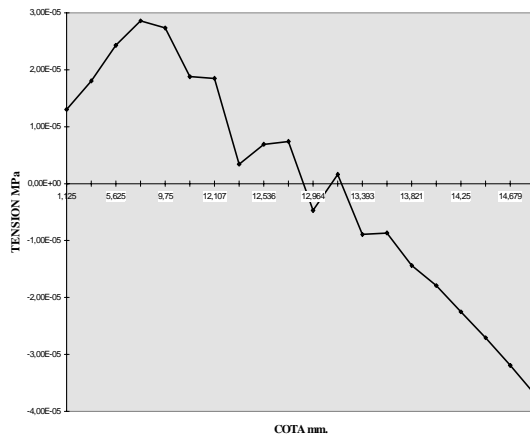


Fig. 2. Stresses τ_{xz} in the interface between layers 2 and 3 obtained with ANSYS

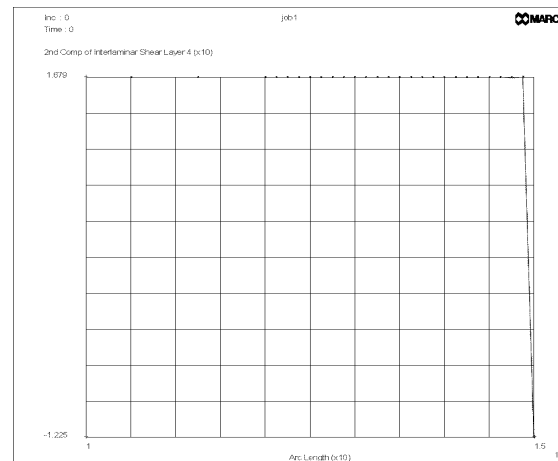


Fig. 3. Stresses τ_{xz} in the interface between layers 2 and 3 obtained with MARC

Full Three Dimensional Calculations

The opposite way to the laminated shell approach useful for calculating composite parts to know the real stress field, is performing a full three dimensional analysis with brick elements including at least one element in thickness for each layer. This procedure leads to very accurate results, nevertheless its computational cost is enormous. It should be beard in mind that interlaminar stresses usually appear in a dimension from the free edge that is similar to the thickness of the laminate. This means that the number of elements to be introduced in the vicinity of the free edges is very large. As FEM requires connectivity between nodes to ensure displacement continuity, the total mesh will have many thousands of elements even for very simple plates.

The next figures show the result of the calculations performed using ANSYS, where interlaminar normal stresses σ_z and interlaminar shear stresses τ_{xz} can be seen at different interfaces between layers of the material. These stresses have been evaluated at the integration points and they have been directly extrapolated to the nodes without performing any averaging [10].

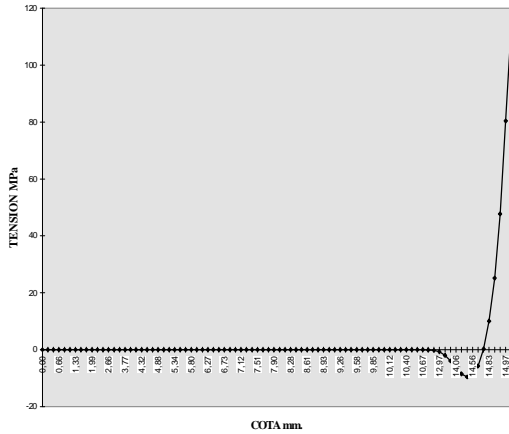


Fig. 4. Interlaminar normal stress in the symmetry plane

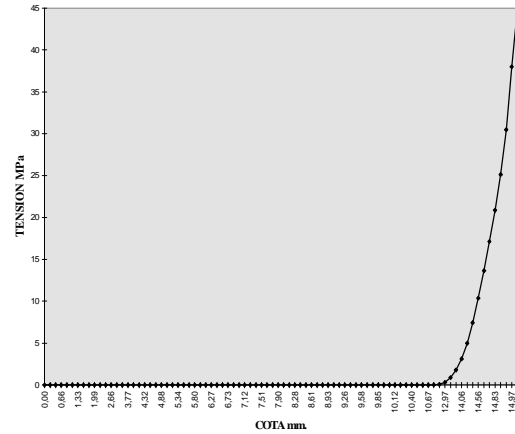


Fig. 5. Interlaminar shear stresses τ_{xz} in the interface 2-3 (+45°-45°)

This figures should be compared with the ones obtained by Pipes and Pagano and many other in Bibliography. This comparison shows that the shape of the stress distribution is the expected one.

Now, the same calculations are repeated but using the commercial FEM code MARC to check results between both of them. Results and FEM meshing can be seen in the next figures.

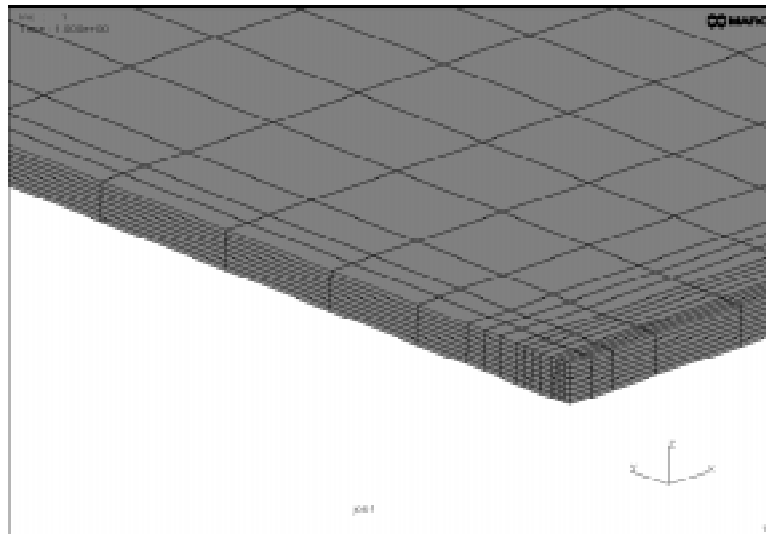


Figure 6. Detail of the FEM meshing performed with MARC

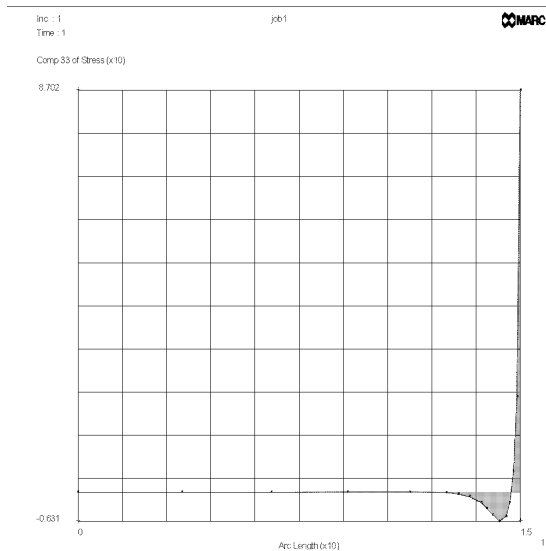


Fig. 7. Interlaminar normal stress in the symmetry plane

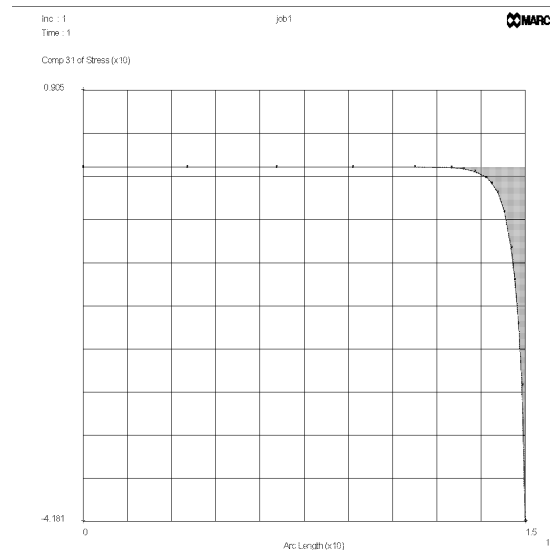


Fig. 8. Interlaminar shear stresses τ_{xz} in the interface 2-3 (+45°-45°)

Differences between both codes is small, as the calculations performed with ANSYS show maximum values of 112.82 MPa and 44.695 MPa for the interlaminar normal stress and the interlaminar shear stress respectively while in MARC, these stresses are 99 MPa for the interlaminar normal stresses σ_z and 42 MPa for the interlaminar shear stresses τ_{xz} .

Differences in the interlaminar normal stresses are caused by the different mesh density used in both models, and, more important, the stresses in MARC are in the nodes, so, extrapolation from the integration points has been performed producing the differences that can be seen in the results.

Results from these calculations are very accurate to calculate interlaminar stresses, nevertheless its cost is too high as to perform these analysis on real structures. This is the main reason why another approach should be followed if these kind of calculations must be done.

Three Dimensional Approach with Different Mesh Densities

It is perfectly known that interlaminar stresses are only a concern in several restricted areas of composite materials. Only in the vicinity of free edges, changes in the thickness of the structure, holes and damages or impacts problems caused by these out of plane stresses can be expected.

Performing normal FEM models have the problem that to ensure the mesh required in the areas of interest, and due to connectivity reasons, the mesh density in the entire model will be too high. A possible way to solve this problem is performing mesh transition between the area of interest and the rest of the model but this point will mean that tetrahedral will appear increasing the “numerical stiffness” of the structure and leading to a lack of accuracy in the calculations. Besides that, to have a reasonable mesh with tetrahedral, the number of elements must be much higher than meshing with hexahedra.

MARC commercial FEM code, specially devoted to non linear and contact calculation, has a very interesting possibility using contact [11]. With this possibility, a glued contact between two parts of a structure with different meshes can be performed. This means that a coarse mesh can be made in the area where stresses are not going to be a concern while a much finer

mesh can be made in the area where interlaminar stresses will appear. The basis of this method can be seen in the next figure.

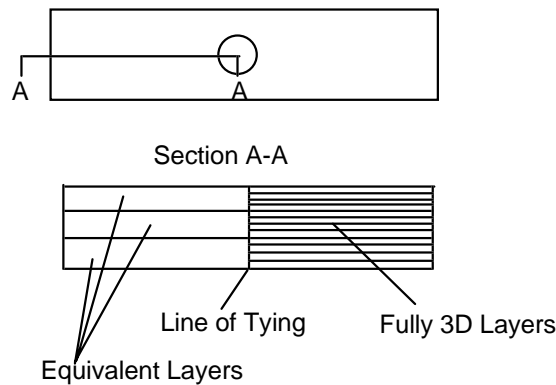


Fig. 9. Sketch of the calculations with mesh transition

In the case the analyst does not know beforehand the behaviour of the structure a first calculation performed with inexpensive laminated shell elements can be performed before starting with the full three dimensional calculations. After knowing the stresses an expansion of the dimension of the elements to obtain a full three dimensional model can be performed.

The area in which the elements are simulating a group of layers must be modelled with their equivalent properties or three dimensional layered brick elements must be used. If the first possibility is used, the group of layers must be symmetrical for being capable of having a subset whose properties are orthotropic. The way to obtain the equivalent layer material properties is through the CLT. Total stiffness matrix [A] or [D] for the group of layers must be formulated depending on the loads introduced to the laminate (the first for plane stress and the second for bending). This matrix is composed of three submatrices in the following form:

Engineering constants to be introduced in the equivalent single layer can be obtained, in the case of plane stress, from the normalized plane stiffness matrix [a*]. Terms in [a*] are calculated as [12]:

$$A_{ij} = \sum_{k=1}^N [\overline{Q}_{ij}] (h_k - h_{k-1})$$

$$[a] = [A]^{-1}; [a^*] = h[a]$$

In this expression, $[\overline{Q}_{ij}]_k$ is the stiffness matrix of each lamina k, referred to the plate axis, h is the total thickness of the laminate and h_k and h_{k-1} are the position of the upper face and the lower one for each layer referred to the center plane of the laminate. From here, engineering constants are obtained as:

$$E_1 = \frac{1}{a_{11}^*}, E_2 = \frac{1}{a_{22}^*}, E_6 = \frac{1}{a_{66}^*}$$

$$\mu_{21} = \frac{-a_{21}}{a_{11}}, \mu_{61} = \frac{-a_{61}}{a_{11}}, \mu_{62} = \frac{-a_{62}}{a_{11}}$$

$$\mu_{12} = \frac{-a_{12}}{a_{22}}, \mu_{16} = \frac{-a_{16}}{a_{66}}, \mu_{26} = \frac{-a_{26}}{a_{66}}$$

For the case of bending, equations are obtained in the same manner but substituting the matrix $[a^*]$ by $[d^*]$ that is computed from:

$$D_{ij} = \frac{1}{3} \sum_{k=1}^N [\overline{Q}_{ij}] (h_k^3 - h_{k-1}^3)$$

$$[d] = [D]^{-1}; [d^*] = \frac{h^3}{12} [d]$$

In the case of the laminate used in the example, there is an only possibility to obtain a single equivalent layer symmetrical, as is taking the full material as a layer. This means that the area far from the point of interest will have an only element in the thickness direction, while the full three dimensional mesh will have eight elements in thickness (one for each layer).

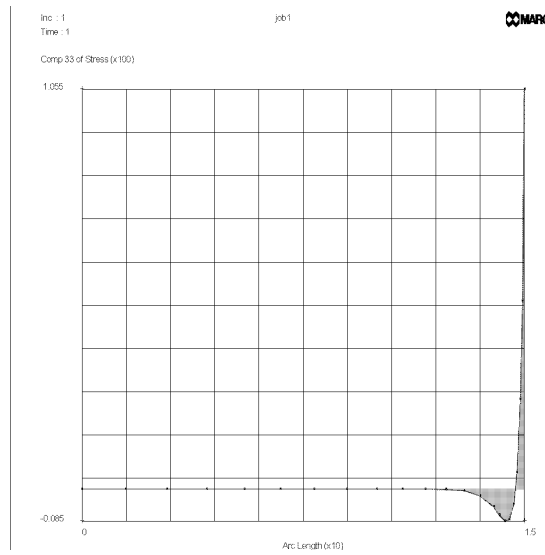


Fig. 10. Interlaminar normal stresses σ_z in the plane of symmetry with mesh transition

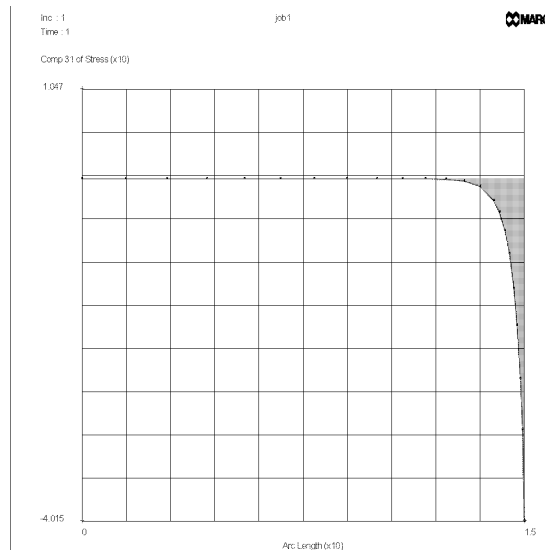


Fig. 11. Interlaminar shear stresses τ_{xz} in the interface 2-3 with mesh transition

A detail of the transition between the area with one element in thickness direction (equivalent single layer) and the full three dimensional mesh with one element for each layer can be seen in the next figure.

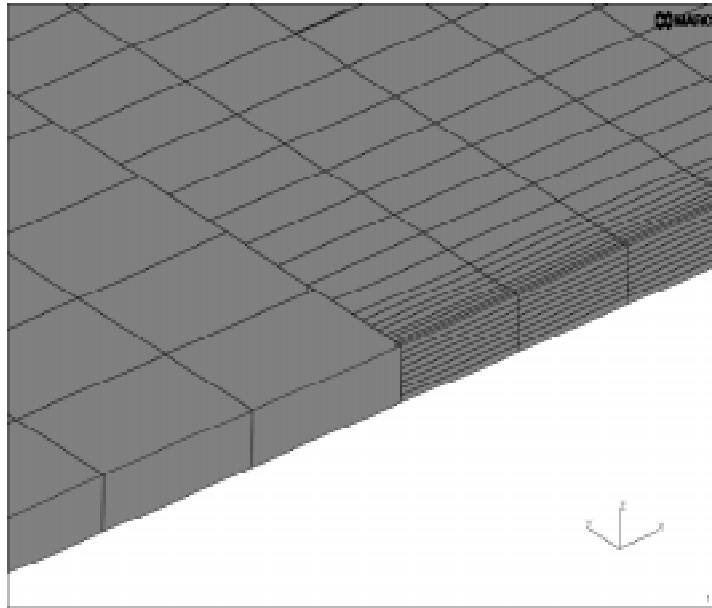


Fig. 12 Detail of the mesh transition

It can be seen how with this approach, interlaminar normal stresses σ_z obtained are 107.4 MPa while interlaminar shear stresses τ_{xz} are 40.15 MPa. These values should be compared with the ones obtained in previous three dimensional analysis to check the accuracy of this method.

Next table shows a summary of the results.

Table 2. Comparison of results

Calculation	σ_z (MPa)	τ_{xz} (MPa)
(1) ANSYS 3-D	112.82	44.695
(2) MARC 3-D	87	41.8
Difference (1)-(2)	22.8%	6.46%
(3) MARC contact	107.4	40.15
Difference (1)-(3)	4.8%	10.16%
Difference (2)-(3)	19%	3.95%

Submodelization Techniques

A second choice, or even better in coordination with previous approach of rigid contacts, as submodelization techniques are, can be used to perform simpler analysis using approaches not demanding so much resources, and performing a second detailed three dimensional analysis on the area where stresses are higher or delamination failures are suspected to appear. Besides that, this technique becomes a powerful tool if different codes are to be used in the analysis as it allows for an straightforward portability of the models provided adequate boundary conditions are computed in the cutting areas.

The basic idea of this procedure, proposed in ANSYS manuals [13], can be splitted into four main steps:

1. Performing a FEM analysis on a coarse inexpensive mesh.
2. Cutting and saving to a file the displacement field obtained in the boundaries of the area where a new model is to be made.
3. Meshing the new area with a finer mesh. This step can include transition between shell and solids if necessary.
4. Interpolation of the displacements saved to a file to apply them to the new nodes in the boundary of the remeshed area. After this, rerun the problem

Application of this procedure to the calculation of composite structures can be made as proposed in the next figure.

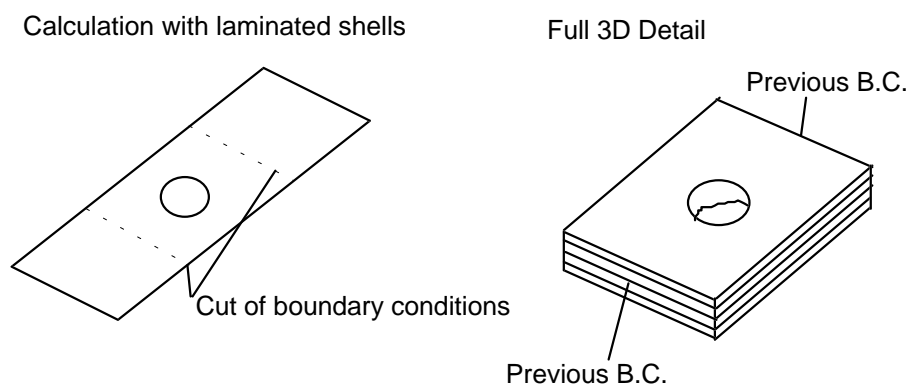


Fig.13 Sketch of submodelization

From the trials already performed by the author, the best approximation can be a mixture between the submodelization and the mesh transition. This is so because cutting of boundaries must not be performed too close to the area of interest to avoid Saint Venant effects. If cut is made far away of that zone, three dimensional mesh can be again too large to be solved in an economical way. So, if submodelization is made far away from the interesting area, followed by a mesh transition procedure with contacts, total number of degrees of freedom can be reasonable without penalising accuracy.

CONCLUSIONS

Along this paper, different possibilities for calculating the three dimensional stress field in composite structures has been shown. Two of the proposed techniques are very attractive to the designer as accurate results can be obtained without requiring too much computer resources for solving the set of equations.

REFERENCES

1. S. W. Tsai and H. T. Hahn. Introduction to Composite Materials. Ed. Technomic Westport CT. 1980.
2. R. M. Jones. Mechanics of Composite Materials. McGraw-Hill Book Company (Scripta Book Company). 1975
3. Michael C. Y. Niu. Composite Airframe Structures. Ed. Conmilit Press Ltd. Second Print Sept 1993
4. I. K. Partridge. Advanced Composites. Elsevier Applied Science. 1989
5. R.N. Pipes and N.J. Pagano. Interlaminar Stresses in Composite Laminates under Uniform Axial Extension, Journal Composite Materials, 4 (1970) 538
6. J. N. Reddy and A. Miravete. Practical Analysis of Composite Laminates. Ed.. CRC Press 1995
7. J. Sancho. Estudio de Fenómenos de Delaminación en Materiales Compuestos. Ier Congreso Nacional de Materiales Compuestos. Ed. F. París, J. Cañas. 1995
8. Peter C. Kohnke. ANSYS User's Manual. Vol IV Theoretical Manual. 1992. Swanson Analysis Systems 1993
9. MARC. User Information. Volume A. 1994 MARC Analysis Research Corporation
10. J. Sancho. PhD. Dissertation. University of Zaragoza. 1996.
11. A. Bout. Advanced Contact Analysis Using MARC. MARC Analysis Research Corporation. 1996.
12. S. W. Tsai and A. Miravete. Teoría del Diseño de materiales Compuestos. Secretariado de Publicaciones. Universidad de Zaragoza. 1992.
13. ANSYS User's Manual. Vol. I Procedures. Third printing Swanson Analysis Systems 1993.

CALIBRATION OF INFRARED STRESS MEASUREMENT TECHNIQUE FOR CFRP COMPOSITES AND ITS APPLICATION

Sunao SUGIMOTO¹ and Takashi ISHIKAWA²

¹Researcher and ²Section Head,
Airframe Division, National Aerospace Laboratory
6-13-1, Ohsawa, Mitaka, Tokyo, 181, Japan,

SUMMARY : Infrared stress measurement technique is applied as a method of non-destructive evaluation of composites with advantages of in-situ and non-contact nature. Thermo-elastic constants of unidirectional carbon fiber reinforced plastics (UD-CFRP) needed for quantitative measurements are obtained through the infrared stress graphic system. The theoretical thermo-elastic constants are derived through the basic equations and physical properties of constituent materials, which are compared with the experimental values. As a consequence, a reliability of the measured thermo-elastic constants is established and capability of this system for quantitative stress measurement is shown. It is also demonstrated that temperature dependency of a transverse coefficient of thermal expansion and a specific heat at constant stress of UD-CFRP cancel each other so as to decrease temperature dependency of the thermo-elastic constant. Other influential factors on measurements like a frequency effect are also examined.

KEYWORDS: thermo-elastic constant, non-destructive evaluation, coefficient of thermal expansion, specific heat, density, surface temperature, stress amplitude.

INTRODUCTION

The infrared stress measurement is a technique that the reversible temperature change at the surface of a body is measured precisely by an infrared sensor and it is transformed to the stress change. The temperature change is caused by the thermo-elastic effect, or in other words, coupled thermo-elasticity in adiabatic continua. Two experimental key points are to obtain a precise temperature signal in a very small amplitude and to correlate a temperature change to the applied force. The recent measurement system consists of a digital signal thermo-camera with graphic software as a core device. The system used here is referred to as an infrared stress graphic system (ISGS). This technique has been applied to metallic materials and composites not only as stress measurement but also as a non-destructive evaluation (NDE) method. It is featured by the following two intrinsic advantages, in-situ and non-contact natures. These advantages will be enhanced particularly in structural tests. A coefficient by which temperature change is transformed into stress, the thermo-elastic coefficient (TEC) so referred to here, is well established for metallic materials. In spite of its high expense as a NDE device, a few types of ISGSs have been spread gradually into applied mechanics fields.

Several efforts have been conducted for application of this technique to composites^{2)~4)}. It is known that the measured results for carbon fiber reinforced plastics (CFRP) laminates depend on almost solely transverse stress due to its orthotropic thermal expansion nature¹⁾. Therefore, there is no need to separate stress components and it is considered to be an advantage in composite measurement. However, the TEC in CFRP measurement is not as reliable as in metal, at least to the author knowledge. Once the TEC of CFRP is established, the measurement is considered to be easier than metal cases experimentally.

The aim of this paper is to raise a reliability of the TEC of uni-directional (UD) CFRP. For that purpose, the measured TEC through the used ISGS was calibrated using the governing formula and three basic material properties measured as accurately as possible. They are the coefficients of thermal expansion, the specific heat at constant stress and density, which govern TEC. The coefficients of thermal expansion were obtained by a thermal expansion measuring device using laser interferometry. Two other experimental check points, the dependency on loading frequency and the line accumulation numbers in the current ISGS as user's selection, were also examined. Consequently, the fundamentals of quantitative stress measurement technique for CFRP laminates are established.

SPECIMENS AND THE MATERIAL CONSTANTS

Table 1 Physical Property and V_f of Constituents of T400H/#3631

E_{fr}	187.0 GPa ^s	E_m	3.63 GPa [#]
$\kappa (=E_{fr}/E_{fz})$	0.084 ^{ss}	ν_m	0.38 ^{**}
ν_{frz}	0.3 [*]	α_m	$5.21 \times 10^{-5}/K$ ^{&}
$\nu_{fr\theta}$	0.42 [*]	ρ_m	$1.29 \times 10^3 \text{ kg/m}^3$ [#]
α_{fr}	$7.6 \times 10^{-6}/K$ [*]	$C_{m\sigma}$	$1.294 \times 10^3 \text{ Nm/(kgK)}$ ^{##}
α_{fz}	$-7.8 \times 10^{-7}/K$ [*]		
ρ_f	$1.82 \times 10^3 \text{ kg/m}^3$ [#]		
$C_{f\sigma}$	$0.7635 \times 10^3 \text{ Nm/(kgK)}$ [#]	V_f	0.577 ^{&}

^s Ref. 4); ^{ss} Estimated data from Ref. 4), 5); ^{*} Ref. 6).
[&] Measured data in this paper; ^{**} Ref. 6); 828 epoxy data.
[#] Ref. 7); ^{##} Ref. 7); #3900-2 epoxy data.

Specimens used in this paper were fabricated with preregs P1211-15: T400H carbon fiber / #3631 epoxy resin by TORAY Industries, Inc. Dimensions of specimens in mm were 220 x 25^w x 1^t for 0 UD- CFRP, 220 x 12.5^w x 6^t for 45 UD- CFRP and 200 x 25^w x 6^t for 90 UD- CFRP. Both ends of 0 UD-CFRP specimens were protected with tapered GFRP tabs whereas the 45 and 90 UD-CFRP specimens were not protected. In the measurement of the coefficients of thermal expansion, small blocks were cut out from the 0 and 90 UD-CFRP specimens so as to be about 10 mm in length. The both ends of these blocks were ground to be spherical in order to realize point contact to the optical interference plates. The length of blocks were measured precisely with a micrometer. Material constants of this T400H/#3631 system used in this paper are shown in Table 1. Note that some of these values were measured in this paper and the other values were taken from references as footnotes of the Table 1.

THE BASIC THEORY OF INFRARED STRESS MEASUREMENT

It is commonly known that a temperature change is caused by pressure variation in gaseous media under adiabatic conditions. In parallel to gas, it is also caused by stress in solid continua. However, since the temperature change is often very small in the case of solid, it

cannot be observed easily. The temperature change phenomenon in a elastic body under adiabatic conditions is referred to as the thermo-elastic effect in this paper. It is reasonably considered that the temperature change is a reversible process and is basically different phenomenon from the non-reversible temperature change with a visco-elastic nature and internal friction. In an isotropic body, the temperature change amplitude, dT , becomes proportional to the sum of principal stresses on the surface., $d\sigma_i$. However, in an orthotropic body, like CFRP, the basic constitutive equation and its coefficients have to be examined.

In the plane stress state, the temperature change in an orthotropic continuum as UD-CFRP by the thermo-elastic effect is described by Kageyama¹⁾ as the next equation:

$$dT = -\frac{T}{\rho \cdot C_\sigma} (\alpha_L \cdot d\sigma_L + \alpha_T \cdot d\sigma_T) \quad (1)$$

where

dT : Temperature variation amplitude by cyclic stresses,

T : Background temperature (in Kelvin),

ρ : Density,

C_σ : Specific heat at constant stress,

α : Coefficient of thermal expansion,

$d\sigma$: Cyclic stress amplitude,

and where the subscripts, L and T , indicate longitudinal and transverse directions, respectively. In order to simplify Eq. (1), two constants are defined as follows:

$$K_L = \frac{\alpha_L}{\rho \cdot C_\sigma} \quad (2)$$

$$K_T = \frac{\alpha_T}{\rho \cdot C_\sigma} \quad (3)$$

These K s are designated as thermo-elastic constants (TEC) connecting the temperature and the stress variation. Then Eq. (1) is rewritten as:

$$dT = -T(K_L \cdot d\sigma_L + K_T \cdot d\sigma_T) \quad (4)$$

The temperature variation by stress in the longitudinal direction is relatively very small value due to very small TEC in the longitudinal direction which will be examined again in this paper. Taking account of this fact, the measured stress change is almost governed by the transverse stress change on the surface of a body. Hence, Eq. (4) can be approximated into:

$$dT \cong -K_T \cdot T \cdot d\sigma_T \quad (5)$$

Namely, a measurement of the temperature change amplitude in time average provides the transverse stress change amplitude on the surface with an aid of K_T .

NOTES IN ACTUAL MEASUREMENT

In this section, the actual situation of the measurement through the present ISGS will be explained and some important remarks will be stated. A schematic illustration of the temperature and stress history is shown in Fig. 1 for the case of tensile loading. It should be noted first that the loading must be in constant frequency with a constant amplitude in order to obtain a precise time-average of a temperature amplitude. There exist a lower limit of

frequency to satisfy an eventual adiabatic condition, which will be mentioned later. It can be considered that the temperature change off the loading frequency caused by the background atmosphere or visco-elasticity does not affect the generated temperature change by a loading cycles as shown in Fig. 1.

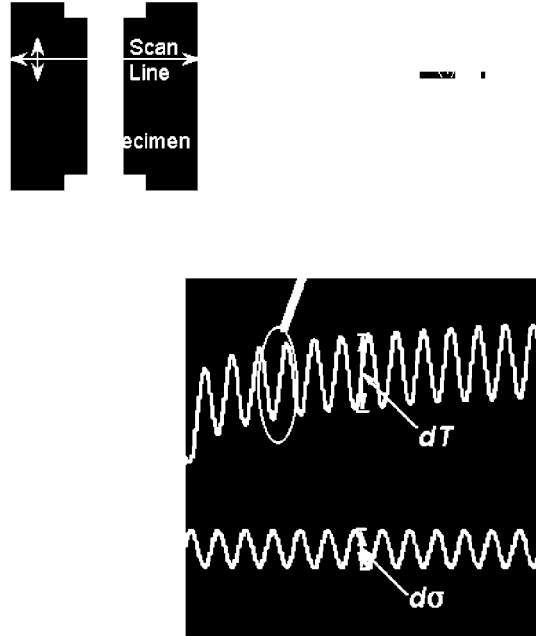


Fig. 1 Schematic Description of the Measurement in Temperature and Load Histories

The other purpose of this paper is to check this phenomena. The used ISGS system here was JTG-8000 made by JEOL Co. LTD in JAPAN. The surface of the specimens were painted in black in order to increase the infrared emission. This effect will be taken into account later. The temperature change was scanned in the horizontal direction by an oscillating mirror in 400 Hz in this system. It will be accumulated and averaged in order to improve a S/N ratio. This procedure is referred to as Line Accumulation in the present ISGS system. As a next procedure, a vertical scanning by the other oscillating mirror creates a two dimensional temperature distribution image of the object surface. This procedure is also repeatedly done for a better S/N ratio, being referred to as Frame Accumulation. Because a total measuring time is roughly governed by Frame Accumulation numbers and total accumulation number affecting quality of image is defined by a multiple of Frame and Line Accumulation numbers, the idea of Line Accumulation is conceived in order to reduce measuring time. Number of Line Accumulation is under operator's definition. He has to make an optimum trade-off between image quality and measuring time.

However, one important point of caution for quantitative measurement exists concerning this Line Accumulation number. An upper part of Fig. 1 should be referred for explanation of this situation where two examples of single (suffix 1) and four (suffix 4) Line Accumulation numbers are given. Suppose that the temperature change at a certain point on the scanned line becomes a sinusoidal curve as shown. Four times of accumulation are done in a loading cycle and an average is assumed to be a temperature peak (or bottom). In the actual measurement, temperature difference dT is determined by a digital operation in a system computer. So, if we compare dT for two cases, it can be understood naturally that dT_1 is always larger than dT_4 and that dT_1 should be maximal if the peak and bottom temperature points are correctly captured. Hence, single Line Accumulation number must be chosen in the system for

quantitative measurement. Although number 4 was erroneously used by the authors in the earlier measurement, those results were not used in the present quantitative discussion. The other point of caution for quantitative measurement is a simple factor, optical cleanness in the lens system for which periodical maintenance is required.

Because an actual procedure is going on as above in the system, the loading must be applied to the specimen in a manner of constant amplitude and frequency. Such loading can be applied by a hydraulic fatigue testing machine, Instron type 8501, of 100 kN capacity. Other loading conditions are tension-tension with 0.1 stress ratio and 5Hz sine wave. It should be also noted that a phase shift between stress peak and temperature bottom happens usually although an elementary theory tells us no phase shift. From the viewpoint of hardware, this system uses the feedback of the loading signals to determine the measurement timing. For the determining the actual phase shift, some preliminary trial is needed.

MEASURED RESULTS OF THE THERMO-ELASTIC CONSTANTS WITH UD-CFRP AND DISCUSSION

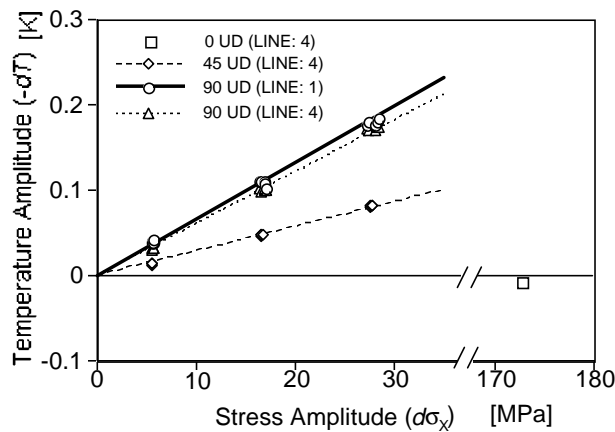


Fig. 2 Relationships between dT and $d\sigma_x$

The temperature change dT was measured by this system to define the TEC of CFRP under the stress $d\sigma_x$ under the loading limitation, where x denotes loading direction. The averages of surface temperature changes in a certain area defined out of the edge effect zone are plotted in Fig. 2 as a function of the applied stress for the 90 UD-CFRP specimens. Figure 2 contains both the previous results by 4 times Line Accumulations and the recent results by single Line Accumulation, which are indicated by subscripts (4) and (1), respectively. These results lead to the following relations between dT and $d\sigma$ through the least square method.

$$dT_{(4)} = -6.07 \times 10^{-9} d\sigma_T \tag{6}$$

$$dT_{(1)} = -6.58 \times 10^{-9} d\sigma_T \tag{7}$$

These relations and measured background temperature of $T=298[K]$ were substituted into Eq. (5) and the TECs were obtained as follows:

$$K_{T(4)} = 2.04 \times 10^{-11} [1/\text{Pa}] \quad (8)$$

$$K_{T(1)} = 2.21 \times 10^{-11} [1/\text{Pa}] \quad (9)$$

Because these values were obtained for the 90 UD-CFRP, Eq. (5) is considered to be exact. The 0 and 45 UD-CFRP specimens were also similarly measured in the same condition as previous series of test and their results are plotted in Fig. 2 for confirming approximation of Eq. (5). If the results of the 45 UD-CFRP are transformed into a transverse stress amplitude, an almost similar coefficient to Eq. (6) can be obtained. In the case of the 0 UD-CFRP, the following TEC, K_L , was obtained in the same manner as the 90 UD-CFRP owing to $d\sigma_T = 0$.

$$K_L = -1.16 \times 10^{-13} [1/\text{Pa}] \quad (10)$$

However, it is needed later that the K_T and K_L must be calibrated with infrared emissivity of the black paint on the surface of the specimens, for increasing infrared emissivity. In practical situations, the thermo-elastic effect of the 0 UD-CFRP are negligible due to the same order of measurement errors because of its material properties. Thus, the approximation of Eq. (5) is regarded as confirmed.

DETERMINATION OF THERMO-ELASTIC CONSTANTS THROUGH THE OTHER PHYSICAL ROUTE

The TECs were theoretically calculated in this section using the basic physical law and experimentally obtained material constants in order to validate the measured TECs by the

ISGS. If density, ρ , specific heat under constant stress, C_σ , and coefficients of thermal expansion, α_T and α_L , are known for UD-CFRP, the TECs, K_T and K_L , are obtained by substituting them into Eqs. (2) and (3). Physical properties, ρ and C_σ , of a UD-CFRP are given as follows if it contains no void and if all constituent ρ and C_σ are known:

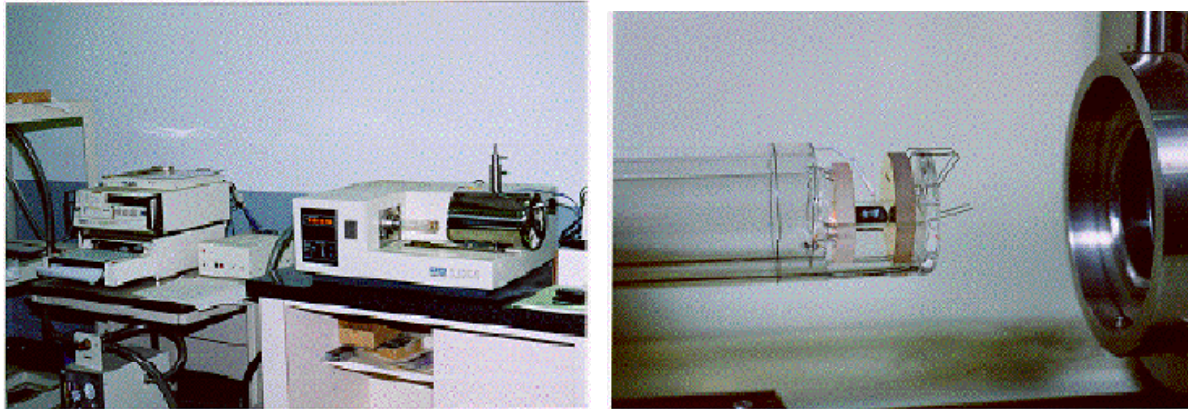
$$\rho = V_f \cdot \rho_f + (1 - V_f) \cdot \rho_m \quad (11)$$

$$C_\sigma = V_f \cdot C_{f\sigma} \cdot \frac{\rho_f}{\rho} + (1 - V_f) \cdot C_{m\sigma} \cdot \frac{\rho_m}{\rho} \quad (12)$$

where subscripts f and m denote fiber and matrix respectively. Instead of Eq. (11), the following value of ρ measured with small pieces cut out of the TEC specimens by using a precision balance, was adopted in the present calculation:

$$\rho = 1.5692 \times 10^3 [\text{kg/m}^3] \quad (13)$$

The physical property, C_σ , was also measured through a type of calorimeter, SH-3000 made by Shinku-Rikoh LTD, JAPAN, with an assistance of a specialist company. The obtained results of C_σ for two specimens are shown in Fig. 3 where a solid line indicates the average. Because the results show temperature dependency, the following value of C_σ at 25 °C is specified as the average between 20 °C and 30 °C, and employed in this paper:



a) Overview,

b) Detail around Specimen

Fig. 4 Pictures of Thermal Expansion Measuring Device by Laser Interferometry: LIX-1

$$C_{\sigma} = 9.77 \times 10^2 \text{ [Nm/(kgK)]} \quad (14)$$

If we admit the material properties in Table 1 and Eq. (13), the following C_{σ} is calculated only for a reference:

$$C_{\sigma} = 9.60 \times 10^2 \text{ [Nm/(kgK)]} \quad (15)$$

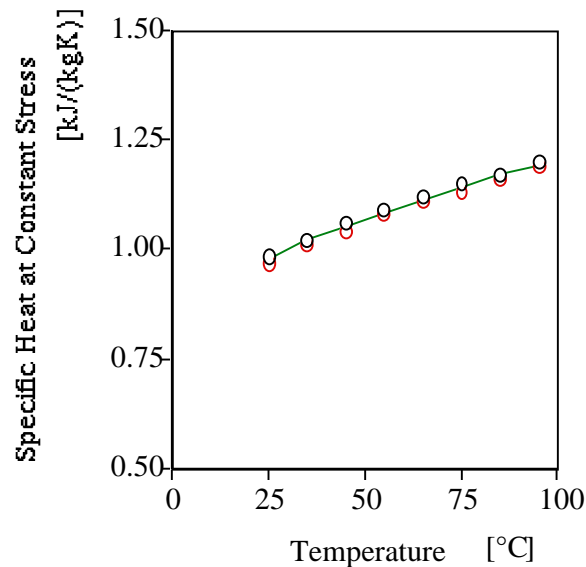


Fig. 3 Measured Results of Specific Heat for T400H/#3631 at Constant Stress

The rest material properties, α_T and α_L , are required to be precisely measured according to the above consideration, and some experimental details are described here. The used equipment was a thermal expansion measurement machine using laser interferometry: LIX-1 made by Shinku-Riko LTD., JAPAN. An overview picture of this machine and a specimen setting detail are shown in Fig. 4. The specimens were initially refrigerated below -10 °C by liquid nitrogen and heated over 100 °C at the rate of 3 °C/mm. The refrigeration was aimed to obtain precise dependency of CTE around the room temperature. Expansion of the specimens within each 10 °C was primarily obtained and it was transformed into the α_T and α_L . Values of α_T and α_L at the central temperature point of the segment were regarded as a representative in that segment. The obtained results of 90 UD-CFRP, α_T , are plotted by a symbol and the average of six specimens are indicated by a dashed curve in Fig. 5. The obtained data were

based on second and third measurement because a hygroscopic effect on CTE is expected strongly in the first heating. The α_L of 0 UD-CFRP were also obtained and plotted in Fig. 6.

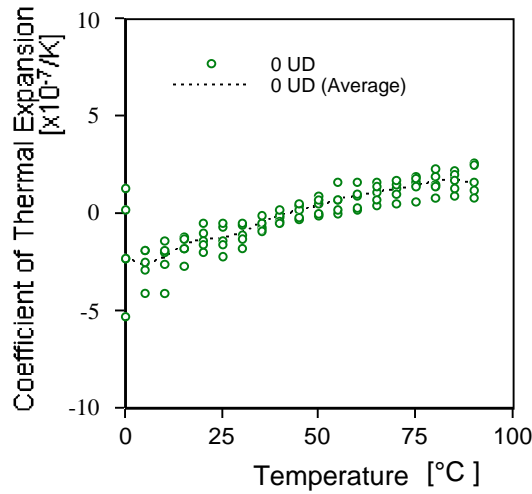


Fig. 6 Measured Results of CTE: 0 UD-CFRP

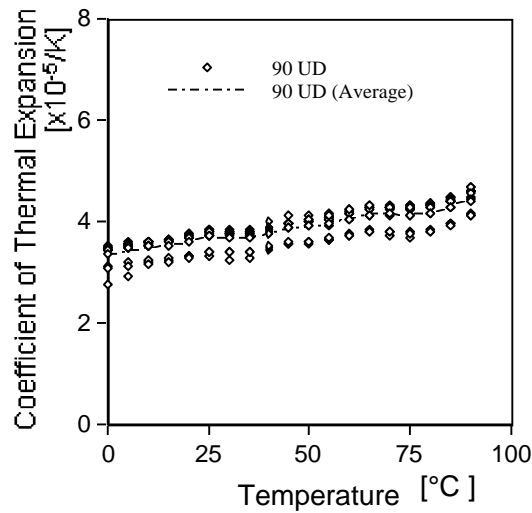


Fig. 5 Measured Results of CTE: 90 UD-CFRP

Because the temperature point at actual measurements of the TECs was 25°C, the values of α_T and α_L at 25 °C were determined as follows from Fig. 5:

$$\alpha_T = 3.680 \times 10^{-5} [1/K] \tag{16}$$

$$\alpha_L = -1.280 \times 10^{-8} [1/K] \tag{17}$$

If we substitute material properties of Eqs. (16), (17) and Table 1 into Eqs. (2), (3), (13) and (14), we have the following TECs:

$$K_T = 2.40 \times 10^{-11} [1/Pa] \tag{18}$$

$$K_L = -8.35 \times 10^{-14} [1/\text{Pa}] \quad (19)$$

In comparison with Eq. (9), Eq. (18) shows close but slightly larger value of K_T . One reason of this tendency can be ascribed to an influence of the emissivity on the surface at infrared stress measurement. It was already measured⁹⁾ that the used black paint has the emissivity value of 0.96 within the present infrared sensor range. The coefficient in Eq. (9) based on 1 Line Accumulation can be modified into the following value:

$$K_T = 2.30 \times 10^{-11} [1/\text{Pa}] \quad (20)$$

It is indicated that Eq. (20) is only 4 % lower than a value of Eq. (18). The result of 4 Line Accumulations does not agree so well with Eq. (18). Further pursuit of the reasons of the difference between Eqs. (18) and (20) is skipped in this paper. Some suspicious factors are nominated as: an imperfection in finding the ideal phase shift, irregularity in temperature variation and so on. From above discussions, it can be concluded at least that the K_T obtained by the infrared stress measurement system exhibits high reliability.

If we compare Figs. 3 and 5, it is clear that both α_T and C_σ show temperature dependencies and that they are expected to cancel out each other by virtue of Eq. (3). Actually, it is demonstrated that temperature dependency disappears in TECs as follows:

$$\alpha_T = 4.181 \times 10^{-5} [1/\text{K}] \quad (21)$$

$$C_\sigma = 11.53 \times 10^2 [\text{Nm}/(\text{kgK})] \quad (22)$$

These values give the following K_T :

$$K_T = 2.31 \times 10^{-11} [1/\text{Pa}] \quad (23)$$

We also need to examine temperature dependency of ρ . By CTE data, ρ at 80 °C is estimated to be only 0.4% smaller than at 25 °C, being negligible in Eq. (23). A trivial temperature dependency of K_T is an importance and an advantage for the quantitative infrared stress measurement around the room temperature.

On the other hand, Eq. (10) can be revised by taking account the infrared emissivity as follows:

$$K_L = -1.21 \times 10^{-13} [1/\text{Pa}] \quad (24)$$

If we compare this value with Eq. (19), it is found that an agreement seems not to be favorable. However, an order of discrepancy between two values is very small if we consider the both measurements were done at the fringe of assured accuracy of the testing systems.

COMMENTS OF OTHER INFLUENTIAL FACTORS FOR MEASURING THE THERMO-ELASTIC CONSTANTS

The infrared stress measurement was done under loading frequency of 5 Hz in this paper unless otherwise stated. The characteristics of loading frequency effect should be discussed here. Hence, the temperature changes were measured under various frequencies for 90 UD-CFRP and 45 UD-CFRP with the same loading amplitude. The results of these trials are shown in Fig. 7 with almost no effect around 5 Hz. Thus, it is verified that measurement at 5 Hz is appropriate. It should be noticed that the data in this figure are the results of 4 times Line Accumulations.

It is a well-known fact that there may be an influence of internal moisture on the coefficient of thermal expansion. For the examination of this influence, the TEC of 90 UD-CFRP was immediately measured after desiccation by a drier at 100 °C air for ten days. However, no clear evidence of the hygroscopic effect on the TEC could be found.

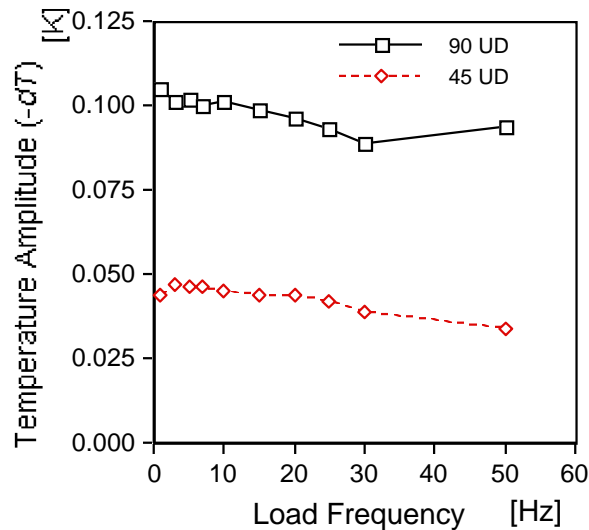
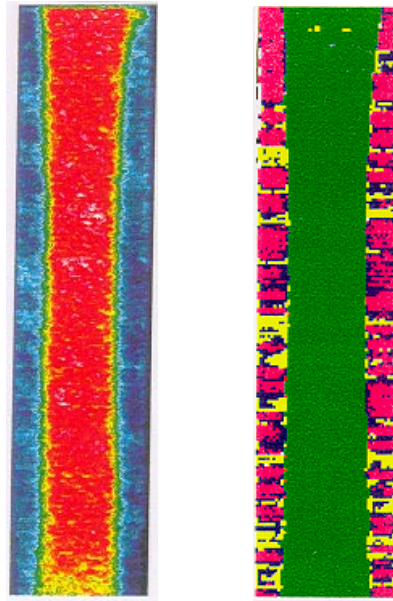


Fig. 7 Load Frequency Effects on Temperature Amplitude

APPLICATION TO DELAMINATION IN CF/EPOXY LAMINATE

Finally, an practical ISGS application of this to composite NDE is described in this section. Quasi-isotropic [(45/-45/0/90)sym.] coupon specimens of 8-ply of CFRP (T400/#3631) laminate were measured under tension - tension cyclic fatigue loading. Free edge delamination starts and propagates during loading for this type of laminates due to Poisson's ratio mismatch. The loading conditions used in the tests in this chapter are as follows; Tension-tension with stress ratio $R=0.1$, load control mode and constant amplitude sine wave of 5 Hz. All surface area of the specimen was inspected by the ISGS and also by a ultrasonic C-scanner at an appropriate interval of loading for comparison. Applied loading level during stress measurements was maintained at a lower level than delamination propagation critical in this area scan. When a ultrasonic C-scan inspection for monitoring delamination propagation is done, specimens were detached from the used hydraulic machine. For a trace purpose of rapidly changing delamination propagation by the ISGS, a line scan inspection was used to reduce a measurement time. It should be noted that measured stress is the stress at the surface normal to the fiber direction.



Stress Measurement C-scan Picture

Fig. 9 A Comparison Measured Stress Pattern with a C-scan Results for CF/Epoxy Coupon Specimen with Edge Delamination

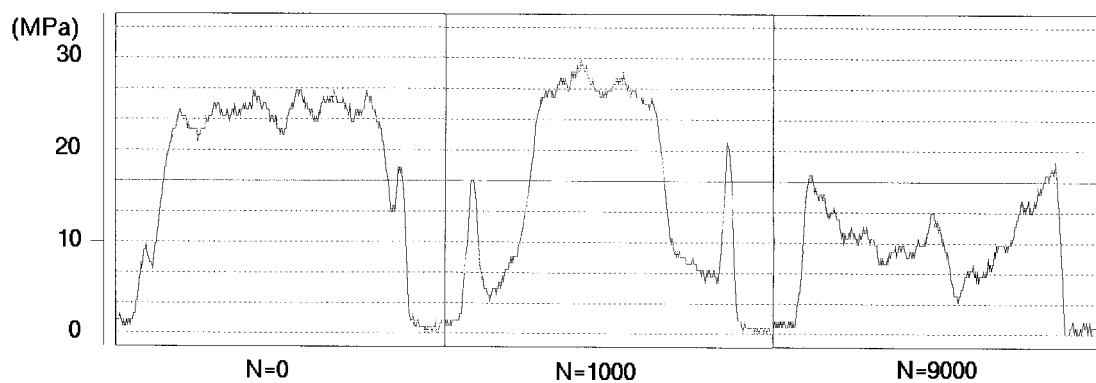


Fig. 8 Measured Results of Transverse Stress on top 45 Layer Surface

Delamination onset and propagation between 0/90 and alternately 90/0 were observed in this fatigue test. These delaminations develop as increasing loading cycles and stop with remained strip of delamination area of 1 ~ 2 mm width. Measured results of stress distribution transverse to the loading direction by the line scan are shown in Fig. 8. In order to clearly indicate C-scan edges and delamination tips symbols of | and ▲ are used in Fig. 8, respectively.

The measured stress pattern obtained by the area scan agrees well with a ultrasonic C-scan delamination image as indicated in Fig. 9. The fact that free edge delaminations liberate surface stresses well plays a key role for such a good correlation. The true delamination pattern in experiments was alternate appearance between in 0/90 and 90/0 interface as mentioned earlier. It can be recognized that width of initial stress plateau is decayed corresponding to delamination propagation and that stresses drop at delamination edges. The stress drop moves inside as the delamination propagates. As a summary, this ISGS system can be used at least as an in-situ mean of non-destructive evaluation for composite laminate if internal damage clearly affects the surface stress state.

CONCLUSIONS

Reliability of TECs for infrared stress measurement is examined and established in comparison with calculated TECs using experimentally determined coefficient of thermal expansion, density and specific heat at constant stress. An excellent correlation between calculated and experimental TECs is achieved if infrared emissivity factor is introduced. Such reliability is required for a quantitative stress measurement of CFRP laminates by using the infrared stress measurement. It is demonstrated that quantitative stress measurement of CFRP by the infrared stress measurement is possible. Also, it is found that the temperature dependency of both the coefficients of thermal expansion and specific heat at a constant stress cancel out each other even at 80 °C. It is a very important advantage for the present stress measurement. No effect of moisture inside the specimens, and insensitivity to loading frequency over 5 Hz were also verified in the present technique. Measurements in one Line Accumulation must be done in order to obtain quantitative result by this system.

ACKNOWLEDGMENT

The authors greatly appreciate a supply of specimens of neat #3631 resin by Mr. J. Matsui of TORAY Co. LTD. They also acknowledge the material data given by Mr. K. Itoh of TORAY Co. LTD.

REFERENCES

1. Kageyama, K., "Application of Infrared Stress Graphic Measurement for FRP (in Japanese)", Journal of Japan Society for Materials science, Vol. 26 No. 1, 1989, pp. 16-21.
2. Ishikawa, T., Sugimoto, S., Matsushima, M. and Hayashi, Y., "Some Experimental Findings in Compression-After-Impact (CAI) Tests of CF/PEEK (APC-2) and Conventional CF/Epoxy Flat Plates", Composite Science and Technology, Vol. 55, 1996, pp. 349-363.
3. Sunao Sugimoto and Takashi Ishikawa, "Application of Infrared Stress Graphic System to Non-Destructive Evaluation of Composites", Proceedings of the 7th J-US Conference on Composite Materials, Kyoto, Japan, June, 1995, pp. 327-334.
4. Ishikawa, T., Matsushima, M. and Hayashi, Y., "Longitudinal Material Nonlinear Properties of Unidirectional Carbon Composites (in Japanese)", Journal of Japan Society for Composite Materials, Vol. 12, No. 1, 1986, pp. 8-15.
5. Ishikawa, T., Koyama, K. and Kobayashi, S., "Elastic Moduli of Carbon Composites and Carbon Fiber (in Japanese)", Journal of Japan Society for Aeronautical and Space Sciences, Vol. 23, No. 263, 1975, pp. 678-684.
6. Ishikawa, T., Koyama, K. and Kobayashi, S., "Thermal Expansion Coefficients of Unidirectional Composites", Journal of Composite Materials, Vol. 12, No. 2, 1978, pp. 153-168.
7. Private communication from TORAY Co. LTD.

8. DUN, S. A., "Analysis of Thermal Condition Effects on Thermoelastic Temperature Measurements for Composite Materials", Transaction of the ASME; Series E (Journal of Applied Mechanics), Vol. 59, No. 9, 1992, pp. 552-558.
9. JEOL Co. LTD., "The Principle of the Infrared Graphic System: Theoretical Manual. (in Japanese)", 1988.

CONTINUOUS MONITORING OF RESIN CONTENT IN COMPOSITE PREPREG NARROW TAPES

Huang Yudong , Liu Li , Zhang Zhiqian and Liu Lixun

*Department of Applied Chemistry 410, Harbin Institute of Technology
Harbin 150001, P.R.China*

SUMMARY: The resin content is the critical factor to ensure the quality of the finished composites product. In response to the need for NDT procedure which can provide immediate information concerning resin content, we have undertaken research to develop a β -ray system that is capable of determining the resin content in the narrow prepreg tape with a width of 3-5mm on-line during unidirectional narrow tape impregnation process by presenting the data in a convenient and useful form. Using a system based on the difference of intensity attenuation with the diversity of resin content in prepreg, we have measured the GF/Epoxy, CF/Epoxy prepreg tapes. A series of calibration curves has been generated to evaluate the resin content in the same prepreg respectively. A good agreement with resin content has been shown by the β -ray system and the conventional weight method. The maximum deviation of resin content is approximately three percent, which indicates β -ray monitoring system is fit to measure the resin content in prepreg tapes.

KEYWORD: resin content, on-line monitoring, prepreg, β -ray monitoring system, intensity attenuation, NDT, composites

INTRODUCTION

Composites have steadily grown due to high strength-to-weight ratio and the requirement for quality assurance is increasing. The uniform resin distribution in prepreg is indispensable in ensuring the quality of the finished composites. Currently there are three basic methods to measure the resin content: solvent wash, acid digestion, and burn off. Generally, the sample is weighed when the resin is removed by the chemical action, combustion, and burn off. Then, the remaining fibers are weighed. From these data, the weight percentage of resin is calculated. Since these methods exhibit some disadvantages such as the high cost of disposing chemical wastes, health and safety concerns associated with the chemicals used, a lack of uniformity from operator to operator, and excessive time required to perform these tests, it can be concluded that NDT method must be improved. NDT methods that can overcome the disadvantages of current destructive methods, including the X-radiography, Eddy-current testing, photometer method, X-ray diffractometer technique[1,2], ultrasonic technique[3,4], and β -ray monitoring technology[5], etc., must be practiced. The β -ray measuring technology is the most effective means to determine the resin content on line.

Conventionally, the β -ray monitoring technology displays the amount of intensity transmitting from some features in the sample as a function of thickness over the sample. In practice, as far as the prepreg is concerned, the resin content is directly related to thickness if the fiber linear density is constant. Namely, it is expected the thickness of prepreg will increase as more resin is applied. Therefore, by using this approach, it is possible to determine the resin content in

prepreg narrow tape. The theory to establish the β -ray measuring system is that the intensity is attenuated when β -particles penetrate the prepreg. Consequently the attenuation corresponds to the exponential principle:

$$I = I_0 e^{-\mu\rho x} \quad (1)$$

where, I_0 and I are the intensities of before and after β -particles penetrating the sample respectively; μ is the material's absorption coefficient; ρ is the density of the measured material; x is the thickness of the measured material.

The method applied to the β -ray measuring system records the variation in intensity (I/I_0) due to β -particles penetrating prepreg tape. These parameters are then correlated to the resin content determined by the weight method in order to establish calibration curves for a set of different prepreg tapes. The calibration curves are subsequently used to safely evaluate the resin content in unknown samples of the same type.

EXPERIMENT

Experiment Instrument

The experimental instrument include a standard β -ray generator and a scintillation detector (which consists of a scintillate, a photo multiplier tube and an amplifier) and a computer, shown in Fig. 1.

Measurement of Dry Fiber

The first step in the experimental phase is to ascertain the extent of fluctuation of the linear density in dry fibers. The long fibers are continuously passed through the space between the β -ray generator and the detector. The β -ray intensity after transmitting the sample is recorded. Then, compared with the initial intensity I_0 , the attenuation quantity is calculated.

On-line Measurement of Resin Content

To measure the variation of the resin content in prepreg tapes on line, it is essential to install the β -ray measuring system in front of the take-up block during unidirectional narrow tape impregnation process. A pair of pressure rolls whose middle position dived a gap with a width of 4 mm is placed in front and in back of this system to ensure prepreg width being precisely 4mm. The effect of width on the accuracy of measurement is the most critical factor. A series of prepreg tapes of different resin content for the GF/Epoxy, CF/Epoxy have been measured using this system on-line. At the same time two calibration curves are established on the basis of the measured parameters.

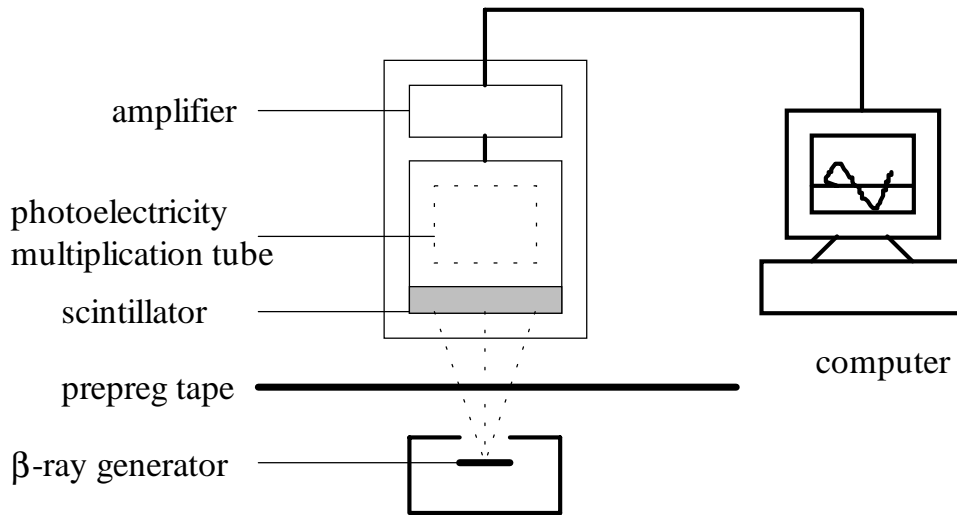


Fig. 1: the schematic diagram of β -ray monitoring system

Weight Method Measurement on Resin Content

The conventional weight method, a type of destructive measurement, is utilized to determine the resin content in above prepreg tapes. The prepreg tape with a length of 20mm accurately cut from the continuous tape is weighed and the resin content is calculated, provided that the fiber linear density is constant.

RESULTS AND DISCUSSIONS

To measure the resin content, the linear density of fiber is first analyzed. The results are listed in Table 1 and 2. From the data in Table 1, we find that the standard deviation is approximately 0.14 percent and the confidence relative deviation is only 0.2 percent, on the condition that the confidence degree is 90 percent and sample size is ten. This indicates that the distribution of GF is uniform, and ensures that the variation of intensity attenuation in the β -ray measuring system manifests the fluctuation of resin content in GF/Epoxy prepreg tapes. The same results are obtained in Table 2 about the CF. Moreover, we note that the extent of variation with the intensity attenuation due to the fiber passing through the measuring system varied significantly for different material systems. Since the densities of fiber vary, there should be a difference in the relationship between the intensity attenuation and the thickness for different fiber system, i.e., the fiber's density. So it is imperative to establish different calibration curves for each sample system. The experiment is based on the fact that the fiber linear density is constant. In cases where the fiber linear density dose vary, a solution would be to install another β -ray measuring system to determine the intensity attenuation aroused by the fiber before the fiber impregnating resin.

Table 1: the statistical analysis of GF density

I [KHz]	I/I ₀	W _f [g/m]	mean of W _f [g/m]	Standard deviation	Confidence interval	Confidence relative standard deviation
61.9	0.993	0.518	0.5184	1.35E-3	[0.5177,0.5191]	0.2%
61.0	0.980	0.520				
61.4	0.986	0.549				
61.6	0.989	0.517				
62.2	0.997	0.517				
62.1	0.996	0.517				
62.1	0.996	0.520				
61.8	0.992	0.520				
61.9	0.993	0.520				
62.0	0.994	0.517				

Table 2: the statistical analysis of CF density

I [KHz]	I/I ₀	W _f [g/m]	mean of W _f [g/m]	Standard deviation	confidence interval	Confidence relative standard deviation
71.8	0.792	0.953	0.9524	1.51E-3	[0.9515,0.9533]	0.19%
71.9	0.793	0.955				
71.6	0.789	0.951				
71.8	0.792	0.952				
72.0	0.794	0.953				
72.1	0.796	0.952				
71.7	0.790	0.951				
71.9	0.793	0.954				
72.0	0.794	0.950				
72.3	0.798	0.953				

where the confidence interval is calculated on the condition that the confidence degree is 90 percent and sample size is ten.

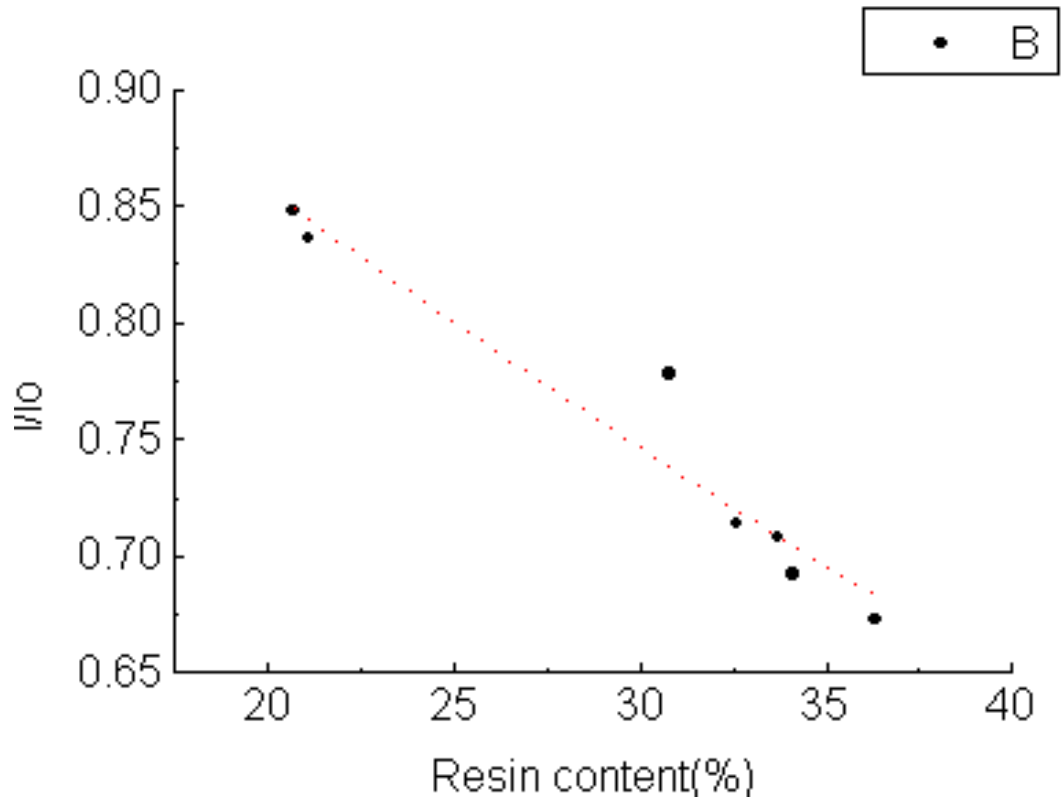


Fig 2: The calibration curve for GF

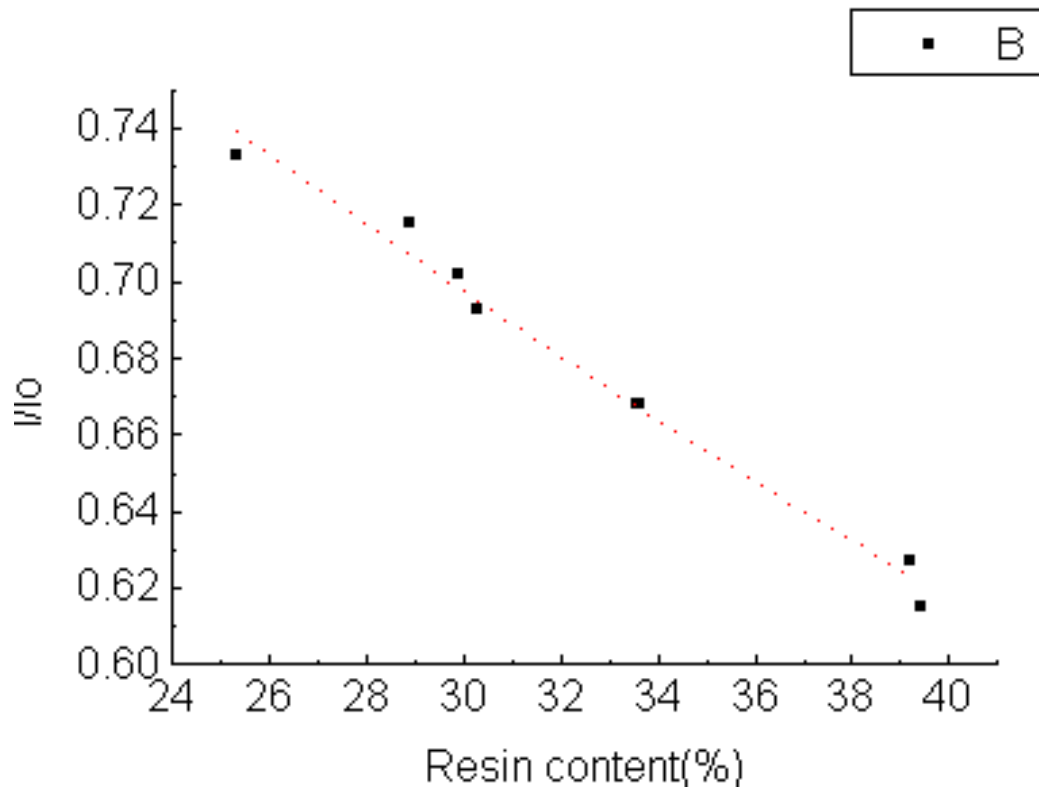


Fig.3: The calibration curve for CF

There are potential problems with using this system for resin content measurement related to the dependence of the thickness on fiber linear density. Keeping fiber linear density constant over the entire range of resin content has been done to ensure that changes in thickness could be correlated with variation in resin content. Based on this, a series of calibration curves, intensity attenuation (I/I_0) versus resin content determined with the weight method have been established for prepreg tapes with the different reinforcement, as shown in Fig.2 and 3.

By observing both calibration curves, the correlation coefficient in both figures is beyond 0.99, which is used reliable in evaluating the resin content in prepreg with the same type.

The Table 3 and 4 list the values of resin content determined by both the conventional weight method and the calibration curves. The maximum deviation is 2.8% for GF/Epoxy and 3.3% for CF/Epoxy by comparing the value in resin content determined with two measurement methods. It shows the β -ray monitoring system may, in comparison, accurately determine the resin content in prepreg tape and its results are more reliable. However, it must be noted that the sample's flutter, when going through the monitoring system, greatly affected the measurement precision since the sample's width contrasted to the β -ray generator may possibly change, and a part of β -particles directly come into the detector. So it is essential to minimize the flutter in the sample in order to precisely measure resin content.

Table 3: the analysis of resin content in GF/Epoxy prepreg tape

W_p	R%	I/I_0	R'%	relative deviation
0.292	28.9	0.75	29	0.3%
0.298	30.3	0.744	30	0.1%
0.305	31.9	0.720	33.0	3.4%
0.309	32.6	0.715	33.4	2.5%
0.322	35.5	0.682	35.0	1.4%
0.323	35.7	0.678	35.7	2.0%

Table 4: the analysis of resin content in CF/Epoxy prepreg tape

W_p	R%	I/I_0	R'%	relative deviation
0.272	29.9	0.695	29.0	3.0%
0.274	30.4	0.692	29.9	1.6%
0.277	31.2	0.690	30.9	1.0%
0.281	32.2	0.673	33.1	2.8%
0.284	32.9	0.659	34.0	3.3%
0.286	33.4	0.655	34.2	2.1%

where R% is the resin content determined by the weight method; R'% is that determined by comparing the calibration curve.

As far as the prepreg tape system is concerned, it consists of fiber and resin that adequately absorb β -particles, i.e., the intensity attenuation detected in the prepreg tape arises from two compounds acting together. Exponential parts of the equation may be displaced by:

$$\mu^p \chi = \mu_m \rho_m \chi_m + \mu_f \rho_f \chi_f \quad (2)$$

The subscripts, m and f, separately stand for the resin and fiber. The equation may be shown as :

$$I/I_0 = e^{-\mu_m \rho_m \chi_m - \mu_f \rho_f \chi_f} \quad (3)$$

If the fiber linear density is constant, the intensity attenuation due to the fiber action may be constant K, then the equation is written as :

$$I/I_0 = Ke^{-\mu_m \rho_m \chi_m} \quad (4)$$

Taking advantage of the least square method, the absorption coefficient of resin is computed as 0.014 for the GF/Epoxy and 0.012 for CF/Epoxy.

Since within the system itself there exists a certain deviation such as the variation in the output intensity including the initial intensity (I_0) and the attenuated intensity (I), we will analyze the effects of these factors on the resin content.

First, presuming the initial intensity (I_0) is steady, we will consider that the variation in I contributes to the deviation of the resin content ($\rho_m \chi_m$). The change of I is written as:

$$dI/I_0 = Ke^{-\mu_m \rho_m \chi_m} (-\mu_m) d(\rho_m \chi_m) \quad (5)$$

i.e.,

$$dI / I = (-\mu_m) d(\rho_m \chi_m) \quad (6)$$

When the variation in I is 1 percent, the deviation of resin content will reach the 3.3 percent for the general purpose since the absorption coefficient (μ_m) range is at 0.01, which is not fit to determine the resin content. Due to the general demands, the relative deviation in resin content is about 1.0 percent and the weight percentage of resin content in prepreg tapes is 30, the relative variation to be under 0.3 percent is needed. The same results may be acquired presuming the I is consistent but the initial intensity (I_0) changes.

In other words, we will discuss the effect on the value of resin content when the absorption coefficient (μ_m) deviates if the β -ray measuring system is steady. According to the equation (4), we can write the relationship between the change in μ_m and the deviation in resin content as:

$$\frac{d(\rho_m \chi_m)}{d\mu_m} = - \frac{K'}{\mu_m^2} \quad (7)$$

Where $K' = \ln(KI_0/I)$. In the light of the equation (7) and the μ_m range at 0.01, that the slight change of absorption coefficient (μ_m) will product the serious error for evaluating the resin content may be turned out. So the measured prepreg tapes must be wholly consistent with

those used for calibration curve since μ_m is the most important factor to affect the measurement result.

CONCLUSION

In conclusion, β -ray measuring system measures the parameters that are correlated highly with resin content, with the thickness being primary parameter. The slight deviation due to the combination with the weight method and the exponential deviation is acceptable. Moreover, by comparison with other measurement methods for resin content, it isn't essential to cut the sample from the roll, but directly measure resin content on line, which is very important to the manufacture of the prepreg tape.

REFERENCES

1. Prakash, R., "Non-Destructive Testing of Composites", *Composites*, No. 10, 1980, pp. 217-224.
2. Teagle, P.R., "The Quality Control and Non-destructive Evaluation of Composite Aerospace Components", *Composites*, Vol. 14, No. 2, 1983, pp. 115-128.
3. Ma, G.L. and Campbell, M.D., *Advanced Composite Material: New Development and Application Conference Proceedings*. Sept. 30- Oct.3, 1991, pp. 377-381.
4. Smith, D.R. and Monson, J., "An Evaluation of Ultrasonic Technique for Measurement Resin Content in Prepreg Materials", *22nd International SAMPE Technical Conference*, Nov., 1990, pp. 237-251.
5. Molyneux, M., "An Instrument for the Non-destructive Determination of Fiber/resin Ratio in Fiber-reinforced Composite Prepreg Materials", *Composites*, Vol. 14, No.2, 1983, pp. 87-91.

THERMAL RESIDUAL STRAIN MEASUREMENT IN A COMPOSITE REPAIR ON A CRACKED ALUMINUM STRUCTURE

A. M. Albat¹, D. P. Romilly² and M. D. Raizenne³

¹ *Department of Mechanical Engineering, University of British Columbia,
2324 Main Mall, Vancouver, British Columbia, V6T 1Z4, Canada*

² *Department of Mechanical Engineering, University of British Columbia,
2324 Main Mall, Vancouver, British Columbia, V6T 1Z4, Canada*

³ *Institute for Aerospace Research, National Research Council of Canada,
Ottawa, Ontario, K1A 0R6, Canada*

SUMMARY: This paper reports results related to thermally induced and process generated residual strains present in a repaired structure consisting of boron/epoxy patches bonded to a cracked aluminum specimen using FM 73M. To measure residual strains within the aluminum and boron/epoxy materials, 44 strain gauges were installed in eight locations at different interfaces of one bonded repair during patch construction and application. The stress free temperature was determined for the repair and found to be well below the curing temperature of 121°C. At room temperature, thermal residual strain magnitudes up to 690 $\mu\epsilon$ in the aluminum and -710 $\mu\epsilon$ in the boron/epoxy patch were measured. In addition, process induced strains were found to be present in the aluminum and oriented perpendicular to the boron fibers. The thermal residual strains present in the bonded repair were also investigated as a function of temperature and indicated a significant change in slope above 90°C.

KEYWORDS: thermal residual strain, residual strain, bonded repair, crack patching, aircraft, film adhesive, boron, aluminum

INTRODUCTION

In the application of composite patches to aluminum aircraft structures, consideration must be given to the residual strain distribution introduced during the repair process. In most composite repairs, the underlying structure is heated locally during the curing process. The unheated surrounding structure will restrain the expansion of the heated area, which leads to a lower effective coefficient of thermal expansion (CTE) for the repaired substructure. In addition, the supporting structure of an aircraft frame will limit the out-of-plane bending and resulting curvature of a single sided repair, which is also caused by the difference in CTE. The magnitude of the thermally induced residual strains (referred to subsequently as thermal residual strains) is therefore dependent upon the difference in the coefficient of thermal expansion between the composite and aluminum as well as the heating and support conditions [2,4].

In contrast to real structure conditions, most materials and procedures are tested using specimens which are typically uniformly heated during the curing process and permitted to expand with little or no restraint (Fig. 1). The key is to understand the relationship between the constraint conditions of the test specimen relative to those of the damaged aircraft structure such that the thermal residual strains can be accounted for properly in the determination of the margin of safety.

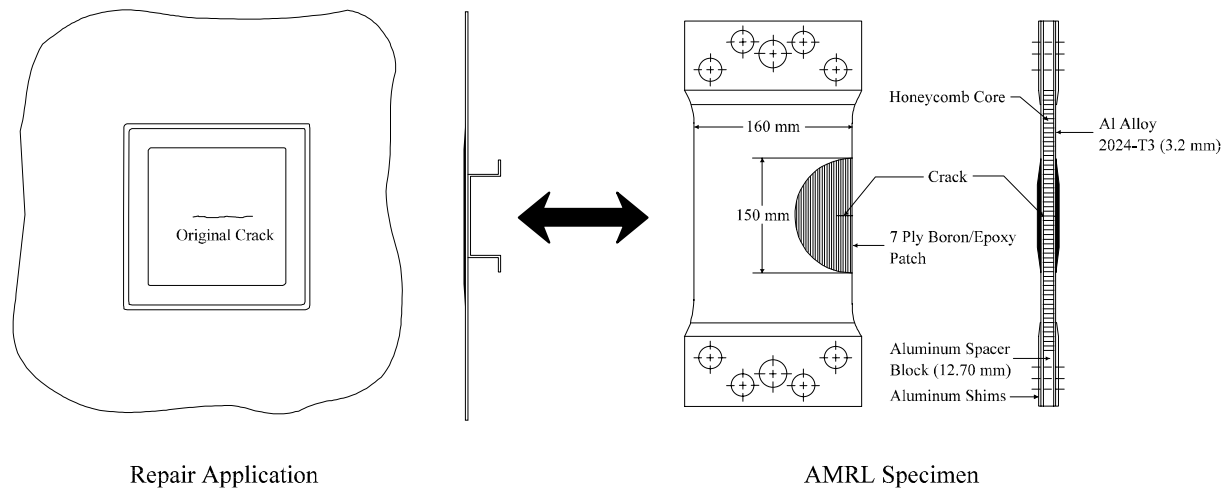


Fig. 1: Small Scale Test Specimen for Composite Repairs [3]

A significant effort has been made through a joint research project between the University of British Columbia (UBC) and the National Research Council of Canada (NRC) to improve the knowledge and potential effect of residual strains induced by the elevated temperature cure in bonded repairs. The magnitude of these residual strains will not only affect the crack propagation life component of a bonded repair, but will also influence the time required for re-initiation of a fatigue crack in the metallic substructure, especially in the presence of a corrosive environment. Although thermal residual strains are the primary focus of this work, the total residual strain due to the elevated temperature cure of any bonded repair consists of both thermal and process induced residual strains, the latter resulting from effects such as anisotropic shrinkage of the patch or adhesive, temperature gradients in the specimen during processing, temperature gradients due to tooling and internal resin flow [6]. While thermal strains are affected by subsequent changes in temperature, process induced residual strains may not be affected. This paper will discuss the results obtained from experimental measurements of residual strain for the bonded repair specimen shown in Fig. 1.

EXPERIMENTAL PROCEDURES

AMRL Test Specimen

The sandwich type specimen (Fig. 1) used in this investigation, which limits out-of-plane bending due to the honeycomb structure, was developed previously by the Aeronautical and Maritime Research Laboratory (AMRL) in Australia. A specially designed fixture employed for the assembly and curing process allowed free in-plane expansion to occur during the cure. Boron/epoxy 5521/4 prepreg, FM 73M film adhesive with a nominal weight of 300 g/m^2 , precracked 2024-T3 aluminum alloy sheets with a thickness of 3.175 mm and HEXCEL honeycomb 3/16-5052-.002 were selected as materials for the specimen. A total of 44 metal

foil strain gauges were employed to monitor the thermal residual strains and total residual strains due to the elevated temperature cure at several locations of the composite repair on one of the two patched face-sheets of the specimen (Fig. 2). Four locations were chosen based on previous documentation which indicated failure initiation sites of the bonded repair occurring around the crack in the aluminum as well as at the tapered end of the patch [1,5]. Within the patched region, strain gauges were placed on each side of the aluminum face-sheet, on top of the adhesive, between the first and second boron/epoxy plies and on top of the patch. In addition, two rosettes were placed outside the repair section on the aluminum face-sheet. Careful planning of the gauge positions and lead wire routing (Fig. 2) was performed to minimize distortions of the true strain distribution.

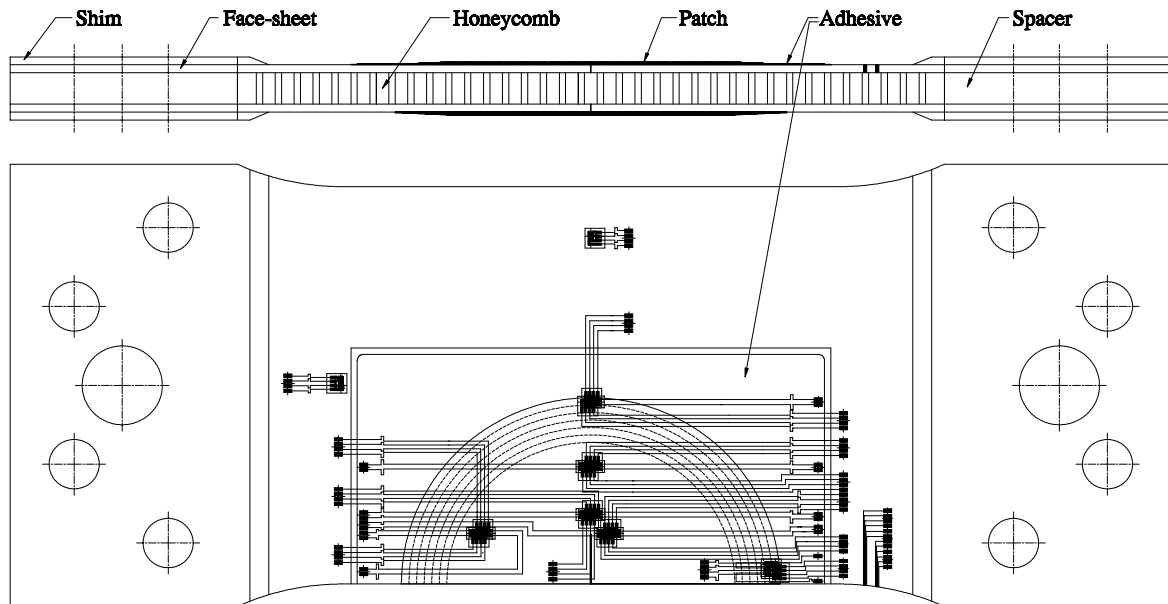


Fig. 2: Instrumented AMRL Specimen

Specimen preparation was divided into five steps: 1) preparation of the face-sheets, 2) gauge mounting on the face-sheets, 3) patch manufacturing including gauge placement, 4) specimen assembly and 5) final gauge installation. First, the aluminum face-sheets were precracked to a crack length of 20 mm. Surface treatment of the aluminum for the bonding process consisted of clad removal, grit blasting with size 220 aluminum oxide grit, a silane treatment and subsequent application of BR 127 primer. Six two-element (90°) and two three-element strain gauge rosettes were then installed in the patch section on both sides of the aluminum face-sheet.

The seven boron/epoxy prepreg plies for each patch were cut in a semi-circular shape with the fiber orientation parallel to the straight edge. The plies were tapered using a 3 mm step between successive plies. The longer outer plies were placed over the inner shorter during lay-up. To minimize distortion of the true strain field, only single element gauges with two 34 gauge lead wires were embedded within the patch. The cocured layer of FM 73M was extended to a rectangular-shape extending beyond the semi-circular shaped seven plies of boron/epoxy prepreg to permit terminal placement and connection of the lead wires, thus avoiding the need to handle the fine diameter lead wires after curing. The patch was C-scanned and X-rayed to check for disbonds and to verify the strain gauge locations after curing at 121°C and 345 kPa pressure.

The bottom of the patches were then grit blasted prior to specimen assembly, which removed a thin layer of the cocured FM 73M. The specimen was then assembled in the aluminum fixture. Single layers of FM 73M were used for bonding the patches to the aluminum. The assembled specimen in the fixture was then cured in the autoclave at 121°C with 345 kPa pressure. In total, 28 gauges were installed at this stage. After removal and clean-up, spacers and shims were installed in the grip region using the room curing adhesive HYSOL EA 9396.

The last step in the instrumented specimen preparation process was the installation of eight, two-element (90°) strain gauges on top of the instrumented patch and outside the repair section. A maximum of two gauges were installed at any one time using M-Bond 610, resulting in the need for four curing cycles. To limit the influence of thermal cycling, the strain gauge glue was cured at 100°C. A final post-cure was then carried out at 107.2°C, which was the highest temperature anticipated for the thermal experiments. This completed the installation of the 44 strain gauges.

Stress Free Temperature

Determination of the thermal residual strains at room temperature requires knowledge of the stress free temperature at which no thermal residual strains are present. In order to determine the stress free temperature for the current application, one identical patch was bonded to a 152.4 mm x 152.4 mm aluminum alloy sheet using one layer of FM 73M. The residual strains caused a significant curvature in the aluminum sheet. To determine the stress free temperature (assuming that process induced strains are negligible in the fiber direction), the specimen was heated until the specimen returned to its initial straight condition in the fiber direction.

This measurement was carried out using a Blue M industrial oven equipped with a Microtrol controller. The specimen was supported with a flat steel bar and a pin (Fig. 3). A halogen light was used to clearly indicate the presence of any gap existing between the curved aluminum sheet and the flat steel bar.

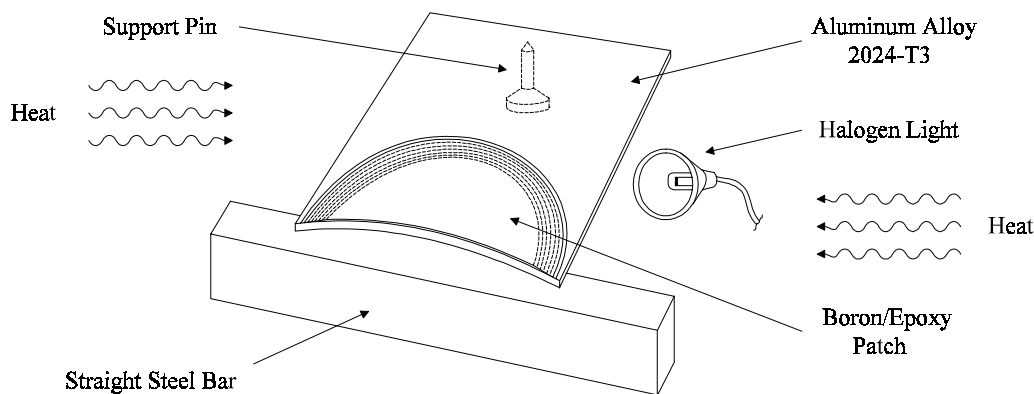


Fig. 3: Stress Free Temperature Measurement Setup

Both the oven and aluminum sheet temperatures were monitored using thermocouples. At 101.25°C, with both the specimen and oven being in thermal equilibrium, the single-side patched aluminum sheet was straight along the supported edge. This experimental set-up had an estimated potential error of 1.5°C based on the stated assumptions (i.e. potential resolution error of 0.5°C + potential temperature measurement error of < 1°C using listed device specifications).

Residual Strain Measurement Procedure

To determine the magnitude of the total residual strains introduced during curing requires knowledge of the strain state both prior to and after completion of the thermal cycle. The strain state prior to curing was obtained using two Vishay 2310 signal conditioning amplifiers, one each for the 120 Ω and 350 Ω quarter bridge configurations. At this point, 120 Ω and 350 Ω precision resistors, respectively, were used in the quarter bridge to zero the two signal conditioning amplifiers. The precision resistors were then removed and replaced by the mounted strain gauges, one gauge at a time, with the indicated resistance change (i.e. strain) being recorded. Since cocuring of the one layer of FM 73M with the seven boron/epoxy plies had introduced some residual stresses in the patch itself (as indicated by the slightly curved patch), the patch was vacuum bagged against a flat aluminum plate for the initial strain recordings to provide a repeatable and representative measurement condition both pre- and post-cure. While this flat patch geometry was representative of the pre-curing setup in the autoclave, it should be noted that the peel ply on the bottom of the patch was not removed for this measurement to protect the bonding surface from contamination. After curing, this measurement condition (including temperature conditions) was maintained and the strain measurement recording procedure repeated. The total residual strains induced during the curing cycle were then determined by calculating the difference in the pre- and post cure strain measurements.

Thermal Residual Strain Measurement Procedure

To quantify the thermal residual strains within the repaired specimen, it was decided to heat the specimen up to the stress free temperature. However, accurate determination of the thermal residual strains in the bonded repair required the measurement of not only thermal strains in the AMRL specimen, but also measurement of the thermal strains for an additional aluminum and a cured boron/epoxy specimen as shown by equations (1) and (2) below.

$$\epsilon_{Al \text{ Thermal Residual}}|_T = \epsilon_{Al}|_{T=\text{Stress Free Temp.}} - \epsilon_{AMRL}|_{T=\text{Stress Free Temp.}} - \epsilon_{Al}|_T + \epsilon_{AMRL}|_T \quad (1)$$

$$\epsilon_{B/Ep \text{ Thermal Residual}}|_T = \epsilon_{B/Ep}|_{T=\text{Stress Free Temp.}} - \epsilon_{AMRL}|_{T=\text{Stress Free Temp.}} - \epsilon_{B/Ep}|_T + \epsilon_{AMRL}|_T \quad (2)$$

In addition, to determine the actual strain experienced by each of the different installed strain gauges, one identical gauge of each type was mounted on a titanium silicate bar having a coefficient of thermal expansion of only $0.03 \pm 0.03 \times 10^{-6}/^\circ\text{C}$. The difference in indicated strain between an identical gauge mounted on a specimen and on the titanium silicate bar thus represents the actual thermal strain in the specimen according to equation (3) below:

$$\epsilon_{\text{Specimen Thermal}}|_T = \epsilon_{\text{Specimen (Indicated)}}|_T - \epsilon_{\text{Titanium Silicate (Indicated)}}|_T \quad (3)$$

The temperature of the AMRL specimen and the titanium silicate bar were both measured using bonded thermocouples. Three-wire strain gauge bridge configurations providing thermal compensation were installed between the terminal blocks mounted on the specimens and the data acquisition system. Measurements of resistance change per $^\circ\text{C}$ and per mm of lead wire length between the strain gauge and terminal blocks were obtained from a lead wire resistance specimen and were subsequently used for strain data correction. To minimize thermal shock, the instrumented AMRL specimen together with the titanium silicate bar and the lead wire resistance measurement specimen were wrapped in breather cloth and covered

with a thin aluminum foil. The same protection was provided for the instrumented aluminum and the boron/epoxy specimens. A Schlumberger Orion datalogger utilizing a high stability, dual current technique allowed simultaneous acquisition of temperature, wire resistance and strain gauge data. To avoid any potential heating effects due to power dissipation at the strain gauge sites, only gauges within a single interface (i.e. ply, layer, etc.) were measured during any single test.

The difference in thermal conductivity and mass between the AMRL and titanium silicate specimens caused a significant difference in the rate of temperature change. Therefore it was decided to establish thermal equilibrium between the specimens and the oven temperature at 21°C (room temperature), 50°C, 80°C and 107°C. The measurements were carried out both during the heating and cooling portions of the thermal cycles. Approximately two hours were required to achieve thermal equilibrium at each of these specified temperatures. To confirm repeatability of the results, measurements were repeated for 12 gauges. For comparison, measurements were also obtained using a 3 fold increase in heating and cooling rates.

All of the recorded strain measurements were subsequently corrected for gauge factor changes due to temperature, lead wire resistance as well as temperature-induced lead wire resistance change, and transverse strain sensitivity for rosettes. The transverse strain sensitivity was estimated to have very little effect on the thermal residual strains for the single element gauges mounted in the boron/epoxy patch (on the order of 0.1%).

RESULTS AND DISCUSSION

The corrected results obtained for the thermal residual strains and the total residual strains due to the elevated temperature cure are presented in Fig. 4. The thermal residual strains were calculated based on the temperature difference between the measured stress free temperature (101.25°C) and 21°C. It should be noted that the thermal residual strains are averaged results based on data obtained from the heating and cooling cycles as well as repeated measurements. Holding for extended periods of time at elevated temperatures caused detectable strain due to creep in the bonded repair, especially perpendicular to the fiber direction (on average < 20 $\mu\epsilon$ with maximum of 90 $\mu\epsilon$ at the tapered end in 55 minutes at 80°C). Very little strain hysteresis due to creep was measured when the experiment was carried out at higher heating and cooling rates without holding at the elevated temperatures. Based on this evidence, the thermal residual strain measurements recorded were corrected for creep while holding at elevated temperatures.

The thermal residual strains for the aluminum within the center section of the repair (specimen locations 'B', 'C', 'D' and 'H') vary in fiber direction of the patch between 491 $\mu\epsilon$ and 686 $\mu\epsilon$ with an average of 541 $\mu\epsilon$ (standard deviation of 14%). The total residual strains due to the elevated temperature cure are very close to this result with an average of 546 $\mu\epsilon$ (standard deviation of 16%), which indicates that process induced strains present are essentially negligible in this direction. In contrast, the total residual strain average due to the elevated temperature cure measured in the aluminum perpendicular to the fiber direction of the patch at these same locations (-164 $\mu\epsilon$ with a standard deviation of 44%) is significantly higher in compression than the thermal residual strain average of -111 $\mu\epsilon$ (with a standard deviation of 20%) indicating that process induced strains are substantially higher in this direction. Unfortunately, the possibility of residual strain relaxation during the first few thermal cycles cannot be verified.

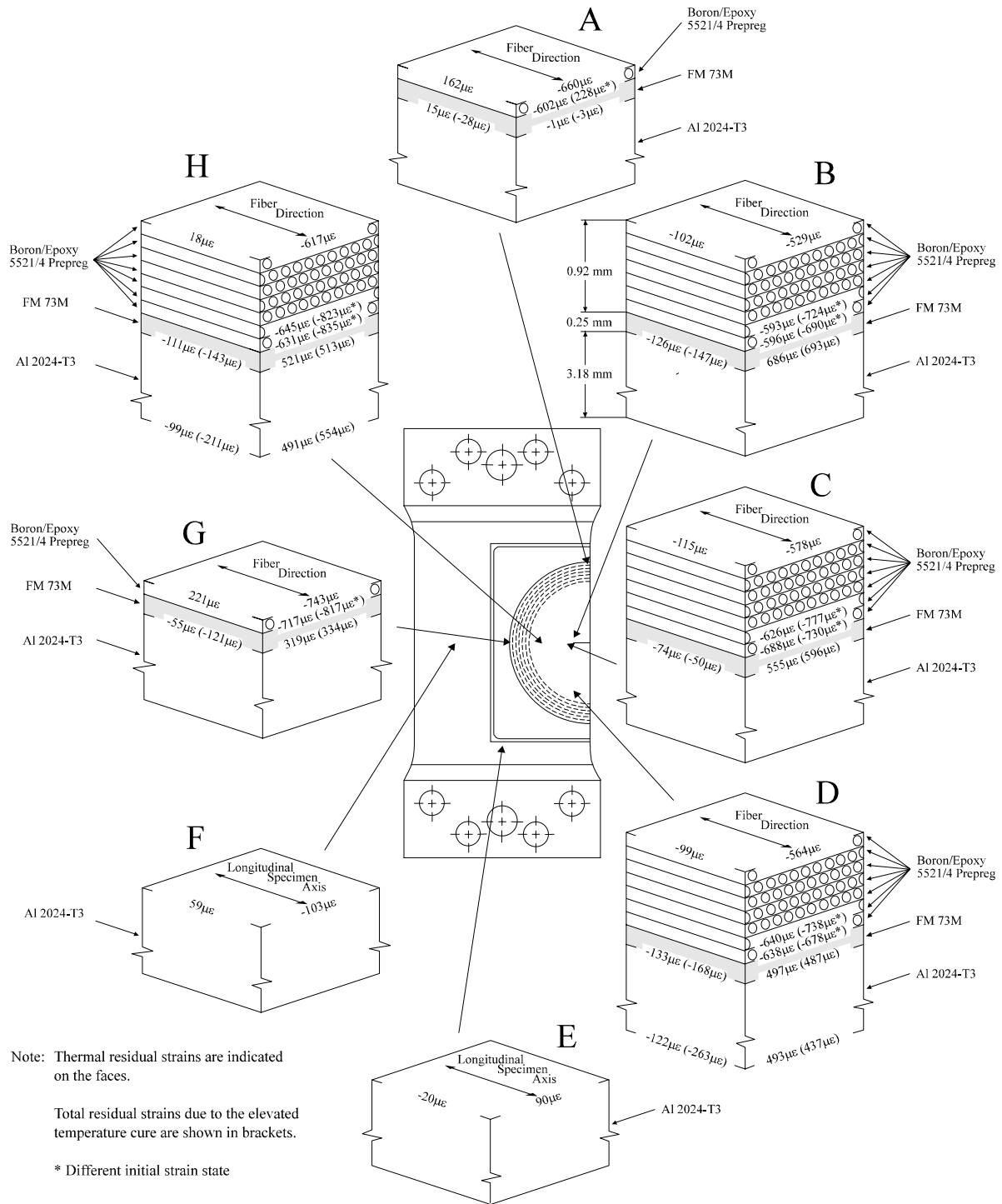


Fig. 4: Thermal Residual and Total Residual Strains due to Elevated Temperature Cure

The thermal residual strains for the boron/epoxy patch at these four locations decline from an average of $-638 \mu\epsilon$ at the patch adhesive interface to $-572 \mu\epsilon$ on top of the patch (standard deviations $< 6\%$). It is important to note that the initial strain state of the boron/epoxy patch cocured with one layer of FM 73M was not identical to the seven ply boron/epoxy specimen which was used for the thermal residual strain measurement thus not allowing identification of process induced strains. In addition, the peel ply was removed after the initial measurement and the bottom of the patch grit blasted, both of which will have an effect on the initial strain

state. The cause for the very large discrepancy in the measured thermal residual strains and total residual strains due to the elevated temperature cure in the boron/epoxy at specimen location 'A' has not yet been identified.

The maximum thermal residual strains found at the strain gauged locations were close to $690 \mu\epsilon$ at the aluminum/adhesive interface (see specimen location 'B'), which is approximately 15% of the aluminum yield strain and should therefore be carefully considered for the determination of the margin of safety of a bonded repair. The thermal residual strains in the boron/epoxy exceeded $-710 \mu\epsilon$ (see specimen location 'G') which can be a concern for repairs under compression loading.

Fig. 5 shows the thermal residual strains versus the temperature for the higher heating rate at specimen location 'B' close to the crack tip. The curves show the thermal residual strains of the aluminum in both the longitudinal and transverse directions of the specimen and at the interface between the adhesive and the first boron/epoxy ply in fiber direction. The thermal residual strains for the aluminum are decreasing nearly linearly with temperature up to approximately 85°C . Above 90°C the change in the thermal residual strain with temperature is small, i.e. the boron/epoxy patch and the aluminum expand nearly at their unrestrained rates.

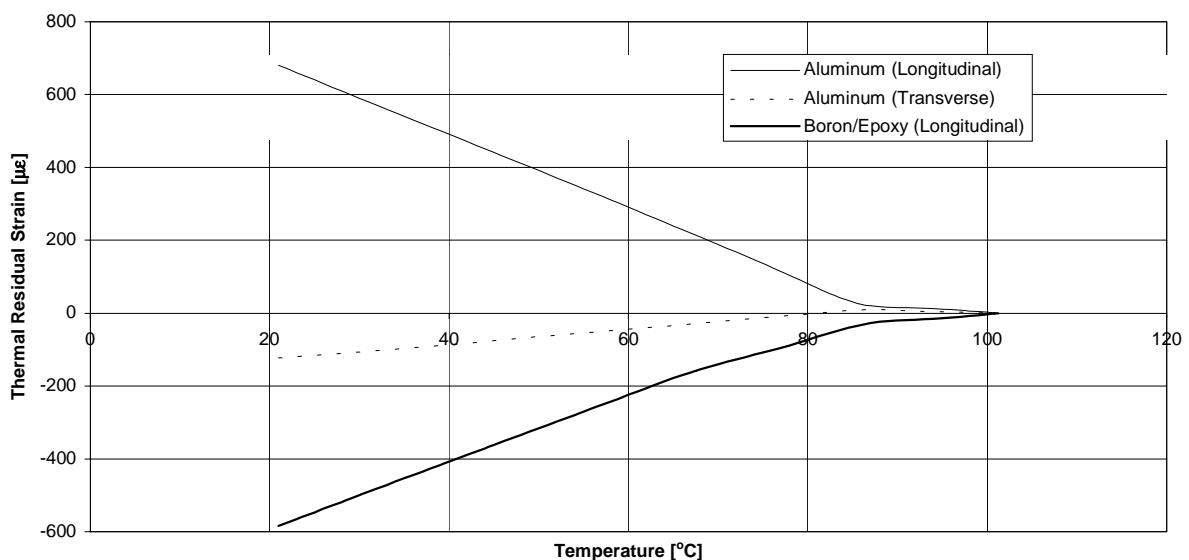


Fig. 5: Thermal Residual Strain versus Temperature

The thermal residual strain versus temperature for the boron/epoxy is initially linear up to approximately 65°C . At this temperature the slope changes slightly and continues to be approximately linear to around 85°C . Above 90°C the residual thermal strain in the boron/epoxy changes only slightly with trends corresponding to those of the aluminum. Note that the thermal strain in the boron/epoxy specimen shows a linear relationship with temperature for the employed temperature range. A possible cause might be the penetration of FM 73 into the boron/epoxy, resulting in the presence of two epoxies with different thermal properties in the patch.

Error estimates indicate that the maximum variation due to hysteresis during these tests was $31 \mu\epsilon$ with an average of only $9 \mu\epsilon$, which does not include creep while holding at elevated temperatures during the experiments. It was noted that an error of 1% in the gauge factor

leads to a change of up to $8 \mu\epsilon$ in the thermal residual strain while the maximum uncertainty of 10 mm in the length of the lead wires connecting the strain gauges with the terminals will only result in an error of $4 \mu\epsilon$. Errors regarding the absolute resistance of all lead wires can be neglected. An error of 2°C in the stress free temperature was found to have only a small effect (approximately $1 \mu\epsilon$).

In summary, the results provided here for a bonded repair utilizing FM 73M indicate that using the difference between the curing and ambient temperature as input to a thermal residual strain model may substantially over-estimate the thermal residual strains present in the repaired structure. Approximately $855 \mu\epsilon$ are predicted using a conventional closed form solution for the uncracked metallic component of a reinforced specimen [1] which is nearly 60% higher than the measured average of $541 \mu\epsilon$ for the cracked aluminum within the center section of the AMRL specimen repair. Unfortunately, the more general question of the real benefit of a lower temperature cure (80°C) for FM 73M cannot be answered at this point since more detailed experiments are required to show the thermal residual strain versus temperature behavior. In addition, the effect of temperature on crack growth retardation in the aluminum must also be considered in any comparison to assess the actual benefits of lower curing temperatures.

CONCLUSIONS AND FUTURE WORK

Thermal residual strains as well as the total residual strains due to the elevated temperature cure were measured using an instrumented sandwich type AMRL specimen. The results indicate that although the FM 73M film adhesive was cured at 121°C and the specimen exhibited a stress free temperature of 101.25°C as determined from current testing, thermal residual strains remained linear with temperature only up to 90°C , beyond which the thermal residual strain gradient was substantially reduced. This phenomenon reduces the expected thermal residual strains at room temperature significantly and suggest that current models employing temperature differences between cure and ambient may substantially over-estimate the magnitude of this residual strain component.

Thermal residual strains at defined strain gauged locations were found to be as high as $690 \mu\epsilon$ in the aluminum (approximately 15% of yield) and $-710 \mu\epsilon$ in the boron/epoxy patch. The results obtained for the thermal residual strains and total residual strains due to the elevated temperature cure for the aluminum in the longitudinal direction of the specimen were found to be nearly equivalent, while it is believed that the difference in the transverse direction of the specimen is caused by process induced strains such as adhesive shrinkage. Although of definite interest, the thermal residual strains and the total residual strains due to the elevated temperature cure for the boron/epoxy cannot be directly compared due to the different initial conditions.

Although the magnitude of thermal residual strains will be less in a constrained structure [7], they should be carefully considered to determine the margin of safety of a bonded repair. The incorporation of thermal residual strains is important for the performance comparison of bonded repairs especially if test specimens with different constraint conditions are used. Continuing work, including a finite element analysis, is being carried out to model the thermal residual strain distribution and dependence on temperature. The results of this work will be correlated with the current results and subsequently utilized to compare with the predict

capabilities of currently available theoretical models. In addition, further experiments are planned to verify the thermal residual strain characteristics of FM 73M film adhesive and to assess thermal residual strains in the high temperature cured AMRL specimen at low temperatures. Further work to quantify the thermal residual strains for the 80°C cure are also being planned in order to establish the actual benefit of lowering the curing temperature.

ACKNOWLEDGMENTS

The financial support of the German Academic Exchange Service (DAAD) for the HSP II scholarship of A.M. Albat is gratefully acknowledged, as well as project funding from the National Research Council of Canada. The assistance of T. Benak and the staff at the Institute for Aerospace Research (NRC) during specimen preparation is also gratefully acknowledged.

REFERENCES

1. Baker, A.A. and Jones, R. (Editors), *Bonded Repair of Aircraft Structures*, Martinus Nijhoff, Dordrecht, 1988.
2. Baker, A.A, Davis, M.J. and Hawkes, G.A., "Repair of Fatigue Cracked Aircraft Structures with Advanced Fibre Composites: Residual Stress and Thermal Fatigue", *Structural fatigue as a design factor: Proceedings of the 10th Symposium*, Brussels, 1979, pp. 4.3/1-4.3/30.
3. Baker, A.A, "Bonded Composite Repair of Metallic Aircraft Components - Overview of the Australian Activities", *AGARD - 79th Meeting of the Structures and Materials Panel, Specialist's Meeting: Composite Repair of Military Aircraft Structures*, 1994, pp. 1.1-1.14.
4. Jones, R. and Callinan, R.J, "Thermal Considerations in the Patching of Metal Sheets with Composite Overlays", *J. Struct. Mech*, Vol. 8, No. 2, 1980, pp. 143-149.
5. Gaudert, P.C., Raizenne, M.D., Bellinger, N.C. and Heath, J.B.R., *Fractographic Investigation of Boron Epoxy 5521/4 Patches*, LTR-ST-1973, National Research Council of Canada, Institute for Aerospace Research, 1994.
6. Johnston, A., Hubert, P., Poursartip, A., *Processing of Fibre-Reinforced Composite Laminates*, MMAT 483 Course-Notes, The University of British Columbia, Department of Metals and Materials Engineering, Composites Group, 1995.
7. Walker, K. and Boykett, R., "Repair Substantiation Fatigue Testing including Temperature and Frequency Effects for a bonded Composite Repair to an F-111 Lower Wing Skin". *Presented at the 1996 USAF ASIP Conference*, San Antonio, Texas, 1996.

COHERENT SIMULATION AND TESTING FOR COMPOSITE BLADE REPAIR

O. O. Ochoa & B. McNichols¹; C. Oztelcan²; J. Martin & K. Sem³

¹*Mechanical Engineering, Texas A&M University, College Station, TX 77843-3123*

²*Intel Corporation 5200 N.E. Elam Young Hillsboro, OR 97124-6497*

³*Bell Helicopter, Textron, P.O. Box 482, Fort Worth, TX 76101*

SUMMARY: The first phase of repair methodology under development is presented to illustrate the salient features on designing, testing and modeling the response of relevant coupons. The present emphasis is on developing appropriate test specimens to evaluate computationally and experimentally the effects of static and cyclic loads on sandwich panels.

KEYWORDS: helicopter blades, sandwich panels, glass/epoxy composite, FEA models

INTRODUCTION

The essentials of excellence in composite component design demand a priori assessment of repair methodology. As the design is enhanced with this knowledge base, the long term maintenance issues become less costly as well as leading to robust performance. The first phase addresses the design of the test coupons representative of overlap and scarf patch repairs and their analysis under static loading. The second phase evaluates the test matrix and the static tests conducted to evaluate the results of the computational effort.

A global blade model is used to identify potential repair sites for a typical flight condition. Identifying this region enables one to generate a local model with the appropriate boundary conditions so that different patch analyses can be carried on as well as recommending specimen configurations for testing. Cross-sectional models are generated from the local model for overlap and scarf patch simulation with finite elements. A failure subroutine, based on the ultimate stress allowable is incorporated into the analysis to detect the initiation and progression of failure. The shear stress distribution in the adhesive layer for the scarf patch model indicated that the stress is much higher in the interior away from the free surface. On the contrary, for the overlap configuration, the shear stress distribution reaches its maximum at the free edges.

In order to assess the structural response experimentally and computationally, composite sandwich test panels with scarf and overlap patches were designed and tested under static and fatigue loads. Two different panel sizes were used, 30.5 cm square (12 in) square for uniaxial tension test and 30.5 by 61 cm (12 by 24 in) rectangular panels for four point flexure test. Corresponding finite element simulations were developed to study the mechanical response.

EXPERIMENTS

The damaged area of the composite skin that is being repaired is circular with a 2.54 cm (1 in) diameter. Both patches, overlap and scarf, are 7.62 cm (3 in) in diameter, leaving 2.54 cm (1 in) between the edge of the damaged area and the end of the patch. The sandwich panels used have 2.54 cm (1 in) honeycomb cores with two 0.2286 mm (0.009 in) lamina on each side. The lamina are in a $\pm 45^\circ$ stacking sequence.

Square Panel

The square panels were tested under static and fatigue loads. The last 2.54 cm (1 in) of honeycomb core on each side of the panel is replaced by an aluminum tab in order to allow the load to be applied to the panel. A peak tensile load of 46.7 kN (10,500 lb) was applied. In tension-tension fatigue, maximum loads of 20.9 kN to 44.5 kN (4,700 to 10,000 lb) and a minimum load of 2.22 kN (500 lb) was applied to the panel.

A total of eight strain gauges were placed on the 30.5 cm (12 in) square panel when tested under static load. They measured axial and transverse as well as shear strain on various positions on the panel. Strain Gauges 1&3 were located between the aluminum tab and the patch and in the center of the patch, Fig. 1.

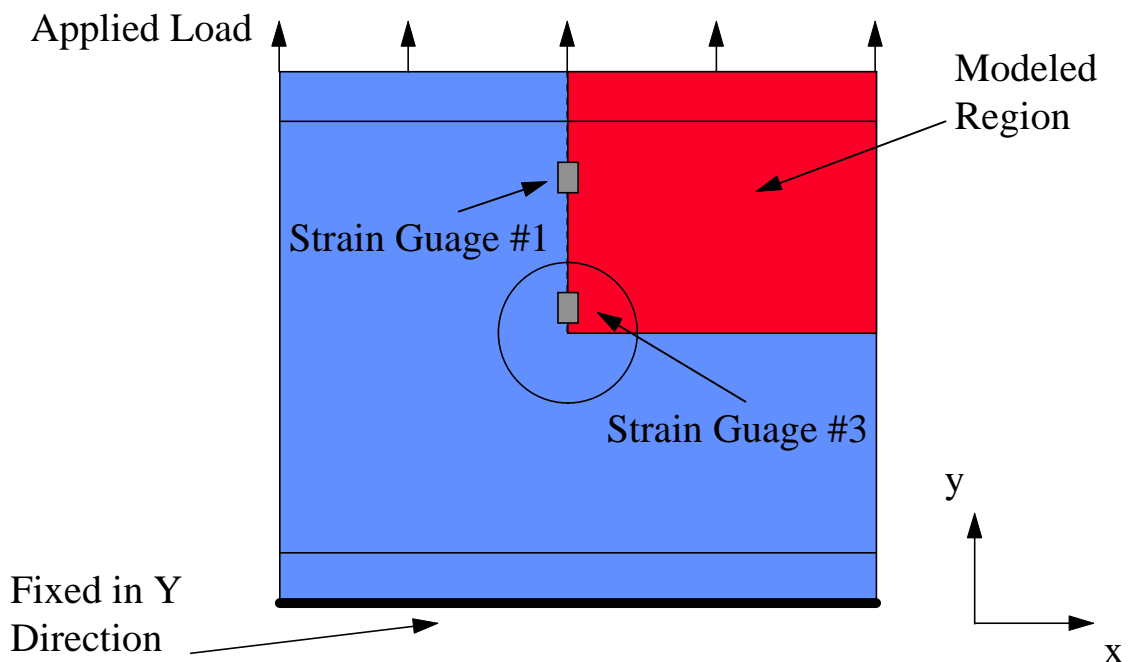


Fig. 1 Configuration of Tension Test on Square Panel

These gauges measured strain in the direction of loading. Cracks consistently initiated from the corners adjacent to the aluminum tabs, before or immediately after they did in the skin surrounding the patch. Cracks grew on a 45° diagonal along the fibers adjacent to the patch. Few or no cracks were seen in the patch and the patch remained in tact during testing. Nonlinearities in the load Vs displacement curve first appear between 17.8 kN & 26.7 kN (4,000 & 6,000 lb) of tensile load. In the tension-tension fatigue tests with an $R=5.5$, visible

cracks in the unpatched panel were observed at the corners around 320,000 cycles. Under equivalent conditions the panel with an overlap patch exhibited initial cracks at 1,500,000 cycles from the patch and at 1,800,000 cycles from the corner. It is noted that as R was increased, earlier crack initiation was routinely observed. The edge effects at the tabs inhibit our ability to experimentally evaluate the response between repaired and original panels.

Rectangular Panel

In order to eliminate stress concentration due to fixture and grips, the 30.5 by 61 cm (12 by 24 in) panels were designed for flex loading. During the testing, the load for core crushing under the loading bars was identified and relevant adjustments were made to the location of support and load bars. The rectangular panel is being tested under four point bending conditions as illustrated in Fig. 2. The distance between the supports was 45.72 cm (18 in). The distance between the loading lines was either 15.24 or 22.86 cm (6 or 9 in).

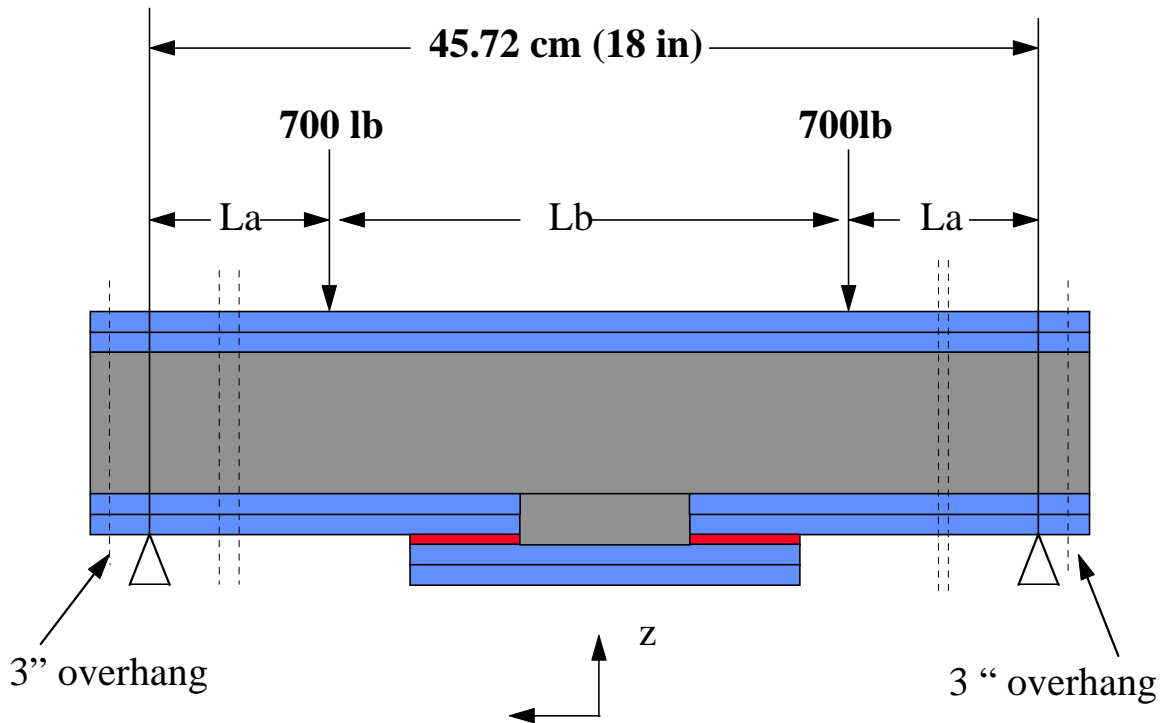


Fig. 2 Side view of Rectangular Bending Tests

COMPUTATIONAL MODELS

A quarter model of the panel is modeled with symmetry boundary conditions. with S8R composite shell elements from the ABAQUS element library. These elements have five degrees of freedom u_x , u_y , u_z , Θ_x & Θ_y at each node. The through the thickness material details were incorporated to address the presence of the patch, adhesive, skin and honeycomb as shown in Fig. 2. The skin and honeycomb were treated as orthotropic where as the adhesive layer was assumed to be an isotropic material. A hypothetical material with minimal

stiffness is used in the unpatched region of the panel to align every integration point (3 per layer) through the thickness of each element

Square Panel: Uniaxial Tension Load

Strains from the ABAQUS models are compared to the test data in Figs. 3 & 4. The skin was modeled with homogenized properties. In the subsequent simulations, the skin was taken as two discrete layers.

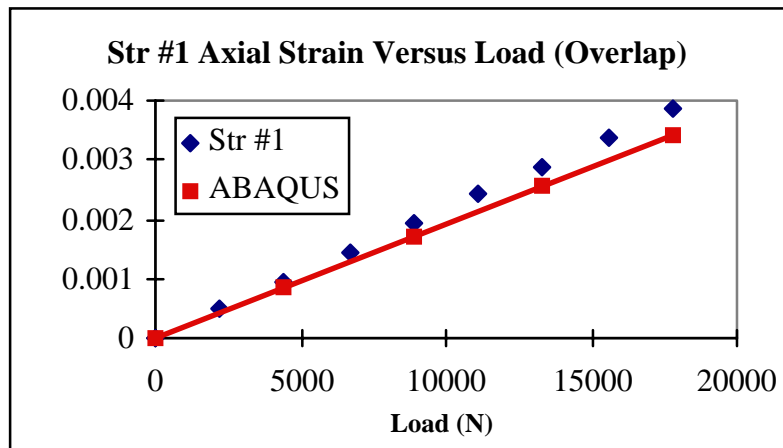


Fig. 3 Experimental & FEA Axial Strains

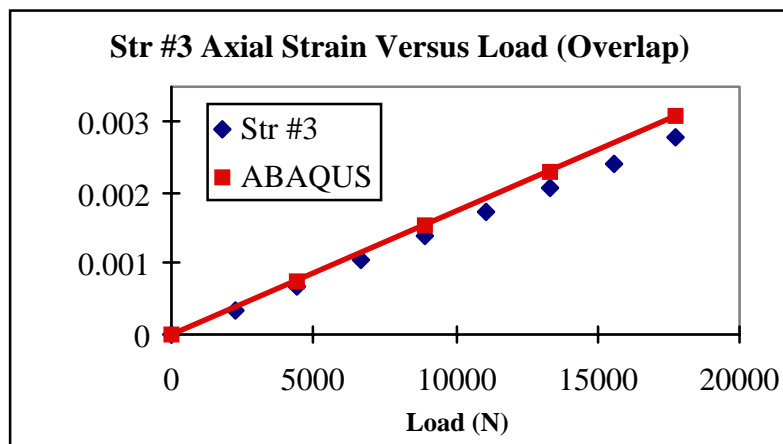


Fig. 4 Experimental & FEA Axial Strains

With a linear analysis simulating 17.8 kN (4,000 lb) of loading and discrete properties for the ± 45 degree layers, peak strains in the panel were at the corner adjacent to the aluminum tab. The ratio of strain to strain allowable in the patch and in the skin surrounding the patch is significantly less than at the corner. Since the strain allowable in the direction transverse to the fiber is less than parallel to the fiber, failure initiation is expected as matrix cracking and splitting. The deformed shape (magnified sixty six times) and the undeformed shape of the panel are presented in Fig. 5 at a tensile load of 17.8 kN (4,000 lb). At this loading conditions there is a reduction in crosshead displacement, D , of 3.4% between the patch with a panel and the unpatched panel. This represents a minimal increase in stiffness due to the addition of an overlap patch over the unpatched panel. Next, the panel was modeled incorporating a user

material subroutine UMAT to model the weakening of the skin after strain allowables have been reached. In this model a total simulated load of 44.5 kN (10,000 lb) is applied in ten increments. The subroutine checks maximum strain theory at each increment and every integration point. Maximum strains in the direction transverse to the fibers in the +45° layer of the modeled

1

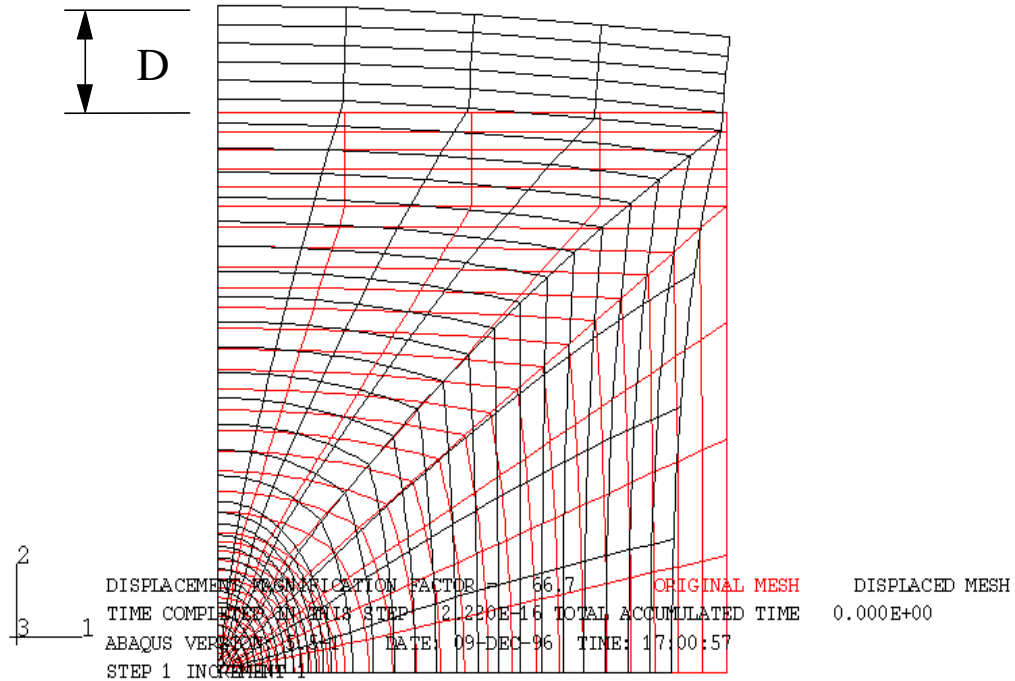


Fig. 5 Deformed & Undeformed Shape of Square Panel

The subroutine checks maximum strain theory at each increment and every integration point. Maximum strains in the direction transverse to the fibers in the +45° layer of the modeled region are seen at the corner node where the aluminum tab is adjacent to the honeycomb core. This is illustrated in Fig. 6, where each point represents an increment and 4.45 kN (1,000 lb) of additional loading to the panel. In the linear range, stresses where the aluminum tab replaces the honeycomb core are roughly twice those around the patch. Once strain allowables are reached at the corner and the material is weakened, higher stress is seen in the skin around the patch. This indicates that edge effects from the tabs are greatly affecting the stress & strain concentrations in the skin surrounding the patch.

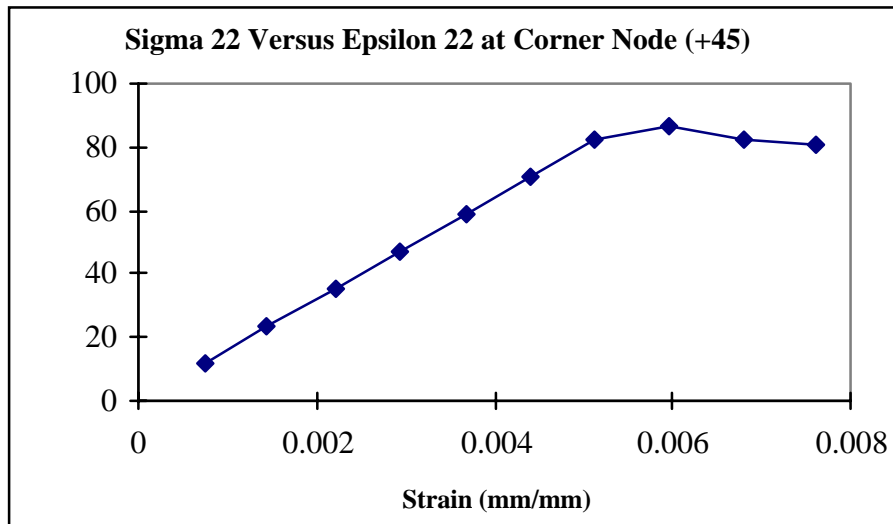


Fig. 6 Stress Versus Strain at Corner Node in Square Model

Rectangular Panel: Flexure Load

Four point flex test geometry was modeled with two different spacings between load and support bars. In both configurations, the patch is located on the tension side of the panel, and the distance between supports is 45.7 cm (18 in). In the first configuration the distance between loading bars is 15.24 cm (6 in), and in the second the distance is 22.9 cm (9 in). On fourth of the panel was modeled with 272 S8R elements from the ABAQUS library. Similar to the square panel case, symmetry boundary conditions were placed along the edges to reduce the overall amount of computation.

The peak strain region in the second configuration first occurs in the skin immediately surrounding the patch. The actual deformed shape is shown in Fig. 7 that corresponds to a total of 6.23 kN (1400 lb).

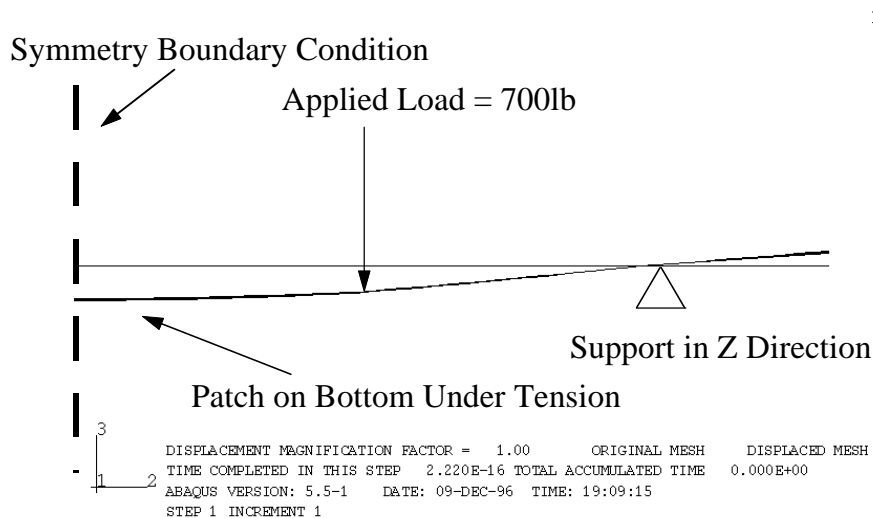


Fig. 7 Actual Displacement of Quarter Point Bending Model

Peak strain ratios, predicted strain divided by strain allowable, indicate that the region of skin immediately surrounding the patch is more likely to fail than the patch itself at a load of 10.2 kN (2,300 lb). Experiments revealed that skin crimping occurred at 11.6 kN (2,600 lb).

CONCLUSIONS

Sandwich panels were designed to establish criteria to assess the effectiveness of relevant blade repairs under static and dynamic load conditions. The integrated computational and experimental approach enabled the successive design improvements to the test panels. The analytical predictions for static tensile and flex load conditions are in excellent agreement with the tests.

The fatigue flexure testing with and without reversed loading is underway and computational assessment for fatigue response is being developed based on energy formulation

ACKNOWLEDGMENTS

The financial support and the technical interaction provided by Bell Helicopter Textron, Inc. is graciously acknowledged.

REFERENCES

1. Oztelcan C, "Design and Analysis of Test Coupons for Composite Blade Repairs", Master's Thesis, Texas A&M University, May 1996
2. Oztelcan C., Ochoa, O.O., Martin, J. and Sem, K., " Design and Analysis of Test Coupons for Composite Blade Repair", *Journal of Composite Structures*, accepted for publication, January 1996.

FAILURE MECHANISMS IN BONDED PATCH REPAIRED STRUCTURES

Naveen Rastogi¹, B. P. Deepak¹, Som R. Soni¹ and Arvind Nagar²

¹ *AdTech Systems Research, Inc., 1342 North Fairfield Road
Beavercreek, Ohio 45432, USA.*

² *WL/FIBE, 2130 Eighth St., Suite 1, WPAFB, OH 45433, USA.*

SUMMARY: Bonded repair of damaged metallic structures using composite patches is finding an increased application in the enhancement of service life of aging aircraft fleets. In this work, the effect of bonded patch repair on the stress fields in the skin, patch and adhesive is studied. The stress field in the bonded composite patch repaired structure is analyzed using three different analytical techniques. The numerical example studied indicates a significant reduction in the magnitude of stresses in the patch repaired skin in the vicinity of damaged zone which is modeled as a rectangular slit in the skin. Also, the presence of high stress gradients at the material interfaces is found to be the characteristic of the bonded repaired structures, and can lead to debonding and failure of the interfaces.

KEYWORDS: bonded repairs, composite patch, high stress gradients, debonding

INTRODUCTION

The enhancement of service life of aging aircraft fleets is a challenging problem for aircraft designers. This is necessary to maximize the return on the money invested by the aircraft operating agencies, and thus, ensure the cost effectiveness in operation of the aircraft fleets. An aircraft is subjected severe aerodynamic and structural loads during its service life. These include loads due to repeated landing and take-off, maneuvering, ground handling, environmental degradation, corrosion, etc., and can cause severe structural damage. Thus, the aircraft structure undergoes several modifications and repairs during its service life. Frequently, the repair process indirectly has an adverse effect on the service life of the aircraft and in most cases shortens the expected life. The shortening of service life of a repaired aircraft can be the result of an inaccurate assessment of strength prediction of the repaired structure, which in turn could be due to the lack of availability of accurate and validated analytical methodologies for stress analysis of repaired zones. It is evident that an accurate strength prediction of the repaired structure would boost the service life of the aircraft.

Most aircraft repairs require reworking of the damaged skin, putting a doubler or a patch over the damaged area, and joining the patch with either mechanical fasteners or by bonding it to the skin. The latter can employ adhesive bonding, welding or brazing of the patch to the skin. Thus, most repairs can be classified into two categories as (a) mechanical repairs (bolted, riveted, screwed, etc.), and (b) bonded repairs (adhesive bonding, brazing, welding, etc.). Denney [1] listed some of the pros and cons of using bonded and bolted repair techniques for metallic structures using composite patches, and advocated for the case of bonded repairs.

Denney pointed out that the bonded repairs are light-weight, eliminate unnecessary fastener holes in an already weakened and damaged structure, enable load transfer more evenly and over the greater area, thus increasing the fatigue life of the repaired structure. In addition bonded composite repairs can be tailored to conform to complex shapes and contours, and meet the variable stiffness requirements in different directions. All these and many other advantages of composites make them ideal materials for application in repair of the damaged zones in the aircraft structures.

COMPOSITE BONDED REPAIRED STRUCTURES

The stress analysis of structures repaired using composite material patches is a complex problem from the mechanics view point. Figure 1 shows a cracked or damaged metallic skin repaired using a composite material patch. The critical issues need to be addressed are:

1. Stress analysis and strength prediction of the damaged (or cracked) zone before any repair is carried out;
2. Reduction of stresses in the damaged (or cracked) material after the patch repair has been performed;
3. Re-initiation of crack propagation in the damaged zone;
4. The rate of crack growth in the metallic structure after its re-initiation;
5. Debonding of composite patch from the metallic structure;
6. Failure in patch material.

The last issue can be precluded from the analysis by assuming the patch material to be much stronger than the skin material. The first five issues require a concerted effort from the researchers and designers in order to effectively utilize composite materials for repair of damaged metallic structures.

In the past, efforts have been made to address the critical issues listed above, and to develop analytical tools for the stress analysis and fatigue life prediction of bonded patch repaired structures. However, most of the existing work involves one-dimensional, semi-empirical and two-dimensional plane stress/strain analysis of the repaired zones using either closed-form solutions or finite element based methods. For example, Harter [2] presented a computer program AFGROW which is a modification of MODGRO computer program to include patch repair analysis capability. Xiong, et al. [3] developed a PC based design package BONDREP for bonded composite repairs. The design software employs closed-form solution approach based on hard inclusion analogy to perform global stress analysis. The bondline stresses are calculated using the one-dimensional model following Hart-Smith [4]. The BONDREP program performs fracture analysis of centrally cracked plate, and obtains stresses in skin, patch and adhesive. Fogarty and Saff [5] developed PGLUE computer program which performs a quasi-three-dimensional finite element analysis of adhesively bonded patch repairs. The PGLUE program provides the stresses and deflection analysis at various points in the three medium, viz., skin, patch, and adhesive. Rastogi, et al. [6] have developed a PC based, Windows 95TM compatible computer program modules for the stress analysis of bonded joints in composite laminates. Bogdanovich and Rastogi [7] have also developed a *novel* three-dimensional variational analysis (MOSAIC) to accurately predict the stresses in the region of high stress gradients in composite bonded joints. The high stress gradients occur at the skin-adhesive and/or patch-adhesive interfaces. The MOSAIC analytical technique is very versatile, and can be effectively utilized to obtain stress fields in the skin, patch and adhesive and predict strength of the bonded repaired structures.

The analytical tools mentioned above are computationally efficient and are easy to use. However, the accuracy of these methodologies in predicting the structural response after repair is not yet validated extensively. Moreover, in most of the situations some of these approximate methods tend to neglect the effect of interlaminar transverse normal and shear stresses along the interfaces in the bonded repaired zones. These stress components can cause debonding of the patch from the skin, and their effect on failure strength prediction of the repaired composite structures can not be ignored. The objective of this work is to study the effect of bonded patch repair on the distributions of stresses in the skin, patch and adhesive. Of particular interest are the regions of high stress concentration in the skin in the vicinity of the damage and the patch repair. A brief discussion on the initiation of failure in the bonded zones is also presented.

STRESSES IN THE BONDED REPAIRED REGION

The bonded repaired configuration shown in Fig. 1 is a double-sided repair design illustrating the application of patch and adhesive from outside as well as inside the skin. A uniform extension is applied at the ends of the aluminum skin. Due to the symmetry of the repaired configuration and applied loading about the three coordinate axes, only 1/8th portion of the repaired configuration as shown in Fig. 2 need be analyzed. Figure 2 illustrates the following unique features of the composite bonded repaired structures:

1. Variation of material properties in the two orthogonal directions of the structure.
2. Double free-edge effect at the corners of the repaired zones which makes the problem all the more complex to analyze.
3. Presence of damaged skin (or cracks) further complicates the analysis of repairs.
4. Thermal expansion mismatch between composite and metals.

The last feature requires consideration of residual stresses in the mechanical analysis. The first three features make the bonded repair analysis extremely complex, and require a full 3-D analysis to accurately solve the problem. The stress analysis of the bonded repaired configuration shown in Fig. 2 is performed using the following three analytical techniques:

A plane stress finite element solution using PGLUE.

1. A 3-D variational analysis using MOSAIC model assuming cubic Bernstein basis functions for the displacement approximations in the three coordinate directions.
2. A three-dimensional finite element analysis using 27-node brick element of the commercial FE package ABAQUS.

The detailed description on the PGLUE analysis program can be found in Ref. [5]. The details on the MOSAIC model can be found in Refs. [6] and [7]. Further details on the ABAQUS FE package can be obtained from Ref. [8]. There were approximately 4000, 27000, and 98000 degrees of freedom in the analytical models of the bonded repaired configuration (see Fig. 2) for PGLUE, MOSAIC and ABAQUS FE analyses, respectively.

Numerical Example

The analysis of a damaged aluminum plate repaired by using FM300 adhesive and unidirectional graphite/epoxy patch is considered for the numerical example. The damaged region is idealized as a rectangular slit in the skin. Various notations used for the geometrical data for the bonded repaired configurations are shown in Figs. 1 and 2. The geometrical and material data used for the purpose of the analyses are given below:

Skin

$L_s = 20.0$ in., $W_s = 10.0$ in., $H_s = 0.25$ in.; $L_c = 0.5$ in., $W_c = 0.25$ in.

$a = L_s/2 = 10.0$ in., $b = W_s/2 = 5.0$ in., $h = 0.38$ in.

$E = 10.7$ Msi, $\nu = 0.25$.

Patch

$L_p = 5.0$ in., $W_p = 2.5$ in., $H_p = 0.25$ in.

$E_1 = 23.86$ Msi, $E_2 = E_3 = 1.426$ Msi, $G_{12} = G_{13} = 0.9825$ Msi, $G_{23} = 0.5306$ Msi

$\nu_{12} = \nu_{13} = 0.2402$, $\nu_{23} = 0.3435$.

Adhesive

$L_a = L_p = 5.0$ in., $W_a = W_p = 2.5$ in., $H_a = 0.005$ in.

$E = 0.5$ Msi, $\nu = 0.3$.

RESULTS AND DISCUSSION

The stress distributions at various locations in the skin, patch and adhesive are obtained from various analytical models. The stresses obtained are normalized by their respective far-field axial normal stress value σ_0 in the aluminum plate.

Stress Reduction in the Patch Repaired Skin

The stress field in the skin before and after the patch repair is analyzed. The distributions of stresses as obtained from the FE analysis in the vicinity of the rectangular slit (or cutout) region are shown in Figs. 3(a), 3(b) and (4). The MOSAIC analysis also provided essentially the same solution for the problem of unrepaired (i.e., without patch repair) skin subjected to uniform extension. As is shown in Fig. 3(a) the axial normal stress σ_x in the unrepaired skin in the vicinity of the rectangular slit region is about 1.4 times the far field (or applied) stress. As expected the areas of stress concentration in the skin are (i) the location $x/a = 0.025$, $y/b = 0.0$ (refer to Fig. 2) where normal stress σ_y attains a high magnitude which is about 94% of the applied stress value (see Fig. 3(b)), (ii) and the location $x/a = 0.0$, $y/b = 0.025$ (refer to Fig. 2) where normal stress σ_x attains a high magnitude which is about 145% of the applied stress value (see Fig. 4). After the patch repair these stress values in the skin reduce to about 2% and 30%, respectively. Thus, the axial stress component in the skin around the rectangular slit shows a reduction by a factor of about 4.6 after the repair. The normal stress σ_y attains an insignificantly small magnitude in the same region after patch repair. In general there is significant reduction in the axial normal stress component σ_x in the patch repaired skin in the vicinity of rectangular slit region (see Figs. 3(a) and 4). It is evident that the reductions in the stress levels in and around the rectangular slit region (or damaged zone) will significantly increase the strength as well as fatigue life of the skin after the patch repair. The low level of stresses would also help in arresting the further growth of cracks in the vicinity of the rectangular slit area (or damaged zone).

Comparison of Stresses in the Skin, Patch and Adhesive

The stress fields in the skin, patch and the adhesive as obtained from the three analyses at the material interfaces along x -direction at $y/b = 0$ are shown in Figs. 5 and 6(a)-6(f). The PGLUE analysis is based on plane stress assumption and does not predict the transverse normal stress σ_z and transverse shear stress τ_{xz} in the skin and the patch. The MOSAIC and FE analyses predict essentially the same behavior of the stress components. The distribution of normalized shear stress component in the FM300 adhesive as obtained from the three analyses is shown in Fig. 5. The magnitude and distribution of this stress component compares fairly well

among various analyses. The magnitude and distribution of axial stress component σ_x in the skin as predicted by the PGLUE analysis compares well with other the two analyses except in the vicinity of the edge $x/a = 0.25$ where it does not show high stress gradients. Also, as shown in Fig. 6(b) the magnitude and distribution of axial stress component σ_x in the patch as predicted by the PGLUE analysis is substantially different from those obtained by the MOSAIC and FE analyses. It can be seen that the simplified analysis of the complex problem of the bonded repaired structures having sharp material and/or geometrical discontinuities can be highly inaccurate. Not only it may result in inaccurate solution of some stress components but also it tends to neglect the high stress gradients of transverse normal stress component σ_z (see Figs. 6(c) and 6(d)) and transverse shear stress τ_{xz} (see Figs. 6(e) and 6(f)) in the skin and the patch at the material interfaces. The high peel and shear stresses are known to be the primary cause of debonding and cohesive failure in the bonded structures.

Singularity of Stresses at Geometrical Discontinuities and Material Interfaces

The stress distributions obtained from the 3-D analysis tend to show singular behavior at the locations of sharp geometrical discontinuities and material interfaces. The numerical values at these locations do not show convergence with the increased degrees of freedom. Hence, the magnitudes of stresses at these physical locations are always questionable. The singular behavior of stresses manifests itself from the way the bonded repaired structure is mathematically modeled for the purpose of analysis. In real-life structures there are no perfectly sharp corners or perfect material interfaces. However, the high stress gradients at the material interfaces or in the vicinity of discontinuities (see Figs. 3-6) are of practical importance to the designers even if their actual values at the point of singularity are not.

Debonding in the Bonded Region

The distributions of the axial normal stress σ_x , transverse normal stress σ_z and transverse shear stress τ_{xz} in the patch as obtained from the MOSAIC analysis are shown in Figs. 7-9 in the patch region. The surface plots of the significant stress components give a better visualization of the high stress gradients occurring at the patch/adhesive interface. A similar behavior for the stresses in the skin at the skin/adhesive interface is obtained. As is shown in Figs. 7-9 the localized effect of high stress gradients can only be studied from a complete 3-D analysis of the bonded region; particularly the behavior of interlaminar stresses σ_z and τ_{xz} which show a variation in the y -direction as well. It may also be noted that the axial normal stress σ_x attains a significantly high magnitude of about 1.3 times the applied stress value in the patch in the vicinity of the free-edge $x/a = 0.25$ (refer to Fig. 2). In this example the patch material is a unidirectional graphite/epoxy composite having a higher tensile strength in axial direction than the aluminum. However, the combination of high stress gradients of the axial normal stress σ_x , transverse normal stress component σ_z and transverse shear stress τ_{xz} at the material interfaces can cause the debonding of the patch (or the skin) from the adhesive at its interface.

CONCLUDING REMARKS

The stress field in the bonded composite patch repaired structures is analyzed using three different analytical techniques. There is a significant reduction in the magnitude of stresses in the skin in the vicinity of rectangular slit region after the patch repair. The reductions in the stress levels in and around the damaged zone will significantly increase the strength as well as fatigue life of the structure after repair. The presence of high stress gradients of transverse

normal stress σ_z and transverse shear stress τ_{xz} is found to be typical of the bonded repaired structures due to the material interfaces and geometrical discontinuities. The high stress gradients can cause debonding and failure in the bonded structures at the skin/adhesive or patch/adhesive interface. Further, the simplified approaches based on plane stress or plane strain assumptions do not seem to represent the stress field in the bonded repaired structures completely, and in some cases provide inaccurate results. Future efforts will focus on validation of other simplified analytical techniques and substantiation of the analytical results of the 3-D solution approaches with experimental observations.

ACKNOWLEDGMENTS

This work has been performed under Contract No. F33615-95-C-2549 of Flight Dynamics Directorate, WPAFB, Dayton, OH-45433. The work is also supported by a grant of HPC time on Cray C916 machine from DoD HPC ASC MSRC, WPAFB, Dayton, Ohio.

REFERENCES

1. Denney, J. J., "Fatigue Response of Cracked Aluminum Panel with Partially Bonded Composite Patch", AFIT/GAE/ENY/95D-7, Air Force Institute of Technology, Wright-Patterson AFB, OH-45433, December 1995.
2. Harter, J., "AFGROW--A Fatigue Crack Growth Analysis Computer Code", *Proceedings of the AIAA/ASME/ASCE/AHS/ASC 37th Structures, Structural Dynamics and Materials Conference and Exhibit*, Salt Lake City, UT, April 15-17, 1996, AIAA-96-1417.
3. Xiong, D. Raizenne and D. Simpson, "Analytical Approaches and PC Based Design Package for Bonded Composite Patch Repair", *Proceedings of FAA-NASA Symposium on Continued Airworthiness*, Atlanta, GA, August 1996.
4. Hart-Smith, L. J., "Analysis and Design of Advanced Composite Bonded Joints", NASA-CR-2218, 1974.
5. Fogarty, J. H. and Saff, C. R., "PGLUE User's Manual - Rev. A", MDC Report No. B0288, McDonnell Aircraft Company, Saint Louis, MO-63166, August 1987.
6. Rastogi, Naveen, Deepak, B. P., and Soni, Som R., "Stress Analysis Codes for Bonded Joints in Composite Structures", *Proceedings of the AIAA/ASME /ASCE/AHS/ASC 38th Structures, Structural Dynamics and Materials Conference*, Orlando, FL, April 7-10, 1997, AIAA Paper No. 97-1341. Accepted for presentation.
7. Bogdanovich, A. E. and Rastogi, Naveen, "3-D Variational Analysis of Bonded Composite Plates", *Proceedings of the ASME Aerospace Division: Structures and Materials for Aerospace Vehicles*, AD-Vol. 52, 1996, The ASME, New York, NY 10017, pp. 123-143.
8. *The ABAQUS User's Manual: Version 5.6*, Hibbit, Karlsson & Sorensen, Inc., Pawtucket, Rhode Island, U. S. A., 1996.

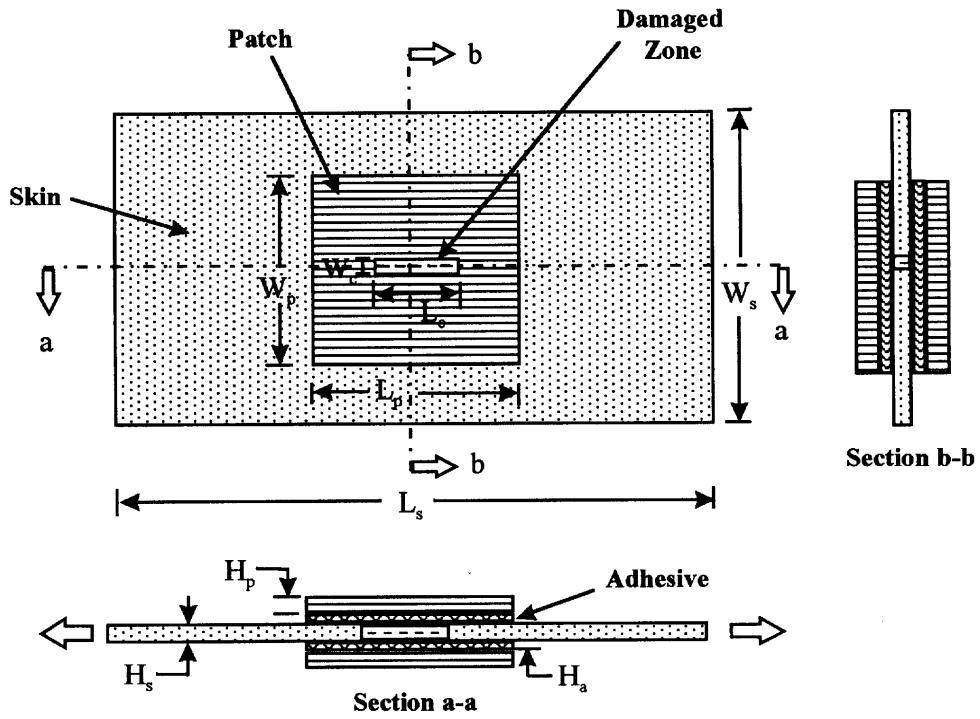


Fig. 1: Schematic diagram for bonded repair of damaged skin using composite material

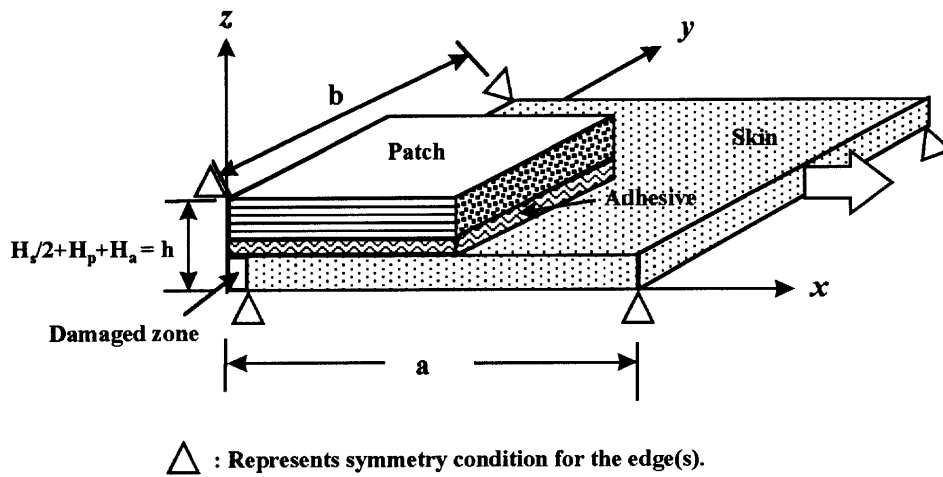


Fig. 2: 1/8th configuration of the bonded repaired skin modeled for analysis.

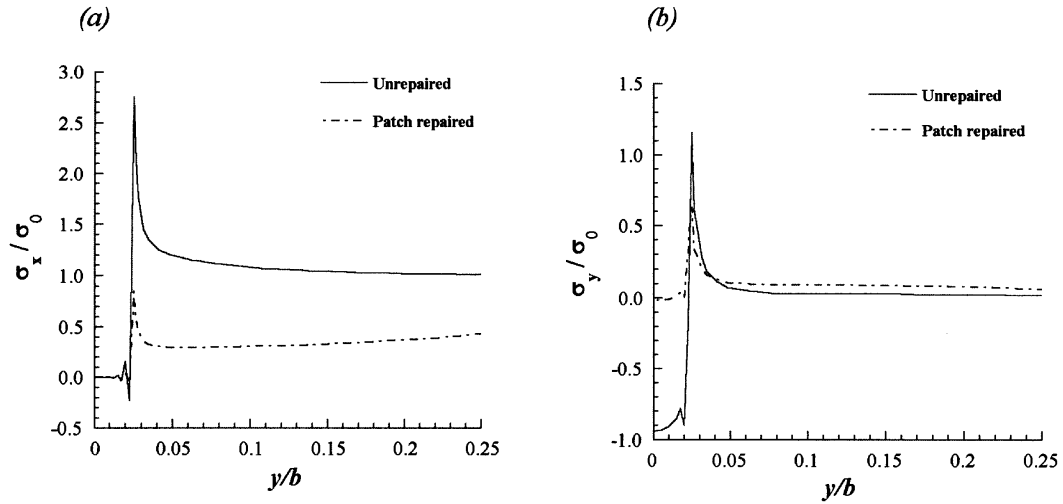


Fig. 3: Distributions of (a) axial normal stress σ_x and (b) transverse normal stress σ_y in the aluminum skin in the rectangular slit region along the y-direction .

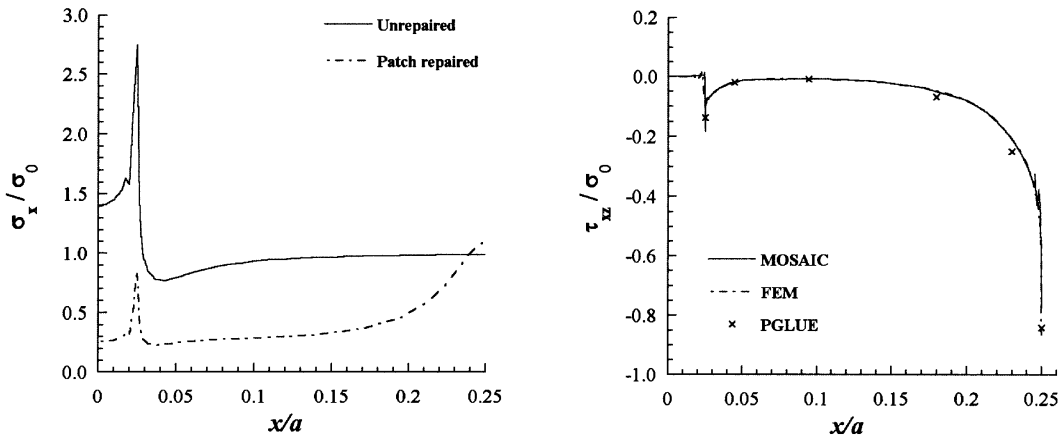


Fig. 4: Distributions of axial normal stress σ_x in the skin along the x-direction in the slit region.

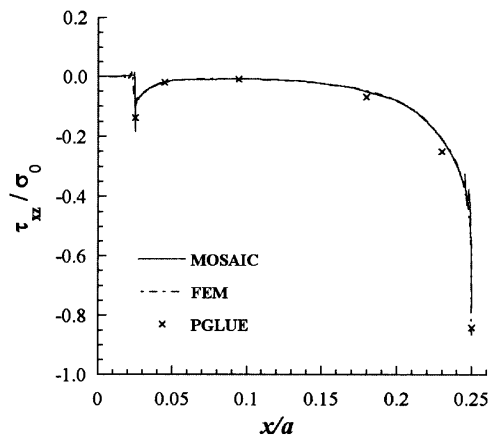


Fig. 5: Distribution of shear stress along the x-direction in the adhesive.

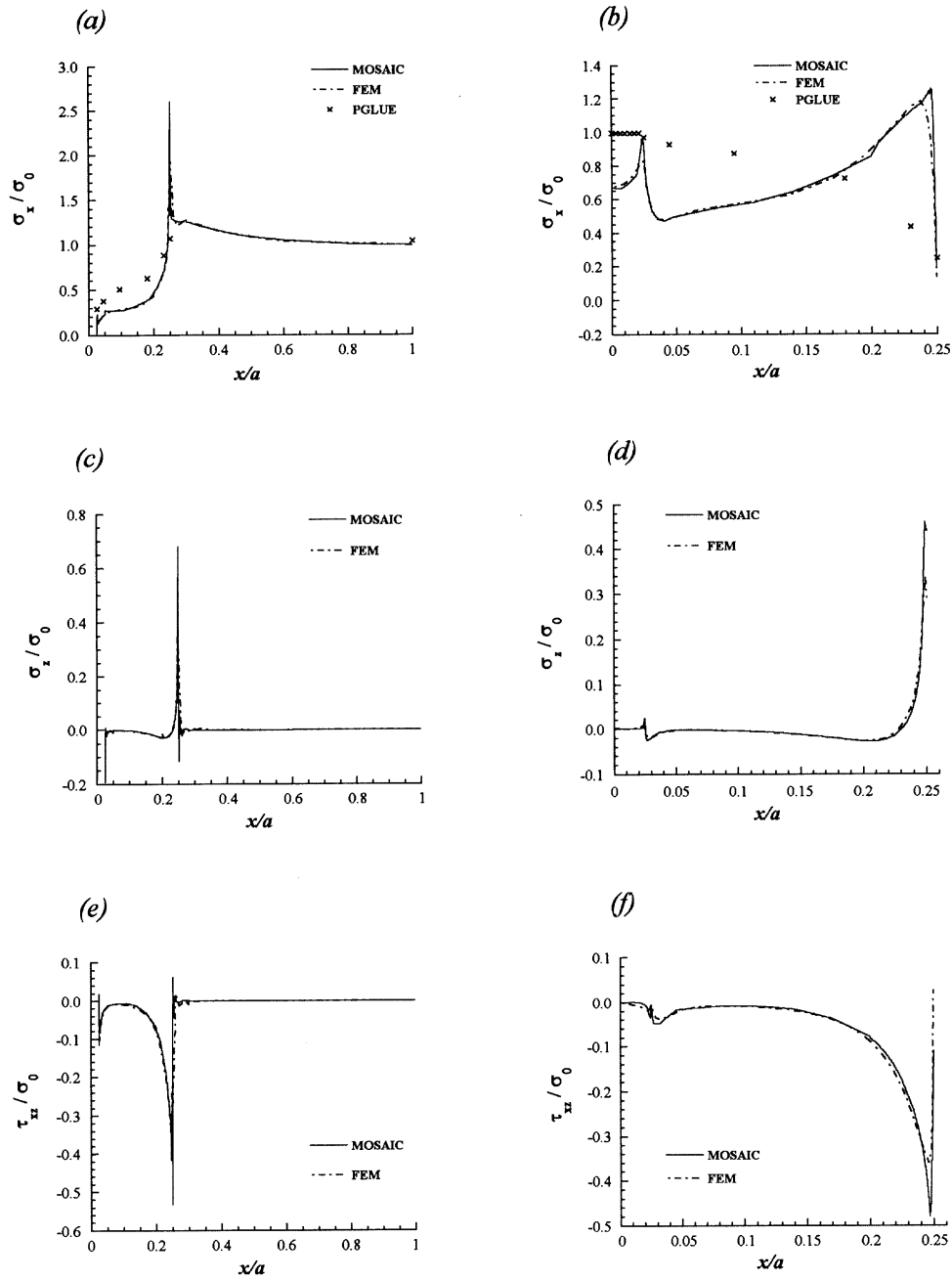


Fig. 6: Distributions of the stresses along the x-direction at $y/b = 0$ in the aluminium skins (a), (c), (e) and the graphite/epoxy patch (b), (d), (f).

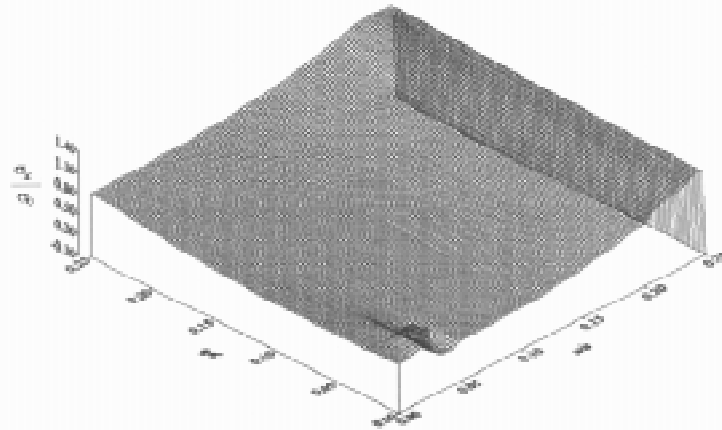


Fig. 7: Variation of patch normal stress σ_x at the patch/adhesive interface.

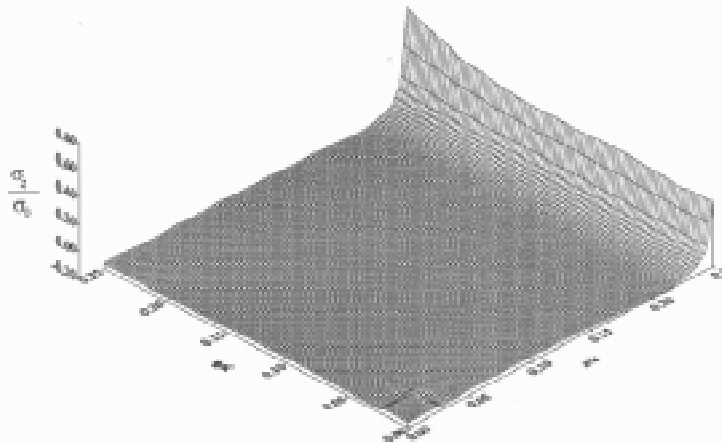


Fig. 8: Variation of patch normal stress σ_y at the patch/adhesive interface.

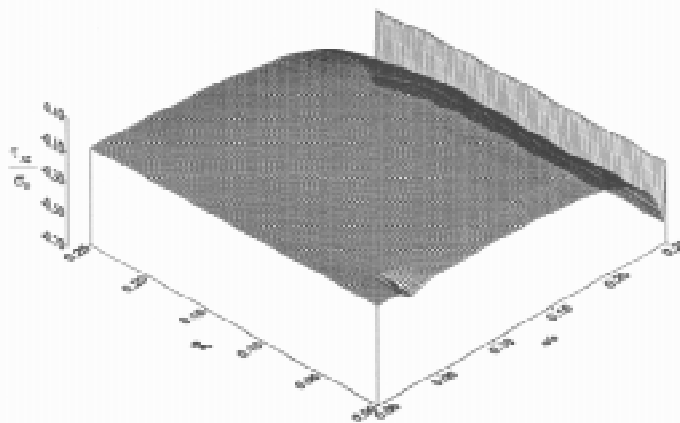


Fig. 9: Variation of patch shear stress τ_{xy} at the patch/adhesive interface.

MONITORING DAMAGE IN BONDED COMPOSITE REPAIRS OF CRACKED METALLIC COMPONENTS USING SURFACE STRAIN MEASUREMENTS

Stephen C. Galea

*Airframes and Engines Division, Defence Science and Technology Organisation,
Aeronautical and Maritime Research Laboratory, 506 Lorimer Street, Fishermens Bend,
Victoria, 3207, Australia.*

SUMMARY: Adhesively bonded fibre reinforced composite patches have been used extensively, over the last two decades, on Royal Australian Air Force (RAAF) aircraft to repair fatigue-cracked metallic aircraft components. The bonded repair to the cracked structure - crack patching - allows the restoration of strength and stiffness of the structure, as well as slowing crack growth by reducing stress intensity. However, especially for critical components with bonded repairs, the crack needs to be inspected at specific intervals in order to monitor crack growth and thus ensure structural integrity is not compromised. This paper reports on an in-situ health monitoring technique of a crack-patched component based on surface strains on the patch to detect and monitor fatigue cracks in the metallic component. Surface mounted electrical resistance strain gauges were installed on the patch of crack-patched specimens. The specimen was then subjected to constant amplitude tension-dominated cyclic loading. Crack lengths, using eddy-current NDI, and surface strain measurements were monitored with increasing number of load cycles. The full field surface stresses were also determined by using a thermoelastic technique. These results were compared with the surface strain gauge measurements. The results showed that the surface strain measurements on the patch commence to deviate, from far-field values, at about 7-8 mm ahead of the crack. Surface strains on the patch in the vicinity of the crack appear to vary linearly with increasing crack length. Also significant variations in residual strains were observed with increasing crack length. These results indicate that monitoring surface strains, and residual surface strains, appear to be a promising technique for detecting and monitoring crack growth beneath composite patches.

KEYWORDS: bonded composite repairs, bonded repairs, bonded composite patches

INTRODUCTION

For economic reasons there is a current trend to operate military aircraft well past their original design life. However, this results in a rapidly increasing number of airframe corrosion and cracking problems and gives rise to the urgent need for cost-effective, efficient repair procedures. This situation is extremely relevant to the Royal Australian Air Force (RAAF) where many aircraft types, such as the F-111, P3C, Macchi will have exceeded their design life well before they can be replaced.

The application of bonded composite patches to repair or reinforce defective metallic structures is becoming recognised as a very effective versatile procedure for many types of

problems. Immediate applications of bonded patches are in the fields of repair of cracking, localised reinforcement after removal of corrosion damage and for reduction of fatigue strain. Adhesively bonded fibre reinforced composite patches have recently been used on the primary structure to repair cracking in the lower wing skin of the F-111C. The bonded repair to the cracked structure - crack patching - allows the restoration of strength and stiffness of the structure, as well as slowing crack growth by reducing stress intensity.

However, especially for critical components with bonded repairs, the crack needs to be inspected at specific intervals in order to monitor crack growth and thus ensure structural integrity is not compromised. Therefore, current studies are focused on the assessment of new techniques in order to achieve in-situ real-time measurement of patch integrity and effectiveness. This application would allow the operator to move away from current costly time-based maintenance procedures toward real-time health condition monitoring of the bonded repair and the repaired structure. These systems would allow timely decisions on preventative and scheduled maintenance before failure of the repair or repaired structure.

This paper reports on an in-situ health monitoring technique of a crack-patched component based on surface strains on the patch to detect and monitor fatigue cracks in the metallic component. Both the surface strains under load and the relative change in residual surface strains were monitored as the crack length increased. The full field surface stresses were also determined by using a thermoelastic technique. These results were compared with the surface strain gauge measurements. The results showed that the surface strain measurements on the patch do vary substantially as the crack passes beneath the strain gauge. Variations in strains were observed 7-8 mm ahead of the crack. Also significant variations in residual strains were observed with increasing crack length. These results indicate that monitoring surface strains, and residual surface strains, appears to be a promising technique for detecting and monitoring crack growth beneath composite repairs.

SPECIMEN

The experimental program was conducted on 2024 T3 specimens 3.14 mm thick having starting cracks with crack length, a , of about 10 mm repaired with unidirectional boron/epoxy 7 ply (0.9 mm) thick semicircular patches. A layer of FM 73 film adhesive was cocured onto the boron/epoxy bonding surface. The patches were then bonded with adhesive FM 73 at 120°C, following surface treatment of the metal using the silane process and the boron/epoxy patches by blasting with alumina grit on the cocured adhesive layer.

The aluminium skins were tested in a back-to-back honeycomb sandwich arrangement by bonding each skin onto aluminium honeycomb as shown in Fig. 1a). This arrangement was used for two reasons:

1. Fabrication considerations, i.e. the skin/patch configuration is unsymmetric therefore the coefficient of thermal expansion (cte) mismatch between the boron patch and the aluminium will cause the panel to bend considerably after the patch has been cured onto the metal skin. Thus by undertaking both processes, i.e. co-curing the patch onto the skin and bonding the skin onto the honeycomb, simultaneously the resultant curvature due to thermal mismatch will be minimised.

2. To minimise the global secondary bending of the panels during testing, due to load path eccentricity in each skin/patch configuration. That is, the bending moments arise from the shift of the neutral axis by the patch. The resistance to bending resulting from the honeycomb support is considered to be a reasonable simulation of the support that would be provided by typical military aircraft structure.

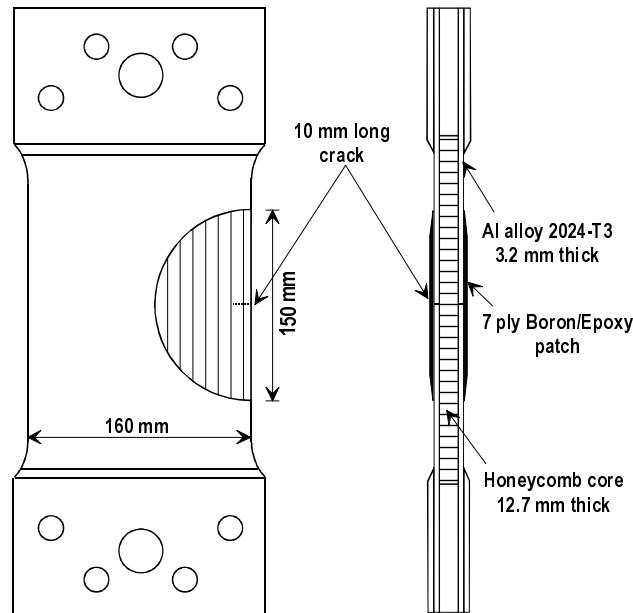


Fig. 1: Schematic of the specimen used for this experimental program.

SENSOR LOCATIONS

In order to study the surface strain behaviour of the patch as the crack grows strain gauges were attached as shown in Fig. 2. Two far-field strain gauges were located on each side of the specimen, these were denoted as 4S1 and 4S2 - far-field gauges on the patch for sides 1 and 2, respectively, and 5S1 and 5S2 - far-field gauges on the aluminium skin for sides 1 and 2, respectively (see Fig. 2). Note that side 1 denotes the side with the strip strain gauges and the sensing direction of all strain gauges was in the loading, y , direction of the specimen.

The strip gauges were attached at three x stations along the crack centreline. The centreline of each strip of gauges was aligned perpendicular to the crack centreline. The first strip, denoted as strip 1, consisted of a column of 10 strain gauges and was located 32 mm ($x = 32$) from the specimen edge and approximately 22 mm ahead of the crack tip, as shown in Fig. 2. The individual gauges are denoted as 1a - 1j with the 5th gauge, 1e, positioned over the crack centreline. These gauges consisted of a sensing length of 1 mm with a pitch of 2 mm. The second strip, strip 2 with gauges 2a - 2e, consisted of a strip of five gauges located 20 mm from the specimen edge ($x = 20$) and approximately 10 mm ahead of the crack tip, as shown in Fig. 2. These gauges consisted of a gauge length of 2 mm with a pitch of 3 mm with the 3rd gauge, 2c, positioned over the crack centreline. The third strip, strip 3 with gauges 3a - 3e, was similar to strip 2 and was located 5 mm ($x = 5$) from the specimen edge and approximately 5 mm behind the crack tip, as shown in Fig. 2. The 3rd gauge, 3c, was positioned over the crack centreline.

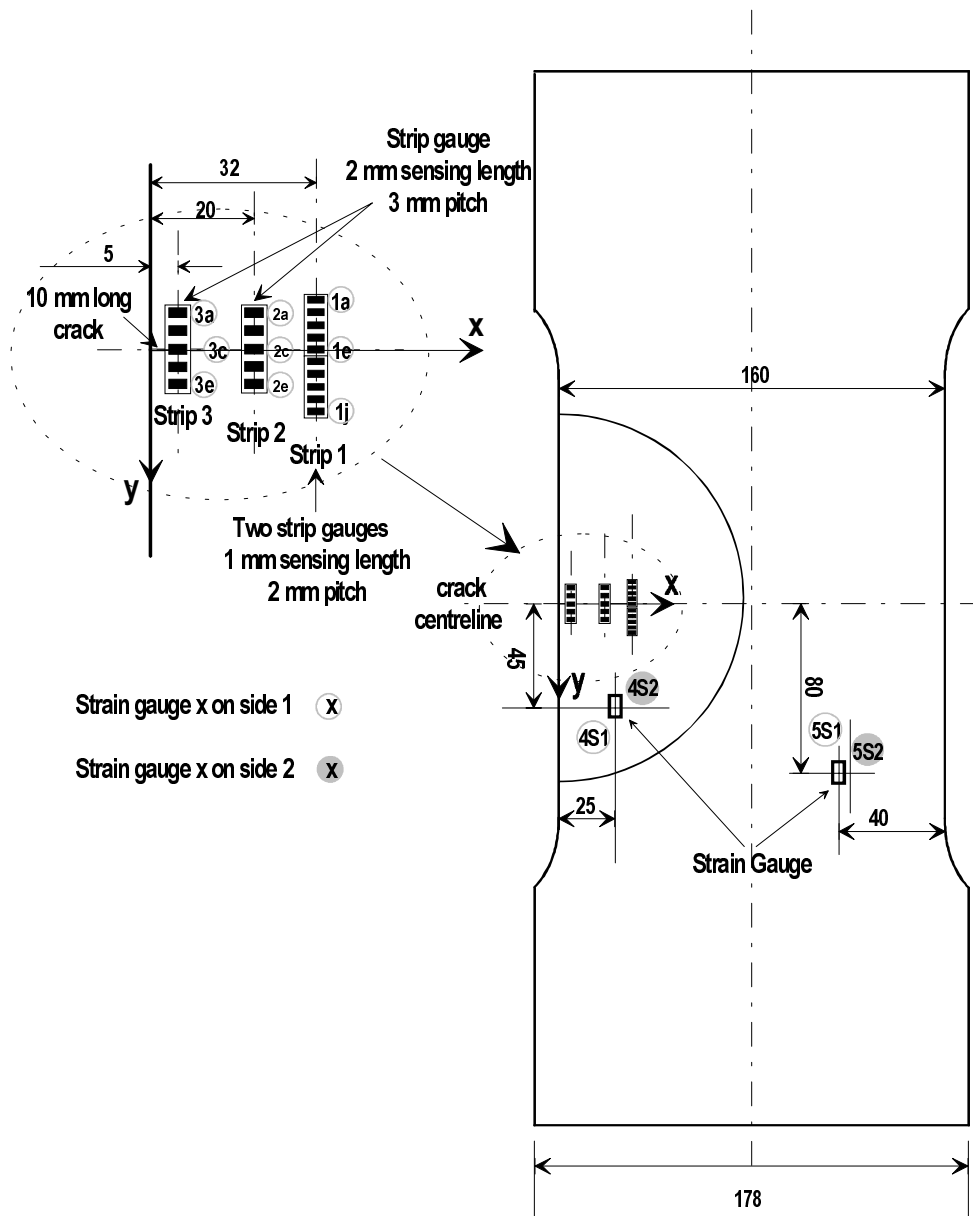


Fig. 2: Location of strain gauges on the specimen Spec1.
(Note that gauges 2c and 2d were defective.)

EXPERIMENTAL SET-UP AND PROCEDURE

Spec1 had the strain gauges attached after the specimen was fully fabricated and so only the strains at load, as well as relative changes in residual strain, could be measured. This specimen was subjected to cyclic in-plane loads, as described below, and strain measurements, at 0 kN and 70 kN load, were taken as the crack progressed. Tests were conducted using the Instron 250kN uni-axial hydraulic testing machine. The cracks were grown under constant amplitude loading for four separate loading conditions, as listed in Table 1. This table lists the required nominal (maximum and minimum) stresses, stress ratios and the applied loads for each of the four loading conditions. Each loading condition was maintained until at least 5 - 8 mm of crack growth was measured, then the next loading condition was applied. The loading frequency during the study was 3 Hz, unless otherwise stated. All tests were undertaken at room temperature.

Table 1: Description of the applied stresses and loads for each load case.

Load Condition		1	2	3	4
Nominal stress, σ (MPa)	Max, σ_{\max}	120.0	135.0	154.0	180.0
	Min, σ_{\min}	12.0	27.0	46.2	72.0
Stress ratio, R ($\sigma_{\min} / \sigma_{\max}$)		0.1	0.2	0.3	0.4
Applied load, P (kN)	Max, P_{\max}	122.0	136.0	156.0	184.0
	Min, P_{\min}	13.0	28.0	47.0	73.0

At every 10000 cycles the cyclic loading was interrupted to undertake strain surveys and crack length measurements. The crack length, a , was measured using an eddy-current surface probe which enabled measurement of the crack length to within an accuracy of about ± 0.5 mm. The strain gauge and load data were recorded using PC-based data acquisition systems. The strain survey was taken during load holds, at every 10 kN, when loading the specimen from 0 to 70 kN at a loading rate of 1 kN/sec. The strain measurements were also taken during the downloading from 70 to 0 kN at every 10 kN increments. Strain gauges were calibrated and zeroed, once only, at the start of the study, i.e. $N = 0$ cycles.

Thermoelastic Analysis

Thermoelastic scans of the patch, for various specimens, using the FAST, Focal-plane Array for Synchronous Thermography, system Ryall and Wong were also undertaken. Provided that adiabatic conditions are maintained it is possible to show that the change in temperature and stress are directly proportional, i.e.

$$-\rho c_{\epsilon} \frac{\Delta T}{T_0} = (\alpha_{11} \Delta \sigma_{11} + \alpha_{22} \Delta \sigma_{22})$$

where ΔT is the local cyclic change in temperature, T_0 is the local absolute temperature, ρ is the density, α_{ii} is the coefficient of thermal expansion, c_{ϵ} is the specific heat at constant strain and $\Delta \sigma_{ii}$ is the cyclic principal stress amplitude. The subscripts 1 and 2 denote directions parallel and perpendicular to the fibre. FAST measures the temperature changes of the coupon under cyclic loading using an infra-red technique and the resultant thermal image effectively represents the stress distribution in the component. For specimens with unidirectional patches, as is the case here, stresses on the surface of the patch are predominantly in the fibre direction, therefore the FAST scan basically represents the σ_{11} surface stress distribution. Specimen 1, with a 45 mm long crack, and a specimen with a 10 mm long crack were scanned using FAST under the load conditions 35 ± 25 kN at 8 Hz.

RESULTS AND DISCUSSION

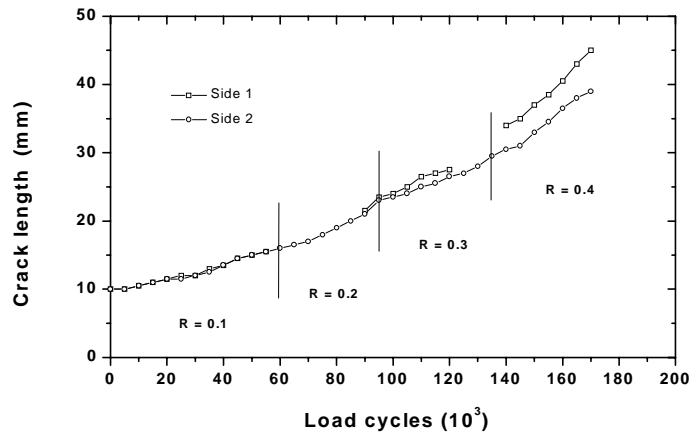


Fig. 3: Plot of crack length with increasing number of loading cycles.

Fig. 3 shows the measured crack growth against number of applied cycles for Spec1. This figure also illustrates the number of cycles, N, applied during each load condition.

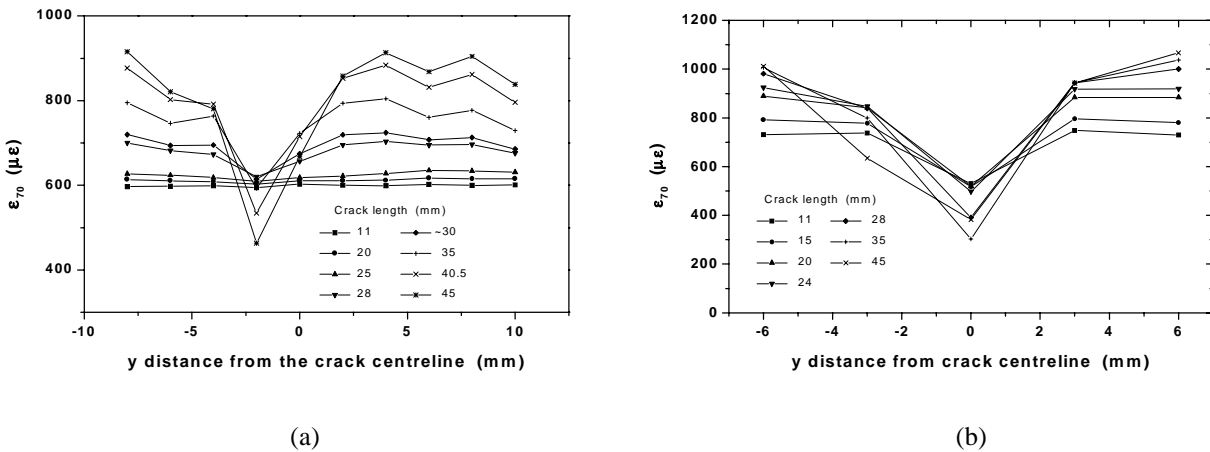


Fig. 4: Variation of strain distributions normal to the crack with increasing crack length for (a) strip 1, $x = 32$ and (b) strip 3, $x = 5$ at 70 kN (ϵ_{70}) load.

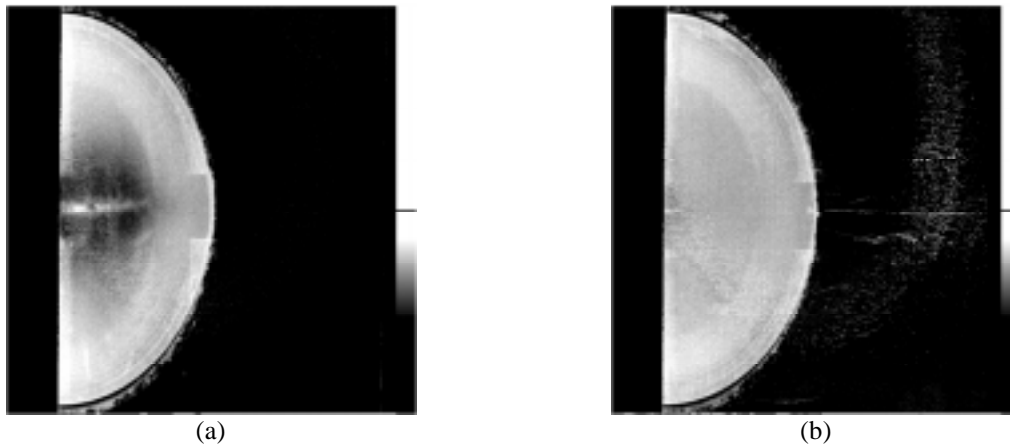


Fig. 5: FAST thermoelastic scans of (a) Spec1, side 1 with $a = 45$ mm, and (b) a specimen with 10 mm long crack, taken under the loading conditions of 35 ± 25 kN at 8 Hz.

Fig. 4 shows the strain distributions at 70 kN load, along a line perpendicular to the crack centreline, at $x = 32$ and 5 , i.e. for strips 1 and 3, respectively. Note that, all the 70 kN load strain data presented in this report has been adjusted such that all strains at zero load were set to zero, i.e. the residual strains were set to zero for all the strain at load cases. This figure illustrates (1) the variation of strain across the crack, and (2) the variation in the strain distribution with increasing crack length. These figures show that the maximum strains do not occur over the crack and are consistent with the FAST scans undertaken on this specimen, Spec 1 with the crack length at 45 mm, and to a lesser extent on a specimen with a 10 mm long crack, see Fig. 5a) and b), respectively. Fig. 5a) shows quite distinctively, a long narrow region of low stresses directly over the crack and regions of high stress above and below the crack. These results are consistent with work undertaken on similar patched cracked specimens [5] and patched cracked specimens with 12 mm thick aluminium cracked skins [4]. Vertical line scans, taken from the scan for Spec1 shown in Fig. 5a), at various positions along the crack are illustrated in Fig. 6. These vertical scans show similar distributions as the strain distributions in Fig. 4. This effect is due to the adhesive shear lag and the local secondary bending. The secondary bending is caused from the load path eccentricity as the load passes through the patch over the crack; the severity of secondary bending will depend on the amount of load path deviation required and the out-of-plane flexibility of the honeycomb core. These regions of high and low stresses become more pronounced, i.e. peaks increase and troughs decrease, as the crack increases in length and the load carried by the patch increases. Note also that the trough appears to be reasonably sharp in nature, however the peaks tend to be broad, see Figs. 4 and 6.

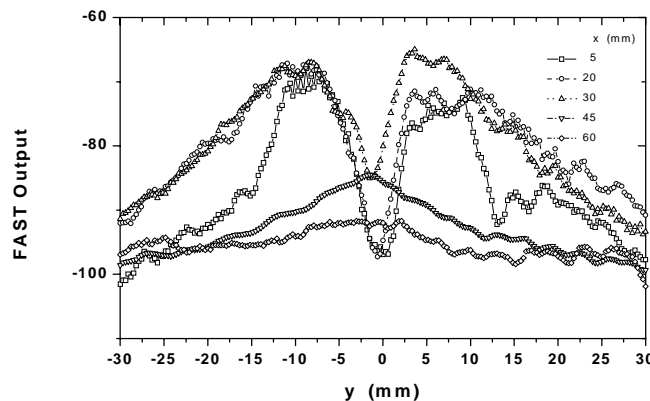


Fig. 6: Vertical line scans from FAST thermoelastic scan of Spec1, side 1 with $a = 45$ mm, taken under the loading conditions of 35 ± 25 kN at 8 Hz.

The strain readings taken at strip 1, Fig. 4a), indicate that the crack has veered about 2 mm upward, from the initial crack centreline, as it passes this strip gauge. This is also illustrated in the FAST scans of Fig. 5 and 6. In fact the vertical line scans show that the location of the minimum strains (ϵ^{\min}) are quite sharp and appear to indicate precisely the location of the crack, whereas the maximum strain peaks are broad plateaus of high strains (ϵ^{\max}). These plateaus have a centre located between 6 - 8 mm above and below the crack and widths between 4 - 8 mm wide. Thus when attempting to detect and monitor the minimum strains, which appear to occur over the crack, then the position of the sensor is critical. However in order to detect and monitor maximum strains the positioning of the sensor appears to be less sensitive to location.

The strain gauges at strip 1, $x = 32$, start to detect the crack when the sensors are approximately 7-8 mm upstream of the crack. That is to say the region of influence of the crack extends to about 7-8 mm ahead of the tip. The extent of this region will be specimen dependent and will depend on factors such as adhesive shear lag and local secondary bending; i.e. on the stiffness of the adhesive, adherands and the honeycomb core.

The measured strains at zero load, ϵ_0 , (residual strains) are shown in Figs. 7a) and 7b) for strips 1 and 3, respectively. These strains are not the true residual strains, since they do not contain the component of residual (thermal) strains due to bonding of the patch onto the aluminium skin. That is, these measurements are basically changes in residual strains in the patch as the crack propagates. This phenomenon is believed to be due to the redistribution of residual thermal strains as the crack propagates under the patch - hence these effects are limited to the immediate vicinity around the crack and are similar to the redistribution of residual thermal stresses experienced in composite laminates after impact has occurred. Fig. 7 shows (1) the spatial variation of residual strain distributions perpendicular to the crack and (2) the variation of residual strain distributions with increasing crack length at stations $x = 32$ and 5. The strain distributions at the two x stations show a surprisingly large change in residual strain with increasing crack length. For strip 1, $x = 32$, the residual strain over the crack drops to $-400 \mu\epsilon$ and the strains above and below the crack increase to $400 \mu\epsilon$ as the crack passes under the strip. Once again changes in residual strains due to the crack appear to occur at about 7-8 mm ahead of the crack. This appears consistent with the strains observed when the specimen is subjected to load, see Fig. 4. The overall features of the residual strain distributions at the two x stations are similar to the strain distributions measured under load.

For the strains measured at strip 1 and 3 variations of the maximum (ϵ^{\max} taken from gauges 1i and 3e) and minimum (ϵ^{\min} taken from gauges 1d and 3c) strains with increasing crack length are illustrated in Figs. 8a) and 8b), respectively. This figure also shows the variations in strains for the two load conditions 0 and 70 kN, ϵ_0 and ϵ_{70} , respectively and illustrates quite clearly the sensitivity of strains to crack length. Fig. 8a) shows once again that the region of influence of the crack extends for about 7-8 mm ahead of the crack tip. Also there appears to be a linear variation in ϵ^{\max} and ϵ^{\min} , for both the residual strains and the 70 kN load case, with crack length for strip 1 once the crack has been detected, i.e. for $a > 25$ mm. Similar results were found by Chang and Sirkis where a linear relationship between strain, in the patch over the crack, and crack length was observed. Fig. 8 also shows that the residual strains have a greater sensitivity to changes in crack length than strain changes measured under load. Therefore it seems that the measurement of residual strains may be a sensitive method for detecting and monitoring crack growth.

Percentage changes in ϵ^{\max} (gauges 1i, 2e, 3e) and ϵ^{\min} (gauges 1d and 3c), compared to far-field measurements, $\epsilon_{70}^{\text{ff}}$ taken from gauge 4S1 at 70 kN load, are then plotted in Fig. 9a) against $a-x_s$. Fig. 9b) shows the variation of the parameter $(\epsilon^{\max} - \epsilon^{\min})/\epsilon_{70}^{\text{ff}}$ with $a-x_s$ for the residual and 70 kN load conditions. The parameter, $a-x_s$, allows the observation of variations in strain from the frame of reference of the sensor where x_s is the x position of the sensor and a is the crack length. Hence negative values, of $a-x_s$, indicate the sensor is upstream of the crack tip and positive values indicate that the crack has passed the sensor and the sensor is downstream of the crack tip. The first figure shows the general linear variation in ϵ^{\max} and ϵ^{\min} with crack growth for the crack upstream and downstream of the sensor. However for conditions where the crack tip has progressed more than 30 mm past the sensor, both the

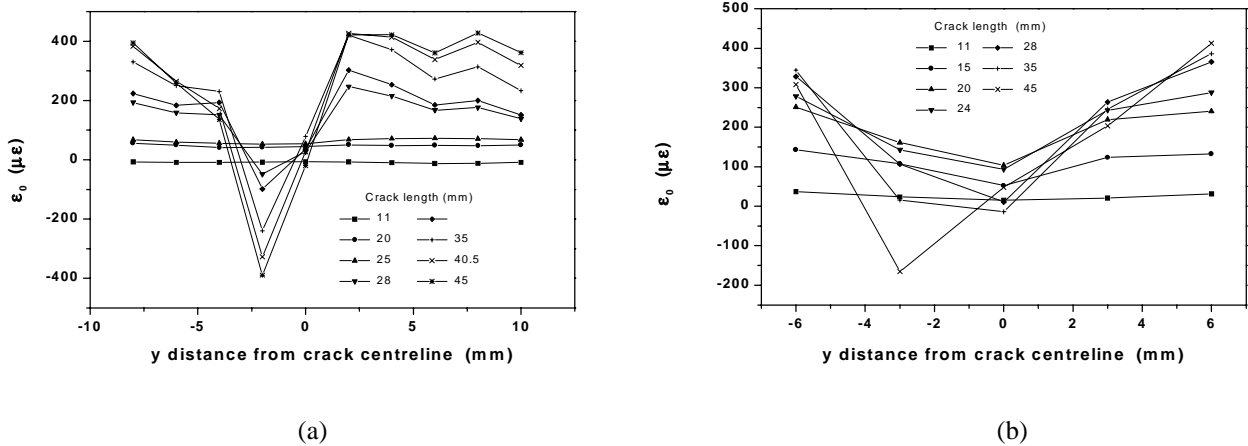


Fig. 7: Variation of strain distributions normal to the crack with increasing crack length for (a) strip 1, $x = 32$ and (b) strip 3, $x = 5$ at 0 kN (ϵ_0) load.

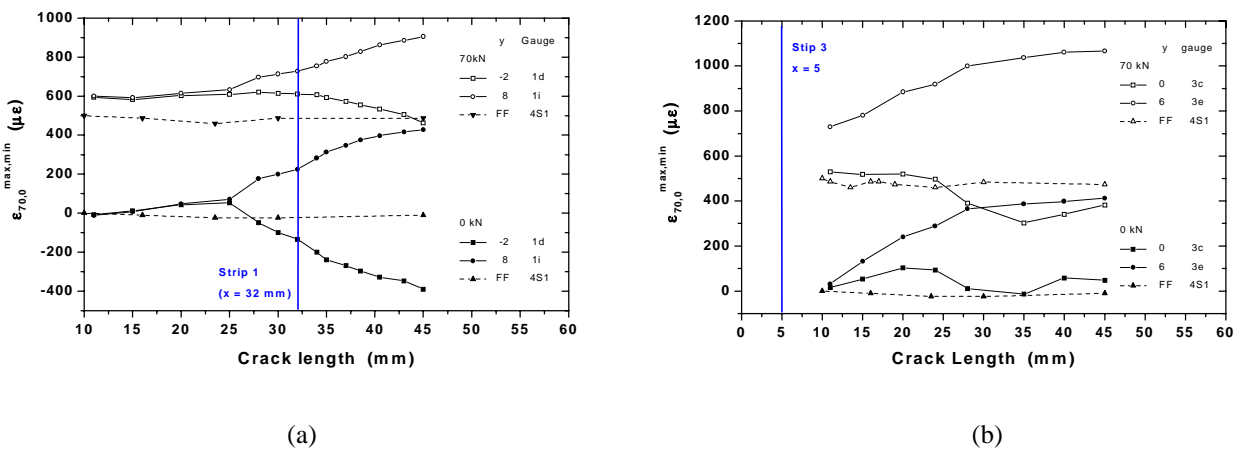


Fig. 8: Variation of maximum and minimum strains with increasing crack length for the two load conditions 0 and 70 kN, ϵ_0 and ϵ_{70} , for (a) strip 1, gauge 1i and 1d, and (b) strip 3, gauges 3e and 3c, respectively. The far-field strains are taken from gauge 4S1.

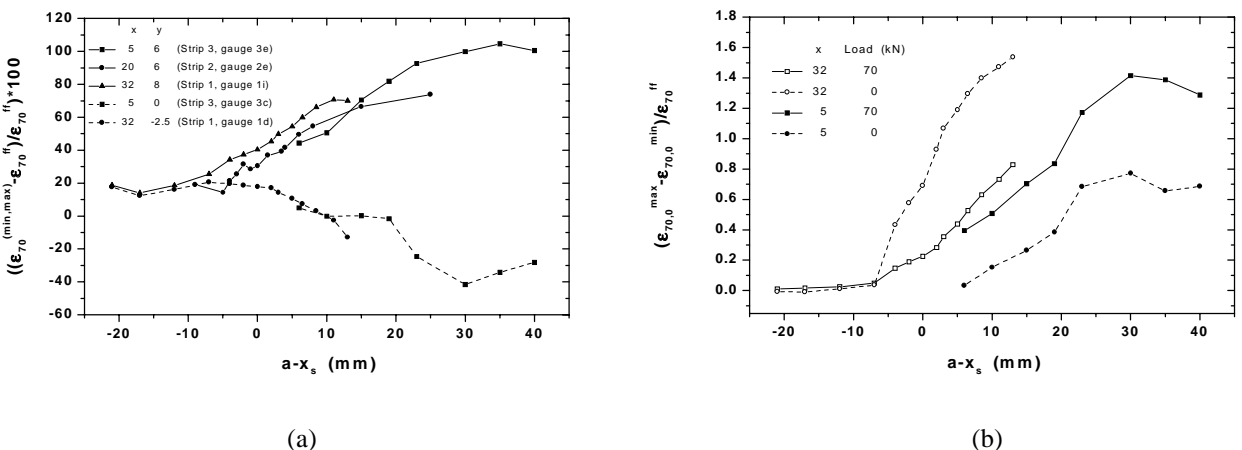


Fig. 9: (a) Percentage variation of maximum and minimum strain with increasing crack length, at 70 kN (ϵ_{70}), for gauges 1i, 2e, and 3e - maximum strain ϵ^{max} - and 1e and 3c - minimum strain ϵ^{min} - compared with the far-field gauge 4S1, ϵ_{70}^{ff} . (b) Variation of the difference between maximum and minimum strain at each strip with increasing crack length.

residual and strains at 70 kN load appear to saturate. Fig. 9b) shows that the parameter $(\epsilon^{\max} - \epsilon^{\min})/\epsilon_{70}^{\text{ff}}$ appears to be extremely sensitive to crack growth - especially for the residual strain case. For example, consider the parameter for residual strains at strip 1, i.e. $(\epsilon_0^{\max} - \epsilon_0^{\min})/\epsilon_{70}^{\text{ff}}$, the variation this parameter is about 150% for a change in crack length of 20 mm whereas the parameter, $(\epsilon_{70}^{\max} - \epsilon_{70}^{\min})/\epsilon_{70}^{\text{ff}}$, varies by only 80%.

CONCLUSIONS

This paper describes a study on surface strains on the patch, of a patched cracked metallic specimen, in order to detect and monitor fatigue cracks in the metallic component. The specimen was subjected to constant amplitude tension-dominated cyclic loading and crack lengths, using eddy-current NDI, and surface strain measurements were monitored with increasing number of load cycles. The full field surface stresses were also determined by using the FAST thermoelastic technique. The following conclusions can be made from the study:

1. Surface strains on the patch, due to an applied in-plane load, show distinctive regions of low strains, over the crack, and high strains, above and below the crack. These results were observed by the strain surveys and by the FAST thermoelastic analysis. The surface strains over the crack, and above and below the crack appeared to be varying quite noticeably with increasing crack length.
2. Similar distributions around the crack were observed for surface residual strains as for strains taken under load. Also, surface residual strains appeared to be extremely sensitive to changes in crack length.
3. Surface strains around the crack region appear to vary linearly with crack length. However strains taken from sensors that were greater than 30 mm downstream from the crack tip appeared to show signs of saturation, and did not change with increasing crack length.
4. The crack appeared to show a region of influence which extended to about 10-15 mm above and below the crack and about 7-8 mm ahead of the crack. However the extent of these regions are specimen dependent and will depend on the stiffness of the adherent, adherends and the honeycomb core.
5. These results indicate that monitoring surface strains, and residual surface strains, appear to be a promising technique for detecting and monitoring crack growth beneath composite patches.

ACKNOWLEDGEMENTS

The author wishes to acknowledge the assistance in the experimental testing by Mr. Onofrio Beninati and Mr. Robert Koning, assistance in undertaking the FAST scans and processing the data by Ms. Petra Cox and Mr. David Rowlands and application of the strain gauges by Mr. Barry Ashcroft and Mr. Phil Ferraroto. He would also wish to thank Dr. Alan Baker for his encouragement and contributions.

REFERENCES

- 1 Baker, A. "Fibre Composite Repair of Cracked Metallic Aircraft Components - Practical and Basic Aspects", *Composites*, Vol. 18, No. 4, 1987, pp. 293-307.
- 2 Baker, A.A., "Bonded Composite Repair of Metallic Aircraft Components", Paper 1 in AGARD-CP-550 Composite Repair of Military Aircraft Structures, 1994.
- 3 Ryall, T.G. and Wong, A.K., "Design of a Focal-plane Array Thermographic System for Stress Analysis", *Experimental Mechanics*, June, 1995, pp 144-147.
- 4 Heller M., Williams J.F., Dunn S., and Jones R., "Thermo-Mechanical Analysis of Composite Specimens", *Composite Structures*, Vol. 11, 1988, pp. 309-324.
- 5 Jones R., Heller M., Lombardo D., Dunn S., Paul J. and Saunders D., "Damage Growth in Composites", *Composites Structures*, Vol. 12, 1989, pp. 291-314.
- 6 Chang, C.-C. and Sirkis, J., "Multiplexed Optical Fibre Sensors for Air Frame Repair Patch Monitoring", *Experimental Mechanics*, Vol. 36, No. 4, 1996, pp353-359.

SHEAR STRESSES IN A STEPPED BONDED REPAIR OF A LAMINATE

Holm Altenbach, Hanno Haars

*Faculty Materials Sciences, Chair Engineering Mechanics,
Martin-Luther-University Halle - Wittenberg, D-06099 Halle (Saale), Germany*

SUMMARY: This paper presents a simplified model for the determination of the shear stress distribution inside a stepped repair of a thin laminated structure. The shear stresses are derived concerning the special material properties of a laminate like non-isotropic material behaviour, differences of the material properties in thickness direction etc. Assuming the laps to be a quasi-homogeneous structure, the bondline is treated as inhomogeneity, which transfers the load via shear stresses from parent laminate into patch and vice versa. The shear stresses in radial and tangential direction and also in-plane shear stresses are derived with help of the proposed model. The model allows a straightforward calculation of the stress distribution without much calculation effort. The efficiency of the model is shown by comparison of example calculations with FE-calculations performed with the FE-system ANSYS[©].

KEYWORDS: composite repair, stepped circular repair, shear stresses, linear elastic material behaviour, macromechanical analysis.

INTRODUCTION

The growing use of fibre reinforced polymers as substitutes for metals and alloys in lightweight engineering areas (automotive and aerospace engineering) leads to an increase of impact damages on fibre-reinforced composite structures. Especially in lightweight engineering applications the structure cannot be designed against impact loads, which may occur in service by drooping tool impacts, carambolages, runway or road debris, etc. Such damages have to be considered in the maintenance procedure (cp. [8], [12]). During the repair - reject decision of a damaged structure, economical subjects as well as ecological ones have to be considered (cp. [7], [11]), because long-fibre reinforced plastics cannot be recycled in an adequate manner. Stiff thinwalled structures are sensitive to impact loads, which mostly lead to damages, even in case of low velocity impacts. After the detection of the damaged area, the question arises, whether the structure can be repaired or has to be replaced. The repair of damaged composites can be performed by a bonded repair where a patch is fitted into or over the damaged area [14]. The use of lap joints, when the patch is simply bonded over the damaged area is not recommended for aerodynamical and also optical reasons. Commonly used joint configurations for that kind of repair are the scarf joint or the stepped joint, because these configurations lead to

a flush surface and do only require access from one side (cp. e.g. [4], [5], [10]). The second configuration is subject of this report.

STEPPED REPAIR

For a macromechanical analysis of a stepped laminate repair, the laminate is assumed to be a quasi-homogeneous material with mechanical properties determined according to the classical lamination theory (e.g. [1], [2]). For the reduction of the complexity of the proposed model, the following assumptions are used:

- constant shear strain across the bondline thickness
- linear elastic material behaviour of laminate and bondline
- shear loads are only transferred by the bondline
- neglect of bending effects of laminate and patch
- ideal connection between the adherends and the bondline

The first assumption can be accepted considering the dimensions of laminate thickness and bondline. The bondline thickness is at least one order of magnitude smaller than the laminate thickness. Linear elastic material behaviour can be assumed for a preliminary approximation of the stress state which leads to equations which can be solved straightforward. Especially the bondline is showing elasto-plastic material behaviour which has to be considered in a more detailed model.

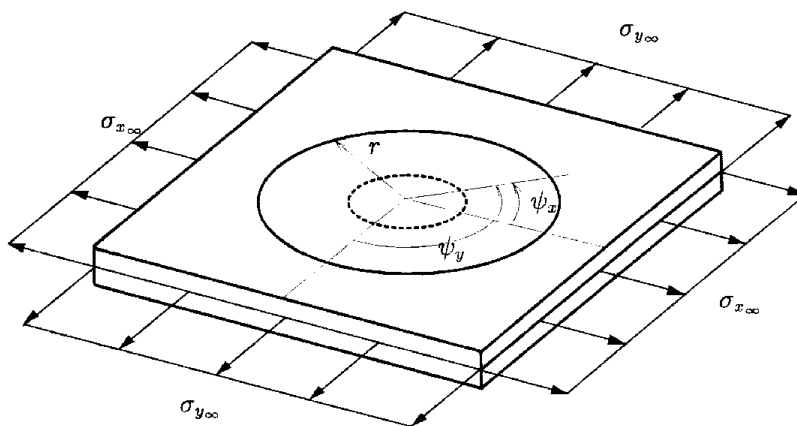


Figure 1: Circular Repair

Considering the assumptions of the classical lamination theory, the laminate is treated as a quasi-homogeneous continuum with the bondline as discontinuity. The shear stiffness of the bondline is in general much lower than that of the laminate, therefore the shear stresses in the laminate can be neglected. Bending effects are not considered, because the structures which are usually damaged by impact loads are thin structures

The repair itself is assumed to have a circular geometry (cp. Fig. 1). Although geometries which are adapted on the stress state and the laminate built up may lead to a more homogeneous stress distribution at the bound of the parent laminate, the circular geometry seems to be more suitable from the manufacturing point of view.

In non-isotropic materials the stress peaks around a circular hole can be much higher than in isotropic materials [9]. The repair will be performed with the aim to re-establish the stress state of the undamaged part as far as possible.

STRESS STATE INSIDE THE BONDLINE

Basing on the models for the determination of the shear stress distribution inside a lap joint (cp. eg. [3], [4], [5], [6], [15]) a model for the shear stress distribution in a stepped repair under plane loading conditions is derived.

The equilibrium at an element inside the repair according to Fig. 2 (the dimension of the bondline-thickness in Fig. 2 is extended for the visualisation of strains inside the bondline and the laminate) with respect to cylindrical coordinates can be expressed as

$$\begin{aligned} \frac{d\sigma_{rr1}}{dr} + \frac{1}{r} \frac{d\tau_{r\psi_1}}{d\psi} + \frac{\sigma_{rr1} - \sigma_{\psi\psi_1}}{r} + F_{rr} &= 0 \\ \frac{d\sigma_{rr2}}{dr} + \frac{1}{r} \frac{d\tau_{r\psi_2}}{d\psi} + \frac{\sigma_{rr2} - \sigma_{\psi\psi_2}}{r} - F_{rr} &= 0 \end{aligned} \quad (1)$$

$$\begin{aligned} \frac{d\tau_{r\psi_1}}{dr} + \frac{1}{r} \frac{d\sigma_{\psi\psi_1}}{d\psi} + \frac{2\tau_{r\psi_1}}{r} + F_{\psi\psi} &= 0 \\ \frac{d\tau_{r\psi_2}}{dr} + \frac{1}{r} \frac{d\sigma_{\psi\psi_2}}{d\psi} + \frac{2\tau_{r\psi_2}}{r} - F_{\psi\psi} &= 0 \end{aligned} \quad (2)$$

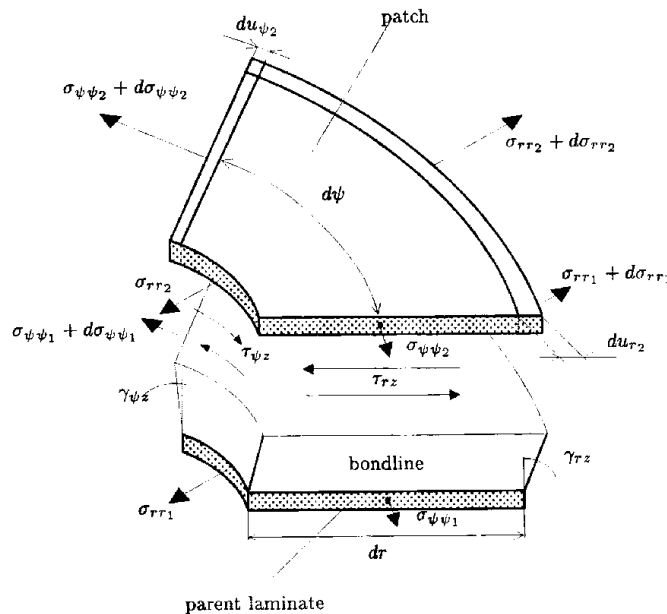


Figure 2: Stresses and strains acting at an element of a stepped repair

Equilibrium inside the repair

The forces F_{rr} and $F_{\psi\psi}$ in Eqs (1) and (2) are transferred by the shear stresses inside the bondline:

$$F_{rr} = \frac{\tau_{rz}}{t_i}, \quad F_{\psi\psi} = \frac{\tau_{\psi z}}{t_i} \quad (3)$$

where the indices i denote the local thicknesses of parent laminate ($i = 1$) and patch ($i = 2$) respectively. The total loads inside the stepped repair have to be the same as in the undamaged structure (index "u"):

$$\sigma_{rr1}t_1 + \sigma_{rr2}t_2 = \sigma_{rru}t_u \quad (4)$$

$$\sigma_{\psi\psi_1}t_1 + \sigma_{\psi\psi_2}t_2 = \sigma_{\psi\psi_u}t_u \quad (5)$$

$$\tau_{r\psi_1}t_1 + \tau_{r\psi_2}t_2 = \tau_{r\psi_u}t_u \quad (6)$$

Using Eqs (1) to (6) the equilibrium of an undamaged structure can be derived:

$$\frac{\sigma_{rr0}}{dr} + \frac{1}{r} \frac{d\tau_{r\psi_0}}{d\psi} + \frac{\sigma_{rr0} - \sigma_{\psi\psi_0}}{r} = 0, \quad (7)$$

$$\frac{d\tau_{r\psi_0}}{dr} + \frac{1}{r} \frac{d\sigma_{\psi\psi_0}}{d\psi} + \frac{2\tau_{r\psi_0}}{r} = 0 \quad (8)$$

These relations lead to the conclusion that the circumferential distribution of the stresses σ_{rr} , $\sigma_{\psi\psi}$ and $\tau_{r\psi}$ inside the damaged shell and the patch is of the same form as in an undamaged structure:

$$\sigma_{rr} = \sigma_\infty \cos^2 \psi, \quad \sigma_{\psi\psi} = \sigma_\infty \sin^2 \psi, \quad \tau_{r\psi} = -\sigma_\infty \sin \psi \cos \psi \quad (9)$$

with σ_∞ as stress acting in the infinity.

Shear stress distribution in radial direction

Equation (9) leads to

$$\frac{d\tau_{r\psi}}{d\psi} = \sigma_\infty (\sin^2 \psi - \cos^2 \psi) \quad (10)$$

which allows a simplification of the equilibrium (1) and (2):

$$\begin{aligned} \frac{d}{dr}\sigma_{rr1} + \frac{\tau_{rz}}{t_1} &= 0, \\ \frac{d}{dr}\sigma_{rr2} - \frac{\tau_{rz}}{t_2} &= 0 \end{aligned} \quad (11)$$

Using the circumferential dependence of the stresses acting at parent laminate ("1") and patch ("2") according to Eqn. (9) results in

$$\begin{aligned} \frac{d}{dr}\sigma_{1\infty} \cos^2 \psi + \frac{\tau_{rz}}{t_1} &= 0, \\ \frac{d}{dr}\sigma_{2\infty} \cos^2 \psi - \frac{\tau_{rz}}{t_2} &= 0 \end{aligned} \quad (12)$$

Considering the assumed compatibility conditions between parent laminate, patch and bondline the relation between the shear strain inside the bondline and the normal strains of laminate and patch can be derived

$$\frac{d}{dr}\gamma_{rz} = \frac{1}{t_b} (\varepsilon_{rr1} - \varepsilon_{rr2}) \quad (13)$$

or using HOOKE'S law

$$\frac{d}{dr}\tau_{rz} = \frac{G_b}{t_b}(\varepsilon_{rr_1} - \varepsilon_{rr_2}) \quad (14)$$

where t_b denotes the bondline thickness and G_b the shear modulus of the bondline. For the plane load case, the elastic relations of laminate and patch are given by:

$$\begin{aligned} \varepsilon_{rr_1} &= s_{11_1}\sigma_{rr_1} + s_{12_1}\sigma_{\psi\psi_1} + s_{13_1}\tau_{r\psi_1}, \\ \varepsilon_{rr_2} &= s_{11_2}\sigma_{rr_2} + s_{12_2}\sigma_{\psi\psi_2} + s_{13_2}\tau_{r\psi_2}, \end{aligned} \quad (15)$$

where the $s_{ij_{1,2}}$ are the components of the compliance matrix of the laminate in radial direction (depending on the circumferential angle ψ).

Shear stress distribution under plane loading conditions

The plane loading condition can be realized by stresses σ_{x_∞} and σ_{y_∞} acting in the infinity. Basing on the equilibrium of forces (Eqs (1) and (2)) the shear stress distribution inside the bondline can be determined. The strains ε_{rr_1} and ε_{rr_2} are dependent on the stresses σ_x and σ_y . To avoid too much indices the index " ∞ " is omitted in the following equations

$$\begin{aligned} \varepsilon_{rr_i} &= \sigma_{x_i} \left(s_{11_i} \cos^2 \psi_x + s_{12_i} \sin^2 \psi_x - s_{13_i} \sin \psi_x \cos \psi_x \right) + \\ &\quad \sigma_{y_i} \left(s_{11_i} \cos^2 \psi_y + s_{12_i} \sin^2 \psi_y - s_{13_i} \sin \psi_y \cos \psi_y \right) \end{aligned} \quad (16)$$

with $i = 1, 2$. Re-arranging yields to

$$\begin{aligned} \varepsilon_{rr_i} &= s_{11_i} (\sigma_{x_i} \cos^2 \psi_x + \sigma_{y_i} \cos^2 \psi_y) \\ &\quad + s_{12_i} (\sigma_{x_i} \sin^2 \psi_x + \sigma_{y_i} \sin^2 \psi_y) \\ &\quad - s_{13_i} (\sigma_{x_i} \sin \psi_x \cos \psi_x + \sigma_{y_i} \sin \psi_y \cos \psi_y) \end{aligned} \quad (17)$$

Considering

$$\psi_y = \psi_x + \frac{\pi}{2} \quad \text{and} \quad \sin\left(\alpha + \frac{\pi}{2}\right) = \cos \alpha, \quad \cos\left(\alpha + \frac{\pi}{2}\right) = -\sin \alpha \quad (18)$$

Eq. (16) can be expressed with $v \equiv \sigma_x/\sigma_y$:

$$\begin{aligned} \varepsilon_{rr_i} &= \sigma_{x_i} \left[s_{11_i} \left(\cos^2 \psi_x + \frac{1}{v} \sin^2 \psi_x \right) \right. \\ &\quad + s_{12_i} \left(\sin^2 \psi_x + \frac{1}{v} \cos^2 \psi_x \right) \\ &\quad \left. - s_{13_i} \left(\sin \psi_x \cos \psi_x - \frac{1}{v} \sin \psi_x \cos \psi_x \right) \right] \end{aligned} \quad (19)$$

If $\sigma_x = \sigma_y$ or $v = 1$ a further simplification of Eq. (19) is possible:

$$\varepsilon_{rr_i} = \sigma_{x_i} (s_{11_i} + s_{12_i}) \quad (20)$$

The differential equation of the shear stress inside the bondline for a uniformly distributed load ($\sigma_x = \sigma_y$) can be calculated to:

$$\frac{d^2}{dr^2}\tau_{rz} = \frac{G_b}{t_b \cos^2 \psi_x} \left[\frac{1}{t_1} (s_{11_1} + s_{12_1}) + \frac{1}{t_2} (s_{11_2} + s_{12_2}) \right] \tau_{rz} \quad (21)$$

For non-uniformly distributed loads ($\sigma_x \neq \sigma_y$ or $v \neq 1$) the differential equation can be derived in a similar way. The general form of this equation is

$$\frac{d^2}{dr^2} \tau_{rz} = \frac{G_b}{t_b \cos^2 \psi_x} \left[\frac{1}{t_1} \left(s_{11_1} \cos^2 \psi_x + \frac{1}{v} s_{11_1} \sin^2 \psi_x \right. \right. \quad (22)$$

$$+ s_{12_1} \sin^2 \psi_x + \frac{1}{v} s_{12_1} \cos^2 \psi_x$$

$$\left. \left. - s_{13_1} \sin \psi_x \cos \psi_x + \frac{1}{v} s_{13_1} \sin \psi_x \cos \psi_x \right) \right.$$

$$+ \frac{1}{t_2} \left(s_{11_2} \cos^2 \psi_x + \frac{1}{v} s_{11_2} \sin^2 \psi_x \right.$$

$$+ s_{12_2} \sin^2 \psi_x + \frac{1}{v} s_{12_2} \cos^2 \psi_x$$

$$\left. \left. - s_{13_2} \sin \psi_x \cos \psi_x + \frac{1}{v} s_{13_2} \sin \psi_x \cos \psi_x \right) \right] \tau_{rz}$$

or

$$\frac{d^2}{dr^2} \tau_{rz} = \lambda^2 \tau_{rz} \quad (23)$$

In the differential equations (21) to (23) the dependence on the circumferential angle is given by the trigonometric functions and the compliances s_{ij} which are also changing with an variation of ψ .

This differential equations can be solved with a solution in form of

$$\tau_{rz} = A \cosh \lambda r + B \sinh \lambda r \quad (24)$$

The constants A and B can be determined with help of the boundary conditions. The average shear stress in radial direction can be estimated with help of a "Load-Transfer-Analysis" as proposed by MYHRE and BECK [13] for a stepped lap joint. This theory assumes the shear stress inside a step to be proportional to the laminate stiffness (in load direction) of that step. The knowledge of the slope of τ_{rz} at the beginning of the step, that means $\frac{d\tau}{dr}(r=0)$ according to Eq. (14) allows the calculation of the constant B :

$$B = \frac{\partial \tau_{rz}}{\partial r}(r=0) \quad (25)$$

which results in

$$B = \frac{G_b}{\lambda t_b} \left[\sigma_1 \left(s_{11_1} \cos^2 \psi + s_{12_1} \sin^2 \psi - s_{13_1} \sin \psi \cos \psi \right) \right.$$

$$\left. + \sigma_2 \left(s_{11_2} \cos^2 \psi + s_{12_2} \sin^2 \psi - s_{13_2} \sin \psi \cos \psi \right) \right] \quad (26)$$

Knowing B and the average shear stress $\tau_{rz_{av}}$ in the step, the constant A can be computed:

$$A = \frac{\lambda \tau_{rz_{av}} l_{Stufe} - B (\cosh (\lambda l_{Stufe}) - 1)}{\sinh (\lambda l_{Stufe})} \quad (27)$$

Shear Stress distribution in tangential direction

With the knowledge of the shear stress distribution in radial direction, the shear stress distribution in tangential direction can be derived. In the equilibrium condition in tangential direction

$$\frac{d}{dr} \tau_{r\psi_i} + \frac{1}{r} \frac{d}{d\psi} \sigma_{\psi\psi_i} + \frac{2}{r} \tau_{r\psi_i} = -\frac{\tau_{\psi z}}{t_i} \quad (28)$$

($i = 1, 2$) the differentiation of $\sigma_{\psi\psi_i}$ according to Eq. (9) with respect to ψ can be performed and the result can be substituted by $\tau_{r\psi_i}$ which leads to

$$\frac{d}{dr} \tau_{r\psi_i} = -\frac{\tau_{\psi z}}{t_i} \quad (29)$$

Substitution of $\tau_{r\psi_i}$ by σ_i according to the stress distribution in radial direction (Eqn. (9)) results in

$$\frac{d}{dr} \sigma_i \sin \psi \cos \psi = \frac{\tau_{\psi z}}{t_i} \quad (30)$$

$\frac{d}{dr} \sigma_i$ can be substituted according to Eqn (12)

$$\frac{d}{dr} \sigma_i = -\frac{1}{t_i} \frac{1}{\cos^2 \psi} \tau_{rz} \quad (31)$$

The differential equation for the shear stress distribution in radial direction (Eq 21) can be re-arranged considering

$$\lambda^{*2} = \lambda^2 / \cos^2 \psi \quad (32)$$

to

$$\frac{1}{\cos^2 \psi} \frac{d^2}{dr^2} \tau_{rz} = \lambda^{*2} \tau_{rz} \quad (33)$$

This differential equation can be solved with a solution of the same form as the original differential equation leading to a shear stress distribution

$$\tau_{\psi z} = -\sin \psi \cos \psi [A^* \cosh(\lambda r) + B^* \sinh(\lambda r)] \quad (34)$$

Resulting shear stress distribution

For the calculation of the resulting shear stress distribution the in-plane shear stresses have to be computed. Assuming that laminate and patch fulfill different in-plane shear deformations, the shear strain inside the bondline can be determined as median of the different shear deformations.

$$\gamma_{r\psi_b} = \frac{1}{2} (\gamma_{r\psi_1} + \gamma_{r\psi_2}) \quad (35)$$

With help of HOOKE's law the corresponding shear stress can be calculated, that the resulting shear stress distribution is determined

$$\tau_{res} = \sqrt{\tau_{rz}^2 + \tau_{\psi z}^2 + \tau_{r\psi}^2} \quad (36)$$

EXAMPLES

For the demonstration of the efficiency of the proposed model, the shear stress distribution inside a stepped repair of a quasiisotropic laminate $[0, 60, 120]_{2s}$ is calculated whereas the number of steps has been varied from 2 steps to 3 steps. The lamina is assumed to be a carbon-fibre reinforced epoxy lamina with the following mechanical properties:

Laminate:		Adhesive:	
Young's Moduli:	E_{\parallel} : 145120 MPa E_{\perp} : 6880 MPa	Shear Modulus:	G : 1000 MPa
Poisson's ratio:	$\nu_{\parallel\perp}$: 0.24	Bondline thickness:	t_B : 0.3mm
		Poisson's ratio:	$\nu_{\parallel\perp}$: 0.4

The laminate is assumed to be uniformly loaded by a tensile stress $\sigma_x = \sigma_y = 30\text{MPa}$.

2-step repair

Due to the built up of the laminate, the shear stress distribution in radial direction is quite inhomogeneous. The inhomogeneity of is dependent on the stacking sequence of the laminate which lead to different mechanical properties in the different steps.

	Parent laminate:	Patch:
1. step	$[0,60,120,0,60,120,120,60]$	$[0,120,60,0]$
2. step	$[0,60,120,0]$	$[60,120,120,60,0,120,60,0]$

Thus the parent laminate of the first step as well as the patch of the second step are relatively stiff in "x"-direction and weak in y-direction (high amount of 0^0 layers). This leads to the high stress peaks in "y"-direction.

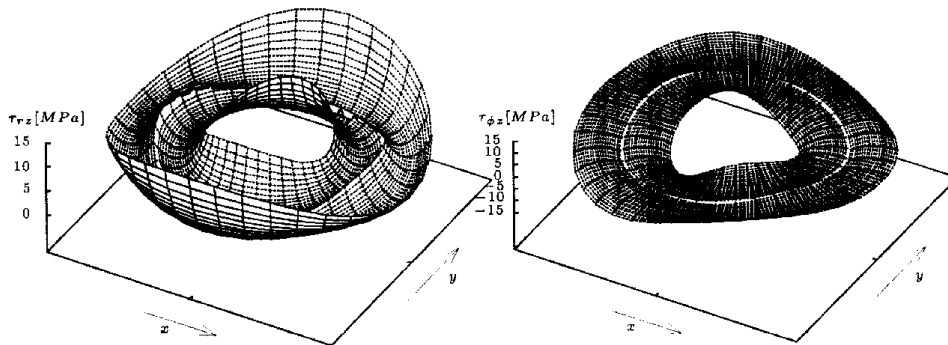


Figure 3: Shear stress distribution, $\sigma_x = \sigma_y = 30\text{MPa}$; QI-laminate $[0,60,120]_{2s}$, 2 steps

3-step repair

Performing a repair with 3 steps in the same laminate, the stiffness changes from step to step are constant (also around the circumference): due to the built up of the laminate, every step is a quasihomogeneous laminate that the elastic properties are not changing from step to step.

	Parent laminate:	Patch:
1. step	[0,60,120,0,60,120,120,60,0]	[120,60,0]
2. step	[0,60,120,0,60,120]	[120,60,0,120,60,0]
3. step	[0,60,120]	[0,60,120,120,60,0,120,60,0]

This repair configuration leads to a more homogeneous shear stress distribution, because the mechanical properties of the steps do remain constant across the circumference of the repair.

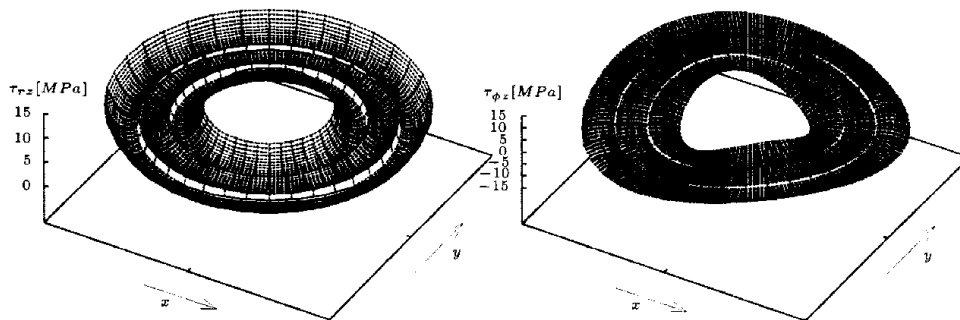


Figure 4: Shear stress distribution, $\sigma_x = \sigma_y = 30$ MPa; QI-laminate $[0,60,120]_{2s}$, 3 steps

For comparison, a finite element model was calculated with the FE-system ANSYS[®]. The laminate was modelled with anisotropic brick elements with mechanical properties calculated according to the classical lamination theory to avoid errors caused by different rheological models. The results obtained by the FE-solution show a good agreement of both models. The shear stress distribution (that means the location of stress maxima and minima) as well as the value of the stresses are in quite good fit. The stresses derived by the proposed model are in general a little higher than the stresses calculated by ANSYS[®] (about 10%).

CONCLUSIONS

The presented model allows a straightforward calculation of the shear stresses inside the bondline of a stepped repair of a laminated structure considering the special mechanical behaviour of laminates. Comparison with FE-calculations shows a satisfactory fit of both models. Considering the modelling and calculation effort, the presented model is suitable for the calculation of the shear stress distribution inside the bondline, at least for preliminary design purposes.

ACKNOWLEDGEMENTS

This work has been supported by the German Research Foundation ("Deutsche Forschungsgemeinschaft (DFG)") (GRK 203/2-96) which is gratefully acknowledged.

REFERENCES

1. J. Aboudi: *Mechanics of Composite Materials*. Elsevier Applied Science Publishers, Amsterdam et. al., 1991.
2. K. Ashbee: *Fundamental Principles of Fiber Reinforced Composites*. Technomic Publishing Co. Inc., Lancaster, Basel, 1989.
3. M. Goland and E. Reissner: *The stresses in cemented joints*. Journal of Applied Mechanics 66(1), P. 17-27, 1944.
4. L.J. Hart-Smith: *Development in Adhesives - 2*. Applied Science Publishers, London, 1981.
5. L.J. Hart-Smith: *Adhesive Bonded Scarf Joints*. NASA National Aeronautics and Space Administration Langley Research Center, Hampton, Virginia, 1973.
6. L.J. Hart-Smith: *Adhesive Bonded Lap Joints*. NASA National Aeronautics and Space Administration Langley Research Center, Hampton, Virginia, 1973.
7. R. Hinterwaldner: *Kleben von Verbundwerkstoffen und deren Recyclingchancen*. Hinterwaldner-Verlag, München, 1992.
8. R. Jones and J. Paul: *Fibre Composite Repairs to Damaged Structural Components*. Computational Mechanics 2(6), pp.247-252, 1987.
9. S.G. Lekhnitski: *Theory of elasticity of an anisotropic elastic body*. Holden-Day, San Francisco, 1963.
10. F.L. Matthews: *Joining Fibre Reinforced Plastics*. Elsevier Applied Science Publishers, Amsterdam et. al., 1987.
11. J.E. McCarty: *Design and Cost Viability of Composites in Commercial Aircraft*. Composites 24(4), pp. 361-365, 1993.
12. S. Müller von Kralik: *Reparaturverfahren bei Composites*. In: 4. Nationales Symposium der SAMPE Deutschland. SAMPE - Society for the Advancement of Materials and Process Engineering, 1990.
13. S.H. Myhre and C.E. Beck: *Repair Concepts for Advanced Composite Structures*. Journal of Aircraft 16(10), pp720-728, 1979.
14. R.H. Stone: *Repair Techniques for Graphite/Epoxy Structures for Commercial Transport Applications*. NASA, 1983.
15. O. Volkersen: *Die Nietkraftverteilung in zugbeanspruchten Nietverbindungen mit konstanten Laschenquerschnitten*. Luftfahrtforschung 15(1), pp. 41-47, 1936

COMPOSITE BONDED REPAIR OF CRACKED PANELS SUBJECT TO ACOUSTIC FATIGUE

R. J. Callinan, S. C. Galea and S. Sanderson

*Aeronautical and Maritime Research Laboratory
506 Lorimer Street, Fishermens Bend, Victoria, 3207, Australia*

SUMMARY: The skin of an aircraft can vibrate as a result of pressure waves caused by engine and/or aerodynamic effects. In modern fighter aircraft such as the F/A-18, sound pressure levels have been recorded up to 170dB over the surface of the skin. In the F/A-18 cracking has occurred in the lower nacelle, typically along the boundaries of the panel. These cracks often originate from a fastener line and grow along the boundary and then turn into the centre of the panel. In the case of the F/A-18, cracking was due to higher than expected pressure levels caused by an aerodynamic disturbance at the inlet lip. Attempts have been made to repair these panels with boron fibre patches, however the cracks have continued to grow. This paper aims at attempting to understand the mechanism's of cracking of the panels subjected to acoustic excitation and the influence of bonded repairs.

KEYWORDS: bonded repair, random response, acoustic fatigue

INTRODUCTION

Acoustic fatigue is due to a very high intensity excitation as a result of pressure waves caused by either engine/or aerodynamic effects. Acoustically-induced cracking has occurred on the external surface of the lower nacelle skin on the F/A-18, illustrated in Fig. 1. In these regions overall sound pressure levels (OASPL) greater than 170 dB have been measured in flight. These high sound pressure levels appear to be a result of an aerodynamic disturbance at the inlet lip [1]. Typical cracks occur along a line of rivets or run parallel to the rivet line and may turn into the centre of the panel, as shown in the inset. Cracking generally occurs along the longer side of the panel where the bending stresses due to out of plane vibrations are a maximum. Up to a third of the F/A-18's in the RAAF fleet are effected by these cracks.

The standard repair for such cracking is to remove and replace the panel. The standard long term fix is to incorporate additional stiffeners on the inside to stiffen the panel. This has two effects firstly to reduce the panels response, i.e. lower stress, for a given load and secondly it increases the resonant frequencies of the panel to frequencies well outside the recorded excitation frequencies.

In order to reduce cost of repairing such cracked structures a bonded repair would be preferred. Such a repair was designed and implemented on an existing cracked aircraft. The benefits of such a repair are reflected in the time required to carry out the repair; typically 60 hours for the mechanical repair and approximately 15-25 hours for the bonded repair. While in the past boron fibre patches have been used as a cost effective means of repairing cracked aircraft structures, in this case however, the cracks continued to grow.

The work reported here will involve the estimation of the root mean square (r.m.s.) response of the stress intensity factor (K) in the cracked and cracked/repaired cases as an attempt to understand the problems involved in patching cracks in such an environment.

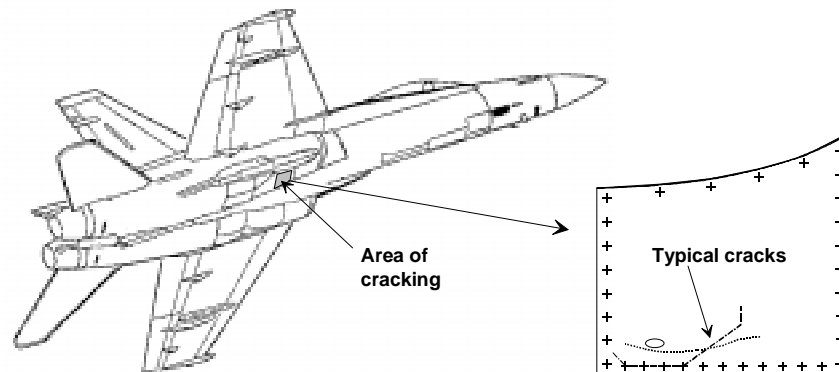


Fig. 1: Location of the cracking in the lower nacelle inlet.

THEORY

Random Response Analysis

The random response analysis capability of the NASTRAN program has been used to solve this problem [2]. This involves a solution in the frequency domain after the transfer function, $H(\omega)$, is generated. Together with the power spectral density (PSD) of the excitation, $S_i(\omega)$, the PSD of the response, $S_j(\omega)$, is determined:

$$S_j(\omega) = |H(\omega)|^2 S_i(\omega) \quad (1)$$

This analysis allows the statistical properties of the system to be evaluated. Random vibrations involve all frequencies at any one instant in time. After calculating the PSD, the root mean square (r.m.s.) of the response can be determined by computing the square root of the PSD area:

$$j_{rms} = \sqrt{\frac{1}{2\pi} \int_0^{\infty} S_j(\omega) d\omega} \quad (2)$$

A similar application of finite element techniques to undertake a PSD analysis to acoustic fatigue problems has been reviewed by Climent and Casalengua [3].

Stress Intensity Factors

In the F.E. model the depth of the plate is modelled using a single layer of 20 noded brick elements, and as such will model bending behaviour of the skin. The skin thickness is approximately 1 mm , hence the condition of plane stress is assumed. The computation of the stress intensity factor may be determined directly from the crack tip element used around the crack tip or from displacements using a crack opening (COD) formula. The r.m.s. crack tip stress intensity factors for mode I and III are derived from the standard asymptotic relations:

$$K_{I rms} = \frac{E V_{rms}}{4} \sqrt{\frac{2\pi}{l}} \quad (3)$$

$$K_{III rms} = G W_{rms} \sqrt{\frac{2\pi}{l}} \quad (4)$$

where E = Young's modulus

G = Shear modulus

V_{rms} = mode I crack opening r.m.s. displacement

W_{rms} = mode III crack opening r.m.s. displacement

l = length of the crack tip element

FEA METHODOLOGY VALIDATION

The complexity of the random response analysis and number of assumptions made is such that validation of the analysis was necessary. Both experimental and analytical work has been carried out by Byrnes [4]. In this case the plate used is that shown in Fig.2 and the PSD of the acoustic excitation is given in Fig. 3. Dimensions of the plate are $B=500 \text{ mm}$, $C=166 \text{ mm}$ and thickness= 1.2 mm with a crack of length A . This plate was clamped along edges except one edge, which was partially restrained. The unrestrained region represented a crack along one side. The length of the crack has been expressed as a ratio A/B . Material properties of the aluminium plate are given in Table 1, with the structural damping coefficient set to 0.055. R.m.s. strains were measured at a point 25 mm ahead of the crack tip, the results are reproduced in Fig. 4 along with an analytical solution also developed by Byrnes [4].

The F.E. results are also shown in Fig.4. Only three experimental data points were published in [4], and in each case the F.E. results are within 10%. However disagreement does exist with the analytical solution for crack length to plate width ratios below 0.4 . It is not clear why this difference occurs. The analytical solution is based on contributions from the first and second mode shapes only. However the F.E. PSD of the response allows for many mode shapes.

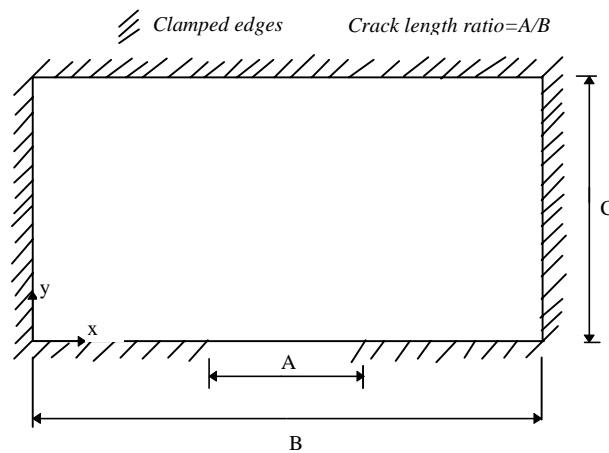


Fig. 2: Geometry of plate used for the validation of the analysis.

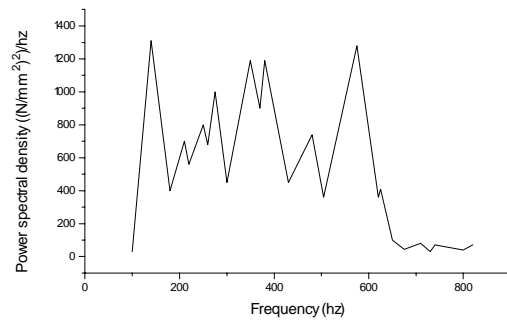


Fig. 3: Power Spectral Density of the pressure excitation used in [4]. results.

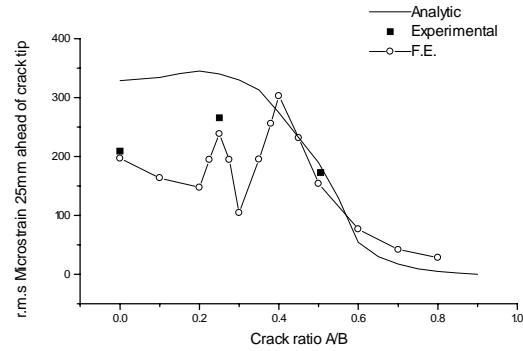


Fig. 4: Comparison of F.E., experimental and analytic results.

FEA OF CRACKED NACELLE INLET

A simplified model has been developed in which the skin is considered to be flat. However, to take account of all shear deformation the structure has been idealised as a fully three-dimensional structure using 20 noded brick elements. The geometry of the structure is shown in Fig. 5. The mesh size of the skin structure is 75x60 elements, while the patch and skin is 40x40 elements. As shown, the patch only extends partially across the panel. Sufficient elements have been used to define the minimum crack length considered. Material properties for the skin, adhesive and boron are shown in Table 1. For the analysis presented here, it is assumed that the boron patch is isotropic. The main reason that 20 noded bricks were used in the skin is that calculations for K can be made corresponding to a bending field. Also, the behaviour of the adhesive has been modelled as a 3 dimensional element, to allow for shear deformation and damping in a future study. A structural damping coefficient of 0.032 has been used [1].

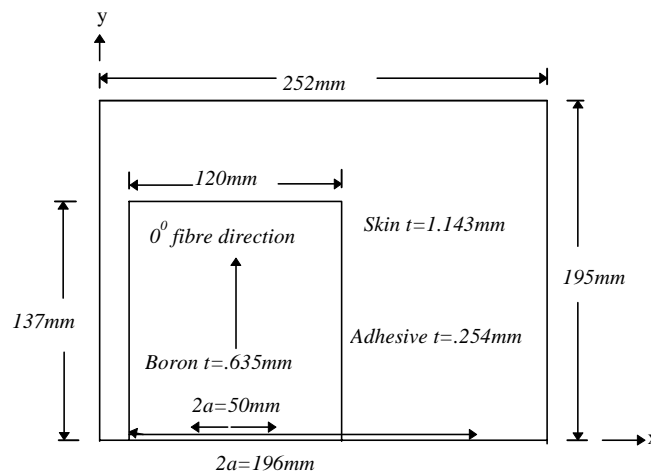


Fig. 5: Dimensions of F/A-18 nacelle inlet panel

The boundary conditions for this model are considered to be fully clamped except for the crack region which is not restrained. The patch above the crack also remains fully constrained. Clearly crack closure will occur at an increasing distance away from the crack tip, however the complexity in introducing such constraints has not been included in this preliminary study.

Table 1: Material properties.

Material	Young's Modulus (MPa)	Poisson's Ratio	Density (Mg/mm ²)
Aluminium	70000.	.33	2.77x10 ⁻⁹
Adhesive	2273.	.35	1.2x10 ⁻⁹
Boron	207000.	.33	2.0x10 ⁻⁹

Flight measurements, Ref. 1, have been made of the one third octave band sound pressure level using microphones located at the nacelle inlet area, and this result is shown in Fig. 6. The spectrum level, relative to the overall sound pressure level (OASPL), is derived from this result and is also shown in Fig. 6. This spectrum is now used as the excitation pressure on the FE model described above.

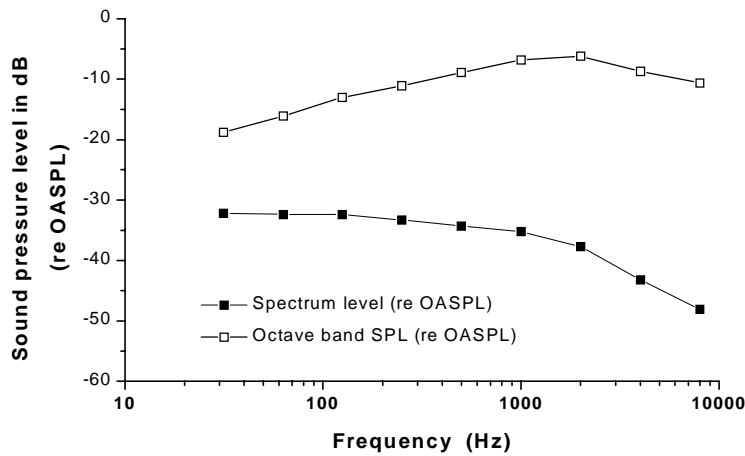


Fig. 6: Maximum sound pressure level and spectrum over nacelle inlet.

The relationship between the spectrum sound pressure level (SPL) and the r.m.s. fluctuating pressure (p) is given in [3] as:

$$p_{rms} = 10^{(SPL/20-4.69897)} \tag{3}$$

and the power spectral density of acoustic pressure, i.e. PSD of the excitation, at any given frequency is given by:

$$PSD = p_{rms}^2 = 10^{(SPL/10-9.3979)} \tag{4}$$

The curve in Fig. 6 has been approximated with the three points shown in Table 2.

Table 2: Input power spectral density

Frequency (hz)	Pressure spectrum level in dB	R.M.S. pressure level ,(MPa) ² /hz
31.5	140	4.0 x10 ⁻⁸
1000	137	2.005x10 ⁻⁸
8000	124.1	1.028x10 ⁻⁹

RESULTS AND DISCUSSION

Shown in Fig. 7 are the natural frequencies versus crack length for the cracked and un-repaired panel and also the repaired panel for the first 3 mode shapes. In the case of the cracked un-repaired structure, increasing the crack length significantly reduces the natural frequency of the panel. Also as expected, repaired panels have little variation in natural frequency with crack length. Furthermore the repaired panels have substantially higher natural frequencies for all modes than the un-repaired panels. The boron repair has a definite influence on the panel stiffness.

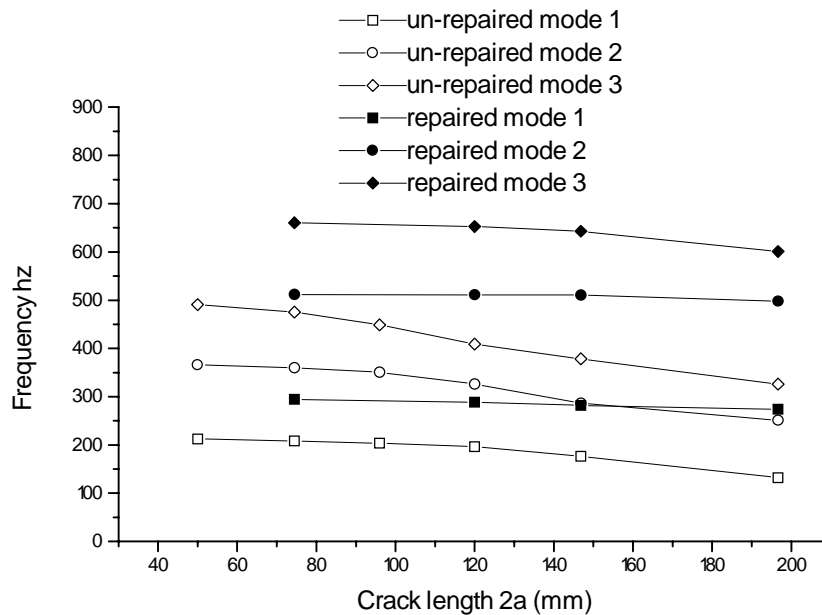


Fig. 7 : Frequency versus crack length for un-repaired and repaired cases.

Mode shapes have been computed corresponding to a short and long crack length for the repaired panel. The first 3 mode shapes for a short crack length (100 mm) which is covered by the patch, is shown in Fig. 8. Clearly the crack tip behaviour is dominated by the mode I stress intensity factor K_I , arising from bending that would occur under excitation of these modes. The mode shape corresponding to a long crack (196 mm) that extends outside the patch is shown in Fig. 9. In this case the unsupported crack has a mode shape that when excited under these modes will also give rise to the mode III stress intensity factor K_{III} .

The modal analysis indicates that both the mode I and III stress intensity factors will be significant. The mode I stress intensity factor K_I for the cracked un-repaired panel is shown in Fig. 10a. As expected, the general response is an increase of K_I with crack length. The left hand crack tip is always closer to the clamped edge of the panel than the right hand crack tip, and since the bending stresses are a maximum midway along the boundary, the right hand tip gives the highest value of K_I . The values of K_I , in relation to the fracture toughness, are significant and explain crack growth.

In the repaired panel the neutral axis is offset and as a result K_I is evaluated at both inner and outer surfaces of the skin, the repair being applied to the outer surface. Being a one sided repair the repair is more effective on the outer surface which is more closely restrained [6].

These bending effects are clearly shown in Fig. 10b. The right hand crack results in the highest values for K_I located on the inner surface. These values of K_I are significantly high before the crack grows out from under the patch, and explains continued crack growth. For a normal 'static' repair in which the only significant events are manoeuvre loads and gust loads the repair would be successful. However in the environment of acoustic fatigue at a frequency of 300 Hz the repair will not be effective

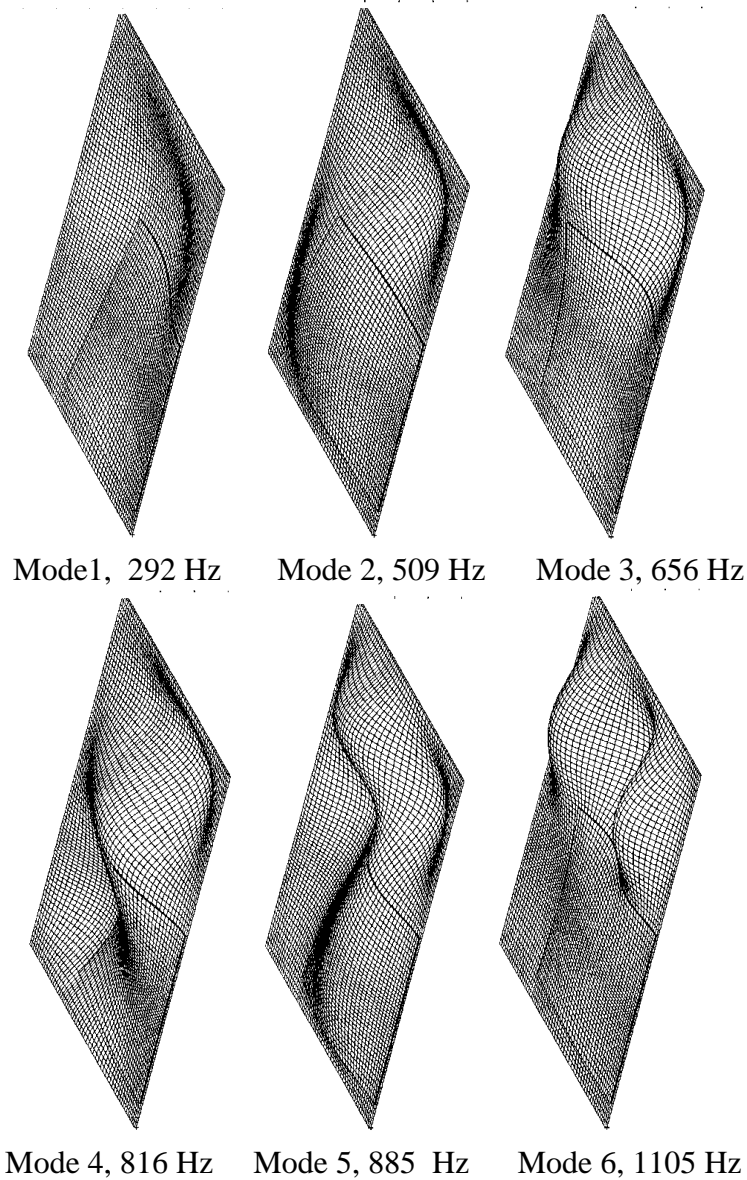


Fig. 8 : Mode shapes for short crack (repaired).

The mode III stress intensity factor K_{III} for the cracked un-repaired panel is shown in Fig.11a. The values of K_{III} increase with crack length significantly for both left and right hand crack tips, and the numerical value of K_{III} is greater than K_I . Clearly K_{III} will contribute significantly to crack growth. In the case of the repaired panel, shown in Fig. 11b, the values K_{III} for a crack not growing outside the patch, are low, but not zero. However, once the crack grows outside the patch (i.e. for crack lengths > 120 mm) K_{III} increases significantly.

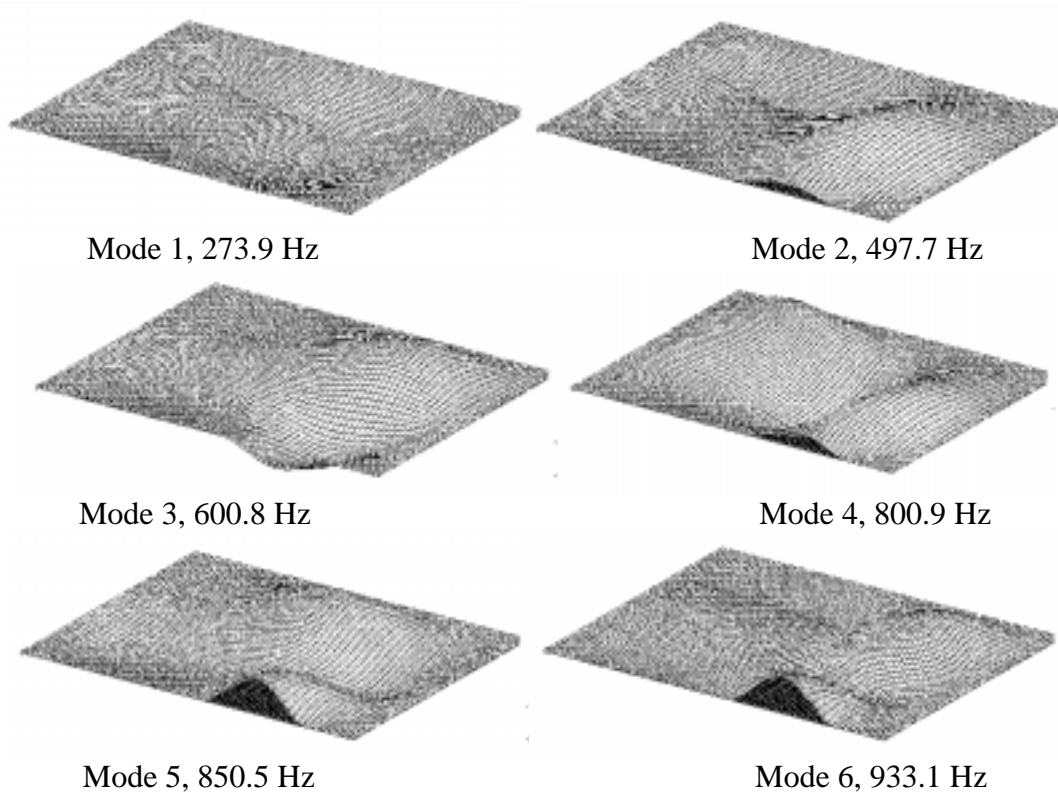


Fig. 9 : Mode shapes for long crack (repaired).

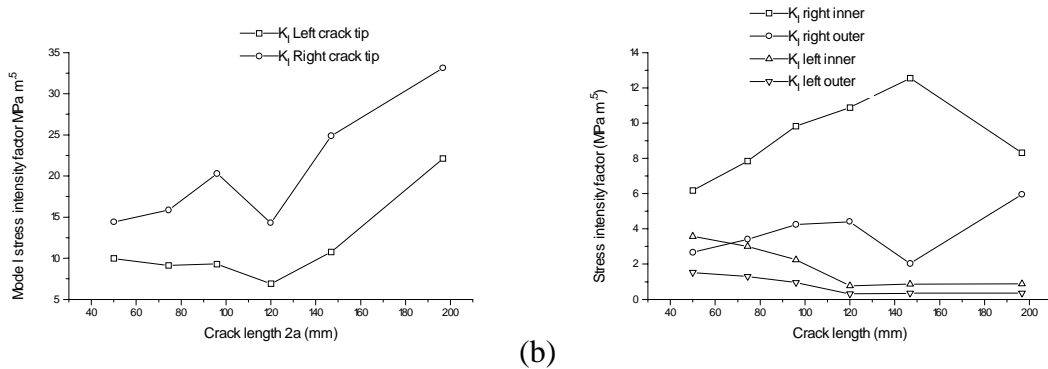


Fig. 10: (a) Stress intensity factor K_I in un-repaired panel for left and right hand crack tips. (b) Stress intensity factor K_I in repaired panel. (Note the change in scale.)

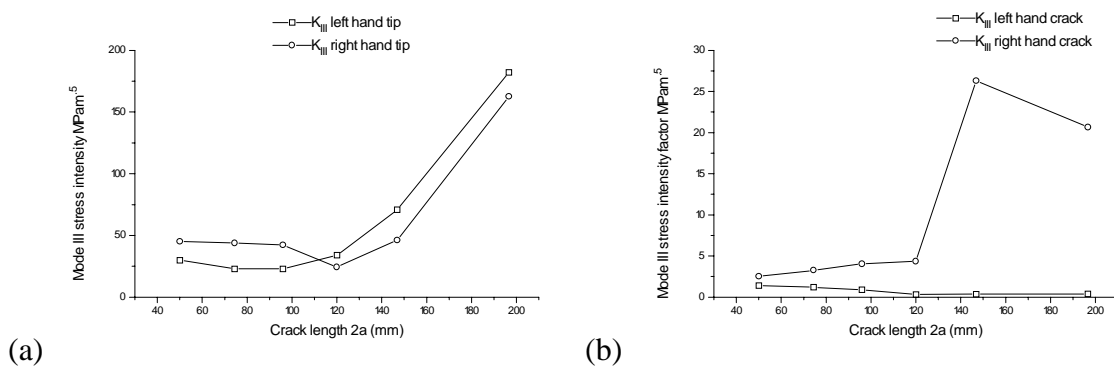


Fig. 11: (a) Stress intensity factor K_{III} for un-repaired panel. (b) Stress intensity factor K_{III} for repaired panel.

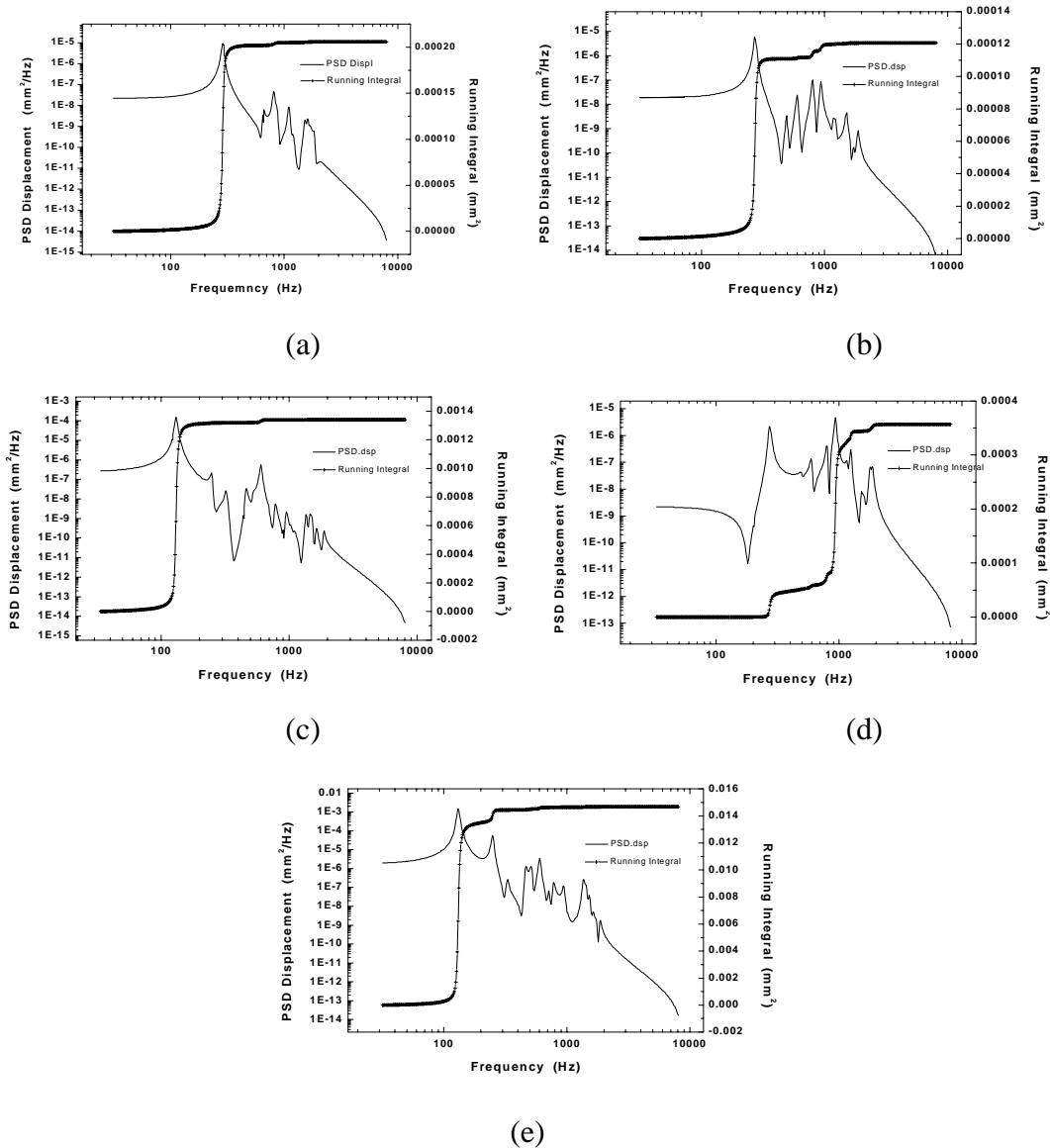


Fig. 12: PSD of displacement ($\propto K_I$) and running integral of the PSD for repaired panel of crack length (a) $2a=96$ mm, (b) $2a=196$ mm and (c) un-repaired panel with crack length $2a=196$ mm. PSD of displacement ($\propto K_{III}$) and running integral of the PSD for (d) repaired panel of crack length $2a=196$ mm and (e) un-repaired panel of crack length $2a=196$ mm.

For a crack length of $2a=96$ mm, the PSD of the response is proportional to the mode I stress intensity factor, and is shown in Fig. 12a. This corresponds to some of the mode shapes shown in Fig. 7. The peak response occurs at a frequency of 291 Hz and corresponds to mode shape 1 in Fig. 7. With increasing frequency the peaks correspond sequentially to the higher modes. The contribution of the modes to the response can be determined by a running integral of the response and is shown in Fig. 12a. These results indicate that about 98% of the response is due to mode 1.

In the case of the repaired panel containing a long crack of 196 mm the response for K_I is shown in Fig. 12b. It is evident from the running integral that mode 1 makes the major contribution to this response followed by modes 4 and 5. However the response for K_{III} ,

shown in Fig. 12d, clearly shows that mode 6 makes the major contribution at a frequency of 933 Hz, followed by mode 1.

In the case of long cracks in the un-repaired panel, the response for K_I and K_{III} is shown in Figs. 12c and 12e, respectively. In this case mode 1 makes the major contribution to these factors.

CONCLUSIONS

Validation of the PSD method has been achieved from both experimental data and analytical formula.

The analysis carried out here has simulated and characterised the growth of the crack in the cracked and repaired panel. It has been found that after patching a significantly high mode I stress intensity factor K_I exists on the inner surface of the right hand crack tip likely to promote crack growth.

For a short crack length in the repaired structure, a running integral of the PSD of the displacement, ($\propto K_I$) has shown that mode shape 1 contributes about 98% of the response at the crack tip. In the case of a long crack in the repaired panel, the running integral showed that mode 6 provided the major contribution to the response for K_{III} . For all other cases considered mode 1 provided the major contribution to K_I and K_{III} .

For the un-repaired panel it is expected that both K_I and K_{III} will have a significant contribution to crack growth.

FUTURE INVESTIGATIONS

The use of thicker patches which extend across the complete panel.

The use of constrained layer damping in a thick adhesive layer.

The trade-off between uni-directional and quasi - isotropic patches.

The application of patches to un-cracked panels to prevent initiation of cracks.

REFERENCES

1. A/B/C/D Aircraft Lower Nacelle Skin Acoustic and Strain Measurements and Sonic Fatigue Analysis. MDC 94B0044. Mar,1994.
2. Blakely MSC/NASTRAN, basic dynamics analysis, user's guide. The MacNeal-Schwendler Corporation, Dec,1993.
3. H. Climent and J. Casalengua. Application of a PSD technique to acoustic fatigue Stress Calculations in Complex Structures. Symposium on ' Impact of Acoustic Loads on Aircraft Structures', Lillehammer, Norway, May 1994.
4. K.P. Byrne Strains Affecting the Growth Rate of Edge Cracks in Acoustically Excited Panels. ISVR Tech. Rep. 59, Nov, 1972.
5. The estimation of r.m.s stress in stiffened skin panels subjected to random acoustic loading. Engineering Sciences Data Unit Number 72005. July, 1984.
6. R.J. Callinan, L.R.F. Rose and C.H. Wang. Three Dimensional Stress Analysis of Crack Patching. To be presented at ICF9 in June, 1997.

TEMPERATURE EFFECTS ON A COMPOSITE REPAIR

R. Boykett and K. Walker

*DSTO, Aeronautical and Maritime Research Laboratory, Airframes and Engines Division
506 Lorimer St, Fishermens Bend, Victoria, 3207, Australia*

SUMMARY: The first bonded composite repair to primary aircraft structure in the Royal Australian Air Force has required comprehensive substantiation. A 48 mm long crack in a wing skin was repaired with a boron fibre epoxy resin patch. Successful validation tests on representative specimens included static residual strength tests at ambient, -40, and +110 degrees Celsius. Residual strains in specimens induced by the bonding cure cycle (80°C) were significant, but were slightly relaxed after fatigue loading. Variation in the frequency of this cyclic loading and raising the temperature did not clearly effect crack growth. The testing program verified the durability and damage tolerance of the repair, thus preventing the scrapping of the aircraft wing. The results suggest that thermal effects, on the integrity of the repaired structure, are less severe than predicted in the current analytic approaches used by AMRL and the RAAF.

KEYWORDS: boron/epoxy composite, aircraft repair, strength tests, crack growth, temperature effects, airworthiness certification

INTRODUCTION

A supersonic F-111C aircraft of the Royal Australian Air Force has been repaired by the application of a Boron Fibre - Epoxy Resin composite patch over a 48 mm long fatigue crack in the lower wing skin. Calculations¹ of the residual strength for the cracked structure predicted a value more than 30% below the original Design Limit Stress, thus compromising flight safety. The repair was designed and applied in accordance with the new RAAF Engineering Standard C5033 to restore flight safety. The validation of such a critical repair to aircraft structure is an important part of the assessment of the aircraft's airworthiness prior to its return to full operational service. In this case, validation by AMRL consisted of two independent methods ; a stress analysis^{2,3} using Finite Element Methods, and experimental testing of representative specimens⁴.

The experimental testing program successfully used three different specimen designs in 28 tests under a range of configurations. This paper concentrates on the performance of medium-sized "Panel" specimens (190 x 300 mm test-section).

DESCRIPTION

The wingskin has raised sections on the inner surface that act as integral stiffeners and attachment lands for the five wing spars⁵. The location of the cracking in the lower wing skin is shown below in Figure 1 in an area below the forward auxiliary spar at a distance of 281.23 inches (7.143 m) from the wing root, known as FASS 281. At this point, the thickness of the integral stiffener is reduced from 8.2 mm to the local skin thickness (3.6 mm minimum) over a length of 20 mm. This depression allows for fuel flow between adjacent bays of the wing-box fuel tank and loss of spanwise stiffness is compensated by two adjacent integral stiffeners.

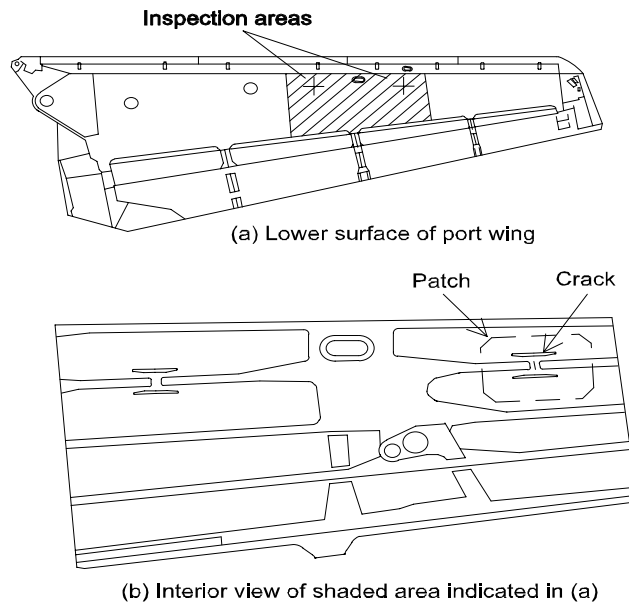


Figure 1: Location of cracking on the F-111 lower wing-skin, at FASS 281, showing also the outline of the repair patch.

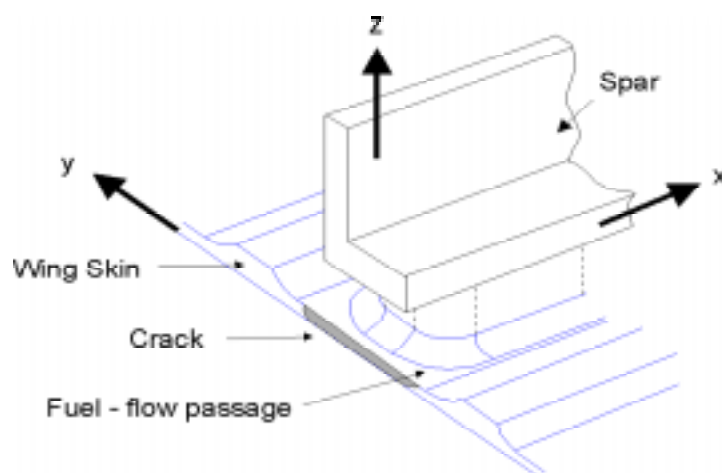


Figure 2: Local geometry of the wing skin in the vicinity of the fuel-flow passage, showing the location of cracking and reference axes used in the text. X is spanwise direction, Y is chordwise direction, Z is upwards.

The crack growth direction was chordwise, driven by the principal stress from the wing bending loads (predominantly tension in the lower skin). The local asymmetrical geometry leads to a significant stress concentration and also to out-of-plane secondary bending at the location where the cracking occurred.

The repair¹ consisted of a composite patch, 470 x 320 mm, bonded to the external surface of the wing skin using Cyanamid FM 73 structural film adhesive. The patch was 14 plies of uniaxial boron fibre epoxy resin (5521-4) pre-preg tape in a $[0_3, \pm 45, 0_2]_s$ lay-up. The edges of the patch were tapered and the corners chamfered to reduce the peel and shear stresses in the adhesive. In the first step, the patch was fully cured with a layer of film adhesive on the faying surface, using a mould of the wing skin contour. The faying surface of the wing skin (including fastener heads) was then carefully solvent cleaned of oil, paint and protective finishes, then grit-blasted with aluminium oxide, before being treated with an adhesion promoter (brush-applied A-187 silane coupling agent) to ensure a good bond surface. The patch was then applied to the structure with a second layer of film adhesive before being cured (101.3 kPa, 80°C) for eight hours. Non-destructive inspection using ultrasonic A-scan techniques confirmed the integrity of the patch and adhesive bondline.

PREDICTED PERFORMANCE

Fracture mechanics calculations of the residual strength assumed a straight-fronted through-thickness crack as shown shaded in Figure 2. The residual strength, σ_{RES} , can be estimated from the simple formula :

$$K_C = \sigma_{RES} \sqrt{(\pi a)} \quad (1)$$

For a handbook value of $K_C = 46 \text{ MPa}\sqrt{\text{m}}$ and a crack half-length, a , of 24 mm, this gives an estimate of 168 MPa for the residual strength of the wing at this location, a significant reduction from the Design Limit Stress of 256 MPa established for this area¹.

This estimate is conservative in two respects. First, the effective fracture toughness for the skin material (2024-T851 aluminium alloy, LT orientation) was found experimentally⁴ to be in the range 57 - 62 $\text{MPa}\sqrt{\text{m}}$, which is significantly higher than the handbook value used above. Secondly, the beneficial effect of the spar bridging the crack has been ignored.

Because the mechanical properties of adhesives and of polymer-matrix composites vary significantly with temperature, and because of the significant mismatch in the thermal coefficients of expansion between the composite patch (3×10^{-6} per °C) and the underlying metallic skin (23×10^{-6} per °C), three load/temperature cases were identified⁶ for demonstrations of adequate static strength.

- At high temperature (110°C), the design limit stress was 143 MPa.
- At ambient (23°C) and low (-40°C) temperature conditions, the design limit stress of 256 MPa was applicable.

The predicted failure or residual stress of the repaired structure can be calculated from the patch repair design⁷. The stress intensity factor, K_∞ , is evaluated for the design condition of elastic behaviour of a one-sided supported repair :

$$K_\infty = \sigma_{design} \sqrt{\frac{E_i t_i \lambda \eta}{G}} \quad (2)$$

Where E_i and t_i are the aluminium adherend's modulus and thickness, λ is the inverse of the elastic transfer length, and η and G are the adhesive's thickness and shear modulus.

Assuming that K_∞ is directly proportional to the applied load and that the aluminium fracture toughness, K_{IC} , is $46 \text{ MPa}\sqrt{\text{m}}$, the residual stress can be estimated from:

$$\sigma_{RES} = \frac{K_{IC}}{K_\infty} \sigma_{design} \quad (3)$$

Hence, predicted failure stresses for the panel specimens can be stated for the temperatures of -40°C (438 MPa) and 23°C (359 MPa), which both exceed the design limit value (256 MPa). However, the manufacturer's data for FM 73 adhesive is not intended for temperatures above 82°C , preventing an estimate for the 110°C condition.

The influence of temperature on crack propagation behaviour after repair with a bonded composite patch is complicated by the following factors:

1. The effective stress ratio, R , is increased due to the thermal residual stress. This will be tension in the aluminium structure and compression in the boron repair in this wing skin example for all conditions below the 80°C cure temperature.
2. The patching efficiency changes because the properties of the adhesive vary considerably with temperature. With an increase in temperature, the shear modulus, G , and the yield strength, τ_p , of the adhesive are reduced and the patching efficiency is also reduced. Note, however, that this effect is opposed by the thermal residual stress.
3. The crack propagation properties of the alloy structure may change with temperature, although this is not significant in this wing skin example over the validation temperature range of -40°C to 110°C .
4. The loading frequency is a potential factor because the time spent at high load is increased with a decrease in frequency and this is the point where the adhesive is loaded into the plastic region in this repair example. Creep effects may also occur at elevated temperature

The thermal residual stress is driven by the difference in the co-efficients of thermal expansion, α , for the bonded materials and the deviation from the cure temperature. However, the aluminium wing structure is only heated in the repair zone, being constrained by the surrounding material. An effective α can be calculated^{7,8} from:

$$\alpha_{eff} = \frac{\alpha(1+\nu)}{2} \quad (4)$$

In this example for aluminium, Poisson's ratio, $\nu = 0.3$ and $\alpha = 23 \times 10^{-6}$ per $^\circ\text{C}$, giving a value for α_{eff} of 14.95×10^{-6} per $^\circ\text{C}$.

SPECIMEN DESIGN

The loading on this cracked section of the aircraft wing skin is predominantly uni-axial tension/compression induced from wing bending loads. Hence, the design of representative specimens⁴ was intended for testing in uniaxial servo-hydraulic testing machines under closed-loop load control. This allowed the application of static loads and cyclic (spectrum and constant amplitude) loads.

Aluminium “panel” specimens were machined from the same alloy as the wing skins, but were not brake-formed, chemical milled or shot-peened. The raised lands of the local geometry in the repair zone were reproduced, including the fastener holes’ size and pitch. The fastener holes conveniently allowed the attachment of a sliding stiffener to prevent the specimen buckling under compressive loads. The test-section width (190 mm) was sufficient to allow crack growth to extend beyond the side stiffeners (95 mm tip to tip crack length) without significant influence from edge effects. The size of the specimen was intended to be small enough to be fitted within an environmental chamber that would allow testing under controlled temperatures. Later tests⁴ used an array of infra-red lamps, controlled by thermocouples, to achieve a better temperature distribution in the test section without enclosing the specimen.

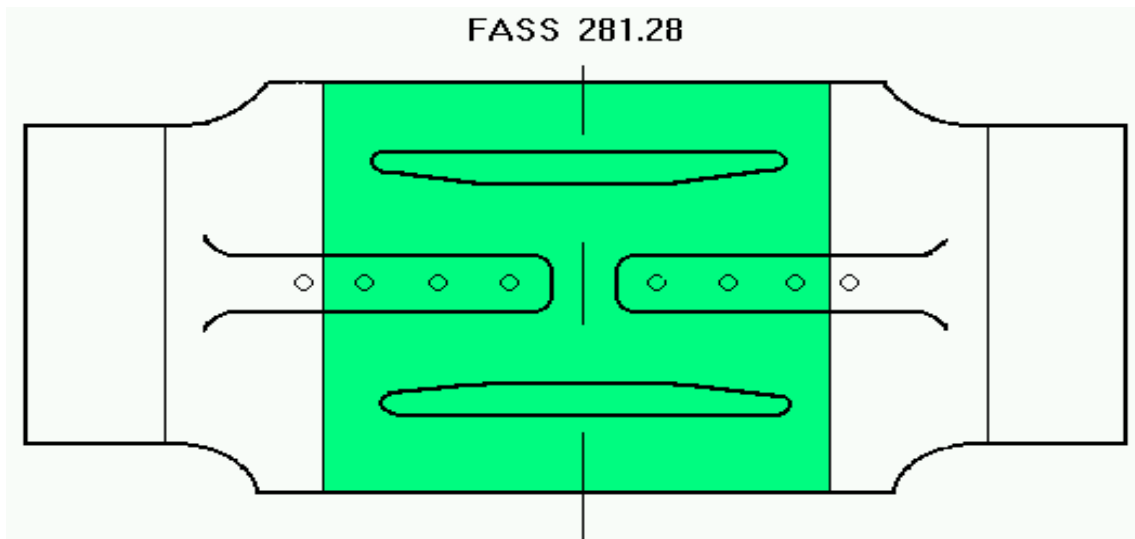


Figure 3: Panel specimen. View onto side representing upper surface of lower wing skin. Boron patch, shown shaded, is bonded to lower surface.

The introduction of the crack defect in the specimen was achieved by creating a small notch in the centre of the side representing the upper surface of the lower wing skin using Electro Discharge Machining. The specimen was then loaded under constant amplitude cyclic tension until a crack appeared the end of the notch and then grew to the required length.

Patching was carried out on cracked specimens in the same manner as the repair on the aircraft, with some exceptions. The repair patch designed for the panel is significantly smaller (190 x 290 mm) than that used on the aircraft (320 x 470 mm); there is no taper at the sides and the chamfer is smaller at the ends, but more importantly, there is less overlap in the length. This is a very conservative approach, giving a measure of the damage tolerance of the repair design either during application or later in service. For convenience, the specimens were autoclave cured under vacuum, whereas the aircraft repair used a positive pressure bag.

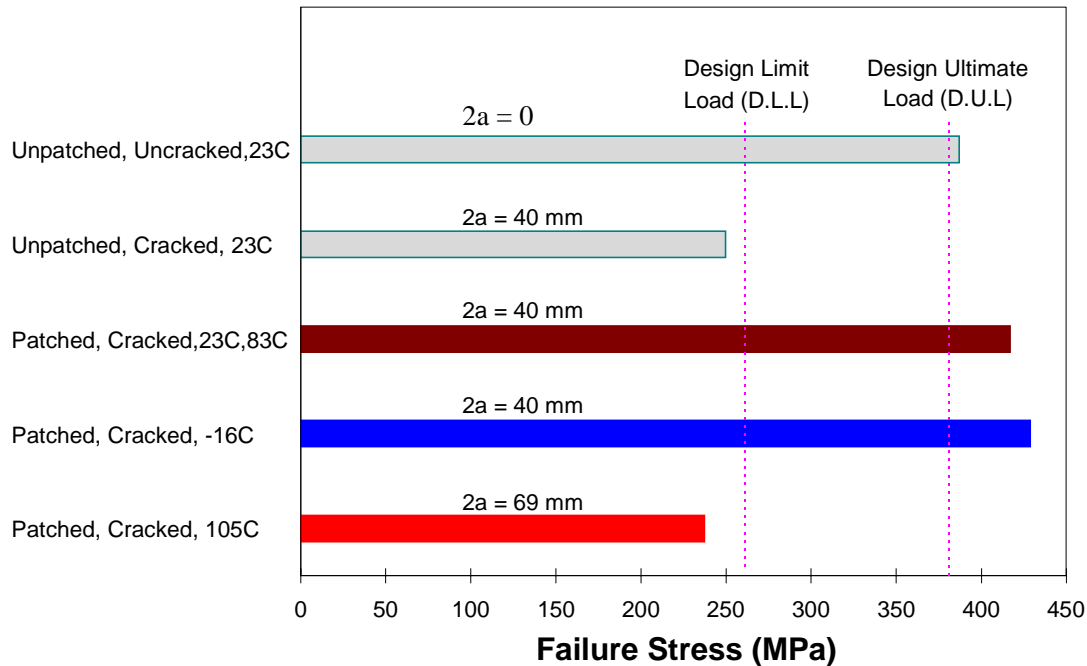
EXPERIMENTAL RESULTS

Static Strength Tests

The results of static residual strength tests are summarised below in Figure 4. The residual strength (stress in MPa) is calculated to be the failure load divided by the nominal cross-sectional area, ignoring the patch and crack.

These results confirm the prediction that a repair is needed to restore the strength of a specimen with a 40 mm long crack to greater than Design Limit Load.

The residual strength of repaired specimens exceeded DUL, but did not vary significantly when the temperature was reduced from ambient to -40°C , although this was an increase as predicted.



*Figure 4: Static strength performance of panel specimens.
Design Limit Load is shown for 23°C and -40°C case; at 110°C , DLL is 143 MPa.*

The temperature gradient across the specimen test section during the cold test (-40°C) ranged from -16.3°C to -42.2°C , while during the hot test (110°C) it ranged from 83.0°C to 119.4°C . The maximum values were at the centre of the test section due to heat transfer from the ends of the specimen into the grips of the testing machine. This temperature range did not significantly change predicted values for the cold test, but was large enough to be quite important at the higher temperature test. The adhesive used in this repair has degraded performance at elevated temperatures; shear modulus, G , is reduced by over 65% when the temperature is increased from 24°C to its maximum rated 82°C , and also the glass transition temperature is less than 110°C .

The hot test was repeated at a later date on another specimen using an improved environmental chamber that limited the temperature range in the test section to between 105°C and 112°C . This specimen had already been used for fatigue loading, with the crack grown to 69.4 mm after 50,000 simulated flight hours. The crack propagated to failure under a load of 204.7 kN (equivalent to 247 MPa), exceeding both the Design and Ultimate stress for the high temperature load case. This is a remarkable result for a specimen, already degraded by extensive fatigue cycling, under a severe load environment and reinforces the result from the previous hot test.

Residual Thermal Strain Tests

An array of electrical resistance strain gauges was fitted to some specimens, mostly on the boron repair patch along the spanwise centreline, over the crack and also at the end of the patch. With the gauges applied before the patch was bonded to the specimen, the thermal residual stresses in the specimen could be measured after the cure was completed. Unfortunately, the response of gauges at the end of the patch, over the ply terminations, was inconsistent and unreliable.

When strain surveys of the instrumented panel specimens were taken at ambient (23°C) and then the cure temperature (80°C), two results were evident, as shown in Figure 5.

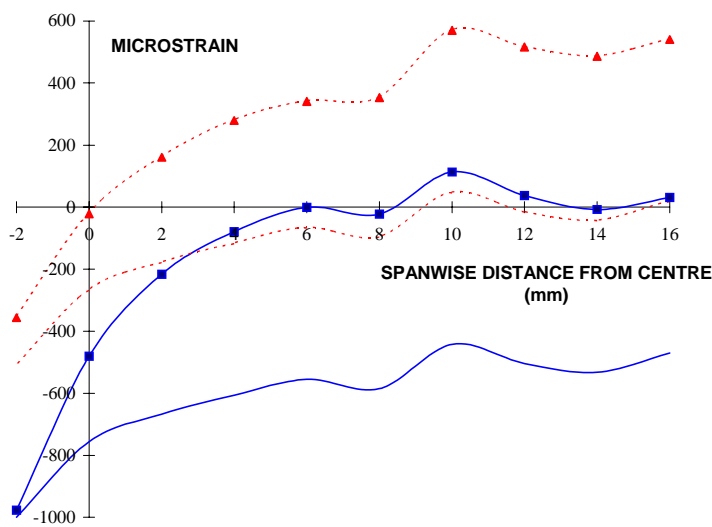


Figure 5: Strain distribution in the patch (the crack in this specimen was 2 mm off-centre). Data for 80°C is shown dashed, Data at 25% DLL is shown with markers.

- The relative strain distribution (in the repair patch) in the local area over the crack was not shown to differ significantly when the temperature increased.

However, in combination with extensive cyclic fatigue loading the residual strain in the patch tended to relax slightly. NDI inspections of fatigue loaded specimens indicated an unbond over a small distance (~ 3 mm) either side of the crack; this remained stable as the crack length increased.

- The magnitude of the thermal residual strain has clearly changed.

At a temperature of 23°C, the “far-field” spanwise residual strain (remote from local geometry effects) was -548 μE in the boron patch and +531 μE in the aluminium panel. The residual tensile strain in the aluminium has the potential to enhance crack growth under fatigue loading conditions. When the temperature was raised to 80°C, these values changed to +137 μE and +1225 μE respectively, which is what would be expected for these materials prior to bonding. The same increase in strain ($690 \pm 5 \mu\text{E}$ for both materials) indicated that the

adhesive bond remained intact over this temperature range and compatibility insured that the whole specimen behaved as a homogenous item.

The individual coefficients of thermal expansion, α , were measured during other tests⁴ in this program for the boron patch lay-up and the aluminium alloy. Over the temperature range of -15°C to $+84^{\circ}\text{C}$, the aluminium specimen α was 21×10^{-6} per $^{\circ}\text{C}$ and for the boron epoxy patch lay-up α was 2.95×10^{-6} per $^{\circ}\text{C}$. This compared well with the published values for 2024-T851 Aluminium (23×10^{-6} per $^{\circ}\text{C}$) and for uniaxial boron epoxy (4.1×10^{-6} per $^{\circ}\text{C}$), when allowing for a reduced expansion from the $\pm 45^{\circ}$ plies in the lay-up.

A patched specimen could then be expected to have an average of these two values (12×10^{-6} per $^{\circ}\text{C}$). The effective co-efficient of thermal expansion measured for the repaired specimen was $690 / 57 = 12.1 \times 10^{-6}$ per $^{\circ}\text{C}$.

The amount of residual strain in these repaired test specimens will be more severe than that experienced on the repaired aircraft where the surrounding wing structure constrains expansion under increased temperatures. An effective co-efficient of thermal expansion, for the wing skin, was calculated to be 14.95×10^{-6} per $^{\circ}\text{C}$ (see section 3). Other tests⁹ at AMRL measured an experimental value for the repair zone on an uncracked, unpatched F-111C wing skin to be 6×10^{-6} per $^{\circ}\text{C}$. This experimental figure is significantly lower than predictions based on Finite Element Methods³ and previous analytic work^{8,10}.

Fatigue Crack Growth Tests

Cyclic loads were applied to specimens as a fatigue spectrum developed¹¹ from flight data for the F-111C fleet in the RAAF. This cycle-by-cycle spectrum contained over 36,000 load points per block of 500 simulated flight hours. It should be noted that the crack growth was not halted by the application of the repair patch to the representative specimens. However, the crack growth rate in repaired specimens was approximately constant, at 0.7 mm per 1000 test hours, less than 3% of that in unrepaired specimens.

Fatigue testing conditions included temperatures at ambient (23°C) and elevated (80°C), and cyclic loading frequencies of 0.5 Hz and 5.0 Hz. Results for crack growth in two panel specimens, under different conditions are shown in Figure 6.

Estimated crack growth rates, calculated from linear regression, give an average of 0.72 mm per 1000 hours, which is similar to the previous tests at ambient temperature. The results did not show a consistent effect of loading frequency or temperature; the variability in crack growth rate is within the bounds of any limited fatigue experiment. Insensitivity to test temperature has been observed¹² in patched, cracked specimens although later work¹³ showed a small increase in crack growth rate with an increase in test temperature. This increase is less than that predicted by theory and may be due to differences between static and dynamic properties of the adhesive.

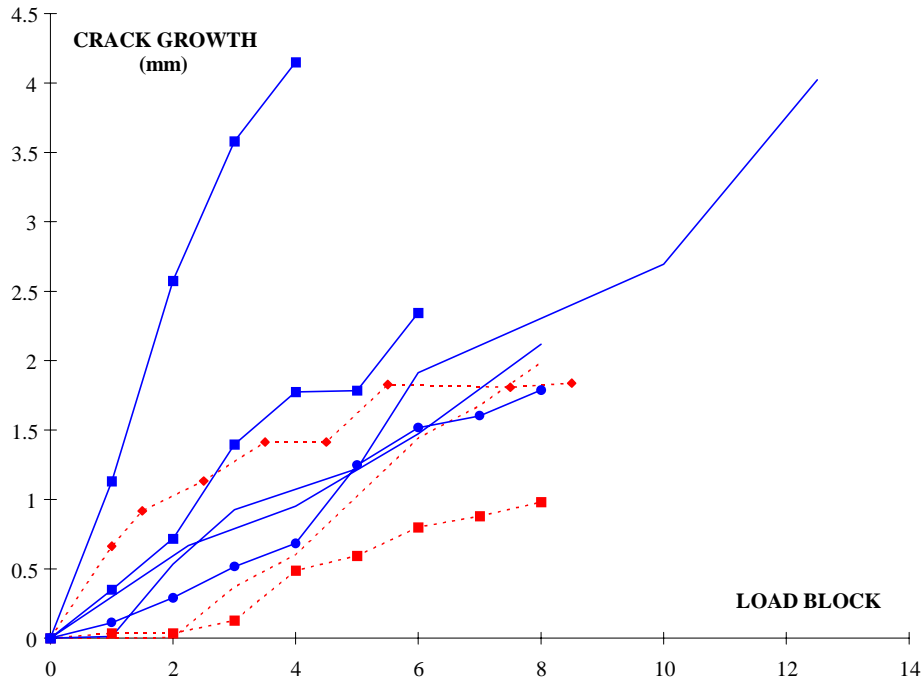


Figure 6: Crack growth comparisons at 23°C and 80°C, and 0.5 and 5.0 Hz. Data for 80°C is shown dashed, Data for 5.0 Hz is shown with markers.

DISCUSSION

The static mechanical properties of film adhesives such as FM-73 are known to vary markedly with temperature. The large difference in thermal coefficient of expansion for Aluminium alloy and Boron Epoxy implies large residual stresses when bonded together. The combination of these two factors could be expected to significantly influence a repair to a supersonic aircraft wing skin. The experimental results indicate a lack of sensitivity to both temperature (under static and dynamic loading) and loading frequency. This suggests that there is scope to reduce conservatism inherent in the current accepted and proven design analysis^{7,8} developed jointly by AMRL and the RAAF. The thermal mismatch has been found to be far lower than predicted, in a full-sized wing, and this is attributed to the actual level of constraint of the structure. This adds another significant factor to the conservatism of the test specimen results.

Baker¹⁰ suggests that one difficulty with the models and analyses that currently over-estimate the thermal effects (particularly under cyclic loading) may be the use of static rather than dynamic mechanical properties for the adhesive. The use of elastic formulae may also be a factor; both these aspects are under investigation at AMRL.

CONCLUSION

A series of static and fatigue tests were successfully conducted on representative specimens of a bonded composite repair to primary aircraft structure. The results substantiate the repair and confirm that current analytic approaches over-estimate the effects of test temperature and loading frequency. Further work is required to fully understand the complex mechanisms involved with these bonded composite repairs; this will lead to improved analysis techniques which reduce unnecessary conservatism.

ACKNOWLEDGEMENTS

The authors acknowledge the assistance and support provided by Dr F. Rose, Dr A. Baker, and R. Callinan, L. Mirabella, of the Airframes and Engines Division at AMRL.

REFERENCES

1. Davis, M.J., Kearns, K.J. and Wilkin, M.O., "Bonded repair to cracking in primary structure ; a case study", *Proceedings PICAST2-AAC6*, Institution of Engineers, Melbourne, Australia, March 1995, pp. 323-330.
2. Keeley, D., Callinan, R. and Sanderson, S., "A validated Finite Element model of an F-111 lower wing skin structural detail at forward auxiliary spar station (FASS) 281.28" *DSTO-TN-0046*, 1996, in publication.
3. Callinan, R.J. and Sanderson, S., "Finite Element Analysis of an F-111 lower wing skin fatigue crack repair", *DSTO Technical Report*, in preparation.
4. Boykett, R. and Walker, K., "F-111C lower wing skin bonded composite repair substantiation testing", *DSTO Technical Report*, in preparation.
5. McHenry, M.I. and Key, R.E., "The F-111 logic; familiar materials; proven process", *Metal Progress*, 93, No.3, 1968, pp. 62-68.
6. Preston, P.F., Rose, L.R.F., Walker, K. and Wilson, E.S., "Repair substantiation for a bonded composite repair to primary aircraft structure", *Proceedings ISASTI '96*, Jakarta, Indonesia, June 1996, in publication.
7. Anon, "Composite materials and adhesive bonded repairs", *RAAF Engineering Standard C5033*, Draft, 1994.
8. Rose, L.R.F., "Theoretical analysis of crack patching", *Bonded Repair of Aircraft Structures*, Martinus Nijhoff, 1988, Chapter 5.
9. Mirabella, L., "Strain gauge and temperature measurements of a heated F-111 wing", *AMRL Laboratory Report*, in preparation.
10. Callinan, R.J., Tran-Cong, T and Walker, K., "Development and validation of a Finite Element based method to determine thermally induced stresses in bonded joints of dissimilar materials", *DSTO Technical Report*, in preparation.
11. Walker, K. and Swanton, G., "Static and Fatigue test loading development for an F-111 bonded composite repair substantiation", *DSTO Technical Report*, in preparation.
12. Baker, A., "Repair efficiency of fatigue cracked aluminium components reinforced with boron epoxy patches", *Fatigue and Fracture of Engineering Materials and Structures*, Volume 16, No. 7, Great Britain, 1993, pp. 753-765.
13. Baker, A., "Fatigue studies related to the certification of composite crack patching for primary metallic structure", *Proceedings FAA-NASA Symposium on Continued Airworthiness of Aircraft Structures*, Atlanta, USA, August 1996, in publication.
14. Fredell, R., *Damage tolerant repair techniques for pressurised aircraft fuselages*, 1994.

ON THE DESIGN OF BONDED PATCHES FOR ONE-SIDED REPAIR

C. H. Wang and L. R. F. Rose

Aeronautical and Maritime Research Laboratory,
Defence Science and Technology Organisation, Melbourne, Australia

SUMMARY: Due to the load-path eccentricity caused by bonding one reinforcement to only one side of a thin plate, which causes a shift of the neutral plane away from that of the plate, one-sided bonded repair has a much lower repair efficiency than two-sided repair. It is shown that for a given patch design, the secondary bending not only results in a higher stress intensity factor as compared with two-sided repair, but also significantly increases the stresses in the bonded reinforcement and the adhesive layer. Three non-dimensional parameters have been identified which completely characterise the stress intensity factor, the stresses in the adhesive layer, and the stress distribution in the reinforcement directly above the crack. A parametric study shows that one efficient strategy to improve the repair effectiveness and to minimise the stresses in the adhesive layer and the patch is to increase the thickness of the reinforcement.

KEYWORDS: bonded repair, one-sided repair, stress intensity factor, design of patches, adhesive stresses.

INTRODUCTION

Bonded repairs can be classified into two categories: symmetrical or unsymmetric, which are frequently termed respectively as two-sided and one-sided. In the former case two identical reinforcements are bonded on the two faces of a cracked plate. This symmetric arrangement ensures that there is no out-of-plane bending over the repaired region, provided the cracked plate is subjected to extensional loads only. In practice, however, one-sided repair is often adopted in which a composite patch is applied to only one face of the panel to be repaired [1,2,3]. This is because most often, only one face of a component to be repaired is accessible and sometimes only one side of a structure is allowed to be patched, e.g., aircraft fuselage and wing sections. If in these cases the thin skin structures are well supported against out-of-plane deflection, for instance, by stiffeners attached to one side, it is acceptable to ignore the out-of-plane bending, thus permitting the problem to be analysed using the method established for symmetrical repairs [4,5,6]. However, if the structure is unsupported, out-of-plane bending may lead to lower repair efficiency as compared with two-sided repairs [7,8,9,10]. Furthermore, the out-of-plane bending near the crack region is expected to result in much higher shear and peel stresses in the adhesive layer. Consequently, rigorous analyses are called for not only to quantify the repair efficiency, but also for the purpose of assessing the strength and durability of the adhesive bonding.

FORMULATION AND NOTATION

The crack geometry to be considered is shown in Fig.1 with the appropriate coordinate system and notations. The plate is repaired by a patch bonded to one face of the cracked plate. The boundary conditions for the problem are that the surfaces of the crack are stress free and there is a prescribed stress system at infinity so that

$$\sigma_{yy} \rightarrow \sigma^\infty, \sigma_{xx} \rightarrow \lambda\sigma^\infty, \tau_{xy} \rightarrow \tau^\infty \quad \text{as } \sqrt{x^2 + y^2} \rightarrow \infty \quad (0 < z < t_p) \quad (1a)$$

and

$$\sigma_{yy} = \tau_{xy} = 0 \quad (|x| < a, y = 0, 0 < z < t_p) \quad (1b)$$

where λ denotes a biaxiality ratio. By using the superposition principle it is easy to demonstrate that it is equivalent to solving the following mixed boundary value problem,

$$\text{plate: } \begin{cases} \sigma_{yy} = -\sigma_0(z), \tau_{xy} = -\tau_0(z) & (|x| < a, y = 0, 0 \leq z < t_p) \\ u_y = \frac{du_y}{dz} = 0 & (|x| \geq a, y = 0, 0 \leq z < t_p) \\ \sigma_{xx} \rightarrow 0, \sigma_{yy} \rightarrow 0, \tau_{xy} \rightarrow 0 & (\sqrt{x^2 + y^2} \rightarrow \infty, 0 \leq z < t_p) \end{cases} \quad (2a)$$

$$\text{patch: } u_y = \frac{du_y}{dz} = 0 \quad (|x| < \infty, y = 0, t_p + t_A \leq z < t_p + t_A + t_R) \quad (2a)$$

Without the bonded patch, it is obvious that $\sigma_0 = \sigma_{yy}^\infty, \tau_0 = \tau_{xy}^\infty$. After patching, however, the stresses along the prospective crack path are no longer equal to those prior to the application of reinforcement. Exact solutions of σ_0 and τ_0 are generally not available except for certain simple reinforcement shapes and loads [4].

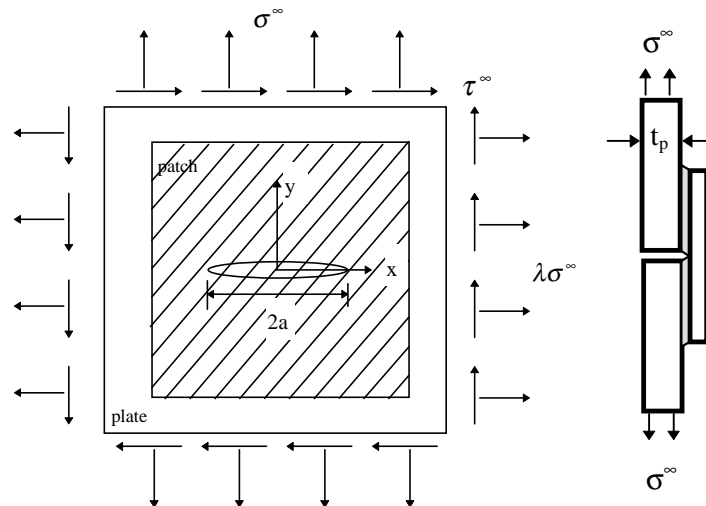


Fig.1 Geometry and coordinate system of repaired crack:
(a) plan view, (b) cross-section along centre line ($x=0$).

In this article we will limit our attention to the tensile mode only, since the shear stress distribution is uncoupled with the bending deflection of the reinforced region, hence the shear mode can be solved by ignoring the bending deflection [11]. In the case of symmetric repair of elliptical shape, i.e. the cracked is fully supported against out-of-plane displacement or two patches are bonded on the two faces of the plate, Rose [4] presented an analytical solution of the stress distribution. The inclusion analogy adopted, however, is not readily applicable to the case of one-sided repairs, where the out-of-plane bending would considerably complicate the analysis. Nevertheless, approximate solutions can be derived assuming the stresses in the

reinforcement and the base plate are uniform everywhere within the reinforced portion, and there is no relative displacement between the plate and the reinforcement. In the special case that the plate and the reinforcement have the identical Poisson's ratio [11], the prospective normal stress in the base plate is given by the following equation [10],

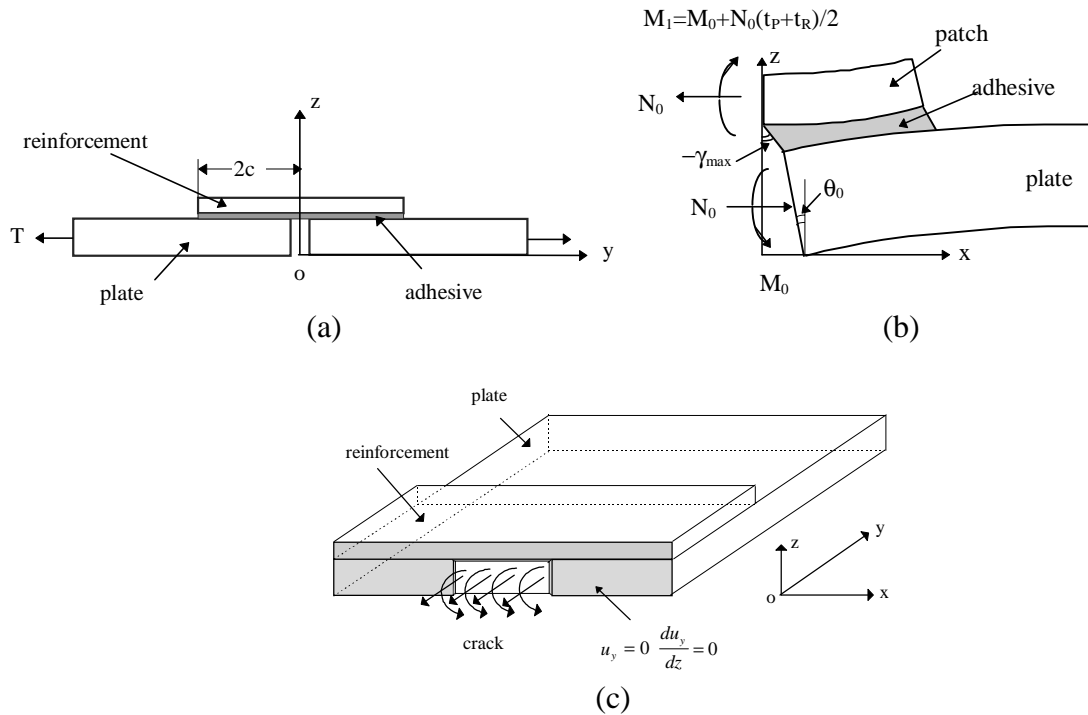


Fig.2 Single strap joint representing one-sided repair: (a) configuration and coordinate, (b) schematic of the bending deformation of an internally loaded strap joint, (c) boundary conditions along the crack plane.

$$\sigma_{yy}(y=0, z) = \frac{\sigma^\infty}{1+S} + \frac{\sigma^\infty t_p (\bar{z} - t_p/2)(\bar{z} - z)}{I_t} \quad (0 < z < t_p) \quad (3)$$

where $S = E_R' t_R / E_P' t_P$ represents the stiffness ratio, I_t and \bar{z} denote the moment inertia and the position of the neutral plane of the composite plate consisting of the base plate and the reinforcement being rigidly bonded.

Since the stress distribution in the plate is linear in the thickness direction, it is convenient to define a membrane force N_0 and a bending moment M_0 ,

$$N_0 = \int_0^{t_p} \sigma_{yy}(y=0, z) dz \equiv \frac{\sigma^\infty t_p}{1+S} + \frac{\sigma^\infty t_p^2 (\bar{z} - t_p/2)^2}{I_t} \quad (4)$$

$$M_0 = \int_0^{t_p} \sigma_{yy}(y=0, z)(z - \bar{z}_p) dz \equiv \frac{\sigma^\infty t_p^4 (\bar{z} - t_p/2)}{12I_t} \quad (5)$$

hence the normal stress at coordinate z is given by

$$\sigma(z) = \frac{N_0}{t_p} - \frac{12M_0}{t_p^3} \left(z - \frac{t_p}{2}\right) \quad (0 < z < t_p) \quad (6)$$

According to the superposition principle, the strain energy release rate for the semi-infinite crack geometry shown in Fig.1(a) is equal to the work done by applying $-N_0$ and $-M_0$ to the crack faces, as depicted in Fig.2. Details are given below.

Asymptotic Limit of the Stress Intensity Factor

The total strain energy release rate for a semi-infinite crack may be expressed as

$$G_{\infty} t_p = N_0 u_0 + M_0 \theta_0 \quad (7)$$

where u_0 and θ_0 denote respectively the mid-plane displacement and rotation of the crack faces, as depicted in Fig.2. The root-mean-square of the stress intensity factor is $K_{\infty, rms} = \sqrt{E_p G_{\infty}}$ [10]. In order to determine these two quantities, it is necessary to analyse first the stresses or strains in the adhesive layer. The governing equations for the adhesive shear and peel strains, which are assumed to be constant through the adhesive thickness, are respectively,

$$\frac{d^3 \gamma^{(A)}}{dy^3} - \beta_s^2 \frac{d\gamma^{(A)}}{dy} = 0 \quad (8)$$

$$\frac{d^4 \varepsilon^{(A)}}{dy^4} + 4\kappa^4 \varepsilon^{(A)} = 0 \quad (9)$$

where

$$\beta^2 = \frac{G_A}{t_A} \left[\frac{1}{E'_p t_p} + \frac{1}{E'_R t_R} \right] \quad (10)$$

$$\kappa^4 = \frac{E_A}{4t_A} \left[\frac{1}{D_p} + \frac{1}{D_R} \right] \quad (11)$$

where G_A and t_A represent the shear modulus and the thickness of the adhesive layer, D_p and D_R refer to the bending stiffness of the plate and reinforcement, $D_{p,R} = E'_{p,R} t_{p,R}^3 / 12$, and $E'_A = 2\mu_A / (1 - \nu)$ is the Young's modulus of the adhesive under plane strain condition. The differential equation (8) has the following solution in the domain $y > 0$,

$$\gamma^{(A)} = \gamma_{\max}^{(A)} e^{-\beta_s y} \quad (12)$$

where $\gamma_{\max}^{(A)}$ represents the maximum shear strain at $y=0$. Similarly the relevant solution for the adhesive peel stress in the case of semi-infinite overlap in the domain $y > 0$ is,

$$\varepsilon^{(A)} = (A \cos \kappa y + B \sin \kappa y) e^{-\kappa y} \quad (13)$$

The three unknowns, $\gamma_{\max}^{(A)}$ and constants A and B need to be determined from the appropriate boundary conditions.

The boundary condition for the shear strain is,

$$\begin{aligned} \left. \frac{d\gamma^{(A)}}{dy} \right|_{y=0} &= \frac{\varepsilon_R(z = t_p + t_A) - \varepsilon_P(z = t_p)}{t_A} \\ &= \frac{1}{t_A} \left[\frac{1}{E'_R t_R} + \frac{1}{E'_P t_p} + \frac{3(t_R + t_p)}{E'_R t_R^2} \right] N_0 + \frac{6}{t_A} \left[\frac{1}{E'_R t_R^2} - \frac{1}{E'_P t_p^2} \right] M_0 \end{aligned} \quad (14)$$

The relevant boundary conditions for the adhesive peel strain at $y=0$ are,

$$\begin{aligned}
 \left. \frac{d^2 \varepsilon^{(A)}}{dy^2} \right|_{y=0} &= \frac{1}{t_A} \frac{d^2(w_R - w_P)}{dy^2} \\
 &= \frac{1}{t_A} \left(\frac{M_R(y=0)}{D_R} - \frac{M_P(y=0)}{D_P} \right) \\
 &= \frac{1}{t_A D_R} \frac{t_R + t_P}{2} N_0 + \frac{1}{t_A D_R} \left[1 + \frac{D_R}{D_P} \right] M_0
 \end{aligned} \tag{15}$$

and

$$\begin{aligned}
 \left. \frac{d^3 \varepsilon^{(A)}}{dy^3} \right|_{y=0} &= \frac{1}{t_A} \frac{d^3(w_R - w_P)}{dy^3} = \frac{1}{t_A} \left(\frac{V_R + \tau_{\max}^{(A)} t_R / 2}{D_R} - \frac{V_P + \tau_{\max}^{(A)} t_P / 2}{D_P} \right) \\
 &= \frac{\mu_A}{2t_A} \left(\frac{t_R}{D_R} - \frac{t_P}{D_P} \right) \gamma_{\max}
 \end{aligned} \tag{16}$$

where the conditions that the shear force V_P and V_R are both zero at $y=0$ have been used.

From condition (14) one obtains

$$\gamma_{\max}^{(A)} = -\frac{1}{2\beta t_A} \left[\frac{1}{E_R t_R} + \frac{1}{E_P t_P} + \frac{3(t_R + t_P)}{E_R t_R^2} \right] N_0 + \frac{6}{2\beta t_A} \left[\frac{1}{E_R t_R^2} - \frac{1}{E_P t_P^2} \right] M_0 \tag{17}$$

and referring to equations (15) and (16) we have,

$$-2\kappa^2 B = \frac{1}{t_A D_R} \frac{t_R + t_P}{2} N_0 + \frac{1}{t_A D_R} \left(1 + \frac{D_R}{D_P} \right) M_0 \tag{18}$$

$$2\kappa^3 (A + B) = \frac{G_A}{2t_A} \left(\frac{t_R}{D_R} - \frac{t_P}{D_P} \right) \gamma_{\max}^{(A)} \tag{19}$$

thus

$$\kappa(A - B) = \frac{G_A t_P}{4\kappa^2 t_A} \left(\frac{t_R}{D_R} - \frac{t_P}{D_P} \right) \gamma_{\max}^{(A)} + \frac{t_R + t_P}{2\kappa t_A D_R} N_0 + \frac{1}{\kappa t_A D_R} \left(1 + \frac{D_R}{D_P} \right) M_0 \tag{20}$$

Denote the rotation of the plate at $y=0$ as θ_0 , since $\partial w_R / \partial y|_{y=0} = 0$ because of symmetry, and $\varepsilon^{(A)} = (w_R - w_P) / t_A$, we have, by definition,

$$\begin{aligned}
 \theta_0 &= \left. \frac{\partial w_P}{\partial y} \right|_{y=0} = \left. \frac{\partial(w_P - w_R)}{\partial y} \right|_{y=0} = -t_A \left. \frac{\partial \varepsilon^{(A)}}{\partial y} \right|_{y=0} = \kappa t_A (A - B) \\
 &= \left\{ \frac{t_P + t_R}{2\kappa D_R} - \frac{G_A}{8\kappa^2 \beta t_A} \left[\frac{t_R}{D_R} - \frac{t_P}{D_P} \right] \left[\frac{1}{E_R t_R} + \frac{1}{E_P t_P} + \frac{t_R(t_R + t_P)}{4D_R} \right] \right\} N_0 \\
 &\quad + \left\{ \frac{1}{\kappa D_R} \left(1 + \frac{D_R}{D_P} \right) - \frac{G_A}{16\kappa^2 \beta t_A} \left[\frac{t_R}{D_R} - \frac{t_P}{D_P} \right]^2 \right\} M_0
 \end{aligned} \tag{21}$$

The opening displacement at the mid-surface of the plate is,

$$\begin{aligned}
u_0 &= -\gamma_{\max}^{(A)} t_A + \theta_0 t_P / 2 \\
&= \left\{ \frac{t_P(t_R + t_P)}{4\kappa D_R} + \left[\frac{1}{E'_R t_R} + \frac{1}{E'_P t_P} + \frac{t_R(t_R + t_P)}{4D_R} \right] \left[\frac{1}{2\beta} - \frac{G_A t_P}{16\kappa^2 \beta t_A} \left(\frac{t_R}{D_R} - \frac{t_P}{D_P} \right) \right] \right\} N_0 \\
&\quad + \left\{ \frac{t_P}{2\kappa D_R} \left(1 + \frac{D_R}{D_P} \right) + \left[\frac{t_R}{2D_R} - \frac{t_P}{2D_P} \right] \left[\frac{1}{2\beta} - \frac{G_A t_P}{16\kappa^2 \beta t_A} \left(\frac{t_R}{D_R} - \frac{t_P}{D_P} \right) \right] \right\} M_0
\end{aligned} \quad (22)$$

A comparison between the present results and the finite element analysis of the single strap joint representing a one-sided repair geometry [10] is shown in Fig.3, demonstrating a very good agreement.

It is now possible to express the crack opening displacement and crack face rotation in terms of the membrane force and the bending moment in a matrix formulation,

$$\begin{Bmatrix} u_0 \\ \theta_0 \end{Bmatrix} = \begin{bmatrix} C_{11} & C_{12} \\ C_{21} & C_{22} \end{bmatrix} \begin{Bmatrix} N_0 \\ M_0 \end{Bmatrix} \quad (23)$$

where

$$\begin{aligned}
C_{11} &= \frac{t_P(t_R + t_P)}{4\kappa D_R} + \left[\frac{1}{E'_R t_R} + \frac{1}{E'_P t_P} + \frac{t_R(t_R + t_P)}{4D_R} \right] \left[\frac{1}{2\beta} - \frac{G_A t_P}{16\kappa^2 \beta t_A} \left(\frac{t_R}{D_R} - \frac{t_P}{D_P} \right) \right] \\
C_{12} &= \frac{t_P}{2\kappa D_R} \left(1 + \frac{D_R}{D_P} \right) + \left(\frac{t_R}{2D_R} - \frac{t_P}{2D_P} \right) \left[\frac{1}{2\beta} - \frac{G_A t_P}{16\kappa^2 \beta t_A} \left(\frac{t_R}{D_R} - \frac{t_P}{D_P} \right) \right] \\
C_{21} &= \frac{t_R + t_P}{2\kappa D_R} - \frac{G_A}{8\kappa^2 \beta t_A} \left(\frac{t_R}{D_R} - \frac{t_P}{D_P} \right) \left[\frac{1}{E'_R t_R} + \frac{1}{E'_P t_P} + \frac{t_R(t_P + t_R)}{4D_R} \right] \\
C_{22} &= \frac{1}{\kappa D_R} \left(1 + \frac{D_R}{D_P} \right) - \frac{G_A}{16\kappa^2 \beta t_A} \left(\frac{t_R}{D_R} - \frac{t_P}{D_P} \right)^2
\end{aligned}$$

It is evident that the cross terms, c_{12} and c_{21} , are non-zero, indicative of the coupling between in-plane and out-of-plane deformation. According to the Maxwell's reciprocal relation, the matrix C should be symmetric, i.e., $C_{12} = C_{21}$. However, due to the approximate nature of the plate theory, the resulting matrix is not exactly symmetric, although the deviation from symmetry is small.

The strain energy release rate is given by

$$G_{\infty} t_P = N_0 u_0 + M_0 \theta_0 \equiv c_{11} N_0^2 + (c_{12} + c_{21}) N_0 M_0 + c_{22} M_0^2 \quad (24)$$

It can be readily proven that the strain energy release rate given by equation (24) is identical to that derived earlier [10], which is plotted in Fig.4 together with finite element results (denoted by symbols). It is seen that the theoretical prediction of the upper bound of the stress intensity factor, $K_{\infty, rms} = \sqrt{E_P G_{\infty}}$, agrees well with the finite element results.

Without losing generality, the extensional and bending stress intensity factors may also be expressed in terms of the membrane force and the bending moment,

$$\begin{Bmatrix} K_m \\ K_b \end{Bmatrix} = \begin{bmatrix} B_{11} & B_{12} \\ B_{21} & B_{22} \end{bmatrix} \begin{Bmatrix} N_0 \\ M_0 \end{Bmatrix} \quad (25)$$

The strain energy release rate can therefore also be expressed as [10],

$$\begin{aligned}
 E_p G_\infty &= K_m^2 + \frac{1}{3} K_b^2 \\
 &\equiv \left(B_{11}^2 + \frac{1}{3} B_{21}^2 \right) N_0^2 + \left(2B_{11}B_{12} + \frac{2}{3} B_{21}B_{22} \right) N_0 M_0 + \left(B_{12}^2 + \frac{1}{3} B_{22}^2 \right) M_0^2
 \end{aligned} \quad (26)$$

Since the strain energy release rate given by equations (24) and (26) should be identical for arbitrary N_0 and M_0 , we have,

$$\begin{aligned}
 B_{11}^2 + \frac{1}{3} B_{21}^2 &= \frac{E_p}{t_p} C_{11} \\
 2B_{11}B_{12} + \frac{2}{3} B_{21}B_{22} &= \frac{E_p}{t_p} (C_{12} + C_{21}) \\
 B_{12}^2 + \frac{1}{3} B_{22}^2 &= \frac{E_p}{t_p} C_{22}
 \end{aligned} \quad (27)$$

It is apparent that matrix [B] is indeterminate unless it is symmetric, as there are only three equations for four unknowns. Since the off-diagonal components b_{12} and b_{21} have different units, they are bound to be difference, hence the matrix [B] cannot be symmetric.

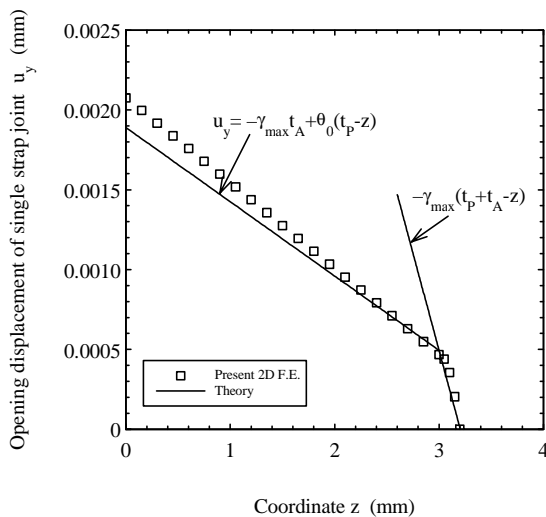


Fig.3 Comparison between theory and finite element analysis of single strap joint.

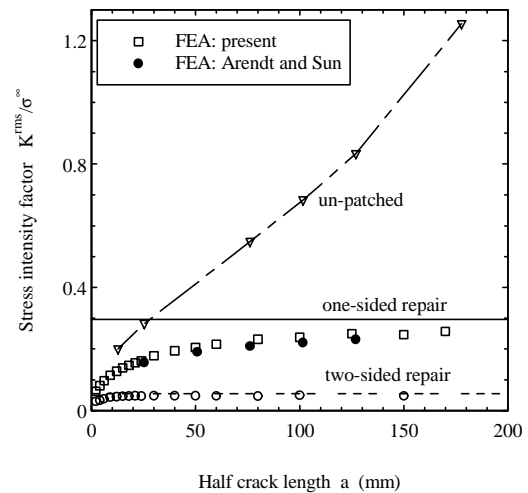


Fig.4 Stress intensity factors

Alternatively we can define the following matrix representation, noting that $N_0 = t_p \sigma_m$ and $M_0 = t_p^2 \sigma_b / 6$,

$$\begin{Bmatrix} K_m \\ K_b \end{Bmatrix} = \begin{bmatrix} d_{11} & d_{12} \\ d_{21} & d_{22} \end{bmatrix} \begin{Bmatrix} \sigma_m \\ \sigma_b \end{Bmatrix} = \begin{bmatrix} t_p b_{11} & \frac{1}{6} t_p^2 b_{12} \\ t_p b_{21} & \frac{1}{6} t_p^2 b_{22} \end{bmatrix} \begin{Bmatrix} \sigma_m \\ \sigma_b \end{Bmatrix} \quad (28)$$

A set of equations similar to equation (27) can be obtained in terms of d_{ij} . Again, unless matrix [d] is symmetric, it is indeterminate. However, for the repair geometry considered in [10], the calculated ratio K_{\min} / K_{\max} by assuming matrix [d] being symmetric is equal to 0.543, while the finite element analysis gave an average of 0.24. It is thus clear that the energy method alone is insufficient to fully determine matrix [b] or [d]; a more rigorous analysis using crack bridging method is called for, which is the subject of a separate article.

Design Considerations against Static and Fatigue Failures

A one-sided bonded repair consists of three layers: the cracked plate, the reinforcement, and the adhesive. While the key objective is to reduce the stress intensity factor for the cracked plate, both the patch and the adhesive have to be adequately designed to sustain service loading without premature failures, either under static or fatigue conditions. For a given cracked plate (characterised by three parameters: E_p , ν_p , t_p), the patch design involves essentially selecting a reinforcement (E_R , ν_R , t_R) and a structural adhesive (E_A , ν_A , t_A) to achieve the maximum reduction in the plate stress intensity factor and to ensure both the patch and the adhesive layer to sustain the design load. This implies that we need to find the optimum combination of six variables. This clearly requires a detailed parametric study to investigate the influences of each individual variable. To this end, it has been shown that the stress intensity factor of a patched crack is fully characterised by three non-dimensional parameters [10], which are

$$F = \frac{E_p t_A}{\mu_A t_p} \quad S = \frac{E_R t_R}{E_p t_p} \quad T = \frac{t_R}{t_p} \quad (29)$$

The first parameter, F , denotes the flexibility of the adhesive layer as compared with the plate [10,12]. Parameter S refers to the stiffness ratio, which is conventionally chosen to be unity [1]. While it suffices to consider the first two parameters for two-sided repairs, the third parameter, T , is an important parameter unique to one-sided repair. As shown later, this parameter plays an important role in deciding the optimum design of patches for one-sided repair. For a given cracked plate, it has been shown that the upper bound of the stress intensity factor decreases with an increase in the thickness ratio, implying that by choosing thicker reinforcement, the stress intensity factor can be significantly reduced.

Apart from the repair efficiency, it is also important to ensure the stresses in the patch and the adhesive layer are also kept sufficiently low so that they do not impose any threat to the structural integrity of a repair system. It is easy to show that the above three parameters also fully characterise the maximum stresses in the patch and the adhesive layer.

For the reinforcement, assuming the stress distribution is linear through the thickness, the maximum stress is given by,

$$\frac{\sigma_{\max}}{\sigma^{\infty}} = \frac{4}{T} + \frac{3}{T^2} \quad (30)$$

It is clear that the maximum patch stress decreases with an increase in the thickness ratio T . It is also noted that the patch stress is much higher than in symmetric repairs or fully supported one-sided repairs, as in this case the maximum patch stress is equal to t_p / t_R .

The maximum shear and peel stresses in the adhesive are respectively,

$$\frac{\tau_{\max}^{(A)}}{\sigma^{\infty}} = -\frac{1}{[FS(1+S)]^{1/2}} \left[2 + \frac{3}{2T} \right] \quad (31)$$

$$\frac{\sigma_{\max}^{(A)}}{\sigma^{\infty}} = \frac{6(1-ST)}{(1-\nu_A)FST} \left[\frac{3(1+ST^2)}{(1-\nu_A)FST^2} \right]^{3/4} \frac{\tau_{\max}^{(A)}}{\sigma^{\infty}} + \frac{6(1+T)}{FST^2(1-\nu_A)} \left[\frac{3(1+ST^2)}{(1-\nu_A)FST^2} \right]^{1/2} \quad (32)$$

which are shown in Fig.5. It is clear that with the constraint of $S=1$ the maximum adhesive shear and peel stresses tend to reach a minimum level of 0.4 as $T \rightarrow \infty$. This level, however,

implies that the repair can be applied only to cracked plates with a maximum design limit of around 75 MPa, as the strength of most structural adhesives is limited to around 30 MPa. In order to design a repair for primary aircraft structures, the adhesive stresses have to be reduced to at least 10% of the plate stress. This means that the balanced reinforcement requirement has to be dropped.

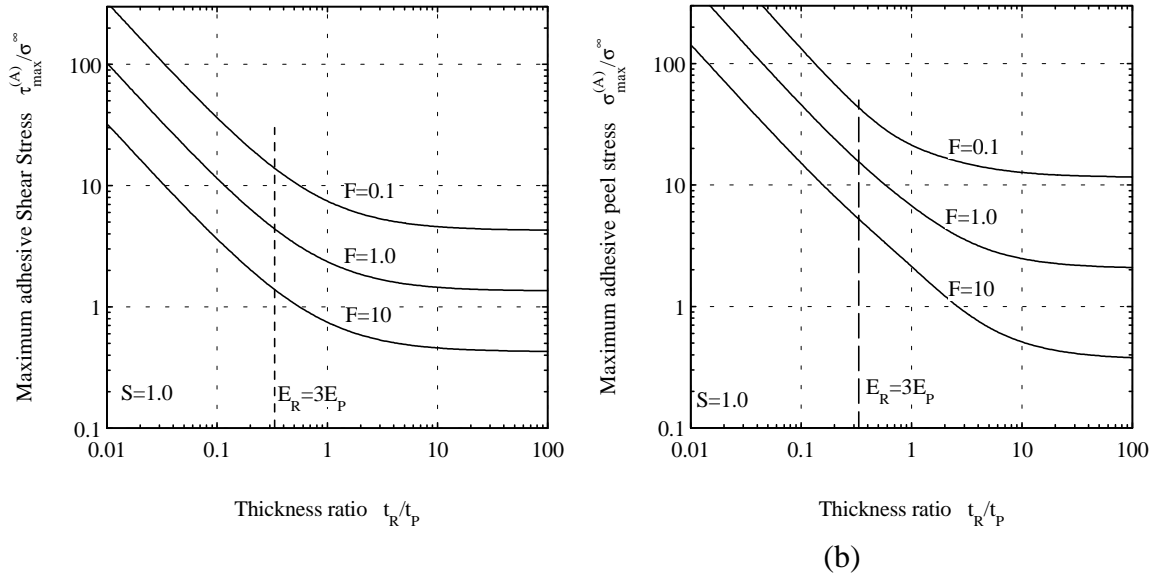


Fig.5 Variations of (a) the adhesive shear stress and (b) adhesive peel stress with the thickness ratio for balanced repair ($S=1.0$)

Let us assume that the patch material has a Young's modulus three times that of the plate, i.e. $E_R = 3E_P$, the respective adhesive shear and peel stresses are plotted in Fig.6. It is seen that by choosing $T = 3$, the above mentioned design requirement can be achieved, provided the adhesive system is designed to give a flexibility ratio of $F=10$.

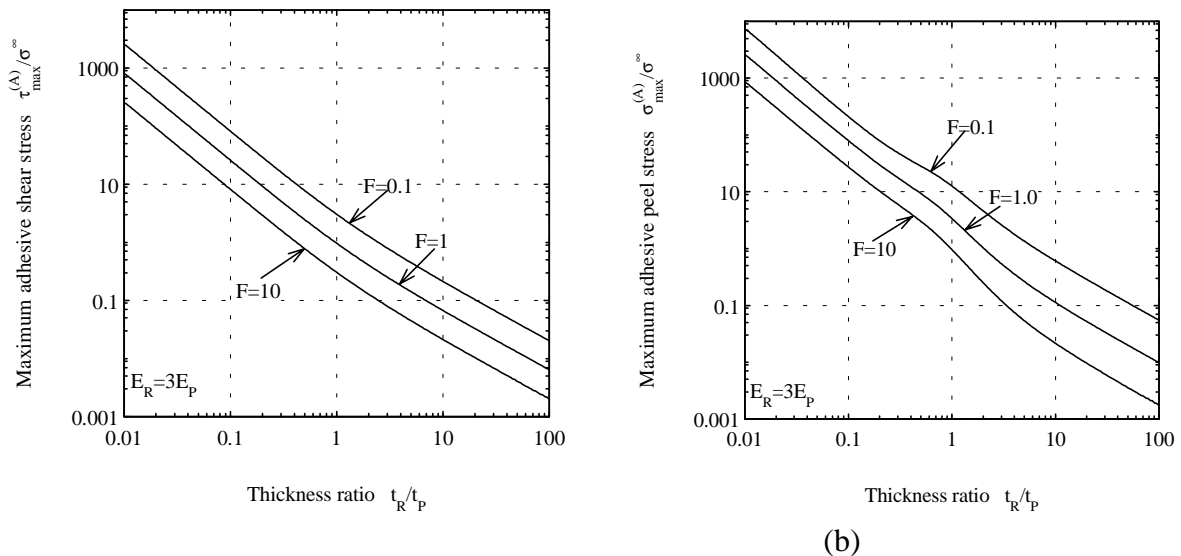


Fig.6 Influences of thickness ratio on (a) the adhesive shear stress and (b) adhesive peel stress.

CONCLUSIONS

The following conclusions can be drawn from the present analysis,

1. Out-of-plane bending in one-sided repair results in lower repair efficiency and higher stresses in the patch and the adhesive layer.
2. Thicker patches are found to be effective in reducing the stress intensity factor of a patched crack and the stresses in the adhesive layer and the reinforcement.
3. Energetic method alone is insufficient to partition the total strain energy release rate into a membrane and bending component, as the relevant matrices are found to be unsymmetrical.
4. Formulas have been derived for the upper bound of the stress intensity factor of repaired cracks, the maximum normal stress in the reinforcement, and the maximum shear and peel stresses in the adhesive.

REFERENCES

1. Baker, A. A. and Jones, R. (editor) (1988) Bonded Repair of Aircraft Structures, Martinus Nijhoff Publishers.
2. Baker, A. A. (1993) Repair efficiency in fatigue-cracked aluminium components reinforced with Boron/Epoxy patches, *Fatigue Fract. Engng. Mater. Struct.*, Vol. **16**, no. 7, pp.753-765.
3. Rose, L. R. F., Callinan, R. J., Baker, A. A., Sanderson, S. and Wilson, E. S. (1995) Design validation for a bonded composite Repair to the F-111 lower wing skin, *Proceedings of 2nd Pacific International Conference on Aerospace Science and Technology*, Vol.1, pp.333-336.
4. Rose, L. R. F. (1981) An application of the inclusion analogy for bonded reinforcements, *Int. J. Solids and Structures*, Vol. **17**, pp.827-838.
5. Rose, L. R. F. (1982) A cracked plate repaired by bonded reinforcements, *Int. J. Fracture*, Vol.**18**, No.2, 135-144.
6. Rose, L. R. F. (1988) Theoretical analysis of crack patching, , in *Bonded Repair of Aircraft Structures*, edited by A.A. Baker and R. Jones, Martinus Nijhoff Publishers, pp.77-105.
7. Ratwani, M. M. (1979) Cracked, adhesively bonded laminated structures, *AIAA Journal*, Vol. **17**, No.9, 988-994.
8. Jones, R. (1983) Neutral axis offset effects due to crack patching, *Composite Structures*, Vol. **1**, 163-174.
9. Arendt, C. and Sun, C. T. (1994) Bending effects of unsymmetric adhesively bonded composite repairs on cracked aluminium panels, *Proceedings of FAA/NASA International Symposium on Advanced Structural Integrity Methods for Airframe Durability and Damage Tolerance*, NASA Conference Publication 3274, Part 1, pp.33-48.
10. Wang, C. H., Rose, L. R. F., and Callinan, R. (1997) Analysis of out-of-plane bending in one-sided bonded repair, *Int. J. Solids and Structures* (in press).
11. Wang, C. H. and Rose, L. R. F. (1997) Bonded repair of cracks under mixed mode loading, accepted for publication in *Int. J. Solids and Structures*.
12. Goland, M and Reissner, E. (1944) The stresses in cemented joints, *J. Appl. Mech*, Vol. **11**, A17-A27.

LOAD HISTORY DEPENDENCE OF GRAPHITE EPOXY JOINTS/REPAIRS: AN EXPERIMENTAL STUDY

W. K. Chiu¹, S. Galea², R. Jones¹ and S. Pitt¹

¹ *Department of Mechanical Engineering, Monash University,
Wellington Rd, Clayton, Vic 3168, Australia.*

² *Airframes and Engines Division, Aeronautical Research Laboratory, Defense Science and
Technology Organisation, 506 Lorimer St, Pt Melbourne, Victoria, 3207, Australia.*

SUMMARY: This paper presents the results of an experimental study into the load history dependence of adhesively bonded joints and therefore, by analogy, adhesively bonded repairs. Here attention is focused on the effects of rate dependence on the failure loads of graphite epoxy scarf joints as well as double and single lap joints. This test program has revealed that, when evaluating the structural integrity and durability of composite joints or bonded repairs, it may be necessary to take load history effects into account. In this test program it was found that increasing the loading rate can either raise or lower the failure load depending on the nature of the joint (or repair). This work also illustrates the need to consider interlaminar failure in the design process and highlights the fact that, designs based on rate independent analyses cannot automatically be assumed to be conservative.

KEYWORDS: bonded joints, composite repairs, failure loads, experimental testing, certification

INTRODUCTION

The island continent of Australia is heavily dependent on transportation and the associated infra-structure for its economic survival. During the post war years Australia experienced rapid economic growth. In this period much of Australia's current infra-structure was constructed. However, there are now doubts on its durability and structural integrity. Economic and market forces have also resulted in utilization of structures beyond their original design life. In the international sphere a number of high visibility aviation accidents have served as a trigger for government and industry action. This "tombstone activity" was largely due to a series of incidents; viz:

- 1) The 1975 Eastern Airlines Flight 66 accident at JFK International which resulted in 113 fatalities;
- 2) The PSA mid-air collision in San Diego in 1978. This resulted in 144 fatalities;
- 3) The Aloha Airlines incident in 1988 which resulted in 1 fatality.

The Aloha incident revealed a number of fundamental weaknesses both in structural design and maintenance. Failure was due to the presence of multiple (interacting) cracks in neighbouring locations, this is now referred to as Multi Site Damage (MSD), coupled with

corrosion damage. Indeed, subsequent investigations have also revealed that multiple mechanical repairs, in close proximity, can also compromise structural integrity.

In the aeronautical scene Australia has developed unique methods which utilize externally bonded composite patches to repair cracked, or damaged, structural components [1]. Although this repair methodology was first used to repair cracks in military aircraft it has recently been applied to civilian aircraft. The application to Boeing 727, 767 and 747 aircraft is described in [2, 3], which outline a series of flight demonstrator programs.

When certifying composite joints and repairs a knowledge of the potential failure mechanisms of composite repairs is mandatory. For bonded joints and composite repairs, failure of the matrix material, i.e. interlaminar failure, often drives the design process, see [4]. From the structural/design view point the necessity of transmitting the load via an adhesive bond, from the composite to the underlying or connecting structure often results in matrix dominated interlaminar shearing forces. Indeed, this was recognised as one of the primary causes of the disbonding of the structural reinforcement of the F111C wing pivot fitting [4, 5, 6]. This failure, which is documented in [4], did not occur instantaneously, upon commencement of the strain hold, but took a significant time to occur. As a result of this failure mechanism attention was subsequently focused on understanding, and thereby preventing, this interlaminar failure process, see [4, 5, 6]. To this end it was recently shown [7, 8] that, for adhesively bonded joints, neglecting the time dependent nature of the stress-strain curves can result in fictitious values for the stresses and strains in the joint. Given the potential importance of this phenomena, i.e. load history dependence of the failure loads, the present paper addresses the question;

Can the non-linear time dependent stress strain response of both the adhesive and the matrix material be reflected by load history dependent failure loads?

SPECIMEN DESCRIPTION

The experimental tests were performed using nine specimens made from graphite fibers and an epoxy resin, viz: (AS4/3501). This material combination is widely in use in both the aircraft industry and in general engineering. For the geometrical layout a scarf joint specimen was chosen which was typical of that used in the wing skin of a modern fighter aircraft, and also in classical (i.e. traditional) composite repairs to composites. The adhesive for the scarf joint was FM300-2 with an approximate layer thickness of 0.2mm. All specimens were clamped in an area 100 mm from each end. The geometry of the specimen was as shown in Figure 1, and the working (test) area was approximately 250 mm. The symmetric adherend(s) consisted of 50 plies with a $[(+45_2, -45_2, 0_4)_3, 90]_s$ ply configuration. Each graphite/epoxy doubler consisted of 16 plies with a $[0_2, +45, -45, -45, +45, 0_2]_s$ ply configuration.

To establish quality of the fabrication process the specimens were C scanned using a 2.5 MHz probe, which was located a distance of 64 mm from the specimens. Except for specimen 8 the scan-images of the nine scarf joint (repair) specimens revealed an acceptable bond quality. This specimen had a major disbond, or delamination, within the scarf joint (i.e. repair). Consequently, Specimen 8 was used as a dummy specimen. This defect subsequently led to a reduced failure load.

To enable the strains to be recorded two gauges were bonded on each specimen. One was located on the center of the patch and the other on the “coupon” material remote from the doubler. The strain gauges used were 5mm self-temperature-compensated gauges with a resistance of 350 Ohm and had a gauge factor of 2.105.

One objective of the test program was to establish the effect of load history on the failure load of the specimens. To investigate this aspect the specimens were loaded under load control an Instron testing machine, using hydraulic grips. The chosen load ramps were approximately 0.01 KN/s, 0.1KN/s, 10KN/s and 1000KN/s. To guarantee the repeatability of the experiments each load rate test was performed with two specimens. Preliminary tests revealed a catastrophic failure and it impossible to detect the location of failure initiation. Consequently, to observe the failure process a high speed video camera (time window 20 sec, 12,000 picture per second) was installed, for tests on specimen 2 and 3. The remaining specimen, specimen number 9, was used to perform a creep tests at 95 kN, 105 kN, 110 kN, 113 kN and 120 kN with load ramps of ≈ 0.01 kN/s.

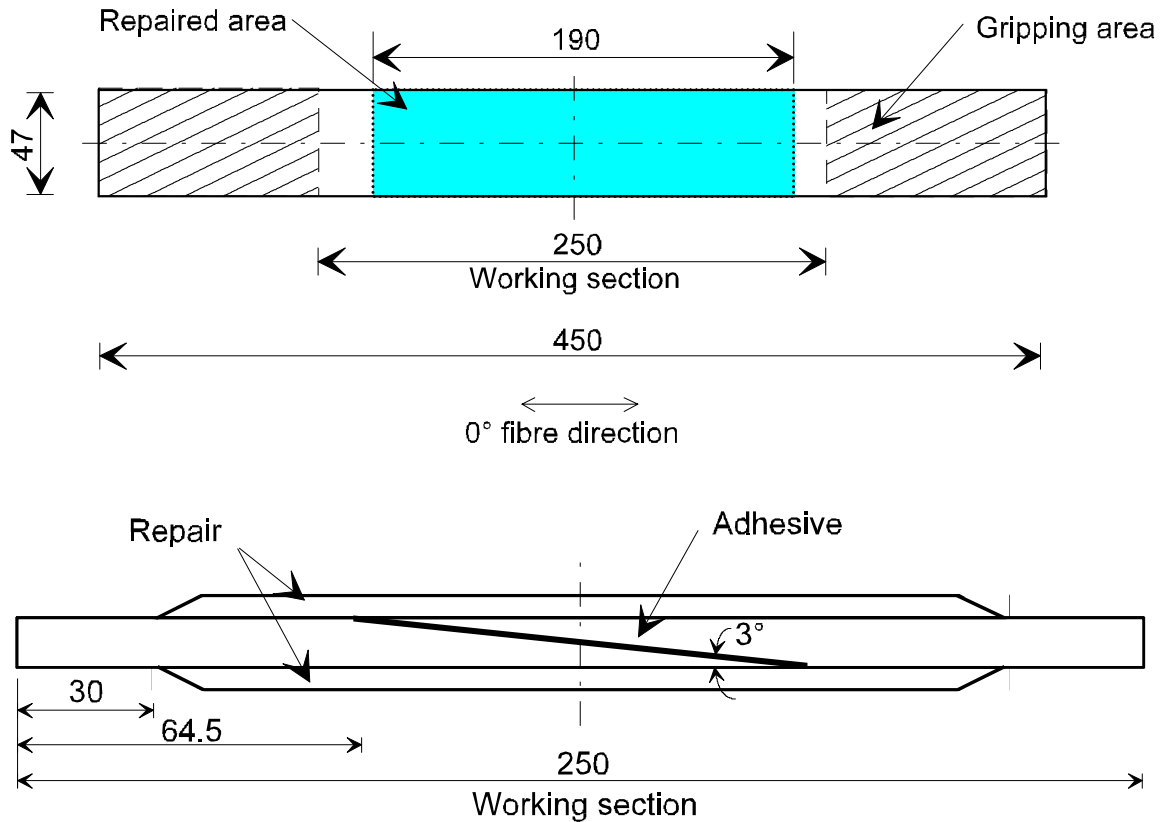


Figure 1: Geometry of the scarf joint specimen

A PC was used to tune an appropriate sample rate and to store the data points. The data acquisition unit recorded the applied load, the actuator displacement and the two strain gauge readings using. The load and displacement values during the tests were provided by the data unit of the tensile testing machine. The strain gauge readings were collected using a self-temperature compensated quarter-bridge. The resultant failure loads are shown in Table 1.

Unfortunately, even at low loading rates, the failure of the specimens was catastrophic, i.e. without any pre-warnings prior to the sudden failure. It was impossible to observe the precise location where the failure initiated. Consequently, a high-speed camera with a picture sequence of 12,000 images per second was used while testing specimens 2 and 3. The resultant images for Specimen number 2 are shown in the Figure 2. In both cases it was apparent that the failure initiated at the patch-coupon interface area. Unfortunately, the resolution of the camera was such that it was not possible to ascertain whether the failure was initiated in the adhesive or in the graphite epoxy adherends.

Following this test program specimen 9 was used to perform a creep test. The specimen was initially loaded slowly ($\approx 0.01\text{kN/s}$) to approximately 95 kN and the load then held for 700 seconds. The specimen was then loaded slowly, at approximately the same loading rate, to approximately 105 kN and the loads held for 800 seconds. Further load holds were performed at 110kN for ≈ 800 seconds, at 114kN for ≈ 1300 seconds and at 120 kN for approximately ≈ 1300 seconds with no apparent creep, or failure, at any of these load holds. Indeed, the test was terminated when after reaching 120kN the specimen had not failed.

Table 1: Summary of Experimental Results

Specimen No.	Loading Rate kN/s	Sample Rate (Hz)	Strain Centre $\mu\epsilon$	Strain Remote $\mu\epsilon$	Failure Load
1	915	1000	1788	3205	84.8
2	800	1000	1614	2847	94.8
3	765	1000	2292	3057	83.3
4	9.7	50	2718	4434	114.2
5	0.125	5	3151	4733	111.5
6	0.1	5	3033	3911	102.5
7	0.012	1	2935	4729	115.0
8 ⁺ Dummy	0.096 Specimen	0.5 used	2609 to set up	3313 the test	93.8 program

⁺ This specimen, had been used as a dummy to calibrate the test rig prior to performing the final test program. It also contained an obvious flaw.

DISCUSSION

The load displacement and the load strain results obtained for each of the nine scarf joint repair specimens were essentially linear to failure. However, the failure loads decreased as the loading rate increased. The range was from 83.3 kN at high load rates to 115.0 kN at low loading rates (or to >120 kN if the results of specimen 9 are included). Indeed, the ratio of the maximum failure load, at low loading rates, to the minimum failure load, at high loading rates, was approximately 1.39. This infers that when designing composite joints the role of rate dependent response of the composite adherends may need to be considered.

The location of the failure initiation was dominantly in the “patch transition area”, i.e. away from the scarf joint. Unfortunately the failure surfaces were such that it was not possible to

determine the exact failure location. A detailed inspection of the failed specimens indicated that the failure surface appeared to jump between the matrix material and the adhesive bond.

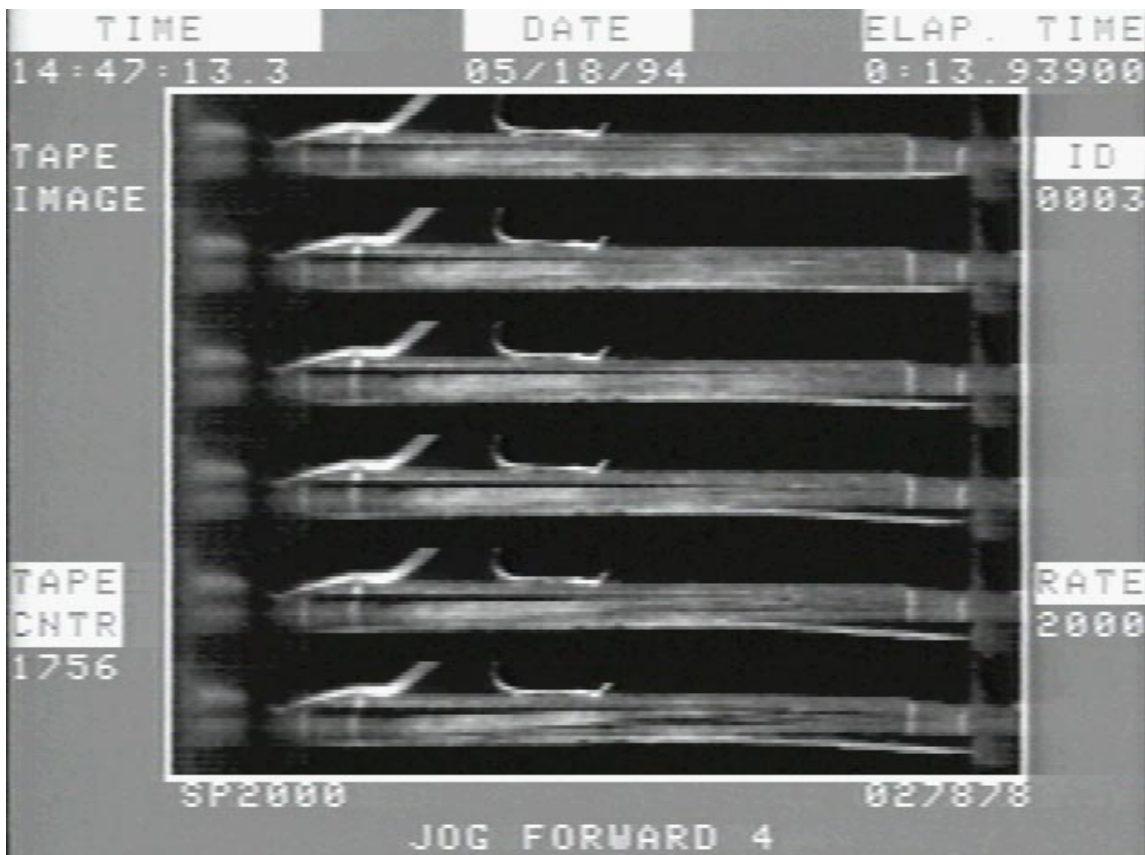


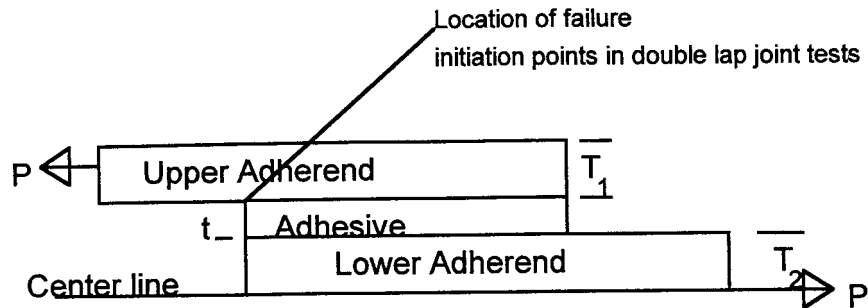
Figure 2: Failure initiation of scarf joint specimen 2 (frame 3)

THE FAILURE OF ADHESIVELY BONDED LAP JOINTS

To further evaluate this effect a series of 8 tests were performed on both single and double, i.e. symmetric, graphite epoxy (AS4/3501) lap joints with loading rates of 0.01, 0.1, 10.0 and 100kN/s. The double lap joints were as shown in Figure 3, with the lower adherend consisting of 8 plies with a ply configuration of $[(+ 45,- 45)_{2S}]_S$ and an upper adherend of $[(+ 45,- 45)_{2S}]_S$ bonded with a single layer of FM300. The single lap joints had the same upper adherends but the lower adherend was $[(+ 45,- 45)_{2S}]_S$, i.e the upper and lower adherends were identical. The specimens had a working section 175 mm long and 40 mm wide, whilst the gripped area was 40 mm x 40 mm and the (bonded) overlap was 25 mm long, see Figure 3. Typical experimental load displacement curves for the double and single lap joints are shown in Figures 4 and 5 respectively.

In both cases we see that, as in the scarf joints, the failure loads and displacement were significantly effected by the loading rates. In contrast to the previous tests, on the scarf joint, increasing the rate of loading increased the failure load and decreased the displacement at failure. Unlike the scarf joint specimens the failure appeared to initiate in the graphite epoxy, see Figure 3, and, in general, left a layer of the upper adherend attached to the lower

adherend. This failure mechanism has previously been discussed in [4, 10, 11] and is common to both composite repairs and step lap joints. Indeed, this was the failure mechanism found in the F/A-18 step lap joint test program, see [9].



No Bending about the center line

Figure 3. Typical geometry for symmetric lap joint tests.

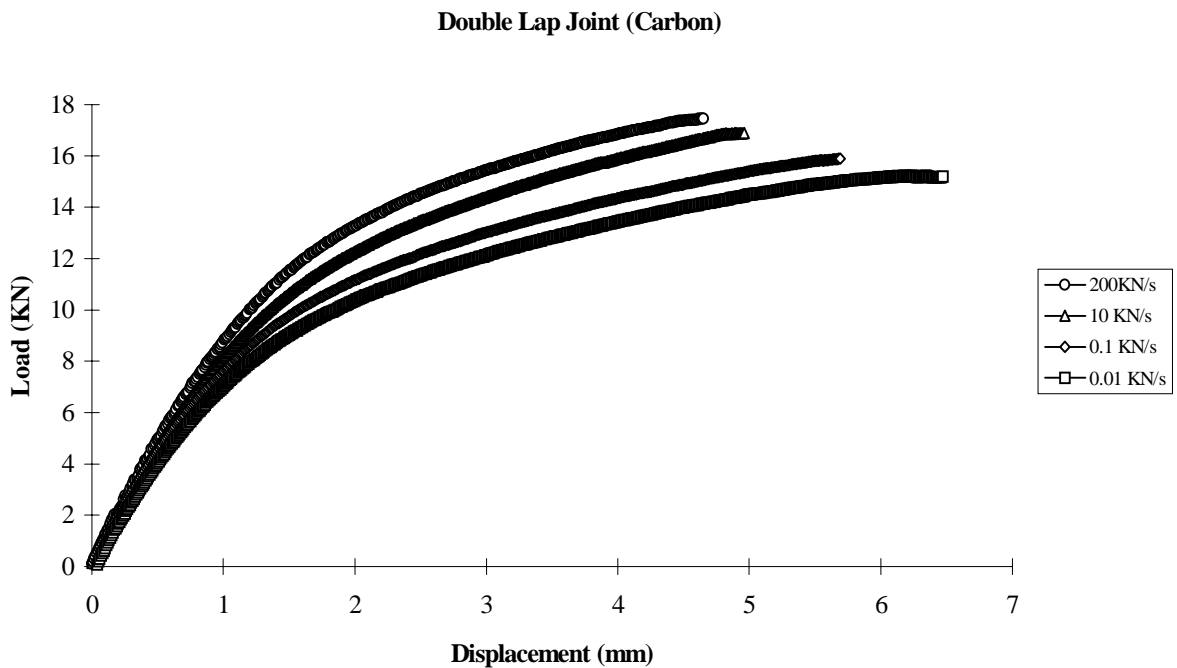


Figure 4. Load displacement results for double lap joint specimens

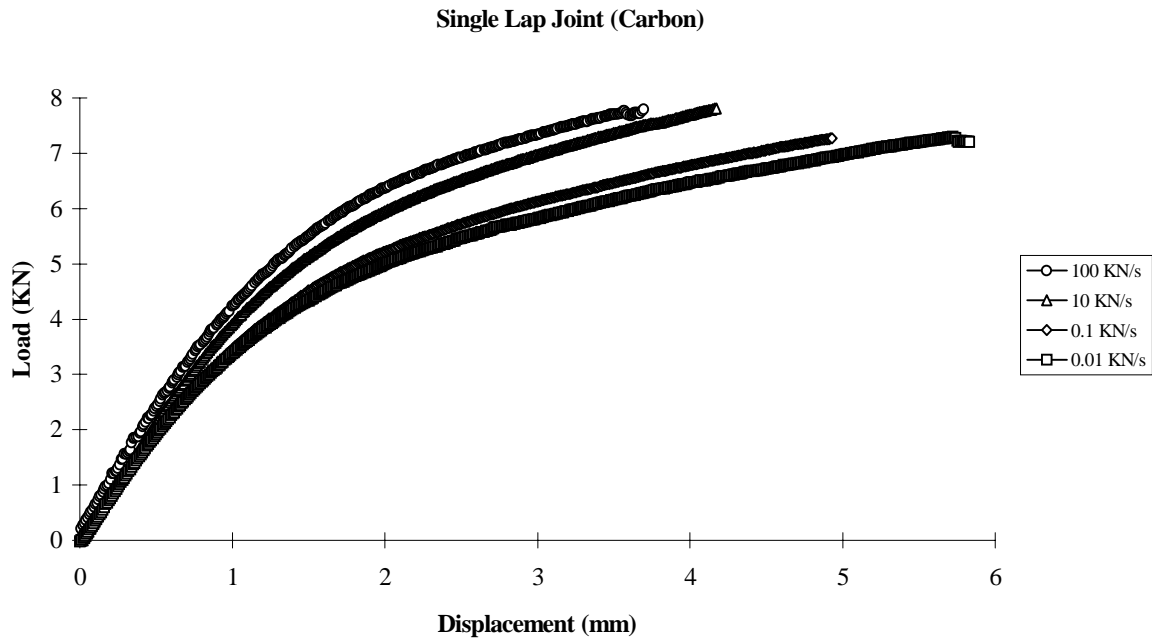


Figure 5. Load displacement results for single lap joint specimens

CONCLUSION

This test program has revealed that when evaluating the structural integrity and durability of composite joints or bonded repairs, see [10, 11] for an aerospace perspective, it may be necessary to take load history effects into account. The results of this experimental study support the conclusions outlined in [7, 8] that for adhesively bonded composite joints and composite repairs current design strategies may need to be extended in order to cater for this observed effect. In this context the present test program has shown that increasing the loading rate can either raise or lower the failure load depending on the nature of the joint (or repair). Hence, designs based on rate independent analyses cannot be assumed to be conservative. It also illustrates the need to consider interlaminar failure in the design process.

REFERENCES

1. Baker A. A. and Jones R., Bonded Repair of Aircraft Structure, Martinus Nijhoff Publishers, The Hague, 1988.
2. Bartholomeus R., Paul J. J. and Roberts J. D., Application of bonded composite Repair technology to Civilian Aircraft- 747 Demonstrator Program, Proceedings International Conference on Aircraft Damage Assessment and Repair, Edited by R. Jones and N. J. Miller, Published by The Institution of Engineers Australia, ISBN (BOOK) 85825 537 5, July 1991.
3. Jones R., "Recent Developments in Repair Technology", Proceedings Int. Conference on Aircraft Damage Assessment and Repair, Published by The Institution of Engineers, Australia, ISBN 85825-537-5, pp. 76-84, 1991.

4. Jones R., Chiu W. K. and Hanna S., Potential failure mechanisms of bonded composite repairs for metal and concrete, *Theoretical and Applied Fracture Mechanics*, 21, 107-119, 1994.
5. Jones R., Molent L., Paul J. J. , Saunders T., Chiu W. K., "Development of a composite repair and the associated inspection intervals for the F111C stiffener runout region", In *NASA Conference Publication 3274*, pp.339-350, 1994.
6. Molent L., Callinan R. J. and Jones R., "Design of an all boron epoxy doubler for the F-111C wing pivot fitting: Structural aspects", *Journal of Composite Structures*, 11, 1, pp. 57-83, 1989.
7. Jones R. , Tripit B., Chiu W. K. and Tomas J., "Lap joint theory revisited", *Journal of Polymers and Polymer Composites*, 1995, vol 3, 1, pp 11-19.
8. Chao M. Chiu , W. K., Jones R., Wang J., and Kelly D., "The Analysis of Bonded Lap Joints", *Proceedings ICCM11*, Australia, (in press).
9. van Blaricum T., Bates P. and Jones R., "An experimental investigation into the effect of impact damage on the compressive strength of step lap joints", *Journal of Engineering Fracture Mechanics*, 32, 5, 667-674, 1989.
10. Jones R. and Smith R., "Continued Airworthiness Of Composite Repairs To Primary Structures For Military Aircraft", *Proceedings 6th Australian Aeronautical Conference*, pp 311-316, 20-23 March, 1995, published by The Institution of. Engineers Australia, NCP 95/1, ISBN (Book) 0 85825 624 X.
11. Jones R., Chiu W. K. and Smith R., "Airworthiness of composite repairs: Failure mechanisms", *Engineering Failure Analysis*, 2, 2, 117- 128, 1995.

OBSERVATION OF STATIC STRENGTH AND FATIGUE LIFE OF REPAIRED GRAPHITE/EPOXY USING TENSILE COUPON

J. W. Choi, W. Hwang, H. C. Park and K. S. Han

*Department of Mechanical Engineering
Pohang University of Science and Technology, Pohang 790-784, Korea*

SUMMARY: The static strength and fatigue life of repaired graphite/epoxy laminates are observed using tensile coupon. The lay-up of investigated laminates was $[0^\circ/\pm 45^\circ/90^\circ]_s$. Static strength was measured from the specimens prepared by various repair techniques such as precured-single patch, precured-double patch and cure-in-place methods. The strength was recovered to the extent of 60-80% of unnotched case. Fatigue life was also measured from the laminates repaired with cure-in-place method. Hwang and Han's MFLPE 1(modified fatigue life prediction equation 1), which was based on the fatigue modulus degradation model and reference modulus, was chosen for fatigue life prediction of repaired specimen and compared with the conventional fatigue life equations such as S-N curve and Basquin's relation. The MFLPE 1 has better agreement with experimental data than S-N curve and Basquin's relation.

KEYWORDS: repaired graphite/epoxy laminates, repaired graphite/epoxy laminates, fatigue modulus, fatigue life prediction equation

INTRODUCTION

The use of advanced composite materials, especially on the aircraft, have been expanding in recent years because of their superior strength-to-weight, stiffness-to-weight ratios and better fatigue resistance compared to the other materials. But unfortunately, most composite materials may contain defects such as cracks, voids and delaminations produced by either fatigue, impact damage or poor design. These defects may cause a bad influence on the various functional capabilities.

To restore a damaged part's structural integrity, attention has recently been focused on developing repair procedures [1, 2]. Considerable effort has been devoted to the development of generic repair technology for advanced composites with aircraft companies as the central figures, but the repair standards are not established yet [3-5]. Some repair designs and application procedures have little chance of success, and in many cases service lives of components have been reduced by poor design.

To establish repair standards, the behavior of repaired composites must be observed not only under static but fatigue loading. In this study, the static and fatigue behavior of repaired composites is observed and analyzed.

THEORETICAL ANALYSIS

The fatigue modulus, F , proposed by Hwang and Han[6, 7] is defined as a function of loading cycle, n , and applied stress, q .

$$F(n, q) = \frac{\sigma_a}{\varepsilon(n)} = \sigma_u \frac{q}{\varepsilon(n)} \quad (1)$$

where F is fatigue modulus, σ_a is applied stress, ε is resultant strain, σ_u is ultimate strength and q is ratio of applied stress to ultimate strength. Initial and final conditions give the following relations:

$$\begin{aligned} F(0, q) &= F_0 = E_0 \\ F(N, q) &= F_f \end{aligned} \quad (2)$$

Fatigue modulus at 0th cycle, F_0 , is assumed to be the same as elastic modulus, E_0 , and fatigue modulus at fracture is defined as F_f at the number of cycles to failure, N . It is reasonable to assume that applied stress has a linear relation with resultant strain at any arbitrary loading cycle if the specimen undergoes constant maximum loading. This assumption follows:

$$\sigma_a = F(n)\varepsilon(n) \quad (3)$$

The fatigue modulus degradation rate at any fatigue cycle can be assumed as a power function of a number of fatigue cycles and the fatigue modulus itself,

$$\frac{dF}{dn} = -A \frac{Cn^{C-1}}{BF^{B-1}} \quad (4)$$

where A , B , and C are material constants. Integration of Equation(4) by substituting the condition (2) gives

$$F_f^B - F_0^B = -AN^C \quad (5)$$

The reference modulus, F_R , is assumed as follows:

$$\begin{aligned} F_0 / F_R &= p \\ F_f / F_R &= f(q) = q \end{aligned} \quad (6)$$

where p and q are material constants and applied stress level, respectively. Substituting Equation (6) into Equation (5), one obtains

$$N = [M(p^B - q^B)]^{1/C} \quad (7)$$

Using the above equation, fatigue life of materials can be predicted as long as the material constants M , B , C , and p are known[8]

EXPERIMENTAL

The parent laminate was fabricated with a stacking sequence of $[0^\circ/\pm 45^\circ/90^\circ]_s$. The prepreg tape manufactured by Han Kook Fiber Company was used. A circular hole was made at the center of each specimen using drilling machine. Four different holes with radii 1, 2, 3 and 4 mm were chosen for static tests and three different holes with radii 1, 3 and 4 mm were chosen for fatigue tests. The width of test laminate was 25 mm and thickness was 1mm. The fatigue test specimen configuration is presented in Figure 1. Static tests were conducted for the specimens repaired by following repair methods. Fatigue tests were performed in load control mode using a sinusoidal wave form with frequency 3Hz which is considered to give a negligible temperature rise during tests.

Cosmetic Treatment

The hole was filled with epoxy which was mixed with chopped graphite fiber and cured in room temperature.

Precured-Single/Double Patch

The patch that had the same lay-up with parent laminate was adhered to the damaged area with adhesive (2216B/A) manufactured by 3M Company. The width of patch was the same as the parent laminate, and the length was 40 mm for single patch and 40 and 60 mm for double patch.

Cure-in-Place Patch

Prepreg was laid up in order of $0^\circ, -45^\circ, 45^\circ$ and 0° from parent laminate with varying the length by 30, 40, 50 and 60 mm, respectively. To reduce the stress concentration at the end of the outer layer of reinforced patch, the outer patch was cut in saw shape[9].

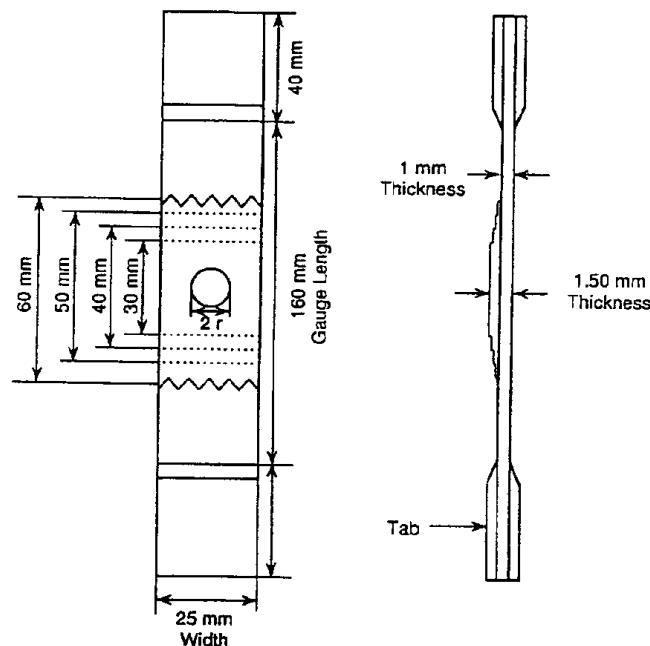


Figure 1. Fatigue test specimen configuration (cure-in-place)

RESULTS AND DISCUSSION

The tensile strength of parent laminate was found to be 608 MPa. Static test results are summarized in table 1. Non-patch method(filling) does not show reinforcing effect, while all patch methods show good results.

The strength recovery to the unnotched tensile strength for various repair methods is presented in Figures 2 and 3. Figure 2 is the case when the flaw size was 2 mm and Figure 3 is when the flaw size was 4 mm. Precured-double patch and cure-in-place patch methods show good results. In both cases, the tensile strength was recovered to the extent of about 60-80% of unnotched tensile strength. As flaw size increases, repaired strength degradation rate decrease more than notched strength degradation rate. In other words, the repair is more effective for large damage than for small damage. From above static test results, it could be concluded that cure-in-place method was the most effective one because it was good for strength recovery and caused minimum weight increase.

For the fatigue test results of repaired specimens, fatigue life was predicted by S-N curve, Basquin's relation and H and H's MFLPE 1. S-N curve and Basquin's relation can be written as follows:

$$\text{S-N curve} \quad q = k \log N + d \quad (8.a)$$

$$\text{Basquin's relation} \quad \sigma_a = \sigma_f' (2N) \quad (8.b)$$

where, N is the fatigue life, σ_a is applied stress and q is applied stress level ($=\sigma_a / \sigma_u$).

To compare the accuracy of these prediction equations, the SSR(residual sum of square) was defined as follows.

$$SSR = \frac{1}{n} \sum_{i=1}^n (\log N_{exp} - \log N_{cal})^2 \quad (9)$$

Table 1. Static test results (MPa)

Radius(mm)	1	2	3	4
Notched	445	373	335	298
Fill	-	369	-	303
Precured Single patch(40mm)	-	401	-	360
Precured Double Patch(40mm)	-	464	-	393
Precured Double Patch(60mm)	-	526	-	512
Cure-in-place Double Patch	-	-	-	451
Cure-in-place Single Patch	466	426	412	377

where N_{exp} is experimental data, N_{cal} is fatigue life predicted by life equations, and n is the number of data.

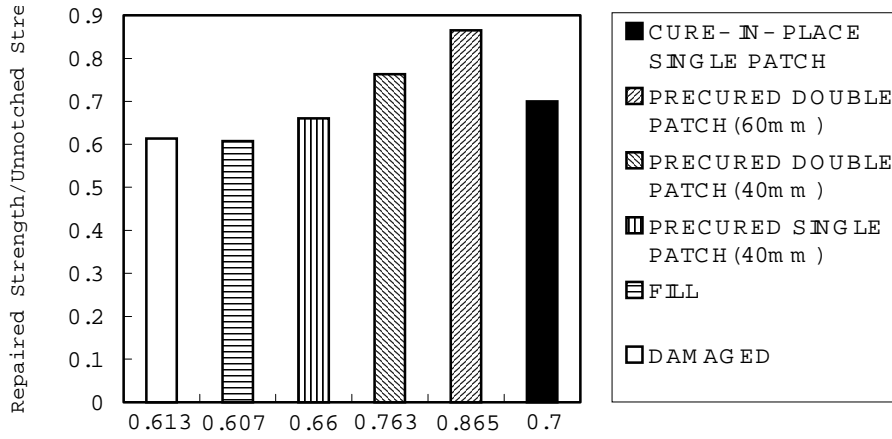


Figure 2. Strength recovery of various repair methods($r=2mm$)

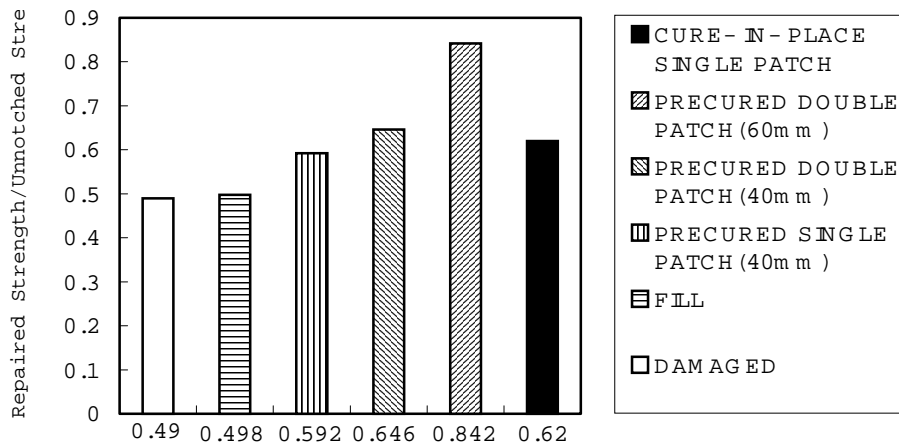


Figure 3. Strength recovery of various repair methods($r=4mm$)

Table 2. Material constants and SSR

Radius(mm)		1	3	4
MFLPE 1	p	0.974	1.091	1.005
	M	353.62	60.03	50.40
	B	2.672	0.158	0.993
	C	0.361	0.110	0.180
	SSR	0.1842	0.1943	0.1680
Basquin's relation	σ_f'	518.18	409.09	413.22
	b	-0.017	-0.019	-0.022
	SSR	0.9784	0.3369	0.3416
S-N curve	k	-0.0324	-0.0370	-0.0440
	d	1.0386	0.9720	1.0594
	SSR	0.7827	0.3129	0.3011

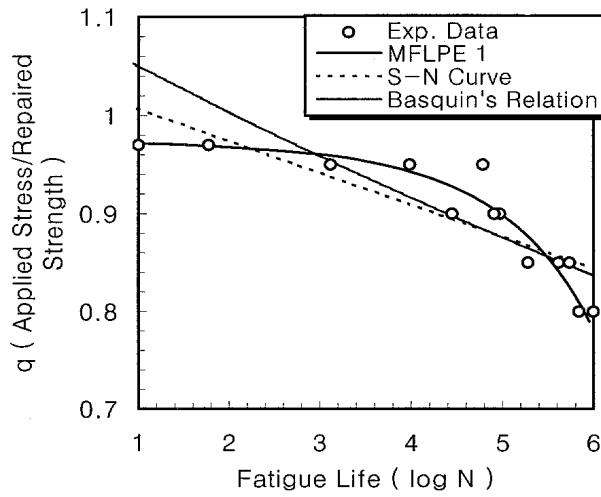


Figure 4. Comparison of MFLPE 1, S-N curve and Basquin's relation($r=1\text{mm}$)

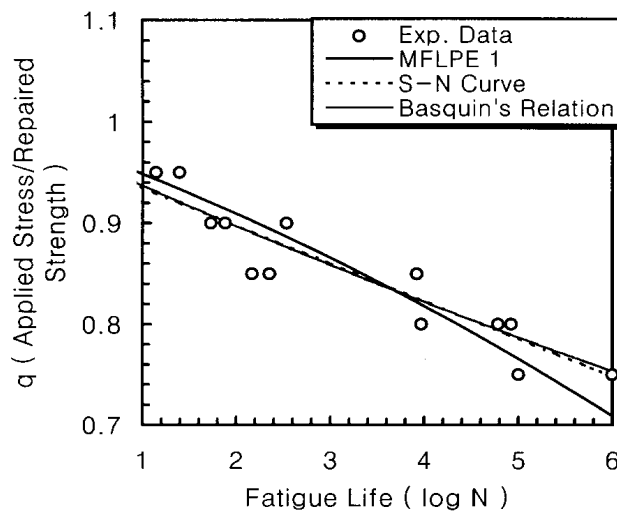


Figure 5. Comparison of MFLPE 1, S-N curve and Basquin's relation($r=3\text{mm}$)

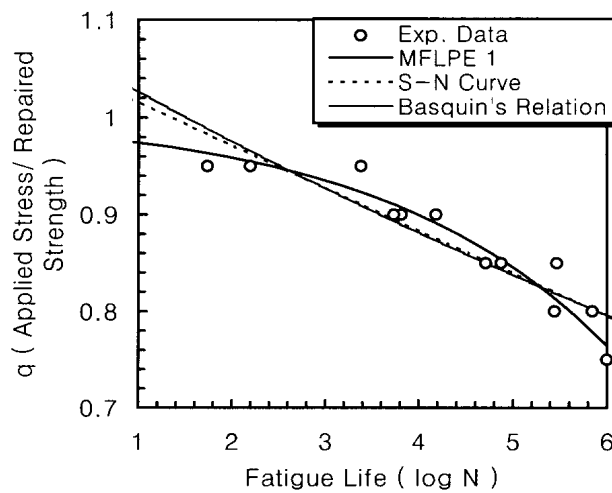


Figure 6. Comparison of MFLPE 1, S-N curve and Basquin's relation($r=4\text{mm}$)

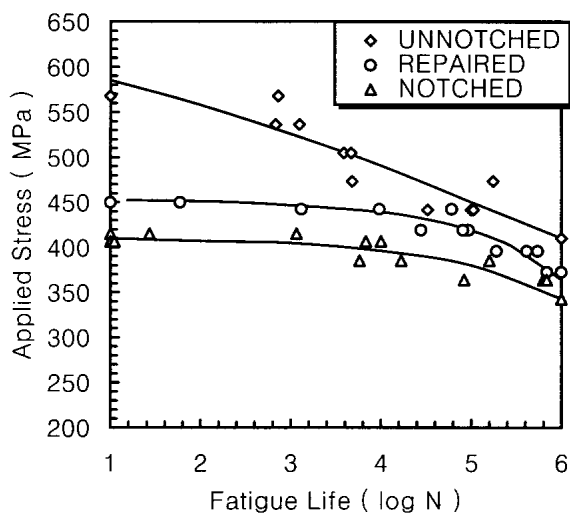


Figure 7. Comparison of fatigue life of unnotched, repaired and notched laminate($r=1mm$)

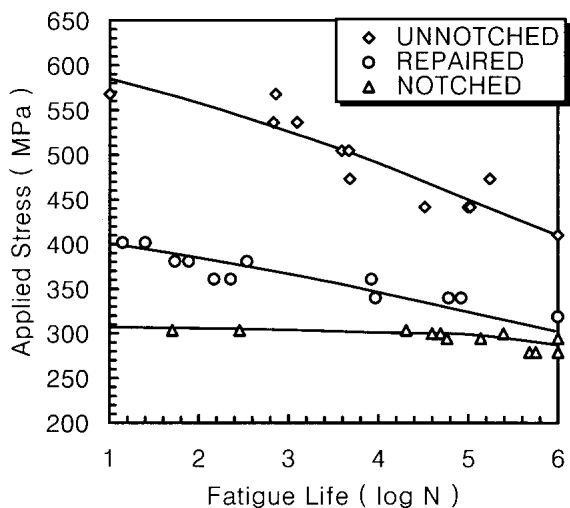


Figure 8. Comparison of fatigue life of unnotched, repaired and notched laminate($r=3mm$)

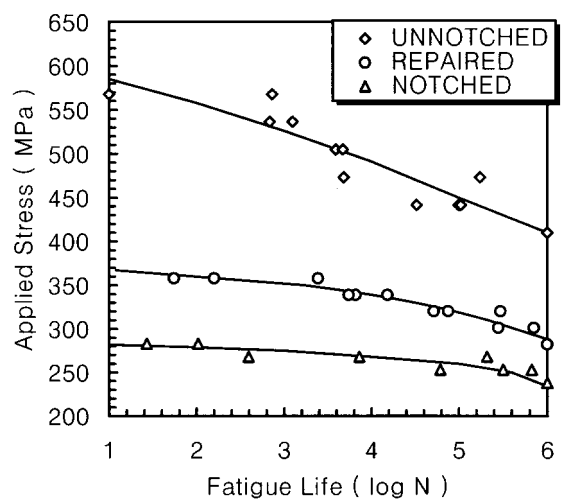


Figure 9. Comparison of fatigue life of unnotched, repaired and notched laminate($r=4mm$)

Table 2 presents material constants and SSR of life prediction equations. The value of SSR is smaller when predicted with MFLPE 1 than when predicted with other life prediction equations, regardless of flaw size. The prediction results are compared with experimental data in Figures 4, 5 and 6 in the case of radius 1, 3 and 4 mm, respectively. The comparison shows that fatigue life of repaired composite laminates could be predicted much better by MFLPE 1 than by S-N Curve or Basquin's relation.

Flaw size effect on the repair was observed by comparing fatigue life of unnotched, notched and repaired laminates. The comparison is presented in Figures 7, 8 and 9 which is the case of radius 1, 3 and 4 mm respectively. In all cases, repaired laminates exhibits higher fatigue strength. One possible explanation of this lies in the higher effective stiffness resulting from load distribution by reinforcing patch. From these figures, one can find that as flaw size increases, the repair efficiency increases, which is same as static cases.

FSRF (fatigue strength reduction factor) was defined to consider the fatigue strength degradation rate

$$FSRF = \frac{\frac{FS_{notched}}{FS_{unnotched}}}{\frac{FS_{repaired}}{FS_{unnotched}}} \quad (10)$$

where $FS_{notched}$ is fatigue strength of notched composites at N_i cycles, $FS_{unnotched}$ is fatigue strength of unnotched composites at N_i cycles, and $FS_{repaired}$ is fatigue strength of repaired composites at N_i cycles. Arbitrary fatigue cycles ($N_1=50$ cycles, $N_2=2500$ cycles, $N_3=125000$ cycles) were chosen to observe the behavior of repaired composites. Figure 10 shows the comparison of FSRF at each arbitrary cycle. At high cycle region (N_3), repaired fatigue strength reduced more than at low cycle region (N_1). It is considered that these phenomena are caused by the failure modes of repaired composites.

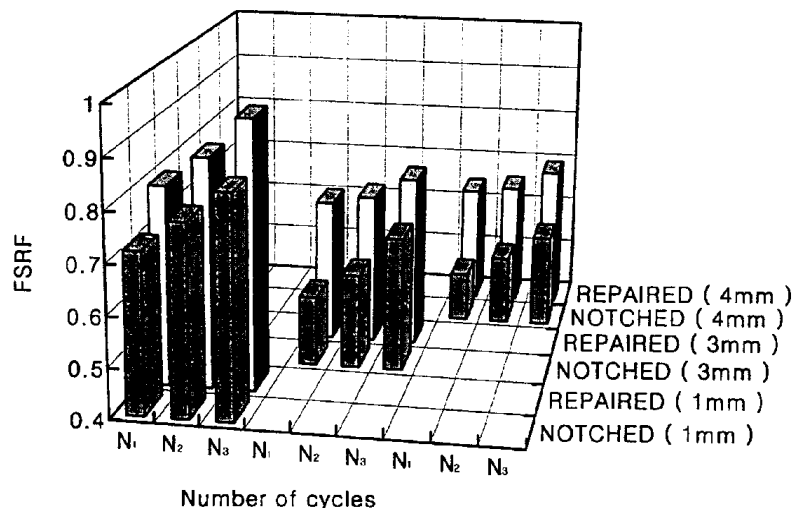


Figure 10. Fatigue strength reduction factor

As fatigue loading cycle progresses, the cure-in-place patch debonded one by one from outer side gradually, and finally debonded entirely from parent laminate about at the mid-cycle of

fatigue life. As a results, fatigue strength degradation rate increases rapidly, so that at high cycle region, fatigue strength increase less than at low cycle region regardless of flaw sizes.

CONCLUSION

Cure-in-place method was found the most effective repair method among a variety of relatively thin laminate repair methods. Static and fatigue strength were restored more as flaw size increases. It was found that MFLPE 1 predicts fatigue life of repaired composites better than conventional S-N curve and Basquin's relation.

REFERENCES

1. Middleton, D. H., *Composite Materials in Aircraft Structures*, Longman, 1990
2. Jones, J. S. and Graves, S. R., "Repair Techniques for Celion /LARC-16 Graphite /Polyimide Composite Structures," NASA CR-3794 ,1984
3. Myhre, S. H., "Advanced Composite Repair-Recent Development and Some Problems," *Composite Repair*, SAMPE Monograph No.1, 1985, pp. 14-25
4. Shyprykevich, P., "Standardization of Composite repair for Commercial Transport Aircraft," *Proceedings of Composite Repair of Aircraft Structures*, 1995, pp. 1-24
5. Davis, M.J., "A Call for Minimum Standards in Design and Application Technology for Bonded Structural Repairs," Int. Symposium on Composite Repair of Aircraft Structure, 1995
6. Hwang, W. and Han, K. S., "Fatigue of Composite - Fatigue Modulus Concept and life Prediction," *Journal of Composite Materials*, Vol.20, 1986, pp. 154-165
7. Hwang, W. and Han, K. S., "Fatigue of Composite Materials - Damage Model and Life Prediction," *Composite materials :Fatigue and Fracture* (Second volume) , ASTM STP 1012, Paul A. Lagace, Ed., 1989, pp. 87-102
8. Hwang, W., Lee, C. S., Park, H. C., and Han, K. S., "Single- and Multi-Stress Level Fatigue Life Prediction of Glass/ Epoxy Composites," *Journal of Advanced Materials*, July 1995, pp. 3-9
9. Stone, R. H., "Development of Repair Procedures for Graphite/Epoxy Structures on Commercial Transport," *Composite Repairs*, SAMPE Monograph No.1 , 1985, pp. 26-39

BONDED REPAIRS IN COMPOSITE STRUCTURES: A FINITE ELEMENT APPROACH

Randolph A. Odi¹, Clifford M. Friend¹

¹*Materials Science and Engineering Department, Cranfield University, Shrivenham Campus, Swindon, SN6 8LA, England*

SUMMARY: This paper reviews the use of the finite element method for the design and analysis of composite structural repairs. It compares a more traditional approach, based on that of Siener [7], with a 3D model and a new quasi-3D approach developed by Bair [8]. The predictive models are compared on the basis of displacement and adhesive tensile and shear stresses in repaired composite panels subjected to tensile loading. This work shows that the approaches are complementary, providing different insights into factors affecting the adhesive and the composite structure itself; both being important for the optimisation of repair joints. This study has also shown the need for an approach which provides an overall view of bonded repairs for composite structures.

KEYWORDS: adhesive bonded repairs, composite plates, finite element models

INTRODUCTION

The use of composite materials in aircraft structures has become increasingly widespread as the need for improved aircraft performance and capabilities grows. Repair engineers increasingly find themselves having to design and analyse suitable repairs for in-service damage beyond the scope of experimentally derived structural repair manuals. Engineers advocate the development of analytical techniques for the design and evaluation of repair techniques. The popularity and widespread use of the finite element method as a numerical analysis tool in engineering make it a suitable candidate for such a task.

This paper reports the findings of the first phase of an on-going research project on the analysis of bonded repairs in composite structures using a PC-based finite element software..

MODELLING APPROACHES

Bonded repairs to composite structures share many features with adhesively bonded joints. As a result, the first approaches proposed for their study using the finite element method were based on models developed to analyse bonded joints. A good insight into the field of bonded repairs can be obtained from the extensive literature on adhesively bonded joints. Published works on bonded joints was extensively reviewed in 1982 by Matthews *et al.* in an excellent article with an emphasis on finite element analysis.

Given the growing popularity of the finite element method as an engineering tool, it is surprising that there is little literature directly concerned with the finite element modelling of composite repairs. This may be due to the fact that repair joints and structural joints share several common features. Thus given the amount of work devoted to understanding the latter, modelling specifically repair joints has not been pursued with the same endeavour. However repairing composite structures is a discipline in its own right. Hall *et al.* [2] have called specifically for an improvement in numerical analysis methods if more efficient repairs are to be designed; a view shared by Heslehurst [1] and also by Davis in his report on the development of a standard for composite repairs for the Royal Australian Air Force. Four modelling approaches have been proposed by Loss and Kedward, Jones *et al.*, Siener and Bair *et al.* which are milestones in the modelling of composite repairs.

This preliminary study has been carried out to evaluate different modelling approaches to composite repairs. In addition to full 3D models, two main alternatives have also been investigated following an extensive literature survey: Siener's model which is an extension of the traditional plane strain 2D model used for adhesive bonded joints and Bair's model which is a promising new approach. These models have been selected because of their suitability for PC-based finite element applications using commercial codes. The main objective of the present study was to explore the advantages and problems associated with each approach through a linear static analysis of a representative composite repair.

SIENER'S MODEL

The main feature of this model is the plane strain assumption. This reduces the analysis to a 2D problem. It has been used before to model bonded joints successfully and thus represents a natural first step into modelling repair joints. In his modelling of composite patch repairs, Siener [7] followed a method similar to Loss and Kedward [5] by working out equivalent orthotropic properties for the composite adherends and inputting them into the FE model.

Siener's investigation addressed the problem of reducing the repair joint overlap length in scarf repairs whilst providing sufficient strength restoration. It was shown that joint strength can be increased while reducing the overlap length by increasing the repair patch stiffness using different lamination sequences. However his attempt to accurately predict joint strength using this FE model was not very successful because it relies on equivalent orthotropic properties and material non-linearity was omitted.

From the laminate stacking sequence and material properties, effective properties are calculated using laminate analysis theory. These effective properties (Young's moduli, Poisson's ratios etc.) are then used in the material definition of the finite element model.

BAIR'S MODEL

The study by Bair *et al.* [8] is one of the very few published papers dedicated exclusively to the modelling of composite repairs. Unlike the previous model, a plane strain state is not assumed by cutting through the repair joint. Instead a quasi-3D model is built using 3D composite shell elements. The 3D composite shell elements include deformations due to membrane, bending, membrane-bending coupling and transverse shear effects and are made up of a number of perfectly bonded orthotropic layers. A repaired panel is therefore modelled

zone by zone with an appropriate number of dummy layers of very small stiffness is added to make up the maximum number of layers (Fig. 1); the number of layers staying the same across the whole model.

For the panel shown in Fig. 1, the dummy layers are indicated for zone A to illustrate this concept where a number of dummy layers are added to make up the same total number of layers as in the central part of the repair patch. The results from Bair's analysis have been compared to experimental data. Both data sets agree very well for strain measurements. Bair's model has its merits but there are doubts about whether features such as adhesive fillets and local geometric rounding can be represented using this approach. Furthermore, no indication has been given about material non-linearity. The main conclusion reached from this work was that the FEM could be used successfully on a day to day basis to design and analyse composite repairs for large area damage on a personal computer.

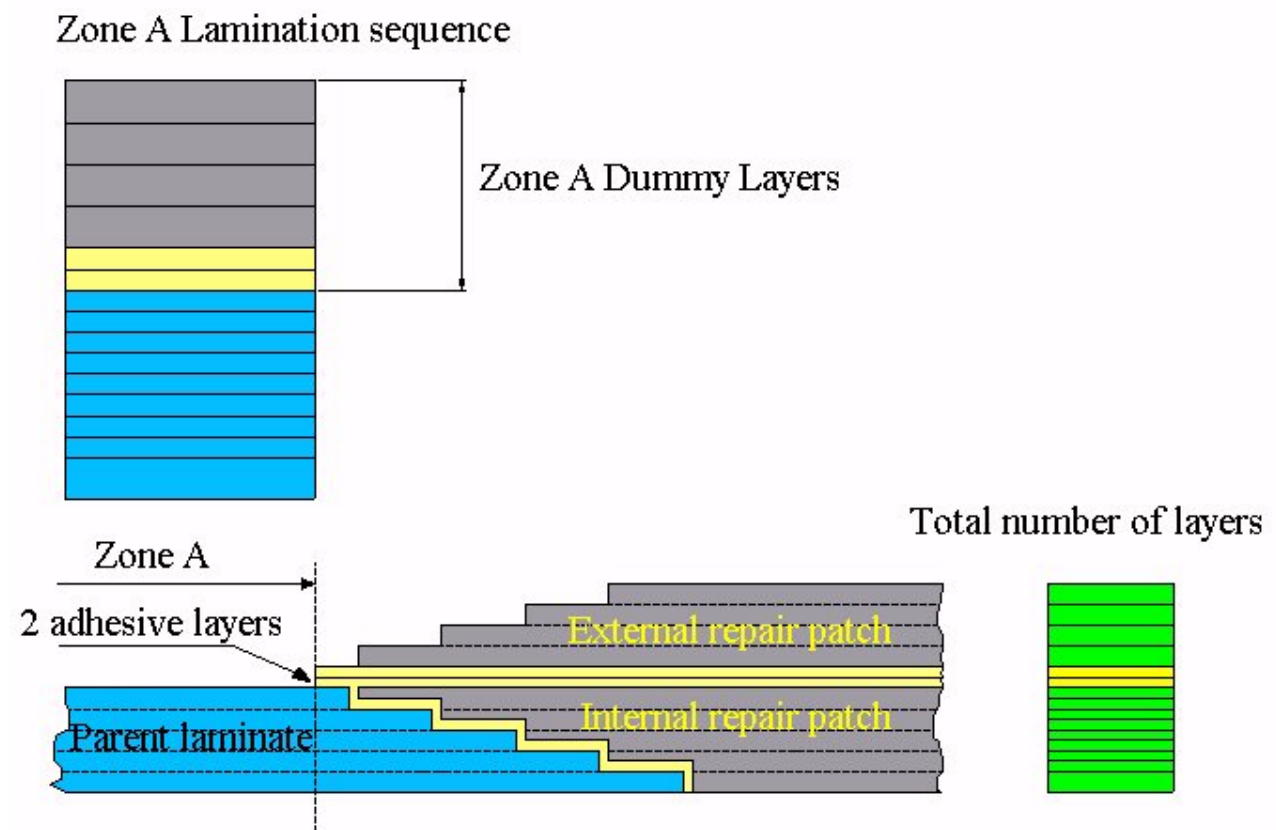


Fig. 1 Repaired panel configuration used by Bair et al.(8)

3D MODEL

This model employs 3D solid elements to represent both the adhesive and the composite adherends. For the former, simple isoparametric solid elements are used and for the latter composite solid elements. The aim is to obtain a full three dimensional representation of the stress state. The composite solid elements are also made of perfectly bonded orthotropic layers. Each adherend ply is modelled individually.

APPLICATION TO BONDED REPAIRS

These three approaches were used to model a scarf repair of a damaged composite plate. Siener's approach could be used to model an exact scarf, however, for the Bair approach the scarf joint was approximated by a five step lap joint. For the 3D model both types of repair were to be modelled. For reference purposes, undamaged and damaged plates were also modelled.

UNDAMAGED PLATE

The undamaged plate was a Hercules AS4/3501-6 carbon/epoxy composite with a stacking sequence of $[0_2 / \pm 45 / 90 / \pm 45 / 0_2]_s$. The laminate was 300 mm long, 25 mm wide and 2.5 mm thick, giving a layer thickness of 0.1389 mm for each lamina. Modelling the undamaged plate was straightforward. The three modelling approaches were used. The displacement and stress output from these models were used as references for the repaired plate as the aim in any repair scheme is to restore a damaged component to a fully functional state. 3D composite shell elements (NISA-NKTP 32) were used in Bair's approach, general shell elements (NKTP 20) for Siener's and both 3D solid elements (NKTP 4) and composite solid elements (NKTP 7) for the 3D model. Plane strain elements (NKTP 2) could have been used for Siener's model and hybrid solids (NKTP 9) for the adhesive in the 3D model. These hybrid solids are more suitable for thin structures but are more expensive to run in terms of computing power and time.

DAMAGED PLATE

The damaged plate had similar dimensions to the undamaged plate but with a central 10 mm hole. The damaged state corresponds to that where damaged material has been cut out of the plate leaving a circular hole. This represents the plate just before the repair is carried out. Damage propagation was not considered. The damaged plate was modelled to show the effect of the hole in the structure. The finite element model was constructed using the automeshing facility in NISA/DISPLAY with a stress accuracy option. The resulting mesh was thus fine enough to warrant accurate stress calculations around the hole. This area was more likely to have stress concentrations. The modelling was again straightforward.

REPAIRED PLATE

Using Siener's approach two models were constructed representing the two repair schemes: a scarf repair with a scarf angle of 3° and a stepped repair with five steps (Fig. 2a and 2b). A laminate analysis programme, LAP, was used to generate equivalent orthotropic properties for the laminate material and stacking sequence. This computer software is based on Classical Laminate Theory in which laminates are assumed to be infinite in length and width with plane stress assumed for each layer. This programme was also used to check results from the undamaged plate in tension.

For Bair's approach, only a stepped repair could be constructed (Fig. 2a). The adhesive thickness at each step was 0.1389 mm with a step length of 7.96 mm. The butt faces at each

step were 0.01 mm apart as shown on Fig. 2a. The repair length was only 39.80 mm compared to the scarf repair length of 47.70 mm.

Initially the same stepped repair used in Bair's approach was to be modelled using 3D solid elements with the same adhesive thickness but with a step length of 9.51 mm and butt faces 0.15 mm apart to be in line with practical repairs. A scarf repair model was also planned. However, for the latter, wedge shaped composite solid elements were required to represent the ideal scarf joint in Fig. 2b. As these are not available in NISA, the model was constructed with a step at each ply as shown in Fig. 2c. From this point of view, the repair modelled using 3D solid elements was closer to actual bonded repairs in its representation of the joint. As a result, the stepped repair used in Bair's approach (Fig. 2a) was not modelled.

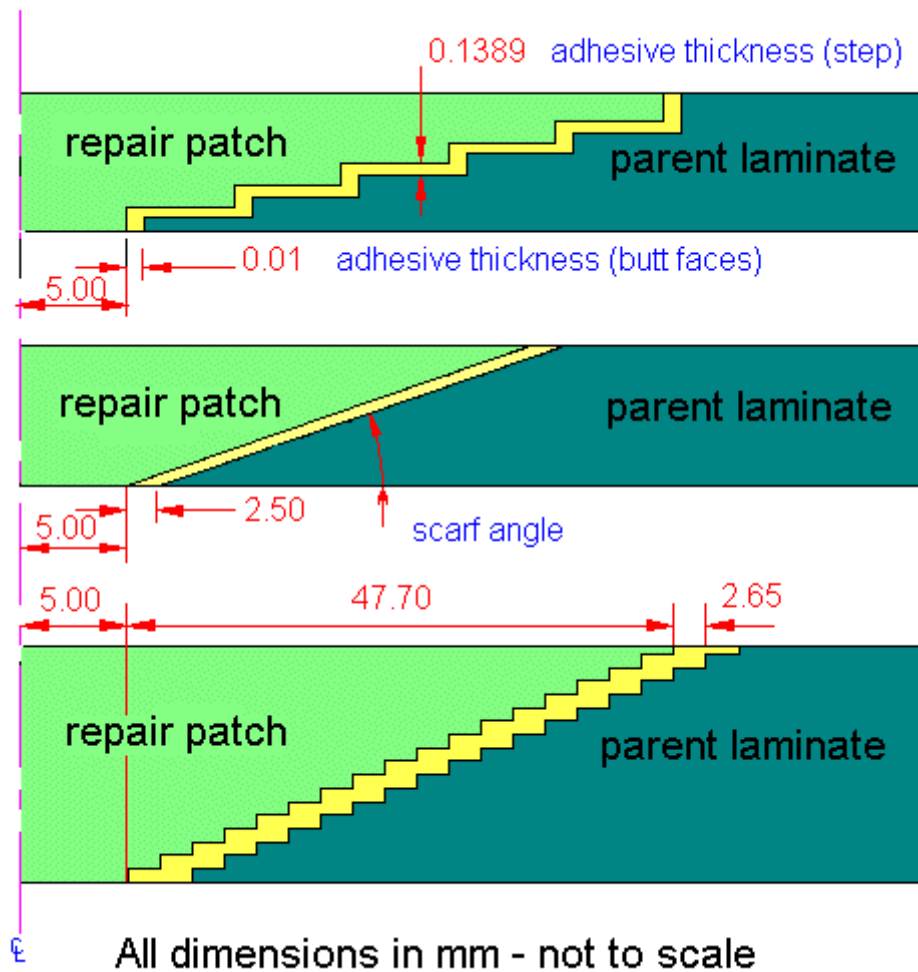


Fig. 2: Repair schemes : (a) stepped lap joint (b) scarf joint (c) 18 step scarf joint approximation

MODELLING DATA

For all three states, the plate was loaded in tension by 10 kN with the appropriate boundary conditions to simulate a tensile test. Where appropriate, extensive use of symmetry was

made. The data in Table 1 were used for the adhesive and those in Table 2 for the carbon fibre composite.

*Table 1 Epoxy Adhesive Material Data
(Picket and Holloway)*

Young's modulus E	3000	MPa
Shear modulus, G	1103	MPa
Poisson's ratio	0.36	

Table 2 AS4/3501-6 Material Data (Source: NPL, UK)

PROPERTY(°)	Value	Unit
Young's modulus in x-direction (EX)	135584	MPa
Young's modulus in y-direction (EY)	9244	MPa
Young's modulus in z-direction (EZ*)	9244	MPa
In plane (XY) shear modulus (GXY)	5019	MPa
Out-of-plane (XZ) shear modulus (GXZ*)	5019	MPa
Out-of-plane (YZ) shear modulus (GYZ*)	5019	MPa
Poisson's ratio (NUXY)	0.3072	
Poisson's ratio (NUXZ*)	0.3072	
Poisson's ratio (NUYZ*)	0.3072	
Tensile strength in x-direction (FXT)	2178	MPa
Compressive strength in x-direction (FXC)	484	MPa
Tensile strength in y-direction (FYT)	53.4	MPa
Compressive strength in y-direction (FYC)	134	MPa
In-plane shear strength (FSXY)	34.6	MPa

* assumed

(°) nomenclature from NISA/DISPLAY

RESULTS AND DISCUSSION

The aim of this study was to compare these different modelling approaches. The results obtained are grouped in three main parts: displacement, adhesive tensile stress and adhesive shear stress results. These parameters provide a useful comparison of the data obtained. The main reason for the choice of these quantities as comparison parameters is the fact that in a repair joint, ultimate characteristics such as strength and efficiency, are strongly influenced by the adhesive stresses (in particular the shear stress). Thus a model's ability to evaluate these stresses is a good indication of its usefulness. Accurate displacement calculation is the first basic requirement that any finite element model must meet. A linear static analysis with a relatively low load also allows an investigation of the structural response predicted by the models.

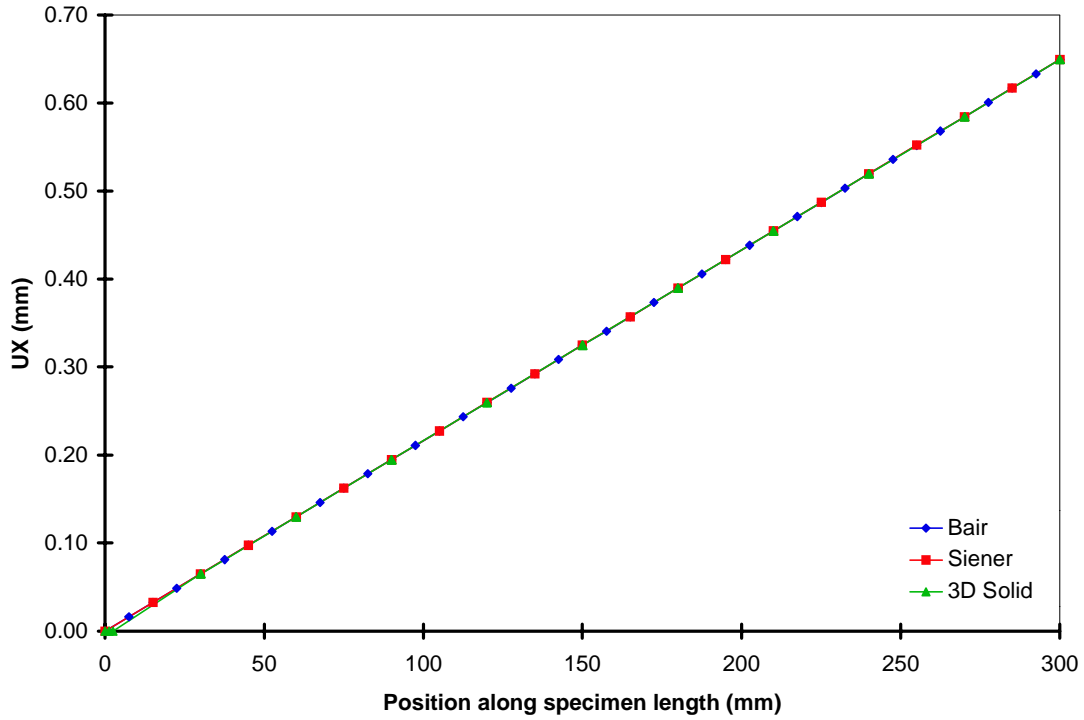


Fig. 3(a): Longitudinal displacement (undamaged)

Fig. 3 compares the displacements along the plate centre line, predicted by the models for both undamaged and repaired states. The reference (undamaged) displacement shows good agreement between the models (Fig. 3(a)). However the mesh used for the Bair and 3D models was finer.

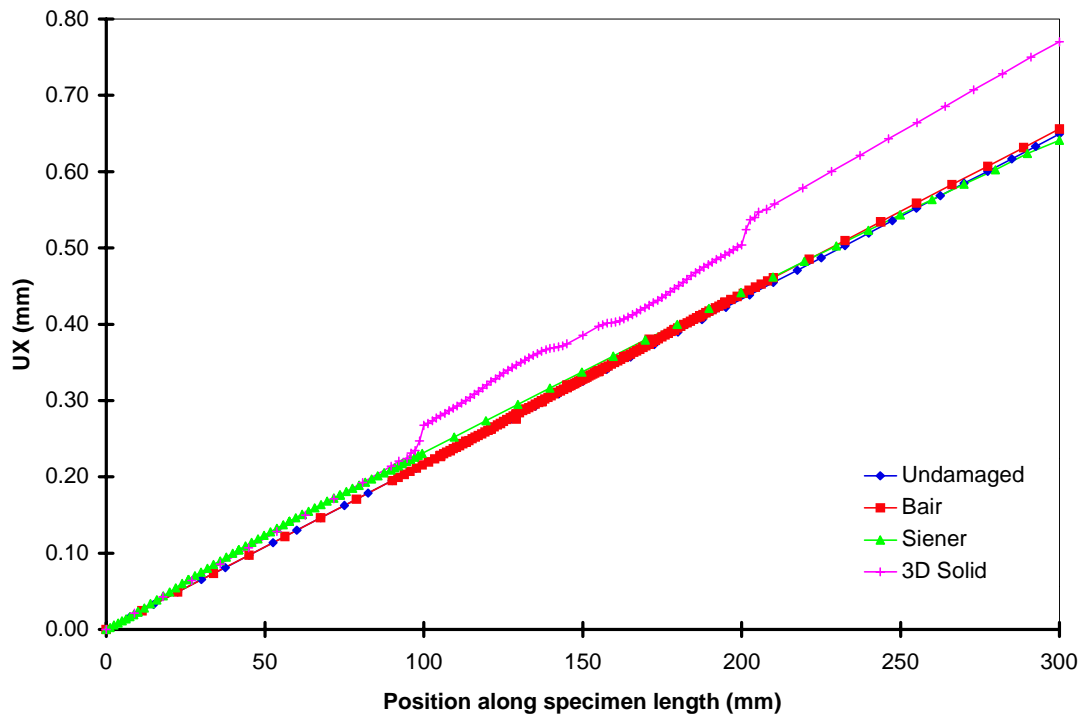


Fig. 3(b): Longitudinal displacement (repaired)

Fig. 3(b) also confirms that the repairs were effective as far as matching the undamaged plate displacement is concerned for both the Siener and Bair models. However, the presence of the repair patch in the 3D model is more apparent. The discontinuities in this displacement curve are located where the patch begins and ends. The curve shows the nodal displacement on the top surface of the plates and the shifts in the 3D solid curve are due to the presence of adhesive at the edge of the repair patch which is much more compliant than the adherends.

The next step is to consider adhesive tensile stress. The right hand top repair step (step 5) for the Siener and Bair models is shown in Fig. 4. The corresponding location for the 3D model are steps 13 and 14 shown in Fig. 5. The tensile stresses at these steps are plotted in Fig. 6.

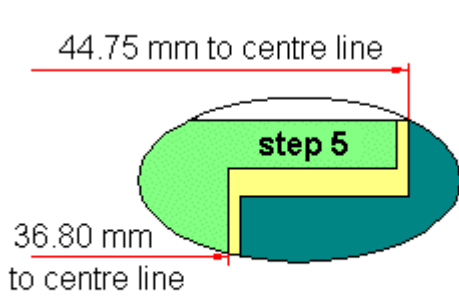


Fig. 4: Top repair step location (3D model)

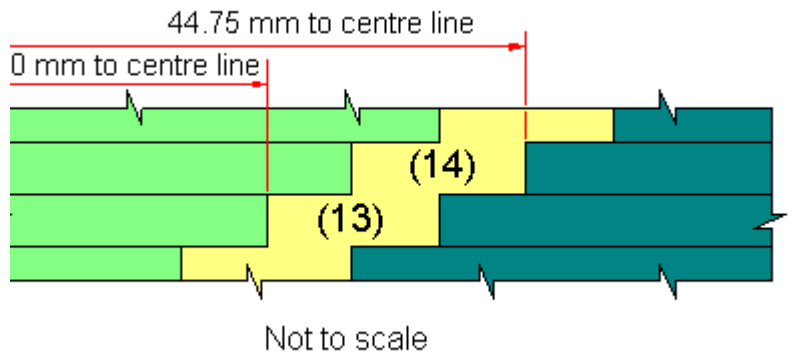


Fig. 5: Steps 13 and 14 (Bair and Siener models)

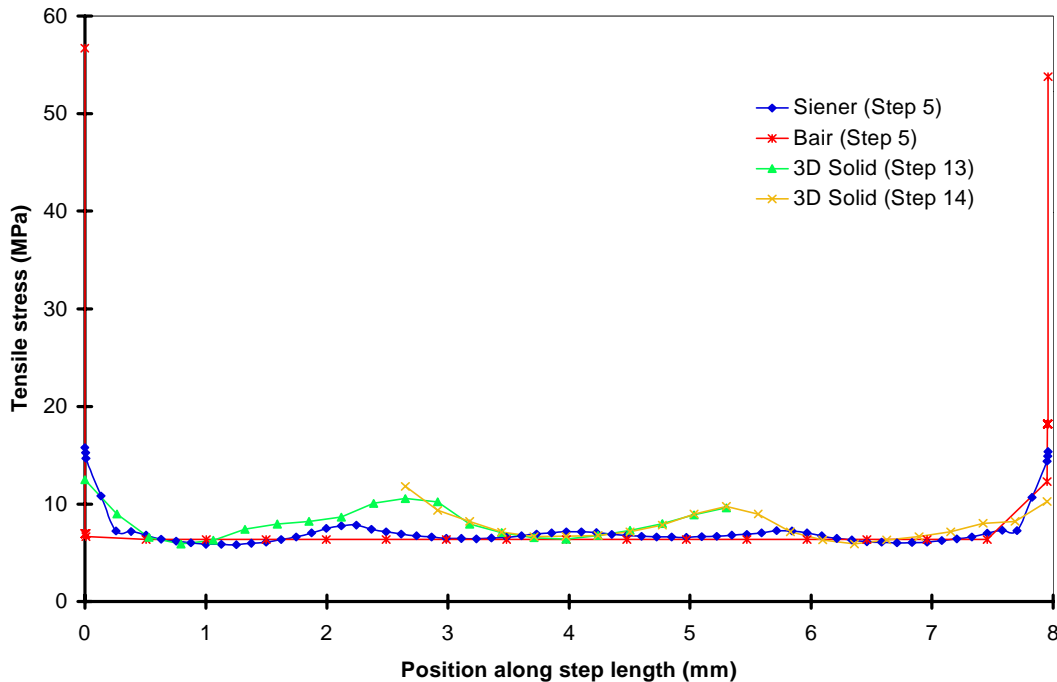


Fig. 6: Adhesive tensile stress

Fig. 6 indicates that there is good agreement between all three models away from step ends; the peaks observed for steps 13 and 14 of the 3D model were due to the end of the ply above each adhesive step which act as stress raiser. All three models predict high stresses at the step ends.

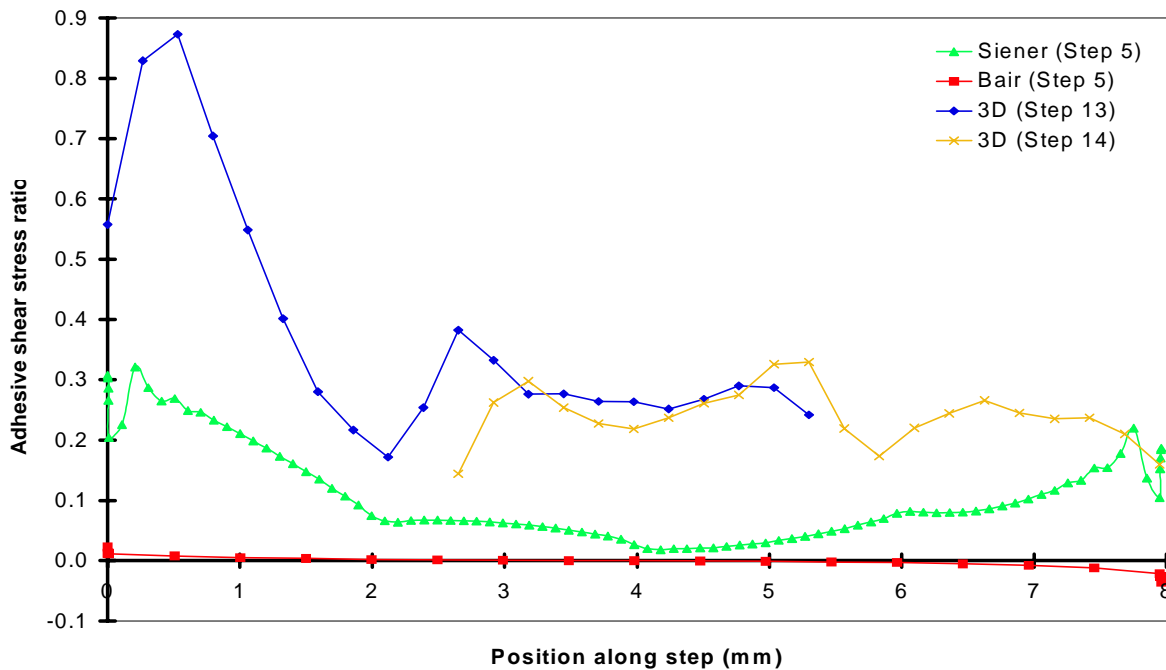


Fig 7: Adhesive shear stress (Stepped repair)

The final comparison parameter, the adhesive shear stress, is shown in Figs. 7 and 8 for different repair schemes using the three approaches. This stage of the comparison highlights some interesting results.

Fig. 7 shows the adhesive shear stress ratio plotted for the same steps as in Fig. 6. This ratio expresses the adhesive shear stress as a fraction of the average applied stress which is 8.37 MPa for the stepped repair used in the Bair and Siener models and 8.38 MPa for the 3D model. The values obtained from Bair's model were very small compared to Siener's and the shape of the curve was completely different from that expected. For the 3D model, the shear stress is higher with larger maximum values because the step length was shorter. However the shape of the curve is similar to Siener's model and is in accordance with previously published work [10, 11].

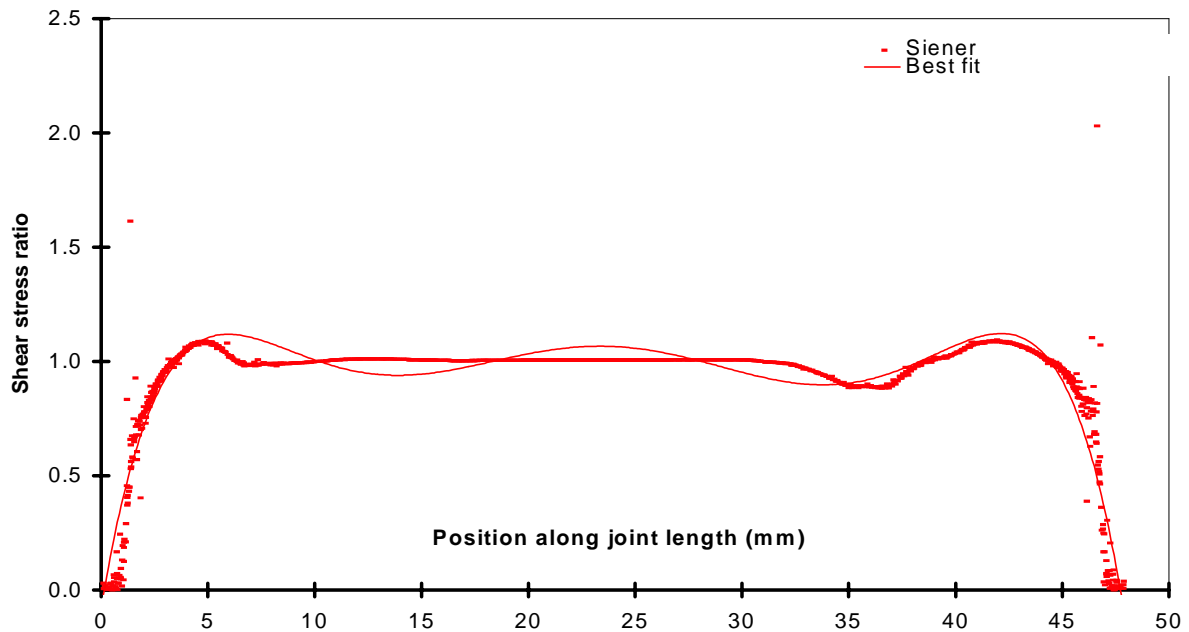


Fig. 8: Adhesive shear stress (Scarf repair)

When using Siener's model for the scarf repair, the shear stress was close to the average applied stress (10.05 MPa) in the central part of the adhesive (Fig. 8). One notices that in the case of the stepped repair using Siener's approach (Fig. 7), the maximum value of shear stress ratio was approximately 0.3 i.e. less than half the average applied stress. This is because in that stepped repair a large proportion of the load was transferred by the adhesive between the butt faces rather than by shear. Increasing the thickness of the adhesive between the butt faces would increase the proportion of load transferred by shear. This is apparent for the 3D model (Fig.7) which has no butt faces (Fig. 5). Given the rather small thickness of the adhesive between the butt faces in the current Bair and Siener models (0.01 mm), there are doubts on the practicality of such repair joints.

Generally, when using Siener's model, stress data for the parent laminate and the repair patch were not accurate since equivalent properties were used to generate the model. The tensile stress, for example, was uniform and approximately 160 MPa for the undamaged plate, which is inaccurate compared to the 292.7 MPa in the top layer predicted by Bair's model, 293.1 MPa by the 3D model and 292.76 MPa by the laminate analysis programme.

The results from the full 3D model were generally the most accurate. However, the solid elements used are expensive to run in terms of computing time. The same models took on average more than twice as long to run on the same machine and with the same mesh using the simplest 3D solid elements. Also, the number of composite solid element types is limited in the current version of NISA and are not available for non-linear analysis which could be a serious handicap for further study of repair joints.

CONCLUSION

This comparative study has highlighted some important features:

- Bair's model shows good agreement with traditional 2D models for direct stress calculations in the adhesive
- Bair's model gives better layer-stress results in the repair patch and parent laminates
- Bair's model produces less reliable results for adhesive shear stresses. These are best obtained using Siener's approach
- Siener's model produces poorer values for layer-stresses. This is inherent in this modelling approach
- A 3D model gives more accurate results but 3D solid elements are expensive to run

These modelling approaches should be viewed by repair engineers as complementary, providing different insights into factors affecting the adhesive and the composite structure itself; both being important for the optimisation of repair joints. This study has also shown the need for an approach which provides an overall view of bonded repairs for composite structures.

REFERENCES

-
1. HESLEHURST, R B; "Analysis and modelling of damage and repair of composite materials in aerospace", *Numerical Analysis and Modelling of Composite Materials*, ed. J W Bull, Chapman and Hall, 1996, pp. 28-59.
 2. HALL, S R; RAIZENNE, M D; SIMPSON, D L; "A proposed composite repair methodology for primary structures" *Composites*, Vol. 20, No. 5, Sept. 1989, pp. 479-483.
 3. MATTHEWS, F L; KILTY, P F; GODWIN, E W; "A review of the strength of joints in fibre reinforced plastics part 2: Adhesively bonded joints", *Composites*, Vol. 13, 1982, pp. 29-37
 4. DAVIS, M J; "The development of an engineering standard for composite repair", AGARD CP-550, AGARD, NATO, 1995, pp. 24.1-24.11.
 5. LOSS, K R; KEDWARD, K T; "Modeling and analysis of peel and shear stresses in adhesively bonded joints", Paper 84-0913, AIAA, 1984.
 6. JONES, R; CALLINAN, R J; AGGARWAL, K C; "Analysis of bonded repairs to damaged fibre composite structures", *Engineering Fracture Mechanics*, Vol. 17, No. 1, 1983, pp. 37-46.
 7. SIENER, M P; "Stress field sensitivity of a composite patch repair as a result of varying patch repair thickness", *Composite Materials: Testing and Design*, ASTM STP 1120, Vol. 10, 1992, pp. 444-464.
 8. BAIR, D L; HUDSON, P O; GHANIMATI, G R; "Analysis and repair of damaged composite laminates", *Proceedings 36th International SAMPE symposium*, SAMPE, Covina, CA, USA, Vol. 36, Book 2, 1991, pp. 2264-2278.
 9. PICKETT, A K; HOLLOWAY, L; "The analysis of adhesive stresses in bonded lap joints in FRP structures", *Composite Structures*, Vol. 3, 1985, pp. 55-79.
 10. ADAMS, R D; "Theoretical stress analysis of adhesively bonded joints", Chapter 5, *Joining of Fibre-reinforced Plastics*, ed. F L Matthews, Elsevier, 1987, pp. 185-226
 11. ODI, R A; FRIEND, C M; "Finite element analysis of bonded repairs in composite structures", *Proceedings 4th International Conference on Deformation and Fracture of Composites*, 24-26 March 1997, Manchester, UK

INFLUENCE OF IMPACT DAMAGE AND REPAIR SCHEMES ON THE STRENGTH OF FOAM-CORED SANDWICH BEAMS

S.D. Clark¹, R.A. Shenoi¹ and H.G. Allen²

¹ *Department of Ship Science, University of Southampton,
Southampton, S017 1BJ, U.K.*

² *Department of Civil Engineering,
University of Southampton, Southampton, S017 1BJ, U.K.*

SUMMARY: The main emphasis of this paper is to identify the effects of impact damage and repair work on both the static and long term fatigue behaviour of composite FRP sandwich beams incorporating a PVC foam core. Experimental results are presented for four beam configurations incorporating two dominant failure modes; core shear and skin tensile/compression failure. It has been observed that impact damage and repair have a major degradation effect on the skin tensile failure mode under both static and fatigue loading. Conventional repair strategies of damaged beams have shown that the skins of sandwich beams are further weakened thus rendering the repair ineffective. Investigation of different repair strategies under static loading, have shown that careful selection of materials and a different approach to the way repairs representative of current marine practice are undertaken, can show marked improvements in static and fatigue strength.

KEYWORDS: sandwich beam, impact damage, repair, foam core, static behaviour, fatigue

INTRODUCTION

Polymeric sandwich beams are being increasingly used for many applications such as aircraft, ship and land-based vehicle structures. These structures need to be designed to withstand static ultimate limit loads and cyclic fatigue loads. The subject of static strength has been well documented in standard textbooks [1] and been confirmed in respect of modern applications [2]. Failure modes ranging from core shear fracture and skin tensile failure through to local skin wrinkling have been studied. Fatigue too has been the subject of a number of recent studies [3,4]. The principal failure modes considered have been core shear and skin tensile failure.

These static and fatigue limit states are affected if the beams have been subject to impact damage. The effect of impact damage on the static strength has been studied already [5]. The purpose of this paper therefore, is to outline the results from a study on the post-impact fatigue strength of sandwich beams and the influence of repair techniques on damage tolerance.

TEST PROGRAMME

The Basis

Sandwich beams are effective carriers of loads, with the skins taking the in-plane stresses due to bending and the core being responsible for shear transfer. Ensuring structural integrity of the beams thus requires examination of the load bearing ability of both the skins and the core. Impact in a structure can occur at different locations in a panel. Two extreme conditions, however, are those pertinent to skin damage in areas where the beam carries large bending moments (and hence high induced stresses in the skins) and skin/core damage in areas of high shear force (and thus high shear stresses in the core).

The principal variables defining the sandwich topology are skin and core thickness, skin make-up and core density. Further in many practical cases it is desirable to have asymmetric skins (i.e. unequal thickness), with the thicker skin being in compression. For investigation purposes, it is essential to have the materials combined in such a manner as to have core shear as well as skin tensile/compressive failures under virgin beam conditions.

The induced impact damage is such as to achieve penetration of the skins and puncturing of the core to sufficient depth to mimic localised collision damage in marine vessels.

Sandwich Materials

Sandwich configurations were chosen comprising FRP skin materials of glass fibres or hybrid glass/Kevlar fibres embedded in epoxy resin. Foam core materials comprised of closed cell PVC based polymer blends. Two beam configurations, corresponding to Case A & B beams respectively, were selected for fatigue tests of both damaged and repaired beams. Case C & D beams, with various repair strategies, were chosen for further static tests.

The skin materials, corresponding to the various beam cases, are shown in Table 1(a). The core material properties, as taken from manufacturers data, are shown in Table 1(b).

Table 1(a) Properties of Sandwich Facings

Skin Type	Lay-up	Thickness (mm)	Young's Modulus (N/mm ²)	Tensile Strength (N/mm ²)
Type 1	2×QE1200	2.0	15.0	265
Type 2	RE210 5×QEA1200	5.5	18.0	289
Type 3	2×QEA1200	2.5	18.0	289

Lay-up code :

E	E-glass
A	aramid
R	reinforced balanced 0°/90° woven roving
Q	balanced quadriaxial 0°/90°/+45°/-45° woven roving
No.	weight of cloth per unit area (g/m ²)

Table 1(b) Properties of Core Materials

Core Type	Nominal Density (kg/m ³)	Thickness (mm)	Tensile Young's Modulus (N/mm ²)	Shear Modulus (N/mm ²)	Shear Strength (N/mm ²)
Airex C70.130	130	100	120.0	50.0	1.90
Divinycel H200	200	70	230.0	85.0	3.30

The sandwich beams used in this testing programme are representative of structures used in boat hulls. They are full scale structures manufactured in 'boatyard' conditions rather than ideally made coupon specimens. The four sandwich configurations pertaining to Case A, B, C & D beams are listed below:

- Case A: C70.130 core, Type 1 inner and Type 2 outer skins (damage/repairs to inner skin)
- Case B: C70.130 core, Type 2 inner and outer skins (damage/repairs to inner skin)
- Case C: H200 core, Type 3 inner and Type 2 outer skins (damage/repairs to inner skin)
- Case D: H200 core, Type 3 inner and outer skins (damage/repairs to outer skin)

All beams had a width of 200mm with a total length of 1600mm and a depth dependent on the selected beam case core and skin thickness'. For all sandwich beam tests, the inner skin of the beam was in tension and the outer skin in contact with the load was in compression.

EXPERIMENTAL PROCEDURE

Outline of Test Rigs

The static and fatigue tests were conducted in a specially designed rig, shown conceptually in Figure 1. Load is applied to the beam through eight air-driven rams each of which bears a hard rubber pad on the surface of the beam under test, to prevent local indentations. The air supply system is controlled by a shut-off gate, a solenoid and two adjusting valves. One of these controls the maximum pressure on the loading side of the ram; the other controls a small back pressure on the unloading side. This back pressure is used to counteract the weight of the beams. The minimum value of the load applied to the beam is therefore zero. The solenoid has two positions; one allows compressed air to reach the rams while the other releases air from the system. A computer-controlled system operates the solenoid at the required frequency.

Deflections are measured at mid-span by means of a transducer mounted on a swivelling arm with quick release brackets. Load on the beam can be obtained from the recorded air pressure. This value is continuously compared with readings from load transducers mounted on two rams. For all the tests, a frequency of 0.5Hz with an applied stress ratio, R (ratio of minimum to maximum stress) was chosen. Tests were conducted at room temperature 23 ± 5 °C.

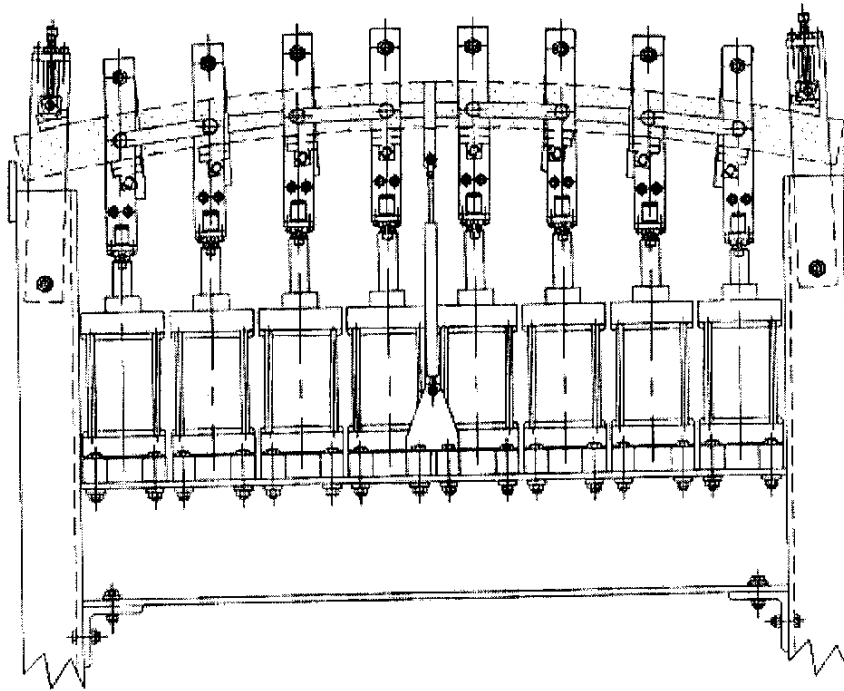


Figure 1 Static and Fatigue Rig

Impact damage was induced in a drop test rig, where the impactor was guided on to a beam at the desired location. Figure 2 shows the impactor used in this series of tests.

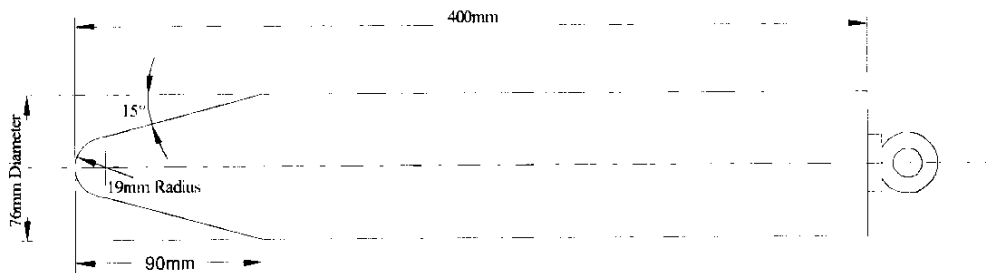


Figure 2 Schematic of Projectile used for Impact Damage

Outline of Repair Schemes

Case A & B sandwich beams were repaired after damage using one repair scheme characteristic of that used in the marine industry. The repair strategy is shown schematically in Figure 3.

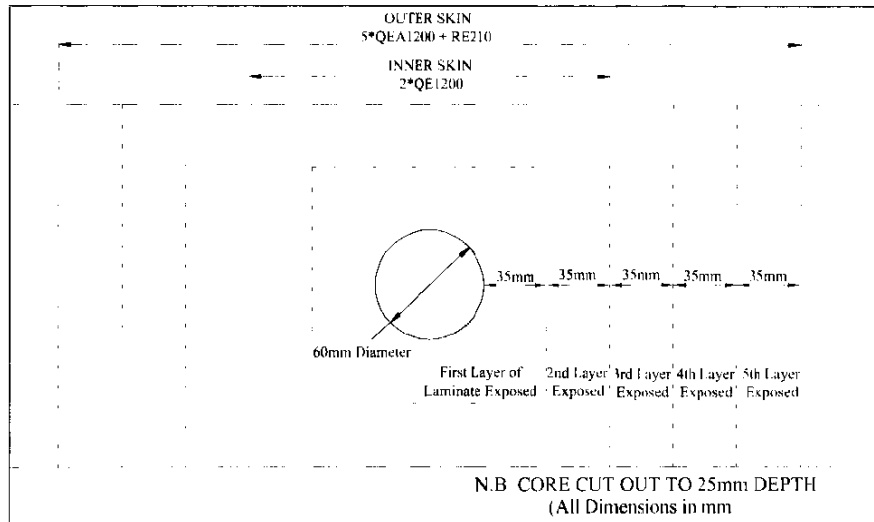


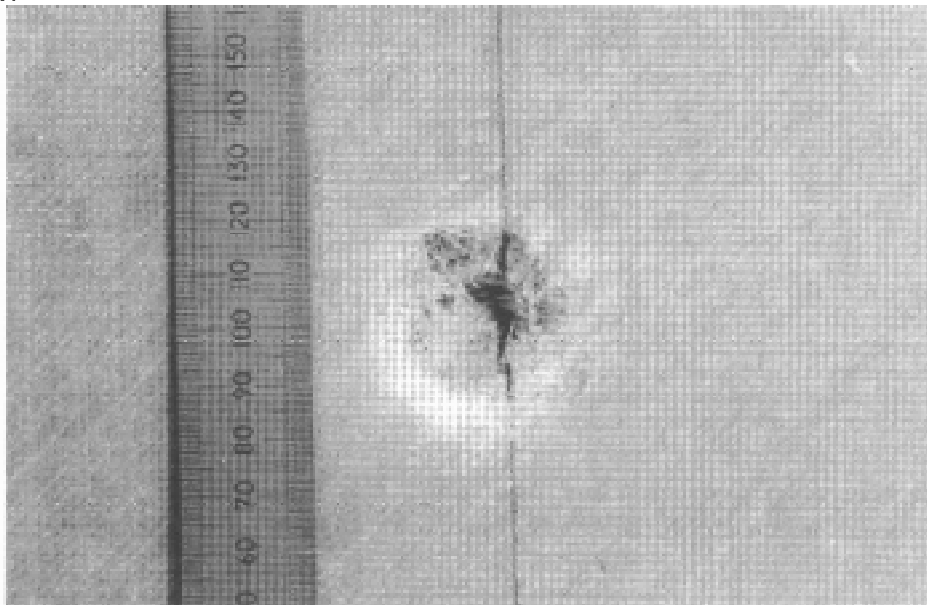
Figure 3 Schematic of Typical Repair Strategy

Further repair strategies on Case C & D beams were investigated under static loading conditions. Table 3 shows the varying overlaminating fabrics, the different resins used for the tests. Repairs were undertaken at midspan on both the tensile and compressive faces for Case C and D beams respectively.

RESULTS

Impact Damage Outline

The beams were subjected to various damage configurations, namely centre damage, end damage and both centre and end damage. Figure 4 shows a typical damaged region due to impact before commencement of fatigue testing. The damage zones were found to be very localised when compared to single skin laminate materials. Very little damage occurred in the immediate area of the impact damage site. This feature partially reflects the energy absorbing capabilities of the core material.



The beams were damaged at different locations, in order to investigate the influence of damage on two main fatigue failure modes, namely core shear and skin tensile failure. For Case A virgin beams, core shear fatigue failure occurred at the ends whilst for Case B virgin beams, tensile fatigue failure was observed at midspan of the inner skin. The damage configurations are shown in Table 2.

Table 2 Sandwich Fatigue Tests on Damaged and Repaired Beams

Beam Case	Damage/Repair Location*	Damage Particulars	No. of Beams	Failure Mode
Case A (Damaged) [#]	end	11.8 kg from height of 4m	2 static + 2 @ 2 loads (18 in total)	skin (tensile)
	centre			
	end & centre			
Case A (Damaged) [#]	end	21.7 kg from height of 4m	2 static + 2 @ 2 loads (18 in total)	core shear
	centre			
	end & centre			
Case B (Damaged & Repaired) ^{\$}	end	11.8 kg from height of 4m	2 static + 2 @ 2 loads (18 in total)	skin (tensile)
	centre			
	end & centre			
Case B (Damaged & Repaired) ^{\$}	end	21.7 kg from height of 4m	2 static + 2 @ 2 loads (18 in total)	core shear or skin compression/ wrinkling
	centre			
	end & centre			

Beams damaged using RNLI projectile (see Figure 2)

\$ Beams repaired after damage using RNLI repair technique (see Figure 3).

* End damage on top skin near supports (570mm from midspan on centreline)
Centre damage on top skin at midspan on centreline

Fatigue of Damaged Beams

The fatigue performance of Case A & B beams, with the various damage configurations, detailed in Table 2, are shown in S-N format in Figures 5 & 6 respectively. In all cases, the skin tensile stress and core shear are calculated from beam theory, without taking into account the reduction in cross-sectional area due to damage or repair. It is observed that end damage has little effect on the fatigue life. For Case A beams, damage at the beams' midspan resulted in a reduction in the beams load carrying capabilities under fatigue by a factor of approximately 25%. However under static loading, the load carrying capability was less than 25%. For Case B beams, neither static nor fatigue strength were significantly affected.

Fatigue of Repaired Beams

Case A & B beams, with repair locations given in Table 2, are shown in S-N format; see Figures 5 & 6 respectively. It is observed that for both Case A & B beams, repairs near the supports appear to have little influence on the fatigue life, when compared to undamaged S-N data. For Case A beams which are skin critical, the tensile stress near the supports is small and therefore end repairs in the skin do not have to support much load. For Case B beams which are core critical, the core is repaired by gluing in a new piece of core material with epoxy resin. The resin has a higher modulus than the core material thus the overall strength of the core material is not weakened.

Centre repairs on Case A beams show considerable reduction in load carrying capabilities with respect to static strength and fatigue life. Typically this is 50% less than the load carrying capabilities of an undamaged beam. The beam failed along the bond line between the overlaminating repair and the parent skin material. The static strength and fatigue life of Case B beams are not affected by centre repairs as the reduced strength of the skins is still relatively greater than that of the core. Centre repairs on Case B beams show little reduction in the static strength and fatigue life of the beam as a whole. For an undamaged beam, no skin failures were observed owing to a large reserve of skin strength; the failure mode was core shear. As with Case A beams, the repair does have a significant detrimental effect on the skin strength with the result that skin and core failures were observed in the repaired Case B beams.

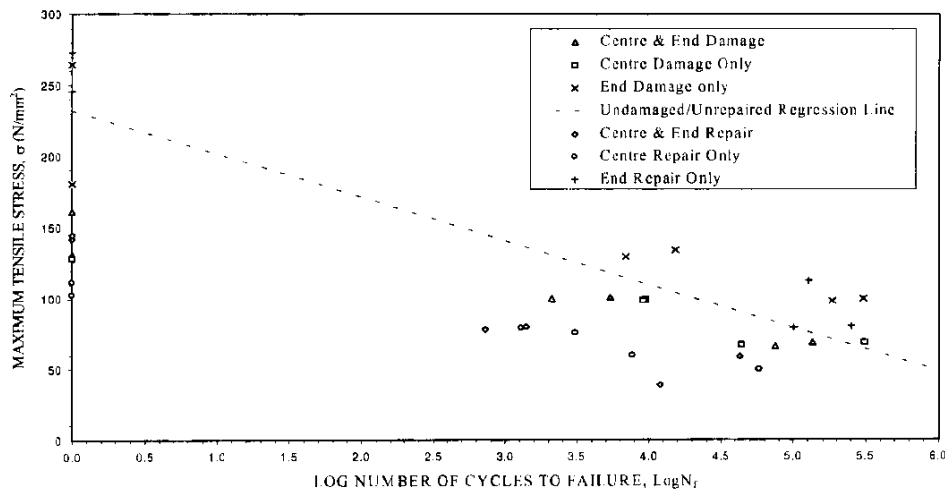


Figure 5 S-N Fatigue Curves for Impact Damaged & Repaired Case A Beams

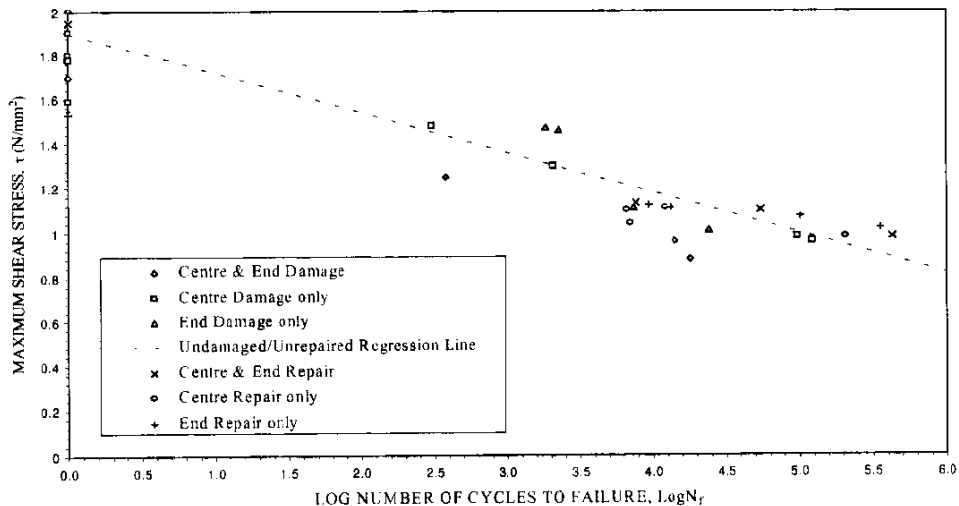


Figure 6 S-N Fatigue Curves for Impact Damaged & Repaired Case B Beams

Static Tests on Repair Specimens

Repairs to Case A skin sensitive beams, significantly reduce both the static and fatigue strength. The reduction occurs to such an extent, that unrepaired beams generally show greater strength. A preliminary investigation was carried out improve repair design. A number of

different repair strategies were considered and the results from static tests are shown in Table 3. The expected failure stress was calculated using the effective load carrying cross section of the skin after the laminate has been cut during the repair process. This method assumes that the repair has no load carrying capability.

Table 3 Repair Strategies for Static Tests on Case C Beams

Repair Type	Description	Compression Failure Load, Case D beam (N/mm)		Tension Failure Load, Case C beam (N/mm)	
		Actual	Expected	Actual	Expected
Type i	scarfed stepped layers & Ampreg 26 epoxy	19.2	19.0	19.5	25.6
Type ii	scarfed stepped layers & 7822 toughened epoxy & lightweight fabrics	24.3	19.0	25.6	25.6
Type iii	scarfed stepped layers & 7822 toughened epoxy & thick fabrics	26.4	19.0	38.6	25.6
Type iv	elliptical cured laminate patch bonded over damage with 5931 toughened epoxy.	35.7	28.6	48.6	42.8
VIRGIN	undamaged/unrepaired	40.0	40.0	53.6	53.6

Typical static load deflection plots are shown in Figure 7.

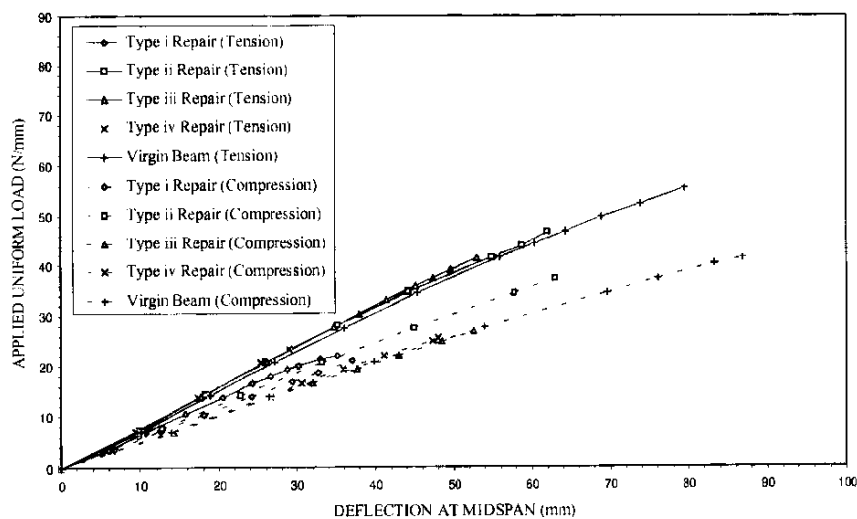


Figure 7 Static Load - Deflection Plots for Tension and Compression Failures

The results indicate that whilst the overall beam stiffness for both tension and compression failures does not significantly change, the failure load for many repair types is significantly reduced. In almost all cases, failure was characterised by debonding between the parent material and the overlaminating repair layers. The greatest static strength is observed in cases where none of the parent material is cut away during repair. This is justified by comparing the actual failure load with the expected failure load based on the uncut skin cross-sectional area. The values in most cases are very similar indicating that the repair is ineffective. In addition,

slight improvements in static strength using a toughened epoxy were observed rather than an ordinary epoxy.

DISCUSSION

Influence of Core and Skin Damage on Static and Fatigue Loading

The static and fatigue strength of undamaged sandwich beams has been found to correspond directly to the skin and core component materials with negligible interaction between the components occurring. For two general failure modes, core shear or skin compression/tension, they are the core or the skin components respectively. The reduction in static and fatigue core strength for a damaged beam is insignificant in this case compared to associated skin damage. This feature was found to be independent of damage location. This is namely because the ratio of the damaged cross-sectional area to the undamaged area of the core was typically much less than for the skin material. In this case only 5% of the cores cross-sectional area was damaged compared to 50% for the skins. The effect of damage also did not appear to greatly aid crack initiation and propagation in the core, due to the high toughness of the core material. The effect of damage on the skins is much more dramatic. In cases where the location of skin damage is not in or near a critical region where tensile/compressive stresses are highest, little difference in static or fatigue behaviour were observed. In cases where the location of damage coincides with a maximum stress region, reduced fatigue lifetimes and static strengths are noticed. In these cases, the static failure load was found to be less than the reduction in cross sectional area of the skin would suggest whilst the fatigue lifetimes appear to be approximately proportional to the reduced effective skin cross sectional area. Whilst the reason for this behaviour is not immediately apparent it was thought to be due to non-linear effects. During fatigue loading, the material response is usually well within the linear domain but in the static case, material non-linearity's can become apparent at extremes of loading.

Influence of Repair Strategies on Static and Fatigue Loading

The static and fatigue behaviour of repaired beams was found to be similar in nature to that for damaged beams though in some cases the failure loads were much reduced. For core sensitive beams, there is no reduction in fatigue life of repaired beams when compared to undamaged beams because the core was not sufficiently weakened by the repair process. For skin sensitive beams, premature skin failures only took place if the repair was at or near a region of high tensile/compressive stress. It was observed again that where the repair coincided with the region of maximum tensile stress in the skin, the fatigue life was approximately proportional to the reduction in cross sectional area caused by the removal of the parent skin material during the repair, thus in this case the repair is ineffective. In fact the performance was seriously impaired compared to that of the damaged beams by a factor of about 20%. This is essentially because the skin is cut back substantially beyond the original damage bounds thus creating a larger area of discontinuity in the fibres. The main failure mode was found to be debonding of the repairing layers from the parent skin material indicating that repair strategies need to be reviewed particularly with respect to bonding techniques.

From results of differing repair strategies, two main points have emerged. One is that the use of toughened resins compared to normal epoxies have shown improved repair performance. The second is that the skin should be cut back as little as possible to minimise the area of discontinuous fibres. The most effective repair was one where the damage area was simply

filled in with an epoxy based filler and a single thick overlamine bonded to the surface using a toughened epoxy. For better repair performance, a chemical bond rather than the achieved mechanical bond would be desirable. It is likely that a repair showing improved static strength when compared to the original repair strategy will also display an increased fatigue performance.

CONCLUSIONS

The effect of impact damage on core materials is generally negligible in cases where the load carrying cross sectional area is not significantly reduced.

Impact damage assumes more importance for skin materials where the loading carrying skin cross section may be seriously reduced by impact damage. Static and fatigue strength reduction is most marked in regions where the skin tensile/compressive stresses are a maximum.

Repairs have shown to significantly reduce the static and fatigue of sandwich beams even when compared to damaged beams. Much thought out to be given to the repair strategy before cutting away any of the skin material surrounding the damaged region. Unless a true chemical bond between parent material and the repair laminates can be achieved, none of the skin materials should be cut away.

The use of toughened high elongation resins have shown slight improvements in strength.

REFERENCES

1. Allen, H.G., "Analysis and Design of Structural Sandwich Panels", Pergamon Press, London, 1969.
2. Theotokoglou, E.E., "Analytical Determination of the Ultimate Strength of Sandwich Beams", *Applied Composite Materials*, Vol. 3, 1996, pp. 345-353.
3. Bergen, P.G., Buene, L., Echtermeyer, A.T., Hayman B., "Assessment of FRP Sandwich Structures for Marine Applications", *Marine Structures*, Vol. 7, 1994, pp. 457-473.
4. Sheno, R.A., Clark, S.D., Allen H.G., "Fatigue Behaviour of Polymer Composite Sandwich Beams", *Journal of Composite Materials*, Vol. 29, No. 18, 1995, pp. 2423-2445.
5. Mines, R.A.W., Worrall, C.M., Gibson A.G., "The Static and Impact Behaviour of Polymer Composite Sandwich Beams", *Composites*, Vol. 25, No. 2, 1994, pp. 95-104.

ACKNOWLEDGEMENTS

The work reported here was funded by the RNLI and EPSRC. The authors are grateful to Mr. Hicks of the RNLI for invaluable discussions and guidance on the experimental simulation of impact damage.

REPAIR DESIGN OF COMPOSITES AND EFFICIENCY OF SCARF PATCH REPAIRS

C. Soutis and F. Z Hu

*Department of Aeronautics, Imperial College of Science, Technology & Medicine, Prince
Consort Road, London SW7 2BY, UK*

SUMMARY: Adhesive bonding of polymeric composites is a widely used technology in the aerospace industry. It is particularly important for joining or repairing composite components because load transfer paths through mechanical fasteners can cause local overloads and damage in the relatively brittle composites. In this paper, a simple closed form solution for a scarf joint is presented together with a 3-D finite element (FE) stress analysis for a scarf patch repaired laminate under uniaxial compression. The FE stress results are used with stress based failure criteria to predict the residual compressive strength. It is found that carefully designed repairs can recover more than 80% of the undamaged strength. The optimum scarf angle for the carbon fibre-epoxy system examined is approximately 7° compared to 4° predicted analytically for the simple scarf joint. This is an important result, since a smaller scarf angle would involve the removal of a significant amount of parent material.

KEYWORDS: CFRP, flush scarf patch repairs, finite element stress analysis, optimum scarf angle, average stress criterion, failure load prediction, compressive strength

INTRODUCTION

Composite patches can be used to repair both composite and metallic structures. The repair of a composite structure with a composite patch may use mechanical fastening or adhesive bonding, external or flush patches. Flush, scarf-type, bonded repairs are used on critical, highly loaded, components where load concentration and eccentricities, especially for compressive loading, must be avoided [1-3]. Thick monolithic structures lend themselves to such repairs since external patch would cause excessive out-of-mouldline thickness and unacceptably high bondline peel and shear stresses [3-5].

Design methods for adhesively bonded repairs require criteria to predict both strength and durability. In this work, a three-dimensional stress analysis is performed to determine the stresses in a flush scarf repaired laminate under uniaxial compression, Fig.1, so that predictions can be made of the likely points of failure. These predictions are then used with observations of actual fracture paths to give a designer a qualitative and quantitative understanding of the mechanics of bonded scarf repairs.

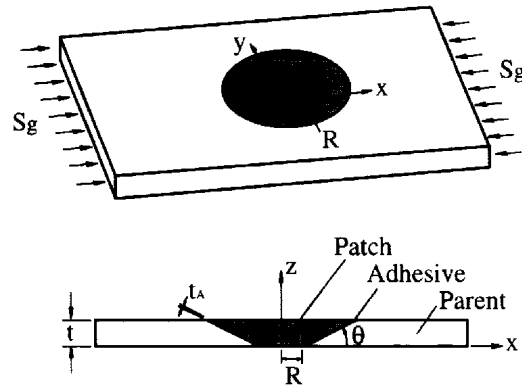


Fig. 1: Flush scarf patch repair ($L=304.8$ mm, $W=152.4$ mm, $R=25.4$ mm, $t=2.27$ mm, $t_A=0.129$ mm)

SCARF JOINT AND OPTIMUM SCARF ANGLE

In this section, a simple two-dimensional stress analysis presented in [6, 7] for a scarf joint is briefly discussed. The joint of interest has identical adherends, use a relatively brittle adhesive and have small scarf angles, Fig.2. For this simple case, the solution of reference [6] predicts uniform adhesive shear stresses and the optimum scarf angle for a maximum strength joint is given by

$$\theta_{opt} = \tan^{-1}(\tau_s / \sigma_{un}) \quad (1)$$

where τ_s is the shear strength of the adhesive and σ_{un} is the ultimate strength of the composite material. Because the analysis of reference [6] neglects the heterogeneous laminar nature of the adherends eqn.(1) was modified in reference [8] to account for the stress concentration developed in the adhesive due to stiffness differences. Eqn.(1) is rewritten as

$$\theta_{opt} \cong \tan^{-1}(0.816 \tau_s / \sigma_{un}) \quad (2)$$

and the failure stress of the scarf joint for small θ is determined by

$$S_{g,f} = \sigma_{un} / K_L = \tau_s / (K_A \sin \theta) \quad (3)$$

where K_A and K_L are the stress concentration factors (SCFs) in the adhesive and adherend, respectively. Based on the correlation with experimental data, Ref. [8] obtained $K_A = 2.88$ and $K_L = 1.35 \cos^2 \theta + 1 \cong 2.35$, for $\theta \leq 10^\circ$. The potential load carrying capability of the adhesive and the adherends in the joint is plotted in Fig.3 as a function of scarf angle. The load carried by the adhesive increases with decreasing scarf angle because the bond area increases. The optimum scarf angle occurs when the adhesive failure load is equal to the adherend failure load. For the system examined, the theoretical optimum scarf angle is 4° , which is about 20% lower than that predicted by eqn.(1), assuming $\tau_s = 40$ MPa and $\sigma_{un} = 454$

MPa. The analysis used room temperature adhesive properties, which would not be conservative at elevated temperatures. Adding a safety factor to the theoretical value to account for temperature effects, manufacturing anomalies, fatigue and endurance life will reduce θ down to 2° - 3° .

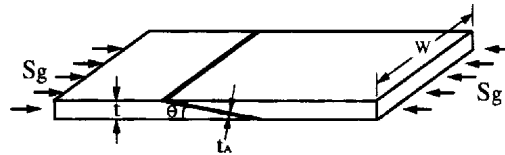


Fig.2: Scarf joint geometry

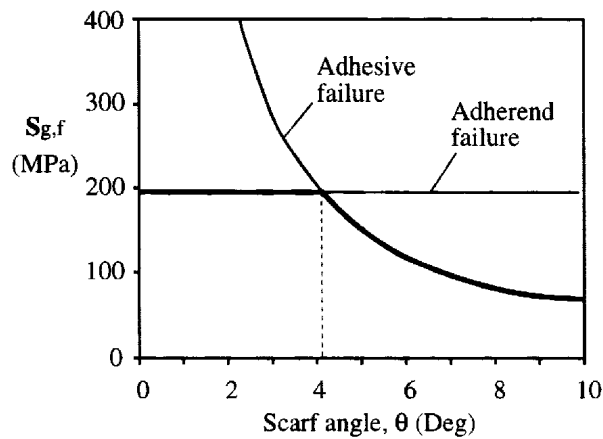


Fig.3: Ultimate strength of a scarf joint based on maximum stress failure criterion [7]

FLUSH SCARF PATCH REPAIR

The scarf patch repaired laminate, shown in Fig.1, is generally a three-dimensional (3-D) problem which is over simplified by the scarf joint model described earlier. In a scarf joint, all loads are transferred through the adhesively bonded interface. In fact, the parent plate can still carry load after losing the support of the patch (a plate with a tapered open hole). Therefore, the 2-D analysis would underestimate the strength of the repaired laminate and a 3-D stress analysis should be performed. However, this is difficult to solve analytically and in the following section a finite element (FE) method is used to calculate stresses developed in the patch, adhesive layer and parent laminate.

Elastic FE Analysis

The finite element analysis is now a well-established means for mathematically modelling stress problems. In the current investigation the FE-77 finite element package [9] is employed to determine the 3-D stress field developed in the repaired laminate; the analysis is based on displacement formulation employing an isoparametric 8-node solid element. Due to the

symmetry of loading and hole location, only one-quarter of the laminate is modelled. Because a stress concentration is expected near the bonded interface, a very high mesh refinement is required in this area. The smallest element size in the radial direction is 0.0125 mm; a typical FE mesh is shown in Fig.4. The laminate and the patch are treated as homogeneous, elastic and orthotropic materials with the properties shown in Table 1. The adhesive layer of thickness $t_A=0.129$ mm is modelled by isotropic 8-node solid elements. The total length of the parent plate is 304.8 mm long by 152.4 mm wide and the hole radius R is 25.4 mm.

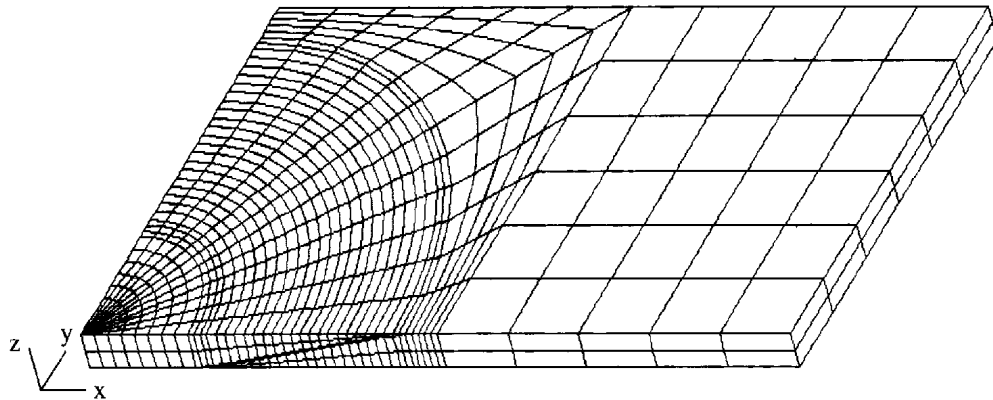


Fig.4: Finite element mesh for one quarter of a scarf patch repaired panel

Table 1: Material properties

	Materials	Mechanical properties
Adherends (parent and patch)	Carbon/epoxy [0/±45/90] _{2S}	$E_{XX}=E_{YY}=53.8$ GPa $E_{ZZ}=11.3$ GPa $G_{XY}=20.5$ GPa $G_{XZ}=G_{YZ}=4.85$ GPa $\nu_{XY}=0.3098$ $\nu_{XZ}=\nu_{YZ}=0.1853$ $\sigma_{XC}=454$ MPa
Adhesive	Epoxy adhesive	$E=3.4$ GPa $G=1.26$ GPa $\nu=0.35$ $\tau_S=40$ MPa

Stress Results

The stress variations in the parent laminate, patch and adhesive layer are plotted for different scarf angles in Figs.5-7. It is found that the dominant stress components are σ_x in the laminates (adherends) and τ_{zx} in the adhesive. Other in-plane and through thickness stress components are relatively small and could be neglected in the failure load calculations.

Fig.5 shows the σ_x stress distribution along the loading x-axis from the scarf tip for $\theta=3^\circ$. It has steep gradient near the tip of the scarf, suggesting the existence of stress singularity, and approaches unity within eight plies (1 mm). Since a mathematical stress singularity exists at the scarf tip due to stiffness discontinuity, the computed stresses are presented near but not at the tip of the scarf, Fig.6. The stresses closest to the scarf tip are at $r-R=0.5h$; that is at a distance of 0.0625 mm. As the distance from the tip ($r-R$) increases, the in-plane stress σ_x rapidly decreases. The largest compressive stress occurs at $\phi=0^\circ$, from the loading axis and is reduced down to 1.06 at $\phi=90^\circ$ for all radial locations, compared to 3.51 for the case with an open hole; σ_x shows no variation along the y-axis. Fig.6 suggests that σ_x is quite significant in the region $-60^\circ \leq \phi \leq 60^\circ$ at $r-R < 10h$.

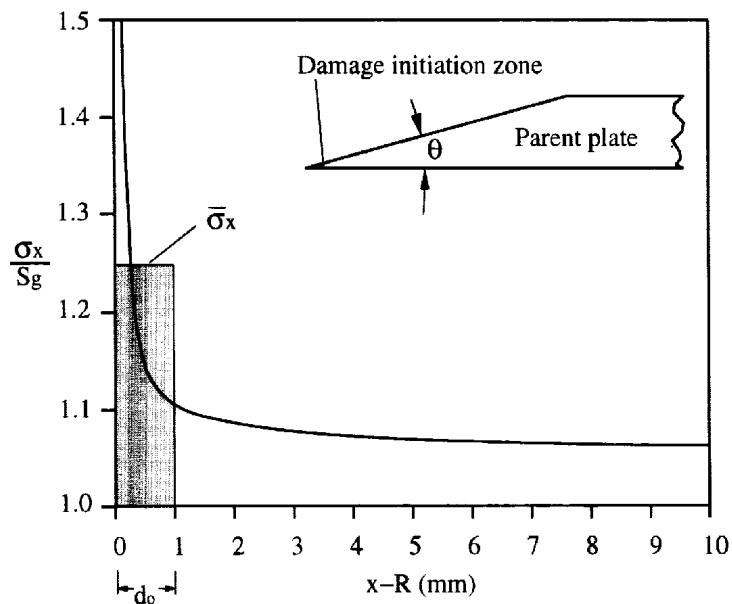


Fig.5: σ_x/S_g distribution in the parent plate along x-axis ($\theta=3^\circ$)

The shear stress varies mainly in the circumferential direction; its maximum value occurs at $\phi=0^\circ$ (from x-axis) and becomes zero at $\phi=90^\circ$ (y-axis). Fig.7 shows the radial shear stress distribution at the angular position $\phi=0^\circ$ for three different scarf angles; its magnitude is inversely proportional to the length of the bond line. τ is almost constant along the bond line except at the joint ends where it goes up slightly and then drops to zero rapidly. This is one of the advantages of the scarf joint configuration over the external patch in which the load is transferred only by a narrow region near the edge [1,4].

Table 2 summarises the stress results for different geometric configurations and illustrates the influence of the scarf angle on the stress concentration factors. The stress factor, $(\sigma_x)_{max}/S_g$, at points A and B in the adherends ($x-R=0.25$ mm) is almost independent of θ while the shear stress concentration, τ_{max}/S_g , in the adhesive (line C) increases rapidly as the scarf angle increases. For $\theta=9^\circ$, τ_{max}/S_g is three times higher than the value obtained for $\theta=3^\circ$ and therefore the repaired laminate is expected to fail at a lower applied load.

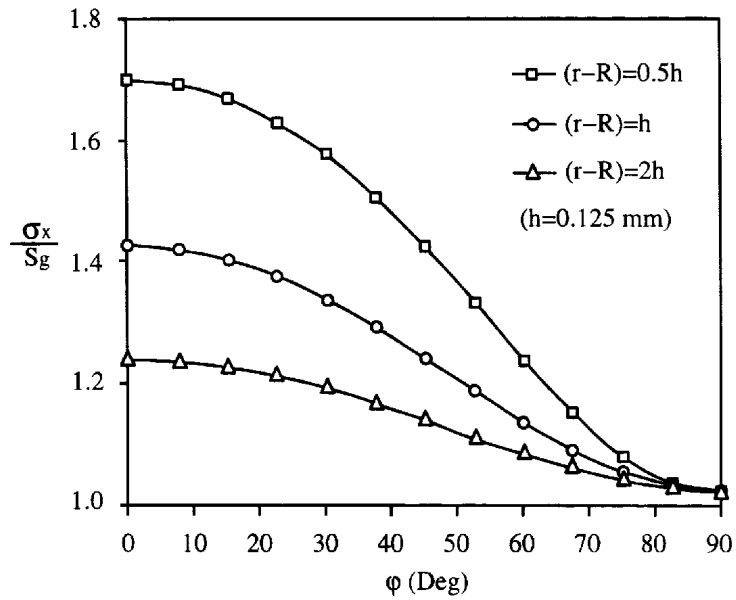


Fig.6: σ_x/S_g circumferential distributions in the parent laminate ($\theta=30^\circ$)

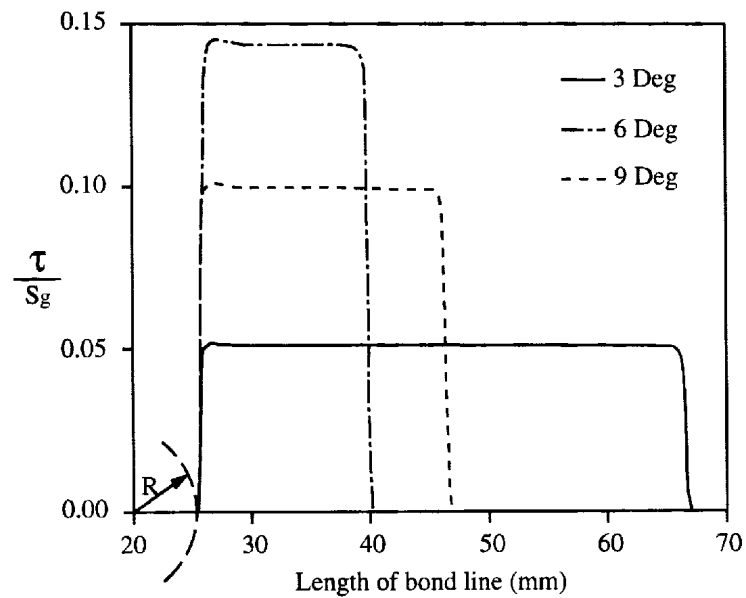
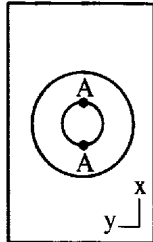
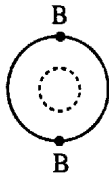



Fig.7: Normalised shear stresses distributions, τ/S_g , in the adhesive layer along the bond line for different scarf angles

Table 2: Normalised local stresses at critical stress locations of a scarf patch repaired laminate ($x-R=0.25\text{ mm}=2h$) and the influence of scarf angle

	Parent	Patch	Adhesive
			
θ	$(\sigma_x)_{\max}/S_g$ Location	$(\sigma_x)_{\max}/S_g$ Location	τ_{\max}/S_g Location
3°	1.238 A	1.220 B	0.0515 C
6°	1.295 A	1.287 B	0.1002 C
9°	1.326 A	1.323 B	0.1442 C

Strength Prediction

After one has obtained the stresses in the adherends and the adhesive layer, the next step is to use these data to predict the failure load of the repaired laminate, which is the load at which failure occurs either in the adherends or in the adhesive. The stress analysis above, has shown that the dominant stress components are σ_x and τ for the adherends and the adhesive layer, respectively. The maximum stress failure criterion could now be applied to determine the load carrying capability of the repaired laminate. If the composite were perfectly brittle, failure would occur when the maximum stress in the material (adherend or adhesive) equals the ultimate strength. For adherend failure have,

$$\sigma_R = \frac{1}{K_t} \sigma_{un} \tag{4}$$

where K_t is the stress concentration factor near the tip of the scarf ($\phi=0^\circ$) and σ_{un} ($=454\text{ MPa}$) the undamaged compressive strength. Fig.6 shows that $K_t=1.7$ at distance $r-R=0.5h$, predicting a residual strength of 267 MPa, which is about 25% less than the measured value [7]. The stress factors presented in Table 2, correspond to $r-R=2h$, would produce better agreement. This suggests that stress redistribution occurs in the repaired region before final failure and a simple elastic stress concentration factor underestimates the residual strength.

From the literature [10, 11], it can be seen that the approach for predicting failure in such laminates has been that of averaging the stresses over a distance from the tip of the scarf, indicating that the exact values of the stresses at the tip are not too important. Stress singularities at the repaired region may not occur in real laminates owing to local stress redistribution; material non-linearities and probable plasticity of the adhesive may reduce the

local peak stresses. Modern structural adhesives can develop a large plastic strain and often yield plastically before the joint fails.

The average stress failure criterion (ASFC) assumes that failure occurs when the average stress over a characteristic length d_o from the scarf tip equals the ultimate strength of the material. The average of the stress component σ_x is shown in Fig.5 and defined as:

$$\bar{\sigma}_x = \frac{1}{d_o} \int_R^{R+d_o} \sigma_x dx \quad (5)$$

Failure occurs when:

$$\begin{cases} \bar{\sigma}_x = \sigma_{un} & \text{(for adherends)} \\ \tau = \tau_s & \text{(for adhesive)} \end{cases} \quad (6)$$

Assuming $d_o=1$ mm, the failure load of the repaired laminate is obtained as a function of the scarf angle, Fig.8; for the composite system examined, the optimum scarf angle is almost 7° compared to 4° obtained for the 2-D scarf joint. The experimental strength data presented in [7] are in good agreement with the theoretical predictions. Also, the peak stress positions predicted by the FE analysis, Fig.6, coincide with experimentally observed failure locations [7], Fig.9, giving further confidence to the present calculations. However, the adjustable parameter d_o has not yet been related to micromechanical features and does not result from a mechanics analysis.

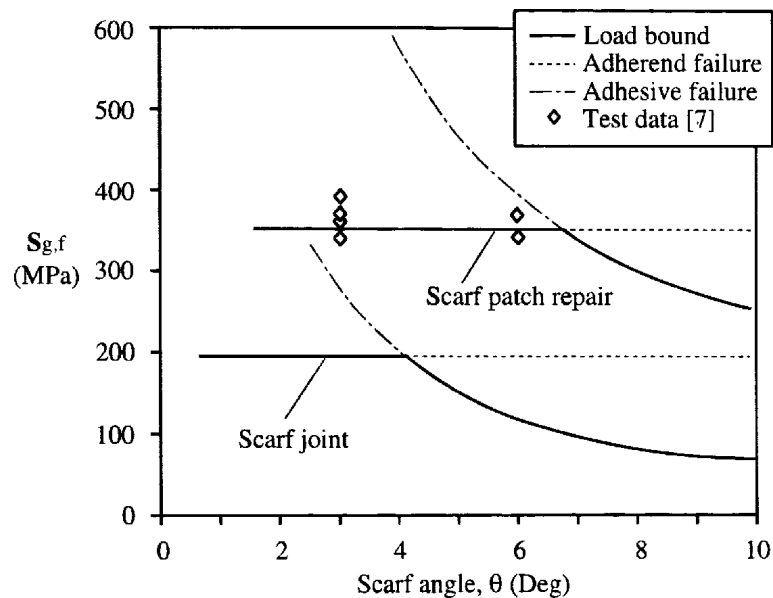


Fig.8: Failure load of a scarf patch repaired laminate versus scarf angle. Average stress, $\bar{\sigma}_x$, over a characteristic length $d_o = 1$ mm is used to correlate test results.

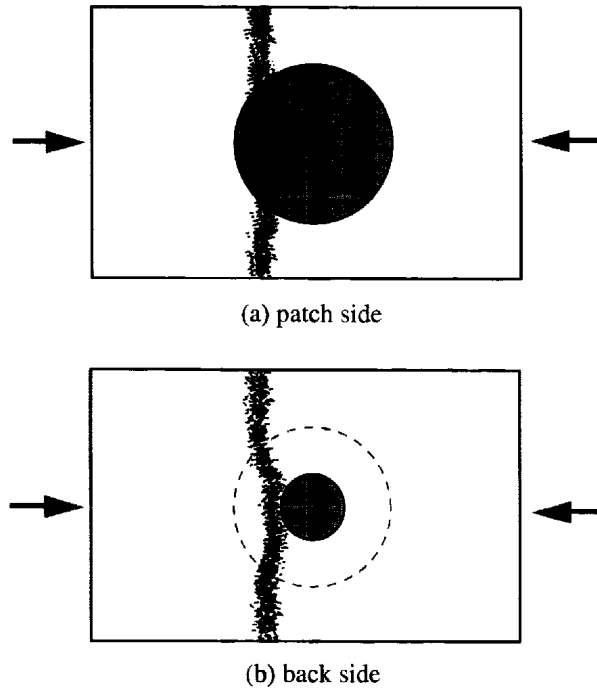


Fig.9: A schematic representation of final failure mode of the scarf patch repaired laminate [7]

DISCUSSION AND CONCLUDING REMARKS

Simple analytical and numerical models were presented to determine the optimum geometry and compressive strength of flush composite repairs. The 2-D analysis for the carbon fibre-epoxy laminate examined predicts an optimum scarf angle of 4° compared to almost 7° obtained from a 3-D linear elastic finite element analysis. A 4° scarf angle would remove too much undamaged material and probably weaken the repaired laminate. To account for material non-linearities and plastic deformation of the adhesive the average stress failure criterion is used with the FE stress distributions to estimate the ultimate strength of the repaired configuration. This avoids the need for a non-linear analysis, saving on computing time and memory requirements. The good agreement between predictions and measurements justifies the approach. In future work, an attempt will be made to relate the characteristic length d_0 used in the ASFC to the laminate fracture toughness (damage tolerance). Additional work is also required to determine thermal and moisture effects on the scarf geometry, strength and durability of the repair.

ACKNOWLEDGEMENTS

The authors are grateful for funding from the Engineering and physical Sciences Research Council (EPSRC, GR/K54892).

REFERENCES

1. Matthews, F.L. (ed.), *Joining fibre-reinforced plastics*, Elsevier Applied Science, 1987.
2. Matthews, F.L. and Rawlings, R.D., *Composite Materials: Engineering and Science*, Chapman & Hall, 1994.
3. Baker, A.A. and Jones, R. (eds.), *Bonded repair of aircraft structures*, Martinus Nijhoff Publishers, 1988.
4. Soutis, C. and Hu, F.Z. "Design and performance of bonded patch repairs of composite structures", An Aerospace Industries Division Seminar on 'Airworthiness Aspects of New Technologies', sponsored by IMechE and the RAeS, Report no S453, 20 November 1996, Bristol, UK.
5. Baker, A.A., Chester, R.J., Hugo, G.R. and Radtke, T.C., "Scarf repairs to graphite/epoxy components", *AGARD-CP-550*, 1995.
6. Hart-Smith, L.J. "Adhesive-bonded scarf and stepped-lap joints", *NASA CR-112237*, 1973.
7. Jones, J.S. and Graves, S.R., "Repair techniques for Celion/LARC-160 graphite/polyimide composite structures", *NASA-CR-3794*, 1984.
8. "Advanced composite design guide", *AFML Wright-Patterson Air Force Base*, United States Air Force, Vol.II, Analysis, 1973.
9. Hitchings, D., "Finite element package FE77 user's manual", Imperial College, 1995.
10. Brewer, J.C. and Lagace, P.A., "Quadratic stress criterion for initiation of delamination", *J. Comp. Materials*. Vol.22, 1988, pp.1141-51.
11. Hu, F.Z., Soutis, C. and Edge, E.C., "Interlaminar stresses in composite laminates with a circular hole", to appear in *Composite Structures*, 1997.

EPOXY FILM ADHESIVE FOR ALUMINUM AND COMPOSITE REPAIRING

Bin Liang , Qingfang Liu and Linan Liu

Beijing Institute of Aeronautical Materials, Beijing 100095 P.R. of China

SUMMARY: A new carboxyl terminated butadiene-acrylonitrile (CTBN) modified epoxy film adhesive, designed as SY-41, which was mainly a mixture of diglycidyl-ether of bisphenol A and Curing agent 328, has been developed for Aluminum and Composite structure repairing . After 4 hours curing at 90°C, under pressure of 0.1MPa, the bonding strengths to Phosphoric Acid Anodizing(PAA) surface treated aluminum adherend were equivalent to those of structural adhesives curing at 120°C. The lap-shear strengths at room temperature and 82°C were 42.7MPa and 30.8Mpa, respectively., while the Bell peel strengths at room temperature and 82°C are 6.0kN/m and 8.7kN/m. After hygrothermal aging 500 hours at 70°C, R.H. 95-100%, the adhesive maintained a high retention lap-shear strength of 31MPa. In addition , the shelf life of the adhesive at room temperature is longer than 1 month.

KEYWORDS : film adhesive, toughness, field repairing , formula optimization

INTRODUCTION

The damage of aluminum (Al) alloys and composites in aircraft structures were often required to be repaired by adhesively-bonding .The adherends were usually Al-Al, Al-composite or composite-composite. The adhesives employed for these repairs need high temperature and high pressure were usually 121°C or 177°C curing epoxy film adhesives. But for field repair where electrical-heating blanket and vacuum bagging pressure were only available, such strict preparing condition was not easy to satisfy. Furthermore, the maldistribution of temperature will raise thermal residual stress because of large differences of thermal expansion coefficient between the aluminum and composite. It was reported that curing above 100°C of bonded repairs may result in blistered or deteriorated adhesive, caused by the action of absorbed moisture between laminates during the curing temperature cycle, which may result in a lower bonding strength [1].

Therefore, to develop a film adhesive curable at temperature below 100°C and vacuum pressure and with mechanical properties equivalent to those of 121°C curing film adhesives will greatly enhance the reliability of field repairing. In this paper, a CTBN modified epoxy film adhesive SY-41, curable at 90°C, with the pressure of 0.1MPa and suitable to field repair of aluminum alloys and composite structures was introduced. The formula design and optimization of the adhesive, its thermal reactive characteristics and mechanical properties of aluminum adherend bonding were also presented. Bonding properties concerning composite adherend will be discussed in another paper.

EXPERIMENTAL

Materials and Process

The epoxy resins employed were two kinds of diglycidyl-ether of bisphenol A(DGEBA) having epoxide equivalent weight of approximately 220g/mole and 900 g/mole respectively and a liquid trifunctional amino-epoxy resin having epoxide equivalent weight of 120 g/mole. The curing agent was a modified amine and commercially available as Curing agent 328 . The rubber used to tough the epoxy resins was a liquid carboxyl-terminated butadiene-acrylonitrile (CTBN) with 26wt% bonding AN and above 3000 number average molecular weight(Mn).

The prepolymer was prepared by initially adding the required quantity of CTBN and epoxy resins to a stirred glass vessel followed by heating to 170°C and holding 2 hours while the Nitrogen atmosphere was used to protect the mixture from oxidation. After finishing the prepolymerization, the formed epoxy-CTBN-epoxy adducts in the mixture were confirmed by Infrared Spectra. The film adhesive was then prepared by mixing the prepolymer and Curing agent 328 in a two-roll mixer and hot pressing into film. The thickness of the film was controlled around 0.3mm.

Specimen Preparing and Testing

Adherend aluminum alloys were LY12CZ with thickness of 2mm and 0.5mm for lap-shear strength and Bell peel strength testing . All of the adherends were phosphoric acid anodized (PAA) per ASTM D3933. All of the adhesively bonded specimen were press cured at 90°C , 0.1 MPa for different time of 3 to 5 hours per design. The lap-shear strength was tested per ASTM D 1002 and the Bell peel strength was tested according to ASTM D 1876.

DSC Analysis

A Perkin Elmer Differential Scanning Calorimeter(DSC) model DSC-2, was operated to obtain DSC curves at different heating rates 5°C/min,10°C/min and 20°C/min from 25°C to 250°C under dry nitrogen.

Gel Time

Gel times were tested by probing the adhesive resin in a thermal plate at controlled temperature with a glass rod to observe long strands drawn out from the adhesive resin. Gelation is the point where no such stringing of the resin was noticed and the probed material has rubber feel. Gel time is the elapsed time when the adhesive reached the point of gelation as measured by a stop watch under the controlled temperature .

RESULTS AND DISCUSSION

The Composition of Adhesive

The toughening effect of a CTBN modified epoxy system not only depended on acrylonitrile bonding content, carboxyl content and molecular weight of CTBN and prepolymerization or not, the procedure of prepolymerization and curing agent of the resin system, but also in close relation to the type and the molecular weight of the epoxy resins. Our previous research indicated that the higher the average epoxide equivalent of the epoxy mixture, the longer the average crosslink length of epoxy matrix, which resulted in CTBN to initiate much plastic deformation energy consumption of the matrix.^[2] Both solid epoxy resin with long molecular chain and liquid epoxy resin with short molecular chain were used in the adhesive to balance its toughness and tackiness. In the mean time, a trifunctional amino-epoxy resin was used to improve crosslink density and heat resistant characteristics of the cured product.

Curing agent was a very important composition for an adhesive. A typical curing system which can cure epoxy resin around 90°C comprises three parts: (1) a room temperature stable, elevated temperature decomposable nitrogen containing compound, (2) a hydroxyl containing organic compound and (3) an organo lead or mercury compound[3]. An epoxy adhesive containing this curing system has a long ambient temperature shelf life, after 6 hours cure at 82°C, the lap shear strength of aluminum adherend is about 31MPa. Other curing system such as curing agent D and dicyandiamide plus Accelerator No.1 can also cure epoxy resins at 90-110°C.^[4,5] But none of them meets our requirement. Curing agent 328 used in this study is a modified amine, it has excellent latency at ambient temperature while reacts quickly with epoxy resins at elevated temperature.

The Optimization of the Adhesive Formula

Our previous research shows, when the quantity of epoxy resins were 100 phr(wt), 10-27.5phr CTBN and 13-23phr Curing agent 328 should be used in the adhesive formula in order to get a cured system with high crosslink density and high strength and good toughness.

The first order and second order orthogonal-regression optional design were then applied to optimize formulation of the adhesive in above mentioned scope. The curing time in the optimization experiment was settled down to 3 hours. The result showed that the confidence level of the first order regression equation was greater than 99%, but that of the second order regression equation was less than 90%. The experiment verification met to the prediction of the first order regression equation.^[6] So it can be concluded that the first order orthogonal regression experiment was successful and the regression equation can reflect the change of the adhesive characteristics in the experimental zone. According to the first order regression equation, with the help of computer, an optimum formula of the adhesive having lap shear strength of 38.8MPa and Bell peel strength of 4.83kN/m was developed. The predicted curves of the shear strength and Bell peel strength of the adhesive are shown in Fig. 1 and Fig. 2 respectively.

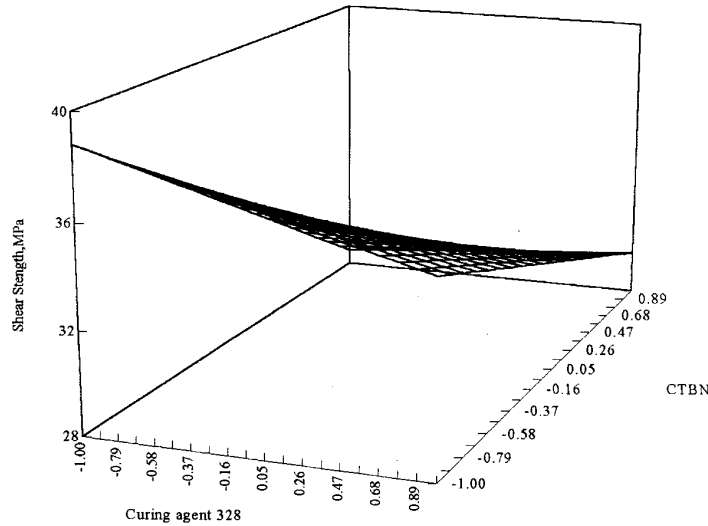


Figure 1: The predicted shear strength curve according to the first order regression equation

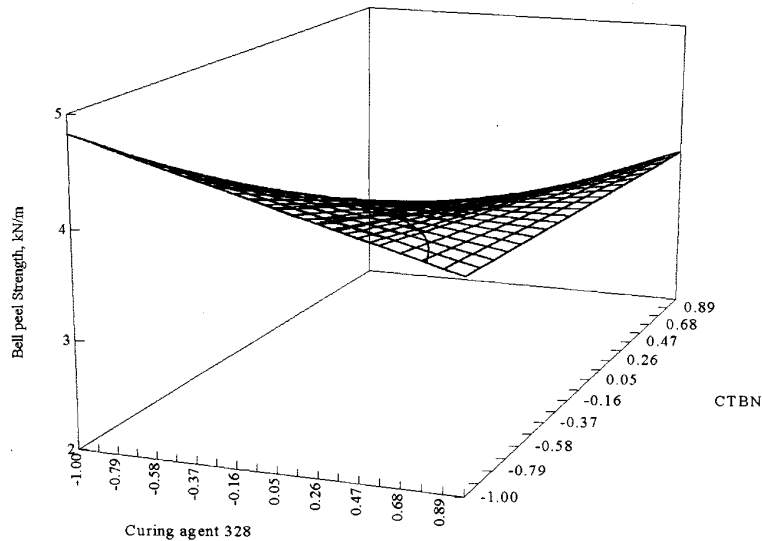


Figure 2: The predicted Bell peel strength curve of the first order regression equation

The Thermal Reactive Characteristics

The gel time-temperature curve of SY-41 was shown in Fig. 3. It was obvious that the slope of the curve changes greatly in the temperature range of 80-100°C, which indicated that the polymerization of the adhesive reacts greatly and the curing temperature of the adhesive can be selected in the range of 80-100°C. The apparent activation energy before gel calculated according to Flory's gel theory was 68.5kJ/mole. [7]

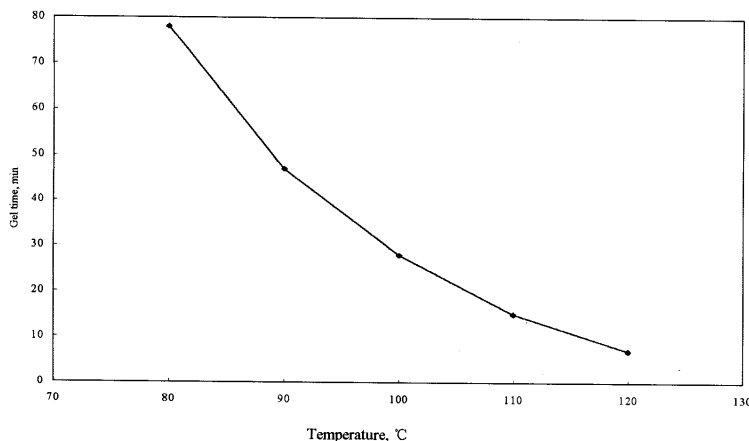


Figure 3: The gel time-temperature curve of SY-41

DSC analysis results of different heating rate of 5°C/min, 10°C/min, 20°C/min and extrapolation to 0 °C/min were listed in Table 1. T_{onset} and T_{peak} in the table mean the curing onset temperature and peak exotherm temperature of the DSC curves respectively. The apparent activation energy of the whole curing reaction calculated based on Kissinger's method was 93.2 kJ/mole.^[8] According to Table 1, the best curing temperature range should be 105°C-119°C. But if prolong the curing time, excellent adhesion properties can still be obtained when cure the adhesive at 90°C which will be confirmed in the following experiment.

Table 1: The characteristic Temperature of DSC curves at different heating rate

heating rate, °C/min	T_{onset} , °C	T_{peak} , °C
5	110	125
10	117	132
20	127	143
0	105	119

The Study of the Curing Procedure

The optimum formula adhesive has a high shear strength and a low peel strength, this may be attribute to the short curing time and low crosslink density because of the sensitivity of peel strength to the degree of cure. The shear strength and Bell peel strength of the adhesive cured at various curing time were shown in Table 2. It was obvious that with the curing time of the adhesive prolonged, the Bell peel strength increased steadily while the shear strength changed little. After 4 hours curing, both the shear strength and Bell peel strength satisfied the requirement of 120°C curing adhesive Metlbond 1113.06. The curing time was then fixed 4 hours in the following study. Furthermore, if higher peel strength was required, the curing time can be prolonged more.

Table 2: The influence of curing time on the adhesion properties

Curing time, hours	3	4	5
Shear strength, MPa	38.8	42.7	39.0
Bell peel strength, kN/m	4.83	6.03	6.40

The Primary Mechanical Properties of SY-41

Table 3 listed the heat resistant, hygrothermal resistant and room temperature storage properties. The requirements of moderate temperature (120°C) curing adhesive film Metlbond 1113.06 were also listed in Table 3 for comparison.

Table3: The primary mechanical properties of SY-41(Typical Value)

	SY-41				Metlbond 1113.06	
	Shear strength, MPa	Retention rate,%	Bell peel strength, kN/m	Retention rate, %	Shear strength, MPa	Bell peel strength, kN/m
R.T.	42.7		6.03		>33	>6
82°C	30.8	72.1	8.87	147	>21*	>4.5*
after immersed in boiling water for 24 hours	34.1	79.8	6.75	112		
after exposure to 70°C, R.H.95-100% for 500 hours	31.0	72.6			>25	>4.5
after store at 22-26°C for 30 days	42.7	100	6.0	99.5	>33	>6

* Requirements of Metlbond1113.06 at 70°C

It can be concluded from the data in table 3 that SY-41 has a high heat resistant property, its shear strength and Bell peel strength at 82°C were higher than those of Metlbond 1113.06 at 70°C. Moreover, the Bell peel strength at 82°C was 47% higher than that of at room temperature. In the mean time, SY-41 has a good hygrothermal resistant property after immersed in boiling water for 24 hours, the retention shear strength was 34.1 MPa, with a retention rate of 80%, while the Bell peel strength increases to 6.76kN/m, with a retention rate of 112%. After store at 22-26°C for 30 days, the shear strength and Bell peel strength appear no obvious decrease which means its room temperature shelf life exceeds 1 month.

CONCLUSION

SY-41 was a kind of epoxy film adhesive with high strength, high toughness, good heat and hygrothermal resistant properties. Excellent mechanical properties can be obtained when curing at 90°C, 0.1MPa for 4 hours which makes the adhesive can be used in field repair. Its room temperature shelf life exceeds 1 month.

REFERENCES

1. S.H. MYHRE, J.D. LABOR and S.C.AKER "Moisture Problems in advanced Composite Structural Repair", COMPOSITES, JULY 1982, 289-297
2. Liu Qingfang ,Liu linan, Liao Zilong et. al. "Influences of Composition and Viscosity of CTBN Modified Epoxy System on Properties of Prepregs and Composites", Proceedings of ICAM'96 ,Vol. 2, 21-27.
3. USP 3,562,215.
4. Fu Chunming, "Latent System Curing at the Moderated Temperature", Technology on Adhesion & Sealing, 1987, No.4 ,18-21.
5. Li Weilong "Study on No.1 One-component Epoxy Adhesive", CHINA Adhesives, 1994 ,No.5,11-13.
6. Bin Liang, Qingfang Liu and Linan Liu , "The Study of 90°C Curable Structural Adhesive Film SY-41" J. of Material Engineering 1996, 203-204.
7. D. J. Flory "Principles of polymer chemistry" Cornell University Ithaca NY(1953).
8. H. E. Kissinger, J. Res. Natl. Bur. Std. , 57, 217(1956); Anal. Chem. , 29, 1702(1957).

REPAIR OF TYPE B DAMAGE TO MARINE SANDWICH STRUCTURES

Rodney S. Thomson¹, Raoul E. Luescher¹, Ivan Grabovac²

¹ *Cooperative Research Centre for Advanced Composite Structures Limited,
506 Lorimer Street, Fishermens Bend, Victoria, 3207, Australia.*

² *Department of Defence, DSTO, Aeronautical and Maritime Research Laboratory,
PO Box 4331 Melbourne, Victoria, 3001, Australia.*

SUMMARY: Marine vessels manufactured from sandwich structures with glass reinforced polymer (GRP) composite skins and PVC core are now common. These vessels will inevitably be subjected to damage and the approach used in carrying out the repair is critical to maintain the strength and stiffness of the structure. This paper concerns the repair of Type B damage to sandwich structures, defined as damage to one skin and the core. The Royal Australian Navy (RAN) repair technique was evaluated and found to be difficult to carry out and could result in a poor quality repair. Static flexural testing indicated that the presence of voids in the bondline seriously affected the strength of the repair. A modified repair technique was proposed to simplify several aspects of the repair procedure and to improve the repair quality. Test results showed that the modified repair technique overcame the problems associated with the RAN technique.

KEYWORDS: sandwich structures, repair, marine structures

INTRODUCTION

Glass reinforced polymer (GRP) composites are being used increasingly in the maritime industry for the manufacture of hulls, superstructures and fittings. In Australia, the Bay class Inshore Minehunters were manufactured entirely from GRP sandwich construction [1]. The Huon Class Coastal Minehunters are also being manufactured from GRP, but use a monolithic construction technique. Fairings on the Collins class submarines are also manufactured from GRP. In addition to this, GRP finds extensive uses in the civil maritime industry. These structures will inevitably be subjected to damage and effective repair methods must be developed.

Sandwich panels consist of two high strength and stiffness skins separated by a low density, lower strength and stiffness core. Such structures can be subjected to three damage scenarios. The damage can be limited to one skin (Type A), to one skin and the core (Type B), or to both skins and the core (Type C). This paper details an investigation into the repair of Type B damage to GRP/PVC foam sandwich structures representative of the Bay Class minehunters. Type B damage can involve delamination and cracking of the skin, skin to core debonding, and crushing or shear cracking of the core. The approach used in carrying out the repair is critical to maintain the strength and stiffness of the structure. However, the performance of a repair technique must be judged both on its ability to restore the mechanical properties and on the ease of carrying it out.

Various approaches for the repair of such damage have been proposed including those for the United States Coast Guard [2] and the Swedish Mine Counter Measure Vessels [3]. In this research, the technique used by the Royal Australian Navy (RAN) for the repair of Type B damage to the Bay class minehunters was first evaluated. A modified method which simplified the repair procedure while improving the quality was then evaluated. The mechanical performance of the repairs was evaluated by testing specimens under four-point bending.

REPAIR TECHNIQUES FOR “TYPE B” DAMAGE

RAN Technique Description

The RAN repair procedure for Type B damage to GRP/foam sandwich structures of the Bay class minehunters [4] is shown schematically in Fig. 1. The skins of the Bay class minehunters are laminated from alternating plies of 300 g/m² chopped strand mat (CSM) and 600 g/m² woven rovings (WR). A set of one CSM and one WR ply is defined as a layer. The RAN repair procedure is performed in the sequence:

1. *Remove damaged material:* Remove the damaged skin, working from the centre of the damaged region outwards until sound material is encountered. Remove the exposed damaged core leaving the other skin intact.

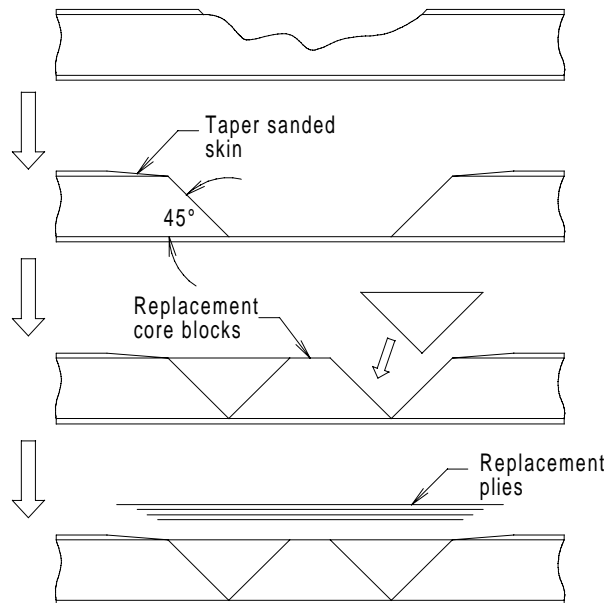


Fig. 1: RAN repair method for Type B damage to GRP/foam sandwich structures.

2. *Prepare the area for repair:* Prepare the foam core to an angle of 45°. Sand the edge of the laminate to a taper of 20 mm per layer which provides a scarf angle of approximately 6°.
3. *Install the replacement foam:* Use the appropriate grade of foam. Use the minimum amount of adhesive designed for bonding PVC foam (bondline thickness 3 mm maximum). No voids should exist between the undamaged skin and the replacement foam.

4. *Replace the skin:* Use the same number of layers as the original skin. Each successive layer is to be 40 mm longer and wider than the previous layer. Apply one extra layer of GRP extending 100 mm beyond the extent of all damage.

Modified Repair Technique Description

Modifications to the repair technique were based on conclusions drawn from the manufacture and testing of the RAN repair technique. These focussed on ensuring a good quality bondline between the skin and replacement core while simplifying the repair preparation. This was achieved by replacing the 45° bevelled edge on the foam with a 90° bevel. Additionally, the replacement foam core used was in one piece wherever practical. Holes drilled through the replacement core were used to prevent air entrapment as the core was positioned. The repair was also placed under vacuum while the core was being bonded in place to ensure a uniform, thin, high quality bondline. The modified Type B repair method, shown in Fig. 2, is detailed below:

1. *Remove damaged material:* Remove the damaged skin, working from the centre of the damaged region outwards until sound material is encountered. Remove the exposed damaged core leaving the other skin intact.

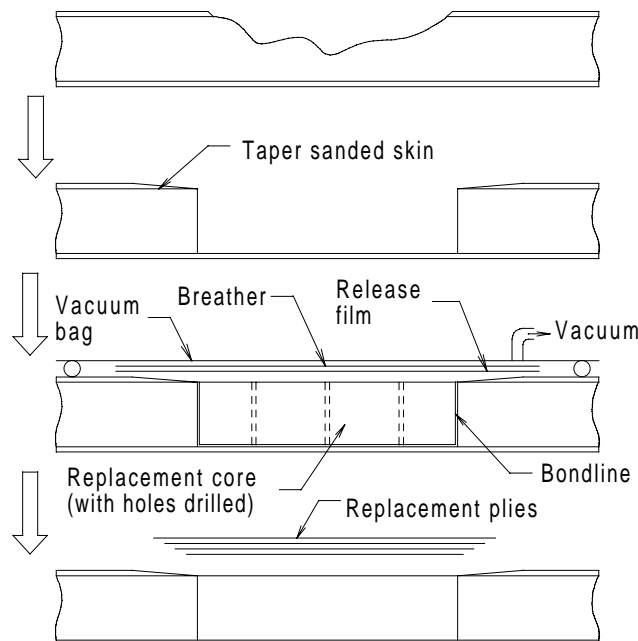


Fig. 2: Modified repair method for Type B damage to GRP/foam sandwich structures.

2. *Prepare the area for repair:* Prepare the foam core to an angle of 90°. Sand the edge of the laminate to a taper of 20 mm per layer.
3. *Install replacement foam:* Cut out a piece of the appropriate grade foam allowing 1 mm all round for the bondline. Drill 3 mm diameter holes through the core at approximately 100 mm centres. Apply an adhesive designed to be used with PVC foam to the existing skin and core. Carefully place the replacement core, forcing it down lightly to remove entrapped air.

4. *Vacuum bag the core:* Apply a layer of perforated release film and breather over the repair area. Position the vacuum bag over the repair area, sealing it to the surrounding structure. Apply vacuum (20 inHg) until the adhesive has cured. Clean up the area for laminating.
5. *Replace the skin:* Use the same number of layers as in the original skin, keeping the orientations the same also. Each successive layer is to be 40 mm longer and wider than the previous layer. Apply one extra layer of GRP extending 100 mm beyond the extent of all damage.

FOUR-POINT BEND TESTS

Test Methodology

The four-point bend test, as specified in ASTM C-393 [5], was selected to evaluate the mechanical performance of the repair. This test places the core under shear and will thereby identify deficiencies in the core itself or the bond between the replacement core and existing core or skin. While the skins do carry the bending loads under four-point bending, these were not anticipated to be high enough to cause skin failure. Two spans between the outer supports were used; 300 mm and 400 mm. The tests were conducted with the repair facing up (normal position) or facing down (inverted position) which placed the repaired skin under compression or tension respectively. The location of the end of the repair was midway between the outer supports where constant shear stress was carried by the core. The tests were carried out using a four-point bend rig mounted in a Riehle 300 kN testing machine. The tests were conducted in displacement control at a rate of 3 mm per minute. The load, displacement, acoustic emissions, failure load and failure mode were recorded during testing. Except where otherwise stated, six specimens of each repair type, span and position were tested.

Four-Point Bend Specimen Fabrication

A large sandwich panel was first fabricated from which the specimens would be obtained. The skins were fabricated using the hand laminating technique with 300 g/m² CSM, 600 g/m² WR and Derakane 411 vinylester resin. The lay-up of the skins was CSM/WR/CSM giving a nominal thickness of 2.1 mm. The core material was 30 mm thick Divinycell HT90 rigid, crosslinked, PVC foam. Following lamination of both skins, the panel was cut into three sections from which the reference, 300 mm span and 400 mm span specimens were obtained. On two of the sections, the RAN repair for Type B damage was performed as detailed previously. Divillette polyester based thixotropic adhesive was used to bond the replacement core. Since the skins were relatively thin, one ply of CSM was applied over the repair instead of one extra layer. Following complete cure of the panels, 40 mm wide four-point bend specimens were cut.

The same approach and materials were used in the fabrication of the modified repair technique specimens. Again, one ply of CSM was applied over the repair instead of one extra layer.

Reference Specimen Test Results

Reference specimens obtained from the RAN and modified repair panels were tested independently under four-point bending. A total of eight 300 mm span specimens were tested and exhibited consistent load-displacement behaviour. All specimens failed through local skin wrinkling/core crushing under the loading points. This failure mode was characterised by the

load reaching a plateau then slowly dropping as compressive failure of the skin occurred under bending. A large drop in load then occurred associated with tension failure of the same skin. Six 400 mm span reference specimens were tested and behaved consistently although one specimen failed through core shear. The reference specimens from the modified repair panel exhibited slightly lower load carrying capability, as summarised in Table 1. This was the result of minor differences in materials and manufacturing between the two panels.

RAN Repair Test Results

The fabrication quality of the RAN repaired specimens was variable, with a number of defects observed in the bondline between the existing skin and replacement core as well as in the 45° join in the core. Some defects represented 50% of the bondline area. The average strength of the 300 mm span repaired specimens tested in the normal position was 14% lower than the reference specimens, as summarised in Table 1. All specimens failed through core shear and a typical failure is shown in Fig. 3. In the inverted position, the average strength was 7% lower but the scatter in results was much higher. This was due to the bondline between the core and the existing skin being positioned on the compression side of the beam making the presence of any defects more critical. The results of such defects are shown in Fig. 4 and Fig. 5.

Similar behaviour was observed for the 400 mm span specimens. The specimens tested in the normal position exhibited similar average strength to the reference specimens and all failed through core shear. The average strength of those tested in the inverted position were 14% lower with most specimens failing through debonding of the skin. Again, the scatter was high in the inverted position.

The stiffness of the repaired specimens was generally higher than the reference specimens. The repaired specimens tested in the normal position were in the order of 10% stiffer than the reference specimens while those tested in the inverted position were in the order of 20% stiffer. The repaired specimens had an extra ply of CSM in the repaired skin and a thicker bondline which contributed to the bending stiffness.

Table 1: Summary of the average strength of the two repair techniques.

Test Group	300 mm Span		400 mm Span	
	Average Maximum Load (N/mm)	Standard Deviation (N/mm)	Average Maximum Load (N/mm)	Standard Deviation (N/mm)
RAN - Reference	79.6	1.5	75.4	0.6
RAN - Normal	68.3	4.3	75.4	1.3
RAN - Inverted	74.2	20.1	64.5	33.2
Modified - Reference	75.3	5.9	73.2	2.0
Modified - Normal	83.3	1.9	78.0	4.2
Modified - Inverted	81.8	2.2	77.4	1.2

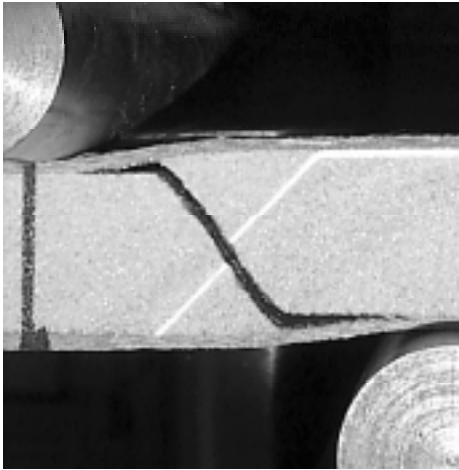


Fig. 3: Typical core shear failure for a RAN repaired specimen in the normal position.

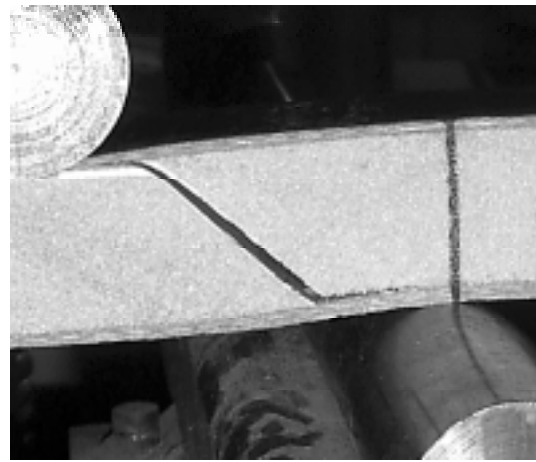


Fig. 4: Failure initiating from a defect in the 45° bondline of a RAN repair tested in the inverted position.

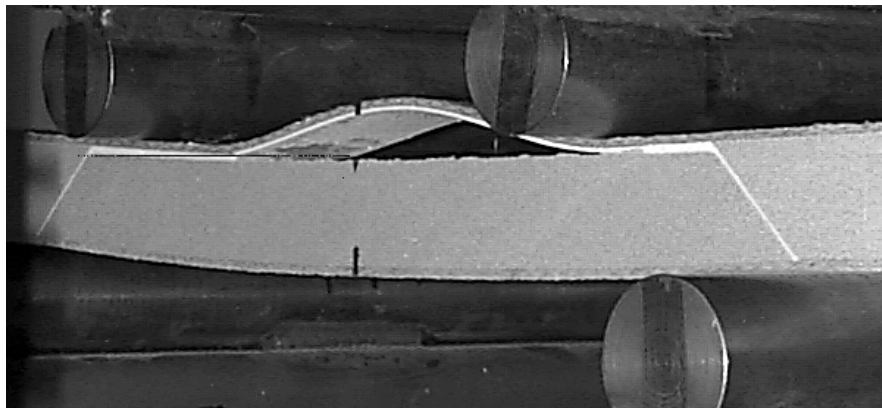


Fig. 5: Debonding failure due to a defect in the replacement core to skin bondline of a RAN repair tested in the inverted position.

Modified Repair Test Results

The fabrication quality of the specimens repaired using the modified technique was very good, although a small number had minor defects in the bondline between the existing and replacement core. The average strength of the 300 mm span repaired specimens tested in the normal and inverted positions was 11% and 9% greater respectively than that of the reference standards. The test results are summarised in Table 1. Similar results were achieved for 400 mm span specimens with the average strength in the normal and inverted positions being 7% and 6% greater respectively than the reference standards. Approximately one third of the specimens failed through skin wrinkling under the loading points while the remainder failed through core shear. No specimens suffered skin debonding failures. Failure initiated from defects in the core to core join in only three of the specimens, as shown in Fig. 6. However, these specimens did not suffer a significant reduction in failure load.

The stiffness of specimens repaired using the modified technique was approximately 8% greater than the reference specimens in both the normal and inverted positions.

DISCUSSION

The RAN repair technique proved difficult to perform, even under laboratory conditions. The major difficulty was associated with finishing the core to a 45° angle. The angle needed to be accurately maintained to ensure good fit of the replacement core and a consistently even, thin bondline. Under field conditions, preparing the repair area would be more difficult with the use of hand held tools. Additionally, typical repairs would be elliptical in shape. The modified repair technique eliminated the 45° join, which made the repair preparation very straightforward. Drilling holes through the core successfully prevented air entrapment. The use of vacuum when bonding the core into position did increase the complexity of the repair. However, the results indicate that this additional process is justified in achieving excellent repair quality and low scatter in the repaired strength and stiffness. Most facilities where such repairs would be carried out would have access to the required vacuum equipment.

Generally, if the bondline were defect free, the strength of the repaired specimens exceeded that of the reference specimens due primarily to the influence of the extra layer laminated into the repaired skin. However, the presence of defects seriously reduced the strength of the sandwich structure, especially when the affected bondline was under compressive loading.

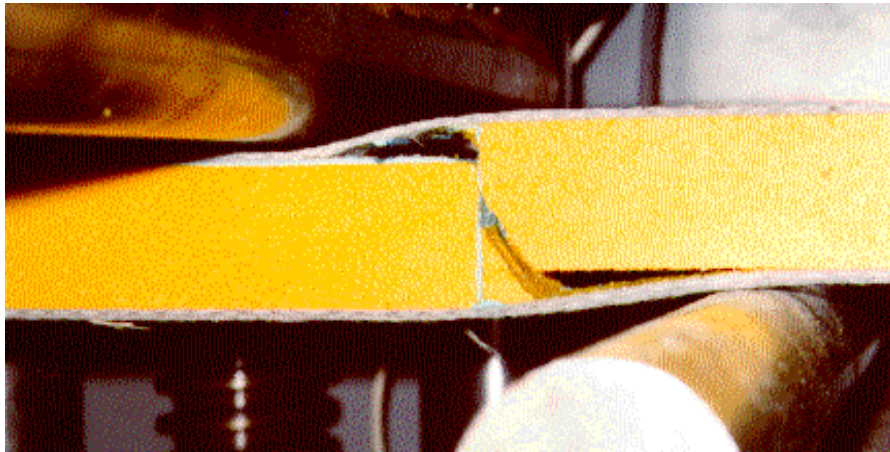


Fig. 6: Failure of a modified repair specimen from a defect in the bondline.

Compressive loading made the presence of defects more critical as they tended to open up, buckle and grow. In the RAN repaired specimens, defects were noted in the bondline between the existing skin and replacement core as well as in the 45° join between the foam. These voids were the result of air entrapment as the replacement core was positioned. Both cases were subjected to compressive loading under four-point bending in the inverted position.

The average strengths under four-point bending of the specimens repaired using the RAN technique were significantly lower than the reference specimens. Also, the standard deviations of the specimens tested in the inverted position were unacceptably high. This was due primarily to the presence of defects in the bondline formed during the repair process. During testing, debonding and local buckling of the skin occurred when these defects were under compressive loading. Once the skin separated from the core, it carried very little of the bending loads rendering the sandwich structure ineffective. Voids in the bondline between the existing and replacement core also affected the ability of the core to effectively carry shear stress. It was imperative that all bondlines be free of defects to produce an effective repair.

On the other hand, the average strengths of the modified repair specimens were greater than the reference specimens due to the low incidence of defects in the bondline. Some small defects were present in the 90° core join, but were found to be less critical than equivalent defects in the RAN repair technique. This was due to the join in the modified repair technique not being aligned with the direction of the shear stress in the core.

The stiffness of the modified repair technique was slightly lower than the RAN technique, but both were significantly higher than the reference standards. This could lead to the presence of a “hard spot” in the structure resulting from the repair which, in a stiffness critical area, could lead to load redistribution or the potential for failure at the edge of the repair.

CONCLUSIONS

The current recommended RAN technique for the repair of Type B damage to GRP/foam sandwich structures was evaluated and two main deficiencies identified. The first concerned the bevelling of the foam at a 45° angle which was found to be difficult to maintain resulting in an uneven bondline thickness. The second deficiency concerned the formation of large voids between the replacement core and the existing skin or core. These were the result of air entrapment when the foam was positioned. These voids were found to seriously reduce the strength of the repair when the bondline was under compressive loading. A less critical problem concerned the increased stiffness of the repaired structure which could result in a “hard spot”.

A modified repair technique for Type B damage to GRP/foam sandwich structures has been proposed. This technique simplifies several aspects of the repair procedure as well as improving the repair quality and repeatability. This was achieved using 90° butt joins in the foam core, drilling holes through the replacement foam core and by using vacuum bagging when bonding the foam in place. The averaged strengths of specimens using the modified repair technique were greater than the reference specimens while the averaged stiffness was similar to that of the RAN repair technique. The results from the evaluation indicate that the problems associated with the RAN technique for the repair of Type B damage have largely been solved by the proposed modified repair technique.

REFERENCES

1. Hall, D.J. and Robson, B.L., "A Review of the Design and Materials Evaluation Programme for the GRP/Foam Sandwich Composite Hull of the RAN Minehunter," *Composites*, Vol. 15, No. 4, October 1984, pp 266-276.
2. "Marine Composites: Investigation of Fiberglass Reinforced Plastics in Marine Structures," Eric Greene Associates, Inc., U.S. Department of Commerce, National Technical Information Service, PB91-129270.
3. Sjogren, J., Celsing, C. G., Olsson, K. A., Levan, C. G. and Hellbratt, S. E., "Swedish Development of MCMV-Hull Design and Production," *RINA Symposium, London, June, 1984*.
4. "Bay Class Minehunter Inshore Glass Reinforced Plastic Repair Manual", Defence Instruction (Navy) ABR 5803, Royal Australian Navy, July 1992.
5. ASTM C-393, "Standard Test Method for Flexural Properties of Flat Sandwich Constructions," American Society for Testing and Materials, 1988.

USE OF OPTICAL FIBRE SENSORS TO DETECT AND MONITOR DAMAGE IN BONDED COMPOSITE REPAIRS OF CRACKED METALLIC COMPONENTS

Edward Tapanes¹ and Stephen C. Galea²

¹*Future Fibre Technologies Pty Ltd, 2 Ralton Avenue, Glen Waverley, Victoria, 3150.*

²*Airframes and Engines Division, Defence Science and Technology Organisation, Aeronautical and Maritime Research Laboratory*

SUMMARY: The application of bonded composite patches to repair or reinforce defective metallic structures is becoming recognised as a very effective versatile procedure for many types of problems. Immediate applications of bonded patch applications are in the fields of repair of cracking, localised reinforcement after removal of corrosion damage and for reduction of fatigue strain. The goal for very demanding repair applications is to incorporate sensors, actuators and electronics in repair systems - smart repair systems - to monitor and report on the health of the repair and the repaired structure, as well as to actuate in order to prevent damage or failure of the repaired structure. The current research is mainly focusing on the assessment of new sensors which may be incorporated in bonded repair systems in order to achieve in-situ real-time measurement of patch integrity and effectiveness. This application would allow the operator to move away from current costly time-based maintenance procedures toward real-time health condition monitoring of the bonded repair and the repaired structure. These systems would allow timely decisions on preventative and schedule maintenance before failure of the repair or repaired structure.

A study was conducted in evaluating the use of embedded and surface mounted optical fibre sensors in detecting and monitoring crack growth of cracked metallic structures repaired with bonded patches. Techniques for embedding optical fibres in boron fibre/epoxy resin patches were developed in this work. The experimental work on a crack patched specimen has shown that optical fibre sensors embedded in composite patches have the potential to detect and monitor crack growth in the metallic sub-structure.

KEYWORDS: smart structures, smart materials, optical fibre sensors, smart patches, intelligent materials and structures

INTRODUCTION

There is a current trend of operating aircraft past their original design life, which has resulted in an increase in the number of structurally significant defects. This problem is extremely relevant to the RAAF where a large number of aircraft, such as the F-111, P3C, Macchi, etc., will have exceeded their original design life before a replacement is put into service. Therefore, the application of bonded composite patches to fix defective structures will become an ever increasing occurrence. However, the application of bonded repairs to primary structures is restricted by certification concerns. For example, the bonded repair on the F-111c wing skin has been substantiated by a substantial analysis and testing program to

ascertain 1) residual strengths, 2) damage tolerance and 3) durability. This approach will be needed for most critical repairs, meaning that feasible repairs may not be undertaken in the future due to the high development costs required to substantiate these types of repairs.

Damage tolerance and durability concerns (i.e., environmental durability and damage resistance of the bond) can be partially overcome by monitoring the condition of the patch during service. In other words, embedding sensors in the patch would allow in-situ NDI to be undertaken on the patch in order to monitor its condition, either on-line or off-line. This approach would considerably ease the operator's concerns during service. Interrogation of the patch, in-situ, should be able to assess 1) crack growth rates and 2) quality of the bond.

Fibre optic technology offers a means by which these essential functions can be performed through the use of embedded fibre optic sensors. Fibre optic sensors (FOSs) offer a new approach to this problem and should allow continuous, in-situ condition monitoring. FOSs offer the advantage of being able to be embedded in a patch without degrading its mechanical properties. Other advantages of FOSs include:

- extreme sensitivity (sensitivity is increased if the sensors are embedded)
- robustness
- monitor temperature for cure purposes
- monitor residual strains in patch (during curing and during service)
- on-line or off-line sensing in-situ

To implement FOSs in composite patches there are a number of factors which need to be addressed. These include the (1) practicality of fabrication, (2) performance (i.e. sensitivity, maximum strain, durability of the fibre, etc.), (3) optimisation (i.e. location, sensing length, etc.) and (4) effects on the mechanical properties of the composite.

The aim of this project is to evaluate the practicality of fabrication and performance of FOSs, embedded in two composite patches and surface bonded to one composite patch, for monitoring the growth of a crack in a metallic structure. As part of the investigations, sensors were embedded or surface bonded at various locations and with various sensing lengths in order to determine the optimum location of application and sensing length. This paper will only report on the embedded sensor results.

TECHNICAL BACKGROUND

Foptic™ Vibration Sensor

Multimode fibre optic sensors generally suffer from optical signal fading and drift. The optical fibre industry has overcome the inherent weaknesses of multimode fibres by the use of singlemode fibre systems, but these are more difficult to handle, and utilise quite expensive components. This significant disadvantage offsets the multimode fibre's advantages of low cost and ease of application.

In recent years, Future Fibre Technologies (FFT) has developed the Foptic™ Vibration Sensor. Based on a unique fibre optic modalmetric sensor configuration, it overcomes the inherent weaknesses of multimode fibre optic sensors, is easy to fabricate and costs relatively little to assemble. The Foptic™ Vibration Sensor provides the first fibre optic sensor in the world which offers an inexpensive method for producing truly localised and mechanically

stable fibre optic multimode sensors, with the flexibility to use virtually any desired optical fibre and components. Fig. 1 illustrates the general configuration of the Foptic™ Vibration Sensor.

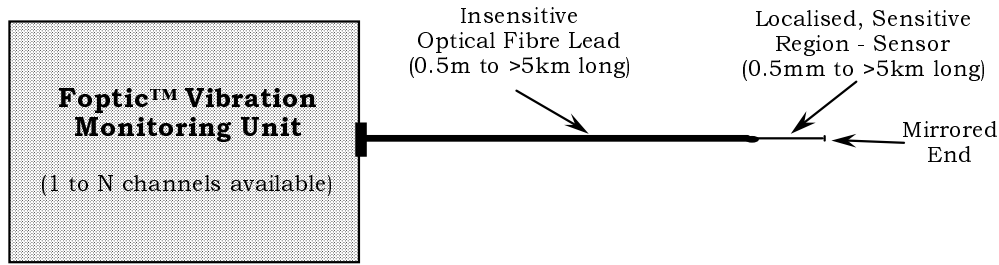


Fig. 1: Foptic™ Vibration Sensor configuration.

The Foptic™ Vibration Sensor is best suited for dynamic measurements. The Foptic™ Vibration Sensor response is a direct function of the dynamic disturbance on the sensitised portion of the fibre. The disturbance may be in the form of physical movement (ie., compression (radially or axially), elongation, twisting or vibration) or microphonic effects (ie., travelling stress waves or acoustic emissions). In the experimental arrangement used in this project, the dynamic elongation and longitudinal compression of the sensitised portion of the fibre results in load-dependent strains in the optical fibre which create intensity modulations. These intensity modulations (the sensor's response) can be measured and calibrated to the known loads or to co-located reference electrical strain gauges.

SPECIMEN MANUFACTURE

Preliminary Study

Preliminary work studied the feasibility of embedding fibre optic sensors in boron/epoxy (B/E) laminates and in FM73 film adhesive. Standard telecommunications optical fibre with 125/250 μm cladding/buffer diameter was used. The cladding and buffer material was glass and acrylate, respectively. A square B/E specimen, consisting of five unidirectional plies, was prepared and cured under standard conditions. The optical fibres were embedded co-linearly with the boron fibres between the first and second plies, as well as the fourth and fifth plies, during the lay-up procedure. The fibres were embedded in pairs and the distance between the fibres was varied between 0.1 and 2 mm. In order to provide strain relief to these optical fibres, where they exited the material, approximately 2 to 3 mm of the buffered section of the fibres was embedded in the composite. Two sensors with buffer included, fibres 1 and 2, were embedded between the fourth and fifth plies. Owing to the arrangement used, the transmissive-mode sensors had an entry point into the composite as well as an exit point on the opposite side of the specimen. In addition, a reflective-mode sensor (fibre mirrored on end face) was embedded between the third and fourth plies. Fig. 2 illustrates the top and cross-sectional views of the embedding arrangement, respectively.

Following cure, visible laser light was launched into each input fibre of the transmissive-mode sensors and the output fibres were observed in order to determine if the sensor had survived the curing procedure. All ten transmissive-mode sensors had survived the cure. The reflective-mode sensor was connected to the Foptic™ Vibration Monitor unit and was tested. Two unbuffered optical fibres were also placed between two layers of the FM-73 adhesive and this arrangement was co-cured between two pieces of thin aluminium. These fibres were not tested for through-put, due to the success rate of the work with the B/E. The B/E and FM-

73 specimens were then cut-up into several pieces, with the saw-lines perpendicular to the optical fibre direction. Each specimen was then polished for viewing under an optical microscope. Fig. 3 shows typical macrographs of the cross-sectional views.

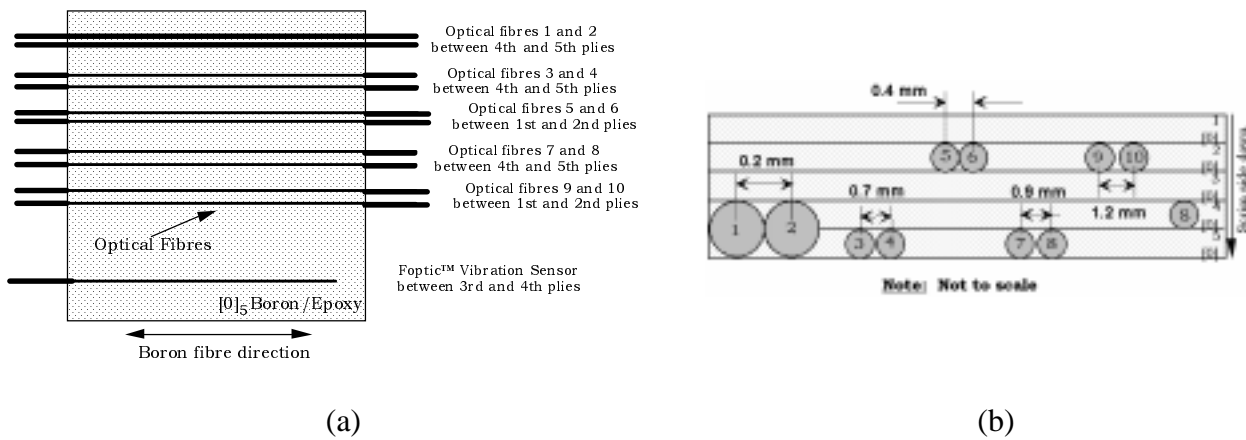


Fig. 2: (a) Top and (b) cross-sectional view of boron/epoxy laminate with embedded optical fibres.

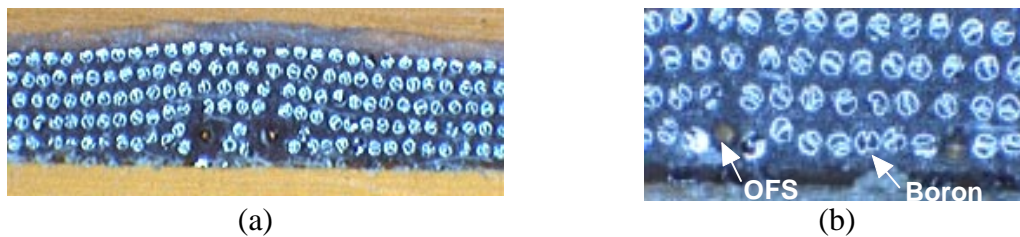


Fig. 3: (a) Buffered fibres, fibres 1/2, embedded in the B/E laminate. (b) Unbuffered fibres, fibres 3/4, at 0.7 mm spacing in the B/E laminate.

From these macrographs the following points were observed:

1. No significant difficulties were encountered during the installation or fabrication stages. All the fibres, emerging from the B/E, remained intact and rugged, and showed no signs of brittleness.
2. The relatively-large diameter buffered fibre significantly displaced the surrounding material fibres, see Fig. 3a. It was concluded that only unbuffered fibre should be used.
3. The unbuffered fibres, having approximately the same diameter as the boron fibres, did not significantly effect the arrangement of the surrounding material fibres when the optical fibres were located around 1 mm or greater apart (see optical fibres 3 and 4 in Fig. 3b). However, if the unbuffered optical fibres were placed much less than 1 mm apart they did have some effect on the surrounding material fibres. It was concluded that the optical fibres should not be embedded closer than 1 mm from each other, in B/E.
4. During the cure process, the scrim of the ply above an optical fibre tended to push the fibre downwards into the ply below and the scrim of the ply below a fibre tended to restrict its downward movement to within the corresponding ply, as seen in Fig. 3b.
5. The two fibres embedded in the FM-73 moved downwards into the bottom layer by the same distance.

Crack Patched Specimens

Standard telecommunications optical fibre with 125/250 μm cladding/buffer diameter was used. The cladding and buffer material was glass and acrylate, respectively. The sensors were individually tested and monitored using the Foptictm Vibration Monitor unit before and during the installation process to ensure that all the sensors were operative prior to the cure process.

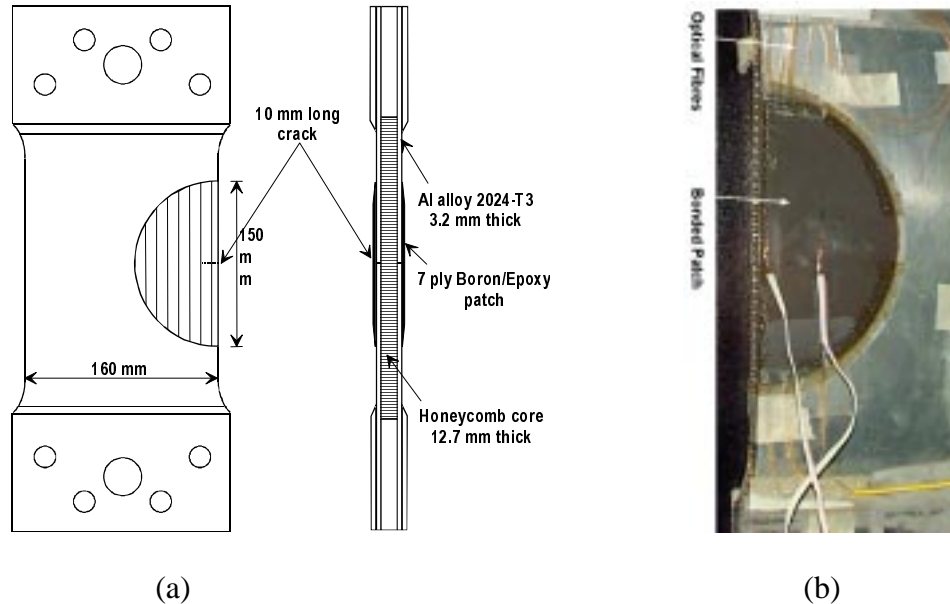


Fig. 4: (a) Schematic of the specimen used for this experimental program. (b) Photograph of the boron/epoxy repaired specimen with embedded optical fibre sensors.

The two test specimens were specified and manufactured and consisted of two cracked aluminium panels, with a B/E patch over the crack, tested back-to-back using a honeycomb sandwich panel, as shown schematically in Fig. 3a. The semi-circular B/E patches were constructed in a 7 ply, unidirectional (i.e., $[0]_7$) laminate arrangement and were adhered to the aluminium panel with two layers of FM-73 adhesive. The patches were constructed in a tapered arrangement, with a radius of curvature of 75 mm for the largest ply and 60 mm for the smallest ply.

The optical fibres were embedded co-linearly with the boron fibres. In order to provide strain relief to these optical fibres, where they exited the material, approximately 2 to 3 mm of the buffered section of the fibres was embedded in the composite. Precautionary measures were taken to prevent the epoxy from running along the optical fibres (by capillary action) during the cure process, because, once cured, the epoxy is brittle and could also make the optical fibres brittle. This was achieved by placing teflon tape over sections of the fibres close to the patch and creating dams with a high temperature vacuum sealant. Previous work taught us that preventing the epoxy from running along the fibre helps to maintain the fibres flexibility and strength. Once the patches were cured, they were prepared for attachment to the cracked metallic test specimen. One patch was co-cured to the cracked metallic test specimen (side B) and the second patch was simultaneously secondary bonded to the same cracked metallic test specimen (side A). Following the final cure process, the sensors were connected to the Foptictm Vibration Monitor unit and tested in order to determine if the sensors had survived the curing procedure.

EXPERIMENTAL PROCEDURE

Jacketed, connectorised fibre optic leads were fusion spliced to all the FOSs which had survived the installation and attachment procedures, in order to couple the sensors to the Foptictm Vibration Monitor units. The linearity of the Foptictm Vibration Sensor response has been shown to be good over a 1000+ $\mu\epsilon$ range in other work. However, the sensor must be calibrated to obtain quantitative results. The results obtained with the FOSs in this work may be approximated with respect to the known loads applied with the hydraulic uniaxial testing machine or, preferably, the localised strain measured by the reference electrical strain gauges (ESGs). However, it is difficult to make a generalised calibration on the Foptictm Vibration Sensor without the sensors being exactly co-located (such that they both experience the exact same strain/load conditions). This is difficult to achieve, particularly with regard to the embedded FOSs, and generally impractical in field conditions. However, the synchronised, relative peak-to-peak values of the two sensor responses (FOSs and ESGs) may be compared over time, during fatigue cycling, to determine whether the in-situ strain conditions monitored by the FOS are changing as the crack in the test specimen grows. This may be useful in determining whether there is a general trend in the FOS response as the crack tip in the specimen approaches and passes the location of the FOS, since the localised strains vary significantly as this occurs. This technique is used to assess the response of the FOS to crack growth.

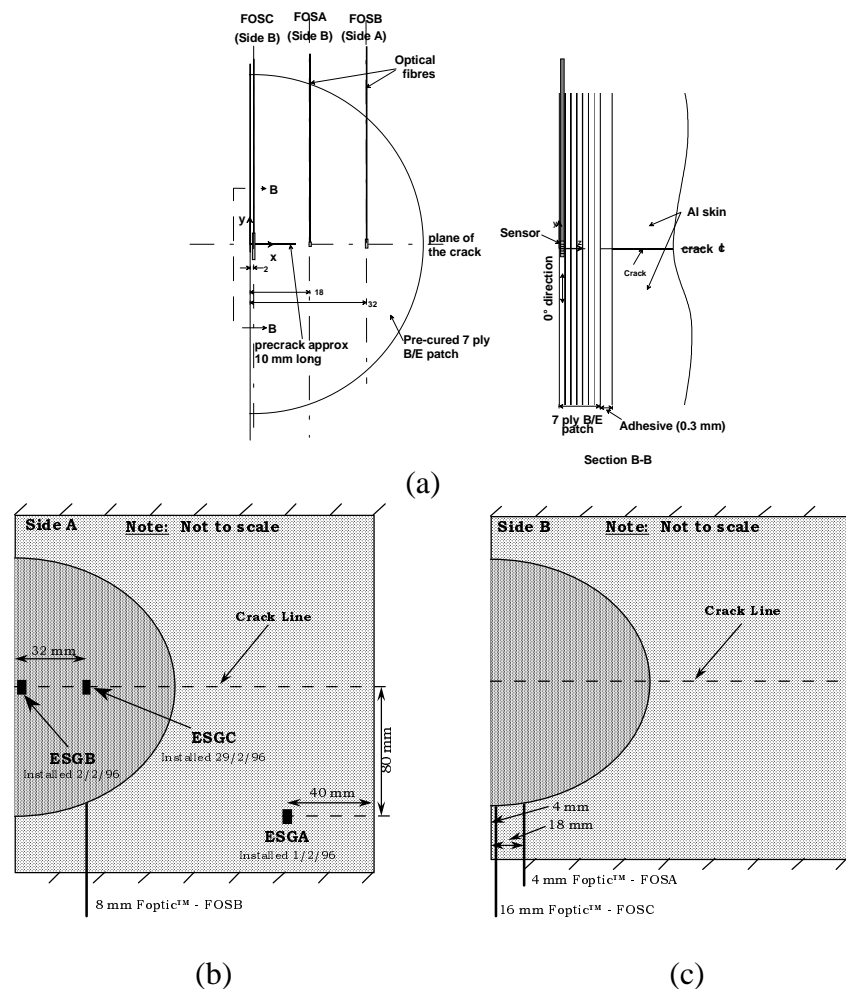


Fig. 5: (a) Position of FOSA, FOSB and FOSC on specimen. (b) Side A and (c) Side B with foil strain gauges ESGA, B and C indicated.

In all the testing, the FOS signals were captured and displayed on an AMLAB[®] I digital signal processing workstation. Sometimes the signals were Fast Fourier Transform analysed and recorded in real-time in order to determine the frequency characteristics of the sensor signals. This was carried-out mainly to confirm the frequency of the applied load, when appropriate. Three ESGs were attached to the test specimen, at various locations, in order to compare the responses of the sensors. Diagrams of the locations of FOSs and strain gauges on side A (side with secondary bonded patch) and side B (side with co-cured patch) are illustrated in Fig. 5. The responses of ESGs were simultaneously captured, displayed and recorded for comparison with the FOSs.

The test specimens were subjected to tension-dominated fatigue loading, at a frequency of 3 to 4 Hz, using a 250 kN capacity Instron hydraulic uniaxial testing machine. Initially, a static pre-load of 77 kN was applied and then it was subjected to tensile-dominated cyclic load of ± 63 kN for a total of 190,000 cycles. The initial crack length was 10 mm. At every 5,000 cycles, the testing was paused and a crack measurement was made manually using an eddy current probe. In addition, static strain surveys were performed with the ESGs at various stages of the testing, and manually recorded.

The signals from the three FOSs and the three ESGs, shown in Fig. 5, were captured and displayed in real-time using the AMLAB[®] unit. Since the data acquisition unit has only four analog input channels, it was decided to monitor the three FOSs with the first three channels and the three ESG signals were captured, one at a time (in turn), using the fourth available channel. Recordings of the sensors signals were made every 1,000 cycles.

RESULTS AND DISCUSSION

Embedding FOS in Boron/Epoxy Patches

Following the curing process, many of the optical fibre leads of both patches showed significant signs of brittleness and several fibres were visibly damaged. Furthermore, the fibre buffer appeared to be considerably deformed and was even absent in some regions of the fibre. Neither of these problems had been encountered in previous work. At this stage, we realised that a previously unencountered factor was acting to significantly degrade the acrylate buffer and weaken the optical fibres.

Previous work with graphite/epoxy and boron/epoxy laminates yielded 100% embedded sensor survivability. However it now appears that the volatile chemicals produced or released from the FM-73 adhesive during cure (in particular, methyl ethyl ketone - MEK) may have reacted with the acrylate coating of the optical fibres and significantly weakened the sensors. This conclusion was strengthened by the fact that less than 50% of sensors survived on the side of the patch closest to the vacuum port, whereas over 70% survived on the opposite side. This was considered relevant because any volatiles produced during cure would tend to migrate towards the vacuum port as the vacuum was being applied and so would run along the fibre in the process. In addition, this conclusion was also supported by the fact that the majority of fibres failed near the edge of the secondary bonded patch, and mostly on the side closest to the vacuum port. Therefore, any future work involving FM-73, will necessitate the use extra precautions to protect the integrity of the optical fibres with the acrylate coating or to use an optical fibre with a more rugged buffer material, such as polyimide. However,

polyimide is much more difficult to work with than acrylate and will significantly increase the time required to fabricate the sensors and install them in composites.

Dynamic Fatigue Test Results

As expected, the strains measured with ESGA remained relatively constant throughout the test. However, the strains measured by ESGB approximately doubled during testing from 40,000 cycles to 150,000 cycles, as illustrated in Fig. 6, and the residual strain detected at the end of testing was quite significant (178 $\mu\epsilon$). The background noise of the optical fibre system was negligible, unless the AMLAB[®] gain was increased significantly in order to determine the minimum sensitivity of the FOSs. The signal-to-noise ratios of FOSA and FOSB were typically in the same range as the surface bonded ESGs. The signal-to-noise ratio for FOSC, however, was lower but reasonable.

The responses from the FOSs represent the localised strain and bending effects acting on the fibre. Any changes in the sensor's signal is a direct indication that a condition has changed, no matter how unusual or unexpected those signals may be. As previously discussed, the Foptic[™] Vibration Sensor must be calibrated to obtain quantitative results. The results obtained with the FOSs in this work may be approximated with respect to the localised strains measured by the reference ESGs. However, it is difficult to make a generalised calibration on the Foptic[™] Vibration Sensor without the sensors being exactly co-located (such that they both experience the exact same strain/load conditions). This is difficult to achieve, particularly with regard to the embedded FOSs. Nonetheless, the synchronised, relative peak-to-peak values of the two sensor responses (FOSs and ESGs) may be compared over time, during fatigue cycling, to determine whether the in-situ strain conditions monitored by the FOS are changing as the crack in the test specimen grows. This may be useful in determining whether there is a general trend in the FOS response as the crack tip in the specimen approaches and passes the location of the FOS, since the localised strains vary significantly as this occurs.

The peak-to-peak values of the signals were calculated at each 1,000 cycle interval. These values were then plotted as a function of the number of fatigue cycles for each sensor. Fig. 6 - 9 illustrate the peak-to-peak responses of the FOSs and ESGs as a function of the number of fatigue cycles. The response of ESGA remained relatively constant. On the other hand, the response of ESGB increased linearly throughout the test and nearly doubled in amplitude by the end of the testing. The response from ESGC showed a slight downward trend until N=164,000 and CLA=39 mm, where it began a slight trend upwards, at approximately the same slope as ESGB.

As can be seen in Fig. 7, the peak-to-peak responses of all three FOSs showed significant downwards trends at the start of the testing, until approximately N=57,000 cycles and CLA=16 mm, and then underwent several changes for the remainder of the testing. In Fig. 8, the peak-to-peak response of FOSB is illustrated. The sensor's response decreased until approximately N=67,000 cycles and CLA=17.5 mm. The sensor's response then increased linearly until a sudden, large decrease at approximately N=121,000 cycles and CLA=30 mm. The decrease in response continued in a linear manner until N=133,000 cycles and CLA=32 mm, which is exactly where the sensor was located, when it suddenly increased in the exact same manner as it had decreased. As can be seen in the figure, the decrease and then increase in the sensor's response, centred about N=133,000 cycles, was symmetric about the vertical direction. At N=148,000 cycles and CLA=34 mm the signal from FOSB decreased by one

order of magnitude, suggesting that the sudden increase in strains may have damaged the fibre or that the fibre may have disbonded from the B/E matrix. The latter explanation is more probable since the sensor was still detecting a sinusoidal signal, whereas a fractured fibre would not respond at all. In any case, it may be concluded that FOSB's response showed a definite trend as the crack approached and passed the location of the sensor.

In Fig. 9, the peak-to-peak response of FOSA is illustrated. The sensor's response decreased until approximately $N=58,000$ cycles and a crack length on side B (CLB) of 16.5 mm, close to where the sensor was located. The sensor's response then increased linearly in the same manner as it had decreased until approximately $N=67,000$ cycles and $CLB=19$ mm, where it began to modulate. At approximately $N=98,000$ cycles and $CLB=25$ mm, the sensor's response settled and decreased until approximately $N=140,000$ cycles and $CLB=34.5$ mm, where it began to increase and then modulate further. As can be seen in the figure, the decrease and then increase in the sensor's response, centred about $N=58,000$ cycles, was symmetric about the vertical direction, as was the case for FOSB when the crack approached and passed its location. This suggests that FOSA's response showed a trend as the crack approached and passed the location of the sensor, although it was not as clear as the case with FOSB.

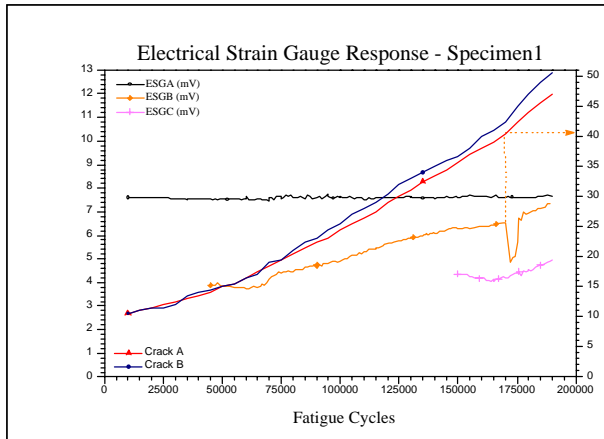


Fig. 6: Electrical strain gauge response versus fatigue cycles.

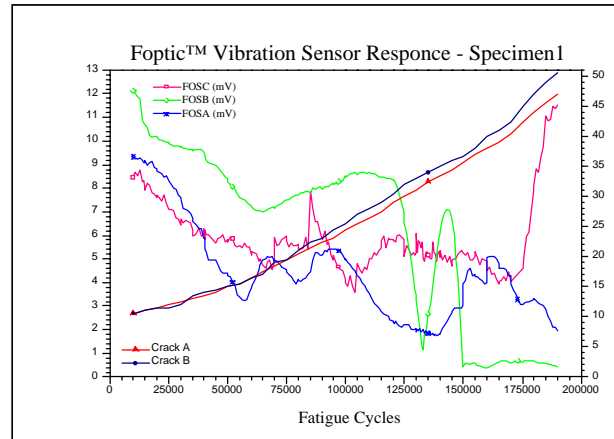


Fig. 7: Foptic™ Vibration Sensor response versus fatigue cycles

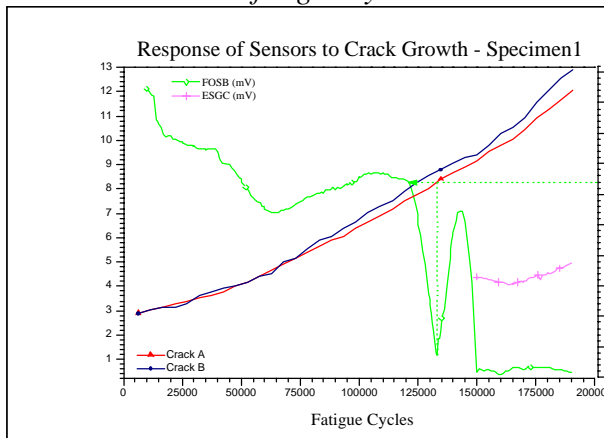


Fig. 8: Response of FOSB and ESGC to crack growth.

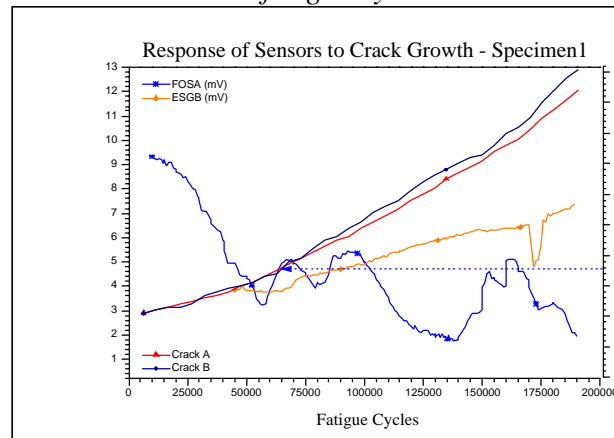


Fig. 9: Response of FOSA and ESGB to crack growth.

During fatigue loading, it was noted that the B/E patch was undergoing considerable bending in the region near the base of the crack (the edge of the specimen with the start of the crack),

particularly once the crack length grew beyond 20 mm. Since FOSC was embedded within this region it too was subjected to these bending effects. Therefore, FOSC was actually responding to both the tensile loading as well as the bending effects. In fact all sensors experience significant local secondary bending as the crack passes under them. It is suspected that this may help to explain the quality of the response of the sensor.

CONCLUSION

A number of Foptic™ Vibration Sensors were embedded in two boron/epoxy patches during the lay-up stage. The two patches were then cured and prepared for attachment to a cracked metallic test specimen. One patch was co-cured to the cracked metallic test specimen and the second patch was simultaneously secondary bonded to the same cracked metallic test specimen. Considerable difficulties were encountered with fibres failing during the various cure stages of the B/E patches. Although previous work with graphite/epoxy and boron/epoxy patches yielded 100% embedded sensor survivability, in this case a low percentage of fibres survived the cure stages. It is believed that the volatile chemicals produced or released from the FM-73 adhesive during cure reacted with the acrylate coating of the optical fibres and significantly weakened the sensors. It is recommended that work involving FM-73 will require enhanced protection of the fibres with the acrylate coating or to use an optical fibre with a more rugged buffer material, such as polyimide.

The test specimen with the three embedded fibre optic sensors was fatigued. Three electrical strain gauges were also attached to the specimen as reference strain gauges. The results of the fatigue testing clearly demonstrate that the responses of the embedded fibre optic sensors underwent significant changes as the length of the crack increased. Furthermore, the analysis of the sensors' responses indicate that the fibre optic sensors exhibited distinct trends as the crack approached and passed the location of the embedded sensors. The 4 mm long sensors required higher gains than the longer sensors and often displayed a lower signal-to-noise ratio. The responses from the 16 mm long sensors were not as consistent as the 8 mm long sensors, perhaps because they integrated many signals or effects over their relatively long lengths. The 8 mm long sensors appeared to perform relatively well and had good signal-to-noise ratios.

During the testing, it was observed that the B/E patches were undergoing considerable bending in the region near the base of the cracks. It is suspected that the bending effects on the B/E patches may have contributed to the response characteristics of the sensors and that this may have had a significantly higher effect on the response of the shorter sensors. Overall the test series demonstrated that the Foptic™ Vibration Sensor technology has good potential for monitoring the crack growth of a crack in a metallic structure, although embedding procedures for the fibre optic sensors must be improved.

ACKNOWLEDGMENTS

The authors wish to acknowledge the assistance of Mr. Ivan Stoyanovski and John Roberts for assistance in manufacturing the specimens and Mr. Onofrio Benninati for undertaking the testing.

REFERENCES

1. Baker, A. "Fibre Composite Repair of Cracked Metallic Aircraft Components - Practical and Basic Aspects", *Composites*, Vol. 18, No. 4, 1987, pp. 293-307.
2. Baker, A.A., "Bonded Composite Repair of Metallic Aircraft Components", Paper 1 in AGARD-CP-550 Composite Repair of Military Aircraft Structures, 1994.
3. Galea, S.C. " Monitoring Damage in Bonded Composite Repairs of Cracked Metallic Components using Surface Strain Measurements", Proceedings of Eleventh International Conference on Composite Materials (ICCM-11), Gold Coast, Australia, 14 - 18 July, 1997.

ELASTICITY SOLUTION OF POLYMERIC PIEZOELECTRIC C-BLOCK COMPOSITE ACTUATOR

Haozhong Gu and Aditi Chattopadhyay

*Department of Mechanical and Aerospace Engineering, Arizona State University
Tempe, AZ 85287-6106, USA*

SUMMARY: An elasticity solution is developed to investigate the mechanical behavior of polymeric piezoelectric C-block composite actuators, which were recently proposed to overcome the limitations of conventional bimorph and stack configurations. The stress functions are used to derive the general equations governing the behavior of induced strain actuation under various load conditions. Closed-form expressions are presented for the displacements and stresses. Comparisons of present approach are made with classical elasticity solutions for curved beams and existing approximate solutions for curved actuators for a simplified case. The results from the current solution also provide physical insight into the mechanism of C-block actuators.

KEYWORDS: elasticity solution, c-block, actuator, smart structures, induced strain

INTRODUCTION

Smart materials have received considerable attention in recent years for vibration control, shape control, damage assessment and active noise reduction of engineering structures^[1]. The advantage of incorporating these type of materials into the structure is that the sensing and actuation mechanisms become an internal part of the structure by sensing and actuating strain directly. The application of smart materials is currently being investigated for in rotary- and fixed-wing aircrafts and large flexible space structures. Significant effort has been focused on piezoelectric materials due to their fast response, low power consumption and relative large induced strain for an applied voltage. The limitations of most commonly used flat bimorph configuration include relatively smaller deflections and the low forces. Therefore, a new class of polymeric piezoelectric composite actuators, called C-blocks (Fig.1) because of their curved shape, has been developed to overcome the limitations of conventional bimorph and stack piezoelectric configurations. These actuators have been shown better force and deflection capabilities^[2].

Since the concept of curved actuators is relatively new, very few research efforts have been reported in developing rigorous mathematical models for investigating the mechanical behavior of the C-block actuators. Questions still remain regarding a complete understanding of the physical phenomena involved. The research was initiated by Brei who developed an approximate approach using the curved Bernoulli-Euler beam model which is only valid in pure bending cases^[2,3]. Castigliano's second theorem was employed to derive the end

deflection, the end force and the end moment. Later, Seeley, Chattopadhyay and Brei presented a new hybrid optimization procedure to optimize the design of the C-block actuators by using this approximate curved beam model^[4]. Recently, Chattopadhyay, Mitchell and Gu developed the refined approach based on the first-order shear deformation theory to overcome the limitation of the pure bending assumptions^[5]. The major limitations of the approximate curved beam model are pure bending assumption and the inplane displacement distribution through the thickness, particularly for laminates in which the stiffness properties vary dramatically from layer to layer. Another important limiting factor is that the beam-type constitutive relations eliminate the possibility of rigorous calculation of interlaminar stresses. For actuators, the curved beam solution also does not account for the local effect of the induced strain, which eventually changes the stress and displacement distributions in multi-layered actuators.

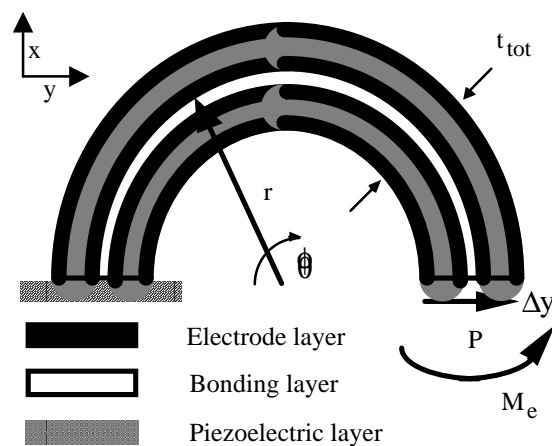


Fig.1 Geometry of a piezoelectric C-block actuator

As a remedy to these limitations, the elasticity solution is developed for this class of polymeric piezoelectric C-block composite actuators in this paper. The general behaviors of the C-block actuator are classified, for a convenient solution procedure, as the combination of the actuator with only the induced stain, the actuator with only the end moment and the actuator with only the end force. The governing equations are derived and solution forms are obtained in each classified problem within the individual layer. The continuity conditions at layer interfaces and the boundary conditions are then applied to solve the entire problem. Numerical results obtained using the current research show general agreement with existing solutions for end deflection and more complicated stress and displacement distributions which differ significantly from existing solutions.

GOVERNING EQUATIONS

The C-block actuators are constructed out of two curved piezoelectric layers in a bimorph configuration resulting in a half circle as shown in Fig. 1. The piezoelectric layers are surrounded on both sides by an electrode layer of silver ink. The bonding layer consists of a common epoxy used to connect the two piezoelectric layers. These layers are actuated with equal but opposite electric fields to produce a bending moment which is used as the actuation mechanism. The ratio of total actuator thickness to the piezoelectric material thickness is

small^[6]. The general governing equations for the C-block actuator, which is valid within each layer, is developed here based on the linear theory of elasticity. For a two dimensional elastic body defined in a cylindrical coordinate system (r, θ) (see Fig.1), the compatibility equations are written in terms of the normal strains ε_r and ε_θ , defined along the radial and the circumferential direction, respectively, and the shear strain $\gamma_{r\theta}$ as follows^[7].

$$\left(\frac{\partial^2}{\partial \theta^2} - r \frac{\partial}{\partial r} \right) \varepsilon_r + r \frac{\partial^2}{\partial r^2} (r \varepsilon_\theta) - \frac{\partial^2}{\partial r \partial \theta} (r \gamma_{r\theta}) = 0 \quad (1)$$

For actuators with induced strain, constitutive relations are written within an individual layer, as follows.

$$\begin{aligned} \varepsilon_r &= a_{11}\sigma_r + a_{12}\sigma_\theta + a_{16}\tau_{r\theta} \\ \varepsilon_\theta &= a_{12}\sigma_r + a_{22}\sigma_\theta + a_{26}\tau_{r\theta} + \Lambda \\ \gamma_{r\theta} &= a_{16}\sigma_r + a_{26}\sigma_\theta + a_{66}\tau_{r\theta} \end{aligned} \quad (2)$$

where, a_{ij} are the compliances for anisotropic material and Λ is the induced strain due to actuation. Denoting d_{31} as the piezoelectric coefficient and E_3 as the applied electric field, the induced strain can be expressed as

$$\Lambda = d_{31}E_3 \quad (3)$$

In each individual layer, the stress function is employed to solve the problem. The stress components can be expressed in terms of the stress function, ϕ , as follows.

$$\begin{aligned} \sigma_r &= \frac{1}{r} \frac{\partial \phi}{\partial r} + \frac{1}{r^2} \frac{\partial^2 \phi}{\partial \theta^2} - \frac{a_{16}a_{26} - a_{12}a_{66}}{\Delta} \Lambda \\ \sigma_\theta &= \frac{\partial^2 \phi}{\partial r^2} - \frac{a_{11}a_{66} - a_{12}^2}{\Delta} \Lambda \\ \tau_{r\theta} &= -\frac{\partial^2 \phi}{\partial r \partial \theta} \left(\frac{\phi}{r} \right) - \frac{a_{12}a_{16} - a_{11}a_{26}}{\Delta} \Lambda \end{aligned} \quad (4)$$

where

$$\Delta = a_{11}a_{22}a_{66} + 2a_{12}a_{16}a_{26} - a_{22}a_{16}^2 - a_{11}a_{26}^2 - a_{12}a_{66}^2 \quad (5)$$

Using Eqs.(1), (2) and (4), the compatibility equation for anisotropic composite material can finally be written in terms of the stress function.

$$\begin{aligned} &\left(\frac{\partial^2}{\partial \theta^2} - r \frac{\partial}{\partial r} \right) \left[a_{11} \left(\frac{1}{r} \frac{\partial \phi}{\partial r} + \frac{\partial^2 \phi}{\partial \theta^2} \right) + a_{12} \frac{\partial^2 \phi}{\partial r^2} - a_{16} \frac{\partial^2}{\partial r \partial \theta} \left(\frac{\phi}{r} \right) \right] + r^2 \frac{\partial^2}{\partial r^2} \left[a_{12} \left(\frac{\partial \phi}{\partial r} + \frac{1}{r} \frac{\partial^2 \phi}{\partial \theta^2} \right) + \right. \\ &\left. a_{22} r \frac{\partial^2 \phi}{\partial r^2} - a_{26} r \frac{\partial^2}{\partial r \partial \theta} \left(\frac{\phi}{r} \right) \right] - \frac{\partial^2}{\partial r \partial \theta} \left[a_{16} \left(\frac{\partial \phi}{\partial r} + \frac{1}{r} \frac{\partial^2 \phi}{\partial \theta^2} \right) + a_{26} r \frac{\partial^2 \phi}{\partial r^2} - a_{66} r \frac{\partial^2}{\partial r \partial \theta} \left(\frac{\phi}{r} \right) \right] = 0 \end{aligned} \quad (6)$$

Since the induced strain is constant within the piezoelectric layer, it automatically disappears in Eq.(6) after taking derivatives.

ELASTICITY SOLUTION

According to the linear theory of piezoelectricity, the supposition technique can be used to simplify the solution procedure. Therefore, the general problem associated with the C-block actuators is classified into a few basic problems, such as the C-block with only induced strain, the C-block with an end moment and the C-block with an end force (Fig.2). In each one of these problems, the solution forms are defined in accordance to its characteristics. This is the key issue in this research.

Induced Strain

For C-blocks with only induced strain, the behavior characters are identical along the circumferential direction (except at the very near field at tow ends). Therefore, it is an axisymmetric problem. The solution can be obtained with the help of a stress function depending only on the single variable, r , that is, $\phi = \phi(r)$. Assuming

$$F = \frac{\partial \phi(r)}{\partial r} \tag{7}$$

Eqs.(4) and (6) yield the following

$$(a_{22}rF' + a_{12}F)' - (a_{12}F' + a_{11}F/r) = (a_{22} - a_{11})C_o \tag{8}$$

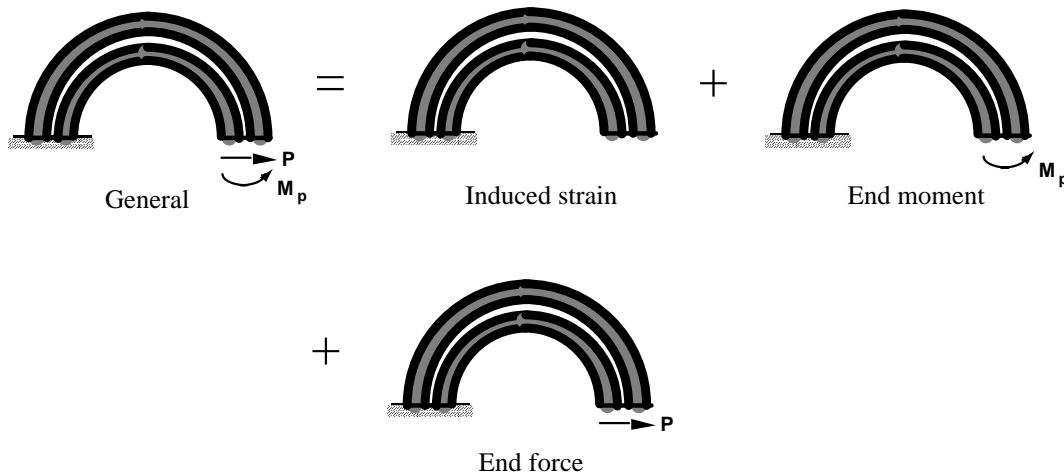


Fig.2 Modeling technique

where ()' is refers to differentiation. Let $r = e^t$ and $\dot{F} = \frac{dF}{dt}$, then the characteristic equation of Eq.(7) can be expressed as follows.

$$a_{22}\ddot{F} - a_{11}F = 0 \tag{9}$$

Solving Eq.(9), the two roots are obtained

$$\lambda_{1,2} = \pm \sqrt{\frac{a_{11}}{a_{22}}} \quad (10)$$

Therefore, the solution of the specified stress function F takes the following form

$$F = A_0 r^{\lambda_1} + B_0 r^{\lambda_2} + C_0 r \quad (11)$$

The material axes and the geometric coordinates in the C-blocks are identical, which yields $a_{16} = a_{26} = 0$. Using Eqs.(4) and (11), the following expressions are obtained for the stresses

$$\begin{aligned} \sigma_r &= \frac{F}{r} + \frac{a_{12}}{a_{11}a_{22}} \Lambda = A_0 r^{\lambda_1-1} + B_0 r^{\lambda_2-1} + C_0 + \frac{a_{12}}{a_{11}a_{22}} \Lambda \\ \sigma_\theta &= F' - \frac{a_{11}a_{66} - a_{12}^2}{a_{11}a_{22}a_{66}} \Lambda = A_0 \lambda_1 r^{\lambda_1-1} + B_0 \lambda_2 r^{\lambda_2-1} + C_0 - \frac{a_{11}a_{66} - a_{12}^2}{a_{11}a_{22}a_{66}} \Lambda \\ \tau_{r\theta} &= 0 \end{aligned} \quad (12)$$

where, A_0 , B_0 and C_0 are unknown constants which will be solved only after the global equations is established. Using the stress expressions in Eq.(12), the strain components can be obtained by using Eq.(2). The displacements at the radial direction u and the circumferential direction v can also be derived using following equations.

$$\varepsilon_r = \frac{\partial u}{\partial r}, \quad \varepsilon_\theta = \frac{u}{r} + \frac{1}{r} \frac{\partial v}{\partial \theta}, \quad \gamma_{r\theta} = \frac{1}{r} \frac{\partial u}{\partial \theta} + \frac{\partial v}{\partial r} - \frac{v}{r} \quad (13)$$

As noted before, the stress and displacement solutions, Eqs.(12) and (13), are only valid within each individual layer. To derive the global equation for the entire C-block, the continuity equation at layer interfaces and the boundary conditions at two ends, top and bottom surfaces are must be applied. Using the superscription (i) to identify quantities in the i^{th} layer and h_i to denote the thickness of the i^{th} layer ($i=1,2,\dots,k$, where k is the number of layers), the tractions and displacements at the layer interfaces must satisfy the following continuity equations defined in the local coordinate

$$\begin{aligned} \tau_{r\theta}^{(i)}(h_i, \theta) &= \tau_{r\theta}^{(i+1)}(h_i, \theta), & \sigma_r^{(i)}(h_i, \theta) &= \sigma_r^{(i+1)}(h_i, \theta) \\ u^{(i)}(h_i, \theta) &= u^{(i+1)}(h_i, \theta), & v^{(i)}(h_i, \theta) &= v^{(i+1)}(h_i, \theta) \end{aligned} \quad (14)$$

The boundary conditions at the top and the bottom surfaces of the C-block are as follows.

$$\tau_{yz}(r_i, \theta) = \tau_{yz}(r_e, \theta) = 0, \quad \sigma_r(r_i, \theta) = \sigma_r(r_e, \theta) = 0 \quad (15)$$

where, r_i and r_e are the radius of the inner surface and the outer surface of the C-block, respectively. The boundary conditions at the clamped end, $\theta = 0$, are

$$u = v = \frac{\partial v}{\partial r} = 0, \quad \text{at } r = \frac{r_i + r_e}{2} \quad (16)$$

The boundary conditions at the free end, $\theta = \pi$, in this case are

$$\int_{r_i}^{r_e} \sigma_{\theta} dr = \int_{r_i}^{r_e} \sigma_{\theta} r dr = 0 \quad (17)$$

Using Eqs.(12) - (16), the final global equation is constituted for the entire C-block to solve for the constants defined in Eq.(12) and in displacement formulas (not shown due to the length limit). In general, this equation can be expressed in matrix form as follows.

$$\mathbf{Ax} = \mathbf{f} \quad (18)$$

where, the vector \mathbf{x} consists of the undetermined constants in stress and displacement functions and the vector \mathbf{f} consists of applied displacements, the applied forces and the equivalent forces caused by induced strains.

End Moment

For C-blocks with only an end moment, M , a similar solution procedure described above are used. However, the induced strain Λ is set to zero in all equations, Eqs.(12) - (17), and the second equation in Eq.(12) is modified to take into account the free end moment as follows.

$$\int_{r_i}^{r_e} \sigma_{\theta} r dr = -M \quad (19)$$

End Force

For C-blocks with only an end force, P , the bending moment at any cross section is proportional the $\sin(\pi-\theta)$ and the normal stress σ_{θ} is proportional to the bending moment^[8]. The stress function is found to be in the form

$$\phi = F(r) \sin \alpha \quad (20)$$

where

$$\alpha = \pi - \theta \quad (21)$$

For C-block actuators, the material axes and the geometric coordinates are always identical. This implies that $a_{16} = a_{26} = 0$. Therefore, Eq.(6) is simplified as follows.

$$\left(\frac{\partial^2}{\partial \theta^2} - r \frac{\partial}{\partial r} \right) \left[a_{11} \left(\frac{1}{r} \frac{\partial \phi}{\partial r} + \frac{\partial^2 \phi}{\partial \theta^2} \right) + a_{12} \frac{\partial^2 \phi}{\partial r^2} \right] + r^2 \frac{\partial^2}{\partial r^2} \left[a_{12} \left(\frac{\partial \phi}{\partial r} + \frac{1}{r} \frac{\partial^2 \phi}{\partial \theta^2} \right) + a_{22} r \frac{\partial^2 \phi}{\partial r^2} \right] + a_{66} \frac{\partial^2}{\partial r \partial \theta} \left[r \frac{\partial^2}{\partial r \partial \theta} \left(\frac{\phi}{r} \right) \right] = 0 \quad (22)$$

Substituting Eq.(20) into Eq.(22), the stress function, F , satisfy the following equation

$$r^4 F^{IV} + 2r^3 F''' - \beta r^2 F'' + \beta(rF' - F) = 0 \quad (23)$$

where

$$\beta = \frac{2a_{12} + a_{11} + a_{66}}{a_{22}} \quad (24)$$

Following the same solution procedure to the characteristic equation, described in Eqs.(9) - (11), the solution formulation in this case can be derived as

$$F = A_1 r^{\lambda_1} + B_1 r^{\lambda_2} + C_1 r + D_1 r \log r \quad (25)$$

with

$$\lambda_{1,2} = 1 \pm \sqrt{1 + \beta} \quad (26)$$

Therefore, the stress components can be written as follows

$$\begin{aligned} \sigma_r &= \left(\frac{F'}{r} - \frac{F}{r^2} \right) \sin \alpha = \left[A_1 (\lambda_1 - 1) r^{\lambda_1 - 2} + B_1 (\lambda_2 - 1) r^{\lambda_2 - 2} + D_1 r^{-1} \right] \sin \alpha \\ \sigma_\theta &= F'' \sin \alpha = \left[A_1 \lambda_1 (\lambda_1 - 1) r^{\lambda_1 - 2} + B_1 \lambda_2 (\lambda_2 - 1) r^{\lambda_2 - 2} + D_1 r^{-1} \right] \sin \alpha \\ \tau_{r\theta} &= - \left(\frac{F}{r} \right)' \cos \alpha = - \left[A_1 (\lambda_1 - 1) r^{\lambda_1 - 2} + B_1 (\lambda_2 - 1) r^{\lambda_2 - 2} + D_1 r^{-1} \right] \cos \alpha \end{aligned} \quad (27)$$

Next, the procedure described in Eqs.(13) - (17) is followed to derive the global equation governing the entire C-block actuator. An additional boundary condition describing the free end force is required to solve for all the unknown constants, and is

$$\int_{r_i}^{r_e} \tau_{r\theta} dr = -P \quad (28)$$

The final step involves the superposition of all three solutions to characterize the general behavior of the C-block actuators.

RESULTS AND DISCUSSIONS

Numerical results obtained using the current elasticity approach are compared with those obtained using the existing curved beam approach^[2-4], the first-order shear deformation theory based approach^[5] and the classical elasticity solution with only the equivalent moment^[6]. The material properties used for the C-blocks are listed in Table 1, where the subscripts p , b , e are used to denote the properties for the piezoelectric layer, the bonding layer and the electrode layer, respectively, E is the Young's modulus and ν is the Poisson's ratio. The dimensions of the C-blocks are listed in Table 2, where t represents of the layer thickness. In all example, the induced strains have the same magnitude and the opposite sign in different layers.

Table 1. Material properties and miscellaneous parameters.

Material Properties		Other Parameters	
E_b (N/m ²)	1.9x10 ⁹	v_{max} (volts)	500
E_p (N/m ²)	5.4x10 ⁹	E_3 (V/m)	30.0x10 ⁵
E_e (N/m ²)	7.0x10 ⁸	d_{31} (m/V)	2.3x10 ⁻¹¹
ν_p	0.31	ν_b, ν_e	0.25

Table 2. Dimensions of the C-Blocks

Property	Two Layer Thick	Two Layer Thin	Three Layer
t_b (mm)	0.0	0.0	0.020
t_e (mm)	0.0	0.0	0.0
t_p (mm)	0.035	0.0007	0.025
r_i (mm)	0.065	14.9883	0.065
r_e (mm)	0.135	15.0117	0.135

In Fig.3, comparisons are made to examine the end deflection of both thin and thick two layered C-blocks with only the induced strain. The solution excluding the local induced strain effect can be calculated from classical elasticity method for curved beams with an equivalent moment. The current elasticity solution agrees with the existing curved beam approach, while both the first-order theory based approach and the classical elasticity solution over estimate the end deflection. This indicates that transverse effects tend to make the end deflection larger and the local induced strain effect reduces the end deflection. Finally these two effects cancel out with each other in the presence of only induced strain. This explains why the curved beam approach^[2,3], although technically inaccurate since it excludes both of these effects, arrives at the right numbers and also shows good correlations with the experimental data^[2-4].

The stress distributions of a thick two-layered C-block actuator are presented in Figs.4 and 5. The local induced strain dramatically changes the stress distributions. The current elasticity solution shows reduction in both maximum normal stress in circumferential direction and maximum transverse normal stress in radial direction due to the local induced strain effect. The maximum stress in circumferential direction is reduced by more than 50 percent and the maximum transverse normal stress in radial direction is reduced by approximately 34 percent compared to the classical elasticity solution. The induced strain effect also causes the discontinuity of the stress distribution or its slope at the layer interface. This phenomenon, generally observed at the layer interface of composite laminates with different ply orientations, is observed here for C-blocks with identical piezoelectric layers.

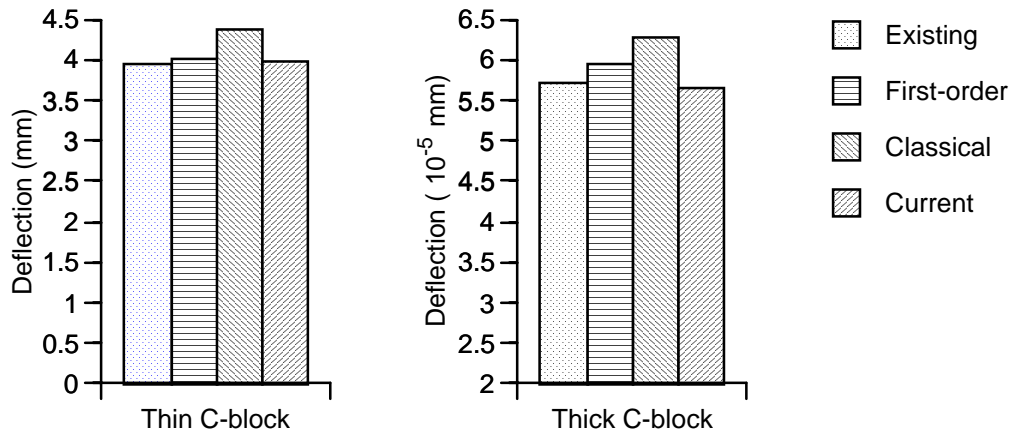


Fig.3 Comparison of end deflection for both thin and thick two layered C-blocks

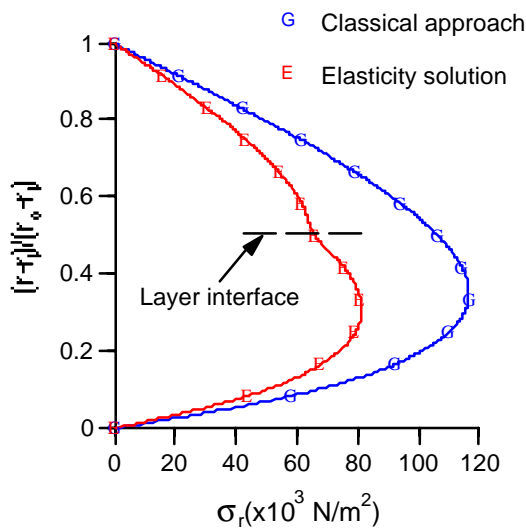


Fig.4 Comparison of transverse normal stress through two layered C-block thickness

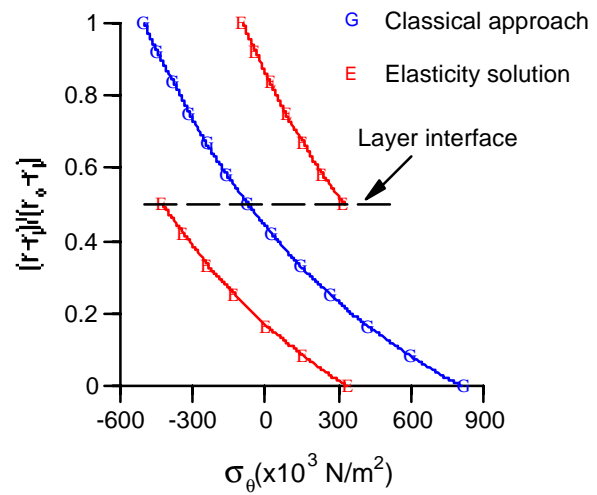


Fig.5 Comparison of normal stress through two layered C-block thickness

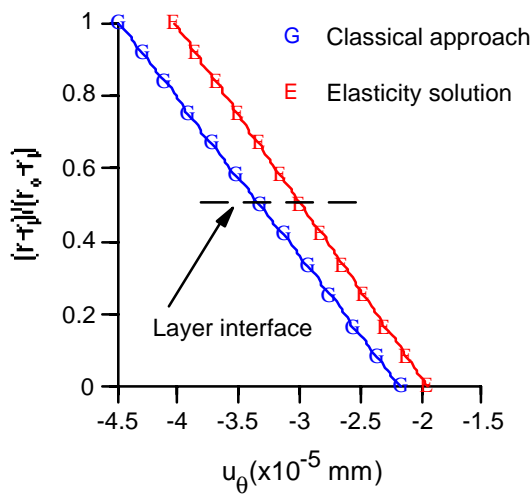


Fig.6 Comparison of circumferential displacement at free end for two layered C-block

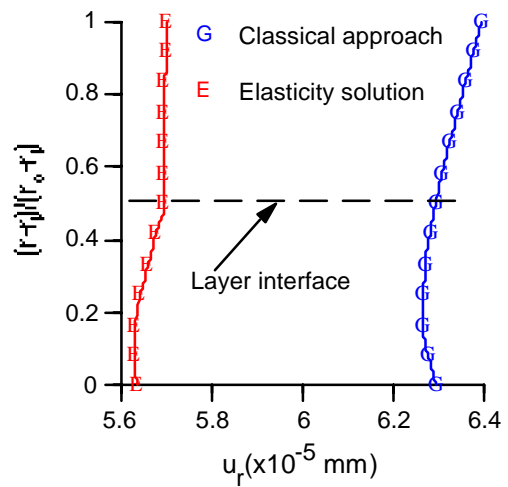


Fig.7 Comparison of radial displacement at free end for two layered C-block

The displacement distributions of the thick two layered C-block actuator are also shown in Figs.6 and 7. The local induced strain also changes the displacement distributions resulting in reduced displacements in the current elasticity solution. The local induced strain effect reduces the circumferential displacement by about 11% and the radial displacement by about 12% compared to the classical elasticity solution. The induced strain effect also causes the slope discontinuity of the radial displacement at the layer interface and changes its shape. This is also a phenomenon that is generally observed for composites with different layers.

In the next example, an end resistant force (Fig.2) is considered in conjunction with piezoelectric actuations for a three layered C-block actuator. In this example, the end resistant force is set to be 1 N/m and its direction of application is assumed to be opposite to the end deflection due to the induced strain. Figures 8-10 present the stress distributions for C-blocks without and with the end resistant force. The end resistant force dramatically changes the stress distributions, particularly for the transverse normal and the transverse shear stresses. It reduces the normal stress in circumferential direction and increases the transverse normal stress. The magnitudes of these changes depend on the magnitude of the end resistant force. Again, the transverse normal stress and the transverse shear stress change their slopes at layer interface and the circumferential normal stress shows discontinuity at the layer interface. It is noted that with presence of the end resistant force, the transverse shear deformation becomes significant. As shown in Figs.8 and 9, the transverse shear stress is larger than the transverse normal stress. Since shear modulus of a material is much smaller compared to its Young's modulus, the evidence indicates that the transverse shear deformation can be significantly larger. As mentioned before, the transverse normal effect is an important factor for C-blocks with only the induced strain. In the presence of the end resistant force, the transverse shear effect is expected to play more important role in the mechanical behavior of C-block actuators.

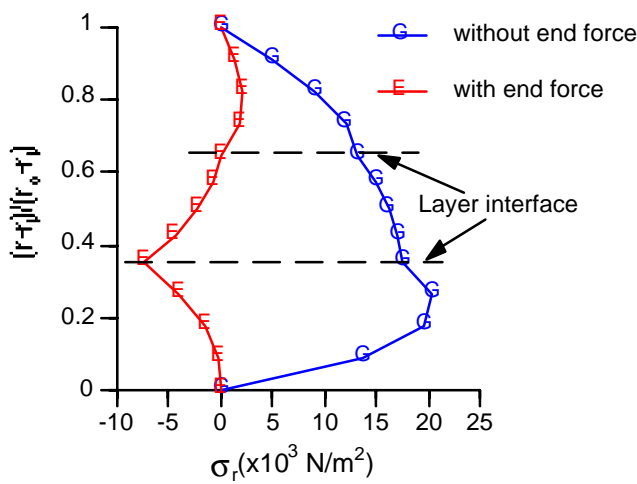


Fig.8 Transverse normal stress distribution near the clamped end for three layered C-block

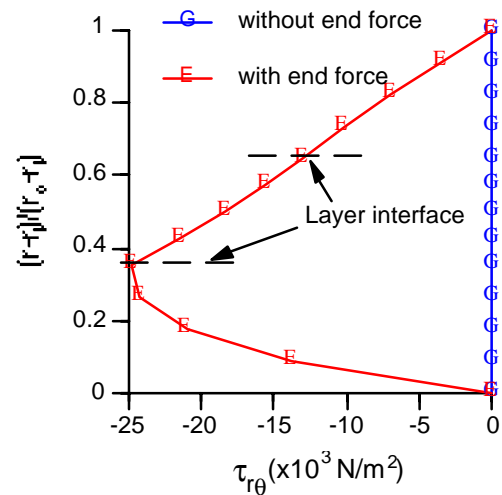


Fig.9 Transverse shear stress distribution at $\theta = 90^\circ$ for three layered C-block

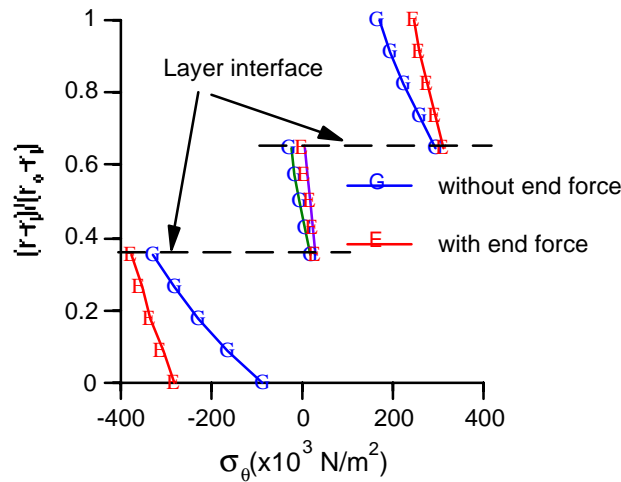


Fig.10 Normal stress distribution near the clamped end for three layered C-block

CONCLUSIONS

An elasticity solution is developed for the mechanical behavior of polymeric piezoelectric c-block composite actuators, which were developed recently to overcome the limitations of conventional bimorph and stack piezoelectric configurations. Since the solutions are exact within the assumptions of linear piezoelectricity, they are free from the simplifying assumptions imposed by the existing approaches. Therefore no distinctions need to be made in the analysis for thick or thin C-blocks and both transverse shear deformation and transverse normal deformation are automatically taken into account. The following important observations have been made from this study.

- (1) The developed solution technique provides a framework against which comparisons can be made of classical and other existing approaches. It also provides insight into the basis of assumptions that are necessary in the formulation of a more general theory for curved actuators.
- (2) The current elasticity solution for end deflections agree well with the existing curved beam approach which have been validated through experiments.
- (3) The transverse deformation and the local induced strain have the opposite effects on end deflections. Refined approaches including only one of these effects will introduce more error than the simple approach which excludes both.
- (4) The local effect of the induced strain dramatically changes the stress and displacement distributions and causes the discontinuity of these distributions or their slopes at the layer interface for multilayered C-blocks.
- (5) The transverse shear deformation is more critical in the case of multilayered C-blocks with the end resistant force.

ACKNOWLEDGMENT

The research is supported by the Air Force Office of Scientific Research, grant number: F49620-96-0195, technical monitor Dr. Brian Sanders.

REFERENCES

1. Crawley, E. F. and de Luis, J., "Use of Piezoelectric Actuators as Elements of Intelligent Structures", *AIAA Journal*, Vol. 5, No. 10, 1987, pp. 1373-1385.
2. Brei, D., "Design and Development of a New Class of Piezoelectric Actuators for Force Improvement", *Proc Society of Engineering Science 31st Annual Technical Meeting*, College Station TX, Oct. 10-12, 1994.
3. Brei, D., "Design and Development of a Piezoelectric Microactuator Building Block for Deflection Improvement" *Proc. Symposium on Micro-Mechanical Systems, ASME Winter Annual Meeting*, Chicago IL, Vol. 2., Nov. 6-11, 1994, pp. 717-723.
4. Seeley, C. E., Chattopadhyay, A. and Brei, D., "Development of a Piezoelectric C-block Actuator Using Hybrid Optimization Technique", *AIAA Journal*, Vol. 34, No.1, 1996, pp. 123-128.
5. Chattopadhyay, A., Mitchell, L.A. and Gu, H., Refined Modeling of Adaptive Composites with Curved Actuators, *Society of Engineering Science, 33rd Annual Technical Meeting Smart Structures and Materials Symposium*, Oct.20-23, 1996, Tempe, AZ
6. Crawley, E. F. and Anderson, E. H., "Detailed Models of Piezoelectric Actuation of Beams", *Proc. of the 30th AIAA/ASME/ASCE/AHS/ASC Structures, Structural Dynamics and Materials Conference*, Mobile, Al., April 1989, pp. 2000-2010.
7. Lekhnitskii, S. G., *Theory of Elasticity of an Anisotropic Body*, Mir Publishers, Moscow, 1981
8. Timoshenko, S. P. and Goodier, J. N., *Theory of Elasticity*, International student Edition, McGraw-Hill Kogakusha, Ltd., 1970

ANISOTROPIC PIEZO-ELECTRO-THERMO-VISCOELASTICITY THEORY WITH APPLICATIONS TO COMPOSITES

H. H. Hilton¹, J. R. Vinson² and S. Yi³

¹*Aeronautical and Astronautical Engineering Department and National Center for Supercomputing Applications, University of Illinois at Urbana-Champaign, 104 South Wright Street, Urbana, IL 61801-2935 USA*

²*Mechanical and Aerospace Engineering and Center for Composite Materials, University of Delaware, 126 Spencer Laboratory, Newark, DE 19716-3140 USA*

³*School of Mechanical and Production Engineering, Nanayang Technological University Nanyang Avenue, Singapore 2263, Rep[ublic of Singapore*

SUMMARY: The general nonlinear 3-D large deformation theory of anisotropic piezo-electro-thermo-viscoelasticity is formulated and represents the confluence of anisotropic elasticity and thermo-viscoelasticity, nonhomogeneous layered media and piezoelectricity. In addition to piezoelectric contributions, the anisotropic nonlinear viscoelastic constitutive relations also included thermal expansion, curing and aging effects. For linear materials and small deformations, a piezoelectric/piezo-viscoelastic⁴ analogy is established in terms of integral Fourier and Laplace transforms. In order to demonstrate the effectiveness of the above piezo-viscoelastic constitutive relation derivations, piezoelectric examples of beam solutions have been re-formulated in terms of piezo-viscoelastic constitutive relations and solved analytically and numerically using viscoelastic finite element analyses. Comparisons with piezoelectric solutions are made and viscoelastic influences on generated voltages and structural control are discussed.

KEYWORDS: nonlinear piezo-electro-thermo-viscoelasticity, constitutive relations, finite element analysis, interlaminar stresses, polymer matrix, viscoelastic laminated composites, beams

1 INTRODUCTION

Bailey & Hubbard [1] have reported on the design of experiments with a distributed piezoelectric-polymer active control of a cantilever beam, but unfortunately did not offer an accompanying viscoelastic analysis of the system. A limited number of analytical and experimental publications on linear piezo-viscoelastic materials may be found in Law *et al.* [2], Perrissinfabert & Jayet [3] and Thomas *et al.* [4].

However, constitutive relations for small deformation piezoelectricity have been derived from first principles by Mindlin [5], Tiersten [6], Leibowitz & Vinson [7-9], Tzou [10] and Yu [11], for large deformations by Toupin [12] and Eringen [13], and for elastic composites by Jones *et al.* [14] and Vinson [15-18], to mention only a few.

Larson & Vinson [19, 20], Leibowitz & Vinson [7-9] and Newill & Vinson [21] have formulated extensive analyses for the behavior of piezoelectric materials in association with

elastic composites and sandwich construction in beams, plates and shells. They have demonstrated the feasibility of control in structural components and structures.

Aging effects in composites are beginning to receive serious analytical and experimental attention (Brinson & Gates [22], Feng [23], Gates & Feldman [24, 25], Monaghan *et al.* [26] Struik [27]), but no published data seems available on PVM aging.

2 ANALYSIS

2.1 Modeling of Constitutive Piezoelectric Viscoelastic Relations

Piezo-viscoelastic constitutive relations can be deduced from their elastic counterparts, consequently the elastic relations are first extended and generalized to anisotropic large deformations including thermal expansions as

$$\tau_j^{ie} = C_{ji}^{ik} \gamma_k^{le} - C_{ji}^{iE} E^{le} - C_{ji}^{ikT} \mathcal{A}_k^l T \quad (2.1.1)$$

and

$$D^{ie} = C_i^{ikE} \gamma_k^{le} + C_i^{iE} E^{le} \quad (2.1.2)$$

where τ_j^{ie} are the elastic Cauchy stress tensors, γ_k^{le} the Green-Zerna [28] elastic large strain tensors, C_{ji}^{ik} and C_{ji}^{ikT} the elastic stiffness matrices, C_{ji}^{iE} the electrical elastic stiffness matrix or the piezoelectric stress/charge matrix, C_i^{iE} the dielectric permittivity matrix, E^{le} the electrical field intensity vectors, $\mathcal{A}_k^l T$ the thermal expansions and D^{ie} the electric displacement vectors. Correspondingly, all similar variables without the superscript *e* refer to viscoelastic quantities.

Secondly, following the developments of Hilton & Dong [29] and Hilton & Yi [30], these relations can be extended to piezo-viscoelastic behavior in terms of corresponding relaxation or creep functions ϕ or ψ in spatial intrinsic curvilinear coordinates $\theta = (\theta^i) = (\theta^1, \theta^2, \theta^3)$ and time t as

$$\begin{aligned} \tau_j^i(\theta, t) = & \int_{-\infty}^t \frac{\partial \phi_{ji}^{ik}(\theta, t, t')}{\partial t'} \gamma_k^l(\theta, t') dt' - \int_{-\infty}^t \frac{\partial \phi_{ji}^{iE}(\theta, t, t')}{\partial t'} E^l(\theta, t') dt' \\ & - \int_{-\infty}^t \frac{\partial \phi_{ji}^{ikT}(\theta, t, t')}{\partial t'} \mathcal{A}_k^l T(\theta, t') dt' - \int_{T^*}^T \phi_j^{sth}(\theta, t, t') dt' - \int_{\alpha^*}^{\alpha} \phi_j^{ich}(\theta, t, t') dt' \end{aligned} \quad (2.1.3)$$

and

$$D^i(\theta, t') = \int_{-\infty}^t \frac{\partial \phi_i^{ikE}(\theta, t, t')}{\partial t'} \gamma_k^l(\theta, t') dt' + \int_{-\infty}^t \frac{\partial \phi_i^{iE}(\theta, t, t')}{\partial t'} E^l(\theta, t') dt' \quad (2.1.4)$$

where ϕ_j^{sth} are thermal anisotropic relaxation functions, ϕ_j^{ich} are chemical shrinkage anisotropic relaxation functions and $T^*(\theta, t^*)$ and $\alpha^*(\theta, t^*)$ respectively are stress-free reference temperatures and the corresponding degrees of cure, occurring at some initial time t^* . The last two integrals in Eqn 2.1.3 are only present during manufacturing processes and are excluded during service conditions. For chronologically simple materials, reduced linear isotropic aging times ξ have been presented by Brinson & Bates [22], Feng [23], Monaghan *et al.* [26] and Struik [27]. Such ξ s have been extended by Hilton & Yi [30] to include nonlinear anisotropic effects, but would call for as many as 45 individual ξ s for PVMs. The ξ approach is, therefore, unmanageable for stress-displacement analyses, but remains most useful for characterizing material behavior under variable environmental exposures.

The Brinson & Gates [22] isotropic aging shift function model has been generalized by Hilton & Yi [30] to 3-D anisotropic viscoelasticity and can now be further generalized to

model PVMs by the inclusion of piezoelectric effects, such that the aging shift functions a_{jl}^{ikag} become

$$a_{jl}^{ikag} = \left[\frac{t_e}{t_e + t} \right]^{\mu_{jl}^{ik}} \quad (2.1.5)$$

where t_e is the aged time before service, t the service time and $\mu_{jl}^{ik}(T, M, I, I^{\mathbf{E}})$ are anisotropic material property parameters for PVMs. At the moment, there is insufficient experimental data available to properly characterize the μ_{jl}^{ik} functions and it is unknown how they are affected by electric and/or strain environments. However, corresponding reduced times ξ_j^{ikag} can be defined in a general functional manner as

$$\xi_j^{ikag}(\theta, t) = \int_0^t a_{jl}^{ikag}[\theta, s, T(\theta, s), M(\theta, s), I(\theta, s), I^{\mathbf{E}}(\theta, s)] ds \quad (2.1.6)$$

All these relaxation functions depend on environmental conditions and in nonlinear cases on strain rates as well, such that any $\phi(\theta, t, t', t_e) = \phi[\theta, t, t', t_e, M(\theta, t'), T(\theta, t'), \alpha(\theta, t'), \dot{I}(\theta, t')]$, with $M(\theta, t, T, \alpha)$ the moisture content, $\dot{I} = \{\dot{I}_i(\theta, t)\}$ the three fundamental strain rate invariants and $\alpha(\theta, t, M, T)$ the degree of cure. During cure $0 \leq \alpha \leq 1$, but while PVMs are in service when $\alpha = 1$, α makes no contribution to any portion of the above relations. In particular, relaxation functions denoted by the superscript \mathbf{E} , but also all other ϕ s, can additionally and independently be made functions of an invariant of E^l (the viscoelastic electrical field intensity vectors), such as $I_a^{\mathbf{E}}(\theta, t) = tr\{E^l\}$, resulting in nonlinear material property electrical intensity effects or conversely exhibiting a dependency on electric displacements through $I_b^{\mathbf{E}}(\theta, t) = tr\{D^l\}$, where $I^{\mathbf{E}}$ represents either electric invariant.

The functional dependence of any and all of the above nonlinear anisotropic relaxation functions can in general be defined as

$$\phi_{jl}^{ik}(\theta, t, t', t_e, M, T, \alpha, \dot{I}, I^{\mathbf{E}}) = \quad (2.1.7)$$

$$\sum_{\underline{m}=0}^{\underline{M}_{jl}^{ik}} \sum_{\underline{p}=0}^{\underline{P}_{jl}^{ik}} \sum_{\underline{q}=0}^{\underline{Q}_{jl}^{ik}} \sum_{\underline{r}=0}^{\underline{R}_{jl}^{ik}} B_{\underline{j}lmpqr}^{ik}(\theta, t, t', t_e, M, T, \alpha) (\dot{I}_1 - 3)^{\underline{m}} (\dot{I}_2 - 3)^{\underline{p}} (\dot{I}_3 - 1)^{\underline{q}} (I^{\mathbf{E}} - 3)^{\underline{r}}$$

where underscores indicate no summations over the affected indices, and where the parameters \underline{M}_{jl}^{ik} , \underline{P}_{jl}^{ik} , \underline{Q}_{jl}^{ik} and \underline{R}_{jl}^{ik} and the functions $B_{\underline{j}lmpqr}^{ik}$ are material dependent and represent distinct functional sets for each of the directional ϕ_{jl}^{ik} , $\phi_{jl}^{i\mathbf{E}}$, $\phi_l^{ik\mathbf{E}}$, $\phi_j^{i\mathbf{E}}$, $\phi_j^{ik\mathbf{T}}$, $\phi_j^{i\mathbf{th}}$ and $\phi_j^{i\mathbf{ch}}$, which must be experimentally generated for each material and environmental condition. Since the curing time scale is relatively short (about 300 min), the degree of cure α and the manufacturing process relaxation functions $\phi_j^{i\mathbf{th}}$ and $\phi_j^{i\mathbf{ch}}$ are unaffected by t_e . For linear materials, none of the parameters are dependent on any of the invariants of strains and/or of the electric field intensity and displacement. Additionally, for small deformations the stresses τ_j^i and strains γ_j^i reduce to their Cartesian engineering counterparts σ_{ij} and ϵ_{ij} and $x_i = \theta^i$.

Thus, linear and nonlinear isotropic and anisotropic viscoelastic PVM behaviors are completely defined in terms of the modeled constitutive relations, but experimental determination of the Eqn 2.1.7 material B functions remains to be carried out and represents a formidable task.

2.2 Field Equations

The field equations, being of a geometric nature, are unaffected by the choice of constitutive relations and conceptually apply equally to piezoelectric and piezo-viscoelastic formulations. They consist of relations for conservation of linear momentum

$$\tau^{ij}||_i + \rho F^j = \rho \frac{\mathcal{D}^2 v^j}{\mathcal{D}t^2} \quad (2.2.1)$$

and of strain definitions in terms of displacement vectors v_i or metric tensors G_{ij} and g_{ij} of the deformed and undeformed space

$$\gamma_{ij} = \frac{1}{2}(v_i|_j + v_j|_i + v^r|_i v_r|_j) = \frac{1}{2}(G_{ij} - g_{ij}) \quad (2.2.2)$$

where the single | refer to covariant differentiation in the undeformed space and the double ones, ||, denote covariant derivatives in the deformed space. The r. h. s. of Eqns 2.2.1 contain the acceleration (inertia) terms, ρ is the density and F^j are components of body forces other than inertia generated by all the integrals of Eqns 2.1.3 except the first.

The boundary conditions are given in the usual two parts as

$$\tau^{ij} n_j = P^i \quad \text{on } \Gamma_\tau(\theta, t) \quad (2.2.3)$$

$$v_i = \tilde{v}_i \quad \text{on } \Gamma_v(\theta, t) \quad (2.2.4)$$

where n_j are the components of the unit outward normal to the boundary surface Γ_τ over which the force P^i act and \tilde{v}_i are the displacement vectors on the boundary surface $\Gamma_v \neq \Gamma_\tau$.

Additional field relations due to electrodynamics are

$$D^i||_i = 0 \quad \text{in } V(\theta, t) \quad (2.2.5)$$

where the D^i are defined by Eqns 2.1.4 and with boundary conditions

$$D^i n_i = S \quad \text{on } \Gamma_S(\theta, t) \quad (2.2.6)$$

$$\Phi = \tilde{\Phi} \quad \text{on } \Gamma_\Phi(\theta, t) \quad (2.2.7)$$

where S and $\tilde{\Phi}$ are respectively the surface charge and surface potential on their boundary surfaces Γ_S and Γ_Φ , V is the total body volume enclosed by the total surface $\Gamma = \Gamma_\tau + \Gamma_v + \Gamma_S + \Gamma_\Phi$. For small deformations, fixed coordinates $x = (x_i)$ replace the embedded θ^i ones and covariant derivatives reduce to the usual partial ones, i. e. $F^i|_j \equiv \partial F_i / \partial x_j \equiv F_{i,j}$. It should be noted that deformations may be large enough in nonlinear formulations, so that any or all boundary surfaces Γ and volumes V depend implicitly on displacements and thereby become part of the solution themselves as well as in addition to the usual variables T, γ, E^l and D^i .

2.3 Solution Strategies

Piezoelastic and piezo-viscoelastic formulations yield the additional coupled relations (2.1.2) or (2.1.4) and (2.2.5) - (2.2.7) and extra unknowns E^{ie} or E^l . Nonlinearities arise independently from two sources: (a) nonlinear material properties and (b) large deformations. Due to the ever present body forces caused by piezoelectric contributions in Eqns 2.2.1, no separation of variable solution can be achieved even when the formulation is totally linear and isotropic (Christensen [31], Hilton [32]) nor in the anisotropic linear case even in the absence of body forces, except under trivial unrealistic material characterizations (Hilton [33]). However, in the linear case sums of separable solutions of the type

$$\sigma_{ij}(x, t) = \sum_{n=1}^{\infty} A_n(x) B_n(t) \quad (2.3.1)$$

can be obtained for certain classes of problems and convergence must be established on an individual basis.

For linear materials and small deformations, a piezoelastic/piezo-viscoelastic analogy can be established in terms of integral Fourier (FT) and Laplace (LT) transforms. The FT of the elastic solution are

$$\overline{\sigma}_{ij}^e(x, \omega) = \overline{\sigma}_{ij}^e(x, \omega, C_{ijkl}^E, C_{ijkl}^E, C_{ikl}^E, C_{il}^E, C_{ijkl}^T, \overline{\overline{\mathcal{A}}}_{kl} \overline{\overline{T}}, \overline{\overline{S}}, \overline{\overline{\Phi}}, \overline{\overline{P}}_i, \overline{\overline{v}}_i) \quad (2.3.2)$$

and

$$\overline{\overline{E}}_i^e(x, \omega) = \overline{\overline{E}}_i^e(x, \omega, C_{ijkl}^E, C_{ijkl}^E, C_{ikl}^E, C_{il}^E, C_{ijkl}^T, \overline{\overline{\mathcal{A}}}_{kl} \overline{\overline{T}}, \overline{\overline{S}}, \overline{\overline{\Phi}}, \overline{\overline{P}}_i, \overline{\overline{v}}_i) \quad (2.3.3)$$

where the underscore indicates no summation.

The FT of the piezo-viscoelastic solution look similar, but with elastic material property parameters replaced by the FT of corresponding viscoelastic material property functions, such that

$$\overline{\sigma}_{ij}(x, \omega) = \overline{\sigma}_{ij}(x, \omega, \overline{\overline{\phi}}_{ijkl}, \overline{\overline{\phi}}_{ijkl}^E, \overline{\overline{\phi}}_{ikl}^E, \overline{\overline{\phi}}_{il}^E, t_e, \mu_{ijkl}, \overline{\overline{\phi}}_{ijkl}^T, \overline{\overline{\mathcal{A}}}_{kl} \overline{\overline{T}}, \overline{\overline{S}}, \overline{\overline{\Phi}}, \overline{\overline{P}}_i, \overline{\overline{v}}_i) \quad (2.3.4)$$

and

$$\overline{\overline{E}}_i(x, \omega) = \overline{\overline{E}}_i(x, \omega, \overline{\overline{\phi}}_{ijkl}, \overline{\overline{\phi}}_{ijkl}^E, \overline{\overline{\phi}}_{ikl}^E, \overline{\overline{\phi}}_{il}^E, t_e, \mu_{ijkl}, \overline{\overline{\phi}}_{ijkl}^T, \overline{\overline{\mathcal{A}}}_{kl} \overline{\overline{T}}, \overline{\overline{S}}, \overline{\overline{\Phi}}, \overline{\overline{P}}_i, \overline{\overline{v}}_i) \quad (2.3.5)$$

While the use of FT analogies provides elegant analytical solutions, in more complicated problems where finite element analyses (FEA) have to be employed and where body forces are present, it has been shown (Yi & Hilton [34, 35]) that their computational effectiveness is severely limited and real time numerical solutions are the method of choice.

2.4 Bending of Beams

As an illustrative example, consider a dynamic linearly viscoelastic beam with top and bottom piezoelectric actuator layers patterned after the elastic problem configurations of Larson & Vinson [19, 20] and Leibowitz & Vinson [7-9] as shown in Fig. 1.

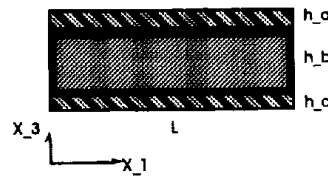


Fig. 1 - Piezoelectric Beam

At uniform temperatures and moisture contents and in the absence of aging effects, the homogeneous beam and actuator both obey distinct 1-D constitutive relations of the type

$$\sigma_{11}(x_1, x_3, t) = \int_{-\infty}^t \frac{\partial \phi(t-t')}{\partial t'} \epsilon_{11}(x_1, x_3, t') dt' \quad (2.4.1)$$

with individual relaxation functions ϕ . Applying the FT analogy of the previous section immediately produces the governing differential-integral equation for the outer surface strains ϵ^{sur}

$$6 \rho_a h_a \frac{\partial^4 \epsilon^{\text{sur}}(x_1, t)}{\partial t^2 \partial x_1^2} - 6 \left(\frac{2 \rho_b}{h_b} + \frac{4 \rho_a h_a}{h_b^2} \right) \frac{\partial^2 \epsilon^{\text{sur}}(x_1, t)}{\partial t^2} = \int_{-\infty}^t \frac{\partial [h_b \phi_b(t-t') + 6 h_a \phi_a(t-t')]}{\partial t'} \frac{\partial^4 \epsilon^{\text{sur}}(x_1, t')}{\partial x_1^4} dt' \quad (2.4.2)$$

with subscripts a and b referring to the actuator and beam respectively and with h denoting thicknesses. The natural boundary and kinematic conditions given by Larson & Vinson [19, 20] and Leibowitz & Vinson [7-9] are all, save one, material independent and the latter now becomes

$$\int_{-\infty}^t \frac{\partial [h_b \phi_b(t-t') + 6h_a \phi_a(t-t')]}{\partial t'} \epsilon^{\text{sur}}(x_1, t') dt' = 3h_a \int_{-\infty}^t \frac{\partial \phi_a(t-t')}{\partial t'} \Lambda(x_1, t') dt' =$$

$$3 \int_{-\infty}^t \frac{\partial \phi_a(t-t')}{\partial t'} \left\{ \int_{-\infty}^{t'} \frac{\partial \phi^{\text{E}}(t'-\hat{t})}{d\hat{t}} \mathbf{V}(x_1, \hat{t}) d\hat{t} \right\} dt' \quad (2.4.3)$$

where Λ is the strain induced by an applied piezoelectric voltage \mathbf{V} and for a PVM it is equal to the expression between the braces $\{ \}$ in Eqn 2.4.3 divided by h_a . In essence, Eqn 2.4.3 can be considered as either prescribing the surface strains ϵ^{sur} or the necessary piezoelectric voltage \mathbf{V} to maintain desired strains and deformations. The initial conditions dictate that all variables equal their corresponding elastic values at $t = 0$ with relaxation function values $\phi(x, 0)$ and relaxation moduli $E(x, 0) = \partial \phi(x, 0) / \partial t$.

It is to be noted that this problem formulation is "simple" enough to lend itself to analytical solutions by FT and proper interpretation of corresponding elastic solutions with the introduction of appropriate complex relaxation functions $\bar{\phi}(\omega)$. In more "complicated" problems with temperature, moisture, degree of cure dependent nonhomogeneous and/or nonlinear materials, the above relaxation function definitions $\phi(t-t')$ are replaced by the general expressions (2.1.7) with $\theta = x$. In these circumstances, analytical solutions are not achievable and numerical spatial FEM and temporal FD must be employed (Yi *et al.* [34-36]).

3 DISCUSSION OF RESULTS

Typical mechanical and dielectric viscoelastic material property data have been given respectively by Nashif *et al.* [37] and McCrum *et al.* [38]. Under constant environmental conditions, linear relaxation functions of Eqns 2.4.1 for the beam (ϕ_b), piezoelectric actuator elements (ϕ_a) and for the voltage-displacement (ϕ^{E}) may be characterized as

$$E_b(t) = \frac{d\phi_b(t)}{dt} = \sum_{n=0}^{N^b} \phi_n^b \exp(-t/\tau_n^b) \quad E_a(t) = \frac{d\phi_a(t)}{dt} = \sum_{n=0}^{N^a} \phi_n^a \exp(-c^a t/\tau_n^a)$$

$$E^{\text{E}}(t) = \frac{d\phi^{\text{E}}(t)}{dt} = \sum_{n=0}^{N^{\text{E}}} \phi_n^{\text{E}} \exp(-c^{\text{E}} t/\tau_n^{\text{E}}) \quad (3.1)$$

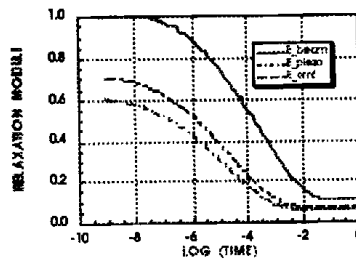


Fig. 2 - Beam and Piezoelectric Relaxation Moduli

where c is a shift function, which together with the ϕ_n s, τ_n s and N s represent material property parameters to be experimentally determined. These relaxation moduli $E = d\phi/dt$ are shown in Fig. 2 with $\phi_b(0) = 1$, $\phi_b(\infty) = .1$, $\phi_a(0) = .7$, $\phi_a(\infty) = .07$, $c^a = 10$, $\phi^E(0) = .6$, $\phi^E(\infty) = .06$ and $c^E = 15$ with all ϕ s normalized w. r. t. the beam elastic Young's modulus E_o^b . For the sake of simplicity, $\tau_n^a = \tau_n^b = \tau_n^E$ for corresponding n s.

The nondimensionalized quantities for the cantilever beams are $b = 1$, $h_a = .05$, $h_b = 9.5$, $L = 100$, $\rho_a = 2$ and $\rho_b = 1$. Two type of cantilever loads at $x = L$ were considered: (1) a constant end load $f = 1$ and (2) a time dependent one $f = \sin(\Omega t)$. Typical forcing frequencies Ω are 10^5 and 10^{10} Hz, as related to the operational times of Fig. 2. Additional details may be found in Hilton *et al.* [39]. The numerical computations associated with Eqns 2.4.1 - 2.4.3 and 3.1 were carried out in the Fourier transform domain ω on a MacintoshTM using MATLABTM for fast Fourier transforms and inversions.

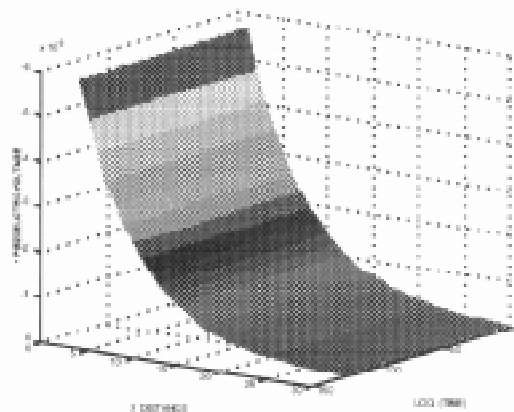


Fig. 3 - Voltages in Piezoelectric Beam Strip (const. load)

Representative piezoelectric voltages generated by these configurations are displayed

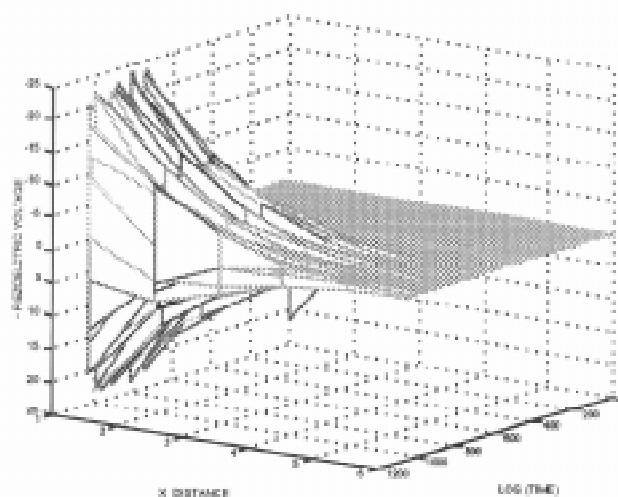


Fig. 4 - Voltages in Piezoelectric Beam Strip ($\Omega = 10^5$ Hz)

in Figs. 3 - 5. The $t = 0$ solutions are the corresponding elastic ones and the viscoelastic contributions for the cases considered indicate exponential decays in piezoelectric voltage responses in the x_1 axial direction, while bending stresses decrease linearly with x_1 for cantilever beams with single end loads. Note that for sinusoidal forcing functions $f = \sin(\Omega t)$, the effect of an increasing frequency is to generate an earlier emf since the forced oscillations begin at smaller t s for larger Ω s in relation to the moduli of Fig. 2. These results are also of importance in inverse problems, where voltages may be input to generate controlled displacements as prescribed by Eqns 2.1.2.

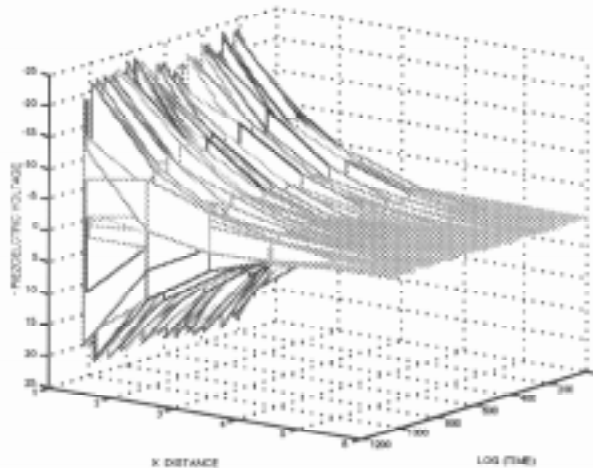


Fig. 5 - Voltages in Piezoelectric Beam Strip ($\Omega = 10^{10}$ Hz)

CONCLUSIONS

The illustrative linear numerical examples based on the formulation of nonlinear anisotropic piezoelectric viscoelasticity indicate the feasibility of generating substantial voltages. Conversely, such voltages can be used to control viscoelastic deformations and failure envelopes of composite structural elements.

REFERENCES

1. Bailey, T. and James E. Hubbard, J.E., "Distributed piezoelectric-polymer active vibration control of a cantilever beam," *Journal of Guidance, Control and Dynamics*, Vol. 8, 1985, pp. 605-611.
2. Law, H.H., Rossiter, P.L., Koss, L.L. and Simon, G.P., "Mechanisms in damping of mechanical vibration by piezoelectric ceramic polymer composite materials," *Journal of Materials Science*, Vol. 30, 1995, pp. 2648-2655.
3. Perrissinfabert, I. and Jayet, Y., "Simulated and experimental study of the electric impedance of a piezoelectric element in a viscoelastic medium," *Ultrasonics*, Vol. 32, 1994, pp. 107-112.
4. Thomas, V., Giacomini, A.J. and Wolfenden, A., "A rheometer to measure the viscoelastic properties of polymer melts at ultrasonic frequencies," *Review of Scientific Instruments*, Vol. 65, 1994, pp. 2395-2401.
5. Mindlin, R.D., "Forced thickness-shear and flexural vibrations of piezoelectric crystal plates," *Journal of Applied Physics*, Vol. 23, 1952, pp. 83-88.

6. Tiersten, H.F., *Linear Piezoelectric Plate Vibrations; Elements of the Linear Theory of Piezoelectricity and the Vibrations of Piezoelectric Plates*, Plenum Press, New York, 1969.
7. Leibowitz, M.M. and Vinson, J.R., "The use of Hamilton's principle in laminated piezoelectric and composite structures," *Proceedings 1993 ASME Winter Annual Meeting, Adaptive Structures and Materials Systems*, Garman, G.P. and Garcia, E., Eds., ASME, New York, Vol. AD-35, 1993, pp. 257-268.
8. Leibowitz, M.M. and Vinson, J.R., "On active (piezoelectric) constrained layer damping in composite sandwich structures," *Proceedings of the Fourth International Conference on Adaptive Structures*, Cologne, Germany, 1993.
9. Leibowitz, M.M. and Vinson, J.R., "The coupling between generally anisotropic composite structures and piezoelectric materials," *Proceedings of the Eighth Annual Conference of the American Society for Composites*, Cleveland, OH, 1993, pp. 151-161.
10. Tzou, H.S., *Piezoelectric Shells - Distributed Sensing and Control of Continua*, Kluwer Academic Publishers, Dordrecht, 1993.
11. Yu, Y.Y., *Vibrations of Elastic Plates - Linear and Nonlinear Dynamical Modeling of Sandwiches, Laminated Composites and Piezoelectric Layers*, Springer, New York, 1996.
12. Toupin, R.A., "The elastic dielectric," *Journal of Rational Mechanics and Analysis*, Vol. 5, 1956, pp. 849-915.
13. Eringen, A.C., *Nonlinear Theory of Continuous Media*, McGraw-Hill Book Co., New York, 1962.
14. Jones, R., Tay, T.E. and Williams, J.F., "Thermomechanical behaviour of composites," *Composite Material Response: Constitutive Relations and Damage Mechanisms*, Sih, G.C., Smith, G.F., Marshall, I.H. and Wu, J.J., Eds.), Elsevier Applied Science, London, 1987, pp. 49-59.
15. Vinson, J.R. and Sierakowski, R.L., *The Behavior of Structures Composed of Composite Materials*, Kluwer Academic Publishers, Hingham, MA, 1987.
16. Vinson, J.R., *Structural Analysis of Laminated Composites*, Technomic Publications Co., Lancaster, PA, 1988.
17. Vinson, J.R., *The Behavior of Thin Walled Structures: Beams, Plates and Shells*, Kluwer Academic Publishers, Boston, 1993.
18. Vinson, J.R., *The Behavior of Shells Composed of Isotropic and Composite Materials*, Kluwer Academic Publishers, Boston, 1993.
19. Larson, P.H. and Vinson, J.R., "The use of piezoelectric materials in curved beams and rings," *Proceedings 1993 ASME Winter Annual Meeting, Adaptive Structures and Materials Systems*, Garman, G.P. and Garcia, E., Eds., ASME, New York, Vol. AD-35, 1993, pp. 277-286..
20. Larson, P.H. and Vinson, J.R., "On the analysis of adaptive structures employing piezoelectric materials," *Proceedings of the Eighth Annual Conference of the American Society for Composites*, Cleveland, OH, 1993, pp. 141-150.
21. Newill, J.F. and Vinson, J.R., "Use of piezoelectric intelligent materials to control vibrations in sandwich structures," *Proceedings Third International Conference on Sandwich Structures*, 1996, pp. 351-362.
22. Brinson, L.C. and Gates, T.S., "Effects of physical aging on long term creep of polymers and polymer matrix composites," *Journal of Solids and Structures*, Vol. 32, 1995, pp. 827-846.

23. Feng, W.W., "A constitutive equation for the aging of elastomers," *Recent Advances in Elasticity, Viscoelasticity and Inelasticity*, Rajagopal, K.R., Ed., World Scientific, Singapore, 1995, pp. 7-16.
24. Gates, T.S. and Feldman, M., "Time dependent behavior of graphite thermoelastic composite and the effects on stress and physical aging," *NASA Langley TM 109047*, 1993.
25. Gates, T.S. and Feldman, M., "The effects of physical aging at elevated temperatures on the viscoelastic creep of IM7/K3B," *NASA Langley TM 109114*, 1994.
26. Monaghan, M.R., Brinson, L.C. and Bradshaw, R.D., "Analysis of variable stress history on polymeric composite materials with physical aging," *Composite Engineering*, Vol. 4, 1994, pp. 1023-1032.
27. Struik, L.C.E., *Physical Aging in Amorphous Polymers and Other Materials*, Elsevier Scientific Publishing, New York, 1978.
28. Green, A.E. and Zerna, W., *Theoretical Elasticity*. Oxford University Press, New York, 1968.
29. Hilton, H.H. and Dong, S.B., "An analogy for anisotropic, nonhomogeneous, linear viscoelasticity including thermal stresses," *Development in Mechanics*, Pergamon Press, New York, 1964, pp. 58-73.
30. Hilton, H.H. and Yi, S., "Theory of anisotropic nonlinear viscoelasticity with applications to composites," in press *Proceedings of the Second World Congress of Nonlinear Analysts*, Athens, 1996. Also *University of Illinois UIUC, Technical Report UILU-ENG 96-0516*, 1996.
31. Christensen, R.M., *Theory of Viscoelasticity - An Introduction*, Second Edition, Academic Press, New York, 1982.
32. Hilton, H.H., "An introduction to viscoelastic analysis," *Engineering Design for Plastics*, Baer, E., Ed., Reinhold Publishing Corp., New York, 1964, pp. 199-276.
33. Hilton, H.H., "On the inadmissibility of separation of variable solutions in linear anisotropic viscoelasticity," *International Journal of Mechanics of Composite Materials and Structures*, Vol. 3, 1996, pp. 97-100.
34. Yi, S. and Hilton, H.H., "Anisotropic viscoelastic finite element analysis of mechanically and hygrothermally loaded composites," *International Journal of Composite Engineering*, Vol. 3, 1993, pp. 123-135.
35. Yi, S. and Hilton, H.H., "Dynamic finite element analysis of viscoelastic composite plates in the time domain," *International Journal for Numerical Methods in Engineering*, Vol. 37, 1994, pp. 4081-4096.
36. Yi, S., Hilton, H.H. and Ahmad, M.F., "Nonlinear thermoviscoelastic analysis of interlaminar stresses in laminated composites," *ASME Journal of Applied Mechanics*, Vol. 63, 1996, pp. 218-224.
37. Nashif, A.D., Jones, D.I.G. and Henderson, J.P., *Vibration Damping*, John Wiley & Sons, New York, 1985.
38. McCrum, N.G., Read, B.E. and Williams, G., *Anelastic and Dielectric Effects in Polymeric Solids*, Dover Publications, Inc., New York, 1991.
39. Hilton, H.H., Vinson, J.R. and Yi, S., "Anisotropic piezo-electro-thermo-viscoelasticity theory with applications to composites," *University of Illinois UIUC, Technical Report UILU-ENG 97-0501*, 1997.

SPATIAL DESIGN OF PIEZOELECTRIC SENSORS AND ACTUATORS FOR VIBRATION CONTROL OF LAMINATED COMPOSITE PLATES

Seung-Jo Kim, Ji-Hwan Kim, Keun-Young Park, and Jung-Kyu Ryou

Department of Aerospace Engineering, Seoul National University, 151-742, KOREA

SUMMARY: Distributed piezoelectric sensor and actuator have been designed for efficient vibration control of laminated composite plate. Electrode pattern of anisotropic piezoelectric film is adopted as design variables. Finite element method is used to model the structure that includes the piezoelectric sensor and actuator. To utilize the anisotropic characteristics of the PVDF film, various lamination angles of the PVDF transducer are considered.

Electrode of the PVDF film bonded over the plate is modeled with lots of small rectangular segments. Electrode pattern is optimized by deciding *on* or *off* of each electrode segment. Actuator design is based on the criterion of minimizing the system energy under a given initial condition. Sensor has been designed to minimize the observation spill-over. Modal forces for the residual modes have been selected as a performance index to be minimized during the sensor design. Genetic algorithm, which is suitable for this kind of discrete problems, is used for optimization. Discrete LQG is used to generate control law. Performance of the sensor, the actuator, and the integrated smart structure shows good agreement between analysis and experiment.

KEYWORDS: active vibration control, PVDF sensor and actuator design, distributed sensor/actuator, spatial filtering, electrode pattern

INTRODUCTION

Piezoelectric materials are widely used as sensors and actuators in active vibration control of structures. Lead zirconate titanate (PZT) and polyvinylidene fluoride (PVDF) are most popular ones. As PVDF has different characteristics from PZT, there needs different approach to utilize its advantages. In this research, PVDF is used as a sensor and an actuator. Although PVDF has shortcomings such as small actuation force compared with PZT, the electrode of PVDF can be shaped easily. Easiness of electrode pattern shaping is a big merit of PVDF.

The active control of composite plates is usually more difficult than that of the isotropic one. This is mainly due to the possibility of high modal density of the composite structures. As modal density increases, control modes and residual (uncontrolled) modes can lie more closely in frequency domain. Then, the controller, a kind of time domain filter, cannot sufficiently fulfill the conflicting requirements: Large control gain in control modes; and the necessity to avoid the instability in residual modes caused by spill-over [1]. Spatial domain filtering by use of the distributed sensor/actuator is beneficial to this kind of difficulties.

As researches on the distributed sensor/actuator, Baliey and Hubbard [2] introduced the concept of spatial filter. Lee and Moon [3] proposed the modal sensor/actuator in beam

structure by changing the shape(width) of the electrode. As researches on the anisotropy of PVDF, Lee[4] devised a sensor and an actuator which can sense and actuate the torsional mode using the lamination angle. Yu, Kang and Kim[5] investigated the control effectiveness by changing the lamination angle of the PVDF actuator.

Modal sensor/actuator is a promising solution for the spill-over problem, but it can not be implemented in two-dimensional structures. In this research, modal sensor/actuator concept is extended to two-dimensional structure by introducing electrode segments and deciding the electrode pattern through optimization.

SYSTEM MODEL

Effect of Anisotropy of PVDF and the Electrode Shape

There exists reciprocity between piezoelectric sensor and actuator[6]. A piezoelectric sensor that yields large amount of charge for a specific vibration mode will have large actuating force for that mode when used as an actuator. Sensor equation derived by Lee[6] says that the amount of induced charge, q in a piezoelectric sensor is

$$\begin{aligned}
 q &= -z \int_S \left[\bar{e}_{31(xy)} \frac{\partial^2 w}{\partial x^2} + \bar{e}_{32(xy)} \frac{\partial^2 w}{\partial y^2} + \bar{e}_{36(xy)} \frac{\partial^2 w}{\partial x \partial y} \right] dS \\
 &= \int_S \left[\bar{e}_{31(xy)} \varepsilon_x + \bar{e}_{32(xy)} \varepsilon_y + \bar{e}_{36(xy)} \frac{\gamma_{xy}}{2} \right] dS
 \end{aligned} \tag{1}$$

where, z is the distance from the neutral plane to the mid-plane of the sensor, and w is lateral displacement. S is the effective area of the sensor covered with electrode. \bar{e} 's and ε 's are piezoelectric constants and strain components, respectively. From the above equation, we can see that the amount of induced charge will increase if the piezoelectric sensor is located in highly strained region. Let's consider the case that the sign of strain changes from point to point in the region covered with a piezoelectric sensor. The charge induced in the positively strained area is canceled out by the charge induced in the negatively strained area, which leads to decrease of total induced charge. The piezoelectric constants, $\bar{e}_{ij(xy)}$, vary with the lamination angle of the anisotropic PVDF film. Therefore, both the electrode pattern and the lamination angle of the anisotropic PVDF transducer becomes more important. For PZT, the size and position of transducer have been given attentions in the same reason[7]. While PZT does not have any preferred direction in plane, PVDF has anisotropy. That is, its piezoelectric constant d_{31} is different from d_{32} , and consequently the piezoelectric constant e_{31} is different from e_{32} . Therefore, the sensing characteristics of the PVDF transducer vary with the lamination angle. The induced charge strongly depends on the lamination angle of the PVDF sensor. As the strain distribution is different from one vibration mode to another, the electrode shape that induces maximum charge will change from mode to mode.

Modeling of the Structure and Control Environment

Finite element method has been used to model the laminated composite plate integrated with piezoelectric sensor and actuator. The mass and stiffness of the integrated structure have been modeled using the Mindlin plate element with nine nodes. The piezoelectric sensor/actuator is divided into many rectangular electrode segments in each finite element. These electrode segments are determined to be *on* or *off* during the optimization process of the sensor/actuator.

Electrode of the segment selected to be *off* will be removed and thus this segment has no actuating force. All the segments selected to be *on* are electrically connected together. For example, let's assume 4 electrode segments in a plate element as shown in Fig. 1. If electrode segments ①, ②, and ③ are selected to be *on* and ④ is selected to be *off*, then the total actuation force by the piezoelectric actuator is as follows.

$$F_p = 1 \times (F_p^{(1)} + F_p^{(2)} + F_p^{(3)}) + 0 \times F_p^{(4)} \quad (2)$$

where, $F_p^{(i)}$ is the actuation force vector of i -th electrode segment. Notation of B_a instead of F_p will be used to represent the actuating force.

Equation of motion of the integrated structure is expressed as,

$$M\ddot{u} + Ku = B_a V_a \quad (3)$$

where, M and K are the mass matrix and stiffness matrices, respectively. u is discretized nodal displacement vector. Subscript a denotes actuator, and V_a is applied voltage.

Assuming modal viscous damping, Eqn 3 is expressed in modal coordinates. For computational efficiency, modal reduction is introduced;

$$\ddot{\eta}_R + c_R \dot{\eta}_R + \Lambda_R \eta_R = \Phi_R^T B_a V_a \quad (4)$$

where, η_R is a modal displacement, $c_R = \text{diag}(2\zeta_1\omega_1, \dots, 2\zeta_n\omega_n)$, $\Lambda_R = \text{diag}(\omega_1^2, \dots, \omega_n^2)$.

Φ_R is a matrix composed of eigenvectors. We define $\Phi_R^T B_a$ as modal force per unit voltage and it is used as a parameter for characterizing the piezoelectric sensors and actuators. If actuation force by a piezoelectric transducer is B_s , then charge induced to this transducer when used as a sensor is

$$q = B_s^T u. \quad (5)$$

A charge amplifier is used as an interfacing amplifier. The output signal through the amplifier is

$$y_{ca} = \frac{1}{C_a} B_s^T \Phi_R \eta_R. \quad (6)$$

where, $1/C_a$ is the gain of the charge amplifier.

Discrete LQG[8] has been used as a control law. To avoid aliasing, two low-pass filters have been used before the AD converter and after the DA converter. Filter was second order butterworth type. Since the size of the controller is limited by physical constraints, every structural mode can not be controlled. First two modes were selected to be controlled. These two modes have been considered during controller design. Fig. 2 shows the block diagram for the total system. The cut-off frequency of the low-pass filter was selected to lie between the third and fourth natural frequencies of the structure. These two filters in addition to the two structural modes will be considered during controller design. There are total eight state variables in the controller.

DESIGN OF SENSOR AND ACTUATOR

Electrode pattern of PVDF sensor/actuator with various lamination angles is optimized in this study. Genetic algorithm[9], which is suitable for this kind of discrete optimization problem, is used to decide whether a specific electrode segment is *on* or *off*. Schematic view of the integrated structure is shown in Fig. 4. The stacking sequence of the host structure is $[\pm 45^\circ]_s$. Mode shapes of the first two modes are presented in Fig. 5, and the natural frequencies of the first five modes are listed in Table 1. As shown in Fig. 5, the mode shape is unsymmetric

w.r.t. the center line, which comes from the coupling stiffness, D_{16} and D_{26} of the composite laminate. Therefore, PVDF transducer whose lamination angle of 45° and that of -45° have different modal effects. In this study, we adopted lamination angles of 45° , 30° , 15° , 0° , -15° , -30° , and -45° . With each lamination angle, optimal electrode pattern has been designed.

Among the natural frequencies of the integrated structure in this study, the second one and the third one are closely located. We decided to control the vibration upto the second mode. Time domain low-pass filter cannot successfully eliminate the signal that comes from the third mode vibration. And it is not desirable to use actuator that has the third and higher modal force components. PVDF sensor/actuator is optimized as follow:

Sensor Design Criteria

We want to maximize the modal forces for the control modes(1st and 2nd modes), and to minimize the modal forces for the residual modes(3rd to 5th mode). In other words, we want to maximize sensing signal from control modes, while minimizing that from the uncontrolled modes.

The performance index used is

$$J = \min(|\Phi_c^T B_s|) - \max(|\Phi_u^T B_s|) \quad (7)$$

where, subscript c and u represent the control and uncontrolled modes, respectively.

Actuator Design Criteria

System energy was selected as performance index:

$$J = E(0) / \int_0^\infty (\dot{\eta}_c^T \dot{\eta}_c + \eta_c^T \Lambda_c \eta_c + \rho g^T g) dt \quad (8)$$

Here $E(0)$ represents initial energy, and ρ is the weighting for the control signal g . This ρ does not affect the actuator design result. Specific mode can be weighted by changing the initial condition of the system. That is, if initial condition is pure first mode, then the acquired result will be a shape that maximizes the modal control force for the first mode. The larger a actuator retains modal actuation force in control mode, the sooner the system energy decays out. The system energy in the denominator in Eqn 8, therefore, will decrease.

Design Result and Discussion

To see the effect of anisotropy of the PVDF transducer, optimization of electrode pattern has been performed for various lamination angles. Selected initial conditions for the actuator design were pure first mode and pure second mode. Fig. 6 shows the variation of PVDF actuator's modal control forces with lamination angles. For comparison, modal control forces of actuator whose electrode covers the entire surface of plate(labeled AC) are included together. Optimized results in Fig. 6(a) are obtained with the initial condition of pure first mode and Fig. 6(b) with the initial condition of pure second mode.

From Fig. 6(a), we can see that there are not much differences in modal force between the optimized ones and those labeled AC. As the strain distribution of the first mode shape is of the same sign over the entire surface, almost all electrode segments are *on* except a few segments. Modal control forces for positive lamination angles differ from that for negative lamination angles. Unsymmetry of mode shape about the center line causes this difference.

Design results for the second mode show more severe unsymmetry. Differences exist between the optimized ones and those labeled *AC*. This is due to the fact that the second mode has relatively more complex (sign changing) strain distribution. The lamination angle which shows maximum control for the second mode is -45° as shown in Fig. 6(b). This also can be explained from the mode shape. As shown in Fig. 5, the second mode deflects more flexibly along the -45° direction and therefore has larger normal strain in that direction. Consequently, -45° lamination angle shows maximum force.

Based on the design criteria for PVDF transducer explained above, an actuator [labeled *A2(-30°)*] and a sensor [labeled *S(-15°)*] have been chosen for our integrated smart structure. Electrode patterns of these transducers are shown in Fig. 7. All the electrode segments in black are electrically connected together. Modal control forces of these transducers are listed in Table 2. Label, *A2(-30°)* means optimized actuator design result for the 2nd mode with lamination angle of -30° . Label, *S(-15°)* indicate optimized sensor with lamination angle of -15° . To show the effect of electrode pattern optimization, additional two transducers are included in Table 2. Labels, *AC(-15°)* and *AC(-30°)* mean that the electrode covers the entire surface of plate with lamination angles of -15° and -30° , respectively.

From Table 2, we can clearly see that the sensor, *S(-15°)* retains very small modal forces for the residual modes. Modal forces for the control modes are large enough. Therefore, the output signal from the residual modes can be negligible. This sensor is a kind of band-stop filter in modal coordinates.

Concerning the characteristics of actuator, the 2nd modal force of *A2(-30°)* is larger than that of *AC(-30°)* and *AC(-15°)*. This is the result of electrode pattern optimization.

EXPERIMENT

Experiment has been carried out to show the performance of our integrated structure. Transfer functions of the designed PVDF sensor and actuator are obtained by the impact hammer test. Experimental result has been compared with the result from analysis. During digital control using LQG, we get the closed-loop transfer function. Comparing this with the transfer function of sensor, we have demonstrated the vibration control capability of our integrated structure.

Specimen Preparation

Composite laminate was fabricated with HFG HT145/RS1222 carbon/epoxy prepreg. Nominal thickness of the prepreg is 0.125mm. Standard curing cycle recommended by the prepreg manufacturer is followed. Thickness of the PVDF film used in this experiment is 52 μ m. Photosensitizer is applied over the entire surface of PVDF film and dried in temperature controlled oven. After being exposed to light through the negative image of the optimized electrode pattern, the film is developed to leave protective coating on the active electrodes. Evaporatively deposited copper-nickel electrode is chemically etched out to shape the optimized electrode pattern. Ferric chloride is used as etchant. After washing out the etchant with water and the PVDF film is dried in air. The PVDF sensor is bonded on one surface and the actuator on the other surface with epoxy adhesive. Integrated structure is completed by attaching the electric lead wire and mounts for fixture.

Experimental Setup

Fig. 3 shows the experimental setup. The charge amplifier gain is 10^8 Volt/Farad and cut-off frequency of the low-pass filter is 100 Hz. Sensing signal is digitally sampled 5000 times per second at the AD converter just before the controller. Control output through the DA converter is limited to ± 4 Volt and applied to actuator via the high voltage amplifier whose gain is set to 100 Volt/Volt.

Excitation force from the impact hammer and the sensing signal from the charge amplifier are processed at the FFT analyzer to yield the transfer function of the integrated structure.

Experimental Result and Discussion

Experimentally obtained transfer functions are shown in Figs. 8(a) ~8(c). Comparing with the modal control forces listed in Table 2, designed PVDF sensor and actuator behave as expected in the finite element analysis. We can discriminate against the signal which comes from the residual modes with our optimized sensor, $S(-15^\circ)$. This is helpful to reduce the effect of observation spill-over. Our optimized actuator, $A2(-30^\circ)$, can effectively excite the structure to the second mode. Although the actuator retains modal forces of higher modes, the associated sensor does work to retard the instability of the integrated structure. Transfer function of the closed-loop system in Fig. 8(c) and that of the open-loop system in Fig. 8(a) show the vibration reduction in the amount of 9dB and 11dB for the first and the second modes, respectively.

CONCLUSION

Design methodology for distributed PVDF sensor and actuator for vibration control of laminated composite plate has been presented. Using the anisotropy of the PVDF film and the electrode shaping, PVDF transducer, which works as a spatial filter, has been designed. It is an extension of the concept of modal transducer to two-dimensional structure. Lamination angle of the PVDF film has influence on the characteristics of the transducer.

Sensor has been optimized to reduce the observation spill-over, and actuator has been optimized to maximize the modal force for a specific vibration mode. We can successfully reduce the signal from the residual modes and increase the modal force of the control mode. Experimental verification has been accomplished for the performance of the optimized sensor and actuator. Real time vibration control has been accomplished for the laminated composite plate integrated with the optimized sensor and actuator.

REFERENCES

1. Mark J. Balas, "Feedback Control of Flexible Systems," *IEEE Transactions on Automatic Control*, Vol. AC-23, No. 4, 1978, pp. 673-679.
2. T.Bailey and J.E.Hubbard,Jr., "Distributed Piezoelectric-Polymer Active Vibration Control of a Cantilever Beam," *J.Guidance, Control and Dynamics*, Vol.8, No.5, 1985, pp.605-611.
3. C.K. Lee, F. C. Moon, "Modal Sensors/Actuators," *J. of Applied Mechanics*, Vol. 57, 1990, pp. 434-441.

4. C.K. Lee, and F.C. Moon, "Laminated Piezoelectric Plates for Torsion and Bending Sensors and Actuators," *J. Acoust. Soc. Am.*, Vol. 85, pp. 2432-2439, 1989.
5. Jeong-Yoel Yu, Woo-Young Kang, and Seung-Jo Kim, "Elastic Tailoring of Laminated Composite Plate by Anisotropic Piezoelectric Polymers - Theory, Computation, and Experiment," *J. of Composite Materials*, Vol.29, No.9, 1995, pp. 1201-1221.
6. C.K. Lee, "Piezoelectric Laminates : Theory and Experiments for Distributed Sensors and Actuators," *Intelligent Structural Systems*, Kluwer Academic Pub., 1992, pp.75-167.
7. S. Devasia, T. Meressi, B. Paden, and E. Bayo, "Piezoelectric Actuator Design for Vibration Suppression: Placement and Sizing," *J. of Guidance, Control, and Dynamics*, Vol. 16, No.5, 1993, pp. 859-864.
8. J.M. Maciejowski, *Multivariable Feedback Design*, Addison-Wesley, 1989.
9. David E. Goldberg, *Genetic Algorithms in Search, Optimization & Machine Learning*, Addison-Wesley, 1989.

Table 1: Natural frequencies of the integrated structure, in Hz

1st mode	2nd mode	3rd mode	4th mode	5th mode
14.0	66.4	86.1	199.6	233.6

Table 2: Modal control force of various electrode shapes

	AC(-15°)	ACI(-30°)	A2(-30°)	S(-15°)
1st mode	-3.7871e-4	-3.3355e-4	-2.7252e-4	-3.0736e-4
2nd mode	9.7002e-4	1.2114e-3	1.3716e-3	5.4544e-4
3rd mode	-7.0975e-4	-3.5084e-4	-5.7741e-4	-4.9298e-6
4th mode	-1.7810e-3	-2.1646e-3	-1.9190e-3	2.8636e-6
5th mode	-8.0549e-4	-2.9311e-4	2.1256e-4	1.7926e-6

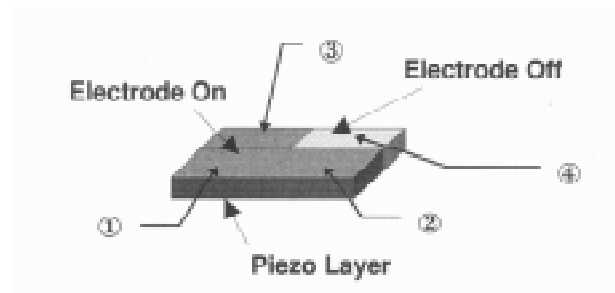


Fig. 1: A finite element with 4 electrode segments

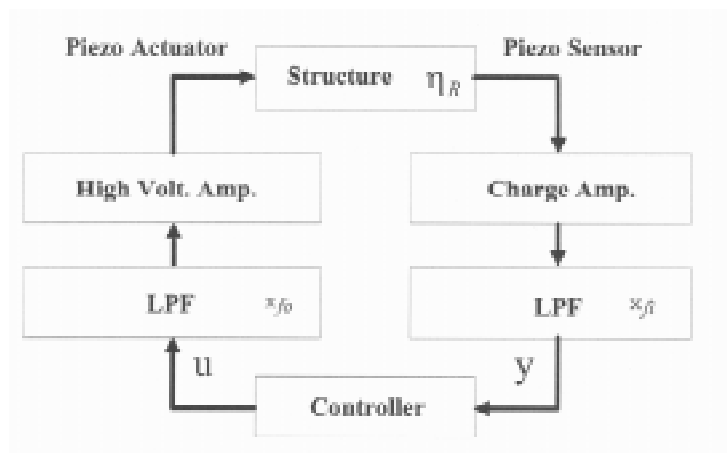


Fig. 2: Block diagram for the total system

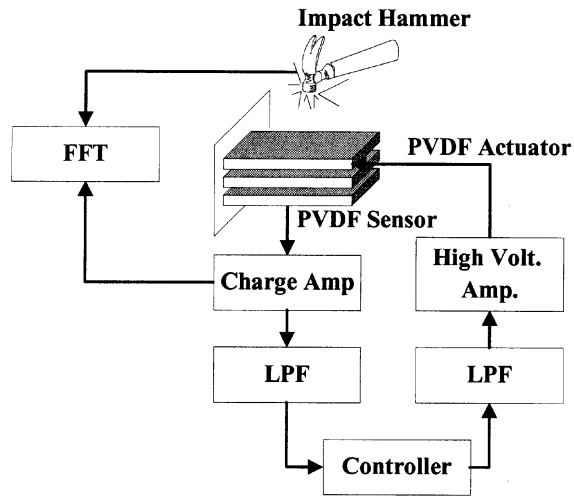


Fig. 3: Experimental Setup

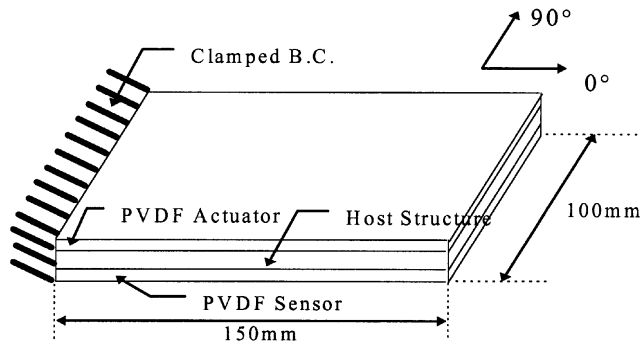


Fig. 4: Schematic view of the specimen

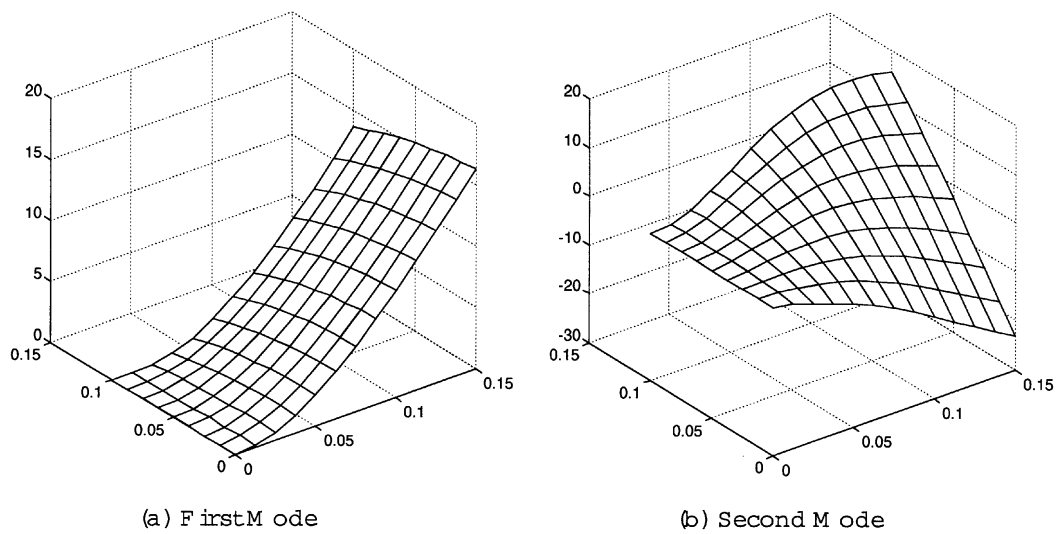
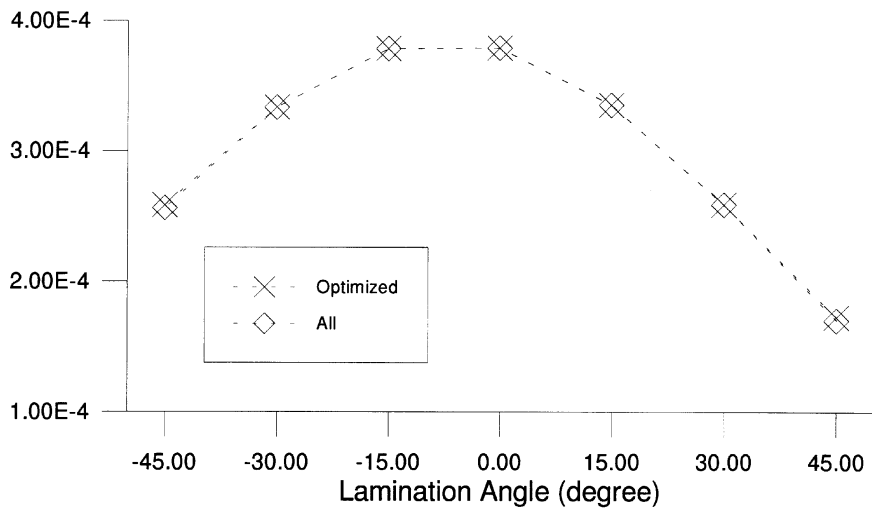
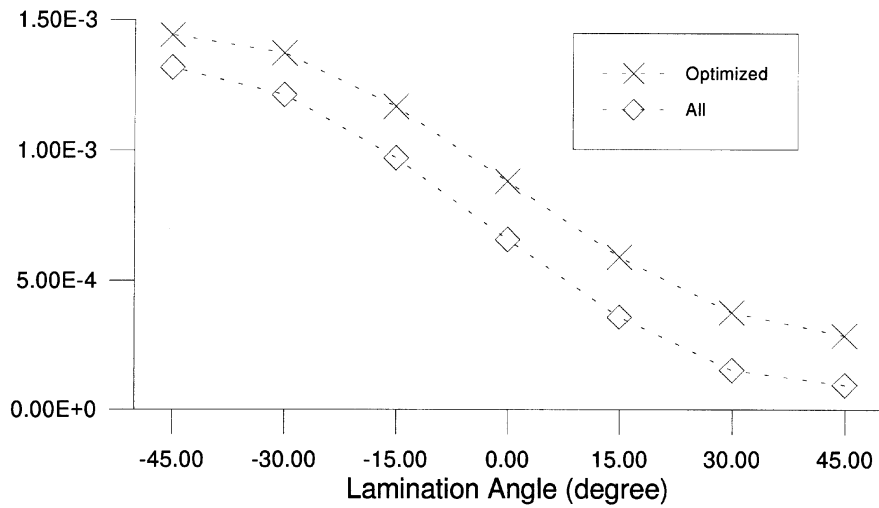


Fig. 5: Mode shapes of the integrated structure

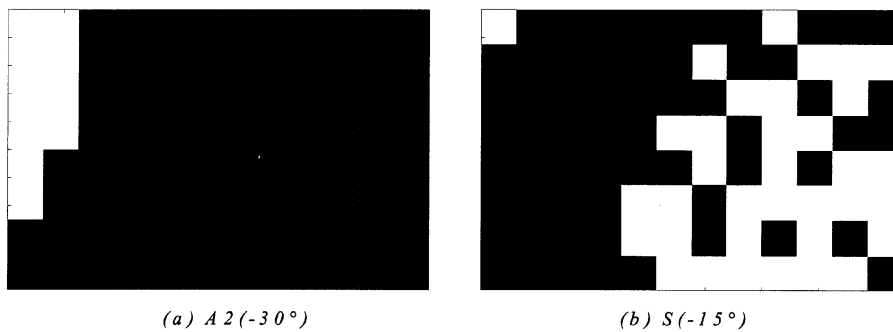


(a) Variation of Modal Control Forces for the First Mode



(b) Variation of Modal Control Forces for the Second Mode

Fig. 6: Variation of modal control force by lamination angle and electrode shape



(a) A2 (-30°)

(b) S (-15°)

Fig. 7: Electrode patterns of the optimized transducers (L.H.S. edges are fixed boundary)

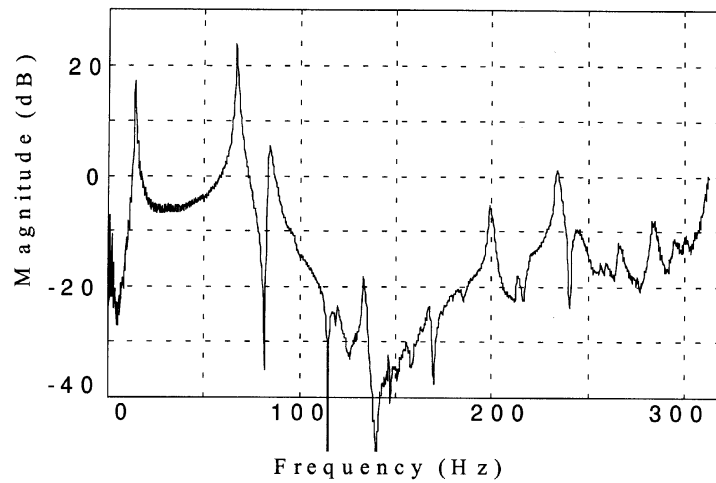


Fig. 8(a): Open-loop Transfer Function of Optimized Sensor, $S(-15^\circ)$

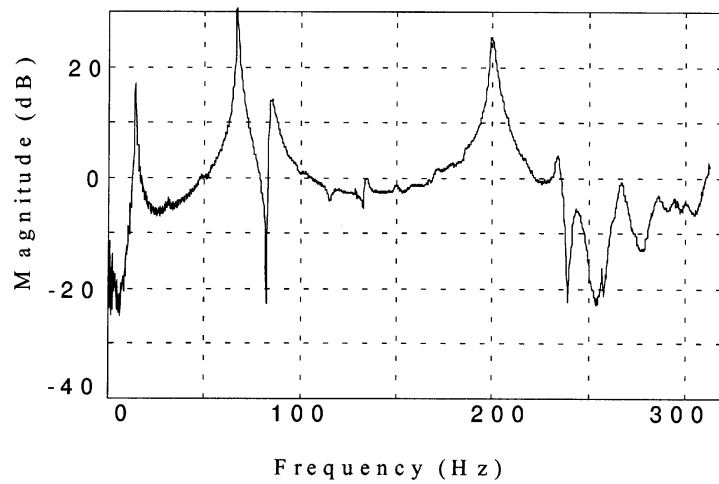


Fig. 8(b): Open-loop Transfer Function of Optimized Actuator, $A2(-30^\circ)$

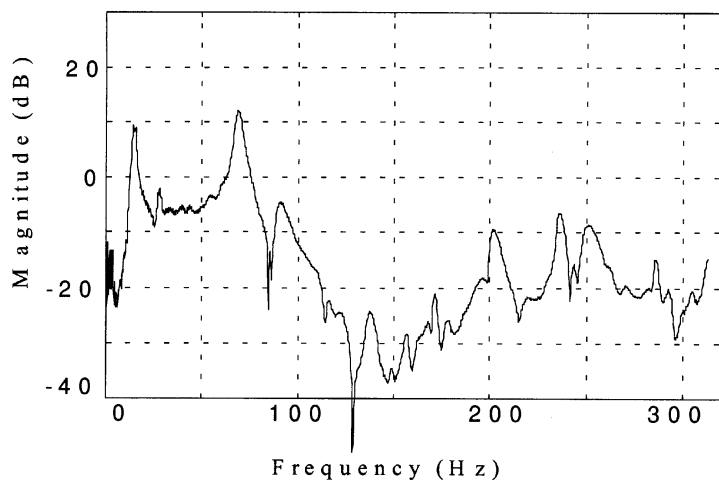


Fig. 8(c): Closed-loop Transfer Function of Integrated Structure

PREDICTION OF MAGNETOELECTRIC COUPLING AND EFFECTIVE PROPERTIES OF INTELLIGENT MATERIALS: PIEZOELECTRIC/PIEZOMAGNETIC COMPOSITES

Jin H. Huang, Ya-Hui Chiu, and Jui-Che Hsu

*Department of Mechanical Engineering
Feng Chia University, Taichung 407, Taiwan, Republic of China*

SUMMARY: A unified method based on the inclusion formulation is proposed to determine the magnetic, electric and elastic fields in a composite with piezoelectric and piezomagnetic phases. The composite reinforcements are treated as ellipsoidal inclusions that enable the reinforcement geometries ranging from thin flakes to continuous fibers. Utilizing the proposed method, the magneto-electro-elastic tensors analogous to Eshelby tensors for elastic ellipsoidal inclusions are obtained. With these tensors, the magnetic, electric and elastic fields around the inclusion as well as concentration factors are determined. Furthermore, based upon the Mori-Tanaka mean field theory to account for the interaction between inclusions and matrix, the effective magneto-electro-elastic constants (elastic moduli, piezoelectric coefficients, dielectric constants, piezomagnetic coefficients, magnetoelectric, and magnetic permeability) of the composites are expressed explicitly in terms of phase properties, volume fraction, and inhomogeneity shape. The numerical examinations have been conducted for the three-dimensional $\text{BaTiO}_3\text{-CoFe}_2\text{O}_4$ composite, and the overall composite behavior have been examined numerically. It is found that the composite reveals interesting magnetoelectric coupling which is absent in each constituent.

KEYWORDS: magneto-electro-elastic Eshelby tensor, anisotropic inclusion method, magnetoelectric coupling effect, Mori-Tanaka theory.

INTRODUCTION

The present paper is to develop a unified and explicit method for determining the magneto-electro-elastic fields around an ellipsoidal inclusion and the effective properties of a piezoelectric/piezomagnetic composite. The inclusions and the matrix are assumed to be perfectly bonded, without any sliding, void nucleation, or growth on their interfaces. The proposed method is based on the anisotropic inclusion method [1] in elasticity in a manner analogous to the that for uncoupled magnetic, electric, and elastic behavior. With this method, the expression for the coupled elastic, electric, and magnetic fields around an ellipsoidal inclusion is expressed in the unified form of surface integral. Then, a unified expression for the magneto-electro-elastic tensors analogous to Eshelby [2] tensors for elastic ellipsoidal inclusions is obtained. The resulting magneto-electro-elastic fields and Eshelby tensors can further be applied to obtain magneto-electro-elastic concentration factors. Finally, based on the Mori-Tanaka [3] theory to account for interaction at finite concentrations of inclusions, the effective elastic moduli, piezoelectric coefficients, dielectric constants,

piezomagnetic coefficients, magnetoelectric, and magnetic permeability of the composite in terms of phase properties, volume fraction, and inclusions' shape are presented in closed forms.

CONSTITUTIVE EQUATIONS

Consider a composite material with piezoelectric and piezomagnetic phases. Suppose that the elastic displacement vector u_i , the electric potential ϕ , and the magnetic potential ψ are chosen as independent variables, while the dependent variables are the elastic stress tensor σ_{ij} , the electric displacement vector D_i , and the magnetic induction B_i . Due to the coupled interaction between the two phases, the constitutive equations coupled the deformations, electric fields, and magnetic fields are

$$\begin{aligned}\sigma_{ij} &= C_{ijmn}\epsilon_{mn} - e_{nij}E_n - q_{nij}H_n, \\ D_i &= e_{imn}\epsilon_{mn} + \kappa_{in}E_n + \lambda_{ni}H_n \\ B_i &= q_{imn}\epsilon_{mn} + \lambda_{in}E_n + \Gamma_{in}H_n,\end{aligned}\quad (1)$$

where ϵ_{mn} is elastic strain tensor, E_n electric field, H_n magnetic field, C_{ijmn} elastic moduli, e_{nij} piezoelectric coefficient, q_{nij} piezomagnetic coefficient, κ_{in} dielectric constant, and Γ_{in} magnetic permeability. The magnetoelectric coefficient λ_{in} is a new material property of the composite, since it is not present in the constituents.

To treat the elastic, electric and magnetic variables on equal footing, Eq. (1) is compactly expressed in the following shorthand notation as

$$\Sigma_{ij} = L_{iJMn}Z_{Mn}, \quad (2)$$

where

$$\Sigma_{ij} = \begin{cases} \sigma_{ij} & J \leq 3, \\ D_i & J = 4, \\ B_i & J = 5, \end{cases} \quad Z_{Mn} = \begin{cases} \epsilon_{mn} = (u_{m,n} + u_{n,m})/2 & M \leq 3, \\ -E_n = \phi_{,n} & M = 4, \\ -H_n = \psi_{,n} & M = 5. \end{cases} \quad (3.a)$$

$$L_{iJMn} = \begin{cases} C_{ijmn} & J, M \leq 3, \\ e_{nij} & J \leq 3, M = 4, \\ q_{nij} & J \leq 3, M = 5, \\ e_{imn} & J = 4, M \leq 3, \\ -\kappa_{in} & J = 4, M = 4, \\ -\lambda_{in} & J = 4, M = 5; J = 5, M = 4, \\ q_{imn} & J = 5, M \leq 3, \\ -\Gamma_{in} & J = 5, M = 5, \end{cases} \quad (3.b)$$

Throughout this paper, conventional indicial notation is used where repeated lowercase subscripts are summed over 1 to 3, while uppercase subscripts are summed over 1 to 5. For example, $T_j U_j = T_1 U_1 + T_4 U_4 + T_5 U_5$, where $j = 1 \rightarrow 3$.

COUPLED MAGNETO-ELECTRO-ELASTIC FIELDS INSIDE AN ELLIPSOIDAL INCLUSION

Consider a three dimensional, infinitely extended composite D which consists of piezoelectric and a piezomagnetic phases. This composite exhibit a magnetoelectric effect that is entirely absent in the two phases. In order to have a unified analysis, both phases will be assumed piezomagnetoelastic. Let the matrix with magneto-electro-elastic moduli L_{iJMn} contain an ellipsoidal inclusion defined by

$$\Omega: \frac{x_1^2}{a_1^2} + \frac{x_2^2}{a_2^2} + \frac{x_3^2}{a_3^2} \leq 1, \quad (4)$$

where a_1 , a_2 , and a_3 are the lengths of the semiaxes of the ellipsoid. The consideration that the shape of the inclusion is ellipsoidal enables the model to treat composite reinforcement geometries ranging from thin flakes to continuous fiber reinforcement. The composite is allowed to undergo an eigenstrain ϵ_{mn}^* (or stress-free transformation strain), eigenelectric field E_n^* (or electric displacement-free electric field), and eigenmagnetic field H_n^* (or magnetic induction-free magnetic field) in the inclusion, while subject to the constraints of the surrounding matrix. Designate Z_{Mn}^* as the unified form of the eigenstrain ϵ_{mn}^* , eigenelectric field E_n^* , and eigenmagnetic field H_n^* :

$$Z_{Mn}^* = \begin{cases} \epsilon_{mn}^* & M \leq 3, \\ -E_n^* & M = 4, \\ -H_n^* & M = 5. \end{cases} \quad (5)$$

It is noted that the eigenfield Z_{Mn}^* is zero in the matrix $D - \Omega$. The eigenfield generally induces elastic displacement, electric potential, and magnetic potential, :

$$U_M = \begin{cases} u_m & M \leq 3, \\ \phi & M = 4, \\ \psi & M = 5. \end{cases} \quad (6)$$

Then, the corresponding stress, electric displacement, and magnetic induction, Σ_{ij} , can be obtained from the linear constitutive equation (2), as

$$\Sigma_{ij} = L_{iJMn} (U_{M,n} - Z_{Mn}^*), \quad (7)$$

in which the comma denotes partial differentiation with respect to the coordinate variable whose subscript follows the comma. In the absence of body forces, free charge, and free magnetic dipole, the coupling equilibrium equation is expressed as

$$\Sigma_{ij,i} = 0. \quad (8)$$

Substitution of Eq. (7) into (8) leads to

$$L_{ijMn} U_{M,ni} = L_{ijMn} Z_{Mn,i}^* \quad (9)$$

From the preceding equation it is seen that $L_{ijMn} Z_{Mn,i}^*$ behaves like a body force, a electric charge, and a magnetic dipole in the composite.

Following the works of Huang and Yu [4] and assuming the eigenfield Z_{Mn}^* as being uniformly distributed in the ellipsoidal inclusion, the fundamental equation (9) can be solved for $U_M(\mathbf{x})$ in terms of the Green's function $G_{MJ}(\mathbf{x} - \mathbf{x}')$ as

$$U_M(\mathbf{x}) = \frac{1}{4\pi} L_{iJAb} Z_{Ab}^* \bar{G}_{MJin} x_n, \quad (10)$$

where

$$\bar{G}_{MJin} = \int_{-1}^1 \int_0^{2\pi} N_{MJ}(\bar{\xi}) D^{-1}(\bar{\xi}) \bar{\xi}_i \bar{\xi}_n d\theta d\bar{\xi}_3, \quad (11)$$

with $N_{MJ}(\bar{\xi})$ and $D(\bar{\xi})$ being the cofactor and the determinant of the 5×5 matrix $L_{iMJn} \bar{\xi}_i \bar{\xi}_n$, respectively.

Combining Eqs. (3.a) and (10), the induced strain, electric and magnetic fields, Z_{Mn} , due to the uniform eigenfield in the inclusion are given by

$$Z_{Mn} = S_{MnAb} Z_{Ab}^*, \quad (12)$$

where S_{MnAb} are referred to as the magneto-electro-elastic Eshelby tensors for anisotropic piezoelectric/piezomagnetic composites. Equation (12) has the same features as that of the Eshelby solution for ellipsoidal inclusions in uncoupled elastic media, *i.e.*, the induced elastic strain, electric and magnetic fields inside the ellipsoidal inclusion are uniform when the prescribed eigenfield is constant. It is also seen from the preceding equation that the resulting magneto-electro-elastic Eshelby tensors are a function of the shape of ellipsoid and the magneto-electro-elastic properties of the surrounding matrix.

By substituting Eq. (12) into (7), the stress, electric displacement, and magnetic induction inside the inclusion are obtained as

$$\Sigma_{ij} = L_{ijMn} (S_{MnAb} - I_{MnAb}) Z_{Ab}^*, \quad (13)$$

where I_{MnAb} are the second order and the fourth order identity tensors, *i.e.*,

$$I_{MnAb} = \begin{cases} (\delta_{ma} \delta_{nb} + \delta_{mb} \delta_{na}) / 2 & M, A \leq 3, \\ \delta_{nb} & M = A = 4, \text{ or } M = A = 5, \\ 0 & \text{otherwise.} \end{cases} \quad (14)$$

In general, the expression \bar{G}_{MJin} cannot be carried out in closed form for an ellipsoidal inclusion in anisotropic media. However, it can be easily computed numerically when the integrands $N_{MJ}(\bar{\xi})$ and $D(\bar{\xi})$ are obtained. Once \bar{G}_{MJin} is evaluated, the magneto-electro-elastic fields characterized by Eqs. (10), (12) and (13) easily follow.

EFFECTIVE MAGNETO-ELECTRO-ELASTIC PROPERTIES

For obtaining the effective properties of a piezoelectric/piezomagnetic composite, we consider a sufficiently large two-phase composite D consists of randomly oriented ellipsoidal inhomogeneities Ω ($=\Omega_1 + \Omega_2 + \dots + \Omega_N$) with electro-elastic (or magneto-elastic) constants L_{iJMn}^* and volume fraction f . The surrounding matrix is denoted by $D-\Omega$ and has magneto-elastic (or electro-elastic) constants L_{iJMn} . Here $L_{iJMn} = L_{iJMn}^* = 0$ for a piezomagnetic (piezoelectric) material when one of subscripts is 4 (or 5).

To deal with such a piezoelectric-piezomagnetic composite with randomly oriented inclusions, the Mori-Tanaka mean field theory will be employed to predict the effective elastic, piezoelectric, dielectric, piezomagnetic, magnetoelectric, and magnetic permeability constants of the composite. This theory generally yields the same effective magneto-electro-elastic moduli for the cases when either a traction-electric displacement-magnetic induction or an elastic displacement-electric field-magnetic field is prescribed on the boundary of the composite [5].

The effective magneto-electro-elastic compliance of the composite can be shown as [6]

$$\bar{L}_{MniJ}^{-1} = [I_{MnAb} - f U_{MnqR}^{-1} (L_{qRAb}^* - L_{qRAb})] L_{AbiJ}^{-1} \quad (15)$$

where

$$U_{iJAb} = (L_{iJMn}^* - L_{iJMn}) [(1-f) S_{MnAb} + f I_{MnAb}] + L_{iJAb} \quad (16)$$

The effective magneto-electro-elastic moduli \bar{L}_{iJMn} calculated for the elastic displacement, electric and magnetic fields prescribed body is derived as

$$\bar{L}_{iJMn} = L_{iJAb} [I_{AbMn} + f V_{AbqR}^{-1} (L_{qRMn}^* - L_{qRMn})], \quad (17)$$

where

$$V_{iJAb} = (1-f)(L_{iJMn}^* - L_{iJMn}) S_{MnAb} + L_{iJAb} \quad (18)$$

Numerical examinations have been conducted for a $BaTiO_3$ - $CoFe_2O_4$ composite. The material constants are given as follows [7, 8]:

$BaTiO_3$ inclusion:

$$C_{11} = 166 \text{ GPa}, C_{33} = 162 \text{ GPa}, C_{44} = 43 \text{ GPa}, C_{12} = 77 \text{ GPa}, C_{13} = 78 \text{ GPa},$$

$$e_{31} = -4.4 \text{ C/m}^2, e_{33} = 18.6 \text{ C/m}^2, e_{15} = 11.6 \text{ C/m}^2,$$

$$\kappa_{11} = 11.2 \times 10^{-9} \text{ C}^2/\text{Nm}^2, \kappa_{33} = 12.6 \times 10^{-9} \text{ C}^2/\text{Nm}^2,$$

$$\Gamma_{11} = 5.0 \times 10^{-6} \text{ N s}^2/\text{C}^2, \Gamma_{33} = 10.0 \times 10^{-6} \text{ N s}^2/\text{C}^2.$$

$CoFe_2O_4$ matrix

$$C_{11} = 286 \text{ GPa}, C_{33} = 269.5 \text{ GPa}, C_{44} = 45.3 \text{ GPa},$$

$$C_{12} = 173.0 \text{ GPa}, C_{13} = 170.5 \text{ GPa},$$

$$q_{31} = 580.3 \text{ N/Am}, q_{33} = 699.7 \text{ N/Am}, q_{15} = 550 \text{ N/Am},$$

$$\begin{aligned}\kappa_{11} &= 0.08 \times 10^{-9} \text{ C}^2/\text{Nm}^2, \quad \kappa_{33} = 0.093 \times 10^{-9} \text{ C}^2/\text{Nm}^2, \\ \Gamma_{11} &= -590 \times 10^{-6} \text{ Ns}^2/\text{C}^2, \quad \Gamma_{33} = 157 \times 10^{-6} \text{ Ns}^2/\text{C}^2.\end{aligned}$$

Figures 1 through 5 illustrate the effect of the inclusion shape on the resulting composite properties; the inclusion volume fraction is set at $f = 0.5$ for these figures. Figure 1 shows the predicted elastic constants against the aspect ratio a_3/a_1 . Both $\bar{C}_{11}(=\bar{L}_{1111})$ and $\bar{C}_{33}(=\bar{L}_{3333})$ decrease with the ratio due to the fact that the BaTiO_3 inclusion is lower in elastic moduli than the CoFe_2O_4 matrix. Figure 2 exhibits the piezoelectric constants of the composite. Since the matrix is absent in piezoelectric effects, the piezoelectric behavior of the composite is therefore dominated by the fiber, especially for the properties along fiber direction. It can be seen that \bar{e}_{33} and $\bar{\kappa}_{33}$ increase significantly with the aspect ratio, while the \bar{e}_{15} and $\bar{\kappa}_{11}$ remain essentially unchanged. The resulting magnetic permeabilities $\bar{\Gamma}_{ij}$ of the composite are shown in Fig. 3; both decrease with the ratio. Note that $\bar{\Gamma}_{11}$ is negative and thus its absolute value is increased when the aspect ratio increases. The resulting piezomagnetic coefficients are shown in Fig. 4. It can be seen that as the aspect ratio increases, both \bar{q}_{31} and \bar{q}_{33} slightly decrease, while \bar{q}_{15} significantly increases. The magnetoelastic coupling coefficients are displayed in Fig. 5, indicating that $\bar{\lambda}_{11}$ are rather small, while $\bar{\lambda}_{33}$ increases notably with the ratio.

The magnetoelastic coupling $\bar{\lambda}_{ij}$ is a unique property of the composite, since it is absent in both constituents. The results for $\bar{\lambda}_{11}$ are plotted in Fig. 6, showing that the values of $\bar{\lambda}_{11}$ are negative at $a_3/a_1=1$ and become positive when a_3/a_1 is higher than 4. As plotted in Fig. 7, the $\bar{\lambda}_{33}$ shows the same trend in its sign. However, the magnitude of $\bar{\lambda}_{33}$ is much larger than that of $\bar{\lambda}_{11}$. Both coefficients are found to vanish at $f=0$ (pure matrix) and $f=1$ (pure fiber) in which cases the materials become monolithic. The most significant coupling effect is found to occur between $f=0.8\sim 0.9$ for $\bar{\lambda}_{11}$, while the maximum values of $\bar{\lambda}_{33}$ occur approximately at $f=0.5$ for $a_3/a_1=1$ and at $f=0.9$ for $a_3/a_1=64$. Thus, this induced coupling effect is determined not only by the inclusion volume fraction, but also by the inclusion shape.

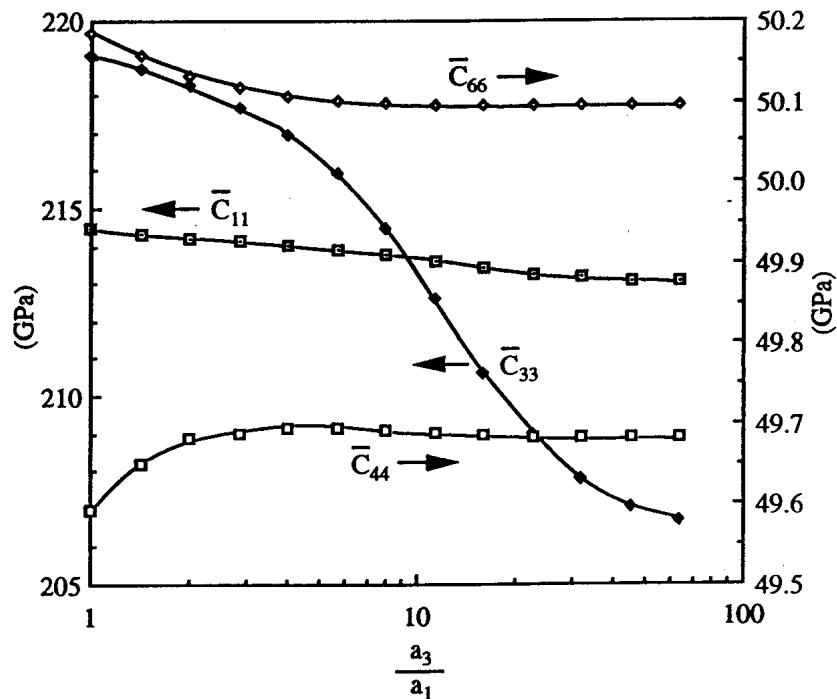


Fig. 1 The predicted composite elastic constants against the aspect ratio a_3/a_1 ($f=0.5$).

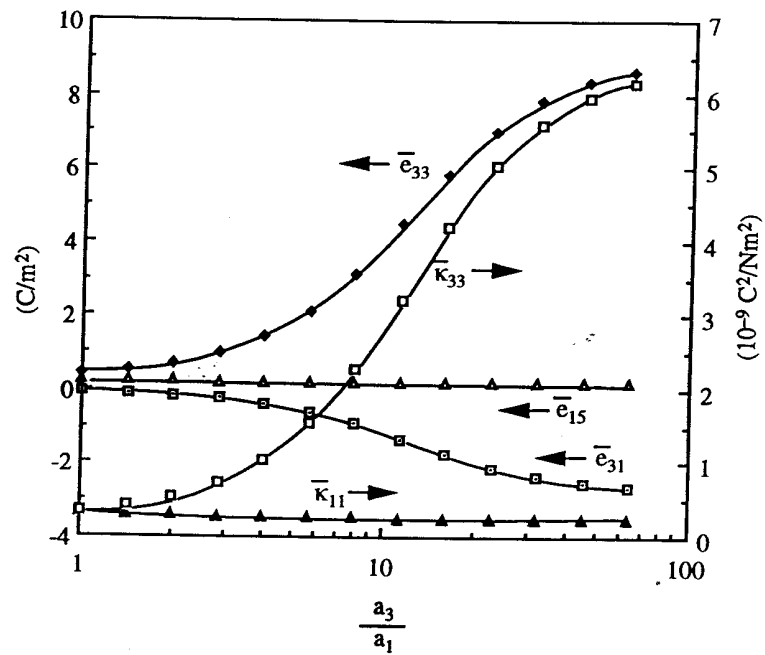


Fig. 2 The predicted composite piezoelectric constants against the aspect ratio a_3/a_1 ($f=0.5$).

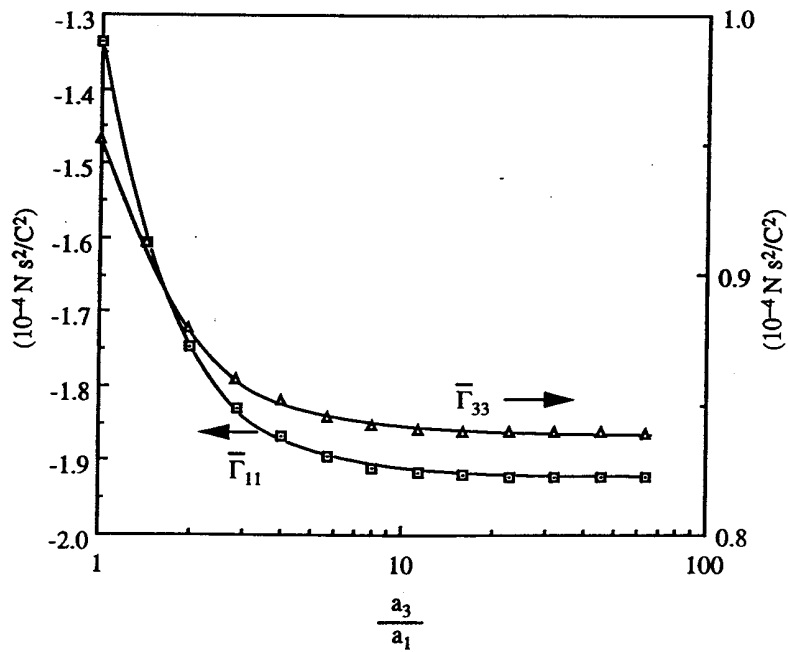


Fig. 3 The predicted composite magnetic permeabilities against the aspect ratio a_3/a_1 ($f=0.5$).

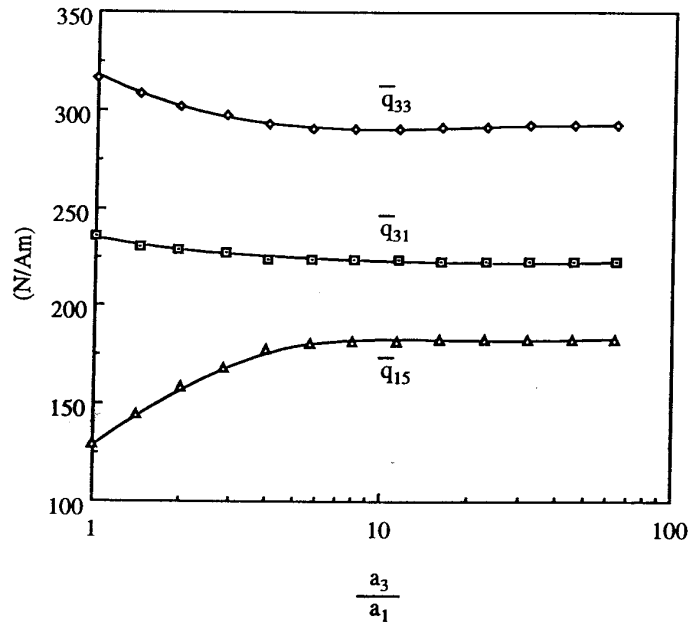


Fig. 4 The predicted composite piezomagnetic coefficients against the aspect ratio a_3/a_1 ($f=0.5$).

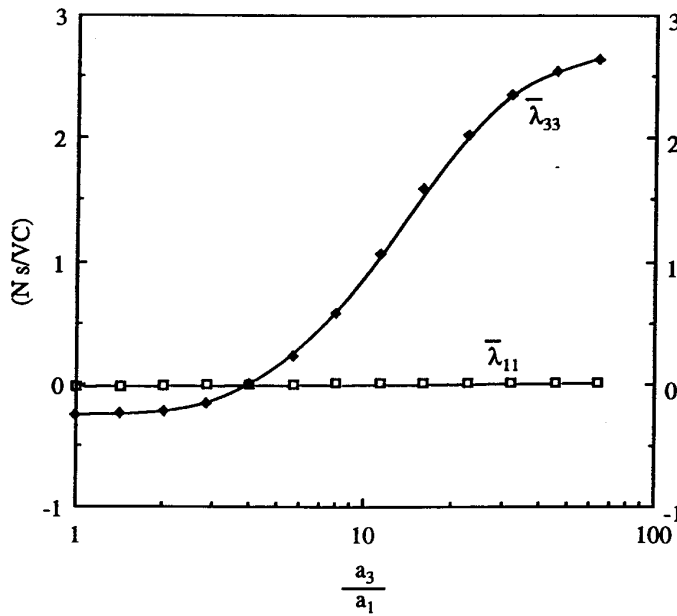


Fig. 5 The predicted composite magnetolectric coupling against the aspect ratio a_3/a_1 ($f=0.5$).

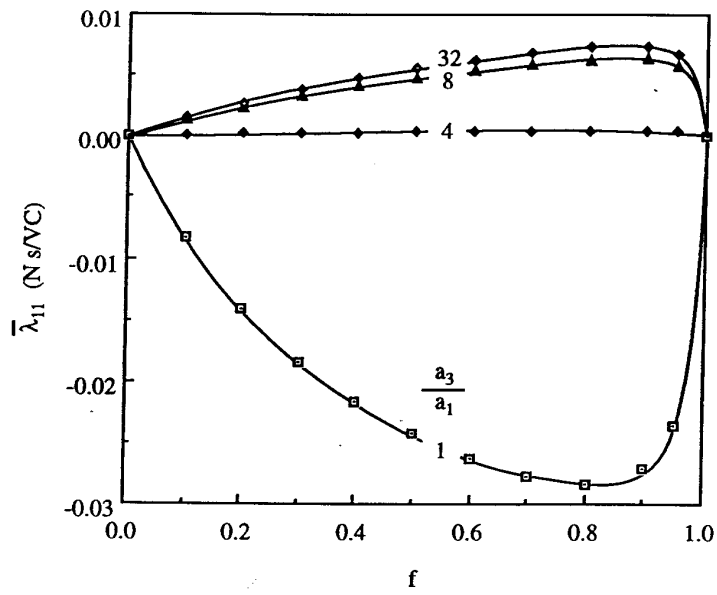


Fig. 6 Effect of inclusion volume fraction and aspect ratio on $\bar{\lambda}_{11}$.

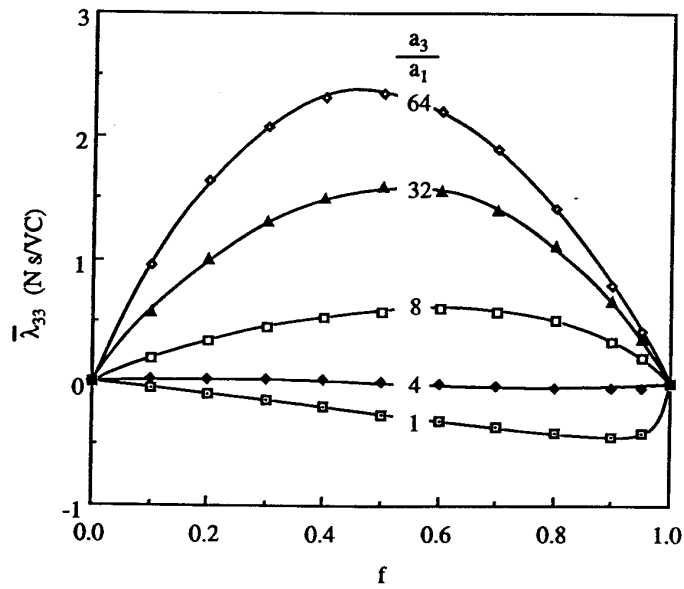


Fig. 7 Effect of inclusion volume fraction and aspect ratio on $\bar{\lambda}_{33}$.

CONCLUSIONS

The anisotropic inclusion method has been extended to derive the magneto-electro-elastic fields around a piezoelectric (or piezomagnetic) ellipsoidal inclusion embedded in an infinitely extended piezomagnetic (or piezoelectric) matrix. Explicit forms have been obtained for the magneto-electro-elastic Eshelby tensors. It has been shown that the magneto-electro-elastic Eshelby tensors are functions of the shape of inclusion and the properties of the surrounding matrix. When magnetoelectric coupling is absent, the resulting Eshelby tensors reduce to those for uncoupled elastic inclusion problems. In addition, it is demonstrated that the coupled magnetic field, electric field, and elastic strain inside the inclusion are constants when eigenfield is uniformly distributed in the inclusion. With the explicit expressions for magneto-electro-elastic fields in hand, a micromechanics model has been developed to predict the effective magneto-electro-elastic moduli of for the BaTiO₃-CoFe₂O₄ composite, in which the matrix is magnetostrictive. The magnetoelectric coupling is a unique effect to the composite, and how it relates to the inclusion volume fraction and aspect ratio has been discussed in detail.

ACKNOWLEDGMENTS

This research was supported by the National Science Council of Taiwan under Grant NSC 86-2216-E-035-005.

REFERENCES

1. Mura, T., *Micromechanics of Defects in Solids*, second, revised edition, Kluwer Academic Publishers, 1987.
2. Eshelby, J. D., "The Determination of the Elastic Field of an Ellipsoidal Inclusion. and Related Problems," *Proceeding of the Royal Society*, Vol. A241, 1957, pp. 376-396.
3. Mori, T. and Tanaka, K., "Average Stress in Matrix and Average Energy of Materials with Misfitting Inclusions," *Acta Metallurgica*, 21, 1973, pp. 571-574.
4. Huang, J. H. and Yu, J. S., Electroelastic Eshelby's Tensors for an Ellipsoidal Piezoelectric Inclusion. *Composite Engineering*, Vol. 4, 1994, pp. 1169-1182.
5. Huang, J. H., Furuhashi, R. and Mura, T., "Frictional Sliding Inclusions," *Journal of Mechanic and Physics of Solids*, Vol. 41, 1993, pp. 247-265.
6. Huang, J. H. and Kuo, W. S. "The Analysis of Piezoelectric/Piezomagnetic Composite Materials Containing Ellipsoidal Inclusions," *Journal of Applied Physics*, 1997, in press.
7. Gray, D. E., "American Institute of Physics Handbook," third edition, McGraw-Hill, 1987.
8. Avellaneda, M. and Harshe, G. R., "Magnetoelectric Effect in Piezoelectric-Magnetostrictive Multilayer (2-2) Composites," *Journal of Intelligent Materials Systems and Structures*, Vol. 5, 1994, pp. 501-513.

MATERIAL CHARACTERIZATION OF THIN FILM PIEZOELECTRIC POLYMERS

Frank Holloway¹ and Aleksandra M. Vinogradov¹

¹ *Department of Mechanical and Industrial Engineering, Montana State University, Bozeman, MT 59717 USA*

SUMMARY: The paper describes an experimental program developed to characterize the material properties of thin film piezoelectric polymers PVF₂, a co-polymer of PVDF (polyvinylidene fluoride). These unidirectional materials have been used as active elements in composite devices for noise suppression and position control. Static and dynamic test results presented in the paper indicate that the mechanical response of PVF₂ thin films at room temperature is time-dependent. The creep rates tend to accelerate at elevated temperatures. It is shown that within certain limits, i.e., approximately 57% of yield stress, the properties of the material can be described by the constitutive equations of linear hereditary viscoelasticity. Above this limit, a stress-dependent nonlinear viscoelastic theory must be used to characterize the properties of piezoelectric thin films.

KEYWORDS: piezoelectric polymers, thin films, creep, viscoelasticity

INTRODUCTION

Piezoelectric materials have been extensively used in the design of intelligent structures. Such structures represent hybrid composite systems used in a variety of applications including vibration control, noise suppression, alignment precision control and damage detection. In general, active control devices are designed in the form of laminated composites the response of which directly depends on the material properties of their piezoelectric components.

In general, piezoelectric materials include piezoelectric ceramics and polymers that produce measurable electrical charges in response to mechanical stress. Because of the brittle nature of ceramics, piezoelectric polymers such as polyvinylidene fluoride (PVDF) and its co-polymer PVF₂ are often used to design compliant sensors and actuators. Typically, piezoelectric polymers are formed in thin films which are electrically poled in one or two directions. In practice, such materials are treated as linearly elastic, and their constitutive properties are defined by the Hooke's law coupled with piezoelectric relations [1].

However, experimental evidence suggests that the mechanical properties of PVF₂ thin films are time-dependent. Samples of this material tested at room temperature under sustained loading conditions develop creep deformations. Hence, it is critical in terms of accurate analysis and design of adaptive structures to fully understand and adequately describe the mechanical response of piezoelectric polymers. The objective of this study is to characterize the creep properties of PVF₂ thin films through a consistent experimental program leading to the development of an accurate constitutive model of this material.

THEORETICAL APPROACH

In many applications, the creep properties of polymers at room temperature can be defined by the constitutive equations of linear hereditary viscoelasticity [2,3]. The theory is based on the Boltzmann's superposition principle leading to the stress-strain relation in the form

$$\sigma = R^* [\epsilon] \quad (1)$$

where R^* denotes a linear integral operator of the Stieltjes convolution type

$$R^* = E \left(1 - \frac{1}{E} \int_0^t R(t-\tau) d\tau \right) \quad (2)$$

In Eqn 2, the kernel $R(t)$ represents the relaxation properties of the material.

An alternative viscoelastic constitutive equation can be presented in the form

$$\epsilon(t) = \sigma D(t) + \int_0^t D(t-\tau) \frac{d\sigma}{d\tau} d\tau \quad (3)$$

An alternative viscoelastic constitutive equation can be presented in the form

where the time-dependent material response to a given stress history $\sigma(t)$ is defined by the function $D(t)$ known as the creep compliance. This function is determined experimentally, typically, from static tension/compression creep tests conducted under sustained loading conditions with $\sigma = \sigma_s = \text{const}$, in which case Eqn 3 reduces to

$$\epsilon(t)/\sigma_s = D(t) \quad (4)$$

It is clear that $D(t)$ must be independent of the experimental stress level σ_s , alternatively, if the creep compliance is shown to depend on stress, the assumptions of linear viscoelastic theory become invalid, and a nonlinear theory must be used to characterize the time-dependent properties of the material [4-6].

An alternative dynamic testing procedure for material characterization of polymers can be used to directly determine the creep or relaxation properties of the material. In this case, samples are subjected to harmonic oscillations, and the material response is defined in terms of a complex modulus or a complex creep compliance. In particular, the complex modulus in the frequency domain is of the form

$$\tilde{E}(\omega) = E'(\omega) + iE''(\omega) \quad (5)$$

where the storage and loss moduli E' and E'' are defined by

$$E'(\omega) = \frac{\sigma^o}{\epsilon^o} \cos \delta ; \quad E''(\omega) = \frac{\sigma^o}{\epsilon^o} \sin \delta \quad (6)$$

In Eqn 6, σ^0 and ε^0 denote, respectively, stress and strain amplitudes, and δ is the phase angle between stress and strain. Note that, in general, σ^0 and δ are functions of ω .

Substitution of experimentally determined σ^0 and δ for each prescribed value of ε^0 into Eqn 6 provides the functions $E'(\omega)$ and $E''(\omega)$ over the experimental range of frequencies. On this basis, the relaxation function in Eqn 2 can be obtained by the inverse Fourier transformation from the frequency domain to the time domain.

The above method, however, requires that a large volume of experimental data be obtained over a wide range of frequencies because the time range of the transformed functions is that of $1/\omega$. This, in turn, requires an extensive long-term testing program.

Typically, the effectiveness of the dynamic testing technique can be enhanced by utilizing the properties of thermorheologically simple viscoelastic materials, [2,7]. This class of materials is characterized by an experimentally determined function, known as the shift factor a_T , that allows to determine the properties of the material at any temperature T from the respective properties measured at a reference temperature T_0 by expanding or compressing the time scale proportionally to a_T . Based on this property, known as the time-temperature correspondence principle, the frequency range of the complex modulus in Eqn 5 can be expanded using the relation

$$\tilde{E}(\omega, T) = \tilde{E}(\omega a_T, T_0) \quad (7)$$

Once the complex modulus $\tilde{E}(\omega)$ is obtained over an expanded frequency range, the complex compliance of the material can be obtained in the form

$$\check{D}(\omega) = D'(\omega) + iD''(\omega) \quad (8)$$

where $D'(\omega)$ and $D''(\omega)$ denote the storage and loss compliances related to E' and E'' by

$$D'(\omega) = \frac{1}{E'(\omega)[1 + \tan^2 \delta]} \quad (9)$$

$$D''(\omega) = \frac{1}{E''(\omega)[1 + \tan^2 \delta]} \quad (10)$$

Similarly to transforming the relaxation function from the frequency domain to the time domain, the creep compliance of the material as a function of time can be obtained from Eqn 8 using inverse Fourier transformation.

Determination of both the relaxation modulus and creep compliance completes the material characterization based on linear viscoelastic theory.

EXPERIMENTAL PROGRAM

As a first step in this study, a series of static tests were conducted in order to determine the range of stresses for which the creep compliance is stress independent. Within this range, linear viscoelastic theory can be used to characterize the material properties of PVF₂. With

this objective, creep tests of (2.54x10.16) cm PVF₂ thin film samples at constant stress levels ranging from 13.8 % to 122.1 % of the yield stress were performed for 2 hour durations. The results of these tests have identified the response range for linear viscoelastic characterization.

Further, a dynamic testing program was developed to determine the complex modulus of PVF₂ thin film in the frequency domain. Material samples with dimensions (10.16x2.54) cm and thickness of 20 μ were subjected to a prescribed loading history involving certain prestress conditions to insure tensile deformations with superimposed oscillatory strain of relatively small amplitude. The testing apparatus shown in Fig. 1 was designed to allow control of the prestress level using an adjustable grip, and to apply harmonic strain using a digitally controlled electrodynamic vibration exciter. A temperature chamber was used for temperature control.

Dynamic tests were conducted at a constant temperature, a constant prestress level of 20 % of yield stress, a constant strain amplitude of 0.073%, and frequencies ranging from 6.3 rad/sec to 315 rad/sec. An in-line load cell, and a temperature and phase compensated LVDT were used to

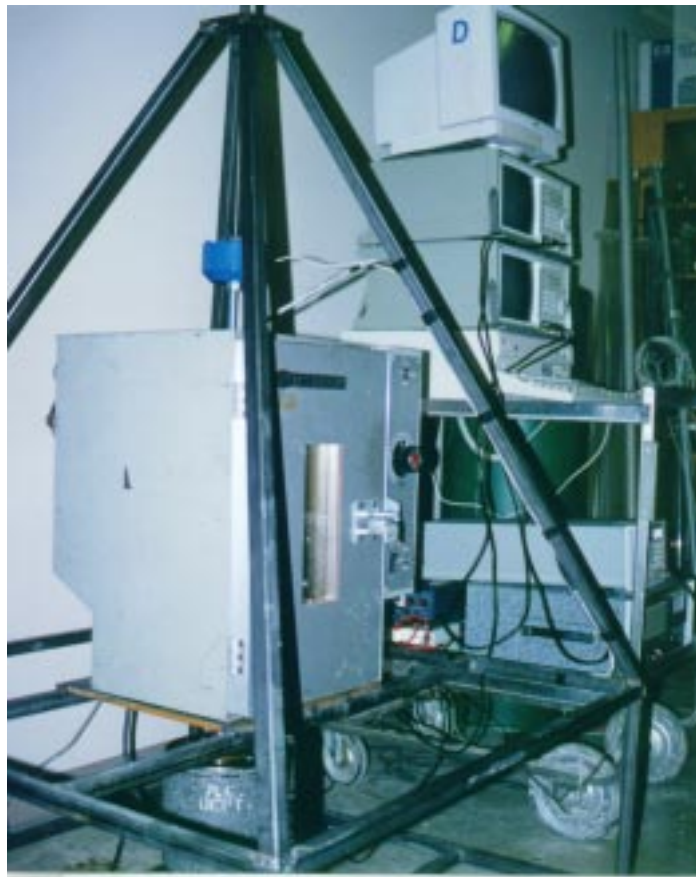


Fig. 1: Testing apparatus.

record the response of PVF₂ samples in terms of the phase angle δ and the stress-strain amplitude ratio σ^0/ϵ^0 as defined by Eqn 6.

Finally, in order to expand the experimental range of frequencies using the time-temperature correspondence principle, each set of experiments was repeated at elevated temperatures in the range from 25.5°C to 81.1°C

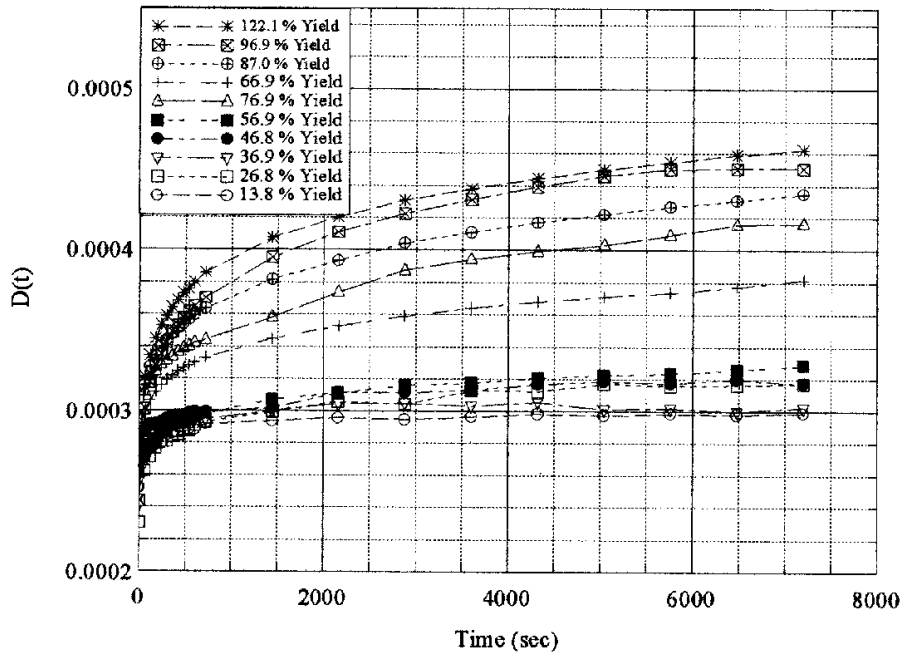


Fig 2: Creep compliance of PVF₂

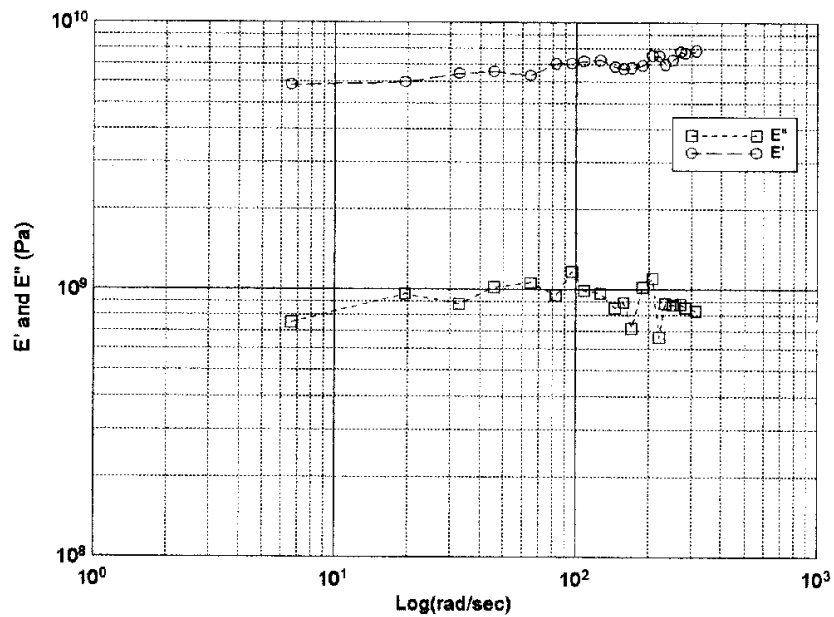


Fig. 3: Dynamic storage and loss moduli for PVF₂ (25.5°C and 23.5% yield)

RESULTS

Resulting from static creep tests, the creep compliance $D(t)$ of PVF₂ has been determined for different stresses σ_s , as shown in Fig. 2. From these diagrams it is clear that, for stresses below 57% of the yield stress, the creep compliance $D(t)$ is stress independent. Respectively, within this range, the theory of linear viscoelasticity can be used to characterize PVF₂ thin film.

Further, dynamic tests of PVF₂ samples at room temperature and different frequencies has allowed to determine the storage and loss moduli E' and E'' , as defined by Eqn 6. These results, plotted on a log-log scale are presented in Fig. 3.

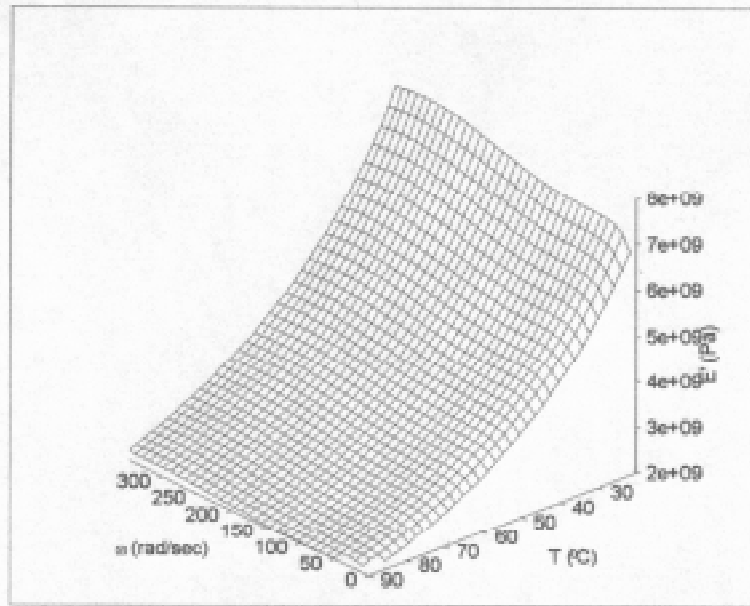


Fig. 4. Dynamic storage modulus for PVF₂ at elevated temperatures.

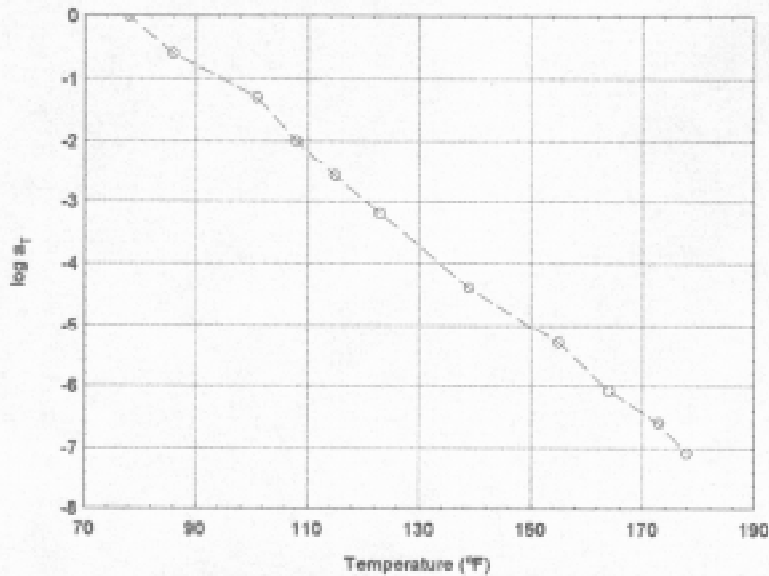


Fig. 5: Temperature dependent shift factor

Repetition of the same set of dynamic experiments under elevated temperature conditions has provided the following results: the storage and loss elastic moduli as functions of frequency and temperature, see Fig. 4, and the shift factor $a_T(T)$ over the temperature range shown in Fig. 5.

Based on this information, dynamic storage and loss compliances have been determined in the frequency domain using Eqns 9 and 10. These results are presented in Figs. 6 and 7.

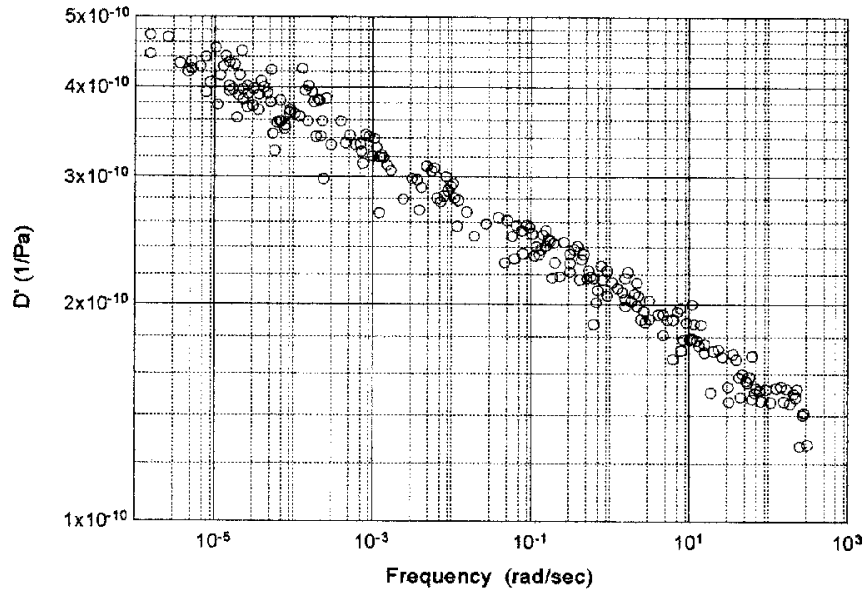


Fig. 6: Shifted dynamic storage compliance : 25.5°C - 81.1°C

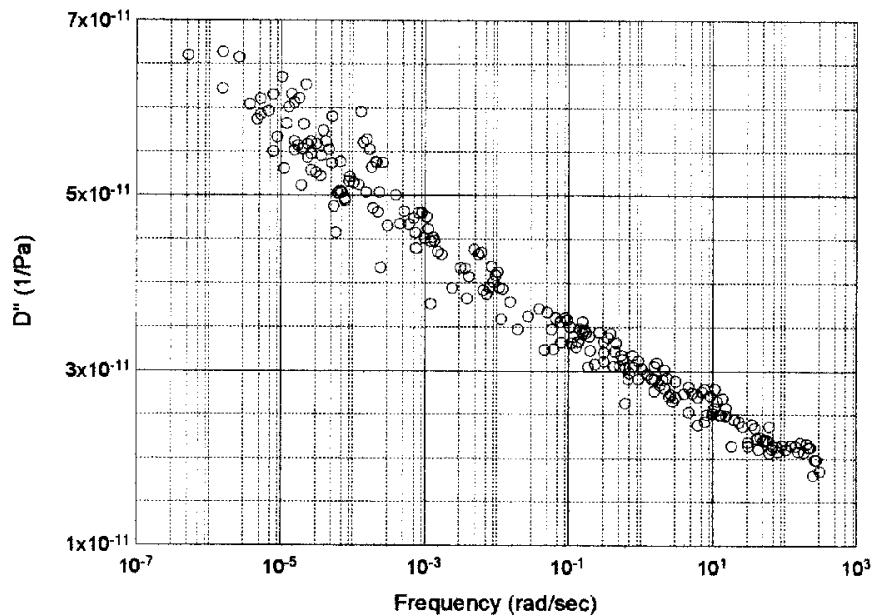


Fig. 7: Shifted Dynamic Loss Compliance : 25.5°C - 81.1°C

Finally, analytical functions obtained by a curve fit of data shown in Figs. 6 and 7 have been used to obtain the creep compliance $D(t)$ in the time domain through an approximate transformation by Ninomiya and Ferry [2] in the form

$$D(t) = D'(\omega) + 0.40D''(0.40\omega) - 0.014D''(10\omega) \Big|_{\omega=1/t} \quad (11)$$

This creep compliance, obtained on the basis of dynamic tests, has been used to predict the creep behavior of thin film PVF₂ for the time duration of 1.92×10^6 sec (about 22 days). An analytical function in the form

$$D(t) = 3.424 (t^{0.0006} - 0.991) \times 10^{-8} \quad (12)$$

has been found to provide the best curve fit for the creep compliance of the material.

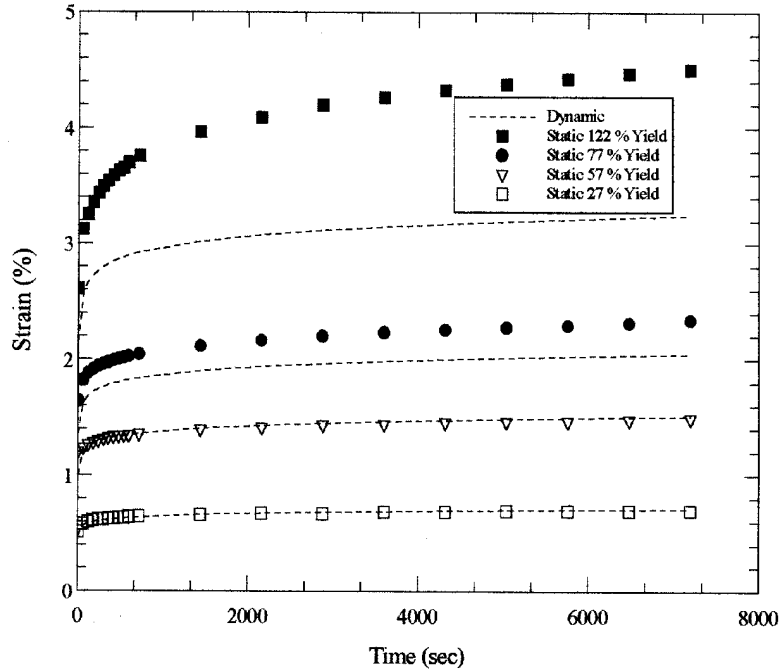


Fig. 8: Comparison of static and dynamic test results

A comparison of the creep curves obtained from the dynamic and static tests shown in Fig. 8 indicates that, within the range of stresses up to 57% of the yield stress, both experimental methods provide practically identical results. Above this limit, the dynamic testing technique predicts lower creep rates than those obtained from the static experiments. These latter results confirms that below the indicated stress limit the creep properties of PVF₂ can be characterized using the constitutive equations of linear viscoelasticity.

CONCLUSIONS

The results of this study clearly indicate that the mechanical response of piezoelectric polymers PVF₂ is time dependent. Linear viscoelastic theory based on the Boltzmann's superposition principle can be used to characterize the creep properties of the material for stresses below 57% of the yield stress. In the temperature range from 25 °C to 81 °C piezoelectric thin films PVF₂ can be treated as thermorheologically simple materials that follow the time-temperature correspondence principle. It is shown that within the indicated range of stresses, both static and dynamic test results are in good agreement. Based on these results, a power function has been used to describe the creep compliance of PVF₂.

It is important to note that the development of a complete constitutive model of piezoelectric polymers requires further research. In particular, an expanded experimental program is required to obtain the nonlinear viscoelastic stress-strain-time relations that will accurately describe the time dependent response of the material beyond the applicability range of the linear viscoelastic theory. In addition, research must be also directed towards time-dependent material characterization of piezoelectric coefficients that determine coupling effects between

electrical and mechanical responses of the material. However, such objectives remain out of the scope of present work.

ACKNOWLEDGMENTS

Funding of this research by NASA and Montana State University under the NASA EPSCoR Program (Grant NCCW-0058) is gratefully acknowledged. The authors also wish to thank Dr. Hugo Schmidt, Professor of Physics, and Dr. Vic Cundy, Head of the Mechanical and Industrial Engineering Department at MSU, for their assistance and interest in this work.

REFERENCES

1. Ikeda, T., Fundamentals of Piezoelectricity, Oxford University Press, New York, 1990.
2. Ferry, J.D., Viscoelastic Properties of Polymers (Third ed.), John Wiley and Sons, New York, 1980.
3. Christensen, R.M., Theory of Viscoelasticity, Academic Press, New York, 1971.
4. Smart, J. and Williams, J.G., "A Comparison of Single-Integral Nonlinear Viscoelasticity Theories, J. Mech. Phys. Solids, Vol. 20, 1972. pp. 313-318.
5. Schapery, R.A., "On the Characterization of Nonlinear Viscoelastic Materials", Polymer Engineering and Science, No. 9, 1969. pp. 295-310.
6. Lou, Y.G., and Schapery, R.A., "Viscoelastic Characterization of a Nonlinear Fiber-Reinforced Plastic, J. Composite Materials, Vol.5, No.4, 1971. pp. 208-234.
7. Strganac, T.W., Letton, A., Payne, D.F., and Biskup, B.A., "Characterization of Nonlinear Viscoelastic Behavior using a Dynamic Mechanical Approach", AIAA Journal, No. 5, 1995, pp. 904-910.

IMPROVEMENT OF DAMPING PROPERTY OF CFRP COMPOSITE BEAM INTERLEAVED WITH SHAPE MEMORY POLYMER BY USING CFRP LAMINATE AS A HEATER

Nobuo OSHIMA¹, Takehito FUKUDA² and Daisuke INUI³

¹*Graduate School of Engineering, Osaka City University,
3-3-138, Sugimoto, Sumiyoshi-ku, Osaka 558, Japan*

²*Faculty of Engineering, Osaka City University,
3-3-138, Sugimoto, Sumiyoshi-ku, Osaka 558, Japan*

³*Under Graduate School of Engineering, Osaka City University,
3-3-138, Sugimoto, Sumiyoshi-ku, Osaka 558, Japan*

SUMMARY: In the present paper, the damping properties of a carbon fiber reinforced plastic (CFRP) and glass fiber reinforced plastic (GFRP) hybrid composite laminate are controlled by CFRP laminate itself as a heater in order to construct so-called smart structures. An shape memory polymer (SMP) film is interleaved between the CF/GF hybrid laminate as a damping material and heated at the desirable temperature. From the preliminary experiments, it is found that the heating capability of the CFRP laminate heater is enough to control the temperature of the composite specimen. It is also verified that the surface temperature is almost uniformly distributed in overall specimen. The damping properties of the composite beam including SMP are analyzed by the Ross-Kerwin-Unger analysis.

KEYWORDS: CF/GF hybrid laminate, damping control, sandwich composite beam, shape memory polymer, CFRP heater, free vibration test, smart materials, Ross-Kerwin-Unger analysis.

INTRODUCTION

Fiber reinforced plastics (FRP) have excellent specific strength and specific modulus. Therefore, FRP are widely used for machines and constructions which require light weight. FRP are not only light weighted materials, but also tailor made materials.

Recently, numerous studies of constructing smart materials and structures prosper as one of methods which produces more high performance materials. The smart materials and structures have sensors and actuators to adapt themselves to environment and control their properties. FRP consists of two or more materials. This property is suitable for embedding sensors or actuators in its molding process. The idea of constructing smart materials and structures matches with such a concept for the idea of composite materials that the properties of composite materials can be tailored by combining with materials having different properties.

The damping property is one of important factors for improving the fatigue life of materials and structures. CFRP laminates have excellent specific strength and specific modulus, but their damping property laminate is not so high. There are some methods for improving damping property of CFRP laminate. One of methods is adding visco-elastic materials to CFRP laminate. There are two techniques to add the visco-elastic layers. One is attaching the visco-elastic layers to the surface of the composite laminates, so called free visco-elastic layers, and another is to interleave visco-elastic layers between the composite laminates, so called constrained visco-elastic layers [1],[2]. The former is easier to construct them, while the latter is more effective to improve the damping properties of them. In the present paper, the latter technique is adopted and an SMP film is interleaved as a visco-elastic layer. The SMP is very sensitive to the temperature. Especially, near glass transition temperature (T_g) the visco-elastic properties of the SMP have a large change. The dynamic properties of the composite beam have strong dependency of the visco-elastic properties of sandwiched visco-elastic layer. It is expected that the composite beams having various dynamic properties are produced by controlling the temperature of the SMP.

The temperature of the composite beam is influenced by the change of the environment temperature [3],[4],[5]. A carbon fiber is not only a strong material, but also an electrically conductive material. Therefore, in order to make the composite beam smart, CFRP layers are utilized for controlling the temperature of specimen as a heater. Since CFRP has strong anisotropy in electric resistance, CFRP laminate having $\pm 45^\circ$ fiber orientation was adopted.

The damping property of the composite beam is measured under clamped-free condition as changing the temperature of the composite beam by using CFRP laminate as the heater. The damping property of the composite beam is also calculated by Ross-Kerwin-Ungar analysis. The calculated values showed good agreement with the experimental values.

SHAPE MEMORY POLYMER

Visco-elastic properties of SMP are extremely changed above and below the T_g . In this paper, this characteristics are utilized for improving damping properties of the composite beam. A polyurethane based SMP is adopted. The complex shear moduli and the loss tangent of the SMP are shown in Fig. 1. In this figure, G' and G'' are the storage shear modulus and the loss shear modulus, respectively and $\tan \delta$ means the loss tangent. The T_g is about 45°C . It is found that this SMP change the maximum elasticity at T_g .

SPECIMEN

The composite beam specimen consists of 9 layers as shown in Fig. 2. The fiber orientation of the composite beam is $[0^\circ\text{GF}/+45^\circ\text{CF}/-45^\circ\text{CF}/0^\circ\text{GF}/\text{SMP}/0^\circ\text{GF}/-45^\circ\text{CF}/+45^\circ\text{CF}/0^\circ\text{GF}]$, where CF and GF mean carbon fiber and glass fiber prepreps, respectively. Since CFRP is an electric conductive material, CFRP layers in such a beam are also used as a heater to increase the temperature of the composite beam. But, there are some problems for utilize CFRP laminates as the heater.

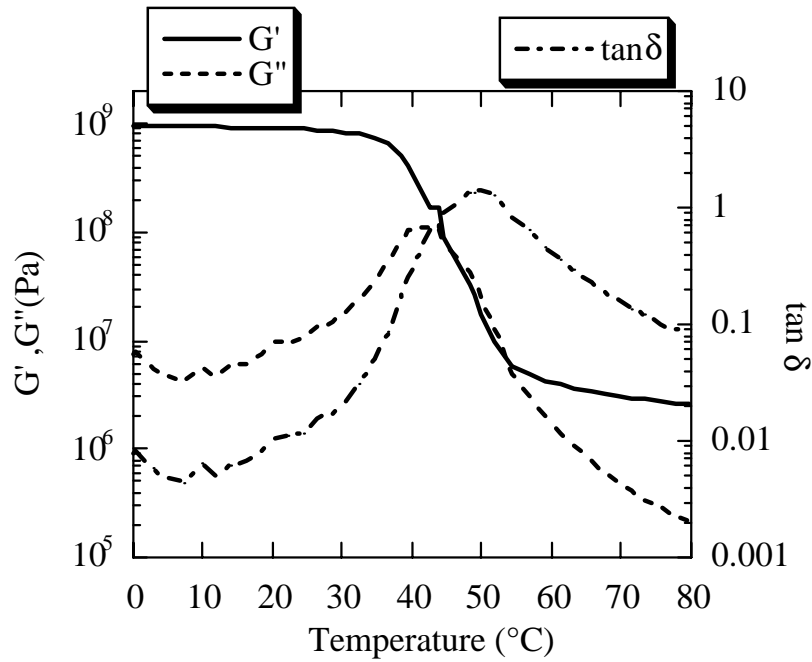


Fig 1: Visco-elastic property of shape memory polymer

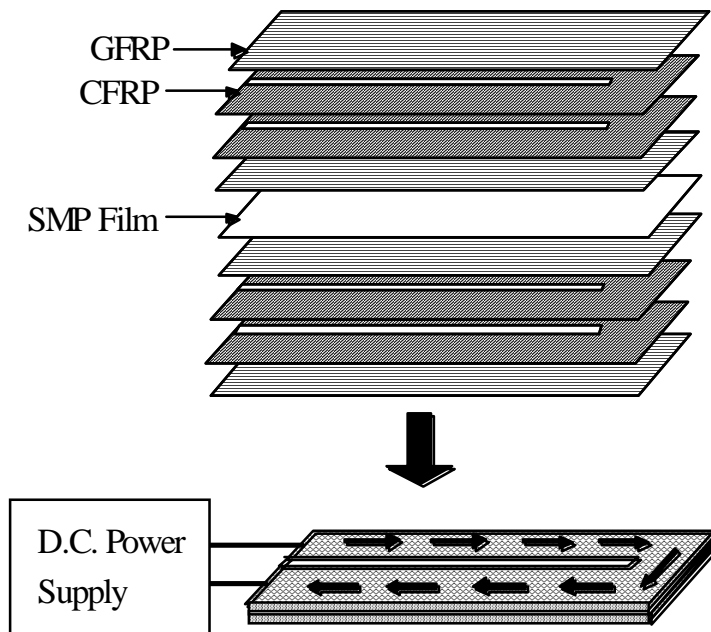


Fig 2: Schematic view of composite beam specimen with stacking sequence of CF and GF prepregs

INFLUENCE OF FIBER ORIENTATION ON THERMAL CHARACTERISTICS OF CFRP LAMINATE

Two kinds of CFRP laminates having fiber orientations $[0^\circ]$ and $[\pm 45^\circ]$ are prepared and tested. A specimen having $[0^\circ]$ fiber orientation was not uniformly heated when applied the electric voltage by an electric D.C. power supply. The temperature at the free end of the specimen was much higher than the temperature at other parts of specimen. This

phenomenon is explained by Ohm law. The generation of heat per unit area is related to the electric resistance and the electric voltage. That is, the generation of heat per unit area is in proportion to the electric resistance per area of the specimen. In the carbon fiber direction, the electric conduction is caused by carbon fibers which may role as a conductive wire. On the other hand, it is mainly caused by the contact of the carbon fibers in the perpendicular direction to the carbon fibers. Therefore, the lack of uniformity in heating was observed at the top end of CFRP [0°] laminate. Based on such an idea that the CFRP [$\pm 45^\circ$] laminate which has isotropy in electric resistance, the specimen using CFRP [$\pm 45^\circ$] laminate is adopted. In this case, the uniform heat of generation was observed in overall specimen.

THERMAL PROPERTIES OF COMPOSITE BEAM

In order to examine the thermal capability of CFRP laminate as a heater, the heating test is conducted at the room temperature. The specimen is supported under the clamped-free condition and the electric power is supplied to the fixed end of the CFRP laminate by the D.C. power supply. The temperature on the surface of the specimen is measured by a thermocouple. The relation between the temperature on the surface of the specimen and the electric voltage supplied to the CFRP laminate is shown in Fig. 3. In this figure, it is known that each saturated temperature is increased as increasing applied electric voltages. The heating changes of the specimen are shown in Fig. 4. The specimen is heated faster as increasing applied electric voltages. In this experiment the maximum voltage applied to the CFRP heater was 24V due to the restriction of the experimental system.

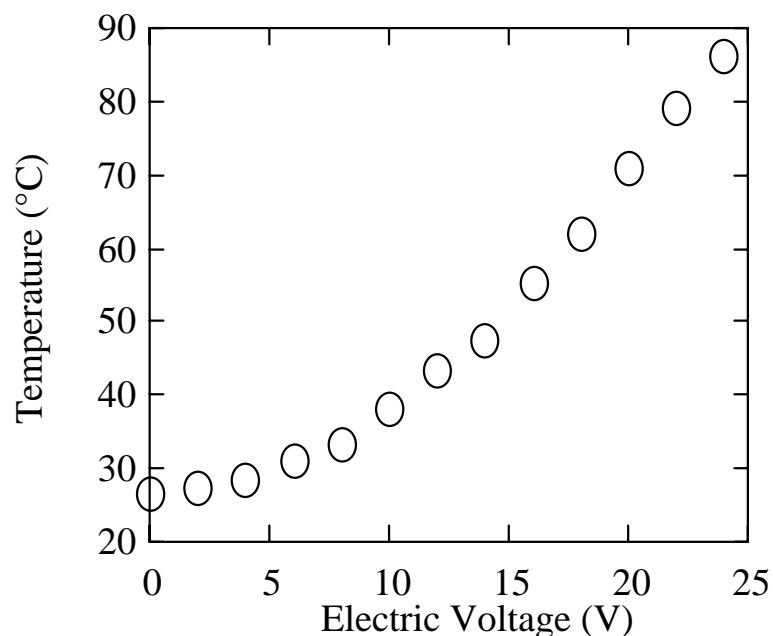


Fig 3: Temperature on the surface of composite beam specimen and electric voltage supplied to CFRP heater

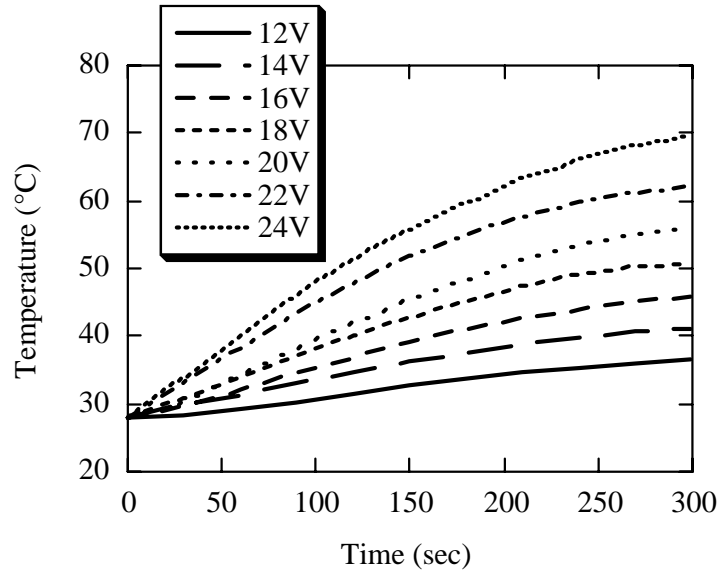


Fig 4: Temperature changes of composite beam specimen with various electric voltages supplied to CFRP heater

DAMPING PROPERTIES OF CFRP COMPOSITE BEAM

Experiments by using CFRP heater

The experimental set-up is shown in Fig. 5. It consists of a composite beam specimen supported under the clamped-free condition, a non-contacting laser pick-up, an FFT analyzer, a D.C. power supply and an impulse hammer. The experiment was performed by the free vibration test. The impulse input at the free end of the specimen is given by the impulse hammer. The response at the free end of the specimen is measured by the non-contacting laser pick-up and recorded by the FFT analyzer. The composite beam is heated up by the CFRP heater to which the electric voltage is provided by the D.C. power supply.

Results and Discussion

The logarithmic decrement vs. the temperature of the specimen is shown in Fig. 6. At the room temperature the logarithmic decrement is less than 0.02. From about 45°C, the logarithmic decrement is increased as the temperature of the specimen increases. At 70°C, the logarithmic decrement reaches to 0.45. This value is more 20 times larger than the one at the room temperature.

The natural frequency of the specimen vs. the temperature of the specimen is also shown in Fig. 6. At the room temperature, the natural frequency is around 33Hz. From 45°C, the natural frequency is decreased as the temperature increases. The reason of this phenomenon is that when the damping property of constrained layer system is increased, not only the loss shear modulus, but also the shear deformation of the constrained layer are increased as a result of decreasing the storage shear modulus. From this result, the composite beam which has suitable dynamic properties can be produced by controlling the temperature of the specimen by using the CFRP heater.

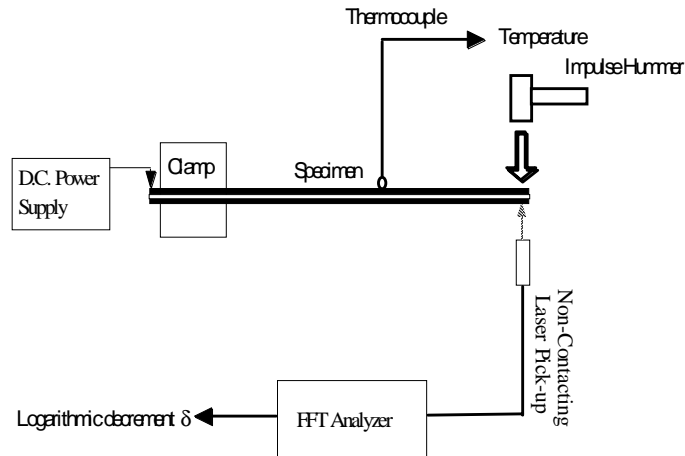


Fig 5: Experiment set-up of free vibration test by using CFRP heater

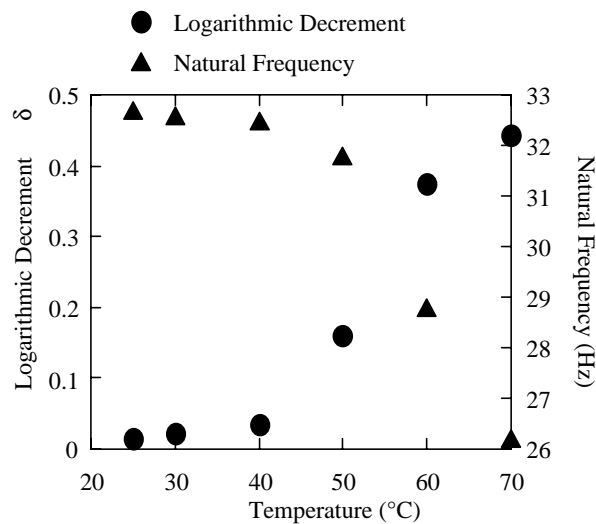


Fig 6: Logarithmic decrement and natural frequency vs. temperature of composite beam specimen by using CFRP heater

Experiments in a thermostatic chamber

The experimental set-up is shown in Fig. 7. A specimen having a strain gage is tested in a thermostatic chamber. In this experiment, the composite beam is heated up by the thermostatic chamber where the desirable temperature is controlled. The composite beam is supported under the clamped-free condition and the similar experiment is taken by free vibration test. The free vibration test is performed by a wire cut method, because of the restriction of the experimental set-up. The strain response at the fixed end is measured by the strain gage. The strain response is recorded by the FFT analyzer and converted to the vibration deflection response at the free end of the composite beam by using the beam theory.

Results and Discussion

The logarithmic decrement vs. the temperature of the specimen is plotted in Fig. 8. From this figure, it is found that the change of the logarithmic decrement is almost the same as the former case using the CFRP heater. But, the rate of the increment in this case is a little smaller than the one in the case using the CFRP heater. This may be supposed due to the reason that when the CFRP heater is used, the surface temperature of the specimen is a little different from the internal temperature of the specimen. Especially, over 50°C, the surface of the specimen is cooled by the room atmosphere. Thus the internal temperature of the specimen would be higher than the surface temperature. The damping property of the composite beam involving the SMP film depends on the visco-elastic property of the SMP. Therefore, it is important to recognize the internal temperature of the composite beam.

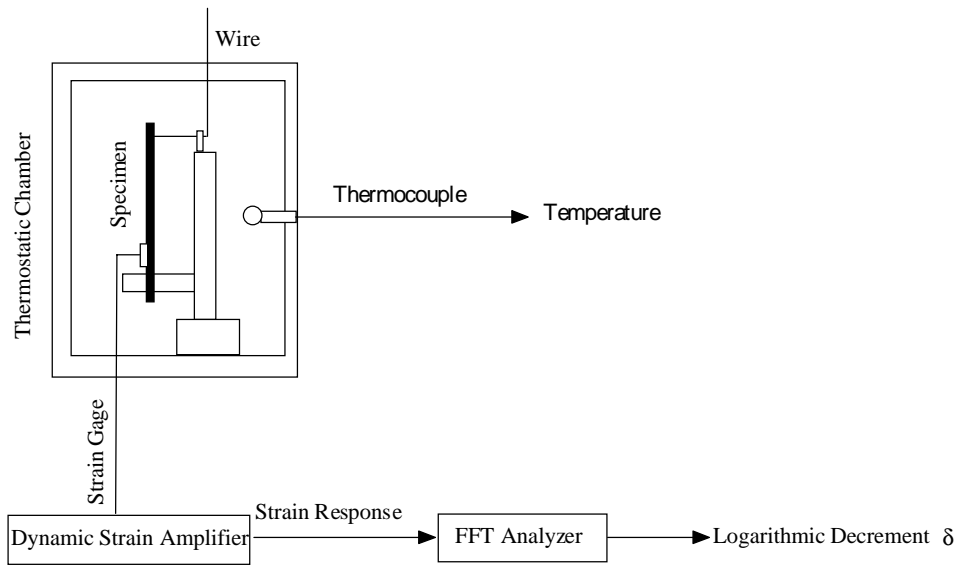


Fig 7: Experimental set-up of free vibration test by using thermostatic chamber

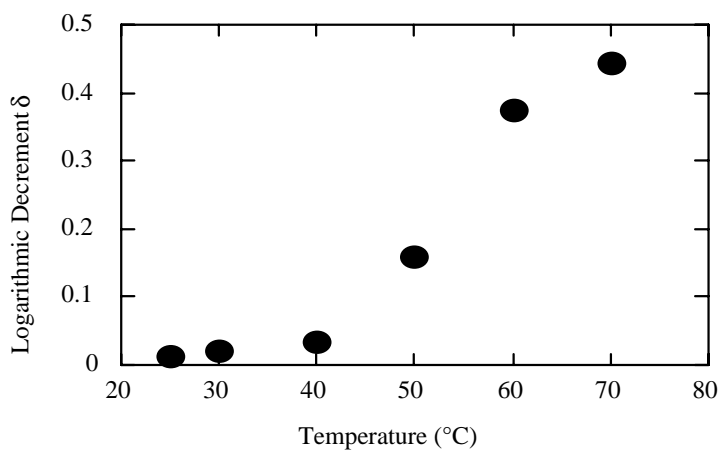


Fig 8: Logarithmic decrement vs. the temperature of composite beam specimen in thermostatic chamber

ANALYSIS

Ross-Kerwin-Ungar Analysis

Ross-Kerwin-Ungar analysis is used in order to predict the logarithmic decrement of the composite beam [6]. This RKU analysis has been developed for a three layer system. It is usually used to handle both extensional and shear types of treatment.

The flexural rigidity, EI^* , of the three-layer system shown in Fig. 9 is

$$\begin{aligned}
 EI^* = & E_1^* \frac{H_1^3}{12} + E_2^* \frac{H_2^3}{12} + E_3^* \frac{H_3^3}{12} - E_2^* \frac{H_2^2}{12} \left(\frac{H_{31} - D^*}{1 + g^*} \right) \\
 & + E_1^* H_1 D^{*2} + E_2^* H_2 (H_{21} - D^*)^2 + E_3^* H_3 (H_{31} - D^*)^2 \\
 & - \left[\frac{E_2^* H_2}{2} (H_{21} - D^*)^2 + E_3^* H_3 (H_{31} - D^*) \right] \left(\frac{H_{31} - D^*}{1 + g^*} \right)
 \end{aligned} \quad (1)$$

where,

$$D^* = \frac{E_2^* H_2 \left(H_{21} - \frac{H_{31}}{2} \right) + g^* (E_2^* H_2 H_{21} + E_3^* H_3 H_{31})}{\left(E_1^* H_1 + \frac{E_2^* H_2}{2} \right) + g^* (E_1^* H_1 + E_2^* H_2 + E_3^* H_3)}$$

$$H_{31} = \frac{(H_1 + H_3)}{2} + H_3, \quad H_{21} = \frac{(H_1 + H_2)}{2}, \quad g^* = \frac{G_2^*}{E_3^* H_3 H_2 p^2}, \quad p = \frac{\xi_n}{L},$$

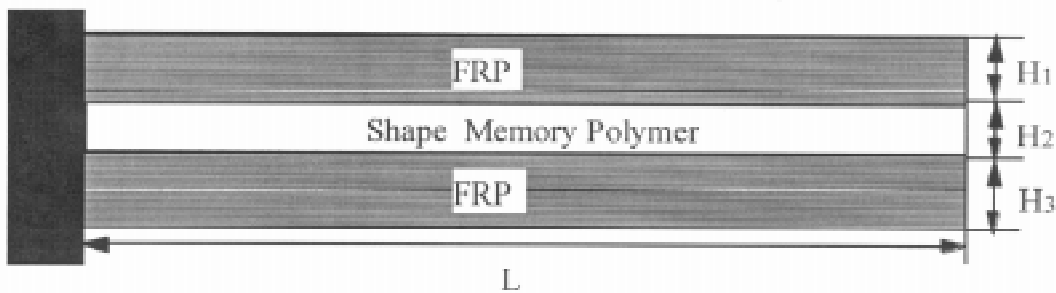


Fig. 9: Composite beam model with shape memory polymer film

and E^* is the Young's modulus of elasticity, G^* is the shear modulus, I is the second moment of area, H is the thickness and ξ_n is the n th eigenvalue. Subscript 1 refers to the base structure, subscript 2 to the damping layer, subscript 3 to the constraining layer, and no subscript refers to the composite system. D is the distance from the neutral axis of the three layer system to that of the base structure. The logarithmic decrement is calculated from the imaginary part and the real part of flexural rigidity.

Results and Discussions

Fig. 10 shows a comparison of the experimental logarithmic decrement and the calculated ones. In this calculation, $H_1=H_3=0.4\text{mm}$, $H_2=0.2\text{mm}$, $\xi_n=22.373$ and $L=200\text{mm}$ were used. From this figure, it is found that the calculated value shows good agreement with the experimental value except that the calculated value is shifted to slightly lower region. The reason is explained as follows; any kind of chemical reactions are not considered in the analysis, and it is assumed that the composite beam consists of the completely separated the three layer system. However, actually, the chemical reaction might take place between the matrix resin for the prepreg sheet and the SMP film at the higher molding temperature. Thus, it is supposed that the interface between the prepreg sheet and the SMP film is not clearly distinct.

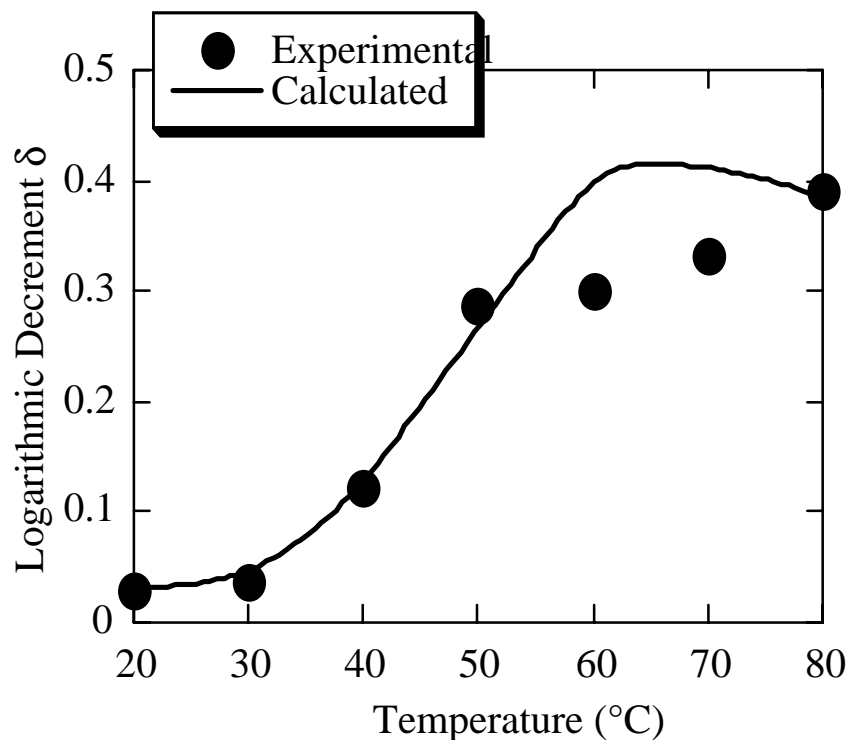


Fig 10: Comparison of experimental and calculated logarithmic decrements

CONCLUSION

It has been shown that the damping property of the CF/GF hybrid composite beam including shape memory polymer can be changed by controlling the temperature of the composite beam with the CFRP heater. The results obtained here are summarized as follows;

- 1) The CFRP laminate has a thermal capability which is enough to heat up the composite beam. CFRP [$\pm 45^\circ$] laminate is adopted to obtain the isotropy in electrical resistance.
- 2) The saturated temperatures of the composite beam are increased as increasing electric voltages applied to the CFRP heater. Increasing applied electric voltages, the specimen is heated faster.

- 3) The composite beam possessing a suitable damping property can be produced by controlling the temperature of the specimen by using the CFRP heater.
- 4) The damping property of the composite beam can be explained by Ross-Kerwin-Ungar analysis.

ACKNOWLEDGMENT

The authors wish to thank Prof. H. Fukuda of Tokyo Science University, Prof. H. Asanuma of Chiba University for significant discussions on the use of CFRP laminates as a heater. They also acknowledge Mitsubishi Heavy Industries, Ltd. for providing the shape memory polymer.

REFERENCE

1. Fujimoto, J., Ugo, R., and Todome, K., "Damping Materials for Spacecraft Structures", *Proc of the 1st Japan International SAMPE Symposium*, pp. 1704-1709, 1989.
2. Fujimoto, J., Tamura, T., Todome, K., Tanimoto, T., Suzuki, Y., Kauchi, K., "Mechanical Properties for CFRP/Damping Material Laminates", *Proc. of ICCM-8*, pp. 34-D-1-34-D-10, 1991.
3. Fukuda, T., Oshima, N. and Hourai, K., "Vibration Characteristics of Fiber Composite Laminates with Shape Memory Film", *Proc. of Japan-Europe Symposium on Composite Materials*, pp. 37-42, 1993.
4. Fukuda, T., Oshima, N. and Hourai, K., "Use of Shape Memory Polymer for Damping Control of Fiber Composite Materials", *Proc. of ICCM-9*, Vol. V, pp. 323-328, 1993.
5. Fukuda, T., Oshima, N., "Damping Properties of Fiber Composite Laminate with Shape Memory Polymer Film as an Interleaf", *Memoirs of Faculty of Engineering Osaka City University*, Vol. 35, pp. 1-13, 1994.
6. Nashif, A. D., Jones, D. I. G. and Henderson, J. P., *Vibration Damping*, Chapter 6, Surface Damping Treatment, New York, John Wiley & Sons, 1985.

ACTIVE CONTROL OF CRACK-TIP STRESS INTENSITY BY CONTRACTION OF SHAPE MEMORY TiNi FIBERS EMBEDDED IN EPOXY MATRIX COMPOSITE: DEPENDENCY OF STRESS INTENSITY FACTOR ON CRACK-TIP DOMAIN SIZE

Akira Shimamoto¹, Yasubumi Furuya² and Minoru Taya³

1 Department of Mechanical Engineering, Saitama Institute of Technology, Okabe-cho, Saitama 369-02, Japan

2 Department of Material Processing, Tohoku University, Sendai 980, Japan

3 Department of Mechanical Engineering, University of Washington, Seattle, WA 98105, USA

SUMMARY: Shape memory TiNi fiber reinforced/epoxy matrix composite is fabricated to demonstrate the suppression effect of crack-tip stress concentration and the increase of fracture toughness (K value) of the composite. The increase of fracture toughness is attributed to the compressive stress field in the matrix which is induced when the prestrained TiNi fibers contract to the initial length upon heating above austenitic finish temperature of TiNi fiber ($T > A_f$). The dependence of K value on the prestrain value of TiNi fibers as well as the compressive stress domain size between a crack-tip and fiber are discussed based on the analytical equivalent inclusion model for a composite. The experimental data agreed well to theoretical predictions.

KEYWORDS: shape memory alloy, smart composite, stress intensity factor, photoelasticity, phase transformation, fracture toughness, crack closure

INTRODUCTION

Enhancement of the mechanical strength (stiffness, yield strength and fracture toughness) and suppression of the degradation damage (crack, delamination) during in service time are very important subjects in the development of engineering composite systems. Recently, the authors developed a new type of "smart" composite where shape memory TiNi fiber was used as a reinforcement and actuator to improve the mechanical properties of the composite at higher use temperatures above the inverse transformation temperature ($T > f$) of TiNi alloy [1,2,3,4] up to the present, the enhancing effects of the tensile yield strength, the suppression effect of fatigue crack propagation in TiNi fiber reinforced Al matrix composite (TiNi/Al) [5] and the increase of the fracture toughness (K-value) in a TiNi/epoxy composite have been experimentally confirmed because of the large compressive stresses in the matrix by the shape memory shrinkages of embedded fibers.

In the present paper, shape memory TiNi fiber reinforced/epoxy matrix composites are fabricated to re-verify the active damage control for cracks in the composite by using

experimental photoelasticity method. The suppression effect of crack-tip stress concentration and the increase of fracture toughness (K) are investigated. Especially, the dependencies of K value on not only the prestrains of TiNi fibers but also the compressive stress domain size between a crack-tip and the embedded fibers are discussed based on the analytical equivalent inclusion model for a composite.

DESIGN CONCEPT FOR SHAPE MEMORY COMPOSITE

Thermoelastic shape memory effect (i.e. shape memory and recovery phenomenon) takes place during martensite (M) to austenite (A) phase transformation in SMA with increasing temperature. Therefore, material functional properties of SMA changes clearly depending on the changes of temperature as summarized in Fig. 1. It should be noticed as a unique property that SMA shows more higher stiffness (2-3 times) and large recovery stress at the higher temperature region due to inversely thermoelastic phase transformation in opposition to weakening of those properties in the general metals.

In consequence, SMA natively has the smart functions, i.e., (1)sensor (thermal), (2)actuator (shape memory deformation) and (3) memory and shape recovery (namely, processor function). These unique properties natively with SMA can be utilized to strengthen the composite.

The design concept of enhancing the mechanical properties of the SMA composite is schematically shown in Fig.2. TiNi fibers are heat-treated to shape-memorize their initial length at higher temperatures ($>T_f$), then quenched to room temperature (nearly, martensite start temperature $=M_s$), given tensile prestrain $\epsilon_T (>0)$ and embedded in the matrix material to form a composite. The composite is then heated to temperature ($>A_f$) at which the TiNi fibers tend to shrink back to their initial length by the amount of prestrain ϵ_T , then the matrix is subjected to compressive stress. It is this compressive stress in the matrix that contributes to the enhancement of the tensile properties of the composite and fracture toughness.

EXPERIMENT

Experimental processing, mechanical testing of TiNi/epoxy composite is described. The shape memorized TiNi fibers (Ti-50.2at%Ni) of 400 μm diameter supplied by Kantoc Ltd., Fujisawa, Japan were arranged in a mold to which photoelastic epoxy and specified amount of hardener were poured and then kept at 130°C for 2 hours for curing. After curing, as-molded composite was cooled to room temperature. During the process, TiNi fibers were kept in tension with four different prestrains of 0, 1, 3 and 5%. A side notch which has three different lengths 3, 4, 4.8mm were then cut into the as molded composite specimen for changing the domain size (D) between a crack-tip and a fiber. The geometry of the composite specimen is shown in Fig.3. In order to determine the transformation temperatures and stress-strain relations of TiNi fiber, tensile test of TiNi fiber at different temperatures (T) was conducted. The stress vs. strain curves at constant temperature: T=20, 40, 60, 80 and 100°C were obtained as shown in Fig.4. From another relationship between strain vs. T at constant stress of 94MPa, four transformation temperatures of TiNi fiber were determined: Martensitic start $M_s=31^\circ\text{C}$, Martensite finish $M_f=1^\circ\text{C}$, Austenitic start $A_s=57^\circ\text{C}$, and Austenitic finish $A_f=63^\circ\text{C}$. A constant load of 392N was applied to TiNi/epoxy specimen by the controlled tensile test machine to form the third or fourth photoelastic fringe pattern. The changes of

number of fringe pattern lines developed around the notch tip were measured at different constant temperatures of 20, 30, 40, 50, 60, 70, 80, 90 and 100°C.

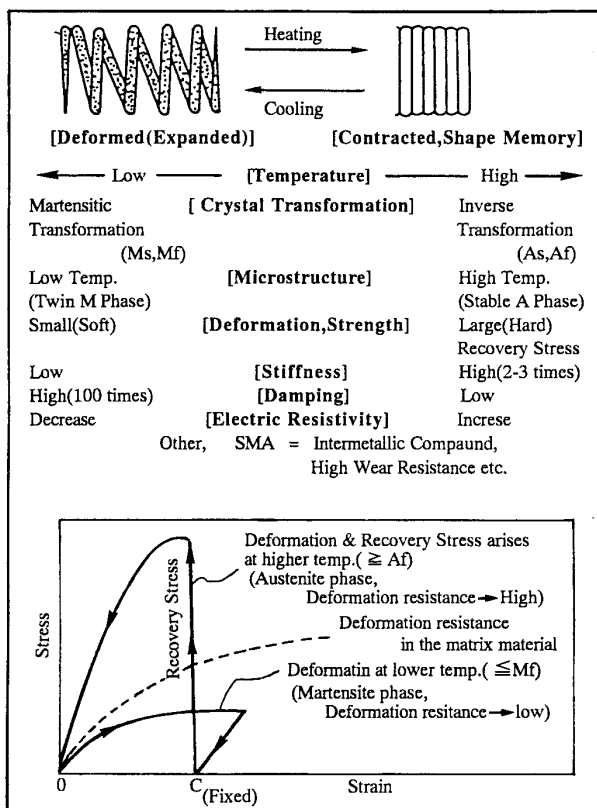


Fig.1: Material properties of shape memory alloy with increasing temperature

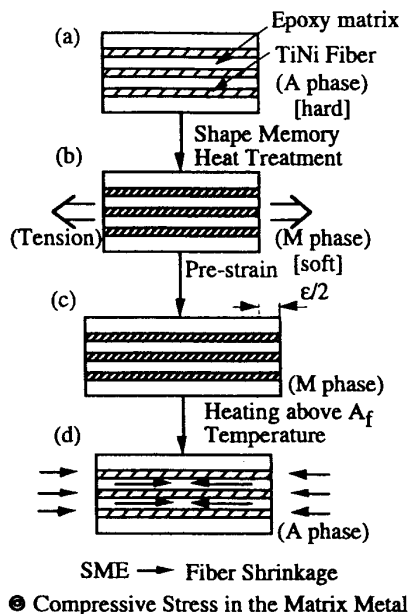


Fig.2: Design concept of SMA smart composite

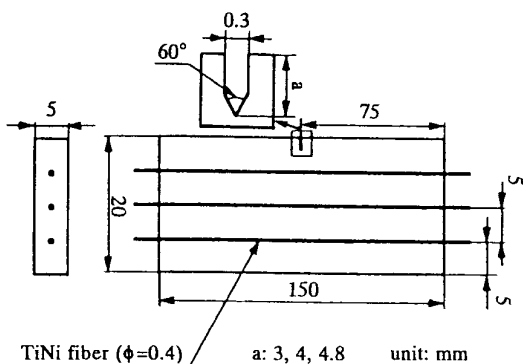


Fig.3: Geometry of TiNi/epoxy composite specimen with a side notch.

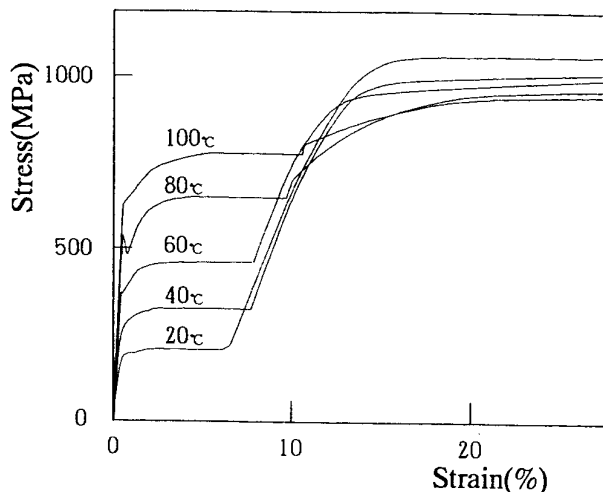


Fig.4: Stress-strain curves of TiNi fiber at different temperatures.

RESULTS AND DISCUSSION

Dependence of Stress Intensity Factor (K-value) on the Prestrain Value(e)

The results of the photoelasticity experiment are shown in Fig.5. Fig.5.(a),(b),(c) and (d) denote the fringe pattern developed around the notch tip in the composite with prestrain 0,1,3 and 5% tested at 80°C, respectively. Fig.5 demonstrates clearly the shape memory effect as the stress intensity factor measured at 80°C above Af, respectively. From the Fig.5, shape memory effect of the embedded TiNi fibers reduce the stress concentration with increasing prestrain value. Stress intensity factor KI can be computed from

$$K_I = \frac{n\sqrt{2}\pi r_m}{\alpha t \sin\theta_m} \left[1 + \left(\frac{2}{3 \tan\theta_m} \right)^2 \right]^{-0.5} \left[1 + \frac{2 \tan(3\theta_m/2)}{3 \tan\theta_m} \right] \quad (1)$$

where n is the number of the fringe, t is the composite plate thickness, α is the epoxy photo-elasticity sensitivity constant, r and θ_m are, respectively, the distance and angle in polar coordinates at point M, shown schematically in Fig.6. The experimental results of the reductions in the stress intensity factor KI are plotted in Fig.7 as a function of temperature along X-axis under three different prestrains in a case of notch length of 4.8mm. The value of KI ratio in Y axis means the normalized value of KI which can be calculated from dividing absolute KI value in a certain prestrained specimen by the KI value of zero-prestrained specimen. KI ratio clearly decreases with increasing temperature above 60°C which is nearly equal to Af temperature of TiNi fiber. It indicates that the shape memory shrinkages of TiNi fibers above 60°C can suppress the stress intensity at a crack-tip. Fig.8 shows the relationship between KI-value ratio and prestrain value in three cases of notch lengths. Stress intensity decreases with increasing prestrain value where the decrease of KI experimentally seems most intense in the most small domain size at a=4.8mm.

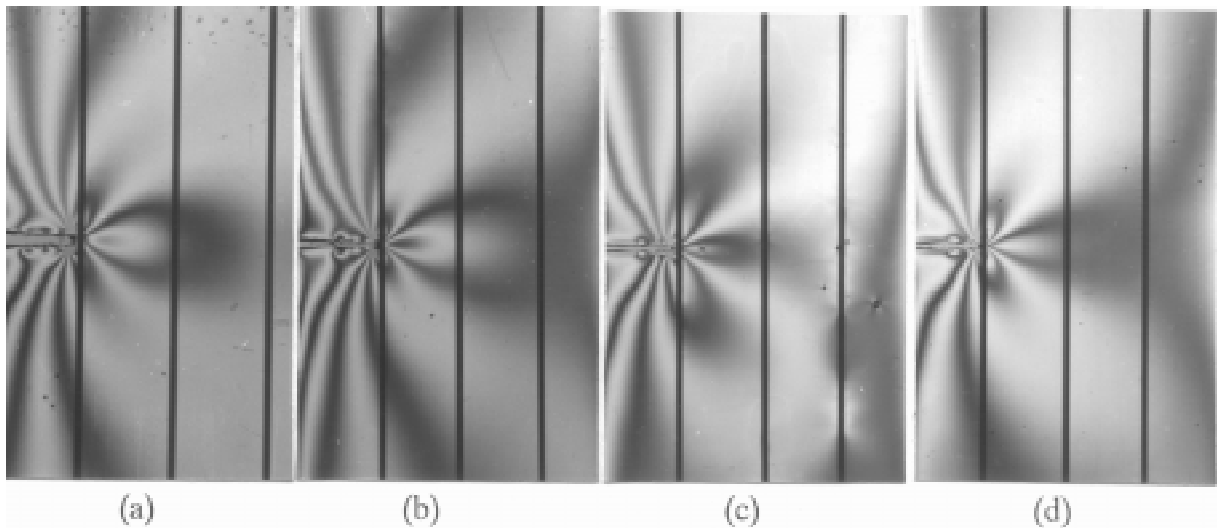


Fig.5 Photoelastic fringe patterns around a side notch of TiNi/epoxy specimen loaded by 392N at 80 °C with different prestrains: (a) 0%, (b) 1%, (c) 3% and (d) 5%

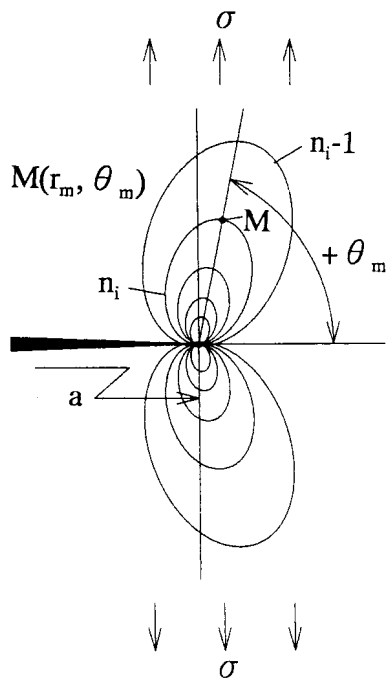


Fig.6 Photoelastic fringe pattern schematically developed in front of a crack size a .

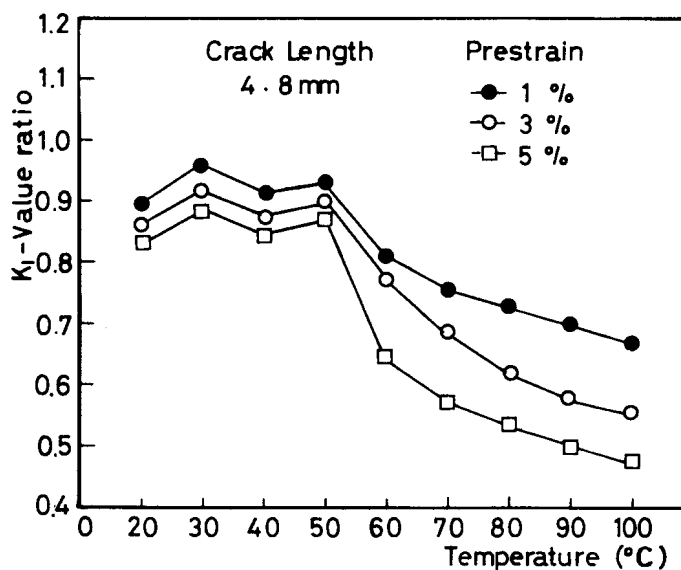


Fig.7 Stress intensity factor KI -ratio as a functions of temperature under three different prestrains in a case of crack length of 4.8mm.

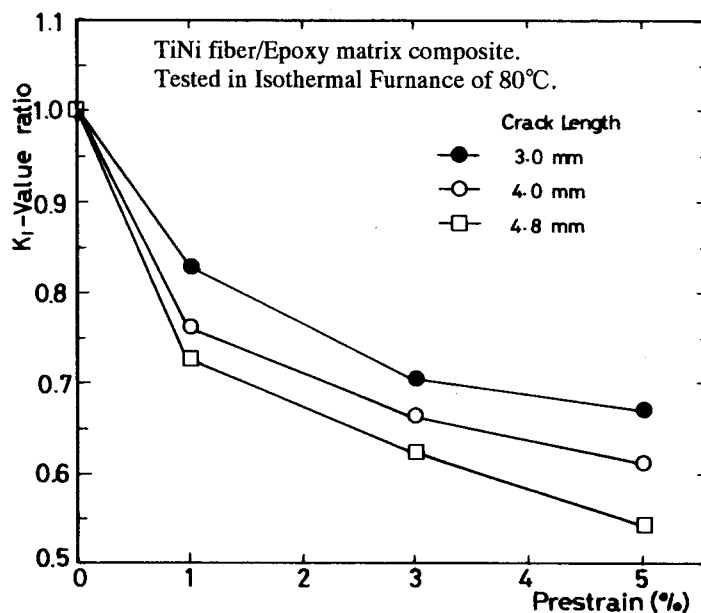


Fig.8 Stress intensity factor KI -value ratio vs. prestrain in three different cases of crack lengths.

Dependence of Stress Intensity Factor (K-value) on the Domain Size (D)

Lastly, the reduction in stress intensity factor due to prestrain and shape memory effect is estimated by the analytical modeling which generally consists of the steps: (1) computation of the compressive residual stress in the matrix, (2) prediction of crack-tip stress intensity factor change ΔK_I . Following Eshelby's equivalent inclusion method [5,6,7] by using eigen strain concept as well as the equilibrium equation of force between TiNi fiber stress and average matrix stress in axisymmetry along the axis of fiber direction, average stress change of the matrix (q) can be calculated. When a crack tip is subjected to compressive stress q, then, the stress intensity factor K_I is given by following equation [8].

$$\Delta K_I = 2q \sqrt{\frac{2D}{\pi}} \quad (2)$$

where D is the length of the compressive stress domain between a crack-tip and the embedded fiber. Eqn(2) was originally formulated by Tada et al. has been used by several researchers [9,10]. The values of D in the present experiment are 2,1 and 0.2 mm respectively for three notch depths as shown in Fig.3. The value of q is in unit of MPa, and computed from the residual stress model for matrix.

As a result, the predicted values of K_I are plotted as solid points in Fig.9. As to the relationship between K_I ratio and prestrain, the analytical model explains the same trend as the experimental results, i.e., K_I -value decreases with increase in prestrain, however, the predictions are apt to show larger values than those of the experiment.

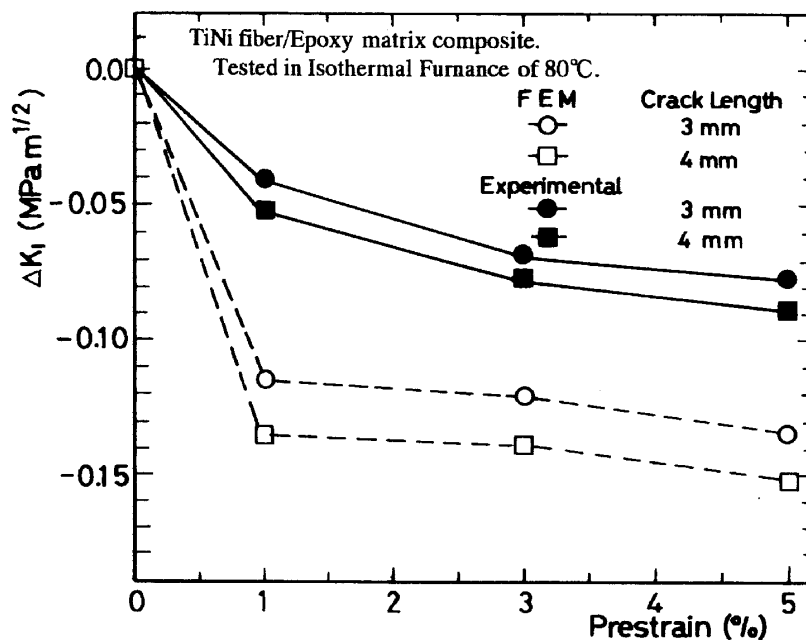


Fig.9 Relationship between K_I change and prestrain in experimental data and FEM analysis.

CONCLUSION

Shape memory TiNi fiber reinforced /epoxy matrix composite was fabricated to demonstrate the suppression effect of crack-tip stress concentration and the increase of fracture toughness (K value) of the composite. The increase of fracture toughness was attributed to the compressive stress field in the matrix which was induced when the prestrained TiNi fibers contract to the initial length upon heating above austenitic finish temperature of TiNi fiber ($T > A_f$). As to the dependence of K values on the prestrain value of TiNi fibers and the compressive stress domain size between a crack-tip and fiber, the analytical model explains the same trend as the experimental results.

REFERENCES

1. Furuya, Y., Sasaki, A. and Taya, M., "Enhanced Mechanical Properties of TiNi Shape Memory Fiber/Al Matrix Composite", *Mater. Trans. JIM*, Vol.34(3), 1993, pp.224-227.
2. Shimamoto, A. and Taya, M., "Reduction in KI by shape memory effect in a TiNi shape memory fiber reinforced epoxy matrix composite" *J. JSME*, 63-605-A, 1997, pp.26-31.
3. Shimamoto, A., Furuya, Y. and Taya, M., "Mechanical Strength of Shape Memory TiNi Fiber Reinforced Epoxy Matrix Composite, 1st. Report: Active Control of Crack-Tip Stress Concentration", The 71st. JSME Spring Annual Meeting, 1994, pp.660-662.
4. Shimamoto, A., Furuya, Y. and Taya, M., "Active Control of Crack-tip Stress Intensity By Contraction of Shape Memory TiNi Fibers Embedded In Epoxy Matrix", *Proceedings of the International Symposium on Microsystems Intelligent Materials Robots*, 1995, pp.463-466.
5. Furuya, Y. and Taya, M., "Improvements of tensile strength and fatigue resistance by shape memory effect in TiNi Fiber/Al Matrix Composite", *Material Trans. JIM*, 34-12, 1996, pp.346-354.
6. Eshelby, J.D., "The Determination of The Elastic Field of An Ellipsoidal Inclusion and Related Problems", *Proc. Roy. Soc. Lond.* A244, 1957, pp.376-396.
7. Taya, M. and Arsenault, R.J., "Metal Matrix Composite: Thermomechanical Behavior", Pergamon Press, 1989.
8. Tada, H., Paris, P.C. and Irwin, G.R. *The Stress Analysis of Cracks Handbook*, Del Research Corp. Hellertown, PA, 1973, pp.3.7.
9. Evans, A.G., Heuer, A.H. and Porter, D.L., "The Fracture Toughness of Ceramics", *Proc. Intl. Conf. Fract.-4 I*, 1977, pp.529-556.
10. Taya, M., Hayashi, S., Kobayashi, A.S. and Yoon, H.S., "Toughening of A Particulate-reinforced Ceramics-matrix Composite by Thermal Residual Stress", *J. Am. Ceram. Soc.* 73(5), 1990, pp.1382-1391.

A TWO-DIMENSIONAL SHAPE MEMORY ALLOY ACTUATOR

Weida Wu and Faramarz Gordaninejad

Department of Mechanical Engineering, University of Nevada, Reno, Nevada 89557, USA

SUMMARY: A theoretical model for the response of a two-dimensional, thermally-driven, shape memory alloy (SMA) actuator is developed. The actuator is assumed to be constructed from a thin layer of SMA bonded to a layer of elastomer. The plate is under a uniformly distributed transverse load. The governing equations is developed by utilizing the classical laminated plate theory, energy balance equations, and a two-dimensional transition model of the SMA layer. A finite element method is employed to solve the nonlinear transient system of equations. Parametric studies are conducted to demonstrate the effects of the elastomer thickness and thermal conductivity, input heating power, and heat sink strength on the overall time response of the SMA actuator.

KEYWORDS: shape memory alloy, elastomer, actuator, two-dimensional, composites, time response, heat sink strength, heating power

INTRODUCTION

The focus of this study is on the time response of a two-dimensional SMA actuator composite plate which is assumed to be constructed from a thin layer of SMA perfectly bonded to a layer of elastomer. In a recent study, the temperature-stress-strain and time responses of a SMA composite beam were investigated by using the energy balance equation for SMA, the equilibrium equations, the constitutive equations, the state equation of phase transition, and a shear-lag stress model [1].

The SMA reinforced composites have been widely studied in recent years. Rogers and baker [2] demonstrated an application of SMA composite in the active structural vibration control of a clamped-clamped graphite/epoxy beam with embedded SMA actuators at the neutral axis. The application of the SMA reinforced composite in structural acoustic radiation control was investigated by Saunders *et al.* [3]. Baz and Tampe [4] have shown that discrete SMA actuator can be used to control buckling of flexible structure. Lagoudas and Tadjbakhsh [5] studied a generalized theory to model the resultant forces and moments for a flexible rod with an embedded line actuator.

Models to simulate the martensitic transformation were developed by Tanaka [6], and Liang and Rogers [7]. Also, a one-dimensional thermo-mechanical constitutive relations for SMAs were developed by Rogers, *et al.* [8]. In order to simulate the thermal-stress behavior of a SMA in a two-dimensional geometry, Ikuta and Shimizu [9] introduced a so called “variable sublayer model.”

In this study, a two-dimensional nonlinear transient analysis of a thermally-driven SMA actuator is presented. The classical laminated plate theory is utilized. The energy balance equation for the SMA layer is developed to model the thermal behavior of the SMA layer. The nonlinear constitutive equations of the SMA layer is obtained by combining the plate's constitutive equations with the variable sublayer model for the two-dimensional martensitic transformation. The governing nonlinear system of equations are solved by using a finite element method.

SMA-ELASTOMER ACTUATOR MODELING

Let us consider the actuator shown in Figure 1. The xy coordinate are fixed at the midplane. The plate is composed of two isotropic layers, a SMA layer with thickness, t , and an elastomer layer with thickness, $h - t$. The elastomer layer is perfectly bonded to a heat sink maintained at temperature T_0 . The four edges of the plate are assumed to be simply supported. The plate is subjected to a uniformly distributed transverse load, q .

Initially, the SMA layer is prestrained in the martensitic phase before the transverse load is applied. The stress-strain state in the SMA is indicated schematically as state 1 in Figure 2. Due to the applied load an additional elastic strain is built in the SMA which is indicated as state 2. When heated by passing an electric current above the austenite start temperature, A_s , the SMA transforms into the austenitic phase, attempting to recover the elastic strain and the prestrain. Since the focus in this work is on the time response and the actuation mechanism of the SMA, only small deformation of the plate is considered. Hence, the recover strain is kept within the range of the linear elastic strain (i.e., state 3 indicated in Figure 2). This is the limit for the recovery strain. As a result of strain recovery process, the deflection of the plate is reduced. After the electric current is reduced or removed, the SMA cools down to the martensite phase via conduction through the elastomer to the heat sink. When the SMA reaches the martensite phase, the stress-strain state of the SMA returns to state 2.

By combining the phase transformation, kinematics, strain-displacement, constitutive and equilibrium equations, the following nonlinear system of PDE, in dimensionless form, are developed [10]:

$$A_{44} \frac{\partial}{\partial X} \left(\theta_x + \frac{\partial W}{\partial X} \right) + A_{55} \frac{\partial}{\partial Y} \left(\theta_y + \frac{\partial W}{\partial Y} \right) + \Phi = 0 \quad (1a)$$

$$\begin{aligned} & D \frac{\partial}{\partial X} \left(\frac{\partial \theta_x}{\partial X} + v_e \frac{\partial \theta_y}{\partial Y} \right) + D_{33} \frac{\partial}{\partial Y} \left(\frac{\partial \theta_x}{\partial Y} + v_n \frac{\partial \theta_y}{\partial X} \right) + (D_A + D_{MA} \xi) \frac{\partial}{\partial X} \left(\frac{\partial \theta_x}{\partial X} + v_e \frac{\partial \theta_y}{\partial Y} \right) + \\ & D_{MA} \frac{\partial \xi}{\partial X} \left(\frac{\partial \theta_x}{\partial X} + v_n \frac{\partial \theta_y}{\partial Y} \right) + D_{33MA} \frac{\partial \xi}{\partial Y} \left(\frac{\partial \theta_x}{\partial Y} + \frac{\partial \theta_y}{\partial X} \right) + (D_{33A} + D_{33MA} \xi) \frac{\partial}{\partial Y} \left(\frac{\partial \theta_x}{\partial Y} + \frac{\partial \theta_y}{\partial X} \right) - \\ & A_{44} \left(\theta_x + \frac{\partial W}{\partial X} \right) = 0 \end{aligned} \quad (1b)$$

$$\begin{aligned} & D \frac{\partial}{\partial X} \left(\frac{\partial \theta_x}{\partial X} + v_e \frac{\partial \theta_y}{\partial Y} \right) + D_{33} \frac{\partial}{\partial Y} \left(\frac{\partial \theta_x}{\partial Y} + v_n \frac{\partial \theta_y}{\partial X} \right) + (D_A + D_{MA} \xi) \frac{\partial}{\partial X} \left(\frac{\partial \theta_x}{\partial X} + v_e \frac{\partial \theta_y}{\partial Y} \right) + \\ & D_{MA} \frac{\partial \xi}{\partial X} \left(\frac{\partial \theta_x}{\partial X} + v_n \frac{\partial \theta_y}{\partial Y} \right) + D_{33MA} \frac{\partial \xi}{\partial Y} \left(\frac{\partial \theta_x}{\partial Y} + \frac{\partial \theta_y}{\partial X} \right) + (D_{33A} + D_{33MA} \xi) \frac{\partial}{\partial Y} \left(\frac{\partial \theta_x}{\partial Y} + \frac{\partial \theta_y}{\partial X} \right) - \\ & A_{55} \left(\theta_y + \frac{\partial W}{\partial Y} \right) = 0 \end{aligned} \quad (1c)$$

where the dimensionless, stiffness coefficients D , D_{33} , D_A , D_{MA} , D_{33A} , D_{33MA} , A_{44} , A_{55} , generalized displacements (W , θ_x , θ_y), coordinates (X, Y), and the transverse load Φ are defined in Table 1. ξ is the martensite fraction, and ν_e , ν_n are the Poisson's ratios for the elastomer and SMA, respectively.

Now, let us consider a differential element of the SMA. If the heat loss on the top surface of the SMA is neglected, the energy balance on the SMA becomes

$$C_n \frac{\partial T}{\partial t} - Q_n \frac{\partial \xi}{\partial t} - k_n \frac{\partial^2 T}{\partial x^2} - k_n \frac{\partial^2 T}{\partial y^2} + K_e(T - T_0) = P \quad (2)$$

where $c_n \frac{\partial T}{\partial t}$ is the change in the internal energy of the SMA layer with $C_n = \rho_n c$, where ρ_n is the density and c is the specific heat of the SMA. $-Q_n \frac{\partial \xi}{\partial t}$ is the energy contributed to the phase transformation of the SMA with $Q_n = \rho_n q_n$, where q_n is the heat of transition of the SMA. $-k_n \frac{\partial^2 T}{\partial x^2} - k_n \frac{\partial^2 T}{\partial y^2}$ is the heat conduction in x and y directions through the SMA layer and k_n is the SMA's thermal conductivity. $K_e(T - T_0)$ is the quasi-steady model for the heat conduction lost through the elastomer layer. $K_e = k / [t(h - t)]$, where k is the thermal conductivity of the elastomer. P is the ohmic heating generated by the electric current passed through the SMA layer in the heating process. P is equal to zero if Eq. (2) is used for the cooling process. Equation (2) may be written in dimensionless form as

$$\frac{\partial \Theta}{\partial \tau} - R_{MA} \frac{\partial \xi}{\partial \tau} - \frac{\partial^2 \Theta}{\partial X^2} - \frac{\partial^2 \Theta}{\partial Y^2} + R_k \Theta + S - R_p = 0 \quad (3)$$

where Θ is temperature of the SMA layer, τ is the time, R_{MA} is the heat of transition of the SMA, R_k is the thermal conductivity of the elastomer, S is the heat loss from the SMA layer through the elastomer to the heat sink, and R_p is the ohmic heating.

A linear model for the martensite fraction for the heating and cooling transition processes, respectively, is in the following form [11]

$$\xi = 1 - \frac{T - A_s}{A_f - A_s} + \frac{\sigma}{C_A(A_f - A_s)} \quad (4)$$

$$\xi = 1 - \frac{T - M_f}{M_s - M_f} + \frac{\sigma}{C_M(M_s - M_f)} \quad (5)$$

where C_A and C_M are the material constants which indicate the influence of the stress on the transformation temperatures, A_s and A_f are the start and finish temperature of the phase transformation from martensite to austenite, respectively, M_s and M_f are the start and finish temperature of the phase transformation from austenite to martensite, respectively, and σ is the stress in the SMA which is contributed to the shift of the transformation temperatures. By combining the phase transformation, strain-displacement, constitutive equations with Eqs. (4) and (5), the following relation can be developed:

$$\xi = 1 - \Theta + \frac{(h - t)}{3hC_A(A_f - A_s)(1 - \nu_n)} [(1 - \xi)E_A + E_M \left(\frac{\partial \theta_x}{\partial X} + \frac{\partial \theta_y}{\partial Y} \right)] \quad (6)$$

Equations (1), (2) and (6) form a nonlinear system of equations governing the bending of the SMA composite plate subject to both thermal and mechanical loads, where $w, \theta_x, \theta_y, \Theta$ and ξ are independent variables. A finite element model was developed by using the variational method and the following two-dimensional four-node linear element [10]

$$W = \sum_{i=1}^4 \Phi_i W_i \quad \theta_x = \sum_{i=1}^4 \Phi_i \theta_{xi} \quad \theta_y = \sum_{i=1}^4 \Phi_i \theta_{yi} \quad \Theta = \sum_{i=1}^4 \Phi_i \Theta_i \quad \xi = \sum_{i=1}^4 \Phi_i \xi_i \quad (7)$$

where Φ_i ($i = 1, 2, 3, 4$) are the interpolation functions.

RESULTS AND DISCUSSION

The actuator is assumed to be constructed from a layer of 55-Nitinol perfectly bonded to a layer of Dow Corning SYLGARD elastomer. The material properties are listed in Table 3. The boundary conditions of the plate are assumed to be simply supported and thermally insulated on all four edges. A 4×4 mesh of linear rectangular elements is utilized to model the domain. The Crank-Nicolson method is used for the temporal approximation and a time increment of $\Delta\tau = 0.05$ is considered.

To verify the finite element solution, two special cases were compared to closed-form solutions. First, the finite element and closed-form solutions for dimensionless maximum center deflection ($W = wEh^3/qA^4$) of a simply supported isotropic plate ($\nu = 0.3$) were compared, as follows:

Mesh	FEM Results			Closed-Form Solution [12]
	2 x 2	3 x 3	4 x 4	
	0.04337	0.04397	0.04416	0.044341

Next, the stress-free time response for the complete heating and cooling phase transitions of the actuator was compared to the closed-form solution of Ref. [13], as follows ($R_p = 3, S = 1.5$ and $R_{MA} = 1.4$):

Heating Time Response		Cooling Time Response	
FEM	CFS Ref. [13]	FEM	CFS Ref. [13]
$\tau = 0.78$	$\tau = 0.78$	$\tau = 0.63$	$\tau = 0.63$

The effects of dimensionless thermal conductivity of the elastomer and the heating power on the overall time response of the actuator are shown in Figure 3. As can be seen, by increasing the heating power the overall time response decreases nonlinearly. Also, one can observe that by enhancing the thermal conductivity of the elastomer the time response is reduced nonlinearly. In addition, it is interesting to note that for any applied heating power there is an optimal value for the thermal conductivity of elastomer beyond which the overall time response of the actuator increases. This optimal value increases as the applied heating power increases. Figure 4 shows the effect of dimensionless thermal conductivity of the elastomer on the overall time response of the actuator for different heat sink strengths. The same

phenomenon, as described for Figure 3, can be seen here. The only difference is that the value of the optimal thermal conductivity reduces by increasing the heat sink strength.

The effects of the thickness of the elastomer layer and the heating power on the overall time response of the actuator are presented in Figure 5. The response time increases nonlinearly by increasing the thickness of the elastomer layer and decreases nonlinearly by increasing the heating power. It is also observed that there is an optimal value for the applied heating power beyond which there is no change on the overall time response. Figure 6 shows the overall time response of the plate as a function the elastomer layer thickness for different heat sink strengths. Again, the response time increases nonlinearly by increasing the thickness and decreases by increasing the heat sink strength. However, beyond a critical value, for the heat sink strength, the time response increases. This means that the actuator's heat loss is faster than the input heat, thus delaying the transformation process.

CONCLUSIONS

A non-linear model for the response of a two-dimensional, thermally-driven SMA-elastomer actuator was developed based on the Classical Laminated Plate Theory, the variable sublayer stress model and a two-dimensional martensitic transformation approximation. A finite element formulation was developed to solve the proposed nonlinear model. The numerical results demonstrated that the input heating power, heat sink strength, the thermal conductivity and the thickness of the elastomer layer play important roles on controlling the time response of the actuator.

REFERENCES

1. Wu, W., Gordaninejad, F. and Wirtz, R. A., "Modeling and Analysis of A Shape Memory Alloy - Elastomer Composite Actuator," *Journal of Intelligent Materials, Systems and Structures*, July, 1996, pp. 441-447.
2. Rogers, C. A. and Baker D., "Experimental Studies of Active Strain Energy Turning of Adaptive Composites," *Proceedings of the 31st Structures, Structural Dynamics and Materials Conference*, Long Beach, CA., April 2-4, 1990, pp. 2234-2241.
3. Saunders, W. R., Robershaw, H. H. and Rogers, C. A., 1991, "Structural Acoustic Control of a Shape Memory Alloy Composite Beam," *Journal of Intelligent Materials, System and Structures.*, Vol. 2, pp. 508-527.
4. Baz, A. and Tampe, L., "Active Control of Buckling of Flexible Beam," *Proceedings of the ASME Design Technical Conference*, Montreal, Canada, Vol. 1. DE-16, 1989, pp. 211-218.
5. Lagoudas, D. C. and Tadjbakhsh, I. G., "Deformation of Active Flexible Rods with Embedded Line Actuators," AMD-Vol. 167, *Recent Developments in stability, Vibration, and Control of Structural Systems*, 1993, pp. 89-106.

6. Tanaka, K. and Nagaki, S., "A Thermomechanical Description of Material with Internal Variables in the Process of Phase Transformation," *Ingenieur Archiv*, 51, 1982, pp. 287-299.
7. Liang, C. and Rogers, C. A., "One-Dimensional Thermomechanical Constitutive Relations for Shape Memory Materials," AIAA-90-1027-CP, 1990.
8. Rogers, C. A., Liang, C. and Jia, J., "Behavior of Shape Memory Alloy Reinforced Composite Plates, Part 1: Model Formulation and Control Concepts," *Proceeding of the 30th Structures, Structural Dynamics and Materials Conference*, AIAA-89-1989, 1989.
9. Ikuta, K. and Shimizu, H., "Two Dimensional Mathematical Model of Shape Memory Alloy and Intelligent SMA-CAD", *Proceedings of the 1993 IEEE Micro Electro Mechanical System - MEMS 1993*, Piscataway, NJ, 1993, pp. 87-92.
10. Wu, W., "Modeling and Analysis of One and Two-Dimensional Shape Memory Alloy-Elastomer Actuators," *Ph.D. Dissertation*, Department of Mechanical Engineering, University of Nevada, Reno, 1996.
11. Lin, M. W. and C. A. Rogers, "Analysis of Stress Distribution in a Shape Memory Alloy Composite Beam," AIAA-91-1164-CP, 1991.
12. Timoshenko, S. and Woinowsky-Krieger, S., *Theory of Plate and Shells*, Mc Graw Hill, 1959.
13. Wirtz, R. A., Gordaninejad, F. and Wu, W., "Free Response of A Thermally Driven Composite Actuator," *Journal of Intelligent Materials, Systems and Structures*, May, 1995, pp. 398-406.

Table 1. Dimensionless Stiffness.

$D = \frac{(h_0^3 - h_1^3)}{3(1 - \nu_e^2)h_0^3}$	$D_{33} = \frac{(h_0^3 - h_1^3)}{3(1 + \nu_e)h_0^3}$
$D_A = \frac{(h_0^3 - h_1^3)E_A}{3(1 - \nu_e^2)h_0^3E_e}$	$D_{MA} = \frac{(h_0^3 - h_1^3)(E_M - E_A)}{3(1 - \nu_e^2)h_0^3E_e}$
$D_{33A} = \frac{(h_1^3 - h_2^3)E_A}{3(1 + \nu_n)h_0^3E_e}$	$D_{33MA} = \frac{(h_1^3 - h_2^3)(E_M - E_A)}{3(1 + \nu_n)h_0^3E_e}$
$A_{44} = \frac{5}{4} \sum_{i=1}^2 G_i \left[h_i - h_{i-1} - \frac{4}{3} (h_i^3 - h_{i-1}^3) \frac{1}{h^2} \right]$	$A_{55} = \frac{5}{4} \sum_{i=1}^2 G_i \left[h_i - h_{i-1} - \frac{4}{3} (h_i^3 - h_{i-1}^3) \frac{1}{h^2} \right]$

Table 2. Dimensionless Parameters.

Quantity	$M \rightarrow A$ heating	$A \rightarrow M$, Cooling
Time, τ	$k_n t / h^2 C_n$	$k_n t / h^2 C_n$
Temperature, Θ	$(T - M_f) / (A_f - A_s)$	$(T - M_f) / (M_s - M_f)$
Heat of transition, R_{MA}	$q_n / C_n (A_f - A_s)$	$q_n / C_n (M_s - M_f)$
Power ratio, R_p	$Ph^2 / k_n (A_f - A_s)$	
Temperature ratio, S	$(M_f - T_o) / (M_s - M_f)$	$(M_f - T_o) / (M_s - M_f)$
Load, Φ	q / E_e	
Deflection, W	w / h	w / h
Location, X	x / h	x / h
Location, Y	y / h	y / h
Conductivity, R_k	$K_e h^2 / K_n$	$K_e h^2 / K_n$

Table 3. Themophysical Properties of 55-Nitinol and Dow Corning SYLGARD.

Property	Units	55-Nitinol	SYLGARD
Density, ρ	kg/m^3	6500	1050
Specific heat, c	$J / kg, ^\circ C$	883	1422
Thermal conductivity, k	$W / m, ^\circ C$	N/A	0.146
Heat of transition, q_n	J / kg	12600	N/A
Material constant, C_A	$MPa / ^\circ C$	10.3	N/A
Material constant, C_M	$MPa / ^\circ C$	10.3	N/A

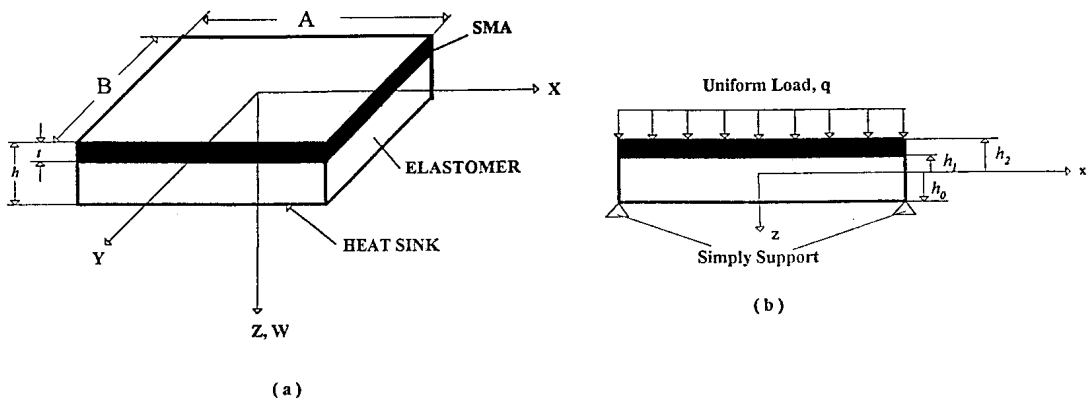


Figure 1. Geometry of the laminated SMA-elastomer actuator.

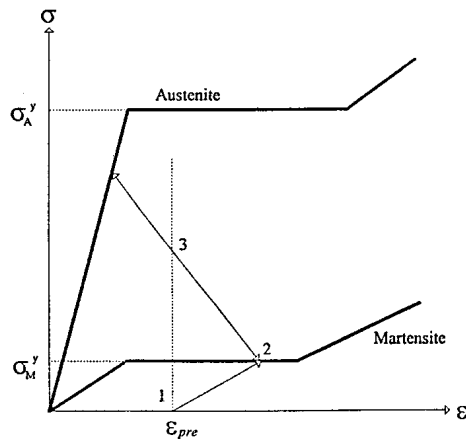


Figure 2. SMA stress-strain relations in austenite and martensite phases.

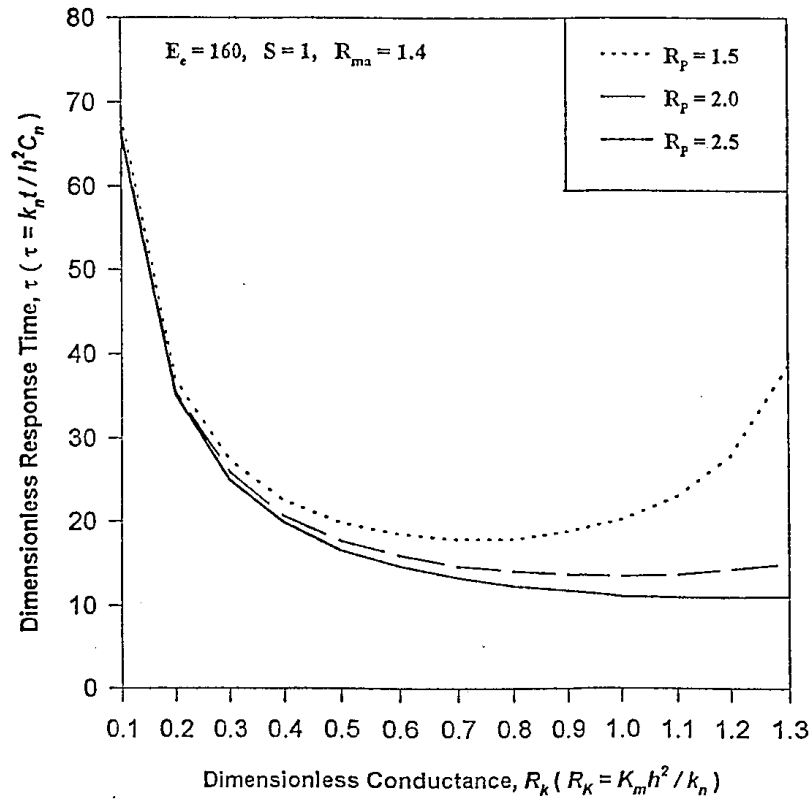


Figure 3. Effects of input heating power and the thermal conductivity of elastomer layer on the overall time response of the actuator.

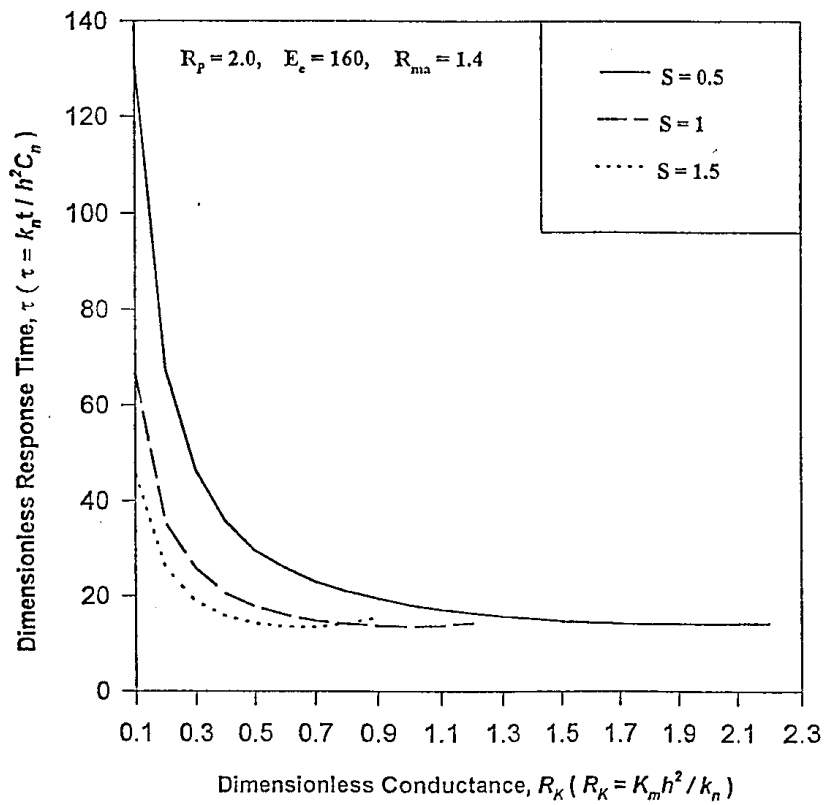


Figure 4. Effects of heat sink strength and the thermal conductivity of elastomer layer on the overall time response of the actuator.

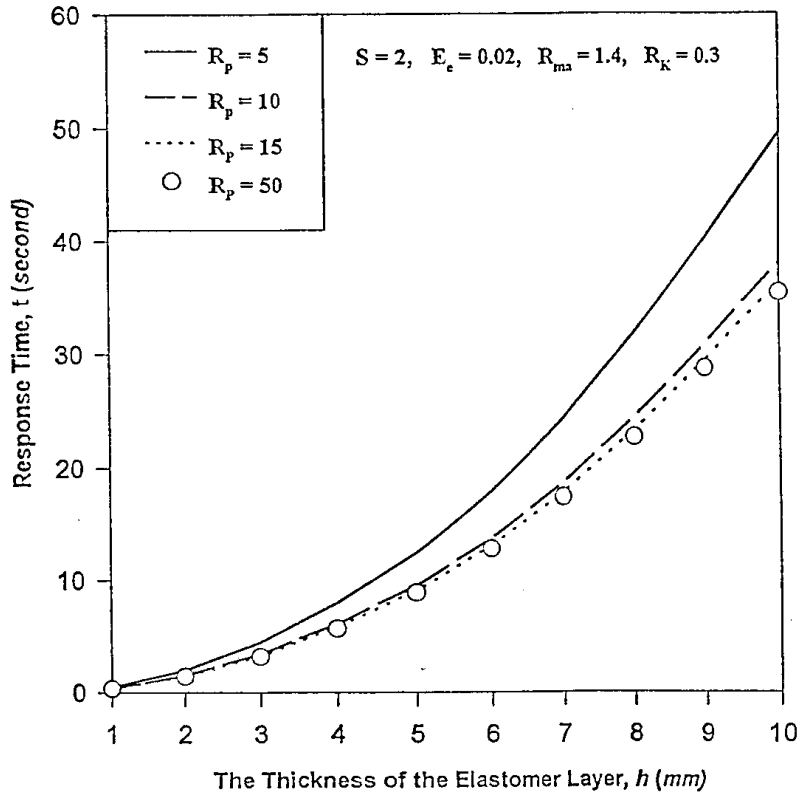


Figure 5. Effects of input heating power and the thickness of the elastomer layer on the overall time response of the actuator.

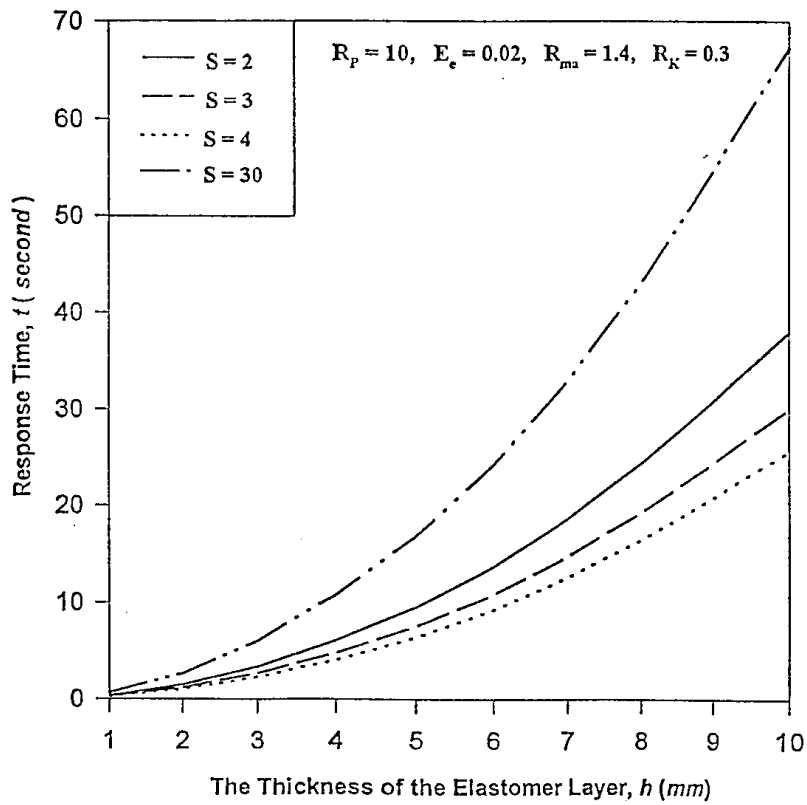


Figure 6. Effects of heat sink strength and the thickness of elastomer layer on the overall time response of the actuator.

FABRICATION AND CHARACTERIZATION OF SQUEEZE CAST AC4A AL/TI NI SHAPE MEMORY COMPOSITES

Youngsu Cho¹, Ildong Choi², Ikmin Park¹, Kyungmox Cho¹,
Busob Kim¹, and Deukman An³

¹*Dept. of Metall. Eng., Pusan National University, Pusan 609-735, Korea*

²*Dept. of Mat. Eng., Korea Maritime University, Pusan 606-791, Korea*

³*Dept. of Mech. and Product. Eng., Pusan National University Pusan 609-735, Korea*

SUMMARY: Reinforcement of shape memory alloys within light weight metal matrix reveals compressive residual stresses in the matrices resulting in improved tensile properties of the composites. In the present study, Al/TiNi shape memory composites were fabricated by the squeeze casting technique. Optimal fabrication conditions for squeeze casting were obtained experimentally. Fairly good microstructure and matrix/reinforcement bonding observed in the squeeze cast Al/TiNi composites. Tensile tests of the composites were carried out above A_f (austenite finishing temperature) which was found from DSC analysis. The amount of prestrain to induce the compressive residual stress in Al matrix and the recovery force of the TiNi were determined from tensile curves of TiNi wire. Improved strength of the composite due to TiNi reinforcement as well as compressive residual stresses in Al matrix was identified. It was found that the total interfacial area between matrix and reinforcement which depends on the wire diameter also affected the strength enhancement.

KEYWORDS: interfacial bonding strength, compressive residual stress, stress-induced martensite, shape memory recovery, Al/TiNi composite

INTRODUCTION

Al, Mg, Ti alloy metal matrix composites reinforced with ceramic fibers have good properties such as low specific gravity, high specific strength and stiffness. They are being expected as materials of automotive parts because of their good wear resistance, thermal property and low thermal expansion coefficient (CTE) [1],[2]. These potential materials, however, have demerits such as the interfacial weakness due to their poor chemical attraction and wettability between the metal matrices and ceramic reinforcements, high manufacturing cost and complexity of production processes. Moreover, tensile strength and mechanical properties of composites are deteriorated by the tensile residual stress in the matrix which is caused by the CTE mismatch between metal matrix and ceramic reinforcement during the cooling process. Therefore, in the present study, shape memory composite (SMC : AC4A Al/TiNi) was chosen to solve problems of metal/ceramic composites. Recovery force of prestrained shape memory alloy upon heating above A_f gives compressive residual stress in the matrix and it can improve mechanical properties of composite such as strength and crack close [3].

The effect of shape memory alloy reinforcement on the mechanical properties of SMC was evaluated by the process described in Fig. 1 [4],[5]. This figure shows the enhancing

mechanism of the mechanical properties by using compressive residual stresses in the matrix of Al/TiNi composites. After TiNi wires of austenite phase was composed in Al matrix, the composites are quenched. The as-fabricated composite is aged at shape-memorizing temperature and then the composite is cooled to martensite phase. When this composite of martensite phase is subjected to tensile prestrain and heated above austenite finish temperature(A_f), TiNi wire shrinks to the original length by shape memory effect. Thus this shrinkage induces the compressive residual stress in Al matrix along the fiber axis while the fiber is in tension.

Al/TiNi composite can be fabricated by powder metallurgy or casting method. In this study, Al/TiNi composite was fabricated by squeeze casting method [6],[7]. To get the optimum condition in fabrication of squeeze cast Al/TiNi composite, processing factors such as the temperature of molten Al, preheating temperature of TiNi wire and mold, applied pressure, and duration time were considered. The interface between Al matrix and TiNi reinforcement of fabricated SMC was analyzed using SEM and EDX. Tensile tests of TiNi wire and the composite were carried out to characterize the shape memory effect in SMC.

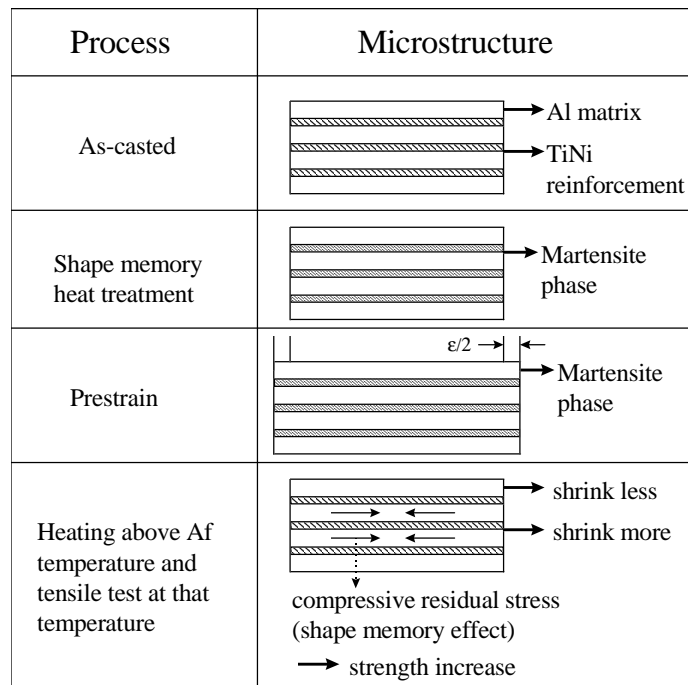


Fig. 1 Enhancing mechanism of SMC

EXPERIMENTAL

Fabrication of Al/TiNi shape Memory Composites

AC4A Al was chosen as matrix because of their good castability, strength and corrosion resistance under high pressure. Diameter of 0.38 and 1mm TiNi wire were chosen as reinforcement because of their large shape memory effect and high stiffness. First of all, the interfacial bonding strength of Al/TiNi composites was investigated as a fundamental study in order to decide manufacturing conditions of composites. The squeeze casting was performed with a range of pouring temperature of 700~900°C and mold preheating temperature of 300~500°C. The applied pressure was fixed at 75MPa. The pull-out strength of fabricated composites was obtained through pull-out test designed as shown in Figure 2. The surface

condition of TiNi wire affected the interfacial property. The specimen with acid cleaned surface had higher pull-out strength, but the wire without acid cleaning pulled out easily. However, the interfacial bond strength of Al/TiNi didn't change much according to the conditions of pouring temperature and mold preheating temperature. Therefore, in this study, the wire was cleaned in acid solution to have good wettability between matrix and reinforcement and the squeeze casting conditions were set as 400°C of mold preheating temperature and 750°C of pouring temperature of molten Al in considering infiltration velocity of Al melt, matrix microstructure and preform deformation.

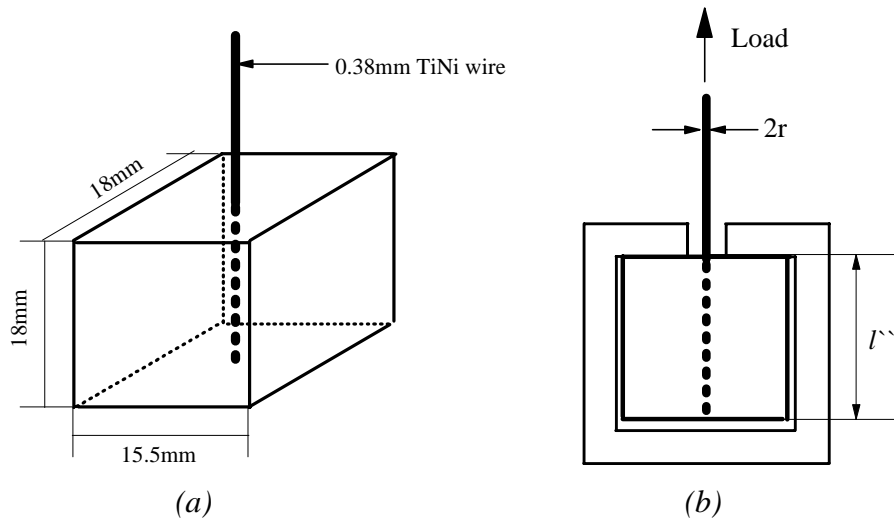


Fig. 2 (a) Pull-out test specimen, (b) Loading for pull-out test

The preform was woven by TiNi wire into the perforated jig(sus.304) as shown in figure 3. The volume fraction of reinforcement was 5-7%. To get off the oxidation film on TiNi wire, the preform was acid cleaned for 120-180 second in 16% HNO_3 + 1% HF bath. Squeeze casting was carried out by pouring molten Al of 750°C into the TiNi preform, which was placed in the mold preheated to 400°C, and then by applying pressure of 75MPa. In applying pressure, delay time and duration time were 7 and 60 seconds, respectively. The processing chart is shown in figure 4.

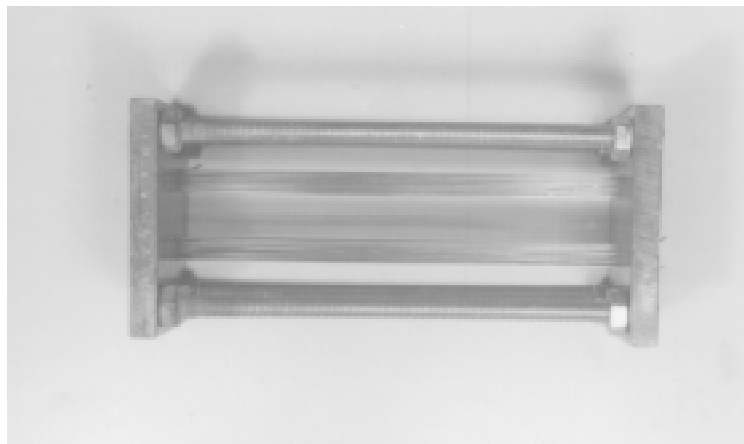


Fig. 3 Preform fabricated with 0.38mm TiNi wire

The direction of applied pressure was perpendicular to longitudinal direction of TiNi wire. The squeeze cast block was quenched into water after applying pressure and the composite block fabricated through this process is shown in figure 5(a). Squeeze cast Al/TiNi composites were tested by X-ray to confirm the straightness of TiNi wire in composites (figure 5(b)). Composites with bending deformation of TiNi wire were discarded .

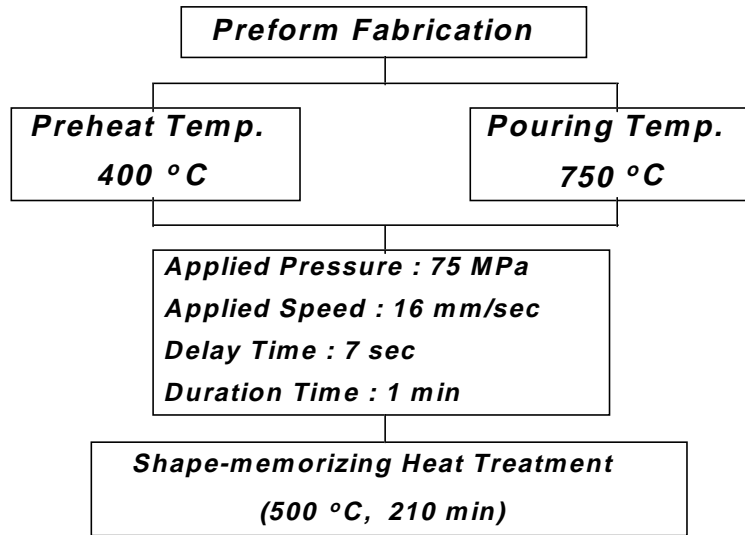


Fig. 4 Flowchart for Al/TiNi SMC manufacturing process by squeeze casting method

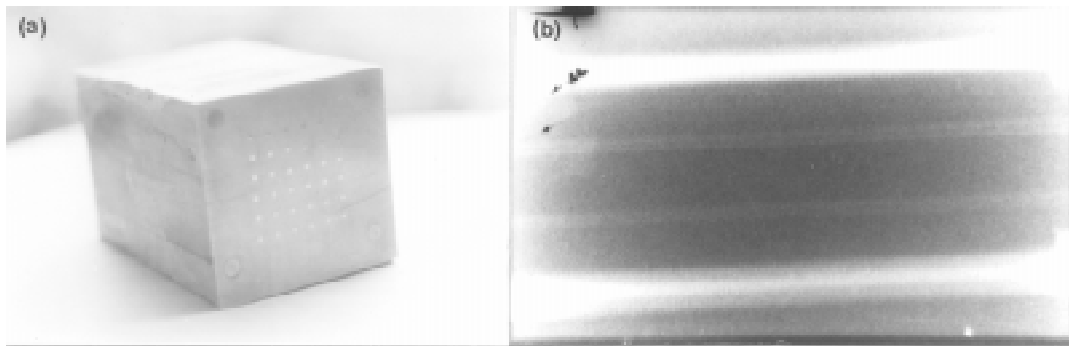


Fig. 5 (a) Squeeze cast shape memory composite fabricated
(b) Non-destructive test by X-ray

Microstructure and Tensile Test

Solidification microstructure of composites was examined and analyzed with optical microscope and SEM (JEOL JSM-5400) and the diffusion distance of Al/TiNi interface was checked with EDX analysis.

Transformation temperatures of TiNi wire which was aged at 500°C for 210 minutes followed by water quenching to induce martensitic transformation of TiNi fiber were measured using differential scanning calorimeter with a heating rate 10°C/min to decide the temperature of

tensile testing. The superelastic region caused by the stress-induced martensitic phases was identified by the tensile test of TiNi wire.

Tensile specimens of composites were machined by electro-discharge machine and the dimension of tensile specimen is shown in Figure 6. Each coupon was heat treated for shape memorizing at 500°C for 210 minutes followed by water quenching to induce martensitic transformation. From the results of TiNi wire tensile test, composites with martensitic TiNi reinforcement were prestrained up to 4% elongation. Tensile tests were carried out at 90°C (above A_f : austenite finish temperature) with strain rate of 1mm/min.

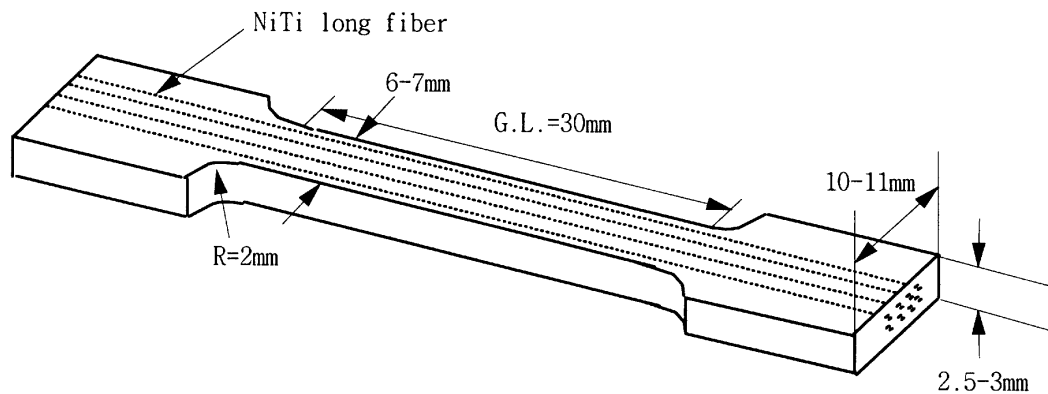


Fig. 6 Size of tensile test specimen.

RESULTS AND DISCUSSION

Microstructure

Figure 7 is the optical micrograph of the squeeze cast Al/TiNi shape memory composite. The marking of a and b in figure represent TiNi continuous fiber and AC4A matrix, respectively. Fine microstructure which had no cast defect in Al matrix and the matrix/reinforcement interface was obtained. Matrix is typical Al-Si cast microstructure that consists of eutectic structure around the primary. It is considered that all TiNi did not have much role as nucleation sites because matrix/reinforcement interface mainly composed of eutectic structure with few primary which is nucleated at high temperature.

SEM-EDX analysis was carried out in order to identify the diffusion distance of each element at Al/TiNi interface. Figure 8 shows the interface of Al/TiNi composite which was infiltrated by 75MPa at optimum condition (750°C of pouring temperature, 400°C of mold preheat temperature) and was subjected to heat treatment at 500°C for 210 minutes to shape-memorize TiNi wire. It was estimated that Al was diffused by 1.09 μ m from Al to TiNi and this specimen showed fairly good pull-out strength. Al/TiNi composites with small diffusion distance fabricated at other conditions exhibited easy pull-out of TiNi wire from matrix.

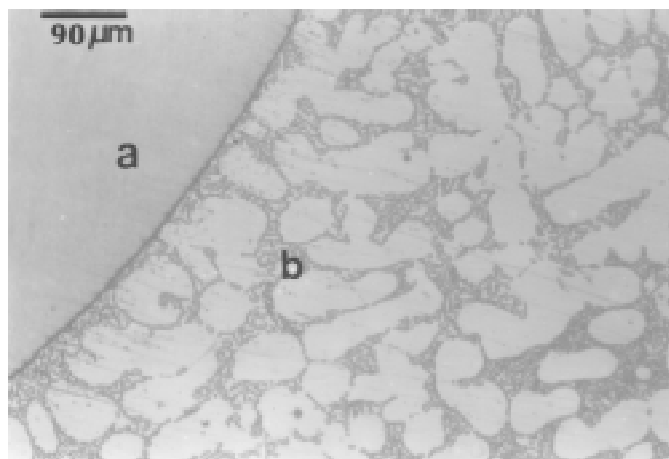


Fig. 7 Optical micrograph of AC4A Al / TiNi shape memory composite.
(a : TiNi reinforcement, b: Al matrix)

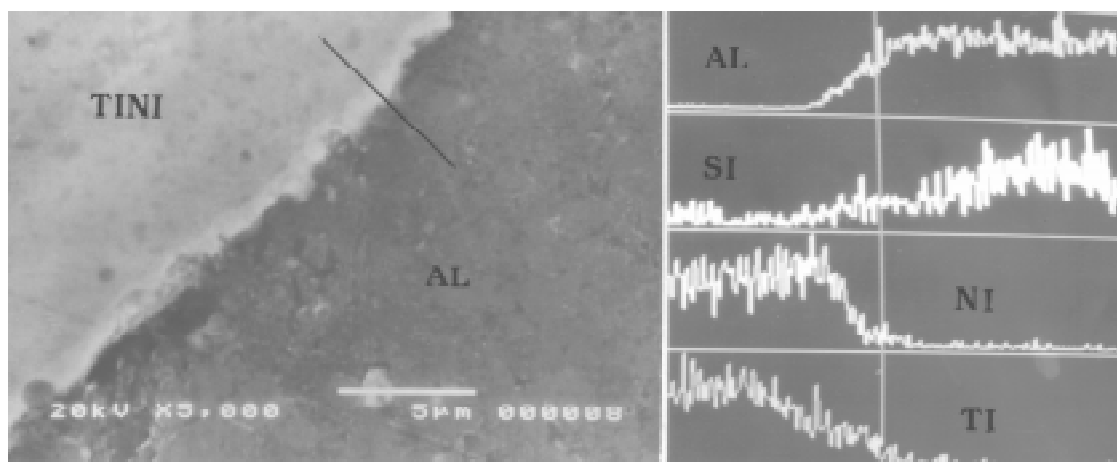


Fig. 8 SEM microstructure and EDX analysis of the interfaces of shape memory composite aged at 500°C for 210 min to shape-memorize. ($X_{Al} = 1.09$: Diffusion distance from Al into TiNi)

Tensile Properties of TiNi Wire

The transformation temperature(martensite-austenite) and tensile property of shape memory alloy have been reported to change with the condition of shape-memorizing heat treatment[8],[9],[10]. Accordingly, tensile and transformation behavior of TiNi wire must be ascertained in advance to evaluate tensile properties of squeeze cast Al/TiNi composites.

Austenite finish temperature of TiNi wire aged to shape-memorize at 500°C for 210 minutes was 57.7°C from the result of DSC(differential scanning calorimetry) analysis. The composite was subjected to tensile prestrain when TiNi wire was in martensitic phase and then heated above A_f . The tensile test of composite at this temperature showed the effect of compressive residual stress due to the shape recovery by the austenite transformation of TiNi in Al matrix. The prestrain and the shape recovery force can be deduced from the tensile test of TiNi wire as shown in figure 9. At room temperature, TiNi wire exhibits the superelastic region(flat

region) of 7-8% due to stress-induced martensite. The superelastic region is appeared in tensile curve of TiNi wire tested at room temperature and 50°C, but this region is not shown at 90°C. This fact is useful in determining the temperatures at which prestrain is to be made, and also at which tensile testing of the composite specimen is to be conducted. Accordingly, in this study, the prestrain was determined as 4% at room temperature and tensile test was carried out at 90°C. It can be predicted that shape recovery force of TiNi wire is about 250MPa if wire is prestrained at room temperature and tested at 90°C.

Tensile Properties of Al/TiNi Composite

Figure 10(a) is the result of tensile test of squeeze cast Al/TiNi composite. The volume fraction of TiNi reinforcement was 5.5% and 6.6% in as-fabricated composite. Al/6.6%TiNi composite without prestrain exhibited the strength increment of 50MPa by fiber strengthening in comparison with that of Al matrix at the test temperature of 90°C. The strength of Al/6.6%TiNi composite with 4% prestrain increased with 45MPa in comparison with that of 0% prestrain. This was caused by the compressive residual stress due to the shape recovery force of TiNi reinforcement. The strength increment was also shown in Al/5.5%TiNi composite. But this increment was smaller than that of Al/6.6%TiNi composite. Thus the strength increment is increased with increasing the volume fraction of TiNi reinforcement.

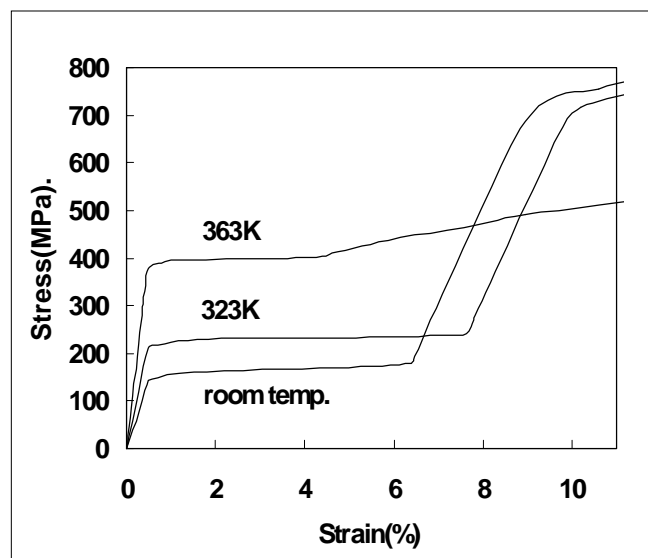


Fig. 9 Tensile curves of TiNi wire heat treated at 500 for 210 min.

The strength increment by shape recovery force with the strain in Al/6.6%TiNi is shown in figure 10(b). The strength is increasing gradually up to 1% strain, thereafter the strength increment is constant as 45MPa. When the yield strength of TiNi wire and Al matrix are 400MPa and 100MPa, respectively, from tensile curves of figure 9 and figure 10(a), the experimental data of composite yield strength have higher value than theoretical value predicted by rule of mixture. But the discrepancy between experimental and theoretical value will be decreased with considering the additional strength increment and the back stress which are caused by TiNi strengthening with the plastic deformation of Al matrix.

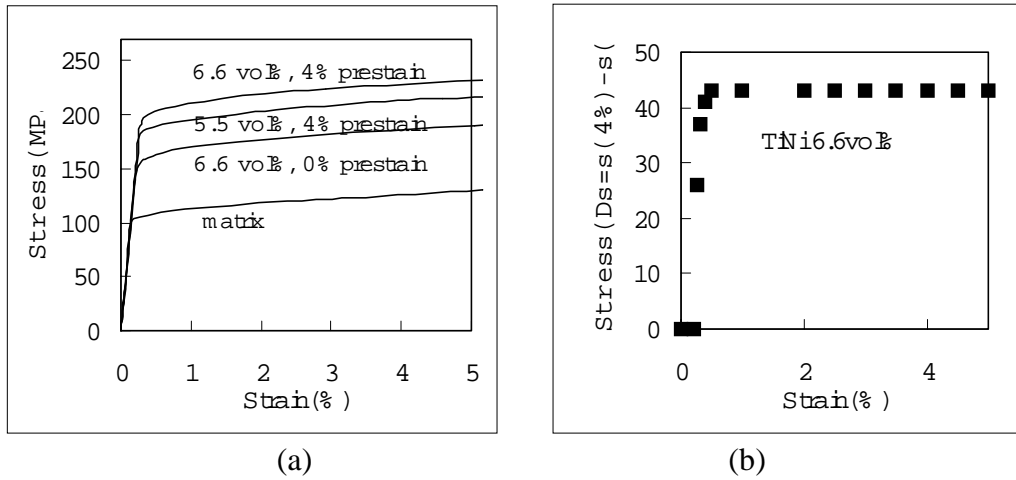


Fig. 10 The result of tensile test of the composite reinforced by 0.38mm TiNi

Figure 11 shows the result of tensile test of composite reinforced with 1mm TiNi wire. The volume fraction of reinforcement is 7%. The strength of this composite without prestrain is nearly the same as that of the composite reinforced with 0.38mm TiNi wire. The strength of composite with 4% prestrain increased with 20MPa in comparison with that of 0% prestrain. The compressive residual stress due to the shape recovery force of TiNi reinforcement is also identified in Al/1mm TiNi composite. However, the strength increment of this composite is smaller than that of the Al/0.38mmTiNi composite. This is caused by the difference of Al/TiNi interfacial area. The interfacial area of Al/0.38mmTiNi composite is about twice as large as that of Al/1mmTiNi composite. Therefore, the effect of compressive residual stress due to the shape recovery force of TiNi on the strength of SMC is dependent on the area of Al/TiNi interface, that is, the strength of SMC is increased with decreasing the diameter of TiNi wire under condition of the same volume fraction of reinforcement. Even if there is an analysis only as a function of the volume fraction of reinforcement [11], no analytical study for the effect of the interfacial area has been performed yet for the strengthening mechanism of SMC. Therefore, more systematic theoretical analysis is needed to confirm the strengthening of SMC due to the interfacial area.

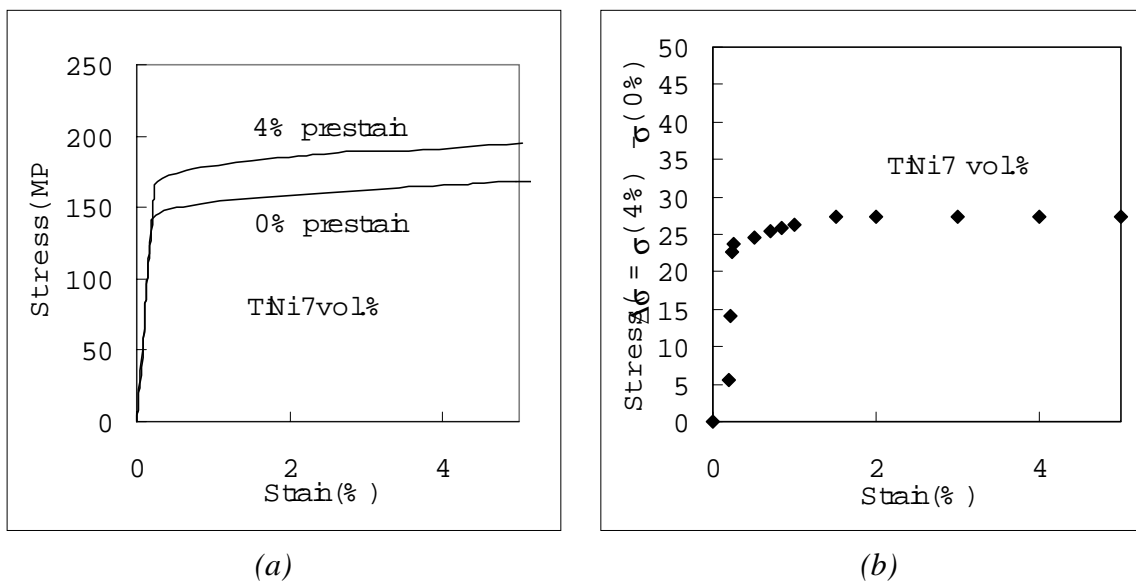


Fig. 11 The result of tensile test of the composite reinforced by 1mm TiNi.

CONCLUSION

The optimum condition to fabricate Al/TiNi composite by squeeze casting was deduced. The composite fabricated at this condition had good interfacial bonding between Al matrix and TiNi reinforcement. In order to improve the interfacial bonding, TiNi wire was cleaned in acid solution. Transformation and tensile behaviors of TiNi wire was investigated to characterize the tensile property of the squeeze cast Al/TiNi composite. The composite was subjected to 4% prestrain at room temperature to induce compressive residual stress and then tensile test of the composite was carried out at 90°C. Improvement of strength was obtained by 50MPa and 45MPa in Al/0.38mmTiNi composite due to TiNi fiber strengthening and induced compressive residual stress, respectively. However, the strength increment due to compressive residual stress of Al/1mmTiNi composite was 20MPa. This difference of strength increment is caused by that of Al/TiNi interfacial area. Therefore, the effect of compressive residual stress due to the shape recovery force of TiNi on the strength of SMC is increased with decreasing the diameter of TiNi wire.

ACKNOWLEDGMENT

This work was supported by the Ministry of Education Research Fund for Advanced materials in 1995.

REFERENCES

1. I.K.Park, W.J.Park, and N.J.Kim : Jr. of Korea Society of Automotive Engineers, 16,4(1993)23.
2. W.J.Park, and I.K.Park : Jr. of Korea Society of Automotive Engineers, 16, 3(1994)36.
3. C.A. Rogers : Jr. of Intelligent Material Systems and Structures, 4(1993)4.
4. Y.Furuya, A.Sasaki and M.Taya : Mat. Trans., JIM, 34(1993)224.
5. W.D.Armstrong and H.Kino : Jr. of Intelligent Mat. Systems and Structures, 6(1995)809.
6. K.C.Lee, Y.C.Park, and Y.Furuya : Bulletin of the Korean Institute of Metals and Mat., 7(1994)319.
7. I.M.Park : Proc. of the 2nd Symposium on Solidification Process, Seoul, Korea, (1991)86.
8. S.Miyazaki, S.Kurooka, A.Ishida and M.Nishida : The 3rd IUMRS Int'nl. Conf. on Ad. Mat., Tokyo, Edit by K. Otsuka and Y. Fukai, 18(1993)1041.
9. P.G.McComick, Y.Liu, X.Chen and D.Favier : The 3rd IUMRS Int'nl. Conf. on Ad. Mat., Tokyo, Edit by K. Otsuka and Y. Fukai, 18(1993)1005.
10. S.D.Wang, X.Z.Wu, J.P.Zhang, H.Q.Su, J.L.Jin and B.T.Song : The 3rd IUMRS Int'nl. Conf. on Ad. Mat., Tokyo, Edit by K. Otsuka and Y. Fukai, 18(1993)1061.
11. M.Taya, Y.Furuya, Y.Yamada, R.Watanabe, S.Shibata, and T.Mori. : Proc. 1993 North American Conf. on Smart Structure and Materials, Albuquerque, New Mexico (1993).

VIBRATION CONTROL OF ACTIVE STRUCTURES WITH PIEZOELECTRIC MODAL SENSORS AND ACTUATORS

Changqing Chen and Yapeng Shen

*Department of Engineering Mechanics, Xi'an Jiaotong University
Xi'an, Shaanxi Province, 710049, P. R. China*

SUMMARY: The finite element method (FEM) is applied to model the sensing and actuating mechanism of piezoelectric sensors and actuators. With the aid of Independent Modal Space Control (IMSC) method, optimal design of vibration control of active structures is performed. And the controllability and observability conditions for single mode are presented. Based on the IMSC method, a new set of modal sensor and actuator is proposed which consist of several piezoelectric patches. Although they are to some extent approximate when compared to those developed by Lee and Moon[1], design and application of them are much simpler. Numerical results are presented to illustrate the feasibility of the developed approximate modal sensors and actuators.

KEYWORDS: piezoelectric material, modal sensor and actuator, optimal control, vibration suppression, finite element method

INTRODUCTION

Due to the two characteristics, i.e. the direct and the inverse piezoelectric effects, piezoelectric materials have been widely used as sensors and actuators in the area of smart structures. Extensive research has been done to understand and model the sensing and actuating mechanisms. Analytical models of piezoelectric sensors and actuators embedded in or surface-bonded on smart beams, plates, and shells are proposed by numerous researchers (see, for example, [2-4]). And the finite element method[5-7] is shown to be the most rigorous way to analyze the piezoelectric structures.

Application of the piezoelectric smart structures into vibration suppression has been demonstrated to be a feasible way not only numerically but also experimentally. Optimal design of the vibration control with piezoelectric smart sensors and actuators is highly desirable [8-10]. Moreover, it is well known that, in a closed-loop control system, observation spillover may bring about unstable dynamic response of undamped structures and control spillover may excite uncontrolled residual modes. To avoid these phenomena, Lee and Moon [1] introduced modal sensors and actuators for one dimensional piezoelectric structures, which can monitor and actuate specified modes. However, design of them is much complicated. And their application is limited to structures of simple and regular appearance. In this paper, the Independent Modal Space Control (IMSC) method is employed to perform the optimal control. And the controllability and observability of specified modes for surface-

bonded piezoelectric structures is proposed. After designing the sensing and control algorithms, a new type of modal sensor and actuator is achieved. Implementation of the developed modal sensors and actuators into structures is much simple. Numerical results are presented to show the feasibility of the modal sensors and actuators.

FINITE ELEMENT DISCRETION

The motion equation of a plate-type active structure with surface-bonded piezoelectric sensors and actuators can be modeled by the following finite element equations [7]

$$\begin{aligned} [M]\{\ddot{x}\} + [K_{uu}]\{x\} - [K_{u\phi}]\{\phi\} &= \{F_m\} \\ [K_{\phi u}]\{x\} + [K_{\phi\phi}]\{\phi\} &= -\{Q\} \end{aligned} \quad (1)$$

where $\{x\}$ is the generalized nodal displacement vector, $\{\phi\}$ the element voltage vector of piezoelectric patches, $[M]$ and $[K_{uu}]$ the mass and the elastic stiffness matrices, $[K_{\phi u}]$ and $[K_{u\phi}]$ the electric-mechanical coupling matrices, $[K_{\phi\phi}]$ the dielectric matrix, and $\{F_m\}$ and $\{Q\}$ are, respectively, the mechanical force vector and the external applied electric free charge vector acting on piezoelectric element. It should be noted that, in Eq. (1), the electric potential of every point on the surface of piezoelectric element is assumed to have a same value. Moreover, each piezo patch is modeled by a layer of a finite element in this paper. Therefore, for an active element (i.e. an element has a surface-bonded piezoelectric patch), an electric voltage variable must be included in the generalized mechanical displacement vectors.

SENSING AND ACTUATING EQUATIONS

With the aid of Eq. (1), the sensing and/or actuating equations of a piezoelectric patch can be obtained readily. When the patch is acted as a sensor (via the direct piezoelectric effect), as we know, no free charge density is applied on the major surfaces (edge surface are negligible). Consequently, the induced electric charge is

$$Q^e = [K_{\phi u}^e]\{x^e\} \quad (2)$$

And the corresponding induced electric voltage of the active element due to deformation is

$$\phi^e = -[K_{\phi\phi}^e]^{-1}[K_{\phi u}^e]\{x^e\} \quad (3)$$

Eqs. (2) and (3) constitute the sensing equations of a piezoelectric element.

On the other hand, the piezoelectric element may be used as actuator (through the inverse piezoelectric effect). And both the external free charge and electric voltage can be acted as driving signals to be imposed on the surface of the element. When the driving signal is the free charge, the deformation equation of the active structure is obtained by substituting Eq. (1b) into (1a), i.e.

$$[M^e]\{\ddot{x}^e\} + [K_{uu}^e]\{x^e\} = \{F_m^e\} + [K_{u\phi}^e][K_{\phi\phi}^e]^{-1}(-\{Q^e\} - [K_{\phi u}^e]\{x^e\}) \quad (4)$$

And when electric voltage is applied on the surface of actuator, the induced deformation equation is much simple

$$[M^e]\{\ddot{x}^e\} + [K_{uu}^e]\{x^e\} = \{F_m^e\} + [K_{u\phi}^e]\{\phi^e\} \quad (5)$$

Eqs. (3)-(5) are the sensing and actuating formulations on element level and they can be assembled into global ones.

OPTIMAL CONTROL

In order to achieve optimal control, the linear second order equations (1) are usually transformed into the state equation of first order. After introducing a quadratic performance index, one can obtain the control algorithm by minimizing the index function, i.e. solving a matrix Riccati equation. However, for a real structure, the degree of freedom is so large that solution of the derived matrix Riccati equation is time-consuming and impracticable expensive. Independent Modal Space Control (IMSC) method is shown to be more preferable, in which it is assumed that each mode can be controlled separately [9-10]. Instead of solving matrix equation, only a set of uncoupled algebraic equations is needed to be solved in IMSC. And it is introduced briefly in this paper.

Without losing generality, the closed-loop feedback control equation of a active structure can be written as,

$$[M]\{\ddot{x}\} + [K_{uu}]\{x\} = \{F\} \quad (6.)$$

where $\{F\}$ is the termed as control force vector and will be determined by IMSC.

With the modal transformation technique,

$$\{x\} = [\Psi]\{y\} \quad (7.)$$

one can rewrite Eq. (6) into a set of uncoupled equations in the modal space, that is,

$$\begin{Bmatrix} \ddot{y}_1 \\ \vdots \\ \ddot{y}_n \end{Bmatrix} + \begin{bmatrix} \omega_1^2 & & \\ & \ddots & \\ & & \omega_n^2 \end{bmatrix} \begin{Bmatrix} y_1 \\ \vdots \\ y_n \end{Bmatrix} = \begin{Bmatrix} f_1 \\ \vdots \\ f_n \end{Bmatrix} \quad (8.)$$

where n is the number of natural modes, ω_i the eigenfrequency, and f_i is the modal control force given by

$$f_i = \{\varphi_i\}^T \{F\} \quad (9.)$$

in which $\{\varphi_i\}$ is the i th modal vector.

In IMSC, the modal control force f_i is assumed to have the form of

$$f_i = -(g_{1i}\omega_i y_i + g_{2i}\dot{y}_i)/r \quad (10.)$$

where r is a weight factor and g_{1i} and g_{2i} are given by

$$\begin{aligned} g_{1i} &= -\omega_i r + \sqrt{(\omega_i r)^2 + \omega_i^2 r} \\ g_{2i} &= \sqrt{2r\omega_i \left(-r\omega_i + \sqrt{(r\omega_i)^2 + r\omega_i^2} \right) + r\omega_i^2} \end{aligned} \quad (11.)$$

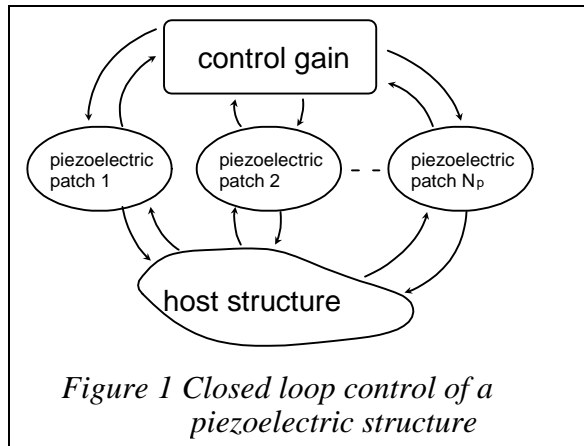
Eqs. (11) are obtained by minimizing the following performance index

$$J = \int_0^\infty \omega_i^2 y_i^2 + \dot{y}_i^2 + r f_i^2 dt \quad (12.)$$

in which the first term, the second term, and the third term of right hand side of Eq. (12) refer to the potential energy, the kinetic energy, and the control effort, respectively.

Controllability and observability of the IMSC have been studied by Hughes and Skelton [11] and Laub and Arnold [12]. In this paper, however, only the controllability and observability

of specified modes are considered. Since for structure control, only those modes are of most interest.



The closed-loop feedback control system of piezoelectric active structures is illustrated in Fig. 1. And each patch shown in it is a self-sensing actuator [13], which means a piezo element is used simultaneously as a sensor as well as an actuator. Although both the electric charge and electric voltage can be sensed and then be fed back to act as driving signal, the induced electric charge is outputted as sensed signal while electric voltage is imposed on the actuator to drive it in this paper. Moreover, both constant velocity feedback controller and

constant position feedback controller are employed. Therefore, the sensing electric charge and driving voltage have the form of, respectively,

$$\begin{Bmatrix} Q_1^e \\ \vdots \\ Q_{N_p}^e \end{Bmatrix} = \begin{Bmatrix} \{K_{\phi u}^e\}_1 \\ \vdots \\ \{K_{\phi u}^e\}_{N_p} \end{Bmatrix} \{x\} \quad (13.)$$

$$\begin{Bmatrix} \phi_1^e \\ \vdots \\ \phi_{N_p}^e \end{Bmatrix} = \begin{bmatrix} G_{11} & \cdots & G_{1N_p} \\ \vdots & \ddots & \vdots \\ G_{N_p 1} & \cdots & G_{N_p N_p} \end{bmatrix} \begin{Bmatrix} Q_1^e \\ \vdots \\ Q_{N_p}^e \end{Bmatrix} + \begin{bmatrix} \tilde{G}_{11} & \cdots & \tilde{G}_{1N_p} \\ \vdots & \ddots & \vdots \\ \tilde{G}_{N_p 1} & \cdots & \tilde{G}_{N_p N_p} \end{bmatrix} \begin{Bmatrix} \dot{Q}_1^e \\ \vdots \\ \dot{Q}_{N_p}^e \end{Bmatrix} \quad (14.)$$

where subscript N_p is the number of piezoelectric elements, $[G]$ and $[\tilde{G}]$ the feedback gain matrices to be determined, ϕ_i^e the feedback voltage acting on the i th piezoelectric element, and Q_i^e is the sensing charge of the i th piezoelectric element. G_{ij} and \tilde{G}_{ij} having the meaning of that the sensed charge of j th piezo element is fed back to control the i th piezoelectric element.

When electric voltage is acted as feedback signal, the control force is

$$\{F\} = \left[\begin{Bmatrix} \{K_{\phi u}^e\}_1^T & \cdots & \{K_{\phi u}^e\}_{N_p}^T \end{Bmatrix} \right] \begin{Bmatrix} \phi_1^e \\ \vdots \\ \phi_{N_p}^e \end{Bmatrix} \quad (15.)$$

Substituting Eq. (15) into (9) yields the modal control force

$$f_i = \{\varphi_i\}^T [K_{u\phi}] \{\phi\} \quad (16.)$$

For a given piezoelectric active structure, the modal vector $\{\varphi_i\}$ and the coupling matrix $[K_{u\phi}]$ are prescribed. Following Eq. (16), we can see that the i th mode is uncontrollable if the following express exists

$$\{\varphi_i\}^T [K_{u\phi}] = \mathbf{0} \quad (17.)$$

Actually, Eq. (17) is also the sufficient condition of the unobservability of the i th mode for a piezoelectric active structure. Combining Eq. (17) and (13), we have

$$\{Q\} = [K_{\phi u}] \{x\} = [K_{\phi u}] \sum_{\substack{k=1 \\ k \neq i}}^n \{\phi_k\} y_k \quad (18.)$$

which implies that the i th mode is unobservable.

MODAL SENSOR AND ACTUATORS

In a distributed structural control system, it is highly desirable that sensors only monitor those modes to be controlled. However, in reality, those sensors also respond to those uncontrolled residual modes from which observation spillover can introduce unstable dynamic response of undamped structures. At the same time, for certain cases, only single mode or a group of natural modes need to be controlled (such as vibration excited noise control). Modal sensors can also be used to identify which mode plays a primary role in the motion of a structure, then a corresponding modal actuator can be adopted to control the motion. An adaptive structure can thus be developed. To these ends, Lee and Moon [11] proposed spatially distributed modal sensors and actuators. Because the modal sensors and actuators depend on the shape of the master structures, the design of them is much complicated, i.e. for one-dimensional structures (e.g. beam and ring) the shape design of them is two-dimensional while for two-dimensional structures it is three-dimensional. As a result, application of them is limited to structures of simple form.

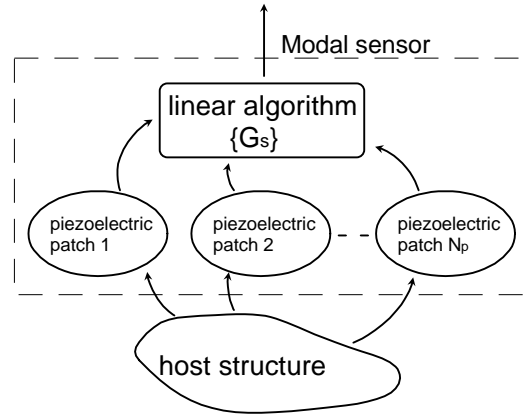


Figure 2 Illustration of the modal sensor

In the following part, a different type of modal sensors and actuators are proposed through the feedback gain design instead of shape design. The modal sensor shown in Fig. 2 consists of several piezo patches, and its output electric charge is defined as

$$Q_m = \{G_s\}^T \begin{Bmatrix} Q_1^e \\ \vdots \\ Q_{N_p}^e \end{Bmatrix} \quad (19.)$$

Substituting Eq. (13) into (19) produces

$$Q_m = \{G_s\}^T [K_{\phi u}] \{x\} \quad (20.)$$

Combining Eqs. (8) and (20), the modal sensor output has the form of

$$Q_m = \sum_{i=1}^n \left(\sum_{j=1}^{N_p} G_{sj} [K_{\phi u}^j] \{\phi_i\} \right) y_i \quad (21.)$$

When $\{G_s\}$ is chosen such that for $i = 1, 2, \dots, n$

$$\sum_{j=1}^{N_p} G_{sj} [K_{\phi u}^j] \{\phi_i\} = \begin{cases} \alpha_i, & i = k \\ 0, & i \neq k \end{cases} \quad (22.)$$

where α_i is an arbitrarily chosen constant. The k th modal sensor is then developed, that is,

$$Q_m = \alpha_k y_k \quad (23.)$$

If the modal sensor is to monitor a group modes, e.g. mode m_1, m_2, \dots , and m_p , Eq. (22) should be replaced by

$$\sum_{j=1}^{N_p} G_{sj} [K_{\phi u}^j] \{\varphi_i\} = \begin{cases} \alpha_i, & i = m_1, m_2, \dots, m_p \\ 0, & i \neq m_1, m_2, \dots, m_p \end{cases} \quad (24)$$

Since the number of piezoelectric patches is fewer compared to that of natural modes, Eqs. (22) or (24) can not be satisfied exactly. There are several ways to evaluate the linear algorithm $\{G_s\}$ in Eqs. (22) or (24). Conventionally, the generalized pseudo inverse method can give a reliable solution. In view of structure control, the equations on the lowest N_p modes in Eqs. (22) or (24) are chosen to be satisfied in this paper (i.e., the mode truncation method is employed). Solution of Eqs. (22) or (24) can then be obtained.

In addition to modal sensors, modal actuators can be formulated in a similar way. Substituting Eq. (14) into Eq. (15), we get the control force vector of the closed loop feedback control system as,

$$\{F\} = [K_{u\phi}] \left([G][K_{\phi u}] \{x\} + [\tilde{G}][K_{\phi u}] \{\dot{x}\} \right) \quad (25)$$

Then, the modal actuating force can be written as

$$f_i = \{\varphi_i\}^T [K_{u\phi}] \left([G][K_{\phi u}] \sum_{k=1}^n \{\varphi_k\}^T y_k + [\tilde{G}][K_{\phi u}] \sum_{k=1}^n \{\varphi_k\}^T \dot{y}_k \right) \quad (26)$$

in which n is the number of natural modes.

Comparing Eq. (26) with (11) yields

$$\{\varphi_i\}^T [K_{u\phi}] [G] [K_{\phi u}] \{\varphi_k\}^T = \begin{cases} -g_{1i} \omega_i / r, & k = i \\ 0, & k \neq i \end{cases} \quad (27)$$

$$\{\varphi_i\}^T [K_{u\phi}] [\tilde{G}] [K_{\phi u}] \{\varphi_k\}^T = \begin{cases} -g_{2i} / r, & k = i \\ 0, & k \neq i \end{cases} \quad (28)$$

Similar to the modal sensors in the previous part, there are $N_p \times N_p$ unknowns in Eqs. (27) and (28) while the number of equations to be satisfied is $n \times n$. And the feedback gain matrices $[G]$ and $[\tilde{G}]$ are determined by choosing $N_p \times N_p$ relations in Eqs. (27) and (28) concerning the modes of most interest in structure control.

The modal sensor and modal actuator developed herein are to some extent approximate. It is obvious inferior to those proposed by Lee and Moon [1]. However, the present modal sensor and actuator make the application of them into complex structures become possible.

Table 1 Material properties of piezoelectric material and the elastic plate

	E (Pa)	ν (Poisson ratio)	ρ (Kg/m³)	d_{31} (CN⁻¹)
elastic plate	73.0×10 ⁹	0.3	2630	
piezoelectric material	63.0×10 ⁹	0.35	7600	37.0×10 ⁻¹¹

Table 2 The first eight natural frequencies of the plate

mode	1	2	3	4	5	6	7	8
frequency (Hz)	11.0	71.8	152.5	212.1	362.0	440.7	484.6	768.1

NUMERICAL RESULTS AND DISCUSSION

In order to illustrate the feasibility of the proposed modal sensor and actuator, a cantilevered plate with surface-bonded piezoelectric patches is studied, shown in Fig. 3. A sinusoidal force is applied at the middle point of the free end to excite the plate. The plate is modeled by 4×10 shear deformable plate elements. The finite element code developed by Chen *et al.* [7] is adopted to simulate the optimal control.

The material properties of piezoelectric material and the elastic plates are given in Table 1. Table 2 lists the natural frequencies of the cantilevered plate without piezo patches. It should be noted that the 1st, the 2nd, and 4th modes are deflection modes, 3rd mode the twist mode, and 5th, 6th, 7th and 8th modes are hybrid modes. In this paper, eight and three patches, shown in Fig. 4, are used to simulate the modal sensor and actuator, respectively. Fig. 5 presents the frequency response curves of modal sensors which monitor single mode or a group of modes. Since the modal sensors shown here are made up of only eight patches, they are, in general, approximate. And observation spillover occurs when the frequency is above 700 Hz. Fortunately, the response at high frequency is not of most importance in structure control. And the spillover can be avoided by several methods, such as low frequency filter.

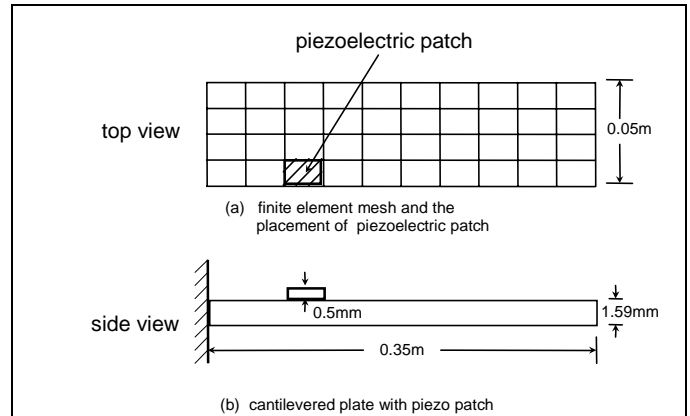


Figure 3 A cantilevered plate and its finite element mesh

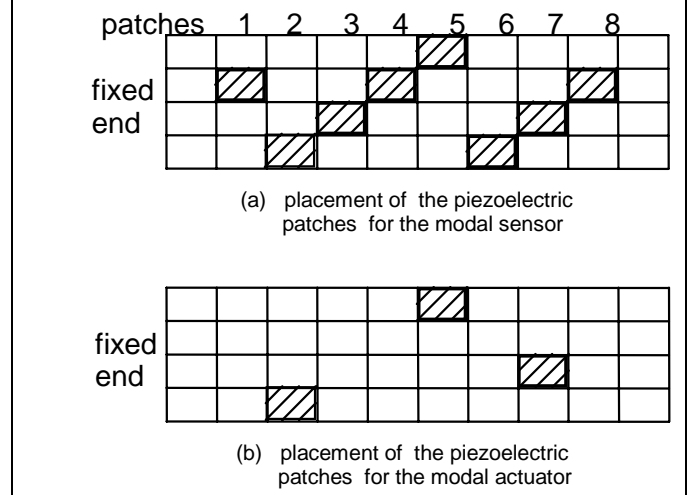


Figure 4 displacement of the piezoelectric patches

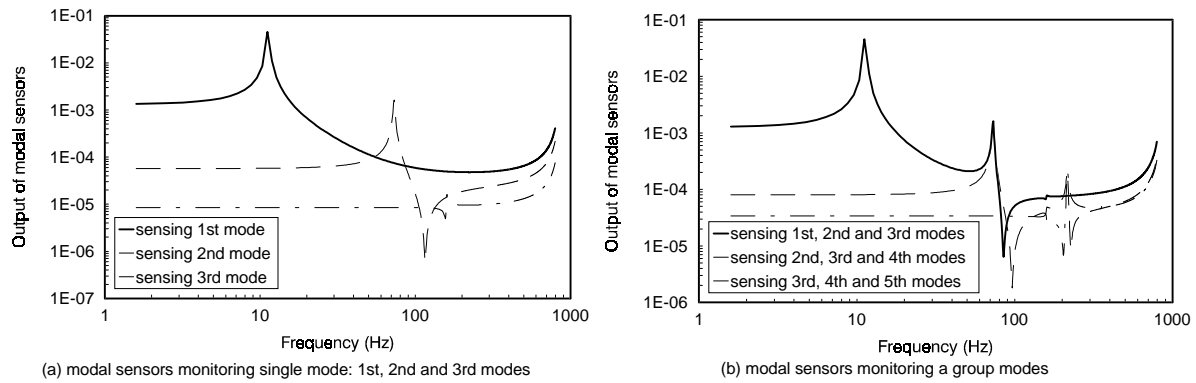


Figure 5 Frequency characteristics of the modal sensors

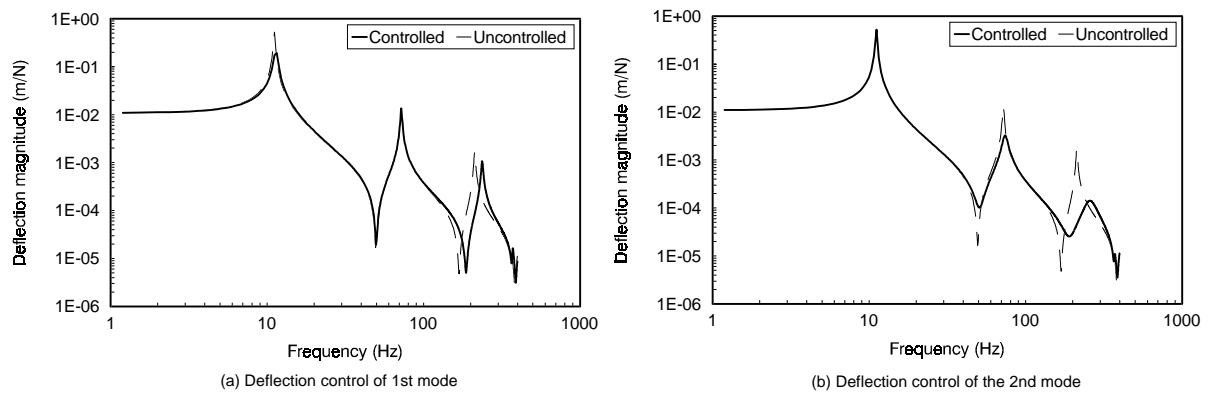


Figure 6 Frequency characteristics of the modal actuators

Application of modal actuators to control single mode is illustrated in Fig. 6. The deflection magnitude is the deflection of the free end along the axial direction. As we can see that the modal actuators can give viable control for specified modes.

From the above results, we can conclude that the developed modal sensors and actuators have the ability to monitor and actuate specified modes. And the application of them into complex structure is much easy although the host structure studied in this paper is quit simple, e.g. a plate. With the modal sensors and actuators, an adaptive structure is easy to make into practice: a structure can identify its motion in accordance with the output of modal sensors, and then select a corresponding modal actuator to control it motion.

However, it should be noted that the developed modal sensor and actuator depend strongly on the modal information and it is implicitly assumed that the modes are distinctive. Therefore, further study of it should be performed investigate how the design the modal sensors and actuators when the obtainable mode information is not sufficiently exact and repeated eigenfrequencies exist.

REFERENCES

1. Lee, C.K. and Moon F.C., "Modal sensors/actuators", ASME J. Appl. Mech., Vol. 57, 1990, 434-441
2. Crawly, E.F. and de Luis J., "Use of piezoelectric actuators as elements of intelligent structures", AIAA J., Vol. 25, 1987, 1373-1385
3. Wang, B.T. and Rogers, C.A., "Laminated plate theory for spatially distributed induced strain actuators", J. Composite Mater., Vol. 25, 1991, 433-452
4. Tzou, H.S. and Gadre, M., "Theoretical analysis of a multilayered thin shell coupled with piezoelectric shell actuators for distributed vibration controls", J. Sound Vib., Vol. 132, 1989, 433-450
5. Chandrashekhara, K. and Agarwal, A.N., "Active vibration control of laminated composite plates using piezoelectric devices: A Finite Element Approach", J. Intel. Mater. Syst. and Struct., Vol. 4, 1993, 496-508
6. Hwang, W.S. and Park, H.C., "Finite element modeling of piezoelectric sensors and actuators", AIAA J., Vol. 31, 1993, 930-937
7. Chen, C.Q., Wang, X.M. and Shen, Y.P., "Finite element approach of vibration control using self-sensing piezoelectric actuators", Comput. and Struct., Vol. 60 (3), 1996b, 505-513
8. Baz, A. and Poh, S., "Performance of an active control system with piezoelectric actuators", J. Sound Vib., Vol. 126 (2), 1988, 327-343
9. Khot, N.S., Oz, H., and Grandhi, R.V., "Optimal structure design with control gain norm constraint", AIAA J., Vol. 29 (12), 1988, 2047-2053
10. Lammering, R., Jia, J.H. and Rogers, C.A., "Optimal placement of piezoelectric actuators in adaptive truss structures", J. Sound Vib. Vol. 171 (1), 1994, 67-85
11. Hughes, P.C. and Skelton R.E., "Controllability and observability of linear matrix second order systems", ASME J. Appl. Mech., Vol. 47, 1980, 415-420
12. Laub, A.J. and Arnold, W.J., "Controllability and Observability criteria for multivariable linear second-order models", IEEE Trans. Automat. Contr., Vol. AC-29 (2), 1994, 163-165
13. Garcial, E., Dosch, J., and Inman, J., "The application of smart structure to the vibration suppression problem", J. Intell. Mater. Syst. and Struct., Vol. 3, 1992, 659-667

DESIGN OF THE SMART COMPONENTS BASED ON SHAPE MEMORY EFFECT

D. J. Lee and T. H. Jeong

*Dept. of Mechanical Engineering, Yeungnam University
Gyongsan, Gyungbuk, Korea 712-749*

SUMMARY: A simple one-dimensional model and 2-D multi-fiber finite element (FE) model are employed to study not only the thermally induced stresses and strains but also the thermal expansion of polymer matrix composite (PMC) with continuous TiNi fiber. It is found that both the back stress in the PMC induced by stiffness of TiNi fibers and the compressive stress in the matrix are the major source of the strengthening mechanisms and low thermal expansion of composite. Based on the concept of so-called shape memory composite (SMC), the critical modulus ratio (CMR) between TiNi fiber and matrix is predicted to design and manufacture the smart components that have no or minimum thermal deformation under the repeated heating and cooling cycles. It is also found that SMC with modulus ratio that is larger than CMR shows no shape memory effect as the number of heating/cooling cycle increases. Experimentally, thermal deformation and tensile strength of SMC are measured to compare with the theoretical and numerical prediction. SMC shows the constant thermal strain after many thermal cycles.

KEYWORDS: shape memory composite, intelligent or smart material, shape memory alloy, thermal expansion coefficient, critical modulus ratio, thermal cycle

INTRODUCTION

Noise due to thermal non-uniformity within the various electronic packages can be a major source of consumer's dissatisfaction. If the thermal stress in several components coming from thermal non-uniformity can not be removed by the simple design changes due to the various reasons such as structural integrity, etc. The thermal stress as a source of noise should be offset by other means such as shape memory effect using shape memory alloys.

The phenomenon known as shape memory effect (SME) is the occurrence of a martensitic phase transformation and its subsequent reversal upon heating or cooling to a critical temperature. Basically, a shape memory alloy (SMA) is deformed in the martensitic condition and the shape memory recovery occurs during heating when the specimen undergoes a reverse transformation of the martensite to its parent phase [1,2,3]. Material functional properties of SMA change depending on the temperature. As a unique mechanical property, SMA shows a higher stiffness (2-3 times), higher yield stress and larger recovery stress at the higher temperature region due to inversely thermoelastic phase transformation in opposition to becoming weak in the general metals. Also, SMA has a high damping and high wear resistance. Another phenomenon due to the transformation between austenite and martensite is superelasticity. In this case, the strain recovers just by unloading at the temperature above a

reverse transformation temperature (A_f). This is caused by the strain-induced martensitic transformation upon loading and the reverse transformation upon unloading.

Using this SMA, an active composite can be made by a pre-stressed martensitic SMA fiber with a non-SMA matrix material. When the composite is heated, the fiber contracts due to transformation, thereby producing the large recovery energy to heal the damage in the composite structures and to improve various mechanical properties. Upon cooling, the austenite transforms into martensite, and the internal stresses within the matrix partially return the composite structure to its original shape. Recently, this active composites or SMC as known as intelligent material are widely studied[6-9].

In the present work, the simple theoretical and 2-D elastic-plastic FE analyses have been used to examine the effects of modulus ratio(MR) between fiber and matrix, fiber volume fraction, fiber shape, the stress/strain system in the composite. And their effects on the thermo-mechanical behavior of composite are studied in the aspect of shape memory composite(SMC) that showed the permanent effects for the repeated heating/cooling cycles with no or minimum thermal deformation.

ANALYTICAL MODELLING

The effective thermomechanical responses of SMA fiber and SMC will be evaluated first in theoretical section. Based on the micromechanics scheme by the Mori-Tanaka method[7-9], the thermomechanical constitutive equations for the TiNi SMA fiber are developed. Also, a simple 1-D model is developed to study the thermal expansion coefficient(CTE) of this active composite.

Theoretical Approach

The thermomechanical behavior[10] of a NiTi SMA fiber is expressed for uniaxial tension as

$$\sigma = E\varepsilon + \Phi T + \Omega \xi \tag{1}$$

$$\text{and } \xi = f(\sigma, T) \tag{2}$$

where E is SMA material elastic modulus, Φ is the thermal elastic modulus, Ω is the transformation constant and ξ is the volume fraction of martensite.

From Eqn(2), volume fraction of martensite is function of temperature and stress. And during martensite transformation(cooling), ξ is

$$0 = f(0, M_s), \quad 1 = f(0, M_f) \tag{3}$$

and during austenite transformation

$$1 = f(0, A_s), \quad 0 = f(0, A_f) \tag{4}$$

where M and A refer to martensite and austenite also the subscripts s and f refer to start point and finish point of transformation.

In above equation, the elastic modulus and the average elastic modulus as a function of temperature are

$$E = E_A + \xi (E_M + E_A) \quad \text{and} \quad E_{avg} = (E_M + E_A)/2 \quad (5)$$

where the subscripts M and A refer to martensite and austenite, respectively.

Based on the 1-D model for SMA material[7,10], the equations for SMA fiber martensite transformation can be given as

$$\xi = 1 - \exp [b_M c_M (M_s - T) + b_M \sigma] \quad M_s \leq T \leq M_f \quad (6)$$

and for a reverse transformation can be

$$\xi = \exp [b_A c_A (A_s - T) + b_A \sigma] \quad A_s \leq T \leq A_f \quad (7)$$

where the material parameters c_M , b_M , c_A and b_A are given in Ref.[10].

Shape memory effect is occurred during a reverse transformation and the shape memory thermal strain is

$$\varepsilon = \varepsilon_M^f + (\Omega / D) (\xi_M^f - \xi) \quad (8)$$

where the transformation constant, Ω , is variable depending on pre-strain. And if the transformation is complete when $\xi = 0.99$. And the volume fraction of martensite from the beginning point of a reverse transformation can be

$$\xi = \xi_M^f \exp [b_A c_A (A_s - T) + b_A \sigma] \quad A_s \leq T \leq A_f \quad (9)$$

From Eqn. (8)

$$Pre - strain (PS) = \frac{\Omega}{D} = \frac{\varepsilon - \varepsilon_M^f}{\xi_M^f - \xi} \quad (10)$$

Combining Eqns. (5) and (10)

$$\Omega = PS [E_A + \xi (E_M - E_A)] \quad (11)$$

If a reverse transformation is completed, the SMA fiber will be recovered up to pre-strain since $\xi_M^f = \xi$. Therefore, it is possible to predict the thermal constitutive behavior of pre-strain SMA fiber as a function of temperature. As a composite with SME, Fig. 1 shows the basic model for continuous SMA fiber reinforced composite. Step(a) is a composite model with martensite TiNi fiber and epoxy matrix under pre-strain. Both fiber and matrix have no stresses but have a residual tensile pre-strain(ε_p). As the temperature increases above A_f , Step(b) shows a condition that the matrix tends to have a tensile thermal strain due to thermal

expansion while the SMA fiber tends to shrink up to the pre-strain due to SME. Therefore, as shown in Step(c), there will be a tensile stress in the TiNi fiber and a compressive stress in the matrix due to the thermo-mechanical coupling. As a composite material, amount and direction of thermal strain of this intelligent material will be determined not only by the degree of SME, volume fraction and distribution of SMA fiber but also by the properties of matrix. So, it is possible to predict and control the thermo-mechanical properties of this TiNi/matrix composite using theoretical and numerical analyses.

At Step(b), if it is assumed that both matrix and fiber deform under iso-strain condition and their interface also deforms as a continuous media with increasing the temperature uniformly, the equilibrium equation of this composite material will be

$$\sigma_m v_m + \sigma_f v_f = 0 \quad (12)$$

where the subscripts m and f represent matrix and fiber, respectively. V is a volume fraction of material. Therefore, at Step(b), the matrix will have a compressive stress due to the thermo-mechanical bonding and the compressive strain will be

$$\alpha_m \Delta T + \epsilon_c = \frac{\sigma_m}{E_m} \quad (13)$$

where α_m is the thermal expansion coefficient of matrix and ϵ_c is the thermal strain of composite. Also, the fiber will have a tensile stress and the tensile strain will be

$$\alpha_f \Delta T + \epsilon_c = \frac{\sigma_f}{E_f} \quad (14)$$

where α_f is the shape memory thermal expansion coefficient(SMTEC) of pre-strain fiber with increasing temperature above A_f .

Combining Eqn(13) and Eqn(14), the compressive stress in the matrix can be obtained as

$$\sigma_m = \frac{(\alpha_m - \alpha_f) \Delta T E_m E_f v_f}{E_f v_f + E_m v_m} \quad (15)$$

Also, the tensile stress in the fiber can be determined by

$$\sigma_f = \frac{(\alpha_m - \alpha_f) \Delta T E_m E_f v_m}{E_f v_f + E_m v_m} \quad (16)$$

From Eqn. (14), one can write

$$\frac{\epsilon_c}{\Delta T} = \frac{\alpha_f E_f v_f + \alpha_m E_m v_m}{E_c} = \alpha_c \quad (17)$$

where $E_c = E_f v_f + E_m v_m$ and α_c is the SMTEC of composite material. Therefore, it is possible to predict the SMTEC of composite as a function of V_f . However, there will be a nonlinear deformation in the elastoplastic matrix due to a large compressive stress coming from a

reverse transformation of TiNi fiber. It is necessary to expand the 1-D elastic theory to elastic-plastic model. Several different approaches have been employed. It will be published later.

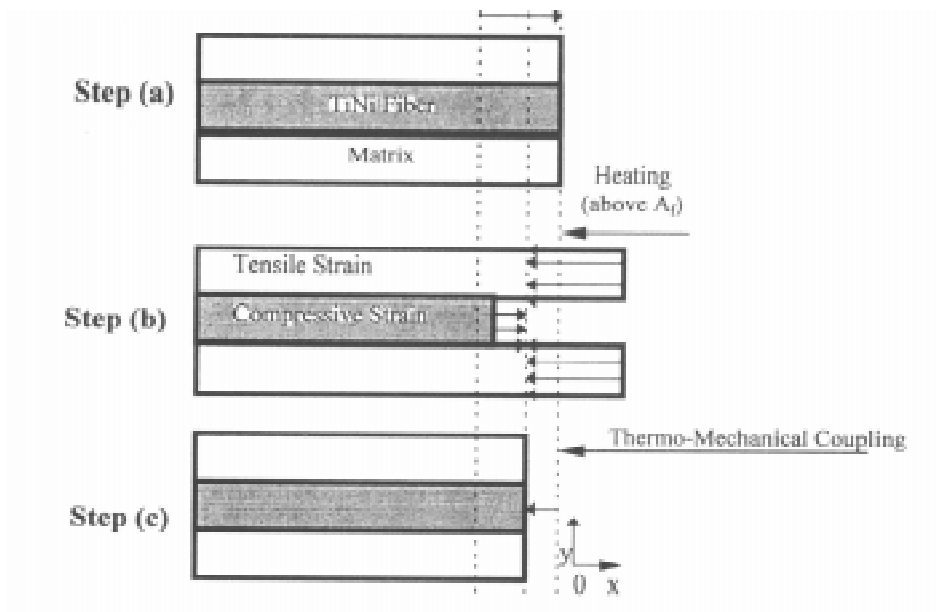


Fig. 1 Analysis model of continuous TiNi fiber reinforced composites.

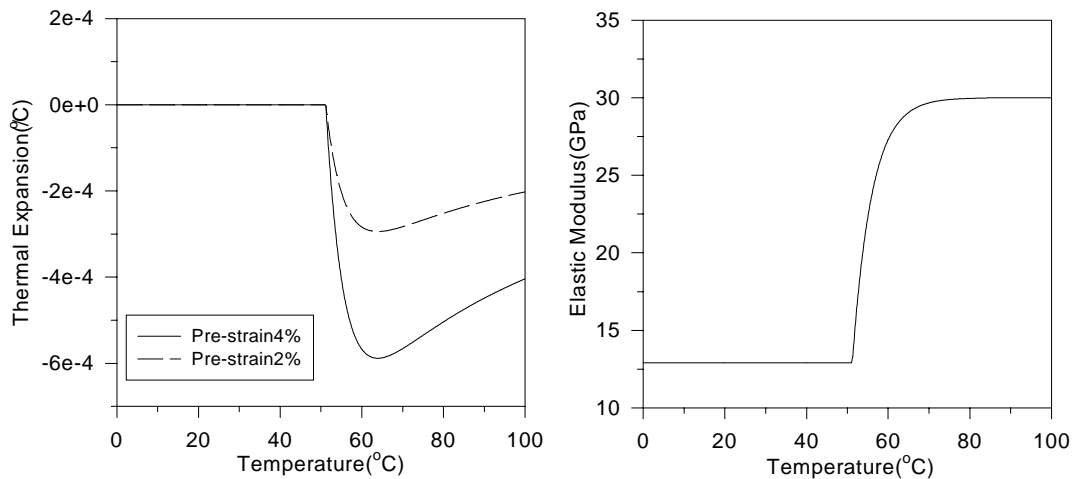


Fig. 2 Thermal expansion (a) and elastic modulus (b) of TiNi fiber as a function of temperature and pre-strain.

Numerical Analysis

The model used for FE analysis is the same as the theoretical approach with continuous fiber. The used temperatures are $M_f=5^\circ\text{C}$, and $M_s=23^\circ\text{C}$ as the finish and starting temperatures for martensite transformation. $A_s=29^\circ\text{C}$ and $A_f=51^\circ\text{C}$ are the starting and finishing temperatures for reverse transformation temperature as independent properties, respectively. Also elastic modulus is $E_M=13\text{Gpa}$ and $E_A=30\text{Gpa}$, Poisson's ratio is 0.33 for matrix and fiber. And tangent modulus of TiNi is 1% of elastic modulus. The elastic modulus and the thermal expansion coefficient are changing according to Eqns.(5) and (8), respectively and are shown in Fig. 2. This data is used for all numerical computation. For the matrix, elastic modulus is $D_{ave.}/MR$, and thermal expansion coefficient is $55\text{E-}6(/^\circ\text{C})$ as a temperature independent properties. All these properties data are selected from the published data[10]. FE analysis is performed by changing the temperature from 0°C to 100°C , the fiber volume fraction of 0.5% and 1%. The used element type is 4-node isoparametric element. The numbers of element are chosen for optimum condition and are same for all analyzing model types. Also, the stress-strain curves, determined by the bilinear kinematics hardening rule, materials' elastic modulus and yield stress are given as input data. To obtain stress-strain behavior numerically, a far field tensile strain is loaded from 0% and 5% stepwise. Each step has 20 small substeps and iteration of substeps is carried out until satisfying the permit error of $10\text{E-}4$. To solve the non-linearity, Newton-Raphson's method has been employed. All computations are performed by the general purpose FE program, ANSYS 5.0[11]. And their boundary conditions are $u=0$ at $x=0$ and $v=0$ at $y=0$ where u and v is amount of displacement in the x and y directions, respectively. Both stresses and strains in the fiber and matrix are obtained based on the average values from the total volume of model. Then, the average stresses and strains of composite are determined as

$$[\varepsilon]_c = [\varepsilon]_m v_m + [\varepsilon]_f v_f \quad \text{and} \quad [\sigma]_c = [\sigma]_m v_m + [\sigma]_f v_f \quad (18)$$

EXPERIMENTAL

Materials

TiNi fiber(Ti-50.2% Ni) of 0.1, 0.3 and 0.5 mm diameter are obtained from Nilaco Inc., Japan. The specimens are made with 0.5 and 1 volume percentage of SMA fiber. The epoxy resins used in this study are Type GT Series(Che-il Ciba-Geigy). Before making the composite specimens, the single fiber pull-out test is performed to obtain the best interfacial properties in the SMA fiber/epoxy system. It is found that the specimens with SMA etched the surface with 25% nitric acid for 25 sec. show the best interfacial strength among many surface treatments such as oxidation and mechanical abrasion techniques. The fibers are then vacuum heat treated for 1 hour at 50°C to remove all remaining solution inside the surface grooves and holes.

Specimen Fabrication

In this study, the continuous TiNi fiber reinforced composites as a candidate for this purpose are made. The fiber holder is used to apply 2 & 4 % pre-strain and hold for curing in a mold. Then, the fibers can be embedded in epoxy to depths in the range of 0.5 with the fiber axis perpendicular to the surface. The epoxy is allowed to harden according to manufacture's

guideline. The ASTM D638 tensile specimens with 2 mm thickness are used to measure the tensile properties of unfilled epoxy resin and SMA filled composite. The bar specimens(1.8 cm x 10 cm x 0.2 cm) are used to measure the CTE.

Experimental Procedure

To measure the thermal deformation of TiNi/epoxy composite, two strain gages positioned over the center of fiber and matrix are used in the middle of specimen. The temperature is controlled as shown in the following table.

Initial Temp.	→ Heating.	→ Max. Temp.	→ Constant Temp.	→ Cooling	→ Setting Temp.
25 °C		70 °C	65 °C		25 °C

The temperature within the electric furnace is representing the temperature in the specimen surface. The typical heating time is about 150 min. and cooling time is about 600 min for stable temperature changes. The holding temperature of 65 °C for 10 min is to measure the thermal deformation at constant temperature. This thermal cycle is continued until specimen shows the same thermal behavior. To measure the thermal strain, the multichannel system(Model AS1302, NEC Sanei Instrument, Ltd) is used. To obtain and compare the mechanical properties of TiNi fiber as a function of temperature, both the shape memorized and original fibers with 0.5 mm are used. All test are performed at 3 different temperatures(20, 45 and 65 °C) and repeated to assure the accurate data. All reported results are obtained by testing at least three samples of each condition. The testing machine is Shimadzu Autograph (Model AG-5000E) tensile machine. The tensile specimen is loaded monotonically to failure at crosshead speed of 2mm/min.

RESULTS AND DISCUSSION

Figs. 3(a) and 3(b) show the theoretical prediction of thermal strain with $V_f=1.0\%$ with pre-strain of 2% and 4% respectively. As the modulus ratio(MR) between matrix and TiNi fiber increases, the thermal deformation is restricted due to simple reinforcing effects by the fibers before transformation and even decreases due to shape memory effects after transformation temperature. As shown, the degree of compressive strain increase with the MR(softer matrix) as expected. Since the one-way SMA fibers can return to pre-strain state only once upon transformation temperature, there will be no SME upon cooling. This means that the SMA fiber in the composite show the compressive shrinkage, the composite will have only the simple reinforcing effects without SME. From these types of curves, it is possible to predict the critical modulus ratio(CMR) of SMC under the given V_f that shows the tensile deformation due to thermal expansion(0) instead of shrinks due to SME of fibers. If the modulus ratio of composite with given V_f is less than CMR, the composite will show the permanent effects of reducing thermal expansion and increasing tensile strength. But the modulus ratio of composite with given V_f is larger than CMR, the composite will show large shrinkage in the first heating/cooling cycle with a simple reinforcing effect after the first cycle.

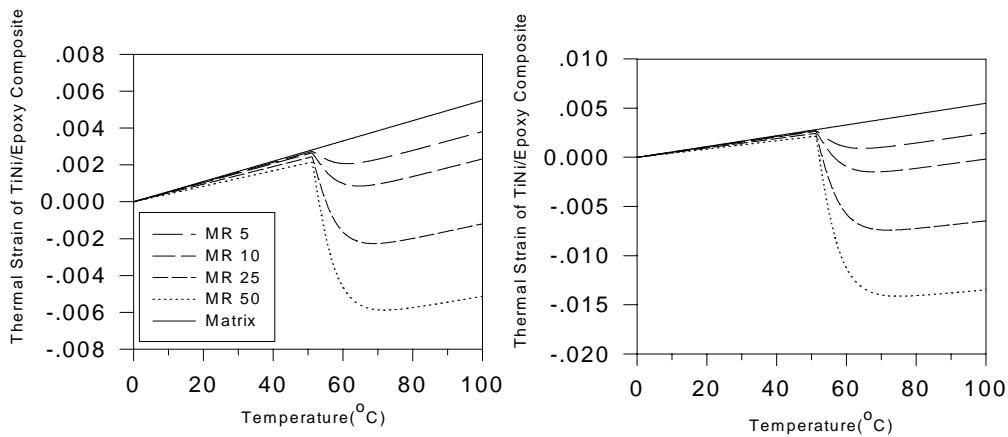


Fig. 3 Theoretical prediction of thermal strain in TiNi/epoxy composite($v_f=10\%$) with 2% pre-strain (a) and 4% pre-strain (b).

Based on the theoretical analysis, Figs. 4 show the numerical prediction with elastoplastic analysis when $V_f=0.5\%$ and the applied pre-strain is 4%. Fig. 4(a) shows the thermal strain of fiber after transformation. As the MR increases, the TiNi fiber shows the compressive strain. And as the MR decrease, the TiNi fiber shows the tensile strain due to thermal expansion of matrix. Fig. 4(b) shows the thermal strain of matrix. Before the transformation, matrix shows the thermal expansion with the simple reinforcing effects by the fiber. After the transformation, composite shows the thermal expansion due to matrix as temperature increase for low MR. As the MR increases, composite will have a thermal shrinkage due to SME of the fiber. Based on this figure, there will be no thermal deformation of matrix around 60 when MR is 50 to 1.

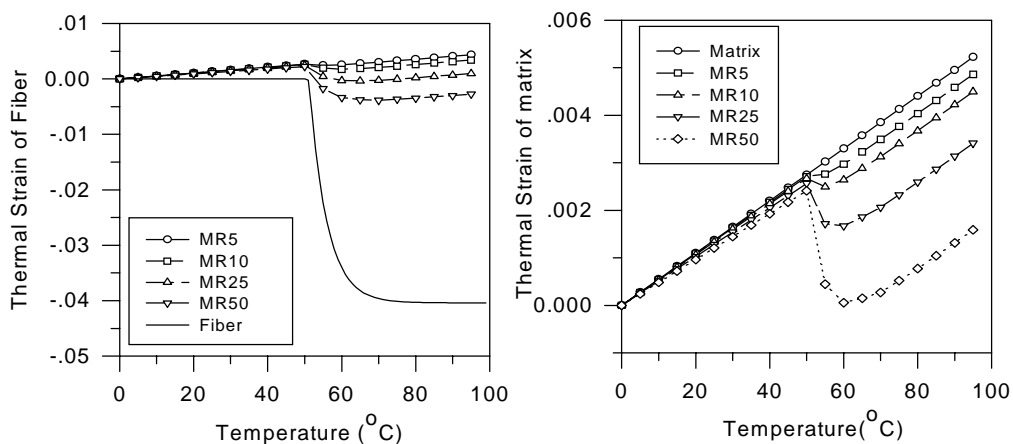


Fig. 4 Numerical prediction of thermal strain in fiber(a) and matrix(b) as a function of temperature and modulus ratio.

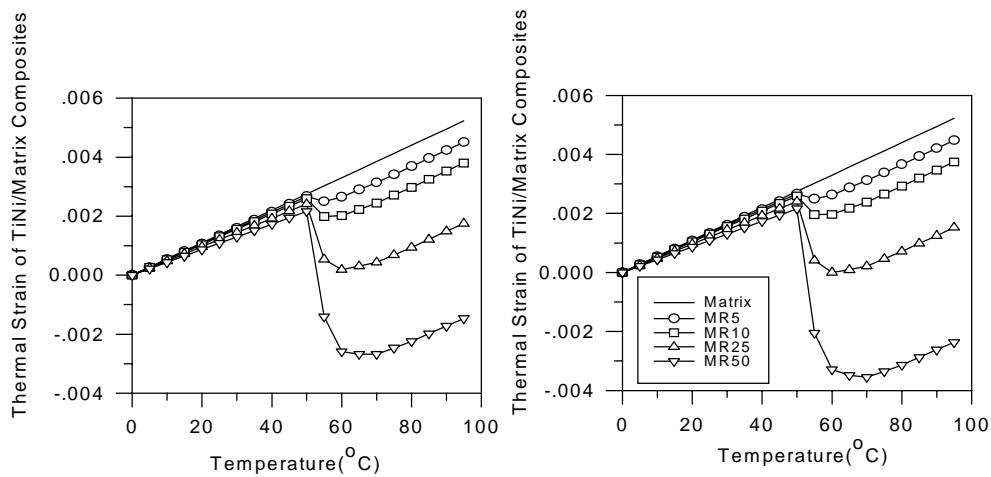


Fig. 5 Numerical prediction of thermal strain in TiNi/matrix composite($v_f=1.0\%$) with (a)2% pre-strain and (b) 4% pre-strain.

Compared to Fig. 3, Figs. 5 show the numerical prediction of thermal strain of SMC with $V_f = 1.0\%$ when the given pre-strain is 2% and 4% respectively. Compared to Figs. 3, the thermal strains of SMC with 2% and 4% pre-strain after transformation are similar to matrix when MR is low. As the MR increases, the effects of pre-strain also increase. In the case of SMA fiber with 2% pre-strain, the compressive strain(ϵ_c) is occurred when MR is 50:1. With 4% pre-strain, SMC has ϵ_c even when MR is 25:1. This is quite different MR ranges compared with the theoretical prediction(Figs. 3). And this data shows the need to develop the theoretical model that considers the elastoplastic behavior.

Figs. 6 show the minimum thermal strain of different conditions as a function of MR after transformation for TiNi fiber and SMC, respectively. As shown in both figures, the thermal strain decreases linearly as the temperature increases. From Fig. 6(a), it is possible to predict the relationship between V_f and pre-strain. For low MR, the thermal behavior of TiNi fiber depends on the matrix after transformation while TiNi fiber exhibits SME as the MR increases. Therefore, the critical modulus ratio(CMR) can be determined from this type of figures. Table 1 shows the CMR of TiNi/epoxy composite predicted by FEM.

Table 1. FEM Prediction of Critical Modulus Ratio

Modulus Ratio(M_f/M_m)	$v_f=0.5\%$ Prestrain 2%	$v_f=0.5\%$ Prestrain 4%	$v_f=1\%$ Prestrain 2%	$v_f=1\%$ Prestrain 4%
TiNi Region	29.5	22.5	14.5	11.3
Composite	54.2	51.2	26.8	24.2

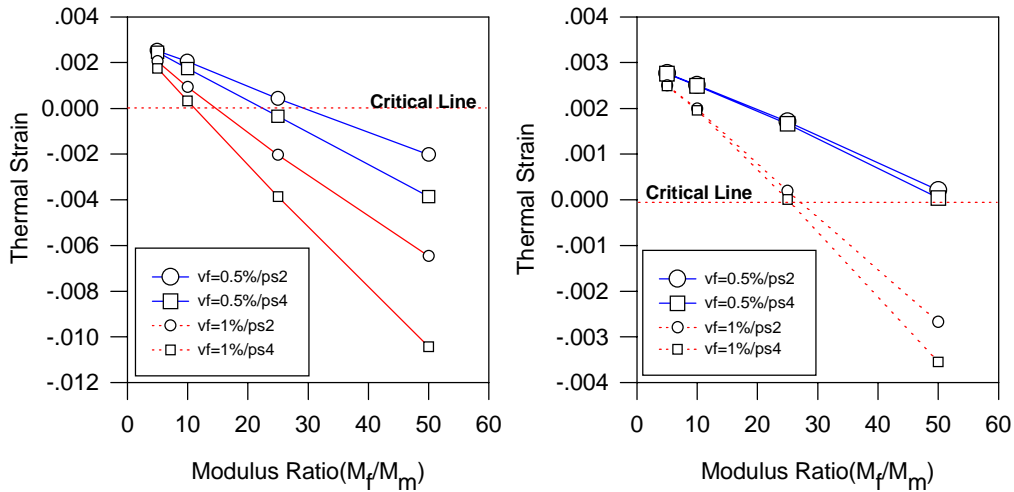


Fig. 6 Minimum thermal strain of TiNi fiber(a) and composite(b) as a function of modulus ratio and volume fraction.

Fig. 7(a) shows the stress-strain curves of TiNi fiber at 20, 45 and 65 °C. As known for SMA, both elastic modulus and yielding stress increase with the temperature. Fig. 7(b) shows the loading and unloading responses of TiNi fiber with 4% and 6% pre-strain . Regardless of the pre-strain amount, the SME of fiber is good.

Fig. 8 shows the thermal strain of TiNi fiber/epoxy with 4% pre-strain and 0.5 mm fiber as a function of temperature and thermal cycles. During few thermal cycles in the beginning, thermal expansion is much low due to SME of fiber. As the number of thermal cycle increases, thermal expansion becomes large. This trend is observed with even 0.1 mm TiNi fiber. Fig. 9 shows the thermal strain at 65 °C as a function of thermal cycles. As the number of thermal cycle increases, thermal expansion of SMC becomes constant. This represents the recovery of the major part of SME within few heating/cooling cycles regardless of fiber volume fraction in the case of large diameter of SMA fiber. However, the composite with the smaller fiber diameter shows the longer SME. Thermal strain measured with strain gage in the middle of specimen over the matrix is lower than thermal strain with gage above the fiber. For this type of specimen with fiber diameter 0.5 cm, two SMA fibers are embedded in the middle section. Gage over the matrix in the middle of specimen gets affect from both SMA fibers while gage over the fiber gets influence by one fiber only. As shown in figure, the total thermal strain of SMC is much less than that of the matrix alone.

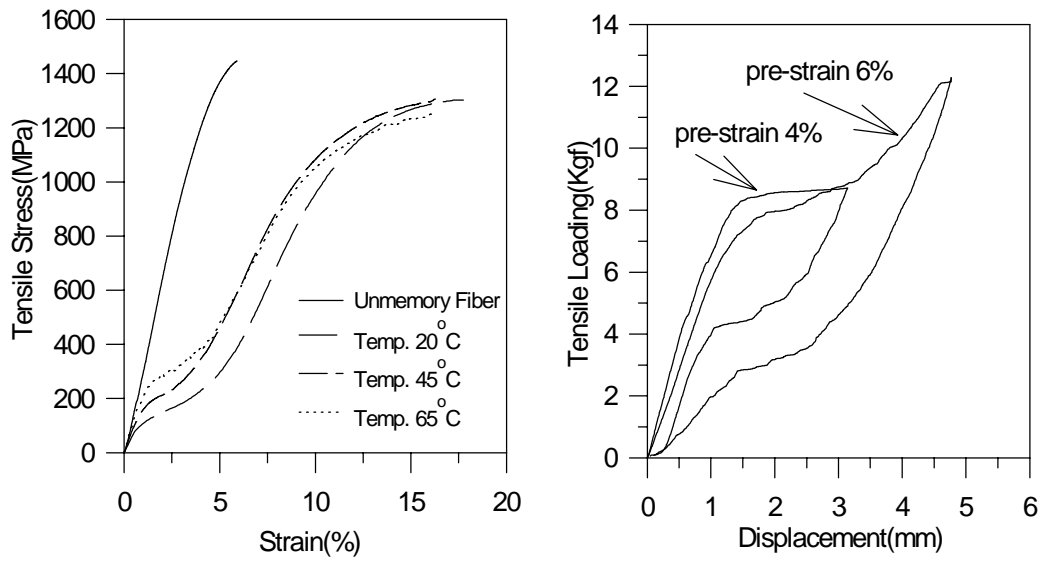


Fig. 7a Tensile stress-strain curves of TiNi as a function of temperature.
 Fig. 7b Tensile loading/unloading response for TiNi.

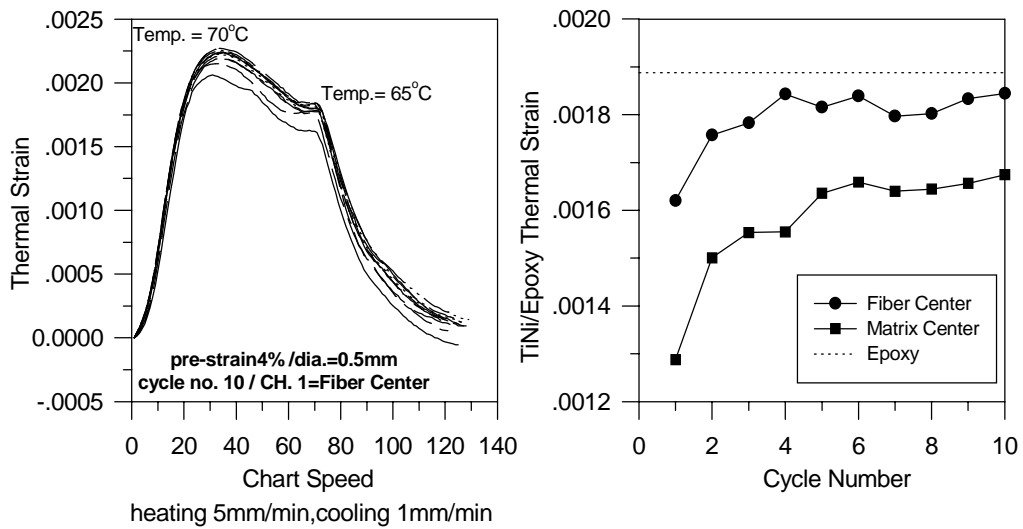


Fig. 8 Thermal strain of TiNi/epoxy for heating and cooling cycle.

Fig. 9 Thermal strain of TiNi/epoxy for heating/cooling with cycle number at 65°C.

CONCLUSION

A new design concept of SMC for no or minimum thermal deformation under repeated heating and cooling cycles is proposed. The 1-D theoretical model for continuous TiNi fiber reinforced composite has been developed to study the thermal behavior as a function of modulus ratio(MR). Based on theoretical and numerical analyses, the critical modulus ratio (CMR) for several types of SMC is suggested for design and manufacturing of smart components. After making composite with TiNi fiber and epoxy, the thermal behavior is measured and compared. Both simple reinforcing effects and SME of TiNi fiber are observed. It is also found that SMC with MR that is larger than CMR shows no SME as the number of heating/cooling cycle increases. Also, SMC shows the constant thermal strain after many thermal cycles.

ACKNOWLEDGMENT

This study is supported by Korean Ministry of Education through Research Fund under Grant Number ME95-C-12, which is gratefully acknowledged.

REFERENCES

1. Taya, M. and Aresenault, R. J., *Metal Matrix Composites : Thermo-mechanical Behavior*, Pergamon Press, 1989, pp.25-28.
2. Tadaki, T., Otsuka, K., "Shape Memory Alloy", *Ann. Rev. Mater.Sci.*, 1988, pp.25-45
3. Tarbrush, H., Tamara, K., "Pseudoelasticity of TiNi Shape Memory Alloy", *JSME*, Vol.36, No.3,1993, pp. 314-318
4. Liu, C. T., Kunsmann, H., Otsuka, K., "Shape Memory Materials and Phenomena Fundamental Aspects and Applications", *Proc. of Mat. Res. Society*, Vol.246, 1992,
5. Furuya, Y., Sasaki, A., Taya, M., "Enhanced Mechanical Properties of TiNi Shape Memory Fiber/Al Composites", *Materials Trans.,Jim*, Vol.34,No.3, 1993, pp.224-227
6. Yamada, Y., Taya, M., "Strength of Metal Matrix Composite by Shape Memory Effect", *Materials Trans. Jim*, Vol. 34, No. 3, 1993,pp.254-260.
7. Boyd, J. G., Lagoudas, D. C., "Thermomechanical Response of Shape MemoryComposites", *J. of Intelligent Syst. and Struct.*, Vol. 5, 1994, pp.333-346
8. Lagoudas, D. C., Tadjbakhsh, I. G., "Active Flexible Rods with Embedded SMA Fibers", *Smart Mater. Struct.*, Vol. 1, 1992,pp.162-167
9. Lagoudas, D. C., Boyd, J. G., "Micromechanics of Active Composites With SMA Fibers" *J. of Engineering Mat. and Tech.*, Vol.116, 1994, pp.337-347
- (10) 田中喜久昭, "形状記憶合金の機械的性質",養賢堂, 1993,pp.62-122
11. Peter Kohnke, "ANSYS User's Manual for Revision5.0", Swanson Analysis System Inc. 1994

FINITE ELEMENT ANALYSIS OF MECHANICAL PROPERTIES OF SHAPE MEMORY ALLOYS

Yen Jinliang¹, Shen Yapeng¹, Chen Ru²

¹Department of Engineering Mechanics, Xi'an Jiaotong University,
Xi'an, Shaanxi Province, 710049, P.R.China

²China Academy of Engineering Physics
P.O. Box 521-50, Chengdu, Sichuan Province, 610003, P.R.China

SUMMARY: This paper reviews the three-dimensional constitutive relation of Shape Memory Alloys presented by Boyd and Lagoudas. A linear incremental constitutive equation is derived from the nonlinear one. The finite element equations in Total Lagrangian form are attained and the program is also developed. To verify the effectiveness of the program, a simple test case are examined and the result shows the reliability of the program. The finite element program is utilized to simulate the mechanical behavior of the pipe connector made by shape memory alloy, and the result of stress distribution reveals greatly unusual. Some difficulties never mentioned before are found in calculation. Measures are taken to overcome the difficulties. Since the constitutive equation of shape memory alloys is very complex, the finite element program is then shown to be a powerful tool for studying various applications of shape memory alloys.

KEYWORDS: shape memory alloys, non linear finite element program, total Lagrangian approach

INTRODUCTION

Shape memory alloys (SMA) are the alloys which have shape memory effect (SME), that means the alloys are able to sustain a large recoverable strain (of the order of 10%) without plastic deformation and to remember its initial configuration and return to it as being heated. The phenomena of SME have attracted a lot of notice of investigators since it was first observed in TiNi alloy in 1960s. Many kind of alloys, such as TiNi, Cu-based alloys, In-based alloys, austenite steels, etc., have been found to have the property of SME. The application of SMA is widely recognized not only in the science filed but also in the engineering field.

The unusual character of SMA is now known to be associated with the thermoelastic martensitic transformation and its reverse course. There are four important temperature point of the phase transformation, M_s , M_f , A_s , A_f , which denote martensite start, martensite finish, austenite start, austenite finish respectively. The martensitic fraction (ξ) is the quantity of SMA in the martensitic phase: $\xi=0$ means that the material is fully austenite, while $\xi=1$ represents that the material is fully martensite. The martensitic fraction changes as a function of temperature under stress-free conditions. More generally, the martensitic fraction is known to change as a function of both stress (S) and temperature (T). A cosine model of variety of martensitic fraction is employed. The expressions are as follows:

for austenite to martensite

$$\xi = \frac{1}{2} \left\{ \cos \left[a_M (T - M_f) + b_M S_i \right] + 1 \right\} \quad (1)$$

$$a_M = \frac{\pi}{M_s - M_f}, b_M = -\frac{a_M}{c_M}$$

for martensite to austenite

$$\xi = \frac{1}{2} \left\{ \cos \left[a_A (T - A_s) + b_A S_i \right] + 1 \right\} \quad (2)$$

$$a_A = \frac{\pi}{A_f - A_s}, b_A = -\frac{a_A}{c_A}$$

In Eqn 1 and Eqn 2, C_A and C_M represent material constants of SMA which determine the influence of stress on transformation temperature, and S_i is the equivalent stress.

CONSTITUTIVE RELATIONS

In this paper, the constitutive relations presented by Boyd and Lagoudas^[2] are adopted. Here we briefly review the constitutive law which will be used later.

Assuming that response will remain elastic, the three-dimensional form of the stress-strain equation may be written as

$$S^{KL} = C^{KLMN} E_{MN}^e = C^{KLMN} (E_{MN} - E_{MN}^t - \alpha_{MN} \Delta T) \quad (3)$$

where S_{KL} is the second Piola-Kirchhoff stress, E_{MN}^e , E_{MN} and E_{MN}^t are the elastic strain, the Green strain, the transformation strain, and $\Delta T = T - T_0$, where T_0 is the initial temperature. The elastic stiffness tensor C_{KLMN} and the thermoelastic expansion tensor α_{MN} are given by

$$C^{KLMN} = C_A^{KLMN} + \xi (C_M^{KLMN} - C_A^{KLMN}) \quad (4)$$

$$\alpha_{MN} = \alpha_{A_{MN}} + \xi (\alpha_{M_{MN}} - \alpha_{A_{MN}}) \quad (5)$$

The subscripts A , M denote austenite and martensite respectively.

In describing the response of SMA materials, incremental constitutive equations are required. Taking the time derivative of 3 results in the equation

$$\dot{S}^{KL} = C^{KLMN} (\dot{E}_{MN} - \dot{E}_{MN}^t - \dot{\alpha}_{MN} \Delta T - \alpha_{MN} \dot{T}) + \dot{C}^{KLMN} E_{MN}^e \quad (6)$$

The three-dimensional transformation strain rate \dot{E}_{MN}^t is obtained from

$$\dot{E}_{MN}^t = \Lambda_{MN} \dot{\xi} \quad (7)$$

where

$$\Lambda_{MN} = \begin{cases} -\frac{3}{2} \frac{\Omega}{\bar{D}} \frac{S'_{MN}}{S_i}, \dot{\xi} > 0 \\ -\frac{\Omega}{\bar{D}} \frac{E'_{MN}}{E'_i}, \dot{\xi} < 0 \end{cases} \quad (8)$$

and where

$$E'_i = \sqrt{\frac{2}{3} E'_{MN} E'_{MN}} \quad (9)$$

$$\bar{D} = \frac{1}{2} (D_A + D_M)$$

The rates \dot{C}_{KLMN} and $\dot{\alpha}_{MN}$ may be obtained from 4 and 5 using the chain rule for the time derivative of ξ , i.e.

$$\dot{\xi} = \frac{\partial \xi}{\partial T} \dot{T} + \frac{\partial \xi}{\partial S_i} \dot{S}_i \quad (10)$$

This completes the three-dimensional SMA constitutive equations.

ONE-DIMENSIONAL ANALYSIS

In one-dimensional domain, Eqn 8 may be rewritten as

$$\Lambda = -\frac{\Omega}{D} \quad (11)$$

It has the same form for both martensitic transformation and the reverse transformation, so Eqn 7 changes to

$$E' = -\frac{\Omega}{D} \xi \quad (12)$$

Substituting the above equation into Eqn 3, one gets

$$S = D(\xi) \left(E + \frac{\Omega}{D} \xi - \alpha \Delta T \right) \quad (13)$$

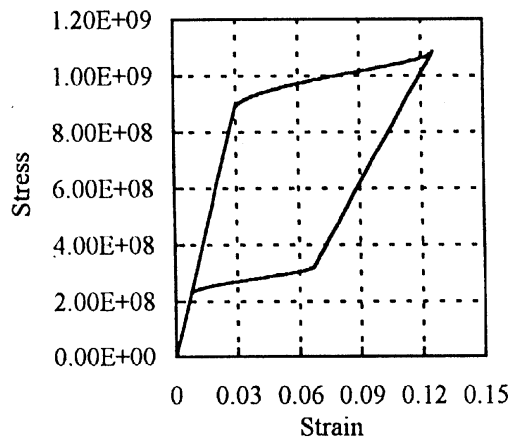


Fig. 1(a). $T=A_f+50\text{ }^\circ\text{C}$

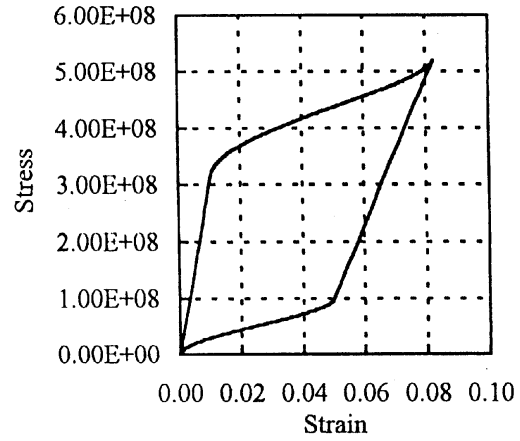


Fig. 1(b). $T=A_f$

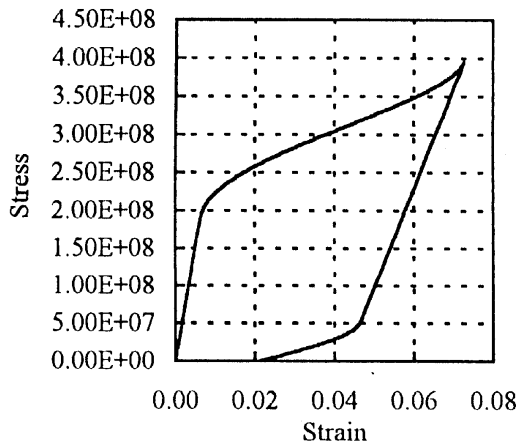


Fig. 1(c). $T=(A_f+A_s)/2$

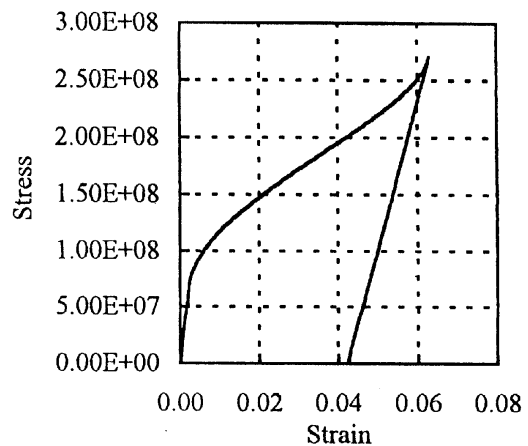


Fig. 1(d). $T=A_s$

Fig.1 Stress-strain curve of SMA at various temperature

It should be noticed that if $\xi=1$ in Eqn 12, the maximum of transformation strain will be obtained, i.e.

$$E'_{\max} = -\frac{\Omega}{D}$$

which points out the physical meaning of the variable Ω .

NUMERICAL FORMULATIONS

Using the Total Lagrangian approach, the Green strain is presented as

$$E_{KL} = \frac{1}{2}(U_K|_L + U_L|_K + U_M|_K \cdot U^M|_L) \tag{14}$$

The increment of the Green strain is

$$\begin{aligned}\Delta E_{KL} &= E_{KL}^{(N+1)} - E_{KL}^{(N)} \\ &= \frac{1}{2}(\Delta U_K|_L + \Delta U_L|_K + \Delta U_M|_K \cdot U^M|_L + U_M|_K \cdot \Delta U^M|_L + \Delta U_M|_K \cdot \Delta U^M|_L)\end{aligned}\quad (15)$$

Neglecting body force, the principle of virtual work of continuous body in equilibrium, with the second Piola-Kirchhoff stress and its increment, can be written as

$$\iiint_V (S^{KL} + \Delta S^{KL}) \delta(E_{KL} + \Delta E_{KL}) dV^{(0)} - \iint_{S_\sigma} (\bar{T}^M + \Delta \bar{T}^M) \delta \Delta U_M dS^{(0)} = 0 \quad (16)$$

Substituting Eqn 15 into Eqn 16 and neglecting the higher order terms, we obtain

$$\begin{aligned}\iiint_V (\Delta S^{KL} \delta \Delta E_{KL}^0 + S^{KL} \Delta U_M|_K \delta \Delta U^M|_L + S^{KL} \delta \Delta E_{KL}^0) dV^{(0)} \\ - \iint_{S_\sigma} (\Delta \bar{T}^M + \bar{T}^M) \delta \Delta U_M dS^{(0)} = 0\end{aligned}\quad (17)$$

where

$$\Delta E_{KL}^0 = \frac{1}{2}(\Delta U_K|_L + \Delta U_L|_K + \Delta U_M|_K \cdot U^M|_L + U_M|_K \cdot \Delta U^M|_L)\quad (18)$$

From Eqn 6, we have

$$\Delta S^{KL} = C^{KLMN} (\Delta E_{MN} - \Delta E_{MN}^t - \alpha_{MN} \Delta T - \Delta \alpha_{MN} T) + \Delta C^{KLMN} E_{MN}^e \quad (19)$$

If we directly substitute Eqn 19 into Eqn 17, the finite element equations can be obtained. However, Eqn 19 is nonlinear and it is very difficult for numerical calculation to converge, yet it must be modified to be available for use. For convenient, here the derivation of modifying the constitutive equations is presented in the form of matrix.

Substituting Eqn 4 and Eqn 5 into Eqn 19, and using Eqn 1 and Eqn 2, Eqn 19 in the form of matrix changes as

$$\{\Delta S\} = [C][D]\{\Delta E\} - [C] \left(\{V\} \frac{\partial \xi}{\partial T} + [D]\{\alpha\} \right) \Delta T \quad (20)$$

where

$$\{V\} = [D] \left[\{\Lambda\} + (\{\alpha_M\} - \{\alpha_A\})(T - T_0) \right] - ([D_M] - [D_A]) \{E^e\} \quad (21)$$

$$[C] = \left([I] + \{V\} \cdot \left\{ \frac{\partial S_i}{\partial S} \right\}^T \cdot \frac{\partial \xi}{\partial S_i} \right)^{-1} \quad (22)$$

From Eqn 17—22, the equation for finite element method is attained

$$([K_0] + [K_U] + [K_S]) \{\Delta U\} = \{\Delta Q\} + \{\Delta F\} + \{\Delta W\} \quad (23)$$

where the matrix $[K_0]$ is the incremental stiffness matrix, the matrices $[K_U]$ and $[K_S]$ are respectively the initial displacement stiffness matrix and initial stress stiffness matrix

influenced by the finite displacement, $\{\Delta Q\}$, $\{\Delta F\}$ represent the vector of applied load and the residual vector, respectively, $\{\Delta W\}$ is the vector of thermoload.

A finite element program (FEP) based on the derivation has been developed. To testify the availability of the program, a special test case is examined: a thin cylinder with internal pressure at the ratio (thickness/radius) of 1/1000. Comparison between results of FEP and the analytical one of one-dimensional case shows well agreement (Fig.2).

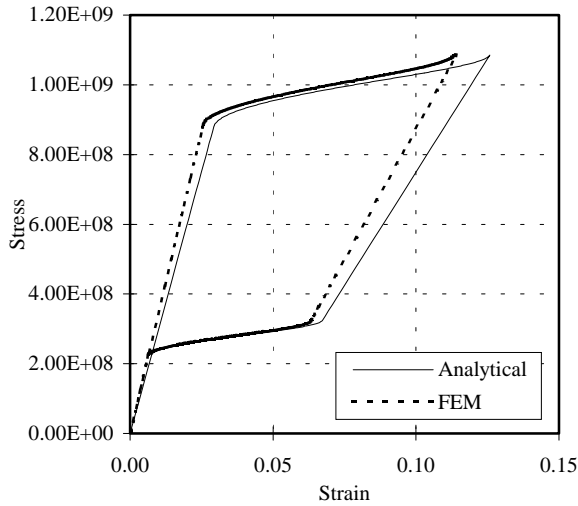


Fig.2(a). $T=A_f+50^\circ C$

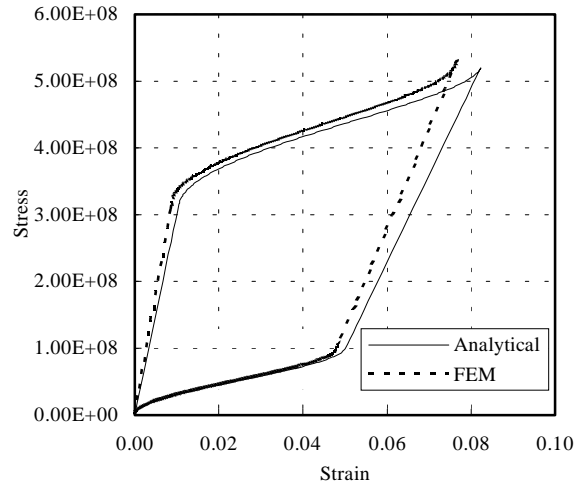


Fig.2(b). $T=A_f$

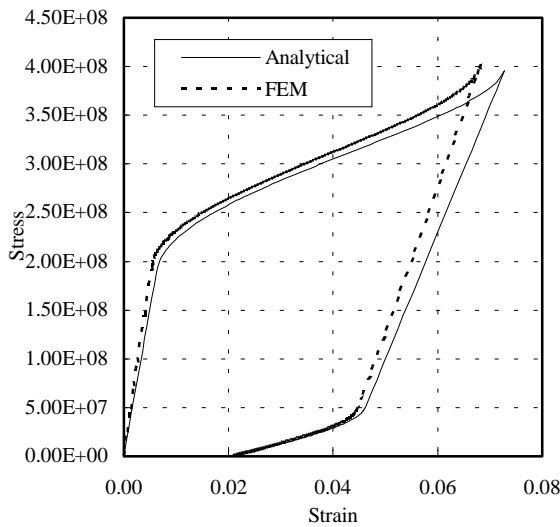


Fig.2(c). $T=(A_f+A_s)/2$

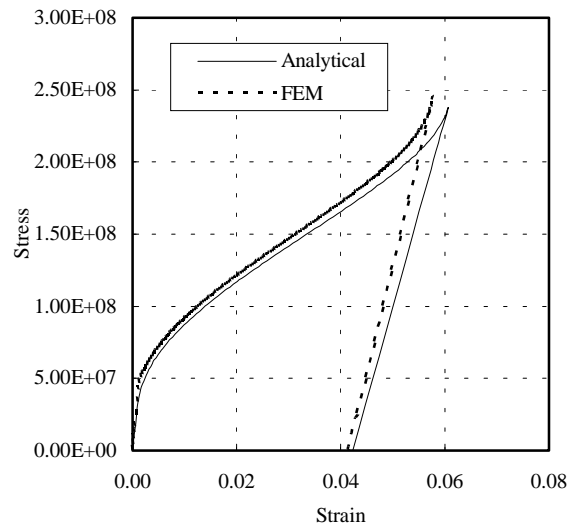


Fig.2 (d). $T=(A_s+M_s)/2$

Fig.2 FEP result at various temperature compared with the analytical one

APPLICATION TO SMA PIPE COUPLING

One of the most established uses for shape memory alloys is that of connectors for tubing. The procedure in these applications is to manufacture a ring of shape memory alloy that has a somewhat smaller inner diameter in the austenitic state than the outer diameter of the pipes to be connected. At a temperature less than A_s the ring is then deformed and change to the martensitic state so that its inner diameter exceeds slightly that of the tubing. The ring is

placed over the pipes in this phase and then heated. As the transformation to austenite takes place, the material attempts to recover the residual strain. However, being partially restrained by the pipes, the connector subsequently recovers only part of its residual strain and finally builds up large internal stresses.

The FEP developed in this paper is utilized to simulate the whole course, add mechanical load so that the SMA connector totally transform to martensite, remove the load and the strains remained, place the connector over the pipes and warm it up. The results of stress in θ -direction of the connector and that at the SMA-pipes interface are shown in fig.3-7. with a thicker SMA connector (thickness/radius=30%)

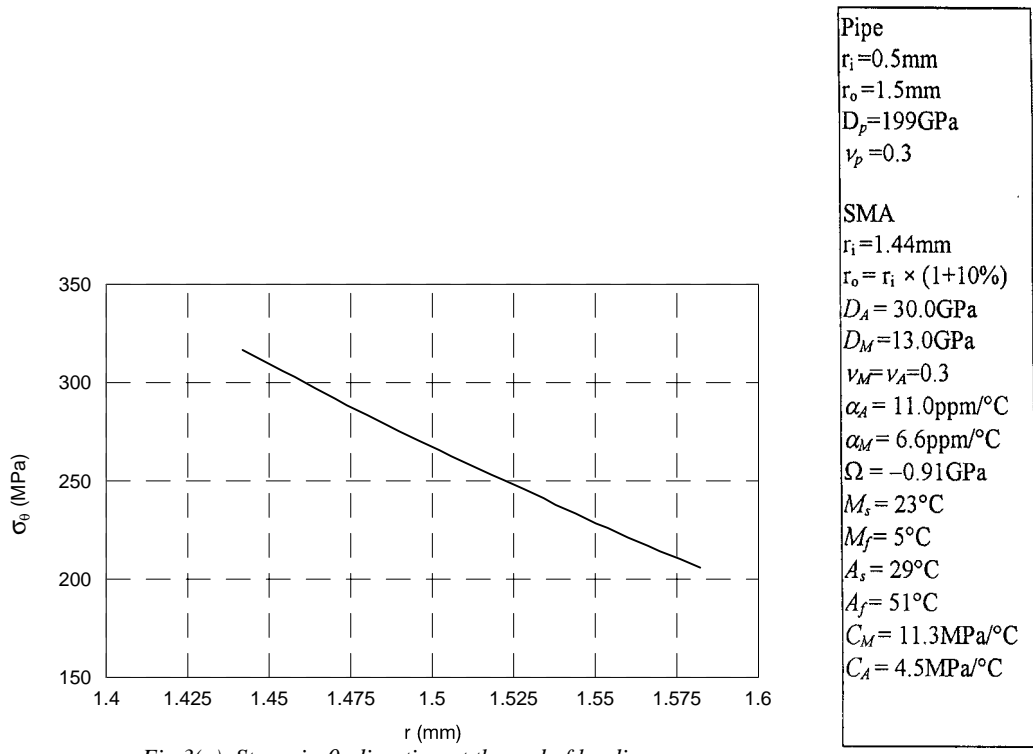


Fig.3(a). Stress in θ -direction at the end of loading

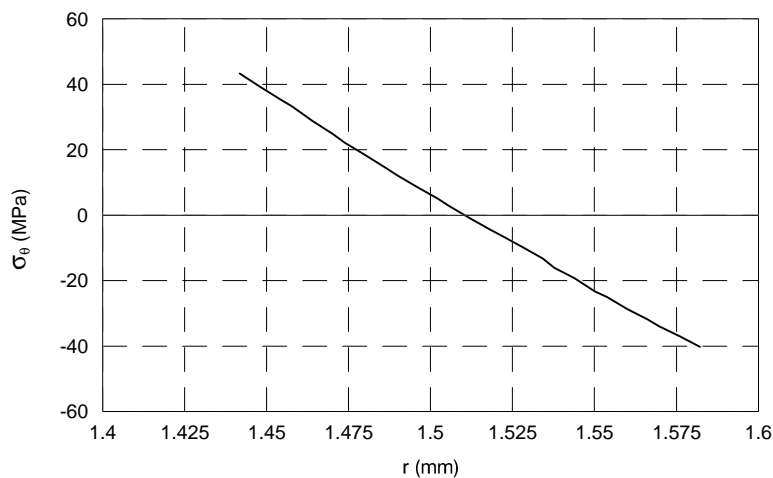


Fig.3(b). Residual stress in θ -direction after removing load

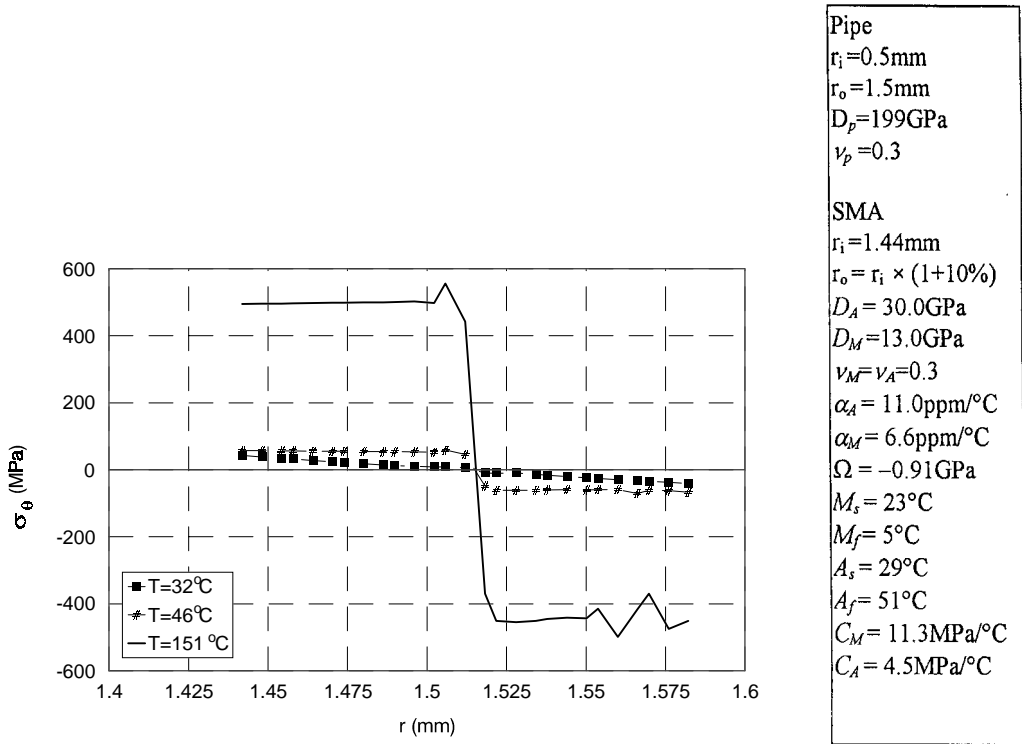


Fig.3(c). Stress in θ -direction during heating

Fig.3 Stress of SMA in θ -direction during whole course

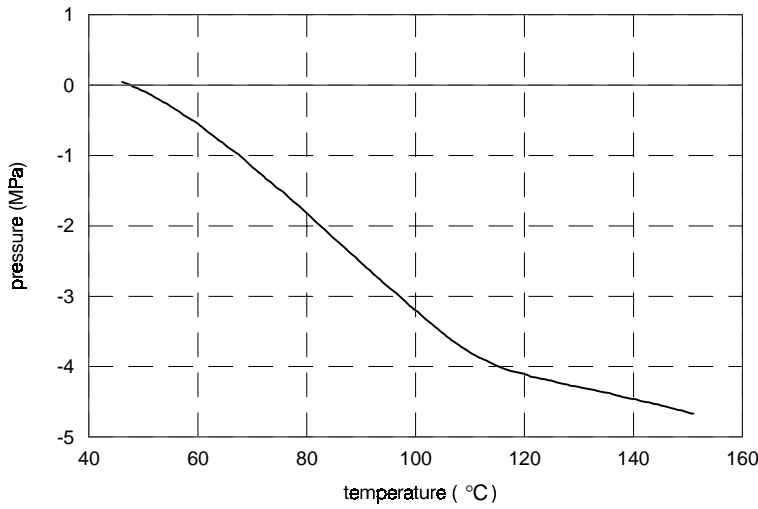


Fig.4 The interface stresses at various temperature
the initial temperature is 23°C , the final temperature is 151°C

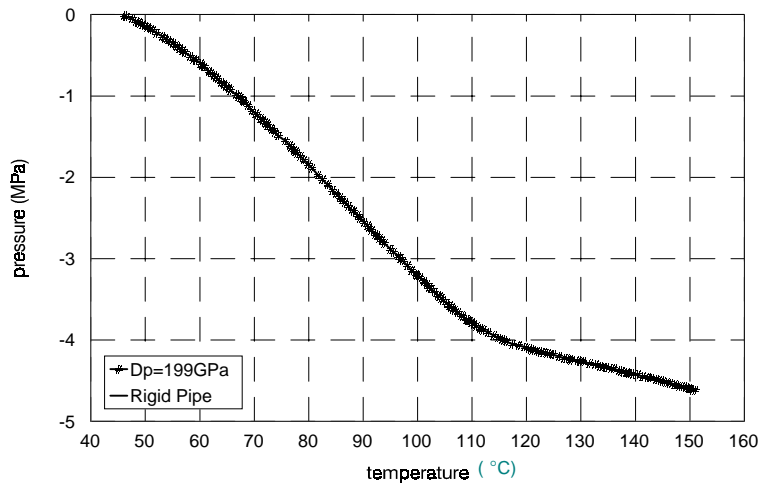


Fig.5 The interface stresses at various temperature with different Young's modulus for the pipes (D_p)

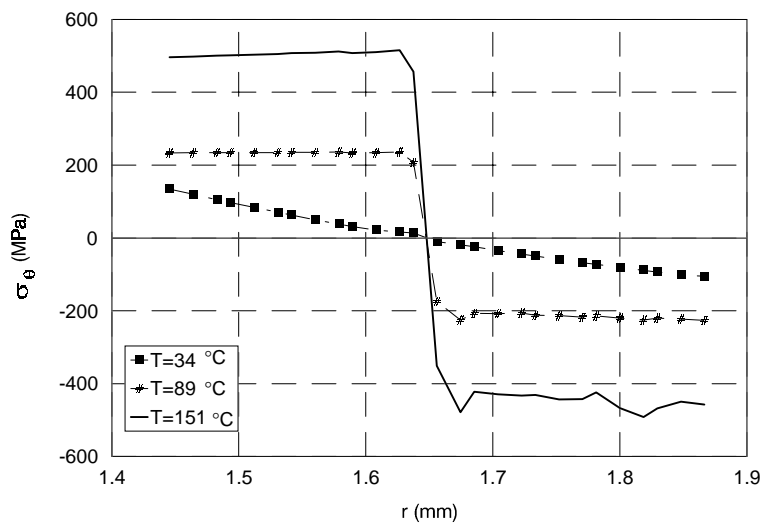


Fig.6 Stress of SMA in θ -direction during heating with a thicker SMA connector (thickness/radius=30%)

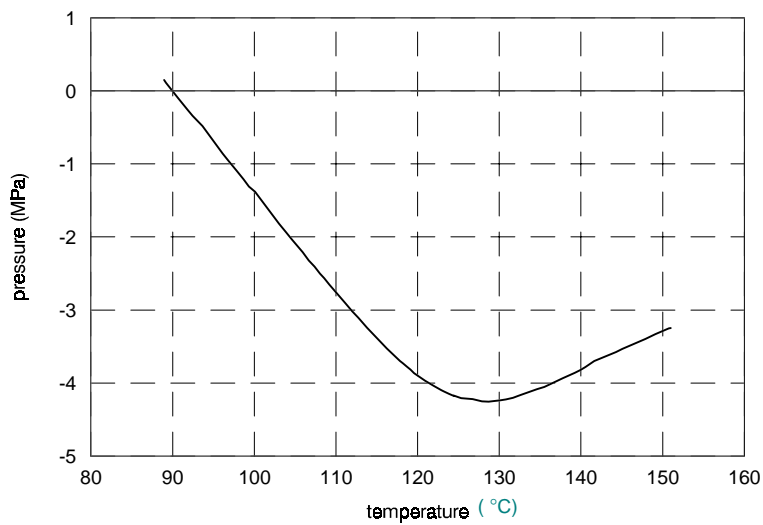


Fig.7 The interface stresses at various temperature

CONCLUSION

This paper has developed a nonlinear three-dimensional axisymmetric finite element program for shape memory alloys behavior. Since the nonlinear constitutive relation is unsuitable for calculation due to the difficulties of convergence, an incremental linear constitutive relation has been proposed based on the nonlinear one, and used in the FEP.

The numerical analysis meets with some difficulties. When the SMA connector is being heated to beyond the critical temperature at which the martensite starts to transform to the austenite, the right hand side of the finite element equations changes greatly, thus bringing considerable calculation errors. It is the reason why the stresses in Fig.3(c) and Fig.6 are not smooth. To overcome the difficulties, the program is designed to be able to automatically choose a variable temperature step according to the material state. In this way, the errors of the critical step can be acceptable; meanwhile the calculation does not take too much CPU time. Another difficulty is the discontinuity of residual stress (Fig.3(c), Fig.6). When the connector is heated, the material starts to transform to Austenite. However, the reverse transformations of different points do not happen at the same time. The heterogeneous reverse transformation leads to the discontinuity of the stress in θ -direction. So the finite element meshes for calculation must be sufficiently fine to avoid the difficulties.

A special phenomenon is seen that the stress on the interface reduces while the temperature increases in some cases (Fig.7). It is induced by the large internal stresses. Since the internal stresses get greater when the thickness of SMA connector is thicker, it seems that the thickness of SMA connector should be as thin as possible to amend the interface pressure.

The results of stresses at the interface for various strengths of the pipe material are shown in Fig.5. The modulus of the pipe is much greater than that of the austenite. It is clear that the results are converging on the case of rigid pipe as one would expect.

ACKNOWLEDGMENT

This paper is supported by China Academy of Engineering Physics and National Natural Science Foundation.

REFERENCES

1. Barrett, D. J., A One Dimensional Constitutive Model for Shape Memory Alloys, *J. of Intell. Mat. Sys. and Struct.*, Vol.6, No.3, 1995
2. Boyd, J. G. and Lagoudas, D. C. , Thermomechanical Response of Shape Memory Composites, *J. of Intell. Mat. Sys. and Struct.*, Vol.5, No.3, 1994
3. Kikuaki Tanaka, Shigenori Kobayashi and Yoshio Sato, Thermomechanics of Transformation Pseudoelasticity And Shape Memory Effect in Alloys, *International Journal of Plasticity*, Vol.2, pp.59—72,1986

4. L. C. Brinson and R. Lammering, Finite Element Analysis of The Behavior of Shape Memory Alloys and Their Application, *Int. J. Solids Structure*, Vol.30, No.23, pp.3261—3280, 1993
5. Liang and C. A. Rogers, Design of Shape Memory Alloy Springs With Applications in Vibration Control, *J. of Vibration and Acoustics*, Jan 1993, Vol.115
6. Qing Ping Sun and Keh Chih Hwang, Micromechanics Modelling for The Constitutive Behavior of Polycrystalline Shape Memory Alloys - I. Derivation of General Relations, *J. Mech. Phys*, Vol.41, No.1, pp.1-17, 1993
7. Qing Ping Sun and Keh Chih Hwang, Micromechanics Modelling for The Constitutive Behavior of Polycrystalline Shape Memory Alloys - II. Study of The Individual Phenomena, *J. Mech. Phys*, Vol.41, No.1, pp.19-33, 1993
8. Sullivan, Analysis of Properties of Fiber Composites with Shape Memory Alloy Constituents, *J. Intell. Mat. Sys. and Struct.* ,Vol.5, No.6, 1994
9. Washizu, Variational Methods In Elasticity And Plasticity, Third Edition, Pergamon Press Ltd. ,Oxford, 1982

INTEGRATED FINITE ELEMENT MODELLING OF SMART COMPOSITE STRUCTURES

Tamunoyala S. Koko, Irewole R. Orisamololu and Malcolm J. Smith

Martec Limited, 400-1888 Brunswick Street, Halifax, N.S., Canada B3J 3J8

SUMMARY: With the increasing use of smart materials and smart structural systems for space and other structural applications, there is an increasing need for advanced analysis and design tools for this class of structures. The study presented herein was undertaken to develop a computational tool which is suitable for the design/analysis of smart materials and structures with integrated control capabilities. In this paper an integrated finite element-control modelling capability for composite structures with piezoelectric sensors and actuators is presented. The method is based on a 20-node thermopiezoelectric finite element and the linear quadratic regulator (LQR) and independent modal space control (IMSC) algorithms. A design/analysis software, called SMARTCOM, has been developed based on the methodology. The efficacy of the method is demonstrated by analyzing several active and sensory structural systems with control capabilities. The results show that SMARTCOM can be efficiently used for the analysis and design of composite structures with piezoelectric sensors and actuators, with various loading conditions and control requirements.

KEYWORDS: thermopiezoelectricity, LQR, IMSC, vibration control, smart materials and structures, SMARTCOM

INTRODUCTION

Smart materials and smart structural systems are increasingly attracting attention from the research community because of their importance in current and future high performance structural applications. Examples of high performance structures requiring smart material and smart structures concepts include space antennas, precision optical systems and large solar arrays. The concepts have commonly been demonstrated for vibration and shape control of structural components such as beams and plates. These active structures have their own sensors, actuators and control capabilities in an integrated fashion. Piezoelectric materials have shown promise as sensor and actuators for many applications and control has been achieved by several methods, such as the independent modal space control (IMSC) and the linear quadratic regulator (LQR) methods [1,2].

In order to design or analyze smart structures for existing or new structural systems, it is essential to understand the behaviour of the integrated structure comprising of the structure, sensors, actuators and the control method. Because of the complex behaviour of these structural systems, the finite element method is considered to be an effective method for analyzing them. Some studies on finite element modelling of composite structures with piezoelectric sensors and actuators with control capabilities have been carried out in recent years [1,3-8]. However, in spite of these efforts there is still an increasing need for advanced analysis and design tools for this class of structures because most of the currently available

tools are based on specialized programs which are not suitable for many realistic problems, and are also not widely available. This study was undertaken to develop a computerized tool, within the framework of a general purpose finite element analysis software, which is suitable for the design/analysis of various types of smart materials/structures and control capabilities. The overall objectives of the study also include fuzzy and probabilistic based optimization and reliability assessment of the structure-integrated control systems.

In this paper an integrated finite element modelling capability for composite structures with surface bonded piezoceramic sensors and actuators is presented. The method, which is completely general, is based on a 20 node thermopiezoelectric finite element and control algorithms based on the linear quadratic regulator (LQR) and the independent modal space control (IMSC). The finite element solution strategy is derived from the general purpose finite element program called VAST [9] and the method has been implemented in the overall smart structures design/analysis software called SMARTCOM [10]. The theoretical foundations on which the method is based are described and some applications of the computational tool for the analysis/design of structures for vibration control are presented.

THEORETICAL FORMULATIONS

Finite Element Model

As stated above, the finite element method is used to model the smart structure comprising the structure, sensors and actuators. Each of these structural components of the smart structure is modelled by a twenty node layered composite brick element with thermopiezoelectric properties. The choice of this element was based on the fact that being a quadratic element it is more accurate than the eight noded brick element frequently used to model piezoelectric materials. In addition it does not require the use of incompatible displacement modes to improve bending response as does the eight noded brick, and it would require fewer elements to model the structure. The fact that fewer elements can be used to provide reasonably accurate results makes it suitable for design. However, it should be pointed out that this element is more computation intensive than the eight node solid element.

The most general formulation of the element, with mechanical, thermal and electrical effects considered, was developed and implemented in SMARTCOM. The element was developed as a layered composite element with orthotropic material properties. As SMARTCOM is expected to be a stand alone finite element design package, the formulation of the element was done so that problems with only mechanical, thermal, electrical, or any possible combinations of these effects with or without control can be analyzed. In the following subsections, a brief description of the thermopiezoelectric finite element formulation is provided. Details can be found in [5,6,11].

Finite Element Discretization and Shape Functions

The element has 20 nodes and the node numbering and shape functions are the same as the standard twenty noded brick element. The effects of the mechanical, electrical and thermal

(u, ϕ, θ , respectively) variables are included, such that there are five degrees-of-freedom at each element node. The element extended displacement field is given by $\bar{u}_i = \sum_{j=1}^{20} \delta_{ij} N_j$ where $\delta_{ij}^T = [u_1, u_2, u_3, \phi, \theta]$ are the displacements for $i=1,2,\dots,5$ at the nodal points $j=1,2,\dots,20$. N_j are the element shape functions which can be found in any standard text (eg Ref. 12).

Strain-Displacement Relations

The relationships between the extended strains $\bar{\epsilon}_s$ and the extended displacements are given by

$$\begin{aligned} \bar{\epsilon}_s^T &= [\epsilon_{11} \ \epsilon_{22} \ \epsilon_{33} \ 2\epsilon_{12} \ 2\epsilon_{23} \ 2\epsilon_{31} \ -E_1 \ -E_2 \ -E_3 \ -g_1 \ -g_2 \ -g_3] \\ &= [B_u \{\delta^u\}, B_\phi \{\delta^\phi\}, B_\theta \{\delta^\theta\}] \end{aligned} \quad (1)$$

where $B_u = [\mathcal{L}_u] \{\delta^u\}$, $B_\phi = [\mathcal{L}_\phi] \{\delta^\phi\}$ and $B_\theta = [\mathcal{L}_\theta] \{\delta^\theta\}$, $[\mathcal{L}_u], [\mathcal{L}_\phi], [\mathcal{L}_\theta]$ are linear operators [11,12], $\{\delta^u\}^T = [u_1, u_2, u_3]$, $\{\delta^\phi\} = \{\phi\}$, $\{\delta^\theta\} = \{\theta\}$, $\epsilon_{11}, \epsilon_{22}, \dots, \epsilon_{31}$ are the strain components, E_1, E_2, E_3 are the electric field components and g_1, g_2, g_3 are the thermal gradients in the three directions.

Constitutive Relations

The equations for quasistatic thermopiezoelectricity are:

$$\begin{aligned} \{\sigma\} &= [C] [\{\epsilon\} - \{\epsilon^0\}] - [e] \{E\} - \{\gamma\} \theta \\ \{D\} &= [e]^T [\{\epsilon\} - \{\epsilon^0\}] + [\epsilon] \{E\} + \{p\} \theta \\ \eta &= \gamma^T [\{\epsilon\} - \{\epsilon^0\}] + [p] \{E\} + \alpha_v \theta \\ \{h\} &= [k] \nabla \theta \\ \{E\} &= -\nabla \phi \end{aligned} \quad (2)$$

where $\{\sigma\}$ is the stress vector, $\{D\}$ is the electric displacement field, η the entropy per unit volume, $\{\epsilon\}$ is the strain vector, $\{\epsilon^0\}$ is the initial strain vector, $\{E\}$ is the electric field vector, $[C]$ the elasticity matrix, $[e]$ the permittivity matrix, $[k]$ the conductivity matrix, $[e]$ is the piezoelectric matrix, $\{\gamma\}$ is the vector of thermal expansion coefficients, $\{p\}$ is the vector of pyroelectric constants, $\{h\}$ the vector of heat flux, ∇ is the gradient operator, $\alpha_v = \rho C_v \theta_o^{-1}$, ρ is the density, C_v is the specific heat at constant volume, θ_o is the reference temperature, θ the temperature rise from reference temperature and ϕ is the electric potential (voltage).

Equations of Motion

The finite element equations are obtained by variational principles. Three energy functionals corresponding to the mechanical displacement, electric and temperature fields are first derived and variations with respect to the independent displacement, electric and temperature variables are then taken to obtain the global system equations as [5,6,11]:

$$\begin{bmatrix} M_{uu} & 0 & 0 \\ 0 & 0 & 0 \\ 0 & 0 & 0 \end{bmatrix} \begin{Bmatrix} \ddot{U} \\ \ddot{\phi} \\ \ddot{\theta} \end{Bmatrix} + \begin{bmatrix} C_{uu} & 0 & 0 \\ 0 & 0 & 0 \\ \theta_0 K_{\theta u} & -\theta_0 K_{\theta \phi} & H_{\theta \theta} \end{bmatrix} \begin{Bmatrix} \dot{U} \\ \dot{\phi} \\ \dot{\theta} \end{Bmatrix} + \begin{bmatrix} K_{uu} & K_{u\phi} & -K_{u\theta} \\ K_{\phi u} & -K_{\phi\phi} & K_{\phi\theta} \\ 0 & 0 & K_{\theta\theta} \end{bmatrix} \begin{Bmatrix} U \\ \phi \\ \theta \end{Bmatrix} = \begin{Bmatrix} F_u \\ F_\phi \\ F_\theta \end{Bmatrix} \quad (3)$$

where M_{uu} is the mass matrix, $K_{uu}, K_{\phi\phi}, K_{\theta\theta}$ are the mechanical, electrical and thermal stiffness

matrices, $K_{u\phi}$, $K_{u\theta}$, $K_{\phi\theta}$ are the coupling matrices, $H_{\theta\theta}$ the thermal rate stiffness matrix, C_{uu} is the damping matrix, and F_u , F_ϕ , F_θ are the mechanical, electrical and thermal load vectors, respectively. The detailed expressions for the element matrices are available in [11]. The matrix coefficients are obtained by Gaussian integration in each material layer [11].

Solution of Finite Element Equations of Motion

In the finite element solution procedure, the thermal, electrical and mechanical displacements are calculated separately to improve the computational efficiency. The thermal field is first obtained by solving the third of Equations (3) using a forward difference time integration scheme. Then the displacement and electrical potential equations are decoupled using Guyan condensation to obtain a reduced system of equations

$$M_{uu} \ddot{U} + D_{uu} \dot{U} + K^* U = F_u + K_{u\phi} K_{\phi\phi}^{-1} F_\phi + (K_{u\theta} - K_{u\phi} K_{\phi\phi}^{-1} K_{\phi\theta}) \theta \quad (4)$$

from which the displacement field U is obtained using the Newmark time integration scheme, where

$$K^* + K_{uu} + K_{u\phi} K_{\phi\phi}^{-1} K_{\phi u} \quad (5)$$

The electrical potential is then obtained from the second of Equations (3) as

$$\phi = K_{\phi\phi}^{-1} (K_{\phi u} U + K_{\phi\theta} \theta - F_\phi) \quad (6)$$

A distinction is made between the electric potential at the sensors and that at the actuators. The electric potential at the sensors is amplified and fed back to the actuators to control the structure as described below.

Control Algorithms

For control problems, the electrical force F_ϕ , assumed to be applied at the actuators, is taken as the control as feedback force F_f given by

$$F_f = [K_{u\phi}^A] [K_{\phi\phi}^A]^{-1} F_\phi \quad (7)$$

and the control law is implemented on the electrical charges as

$$F_\phi = -G \phi^s \quad (8)$$

where the superscripts A and S denote actuators and sensor quantities, respectively, and G is a gain matrix. The control problem effectively reduces to determining the gain matrix and substituting equations (7) and (8) into equation (4) to obtain the closed-loop responses. Among the numerous methods available for calculating gain matrix [2], the linear quadratic regulator (LQR) is used in this study because of its wide use. However, options for the use simple control algorithms such as the independent modal space control (IMSC) and the modified independent modal space control (MIMSC) are provided to facilitate optimization studies. In general, these control laws provide various means of minimizing the performance index

$$J = \frac{1}{2} \int_0^\infty [Z^T Q Z + F_f^T R F_f] dt \quad (9)$$

subject to

$$\dot{Z}(t) = A Z(t) + B F_f \quad (10)$$

where $\{Z(t)\}^T = [U(t) \dot{U}(t)]$ and A and B are the system matrices, Q and R are weighting factors

which are related to the control effectiveness and control energy consumption, respectively [2,11].

NUMERICAL EXAMPLES

Several numerical example problems have been used to verify various aspects of the theoretical formulations, as detailed in Reference [11]. The results obtained generally compared well with other published results [11]. In this paper, simple examples on how the computational tool SMARTCOM can be used for the design of actively controlled structure are presented. The problem configuration is shown in Figure 1. Two layers of polyvinylidene fluoride (PVDF) films are bonded to the top and bottom of an aluminum beam. The PVDF films are 0.001m thick and the aluminium beam is 0.005 m thick and 0.005m wide. Two lengths of the beam, 0.6m and 0.06m, respectively, were considered to study the influence of beam flexibility. The material properties are shown in Table 1. The beam is subjected to a point step load of 0.1N at the free end. The hybrid structure is modelled by a total of nine elements - three for each of the PVDF layers and three for the aluminium beam.

A natural frequency analysis is first carried out and the first 10 natural frequencies for the two beam length cases are shown in Table 2. The effects of the piezoelectric material layers are accounted for in the natural frequency calculations. As shown in the table, the frequencies of the beam with $l=0.06\text{m}$ are much higher than those for the beam with $l=0.6\text{m}$, since the former is much stiffer. Based on the frequencies, time steps equal to or less than 0.005 sec and 0.00005 sec were used for beams with $l=0.6\text{m}$ and $l=0.06\text{m}$, respectively, for the transient analysis. The transient displacement and voltage solutions for the two beam cases are obtained using the modal superposition method. The gain matrix and for the closed loop solution is obtained by the IMSC method.

For the case of the beam with length of 0.6 m , the modal weighting factor R_i was selected as 10 for each of the 10 modes used in the analysis. The open and closed loop displacement solutions are shown in Figure 2 and the corresponding voltages are shown in Figure 3. Control was achieved in about 0.12 seconds. For the case of the beam with length of 0.06 m the weighting factor R_i was also set to 10 for each mode and the open and closed loop displacement solutions are shown in Figure 4. As shown in the figure, control could not be obtained after 3 milliseconds. In fact, the trend of the closed loop solution indicates that it would take a very long time for the solution to stabilize at the mean displacement or voltage. This shows that the value of $R_i = 10$ was not efficient for this structure. Consequently, the value of the weighting factor R_i was changed to $R_i=100$ for each mode. This corresponds to increasing the effort or energy to control the structure. The new displacement and voltage solutions are shown in Figures 5 and 6, respectively. Now control is achieved in about 1.5 milliseconds.

CONCLUSIONS

This paper has presented an integrated finite element control capability for design/analysis of smart composite structures. The structure, sensors, and actuators are modelled by 20-node thermopiezoelectric elements and control is achieved by the IMSC and LQR algorithms. A computational software called SMARTCOM has been developed based on the method. Numerical example problems have been used to verify the software tool and the results obtained show that SMARTCOM can be and effectively used to model actively controlled structures.

ACKNOWLEDGEMENTS

Part of this work was done under subcontract to Expert System Applications, Inc., Solon, Ohio on a NASA funded contract No. NAS3-27816. The funding and support provided by Martec Limited are also gratefully acknowledged.

REFERENCES

1. Rao, S.S. and Sunar, M. "Piezoelectricity and its Use in the Disturbance Sensing and Control of Flexible Structures: A Survey", *Applied Mechanics Review*, Vol. 47, No. 4, April 1994.
2. Rao, S.S. and Pan, T.S., "Modelling, Control, and Design of Flexible Structures: A Survey", *Applied Mechanics Review*, Vol. 43, No. 5 Part 1, May 1990.
3. Kim, J., Varadan, V.V., Varadan, V.K. and Bao X.Q., "Finite Element Modelling of Smart Cantilever Plate and Comparison with Experiments", *Smart Materials and Structures*, Vol. 5, pp. 165-170, 1996
4. Hwang, W-S. and Park, H.C., "Finite Element Modelling of Piezoelectric Sensors and Actuators," *AIAA Journal*, Vol. 31, No. 5, pp. 930-937 (1993).
5. Rao, S.S. and Sunar, M., "Analysis of Distributed Thermopiezoelectric Sensors and Actuators in Advanced Intelligent Structures," *AIAA Journal*, Vol. 31, No. 7, pp. 1280-1286 (1993).
6. Tzou, H.S. and Ye, R., "Piezothermoelasticity and Precision Control of Piezoelectric Systems: Theory and Finite Element Analysis," *ASME Transactions, Journal of Vibration and Acoustics*, Vol. 116, pp. 489-485 (1994).
7. Ha, S.K., Keilers, C. and Chang, F.K., "Finite Element Analysis of Composite Structures Containing Distributed Piezoceramic Sensors and Actuators", *AIAA Journal*, Vol. 30, No. 3, pp. 772-780, March (1992).
8. Saravanos, D.A., Heyliger, P.R. and Hopkins, D.H., "Layerwise Mechanics and Finite Element for the Dynamic Analysis of Piezoelectric Composite Plates," *International Journal of Solids and Structures*, in press, December (1995).
9. Vibration and Strength Analysis Program (VAST): User's Manual Version 7.1, Martec Limited, Halifax, N.S., Canada, October 1995
10. Koko, T.S. and Orisamololu, I.R. "User's Manual for Program SMARTCOM for Analysis of Smart Composite Structures Version 1.0", Martec Limited, Halifax, N.S., Canada, February 1996.
11. Koko, T.S., Orisamololu, I.R. and Smith, M.J., "Fuzzy and Probabilistic Design Tool for Actively Controlled Composite Structures, Martec Report No: TR-96-14, Halifax, NS, Canada, February 1996.
12. Bathe, K.J., *Finite Element Procedures in Engineering Analysis*, Prentice-Hall, Inc. Englewood Cliffs, NJ, 1982.

Table 1. Material Properties for Sensory/Active Beams

Property	PVDF	Aluminium
Elastic Properties		
E ₁₁ (GPa)	2.0	68.9
E ₂₂ (GPa)	2.0	68.9
E ₃₃ (GPa)	2.0	68.9
G ₂₃ (GPa)	0.775	27.6
G ₁₃ (GPa)	0.775	27.6
G ₁₂ (GPa)	0.775	27.6
v ₁₂	0.29	0.25
v ₁₃	0.29	0.25
v ₂₃	0.29	0.25
Piezoelectric Stress Constants (C/m ²)		
e ₃₁	0.046	
e ₃₂	0.046	
Electric Permittivity (10 ⁻¹² F/m)		
ε ₁₁	106.2	0
ε ₂₂	106.2	0
ε ₃₃	106.2	0
Mass Density ρ(kg/m ³)	1800	2769

Table 2 Natural Frequencies of Beams with PVDF Layers

Mode No.	Frequencies (Hz)	
	Case 1: ℓ = 0.6m	Case 2: ℓ=0.06m
1	12.51	1249.0
2	12.52	1249.1
3	79.75	7717.4
4	79.76	7717.6
5	239.94	13605.0
6	239.96	22031.0
7	628.02	22196.0
8	628.44	22369.0
9	1360.5	41117.0
10	1879.9	51530.0

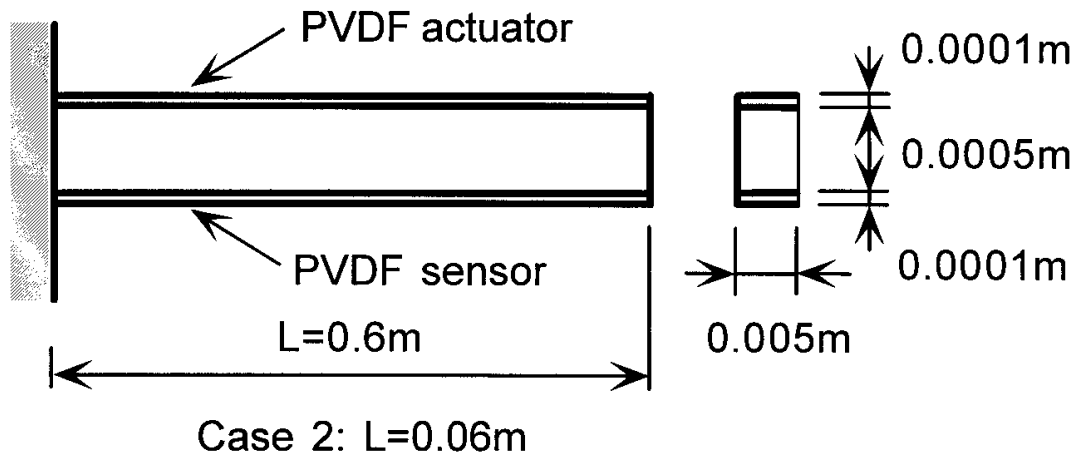


Figure 1: Schematics of Beam with Piezoelectric Sensor and Actuator

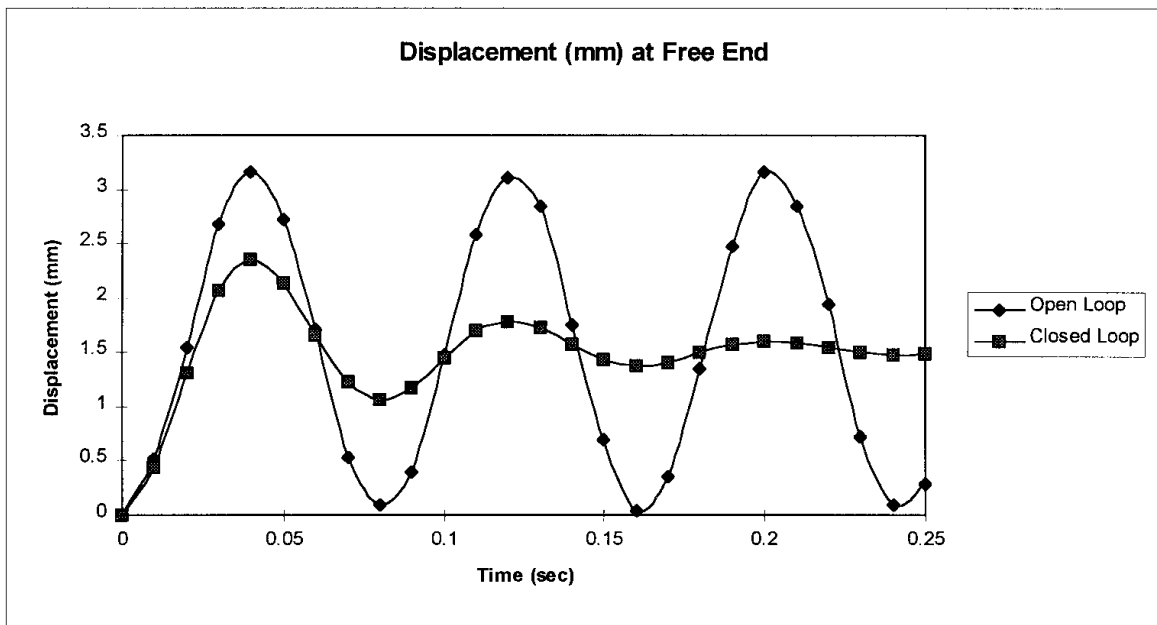


Figure 2: Open and Closed Loop Displacement at Free End of Beam ($\ell = 0.6\text{ m}$)

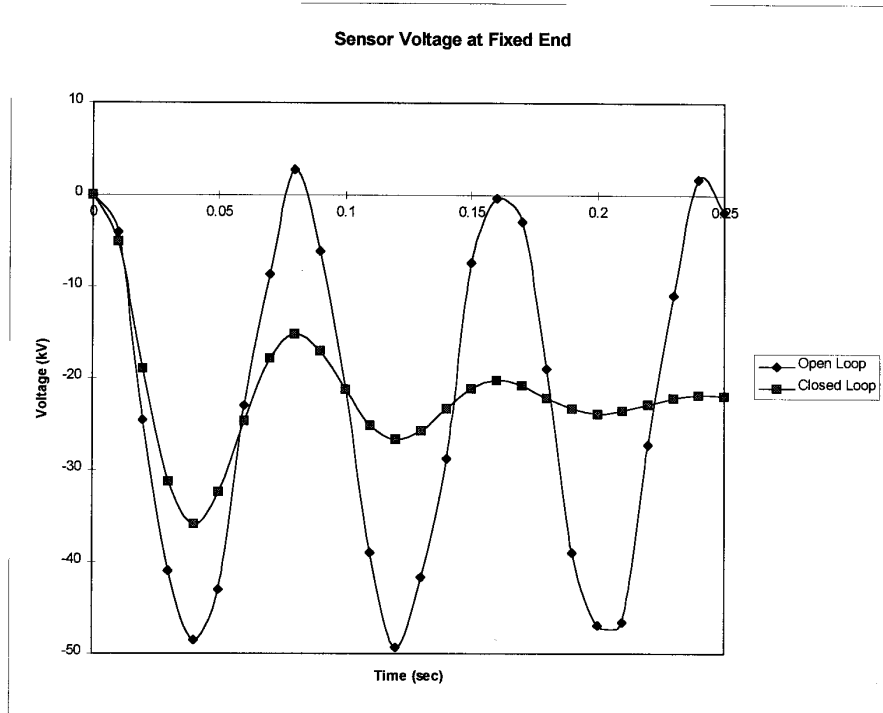


Figure 3: Open and Closed Loop Voltages at Fixed End of Beam ($\ell = 0.6 \text{ m}$)

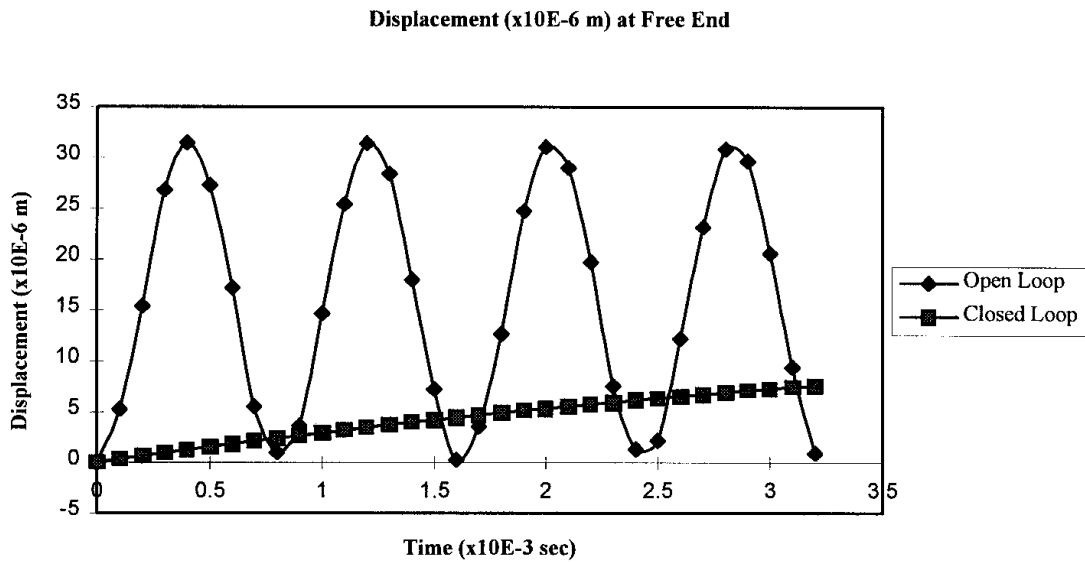


Figure 4: Open and Closed Loop Displacements at Free End of Beam ($\ell = 0.06 \text{ m}$, $R_i = 10$)

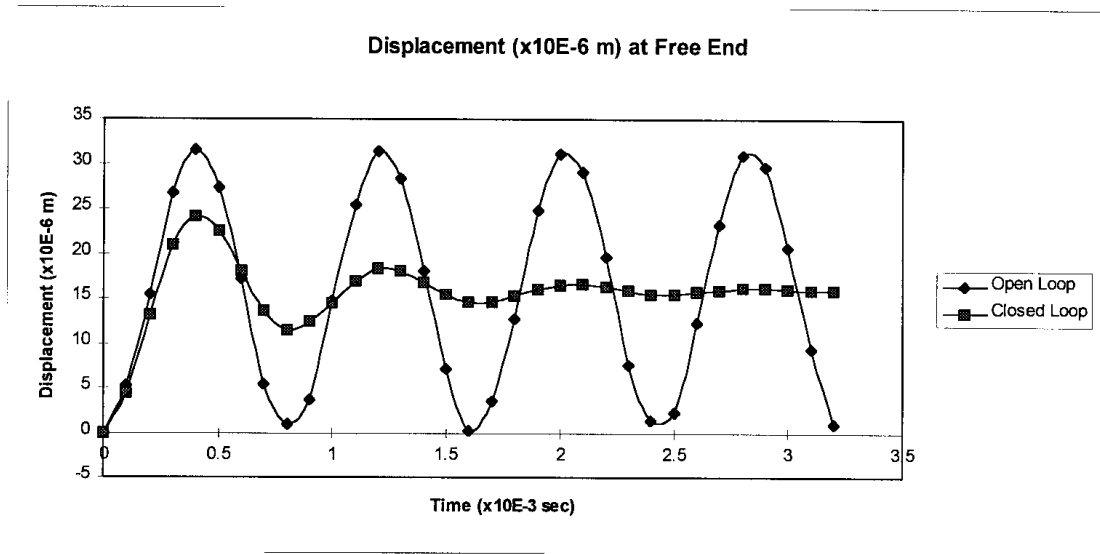


Figure 5: Open and Closed Loop Displacements at Free End of Beam ($\ell=0.06$ m, $R_i = 100$)

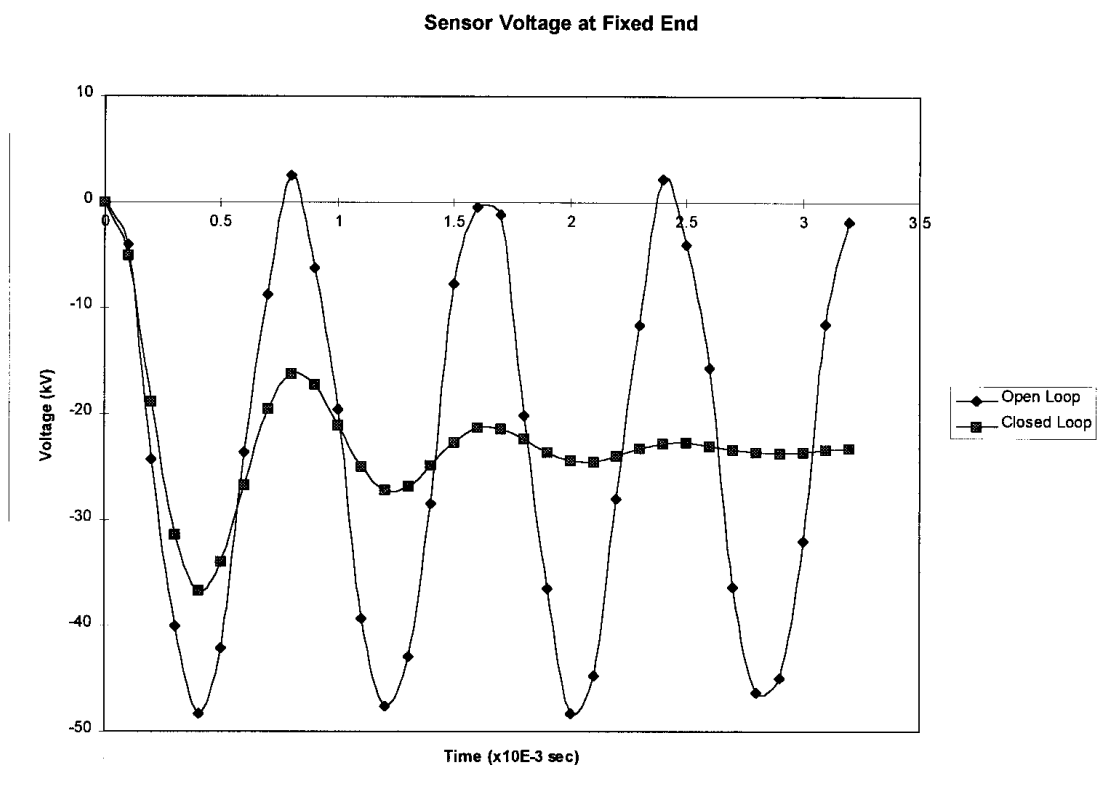


Figure 6: Open and Closed Loop Voltages at Fixed End of Beam ($\ell=0.06$ m, $R_i = 100$)

ACTIVE SHAPE CONTROL OF SHAPE MEMORY ALLOY COMPOSITE STRUCTURES

M.W.M. Van der Wijst, J.Zuidervaart, T. Peijs, and P.J.G. Schreurs

*Eindhoven University of Technology, Centre for Polymers and Composites,
P.O. Box 513, 5600 MB Eindhoven, The Netherlands*

SUMMARY: In this paper the shape control of a flexible composite beam containing embedded Nitinol (a Shape Memory Alloy) wire actuators is investigated both numerically and experimentally. The temperature of an SMA wire cannot be prescribed directly, but has to be changed by an electric current through the wires. A Finite Element model of the beam is presented, that permits calculation of the temperature distribution in the entire SMA composite beam, as well as the deformation of the beam caused by the Shape Memory response to this temperature field. An important part of the FE model is a constitutive model, that describes the stress-strain-temperature behaviour, including hysteresis, of Nitinol wires. Shape control of the beam is established by having a point on the beam follow a desired displacement. This is achieved with a feedback control law for the electric current. The control strategy is examined both with the FE model and in experiments for various trajectories.

KEYWORDS: shape control, shape memory alloy, nitinol

INTRODUCTION

In recent years attention is shifting to the development of materials, of which the mechanical behaviour can be changed during service to meet certain functional or structural requirements. To control actively the properties of such material, actuators must be an integral part, thus forming a composite material. Shape Memory Alloys (SMA's) are an important candidate as such built-in actuators. SMA's have the drawback that they are effective only at low frequencies, but they are capable of causing large deformations. Their mechanical properties can be changed by altering their temperature. By raising the temperature of an unconstrained, previously deformed SMA wire, its length can be reduced. Strains of about 8% can be recovered this way. If the wire is clamped at both ends, a large force can be exerted. This behaviour is due to a change of the micro structure, more specifically a phase transformation [1-3]. Because of the specific properties of SMA's, increasing interest is paid to change the shape of flexible structures employing SMA wires [4, 5]. Other applications include active damping of vibrations [6, 7], and light weight actuators in robotic devices [8-11].

Active control of the temperature of SMA actuators is easiest achieved by means of resistive heating. Although (mainly feedback) control strategies have been applied for active damping of vibrations [12-15], and for position control in robotics [16-19], few attempts have been undertaken to actively control the shape of composite structures. The majority of the investigations on shape control of SMA composite materials are restricted to recording the shape response as a result of electric current. However, to understand in more detail the mechanical and thermal behaviour of SMA composites, a Finite Element model of the entire material has been developed in this study. This model includes a constitutive model of Nitinol wires, the SMA used in this study, relating stress, strain and temperature, and the energy balance of the matrix material and the wires.

The FE model is used to simulate shape control of SMA composites. Shape control is established by controlling actively the electric current through the Nitinol wires. A feedback control law is applied to determine the electric current. Experimental evaluation of the control strategy has also been performed.

The content of this paper is as follows. First a constitutive model of Nitinol wires is presented, see also [20]. Next an SMA composite beam is described, followed by a FEM model of this beam and numerical results. Finally the applied control strategy is introduced, and results, both in simulations and experiments, are presented.

DESCRIPTION AND MODELING OF THE SMA BEHAVIOUR

The behaviour of Nitinol is due to a change of crystal structure from austenite to martensite and vice versa. When an austenitic Nitinol wire is subjected to a number of tensile test cycles at a relatively high temperature, tensile curves like those in Fig.(1) are obtained. The deformation of the wire is described with the Green-Lagrange strain $e = (\lambda^2 - 1)/2$, where $\lambda = l/l_{ref}$: l is the current length of the wire and l_{ref} the reference length of the austenitic, unloaded wire at the reference temperature ϑ_{ref} . The stress in the wire is represented by the 2nd Piola-Kirchhoff stress $p = F/(\lambda A_{ref})$, where F is the force in the wire, and A_{ref} is the reference cross-sectional area. For modelling purposes the curved lines in Fig.(1) are approximated by straight lines. This is not an essential simplification of the real behaviour, but makes the model less complicated.

The mathematical description of the SMA behaviour in terms of the stress p and the strain e is rather complicated. It can be simplified by using alternative variables. One of these variables is the martensite fraction m , being the relative amount of martensite. The domain of this variable is $[0,1]$, where $m = 0$ if the material is purely austenitic and $m = 1$ for a completely martensitic structure. The second alternative variable ξ is such that the rectangle with vertices 1, 4, 6 and 9 in the (e,p) -plane is mapped on a unit square in the (m,ξ) -plane (see Fig.1).

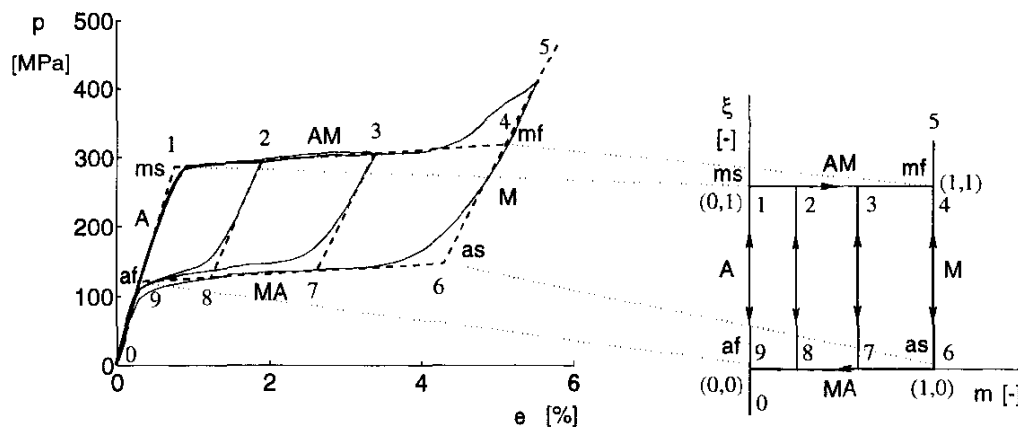


Figure 1: Experimental and modelled tensile curves of a Nitinol wire

Starting in point 0 ($m = 0, \xi < 0$), first the austenite deforms elastically. When the Martensite Start transition stress p_{ms} is reached (point 1, $m = 0, \xi = 1$), martensite starts to form. Upon further loading $\xi = 0, \dot{m} > 0$ and strain increases considerably. The Austenite to Martensite (AM) transformation ends when the stress equals p_{mf} at point 4 ($m = 1, \xi = 1$). Further loading results in elastic deformation of the martensite ($m = 1, \xi > 0$).

Unloading from point 5 does not yield the same curve as that followed during loading. The reverse MA transformation does not start until the stress has dropped to p_{as} (point 6, $m = 1$,

$\xi = 0$), which is significantly lower than p_{mf} . During the MA transformation, which ends in point 9 ($m = 0, \xi = 0$) the martensite fraction decreases from 1 to 0. Continued unloading from point 9 results in elastic deformation of the austenite along the line through points 9 and 0 ($m = 0, \dot{\xi} < 0$). Hence, a closed hysteresis loop occurs in such a loading cycle.

If unloading is started before the austenite has been transformed entirely into martensite ($0 < m < 1, \xi = 1$), e.g. in point 2 or 3, the material is unloaded elastically ($\dot{m} = 0, \dot{\xi} < 0$). If reloading is resumed before the lower MA side ($\xi = 0$) is reached, the same elastic path is followed ($\dot{m} = 0, \dot{\xi} > 0$) until the upper AM side ($\xi = 1$) is encountered. Continued loading then involves continued AM transformation. Within the loop ($0 < \xi < 1$) the martensite fraction cannot change, whereas m can increase only on the AM side ($\xi = 1$), and decrease only on the MA side ($\xi = 0$).

The relation between the strain e and the stress p on the one hand and the alternative variables m and ξ on the other is given by

$$e = e_{af} + \xi(e_{ms} - e_{af}) + m(e_{us} - e_{af}) + \xi m(e_{mf} + e_{af} - e_{ms} - e_{as}) \quad (1)$$

$$p = p_{af} + \xi(p_{ms} - p_{af}) + m(p_{as} - p_{af}) + \xi m(p_{mf} + p_{af} - p_{ms} - p_{as}) \quad (2)$$

The transition strains e_{ms} through e_{af} and transition stresses p_{ms} through p_{af} strongly depend on the temperature ϑ . It is assumed that this dependence is linear. Hence if the value of the parameters is known for two different temperatures ϑ_1 and ϑ_2 then their value for any relevant temperature ϑ can be determined. For example, the martensite start stress p_{ms} at temperature ϑ follows from

$$p_{ms}(\vartheta) = p_{ms}(\vartheta_1) + \frac{\vartheta - \vartheta_1}{\vartheta_2 - \vartheta_1} \{p_{ms}(\vartheta_2) - p_{ms}(\vartheta_1)\} \quad (3)$$

Analogous relations hold for the other transition parameters.

Fig.(2) illustrates the constitutive model for a Nitinol wire in the (e, p, ϑ) -space (left), and in the (m, ξ, ϑ) -space (right). Changes of state within the hysteresis loop are restricted to planes of constant martensite fraction. The shaded planes in Fig.(2) represent two planes of this kind. Table (1) contains experimentally obtained values of the transition parameters.

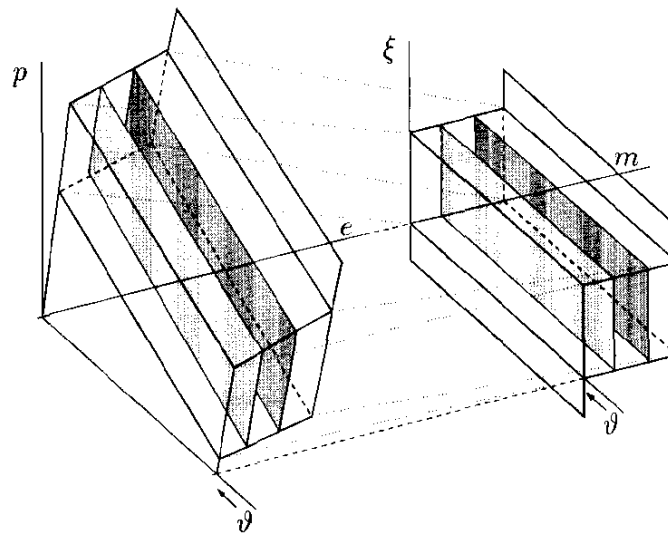


Figure 2: Three-dimensional representation of all possible (e, p, ϑ) and (m, ξ, ϑ) states

Table 1: Constitutive parameters

ϑ_1, ϑ_2 (°C)	transition strains				transition stresses			
	ϵ_{ms}	ϵ_{mf}	ϵ_{as}	ϵ_{af}	p_{ms}	p_{mf}	p_{as}	p_{af}
	(%)				(MPa)			
50	1.08	5.43	4.33	0.39	234	369	218	95
70	1.62	6.45	4.70	0.09	369	561	369	234

SYSTEM DESCRIPTION

A schematic drawing of the SMA composite structure used in this study is shown in Fig.(3). The flexible beam consists of two pairs of Nitinol wires embedded in a Polypropylene (PP) matrix. The beam is 166 mm long, 8.5 mm wide and 1.6 mm thick. The Nitinol wires have a rectangular cross-section of $0.1 \times 0.6 \text{ mm}^2$, and are positioned approximately 0.1 mm below the surface of the beam. Before embedding the Nitinol wires, they were stretched to a strain of 2.2%. According

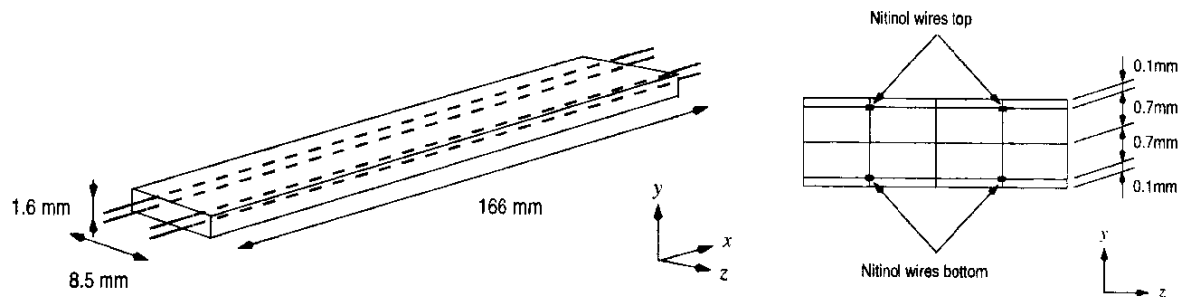


Figure 3: Left: flexible SMA composite beam. Right: cross-section

to the constitutive model this strain corresponds with a martensite fraction of 0.5. The upper two wires are connected in series electrically, as well as the lower two wires. The wires are heated by means of an electric current I . When for example the upper wires are heated, they try to return to their original, smaller, length. However, because the wires are embedded in the matrix material, they are restrained from contracting without a considerable increase of force in the wires. Since the wires lie at a distance (0.7mm) from the neutral axis, a bending moment is exerted on the beam, which causes the beam to bend upwards. Because of this, the wires at the lower side of the beam are stretched, yielding another resisting moment. When the wires at the lower side are heated, the beam bends downwards. Thus, by supplying the wires with an appropriate current, the shape of the beam can be controlled actively. The experimental setup that was used is shown in Fig.(4). The flexible beam is clamped on one side. An optical position sensor is placed at a distance of 100mm. The sensor measures the displacement q of the beam at that location. The measured displacement is converted to a digital value by a 12 bits AD converter. An AT 386 PC equipped with a PCL718 data acquisition card calculates the input, i.e. the electric current I . The obtained value for I is converted to an analog signal, and transmitted to a servo amplifier. The maximum allowed current is 1.0 A.

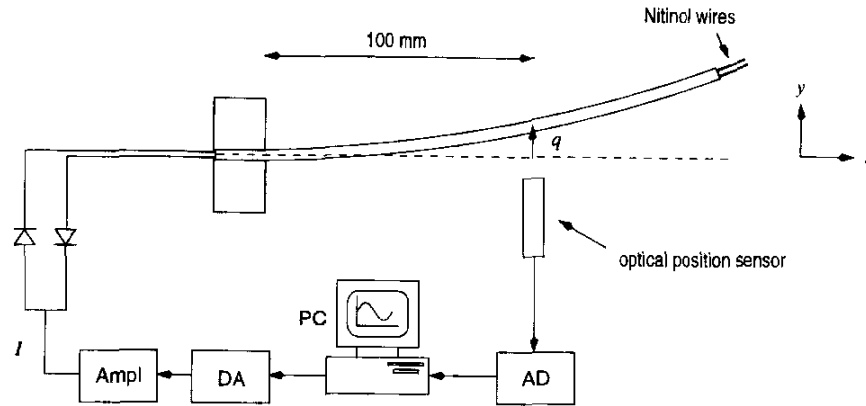


Figure 4: Experimental setup

FINITE ELEMENT MODEL

To be able to analyze both the thermal and mechanical response of the flexible beam to an electric current, a Finite Element model was developed in the FEM package MARC. The matrix material is modelled with $5 \times 4 \times 4$ three-dimensional quadratic isoparametric elements with 20 nodes. All Nitinol wires are modelled with five one-dimensional quadratic truss elements with three nodes. The unknown variables are the displacement field $\underline{u}(\underline{x}, t)$ and the temperature field $\vartheta(\underline{x}, t)$. In every material point the balance laws of force and energy must hold:

$$\vec{\nabla} \cdot \boldsymbol{\sigma} = \vec{0} \qquad \rho c_p \dot{\vartheta} - k \nabla^2 \vartheta = r \qquad (4)$$

where $\boldsymbol{\sigma}$ is the Cauchy stress tensor, ρ the material density, c_p the specific heat, k the thermal conductivity, and r the generated heat per unit volume. The heat generated in the Nitinol wires equals $r = \rho_{ei} i^2$, with ρ_{ei} being the electrical resistivity of Nitinol, and i is the electric current per unit area. No heat is produced inside the matrix. Heat exchange with the surrounding air is assumed to be a purely convective process, with an average heat transfer coefficient of $54 \text{ W.m}^{-2}.\text{K}^{-1}$. Table (2) lists the values of all material parameters that were used for the simulations. The stress in the Nitinol wires is assumed to consist of only one axial component. This stress depends on the axial strain in the wire, and therefore on the displacement field, and the

Table 2: Material parameters

material parameter	symbol	value		unit
		PP	Nitinol	
Young's modulus	E	1.5		GPa
Poisson ratio	ν	0.3		-
mass density	ρ	900	6700	kg.m^{-3}
specific heat	c_p	1700	530	$\text{J.kg}^{-1}.\text{K}^{-1}$
thermal conductivity	k	0.24	56	$\text{W.m}^{-1}.\text{K}^{-1}$
electric resistivity	ρ_{ei}		1.5×10^{-6}	$\Omega.\text{m}$

temperature in the wire through the constitutive model discussed earlier. The material behaviour of the PP matrix is modelled as linear elastic and isotropic. The above set of partial differential equations cannot be solved analytically. Therefore the displacement and temperature field, as well as time are discretized, and a solution is obtained in an incremental-iterative way using a Newton-Raphson procedure. The set of linear FEM equations to be solved for the iterative changes $\delta\vartheta$ and δu in iteration step i of increment j read:

$$\left[\frac{C}{\Delta t} - \Lambda \right] \delta\vartheta = r_j + \frac{C}{\Delta t} \vartheta_{j-1} \quad (5)$$

$$\underline{K}_{i-1} \delta u = f_{ext,j} - f_{int,i-1}(u_{i-1}, \vartheta_j) \quad (6)$$

where C is the specific heat matrix, Δt is the time increment, Λ is the conductivity matrix, and r_j represents the nodal generated heat, which is only present in nodes which are part of Nitinol elements. Matrix K is the global stiffness matrix, f_{ext} are external loads, and $f_{int,i-1}$ are the internal forces calculated in the previous iteration. The internal forces in Nitinol elements are, because of the Shape Memory behaviour, strongly dependent both on the deformation and on the temperature. In each increment first the heat generated by the supplied electric current is determined, after which the temperature distribution is determined with Eq.(5). Then the displacement field is calculated with Eq.(6) using these temperatures.

The open loop response of the flexible beam was examined, i.e. the temperature field and the shape change as a result of a prescribed current. During ten seconds an electric current of 0.7 A

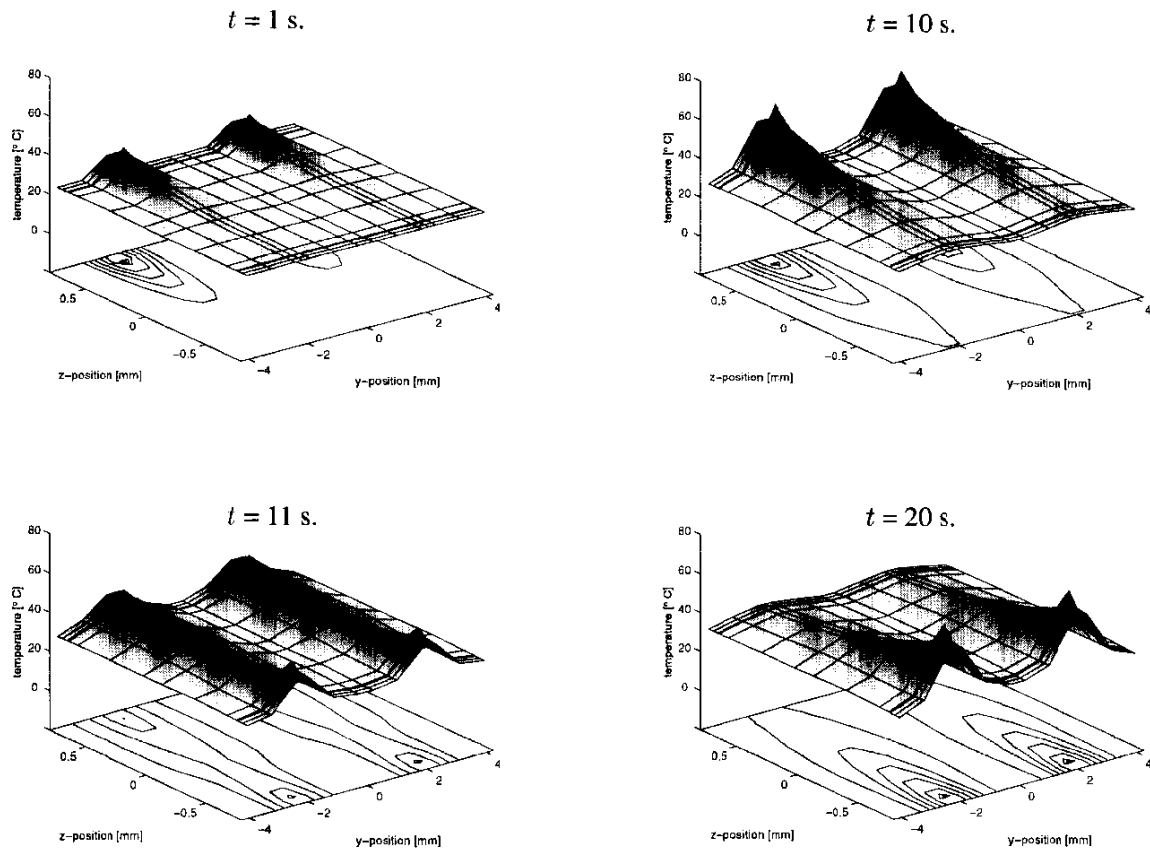


Figure 5: Temperature distribution in cross-section

was supplied to the upper wires. After this period the current was supplied to the lower wires also during ten seconds. Fig.(5) shows the temperature distribution in the cross section of the strip at the sensor location at four consecutive moments. During the first ten seconds the temperature of the two upper wires rises strongly. The position of the wires is easily spotted by the two peaks. The rather low conductivity of PP has two consequences. First, large temperature gradients exist in the matrix material, and secondly, the temperature in the wires is considerably higher than in the adjacent material. After ten seconds no more heat is generated in the upper wires, causing their temperature to drop. At the same time the temperature of the lower wires increases, because of the supplied current. The lower two graphs of Fig.(5) illustrate this process.

Because of the temperature rise of the upper wires during the first ten seconds, the Shape Memory effect is activated, and the stress in these wires increases with temperature. Because of the offset distance of the wires, a moment is generated, causing the beam to bend upwards. During the second stage the stress in the lower wires will exceed the stress in the upper wires. The result is an opposite bending of the beam. These findings are depicted in Fig.(6). The temperature and stress in the middle of a wire on top, and a wire at the bottom, are plotted against time. The bottom left graph shows the displacement of the beam at the sensor location, see Fig.(4).

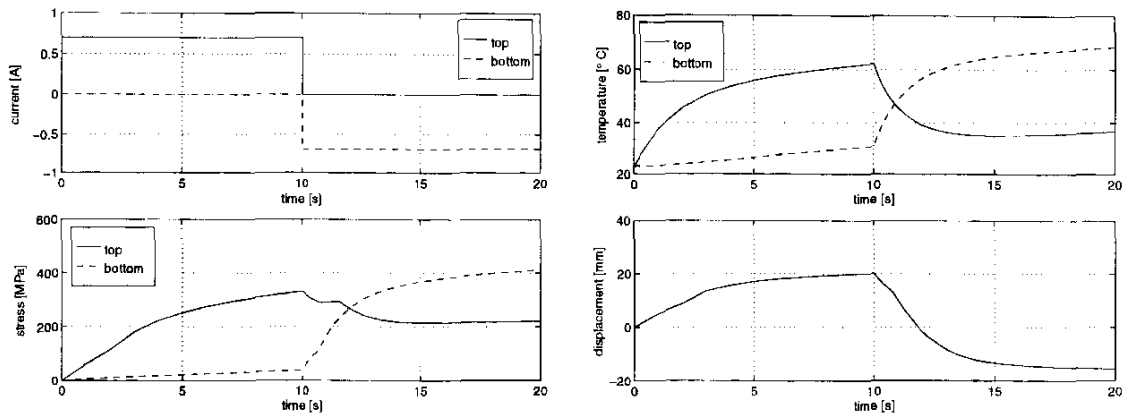


Figure 6: Calculated response of SMA composite

ACTIVE SHAPE CONTROL

Control strategy

In the previous section the electric current was given a fixed, predefined value. However, the objective is to control the shape of the beam by changing the electric current through the wires during service. The control objective is to force the position of the beam at the sensor location $q = q(t)$ to follow a desired path $q_d = q_d(t)$. This must be achieved by prescribing the electric current through the wires. A Proportional-Integral feedback control law [21] is used to calculate the current:

$$I = K_p(q_d - q) + K_i \int_0^t (q_d - q) dt \quad (7)$$

The constants K_p and K_i must be tuned such, that satisfactory tracking performance is obtained, without the system going unstable. The values for K_p and K_i used both in the simulations and

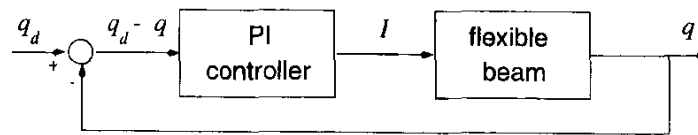


Figure 7: Feedback control scheme

experiments are 1.0 A/mm and 5.0 A/m.s respectively. When the current is positive the upper wires are heated, the lower wires when the current is negative. In practice this is achieved by a pair of diodes. Fig.(7) is a block diagram of this control strategy. The proposed control strategy was examined both numerically and experimentally. The results for various trajectories $q_d(t)$ are discussed below.

Numerical results

The response of the controlled SMA composite was examined for three different periodic trajectories. In the first case the desired position of the beam at the sensor location varies linearly, in the second case it is sinus shaped, and finally a block wave should be tracked. The period time of all trajectories is 2 s, while the amplitude is 1 mm. The total time span of 10 s is divided in time increments of 0.02 s. After each increment the current to be supplied in the next step is determined using the calculated displacement, and the desired displacement at that moment. The three graphs on the left of Fig.(8) show the desired and realized displacements. The SMA

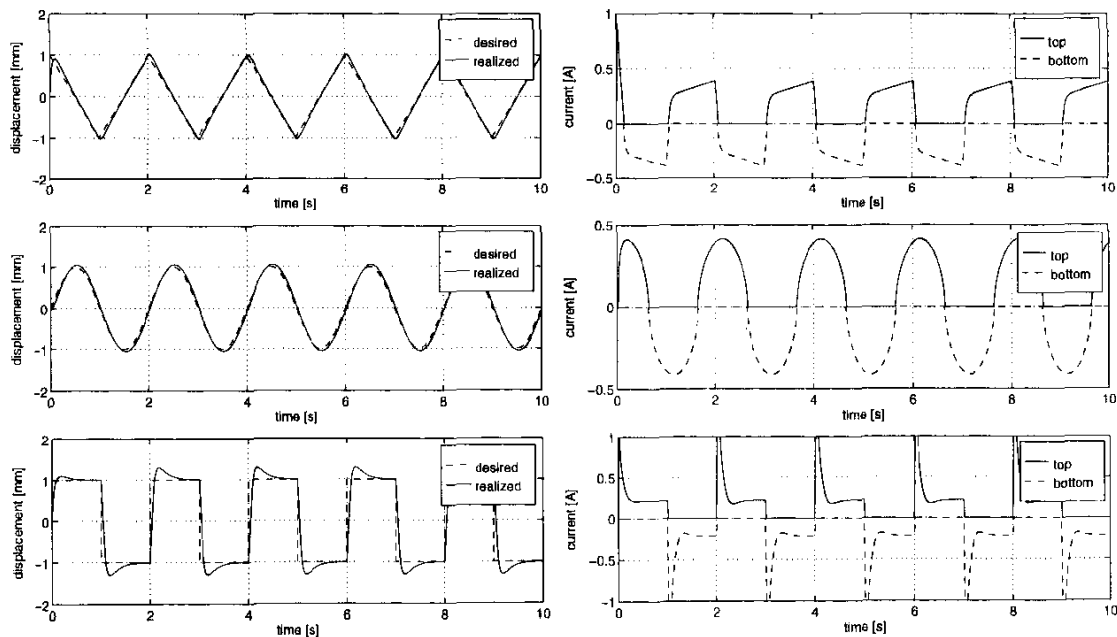


Figure 8: Calculated results for several trajectories

composite beam is able to track all trajectories rather well. The largest tracking errors occur at the extreme points of the desired trajectories. This is mainly caused by the fact that at these points the hysteresis of the Nitinol wires must be crossed. Within the hysteresis both stress and strain change very little with temperature, which slows down the response of the beam. The

currents that are calculated with control law Eq.(7) are plotted in the graphs on the right. In case of a positive current, the two Nitinol wires on top of the beam were heated; a negative current means heating of the wires at the lower side. The peak values occurring for the block wave are the result of the proportional part of control law Eq.(7). At the concerning moments the tracking error becomes large, resulting in a large electric current.

Experimental results

The tracking performance was also investigated experimentally. The results for periodic trajectories with a period time of 5 s are shown in Fig.(9). Again displacements are shown on the left, and the corresponding currents on the right. The same trends as in the simulations are observed. The experimentally observed tracking performance is also quite good. The fact that the electric currents supplied to the lower wires are somewhat higher than the current through the upper wires is probably caused by a difference in offset distance to the neutral axis of the wires: a smaller offset distance requires a higher stress to obtain the same bending moment, and thus a higher temperature.

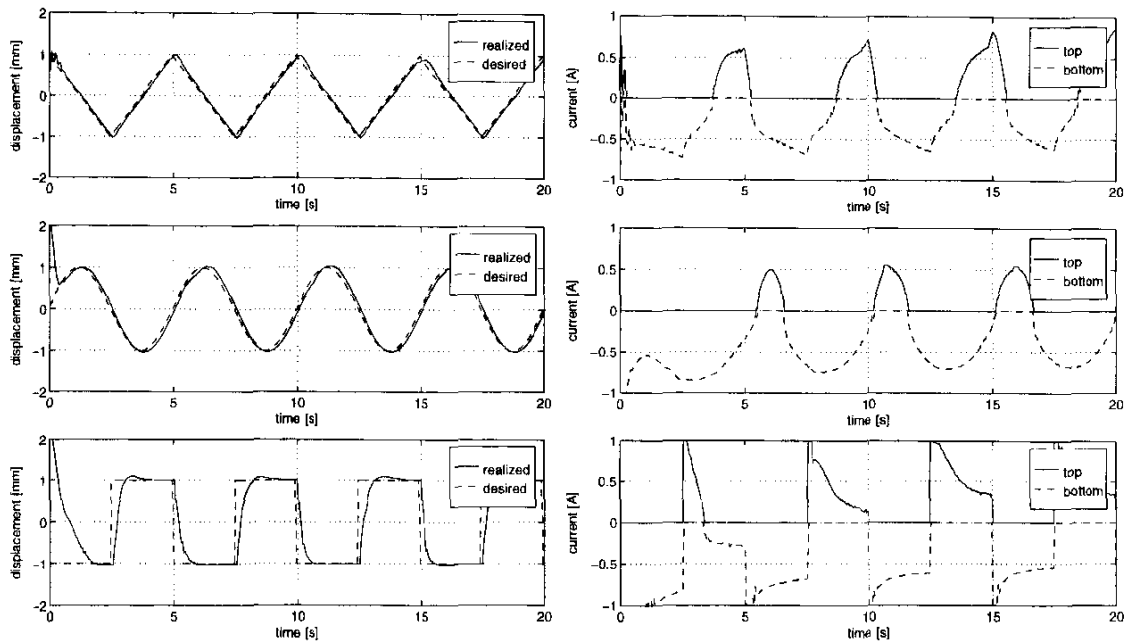


Figure 9: Experimental results for several trajectories

CONCLUSIONS

A numerical and experimental investigation of the shape control of a flexible composite beam with integrated Nitinol wire actuators is presented. The numerical model uses the Finite Element method to simulate the behaviour of the SMA composite beam. A constitutive model, describing the relation between stress, strain and temperature, including hysteresis, of Nitinol wires is developed for this purpose. The calculated thermal and mechanical response of the beam to a constant electric current through the Nitinol wires is discussed. To achieve a desired shape of the beam, a feedback control law is applied to determine the electric current. Both the Finite Element model and the experiments show that a time varying shape can very well be established with this control method.

REFERENCES

- [1] T.W. Duerig, editor, *Engineering aspects of shape memory alloys*, Butterworth-Heinemann, 1989.
- [2] H. Funakubo, *Shape memory alloys*, Gordon and Breach science publishers, 1987.
- [3] J. Perkins, editor, *Shape memory effects in alloys*, Plenum Press, 1975.
- [4] Z. Chaudhry and C.A. Rogers, "Bending and shape control of beams using SMA actuators", *J. of Intell. Mater. Syst. and Struct.*, Vol. 2, October 1991, pp. 581–602.
- [5] Z. Chaudhry and C.A. Rogers, "Response of composite beams to an internal actuator force", *J. of Mechanical Design*, Vol. 114, September 1992, pp. 343–348.
- [6] A. Baz and J. Ro, "Optimal vibration control of Nitinol-reinforced composites", Vol. 4, No. 6, 1994, pp. 567–576.
- [7] B.J. Maclean, G.J. Patterson, and M.S. Misra, "Modeling of a Shape Memory integrated actuator for vibration control of large space structures", *J. of Intell. Mater. Syst. and Struct.*, Vol. 2, January 1991, pp. 72–94.
- [8] Y. Furuya and H. Shimada, "Shape memory actuators for robotic applications", *Materials & Design*, Vol. 12, No. 1, February 1991, pp.21–28.
- [9] K. Kuribayashi, "Millimeter-sized joint actuator using a shape memory alloy", Vol. 20, 1989, pp. 57–64.
- [10] D. Reynaerts and H. van Brussel, "A SMA high performance actuator for robot hands", *Journal de Physique 4 Colloque 4*, Vol. 1, November 1991, pp. 157–162.
- [11] D. Reynaerts and H. van Brussel, "Development of a SMA high performance robotic actuator", *Proc. IEEE MEMS*, Nara, Japan, 1991, pp. 61–66.
- [12] A. Baz, K. Imam, and J. McCoy, "Active vibration control of flexible beams using shape memory actuators", Vol. 140, No. 3, 1990, pp. 437–456.
- [13] R. Ikegami, D.G. Wilson, J.R. Anderson, and G.J. Julien, "Active vibration control using Nitinol and piezoelectric ceramics", *J. of Intell. Mater. Syst. and Struct.*, Vol. 1, April 1990, pp. 189–206.
- [14] S.W. Rhee and L.R. Koval, "Comparison of classical with robust control for SMA smart structures", *Smart Mater. Struct.*, Vol. 2, 1993, pp. 162–171.
- [15] R. Lashlee, R. Damle, V. Rao, and F. Kern, "Identification and robust control of flexible structures using shape memory actuators", *Proc. SPIE Smart Structures and Materials*, Bellingham, USA, 1993, Vol. 1919, pp. 271–282.
- [16] K. Kuribayashi, "Improvement of the response of an SMA actuator using a temperature sensor", *Int. J. of Robotics Research*, Vol. 10, No. 1, February 1991, pp. 13–20.
- [17] R.B. Gorbet and R.A. Russell, "A novel differential shape memory alloy actuator for position control", *Robotica*, Vol. 13, 1995, pp. 423–430.
- [18] D. Honma, Y. Miwa, and N. Iguchi, "Application of shape memory effect to digital control actuator", *Bulletin of JSME*, Vol. 27, No. 230, August 1984, pp. 1737–1742.
- [19] K. Ikuta, "Micro/miniature shape memory alloy actuator", *Proc. IEEE Int. Conf. on Robotics and Automation*, Cincinnati, USA, 1990, pp. 2156–2161.
- [20] M.W.M. van der Wijst, P.J.G. Schreurs, and F.E. Veldpaus, "Application of computed phase transformation power to control shape memory alloy actuators", *Smart Materials and Structures*, in press.
- [21] J.L. Martins de Carvalho, *Dynamical systems and automatic control*, Prentice Hall, 1993.

FABRICATION AND TESTING OF SMART FRP REINFORCEMENTS

Alexander L. Kalamkarov and Douglas O. MacDonald

*Department of Mechanical Engineering, Technical University of Nova Scotia
P.O. Box 1000, Halifax, Nova Scotia, B3J 2X4, CANADA*

SUMMARY: The aspects of fabrication, microstructural evaluation and experimental testing of smart composites are discussed. The technology for the fabrication of fiber reinforced polymer composites with embedded optical fibers is developed. Smart composites are produced by a custom built pultruder. The pultruded carbon reinforced rods with and without optical fiber showed higher shear and tensile strength, as well as greater tensile modulus than did the glass fiber analogue. The embedded optical fibers do not have significant effect on the tensile properties of pultruded rods, but they slightly affected the shear strength of the glass fiber rods. Polyimide coating on optical fiber results in a good interface between optical fiber and host material; whereas acrylate coating cannot withstand the high production temperature and causes severe debonding of optical fiber and resin.

KEYWORDS: smart fiber reinforced polymer composites, pultrusion, optical fiber sensors, tensile and shear strength, interface debonding

INTRODUCTION

Composite materials have recently been used in civil engineering structures, including monitoring, rehabilitation projects, prestressing tendons, reinforcing bars, and most recently as innovative structural members of bridges [1, 2]. For these reasons, composite materials lend themselves as prime candidates for another rapidly expanding field of research known as "smart materials". A smart material is a structure which contains a built in sensing device to continuously monitor the current state and serviceability of the structure. This is referred to as a "passive" smart material which has many applications in civil engineering. Composite materials are good candidates as smart materials because their "build up" fabrication techniques inherently allow for the embedment of sensors and communication lines.

To date, the hand layup in combination with vacuum bagging and autoclaving has been most often used to fabricate smart composites. This can be a labour intensive and time-consuming process in which the quality of the final product is significantly affected by the skill and experience of the technician. Pultrusion, which is the only continuous process, has received little attention in the area of smart composites, and there are currently only a few published papers on this subject [3, 4]. However, by considering the costs and cycle times which are favorable criteria for selection of a manufacturing process, pultrusion is the fastest and most cost effective process. For engineering applications, pultrusion is also well suited to produce prestressing tendons and reinforcing bars, because it can provide the structures with a high degree of axial reinforcement. A part of the work reported here concerns the adaptation of pultrusion techniques into a manufacturing process for smart composite reinforcements.

The diameter of an optical fiber is typically much larger than the diameter of a reinforcing fiber. Thus, when embedding large diameter optical fibers in a composite, some loss of strength of the composite could occur because of optical fiber induced stress and strain concentrations in the host material. The degradation in the mechanical properties of the composite is also related to some other factors, such as the position of the optical fiber within a composite and the bond strength of the optical fiber and host material. The location of an optical fiber within a product may affect the mechanical properties, as well as the sensing capability of the smart materials. Also to be considered is the interface between the optical fiber and host material. To effectively transfer strain from the resin matrix to an embedded fiber optic sensor, a good bond of the optical fiber to host material is required. In general, optical fibers are protected with a buffer coating for increased durability. The bond strength of the optical fiber and host material is therefore dependent upon the characteristics of the buffer coating, i.e. its ability to survive in the harsh composite production environment and its chemical compatibility with the resin matrix system used to produce the composite.

The objective of this research is to develop a continuous manufacturing process for embedding optical fiber and sensors in fiber reinforced plastic composites, and to determine how the embedment of optical fibers and their surface coatings affect the mechanical properties of the composite materials. To achieve these objectives, a microstructural analysis was carried out on both the pultruded profile's cross section, and fracture surfaces obtained from mechanically fractured samples. This analysis was carried out in order to verify the quality of the pultruded composites and to look at the interfaces between optical fibers and host materials.

EXPERIMENTAL

Materials

The resin system which was used for all of the pultrusion tests in this study was a urethane modified bisphenol vinylester. The resin was chosen for its excellent mechanical properties, as well as its low viscosity and high pulling speeds. Two kinds of organic peroxide catalysts were required to cure the resin, and the adequate release from the mold was achieved using an internal lubricant.

Both glass fiber and carbon fiber reinforcements were used to produce composite materials for this study. The sizing on both types of fibers is stated by the manufacturers as being compatible with a vinylester resin system.

Two types of optical fibers were also used for this research. The first was a polyimide-coated single mode optical fiber. Its overall diameter was 155 microns with a 10 micron core and a 125 micron cladding. The second optical fiber was a multimode fiber with an overall diameter of 250 microns, a 50 micron core, and a 125 micron cladding. This fiber contained a UV cured acrylate surface coating.

Processing of Pultruded Rod Samples

In this study, 9.5 mm diameter rod stock was produced using a customized pultrusion machine which was designed and constructed at the Smart Materials Centre of the Technical University of Nova Scotia [1]. This machine is shown schematically in Fig. 1.

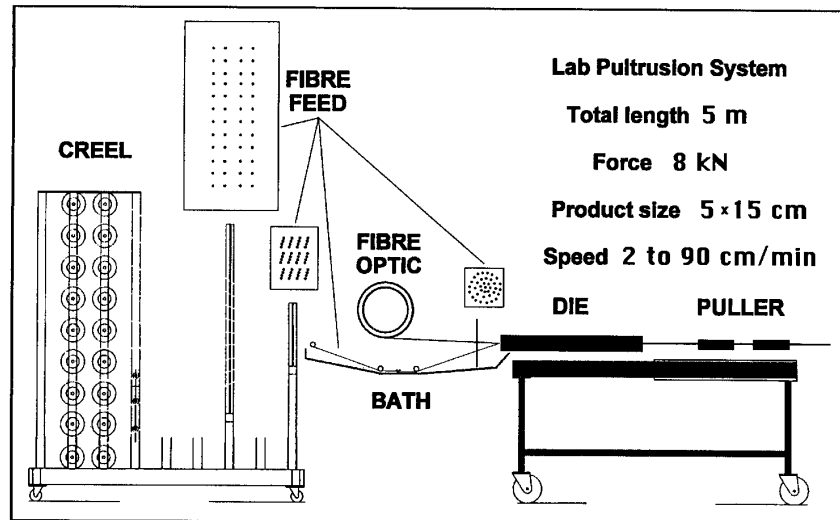


Fig. 1: Schematic diagram of laboratory scale pultrusion system.

Reinforcing fibers (E-glass or carbon rovings) were pulled from a creel system, via a resin tank containing vinylester resin, into a shaping die. The fibers are thoroughly wetted with resin in the dipping tank and polymerization (an exothermic chemical reaction) takes place in an electrically heated die at temperatures of up to 150°C. A rigid cured profile corresponding to the die shape was pulled from the die by a caterpillar pulling system at a constant rate, which for this study was 30 cm/min. Materials produced at higher pulling speeds are not reported at this time. The finished products were cut to the desired length by a cut off saw.

During the production of the pultruded rods, one or two optical fibers were placed at an intended location within the composite with the aid of a positioning device, which was firmly fixed at the entrance to the die.

Both visual inspections and optical microscopy were used as an early quality assessment evaluation for all of the pultruded products.

Mechanical Testing and Microscopic Examination

The tensile and shear properties of the pultruded rods were carried out in accordance with ASTM D3916 and ASTM D4475 respectively, on a hydraulically driven MTS Model 8504RM testing machine using Instron series IX software.

A stereo microscope was used to examine the pultruded profile's cross section and to determine the location of the optical fiber(s). To facilitate this examination, a cross section of each rod was ground on silicon carbide abrasive papers with grit sizes ranging from 120 to 800 microns. The rods were examined at magnifications ranging from 10x to 20x.

Scanning electron microscopy (SEM) was performed on various polished cross sections, as well as on the fracture surfaces from rods which had been subjected to mechanical testing. A Jeol JSM 820 SEM was used to study the interfaces between optical fibers and host materials, as well as the presence of delaminations or voids, in the polished rod sections. A Jeol JXA35 SEM was used to examine fiber pull-out and fiber-matrix debonding in the fractured rod samples. To prepare the samples for the SEM, the ground samples were polished on with 3 and 1 micron diamond suspensions, as well as colloidal silica. A 20 nm gold/palladium coating was applied to each sample via a hummer X sputtering coater.

RESULTS AND DISCUSSION

Pultrusion Processing Equipment

A large quantity of glass and carbon fiber reinforced vinylester rods with and without the embedded optical fiber was fabricated using the laboratory scale pultrusion machine. This pultrusion machine was successful at producing very consistent products. The pultruder shows certain improved performance as compared to the conventional analogue. For example, the specialized fiber feed system is capable of locating the optical fiber with high precision; the caterpillar pulling system which is driven by a DC motor gives highly accurate speed control at less than 0.1 % variation, and at a constant pulling force; and the desktop work platform as well as being portable and modular, provides easy access to the entire work area.

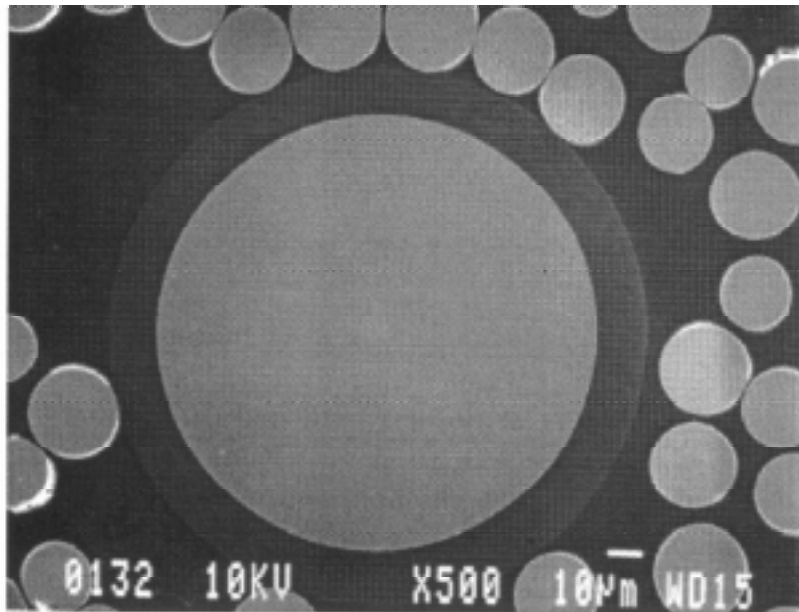


Fig. 2: SEM micrograph shows excellent interface between polyimide coated optical fiber and host material (500 x).

Furthermore, it is capable of pulling speeds of up to 36 inches per minute. This is virtually in good agreement with the statement that pultrusion is the fastest and most cost effective process for fabricating composites as compared to other processes. The verification of other required processing parameters such as temperature control revealed that the customized pultruder has performed satisfactorily according to design specification. Temperature was controlled on 3 separate zones along the length of the die, in order to obtain the required

curing profiles for the vinyl ester resin. Setup of the pultrusion line was made simpler and faster as the system was designed in order to achieve self alignment of the die with the pulling mechanism.

Survivability of Optical Fibers in Pultrusion Process

Previous studies have reported that polyimide coated fibers have a melting point of 385°C, and therefore possess a superior ability to withstand high temperatures [5]. These fibers were thus expected to survive the cure temperatures encountered in the pultrusion process. They were also chemically compatible with resin matrix used, and hence created good interface with host material. Fig. 2 is an SEM micrograph which illustrates that our results were very consistent with the above statements in that the polyimide coated fiber has survived the pultrusion process, and appears to be well bonded to the resin matrix.

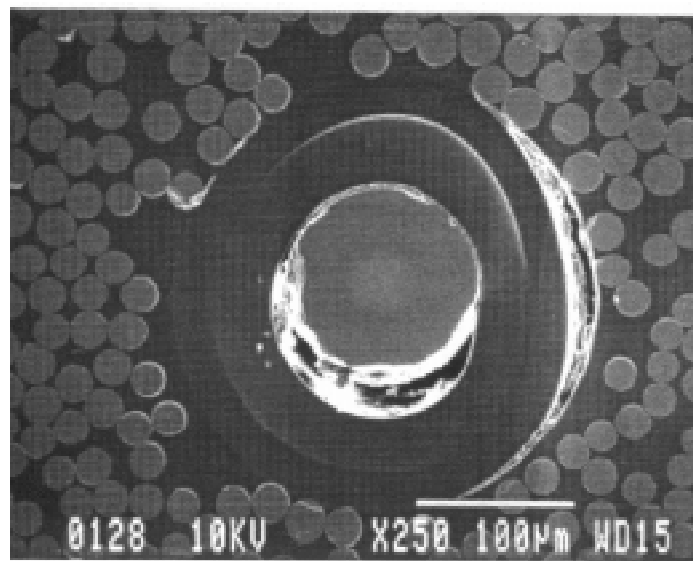


Fig. 3: SEM micrograph shows debonding between acrylate-coated optical fiber and host material (250 x).

It has also been reported that the acrylate coating on common optical fibers could not withstand processing temperatures greater than 85°C [5]. In the current study, the maximum curing temperature was 150°C. Therefore, the acrylate coating was not expected to survive in this harsh production environment. This was supported by the evidence, as shown in the SEM micrograph of Fig. 3. Severe debonding between the acrylate coated optical fiber and the host material occurred, most likely due to melting and distortion of the acrylate coating. For this reason, the majority of the work reported in this study involves an investigation of the embedment of polyimide coated optical fibers within pultruded composites.

Comparison of Pultruded Carbon and Glass FRP Rods

Casual visual inspection of the pultruded carbon and glass reinforced rods indicated some common features. All of the pultruded rods had a consistently circular shape and excellent surface finish. The embedded optical fiber in the cross section of the glass FRP rod was easily visible by eye. However, the location of the optical fiber in carbon FRP required an optical microscope with good lighting.

The mechanical properties of pultruded carbon and glass reinforced composites are given in Table 1. A comparison of tensile properties of these two kinds of pultruded rods is presented in Fig. 4, from which the large difference between the tensile strengths of carbon and glass fiber reinforced samples was observed regardless of the presence of optical fibers. As expected, the use of carbon fiber gave much higher tensile strength (1245 MPa) than glass reinforcement (902 MPa). This is because the fibers are the principal load-carrying agent and in a fiber reinforced unidirectional composite, the properties such as strength and modulus in the fiber direction are fiber-dominated [6]. The inherent tensile strength of carbon fiber is about 64% greater than that of E-glass. The tensile failure modes of all the samples were typical fiber breakage and debonding.

In view of the results in Table 2, the shear strengths of the pultruded rods appear to be insensitive to the type of fiber reinforcement. In principle, the short beam shear test is designed to determine the interfacial adhesion of the resin and fiber, and the strength of the matrix [7, 8]. Both glass and carbon fibers used in this study had been treated with a surface sizing, which is compatible with vinylester resin. Thus similarly good interfaces between

Table 1. Tensile properties of fiber-reinforced vinylester composites

Material	Strength (MPa)	Standard Deviation (MPa)	Tensile Modulus (MPa)	Standard Deviation (MPa)
Glass FRP				
No optical fiber	902	126	48.2	1.1
One polyimide fiber	949	55	47.3	0.7
Carbon FRP				
No optical fiber	1245	118	140.8	
One optical fiber	1246	56	144.2	3.4

Table 2. Shear properties of fiber-reinforced vinylester composites

Material	Shear Strength (MPa)	Standard Deviation (MPa)
Glass FRP		
No optical Fiber	29.3	1.3
One polyimide fiber	27.2	1.1
Two polyimide fibers	25.4	1.0
One acrylate fiber	29.2	2.2
Carbon FRP		
No optical fiber	29.7	1.6
One polyimide fiber	29.5	1.5

these two kinds of fiber reinforcements and vinylester resin within the pultruded rod would be expected. Thus, the shear strength of a pultruded composite in this case is virtually given by the resin matrix. However, it is important to note that embedding an optical fiber into the pultruded part slightly affected the mean shear strength of the glass fiber reinforced composites, as can be seen from Table 2. The reason to be considered for this will be given in the following section.

Effect of Optical Fiber Embeddement on the Mechanical Properties of Smart Materials

Fig. 4 illustrates that the tensile strength and modulus of glass and carbon fiber pultruded FRP rods were virtually unaffected by the embeddement of a single polyimide coated optical fiber. Earlier publications [5,9] also reported that an embedded optical fiber did not have a detrimental influence on tensile properties when embedded in the same direction as the composite's reinforcing fibers. The suggested explanation is that the fiber reinforcement is the only significant factor directly affecting the tensile properties of unidirectional composite [6]. Fig. 5 shows the effect of an embedded optical fiber on the mean shear strength of fiber reinforced vinylester composites. The embedded optical fiber had a total diameter of 155 microns and had a polyimide coating. As the number of the embedded optical fibers increased from 0 through 1 to 2, the mean shear strength of glass FRP rod decreased by 11% and 17% respectively, from 29.9 MPa through 26.9 MPa to 25.6 MPa. Pultruded carbon fiber reinforced rods appeared not to be affected by the presence of a single embedded polyimide coated optical fiber. The mean shear strength values were virtually identical. The shear strength of the carbon rod with an optical fiber (29.5 MPa) was less than 1% lower than the shear strength of the baseline carbon rod with no optical fiber (29.7 MPa). However, this difference falls within the standard deviation of the data obtained for the baseline rod. While the mean strength reduction of 11-17% in the glass FRP rods containing optical fibers appears to be real, and outside of the standard deviation for the baseline rods, it should also be stated that the scatter in the data obtained from the short beam shear test is in the range of 10-15% as well. Increasing the number of samples from 5 to 10 for each test category reaffirmed the reduction in mean shear strength.

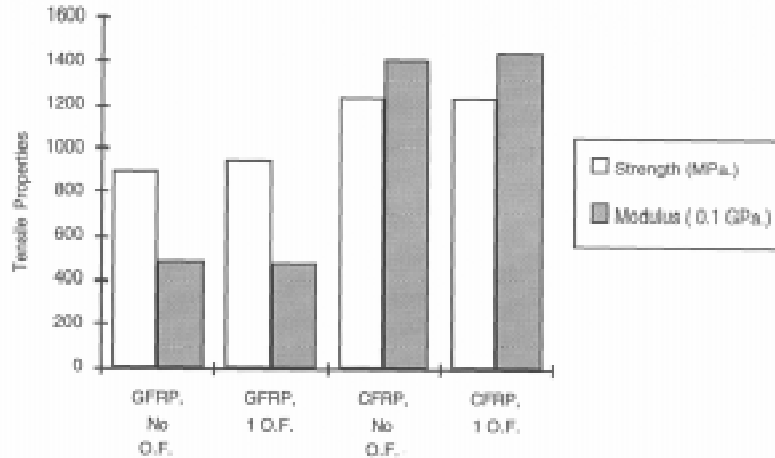


Fig. 4: Comparison of tensile properties of pultruded CFRP and GFRP rods.

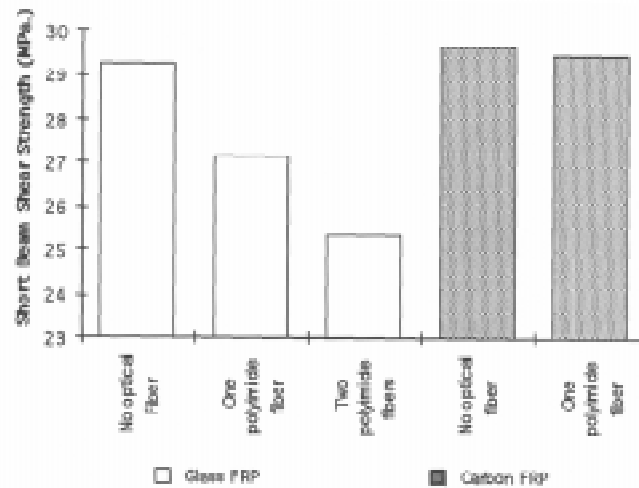


Fig. 5: Comparison of shear properties of pultruded CFRP and GFRP rods.

The degradation in the shear strength is caused by the changes induced by the optical fiber on a micro level within the pultruded composite. It has been reported that the incorporation of optical fibers with a comparatively large diameter of 155 microns, although the embedments were placed in the direction of the reinforcing fiber, may cause the formation of resin-rich regions near the fiber-matrix interface [10]. This effect causes internal material geometry variations in the vicinity of interfaces [11]. This resulted in a large strain concentration, which in turn caused the premature failure of the composite under shear stress. In support of this theory, the quantitative micromechanical analysis and measurement of the strain concentrations caused by embedded fibers were conducted [12]. The results in that study showed that an applied load equal to half the failure load of the eight-ply specimens tested, generated a strain of approximately 0.05 at the fiber-matrix interface.

Adding two optical fibers into the pultruded rod had a more significant effect on the shear strength of glass FRP than did a single optical fiber embedment, see Fig. 5. The obvious reason for this can be inferred from the above discussion. Also, this result is consistent with a previous publication [13], stating that large numbers of embedded optical fibers had a more pronounced influence upon the compressive properties (matrix-dominated properties) of laminates, than did smaller numbers.

In the case of carbon FRP rods, a single embedded optical fiber did not have any noticeable effect on the shear strength, see Fig. 5. The optical fiber having less significant effect on the shear strength of carbon FRP rod was, in this case, thought to be attributed to a good bond strength between carbon fiber and vinyl ester resin [1]. Another interesting factor to be considered is the failure behaviour of the specimens under shear stress. After testing, fracture surfaces were carefully monitored and found to be away from the location of the optical fiber embedded in a rod in the cases of a polyimide coating. At the same time, in the cases of acrylate coated optical fibers, the fracture surface passed through the interface of optical fiber.

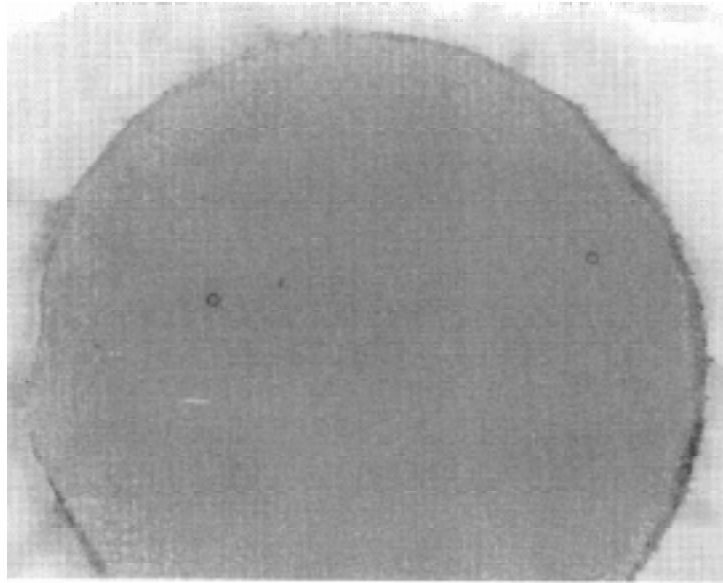


Fig. 6: Optical micrograph shows a cross section of the pultruded Glass FRP rod with two embedded optical fibers (14 x)

It is also interesting to note that the mean shear strength of the pultruded glass FRP rod containing an embedded acrylate coated optical fiber was slightly higher than that for the baseline rod. The acrylate coated optical fiber was expected to deteriorate the mechanical properties of the pultruded glass FRP rod due to its large overall diameter of 250 microns, and because it had failed to survive the pultrusion process, as was shown earlier in Fig. 3. It was also expected to produce mechanical property values that were lower than those for rods containing embedded polyimide optical fibers which were smaller, and had survived the high temperatures of the pultrusion process.

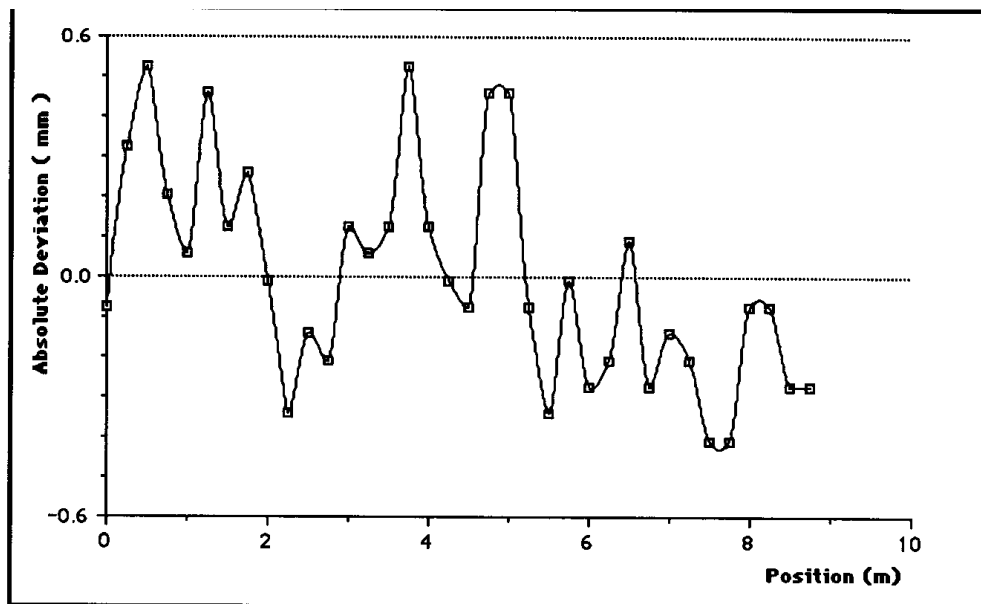


Fig. 7: Variation in relative fiber position of two optical fibers in Glass FRP rod shown in Fig. 6.

Microscopic Analysis

A cross section of a glass FRP rod containing two embedded optical fibers is shown in Fig. 6. The optical fibers are located inside the rod at a fixed distance apart, as determined by the positioning device in the fiber feed system. Fig. 7 illustrates the variation in the distance between the two optical fibers, as determined over an embedded distance of 10 m. It can thus be seen that an embedded optical fiber exhibits little wander or drift inside the composite rod, with a maximum deviation of 0.5 mm from a specific location over a 10 m span.

The absence of delaminations or voids in Fig. 6 appears to indicate that the pultruded rods are of good quality.

CONCLUSIONS

The pultrusion process for the fabrication of FRP smart materials has been successfully set up at Smart Materials Centre at the Technical University of Nova Scotia. The positioning of optical fibers and sensors within a composite was achieved by using a specially designed locating device. Polyimide coating on optical fiber results in a good interface between optical fiber and host material; whereas acrylate coating cannot withstand the harsh environment (high production temperature) and causes severe debonding of optical fiber and resin. Therefore, polyimide-coated optical fiber should be a preferential selection to be used in this study. Embedded optical fibers do not have a significant effect on the tensile properties of the pultruded FRP, but they slightly deteriorate the shear strength of composites. This slight decrease in shear strength was seen for the glass rods, but was not evident in the carbon rods. As the number of embedded optical fibers in the composite is increased, the effect upon the shear strength is also increased.

ACKNOWLEDGMENTS

This work has been supported by the ISIS - CANADA NCE (the Intelligent Sensing in Innovative Structures Canadian Network of Centres of Excellence) through the Project T 3.4 on Smart Reinforcements and Connectors.

REFERENCES

1. Kalamkarov, A.L., Yang, Q., MacDonald, D.O. and Westhaver, P.A.D., "Experimental applications of smart composites", *International Conference on Experimental Mechanics: Advances and Applications (ICEM'96)*, Singapore, Abstracts: p. 40, December 1996, Proceedings in press.
2. MacDonald D.O. and Kalamkarov, A.L., "On the application of pultruded smart composites in civil engineering", *Proc. of the Third International Conference on Composites Engineering*, 1996, pp. 549-550.
3. Friebele, E., Askins, C., Putnam, M., Florio, J., Fasha, A., Donti, R. and Mosley, C., "Distributed strain sensing with fiber Bragg grating arrays embedded in CRTM™ composites", *SPIE Vol. 2361, 2nd European Conference on Smart Structure and Materials*, 1994, pp. 338-341.

4. Friebele, E.J., Askins, C.G., Putnam, M.A., William, G.M., Kersey, A.D., Fosha, Jr., A.A., Florio, Jr., J., Donti, R.P. and Blosser, R.G., "Fabrication and application of low-cost optical fiber sensor arrays for industrial and commercial applications", *Industrial and Commercial Appl. of Smart Structures Tech., SPIE*, Vol. 2447, Crowe, C.R. and Anderson, G.L., Eds., 1995, pp. 305-311.
5. Leka, L. and Bayo, E., "A close look at the embedment of optical fibers into composite structures", *Journal of Composites Technology & Research*, Vol. 11, No. 3, 1989, pp. 106-112.
6. Kalamkarov, A.L., *Composite and Reinforced Elements of Construction*, John Wiley & Sons, Chichester, New-York, 1992.
7. English, L.K., "Composite materials-special report", *Materials Engineering*, September 1987, pp. 15-50.
8. Kubel, E., "Advanced materials star at SAMPE", *Materials Engineering*, June 1985, pp. 63-66.
9. Measures, R.M., Glossop, N.D.W., Lymer, J. and Tennyson, R.C. , "Structurally integrated fiber optic damage assessment system for composite materials", *Proc. SPIE*, Vol. 986, 1988, pp. 120-129.
10. Udd, E., "Overview of fiber optic smart structures for aerospace applications", *Proc.SPIE*, Vol. 986, 1988, pp. 2-5.
11. Measures, R.M., Glossop, N.D.W., Lymer, J., West, J., Tsaw, W. and Tennyson, R.C., "Fibre optic impact damage detection of composite Materials", *Fibre Optics 88, Proc. SPIE*, 1988, pp. 949-952.
12. Czarnek, R., Guo, Y., Bennett, K.D. and Claus, R.O., "Interferometric measurements of strain concentrations induced by an optical fiber embedded in fiber reinforced composites", *Proc. SPIE*, Vol. 986, 1988, pp. 43-54.
13. Jensen, D. and Pascual, J., "Degradation of graphite/bismaleimide laminates with multiple embedded fiber-optic sensors", *Proc. SPIE*, Vol. 1370: Fiber Optic Smart Structures and Skins III, 1990, pp 228-237.

FATIGUE BEHAVIOR OF OPTICAL FIBER SENSOR EMBEDDED IN SMART COMPOSITE STRUCTURES

Tae Seong Jang¹, Jung Ju Lee¹, Dong Chun Lee¹, Dae Cheol Seo¹ and Ho Kim²

¹*Department of Mechanical Engineering, Korea Advanced Institute of Science and Technology, 373-1, Kusong-dong, Yuseong-gu, Taejeon, 305-701, Korea*

²*KIA Motors Corp. R&D Center, 781-1, Soha-dong, Kwang myung-shi, Kyungki-do, 423-701, Korea*

SUMMARY: Fatigue behavior of the optical fiber sensors embedded in composite laminate was studied. The fatigue life of the embedded optical fiber was investigated by measuring the intensity change of the laser signal transmitted through it. Test specimens consisted of three types of stacking sequences; $[0_6/OF/0_6]_T$, $[0_2/90_4/OF/90_4/0_2]_T$ and $[0_3/90_3/OF/90_3/0_3]_T$. From the experiment, it was observed that the optical fiber sensor embedded in composite laminate under fatigue loading was fractured at lower stress level than the average static stress at which the fracture of the embedded optical fiber within the laminate occurred. It was found that the fatigue life of the optical fiber embedded in cross-ply laminate was closely related with the growth of transverse matrix crack. On the other hand, the fatigue fracture of the embedded optical fiber within the unidirectional-ply laminate occurred due to the growth of internal defects of optical fiber. The decrease in fatigue life of the optical fiber embedded in the unidirectional-ply laminate is relatively small compared to the cross-ply laminate case.

KEYWORDS: optical fiber sensor, smart composite structures, fatigue behavior, S-N curve, transverse matrix crack, internal defects, strain concentration, laser signal intensity

INTRODUCTION

There was a considerable increase in the use of composite materials for aerospace, marine and other structural applications because of their high specific stiffness and strength. However, periodical and careful inspection are required due to the limiting features of composite laminates such as transverse matrix cracking and delamination. Recently, smart structure concepts have been applied to composite structures for the effective monitoring of structural integrity. Optical fiber sensor technology has been used for the purpose of monitoring the integrity of composite materials. One such application is that of embedding optical fibers into composite materials. The increasing use of optical fiber sensor as a sensing material has been found because they have several attractive features compared to other sensors [1]. Optical fiber sensors offer following capabilities to smart structures such as structural health monitoring, internal deformation measurement, impact detection, vibration sensing, etc. The effect of the embedded optical fiber on the mechanical behavior of host composite structures was studied. Jensen et al. [2, 3] and Measures et al. [4] reported that embedded optical fibers may degrade the uniaxial tensile and compressive properties of composite laminates. Singh et al. [5] measured the strain of composite material around the embedded optical fiber whose diameters and coating states are different from each other. Seo et al. [6] measured the damage caused by the embedding of optical fiber in terms of the transverse matrix crack density of

cross-ply laminate. Lee et al. [7] performed qualitative investigation on the fatigue behavior of composite laminate with the embedded optical fiber sensor.

However, for the successful application of optical fiber sensor to smart composite structures, in addition to the integrity of the composite laminate with embedded optical fibers, it should be also checked whether the embedded optical fiber sensor can survive and perform their designed functions under the service loading condition of host structures. The structures in service are usually subjected to variable random loading and the materials under fatigue loading are generally fractured at lower stress level than that under static loading. Therefore, it should be investigated whether the embedded optical fiber sensor performs their designed function under the given loading condition. In this paper, the fatigue behavior of optical fiber sensor embedded in composite laminate was investigated. The composite laminate specimens consisted of three types of stacking sequences; a unidirectional-ply laminate $[0_{12}]_T$, and two cross-ply laminates $[0_2/90_4]_S$ and $[0_3/90_3]_S$. One optical fiber was embedded in the neutral plane of each specimen along the loading direction. With these specimens, comparison of the fatigue behavior of the optical fiber embedded in different laminates was performed by measuring fatigue life of each specimen and obtaining the S-N curve.

SPECIMEN FABRICATION

All specimens were fabricated by glass/epoxy prepreg. SUNKYUNG INDUSTRY Co. UGN-150 prepreg was used. The glass/epoxy laminates have the advantage that we can directly observe the bleeding of laser, the initiation and the growth of damage in the specimen, such as delamination, splitting and transverse crack, due to their transparency. Fig. 1 shows three types of stacking sequences, the location and orientation of the embedded optical fiber. The nominal thickness of all specimens is 1.2mm. Optical fibers were embedded in the neutral plane of laminate by using the fiber positioning jig designed to make it easy to align them with the loading direction. The 60mm test section part of the optical fiber coating was removed chemically by acetone to increase the sensitivity to damage.

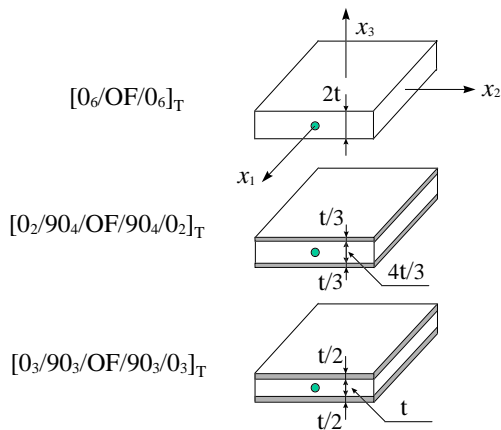


Fig. 1: Schematic diagram of specimen configuration with embedded optical fiber

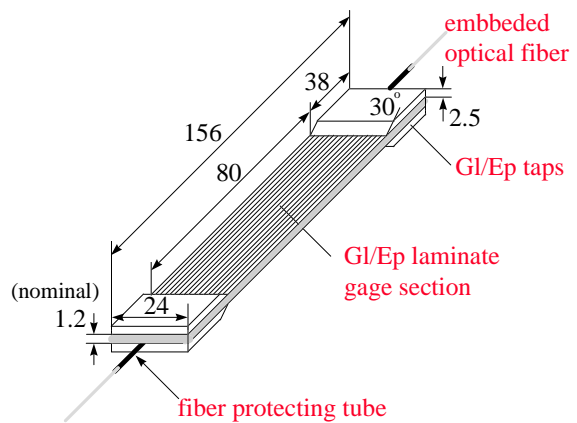


Fig. 2: Geometry of specimen (dimensions in millimeters)

After the laminate was cured in the programmable autoclave along the manufacturer's recommended cure cycle, the HANKOOK FIBER Co. HFG GU-300 E-glass loading tabs were attached at both ends by using CYANAMID FM 73 film adhesive. Then the specimens

were cutted out by using a water-cooled diamond wheel cutter. The final shape of a specimen is shown in Fig. 2.

EXPERIMENTAL

The fatigue tests were performed by using 25ton MTS servohydraulic test machine. Fatigue tests were carried out under load control with a sinusoidal waveform at frequency of 5Hz and stress ratio, R (=minimum stress/maximum stress), of 0.1. The laser was introduced into the optical fiber sensor embedded in composite laminate by using a coupler which was composed of a set of lenses and an optical fiber positioning assembly. The intensity of the laser transmitted through the embedded optical fiber was measured by a photo-diode. Load history and laser intensity signal were recorded automatically during test by using a PC-based data acquisition system. The overall experimental setup is shown schematically in Fig. 3. The fracture of optical fiber was detected by the intensity drop-off of the laser signal transmitted through it and visually confirmed by the bleeding of the laser signal at the location of its fracture. With this experimental setup, we investigated the fatigue life of the optical fiber sensor embedded in composite laminate under the various levels of fatigue loads and then plotted the S-N curve.

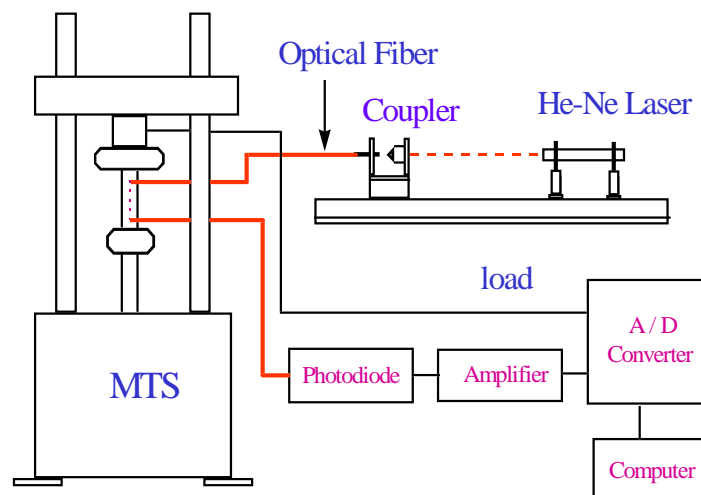


Fig. 3: Schematic diagram of experimental setup

RESULTS AND DISCUSSION

Fatigue behavior of the optical fiber embedded in unidirectional-ply laminate

Fatigue tests for the optical fiber embedded in unidirectional-ply laminate were conducted under various maximum stress levels with the stress ratio, R , of 0.1 to avoid the compressive stress during the fatigue loading. The fracture of optical fiber was detected by observing the change of laser intensity transmitted through it. Fig. 4 shows the typical change of the laser intensity for unidirectional-ply laminate specimen as fatigue cycles increase. As can be seen in this figure, the laser intensity is nearly uniform until the fracture of optical fiber. This laser signal behavior shown in Fig. 4 means that the fracture of optical fiber sensor occurred abruptly without gradual damage accumulation in the embedded optical fiber sensor. To make

certain of this, the specimen was examined macroscopically and microscopically. In macroscopic observations, any evidence was not found for the fracture of reinforcement glass fibers or the internal cracking such as matrix cracks or delaminations until the fracture of optical fiber sensor. In microscopic observations, the debonding between the optical fiber and the matrix, which can cause the fracture of the brittle optical fiber by generating the shear stress in the optical fiber, was not found. The microscopic views around the fractured optical fiber are shown in Fig. 5.

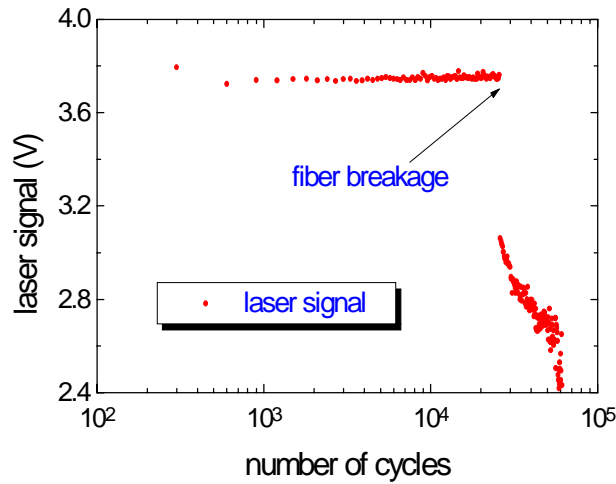


Fig. 4: Laser signal intensity of the unidirectional-ply

The laser intensity drops rapidly when the optical fiber is fractured and then decreases gradually. The gradual decrease of laser intensity is caused by additional fractures at other positions of the optical fiber in the test section and subsequent cracking from the first fracture, as can be seen in Fig. 5.

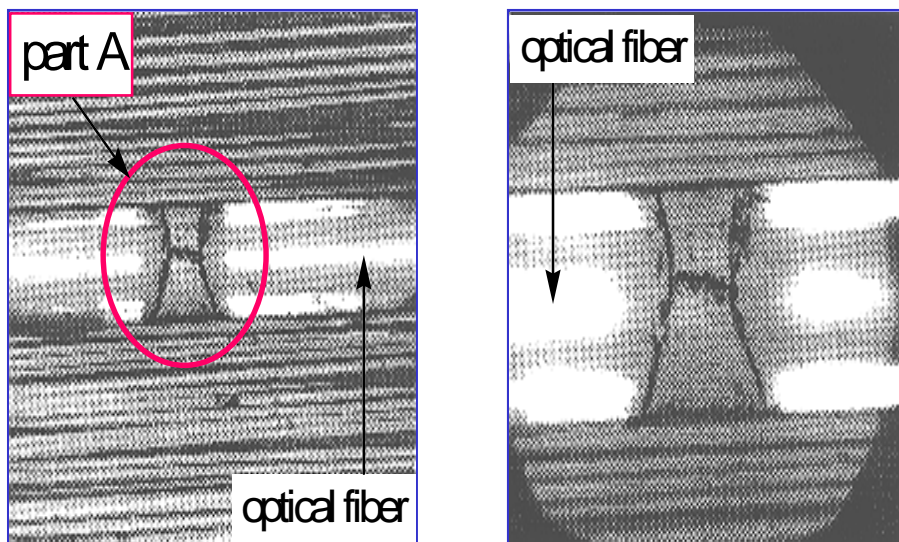


Fig. 5: Microscopic pictures of a failed optical fibre in $[0_6/OF/0_6]_T$, (b) is the magnified photo of Part A in (a)

In these tests, the fatigue fracture of the embedded optical fiber sensor was determined when the abrupt drop-off of laser signal intensity occurred, as shown in Fig. 4. Then the S-N curve was plotted from the cycles at that time as shown in Fig. 6. In this figure, it is not easy to characterize the fatigue behavior of the embedded optical fiber because of wide scatter. Generally, the strength of fibrous materials such as reinforcement glass fibers and optical fibers can not have a unique value due to the inhomogeneous distribution of internal defects within the fiber. The wide scatter means the variety of sizes and locations of internal defects. In Fig. 6, the ordinate axis represents the ratio of maximum fatigue stress applied to laminate with respect to the average static stress at which the embedded optical fiber within the laminate occurred.

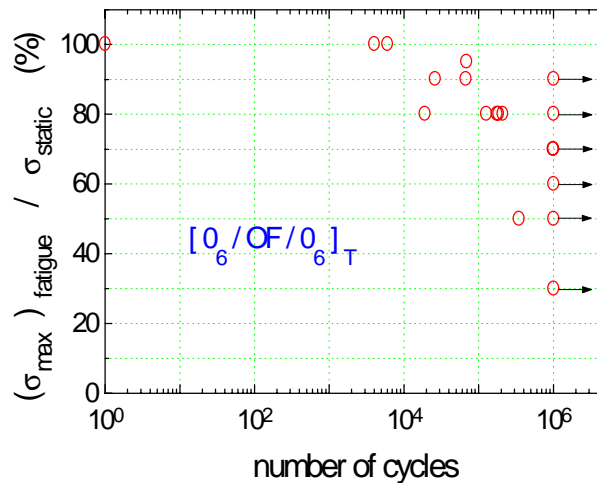


Fig 6: Fatigue life of the optical fiber in $[0_6/OF/0_6]_T$

From these results, it can be said that the optical fiber embedded in unidirectional-ply laminate has relatively good fatigue resistance and the optical fiber embedded in unidirectional-ply laminate is fractured due to the growth of its internal defects under fatigue loading.

Fatigue behavior of the optical fiber embedded in cross-ply laminate

In the above fatigue tests, no defects or damages in the unidirectional-ply laminate were observed until the fracture of optical fiber. In fatigue tests of the optical fiber embedded in cross-ply laminate, a matrix cracking in the transverse plies always preceded the fracture of the embedded optical fiber. After curing, there might exist a number of inherent microcracks in the matrix of the cross-ply laminate. These microcracks, particularly in the transverse plies, grow along the direction of reinforcement fibers as fatigue cycles are increased. A crack that grows faster than others fractures the optical fiber. Because the matrix crack causes the strain concentration, the embedded optical fiber is fractured in a few cycles after the matrix crack arrives at the optical fiber. One noticeable fact is that the embedded optical fiber is fractured just by the matrix crack which arrives at the optical fiber first. In the previous study [8] concerning the fracture of cross-ply laminate with embedded optical fiber under static tensile loading, a lot of matrix cracks were observed until the fracture of optical fiber. However, under fatigue loading, the strain concentration makes a direct cause of the fracture of optical fiber. From the microscopic observations, it can be said that the matrix crack causes the fracture of optical fiber directly, as shown in Fig. 7. The fatigue behavior for two cross-ply laminates $[0_2/90_4/OF/90_4/0_2]$ and $[0_3/90_3/OF/90_3/0_3]$, is shown in Fig. 8. The S-N curves of

optical fibers also show similar trend to those of conventional metals. The fatigue limits of optical fibers embedded in two cross-ply laminates are about 30% value of average static tensile stress at which the embedded optical fiber within the laminate occurred. Fig. 9 shows the fatigue life of optical fiber embedded in different laminates where the ordinate axis represents the maximum stress applied to laminates under fatigue loading.

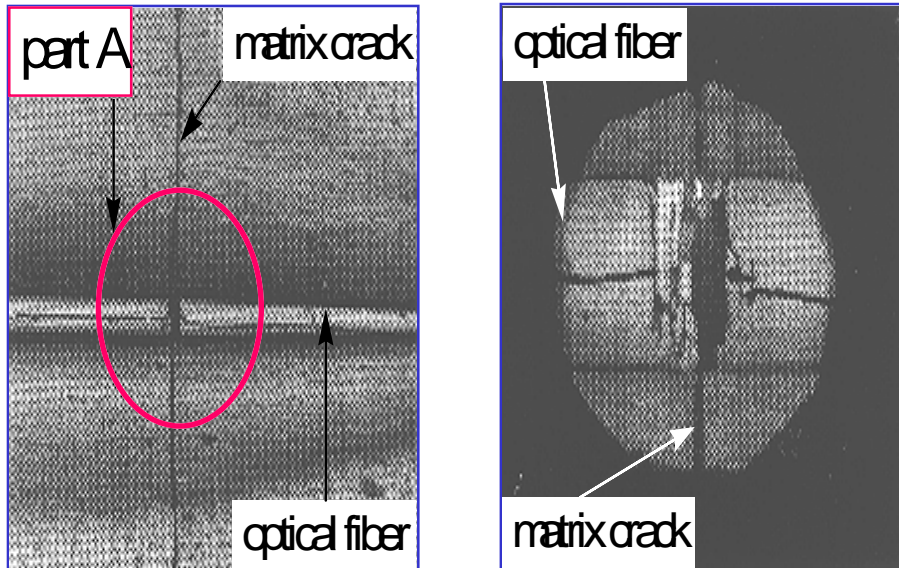


Fig. 7: Microscopic pictures of a failed optical fiber in cross-ply laminate, (b) is the magnified photo of part A in (a)

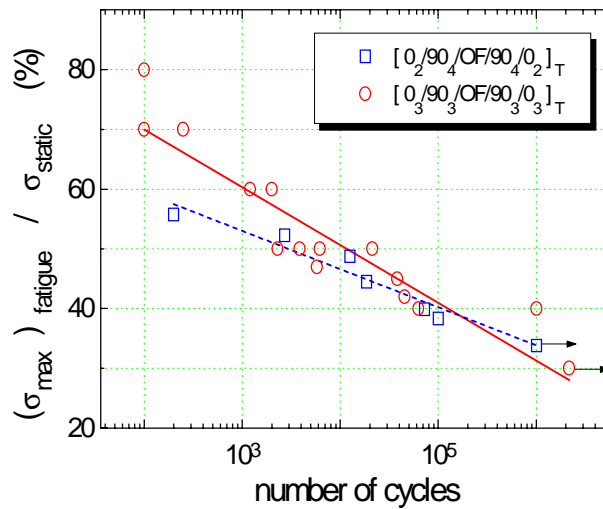


Fig 8: Fatigue life of optical fibers in cross-ply laminates

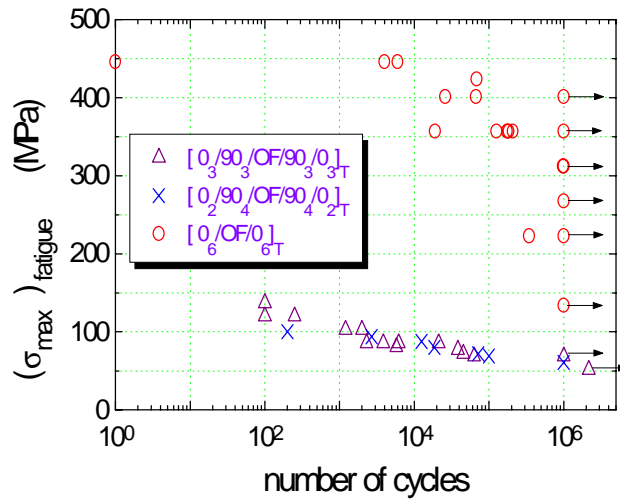


Fig. 9: Fatigue life of optical fibers embedded in different laminates

From these results, it can be said that the strain concentration by the matrix crack causes the fracture of the optical fiber embedded in cross-ply laminate under the fatigue loading. The growth of matrix crack by the fatigue loading can be estimated by the fatigue life of the optical fiber embedded in cross-ply laminate, which is initiated from the free edge. It can be also said that the optical fiber has lower fatigue resistance when embedded in cross-ply laminate than unidirectional-ply laminate. Therefore, smart composite structures under fatigue loading should be designed to ensure the integrity of the embedded optical fiber sensor for the successful applications.

Fatigue behavior of the optical fiber embedded in laminates with different gage length

In this study, the gage length of all specimens is 60mm. Generally, the fibrous materials have different strengths depending on their length. So comparisons of present result with the previous results [8] for 120mm gage length specimens were performed. Fig. 10 is the result for the unidirectional-ply laminate specimens and Fig. 11 is for the cross-ply laminate specimens.

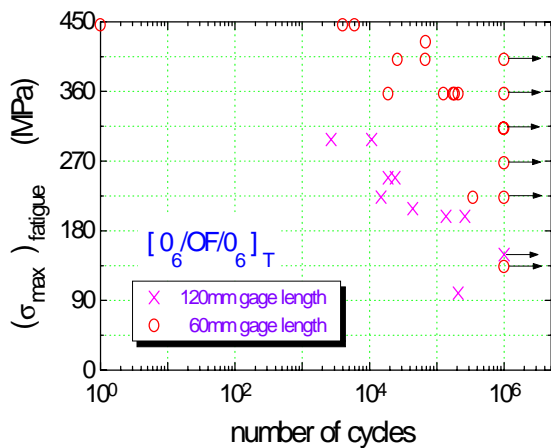


Fig. 10: Fatigue life of optical fibers with

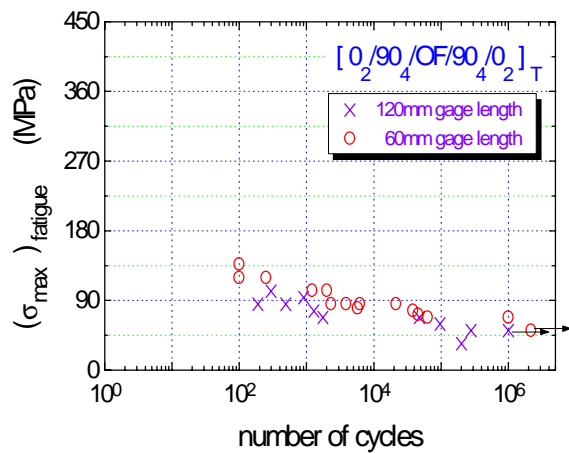


Fig. 11: Fatigue life of optical fibers with

In Fig. 10, we can observe the apparent drop of the fatigue life of the optical fiber with 120mm gage length. This is due to the increase of defects within optical fiber. The scatter is due to the inhomogeneous distribution of defects. In unidirectional-ply laminate, the gage length is very important factor affecting the fatigue life of the embedded optical fiber. However, in cross-ply laminate, the two curves are nearly identical as shown in Fig. 11. This is due to the difference of the fracture mechanism. In other words, the optical fiber under fatigue loading is fractured by the growth of its internal defects when embedded in the unidirectional-ply laminate, while by the strain concentration due to the matrix crack when embedded in the cross-ply laminate. So, the dependence of the fatigue life on the gage length is not found in case of the cross-ply laminate.

CONCLUSIONS

From this study for the fatigue behavior of embedded optical fiber sensors within the composite laminates, the following conclusions were obtained.

1. The optical fiber sensor embedded in laminate under fatigue loading is fractured at lower stress level than the average static stress at which the fracture of the embedded optical fiber within the laminate occurred. The optical fiber, especially embedded in cross-ply laminate, has very low fatigue resistance. Thus, for the successful application of optical fiber sensor to smart composite structures, this point should be carefully considered in the design process.
2. The decrease in fatigue life of optical fiber is relatively small when embedded in unidirectional-ply laminate compared to cross-ply laminate. The optical fiber embedded in unidirectional-ply laminate is fractured by the fatigue damage due to the growth of its internal defects. The optical fiber embedded in cross-ply laminate is fractured by the strain concentration produced at the tip of the primary matrix crack.
3. The fatigue life of optical fiber sensor is not dependent on the gage length when embedded in cross-ply laminate. The matrix crack is the dominant factor affecting the fatigue life of the optical fiber sensor embedded in cross-ply laminate.

ACKNOWLEDGEMENTS

The authors would like to thank KOSEF (Korea Science and Engineering Foundation) for the financial support for this work under the contract No. 96-0200-05-01-3.

REFERENCES

1. Claus, R.O., "Overview of Fiber Optic Sensor-based Smart Materials and Structures", *Proceedings of the Conference on Optical Fiber Sensor-based Smart Materials and Structures*, held at Blacksburg, Virginia, 1991, p. 3.

2. Jensen, D.W., Pascual, J. and August, J.A., "Performance of a Graphite/bismaleimide Laminates with Embedded Optical Fibers. Part I: Uniaxial Tension", *Smart Materials and Structures*, Vol. 1, 1992, pp. 24 - 30.
3. Jensen, D.W., Pascual, J. and August, J.A., "Performance of a Graphite/bismaleimide Laminates with Embedded Optical Fibers. Part I: Uniaxial Compression", *Smart Materials and Structures*, Vol. 1, 1992, pp. 31 -35.
4. Measures, R.M., Glossop, N.D.W., Lymer, J., Leblanc, M., West, M., Dubois, S., Tsaw, W. and Tennyson, R.C., "Structurally Integrated Fiber Optic Damage Assessment System for Composite Materials", *Applied Optics*, Vol. 28, No. 13, 1989, pp. 2626 -2633.
5. Singh, H., Sirkis, J.S. and Dasgupta, A., "Micro-interaction of Optical Fibers Embedded in Laminated Composites", *Proceedings of SPIE Fiber Optic Smart Structures and Skins*, Vol. 1588, 1991, p. 76.
6. Seo, D.C. and Lee, J.J., "Effect of Embedded Optical Fibers on Matrix Crack Spacing in Smart Structures", *Composite Structures*, Vol. 32, 1995, pp. 51 -58.
7. Lee, D.C., Lee, J.J. and Yun, S.J., "The Mechanical Characteristics of Smart Composite Structures with Embedded Optical Fiber Sensors", *Composite Structures*, Vol. 32, 1995, pp. 39 -50.
8. Lee, D.C. and Lee, J.J., "Fatigue Behavior of Composite Structures with Embedded Optical Fiber Sensors", *Proceedings of the Tenth International Conference on Composite Materials*, Vol. 5, 1995, pp. 307 -314.

EFFICIENT PARALLEL DESIGN/PLACEMENT OPTIMIZATION METHODOLOGY OF LARGE SMART STRUCTURES

Rong C. Shieh

MRJ Technology Solutions, 10560 Arrowhead Drive, Fairfax, Virginia 22030 USA

SUMMARY: The title methodology is formulated for optimal sizing of structural members and/or placement of active elements for structural weight minimization and shape control of piezoelectric-type smart structures in a parallel environment. The efficient, stochastic-type Integral Global/Local Optimization algorithm (IGLOA) is first extended to form a discrete design variable (D) version, IGLOA_D, and used to develop optimization procedures to solve this class of mixed integer/discrete/continuous design variable optimization problems. The design variables include both structural sizing (such as cross-sectional area, etc.) and active element placement/design (such as number, location, and/or control gain) variables. Several numerical design/placement optimization examples of 72- and 504-bar piezoelectric-type smart truss structures are presented for demonstration purposes. Excellent computational timing and optimization results have been obtained, indicating that the algorithm/methodology is capable of solving this class of computationally intense, large-size, smart structural optimization problems.

KEYWORDS: optimization method; integer, discrete, and continuous design variables; weight and energy minimization; active element placement; smart structures

INTRODUCTION

An optimal placement problem of active elements for structural shape control with respect to active element number, location, and control gain value is a mixed integer/discrete/continuous design variable (MIDCDV) optimization problem. Solution of this class of mixed design variable problems is particularly computationally intense because one cannot take advantage of gradient (sensitivity derivative) information in the optimization process. Three most widely used (and better) methods for solving MIDCDV problems are the Genetic Algorithms (GAs), Simulated Annealing (SA), and Branch and Bond Method (BBM). Application of these methods (with the most widely used GAs followed by the SA of stochastic-type) in optimal placement optimization problems of active elements or actuators for structural shape or vibration control can be found, among others, in [1-3], respectively. While these methods have been found effective in varying degrees for solving small-to-medium size optimization problems, they are generally not suitable for solving large-scale, MIDCDV-type optimization problems because of the excessive computational time required even in a massively parallel computational environment. Even for engineering optimization problems with continuous design variables (CDVs), some problems exist for the most widely used gradient-based optimization (GBO) methods [4] (such as a tendency to be trapped in a local minima, tendency for inefficiency or for frequently not yielding a convergent solution for large-scale optimization problems, and for less amenability than a stochastic method to a massively parallel computing environment).

Therefore, the author has taken a different unified approach for attacking large-scale engineering design optimization problems of both CDV and MIDCDV-types by formulating and enhancing a powerful, parallel stochastic-type algorithm, Integral Global/Local Optimization algorithm, IGLOA [5], which is a local random search augmented Integral Global Optimization (IGO) algorithm [6]. Application of the algorithm in solving large-scale structural design optimization problems has been made successfully [6]. A comparison study of the IGLOA with a vastly improved version of the widely used, stochastic-type Genetic Algorithms [7] shows that the former outperforms the latter in both computational efficiency and optimal global solution areas [8]. For example, in solving a structural weight minimization problem of an asymmetric 72-bar truss with 72 design variables (cross-sectional areas), the IGLOA was found to be computationally at least two-orders of magnitude more efficient than a significantly improved version of the GAs [7]. Furthermore, the IGLOA was also found to be capable of obtaining the best minimized structural weight result, i.e., 60% smaller than that based on the best improved GA at 100K function evaluations. Thus far, the IGLOA has been formulated mainly for and applied to the CDV optimization problems, although it was also used in an exploratory study of optimal placement problems of active elements for shape control of truss and frame structures [9]. In the present study, formal extension/refinement of the IGLOA algorithm to the MIDCDV case is first made and then applied to the sizing design/active element placement optimization problems of large smart structures. The optimization problems are posed as minimization of objective function of combined structural weight, strain energy, and/or control gain sum with respect to sizing design variables (cross-sectional areas, second moments of inertia, etc.) and/or active element placement/control variables (number, locations, and/or control gains) under a set of design and behavioral constraints. Formulation of the optimization problem is given in Section 2. Solution procedure/ methodology of the optimization problem is formulated in Section 3. Section 4 contains several example problems for demonstration purposes.

FORMULATION OF OPTIMIZATION PROBLEM

The design/placement optimization problems for weight minimization and/or shape control of a smart structure with mixed integer/discrete/continuous design variables (MIDCDVs) can be stated as below. Optimization is to be performed for the objective function F such that

$$Z = F(\{X\}) = \sum_{i=1, N_c} X_{Ci} F \rightarrow \text{Minimum} \quad (1a)$$

with respect to design variables $\{X\} = \{X_S|X_G|X_D|X_I|X_C\}$ and subjected to the constraints

$$\{X^L\} \leq \{X\} \leq \{X^U\}$$

$$(\{X_C^L\} = \{0\}, \{X_C^U\} = \{1\}); \sum_{i=1, N_c} X_{Ci} = 1 \quad (1b)$$

$$\{H(\{X\})\} \leq \{0\} \quad (1c)$$

$$\{L(\{X\})\} = \{0\} \quad (1d)$$

where $\{H\}$ and $\{L\}$ are the inequality behavioral and equality side constraint function vectors, respectively; N_C is the number of subobjective functions, F_i ; $\{X_K\}$ of vector lengths N_K with subscripts $K = S, G, D, I,$ and C denoting the partitioned subvectors of continuous cross-sectional sizing variables, continuous control gain variables, discrete active element location variables, integer variables (such as the number of active elements), and objective function coefficient variables ($N_C =$ number of subobjective functions, F_i), respectively; and superscripts L and U stand for "lower" and "upper" bounds, respectively.

Many subclasses of the smart structural optimization problems stated above exist. The following specific subobjective functions and design variables are considered:

- a) Subobjective functions -- $F_1 =$ structural weight (W), $F_2 =$ strain energy (Q) or maximum displacement (U_{max}), and $F_3 =$ control gain sum ($G_{sum}=G_1+G_2+...G_{N_C}$).
- b) Design variables -- i) $\{X_S\} = N_S$ -groups of independent structural element cross-sectional areas ($\{A\}$) with $N_S \leq N_E =$ number of structural elements for the truss structure case and areas ($\{A\}$) or areas and second moments of inertia ($\{X_S\}^T = \{\{A\}^T | \{J\}^T\}^T$ with $N_S \leq 2N_E$, where superscript T stands for "transpose" of a vector or matrix) for frame structures; ii) $\{X_G\} =$ control gains ($\{G\}$) of displacement amplifiers); iii) $\{X_D\} = \{X_L\} =$ active element (sensor/actuator) locations, which may be jointly expressed with $\{X_G\}$ by assigning X_{Gi} a zero or nonzero positive value ($\{0\} \ll \{G^L \leq \{G\} \leq \{G^U\}$) according to whether the i -th sensor/actuator pair of a structural element is active ($G_i > 0$) and present ($G_i > 0$) or absent ($G_i = 0$) with $N_G \leq n_p \times N_E$, where $n_p =$ maximum number of distributed sensor/actuator pairs in each structural element; iv) $\{X_I\} =$ number of groups of independent active elements (N_A) with $N_I = 1$; and v) $\{X_C\} =$ coefficient variables of $\{F_i\}$ ($i=1, \dots, N_C \leq 3$). If all of these design variables are present, the total number of design variables is $N_X = N_S + 2N_G + N_A + N_C$, of which the numbers of continuous, discrete, and integer variables are $N_S + N_G + N_C$, N_G , and $N_I (=1)$, respectively.
- c) Constraint functions $\{H\}$ -- i) behavioral variable constraints: displacement-type, $\{H_q\} = \{\{q\} - \{q_{max}\}\}$, stress-type, $\{H_s\} = \{s\} - \{s_{max}\}$, and piezoelectric active element voltage carrying capacity-type, $\{H_v\} = \{v\} - \{v_{max}\}$; ii) design variable inequality constraints as given in Eqn 1b, and iii) equality design variable constraints: unity coefficient design variable sum-type, $L_C = \sum_{i=1, N_C} X_{Ci}$ and constant gain sum (G^*)-type, $L_G = \sum_{i=1, N_A} X_{Gi} - G^*$, if appropriate.

PARALLEL SOLUTION PROCEDURE/METHODOLOGY

IGLO_D Optimization Algorithm (IGLOA_D)

As mentioned in the introductory section, the stochastic-type IGLOA is a local (Koosh) search augmented Integral Global Optimization (IGO) algorithm [5]. It is proposed to extend the algorithm to solve the class of mixed integer/discrete/continuous design variable optimization problem of smart structures as follows:

- Step 1. First specify an initial search region and establish an initial average.
- Step 2. The design variable search regions of integer-type (such as the number of active elements), discrete-type (locations of active elements quantified by those elements

having nonzero gain values), and continuous-type (sizing variables of all structural elements and gain values of active elements) are then sampled at random, and the corresponding objective functions evaluated.

- Step 3. Points at which the objective function are below the current average are added to the list of points, called "good" points. When the length of this list grows above some threshold, the average value of the objective function is computed for points on the list. Points at which the value of the objective function is above this new average are removed from the list.
- Step 4. The new search region is then chosen to be an N_X -dimensional rectangle slightly larger than required to hold all points on the current list of good points, where N_X is the number of design variables, which for the most general case of design/placement optimization problem under consideration is $N_X = N_S + N_G + N_L + N_A + N_C$. For continuous design variables and the integer variable (number of active distributed sensor/actuator pairs), the corresponding subregions can be specified by simply providing upper and lower design variable bounds to each design variable. For the discrete variables of sensor/actuator pair locations, a second (auxiliary) list must be established. This list contains the candidate active sensor/actuator pair IDs, from which N_A -design variables of active distributed sensor/actuator elements will be chosen. The simplest acceptable way is to include all candidate sensor/actuator IDs, as in [9]. In the present improved version of the algorithm, only those active element (or unit) IDs that are associated with those good points on the good point list are included in this second (good active element) list. It should be noted that, while the number of on-list active elements remain constant for the former case, it will shrink for the latter (present) case as the optimization search continues. Now the iteration is ready to begin again.
- Step 5. When many points have been examined but few points have been added to the history list of good points under consideration, one goes to local search mode that is called Local (Koosh) search. In this mode, small neighborhoods of the best points on the current good point list (including the auxiliary list) are searched. This is done only long enough to get enough good points on the list to be able to make meaningful updates to the average and search region. The search is then returned to the top level (IGO) algorithm. Depending on how the neighborhoods are defined for the discrete variables of active element locations in the above local search, different local discrete variable space search subalgorithms can be formulated. One concept of neighborhoods for active element locations are that of the structural elements adjacent to the onlist active elements.
- Step 6. These global/local search steps are repeated until meeting a specified stop criterion, which may be either that the original search region has shrunk to a small fraction value or that the percentage of change of two successive objective function values is below a given small percentage value.

In what follows, the study of the algorithm will be confined to a subalgorithm (IGLOA_D1) in which the discrete/integer variable search portions will be confined to the global (IGO) search mode only, while the local search will be done for the continuous design variable portions only, i.e., the algorithm described in Steps 1-6 minus the integer/discrete variable search portions in Step 5. This is because the full algorithm itself merits a separate in-depth study. We are also

interested in applying the subalgorithm to solve some large-scale design/ placement optimization problems of smart structures in a parallel environment.

Parallel Smart Structural Analysis Procedure

To perform design/placement optimization of smart structures, it is required to perform analysis/reanalysis to obtain structural response quantities appearing in the objective functions and/or constraint conditions. For this, only frame and truss-type smart structures comprised of active, distributed piezoelectric sensor/actuator structural elements and regular (passive) elements will be considered. The governing finite element (FE) equations of equilibrium for such structures with piezoelectric sensor/actuator layers bonded on the four outer faces of host structural element with hollow rectangular cross-section have been derived by the writer in [10]. The element end force ($\{f\}_i$)-displacement $\{u\}_i$ relationships for a typical active i -th element following negative position feedback law between a bi-layered sensor/actuator pair are of the form

$$\{f\}_i = [k]_i \{u\}_i - \{p\}_i \quad ([k]_i = [k_e]_i + [k_p]_i) \quad (2a)$$

where $\{p\}_i$ is the force vector associated with the distributed forces; $[k_e]_i$ and $[k_p]_i$ are the elastic and piezoelectric portions of the i -th element stiffness matrix, $[k]_i$, respectively. Note that $[k_p]_i$ and, thus, $[k]_i$ matrices are generally asymmetric. The former is given by

$$[k_p]_i = [b_a]_i [g]_i [b_s]_i \quad (2b)$$

Here, $[b_a]$ and $[b_s]$ are the (12x4) element actuator force ($\{f_a\}$) and (4x12) sensor signal matrices, respectively, and $[g]$ the (4x4) diagonal element position feedback control gain matrix. The $[b_a]$ and $[b_s]$ (and, thus, $[k_p]$) matrices have been derived by the writer for the hollow beam rectangular cross section case with PVDF piezoelectric sensor/actuator pair layers bonded to the four outer beam surfaces (sectors) [10]. The assembled equations of equilibrium for a frame or truss structure, after using the element end and nodal displacement vector ($\{u\}$)- $\{q\}$ relationships, $\{u\}_i = [B]_i \{q\}$ ($i = 1, 2, \dots, N_E$), where $[B]_i$ is a (12x N_q) Boolean matrix, can be written as

$$[K] \{q\} = \{P\} \quad ([K] = \sum_{i=1, N_E} [B]_i^T [k]_i [B]_i = [K_e] + [K_p], \{P\} = \sum_{i=1, N_E} [B]_i^T \{p\}_i) \quad (3)$$

To obtain relevant smart structural responses, Eqn 3 is first solved for $\{q\}$. The element end displacements $\{u\}_i$ are then also known. The actuator voltages can be obtained from voltage-displacement relations [10]. The stress quantities can be obtained in a typical fashion.

In a multiple-instruction-multiple-data (MIMD) computational environment using a message passing paradigm, such as that of the parallel IBM SP computers or PVM or MPI networked parallel workstation clusters, each processor has sufficient random access memory to solve a sufficiently large-size structural reanalysis problem in design optimization, particularly if the Preconditioned Conjugate Gradient (PCG) method of linear system solution is used to solve a typically sparse FE discretized linear system. Therefore, it is particularly efficient to assign a processor to solve a complete structural response solution of the multiple structural solutions (under randomly generated design variable sets) required for optimization.

Parallel Smart Structural Design/Placement Optimization (PSSDPO) Procedure

Processor Assignment Strategy: In a sequential computational environment, over 95 percent and less than 5 percent of computational time are spent on structural response computations/optimization (objective and constraint) function evaluations and remaining IGLO optimization search operations, respectively. Therefore, the former tasks (response computations/function evaluations) are assigned to parallel slave processors, with each processor performing one set of a complete structural response analysis, an associated constraint treatment operation, and a single objective function calculation. The latter (i.e., IGLO optimization search) task is assigned to a single master processor.

Load Balancing Strategy: In conjunction with the above processor assignment strategy, the following efficient load balancing strategy under a homogeneous or heterogeneous processing environment has been formulated and used. In this strategy, the required number of design variable sets are generated sequentially in the master processor and sent to multiple slave processors one-by-one for structural response function analyses and optimization function evaluations. Immediately after receiving a set of design variable/objective function data from a slave processor, the master processor generates a new design variable vector and sends it to that slave processor to perform new set of analyses/evaluations. This will result in keeping all multiple slave processor busy all the time, thus having faster (or in the homogeneous processor configuration case, less busy) processors yielding a larger number of analysis/evaluation sets.

PSSDPO Computational Procedure: These parallel computational/implementation strategies and structural analysis and IGLOA_D-based optimization procedures forms an efficient PSSDPO computational procedure.

PARALLEL IMPLEMENTATION AND NUMERICAL EXAMPLES

Parallel Implementation of the PSSDPO Computational Procedure

The IGLOA_D1-based subset of the foregoing PSSDPO computational procedure for truss and frame structures has been implemented into the writer's previously developed parallel structural analysis/design optimization code, PSTRAND, as PSTRAND_D1, on the IBM high performance SP2 computer platform and used in the following numerical study of example problems. The following three quantities will be used in measuring computational performance of a structural design optimization algorithm, methodology, and/or procedure: (i) number of function evaluations, N_F , in which one evaluation includes all calculations for relevant structural responses and satisfying constraints required for obtaining one objective function; (ii) accumulated cycles of iteration, N_{cyc} , to obtain convergent structural response solutions via the use of Preconditioned Conjugate Gradient (PCG) Method; and (iii) wall-clock (WC) time. The former two are good measurements for numerical performance evaluation independent of computer machine used (parallel or serial).

Assumptions and Design Parameters Used in the Example Problems

In the following examples, all element cross-sections of the host truss structures (Figure 1) are assumed to be of thin-walled, hollow rectangular-type fabricated from aluminum material, on

outface of it a pair of PVDF PZ layers (each with 0.022 cm thickness) is bonded if the element is of active type. The material properties and design parameters are given in Figure 1.

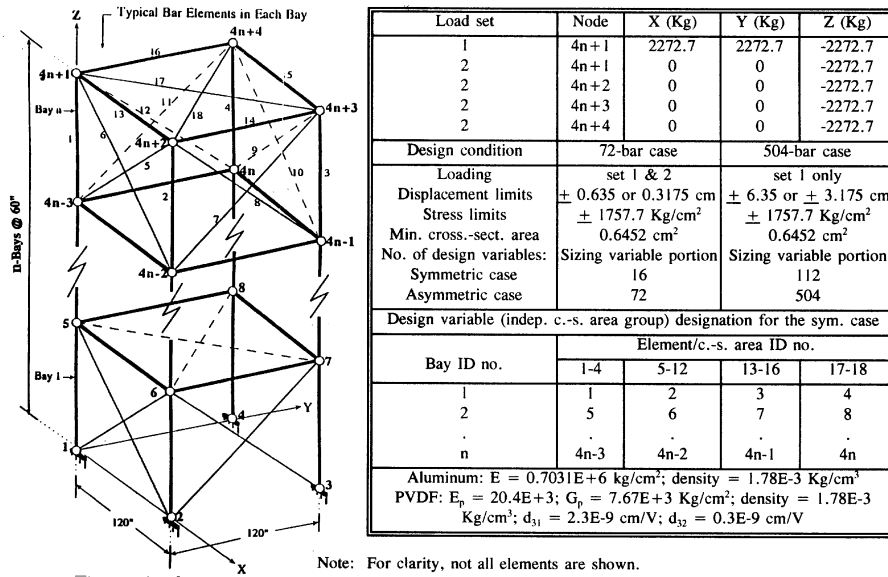


Figure 1. 72-Bar (n=4) and 504-Bar (n=28) Truss Minimum Weight Design Problems.

Symmetric 72-Bar Truss Optimization Cases

The passive host structure is subjected to two loading sets and is under displacement and stress constraints as given in Figure 1, in which the maximum allowable displacements are $q_{max} = 0.635$ and 0.3175 cm corresponding to the baseline and modified (Mod. 1) optimization design cases, respectively. In the optimization, an equivalent 144-bar truss structural model, comprised of two identical 72-bar trusses subjected to the first and second loading sets, respectively, is used.

Host Structural Weight Minimization Cases. The design variables in this case are the 16 independent groups of cross-sectional areas. The best minimum structural weight of $W_0=172.22$ Kg (= 379.66 lbs.) for the baseline case ($q_{max}= 0.635$ cm = 0.25 in) obtained by previous authors is based on a gradient-based optimization (GBO) algorithm of Sequential Quadratic Programming (SQP). The present IGLOA-based PSSDPO capability yielded the best weight result of $W = 1.0044W_0$ requiring only $N_F = 2755$ function evaluations and $N_{cyc} = 53,212$ accumulated PCG iteration cycles, indicating the effectiveness of the IGLOA-based structural optimization method. The corresponding IGLOA-based best weight result for the Mod. 1 design case ($q_{max} = 0.3175$ cm = 0.125 inch) is found to be $W = 1.96W_0$ and $W_1 = 1.95W_0 = 335.85$ Kg at (N_F, N_{cyc}) pairs of (2698, 52983) and (4388, 86460), respectively, corresponding to the cases of using coarser and finer searches.

Smart Structural Technology-Based Weight Minimization Cases: The Mod. 1 host structural weight minimization problem is to be performed with respect to not only the 16-groups of independent cross-sectional (c.-s.) areas as before, but also to 16 groups each of the active element's locations and control gains and a single integer design variable of a number of active elements with 49 design variables in all. The lower and upper bound pairs for these design variables are: (0.6452, 30.0) cm, (1, 16), (1E+09, 1E+12) V, and (1, 16), respectively. The constraint conditions are, as before, the maximum allowable displacement of 0.3175 cm

and 1757.7 Kg/cm². (More realistically, maximum allowable voltage constraints should also be imposed. Without such constraints, one needs to properly set/choose the allowable range of gain voltage and/or PZ layer thicknesses.) The minimum weight design and computational performance (N_F and N_{cyc}) results obtained in the preceding passive structural design, are shown in Table 1.

Table 1. Final Weight Minimization/Active Element Placement and Computational Performance Results for 72-Bar PZ Truss

Bay No.	Areas (cm ²)/Gains (GV) for Intra-Bay truss Member Nos.			
	1-4	5-12	13-16	17-18
1	0.8945/69.023	0.6744/33.510	0.6452/0.000	0.6549/0.000
2	0.8217/133.63	0.6452/39.238	0.6452/0.000	0.6452/0.000
3	0.6452/93.794	0.6452/27.334	0.8233/0.000	0.7309/0.000
4	1.8161/0.000	0.6452/37.812	0.8537/0.000	0.6452/36.296
Optimal results: $N_A = 8$ (46 act. elements); $W = 0.5132W_0 = 88.39$ Kg; $G_{sum} = 2.36E+12$ V; Av. Energy = 2,241.3 Kg-cm; $N_F = 6554$; $N_{cyc} = 179,284$.				

The best minimized weight result is $W_2 = 88.48$ Kg = $0.5132W_0 = 0.263W_1$. Because of the presence of 46 (8 groups) of the optimally placed active elements with optimally designed gain values, the total weight (including those of the optimally designed baseline host structure and additional PZ layers for the active elements) is reduced by nearly 50% while reducing the maximum displacement by 50%. Without such active elements, it requires nearly twice the baseline weight (four times of the smart structural weight) to reduce the maximum displacement of 0.635 cm by 50% to 0.3175 cm.

Smart Structural Energy Function Minimization Case. The baseline structural energy function (work done by external forces) was also minimized with respect to the active element's locations and gain values under a preassigned or optimally obtained number of active elements. Some optimization results are given in Table 2 under different gain sum (G_{sum}) values and number of active element groups (N_A). The weight ratios are seen to be greater than unity because of the additional PZ layer weight due to the presence of active elements.

Table 2. Final Energy Minimization/Active Element Placement Results_a

Case No.	G_{sum} (GV)	N_A	NAE group IDs ^b	W/W ₀	Av. E (kg-cm)	Max. q (cm)	N_F	N_{cyc}
1	2586.	12	3, 7, 8, 11	1.303	1502.	0.2546	3,262	71,883
2		13	3, 4, 7	1.312	2417.	0.4419	2,699	53,806
3		12 ^c	3, 7, 8, 11	1.302	2418.	0.4561	1,901	37,536
4		6 ^c	2, 5, 7, 8, 10, 12, 15, 16	1.149	2553.	0.5656	1,797	36,948

a. Under lower and upper gain value design limits of 1 to 1000 GVs.

b. Non-active element (NAE) group IDs = design area group IDs.

c. These are preassigned number of active elements, while the others (for cases 1-3) are obtained optimally.

For the preassigned cases (3 and 4) of $N_A = 12$ and 6, the final energy values are seen to be slightly and significantly greater than the optimum energy value, as was expected.

Symmetric 504-Bar Truss Optimization Cases (112 Groups of Design C.-S. Areas)

Host (Passive) Structural Weight Minimization Case. The structural configuration, loading set, and design parameters are shown in Figure 1 (with $n = 28$). The maximum allowable displacement now is 6.35 cm (5 inches). The truss is subjected to the first loading set only. The IGLOA-based final best minimized weight for the passive structure case was found to be $W_0 = \sim 3,860$ Kg (8500 lbs. = 5% of the initial average weight) consuming 40 wall-clock minutes on the 24-node NASA AMES SP2 of which approximately 50% of the time was spent on reducing the last 5% of the final weight. This is because (i) the rate of decrease in objective function becomes slower and slower as the average objective function approaches its minimum value and (ii) a stringent computational stopping criterion was used, which required three consecutive decreasing changes in average objective functions under two successive optimization iterations to be less than 0.01%. The number of functions evaluated to get the best optimization results are $\sim 74,000$.

Smart Structural Weight Minimization Case. To further reduce the structural weight, as in the preceding design case, one uses active elements and performs weight minimization/active element placement design with respect to both sizing and active element design variables (c.-s. areas and locations, gains, and/or number of active elements). The weight minimization results are given in Table 3.

Table 3. Optimal Structural Weight/Active Element Placement Design Results for Symmetric 504-Bar Smart Structure Truss ($N_A=20$) on the 16-node MHPCC SP2

Items	W_n/W_0	G_{sum} (V)	Max q (cm)	N_{Fn}	WC (min)
Final results	0.7234	3.152E+13	11.13	$\sim 80,000$	~ 90
20 active elem. group ID nos.	1, 14, 15, 20, 21, 28, 30, 45, 53, 57, 63, 70, 71, 75, 81, 84, 92, 100, 103, 112 (Total number of active elements = 80 in 20 groups)				

The final smart structural weight is seen to be $\sim 72\%$ of the minimized host (passive) structural weight under the same inequality displacement and stress constraint conditions and additional equality gain sum constraint of $3.152E+13$ V. It took $\sim 80K$ function evaluations and ~ 90 minutes of 16 node SP2 wall-clock time to solve this 504-bar smart truss structural optimization problem with 337 design variables. It took $\sim 80K$ function evaluations and ~ 90 minutes of 16 node SP2 wall-clock time to solve this 504-bar smart truss structural optimization problem with 337 design variables.

CONCLUSIONS

The Integral Global/Local algorithm (IGLOA) has been extended as IGLOA_D to solve the mixed integer/discrete/continuous design variable structural sizing/active placement design optimization problems of large smart structures for weight minimization and shape control. An IGLOA_D-based parallel design/placement optimization procedure for frame and truss-type smart structures was then formulated, and its subset (based on IGLOA_D1) was implemented on the IBM SP2 computer platform. Several numerical structural weight and energy minimization examples of plain and smart truss structure-type with 72 and 504 structural elements were presented for demonstration purposes. These study results show that the formulated optimization algorithm and procedure are capable of performing the optimization efficiently and excellently. However, more thorough study of the methodology

is needed, particularly in solving the large-scale/large structural optimization problems, such as the 504-bar truss problem studied here. A comparison study of the methodology with other methods to solve smart structural problems is desirable to further evaluate the parallel IGLOA_D-based methodology.

ACKNOWLEDGEMENTS

The SP2 computer resources used in the present work were provided by Maui High Performance Computing Center (MHPCC).

REFERENCES

1. Furuya, H. and Haftka, R.T., "Genetic Algorithms for Placing Actuators on Space Structures," *Proc. 5th Int. Conference on Genetic Algorithms*, Urbana, IL, July, 1993, pp. 536-542.
2. Chen, G.S., Bruno, R.J., and Salama, M., "Optimal Placement of Active/Passive Members in Structures Using Simulated Annealing," *AIAA Journal*, 29(8), 1991, pp. 1327-1334.
3. Padula, S.L. and Sandridge, C., "Active Strut Placement Using Integer Programming for the CSI Evolutionary Model," *Proc. 4th AIAA Symposium on Multidisciplinary Analysis and Optimization*, Cleveland, OH, Sept. 21-23, 1992, pp. 784-793.
4. Haftka, R.T., Gurdal, Z., & Karoraamat, M., *Element of Structural Optimization*, Second Revised Ed., Kluwer Academic Publishers, Boston, MA, 1990.
5. Shieh, R. and Wilson, G., "A massively Parallel Nonlinear Optimization Code Capability and Its Application in Structural Design," *Proc. 32nd AIAA SDM Conference*, Baltimore, MD, April 8-10, 1991, pp. 636-643.
6. Chew, S. and Zheng, Q., *Integral Global Optimization*, Springer-Verlag, N.Y. 1988.
7. Lin, C.-Y. and Hajela, P., "Genetic Search Strategies in Large Scale Optimization," *Proc. 34th AIAA SDM Conference*, La Jolla, CA, April 19-22, 1993, pp. 2437-2447.
8. Shieh, R.C., "Parallel Finite Element and/or Neural Network Technique-Based Structural Design Optimization Procedures and Computer Code Capabilities," 1996 *NASA Computational Aeroscience Workshop*, Ames Research Center, Moffett Field, CA, August 13-15, 1996.
9. Shieh, R.C., "Massively Parallel Optimal Placement/Specification Design Methodology of Active Elements for Structural Shape Control," *Proc. 5th Int. Conference on Adaptive Structures*, Dec. 5-7, 1994, Sendai, Japan, pp. 95-106.
10. Shieh, R.C., "Finite Element Formulation for Dynamic Response Analysis of Multiaxially Active Piezoelectric Beam Elements and Structures," *Proc. of 34th AIAA SDM Conference*, La Jolla, CA, April 19-21, 1993, pp. 3250-3260.

SENSITIVITY ANALYSIS OF COMPOSITE BEAM STRUCTURAL RESPONSE DUE TO DEFECTS

K. L. Springer and W. S. Chan¹

*Center for Composites Materials
Department of Mechanical and Aerospace Engineering
University of Texas at Arlington, U.S.A.*

SUMMARY: Composite materials contain defects originating from manufacturing processes and/or inservice life. There is a need for an analytically based acceptance and rejection criterion for composite with a defect. Hence, sensitivity analysis of composite structural response due to defects provides a guideline for this criterion. The focus of this paper is to investigate the change in maximum midplane deflection of a composite beam due to ply angle misorientation, fiber waviness and delamination. An cantilever beam made of IM6/3501-b Gr/ep with $[\pm 45/0/90]_{8s}$ was used to illustrate the developed methodology.

INTRODUCTION

Composite materials contain defects originating from manufacturing processes and/or inservice life. Defects such as misarranged fiber orientation, fiber waviness, ply cracking, and delamination can significantly affect the structural response of a system. Instead of re-manufacturing or replacing composite structural components because of defects, designers and engineers want to know what is the overall effect of the defect on the particular system. Therefore, the need for an analytically based acceptance and rejection criterion for composite structures with a defect exists.

In order to quantify the effects of certain parameters on a system, the tools of sensitivity analysis are employed. According to Frank [1], sensitivity analysis provides the basic methods to study the sensitivity of a system to parameter variations. Adelman and Haftka [2] surveyed sensitivity analysis methods applicable to the calculation of structural sensitivity derivatives for structures. Recently, sensitivity analysis has been employed to study the behavior of composite materials. King and Chan[3] studied the effects of taper angle and ply angle orientation on tension and bending loads, Chan and Chou [4] investigated the effects of delamination and fiber waviness on effective axial and bending stiffnesses. Chan and Wang [5] predicted structural properties of laminated composites with fiber waviness.

The focus of this paper is to investigate the change in structural response of a composite beam due to defects. In particular, the effects of ply angle orientation, fiber waviness, and delamination on the maximum midplane deflection of a cantilever composite beam are studied. The maximum midplane deflection equation is derived.

STRUCTURAL RESPONSE OF A CANTILEVER COMPOSITE BEAM

Composite Beam Description

A cantilever composite beam made of IM6/3501-6 graphite epoxy with the lay-up [45/-45/0/90]_{8s} is used. The uniaxial lamina material properties of IM6/3501-6 graphite epoxy are

$$E_1 = 24.8 \times 10^6 \text{ Psi}, E_2 = 1.41 \times 10^6 \text{ Psi}, G_{12} = 0.9 \times 10^6 \text{ Psi}$$

$$\nu_{12} = 0.329, t_{\text{ply}} = 0.0052 \text{ in}, \rho = 0.05 \text{ lbm / in}^3$$

The cantilever composite beam shown in Fig. 1 is loaded laterally with a uniform pressure.

Beam Deflection

The equilibrium equation for the bending of a symmetric laminate under lateral load and with no hygrothermal effects is

$$\frac{\partial^2 M_x}{\partial x^2} + 2 \frac{\partial^2 M_{xy}}{\partial x \partial y} + \frac{\partial^2 M_y}{\partial y^2} + \frac{q_0}{b} = 0 \quad (1)$$

where q_0 is the uniform load. For a beam subjected to M_x only, the above equation becomes

$$\frac{\partial^4 w_0}{\partial x^4} = \frac{d_{11} q_0}{b} \quad (2)$$

where w_0 is the midplane deflection of the beam and d_{11} is the flexibility of the laminate.

It should be noted that because of anisotropy characteristics, a composite beam will not deflect uniformly across its width. In other words, w_0 is not independent of y . Previous work on the beam deflection, the width effect of the beam is neglected [6,7].

By integrating the above differential equation with the following boundary conditions

$$\begin{aligned} w_0(0, y) = 0, \quad \frac{\partial w_0(0, y)}{\partial x} = 0 \\ M_x(L, 0) = 0, \quad V_x(L, 0) = 0 \\ \int_{-b/2}^{b/2} \frac{\partial^2 w_0}{\partial x \partial y} dy \Big|_{x=L} = 0 \end{aligned} \quad (3)$$

the midplane deflection of a cantilever composite beam as function of x and y can be obtained as

$$w_0(x, y) = \frac{d_{11} q_0 x^4}{24b} + \frac{q_0 x^3}{12b} (d_{16} y - 2d_{11} L) + \frac{q_0 x^2}{8b} (2d_{12} y^2 - d_{16} Ly + 2d_{11} L^2) \quad (4)$$

It should be mentioned that the last boundary condition in Equation (3) states that the twisting moment is zero at $x=L$.

The anisotropic coupling terms, d_{12} and d_{16} are generally neglected for orthotropic analysis; however, for beams that are thin and not antisymmetric, neglecting d_{12} and d_{16} can

render non-conservative results [8]. The d_{12} term contributes deflection effects due to Poisson's ratio, and the d_{16} term induces twisting curvature. Note, for beams with a high length to width ratio, the effect of d_{12} is negligible.

By letting $x=L$, the maximum midplane deflection for a cantilever composite beam as a function of y results:

$$w_{max} = \frac{q_0 L^2}{24b} (6d_{12}y^2 - d_{16}Ly + 3d_{11}L^2) \quad (5)$$

SENSITIVITY ANALYSIS

Ply Angle Orientation

Effects on Maximum Midplane Deflection

The change in w_{max} due to θ can be obtained by differentiating w_{max} in Eqn. (5) with respect to θ .

$$\frac{\partial w_{max}}{\partial \theta} = \frac{\partial w_{max}}{\partial d_{11}} \cdot \frac{\partial d_{11}}{\partial \theta} + \frac{\partial w_{max}}{\partial d_{12}} \cdot \frac{\partial d_{12}}{\partial \theta} + \frac{\partial w_{max}}{\partial d_{16}} \cdot \frac{\partial d_{16}}{\partial \theta} \quad (6)$$

The derivatives $\partial w_{max}/\partial d_{11}$, $\partial w_{max}/\partial d_{12}$, and $\partial w_{max}/\partial d_{16}$ can be easily obtained and $\partial d_{11}/\partial \theta$, $\partial d_{12}/\partial \theta$ and $\partial d_{16}/\partial \theta$ are given in Reference [3].

Figure 2 depicts normalized w_{max} (@ $y=0$) versus θ for five 0° ply locations. The results indicated that, a maximum w_{max} is found at $\theta = 60.5^\circ$ and w_{max} increases as the location of the 0° ply moves farther away from the laminate midplane. Figure 3 indicates that w_{max} sensitivity to θ increases as the location of the 0° ply moves farther away from the laminate midplane. Figure 4 show normalized w_{max} versus width for a thick laminate $[45, -45, 0, 90]_{8s}$ and a thin laminate $[45, -45, 0, 90]_{2s}$. As expected, maximum w_{max} does not occur at $y = 0$ due to beam twist (i.e. the d_{16} term). As the beam becomes thinner, the twist becomes more unsymmetrical and the maximum w_{max} shifts farther from the center of the beam.

Fiber Waviness

The geometry of fiber waviness shown in Figure 5 is defined by a sinusoidal wave function in the principal material axis. The fiber orientation ϕ at any given position is defined in Ref. [5] as

$$\phi = \tan^{-1} \left[\pi R \cos \left(\frac{\pi x}{L} \right) \right], \quad R = A/L \quad (7)$$

where R is the fiber waviness factor. It is assumed that all fibers in a given lamina have the same wave function, and the wave functions are parallel throughout the lamina.

Effects on Maximum Midplane Deflection

The change in w_{max} due to R is defined by

$$\frac{\partial w_{max}}{\partial R} = \frac{\partial w_{max}}{\partial d_{11}} \cdot \frac{\partial d_{11}}{\partial R} \quad (8)$$

The terms $\partial d_{11}/\partial R$ and $\partial w_{max}/\partial d_{11}$ were explicitly obtained and given in Ref. [9].

The result shown in Fig. 6 indicates that w_{max} sensitivity to R increases as the ply containing the fiber waviness is placed further away from the laminate midplane.

Delamination

All analysis in this section is based on the assumption that delaminations exist symmetrically in the beam cross section as shown in Fig. 7. This assumption prevents coupling and subsequent introduction of a global [B] matrix.

Structural Response Sensitivity to Delamination Length

Utilizing the following continuity conditions at $x = c$

$$w_0^I = w_0^{II} \quad , \quad \frac{\partial w_0^I}{\partial x} = \frac{\partial w_0^{II}}{\partial x} \quad (9)$$

the midplane deflection for the beam shown in Fig. 7 can be obtained as

$$\begin{aligned} w_0^{II} &= \frac{d_{11}^{II} q_0 x^4}{24b} + \frac{q_0 x}{6b} [c^3 (d_{11}^I - d_{11}^{II}) - d_{11}^I L^3] + \\ &\quad \frac{q_0}{8b} [c^4 (d_{11}^{II} - d_{11}^I) - d_{11}^I L^4] \quad \text{for} \quad 0 \leq x \leq c \\ w_0^I &= \frac{d_{11}^I q_0}{24b} (x^4 - 4L^3 x + 3L^4) \quad \text{for} \quad c \leq x \leq L \end{aligned} \quad (10)$$

The maximum midplane deflection (w_{max}) occurs at $x=0$ is

$$w_{max} = \frac{q_0}{8b} [(d_{11}^{II} - d_{11}^I) c^4 + d_{11}^I L^4] \quad (11)$$

It should be noted that all the d_{11} 's are function of delamination width, a . The sensitivity of the maximum midplane deflection (w_{max}) to delamination length is defined by

$$\frac{\partial w_{max}}{\partial c} = \frac{q_0 c^3}{2b} (d_{11}^{II} - d_{11}^I) \quad (12)$$

Figure 8 depicts normalized w_{max} versus normalized delamination length (c/L) at the following four ply interfaces:

- 1) 90/45 Interface between plies 28 & 29
- 2) 45/-45 Interface between plies 29 & 30

- 3) -45/0 Interface between plies 30 & 31
- 4) 0/90 Interface between plies 31 & 32

The delamination width a remains constant @ $a = 0.2$ in. An interesting observation is made from Figure 8. For delamination occurring at the 0/90 and 90/45 ply interfaces, w_{max} decreases as the delamination length is increased. This observation implies that the beam actually becomes stiffer as the delamination length is increased for delamination at the 0/90 and 90/45 ply interfaces. The 0/90 ply interface is the most sensitive to delamination length, and the 45/-45 ply interface is the least sensitive to delamination length. For the other two ply interfaces, -45/0 and +45/-45, w_{max} increases as the delamination length increases. Figure 9 exhibits w_{max} sensitivity to delamination length vs. normalized delamination length (c/L). At all interfaces, sensitivity to delamination length is not significant until $c/L=0.3$. Similar results to Figure 10 are obtained.

CONCLUSIONS

Closed-form solutions for sensitivity analysis were developed to quantify the effects of defects on the structural response of composite beams. An expression of a cantilevered composite beam deflection accounting for the width effect was also developed. The following conclusions were deduced for a rectangular cantilever composite beam made of IM6/3501-6 graphite epoxy with the lay-up $[45/-45/0/90]_8s$

- 1) The location of the maximum midplane deflection shifts away from the center of the beam width when the laminate with the same layup becomes thinner.
- 2) The maximum midplane deflection sensitivity to ply angle orientation and fiber waviness increases as the ply containing the ply angle orientation or fiber waviness is located farther away from the laminate midplane.
- 3) For delamination occurring at 0/90 and 90/45 ply interfaces, maximum midplane deflection decreases as the delamination length increases, implying that the beam actually becomes stiffer.
- 4) For delamination occurring at -45/0 and 45/-45 ply interfaces, maximum midplane deflection increases as the delamination length.

REFERENCES

1. Frank, P. M., *Introduction to System Sensitivity Theory*, Academic Press, Inc., 1978.
2. Adelman, H. M. and Haftka, R. T., "Sensitivity Analysis of Discrete Structural Systems", *AIAA Journal*, Vol. 24, No. 5, May 1986, pp. 823-832.
3. King, Y. F. and Chan, W. S. "Sensitivity Analysis of Delamination Characterization in Composite Tapered Beams", *J. of Reinforced Plastics and Composites*, Vol. 12, No. 4, April 1993, pp. 386-403.

4. Chan, W. S. and Chou, C. J., "Effects of Delamination and Ply Fiber Waviness on Effective Axial and Bending Stiffnesses in Composite Laminates", *Composite Structures*, Vol. 30, 1995, pp.299-309.
5. Chan, W. S. and Wang, J. S., "Prediction of Structural Properties of Laminated Composites with a Fiber Waviness", *Journal of Thermoplastic Composite Materials*, Vol. 7, No. 3, pp. 243-260, July 1994.
6. Skudra, A. M., Bulavs, F. Y., Gurvich, M. R., and Kruklinsh, A. A., *Structural Analysis of Composite Beam Systems*, Technomic Publishing Company, Inc., 1991.
7. Vinson, J. R. and Sierakowski, R. L., *The Behavior of Structures Composed of Composite Materials*, Kluwer Academic Publishers, 1987.
8. Halpin, J. C., *Primer on Composite Materials: Analysis*, Technomic Publishing Company, Inc., 1984.
9. Springer, K. L., *Sensitivity Analysis of Composite Beam Structural Response*, Master Thesis, University of Texas at Arlington, August 1994.

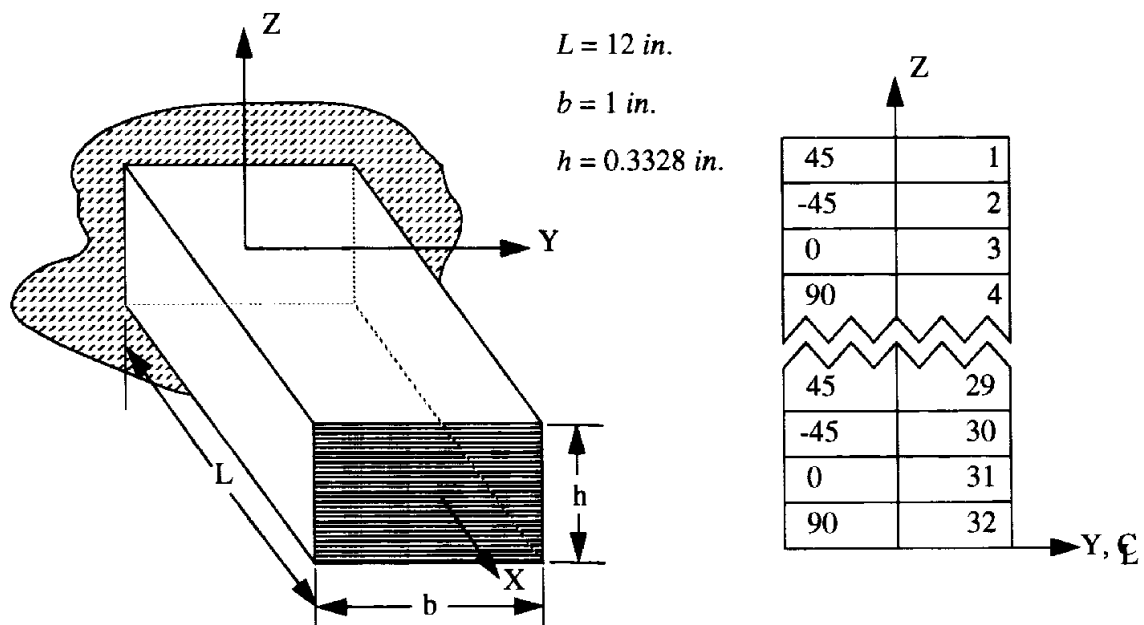


Figure 1. Schematic of Cantilever Composite Beam

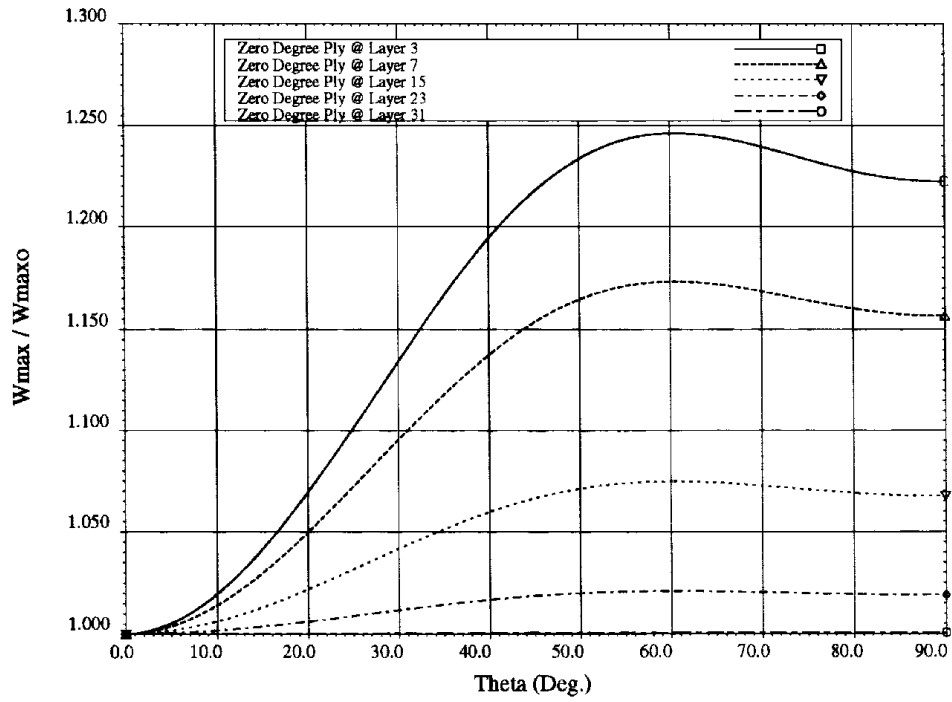


Figure 2. Normalized Maximum Midplane Deflection vs. Ply Angle Orientation (0-90 Degrees)

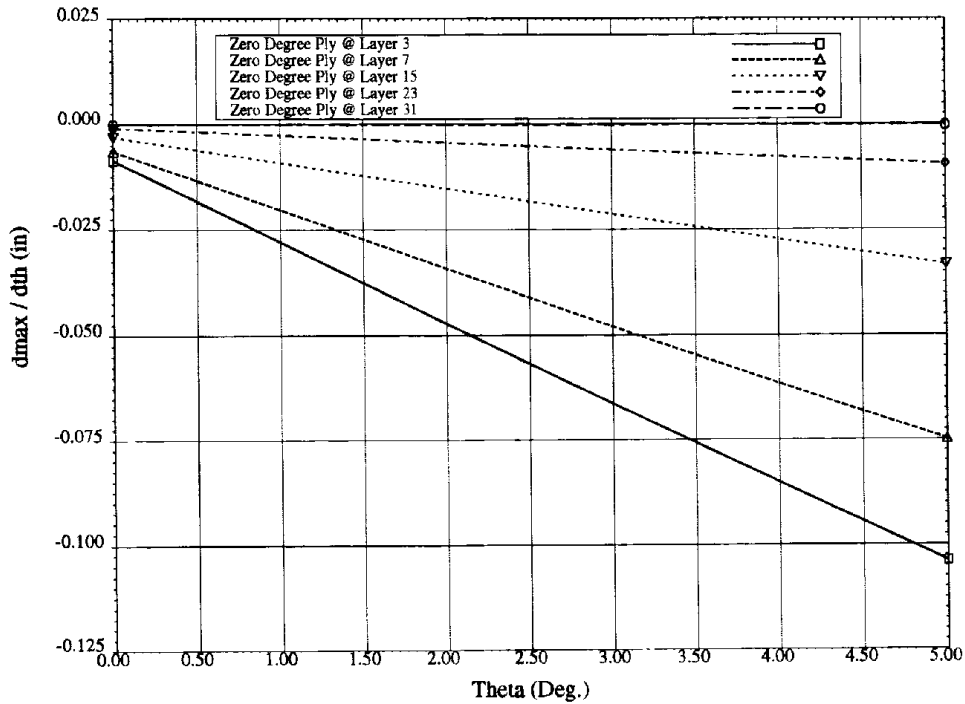


Figure 3. Maximum Midplane Deflection Sensitivity to Ply Angle Orientation (0-5 Degrees)

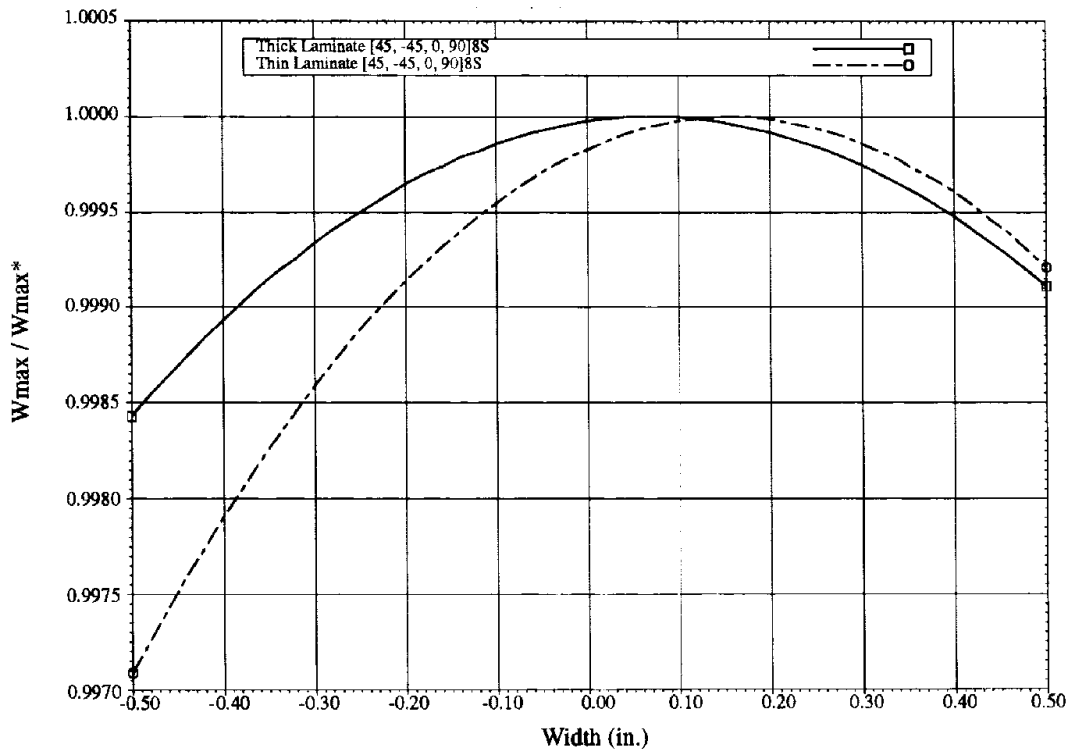


Figure 4. Normalized Maximum Midplane Deflection vs. Width

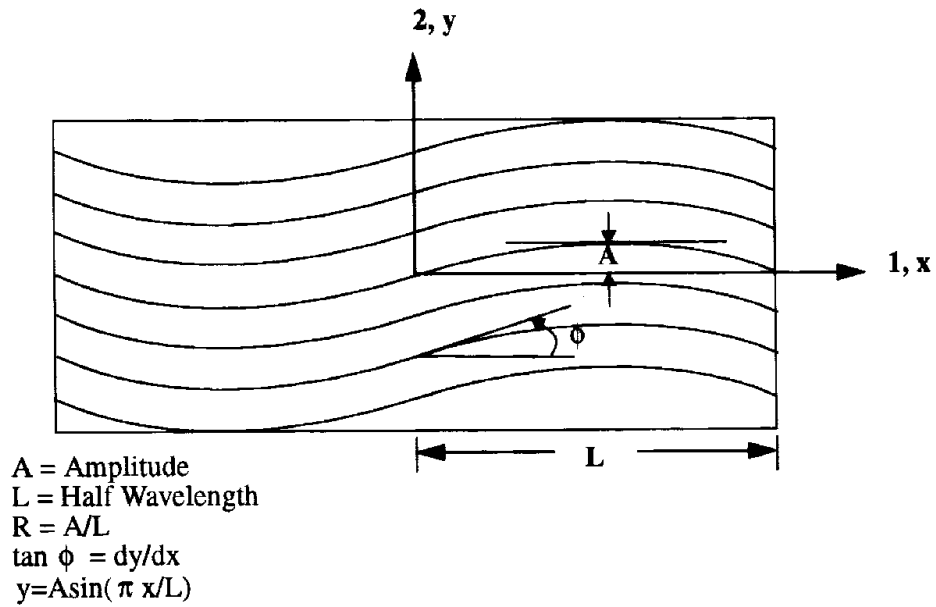


Figure 5. Geometry of Fiber Waviness

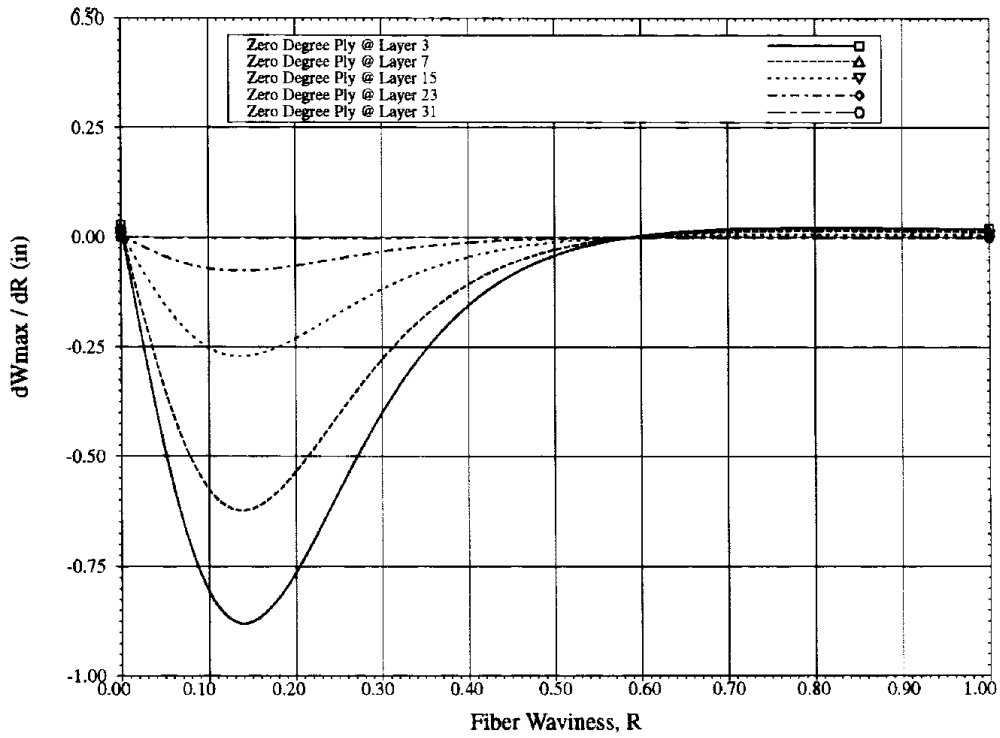


Figure 6. Maximum Midplane Deflection Sensitivity to Fiber Waviness Factor

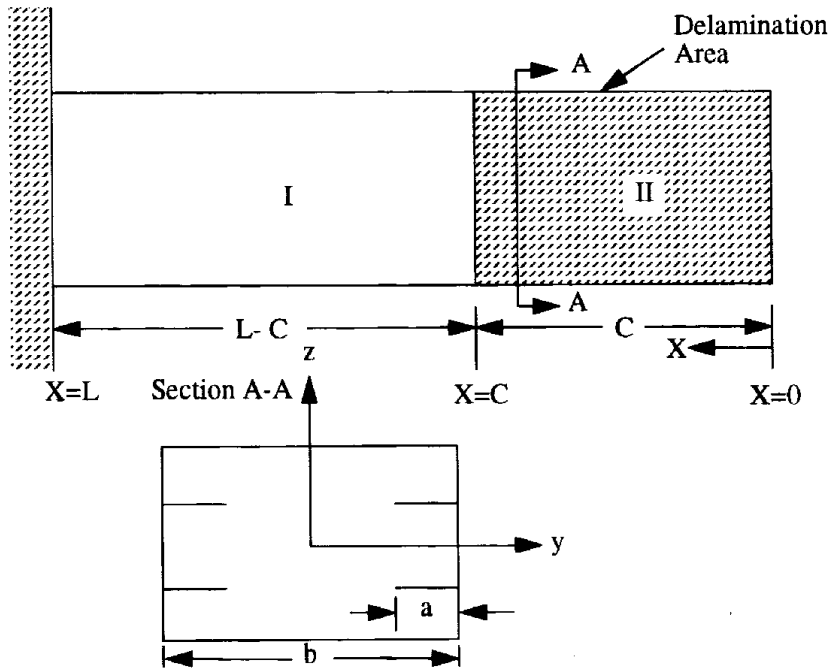


Figure 7. Cantilever Beam With Delaminations

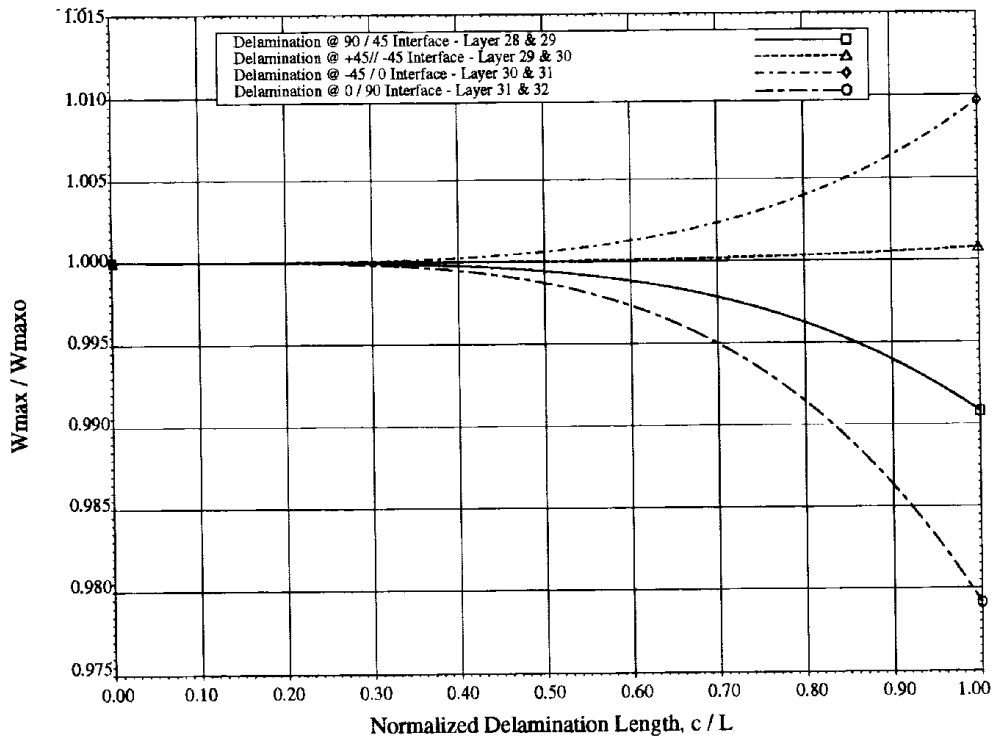


Figure 8. Normalized Maximum Midplane Deflection vs. Delamination Length

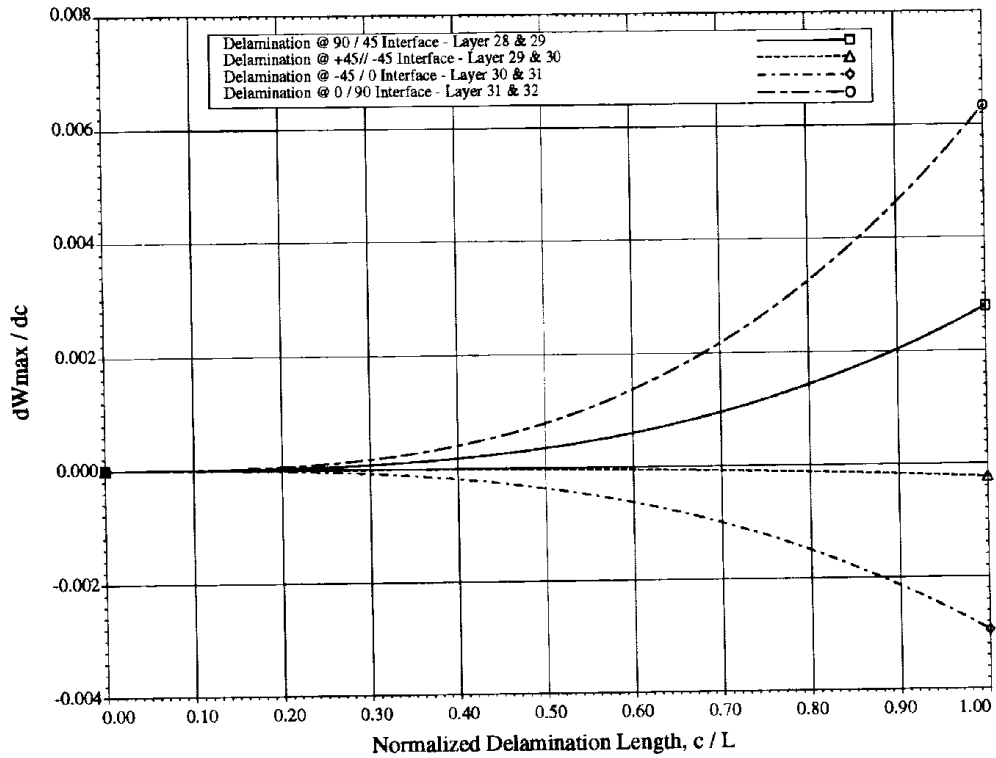


Figure 9. Maximum Midplane Deflection Sensitivity to Delamination Length

A MODEL FOR THE BEHAVIOUR OF THICK COMPOSITE LAMINATES IN HYDROCARBON FIRES

N. Dodds and A. G. Gibson

*Centre for Composite Materials Engineering, University of Newcastle upon Tyne.
Newcastle upon Tyne NE1 7RU. UK.*

SUMMARY: A model for the fire behaviour of thick composite laminates in hydrocarbon fires has been developed and experimentally validated by furnace fire testing. The integrity of certain composite materials in the form of thick laminates under severe fire conditions is demonstrated to be surprisingly good. Heat transfer through the laminate is slow in comparison to metallic materials which leads to long survival times and containment of the fire. The endothermic decomposition of the matrix provides the basic mechanism for slowing down the heat transfer through composite laminates, whilst the overall integrity of the structure is maintained for considerable time due to the non-combustible reinforcement.

KEYWORDS: fire behaviour, structural integrity, fire testing, cone calorimeter, ablation, offshore, modelling

INTRODUCTION

In almost every application for composites the issue of material response to fire is one which must be addressed. Of course, whenever a potentially combustible organic matrix is present the resultant hazards due to heat release, smoke and toxicity must be taken into account: a comprehensive range of standard test procedures is available to characterise behaviour and the composites industry has applied these responsibly for many years. In the past the question of combustibility has prevented the application of composite materials in fire-sensitive areas, but with the adoption of performance-led design procedures, composites are finding increasing application in new structures. Aside from the combustibility issue, it must be recognised that exceptional structural integrity can be achieved in certain types of composite structures under fire conditions. The combination of low thermal conductivity, resin endotherm effects and structural integrity combine to provide excellent fire characteristics for application as structural members, fire walls, blast panels and passive fire protection systems.

The main thrust of this paper concerns the use of composite materials in large engineering structures and their integrity when subjected to fire. Research carried out to support the use of these materials in the offshore industry shows that in the correct circumstances the fire integrity of large composite structures can be superior to that of their steel counterparts.

USE OF COMPOSITE MATERIALS OFFSHORE

Markets for composites of all types (glass, aramid, carbon fibre) in large scale engineering structures are expected to increase considerably in the future. The most promising materials, for cost reasons are glass reinforced plastics (GRP), which are now entering the offshore industry in a range of areas where their lightness and corrosion resistance can be used to special advantage. The authors are principally involved in research related to the offshore industry [1], but clearly many of the issues raised here will relate to other industries involving processing and large scale structures. The most important factor in composites gaining access to the offshore industry has been the recent move away from prescriptive regulations requiring non-combustibility towards a *performance-based* approach to design- a change which is also taking place in other industries.

Two important application areas have led the use of GRP offshore. The first is pipework for aqueous liquids (especially seawater for fire-water distribution mains) [2]. In these applications glass reinforced epoxy (GRE) pipework has been shown to have a lower through-life cost than competing metallic systems, which include duplex stainless steel, Inconel and even titanium. It has been well-known for some time that liquid-filled composite pipes and tanks show excellent resistance to fire. In those cases where pipes under threat may not contain liquid they can, of course, be protected by conventional passive fire protection materials. Comprehensive performance-based guidelines for GRE pipes, issued by the UK Offshore Operators Association [3] have significantly accelerated these applications.

The other significant application is in panelling for both floors and walls. The first major tonnage on a North Sea platform involved fire protection panels for the helideck of the Amerada Hess Rob Roy rig, which was deployed in the 1980s. It is interesting to note that, despite their perceived combustibility, all the early uses of GRP offshore involved applications where fire was an important issue. Offshore applications of composites have been discussed in several recent publications, including references [4] and [5].

STRUCTURAL PERFORMANCE REQUIREMENTS VS. PERCEIVED HAZARDS

The key factors in relation to fire hazard are; smoke and toxicity, ignitability/spread of flame, heat release and structural integrity. These factors assume different degrees of importance, depending upon the engineering application area. In enclosed locations for instance, where personnel may be present, smoke and toxicity, which determine ease of escape and survivability are of paramount importance. Ignitability, spread of flame and heat release, on the other hand, are important in determining the development of a fire when there is a risk of ignition from some other source, such as an electrical fault or some other defined fire hazard. Heat release from the composite material may or may not be important, depending on the overall load of combustible material present. In offshore plant, for instance, when the main hazard is a hydrocarbon fire from a large quantity of stored oil or gas, heat release from the composite materials present may not be of great significance.

Structural integrity is the most important issue when a composite structure is required to retain its function for a period of time during fire exposure. This applies in several structural and semi-structural applications, as in the cases of composite pipework or pultruded gratings and handrails. It will be shown that the most significant factor in maintaining integrity and in preventing the transmission of heat through the structure is the *slow burn-through* effect,

which can be observed in many types of composite, provided the section is of sufficient thickness (usually above about 9mm). Because of the ability of composites to limit heat transmission they are beginning to be used in roles involving passive fire protection, such as in the protection of steel jacket structures and risers offshore.

QUANTIFYING THE FIRE RESPONSE OF COMPOSITE STRUCTURES

A range of different fire performance requirements may apply, depending on the application and environment. There is a similarly broad range of standard tests [6], which may be used to quantify the response of the material. Two major test procedures are the oxygen consumption calorimeter and the furnace fire test. The NBS Cone Calorimeter [7], provides an accurate method of measuring heat release and combustion products in a fire.

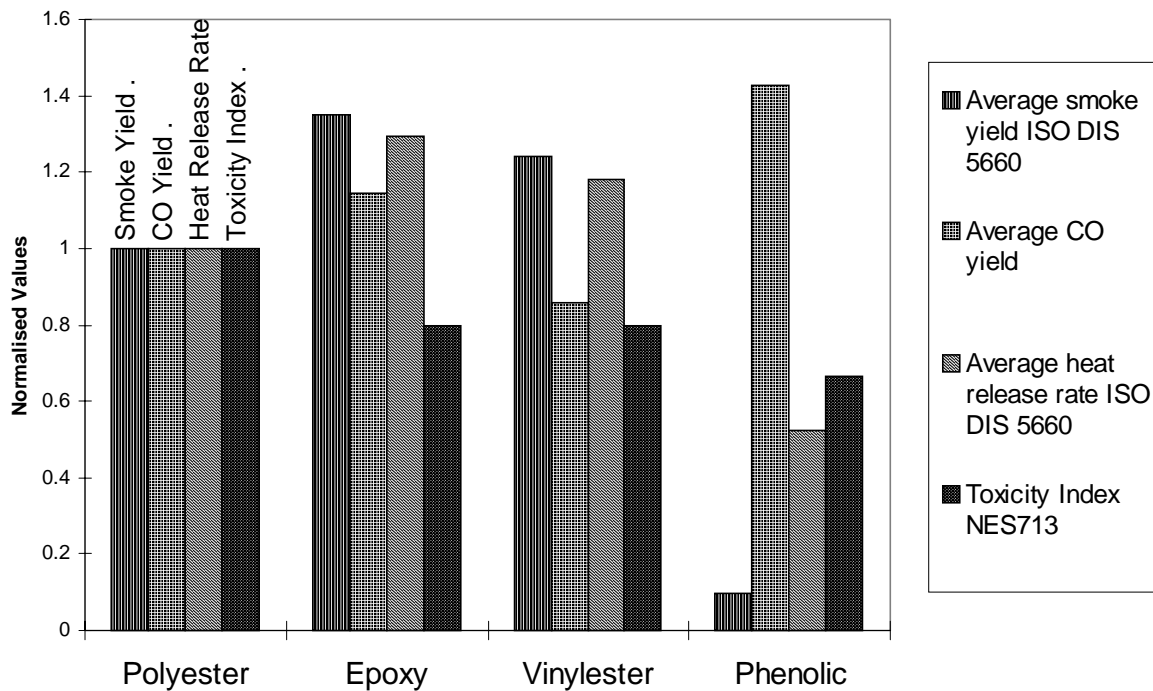


Figure 1 Comparison of the main resin systems used in composite engineering structures. Cone calorimeter results and the overall toxicity index according to standard test procedures are plotted using polyester as the baseline. The composite systems are: isophthalic polyester (Freemans Stypol 73/2785), amine-cured epoxy (Araldite LY1927 HY1927), vinyl ester (Freemans Stypol Atlac 580/05) and phenolic (BP Cellobond J2018/L Phencat 10) 50% w/w glass woven roving laminates. Specimen thickness 6mm. For the cone calorimeter test average values obtained for an irradiance of 50 kw/m² are plotted.

A comparison of the heat release and toxicity of the different matrix systems carried out using standard test procedures is shown in Figure. 1. The baseline is isophthalic polyester. The lower heat release and smoke emission of the phenolic laminates is evident. An increased yield of carbon monoxide is observed for phenolic but the overall toxicity index remains lower than competing resins. Clearly there are strong arguments for the use of phenolic systems in the most personnel-sensitive areas.

Figure 2 shows total heat release values (expressed per unit volume of composite) measured by cone calorimetry, plotted against laminate thickness. All the materials show a thickness effect: the effective heat release falls considerably as the laminate thickness increases, suggesting that composites will perform well when used in thick sections.

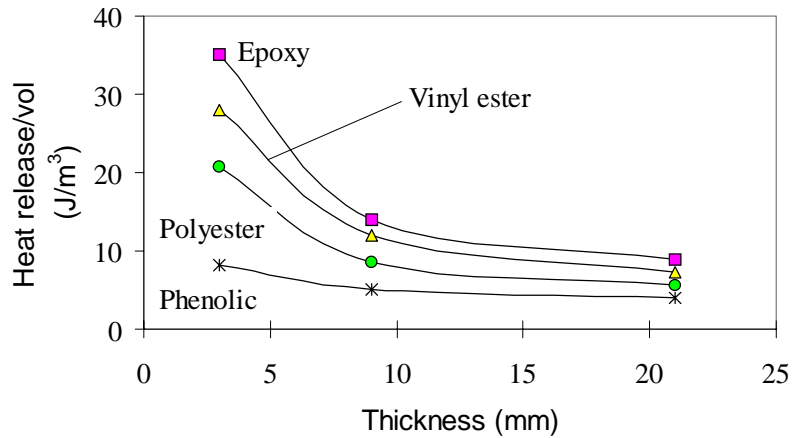


Figure 2 Total heat release per unit volume as a function of laminate thickness. The specimen details are identical to those in Figure 1.

FURNACE TESTS

Furnace tests are used to measure the structural integrity of composites in fires [6]. Experimental fire tests were carried out using a purpose built furnace with an active volume of 3.375 cubic metres, fired by a single portable burner.

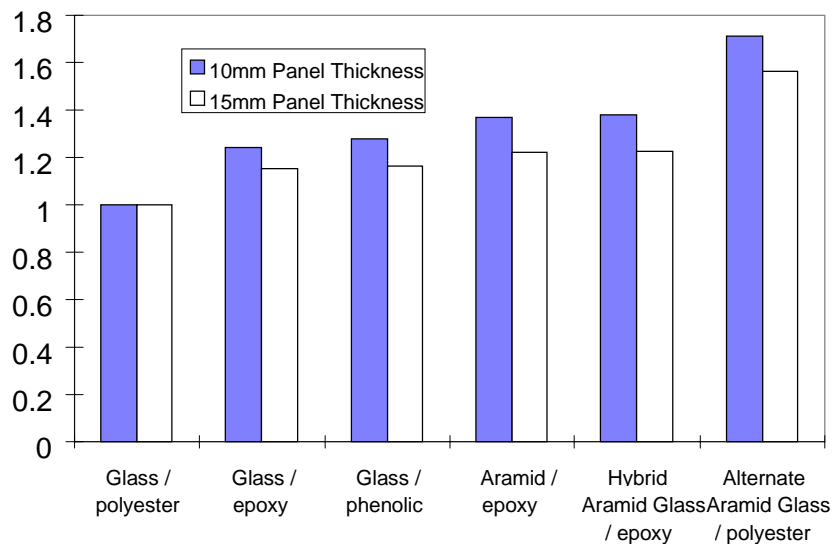


Figure 3 Laminated panel response to hydrocarbon curve furnace fire tests ranked as a Relative Fire Barrier Performance Index. The ranking is the time required for the cold face to reach 160°C normalised with reference to standard polyester glass woven roving laminates.

The test panels were mounted vertically in a specially designed frame forming the door of the furnace. For the purposes of model validation the furnace temperature was programmed to

follow the hydrocarbon fire curve and the fire resistance of the material tested conventionally expressed as the time taken for the cold face of the panel to reach a temperature of 160°C. Experimental relative fire barrier performance data derived from hydrocarbon curve furnace fire testing is shown in Figure 3. The standard development material has been taken as isophthalic polyester / glass woven roving with a glass volume fraction of 55%. The most successful materials in terms of thermal barrier performance are those with the highest endothermic contribution. For panels with an aramid content the reinforcement also decomposes endothermically this is illustrated by the advantageous thermal barrier performance observed in Figure 3, especially when aramid is combined with glass reinforcement for added structural integrity.

In the furnace fire tests the panel cold face is exposed to stationary air, which removes very little heat. If heat is actually removed from one side of the laminate the time to failure can be even further prolonged. This effect can usefully be employed with composite pipework containing a stationary, or better still, flowing fluid, and is one of the reasons why GRE pipes have begun to be so widely-used for offshore fire-water systems.

MODELLING THE MATERIAL RESPONSE TO HYDROCARBON FIRE

The factors which contribute to the slow burn-through effect in composites are thermal conduction through the laminate, transport properties of the residual reinforcement (and carbonaceous char, if present), the endotherm due to resin decomposition and the mass flux or convection of volatiles away from the hot surface.

A thermal model [8], taking into account the decomposition processes mentioned above has been developed to assist in the prediction of fire integrity. This model, based on previously reported models for ablative behaviour [9-11] may be used with a range of different boundary conditions and has been validated by tests on laminates of different thickness'. The basic governing equation expressed in one dimension is of the form:

$$\rho C_p \frac{\partial T}{\partial t} = \frac{\partial}{\partial x} \left(k \frac{\partial T}{\partial x} \right) + M_G \frac{\partial}{\partial x} h_G - \rho A e^{-\frac{E}{RT}} (Q_p - h_c + h_G) \quad (1)$$

where:

- T , t and x are temperature, time and through-thickness coordinate, respectively
- ρ , C_p and k are the density, specific heat and conductivity of the composite
- M_G is the mass flux of volatiles from decomposition
- h_A and h_G are the respective enthalpies of the composite and evolved gas
- Q_p is the endothermic decomposition energy
- A , E and R are the rate constants for the decomposition reaction and the gas constant.

The three terms on the right hand side of equation (1) relate to heat conduction, volatile convection and endothermic resin decomposition, respectively. Modelling of the thermal conductivity and specific heat as the composite is ablated is described fully in reference [12]. The rate constants for the decomposition term are estimated from thermo-gravimetric measurements on laminate samples.

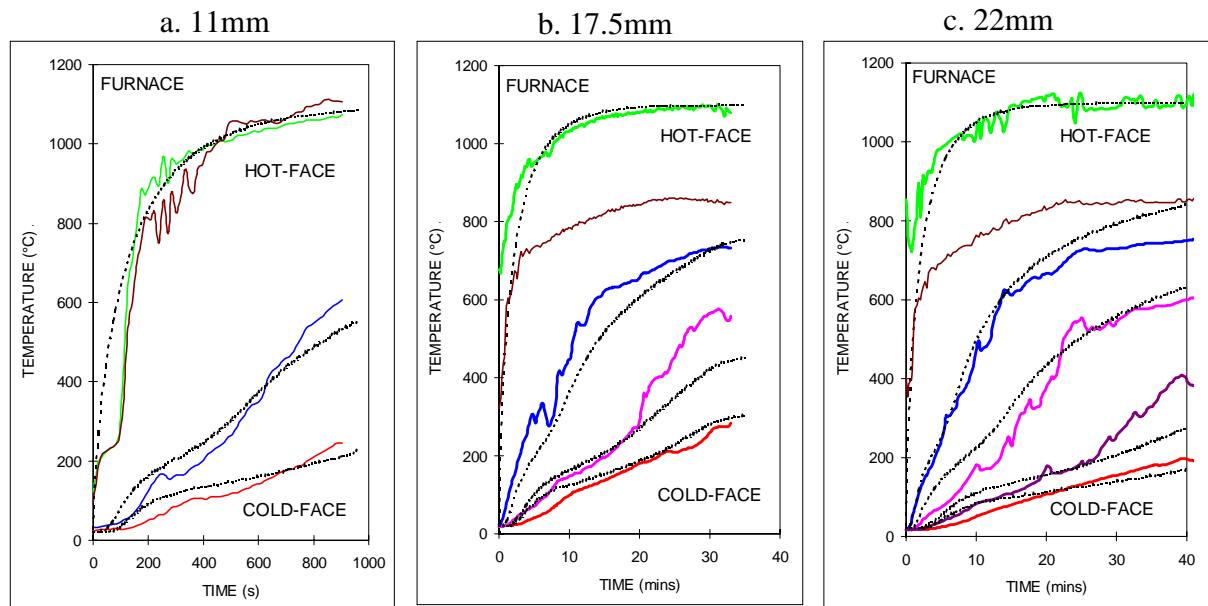


Figure 4 Experimental hydrocarbon curve furnace fire tests results (solid lines) for isophthalic polyester / glass woven roving laminated panels and corresponding one-dimensional modelled response (dotted lines). Intermediate curves are inter-laminar temperatures

Figure 4 shows furnace test results from a range different thickness polyester/glass laminated panels, used to confirm the model constants, demonstrating that good correlation can be obtained between experiment and model over a wide range of laminate thickness'.

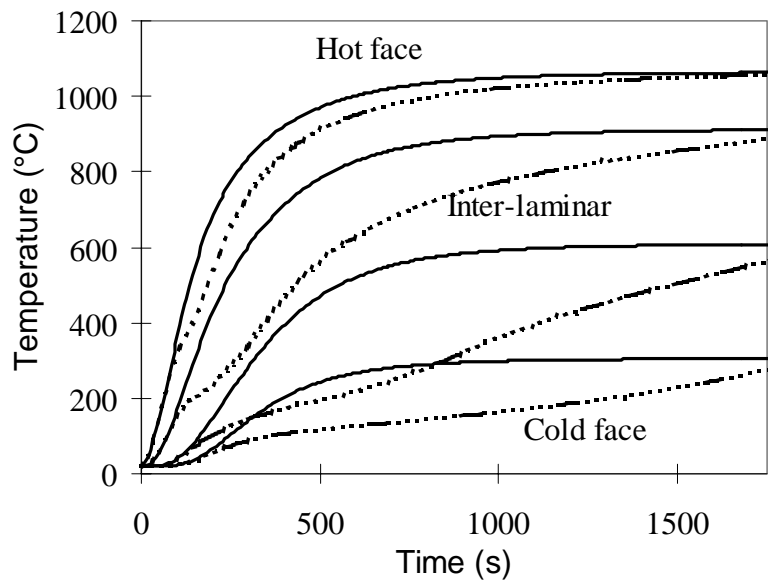


Figure 5 A comparison of the calculated temperature response of a 25mm polyester / glass laminate with (dotted lines) and without (solid lines) the decomposition term.

Comparison of the significance of the terms on the right of equation (1) shows that the most important factor in the slow burn-through effect is not the low conductivity of the composite laminate but the highly endothermic nature of the resin decomposition reaction. This is illustrated in Figure 5 which compares the calculated temperature distribution with and without the decomposition term. The heat absorbed by resin decomposition is the most

important factor limiting the rate of ablation of the laminate and in preventing the transmission of heat through the specimen to the cold face. In fact the decomposition model outlined above is based on an ablative model originally developed to describe the behaviour of wood in fires [10].

The kinetics of the decomposition reaction during a hydrocarbon fire test are illustrated in Figure 6. The rate parameters, A and E, in equation 1 are obtained experimentally by thermo-gravimetric analysis at a fixed heating rate (solid curve Figure. 6(a)). The dotted lines in Figure 6(a) are the calculated resin decomposition curves through the laminate thickness for the variable heating rates applied during a hydrocarbon curve fire test. The differences between the experimental and calculated TGA curves are due to the variation of heating rates during a hydrocarbon fire test.

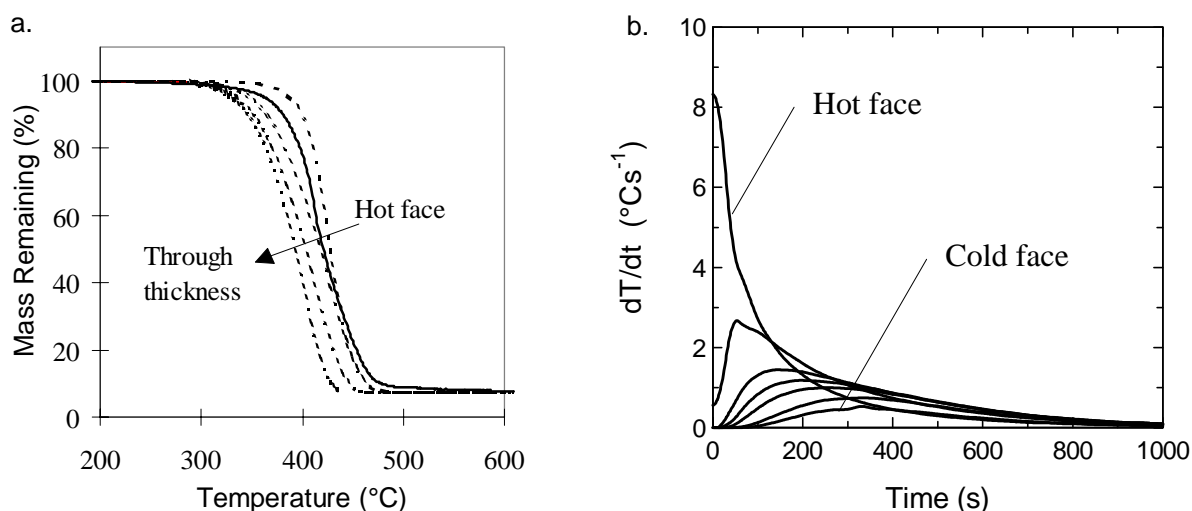


Figure 6 (a) Comparison of experimental thermo-gravimetric data collected at 25°C/min in a nitrogen atmosphere (solid line) with the calculated mass loss at points through the laminate thickness (dotted lines). (b) The calculated effective heating rates for a polyester / glass laminate during a hydrocarbon curve fire test. The highest rate is at the surface, decreasing at points through the thickness.

The calculated variation of the effective heating rate during a hydrocarbon curve fire test is plotted in Figure 6(b) for through thickness positions in an 11mm thick polyester / glass panel. The highest heating rate is at the hot face as expected and the test is predicted to have reached a steady state after ≈ 16 minutes.

APPLICATIONS OF THE THERMAL MODEL

The thermal model may be used to provide design information for the use of composite materials in fire sensitive applications. Design charts prepared using the validated computer model are shown in Figure. 8. Figure. 8a allows polyester woven roving laminate thickness' to be defined by the allowed cold face temperature rise in a hydrocarbon fire, while Figure. 8b shows the cold face response of laminates to a predetermined heat flux.

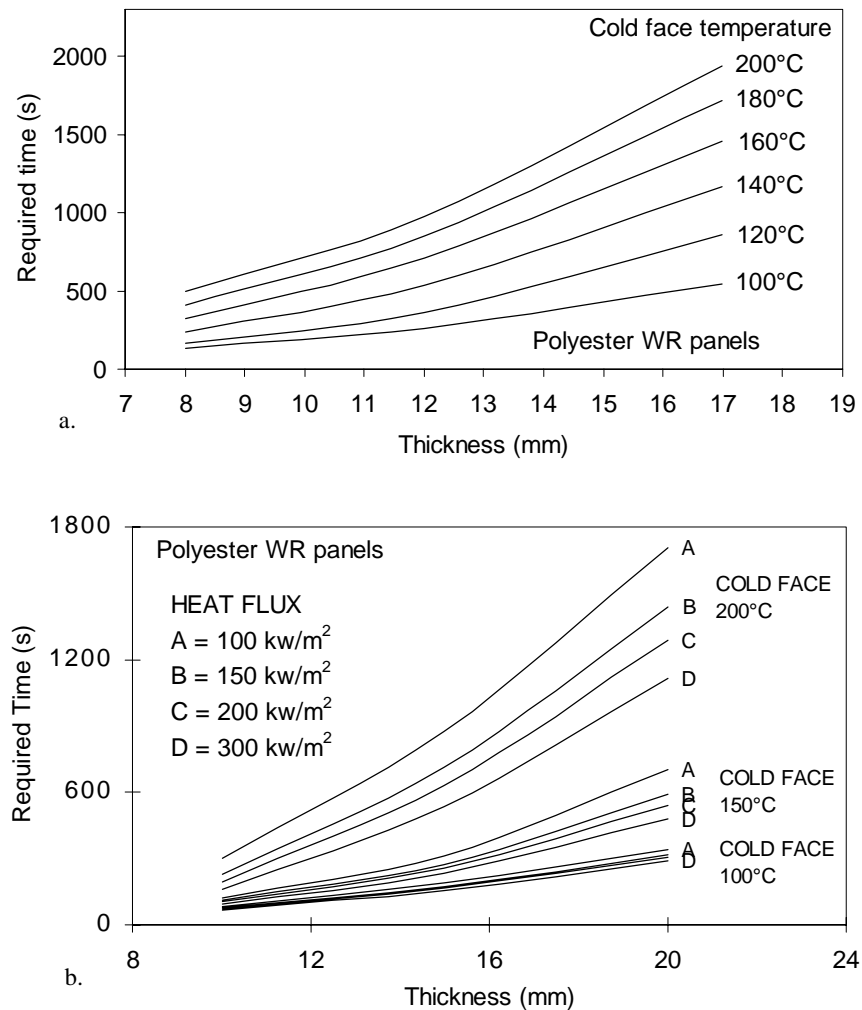
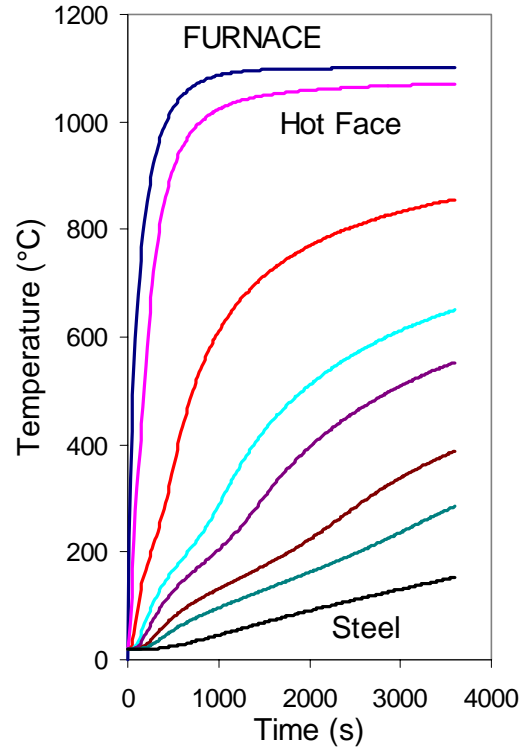
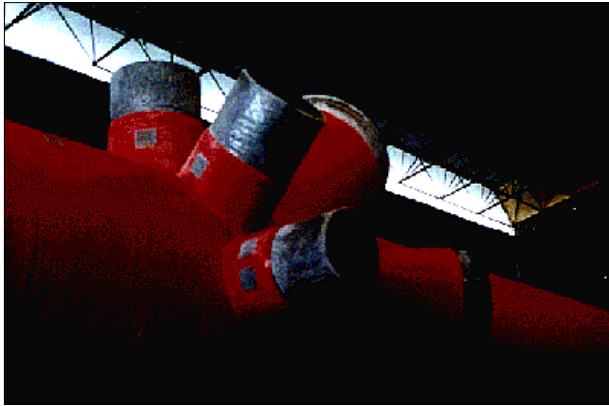


Figure 7 Design charts for polyester glass WR laminates prepared using the thermal model.
 (a) Hydrocarbon curve fire response - thickness required for specified temperature.
 (b) Cold face temperature response for specified incident heat flux vs. Thickness.

The application of composite materials as passive fire protection requires a prediction of the lifetime during a fire. Steel retains its structural properties up to about 500°C but, because of its relatively high thermal conductivity structures tend to reach this temperature quite quickly in fires. For this reason, metallic structures subject to fire hazards need to be protected, usually by an intumescent or other passive heat protection medium. Composite structures, by contrast, transmit heat less rapidly and will often maintain their integrity for longer. Composite materials are increasingly applied in offshore structures as structural members, risers and combined corrosion/fire protection in the splash zone. An example of the use of polyester/glass cladding as passive fire protection offshore is shown in Figure. 8. A steel tubular clad in 30mm polyester/glass is shown in Figure. 8a and the predicted temperature response of the cylindrical section to a hydrocarbon fire is shown in Figure. 8 b. The steel temperature remains below 160°C for more than 60 minutes satisfying design requirements.



a.

b.

Figure 8 (a) Polyester / glass passive fire protection applied to a steel riser. (courtesy of Vosper Thornycroft (UK) Ltd.) (b) Computer simulation of the temperature distribution of the cylindrical section under hydrocarbon fire curve conditions. The cold face temperature, defined at the composite/steel interface, remains below 160°C for up to 60 minutes. (Intermediate curves are inter-laminar temperatures).

CONCLUSIONS

We have attempted to show in this paper that, despite their combustibility, organic matrix composites have considerable potential for use in large load-bearing structures which may be subject to fire. When used in sufficiently thick sections these materials are capable of withstanding severe temperatures and ablative effects by virtue of the endothermic nature of the resin decomposition process.

The thermal response of composite systems subjected to severe hydrocarbon fire conditions can be accurately predicted using an experimentally validated thermal model which provides basic data for performance based design.

Composite materials have already found application as passive fire protection for metallic structures and it is recognised that composite structures will outperform unprotected metallic structures under many severe fire conditions.

ACKNOWLEDGMENTS

The fire modelling work reported here has been carried out in collaboration between the Newcastle Centre for Composite Materials Engineering and Professor J M Davies' Fire Research Group at Manchester University. The following organisations, which have supported the Marinotech Research *Composites Offshore* programme, have contributed greatly to the work presented here. Their support is gratefully acknowledged: AGIP (UK), Amerada Hess, Ameron bv, Amoco Research, Balmoral Group, Bow Valley Petroleum, BP Exploration, Brasoil, British Gas, Ciba, Conoco, Defence Research Agency, Dow Chemicals, DRA, EDF, Elf (Aquitaine), Enichem (SPA), Exxon, Hunting Engineering, Kerr McGee Oil (UK) Ltd, MaTSU, Centre for Marine and Petroleum Technology Ltd., Maunsell Structural Plastics, Mobil Research and Development Ltd, Norsk Hydro, UK Ministry of Defence (Navy), UK Offshore Supplies Office, Phillips Petroleum, Shell, SLP Engineering Ltd, Statoil, Total Oil Marine, UK Department of Energy, VSEL and Vosper Thornycroft.

REFERENCES

1. Marinotech Research multi-sponsor research programme on *The Cost-Effective Use of Fibre Reinforced Composites Offshore*, Phases I, II and III Final Reports, Marinotech Research, Chemistry Link Building, UMIST, P.O.Box 88, Sackville Street, Manchester M60 1QD, UK.
2. S. Ciaraldi, J. D. Alkire and G. Huntoon, 'Fibreglass firewater systems for offshore platforms', Paper OTC 6926, 23rd Annual Offshore Technology Conference, Houston Texas, May 6-9 1991.
3. *Specification and Recommended Practice for the Use of GRP Piping Offshore*, UK Offshore Operators Association, March, 1994.
4. 'Composite Materials for Offshore Operations' Proceedings of the 1st International Workshop', Houston, Texas, 26-28 October, 1993 (NIST Special Publication 887, US Government Printing Office, Washington DC 20402).
5. J. G. Williams, 'Developments in Composite Structures for the Offshore Oil Industry', Paper OTC 6579, 23rd Annual Offshore Technology Conference, Houston Texas, May 6-9 1991.
6. ISO 834:1975 Fire Resistance Tests. Also BS 476.
7. ISO 5660-1 1993. Fire Tests - Reaction to Fire. Cone Calorimeter.
8. A. G. Gibson, Y. S. Wu, H. W. Chandler, J. A. D. Wilcox and P. Bettess, 'A model for the thermal response of thick composite laminates in hydrocarbon fires', 'Composite Materials in the Petroleum Industry', Revue de l'Institut Francais du Petrole (Special Issue), 50, 1, Jan-Feb. 1995, pp69-74.
9. M. C. Adams, 'Recent advances in ablation', American Rocket Society, 29, 9, 1959.

10. E. J. Kansa, H. E. Perlee and R. F. Chaiken, 'Mathematical model of wood pyrolysis including forced convection', *Combustion and Flame*, 29, 1977.
11. R M Sullivan, 'A coupled solution method for predicting the thermo-structural response of decomposing expanding polymeric composites', *Journal of Composite Materials*, 27, 4, 1993.
12. N. Dodds, A.G. Gibson, J. M. Davies. submitted to *Composites*.

EXPERIMENTAL AND NUMERICAL METHOD FOR LARGE TRANSFORMATIONS OF REINFORCED COMPOSITE STRUCTURES

A. Ben Dhia

*Pôle Univeritaire Léonard de Vinci, Education and Research Department of Mechanics
Structures Materials & Process, 92916 Paris La Défense Cedex, France*

SUMMARY: Two approaches are presented to modelise and take into account in a finite element model the nonlinear mechanical behavior of the reinforcements and the matrix of composite materials and structures. Based on homogenization technique and a macro - micro approach, the first method requires the knowledge of experimental tensile stress-strain curves of the constituents and their Poisson's ratio. The second, of a very convenient use as it will be shown, is based on a combined exploitation of experimental data and finite element results. Few a steps of successive comparisons of these results are necessary to make it efficient and accurate enough. While the first approach is described in details only, the second was actually performed to simulate the response of a pressurized Aramid fiber-rubber composite cylinder. The details of this method and of the numerical tools are given and the results are discussed.

KEYWORDS: reinforced composite structures, material nonlinearities, large transformations, finite element modeling, experimental tests.

INTRODUCTION

One of the main difficulties one can face when attempting to modelise composite reinforced materials and structures under large loadings (especially when the constitutive material is highly flexible), is to introduce the nonlinear mechanical behavior of reinforcements and matrix in the numerical model. Although successful attempts were realized on a single reinforced (cord-rubber) ply, the problem becomes much more difficult when real physical structures are involved because of the too large size of the finite element model. Fig. 1 shows the structure under consideration in this paper.

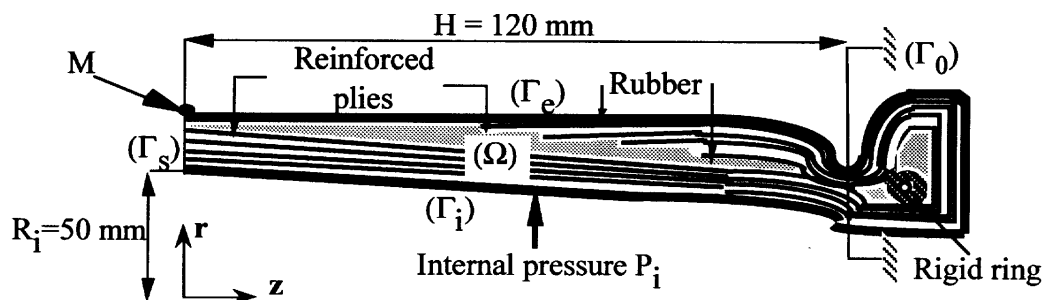


Fig. 1: Description of the structure . Definition of the Axes and boundary conditions

This structure is an axisymmetric multilayer composite cylinder. Because of the symmetry with respect to plane $z = 0$ only its half part is modeled. Each constitutive layer is a reinforced Aramid fiber-rubber composite ply. The fiber's volume ratio, $V_f = 36\%$ and their orientation with respect to z -axis equals to $\pm 14^\circ$ alternatively in two successive plies. In a previous study [1] the author showed that if the mechanical behavior of the constituents and, consequently, of the composite plies is determined under the hypothesis of infinitesimal strains and displacements the numerical solution moves away from the experimental results (see Fig. 6), i.e., the elastic and linear approach becomes unsuitable. This phenomenon occurs at a relatively modest level of the internal pressure since that the fibers and the resin are submitted, locally, to high strain level.

In this paper we developed a finite element model in which the large strains and nonlinear behavior of aramid fiber (see Fig. 2_a) and rubber matrix (see Fig. 2_b) are taken into account. For that, we suggest two approaches : an Incremental Homogenization Method and a Multilinear Domain Approach. The last method was actually performed and led to sufficiently accurate results with fairly good agreement with the experimental ones.

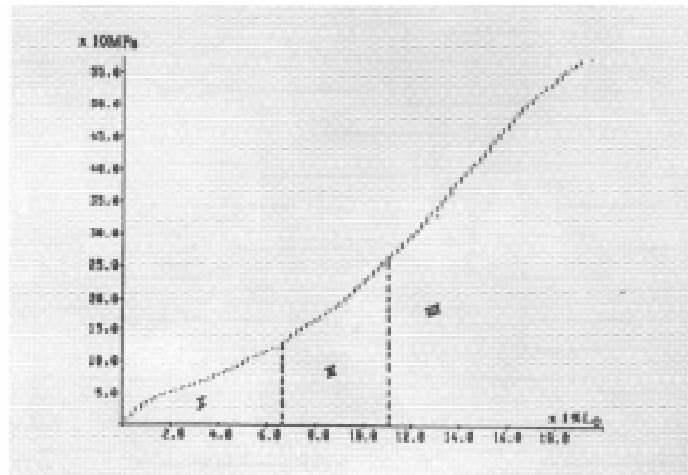


Fig. 2_a. Aramid fiber behavior under uniaxial tensile test

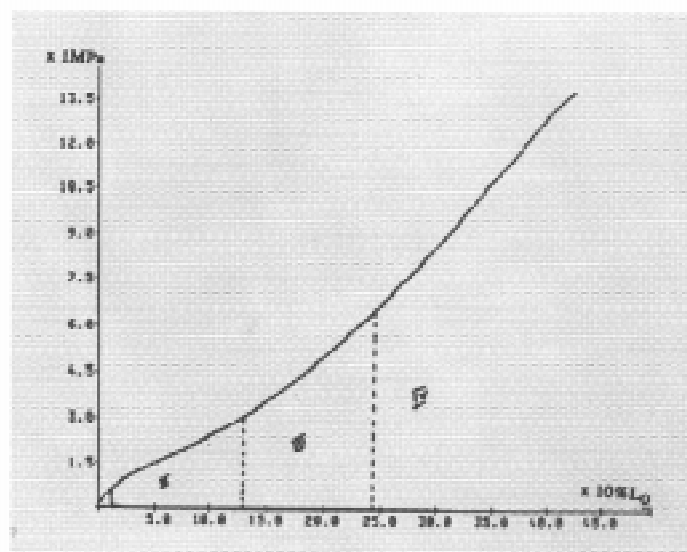


Fig. 2_b. Rubber behavior under uniaxial tensile test

INCREMENTAL HOMOGENIZATION METHOD

The first approach called Incremental Homogenization Method (IHM) requires the knowledge of experimental tensile curves of fibers and matrix, their Poisson ratios, volume fraction of fibers (or matrix) and their local orientation inside the reinforced ply. The (IHM), based on a macro-micro process, is applied in several identical stages and could be summarized as following:

(i) Young's moduli and Poisson's ratio (E^f_1 , ν^f_1) for fibers and (E^r_1 , ν^r_1) for matrix are identified by classical experimental methods. Then, one homogenization technique, called Homogenization Technique of Periodic Cells Structures is performed [2], [3], to obtain the homogenized elastic moduli of the equivalent anisotropic (locally orthotropic in this case) material and denoted by the stiffness tensor $[Q^1]$. This technique was validated [1] in this case through significant experiments.

(ii) *Macroscopic* numerical simulation based on a finite element analysis is realized by introducing the $[Q^1]$ tensor and an incremental algorithm (Newton- Raphson) is used to solve the problem.

(iii) After each *small* increment, the *mesoscopic* (ply-scale) displacement, strain and stress fields solution of the numerical problem are known. We perform then the so called Localization Process [5] to be back to the *microscopic* scale: fiber and matrix. This process allows the determination of displacements, strains and stresses fields in fibers and matrix by using the macroscopic results obtained in the previous step (ii). The Localization Process can be applied, automatically, to each previously chosen relevant elementary volume (the finite element still the smallest) of the model. Using these results, we can extract the slope between the minimum and maximum strain values computed on the elementary volume directly identified on the experimental curves previously introduced in the computer memory.

Thus, we are able to identify the *new* Young's moduli (we are conscious of misusing the expression) of the fiber and the resin denoted by $(E^f_2)_k$ and $(E^r_2)_k$ for the k-th elementary volume : $\delta\Omega_k$. In this case, the variations of Poisson's ratios can reasonably be neglected. (If needed, the computed strain field can yield to the new values of those coefficients). Moreover the knowledge of the displacement field allows the determination of new volume ratio and the local orientation of the fibers.

(iv) The next step consists in applying the following test to each $\delta\Omega_k$:

$$\boxed{|(E^f_2)_k - (E^f_1)_k| \leq \epsilon_1 \text{ ? and } |(E^r_2)_k - (E^r_1)_k| \leq \epsilon_2 \text{ ?}}$$

If the test is satisfied, the load is incremented and the previous steps are reproduced. Otherwise, the ply mechanical behavior is determined like described in the step (i) by injecting the new computed input data. This incremental method could be performed as many times as necessary to reach the desired loading value.

Considerations about the Incremental Homogenization Method

The choice of the three fundamental parameters: Elementary volumes $\delta\Omega_k$ and the test parameters ϵ_1 and ϵ_2 falls to the operator. Nevertheless, this choice must consider, at least, two principal aspects : the estimated experimental uncertainties and the desired accuracy.

This method can be applied systematically and with a very high accuracy to such nonlinear problems and particularly when experimental results are not available on the entire composite structure under consideration. However, it induces high numerical cost when applied to realistic structures. Hence, a careful compromise should be found out between the desired accuracy of the results and the cost by acting, directly, on the fundamental parameters defined above.

In case experimental results are available for the whole structure one can perform a much easier and nevertheless efficient method, that is the multilinear domain approach. Before getting into details of this method we describe briefly the experimental tests carried out on the considered structure and used to perform this approach.

Description of the Experiments

The structure is submitted to an internal pressure denoted by P_i on its internal face (Γ_i) when the top and bottom faces (Γ_U), defined by $z = \pm H$, are built in (see Fig. 1). The load was incremented by constant fraction, $\delta P = 0.01$ MPa (0.1 bar). The total pressure loading was set to 0.39 MPa. At each load we measured the radial displacement (u_r) of the point denoted by M on fig. 1 and the z-component of the total reaction force (R_z) on the built in faces Γ_0 .

Multilinear Domain Approach

The basic idea of the Multilinear Domain Approach (MDA) when applied to composite materials and structures is to share the total strain intervals of the constituents in a finite number of domains in which the behavior can be approximated by an elastic and linear one. Thus, the nonlinear behavior of rubber and aramid fiber is assumed to be taken into account only through the variation of the tensile resistance of the constituents.

In the case under consideration, (see Fig. 2_a and Fig. 2_b) we exhibited 4 domains for the rubber matrix and 3 for the reinforcements (denoted by Romaine numbers).

In table 1 are summarized the different strain intervals and the measured values of the slopes. The Poisson ratios still assumed constants and set to $\nu_r = 0.49$ for rubber and $\nu_f = 0.3$ for fiber.

Table 1: Strain intervals of the constituents

Rubber				
Strain intervals	$0 \leq \epsilon \leq 9$ %	$9 < \epsilon \leq 140$ %	$140 < \epsilon \leq 265$ %	$\epsilon > 265$ %
Slope values $E_r^{(i)}$ $i = 1$ to 4	3.6 MPa	1.3 MPa	2.2 MPa	3.6 MPa

Aramid fiber			
Strain intervals	$0 \leq \epsilon \leq 6.5$ %	$6.5 < \epsilon \leq 11.5$ %	$\epsilon > 11.5$ %
Slope values $E_f^{(j)}$ $j = 1$ to 3	1574 MPa	3040 MPa	4220 MPa

Consequently, the homogenization technique shall be performed nine times to compute the equivalent homogenized anisotropic behavior corresponding to nine possible combinations of the constituents moduli. For this purpose we used the software "LANDRU" [6].

In tables 2.1 to 2.3 are presented the orthotropic elastic moduli corresponding to only three combinations. The fiber's volume ratio still unchanged and equals to 36 %.

Tables 2_1 to 3: Homogenized behavior

$E_r = 1.3 \text{ MPa}$		$E_f = 1574 \text{ MPa}$		$V_f = 36 \%$	
$E_2 \text{ (MPa)}$	$E_3 \text{ (MPa)}$	ν_{23}	ν_{12}	$G_{23} \text{ (MPa)}$	$G_{12} \text{ (MPa)}$
5.800	577.442	0.00409	0.912	0.945	0.787

$E_r = 2.2 \text{ MPa}$		$E_f = 3040 \text{ MPa}$		$V_f = 36 \%$	
$E_2 \text{ (MPa)}$	$E_3 \text{ (MPa)}$	ν_{23}	ν_{12}	$G_{23} \text{ (MPa)}$	$G_{12} \text{ (MPa)}$
9.621	1112.030	0.00363	0.914	1.596	1.332

$E_r = 3.6 \text{ MPa}$		$E_f = 4200 \text{ MPa}$		$V_f = 36 \%$	
$E_2 \text{ (MPa)}$	$E_3 \text{ (MPa)}$	ν_{23}	ν_{12}	$G_{23} \text{ (MPa)}$	$G_{12} \text{ (MPa)}$
15.730	1544.026	0.00427	0.913	2.611	2.180

In these tables, the 3-axis and 2-axis are the longitudinal (fiber direction) and transversal (perpendicular to the fiber direction) directions respectively. The 1-axis completes the direct orthonormal (1,2,3)-local orthotropic basis of the reinforced composite ply.

The anisotropic Poisson coefficients and the anisotropic shear moduli are denoted respectively by ν_{ij} and G_{ij} .

Nine finite element analyses were actually performed with the nine possible combinations listed above. These analyses show that the above three cases were sufficient to describe the whole response of the structure and insure satisfactory correlation between numerical and experimental results.

We shall notice that one more refined partition of strain domains of the constituents induces more and more combinations to consider. Hence, the refinement depends closely on the objectives and on the accuracy of the experimental measurements. The multilinear domain approach is summarized as indicated in fig. 3 in which we denoted by Q^c and Q^e the computed and experimental values, respectively, of any quantity Q .

In our case, three stages were necessary to reach the maximum load value, $P_{\max} = 0.39 \text{ MPa}$.

Finite Element Modeling

Let us denote by Ω the region occupied by the axisymmetric slice of the structure, related to a system of orthonormal axes (O, x_1, x_2, x_3) . Ω is subjected to an internal pressure P_i on a portion Γ_i of the boundary Γ . In this problem we neglect the body forces (such as gravity). On the others parts of the boundary, as could be seen from Fig. 1, we impose a zero displacement condition on Γ_0 , kinematics symmetry condition on Γ_s and a stress free condition on the complementary portion of the boundary Γ_e .

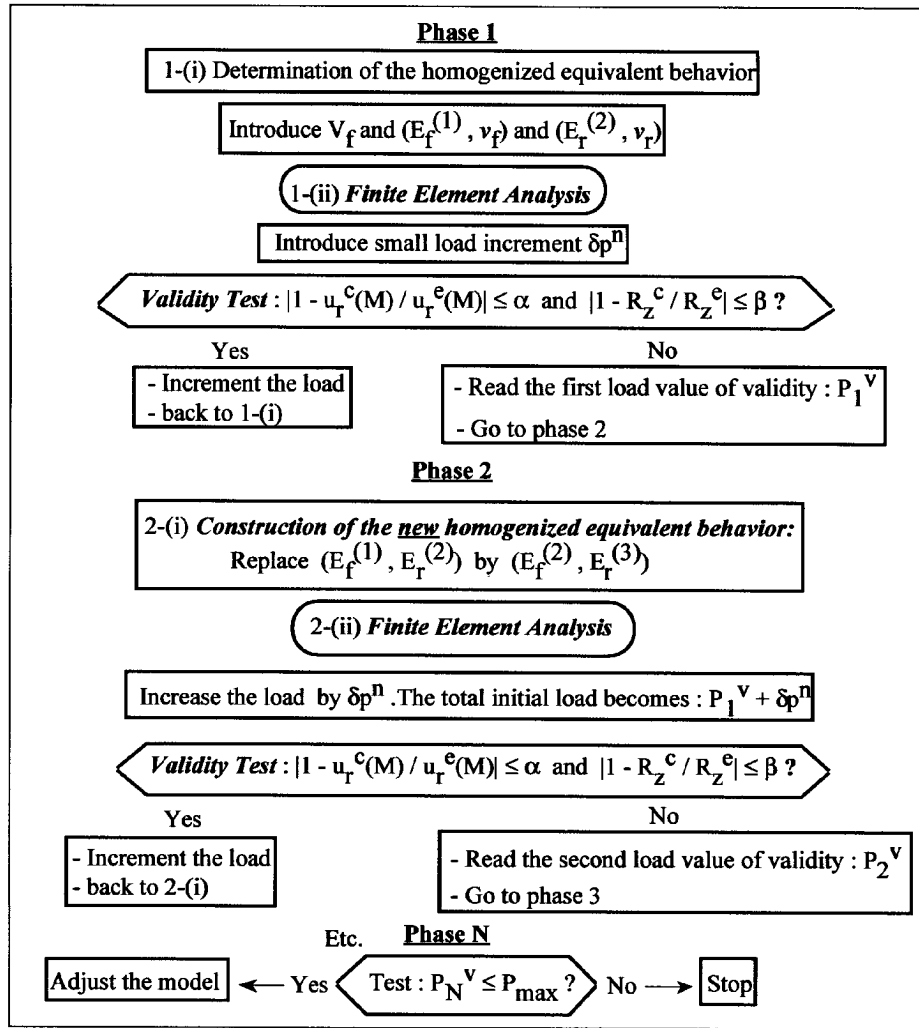


Fig. 3: Multilinear Domain Approach

Numerical method and tools employed

Following the classical process used for hyperelastic materials (P.G. Ciarlet [7]), the problem to be solved is transferred on the reference configuration Ω_0 considered as a natural one. On Ω_0 , the problem to be solved writes as follows :

$$\text{div}_0(F\Sigma) = 0 \quad \text{in } \Omega_0 \quad (1)$$

$$\Sigma = QE \quad \text{in } \Omega_0 \quad (2)$$

$$F = 1 + \text{grad}_0(u) \quad 2E = {}^tFF - 1 \quad (3)$$

$$u_3 \text{ (or } u_z) = 0 \quad \text{on } \Gamma_s^0 \quad (4)$$

$$u = 0 \quad \text{on } \Gamma_0^0 \quad (5)$$

$$(F\Sigma) \cdot n_0 = -P_i n_0 \quad \text{on } \Gamma_i^0 \quad (6)$$

$$(F\Sigma) \cdot n_0 = 0 \quad \text{on } \Gamma_e^0 \quad (7)$$

Where Σ denotes the symmetric second Piola-Kirchhoff stress tensor Q is the homogenized stiffness matrix, F the gradient deformation tensor, E The deformations tensor and n the external outer normal to the domain. The differential operators (divergence and gradient) indexed by 0 are applied on the natural configuration:

To solve the nonlinear problem (1)-(7), we used the Actualized Lagrangian. That approach is based essentially on sharing into a finite number K , the total loading. Let us denote by:

$$(\delta P)^n = (\alpha^{n+1} - \alpha^n)P_i$$

the pressure loading of each step and α^n being defined as follows :

$$0 = \alpha^0 < \alpha^1 < \dots < \alpha^n < \alpha^{n+1} < \dots < \alpha^K = 1$$

The method performed consists in the computation of the successive approximations u^n of the exact solution associated to the successive loading values. The $(n-1)$ th approximation is supposed known after the previous step. Thus, at each step we compute the displacement increase u^{*n} , solution around the known Ω_n -configuration.

Those problems are obtained at the step n by distinguishing in the deformation history of the structure three configurations : two of them are supposed known (Ω_0 , the initial one and Ω_n the just computed one), the third is the searched one Ω_{n+1} as it can be seen on fig. 4.

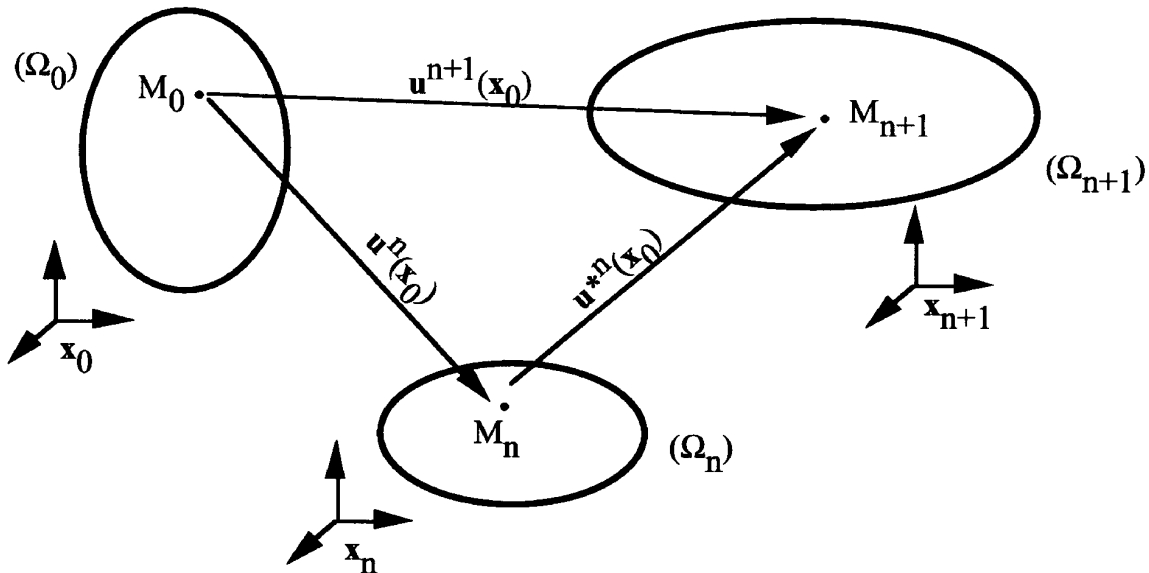


Fig. 4 : The different configurations considered

Using the kinematics process described, one can express the different tensors entering the problem to be solved at the $(n+1)$ th step as follows :

$$F^n = 1 + \text{grad}_0 u^n$$

$$F^{n+1} = 1 + \text{grad}_0 u^n + \text{grad}_0 u^{*n} = F^n + \text{grad}_0 u^{*n}$$

$$E^n = 1/2(t F^n F^n - 1)$$

$$E^{n+1} = E^n + E^{*n}$$

$$E^{*n} = 1/2(t F^n \text{grad}_0 u^{*n} + t \text{grad}_0 u^{*n} F^n + t \text{grad}_0 u^{*n} \text{grad}_0 u^{*n})$$

$$\Sigma^n = Q E^n$$

$$\Sigma^{n+1} = \Sigma^n + \Sigma^{*n}$$

$$\text{where, } \Sigma^{*n} = Q E^{*n}$$

Consequently, the problem obtained at the step $(n+1)$ can be written on the natural configuration by using the expressions above and lastly, knowing the n -th configuration the

problem is transferred on the Ω_n configuration. In order to realize this operation, let us denote Φ^n the tensor defined on Ω_0 as follows :

$$\Phi^n = \Phi^n \Sigma^{*n} + \text{grad}_0 u^{*n} (\Sigma^n + \Sigma^{*n}) \text{ and its image in } \Omega_n \Sigma^n = [\Phi^n \text{ }^t \Phi^n] / \det(\Phi^n)$$

Then, the use of the Piola's identity, applied to Φ^n , allows one to express the problem on the deformed configuration Ω_n . This way, the displacement increment u^{*n} has to satisfy the following equations :

$$\text{div}_n \Sigma^n = 0 \quad \text{in } \Omega_n \quad (8)$$

$$\Sigma^{*n} = Q E^{*n} \quad \text{in } \Omega_n \quad (9)$$

$$2E^{*n} = \text{ }^t F^n (\text{grad}_n u^{*n} F^n) + \text{ }^t (\text{grad}_n u^{*n} F^n) F^n + \text{ }^t (\text{grad}_n u^{*n} F^n) (\text{grad}_n u^{*n} F^n) \quad \text{in } \Omega_n \quad (10)$$

$$u_3^{*n} = 0 \quad \text{on } \Gamma_s^n \quad (11)$$

$$u^{*n} = 0 \quad \text{on } \Gamma_0^n \quad (12)$$

$$\Sigma^n \cdot n_n = -(\delta P)^n n_n - P_i \alpha^{n+1} (\text{tr}(\text{grad}_n u^{*n}) 1 - \text{grad}_n u^{*n}) \cdot n_n \quad \text{on } \Gamma_P^n \quad (13)$$

$$\Sigma^n \cdot n_n = 0 \quad \text{on } \Gamma_e^n \quad (14)$$

where the differential operators indexed by n act on the deformed configuration Ω_n . To solve this nonlinear problem we used the so-called Full Newton Algorithm. The displacement and energy parameters chosen for the convergence assessment have been respectively set to 10^{-3} and 10^{-2} .

For the mesh design three-dimensional first order (linear) isoparametric finite elements (8-nodes) for large strain analysis were used: 2 finite elements across the thickness of each reinforced ply and three elements across the rubber envelops thickness were created (Fig. 5).

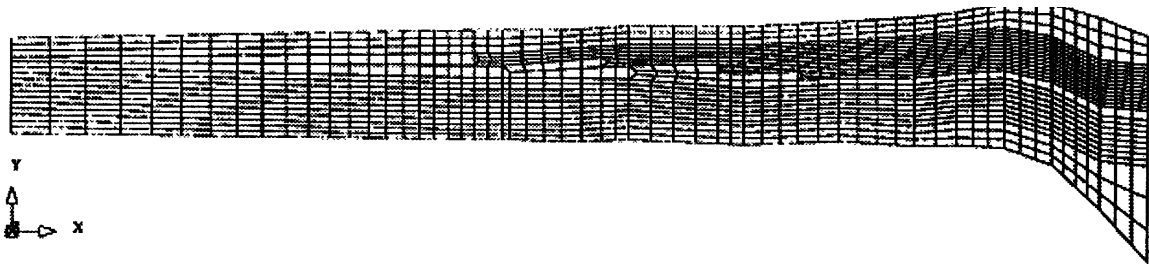


Fig. 5: Mesh design of the structure

The mesh was refined until the asymptotic response of the numerical model was reached. Thus, 1294 finite elements were generated and the problem size is of 5500 degrees of freedom. The calculation was performed on a quadri-processors Convex C240 and the computer time consumed equals to 713 seconds.

Presentation and analysis of results

Considering the experimental uncertainties, the fundamental parameters defined for the validity test (see fig. 3) was set to $\alpha = \beta = 0.08$.

When the equivalent homogenized mechanical behavior of reinforced plies is determined by introducing the elastic moduli of the fiber and the rubber matrix only around the origin, i.e, only stage 1 (see fig. 3) is processed the numerical and measured results of the radial component of the displacement field at M (see fig. 1) and the z-component of the total reaction force on the pinned face Γ_0 (see Fig. 6) are in good agreement until the load value reaches 0.3 bars. Beyond that value the computed structure becomes more flexible than the physical one.

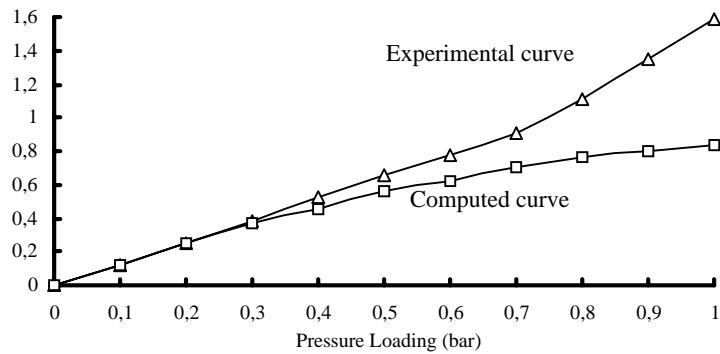


Fig. 6: Computed and experimental z-reaction force.

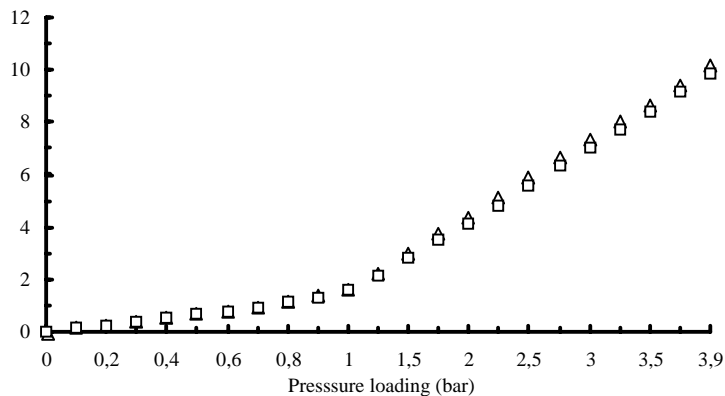


Fig. 7: Computed and experimental z-reaction force. MDA performed

Fig. 7 shows the same results when the Multilinear Domain Approach is performed. We notice the fairly good agreement until the maximum loading value between the computed and measured results. For illustration, fig. 8 shows the computed deformed structure and the Von-Mises stress distribution corresponding to the maximum value of the internal pressure imposed to the structure. An accurate analysis of that distribution shows that the critical value is localised around the free extremities of the reinforced plies. Experimental observations showed that damage and failure actually initiate in this area.

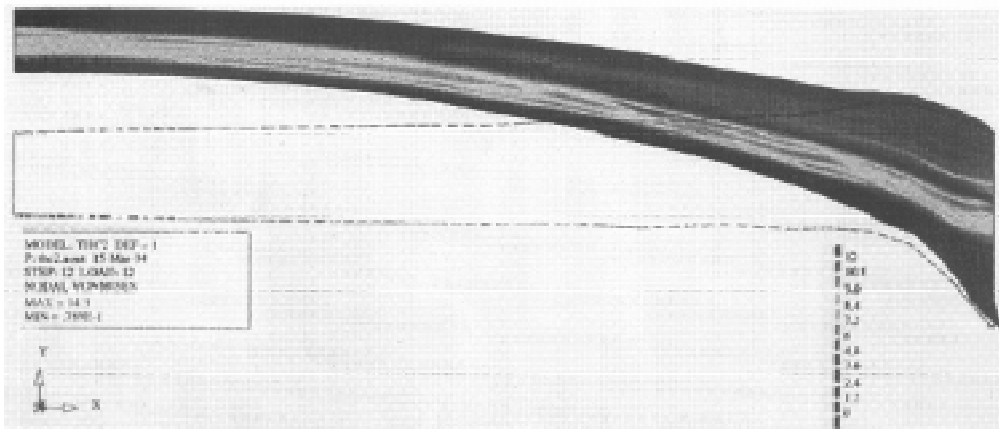


Figure 8. Von Mises Stress field on the displaced structure

Concluding remarks

Two approaches were proposed, the Incremental Homogenization Method and the Multilinear Domain Approach to include in the finite element model of any reinforced composite material and structure the nonlinearities of the reinforcements and the matrix.

This new *strategy* led us to a satisfactory computed results according to their comparison with the measured ones and was extended successfully to others loading types such as tensile, compression combined or not with internal pressure.

REFERENCES

1. Ben Dhia, A., "Caractérisation, Modélisation et Calcul d'une Structure Composite Fibres de Nylon-Résine Caoutchouc", Thèse de Doctorat de l'Université Pierre et Marie Curie, Paris (1994).
2. Sanchez-Palencia, E., "Comportement Local et Macroscopique d'un Type de Milieux Physiques Hétérogènes", Int. J. Eng. Sci., Vol. 12, 1974, pp. 331-351.
3. Bensoussan, A., Lions, J.L. and Papanicolaou, G., "Asymptotic Analysis for Periodic Structures", North Holland, Amsterdam, 1978.
4. Duvaut, G. and Pistre, F. "Calcul des Vecteurs Contraintes en Approximation P1 et P2", C.R.A.S., Vol. II, No. 295, 1982, pp.827-830.
5. Pistre, F., "Calcul des Microcontraintes dans les Matériaux Composites", Doctorat de 3ème Cycle, Université Paris 6, 1984, Paris.
6. Devries, F. and Léné, F., "Homogénéisation à Contraintes Microscopiques Imposées, Implémentation Numérique et Applications", La Recherche Aérospatiale, No. 1, pp.33-51.
7. Ciarlet, P.G. and Geymonat, P. "Sur les Lois de Comportement en Elasticité Non Linéaire Compressible », Comptes Rendus de l'Académie des Sciences, Vol. II, No. 295, pp. 423-426.

THE EFFECT OF ELASTIC CORE ON THE STABILITY OF COMPOSITE CIRCULAR CYLINDRICAL SHELLS

Yin Yunyu

*Beijing Institute of Astronautical Systems Engineering ,
9208-10-10, Beijing ,100076, P.R. China*

SUMMARY: The effect of an elastic core on the thin laminated circular cylindrical shells subjected to uniform axial compression, lateral pressure is analyzed. Moreover, the solution methodology is described, and results are generated for the composite circular cylindrical shells with an elastic core. The results have shown that the material behavior of the core and the boundary conditions of shell have a great effect on stability . The method appears to be worth recommending , especially while designing solid engines.

KEYWORDS: composite material , structural stability , finite difference theory

INTRODUCTION

Circular cylindrical shells find wide uses in complicated aerospace structural systems. Especially, in the recent few years, the constant demand for lightweight efficient structures, led the structural engineers to the use of composite materials. One of the keys of the correct and effective use of these composite shells is to find a good method to analyze the stability of the shells.

In 1975, Tennyson[1] made a review of previous studies on the buckling of laminated cylinders. Several papers were involved in the comparison of the efficiency and accuracy between Flugge's linear shell theory and other shell theories (such as the theory based on Donnell's equations). In the past, the inverse method or energy method [1,2] was widely used to analyzed the shell stability; in the recent, Simitses[3] adopted Galerkin-difference method to analyze the stability of the laminated circular cylindrical shells subjected to axial compression and torsion, and got good results. This method is especially suitable for middle-short shells (length/radius \ll 5).

The stability analysis of metallic circular cylindrical shells with a soft elastic core under axial compression and lateral pressure began in the end of nineteen-fifties[4]. As for the stability research of laminated circular cylindrical shells with an elastic core under axial compression and lateral pressure is very few.

In this paper, the effect of an elastic core on the stability of laminated circular cylindrical shells subjected to axial compression and lateral pressure is analyzed. The Galerkin-difference method is used to solve the modified Donnell's equations. Then, in terms of the stability criterion, the critical loads can be found. The effect of the core is determined by the elastic constant of the core[4]. For convenience, the following assumptions are introduced : 1.

Neglect the shear between the elastic core surface and the inner wall of the shell; 2. The normal displacement of the shell middle surface is equal to the core surface's; 3. The core is isotropic, solid and linear. In general, if the ratio of the inner diameter and the external diameter exceeds 0.55, to simplify the core as solid causes very small errors[4]; 4. Each lamina of the shells is orthotropic.

MATHEMATICAL FORMULATION

The geometry and reference frame are shown on Fig.1. Reference surface is the middle surface.

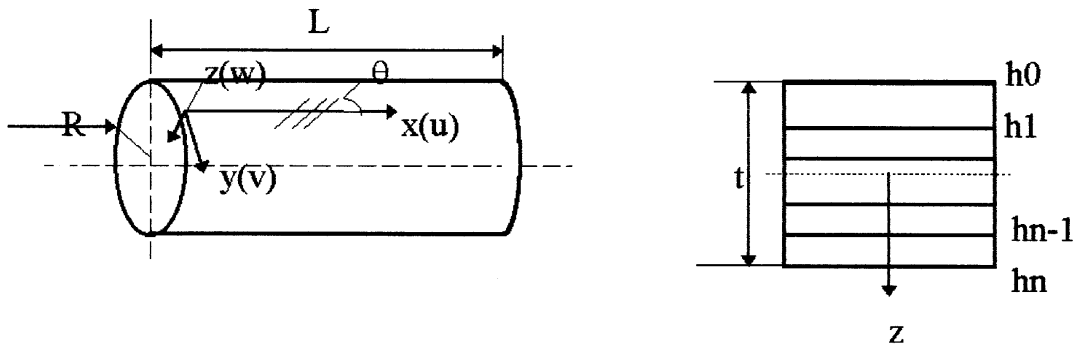


Fig.1. Geometry

The kinematic relations are

$$\begin{aligned}
 \epsilon_{xx} &= \epsilon_{xx}^0 - zk_{xx} \\
 \epsilon_{yy} &= \epsilon_{yy}^0 - zk_{yy} \\
 \epsilon_{xy} &= \epsilon_{xy}^0 - 2zk_{xy} \\
 \epsilon_{xx}^0 &= u_{,x} + w^2_{,x} / 2 \\
 \epsilon_{yy}^0 &= v_{,y} - w / R + w^2_{,y} / 2 \\
 \epsilon_{xy}^0 &= u_{,y} + v_{,x} + w_{,x} w_{,y}
 \end{aligned}
 \tag{1}$$

where

and $k_{xx} = w_{,xx} ; k_{yy} = w_{,yy} ; k_{xy} = w_{,xy} .$

Note that w is the normal displacement of the middle surface, which is positive when moving to the inner, u and v are the displacement components in the middle surface, and $\epsilon_{xx}^0, \epsilon_{yy}^0, \epsilon_{xy}^0$ and k_{xx}, k_{yy}, k_{xy} the middle surface stretching and bending strains.

In this paper, we consider single-direction composite materials. Each lamina is orthotropic and the constitutive equations are

$$\begin{Bmatrix} \sigma_{xx} \\ \sigma_{yy} \\ \sigma_{xy} \end{Bmatrix} = \begin{bmatrix} \frac{E_{11}}{1-\mu_{12}\mu_{21}} & \frac{\mu_{21}E_{11}}{1-\mu_{12}\mu_{21}} & 0 \\ \frac{\mu_{12}E_{22}}{1-\mu_{12}\mu_{21}} & \frac{E_{22}}{1-\mu_{12}\mu_{21}} & 0 \\ 0 & 0 & G \end{bmatrix} \begin{Bmatrix} \varepsilon_{xx} \\ \varepsilon_{yy} \\ \varepsilon_{xy} \end{Bmatrix} = \begin{bmatrix} Q_{xx} & Q_{xy} & 0 \\ Q_{yx} & Q_{yy} & 0 \\ 0 & 0 & Q_{ss} \end{bmatrix} \begin{Bmatrix} \varepsilon_{xx} \\ \varepsilon_{yy} \\ \varepsilon_{xy} \end{Bmatrix} \quad (2)$$

where E_{11} and E_{22} are longitudinal and transverse Young's moduli respectively,

$\mu_{12} = -\frac{\varepsilon_{yy}}{\varepsilon_{xx}}$ and $\mu_{21} = -\frac{\varepsilon_{xx}}{\varepsilon_{yy}}$ are the Poisson's ratio, and G is the shear modulus. In engineering, the fiber direction has an angle with the axial line of the cylindrical shell. Its constitutive equations [5] are :

$$\begin{Bmatrix} \sigma_{xx} \\ \sigma_{yy} \\ \sigma_{xy} \end{Bmatrix} = \begin{bmatrix} Q_{11} & Q_{21} & Q_{16} \\ Q_{21} & Q_{22} & Q_{26} \\ Q_{61} & Q_{62} & Q_{66} \end{bmatrix} \begin{Bmatrix} \varepsilon_{xx} \\ \varepsilon_{yy} \\ \varepsilon_{xy} \end{Bmatrix} \quad (3)$$

where

$$\begin{aligned} Q_{11} &= m^4 Q_{xx} + n^4 Q_{yy} + 2m^2 n^2 Q_{xy} + 4m^2 n^2 Q_{ss} \\ Q_{22} &= n^4 Q_{xx} + m^4 Q_{yy} + 2m^2 n^2 Q_{xy} + 4m^2 n^2 Q_{ss} \\ Q_{21} &= m^2 n^2 Q_{xx} + m^2 n^2 Q_{yy} + (m^4 + n^4) Q_{xy} - 4m^2 n^2 Q_{ss} \\ Q_{66} &= m^2 n^2 (Q_{xx} + Q_{yy}) - 2m^2 n^2 Q_{xy} + (m^2 - n^2)^2 Q_{ss} \\ Q_{61} = Q_{16} &= m^3 n Q_{xx} - mn^3 Q_{yy} + (mn^3 - m^3 n) Q_{xy} + 2(mn^3 - m^3 n) Q_{ss} \\ Q_{62} = Q_{26} &= mn^3 Q_{xx} - m^3 n Q_{yy} + (m^3 n - mn^3) Q_{xy} + 2(m^3 n - mn^3) Q_{ss} \end{aligned}$$

where $m = \cos\theta$, $n = \sin\theta$, ply angle θ is positive in counterclockwise direction. Now we introduce stress and moment resultants,

$$\begin{Bmatrix} N_{xx} \\ N_{yy} \\ N_{xy} \end{Bmatrix} = \int \begin{bmatrix} h_n \sigma_{xx} \\ \sigma_{yy} \\ h_0 \sigma_{xy} \end{bmatrix} dz \quad (4)$$

and

$$\begin{Bmatrix} M_{xx} \\ M_{yy} \\ M_{xy} \end{Bmatrix} = \int z \begin{bmatrix} h_n \sigma_{xx} \\ \sigma_{yy} \\ h_0 \sigma_{xy} \end{bmatrix} dz \quad (5)$$

Use of the principle of the stationary value of the total potential yields the transverse equilibrium equation of laminated cylindrical shell with an elastic core :

$$M_{xx,xx} + 2M_{yx,yx} + M_{yy,yy} + N_{xx}w_{,xx} + N_{yy} \left(\frac{1}{R} + w_{,yy} \right) + 2N_{xy}w_{,xy} + q - p = 0 \quad (6)$$

where q is the lateral pressure, p is core's reaction force ($p = f_{mn}w$), and the core's elastic constant f_{mn} is seen in reference[4]. The compatibility equation is :

$$\varepsilon_{xx,yy}^0 + \varepsilon_{yy,xx}^0 - \varepsilon_{xy,xy}^0 = -\frac{1}{R}w_{,xx} + w_{,xy}^2 - w_{,yy}w_{,xx} \quad (7)$$

Here we do not consider the torsion. Introduction of stress function F , defined below, leads to the identical satisfaction of the two in-plane equilibrium equations.

$$N_{xx} = -N_{xx}^0 + F_{,yy}, N_{yy} = N_{yy}^0 + F_{,xx}, N_{xy} = -F_{,xy} \quad (8)$$

The transverse equilibrium equation and in-plane compatibility equation then can be written solely in terms of F and w respectively, or

$$\begin{aligned} L_1(F) + L_2(w) + F_{,xx} \left(\frac{1}{R} + w_{,yy} \right) + N_{yy}^0 \left(\frac{1}{R} + w_{,yy} \right) + F_{,yy}w_{,xx} - N_{xx}^0 w_{,xx} - 2F_{,xy}w_{,xy} + q - f_{mn}w = 0 \\ L_3(F) + L_1(w) + \frac{1}{R}w_{,xx} - w_{,xy}^2 + w_{,xx}w_{,yy} = 0 \end{aligned} \quad (9)$$

where

$$\begin{aligned} L_1(F) &= b_{21}F_{,xxxx} + (-b_{31} + 2b_{23})F_{,xxxy} + (b_{11} - 2b_{33} + b_{22})F_{,xxyy} + (-b_{32} + 2b_{13})F_{,xyyy} + b_{12}F_{,yyyy}; \\ L_2(w) &= d_{11}w_{,xxxx} + (2d_{13} + 2d_{31})w_{,xxxy} + (d_{12} + 4d_{33} + d_{21})w_{,xxyy} + (2d_{32} + 2d_{33})w_{,xyyy} + d_{22}w_{,yyyy}; \\ L_3(F) &= a_{11}F_{,yyyy} - 2a_{13}F_{,xyyy} + (2a_{12} + a_{33})F_{,xxyy} - 2a_{23}F_{,xxxy} + a_{22}F_{,xxxx}; \\ [a_{ij}] &= [A_{ij}]^{-1}, [b_{ij}] = [a_{ij}][B_{ij}], [d_{ij}] = [B_{ij}][b_{ij}] - [D_{ij}], [A_{ij}] = \sum_{k=1}^N Q_{ij}^{(k)}(h_k - h_{k-1}), \\ [B_{ij}] &= \frac{1}{2} \sum_{k=1}^N Q_{ij}^{(k)}(h_k^2 - h_{k-1}^2), [D_{ij}] = \frac{1}{3} \sum_{k=1}^N Q_{ij}^{(k)}(h_k^3 - h_{k-1}^3); \end{aligned}$$

and N is the ply numbers. When conducting linear stability analysis of the circular cylindrical shells with an elastic core, we can neglect the nonlinear items of the above equations. Let the shell be critical state, then $F = F_c + \Delta F$, $w = w_c + \Delta w$ (10)

where sublabel c represents critical state, and $\Delta F, \Delta w$ are any small value. Put (10) into equilibrium and compatibility equations, we get the linear Donnell's equation, or

$$\begin{aligned} L_1(\Delta F) + L_2(\Delta w) - N_{xx}^0 \Delta w_{,xx} + \frac{1}{R} \Delta F_{,xx} + N_{yy}^0 \Delta w_{,yy} - f_{mn} \Delta w = 0 \\ L_3(\Delta F) + L_1(\Delta w) + \frac{\Delta w_{,xx}}{R} = 0 \end{aligned} \quad (11)$$

SOLUTION METHODOLOGY

Let ΔF and Δw have the following forms:

$$\begin{aligned} \Delta F(x, y) &= \sum_{i=1}^p [C_i(x) \cos \frac{iny}{R} + D_i(x) \sin \frac{iny}{R}] \\ \Delta w(x, y) &= \sum_{i=1}^p [A_i(x) \cos \frac{iny}{R} + B_i(x) \sin \frac{iny}{R}] \end{aligned} \quad (12)$$

where n is the circumferential wave numbers, p is the items of the trigonometric series, and A_i, B_i, C_i, D_i are unknown function about x . Put (12) into (11), adopt Galerkin-difference method, we can reduce (11) into linear equations, or

$$\left\{ \frac{1}{\Delta x^2} \begin{bmatrix} M_3 & M_1 \\ -I & 0 \end{bmatrix} + \frac{1}{2\Delta x} \begin{bmatrix} M_4 & M_2 \\ 0 & 0 \end{bmatrix} \right\} \{\beta_i\}_{j+1} + \left\{ \begin{bmatrix} M_5 & 0 \\ 0 & I \end{bmatrix} - \frac{2}{\Delta x^2} \begin{bmatrix} M_3 & M_1 \\ -I & 0 \end{bmatrix} \right\} \{\beta_i\}_j \quad (13)$$

$$+ \left\{ \frac{1}{\Delta x^2} \begin{bmatrix} M_3 & M_1 \\ -I & 0 \end{bmatrix} - \frac{1}{2\Delta x} \begin{bmatrix} M_4 & M_2 \\ 0 & 0 \end{bmatrix} \right\} \{\beta_i\}_{j-1} = 0$$

where $\{\beta_i\} = [x_i \ \eta_i]^T$, $\{\eta_i\} = \{x_i\}_{,xx}$, $\{x_i\} = [A_i \ B_i \ C_i \ D_i]^T$, $i=1,2, \dots, p$, $j=1,2, \dots, NP$, NP is the mesh points, I is the 4×4 identity matrix, and M_1, M_2, \dots, M_5 are 4×4 matrices with known elements. This is a set of $8p \times NP$ linear algebraic equations with $8p(NP+2)$ unknown variables. According to stability criterion, set $\{\beta_i\} \neq 0$, through the use of that the factor determinant value of (13) is zero, we can find the critical loads.

As the same, we can reduce (11) into standard characteristic equations, that is

$$\left\{ \frac{1}{\Delta x^2} \begin{bmatrix} M_3' & M_1 \\ -I & 0 \end{bmatrix} + \frac{1}{2\Delta x} \begin{bmatrix} M_4 & M_2 \\ 0 & 0 \end{bmatrix} \right\} \{\beta_i\}_{j+1} + \left\{ \begin{bmatrix} M_5' & 0 \\ 0 & 0 \end{bmatrix} - \frac{2}{\Delta x^2} \begin{bmatrix} M_3' & M_1 \\ -I & 0 \end{bmatrix} \right\} \{\beta_i\}_j + \quad (14)$$

$$\left\{ \frac{1}{\Delta x^2} \begin{bmatrix} M_3' & M_1 \\ -I & 0 \end{bmatrix} - \frac{1}{2\Delta x} \begin{bmatrix} M_4 & M_2 \\ 0 & 0 \end{bmatrix} \right\} \{\beta_i\}_{j-1} = \frac{N_{xx}^0}{\Delta x^2} \begin{bmatrix} F_1 & 0 \\ 0 & 0 \end{bmatrix} \{\beta_i\}_{j+1} + \frac{N_{xx}^0}{\Delta x^2} \begin{bmatrix} F_1 & 0 \\ 0 & 0 \end{bmatrix} \{\beta_i\}_{j-1}$$

$$+ \left\{ N_{yy}^0 \begin{bmatrix} F_2 & 0 \\ 0 & 0 \end{bmatrix} - N_{xx}^0 \frac{2}{\Delta x^2} \begin{bmatrix} F_1 & 0 \\ 0 & 0 \end{bmatrix} \right\} \{\beta_i\}_j$$

where $[M_3']$, $[M_5']$, $[F_1]$, $[F_2]$ are 4×4 matrices with known elements. (14) and typical characteristic equation $[E]\{\beta\} = P[G]\{\beta\}$ are the same. If let $[C] = [E]^{-1}[G]$, then the equation can be modified as $[C]\{\beta\} = \frac{1}{P}\{\beta\}$, which we can get the critical values by using the multiply-index method.

EXAMPLES AND DISCUSSION

Stability of Laminated Circular Cylindrical Shells

The critical loads of 3-ply Boron/Epoxy circular cylindrical shells

The material properties are:

$$E_{11} = 0.27586 \times 10^6 \text{ N/mm}^2, \mu_{12} = 0.25, E_{22} = 0.31034 \times 10^6 \text{ N/mm}^2,$$

$$\mu_{21} = 0.028, G = 0.10345 \times 10^5 \text{ N/mm}^2$$

The geometry configuration is $R=152.4\text{mm}$, $L=304.8\text{mm}$ and the total thickness $t=0.9144\text{mm}$. The stacking combinations of angle-ply are listed below, which are $\theta/\theta/0^\circ$ from the outside to inside. The boundary condition is SS-2. The results are seen in Table 1. As we see from Table 1, the results of this paper are approximate to the references'.

The critical loads of Graphite/Epoxy laminated cylindrical shells subjected axial compressure

The material properties are:

$$E_{11} = 0.11999 \times 10^6 N / mm^2, E_{22} = 0.76985 \times 10^5 N / mm^2,$$

$$\mu_{12} = 0.32, \mu_{21} = 0.02051, G = 0.48758 \times 10^4 N / mm^2,$$

The R=100mm, L=200mm, and the stacking combinations are (1) N=3, 90°/-20°/20°, t=0.419mm; (2) N=4, 90°/-45°/-45°/0°, t=0.579mm; (3) N=6, 90°/90°/30°/-30°/-30°/30°, t=0.899mm. The boundary condition is CC-4. The results are seen in Table 2.

The Stability of Laminated Circular Cylindrical Shell with Elastic Core

The critical loads of (3) group shell in 1.2 above with an elastic core under lateral and hydrostatic pressure are listed in Table 3, where the core's $E_c = 4.8275 N / mm^2$

Table 1 ($N_{cr}; N$)

source	θ N_{cr}	10°	20°	30°	40°	50°	60°	70°	80°
[6]		160.21 (11)	195.09 (12)	223.64 (12)	229.07 (12)	211.91 (12)	189.31 (12)	166.69 (12)	147.65 (11)
[7]		159.02 (11)	189.84 (12)	212.26 (12)	221.01 (12)	210.68 (12)	172.78 (12)	143.66 (12)	128.41 (11)
this paper		151.12 (10)	184.90 (13)	208.13 (12)	212.78 (14)	210.34 (12)	173.92 (12)	147.55 (11)	134.46 (10)

Table 2 (N/mm)

source	(1)	(2)	(3)
test	21.114(10)	43.513(8)	146.628(-)
Simitses[3] calculation	23.438--26.478(12)	40.60--63.45(9)	138.86--165.64(9)
this paper calculation	26.14(14)	50.031(12)	160.84(10)

Table 3 ($P_{cr} : 10^{-2} N / mm^2$)

load and boundary condition	μ_c P_{cr}	0.35	0.4	0.45	0.5
lateral pressure SS-1		49.309(9)	50.668(9)	52.358(9)	54.461(9)
hydrostatic pressure SS-1		47.703(9)	48.889(10)	50.358(10)	52.185(10)
lateral pressure CC-4		52.061	53.35(10)	54.944(10)	56.923(10)

In addition to the examples listed above, the critical lateral pressures of two group of composite shells with elastic core under different E_c , boundary conditions, angle-ply and numbers of laminate are calculated. The calculated results show that the core's E_c and boundary condition have great effect on the critical loads, the angle-ply θ has little effect and under thickness unchanged the numbers of laminate have no effect on the critical loads.

CONCLUSION

This paper uses Galerkin-difference method to reduce the Donnell's partial differential equations of laminated cylindrical shell with elastic core to linear equations. Then according to the stability criterion, the critical loads are found by using the multiply-index method to solve the characteristic equations. The FORTRAN program has been programmed, which can be used to calculate critical loads under different cases. The results of examples show that the method adopted in this paper is reliable and has great value to the designing engineers.

REFERENCES

1. R.C. Tennyson , "Buckling of laminated composite cylinders: a review", Composites 1, 17-24, 1975.
2. Cugupinghe and Zhicunyici, "The coupling effect on the buckling of laminated circular cylindrical shells under axial compression", Foreign Rocket Technology, 1985. 2.
3. G.J. Simitses, I. Sheinman and D. Shaw, "Analysis of the nonlinear large deformation behavior of composite cylindrical shells", AD-A133761, 1983.
4. P. Seide, "The stability under axial compression and lateral pressure of circular cylindrical shells with a soft elastic core", J.A.S., July, 1962.
5. Edited by Cai weijun and Thomas , Translated by Yu dechang, "Introduction of composite mechanics", 1981.
6. Zhou chengti and Zhou jianping, "Nonlinear stability analysis of laminated composite cylindrical shells", Applied mathematics and mechanics, 1986.1.
7. N.S. Khot and Uenkayya V.B., "Effect of fiber orientation on initial postbuckling behavior and imperfect sensitivity of composite cylindrical shells", AFFDL-TR-70-125,1970.

HOLE IDENTIFICATION IN COMPOSITE STRUCTURES USING BOUNDARY DATA FROM MULTIPLE LOADING MODES

Chyanbin Hwu and Yan-Chu Liang

*Institute of Aeronautics and Astronautics,
National Cheng Kung University Tainan, Taiwan, 70101, Republic of China*

SUMMARY: Recently, a special boundary element was developed for a two-dimensional composite structure containing an elliptical hole. With this special boundary element doing the forward analysis and the nonlinear optimization techniques doing the inverse analysis, the size, location and orientation of the holes can be identified in principle. However, the hole effects are localized which may not be clearly reflected from the boundary information especially when the data are from static deformation only. To remedy this, we propose a concept of stepwise multiple-loading modes. By combining the special boundary element with the nonlinear optimization technique and the stepwise multiple-loading concept, several numerical examples have been done. The results show that our method for hole identification is always stable and accurate no matter how far-away of the initial guess from its target.

KEYWORDS: two-dimensional composite structure, hole identification, forward analysis, inverse analysis, nonlinear optimization, multiple loading modes

INTRODUCTION

Current development in smart materials has improved the conventional composite materials in the ability of self-monitor during service. The massless sensor of micro-electro-mechanical system makes the work successful to embed the sensor into the composite material without changing the original system. For an ideal on-line identification, the measured values of sensors are obtained during service not from experiment. Due to this important reason, the study of the inverse problem by using the static deformation as the input is gradually an interested research [1,2]. On the other hand, research interest in identifying the hole/crack in a non-destructive manner has considerably increased in the past few years. Indeed, such information about the hole/crack geometry is indispensable for estimating the safety of the structure. In engineering practice, one usually carries out measurements, using techniques such as ultrasonics, magnetic flux leakage, X-rays, penetrant, eddy current, etc. [3], on the exterior boundary of the body to locate the hole/crack. Recently, Qian, et.al [4], Rizos, et.al [5], Shen and Taylor [6], Lim [7], Ricles and Kosmatka [8] and Soeiro and Hajela [9] identified the damage location and magnitude of a beam or plate from the vibration modes.

The determination of the unknown internal hole in a structure for which the boundary conditions are prescribed (measured experimentally) belongs to the category of inverse problems in mechanics. Since the measured data are usually provided on the exterior boundary, the boundary integral technique [10] for the analysis of the forward mechanics problems becomes a promising computational tool, e.g., [11,12,13]. In this paper, a special boundary element developed by Hwu and Yen [14], is employed for the forward analysis. The Green's function used in this special boundary element method was derived by using Stroh's formalism [15]. An overview of the Stroh's formalism, the exact closed-form solutions for infinite domain problems, and the special boundary element method are presented for the convenience of readers' reference. As far as the inverse problems are concerned, the technique of nonlinear optimization is applied. Examples of the application of this technique to damage detection may be found in [6,16,17,18]. When the boundary data are from static deformation only, the localized characteristics of hole effects may decrease our ability to identify hole within the body. To remedy this, a concept of stepwise multiple-loading modes is proposed in this paper.

FORWARD PROBLEMS

In order to analyze the overall mechanical behaviors of the composite materials, the mechanics model of anisotropic elasticity is usually used. Among various analytical formulation, the Stroh's formalism [15] has recently been proved to be a powerful and elegant formalism for treating general problems of two-dimensional linear anisotropic elasticity. By combining the Stroh's formalism for anisotropic elasticity formulation with the method of analytical continuation for the complex variable manipulation [19], the analytical solution for most of infinite domain problems can be obtained explicitly. Infinite domain solutions are very useful for catching the special feature of the discussed problems such as cracks, holes or inclusions [20]. For practical engineering analysis, the infinite domain solutions can also be embedded into the numerical algorithm to accelerate the computation and raise the accuracy. Before doing any work about the hole identification, we will now present the general solutions for two-dimensional linear anisotropic elasticity.

In a fixed rectangular coordinate system $x_i, i = 1, 2, 3$, let u_i and σ_{ij} be the displacement and stress, respectively. A general solution satisfying the strain-displacement relations, the stress-strain laws and the equations of equilibrium can be written as [15,21]

$$\underline{u} = \underline{A}\underline{f}(z) + \overline{\underline{A}\underline{f}(z)}, \quad \underline{\phi} = \underline{B}\underline{f}(z) + \overline{\underline{B}\underline{f}(z)}, \quad (1a)$$

where

$$\underline{A} = [\underline{a}_1 \quad \underline{a}_2 \quad \underline{a}_3], \quad \underline{B} = [\underline{b}_1 \quad \underline{b}_2 \quad \underline{b}_3], \quad (1b)$$

$$\underline{f}(z) = [f_1(z_1), f_2(z_2), f_3(z_3)]^T. \quad (1c)$$

\underline{u} and $\underline{\phi}$ are 3×1 matrices whose elements are u_i and $\phi_i, i = 1, 2, 3$. ϕ_i denotes the stress function and $\sigma_{i1} = -\phi_{i,2}, \sigma_{i2} = \phi_{i,1}$. $f_\alpha(z_\alpha)$ is an arbitrary function of the complex variable $z_\alpha (= x_1 + p_\alpha x_2, \alpha = 1, 2, 3)$, which will be determined by the boundary conditions set for each particular problem. The eigenvalues p_α and the eigenvector matrices $\underline{A}, \underline{B}$ are determined by the elastic constants C_{ijkl} . Note that $\underline{A}, \underline{B}$ are uniquely defined by the normalization $\underline{A}^T \underline{B} + \underline{B}^T \underline{A} = \underline{I}$.

Infinite Domain Solution

Consider an infinite anisotropic plate containing an elliptic hole under a concentrated force \hat{p} applied at point $\hat{x} = (\hat{x}_1, \hat{x}_2)$ in the body. An analytical solution satisfying the traction-free hole boundary condition and the force equilibrium condition around the point \hat{x} can be found in [20,22], which is

$$f(z) = \frac{1}{2\pi i} \ll \log(\zeta_\alpha - \hat{\zeta}_\alpha) \gg A^T \hat{p} + \sum_{k=1}^4 \frac{1}{2\pi i} \ll \log(\zeta_\alpha^{-1} - \hat{\zeta}_k) \gg B^{-1} \bar{B} I_k \bar{A}^T \bar{p} \tag{2}$$

where $\zeta_\alpha = \frac{z_\alpha + \sqrt{z_\alpha^2 - a^2 - p_\alpha^2 b^2}}{a - ip_\alpha b}$ and a, b are the half lengths of the major and minor axes of the ellipse. $\ll \gg$ stands for the diagonal matrix, i.e. $\ll f_\alpha \gg = \text{diag}[f_1, f_2, f_3]$, where each component function is varied according to the index α . I_k denotes the 3×3 matrix whose components are all zero except that the k^{th} diagonal term is equal to 1.

Finite Domain Solution

Due to the mathematical infeasibility, most of the analytical solutions are obtained for infinite domain problems. To get the solution for the problems with finite boundaries, the usual way is by finite element method in which the mesh of the entire body is necessary. For a problem that only the response of the outer boundary is concerned, the boundary element method [10] may become more attractive. Since the measured data are usually provided on the exterior boundary for the hole identification problems, the boundary integral technique for the hole analysis becomes a promising computational tool. Furthermore, to provide an efficient and accurate computational algorithm, the analytical solution shown in eqn.(2) concerning only the internal hole boundary of infinite bodies is used as a Green's function in the boundary element formulation [20]. Since the Green's function already satisfies the traction-free hole boundary conditions, discretization around the hole boundary is avoided. This results in a saving of computer time and storage. Moreover, discretization with relatively coarse meshes can achieve high accuracy. By letting the minor axis of the elliptic hole be zero, this special boundary element can also be used for crack analysis.

The purpose of this paper is to explore the feasibility of identifying a hole by using only the data from static deformation. From the study of Liang and Hwu [23] for the piezoelectric materials, we see that the stress intensity factors are very insensitive to the crack location especially when the crack size is under a certain value. Similar results may occur for the conventional fiber-reinforced composite materials. To be successful in identification, we should be very careful about the choice of parameters which need to be sensitive to the hole size, location and orientation. Therefore, in the following example we like to search the parameters which may be sensitive to the hole size and location. Consider the mean square value ψ_k of stresses or displacements ϕ_{ki} at some near boundary points $i(i = 1, 2, \dots, N)$,

$$\psi_k(a, b, x, y, \theta) = \sum_{i=1}^N [\phi_{ki}(a, b, x, y, \theta) - \phi_{ki}^o(a_o, b_o, x_o, y_o, \theta_o)]^2, \tag{3}$$

in which the argument a, b, x, y, θ denotes, respectively, the size, center location, and orientation of the hole. ϕ_{ki}^o is the prescribed value of ϕ_{ki} at $a_o = 10^{-8}cm, b_o = 10^{-8}cm, x_o =$

$\frac{W}{2}, y_o = \frac{H}{2}, \theta_o = 0^\circ$. Under different loading conditions, the components of stresses or displacements considered are different. For example, only displacement u_2 and stresses σ_{11}, σ_{12} and σ_{22} are considered for opening mode I, i.e., we choose $\phi_{1i} = (u_2)_i, \phi_{2i} = (\sigma_{11})_i, \phi_{3i} = (\sigma_{12})_i, \phi_{4i} = (\sigma_{22})_i$. Similarly, for shearing mode II, we choose $\phi_{1i} = (u_1)_i, \phi_{2i} = (\sigma_{11})_i, \phi_{3i} = (\sigma_{12})_i, \phi_{4i} = (\sigma_{22})_i$. For tearing mode III, we choose $\phi_{1i} = (u_3)_i, \phi_{2i} = (\sigma_{31})_i, \phi_{3i} = (\sigma_{32})_i$.

Example

Consider a square finite plate with $W = H = 0.3m$ and the plate is made of composite materials whose mechanical properties are $E_1 = 114.8GPa, E_2 = E_3 = 11.72GPa; \nu_{12} = 0.21; G_{12} = 9.65GPa$. The variation of the mean square value ψ_1 of displacements with respect to circular hole radius r or half crack length a under different loading mode are plotted [24]. The results show that the displacement u_2 of mode I, the displacement u_3 of mode III for the crack problem and the displacement u_1 of mode II for the hole problem are more sensitive to the hole/crack size than the others. This is helpful for us to choose proper design variables for the inverse analysis. To know the sensitivity of stresses or displacements with respect to the hole location, we vary x , fix all the other variables, and plot the figures under a certain loading mode. Figure 1 is a typical example for studying the effects of the hole location, from which we see that the stress component σ_{32} is more sensitive than the other variables. Note that all the curves in this figure have been shifted vertically to the lowest value of ψ_1 since only relative values are concerned in this figure. It is also noticed that σ_{31} and u_3 are almost indistinguishable with respect to the hole location. This means that if σ_{31} and u_3 are chosen to be the design variables for the inverse analysis, the hole may not be identified under certain loading conditions. Thus, using boundary data from multiple loading modes becomes necessary for hole identification.

INVERSE PROBLEMS

Consider that the internal hole boundary Γ_c^* is not known. A set of experimental measurements are available as

$$\begin{aligned} u_k(\tilde{x}_i, \Gamma_c^*) &= \underline{u}_k^e(\tilde{x}_i, \Gamma_c^*), & \tilde{x}_i &\in \Gamma_{eu}, \\ t_k(\tilde{x}_j, \Gamma_c^*) &= \underline{t}_k^e(\tilde{x}_j, \Gamma_c^*), & \tilde{x}_j &\in \Gamma_{et}, \end{aligned} \quad (4)$$

$i = 1, 2, \dots, m; j = 1, 2, \dots, n$. A total of $(m+n)$ experimental observations are thus available. The identification problem consists of determining the hole geometry Γ_c^* based upon these given experimental values.

In section 2, the forward analysis shows that some combinations ψ_k of stresses and displacements under different loading modes may provide a sensitive parameter for the hole location. Based upon these analyses, in this section we will show the hole size, location and orientation identification by using the concept of multiple loading conditions. Thus, the design variable Γ_c can be represented by the hole size a, b (when $b \rightarrow 0$, it may be recognized as a crack), the rotation angle θ and the hole-centered position x, y . The identification problem now becomes the determination of the hole size a^*, b^* , the orientation θ^* and the hole-centered position x^*, y^* based upon $u_i^e(\Gamma_c^*)$ and $\sigma_{ij}^e(\Gamma_c^*)$. To proceed with this kind of inverse problem, the technique of nonlinear optimization [25] was applied in this paper.

From the results of forward analysis provided in section 2, we know that the hole identification may be achieved by the use of multiple loading conditions. With this concept, we design a multi-step nonlinear optimization as

- minimize:

$$F_M(\Gamma_c) = \sum_{i=1}^{n+m} \sum_{k=1}^4 \omega_k [\Delta\phi_{ki}(\Gamma_c)]^2, \quad \text{for mode M(= I, II, or III)} \quad (5)$$

- subject to:

$$g_{ki} = \left| \frac{\phi_{ki}(\Gamma_c)}{\phi_{ki}^e(\Gamma_c^*)} - 1 \right| - e_M < 0, \quad \begin{cases} k = 1, 2, 3, 4; \\ i = 1, 2, \dots, n + m. \end{cases} \quad (6a)$$

$$0.02W < 2a < 0.98W,$$

$$0.02W < 2b < 0.98W,$$

$$0.02W < x < 0.98W,$$

$$0.02H < y < 0.98H,$$

$$-\frac{\pi}{2} < \theta < \frac{\pi}{2},$$

(6b)

- change mode M, decrease e_M and repeat the optimization stated in (5) and (6) until the final result satisfies our tolerance requirement.

where ϕ_{ki} has been defined following eqn.(3); the objective function is to fit the numerical results $\phi_{ki}(\Gamma_c)$ to the experimental data $\phi_{ki}^e(\Gamma_c^*)$ by varying Γ_c ; $\Delta\phi_{ki}$ denotes the difference between ϕ_{ki} and ϕ_{ki}^e ; ω_k is the weighting factor proportional to the sensitivity of ϕ_{ki} and is defined as

$$\begin{aligned} \omega_1 = 1.0, \omega_2 = \omega_3 = 0.6, \omega_4 = 0.5, & \quad \text{for mode I and II} \\ \omega_1 = 1.0, \omega_2 = \omega_3 = 0.6, & \quad \text{for mode III} \end{aligned} \quad (7)$$

In order to make sure that the hole is inside the plate to prevent a meaningless design, additional side constraints must be included:

$$\begin{aligned} h_1 &= \max(a \cos|\theta|, b \sin|\theta|) - \min(x, W - x) < 0, \\ h_2 &= \max(a \sin|\theta|, b \cos|\theta|) - \min(y, H - y) < 0, \end{aligned} \quad (8)$$

Note that at the beginning of iteration procedure, the tolerance e_M can be chosen to be a large value e.g. $e_M = 10^{-2}$ to accelerate the optimization. When we finish one optimization procedure for a certain mode, we may decrease the tolerance e_M and change to the other loading mode. Repeating these process until e_M is within a small tolerance value ,e.g. $e_M = 10^{-6}$. The convergence is then achieved and the hole is identified. The three different loading conditions are given as follows: the lower face of the plate is fixed; the left and right sides are free and the upper face of the plate is subjected to the traction in x_1, x_2 or x_3 direction corresponding to each mode. The material is chosen to be the same as the one used in the example of section 2 and a square finite plate ($W = H = 30cm$) is considered. The public domain program COPES/ADS [26] is chosen to implement the optimization procedure and the combinations used in this paper are the method of feasible direction plus polynomial interpolation.

Example

In this example, Figure 2 show a small inclined elliptical hole identified by the multi-step nonlinear optimization. Followed by the mode III, II, ... loading conditions, the final identified

value is very close to the target value even by beginning with a far-away initial guess. To see the influence of the initial guess, the starting loading mode, and the sequence of loading mode, many different cases are studied in [24]. The results show that the final identified value will not be influenced by the initial guess, the starting loading mode and the sequence of loading mode. However, the efficiency of optimization may be different. It seems that mode III is a good starting loading mode for our multi-step nonlinear optimization, which is compatible with the results of forward analyses.

CONCLUSION

The purpose of this paper is to explore the feasibility of identifying a hole by using only the data from static deformation. The hole analysis (forward problem) is performed by combining the Stroh formalism with the boundary element method. The hole identification (inverse problem) is then implemented by applying the techniques of nonlinear optimization. Lots of efforts in the forward analysis give us an idea to improve the nonlinear optimization by using the concept of stepwise multiple loading modes. The optimum result of each step can be used as an initial guess of the next step under different loading condition, until the final result satisfies our tolerance requirement. Thus, not only the hole size but also the location and orientation can be identified. From the numerical examples shown in this paper, we see that our method for hole identification is always stable no matter how far-away of the initial guess from its target. However, the efficiency is usually dependent upon the initial guess, starting loading mode and the sequence of loading mode. Moreover, the total CPU time is still too long to be applied to the on-line hole identification. Therefore, the most important thing for us is applying the same concept to the method of neural network.

ACKNOWLEDGEMENTS

The authors would like to thank the support by National Science Council through grant NSC 85-2212-E006-059.

REFERENCES

1. Chen, D.H. and Nisitani, H., 1993, "Detection of a crack by body force method," *Engineering Fracture Mechanics*, Vol. 45, No. 5, pp. 671-685.
2. Atkinson, C. and Aparicio, N.D., 1994, "An inverse problem method for crack detection in elastic materials under anti-plane strain," *Proc. R. Soc. London A*, Vol. 445, pp. 637-652.
3. Bray, D.E. and Stanley, R.K., 1993, *Nondestructive Evaluation - A Tool in Design, Manufacturing and Service*, McGraw-Hill, N.Y.
4. Qian, G.L., Gu, S.N., and Jiang, J.S., 1990, "The dynamic behavior and crack detection of a beam with a crack," *J. of Sound and Vibration*, Vol. 138, No. 2, pp. 233-243.
5. Rizos, P.F., Aspragathos, N., and Dimarogonas, A.D., 1990, "Identification of crack location and magnitude in a cantilever beam from the vibration modes," *J. of Sound and Vibration*, Vol. 138, No. 3, pp. 381-388.
6. Shen, M.H.H., and Taylor, J.E., 1991, "An identification problem for vibrating cracked beams," *J. of Sound and Vibration*, Vol. 150, No. 3, pp. 457-484.
7. Lim, T.W., 1991, "Structural damage detection using modal test data," *Technical Notes*, Vol. 29, No. 12, pp. 2271-274.
8. Ricles J.M., and Kosmatka, J.B., 1992, "Damage detection in elastic structures using

- vibratory residual forces and weighted sensitivity," *AIAA Journal*, Vol. 30, No. 9, pp. 2310-2316.
9. Soeiro, F.J., and Hajela, P., 1993, "Damage detection in composite materials using identification techniques," *J. of Aerospace Engineering*, Vol. 6, No. 4, pp. 363-380.
 10. Brebbia, C.A., Telles, J.C.F. and Wrobel, L.C., 1984, *Boundary Element Techniques - Theory and Applications in Engineering*, Springer-Verlag, N.Y.
 11. Nishimura, N. and Kobayashi, 1991, "A Boundary Integral Equation Method for an Inverse Problem Related to Crack Detection," *Int. J. Numerical Methods in Engineering*, Vol. 32, pp. 1371-1387.
 12. Zeng, X. and Saigal, S., 1992, "An Inverse Formulation with Boundary Elements," *J. Applied Mechanics*, Vol. 59, pp. 835-840.
 13. Hsieh, S.C. and Mura, T., 1993, "Nondestructive Cavity Identification in Structures," *Int. J. Solids Structures*, Vol. 30, No. 12, pp. 1579-1587.
 14. Hwu, C. and Yen, W.J., 1991, "Green's Functions of Two-Dimensional Anisotropic Plates Containing an Elliptic Hole," *Int. J. Solids and Structures*, Vol. 27, No. 13, pp. 1705-1719.
 15. Stroh, A. N., 1958, "Dislocations and Cracks in Anisotropic Elasticity," *Phil. Mag.*, Vol. 7, pp. 625-646.
 16. Yagawa, G., Yoshimura, S., Mochizuki, Y., and Oishi, T., 1992, "Identification of Crack Shape Hidden in Solid by Means of Neural Network and Computational Mechanics," *IUTAM Symposium*, Tokyo, pp.213-222.
 17. Takadoya, M., Notake, M., Kitahara, M., Achenbach, J.D., Guo, Q.C., and Peterson, M.L., 1992, "Neural Network Approach to the Inverse Problem of Crack-Depth Determination from Ultrasonic Backscattering Data," *IUTAM Symposium*, Tokyo, pp.413-422.
 18. Tsou, P. and Shen, M.H.H. , 1994, "Structural Damage Detection and Identification Using Neural Networks," *AIAA J.*, Vol. 32, No. 1, pp. 176-183.
 19. Muskhelishvili, N.I., 1954, *Some Basic Problem of the Mathematical Theory of Elasticity*, Noordhoff Pub., Groningen.
 20. Hwu, C. and Yen, W.J., 1991, "Green's Functions of Two-Dimensional Anisotropic Plates Containing an Elliptic Hole," *Int. J. Solids and Structures*, Vol. 27, No. 13, pp. 1705-1719.
 21. Ting, T.C.T., 1996, *Anisotropic Elasticity - Theory and Applications*, Oxford Engineering Science Series (45), N.Y.
 22. Hwu, C. and Yen, W. J., 1993, "On the Anisotropic Elastic Inclusion in Plane Elastostatics," *ASME J. Applied Mechanics*, Vol. 60, pp. 626-632.
 23. Liang, Y.C. and Hwu, C. , 1995, "Analysis And Identification of Cracks In Piezoelectric Materials," *Proceedings of ICCM-10*, Vol. V, pp. 315-322.
 24. Hwu, C. and Liang, Y.C., 1996, "Crack Identification In Composite Materials ," *National Science Council Report*, NSC 85-2212-E-006-059.
 25. Vanderplaats, G.N., 1984, *Numerical Optimization Techniques for Engineering Design: With Applications*, McGraw-Hill, N.Y.
 26. Vanderplaats, G.N., 1985, *A Fortran Control Program for Engineering Synthesis (COPES) Using the Automated Design Synthesis (ADS) Optimization Program*, Engineering Design Optimization, Inc., Santa Barbara.

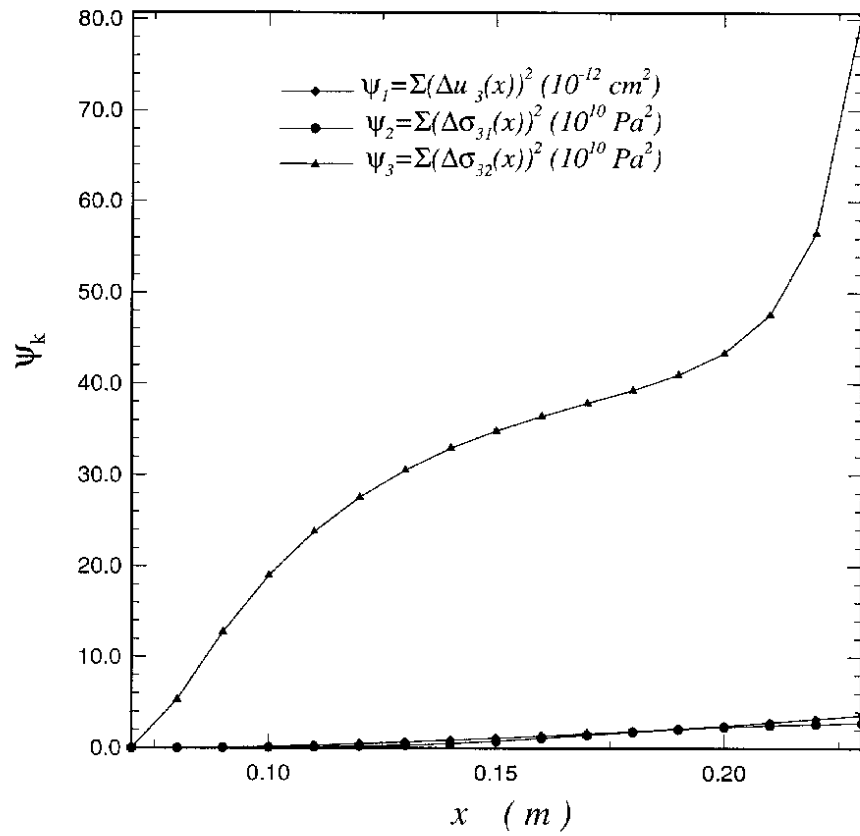


Fig. 1 Variation of stress and displacement with respect to hole horizontal location x (Mode III).

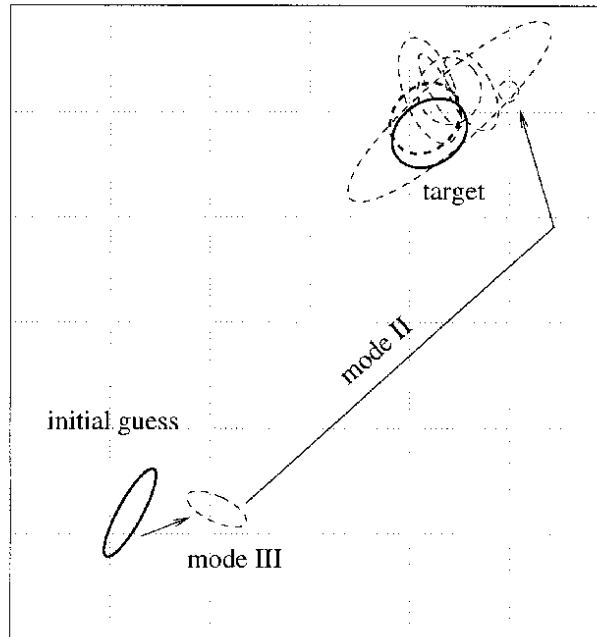


Fig. 2 Hole identification by multi-step nonlinear optimization technique.

material properties: $E_1=114.8\text{GPa}$, $E_2=E_3=11.72\text{GPa}$,
 $\nu_{12}=0.21$, $G_{12}=9.65\text{GPa}$.

	$(2a/W, 2b/H, x/W, y/H, \theta)$
target value	$(.1333, 0.1, 0.7, 0.8, 30^\circ)$
identified value	$(.1254, .1021, .6924, .8234, 39.3^\circ)$
initial guess	$(.006, .16, 0.2, 0.2, -30^\circ)$

FREE-EDGE INTERLAMINAR STRESS ANALYSIS IN COMPOSITE LAMINATES BY THE EXTENDED KANTOROVICH METHOD

Maenghyo Cho and Jin-Young Yoon

Department of Aerospace Engineering, Inha University, 253 Yong-Hyun Dong, Nam-Ku, Incheon, 402-751, Republic of Korea

SUMMARY: The extended Kantorovich method has been applied to analyze the interlaminar stresses at the free edge of composite laminates subjected to a mechanical uniaxial tension. Using the principle of complementary minimum energy and iterating through the extended Kantorovich method, the results given by the present method satisfy the traction-free conditions not only at the free edge, but also at top and bottom surfaces of laminates. For verification of the proposed method, cross-ply, angle-ply and quasi-isotropic laminates are considered. Through the iteration processes of four times, the convergence of the solutions is demonstrated. The present method predicts both the in-plane and out-of-plane stresses accurately. Thus, at the interior as well as near the free edge of laminates, the present method can provide accurate stress predictions.

KEYWORDS: interlaminar stress, free edge, extended Kantorovich method, uniaxial tension, principle of complementary minimum energy, eigenproblem, stress function, iteration

INTRODUCTION

Due to the mismatch of the elastic properties between plies, serious stress concentration/singularity are caused near the free edges of composite laminates. Because the full 3-dimensional stress fields should be considered in these regions, classical laminated plate theory is no longer valid for the reliable interlaminar stress predictions. The interlaminar stresses at the free edge may lead to the initiation of delamination and failure of composite laminates. Thus, the determination of these stresses is an important issue on the strength analysis and design of laminates.

Unfortunately, the exact elasticity solutions do not exist until now. Thus, numerous researchers have used various approximate analytical and numerical methods to predict the interlaminar stresses. Even though a number of approximate methods have been proposed, accurate and efficient methods are rare, which satisfy all the boundary and interface continuity conditions.

In the early stage of this research field, the displacement-based methods such as the finite difference method[1,2] and finite element method[3,4], have been used. However,

those methods have difficulty in predicting the interlaminar stresses accurately because they do not satisfy traction continuities at the interfaces between layers. Furthermore, the convergence is slow and the large computation is required to resolve the stresses. Thus the displacement-based methods are unsuitable for the analysis of the interlaminar stresses.

After Spilker and Chou[5] demonstrated the importance of satisfying the traction-free conditions at the edges, the researches using the stress-based methods have been led. In these studies, stress functions are divided into in-plane and out-of-plane functions. Under the appropriate assumption of stress functions, the interlaminar stresses at the free edge have been calculated. As represented among those approaches, Kassapoglou and Lagace[6] determined the stresses based on the integrated form of the force and moment equilibriums. However, they assumed that in-plane stresses are constant through the thickness in each plies of laminates. The results do not satisfy the pointwise traction-free conditions through the thickness at the free edges. Thus, the accuracy of predicted stresses in out-of-plane direction cannot be guaranteed from this method. Yin[7,8] used the piecewise polynomial approximations for the out-of-plane stress functions. In his formulation, the stress functions are continuous over each layer, and the interlaminar stresses are also continuous at the interface of each layer. However, the formulation is complicated and the predicted interlaminar stresses show undesirable oscillatory behavior along the in-plane direction at the interfaces between layers.

Recently, Flanagan[9] proposed alternative efficient method in which he assumed the solutions of the free vibration of a clamped-clamped beam for the out-of-plane stress functions. Using the principle of complementary minimum energy, a simple method to determine the in-plane stress functions was proposed. The stress functions given by his approach are not satisfied the displacement continuity conditions at the interfaces between plies. Thus, out-of-plane stress distributions are not predicted accurately, and the oscillating trends appear. In addition, his results cannot recover the classical lamination theory (CLT) solution in the interior of the laminate.

In the present study, the analysis of the interlaminar stresses at the free edge in composite laminates has been proposed. The extended Kantorovich method by Kerr[10] is used to predict the accurate stress functions. The Leknitskii stress functions[11] are adopted to divide interlaminar stress expression into in the in-plane and out-of-plane coordinate functions. Using the extended Kantorovich method, the iteration process is carried out. Under the principle of complementary minimum energy through eigenproblem, the in-plane and out-of-plane stress functions are improved repeatedly.

For the accurate calculation of the interlaminar stresses, it should be satisfied that the stresses are zero at the free edge, and top/bottom surfaces in composite plates, and that the stresses and displacements are continuous at the interfaces between plies. In the present study, all above conditions are satisfied through the calculating processes, and the displacement fields are continuous through the thickness in the variational sense. From the analysis of cross-ply, angle-ply and quasi-isotropic laminates, it is found that the present method predicts the interlaminar stresses accurately not only at the free edge of composite laminates but also at the interior without any undesirable oscillatory behaviors.

FORMULATION

The geometry of the composite laminate with free edge under uniaxial tension is given in Fig. 1. The laminate consists of the orthotropic materials. The thickness of each ply is same, and the plies have arbitrary angles with x axis.

The linear elastic constitutive equations of each ply are expressed as

$$\begin{Bmatrix} \epsilon_1 \\ \epsilon_2 \\ \epsilon_3 \\ \epsilon_4 \\ \epsilon_5 \\ \epsilon_6 \end{Bmatrix} = \begin{bmatrix} S_{11} & S_{12} & S_{13} & 0 & 0 & S_{16} \\ S_{12} & S_{22} & S_{23} & 0 & 0 & S_{26} \\ S_{13} & S_{23} & S_{33} & 0 & 0 & S_{36} \\ 0 & 0 & 0 & S_{44} & S_{45} & 0 \\ 0 & 0 & 0 & S_{45} & S_{55} & 0 \\ S_{16} & S_{26} & S_{36} & 0 & 0 & S_{66} \end{bmatrix} \begin{Bmatrix} \sigma_1 \\ \sigma_2 \\ \sigma_3 \\ \sigma_4 \\ \sigma_5 \\ \sigma_6 \end{Bmatrix} \quad (1)$$

where S_{ij} are terms of the transformed compliance matrix.

From above geometry, the boundary conditions at the free edge, top and bottom surface are given in Eqn 2.

$$\begin{aligned} \sigma_2 = \sigma_4 = \sigma_6 = 0 & \quad \text{at } y = 0, b \\ \sigma_3 = \sigma_4 = \sigma_5 = 0 & \quad \text{at } z = \pm h/2 \end{aligned} \quad (2)$$

The laminate is assumed to be in a state of generalized plane strain in the x coordinate. From these assumptions and constitutive equations, all the strains can be expressed in terms of ϵ_1 .

$$\epsilon_i = \hat{S}_{ij}\sigma_j + \frac{S_{i1}}{S_{11}}\epsilon_1 \quad (i, j = 2, 3, \dots, 6) \quad (3)$$

where

$$\hat{S}_{ij} = S_{ij} - \frac{S_{i1}S_{1j}}{S_{11}} \quad (4)$$

The coordinates are nondimensionalized as follows.

$$\eta = z/h, \quad \xi = y/h \quad (5)$$

Leknitskii stress functions are introduced to satisfy the pointwise equilibrium automatically. The interlaminar stress functions can be divided into the in-plane and out-of-plane functions.

$$\begin{aligned} \frac{\partial^2 F}{\partial \eta^2} = \sigma_2, \quad \frac{\partial^2 F}{\partial \xi^2} = \sigma_3, \quad \frac{\partial^2 F}{\partial \eta \partial \xi} = -\sigma_4 \\ \frac{\partial \Psi}{\partial \xi} = -\sigma_5, \quad \frac{\partial \Psi}{\partial \eta} = \sigma_6 \end{aligned} \quad (6)$$

where

$$F = \sum_{i=1}^n f_i(\xi)g_i(\eta), \quad \Psi = \sum_{i=1}^n p_i(\xi)g_i^I(\eta) \quad (7)$$

1st Process : Calculation of In-plane Stress Functions from Initial Assumption

The in-plane stress functions are determined from the assumption of the out-of-plane stress functions. The out-of-plane functions must satisfy the traction-free conditions at the top and bottom surfaces in composite laminates. If the functions and their first derivatives are zero in those regions, then the above conditions are satisfied. In the present study, the out-of-plane functions are assumed as eigenmodes of a clamped-clamped beam which are same as those of Flanagan[9].

$$g_i(\eta) = \cos(\beta_i\eta) + k_i \cosh(\beta_i\eta) \tag{8}$$

where

$$k_i = -\cos(\beta_i/2) / \cosh(\beta_i/2) \tag{9}$$

In above equation, β_i are the solutions of following characteristic equation.

$$\cosh(\beta/2) \sin(\beta/2) + \cos(\beta/2) \sinh(\beta/2) = 0 \tag{10}$$

The governing equations are derived from the assumed out-of-plane stress functions and the principle of complementary minimum energy.

$$\delta U = \int \int \epsilon_i \delta \sigma_i dy dz = 0 \quad (i = 2, 3, \dots, 6) \tag{11}$$

In Eqn 11, the strains are substituted from Eqn 3. Using the Eqn 6, the stresses are expressed in terms of f_i and g_i . Eqn 11 is expressed as follows through integration by parts.

$$\begin{aligned} & \int [a_{ij}^{(4)} f_j^{IV} + a_{ij}^{(2)} f_j^{II} + a_{ij}^{(0)} f_j + b_{ij}^{(2)} p_j^{II} + b_{ij}^{(0)} p_j + r_i] \delta f_i d\xi \\ & + \int [c_{ij}^{(2)} p_j^{II} + c_{ij}^{(0)} p_j + d_{ij}^{(2)} f_j^{II} + d_{ij}^{(0)} f_j + s_i] \delta p_i d\xi = 0 \quad (i, j = 1, 2, \dots, n) \end{aligned} \tag{12}$$

where

$$\begin{aligned} a_{ij}^{(4)} &= \int \hat{S}_{33} g_i g_j d\eta \\ a_{ij}^{(2)} &= \int \hat{S}_{23} (g_i^{II} g_j + g_i g_j^{II}) d\eta - \int \hat{S}_{44} g_i^I g_j^I d\eta \\ a_{ij}^{(0)} &= \int \hat{S}_{22} g_i^{II} g_j^{II} d\eta \\ b_{ij}^{(2)} &= \int \hat{S}_{36} g_i^{II} g_j^{II} d\eta - \int \hat{S}_{45} g_i^I g_j^I d\eta & d_{ij}^{(2)} &= \int \hat{S}_{36} g_i^{II} g_j^{II} d\eta - \int \hat{S}_{45} g_i^I g_j^I d\eta \\ b_{ij}^{(0)} &= \int \hat{S}_{26} g_i^{II} g_j^{II} d\eta & d_{ij}^{(0)} &= \int \hat{S}_{26} g_i^{II} g_j^{II} d\eta \\ c_{ij}^{(2)} &= - \int \hat{S}_{55} g_i^I g_j^I d\eta & r_i &= \int \epsilon_1 \frac{S_{12}}{S_{11}} g_i^{II} d\eta \\ c_{ij}^{(0)} &= \int \hat{S}_{66} g_i^{II} g_j^{II} d\eta & s_i &= \int \epsilon_1 \frac{S_{16}}{S_{11}} g_i^{II} d\eta \end{aligned} \tag{13}$$

The boundary terms induced by integration by parts are eliminated from the condition that g_i and g_i^I are zero at the top and bottom surfaces in laminate.

In Eqn 12, the governing equations are reduced to the ordinary differential equations where $f_i(\xi)$ and $p_i(\xi)$ are coupled. The homogeneous solutions of f_i and p_i are assumed in the following forms,

$$f_i = v_i^f e^{\lambda \xi}, \quad p_i = v_i^p e^{\lambda \xi} \tag{14}$$

Substituting Eqn 14 to Eqn 12, the ordinary differential equations are reduced to the following forms.

$$\begin{aligned}
 a_{ij}^{(0)} v_j^f + (a_{ij}^{(2)} + \lambda^2 a_{ij}^{(4)}) v_j^{fII} + (b_{ij}^{(0)} + \lambda^2 b_{ij}^{(2)}) v_j^p &= 0 \\
 b_{ij}^{(0)} v_j^f + b_{ij}^{(2)} v_j^{fII} + (c_{ij}^{(0)} + \lambda^2 c_{ij}^{(2)}) v_j^p &= 0 \\
 \lambda^2 v_j^f - v_j^{fII} &= 0 \quad (i, j = 1, 2, \dots, n)
 \end{aligned} \tag{15}$$

The third one of Eqn 15 is arbitrarily defined for the conversion to the form of the eigenproblem. Since the interlaminar stresses decay in the interior region of laminates, only the negative roots of λ^2 are selected. From above eigenproblem, $3n$ eigenvalues are obtained, and the homogeneous solutions are obtained by $3n$ term linear combination.

$$\begin{aligned}
 f_i^{(H)} &= v_{ij}^f t_j e^{-\lambda_j \xi} \\
 p_i^{(H)} &= v_{ij}^p t_j e^{-\lambda_j \xi} \quad (i = 1, 2, \dots, n), \quad (j = 1, 2, \dots, 3n)
 \end{aligned} \tag{16}$$

where t_j are constants which should be determined from the boundary conditions.

The particular solutions can be obtained from the assumption that $f_i(\xi)$ and $p_i(\xi)$ in Eqn 12 are constants.

$$\begin{aligned}
 a_{ij}^{(0)} f_j^{(P)} + b_{ij}^{(0)} p_j^{(P)} &= -r_i \\
 b_{ij}^{(0)} f_j^{(P)} + c_{ij}^{(0)} p_j^{(P)} &= -s_i \quad (i, j = 1, 2, \dots, n)
 \end{aligned} \tag{17}$$

Accordingly, the in-plane stress functions are expressed as the sum of the homogeneous and particular solutions.

$$\begin{aligned}
 f_i &= f_i^{(H)} + f_i^{(P)} \\
 p_i &= p_i^{(H)} + p_i^{(P)} \quad (i = 1, 2, \dots, n)
 \end{aligned} \tag{18}$$

The final step of the determination of the in-plane functions is the calculation of t_j . The variables t_j can be determined from the boundary condition that σ_2 , σ_4 , and σ_6 are zero at the free edge.

$$\begin{aligned}
 v_{ij}^f t_j &= -f_i^{(P)} \\
 \lambda_j v_{ij}^f t_j &= 0 \\
 v_{ij}^p t_j &= -p_i^{(P)} \quad (i = 1, 2, \dots, n), \quad (j = 1, 2, \dots, 3n)
 \end{aligned} \tag{19}$$

Substituting the calculated in-plane stress functions into Eqn 6, the interlaminar stresses are determined as follows.

$$\begin{aligned}
 \sigma_2 &= [v_{ij}^f t_j e^{-\lambda_j \xi} + f_i^{(P)}] g_i^{II}(\eta) \\
 \sigma_3 &= \lambda_j^2 v_{ij}^f t_j e^{-\lambda_j \xi} g_i(\eta) \\
 \sigma_4 &= \lambda_j v_{ij}^f t_j e^{-\lambda_j \xi} g_i^I(\eta) \\
 \sigma_5 &= \lambda_j v_{ij}^p t_j e^{-\lambda_j \xi} g_i^I(\eta) \\
 \sigma_6 &= [v_{ij}^p t_j e^{-\lambda_j \xi} + p_i^{(P)}] g_i^{II}(\eta) \quad (i = 1, 2, \dots, n), \quad (j = 1, 2, \dots, 3n)
 \end{aligned} \tag{20}$$

2nd Process : Improvement of Out-of-plane Stress Functions

The in-plane stress distributions calculated by above process are predicted well(Fig. 2), but the out-of-plane distributions are oscillating(Fig. 3). The CLT solutions are not recovered in the interior region(Fig. 5). Thus, one-step iteration is not sufficient for the accurate prediction of the interlaminar stresses accurately.

In the present study, the extended Kantorovich method is introduced to improve the interlaminar stress prediction. Defining the out-of-plane stress functions individually at each layer and reapplying the principle of complementary minimum energy, the out-of-plane functions can be improved.

The in-plane stress functions, f_i and p_i obtained by the 1st process are used in the 2nd process, and the partial derivative of g_i is carried out. As g_i are defined at each layer, the governing equations are also obtained in terms of $g_i^{(k)}$ from integration by parts.

$$\begin{aligned} \delta U &= \int \left[m_{ij}^{(4)(k)} g_j^{(k)IV} + m_{ij}^{(2)(k)} g_j^{(k)II} + m_{ij}^{(0)(k)} g_j^{(k)} + n_i^{(k)} \right] \delta g_i^{(k)} d\eta + \Lambda \\ &= 0 \quad (k = 1, 2, \dots, N), \quad (i, j = 1, 2, \dots, n) \end{aligned} \quad (21)$$

where

$$\begin{aligned} m_{ij}^{(4)(k)} &= \int \left[\hat{S}_{22}^{(k)} f_i f_j + \hat{S}_{26}^{(k)} (f_i p_j + p_i f_j) + \hat{S}_{66}^{(k)} p_i p_j \right] d\xi \\ m_{ij}^{(2)(k)} &= - \int \left[(2\hat{S}_{23}^{(k)} + \hat{S}_{44}^{(k)}) f_i^I f_j^I + (\hat{S}_{36}^{(k)} + \hat{S}_{45}^{(k)}) (f_i^I p_j^I + p_i^I f_j^I) + \hat{S}_{55}^{(k)} p_i^I p_j^I \right] d\xi \\ m_{ij}^{(0)(k)} &= \int \hat{S}_{33}^{(k)} f_i^{II} f_j^{II} d\xi \\ n_i^{(k)} &= \int \epsilon_1 \frac{S_{13}^{(k)}}{S_{11}^{(k)}} f_i^{II} d\xi \end{aligned} \quad (22)$$

In Eqn 21, for the arbitrary $\delta g^{(k)}$, the governing equations are obtained. The homogeneous solutions of $g^{(k)}$ are assumed as the exponential functions with the eigenvalues are $\mu^{(k)}$.

$$g_i^{(k)} = v_i^{g^{(k)}} e^{\mu^{(k)} \eta} \quad (23)$$

Substituting Eqn 23 into Eqn 21, the following equations are derived.

$$\begin{aligned} m_{ij}^{(0)(k)} v_j^{g^{(k)}} + (m_{ij}^{(2)(k)} + \mu^{(k)2} m_{ij}^{(4)(k)}) v_j^{g^{II}(k)} &= 0 \\ \mu^{(k)2} v_j^{g^{(k)}} - v_j^{g^{II}(k)} &= 0 \quad (k = 1, 2, \dots, N), \quad (i, j = 1, 2, \dots, n) \end{aligned} \quad (24)$$

The second equation of Eqn 24 is used to construct formal eigenproblem. The positive as well as negative roots of $\mu^{(k)2}$ are chosen in this process, and the homogeneous solutions are constructed by the $4n$ linear combinations.

$$g_i^{(k)(H)} = v_{ij}^{g^{(k)}} b_j^{(k)} e^{\mu_j^{(k)} \eta} \quad (k = 1, 2, \dots, N), \quad (i = 1, 2, \dots, n), \quad (j = 1, 2, \dots, 4n) \quad (25)$$

where $b_j^{(k)}$ are variables decided from the boundary and continuity conditions.

The particular solutions are calculated from the assumption that $g_i(\eta)$ are constants in Eqn 21.

$$m_{ij}^{(0)(k)} g_j^{(k)(P)} = -n_i^{(k)} \quad (k = 1, 2, \dots, N), \quad (i, j = 1, 2, \dots, n) \quad (26)$$

The out-of-plane stress functions are given as follows.

$$g_i^{(k)} = g_i^{(k)(H)} + g_i^{(k)(P)} \quad (k = 1, 2, \dots, N), \quad (i = 1, 2, \dots, n) \quad (27)$$

The variables b_j are determined from two conditions. The first condition is that the out-of-plane stress functions and their first derivatives are zero at the top and bottom surfaces in composite laminate. The second condition is that the boundary terms caused by the integration by parts in Eqn 21 must be zero. Rearranging the boundary terms, the second condition indicates the stress and variationally consistent displacement continuity conditions at the interfaces between plies. Accordingly, the final interlaminar stresses calculated by 2nd process are given as follows.

$$\begin{aligned} \sigma_2 &= f_i(\xi) \left[\mu_j^{(k)2} v_{ij}^{g(k)} b_j^{(k)} e^{\mu_j^{(k)} \eta} \right] \\ \sigma_3 &= f_i^{II}(\xi) \left[v_{ij}^{g(k)} b_j^{(k)} e^{\mu_j^{(k)} \eta} + g_i^{(k)(P)} \right] \\ \sigma_4 &= -f_i^I(\xi) \left[\mu_j^{(k)} v_{ij}^{g(k)} b_j^{(k)} e^{\mu_j^{(k)} \eta} \right] \\ \sigma_5 &= -p_i^I(\xi) \left[\mu_j^{(k)} v_{ij}^{g(k)} b_j^{(k)} e^{\mu_j^{(k)} \eta} \right] \\ \sigma_6 &= p_i^{II}(\xi) \left[v_{ij}^{g(k)} b_j^{(k)} e^{\mu_j^{(k)} \eta} + g_i^{(k)(P)} \right] \quad (i = 1, 2, \dots, n), \quad (j = 1, 2, \dots, 4n) \end{aligned} \quad (28)$$

3rd Process : Improvement of In-plane Stress Functions

The 2nd process has eliminated the undesirable oscillation of the out-of-plane stress distributions(Fig. 3), and recovered the CLT solutions accurately in the interior domain(Fig. 5). However, the interlaminar stresses obtained from the 2nd process showed still some oscillation of the in-plane distributions as n increases(Fig. 2).

Therefore, the extended Kantorovich method is reapplied. The in-plane stress functions are improved through the iteration. The calculating procedure is the same as that of the 1st process, and instead of the eigenmode of a clamped-clamped beam, the out-of-plane stress functions which are obtained from the 2nd process are applied.

Meanwhile, for the examination of the convergence of the present method, the iterating process of four times is accomplished. It is found that the interlaminar stresses converge to the expected values with only two-time iteration process.

NUMERICAL RESULTS

For verification in accuracy and efficiency of present method, composite laminates are analyzed for various layup configurations. The material properties of a ply are given as follows.

$$\begin{aligned} E_1 &= 20 \times 10^6 \text{ psi}, \quad E_2 = E_3 = 2.1 \times 10^6 \text{ psi} \\ G_{12} &= G_{13} = G_{23} = 0.85 \times 10^6 \text{ psi} \\ \nu_{12} &= \nu_{13} = \nu_{23} = 0.21 \end{aligned}$$

The in-plane length b is assumed to $2h$. Stress distributions of in-plane and out-of-plane are given, and they are compared to those previously reported. In the figures, the results of present method are for those of 3rd iteration process at $n=8$, and the results of Flanagan are same as to those of 1st iteration process.

$[0/90]_S$, $[45/-45]_S$ Laminates

Fig. 2 is the distribution of σ_3 at 0/90 interface in $[0/90]_S$ laminate. The plot shows good agreement of the result of 3rd process with that of Flanagan except at the free edge. As mentioned above, the result obtained by 2nd process is oscillating. It can be found that the peak stress at free edge is significantly improved by the present method. To investigate the tendency of out-of-plane stress distributions, the distribution of σ_3 at free edge in $[0/90]_S$ laminate is shown in Fig. 3. For comparison, Sandhu's result[12] is illustrated together. Sandhu's result were calculated with the finite element method which used 288 continuous traction elements. In contrast to the result given by Flanagan, the present result has no discrepancy with that of Sandhu, and the stress singularity at the interface is predicted well.

The distribution of σ_3 at the free edge of $[45/-45]_S$ laminate is shown in Fig. 4. There exists an excellent agreement between the present result and that of Wang and Choi[13] which is calculated by the finite element method. In addition, the maximum stress at the interface obtained by the present method is far larger than other results.

Quasi-isotropic Laminates

To investigate the recovery of CLT solution at the interior of composite laminate, the distribution of σ_2 at the interior of $[45/-45/0/90]_S$ laminate is shown in Fig. 5. The figure shows that the present method recovers the CLT solution exactly while Flanagan's method does not.

CONCLUSIONS

In the present study, the interlaminar stresses in composite laminates near free edge were analyzed by the extended Kantorovich method. Through the iteration process, the accurate interlaminar stresses can be calculated. The high gradient of the stress at the free edge is correlated well to those of the reported results, and the position of maximum stress is predicted accurately. Since the CLT solution is recovered at the interior of laminates, it is found that the present method predicts the accurate stress distributions over the whole domain of laminates.

In the given numerical examples, four-time iterations are performed. However, the calculation process is not entirely complicated since it requires only two iterative steps which consist of calculating process of out-of-plane stress functions from in-plane functions and inverse process.

Numerical examples demonstrated that the present method provides reliable prediction of free edge interlaminar stresses for various layup configurations.

REFERENCES

1. Pipes, R.B. and Pagano, N.J., "Interlaminar Stresses in Composite Laminates under Uniform Axial Extension", *Journal of Composite Materials*, Vol. 4, 1970, pp. 538-548.

2. Altus, E., Rotem, A. and Shmueli, M., "Free Edge Effect in Angle Ply Laminates - A New Three Dimensional Finite Difference Solution", *Journal of Composite Materials*, Vol. 14, 1980, pp. 21-30.
3. Wang, A.S.D. and Crossman, F.W., "Some New Results on Edge Effect in Symmetric Composite Laminates", *Journal of Composite Materials*, Vol. 11, 1977, pp. 92-106.
4. Whitcomb, J.D. and Raju, I.S., "Superposition Method for Analysis of Free-Edge Stresses", *Journal of Composite Materials*, Vol. 17, 1983, pp. 492-508.
5. Spilker, R.L. and Chou, S.C., "Edge Effects in Symmetric Composite Laminates : Importance of Satisfying the Traction-Free-Edge Condition", *Journal of Composite Materials*, Vol. 14, 1980, pp. 2-20.
6. Kassapoglou, C. and Lagace, P.A., "An Efficient Method for the Calculation of Interlaminar Stresses in Composite Materials", *Journal of Applied Mechanics*, Vol. 53, 1986, pp. 744-750.
7. Yin, W.L., "Free-Edge Effects in Anisotropic Laminates Under Extension, Bending and Twisting. Part 1 - A Stress Function Based Variational Approach", *Journal of Applied Mechanics*, Vol. 61, 1994, pp. 410-415.
8. Yin, W.L., "Free-Edge Effects in Anisotropic Laminates Under Extension, Bending and Twisting. Part 2 - Eigenfunction Analysis and the Results for Symmetric Laminates", *Journal of Applied Mechanics*, Vol. 61, 1994, pp. 416-421.
9. Flanagan, G., "An Efficient Stress Function Approximation for the Free-Edge Stresses in Laminates", *International Journal of Solids and Structures*, Vol. 31, 1994, pp. 941-952.
10. Kerr, A., "An Extension of the Kantorovich Method", *Quarterly of Applied Mathematics*, 1968
11. Lekhnitskii, S.G., *Theory of Elasticity of an Anisotropic Body*, Holden-Day, San Francisco, 1963
12. Sandhu, R.S., Wolfe, W.E., Sierakowski, R.L., Chang, C.C. and Chu, H.R., "Finite Element Analysis of Free-Edge Delamination in Laminated Composite Specimens", *U.S. Air Force Wright Laboratory Report*, WL-TR-91-3022, 1991
13. Wang, S.S. and Choi, I., "Boundary Layer Effects in Composite Laminates : Part 2 - Free Edge Stress Solutions and Basic Characteristics", *Journal of Applied Mechanics*, Vol. 49, 1982, pp. 549-560.

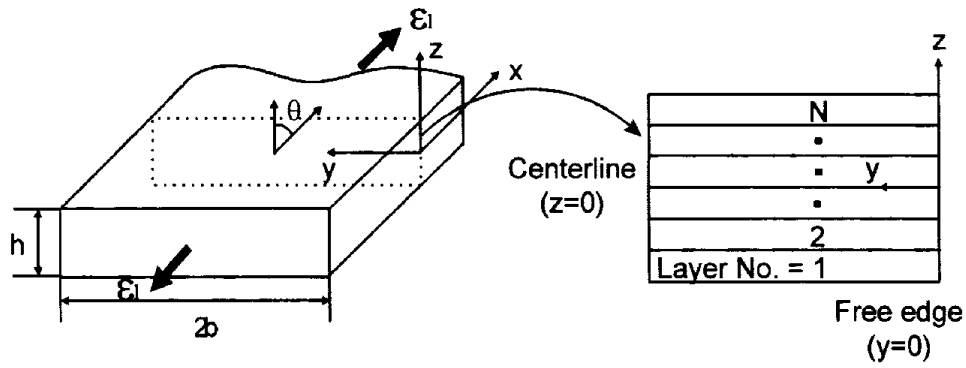


Fig. 1: geometry for the laminate with free edge

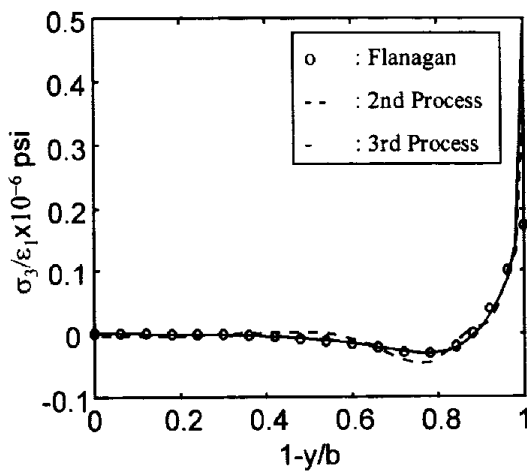


Fig. 2: σ_3 at 0/90 interface ($z/h=0.25$) of $[0/90]_S$ laminate

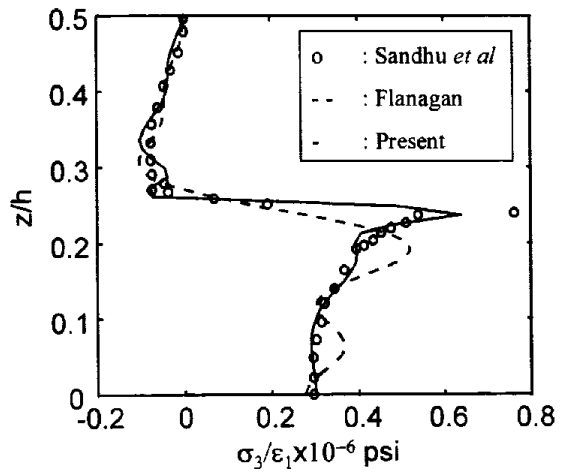


Fig. 3: σ_3 at free edge ($y/h=0$) of $[0/90]_S$ laminate

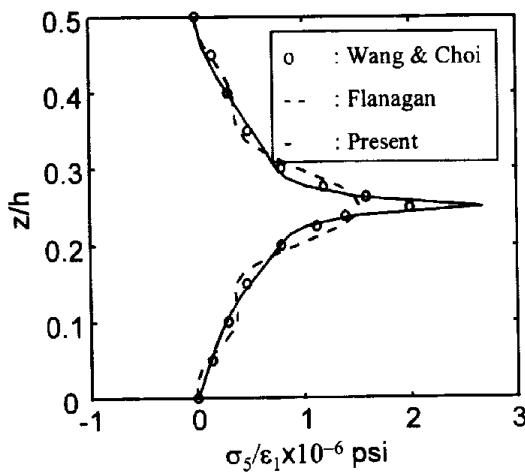


Fig. 4: σ_3 at free edge ($y/h=0$) of $[45/-45]_S$ laminate

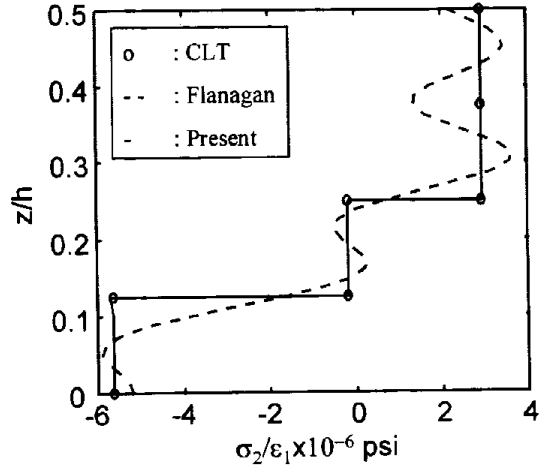


Fig. 5: σ_2 at interior ($y/h=\infty$) of $[45/-45/0/90]_S$ laminate

BUCKLING ANALYSIS OF SKEW COMPOSITE LAMINATE PLATES

Hsuan-Teh Hu and Wen-Long Tzeng

Department of Civil Engineering, National Cheng Kung University,
Tainan, Taiwan 701, R.O.C.

SUMMARY: Up to date, while most stability studies of fiber-composite laminate plates have been focused on the rectangular plates, very little attention has been paid to the skew laminate plates. To fill the gap, this study investigates the elastic stability of skew composite laminate plates subjected to uniaxial inplane compressive forces. Based on the linearized bifurcation buckling formulation, numerical calculations of the critical buckling loads of skew composite plates are carried out by the finite element program ABAQUS. The influence of skew angles, laminate layups, plate aspect ratios, plate thicknesses, central circular cutouts, and end conditions on the buckling resistance of skew composite laminate plates are demonstrated and discussed.

KEYWORDS: buckling, skew, laminate plates, finite element

INTRODUCTION

The composite laminate plates in service are commonly subjected to compressive forces which may cause buckling. Hence, structural instability becomes a major concern in safe and reliable design of the composite plates. In the literature, most stability studies of fiber-composite laminate plates have been focused on the rectangular plates¹⁻⁵. Little attention has been paid to the skew laminate plates. It is known that the buckling resistance of rectangular composite laminate plates depends on end conditions^{2,5}, ply orientations^{2,3,5}, and geometric variables such as aspect ratios, thicknesses and cutouts^{1,2,4,5}. For skew composite plates, in addition to those factors, the plate skew angle, α (Fig. 1), should also be a key factor that influencing the buckling resistance of the plates^{6,7}.

In this investigation, buckling analysis of uniaxially compressed skew composite laminate plates are performed. The skew angle of the plates are varied among 50° to 90° . The laminate layups of these plates are $[\pm\theta]_{NS}$ ($0^\circ \leq \theta \leq 90^\circ$), $[\alpha/0]_{NS}$, $[90/0]_{NS}$ ($n = 2, 10$),

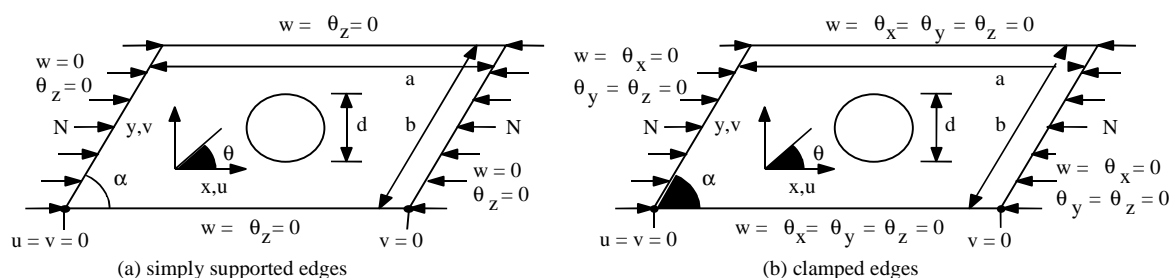


Fig. 1 Skew composite laminate plates with different edge conditions

$[90/45/0/-45]_s$ and $[90/45/0/-45]_{5s}$. The plates in analysis have different end conditions, plate aspect ratios, and may contain central circular cutouts. The critical buckling loads N_{cr} of the skew composite plates are calculated by the bifurcation buckling analysis implemented in the ABAQUS finite element program⁸. Through this study, the influence of skew angles, laminate layups, plate aspect ratios, plate thicknesses, central circular cutouts and end conditions on the buckling resistance of skew composite plates can be clearly understood.

BIFURCATION BUCKLING ANALYSIS

In the finite-element analysis, a set of nonlinear equations results in the incremental form:

$$[K_t] d\{u\} = d\{p\} \quad (1)$$

where $[K_t]$ is the tangent stiffness matrix, $d\{u\}$ the incremental nodal displacement vector and $d\{p\}$ the incremental nodal force vector. When the structural deformation is small, the nonlinear theory leads to the same critical load as the linear theory. The linearized formulation then gives rise to a tangent stiffness matrix in the following expression:

$$[K_t] = [K_L] + [K_\sigma] \quad (2)$$

where $[K_L]$ is a linear stiffness matrix and $[K_\sigma]$ a stress stiffness matrix. If a stress stiffness matrix $[K_\sigma]_{ref}$ is generated according to a reference load $\{p\}_{ref}$, for another load level $\{p\}$ with λ a scalar multiplier, we have

$$\{p\} = \lambda\{p\}_{ref}, \quad [K_\sigma] = \lambda[K_\sigma]_{ref} \quad (3)$$

When buckling occurs, the external loads do not change, i.e., $d\{p\} = 0$. Then the solution for the linearized buckling problem may be determined from the following eigenvalue equation:

$$([K_L] + \lambda_{cr}[K_\sigma]_{ref}) d\{u\} = \{0\} \quad (4)$$

where λ_{cr} is an eigenvalue and $d\{u\}$ becomes the eigenvector defining the buckling mode. The critical load $\{p\}_{cr}$ can be obtained from $\{p\}_{cr} = \lambda_{cr}\{p\}_{ref}$.

CONSTITUTIVE MATRIX FOR FIBER-COMPOSITE LAMINAE

The laminate plates are modeled by eight-node isoparametric laminate shell elements with six degrees of freedom per node. The formulation of the shell element allows transverse shear deformation⁸. For fiber-composite laminate materials, the stress-strain relations for a lamina in the material coordinates (1,2,3) at an element integration point can be written as

$$\{\sigma'\} = [Q'_1]\{\varepsilon'\}, \quad \{\tau'\} = [Q'_2]\{\gamma'\} \quad (5)$$

$$[Q'_1] = \begin{bmatrix} \frac{E_{11}}{1-\nu_{12}\nu_{21}} & \frac{\nu_{12}E_{22}}{1-\nu_{12}\nu_{21}} & 0 \\ \frac{\nu_{21}E_{11}}{1-\nu_{12}\nu_{21}} & \frac{E_{22}}{1-\nu_{12}\nu_{21}} & 0 \\ 0 & 0 & G_{12} \end{bmatrix}, \quad [Q'_2] = \begin{bmatrix} \alpha_1 G_{13} & 0 \\ 0 & \alpha_2 G_{23} \end{bmatrix} \quad (6)$$

where $\{\sigma'\} = \{\sigma_1, \sigma_2, \tau_{12}\}^T$, $\{\tau'\} = \{\tau_{13}, \tau_{23}\}^T$, $\{\epsilon'\} = \{\epsilon_1, \epsilon_2, \gamma_{12}\}^T$, $\{\gamma'\} = \{\gamma_{13}, \gamma_{23}\}^T$. The α_1 and α_2 are shear correction factors calculated by assuming that the transverse shear energy through the thickness of laminate is equal to that of the case of unidirectional bending⁸. The constitutive equations for the lamina in the element coordinates (x,y,z) then become

$$\{\sigma\} = [Q_1]\{\epsilon\}, \quad [Q_1] = [T_1]^T [Q'_1] [T_1] \quad (7)$$

$$\{\tau\} = [Q_2]\{\gamma\}, \quad [Q_2] = [T_2]^T [Q'_2] [T_2] \quad (8)$$

$$[T_1] = \begin{bmatrix} \cos^2\theta & \sin^2\theta & \sin\theta\cos\theta \\ \sin^2\theta & \cos^2\theta & -\sin\theta\cos\theta \\ -2\sin\theta\cos\theta & 2\sin\theta\cos\theta & \cos^2\theta - \sin^2\theta \end{bmatrix}, \quad [T_2] = \begin{bmatrix} \cos\theta & \sin\theta \\ -\sin\theta & \cos\theta \end{bmatrix} \quad (9)$$

where $\{\sigma\} = \{\sigma_x, \sigma_y, \tau_{xy}\}^T$, $\{\tau\} = \{\tau_{xz}, \tau_{yz}\}^T$, $\{\epsilon\} = \{\epsilon_x, \epsilon_y, \gamma_{xy}\}^T$, $\{\gamma\} = \{\gamma_{xz}, \gamma_{yz}\}^T$, and fiber angle θ is measured counterclockwise from the element local x-axis to the material 1-axis. Let $\{\epsilon_0\} = \{\epsilon_{x0}, \epsilon_{y0}, \gamma_{xy0}\}^T$ be the in-plane strains at the mid-surface of the laminate section, $\{\kappa\} = \{\kappa_x, \kappa_y, \kappa_{xy}\}^T$ the curvatures, and h the total thickness of the section. If there are n layers in the layup, the stress resultants, $\{N\} = \{N_x, N_y, N_{xy}\}^T$, $\{M\} = \{M_x, M_y, M_{xy}\}^T$ and $\{V\} = \{V_x, V_y\}^T$, can be defined as

$$\begin{Bmatrix} \{N\} \\ \{M\} \\ \{V\} \end{Bmatrix} = \int_{-h/2}^{h/2} \begin{Bmatrix} \{\sigma\} \\ z\{\sigma\} \\ \{\tau\} \end{Bmatrix} dz = \sum_{j=1}^n \begin{bmatrix} (z_{jt}-z_{jb})[Q_1] & \frac{1}{2}(z_{jt}^2-z_{jb}^2)[Q_1] & [0] \\ \frac{1}{2}(z_{jt}^2-z_{jb}^2)[Q_1] & \frac{1}{3}(z_{jt}^3-z_{jb}^3)[Q_1] & [0] \\ [0]^T & [0]^T & (z_{jt}-z_{jb})[Q_2] \end{bmatrix} \begin{Bmatrix} \{\epsilon_0\} \\ \{\kappa\} \\ \{\gamma\} \end{Bmatrix} \quad (10)$$

where z_{jt} and z_{jb} are the distance from the mid-surface of the section to the top and the bottom of the j-th layer. The [0] is a 3 by 2 matrix with all the coefficients equal to zero. Prior to numerical analyses, the ABAQUS program has been employed to analyze the buckling of composite cylindrical panels with cutout and of isotropic skew plates. These solutions are compared with known benchmark solutions and satisfactory results are obtained⁹.

RESULTS OF THE NUMERICAL ANALYSIS AND DISCUSSION

Laminate Rhombus Plates

In this section composite laminate rhombus plates without cutout and subjected to uniaxial compressive force N per unit length (Fig. 1) are analyzed. The length and width of the plates are $a = b = 10$ cm and the skew angle α varies among 50° and 90° . Two types of edge conditions, i.e., four edges simply supported and four edges clamped, are considered. The lamina in the plates is consisted of Graphite/Epoxy and material constitutive properties are $E_{11} = 128$ GPa, $E_{22} = 11$ GPa, $\nu_{12} = 0.25$, $G_{12} = G_{13} = 4.48$ GPa, $G_{23} = 1.53$ GPa. The thickness of each ply is 0.125 mm. Eight types of laminate layups, $[90/0]_{2S}$, $[\alpha/0]_{2S}$, $[90/45/0/-45]_S$, $[\pm\theta]_{2S}$, $[90/0]_{10S}$, $[\alpha/0]_{10S}$, $[90/45/0/-45]_{5S}$, and $[\pm\theta]_{10S}$ are studied. In the analysis, no symmetry simplifications are made and a 10×10 fine finite element mesh (100 elements) is used to model the entire rhombus plate.

Figure 2 shows critical buckling load N_{cr} versus the skew angle α for $[90/0]_{2S}$,

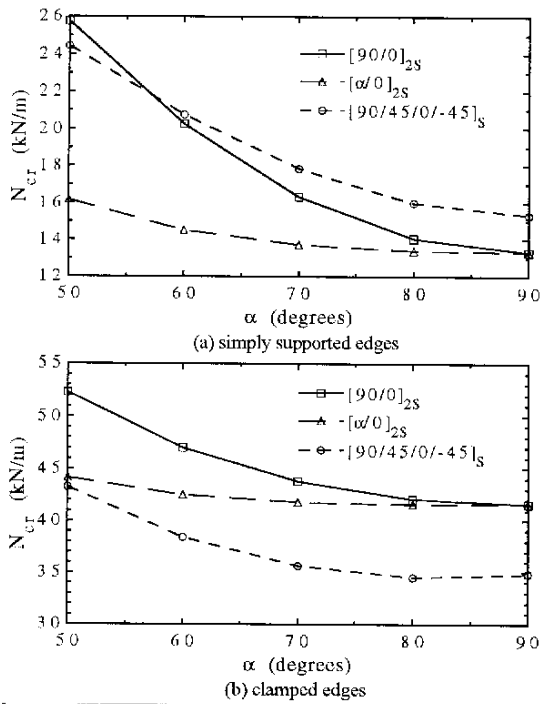


Fig. 2 Effect of skew angle on buckling loads of composite rhombus plates with $[90/0]_{2S}$, $[\alpha/0]_{2S}$ and $[90/45/0/-45]_S$ laminate layouts

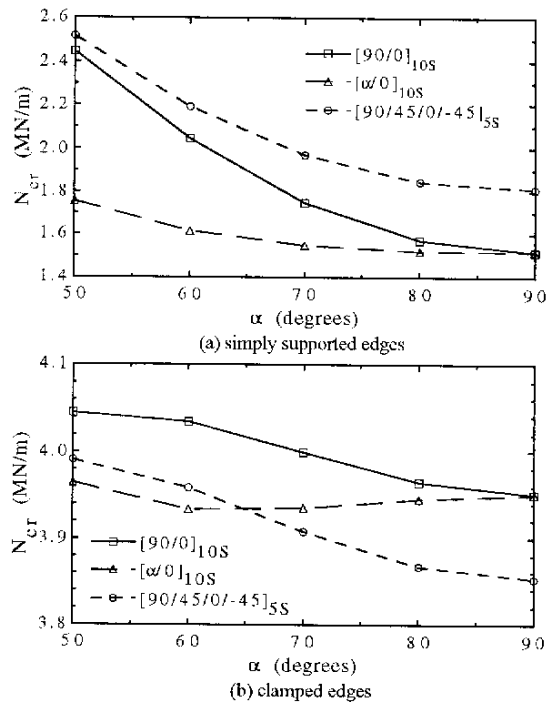


Fig. 3 Effect of skew angle on buckling loads of composite rhombus plates with $[90/0]_{10S}$, $[\alpha/0]_{10S}$ and $[90/45/0/-45]_{5S}$ laminate layouts

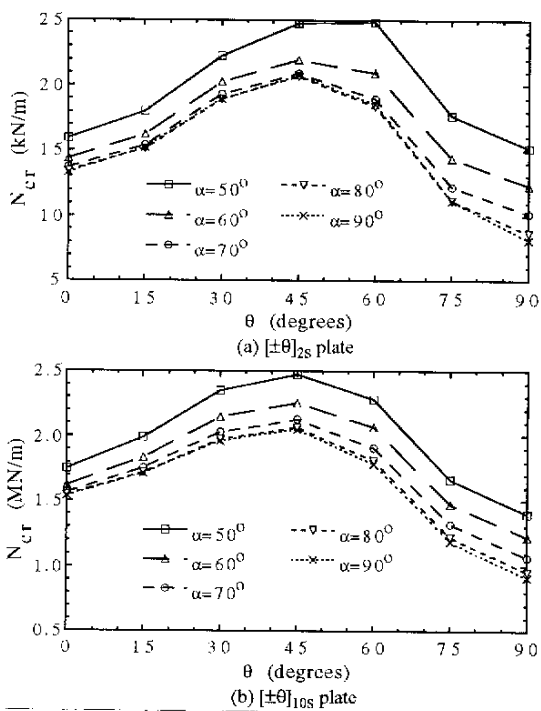


Fig. 4 Effect of skew angle on buckling loads of simply supported $[\pm\theta]_{2S}$ and $[\pm\theta]_{10S}$ composite rhombus plates

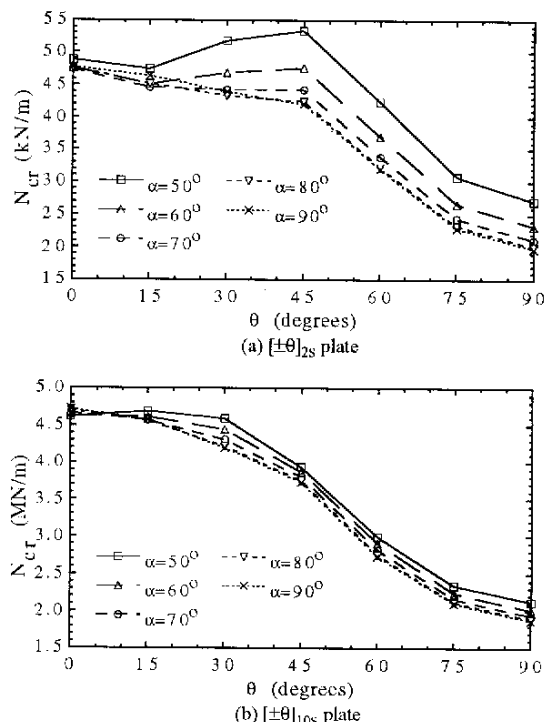


Fig. 5 Effect of skew angle on buckling loads of clamped $[\pm\theta]_{2S}$ and $[\pm\theta]_{10S}$ composite rhombus plates

$[\alpha/0]_{2S}, [90/45/0/-45]_S$ composite rhombus plates. We can see that the critical buckling loads of the plates generally decrease with the increase of α angle. Under the simply supported conditions, the $[\alpha/0]_{2S}$ plates, always have the lowest buckling loads and the $[90/45/0/-45]_S$ plates usually have the highest buckling loads (except $\alpha < 60^\circ$). When the edges of plates are all clamped, the results of analyses are quite different. The $[90/0]_{2S}$ plates have the highest buckling loads and the $[90/45/0/-45]_S$ plates have the lowest buckling loads. Figure 3 shows critical buckling load N_{cr} versus the skew angle α for $[90/0]_{10S}$, $[\alpha/0]_{10S}$, $[90/45/0/-45]_{5S}$ composite rhombus plates. For plates with simply supported conditions, except the magnitude of the buckling loads, the results of analysis for these thicker plates (Fig. 3a) are very similar to those of thin plates (Fig. 2a). Comparing Fig. 3b with Fig. 2b, we can observe that the thickness does have influence on the buckling behavior of clamped rhombus plates. First, the buckling loads of the $[\alpha/0]_{10S}$ plates may increase with the skew angle α when $\alpha > 60^\circ$. Second, the buckling loads of $[90/45/0/-45]_{5S}$ plates may be greater than those of $[\alpha/0]_{10S}$ plates when $\alpha < 70^\circ$.

The last rhombus plates for analysis are the angle ply $[\pm\theta]_{2S}$ and $[\pm\theta]_{10S}$ laminate plates, in which the θ angle varies among 0° and 90° . Figure 4a shows that if the angle θ is fixed, the critical buckling loads of simply supported $[\pm\theta]_{2S}$ plates increase with the decreasing of the skew angle α . When the angle α is smaller, this increasing in buckling loads is more prominent. In addition, it seems that in spite of the skew angle α , these plates would have the highest buckling loads when the fiber angle θ is close to 45° . The only exception is the plates with α equal to 50° , where the highest buckling load may occur with θ around 60° . From Fig. 4b we can see that when the plate thickness is increased, the highest buckling loads of the simply supported $[\pm\theta]_{10S}$ plates all occur with θ around 45° .

If the edge conditions of these plates are changed to clamped edges, we can observe from Fig. 5a that the critical buckling loads of the plates still increase with the decreasing of the skew angle α . However, these plates would have the highest buckling loads when the fiber angle θ is close to 90° . The only two exceptions are the plates with α equal to 50° and 60° , where the highest buckling loads take place with θ around 45° . If the plate thickness is increased, the highest buckling loads of the clamped $[\pm\theta]_{10S}$ plates almost all take place with θ close 0° as shown in Fig. 5b. The only exception is the plates with α equal to 50° , where the highest buckling load occurs with θ around 15° .

Comparing Fig. 5 with Fig. 4, we can observe that the edge conditions have significant influence on the buckling behavior of the rhombus plates. In addition, when the plate thickness is increased, the highest buckling load of rhombus plates with angle ply laminate layup will more consistently take place at the same θ angle (say $\theta = 45^\circ$ for simply supported plates and $\theta = 0^\circ$ for clamped plates). Hence, it may be suggested to use $\theta = 45^\circ$ in the design of simply supported rhombus plates with angle ply $[\pm\theta]_{nS}$ laminate layup (n is an integer) and subjected to uniaxial compressive loading. Though, in some cases, there would have other better θ angle to achieve higher buckling resistance of plates. However, as far as the simplicity is concerned, the use of the $[\pm 45]_{nS}$ laminate layup may be a straightforward and practical choice. On the basis of the same reason, it may also be suggested to use the $[0_2]_{nS}$ laminate layup (all fibers parallel to the loading direction) in the design of clamped rhombus plates subjected to uniaxial compression.

Laminate Parallelogram Plates with Various Aspect Ratios

In this section composite laminate parallelogram plates without cutout and subjected to

uniaxial loading are analyzed (Fig. 1). The laminate layups are $[\pm\theta]_{ns}$, in which $n = 2, 10$, and θ varies among 0° and 90° . The width b of the plates is 10 cm. The length a of the plates may be either 5 cm ($a/b = 0.5$) or 40 cm ($a/b = 4$). The skew angle α of the plates still varies among 50° and 90° and two types of boundaries conditions, four edges simply supported and four edges clamped, are considered. Again, no symmetry simplifications are made in the analysis. A 10×10 finite element mesh (100 elements) is used to model the plates with $a/b = 0.5$ and a 10×20 finite element mesh (200 elements) is used to model the plates with $a/b = 4$.

Figure 6 shows critical buckling load N_{cr} versus the angle θ for $[\pm\theta]_{2S}$ and $[\pm\theta]_{10S}$ composite parallelogram plates with a/b ratio equal to 0.5 and with four simply supported edge conditions. We can see that the maximum buckling loads of the $[\pm\theta]_{2S}$ thin plates all take place when θ angle is equal to 0° (Fig. 6a). For thick plates with $[\pm\theta]_{10S}$ laminate layup (Fig. 6b), the maximum buckling loads take place at θ equal to 0° for most cases. The only exception is the plate with α equal to 0° , where the maximum buckling load may occur with θ around 30° . We can also observe that when θ is greater than 15° , the critical buckling loads generally decrease with the increase of α angle. However, when θ angle is close to 0° , this trend is totally reversed and the critical buckling loads decrease with the decreasing of α angle.

When the edge condition of the short plates is changed to clamped, we can observe from Fig. 7a that the edge conditions do not have significant influence on the trends of the buckling behavior of the $[\pm\theta]_{2S}$ thin plates (except the buckling loads are increased). For $[\pm\theta]_{10S}$ thick plates with four clamped edges (Fig. 7b), it can be seen that when θ angle is greater than 45° , the critical buckling loads increase with the decreasing of α angle. When θ angle is less than 30° , the critical buckling loads increase with the increasing of α angle. In addition, comparing Fig. 7b with Fig. 6b, we can observe that the clamped edge conditions shift the optimal fiber angle θ to values around the region 30° to 45° .

Figure 8 shows critical buckling load N_{cr} versus the angle θ for $[\pm\theta]_{2S}$ and $[\pm\theta]_{10S}$ composite parallelogram plates with a/b ratio equal to 4 and with four simply supported edge conditions. We can see that the maximum buckling loads of the $[\pm\theta]_{2S}$ and $[\pm\theta]_{10S}$ plates all take place with θ angle around 45° . For both thin and thick plates, the critical buckling loads all decrease with the increase of α angle. When the edge condition of the long plates is changed to clamped, we can observe from Fig. 9a that the edge conditions do not have significant influence on the trends of the buckling behavior of the $[\pm\theta]_{2S}$ thin plates (except the buckling loads are increased). Comparing Fig. 9b with Fig. 8b, we can observe that the clamped edge conditions shift the optimal fiber angle θ from 45° to 30° .

Finally, comparing Figs. 8 and 9 with Figs. 6 and 7, we can see that the optimal angle θ for $[\pm\theta]_{2S}$ and $[\pm\theta]_{10S}$ skew plates is influenced by the plate aspect ratio significantly. For both thin and thick plates with simply supported edges and for thin plates with clamped edges, when the plate is short, the optimal angle θ may be close to 0° . However, when the plate is long, the optimal angle θ is usually around 45° . For thick plates with clamped edges, though the optimal angle θ seems to be around 30° for both short and long plates. However, for long and thick plates (Fig. 9b), in spite of the fiber angle θ , the critical buckling loads decrease with the increase of skew angle α . For short and thick plates (Fig. 7b) the critical buckling loads may decrease with the decrease of skew angle α for some θ angle (say $\theta < 30^\circ$).

Laminate Parallelogram Plates with Various Aspect Ratios and Circular Cutouts

In these section, composite laminate parallelogram plates with central circular cutouts and subjected to uniaxial loading are analyzed (Fig. 1). The laminate layup is $[\pm\theta]_{2S}$ and θ varies

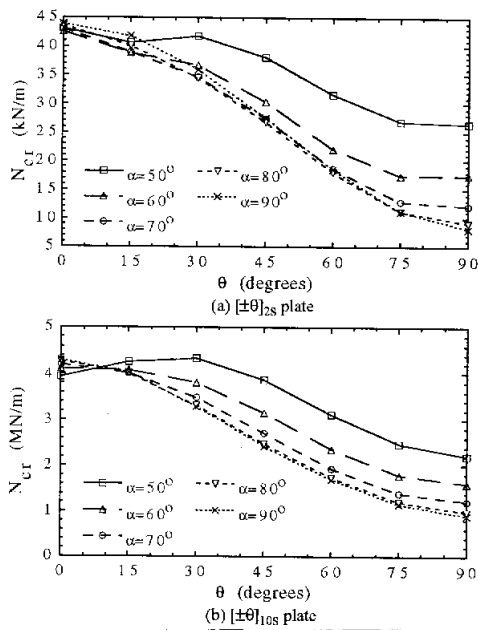


Fig. 6 Effect of skew angle on buckling loads of simply supported $[\pm\theta]_{2S}$ and $[\pm\theta]_{10S}$ composite parallelogram plates with $a/b = 0.5$

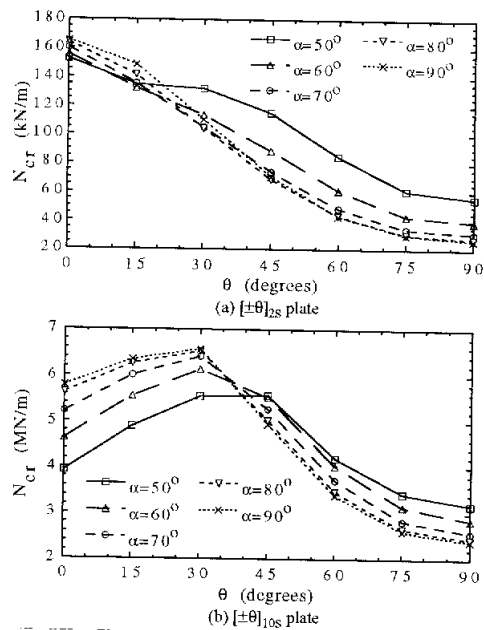


Fig. 7 Effect of skew angle on buckling loads of clamped $[\pm\theta]_{2S}$ and $[\pm\theta]_{10S}$ composite parallelogram plates with $a/b = 0.5$

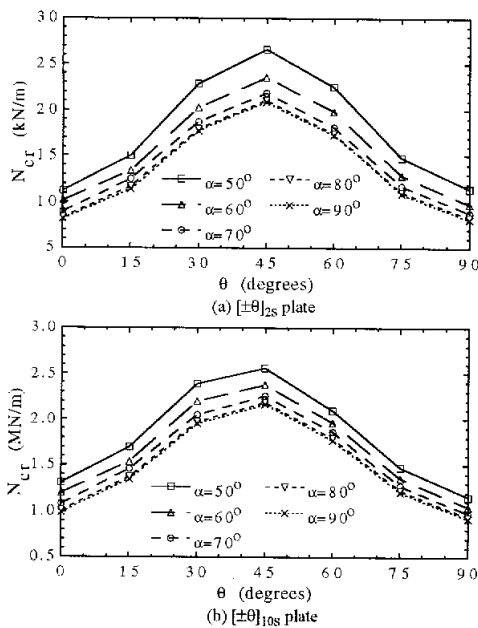


Fig. 8 Effect of skew angle on buckling loads of simply supported $[\pm\theta]_{2S}$ and $[\pm\theta]_{10S}$ composite parallelogram plates with $a/b = 4$

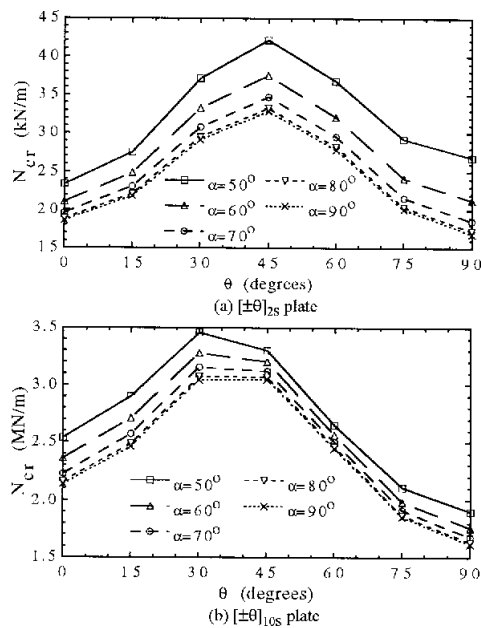


Fig. 9 Effect of skew angle on buckling loads of clamped $[\pm\theta]_{2S}$ and $[\pm\theta]_{10S}$ composite parallelogram plates with $a/b = 4$

among 0° and 90° . The width b of the plates is 10 cm. The length a of the plates may be either 5 cm ($a/b = 0.5$) or 40 cm ($a/b = 4$). In the analysis, the diameter d of the cutout is selected to be 1 cm or 2 cm ($d/a = 0.1$ or 0.2). The skew angle α of the plates still varies among 50° and 90° and two types of boundaries conditions, four edges simply supported and four edges clamped, are considered. No symmetry simplifications are made in the analysis. Due to the presentation of cutouts, at least 500 elements are used to model the plates with $a/b = 0.5$ and at least 800 elements are used to model the plates with $a/b = 4$.

The results of analysis show that no matter of the edge conditions, N_{cr} versus θ curves for short skew plates ($a/b = 0.5$) with central holes are very similar to those of plates without holes. The only different is that the critical buckling loads of plates with holes are lower than those of plates without cutouts. Table 1 lists the reduction (in percentage) of the critical buckling loads for short skew plates with cutouts. From the table it can be seen that the plates with large hole sizes will have large reductions in the critical buckling loads. In addition, under the same fiber angle θ , the plates having small α angles usually have large reductions in the critical buckling loads. If the edge effect is considered, under the same skew angle α and fiber angle θ , the plates with simply supported edges usually (not always) have large reductions in critical buckling loads than those with clamped edges.

For long skew plates ($a/b = 4$) again N_{cr} versus θ curves are very similar to those of plates without holes. Table 2 lists the reduction of the critical buckling loads for long skew plates with cutouts. In the table, there are some negative reduction values, which means that the plates with cutouts may have higher critical buckling loads than the same plates without holes. In addition, for some skew plates (say $\alpha = 80^\circ$, $\theta = 15^\circ$, simply supported edges), the critical buckling loads may increase with the hole sizes. These phenomenon is quite different from our intuition and from the behavior of the short skew plates with central holes. However, past research did show (numerically and experimentally) that introducing a hole into an isotropic plate or a composite plate does not always reduce the buckling load and, in some instances, may increase its buckling load^{4,5,10}. This is because that the buckling load of a plate is not only influenced by cutout, but also influenced by material orthotropy, end condition, and plate geometry. From table 2 we can also find that when the fiber angles θ are less than 45° , the changes of the critical buckling loads are not significant. For same skew plates with cutouts, the change of critical buckling loads are more prominent when the fiber angles θ approach 90° . Finally, comparing Table 2 with Table 1, we can conclude that the cutout usually have more significant effect on short skew plates than on long skew plates.

CONCLUSIONS

From the buckling analyses of uniaxially compressed skew laminated plates, the following conclusions may be drawn:

1. For composite plates with same laminate layups and boundary conditions, the buckling loads increase with the decreasing of the skew angle α . When the angle α is smaller, this increasing in buckling loads is more prominent.
2. For composite rhombus plates with simply supported ends and with $[90/0]_{2ns}$, $[\alpha/0]_{2ns}$, $[90/45/0/-45]_{ns}$ laminate layups, the plates with $[90/45/0/-45]_{ns}$ layup usually have the highest buckling loads and the plates with $[\alpha/0]_{2ns}$ layup have the lowest buckling loads. When the edges of plates are all clamped, the $[90/0]_{2ns}$ plates have the highest buckling loads and the $[90/45/0/-45]_{ns}$ plates usually have the lowest buckling loads.
3. For rhombus $[\pm\theta]_{ns}$ laminate plates ($0^\circ \leq \theta \leq 90^\circ$), the highest buckling loads usually occur with θ around 45° for simply supported plates and with θ close to 0° for clamped plates. This phenomenon is more consistent when the thickness of plate is increased.
4. For skew parallelogram $[\pm\theta]_{2s}$ and $[\pm\theta]_{10s}$ laminate plates with simply supported edges, thickness has very little influence on the optimal fiber angle θ . The highest buckling loads usually occur with θ around 0° for short plates and θ around 45° for long plates. For skew parallelogram $[\pm\theta]_{2s}$ and $[\pm\theta]_{10s}$ laminate plates with clamped edges, thickness has significant influence on the optimal fiber angle θ .

5. For short skew parallelogram $[\pm\theta]_{2S}$ laminate plates with central cutouts, the plates with large hole sizes will have large reductions in the critical buckling loads. Under the same fiber angle θ and same size of cutout, the plates having small α angles usually have large reductions in the critical buckling loads. In addition, under the same skew angle α , same fiber angle θ and same cutout size, the plates with simply supported edges usually (not always) have larger reductions in critical buckling loads than those with clamped edges.
6. For long skew parallelogram $[\pm\theta]_{2S}$ laminate plates with central cutouts, the plates with cutouts may have higher critical buckling loads than the same plates without holes. In addition, for some skew plates, the critical buckling loads may increase with the increasing of the hole sizes. When the fiber angles θ are less than 45° , the changes of the critical buckling loads due to the present of cutouts are not significant. This changes in critical buckling loads are more prominent when the fiber angles θ approach 90° . In addition, the changes of critical buckling loads due to the present of cutouts for short skew plates are more significant than those for long skew plates (but not always).

REFERENCES

1. Rhodes, M. D., Mikulas, M. M. and McGowan, P. E., "Effects of Orthotropy and Width on the Compression Strength of Graphite-Epoxy Panels with Holes," *AIAA Journal*, Vol. 22, 1984, pp. 1283-1292.
2. Leissa, A. W., *Buckling of Laminated Composite Plates and Shell Panels*. AFWAL-TR-85-3069, Flight Dynamics Laboratory, Air Force Wright Aeronautical Laboratories, Wright-Patterson Air Force Base, Ohio, 1985.
3. Muc, A., "Optimal Fibre Orientation for Simply-Supported Angle-Ply Plates under Biaxial Compression," *Composite Structures*, Vol. 9, 1988, pp. 161-172.
4. Nemeth, M. P., "Buckling Behavior of Compression-Loaded Symmetrically Laminated Angle-Ply Plates with Holes," *AIAA Journal*, Vol. 26, 1988, pp. 330-336.
5. Hu, H.-T. and Lin, B.-H., "Buckling Optimization of Symmetrically Laminated Rectangular Plates with Various Geometry and End Conditions," *Composite Science and Technology*, Vol. 55, 1995, pp. 277-285.
6. Morley, L. S. D., *Skew Plates and Structures*, Macmillan, New York, 1963.
7. Liao, C.-L. and Lee, Z.-Y., "Elastic Stability of Skew Laminated Composite Plates Subjected to Biaxial Follower Forces," *International Journal for Numerical Methods in Engineering*, Vol. 36, 1993, pp. 1825-1847.
8. Hibbitt, Karlsson & Sorensen, Inc., *ABAQUS User's Manual, Example Manual and Theory Manual*, Version 5.4, Providence, Rhode Island, 1995.
9. Tzeng, W.-L. Tzeng, *Buckling Analysis of Laminate Parallelogram Plates Subjected to Uniaxial Compression*, Master Thesis, Department of Civil Engineering, National Cheng Kung University, Tainan, R.O.C., 1996.
10. Ritchie, D. and Rhoades, J., "Buckling and Postbuckling Behavior of Plates with Holes," *Aeronautical Quarterly*, Vol. 26, 1975, pp. 281-296.

Table 1 Reduction of buckling loads for $[\pm\theta]_{2s}$ composite parallelogram plates with central circular cutouts ($a/b = 0.5$)

Simply Supported Edges										
%	$\alpha = 50^\circ$		$\alpha = 60^\circ$		$\alpha = 70^\circ$		$\alpha = 80^\circ$		$\alpha = 90^\circ$	
θ	d/b=0.1	d/b=0.2	d/b=0.1	d/b=0.2	d/b=0.1	d/b=0.2	d/b=0.1	d/b=0.2	d/b=0.1	d/b=0.2
0°	18.04	41.20	17.85	42.52	17.75	43.50	17.73	44.16	17.67	44.33
15°	15.31	37.14	14.75	37.08	14.53	37.36	14.56	37.87	14.72	38.53
30°	15.69	37.47	13.39	33.56	12.12	31.25	11.80	30.69	12.11	31.67
45°	18.54	40.95	14.78	35.07	11.64	29.12	10.20	26.08	10.16	26.43
60°	19.63	40.95	16.04	36.55	11.79	29.36	9.279	24.20	8.397	23.14
75°	19.71	39.40	15.69	34.58	12.36	30.51	10.34	27.48	8.921	25.70
90°	22.18	41.80	16.60	34.33	13.08	30.81	12.28	31.72	11.92	33.10
Clamped Edges										
%	$\alpha = 50^\circ$		$\alpha = 60^\circ$		$\alpha = 70^\circ$		$\alpha = 80^\circ$		$\alpha = 90^\circ$	
θ	d/b=0.1	d/b=0.2	d/b=0.1	d/b=0.2	d/b=0.1	d/b=0.2	d/b=0.1	d/b=0.2	d/b=0.1	d/b=0.2
0°	16.08	40.60	16.16	40.38	16.17	40.53	16.26	40.70	16.36	40.70
15°	13.88	35.92	13.53	34.85	13.36	34.68	13.42	35.06	13.89	35.76
30°	13.71	33.23	12.70	30.32	12.00	28.81	11.80	28.49	12.23	29.09
45°	16.19	32.62	14.91	28.63	12.83	26.47	12.11	25.46	12.34	25.61
60°	16.61	30.81	15.44	26.55	13.26	24.67	12.55	23.58	11.76	23.22
75°	15.72	29.07	13.89	24.60	12.74	22.91	11.94	22.05	11.15	21.50
90°	17.08	31.72	14.63	25.81	13.41	23.78	12.94	23.15	12.28	22.70

Table 2 Reduction of critical buckling loads for $[\pm\theta]_{2s}$ composite parallelogram plates with central circular cutouts ($a/b = 4$)

Simply Supported Edges										
%	$\alpha = 50^\circ$		$\alpha = 60^\circ$		$\alpha = 70^\circ$		$\alpha = 80^\circ$		$\alpha = 90^\circ$	
θ	d/b=0.1	d/b=0.2	d/b=0.1	d/b=0.2	d/b=0.1	d/b=0.2	d/b=0.1	d/b=0.2	d/b=0.1	d/b=0.2
0°	1.652	3.562	1.413	3.650	-1.144	-4.041	-1.070	-4.1176	-1.032	-4.022
15°	1.082	2.191	0.880	2.207	0.470	1.898	-0.761	-1.975	-0.736	-2.777
30°	-0.262	0.800	0.795	2.365	0.754	2.364	0.769	2.398	0.802	2.450
45°	1.865	4.685	1.061	3.442	-0.188	2.401	-0.332	2.320	-0.311	2.601
60°	3.551	8.804	1.880	6.848	0.226	4.941	6.120	5.022	0.699	5.734
75°	6.869	13.82	4.109	10.85	2.796	8.948	1.821	7.275	1.773	7.201
90°	11.23	20.37	6.532	15.31	4.414	12.69	3.145	10.80	2.246	9.450
Clamped Edges										
%	$\alpha = 50^\circ$		$\alpha = 60^\circ$		$\alpha = 70^\circ$		$\alpha = 80^\circ$		$\alpha = 90^\circ$	
θ	d/b=0.1	d/b=0.2	d/b=0.1	d/b=0.2	d/b=0.1	d/b=0.2	d/b=0.1	d/b=0.2	d/b=0.1	d/b=0.2
0°	0.090	-1.490	1.464	1.242	1.404	1.925	1.406	2.314	1.428	2.448
15°	-0.022	-0.830	0.717	0.789	1.140	1.629	1.104	1.810	1.137	1.926
30°	1.976	2.760	1.797	3.173	0.873	2.606	0.437	2.359	0.419	2.416
45°	3.386	5.296	2.775	5.387	2.161	5.119	1.998	5.072	2.058	5.180
60°	6.994	7.741	4.331	6.349	3.319	5.914	2.870	5.708	2.835	5.759

BUCKLING OF DELAMINATED BEAM-PLATES WITH REPAIRING FASTENERS

Chien-Chang Lin and Shou-Hsiun Cheng

*Department of Applied Mathematics,
National Chung-Hsing University, Taichung, Taiwan 402, R.O.C.*

SUMMARY: This paper presents an analysis model for predicting the buckling load of a delaminated beam-plate repaired by single or multiple rows of fasteners. The present analysis model is based on a so called "continuous analysis method". According to this method, the upper (thinner) part of the delaminated plate is modeled as a beam-plate supported on a continuously foundation. To obtain an analytical solution for the analysis model the Fourier series method is employed. For illustrative purpose, some numerical examples accounting for the effects of fastener locations, numbers of fasteners, and delamination length on the local buckling are presented. Results show that the present method is effective and useful in engineering application, and the fastener repair is significantly effective on the buckling behavior of delaminated structure.

KEYWORDS: buckling, delaminated beam-plate, fastener repair, continuous analysis method

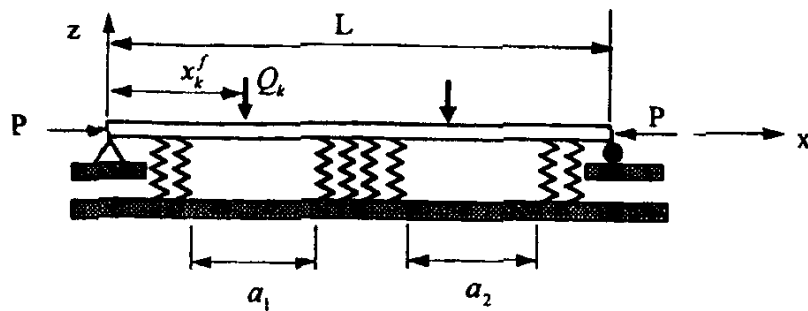
1 INTRODUCTION

Delamination is one of the most common failure modes in composite structures. Because delamination can significantly reduce the compressive strength and stiffness of laminate, repair of such damage composite is necessary if replacement deems to be too costly or can be avoid. Although adhesive bonding repair is generally successful for thin structures with transverse crack, it seemingly may not be effective for composite structures with delamination flaws under in plane compressive load. For this case, an alternate repair, the usage of inserting fasteners/rivets or stitching in the delaminated regions appears to be more effective. However analytic studies on these topics are very limited. Wehrenberg II [1] presented new process by weaving 3-D reinforcement to prevent delamination of composites. Fibers can be woven through the thickness by stitching for reinforcement. Minery et al. [2] investigated the stitching effect to suppress delamination in laminated composites by an experimental procedure and finite element method. Chen et al. [3] discussed the stitching effects of thickness-direction reinforcement on interlaminar fracture toughness of unidirectional laminates. Recently, an analytical study on the buckling of a circular delamination restrained by a fastener was presented by Huang [4] using the Rayleigh-Ritz method. In this study, the "continuous analysis method" proposed by Wang [5,6] is employed for analyzing local buckling of a delaminated beam-plate repaired by single or multiple rows of fasteners.

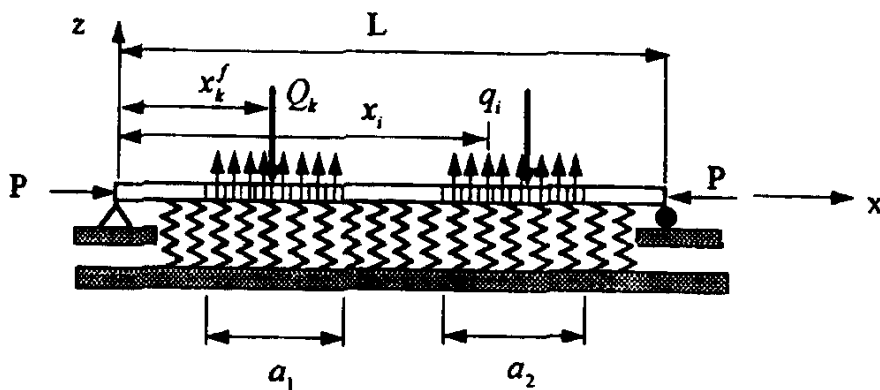
2 FORMULATION

Some assumptions are made for the analysis:(1) the delamination is through-the-width and locates at an interface of adhesive layer with debonds , (2) the thinner (upper) part of the plate is applied by a compressive axial load, (3) only the local buckling is considered in this study, (4) when local buckling occurs at the delamination region the adhesive layer of bonded region acts as an elastic foundation, i.e. the upper part of the plate is acted by a discontinuous elastic foundation (including bonded and debonded regions), (5) the repaired fasteners are assumed to be small enough compared with the delamination size and treated as members of capably carrying axial loads only.

Following these assumptions, we may illustrate the actual model as shown in Fig.1-(a). According to the continuous analysis method, the upper (thinner) part of the delaminated plate is modeled as a beam-plate supported on a continuously foundation but with fictitiously added transverse forces q_i at a suitable number of discrete points x_i in the delaminated region so as to make the net transverse traction (including supported forces of foundation and fictitiously added forces) at each neighborhood region of these points to vanish, the supported force $q(x)$ of foundation is represented by a distributed spring force, i.e. $q(x) = k_w$, and the repaired fasteners are replaced by imposed transversely concentrated loads Q_k at points x_k^f . This continuous analysis model is illustrated as shown in Fig.1-(b). Thus the governing



(a.) Actual model



(b.) Model for the continuous analysis

Fig. 1: A delaminated beam-plates repaired by multiple rows of fasteners

equation of this sub-beam-plate can be derived as

$$D_{11} \frac{d^4 w}{dx^4} + P \frac{d^2 w}{dx^2} + k_f w - \sum_{i=1}^N q_i \delta(x - x_i) + \sum_{k=1}^M Q_k \delta(x - x_k^f) = 0 \quad (1)$$

where $\delta(x)$ is the Dirac delta function, k_f is the elastic constant of adhesive layer, w is the deflection, D_{11} is the bending stiffness of the sub-beam-plate, P is the compressive load, N is the number of divided elements in the delaminated region, M is the number of fasteners.

3 METHOD OF SOLUTION

It has been shown that the influence of boundary conditions on the local buckling of a delaminated beam-plate is negligible except when the delamination region near the edge. In this paper, for the sake of convenience for analysis, only simply supported boundary conditions are considered:

$$W(0) = W''(0) = W(L) = W''(L) = 0 \quad (2)$$

The Fourier series method is used for analytical solution (the problems other than simply supported boundary conditions can be accommodated in conjunction with the Stoke's transformation [6]). Thus the displacement W and Dirac Delta function are expressed in Fourier series as

$$w = \sum_{n=1}^{\infty} w_n \sin \alpha_n x \quad (3)$$

$$\delta(x - x_i) = \sum_{m=1}^{\infty} \left(\frac{2}{L} \sin \alpha_m x_i \right) \sin \alpha_m x \quad (4)$$

$$\delta(x - x_k^f) = \sum_{m=1}^{\infty} \left(\frac{2}{L} \sin \alpha_m x_k^f \right) \sin \alpha_m x \quad (5)$$

where $\alpha_m = m\pi / L$, and coefficients w_m are to be determined. By substituting Eqs (3)-(5) into Eqn (1) and comparing the corresponding coefficients, we obtain

$$w_m = \frac{1}{\lambda_m} \left[\sum_{i=1}^N \bar{q}_i \left(\frac{2}{L} \sin \alpha_m x_i \right) - \sum_{k=1}^M \bar{Q}_k \left(\frac{2}{L} \sin \alpha_m x_k^f \right) \right] \quad (6)$$

where

$$\lambda_m = \alpha_m^4 - \beta^2 \alpha_m^2 + K$$

$$\beta^2 = \frac{P}{D_{11}}, \quad K = \frac{k_f}{D_{11}}, \quad \bar{q}_i = \frac{q_i}{D_{11}}, \quad \bar{Q}_k = \frac{Q_k}{D_{11}}$$

According to the previous assumption, the k^{th} fastener will impose the transversely concentrated inward loading Q_k on the beam-plate in order to restrain the deformation of the sub-plate during local buckling. Each fastener will be elongated by the amount of w at the fastener location during local buckling. Hence, the unknown concentrated loads Q_l can be related to w at $x = x_l^f$ as

$$w = \frac{Q_l L^f}{2E^f A^f}, \quad l = 1, 2, \dots, M \quad (7)$$

where L^f is the fastener length, E^f is Young's modulus, and A^f is the cross-section area of the fastener. By substituting Eqn (3) into Eqn (7), we obtain

$$a_{ik} \bar{Q}_k = \eta_{li} \bar{q}_i, \quad i.e. \quad \bar{Q}_k = b_{kl} \eta_{li} \bar{q}_i \quad (8)$$

or in matrix form, $\{\bar{Q}_k\}_{M \times 1} = [b_{kl}]_{M \times M} [\eta_{li}]_{M \times N} \{\bar{q}_i\}_{N \times 1}$ where $[b_{kl}] = [a_{ik}]^{-1}$ and

$$a_{ik} = \frac{D_{11} L^f \pi^4 \delta_{ik}}{4 E^f A^f L^3} + \sum_{m=1}^{\infty} \frac{1}{\lambda_m} \sin \alpha_m x_k^f \sin \alpha_m x_i^f$$

$$\bar{\lambda}_m = m^4 + \bar{K} - \frac{P}{P_{Euler}} m^2, \quad P_{Euler} = \frac{D_{11} \pi^2}{L^2}, \quad \bar{K} = \frac{k_f L^4}{D_{11} \pi^4}$$

By substituting Eqn (8) into Eqn (6), we obtain

$$w_m = \sum_{i=1}^N c_{mi} \bar{q}_i \quad (9)$$

where

$$c_{mi} = \frac{1}{\lambda_m} \left[\frac{2}{L} \sin \alpha_m x_i - \sum_{k=1}^M \sum_{l=1}^M b_{kl} \eta_{li} \left(\frac{2}{L} \sin \alpha_m x_k^f \right) \right]$$

By substituting Eqn (9) into Eqn (3), we obtain

$$w = \sum_{m=1}^{\infty} \left(\sum_{i=1}^N c_{mi} \bar{q}_i \right) \sin \alpha_m x \quad (10)$$

Finally, we require the net traction at $x = x_j$ in the debond region to vanish,

$$q_j = k_f w(x_j) \Delta x_j \quad (11)$$

or

$$D_{11} \delta_{ij} \bar{q}_i = D_{11} K \left[\sum_{m=1}^{\infty} \left(\sum_{i=1}^N c_{mi} \bar{q}_i \right) \sin \alpha_m x_j \right] \Delta x_j \quad (12)$$

where $\Delta x_j = \Delta x$ is the length of each element related to the force q_j in the delaminated region. While Δx_j can be taken to be a variable quantity, they are considered to be constant in this study. Eqn (12) can also be expressed as

$$\sum_{i=1}^N \left(K \Delta x \sum_{m=1}^{\infty} c_{mi} \sin \alpha_m x_j - \delta_{ij} \right) \bar{q}_i = 0 \quad (13)$$

Eqn (13) can be written in the following matrix form

$$[A] \{\bar{q}\} = 0 \quad (14)$$

The lowest eigenvalue of Eqn (14) provides the critical buckling load.

4 NUMERICAL RESULTS AND DISCUSSIONS

In order to check the accuracy and efficiency of the present method, we consider some special cases in this study where degenerated solutions are compared to existing results. For the convenience of comparison between degenerated solution and the existing solution, a beam-plate having the length L of 31.4 inches and bending stiffness D_{11} being 100 lb-in are considered in all numerical results. While the computer program is prepared for any spring constant k_f , results for $k_f = 100 \text{ lb/in}^3$ have been generated in all numerical examples. To show that there is no limitation on the number of delaminations in the analysis, we divide the present class of problems into two categories including single and multiple delaminations.

4.1 Composite Beam-plates with a Single Delamination

For checking the analysis and computational accuracy, we firstly consider a beam-plate having a central delamination repaired by a row of fasteners at the center line of delamination region. As expected, it can be seen from Table 1 that the buckling load increases as the fastener rigidity $E' A' / L'$ increases or as the delamination length a , decreases. The buckling load for all cases decreases to the value corresponding to the beam-plate without fastener when the fastener's extensional rigidity is reduced below 10^{-7} . This fact shows that the present analysis is accurate and effective. Moreover, results listed in the first column under P_{cr} in Table 1

Table 1 Buckling load for a delaminated beam-plate repaired by a row of fasteners with various rigidities

$\frac{E' A'}{L'}$	P_{cr}				
	$\frac{a}{L} = 0.001$	$\frac{a}{L} = 0.01$	$\frac{a}{L} = 0.1$	$\frac{a}{L} = 0.2$	$\frac{a}{L} = 0.3$
10^3	200.00	199.98	168.83	90.50	52.27
10^2	200.00	199.98	168.83	90.50	52.27
10^1	200.00	199.98	168.83	90.50	52.25
1	200.00	199.98	168.83	90.50	52.20
10^{-1}	200.00	199.98	168.83	90.50	52.15
10^{-2}	200.00	199.98	158.70	90.50	52.10
10^{-3}	200.00	199.92	106.93	57.38	41.04
10^{-4}	200.00	198.99	106.70	47.30	27.40
10^{-5}	200.00	198.87	100.07	46.28	26.00
10^{-6}	200.00	198.86	100.01	46.17	25.86
10^{-7}	200.00	198.86	100.00	46.16	25.85
10^{-8}	200.00	198.86	100.00	46.16	25.85
without fastener [7]	200.00	198.86	100.00	46.16	25.85

show that for debond length ratio a_1/L of 0.001 corresponding to a beam-plate which has almost no debond, the critical buckling load found to be 200.00 lb is in excellent agreement with the buckling load of 200.00 lb for a beam-plate on the Winkler foundation given on Ref.[7]. It is also noted that the critical buckling load for a beam-plate having delamination length ratio a_1/L being 0.3 repaired by a row of fasteners is increased by over 100% of the buckling load of the delaminated beam-plate without repair fastener. Results show that the fastener with rigidity $E^f A^f / L^f = 10^2$ may reasonably be considered to be rigid which is used in all examples.

To explore the effect of the fastener location on the buckling load, we consider a beam-plate having a central delamination repaired by a row of fasteners at various positions. Numerical results shown in Fig. 2 exhibit that the effect of fastener locations on the buckling load is significant. It is most effective to place the fasteners at the center of delamination region resulting in the highest buckling load. To explore the effect of fastener locations on buckling loads for a delaminated beam-plate repaired by multiple rows of fasteners, we consider a beam-plate having a central delamination repaired by three rows of fasteners. One row is located along the center line of delaminated region and each of the others has a distance c from the center line. Numerical results shown in Fig. 3 show that the effect of fastener locations on the buckling load is significant, and is most significant when $c/a_1 = 0.25$.

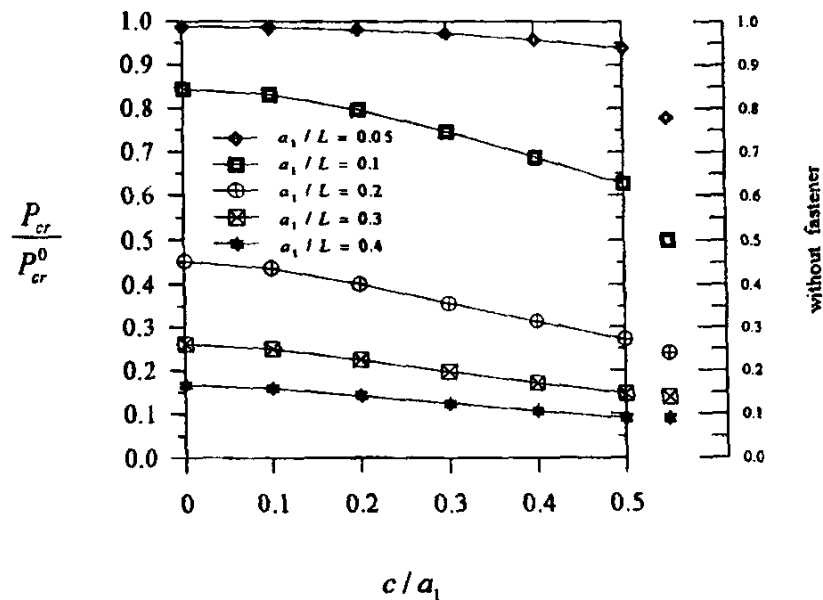


Fig. 2: Effect of fastener locations on buckling load for a beam-plate having a central delamination

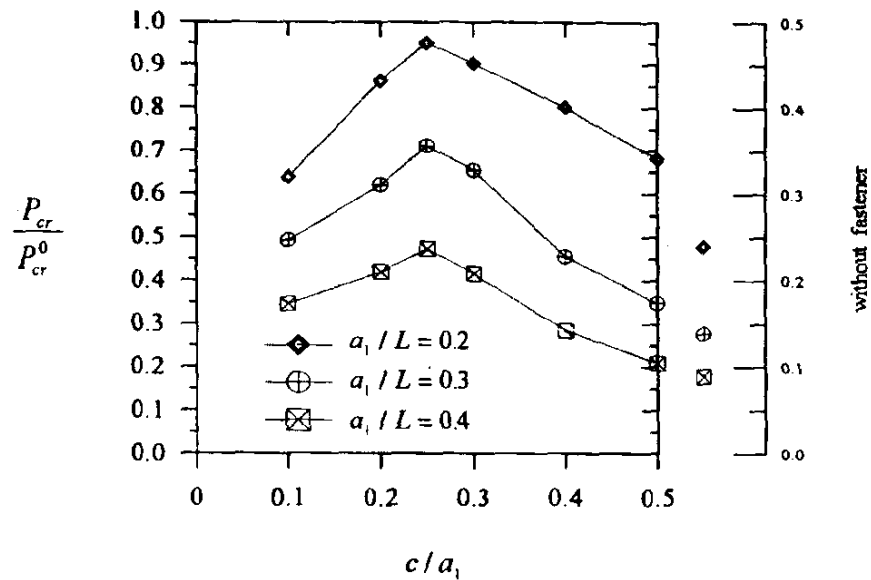


Fig. 3: Effect of fastener locations on buckling load for a delaminated beam-plate repaired by three lines of fasteners

4.2 Composite Beam-plates with Multiple Delaminations

To show the present model has no limitation to the number of delaminations and repair fasteners, we consider a beam-plate having two delaminations of equal size and the delamination centers are located at the one fourth of L and the three fourths of L positions, separately. In each delamination, we consider two examples, in the first example, a single row of repair fasteners located at the center line of each delamination region; however, in the second example, three rows of repair fasteners located at the three lines dividing each delaminated region into four equal parts. Numerical results presented in Fig.4 indicate that the buckling loads of the delaminated beam-plates in the first example increase by about 69% (for $a/L=0.10$), 89% (for $a/L=0.15$), 97% (for $a/L=0.20$), 101% (for $a/L=0.25$), 103% (for $a/L=0.30$), 104% (for $a/L=0.35$) over the buckling load for the plate without fasteners. However, the buckling loads of the delaminated beam-plates in the second example increase by about 100% (for $a/L=0.10$), 204% (for $a/L=0.15$), 288% (for $a/L=0.20$), 375% (for $a/L=0.25$), 440% (for $a/L=0.30$), 476% (for $a/L=0.35$). This reflects the fact that the effect of repair fasteners is more significant for longer delamination lengths and more rows of fasteners.

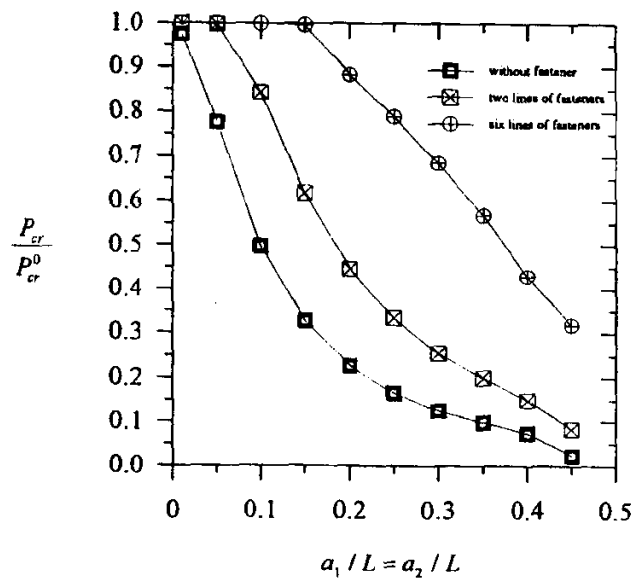


Fig. 4: Effect of fastener on buckling load of a beam-plate with two delaminations of equal size

5 CONCLUSIONS

An analysis method for predicting the buckling load of delaminated beam-plate repaired by single or multiple rows of fasteners has been proposed. According to the results obtained in this study, we have the following concluding remarks :

1. The presented method is simple and effective.
2. The locations of fasteners can significantly affect the delamination buckling load and fastenering at the center of the delamination region is the most significant one.
3. The effect of repairing fastener on the delamination buckling load is more significant when the delamination size is larger.
4. The use of repairing fasteners on the delamination buckling is feasible, and the present model should be useful in engineering application.

ACKNOWLEDGMENT

This study was supported by the National Science Council of the Republic of China under the grant No. NSC 86-2212-E005-018.

REFERENCES

- [1] Wehrenberg II ,R.H., "Composite Get Stronger with 3-D Reinforcement," Materials Engineering, Vol.97, 1983, pp.27-31.
- [2] Minery, L.A., Tan, T.M., and Sun, C.T., "The Use of Stitching to Suppress Delamination in Laminated Composites," STP 867, ASTM, 1985, pp.371-385.

- [3] Chen, V.L., Wu, X.X., and Sun, C.T., "Effective Interlaminar Fracture Toughness in Stitched Laminates," Proceedings of 8th Technical Conference on Composite Materials of American Society for Composites, Cleveland, Ohio, October, 1993, pp.19-21, (Douglas Paper MDC 93K0022).
- [4] Huang, J.Y., "Analysis of a Sublaminar in Compressively Load Laminate under a Transverse Loading at Its Center," Composite Structures, Vol.28, 1994, pp.315-322.
- [5] Wang, J.T.S., "Continuous Analysis of Layered Structures with Debonds," Chinese Journal of Mechanics, 9(2), 1993, pp.81-90.
- [6] Wang, J.T.S., Cheng, S.H. and Lin, C.C., "Local Buckling Of Delaminated Beams and Plates Using Continuous Analysis," J. of Composite Materials, Vol.29, No.10, 1995, pp.1374-1402.
- [7] Brush, Don O., and Almroth Bo O., "Buckling of Bars, Plates, and Shells," McGraw-Hill, 1975.

DURABILITY OF POSTBUCKLING FIBRE COMPOSITE SHEAR PANELS

Rodney S. Thomson¹ and Murray L. Scott²

¹ *Cooperative Research Centre for Advanced Composite Structures Limited,
506 Lorimer Street, Fishermens Bend, Victoria, 3207, Australia.*

² *Department of Aerospace Engineering, Royal Melbourne Institute of Technology,
GPO Box 2476V, Melbourne, Victoria, 3001, Australia.*

SUMMARY: An experimental investigation to characterise the performance of thin, stiffened, composite panels in the postbuckled state has been undertaken. Static and fatigue shear testing was performed on three-blade-stiffened panels with skin thickness of 1 mm and a working section of 250 x 250 mm. Panels with an artificial delamination and others which had been impact damaged were also tested. As well as laboratory testing, a series of environmental exposure tests was conducted under tropical conditions. Initial results indicate that undamaged panels are capable of withstanding cycling at two thirds of the static ultimate load. Panels containing large artificial delaminations suffered considerable delamination growth which stabilised after less than 100,000 cycles. These panels were still capable of carrying significant load, demonstrating their inherent damage tolerance.

KEYWORDS: postbuckling, durability, environmental effects, fatigue, stiffened structures

INTRODUCTION

The progressive introduction of advanced fibre composite materials into primary aerospace structures has enabled significant performance improvements to be achieved. However, the use of composites in stiffened panels has generally been restricted to designs which do not buckle under compression and shear loads for various reasons including some relating to uncertainties associated with their long term durability. In order to improve the relative competitiveness of composites in primary structural applications, this conservative philosophy needs to be reconsidered and postbuckling structures used. Prior to the introduction of designs intended to operate at high buckling ratios, a thorough understanding of both the static and fatigue characteristics of postbuckling composite panels is necessary.

The postbuckling performance of metal panels has been investigated extensively and is relatively well understood. One of the main concerns with metal postbuckling structures is the permanent deformation resulting from the large deflections. Similar stress relief due to yielding is not available in practical composite lay-ups which could result in sudden failure. Due to the poor through-thickness properties of laminated composites, likely failure modes include delamination and stiffener-skin separation. Another area of concern for composite structures is degradation from exposure to moisture, elevated temperature and ultraviolet (UV) radiation. The performance of the panels over long periods of time must also be

evaluated. Much of the work conducted in this area to date has not adequately addressed these aspects.

Experimental and analytical investigations into the buckling and postbuckling response of composite shear panels have been undertaken by a small number of researchers. Some significant work has been performed by Weller and Singer [1] who investigated the buckling and postbuckling response of unstiffened shear webs and “T” and “J” stiffened panels. An aspect of the work involved cycling the shear webs at various load levels for up to 250,000 cycles. It was concluded that such panels could withstand fatigue loading, with reductions in residual strength of up to 20%. The performance of flat, postbuckling, “T” and hat-stiffened composite shear webs was investigated by Agarwal [2]. It was found that these panels could withstand 500,000 cycles with little loss in strength despite delamination and stiffener-skin separation. Panhwar et al [3] investigated the fatigue performance of flat, unstiffened panels under shear. These panels were cycled for up to 3 million cycles and it was concluded that they could operate safely at up to seven times the buckling load.

Environmental and fatigue testing of composite materials are usually conducted in the laboratory under accelerated conditions. To investigate the validity of this testing methodology, an extensive study was carried out by Hoffman and Bielawski [4] into the long term environmental exposure effects on composite materials. Studies were carried out on both laboratory and field specimens over a period of 10 years. It was concluded that the field exposure specimens were necessary, as some important long term behaviour patterns were not predicted by the laboratory testing.

In view of this, the present program of research involves theoretical and experimental investigations of the postbuckling characteristics of thin, stiffened, composite shear panels. Experiments were undertaken using integral-blade-stiffened panels with a skin thickness of 1 mm, tested in shear. Emphasis was placed on assessing the effect of a high number of cycles coupled with long term exposure to adverse environments. Static and fatigue failure modes are being determined and methods to predict the buckling load, postbuckling behaviour and strength have been developed using finite element techniques [5].

APPROACH

Test Specimens

Tests were performed on three-blade-stiffened panels, as shown in Fig. 1. The overall dimensions of the panels were 340 x 340 mm with working dimensions of 250 x 250 mm. The integral blade-stiffeners were 25 mm high with run-out angles of 45°. The skins and stiffeners were co-cured in an autoclave using flexible tooling. The material used to manufacture the panels was T300/914C carbon fibre/epoxy, unidirectional, pre-impregnated, zero-bleed tape. The skins of the panels were 1 mm thick consisting of eight plies of tape and the stiffeners were 2 mm thick consisting of 16 plies. The clamping regions of the panels were built-up to a thickness of 1.5 mm consisting of 12 plies. The stacking sequences of the panels are detailed in Fig. 1. A design criterion was for the stacking sequence of the stiffeners to be symmetrical. As shown in Fig. 2, the top four plies of the skin formed part of the stiffener to improve the interface strength, resulting in the lay-up of alternate bays of the skin not being symmetric. The panels were trimmed and drilled to the geometry shown in Fig. 1 and inspected using through-transmission, ultrasonic C-Scan to detect manufacturing flaws.

To assess the effect of damage, a number of panels were manufactured with a 50 mm diameter piece of teflon film imbedded in the lay-up in the centre of the panel. The location of the film in the stacking sequence is shown in Fig. 3. This situation is representative of a delamination introduced during manufacture or resulting from in-service damage. The presence of the insert was verified by C-Scan of the panel. Other panels were subjected to low speed impact using a 25 mm diameter impactor to produce barely visible impact damage. An incident energy of 3.4 J was used of which approximately 1.0 J was absorbed. The impact location coincided with a buckle peak and the damage area was assessed by C-Scan.

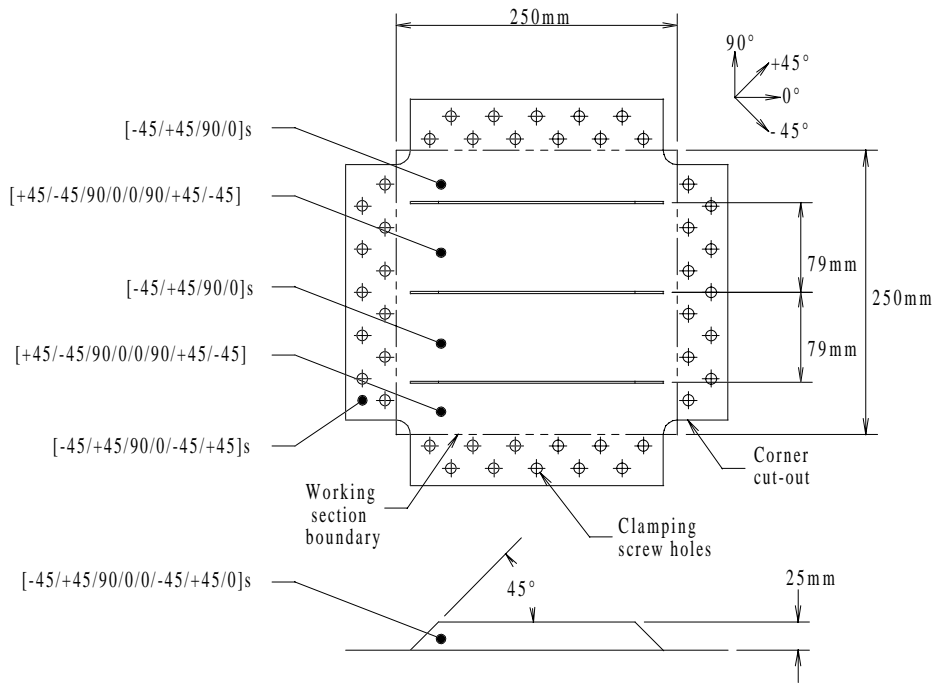


Fig. 1: Three-blade-stiffened panel dimensions.

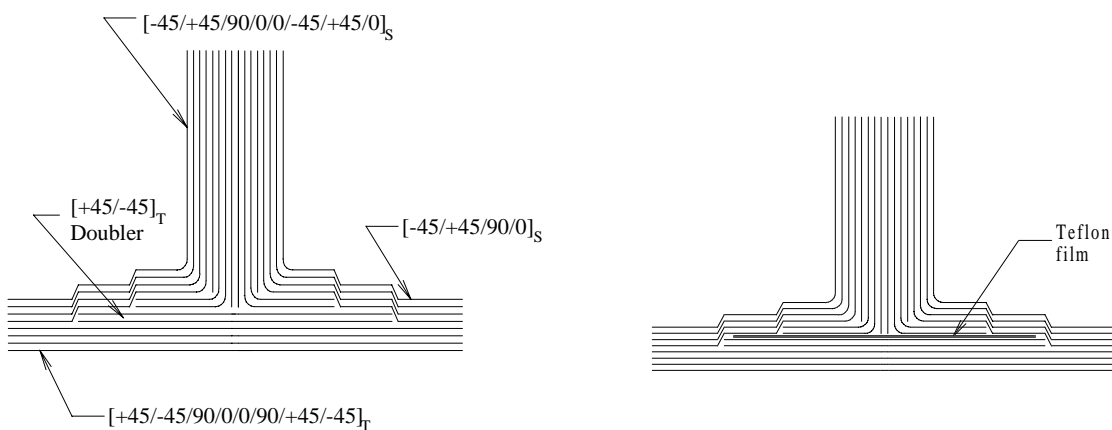


Fig. 2: Detail of the integral stiffener lay-up.

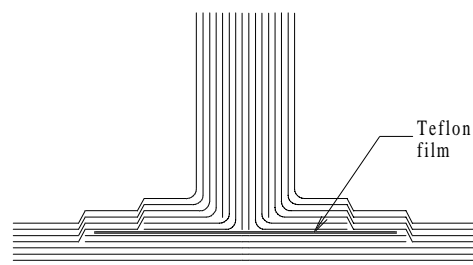


Fig. 3: Location of the teflon insert under the centre stiffener.

Test Procedure

Static Testing

Panels were tested in a “picture frame” shear fixture with anti-slip strips placed between the panel and the rig edge members to achieve effective load transfer through frictional contact. A number of panels were fitted with three-element strain gauge rosettes, located front and back at various locations on the panel. A linear variable differential transformer (LVDT) was employed to measure the out-of-plane displacement of a buckle peak during the tests. The shadow moiré interferometry technique was also used to qualitatively correlate the buckle shapes and out-of-plane displacements with those obtained through analytical techniques [5].

A uniaxial tensile load was applied diagonally through the top and bottom pins using a servo-hydraulic universal testing machine in displacement control mode. The load was applied in the direction of the -45° fibres of the panels; this represents the applied load and has been converted to shear flow throughout this paper. A data acquisition system was used to record the load, stroke, strains and out-of-plane displacement continuously during testing. When using moiré interferometry, the tests were paused at various load levels to photograph the buckled patterns.

Fatigue Testing

Laboratory fatigue testing has been carried out on a number of panels using the “picture frame” shear fixture. Tests have been conducted at stress ratio (R) values of 0.4 and -1.0 with maximum shear buckling ratios of 2.0. The R value of 0.4 was chosen to simulate the cycling of a wing skin from just below buckling load to limit load. The R value of -1.0 represents the fully reversed fatigue loading experienced by aircraft components such as fins or rudders. For all laboratory fatigue tests, loads were applied using a servo-hydraulic universal testing machine in load control mode. Cyclic frequencies between 2 and 4 Hz have been used for the testing.

Environmental Testing

Long term environmental testing was performed at the Australian Defence Science and Technology Organisation (DSTO) tropical test facility located near Innisfail in Northern Queensland. The site is at a latitude of 17° South where the annual rainfall is 3,500 mm and the average daily humidity is 80%. There are 2,300 hours of sunlight experienced per year with an average daily maximum temperature of 28°C . Surface temperatures of up to 84°C have been recorded. Previous tests on carbon fibre/epoxy specimens carried out at the facility by Chalkley and Chester [6] concluded that a moisture content of 0.7% was reached. The specimens were also subjected to hygrothermal cycling as the temperature varied throughout the day.

“Hot/wet” conditions are critical for structures manufactured from carbon fibre/epoxy composites. Reductions in the strength of composites occur when operating temperatures approach the glass transition temperature, T_g . This is the temperature at which the epoxy matrix changes from a glass like state to a rubbery state which is associated with a drastic reduction of properties. Moisture, which is readily absorbed by the epoxy matrix of composite laminates, also adversely affects the properties; this has the effect of plasticising the matrix and reducing T_g . A moisture content of 1% in a laminate can typically reduce T_g

from 175°C to 130°C. The combination of high temperatures and absorbed moisture can lead to significant strength reductions.

Two sets of tests were conducted at the tropical test facility; fatigue tests and static exposures tests. The specimens which were fatigue tested included one undamaged, one impact damaged and another manufactured with a teflon insert. Two teflon insert panels were used as the first was removed part way through the test period due to damage development. The environmental test fixture, shown in Fig. 4, used three "picture frame" shear fixtures, similar to the laboratory fixtures, connected in series. The train of "picture frame" rigs was connected to a hydraulic ram at one end and a load cell located at the other. As the frame was horizontal, a support structure, not shown in the figure, prevented the rigs sagging under their own weight. The fatigue tests were conducted at a peak load level of 38 kN (107 N/mm), cycling with a period of 40 seconds.

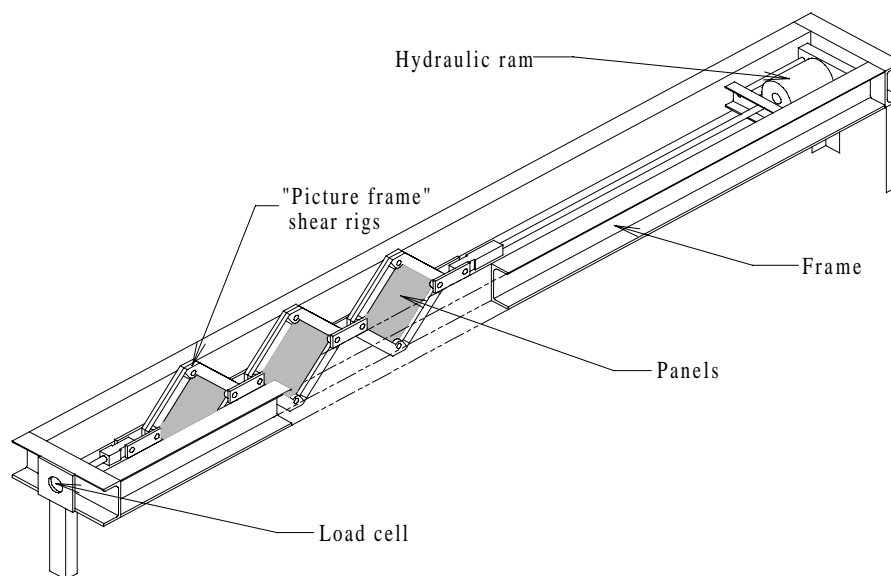


Fig. 4: Environmental test fixture arrangement.

Another three specimens were mounted in a stand, not under load, while being subjected to the same environmental conditions. The stand was positioned so that the specimens were exposed to maximum solar radiation. Following completion of the test period, all specimens were returned to the laboratory to assess the extent of any environmental degradation and damage growth. Residual strength tests will be conducted to determine whether long term cyclic loading combined with environmental exposure has a significant effect on the properties of the postbuckling panels.

RESULTS AND DISCUSSION

Static Testing

Tests on undamaged panels showed that prior to buckling, the skin deflected out-of-plane due to both the unsymmetric lay-up of the skin and the initial imperfections. The panels buckled at approximately 31 kN (88 N/mm) (determined from strain reversal), developing a diagonal tension field typical of shear buckling. This was characterised by three half-waves in the two centre bays of the panel. As the load increased, the wave-length of the buckles decreased

slightly and small buckle peaks at the edges of the bays became more prominent. The out-of-plane displacements during testing were investigated qualitatively using the moiré interferometry technique. The peaks and troughs in the two central bays of the panel were not identical because of the different lay-up in the two bays. The out-of-plane displacements were also recorded using the LVDT with displacements of up to 3.2 mm measured. The buckled shape at a load of 70 kN (198 N/mm) is shown in Fig. 5. The presence of the 50 mm diameter teflon insert did not greatly influence the buckling load of the panels; however, the postbuckling shape was affected. It was observed that shortly after buckling, one of the buckle peaks was elongated and clearly extended into the delaminated region.

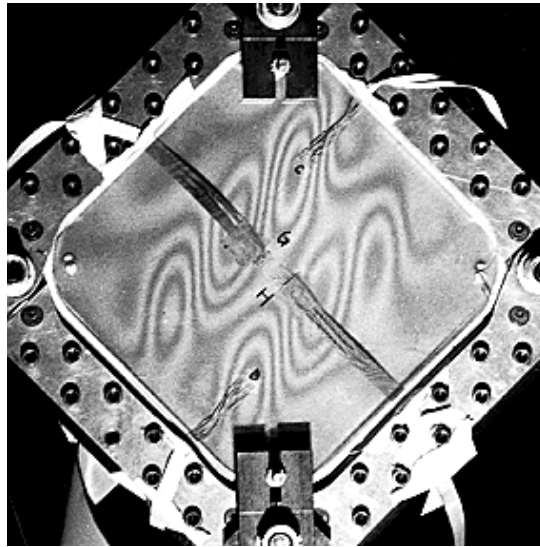


Fig. 5: Buckling shape of an undamaged panel at a load of 70 kN.

The experimental results showed that in the strain gauge locations, surface shear strains up to 22,000 $\mu\gamma$ were experienced before failure. Prior to buckling, the relationship between load and strain was approximately linear. Buckling was clearly identified by bifurcation of the back-to-back gauge strains. Following buckling, the strains increased at a higher rate due to the bending strains resulting from buckling.

The undamaged panels failed at loads of approximately 80 kN (226 N/mm) with fibre axial strains up to 10,000 $\mu\epsilon$ recorded. This was preceded by audible cracking from a load of 62 kN (175 N/mm). Ultimate failure of the undamaged panels was through fibre failure, fibre pull-out and delamination. It was characterised by extensive tension failure and fibre pull-out of the -45° fibres and appeared to initiate from the region where one buckle terminated at the centre stiffener. Failure spread rapidly horizontally across the panel, as shown in Fig. 6. Ultimate failure also resulted in extensive delamination along the vertical diagonal of the panels.

The process of failure in the panels with the teflon insert was very different. As previously mentioned, one of the buckle peaks extended into the delaminated region shortly after buckling. Cracking was heard at a load of 38 kN (107 N/mm) while significant delamination growth was noted at a load of 48 kN (136 N/mm). The resulting delaminated region can be

seen in Fig. 7. Following these events, the growth stabilised and load continued to be carried up to approximately 60 kN (170 N/mm) when significant fibre breakage occurred.

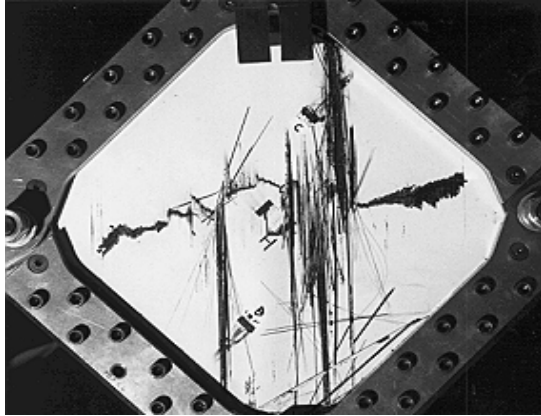


Fig. 6: Typical undamaged panel failure showing tension failure and fibre pull-out

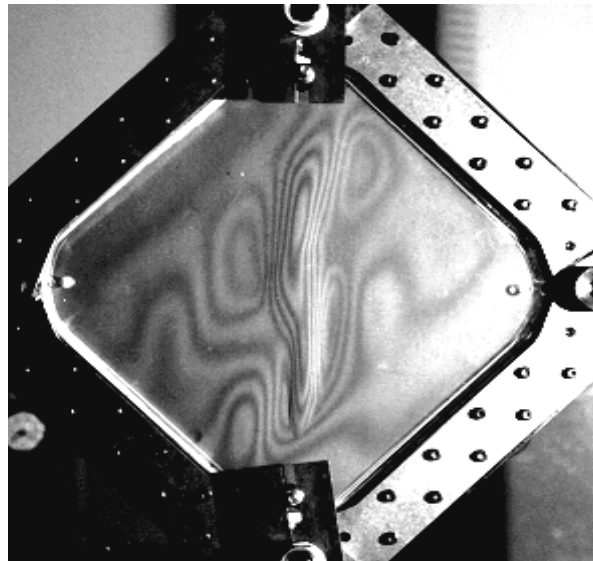


Fig. 7: Teflon insert panel at 50 kN following delamination growth.

Laboratory Fatigue Testing

Fatigue tests have been conducted on several panels. One test was carried out at an R value of 0.4 with a minimum load of 20 kN (57 N/mm) and a peak load of 50 kN (141 N/mm). The peak load was equivalent to two thirds of the static ultimate load of the panel. This loading represents maximum fibre strains of approximately 6,000 $\mu\epsilon$ with out-of-plane displacements of up to 2.0 mm. The panel was cycled at this high strain level for three million cycles at 4 Hz with no resulting damage detected by ultrasonic C-scan. A test was carried out at an R value of -1.0 with a peak load of 50 kN (141 N/mm). This panel has been subjected to 60,000 cycles of fully reversed loading with no resulting damage.

Environmental Testing

The environmental test specimens underwent tropical exposure for up to 20.5 months, during which time the various specimens were subjected to a total of 370,000 cycles. A summary of the conditions experienced during this period are presented in Table 1. The relative humidity at the site was very high being above 90% for 60% of the time, dropping below 60% for only 6% of the time. The average daily maximum temperature was also quite high at 29.3°C. At the end of the test period, the moisture absorbed by the laminate had reached a level of approximately 0.7%, although it is expected that this level would fluctuate depending upon the temperature and humidity.

All specimens have exhibited signs of degradation due to exposure to UV radiation. This was characterised by the breaking down of the outer layer of the epoxy matrix which was then eroded by the wind and rain. In the static exposure specimens, the side that was facing the sun showed extensive signs of degradation. The outer layer of fibres were visible, many of which were loose. These fibres do appear to protect the underlying matrix, however under a

more erosive environment, it would be expected that the degradation could penetrate to a greater depth. This could seriously affect the integrity of the laminate in the long term and provides an indication of the importance of protecting composite structures from UV degradation. The fatigue panels were not subjected to the same levels of UV exposure, but some degradation was clearly evident.

Table 1: Summary of the environmental conditions at the tropical exposure site during the 20.5 month test period.

Average Daily Maximum Temperature	29.3°C
Average Daily Temperature	24.5°C
Average Daily Minimum Temperature	21.0°C
Average Daily Maximum Relative Humidity	99%
Average Daily Relative Humidity	88%
Average Daily Minimum Relative Humidity	65%
Proportion of Time Above 90% Relative Humidity	60%
Proportion of Time Below 60% Relative Humidity	6%
Total Rainfall	5,965 mm
Duration of Rainfall	757 hours
Total Solar Radiation	10,476 MJ/m ²

The undamaged fatigue specimen exhibited no signs of damage development as determined using C-scan following the test period. The impact damaged panel showed insignificant damage growth although the impact site was permanently “bubbled” following testing. The specimen with the 50 mm diameter artificial delamination underwent extensive delamination growth. This was clearly visible after 91,000 cycles when a C-scan was performed which showed delamination growth along the tension diagonal from the central delamination. The C-scan of this panel prior to testing is shown in Fig. 8(a) and after 91,000 cycles in Fig. 8(b). In Fig. 8(b), only the section along the tension diagonal was scanned at a lower resolution and damage was indicated by white regions; dark areas indicate damage in the other figures. The panel was then cycled for another 166,000 cycles before being removed. Another C-scan showed only a small amount of further delamination growth had occurred around the ends of the stiffeners, as shown in Fig. 8(c). A new delamination specimen was then placed in the test fixture for the remaining period. This panel underwent a total of 112,000 cycles and suffered very similar delamination growth to the previous panel after 257,000 cycles, as shown by the C-scan in Fig. 8(d). It should be pointed out that in Fig. 8(c), the damage above and to the left of the artificial delamination is not shown clearly.

From the various C-scans taken of the panels containing artificial delaminations, it appeared that the delamination reached a limit after approximately 100,000 cycles. The damage itself was similar in appearance to that experienced in the static testing of the same panels. However, the delamination growth occurred at a lower load level and became more widespread than in the static tests. In both the static and fatigue tests, the delamination growth was greater in the unsymmetric bay of the panel (the bay above the central stiffener in Fig. 8). After the delamination growth, the panels were still capable of carrying the cyclic load. These preliminary conclusions will be verified after further laboratory testing.

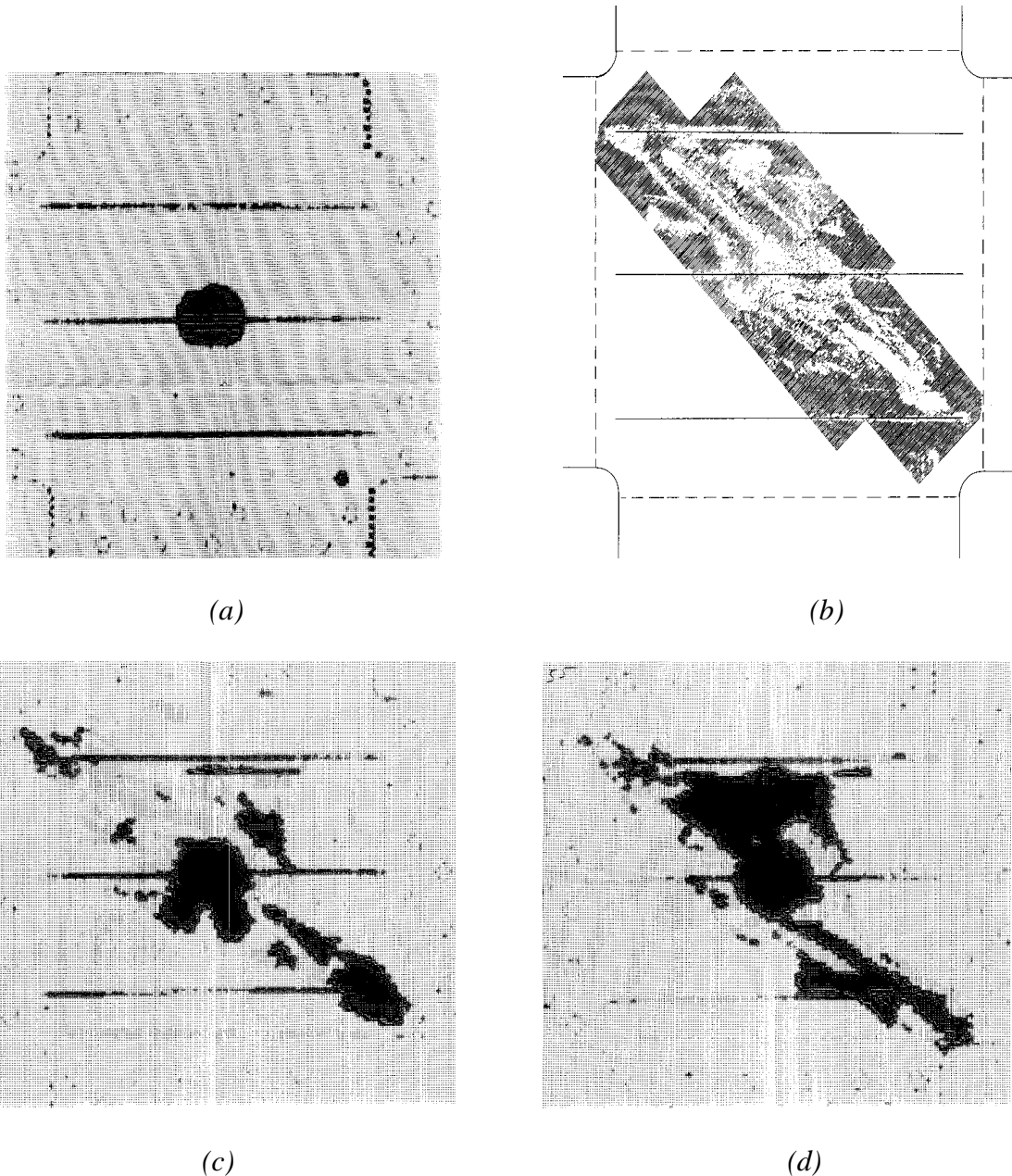


Fig. 8: C-scans of teflon insert panel (a) prior to testing, (b) after 91,000 cycles, (c) after 257,000 cycles and (d) replacement panel after 112,000 cycles.

CONCLUSIONS

The buckling and postbuckling performance of three-blade-stiffened carbon fibre/epoxy panels under shear has been investigated. Static and fatigue tests were conducted in a “picture frame” shear fixture. During static testing, buckling initiated at 31 kN (88 N/mm) and the panels exhibited significant postbuckling strength before failing at approximately 80 kN (226 N/mm). Ultimate failure of the panels was characterised by widespread delamination coupled with extensive fibre breakage of the -45° plies which were in tension. The presence of an introduced delamination affected the buckling mode shape and reduced the strength of the panels by 25%. These panels underwent delamination growth at 48 kN (136 N/mm) before failing at approximately 60 kN (170 N/mm).

The fatigue tests carried out so far have indicated that these panels are resistant to fatigue failures. Undamaged panels have been shown to be capable of sustaining cyclic loading up to two thirds of the static failure load without developing fatigue damage. Environmental testing proved the durability of undamaged and impact damaged panels, however panels containing a 50 mm diameter artificial delamination suffered delamination growth along the tension diagonal. These panels were still capable of carrying the cyclic load and the delamination appeared to stabilise after approximately 100,000 cycles. This testing program has demonstrated the inherent damage tolerance of the stiffened, postbuckling, composite panels.

ACKNOWLEDGMENTS

The authors wish to thank the staff at DSTO-Queensland, in particular Ed Shum and Ian Williams, for their assistance with the environmental testing.

REFERENCES

1. Weller, T. and Singer, J., "Durability of Stiffened Composite Panels Under Repeated Buckling," *International Journal of Solids and Structures*, Vol. 26, No. 9-10, 1990, pp. 1037-1069.
2. Agarwal, B.L., "Postbuckling Behavior of Composite Shear Webs," *AIAA Journal*, Vol. 19, No. 7, July 1981, pp. 933-939.
3. Panhwar, N.M., Thomson, R.S. and Scott, M.L. "Durability of Postbuckling Fibre Composite Panels Under Shear", *Proceedings Fifth Australian Aeronautical Conference*, Melbourne, Victoria, Australia, September 13-15, 1993, Vol. 1, pp. 75-80.
4. Hoffman, D.J. and Bielawski, W.J., "Environmental Exposure Effects on Composite Materials for Commercial Aircraft", *NASA CR-187478*, National Aeronautics and Space Administration, Hampton, Virginia, USA, 1991.
5. Thomson, R.S. and Scott, M.L., "Testing and Analysis of Thin Stiffened Carbon Epoxy Shear Panels," *Proceedings Second Pacific International Conference on Aerospace Science and Technology - Sixth Australian Aeronautical Conference*, Melbourne, Victoria, Australia, March 20-23, 1995, Vol. 2, pp. 655-662.
6. Chalkley, P.D. and Chester, R.J., "The Influence of Tropical Exposure on the Durability of Graphite/Epoxy Laminates," *Theoretical and Applied Fracture Mechanics*, Vol. 13, 1990, pp. 137-144.

POSTBUCKLING AND FAILURE OF STIFFENED COMPOSITE PLATES

Chang-Sun Hong¹, Cheol-Won Kong¹, In-Cheol Lee²

¹*Department of Aerospace Engineering
Korea Advanced Institute of Science and Technology
Taejon 305-701, Korea*

²*Samsung Motors, Kyoung-gi, Korea*

SUMMARY: Postbuckling and failure were studied analytically and experimentally for the stiffened composite plates. In the analysis, the stiffened composite plates were analyzed using the nonlinear finite element method. The progressive failure analysis was done by adopting the maximum stress criterion and complete unloading failure model. In the failure analysis, the considered failure modes are matrix failure, shear failure and fiber failure. In the experiment, the stiffeners were formed by the continuous lay-up of the skin. Therefore, the separation between the stiffener and the skin was not found even after final failure. A shadow moire technique was used to monitor the out-of-plane deformations of the plates. Piezoelectric film sensors were attached to the plate and damages were detected by those. The analytical results on the buckling load, postbuckling behavior, and failure characteristics showed good agreement with the experimental results. The stiffened composite plate, which had been fabricated by secondary bonding, was failed by debonding between the skin and the stiffener. The comparisons of the present cocuring with the secondary bonding for the stiffened composite plate were conducted with respect to postbuckling behavior and failure mode in experiments.

KEYWORDS: postbuckling, failure, stiffened composite plate, cocuring, debonding

INTRODUCTION

The stiffened composite plates are extensively used in aircraft and other structural components to satisfy requirements of increased stiffness and reduced weight. Since the buckling of the stiffened plates does not mean the total collapse of structure, it has been found to be efficient to permit buckling of the stiffened composite plates under postbuckling ultimate load. Therefore, it is essential to investigate the postbuckling behavior and failure characteristics of the stiffened composite plates. In most of previous studies [1, 2, 3] except for ref. [4], the stiffened composite plates have been secondarily bonded between the skin and the stiffener or cocured without ply overlap in the junction part of the skin and the stiffener. These types of the stiffened composite plates losed load carrying capacity due to the separation between the skin and the stiffener. In case of the previous study [3], the postbuckling compressive strength of the secondary bonded plate was higher than that of the cocured one about 18%. In present study, the separation of the cocured plate was eliminated by curing the stiffener with the skin in a continuous laminate. In the analysis, a progressive failure model was introduced into the nonlinear finite element analysis[5, 6]. This finite element program was applied to the stiffened composite plate fabricated by the present cocuring. The postbuckling behavior and the failure characteristics were studied. Two kinds of the stiffened composite plate, which had been fabricated by present cocuring and secondary

bonding respectively, were also tested to compare postbuckling behavior and failure modes in experiments.

FINITE ELEMENT ANALYSIS

The eight-node degenerated shell element is used for the modeling of the stiffened composite plates, and the first order shear deformation theory is adopted in the nonlinear finite element analysis. To estimate the failure load of each failure mode, the maximum stress criterion is applied to the average stresses in the principal material directions of each layer of each element. Also, in order to estimate the postbuckling load-carrying capacity, it is assumed that the stress corresponding to the failure mode of each layer is completely unloaded and the corresponding stiffness is set to zero in each element. This complete unloading failure model can be expressed by the following equations.

If fiber failure occurs, then

$$\sigma_1 = 0, \quad E_1 = 0, \quad \nu_{12} = 0, \quad \nu_{13} = 0$$

If matrix failure occurs, then

$$\sigma_2 = 0, \quad E_2 = 0, \quad \nu_{21} = 0, \quad \nu_{23} = 0$$

If shear failure occurs, then

$$\tau_{12} = 0, \quad \tau_{21} = 0, \quad G_{12} = 0$$

The failure of each element in this model is estimated for the converged stresses during each load step, and the stress component corresponding to the failure mode is unloaded. Therefore, if failure occurred at the previous load step, the force equilibrium is not satisfied at the first iteration of the present load step, and an unbalanced force is induced due to the unloaded stress component. For the postbuckling failure analysis, the effect of the deformation due to the failure-induced unbalanced force should be introduced into the modified arc-length method[5, 6]. In case of modeling the skin and the stiffener with the degenerated shell elements, the incompatibility in degrees of freedom arises from the difference in local coordinates between the two elements to hold the adjacent nodes of the skin and the stiffener in common. The compatibility is enforced to the common nodes by equalizing the displacement in the global x , y , z directions and matching the rotation about the local unit vector.

EXPERIMENTS

The stiffened composite plates were fabricated using graphite/epoxy prepreg, and the material properties used in this study were as follows.

$$E_1=130.0 \text{ GPa}, E_2=E_3=10.0 \text{ GPa}, G_{12}=G_{13}=4.85 \text{ GPa}, G_{23}=3.62 \text{ GPa}, \nu_{12}=\nu_{13}=0.31, \\ \nu_{23}=0.52, X_T=1933 \text{ MPa}, X_C=1051 \text{ MPa}, Y_T=51 \text{ MPa}, Y_C=141 \text{ MPa}, S=61 \text{ MPa}$$

The geometry and the dimension of the stiffened plate are shown in Fig. 1-a. Boundaries are clamped for loaded edges and free along the unloaded sides. The stiffened plate consists of

two stiffeners having the lay-up sequence of $[0/90/45/0/-45]_5$ for web and cap. The stiffeners were formed by the continuous lay-up of skin, $[0/90/\pm 45]_5$. As shown in Fig. 1-b, two types of the stiffeners were used in the composite plates, one was I-shaped stiffeners, and the other was blade-shaped stiffeners. Two 0° plies for the flange were inserted into the skin, and one of them was continued to the stiffener. Unidirectional tape fillers were inserted into intersection between the web and the skin or the cap. After curing, the stiffened plates were inspected using C-scan and no significant defects were detected. The loaded ends of the stiffened plates were potted by casting resins, and they were machined flat and parallel to load uniformly. The stiffened plates were tested to final failure in compression to investigate its postbuckling behavior. Out-of-plane deflections were also monitored by the shadow moire technique. Piezoelectric film sensors were used to detect the event of damages globally.

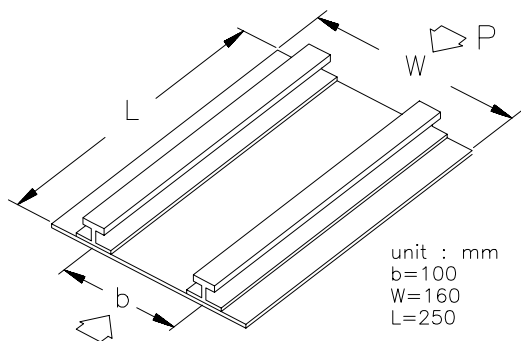


Fig. 1-a: Geometry of I-stiffened plate.

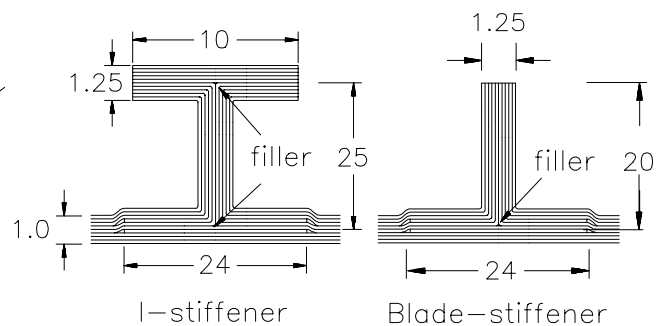


Fig. 1-b: Configuration of stiffeners.

To compare postbuckling behavior of the present cocuring with the secondary bonding, two stiffened composite plates were also fabricated by different method. In case of the secondary bonding, the skin and the stiffener were precured firstly. The typical surfaces of the skin and the stiffener, which would be bonded each other, were abraded with a mesh sandpaper such as #150. The surface roughness was $3\mu\text{m}$ in the direction of fiber and $9\mu\text{m}$ in the vertical direction. American Cyanamid FM-73 adhesive films were inserted into the surface between the skin and the stiffener and cured in an autoclave.

COMPARISON OF ANALYSIS WITH EXPERIMENT

The load-end shortening curves of the I-shaped stiffened plate obtained from experiment and finite element analysis are shown in Fig. 2. The stiffened composite plate carried the applied load about four or five times of the buckling load. The experimental buckling load is in good agreement with the analytical result. But the experimental postbuckling ultimate load differs by 23% from the analytical result because the failure model used in this paper does not consider the delamination. The positions of the first-ply-failure of each mode are indicated on the load-end shortening curve. These failure modes induced the reduction in the stiffness of the plate abruptly. At last the load carrying capacity was lost rapidly. The separation between the stiffener and the skin was not found even after the final failure. The buckling loads were determined by the load- deflection curves at the center of the plate, as shown in Fig. 3.

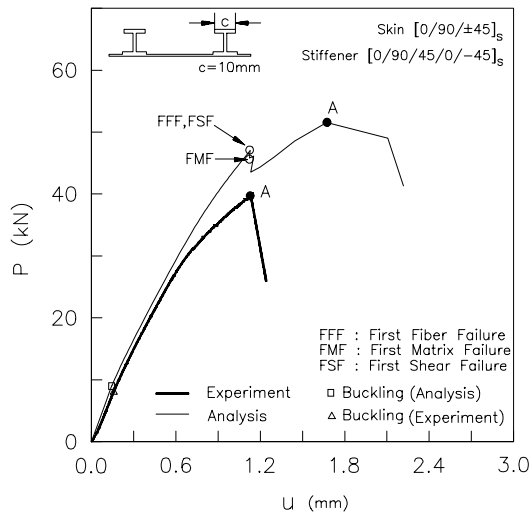


Fig. 2: Load-shortening curves of I-stiffened plate.

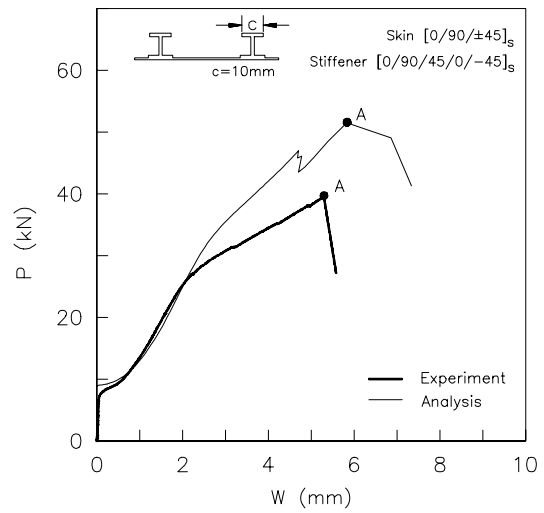


Fig. 3: Load-deflection curves of I-stiffened plate.

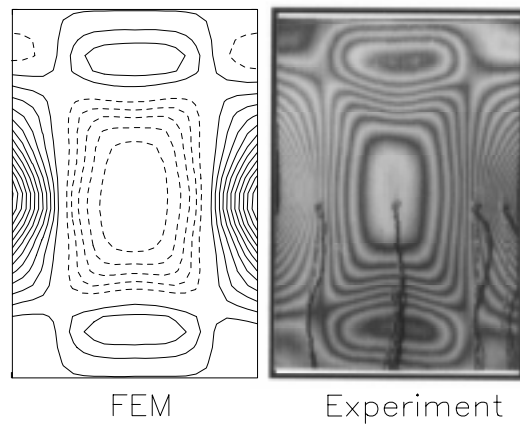


Fig. 4: Contour plots of out-of-deflection

Figure 4 shows the contour plot of the out-of-plane skin deflections generated from the finite element analysis and the photograph of the moire fringe pattern at the point A. These results show very good agreement in postbuckling range. Figure 5-a shows the picture of the stiffened plate after final failure. Delaminations were occurred along the free edges and fiber failures were occurred at the stiffener. Figure 5-b shows the failure pattern of that in analysis. Most of failures were occurred at the center of the stiffeners and the free edges.

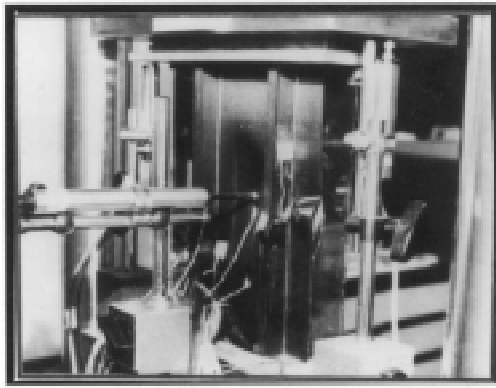


Fig. 5-a: Failure patterns in experiment.

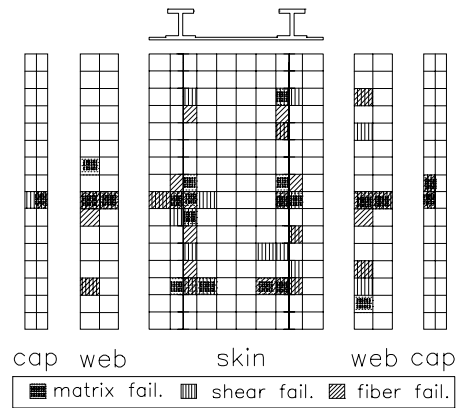


Fig. 5-b: Failure patterns in analysis.

The load-end shortening curves of the blade-shaped stiffened plate obtained from experiment and finite element analysis are shown in Fig. 6. The experimental postbuckling ultimate load differs by 2% from the analytical result. The first-ply failure of analysis was occurred at the point A and damage in experiment was detected near the final failure. Figure 7 shows the event of damage detected by piezoelectric film sensors.

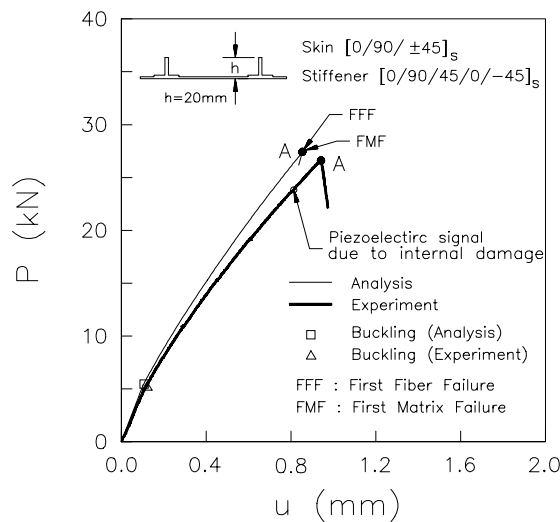


Fig. 6: Load-shortening curves of blade-stiffened plate.

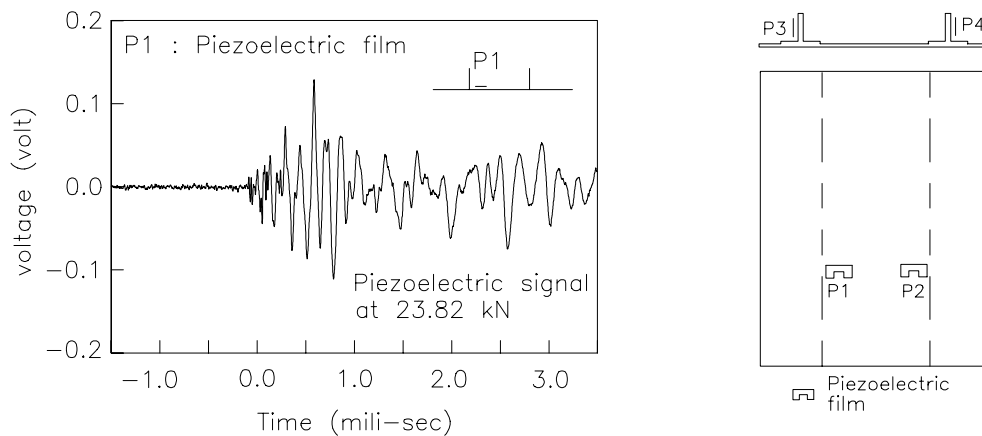


Fig. 7: Piezoelectric film signal due to internal damage.

COMPARISON OF COCURING WITH SECONDARY BONDING

Figure 8 shows two I-shaped stiffeners formed by the present cocuring and the secondary bonding respectively. For both specimens, unidirectional tape fillers were inserted into the intersection between the stiffener and the skin. Figure 9 shows the load-shortening curves of stiffened composite plates loaded in the axial direction. The slopes of load-shortening curves

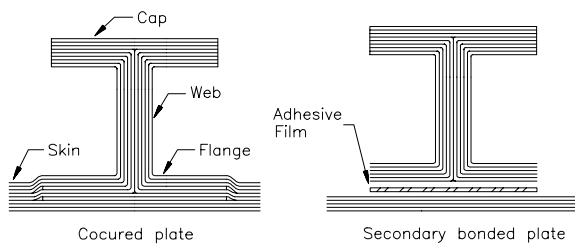


Fig. 8: Two types of the stiffened plate.

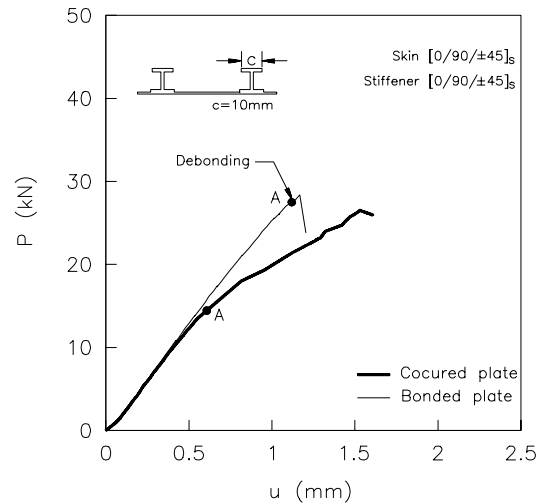


Fig. 9: Load-shortening curves of cocured plate and bonded plate.

matched till the point A but decreased after the point A in cocured case, because the stiffener of the bonded plate sustained more compression load than that of the cocured plate until the peeling was occurred between the skin and the stiffeners. The postbuckling compressive strength of the cocured plate was slightly smaller than that of the bonded plate. But present cocured stiffened plate showed relatively higher postbuckling compressive strength than previous ones[2, 3], when compared with secondary bonded plate.

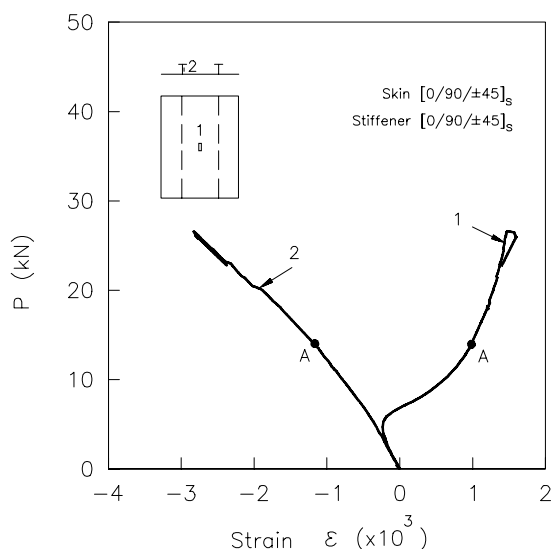


Fig. 10: Load-strain curves of cocured plate.

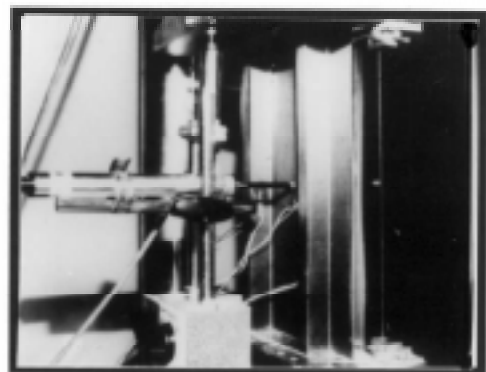


Fig. 11: Failure patterns of cocured plate.

Figure 10 shows load-strain curves of the cocured plate in the skin and the stiffener. In case of skin, the slope of load-strain curve changed at the event of buckling due to the bowing of the skin. But otherwise the slope of load-strain curve of the stiffener changed little till the point A. Therefore the stiffener sustained the compressive load in the axial direction and the skin sustained bending moment till the point A. The slope of the load-strain curve increased in the skin and decreased in the stiffener after the point A, because the buckling mode of the skin was enlarged globally and the bending moment had effects on the stiffener. Figure 11 shows the patterns of failure before final collapse. The stiffener had delaminations under the stiffener due to bending moment. The separation between the stiffener and the skin was not found. Figure 12 shows load-strain curves of the bonded plate in the skin and the stiffener. The slope of the load-strain curve in the stiffener changed little till the point A, because the stiffener with adhesive film sustained compression load till the debonding. The debonding between the skin and the stiffener was occurred suddenly after the point A, as shown Fig. 13.

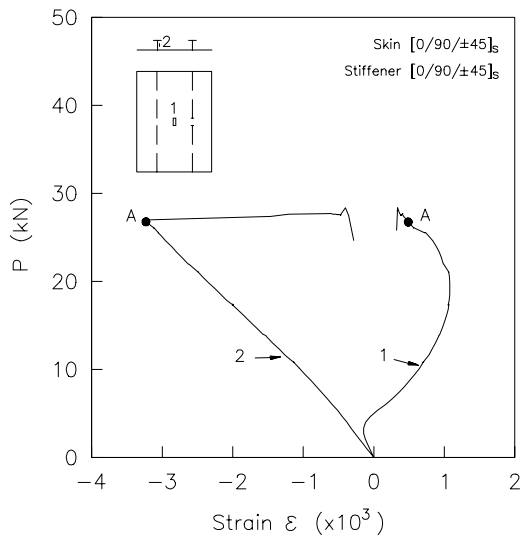


Fig. 12: Load-strain curves of bonded plate.

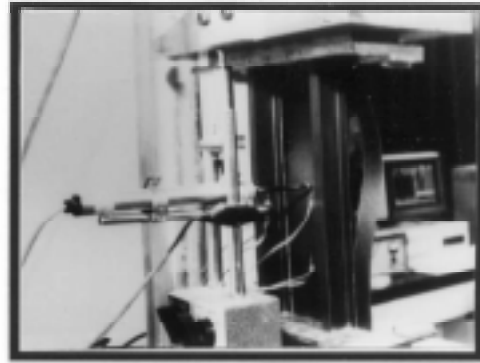


Fig. 13: Failure patterns of bonded plate.

CONCLUSIONS

The finite element program with the progressive failure model was applied to the stiffened composite plates under axial compression. The postbuckling behavior and the failure of these plates were characterized. The stiffeners were fabricated by the continuous plies of the skin and cocured with the skin. Therefore, the separation between the stiffener and the skin, which was main failure mode of the previous cocured or bonded plates, was not found even after final failure. The events of damage were detected by piezoelectric film sensors in experiments and compared with analysis. The results of FEM about the buckling load, the postbuckling behavior, and the failure characteristics showed good agreement with those of experiments. The postbuckling compressive strength of the cocured plate was slightly smaller than that of the bonded plate. But the present cocured stiffened plate showed relatively higher postbuckling compressive strength than previous ones, when compared with the secondary bonded plate. The bonded stiffened plate lost the loading carrying capacity suddenly due to the debonding between the skin and the stiffener, which was not found in the present cocured plate.

REFERENCES

1. Starnes, J.H., Knight, N.F., and Rose, M., "Postbuckling Behavior of Selected Flat Stiffened Graphite-Epoxy Panels Loaded in Compression," *AIAA*, Vol. 23, No 8, 1985, pp. 1236-1246.
2. Stevens, K. A., Ricci, R., and Davies, G.A.O., "Buckling and postbuckling of composite structures," *Composites*, Vol. 26, 1995, pp. 189-199.
3. Lee, S., Elaldi, F., Villalobos, H., and Scott, R.F., "Experimental and Analytical Study of J-stiffened Composite Panels Loaded in Axial Compression," *ICCM-9*, Madrid, Spain, 1993, pp. 519-526.
4. Scott, M.L., and Rees, D.A., "Analysis and Test of Thin Integrally Stiffened Fibre Composite Panels," *ICCM-10*, Whistler, B.C., Canada, 1995, pp. 117-124.
5. Kweon, J.H., and Hong, C.S., "An Improved Arc-length Method for Postbuckling Analysis of Composite Cylindrical Plates," *Comp. And Struct.*, Vol. 53, No. 3, 1994, pp. 541-549.
6. Kweon, J.H., Hong, C.S., and Lee, I.C., "postbuckling Compressive Strength of Graphite/Epoxy Laminated Cylindrical Plates Loaded in Compression," *AIAA*, Vol. 33, No 2, 1995, pp. 217-222.

POSTBUCKLING FAILURE OF CARBON-EPOXY COMPRESSION PANELS

K. A. Stevens, S. Specht and G. A. O. Davies

*Department of Aeronautics, Imperial College of Science, Technology and Medicine,
Prince Consort Road, London SW7 2BY*

SUMMARY: The postbuckled failure of carbon/epoxy compression panels is studied experimentally and theoretically. Four different designs are considered each of which has significant postbuckled strength with a failure load more than twice the buckling load. The mechanisms which can initiate failure through stiffener debonding, prior to imminent explosive collapse, are postulated, taking account of the buckled mode shape. The specific mechanism which leads to failure in each of the particular four designs is identified from careful experiments with complete panels and also by suitably loading transverse strips cut from the panel to be tested. These component tests provide a quantitative guide to the magnitude of a stress resultant which will lead to debond initiation. This stress resultant can then be related to a compression failure load through an FE analysis of the postbuckled panel.

KEYWORDS: postbuckling failure, stiffened carbon/epoxy panels, axial compression

INTRODUCTION

Stiffened compression panels manufactured in carbon fibre composite can have a large reserve of postbuckled strength if the skins are thin ($b/t > 50$). Each of the four panel designs discussed in this paper has a ratio of failure load to buckling load greater than 2. For this strength margin between buckling and failure to be accessible to the designer, say to meet ultimate requirements, a method for predicting the failure load is needed.

Advanced finite element packages facilitate the prediction of displacements and stresses in a postbuckled panel. Even structures undergoing post-critical bifurcations or mode jumps can now be investigated successfully. However, a numerical strategy to predict the failure load of a stiffened panel still presents considerable difficulties, and this is especially true if there is no information from a laboratory test of the panel.

There are a number of reasons why failure prediction is difficult:-

- (i) Failure of these panels is invariably associated with separation of the stiffener from the skin, rather than as a result of in-plane material failure. There will be a number of locations in the panel where failure could be initiated, and in a number of possible ways. A priori the failure mechanism and location are not easily identified by analysis.
- (ii) The skin-stiffener assembly is a complex region involving a large number of variable quantities. The stiffeners may be co-cured or bonded and there will be resin rich

regions and areas where the plies will be curved. Also the flanges of the stiffener may be tapered in some way. All of these details, and of course the particular stiffener configuration, will govern the initiation and locus of the crack which will lead to stiffener debonding.

- (iii) There is a dearth of accumulated experimental evidence in the literature about how stiffener debonding is initiated. This is a consequence of the explosive and destructive nature of the failure which largely precludes any useful examination of the debris. Earlier researchers into postbuckling failure [2,3,4,5] who tested panels with I, blade and hat stiffeners all observed the explosive collapse and the stiffener separation, without identifying the initiating mechanism and its location. Ref. 6 noted "localised flange separation" in J stiffened panels before collapse but did not locate it with reference to the buckle pattern.

A number of workers, for example Ref. 7, have developed analytical techniques for calculating the stress distribution at the skin/stiffener interface. However these are idealised models which cannot reflect the idiosyncrasies of a particular case. They are helpful in regard to parametric studies, e.g. to observe the effect of the relative stiffnesses of the skin and the flange and web of the stiffener on the peak stresses [7].

This paper presents a study of the failure of four types of postbuckled panel having I, J and two forms of hat stiffener. In each case, knowing the buckle mode shape (from an FE analysis) the possibilities for failure initiation due to stiffener debonding are considered.

The results of some component tests which replicate some of the failure mechanisms are then considered before the experimental evidence from the complete panel tests are presented.

Finally a methodology for evaluating postbuckled failure loads is considered.

THE TEST PANELS

Each panel was made from unidirectional prepreg and had four stiffeners. The ends were potted and machined flat and parallel whilst the edges were unsupported. The panels were tested under axial load in a special purpose 250 tonne test machine which had been designed to have the high stiffness necessary for postbuckling studies. The panels varied in length, but each was long enough for there to be at least three half waves along the length when buckled.

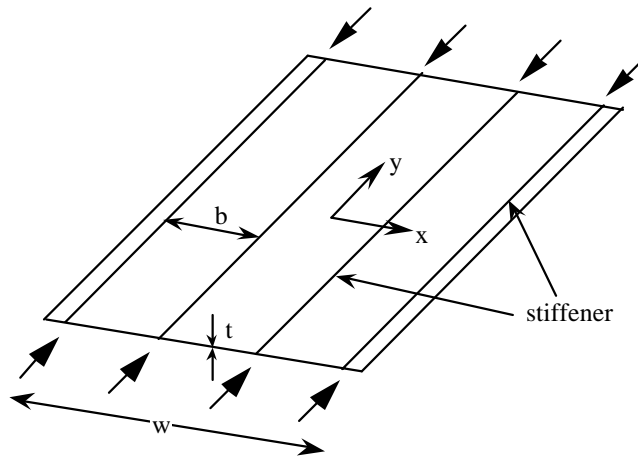
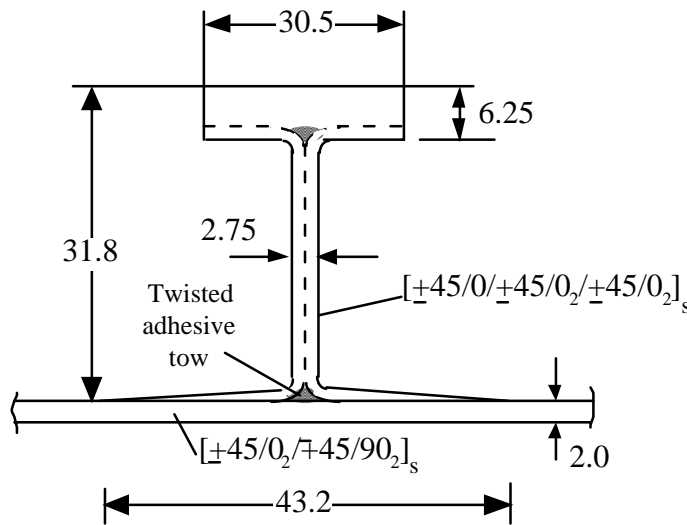


Fig. 1: Four stiffener panel

I-Stiffened Panels

Material T300/914C. The panels had either co-cured or bonded stiffeners. An adhesive layer was present in each case, Fig. 2.

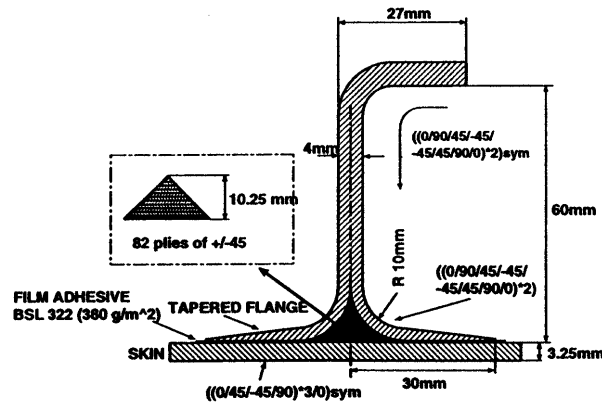


$$w = 610; b/t = 178/2 = 89$$

Fig. 2: I stiffener panel

J-Stiffened Panels

Material T800/924C. The panels were co-cured and incorporated an adhesive layer. The triangular region was filled with $\pm 45^\circ$ laminate, Fig. 3.



$$w = 903; \quad b/t = 270/3.25 = 83$$

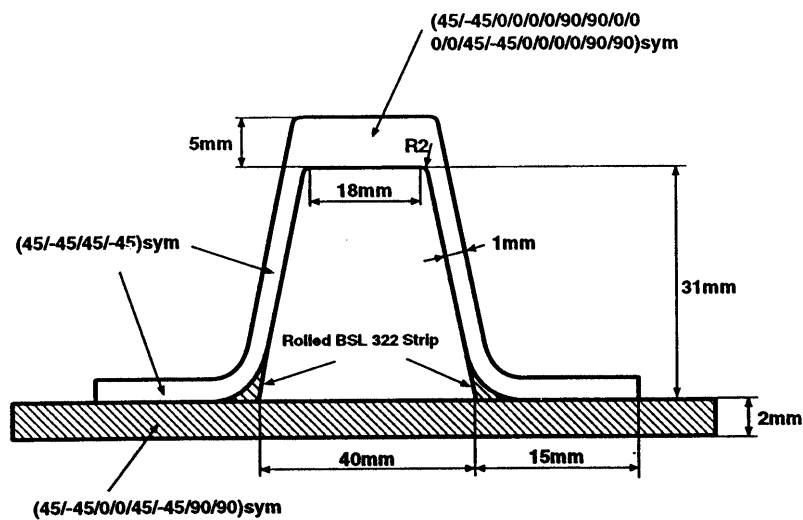
Fig. 3: J stiffened panel

Hat-Stiffened Panels

Material T800/924C. The panels were co-cured and did not incorporate an adhesive layer. The filler material at the base of the webs was twisted adhesive tow.

There were two types of hat panel:

- Ht = stiffeners had tapered flanges.
- Hu = stiffeners had untapered flanges.



$$w = 610, \text{ stiffeners } 178\text{mm apart}$$

$$\therefore b/t \approx 138/2 = 69$$

Fig. 4: Hat stiffened panel (untapered)

BUCKLING MODES

In each case the skin buckled between the stiffeners, which remains essentially undistorted, even at 3 times the buckling load. Thus although a nonlinear FE programme was required for the postbuckling panel analysis the stress analysis of a local model of the skin/stiffener attachment could be treated as a linear problem.

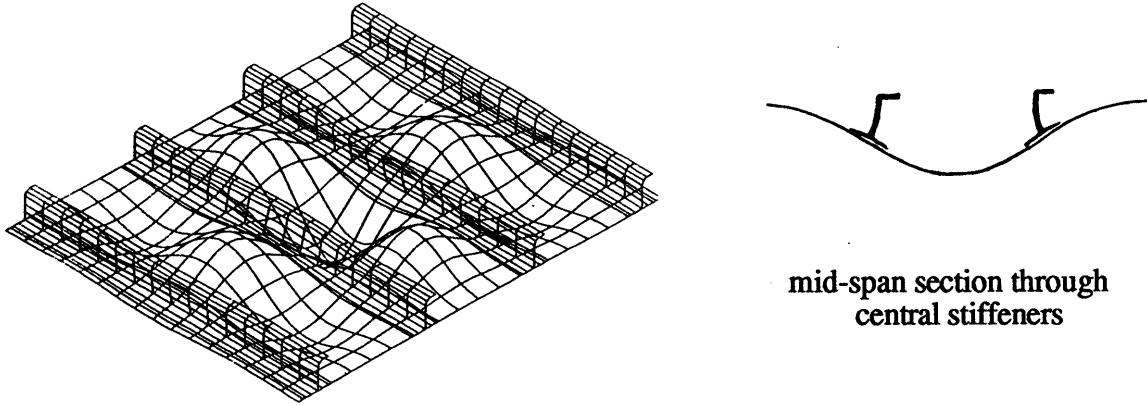


Fig. 5(a): Mode shape for I and J stiffeners

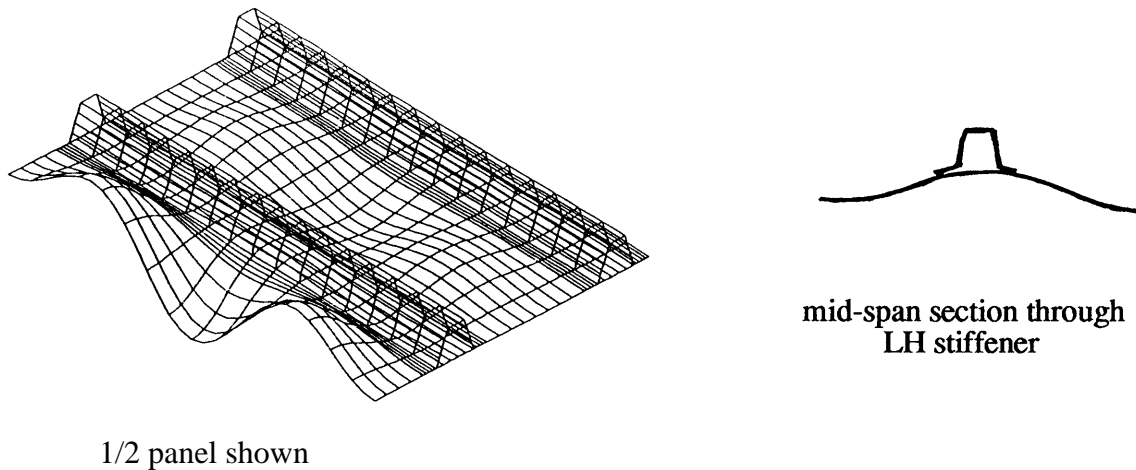


Fig. 5(b): Mode shape for hat stiffeners

Fig. 5(a) shows the mode shape, for I and J stiffened panels. The buckling displacements are asymmetric with respect to a stiffener centre line. However the mode shape for hat stiffened panels, Fig. 5(b), is symmetric with respect to the centre line of a stiffener and this symmetry has an influence upon the possibilities for stiffener debonding, as shown in the next section.

STIFFENER DEBONDING MECHANISMS

In sympathy with the buckle mode shape the stress resultants in the panel will vary periodically having peak values at positions corresponding to nodal and anti-nodal (buckle peak) lines. Thus we might expect the initiation of stiffener debonding to occur at one of these positions.

I and J Stiffener Debonding

The I and J stiffeners behave in the same way. In each case the flange caps of the stiffeners provide a high torsion/bending resistance, leading to a significant moment transfer between the skin and the stiffener (Fig. 6). This moment, M_w , is a maximum at the buckle peak and, as discussed in Ref. 10, can induce debonding under the web. Also at the buckle peak the discontinuity in bending stiffness at the free edge of the flange can cause the skin to peel away from the flange (on the left-hand side in Fig. 6).

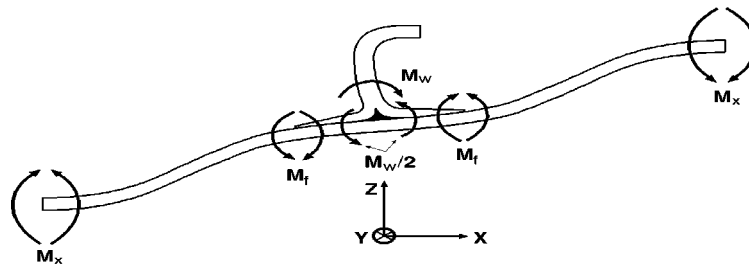


Fig. 6: Moments at an anti-node

A third possible failure mechanism exists on buckle nodal lines, where the bending moments M_w and M_f are zero, but the twisting moment in the skin, M_{xy} , is a maximum. The imposition of compatible shear strains by the skin on the stiffener flange gives rise to shear stresses τ_{yz} at the interface (Fig. 7). If these stresses are high enough debonding can ensue, as will be shown to be the case for the hat stiffened panels.

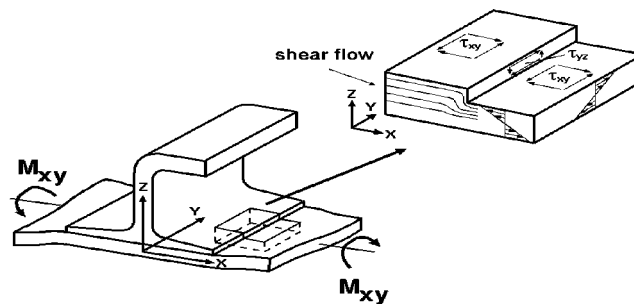


Fig. 7: Conditions on a node line ($M_x = 0$, M_{xy} max)

Hat Stiffener Debonding

Figs. 8(a) and 8(b) show conditions at adjacent buckle peaks on a hat stiffener.

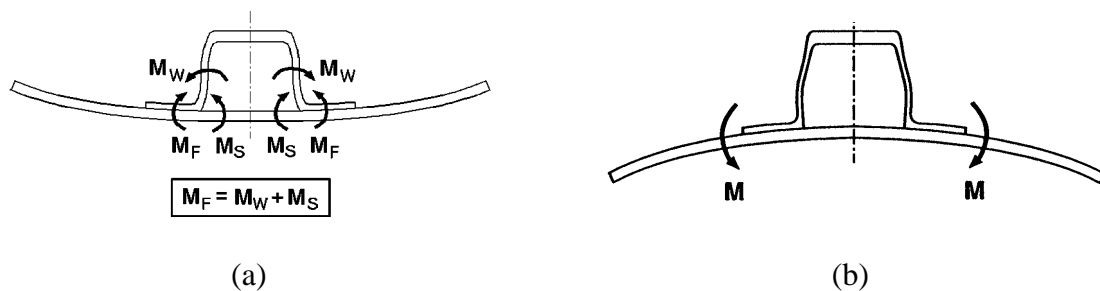


Fig. 8: Moments at adjacent anti-nodes

In Fig. 8(a) the moment M_w is tending to peel the flange away from the skin starting at the inside of the stiffener. In Fig. 8(b) the skin tends to peel from the flange at its free edge due to the flexural stiffness discontinuity.

At the nodal line in a hat stiffened panel the twisting moment M_{xy} is a maximum and the diffusion of the load into the stiffener is associated with the interfacial shear stress τ_{xz} mentioned in 4.1.

COMPONENT TESTS

I and J Stiffeners

Figs. 6 and 8 show ways in which the moment stress resultants on anti-nodal lines might initiate debonding between the stiffener flange and the skin. In Ref. 10 methods were proposed for determining critical values of these bending moments. A "component test" using a strip cut from an I stiffened panel was loaded in a special rig to simulate the web bending which initiates debonding under the web. The onset of debonding from the free edge of the flange can be simulated by loading a strip in 4-point bending (see Fig. 9(b) for hat stiffener). Component tests for the J stiffened panel are the same as those for the I panel.

Hat Stiffened Panels

Figs. 8(a) and 8(b) show that at buckle peaks the loading is symmetric about the stiffener centre line but reverses in sign as we pass to an adjacent peak along the stiffener.

The loading in Fig. 8(a) is reproduced by the 4-point bending test in Fig. 9(a). If the specimen is turned over in the rig then the loading in 8(b) is produced, 9(b).

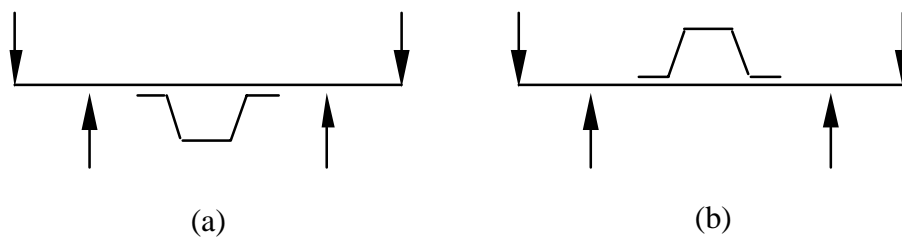


Fig. 9: Component tests for hat stiffened panels at the buckle crests

Debondings initiated by shear diffusion stresses on the nodal line are more difficult to reproduce in a simple component cut from the panel. An idea involving a torsional test is receiving attention.

These component tests, as well as providing guidance with respect to the critical values of stress resultants in the full panel test are also economical for parametric studies, Ref. 1.

PANEL TESTS

I Stiffened Panels

Refs. 9 and 10 reported results for some I stiffened panels. These panels initially debonded under the stiffener web at a buckle peak before explosive collapse. The correspondence between the micrographs at the failure site in the panel, and the component tests was remarkable, both in respect of the measured web bending moments at failure and the progression of the crack. In the co-cured case the crack went into the skin, whilst in the bonded case it remained in the flange (Fig. 7, Ref. 10). These panels typically buckled at about 11.5 tonnes and failed at 45 tonnes.

J Stiffened Panels

These larger panels buckled at approximately 30 tonnes and failed at a load of about 80 tonnes. Failure was initiated at a buckle crest when a crack propagated outwards from under the web (as in the case of the I stiffeners). A diagram of the failure is shown in Fig. 10.

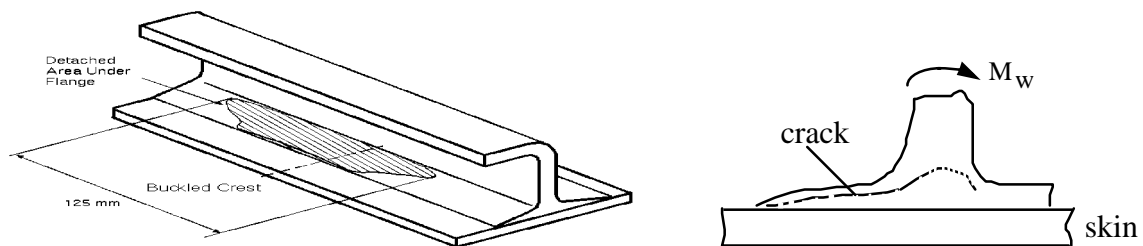


Fig. 10: Failure initiation of J stiffened panel

During the panel test the moment measured in the web at the buckle crest was $M_w = 860\text{N}$ at failure. The mean value of the moment in the skin near the free edge of the flange was only $M_f = 40\text{N}$. This low value for M_f is confirmed by the FE analysis. M_f is changing sign rapidly in this region since there is a point of inflexion in the mode shape.

The 4-point bending component test showed that a moment, $M_f = 480\text{N}$, was required to cause a crack to propagate from the edge of the flange, into the skin, towards the web. The mechanism was very similar to that seen in Ref. 1. At the edge of the flange a crack forms in the outer 0° ply which, in this case, has been used to envelope the inner plies which have been dropped off to form the taper. As seen in Fig. 11 the crack passes the end of the next ply (90°) in the flange and enters the skin through its outer 0° ply. It then propagates towards the web in the $0^\circ/45^\circ$ interface.

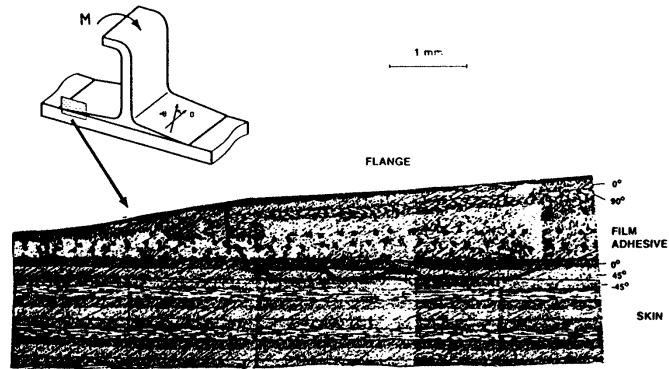


Fig. 11: Failure of J component in 4-point bending

In contrast to the very successful replication of the I stiffened panel failure in the web bending component tests, the J stiffener component tests did not reproduce a web bending type of failure. The failure produced was the same as that first described in the four-point bending test. That is the failure originated in the 0° ply at the edge of the flange. Clearly surface 0° plies, both in the skin and also in the flange, are vulnerable to transverse bending caused by buckling. Strain measurements indicated that the web bending component test did not properly represent the buckle crest conditions because a too high skin bending moment was induced at the edge of the flange.

Hat stiffened panels

(a) Untapered stiffener flanges

In the panel test, and also in the component test, strain gauges were positioned on the stiffener webs to monitor the web bending strains (at the buckle crests in the panel). A component test in the form of Fig. 9(a) showed that a crack would propagate out under the flange when the web moment reached 165N. The FE analysis of the panel calculated that the test panel stiffeners would realise this moment when the panel load reached 48 tonne.

However, in the test of the panel, failure was initiated at 42.5 tonne, after buckling at 13.5 tonne. Also, significantly, failure occurred at a nodal line. The failure took the form of a local debonding of the flange. The crack was at the flange/skin interface, $\pm 45^\circ$, and propagated from the flange edge towards the web, Fig. 12.

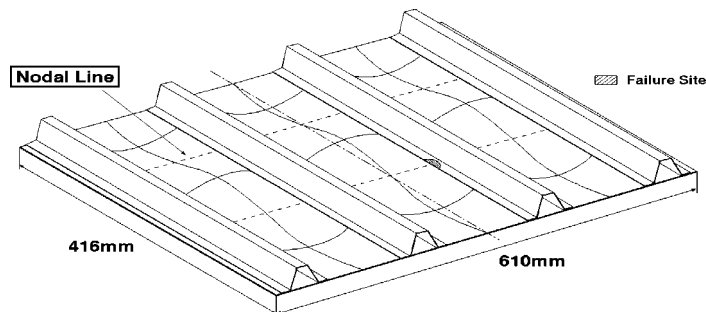


Fig. 12: Flange debonding on the nodal line

Fig. 13 shows the shear strains measured in the panel skin on each side of a stiffener at two nodal lines. If the twisting moments compatible with these shear strains are applied to a local 2-D model, in an FE analysis, then a high interfacial shear stress, τ_{yz} , is found to exist.

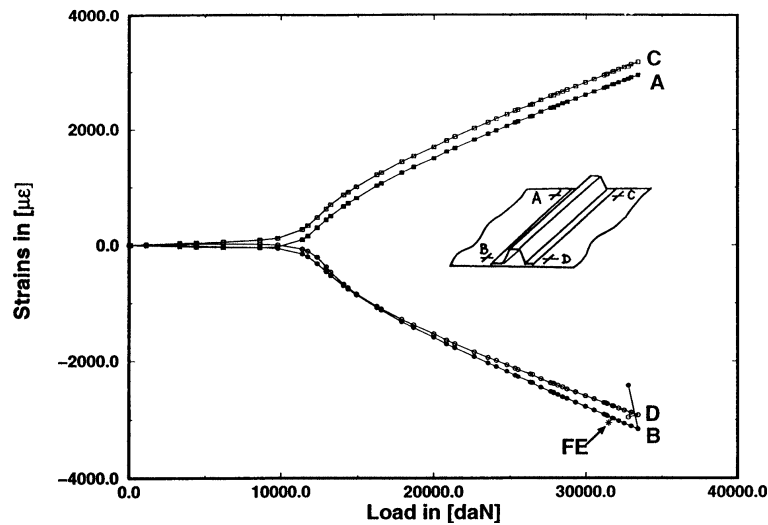


Fig. 13: Shear strains in the skin near the flanges at nodal lines of a Hat panel

When failure of the panel occurred the moment in a stiffener web at a buckle crest was measured to be 159N. Extrapolating from these panel test results it would indicate that the panel would fail due to web bending at a panel load of about 46 tonne – a good agreement with the FE prediction. Fig. 13 also contains a theoretical point, again showing that the postbuckling behaviour is reliably predicted.

(b) *Tapered stiffener flanges*

It was expected that tapering the flanges would move the failure to the buckle crest, since the diffusion stresses would be alleviated at the nodal line. However, for the only panel where initiation could be identified the failure was the same as the case for the untapered flange i.e. a shear debonding opposite a nodal line. The failure load was 43.7 tonne.

CONCLUSIONS

Experiments show that in a stiffened compression panel, failure may be initiated at a nodal line or a buckle crest. This initial crack or delamination leads to stiffener debond and explosive collapse of the panel. However the analytical, a priori, prediction of a failure load would seem to be defeated by the complexity. Not only are there a number of possible failure mechanisms, but the location of crack initiation is not known.

It has been suggested that failure criteria can be established in some simple 2-D component tests which replicate the loading at particular locations in the postbuckled panel. These component tests not only indicate critical values of stress resultants, but also show the locus of the crack. This information is necessary for the complementary energy release calculations of fracture mechanics. These calculations would be done on a local 2-D model.

With an accumulation of evidence from various types of failure initiation it should be possible, either on the basis of component tests or because of design similarity, to identify the location and mode of failure without doing expensive panel tests. An estimation of the failure load can then be made using fracture mechanics, as in Ref. 11. The prediction of a postbuckled failure load for a new panel configuration would seem, at this time, to be very problematic without any guidance from experimental tests.

ACKNOWLEDGEMENTS

The work on the I stiffened panels was done with the support of the EEC Brite Euram Directive. British Aerospace were the project leaders and panel manufacturer.

The research at Imperial College on the other configurations was supported by British Aerospace who, again, supplied the test panels.

REFERENCES

1. Minguet, P.J. and O'Brien, T.K., "Analysis of Composite Skin/Stringer Bend Failure using a Strain Energy Release Rate", *ICCM-10*, Whistler, B.C., Canada, August 1995.
2. Starnes, J.H.Jr., Knight, F.K.Jr. and Rouse M., "Postbuckling Behaviour of Selected Flat Stiffened Graphite Epoxy Panels Loaded in Compression", *AIAA*, Vol. 23, No. 8, 1985, pp. 1236-1246.
3. Knight, F.K.Jr. and Starnes, J.H.Jr., "Postbuckling Behaviour of Selected Curved Stiffened Graphite Epoxy Panels Loaded in Compression", *AIAA*, Vol. 26, No. 3, 1988, pp. 344-352.
4. Romeo, G., "Experimental Investigation on Advanced Composite Stiffened Structures Under Uni-Axial Compression and Bending", *Proceedings AIAA/ASME/ASCE/AHS 26th Structural Dynamics and Materials Conference*, Orlando, Florida, 1985.
5. Bushell, D., Holmes, A.M.C., Flaggo, D.L. and McCornicle, P.J., "Optimum Design, Fabrication and Test of Graphite Epoxy, Curved, Stiffened, Locally Buckled Panels Loaded in Axial Compression", *Buckling of Structures*, Ed. I.Elishakoff et al, Elsevier Science Pub., B.V. Amsterdam, 1988.
6. Lee, S., Elaldi, F., Villaloboo, H. and Scott, R.F., "Experimental and Analytical Study of J Stiffened Composite Panels Loaded in Axial Compression", *ICCM-9*.
7. Wang, J.T.S. and Biggers, S.B., "Skin/Stiffener Interface Stresses in Composite Stiffened Panels", *NASA*, CR 172261, 1984.
8. Cohen, D. and Hyer, M.W., "Influence of Geometric Nonlinearities on Skin-Stiffener Interface Stresses", *AIAA*, Vol. 30, No. 4, April 1992, pp. 1055-1061.
9. Stevens, K.A., Ricci, R. and Davies, G.A.O., "Buckling and Postbuckling of Composite Structures", *Journal of Composites*, Vol. 26, No. 3, 1995, pp. 189-199.

10. Stevens, K.A., Davies, G.A.O. and Ricci, R., "Postbuckling Failure of Composite Compression Panels", *19th ICAS Conference*, ICAS-94-9.8.3, Anaheim, California, 1994, pp. 2975-2981.
11. Martin, R.H., "Local Fracture Mechanics Analysis of Stringer Pull-Off and Delamination in a Postbuckled Panel", *Proceedings ICCM-10*, Whistler, B.C., Canada, 1995.

POSTBUCKLING FAILURE ANALYSIS OF CARBON/EPOXY COMPRESSION PANEL

H. Alesi¹, V. M. Nguyen², R. Jones³, N. Mileskin², D. Kelly⁴

¹Cooperative Research Centre for Aerospace Structures, 506 Lorimer Street, Fishermens Bend, Victoria, 3207, Australia

²RMIT Aerospace, 226 Lorimer Street, Fishermens Bend, Victoria, 3207, Australia

³Mechanical Engineering, Monash University, Wellington Road, Clayton, Victoria, 3168, Australia

⁴UNSW, P.O. Box 1, Kensington, NSW, 2033, Australia

KEYWORDS: airframes, composite structures, stringer/skin panels, postbuckling failure, finite element analysis, global/local procedures, testing

SUMMARY: A finite element methodology that was developed at the Cooperative Research Centre for Aerospace Structures in Australia is applied in the present work for the failure analysis of a postbuckled composite stringer/skin compression panel. Stress analyses are carried out with a global-2D/local-3D finite element model utilising both linear and nonlinear material formulations. Failure analyses on the basis of several phenomenological failure theories lead to failure loads, locations and modes that compare very favourably with results from an experimental test program carried out earlier. Based on the computational results, recommendations for a design improvement of the critical panel region are made. They are consistent with previous empirically derived design changes. The current work suggests that failure initiation in postbuckled composite stringer/skin panels can be effectively modelled with the developed finite element methodology.

NOMENCLATURE

Superscripts, Subscripts and Operators

0	Global coordinate system
e	Effective
x,y,z	Cartesian coordinates
$1,2,3$	Ply coordinates
$\bar{\square}$	Vector or Matrix
$\dot{\square}$	Time derivative

Vectors, Matrices and Tensors

ε_{ij}	Strain tensor
$\dot{\varepsilon}_e^I$	Effective inelastic strain rate vector
$\dot{\varepsilon}_{ij}^I$	Inelastic strain rate tensor
\underline{R}^{**}	Rotation matrix
$\underline{\Omega}_{ij}$	Back stress tensor
S_{ij}	Deviatoric stress tensor
$\sigma_{ij}, \sigma_{ij}^*$	Applied stress tensors

Scalar Values

E, G	Young's modulus and shear modulus
f	Failure index
ε, γ	Direct and indirect strain
K_2, Z	Overstress and drag stress
M, P	Moment and force
N	Shape function or force flow
ν	Poisson's ratio
σ, τ	Direct and indirect stress
x, y, z	Cartesian coordinates
ξ, η, ζ	Intrinsic coordinates
u, v, w	Translational degrees of freedom
$\varphi_x, \varphi_y, \varphi_z$	Rotational degrees of freedom
b, h, l, t, w	Geometric dimensions
A, B, C, P	Node numbers
$A, D_0, n, f_1, f_2, m, Z_0, Z_1, \Omega_s, C_{ij}$	Material parameters
$X_T, X_C, Y_T, Y_C, Z_T, Z_C, S, R, T$	Material allowables

INTRODUCTION

Computational methodologies based on 2D-plate finite element theory were developed in order to support the postbuckling design certification of composite stringer/ skin panels. However, at critical stringer/skin interfaces the accuracy of 2D-plate models is doubtful. Here a structural discretisation based on plate-type elements represents a severe simplification of the real (physical) situation. To overcome the limitations of standard 2D-plate models special purpose 2D and Quasi3D models were developed. These models are computationally more efficient but involve a significant amount of engineering approximation(s) which complicates the interpretation of results. Global-2D/local-3D analysis procedures were suggested as a feasible alternative. Using these procedures the global domain of a structure is modelled with 2D-plate finite elements and a critical local domain is modelled with 3D-solid finite elements.

A postbuckling failure analysis methodology for composite stringer/skin panels based on a global-2D/local-3D approach was developed at the Cooperative Research Centre for Aerospace Structures (CRC-AS) in Australia [1-3]. The methodology was applied in the work that is presented here (in short: the current work) for the failure analysis of a stringer/skin box beam compression panel. The panel investigated failed in experiments through delamination at the stiffener run-outs. Previous finite element simulations [4] concentrated on the analysis of panel deformation and surface strain distribution. The current work aimed to analyse failure load, failure location and failure mode.

TEST SPECIMEN

The composite panel under investigation was fabricated from unidirectional carbon/epoxy CIBA GEIGY/FIB-REDUX 914-TS-5-34 tape that contained T300 high tensile TORAYACA carbon fibres. The panel consisted of a quasi-isotropic skin and blade-type stiffeners that were equally spaced across the working section. A total of five panels were manually layed up and cured in an autoclave using hard tools. The overall panel was made larger than the actual working section to allow panel attachment to a box beam test fixture. The stiffener ends were trimmed back to avoid interference with the test rig. A description of the panel geometry is given in Figure 1.

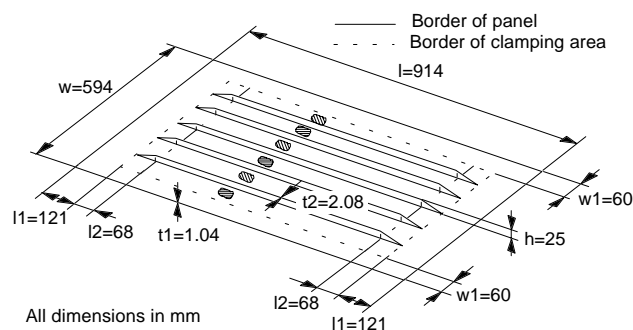


Figure 1 Test panel geometry

Skin regions between the stiffeners were made from eight plies and the stiffeners were made from sixteen plies of unidirectional tape. A symmetric stiffener lay-up was employed. This resulted in a skin lay-up that alternated between being symmetric in some skin bays and unsymmetric in other skin bays, Figure 2 refers. The top three skin plies wrapped from the skin on to the stiffener in order to make the stiffener form a more integral part of the skin.

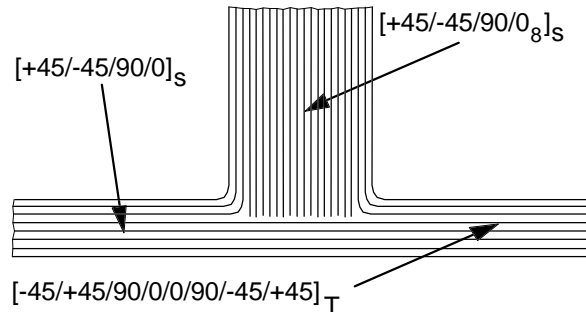


Figure 2 Schematic of ply stacking sequence

APPARATUS AND TEST

Five stringer/skin panels were structurally tested utilising a four point box beam test rig. The test rig consisted of a three bay aluminium box beam, a supporting steel frame and two 20,000 lb load jacks operated in load control. The jack loads induced a constant bending moment into the middle bay where the test panel was located, Figure 3 refers. The test panel was loaded by a distributed force, N , that acted in the plane of the box beam covers.

The middle bay of the box beam contained a detachable skin which allowed for different test panels to be mounted via a mechanical fastening system.

FINITE ELEMENT MODEL

A global 2D-plate finite element model of the compression panel, previously developed in [4], formed the basis for the current investigation. The loading and support conditions for the physically existing panel were translated into the finite element boundary conditions presented in Figure 4.

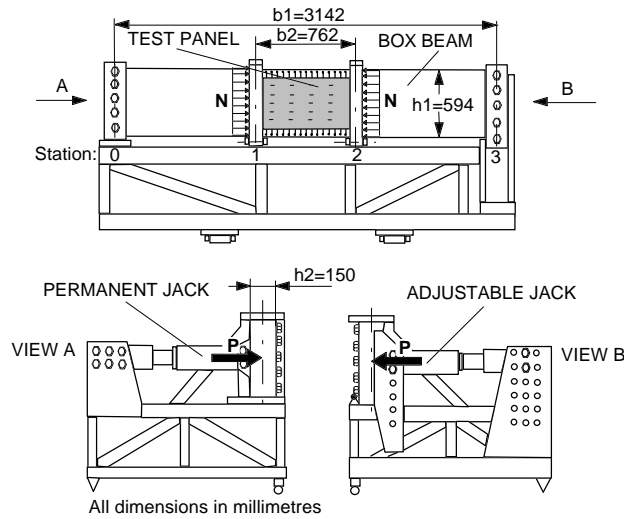


Figure 3 Box beam test rig

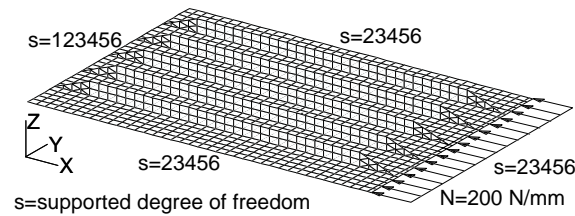


Figure 4 Global 2D finite element model

A local 3D-solid finite element model was developed for the current investigation that represented a critical panel region at the central stiffener run-out, Figure 5 refers. Individual plies were therein modelled with separate layers of hexagonal solid elements. Pentagonal solid elements were employed when necessary in order to generate an overall rectangular solid mesh.

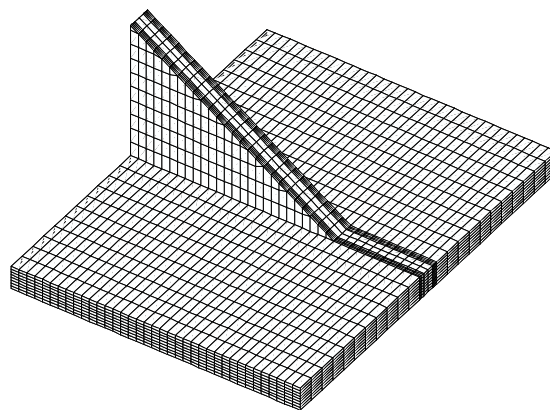


Figure 5 Local 3D finite element model

Each solid element on it's own represented a discrete amount of composite material with constant fibre orientation.

The global 2D model and the local 3D model were connected with the coupling technique presented in [1]. The fundamental equations for the coupling technique were originally developed for the general interface node arrangement shown in Figure 6.

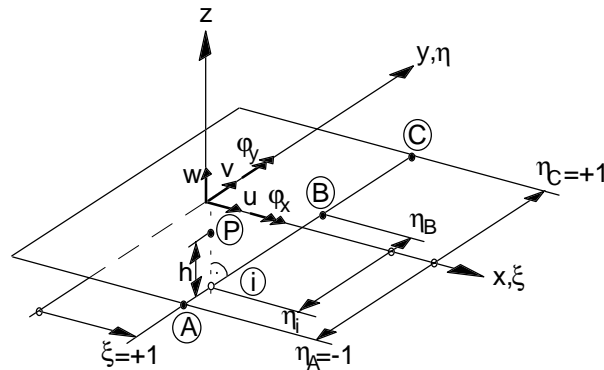


Figure 6 General interface node arrangement

Plate nodes (A),(B) and (C) are situated on the edge of a plate element that is adjacent to a solid element region. Point (i) is situated on the intersection between the line that connects (A) and (C) and the line through solid element node (P) that is orthonormal to line (A)-(C). The displacements of point (i) can be related to the displacements of nodes (A),(B) and (C) by employing the following plate shape functions given by Schaeffer [5]:

$$\begin{aligned}
 N_A &= -0.25(1 + \xi_i \xi_A)(1 + \eta_i \eta_A)(1 - \xi_i \xi_A - \eta_i \eta_A) \\
 N_B &= +0.50(1 + \xi_i \xi_B)(1 - \eta_i^2) \\
 N_C &= -0.25(1 + \xi_i \xi_C)(1 + \eta_i \eta_C)(1 - \xi_i \xi_C - \eta_i \eta_C)
 \end{aligned} \tag{1}$$

The relation between nodal point displacements at plate nodes (A),(B),(C) and displacements at point (i) is as follows:

$$\begin{aligned}
 u_i &= N_A \cdot u_A + N_B \cdot u_B + N_C \cdot u_C \\
 v_i &= N_A \cdot v_A + N_B \cdot v_B + N_C \cdot v_C \\
 w_i &= N_A \cdot w_A + N_B \cdot w_B + N_C \cdot w_C \\
 \varphi_{xi} &= N_A \cdot \varphi_{xA} + N_B \cdot \varphi_{xB} + N_C \cdot \varphi_{xC} \\
 \varphi_{yi} &= N_A \cdot \varphi_{yA} + N_B \cdot \varphi_{yB} + N_C \cdot \varphi_{yC}
 \end{aligned} \tag{2}$$

The kinematic relation between solid node (P) and point (i) can be defined by applying the assumptions of Kirchhoff [6] plate theory. The displacements of node (P) are herewith expressed in terms of the displacements and rotations of point (i), viz:

$$\begin{aligned}
 u_P &= u_i + h \cdot \varphi_{yi} \\
 v_P &= v_i - h \cdot \varphi_{xi} \\
 w_P &= w_i
 \end{aligned} \tag{3}$$

Substitution of Eqs. (2) into Eqs. (3) relates degrees of freedom on solid element node (P) with degrees of freedom on plate element nodes (A), (B) and (C), viz:

$$\begin{aligned}
 \begin{Bmatrix} u_P \\ v_P \\ w_P \end{Bmatrix} &= N_A \cdot \begin{Bmatrix} u_A \\ v_A \\ w_A \end{Bmatrix} + N_B \cdot \begin{Bmatrix} u_B \\ v_B \\ w_B \end{Bmatrix} + N_C \cdot \begin{Bmatrix} u_C \\ v_C \\ w_C \end{Bmatrix} \\
 &+ N_A \cdot h \cdot \begin{Bmatrix} \varphi_{yA} \\ -\varphi_{xA} \\ 0 \end{Bmatrix} + N_B \cdot h \cdot \begin{Bmatrix} \varphi_{yB} \\ -\varphi_{xB} \\ 0 \end{Bmatrix} + N_C \cdot h \cdot \begin{Bmatrix} \varphi_{yC} \\ -\varphi_{xC} \\ 0 \end{Bmatrix}
 \end{aligned} \tag{4}$$

Thus far the equation development was carried out with reference to a plate element coordinate system. The previous equations can not be used in a general context where element coordinate systems and global coordinate system often not coincide. To eliminate this restriction Eq. (4) was formulated in global coordinates by employing the rotation matrix \underline{R}^{**} :

$$\begin{aligned}
 \begin{Bmatrix} u_P^0 \\ v_P^0 \\ w_P^0 \end{Bmatrix} &= N_A \cdot \begin{Bmatrix} u_A^0 \\ v_A^0 \\ w_A^0 \end{Bmatrix} + N_B \cdot \begin{Bmatrix} u_B^0 \\ v_B^0 \\ w_B^0 \end{Bmatrix} + N_C \cdot \begin{Bmatrix} u_C^0 \\ v_C^0 \\ w_C^0 \end{Bmatrix} \\
 &+ N_A \cdot h \cdot \underline{R}^{**} \cdot \begin{Bmatrix} \varphi_{xA}^0 \\ \varphi_{yA}^0 \\ \varphi_{zA}^0 \end{Bmatrix} + N_B \cdot h \cdot \underline{R}^{**} \cdot \begin{Bmatrix} \varphi_{xB}^0 \\ \varphi_{yB}^0 \\ \varphi_{zB}^0 \end{Bmatrix} + N_C \cdot h \cdot \underline{R}^{**} \cdot \begin{Bmatrix} \varphi_{xC}^0 \\ \varphi_{yC}^0 \\ \varphi_{zC}^0 \end{Bmatrix}
 \end{aligned} \tag{5}$$

The previous mathematical approach formed the basis for a generic coupling program which can be used as a pre-processor for a variety of finite element codes, viz: MSC/NASTRAN [7], ABAQUS [8], etc. The coupling program reads a basic data input file and automatically identifies solid element nodes that are situated within a plate/solid interface control volume. The program generates, based on the physical location of plate nodes (A), (B) and (C), the appropriate multi-point-constraint (MPC) statements for solid element nodes that are found within the control volume. The multi point constraint statements are automatically added, in the required format, to the basic data input file of the employed finite element program. This modified data file can then be processed in a normal fashion without solver modifications being required.

Employing this program the global-2D and local-3D models of the box beam compression panel were connected. The coupling program required eight-noded plate-bending elements in order to work. They were simulated by substituting three triangular elements for each four-noded element found at the plate-solid interface, Figure 7 refers.

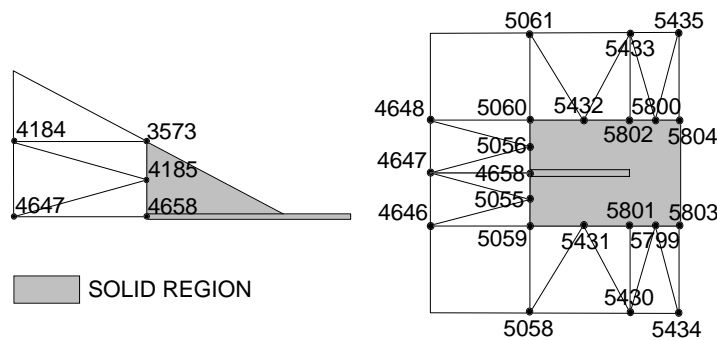


Figure 7 Interface nodes on stiffener and skin

MATERIAL MODEL

Aircraft structures that are made from fibre reinforced composite materials are generally designed such that the fibres carry the bulk of the applied load. The associated in-plane material behaviour is termed fibre-dominated. In a classical composite design a strain limit of around 0.4 % is applied to prevent breakage of the brittle fibres. Within this strain limit the material behaves essentially linear-elastically and the material behaviour can be mathematically expressed with nine elastic constants, Table 1 refers.

Table 1 Material constants for T300/914C [9]

E_{11}	E_{22}	E_{33}
131.90 GPa	9.51 GPa	9.43 GPa
G_{12}	G_{13}	G_{23}
5.27 GPa	7.03 GPa	3.39 GPa
ν_{12}	ν_{13}	ν_{23}
0.326	0.341	0.485

Composite fibres carry far less load in situations where a force flow exists through the thickness of the material, i.e. at free edges, lap-joints or at skin-stiffener interfaces. The associated interlaminar material behaviour is termed matrix-dominated and requires a nonlinear material description for representing the viscoplastic material behaviour of polymeric matrix material, see Mills [10].

A theory by Ramaswamy & Stouffer [11] was employed in the current work to model matrix behaviour. The theory consists of three equations. The first equation represents the constitutive relation between the inelastic strain rate $\dot{\epsilon}_{ij}^I$, the Deviatoric stress S_{ij} , the ‘back stress’ Ω_{ij} , the ‘drag stress’ Z and the effective value of the ‘overstress’ K_2 :

$$\dot{\epsilon}_{ij}^I = D_0 \cdot \exp \left[-\frac{A}{2} \cdot \left(\frac{Z^2}{3 \cdot K_2} \right)^n \right] \cdot \frac{(S_{ij} - \Omega_{ij})}{\sqrt{K_2}} \quad (6)$$

The second equation models the development of the ‘back stress’ - the ‘back stress’ being the level to which an applied stress relaxes during a prolonged strain hold.

$$\dot{\Omega}_{ij} = \frac{2}{3} \cdot f_1 \cdot \dot{\epsilon}_{ij}^I - f_1 \cdot \frac{\Omega_{ij}}{\Omega_s} \cdot \dot{\epsilon}_e^I + f_2 \cdot \dot{S}_{ij} \quad (7)$$

The third equation models work hardening. This is done by introducing a ‘drag stress’ that depends on the amount of accumulated inelastic work, viz:

$$\dot{Z} = m \cdot (Z_1 - Z) \cdot S_{ij} \cdot \dot{\epsilon}_{ij}^I \quad , \quad Z_{(0)} = Z_0 \quad (8)$$

An additional equation was added by the authors to account for materials with non-zero post yield slope, viz:

$$\sigma_{ij}^* = \sigma_{ij} + C_{ij} \cdot \left(\varepsilon_{ij} - \frac{\sigma_{ij}}{G_{ij}} \right) \quad (9)$$

In this equation, C_{ij} represents the post-yield slope parameters and G_{ij} represents the elastic shear moduli of the material.

The material model is adapted to individual materials by specification of material model parameters: $A, D_0, n, f_1, f_2, m, Z_0, Z_1, \Omega_s$ and C_{ij} . The material model parameters for T300/ 914C were identified with an optimisation procedure [12] that gradually reduced the error between the simulated material response and the experimentally measured material behaviour. The recovered material model parameters are presented in Table 2.

Table 2 Material parameters for T300/914C

A	D_0	n	f_1	f_2
1	5e9 1/s	0.237	2.4e4 MPa	0
m	Z_0	Z_1	Ω_s	C_4
0	2.9e5 MPa	2.9e5 MPa	65 MPa	310 MPa

The previous mathematical description formed the basis for a material user routine for the program ABAQUS that is called during element stiffness updates.

The following assumptions were made to simplify the FEM implementation of the material model:

1. Only the matrix dominated stress terms $\sigma_{22}, \sigma_{33}, \tau_{12}, \tau_{13}$ and τ_{23} contribute to viscoplastic material behaviour;
2. In a first order approximation the direct stresses σ_{22} and σ_{33} are assumed to be linear functions of the direct strains ε_{22} and ε_{33} , (see Jones [13]);
3. The nonlinear shear behaviour is similar in the three material planes, (see Alesi et al [12] and Nguyen [14]).

The previous assumptions lead to a constitutive model that contains a linear-elastic/orthotropic representation for the direct stress components and a nonlinear-inelastic/iso-tropic representation for the indirect stress components. The composite material model was implemented by adding the current material model to an existing ABAQUS user subroutine developed by Trippit et al [15].

Several material simulations were carried out in order to validate the material model for strain rates that cover five orders of magnitude - ranging from quasistatic loading to shock-type loading. The finite element results for a single solid element model are compared in Figure 8 with the experimental stress-strain curves.

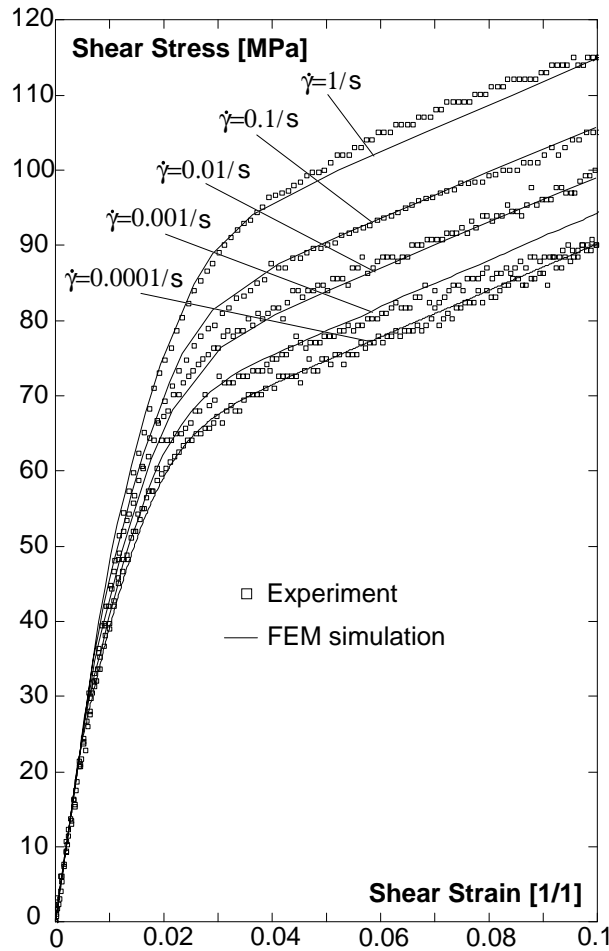


Figure 8 Material shear response

STRESS ANALYSIS

Geometric nonlinear finite element analyses were carried out in the current work with both linear and nonlinear material models. Initial imperfections consistent with the first buckling mode were generated by small lateral forces in order to bias the nonlinear solution to follow the experimentally observed load path.

In the linear material analysis with NASTRAN an exponential increase of stress for at least four stress components was observable in the vicinity of the stiffener tip. This pointed towards a stress singularity. This interpretation was verified by carrying out numerical convergence tests with different stiffener tip mesh sizes. Here it was found that some tip stress components increased dramatically when reducing mesh size. The problem was overcome in a material nonlinear analysis with ABAQUS. In this simulation the material plastified and load was shed to less stressed areas. Employing a nonlinear material model resulted in an overall less 'spiky' stress distribution and a converged stress solution. Figures 9-11 contain interlaminar stress results for one of the 90-degree skin/stiffener plies at the stiffener run-out.

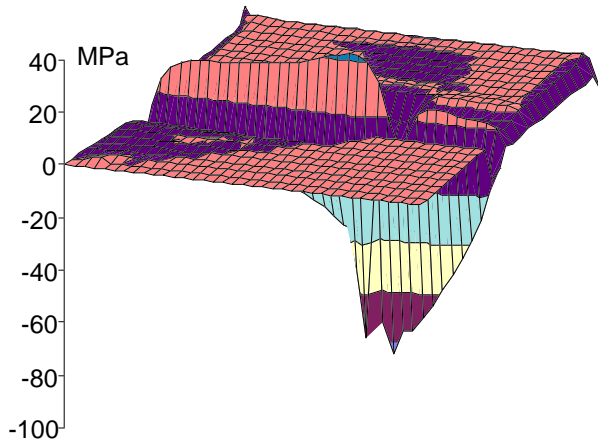


Figure 9 Interlaminar peel stress σ_{33}

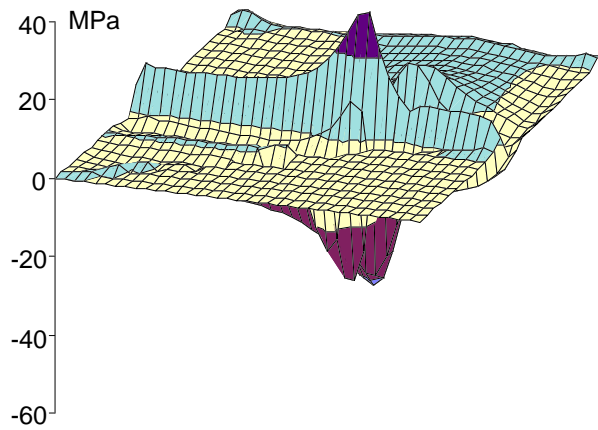


Figure 10 Interlaminar shear stress τ_2

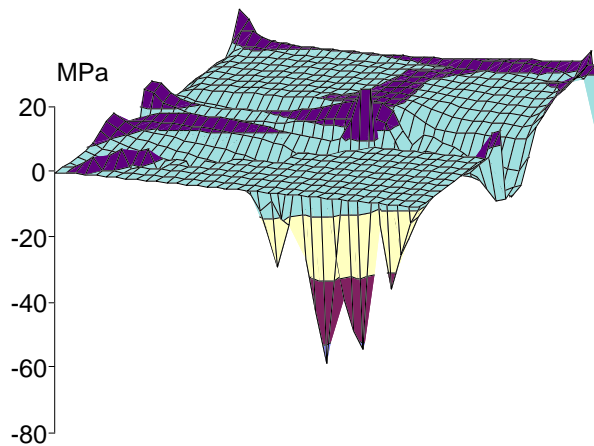


Figure 11 Interlaminar shear stress τ_{31}

FAILURE ANALYSIS

Several more commonly used three-dimensional composite failure theories [16-21] were employed for a prediction of stiffener run-out failure. The associated material strength allowables for T300/914C are presented in Table 3.

The stress results from a geometric and material nonlinear finite element analysis of the global-2D/local-3D model were employed for calculating failure indices for individual solid elements. The failure indices were then used to determine the actual failure load. For a comparison between the computational and experimental failure loads refer to Table 4.

Table 3 Material allowables for T300/914C [9] [MPa]

Material allowable	Symbol	Value
Tensile strength in fibre direction	X_T	1328.0
Compression strength in fibre direction	X_C	1064.0
In-plane transverse tensile strength	Y_T	70.9
In-plane transverse compression strength	Y_C	221.0
Interlaminar peel strength	Z_T	97.6
Interlaminar compression strength	Z_C	242.0
In-plane shear strength	S_{12}	71.2
Interlaminar 1-3 shear strength	R_{13}	94.5
Interlaminar 2-3 shear strength	T_{23}	52.9

Table 4 Comparison of failure loads [N/mm]

Failure Theory	* P_{limit}	** P_{limit}	*** P_{limit} (Test Panel)
1. Max. Stress	106.85	153.74	204.00 (BP01)
2. Hill	75.16	127.94	184.00 (BP03)
3. Hoffman	91.22	178.49	211.00 (BP06)
4. Tsai-Wu	84.26	150.79	187.00 (BP06B)
5. Hashin	75.84	157.98	158.00 (BP10)
6. Quad. Stress	101.49	158.08	
Average values	89.13	154.50	188.80

*FEM Linear Material, **FEM Nonlinear Material, ***Experiment

Four segments of solid elements within the stiffener tip region are displayed in Figure 12. The dark areas represent finite elements with a failure index of greater than one.

From the previous graph it can be seen that at design load, $N=200$ N/mm, critical stress levels occurred only within a very small structural domain in the vicinity of the stiffener run-out tip. Critical stress levels were found in solid elements within the stiffener and the skin in 0-degree plies and also in some solid elements within the 90-degree stiffener plies. This result is consistent with a c-scan image that was taken after the panels had failed experimentally, Figure 13 refers. Here it can be seen that delamination mainly occurred around the stiffener run-outs. The delaminations in the most left skin bay were formed during final panel collapse.

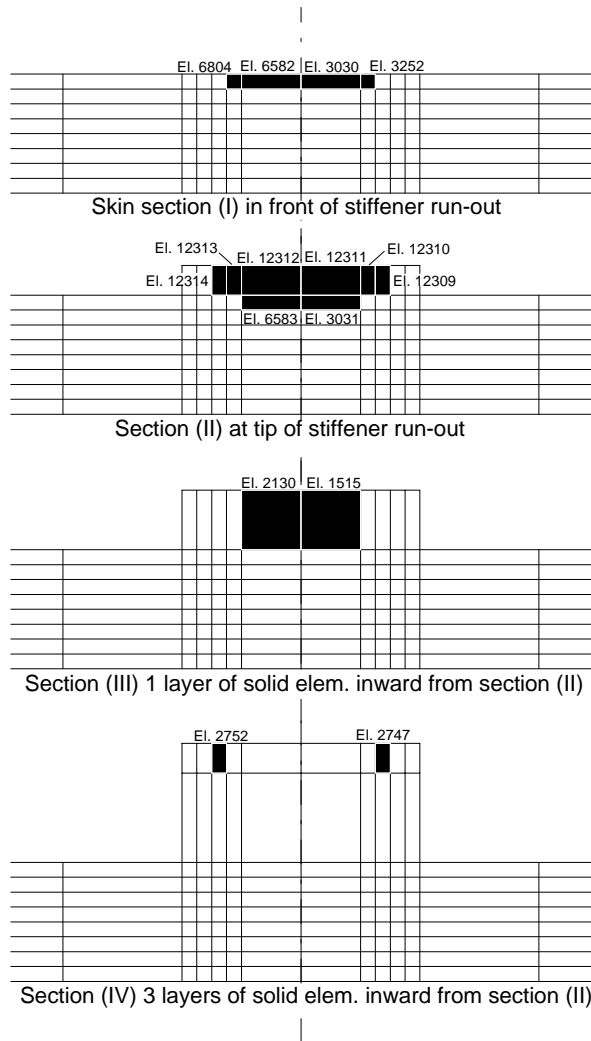


Figure 12 Computational failure locations



Figure 13 C-scan of stiffener run-out area

Table 5 Critical element stresses [MPa]

Elem.	σ_{11}	σ_{22}	σ_{33}	σ_{12}	σ_{13}	σ_{23}	f*
3030	-1376	-15	-74	55	9	-2	1.8
3252	-1384	-40	-86	44	33	13	1.7
6582	-1375	-15	-74	56	-8	2	1.8
6804	-1382	-40	-85	45	-33	-13	1.7
3031	-891	-15	-62	66	10	-4	1.2
6583	-891	-15	-62	66	-9	4	1.2
1515	-313	-12	-37	81	9	-10	1.2
2130	-313	-12	-37	81	-9	10	1.2
12310	-817	-31	-60	82	32	-6	1.6
12311	-709	-18	-58	90	6	-7	1.7
12312	-709	-18	-58	90	-5	7	1.7
12313	-818	-32	-60	82	-32	6	1.6
2747	57	-26	-13	-15	-25	-65	1.3
2752	54	-26	-13	-15	25	65	1.3
12309	84	-82	-76	-42	-26	-62	1.2
12314	84	-82	-76	-42	26	62	1.2

*f=Failure Index

Inspection of the stress components shows that three different failure mechanisms were active at the stiffener run-out, viz: Zero-degree plies under the stiffener, i.e. element 3030-6804, failed in a pure in-plane compression mode and combined compression and shear mode (elements 3031 & 6583). Zero-degree plies within the stiffener, i.e. element 1515-12313, failed due to in-plane (the term ‘interlaminar’ is equally valid at this model location) shear failure. Ninety-degree plies within the stiffener, i.e. element 2747-12314, failed due to interlaminar shear failure.

The information contained in Table 5 allowed the following failure interpretation: The loading mechanism and overall panel response in combination with a relatively small skin bending stiffness resulted in strong skin bending deformations at the stiffener run-out. This resulted in high compression stress being induced in the upper zero-degree plies at the stringer/skin transition. Loading through the skin essentially generated a lap joint problem at the stiffener run-out where compressive skin load had to be transferred via shear into the zero-degree stringer plies. One part of this load was transferred through in-plane shear within the zero-degree skin/stringer transition plies another part via interlaminar shear within the 90-degree stiffener plies into the assembly of zero-degree stringer plies.

Figure 14 contains a photo of the three inner blade stiffeners. Post-failure inspection of the area showed that the stiffener run-out separated from the skin. The stiffener run-out also split at the interface between the ‘block’ of zero-degree stringer plies and the top three stringer/skin cover plies. Both of these experimentally observed failure mechanisms are consistent with the computationally predicted failure modes.

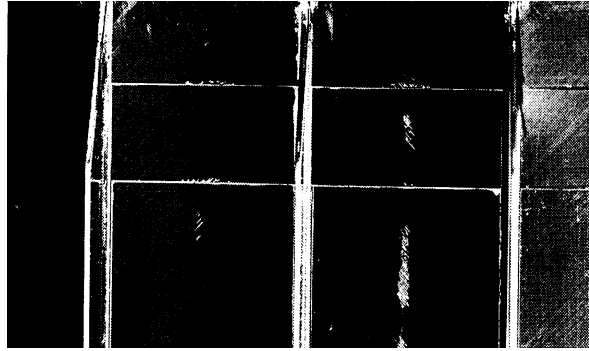


Figure 14 Delamination at stiffener run-outs

CONCLUSIONS

A global-2D/local-3D finite element methodology previously developed at the CRC-AS was employed in the current work for failure analysis of a postbuckled composite stringer/ skin panel. An existing global 2D-plate finite element model of the complete panel was employed in combination with a local 3D-solid finite element model of a critical stiffener region. The global and the local model were kinematically coupled to form a combined global-2D/local-3D finite element model of the panel. Herewith geometric and material nonlinear finite element analyses were carried out. Critical stresses were computed for a region at the tip of the stiffener run-out. The stress state in individual plies was of complex three-dimensional nature. This justified the modelling detail employed in the development of the local 3D model. It is believed that with a plate-type finite element discretisation of the stiffener run-out it would not have been possible to capture the local structural response at the run-out tip.

The three-dimensional stress-strain response of the composite material that was used for the manufacture of the investigated panels was determined in an experimental test program. The material showed strong viscoplastic shear behaviour including nonlinear stress-strain curves and other phenomena such as rate sensitivity, stress relaxation and creep. A viscoplastic material theory was employed for the mathematical representation of this material behaviour.

A linear material analysis of the box beam compression panel produced stress results that were singular at the critical panel region. A material nonlinear analysis based on the developed viscoplastic material model produced physically meaningful stress values that could be employed for a quantitative prediction of failure initiation.

The predicted failure loads for the investigated load case were very close to the ones observed in the experiments, Figure 15 refers. In fact both the computational results for buckling load and failure initiation represent conservative estimates of the experimentally observed values. These findings suggest that failure initiation in postbuckled composite structures can be effectively modelled with the developed global-2D/local-3D finite element methodology.

Stress components and failure indices for solid elements that were identified as being critical are presented in Table 5.

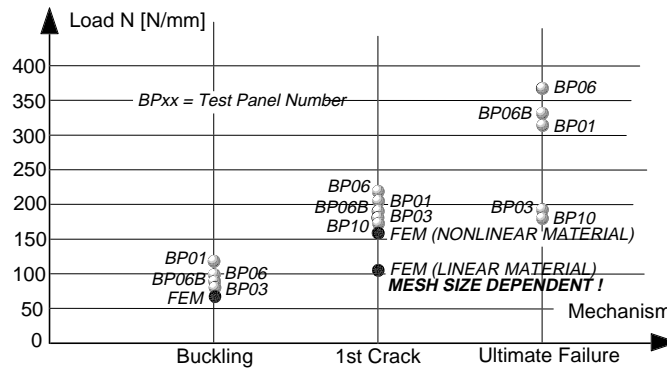


Figure 15 Summary of results

The failure analyses further pinpointed at which plies and through which failure mechanism failure occurred. The computational results for failure location and failure mode compared thereby qualitatively very favourably with the experiments. Previous empirical design improvements of the investigated panels were based on a close inspection of experimental results. Premature failure of the stiffener run-out was there overcome by reinforcement of the panel skin and by subdivision of the zero degree stringer sublaminates. The first measure reduced local skin curvature. The second measure increased the effective shear area, resulting in a more effective load transfer between skin and stringer. The computational results from the present work support both of these changes.

The positive findings from the current work indicate that the developed nonlinear global-2D/local-3D finite element procedure can be employed as part of a general postbuckling composite design methodology.

REFERENCES

1. Alesi, H., Jones, R., Mileskin, N., A technique for coupling plate and solid elements, Proc. Comp. Mech. 95, Vol. 1, Eds. S. N. Atluri, G. Yagawa, T. A. Cruise, Springer Verlag, ISBN 3-540-59114-1, pp 702-707, 1995.
2. JONES, R., ALESI, H., CHIU, W. K., GALEA, S., A preliminary study into the matrix dominated non-linear behaviour of graphite/epoxy laminates, Composite Structures Vol. 30, pp 193-199, 1995.
3. Alesi, H., Thomson R. S., Diegelmann, G., Jones, R., Experimental and computational skin/stiffener analysis of a postbuckled graphite/epoxy shear panel, Proc. First Australasian Congress on Applied Mechanics, The Institution of Engineers Australia Preprints of Papers, pp 273-278, Melbourne, 1996.
4. Trentin, C., Scott, M. L., Alesi, H., Postbuckling behaviour of blade-stiffened fibre composite panels, Proceedings 9th International Conference on Composite Materials, pp. 511-518, Madrid, 1993.
5. Schaeffer, H. G., MSC/NASTRAN Primer Static and Normal Modes Analysis, Wallace Press, pp 143-145, Milford New Hampshire, 1988.
6. Kirchhoff, G. R., Ueber das Gleichgewicht und die Bewegung einer elastischen Scheibe, Journal fuer reine angewandte Mathematik, Vol. 40, pp 51-88, 1850.

7. MSC/NASTRAN Version 66A User Manual Vol. I & II, Editor M. A. Reymond, The MacNeal-Schwendler Corporation, Los Angeles, 1989.
8. ABAQUS Version 5.3 User Manual, Vol. I & II, Hibbitt, Karlsson & Sorensen Inc., Pawtucket, 1993.
9. Benzeggagh, M. L., Khellil, K., Chotard, T., Experimental determination of Tsai failure tensorial terms F_{ij} for unidirectional composite materials, *Composites Science and Technology* 55, Elsevier Science Ltd., pp 145-156, Northern Ireland, 1995.
10. Mills, N. J., *Plastics: Microstructure, Properties and Applications*, Metallurgy and Materials Science Series, Eds. R. W. K. Honeycombe & P. Hancock, Edward Arnold Ltd, pp 153-173, London, 1986.
11. Ramaswamy, V. G., Stouffer, D. C., Laflen, J. H., A constitutive model for the in-elastic multi-axial response of René 80 at 871C and 982C, *Journal of Engineering and Materials Technology*, ASME, 112, pp 281-286, 1990.
12. Alesi, H., Postbuckling analysis of 3D composite structures, Dissertation submitted for examination, Royal Melbourne Institute of Technology, pp 121-153, Melbourne, 1996.
13. Jones, R. M., *Mechanics of composite materials*, McGraw-Hill, pp 339-342, New York, 1975.
14. Nguyen, V. M., Prediction of interlaminar failure in selected Graphite-Epoxy laminates, MEng Thesis, Royal Melbourne Institute of Technology, To be published, 1997.
15. Trippit, B. J., Jones, R., Recent Australian developments in the engineering applications of constitutive modelling, AMD-Vol. 213/MID-Vol.63, *Numerical Implementation and Application of Constitutive Models in the Finite Element Method*, ASME, pp 14-20, New York, 1995.
16. Zocher M. A., Allen D. H., Evaluation of first ply failure in a three dimensional loadspace, *Journal of composite materials*, Vol. 29, No.12, pp 1649-1665, 1995.
17. Hill R., *The mathematical theory of plasticity*, Clarendon Press, Oxford, 1950.
18. Hoffman O., The brittle strength of orthotropic materials, *Journal of composite materials*, Vol. 1, pp 200-206, 1967.
19. Tsai S., Wu E., A general theory of strength for anisotropic materials, *Journal of composite materials*, Vol. 5, pp 58-78, 1971.
20. Hashin Z., A failure criteria for unidirectional fiber composites, *Journal of applied mechanics*, Vol. 47, pp 329-334, 1980.
21. Brewer J., Lagace P., Quadratic stress criterion for initiation of delamination, *Journal of composite materials*, Vol. 22, pp 114-1153, 1988.

FIBER ARCHITECTURE BASED DESIGN OF DUCTILE COMPOSITE REBAR FOR CONCRETE STRUCTURES

Frank K. Ko¹, Win Somboonsong² and Harry G. Harris²

¹ Department of Materials Engineering, Drexel University, Philadelphia, PA 19104, USA

² Department of Civil & Architectural Engineering, Drexel University, Philadelphia, PA 19104, USA

SUMMARY: Fiber Reinforced Plastic (FRP) has been identified as an attractive candidate material for civil infrastructure applications because of its light weight, high strength, non-corrosive and non-magnetic characteristics. In spite of these attractive features, the adaptation of FRP to civil infrastructure applications has been slow especially in concrete reinforcements. This can be attributed to the lack of ductility of the state-of-the-art FRPs which have linear elastic tensile stress-strain behavior up to ultimate load and they fail in a brittle mode. Thus the flexural response of these FRP bars in reinforced concrete beams and slabs exhibit little ductility and therefore makes it impossible to design such members based on ultimate strength principles. There is a need for a FRP rebar system which has a steel-like stress-strain behavior. The aim of this paper is to demonstrate a design concept for a ductile composite rebar utilizing low cost textile preforming technology supported by an integrated fiber architecture based designing methodology.

KEYWORDS: braid fiber architecture, FRP, hybrid, ductile, ribs, reinforced concrete, structural hierarchy, braiding, pultrusion

INTRODUCTION

Structural repair of deteriorated reinforced concrete (R/C) and pre-stressed (P/C) concrete structures is rapidly becoming a more economical option for constructed facilities in the United States. Corrosion of steel reinforcement, which is a primary factor in reduced durability of concrete structures especially in the more severe climates where deicing compounds are used, has prompted the need to seek steel substitutes. In general FRP systems, which usually consist of glass, aramid, or carbon fibers in a polymer matrix, have high strength, low modulus of elasticity and very low ultimate tensile strains as compared to steel as illustrated in Fig. 1. showing the brittle failure behavior of typical GFRP, AFRP, and CFRP systems. The lack of ductility is undesirable for civil engineering structures. As a result it precludes our exploitation of the advantages such as low weight, corrosion resistance, and non-magnetic properties provided by the FRP reinforcement in new and repaired concrete structures.

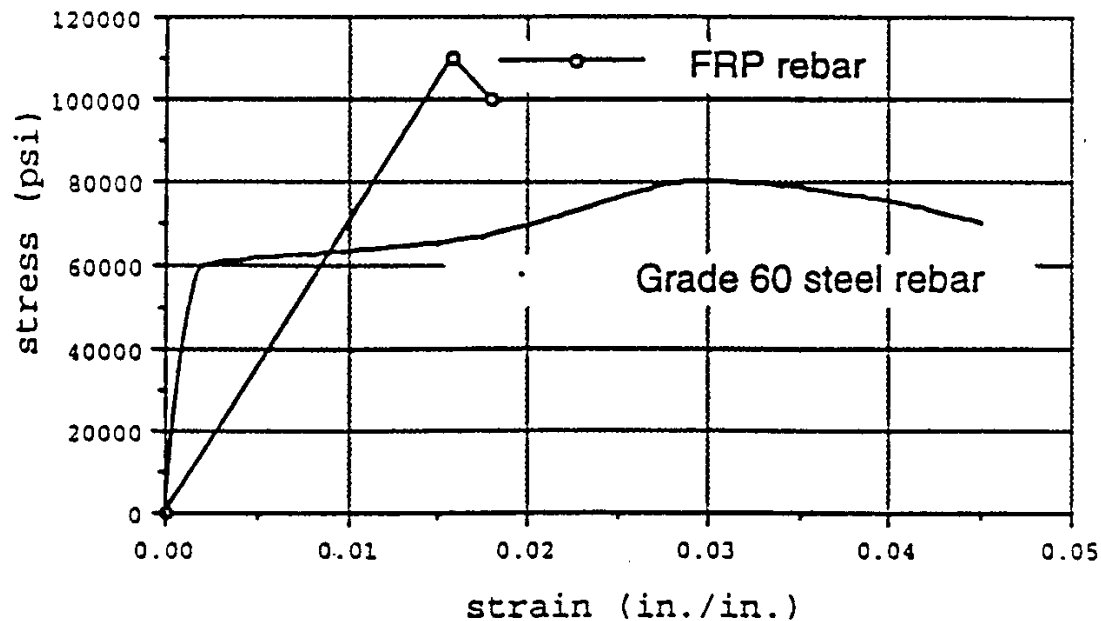


Fig. 1 Comparison of Stress-Strain Properties of FRP Bars with Steel

There is a need for a low cost composite system which has a sufficient level of stiffness and can fail in a ductile or "pseudo-ductile" manner. To facilitate the adaptation of the new design concept and material systems to infrastructure applications, it would be desirable to establish an engineering design base which takes material processing parameters and civil engineering parameters into consideration. It is desirable to develop a composite rebar system which has stress-strain behavior similar to that of the steel reinforcement (Fig. 1).

DESIGN CONCEPT

Taking advantage of the design flexibility and the wide availability of manufacturing capacity in the industry, braided structures will be employed as the primary fiber architecture for the construction of the proposed hybrid FRP rebar system. The technology of braiding, as detailed by Ko [3,4] is a well established technology which intertwines three or more strands of yarns to form a tubular structure with various combinations of linear or twisted core materials. By judicious selection of fiber materials and fiber architecture for the braid sleeve and the core structure, the load-deformation behavior of the braided fibrous assembly can be tailored. As illustrated in Fig. 2, the sleeve structure may be a tough aramid (e.g. Kevlar) fibrous structure whereas the core structure would be high modulus carbon fibers to provide the initial resistance to deformation. The rib effect, as commonly incorporated in steel rebar to increase bond strength between the rebar and concrete, can also be introduced to the sleeve structure during the braiding process. By proper combination of the braided fibrous assembly with a protective resin matrix system to form a composite material system, the stress transfer from the rebar structure to the fibers can be controlled. The end product of this hybridization of material systems and fiber architecture is a composite rebar which has high initial resistance to tensile deformation followed by a graceful failure process manifested by a gradual reduction in the slope of the stress strain curve before reaching a high level of ultimate strain as shown in Fig. 3. Note from Fig. 3 the high initial modulus obtained for the newly developed 5 mm. hybrid FRP bar which has essentially bi-linear stress-strain characteristics. A reduction in the stress fluctuations shown in Fig. 3 will be achieved by modifications to the braid architecture.

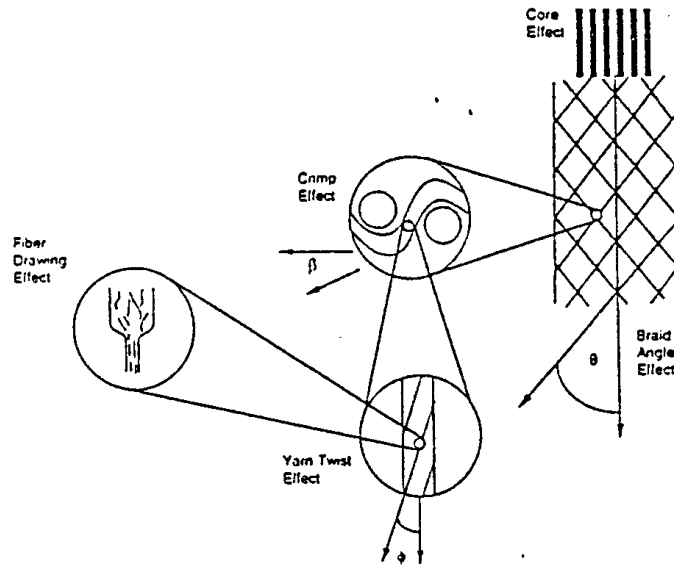


Fig. 2 Structural Hierarchy of the Braided Rebar

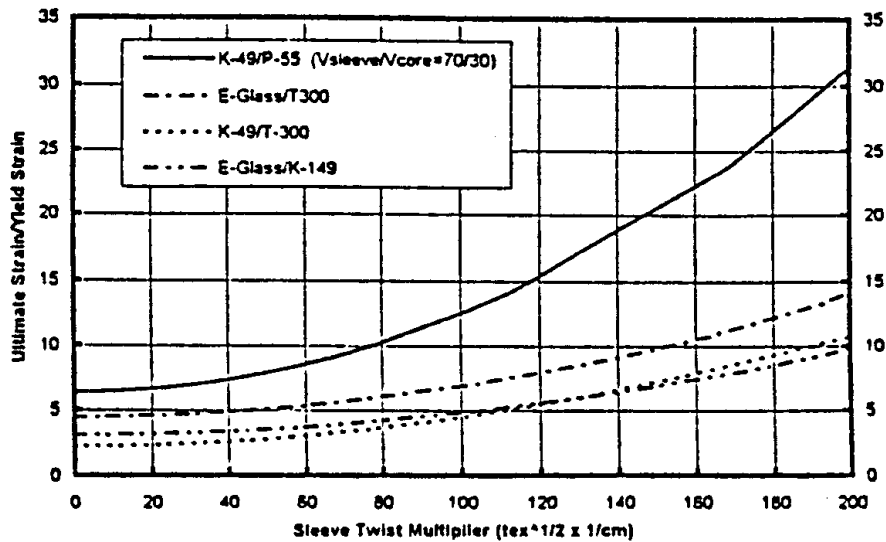


Fig. 3 Stress-Strain Characteristics of Braided Composites.

FIBER ARCHITECTURE BASED DESIGN

The Fabric Geometry Model

The development of the composite rebar system is based on an understanding of the structural hierarchy of the braided reinforcement assembly established at Drexel University over the past decade. This fundamental understanding revealed that the translation of the fiber material properties and effect of braiding process parameters can be related to the mechanistic response of the composite rebar system through the geometric relationships between the various structural levels. The result is a Fabric Geometry Model (FGM) developed by Ko et al

[5] for braided composite systems linking fiber and matrix properties, fiber architecture and processing parameters to the engineering material coefficients required for finite element stress analysis. Based on a modified laminate theory, the FGM quantifies the fiber architecture of the braided structure in terms of a unit cell. A stiffness matrix for each yarn system, $[C_i]$, is then obtained by transforming the stiffness matrix for a comparable unidirectional composite rod, $[C]$, through the following equation:

$$[C_i] = [T_{\Sigma,i}]^T [C] [T_{\Sigma,i}] \tag{1}$$

where $[T_{\Sigma,i}]$ is a transformation matrix containing the directional cosine of each component yarn system. The total stiffness matrix for the braided composite structure can be obtained by the volume averaging of $[C_i]$. Through a piecewise linear approximation, the nonlinear stress-strain relationship resulting from matrix material, interfacial debonding and fiber distortion can be accounted for by an incremental strain analysis. Failure prediction can be accomplished finally by invoking the maximum strain energy criterion.

Hybrid Effect

The combination of different types of fiber and fiber architecture produces a hybrid effect which gives rise to the "pseudo ductile" behavior of the composite. In our study, a low elongation high modulus component - the carbon core fiber bundle, is surrounded by a higher elongation component - the Kevlar braided sleeve. The selection of the relative proportion and the nature of the combination of the types of fiber twist geometry and braid architecture were guided by an analysis of the hybrid effect as shown in Fig. 4.

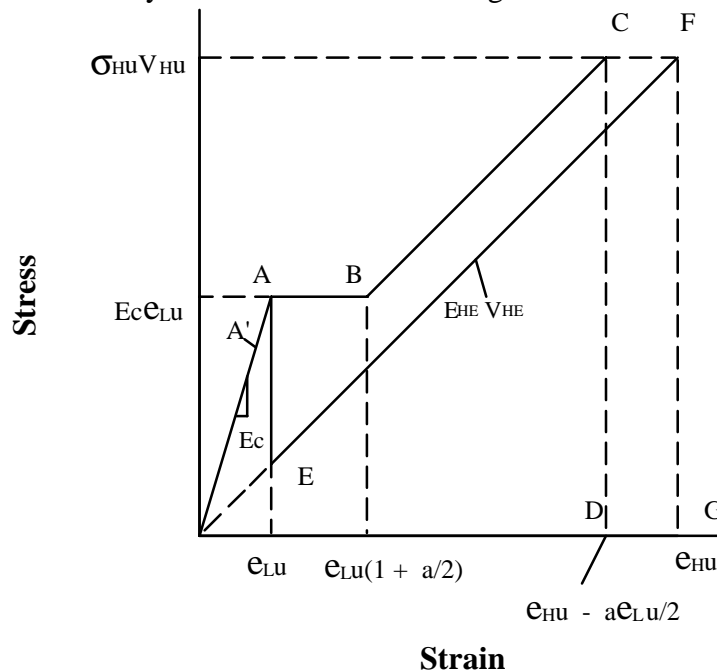


Fig. 4 Hybrid Composite Consisting of High and Low Elongation Components.

As demonstrated by Averston and Kelley [6], a unidirectional hybrid composite consisting of both high elongation and low elongation components can continue to carry the total load after failure initiation in the low elongation component if the following condition is satisfied:

$$V_{HE} \geq [\sigma_{LU} / (\sigma_{HU} + \sigma_{LU} - \sigma_H^1)] \quad (2)$$

where V_{HE} = fiber volume fraction of the high elongation component
 σ_{LU} = failure stress of low elongation fiber
 σ_{HU} = failure stress of high elongation fiber, and
 σ_H^1 = stress of the high elongation fiber at the failure strain of the low elongation component.

In this study we have modified equation (2) using the methodology established by Ko et al [7] to guide our design of the braided hybrid composites.

EXPERIMENTAL

To demonstrate the design concept and to verify the analytical predictions, a series of braided hybrid FRP bars with a nominal diameter of 5 mm. were fabricated. Two basic fibers Kevlar 49 and carbon fiber were used. A very high modulus carbon fiber Type P55 was used in order to produce a high initial modulus for the composite rebar. The Kevlar yarns were used for the braided sleeve whereas the carbon yarns were used for the core structure. In order to achieve reproducibility, a computerized braiding system developed at Advanced Product Development, Inc. was used. This system allows the incorporation of the rib effect automatically, as well as control of braiding angle and fiber volume fraction. To facilitate composite production, the braided structures were fabricated by in-line braiding and pultrusion (Figure 5).

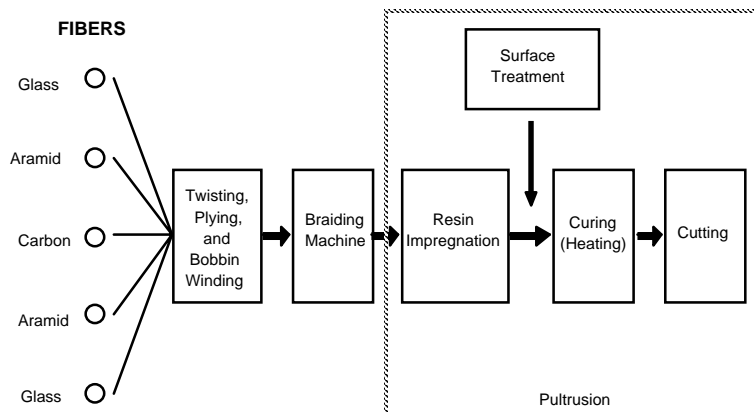


Fig. 5 Schematic of Production of Hybrid FRP Bars.

Tensile Behavior of the Composite Rebar

Three 5 mm. tensile specimens 42.5 cm. long were cut from the FRP bars production line with a water-cooled diamond saw. Simple tensile testing of the braided FRP bars were performed according to ASTM D3039 (1993) standards for tensile strength testing using a Tinius-Olsen T10000 bench top universal testing machine. Cast epoxy beveled tabs were developed to fit the specimen into the tensile grips and minimize stress concentration on the test specimen. The specimen ends were casted in aluminum molds with Epon 828 with room temperature curing agent, Epi-cure 3061. A Tinius-Olsen extensometer with a 50 mm gage

length was equipped with film clamps to minimize the stress concentration from clamping onto the FRP specimens.

All specimens composite bars failed in a similar manner, near the middle of the specimen length. The stress-strain curve exhibited a bilinear behavior with a relatively high initial slope before reaching a pseudo yield point. The yield strain was approximately equal to the ultimate strain of the core yarn. The initial elastic modulus of the braided composite bar was found to be predictable using the rule of mixtures when the geometric effects such as yarn twist, yarn crimp and braiding angle are taken into account. After reaching the yield point, a small drop of stress was experienced by the composite bar before further build up of stresses. The progressive breaking of the small braiding yarns were visible and they occurred in a sequential manner. Each breakage corresponded to a drop in the stress-strain curve. Most of the subsequent drops occurred at a higher stress level than the previous ones. The hybrid FRP bars were able to withstand increasing stress significantly higher than the first yield stress. When the strain was increased to the value near the ultimate strain of the sleeve yarn, the hybrid FRP bars reached their ultimate strength and failed suddenly. Between the first yield stress and the ultimate strength, the stress-strain curve exhibited the transition range where many drops in stress level occurred. This strain harden slip-stick behavior is due to the progressive failure of core and sleeve yarns which creates a ductile failure mechanism for the composite rebar.

A comparison of the theoretical and the experimental tensile stress-strain curves are shown in Figs. 6. As can be seen from Figs. 6, the agreement between the theoretical and experimental curves is good in the initial modulus and in the post yield modulus. The mean slope of these curves paralleled the slope of the theoretically predicted curves. The analytical model however predicts a higher drop in stress at yield.

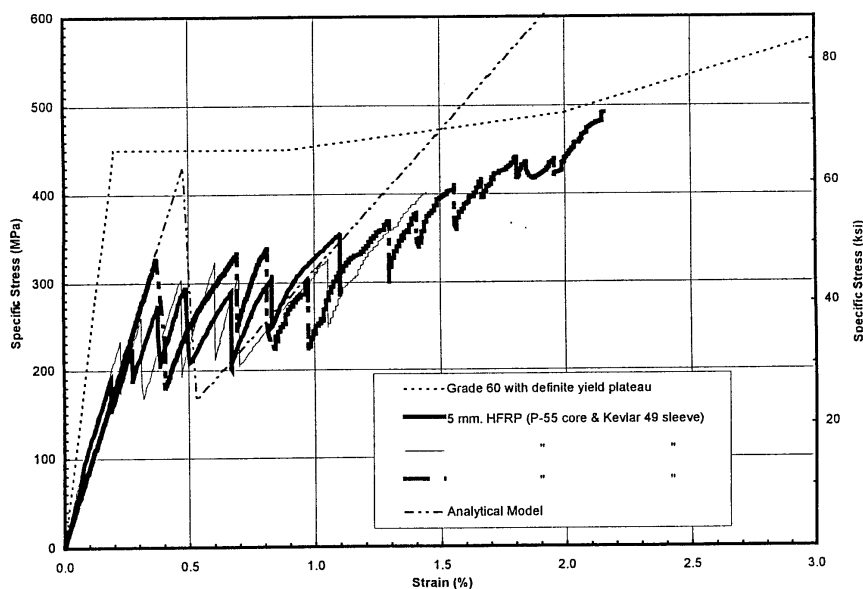


Figure 6. Experimental and Theoretical stress Strain Curves of Braided Composite Bars

Flexural Behavior of Braided Composite Reinforced Concrete

Three concrete beams (50 mm x 100 mm in section and 1.2 m long), each reinforced with 4 braided hybrid FRP bars were prepared for four point flexure test to failure. The composite

bars had a 5 mm nominal diameter and they were placed on the bottom side of the concrete beams. All the beams were casted at the same time and moisture cured for at least 28 days before testing. These beams were designed to have the same ultimate strength capacity as the reference steel reinforced beam. Steel stirrups were used in each beam in order to limit the study to the effects of tensile reinforcements. A Tinius-Olsen T10000 bench top universal testing machine was used with three dial gages and three linear-variable-differential-transformers (LVDT) for monitoring the deflection and the curvature of the beams. The load vs. deflection characteristics of this beam series is shown in Fig. 7. It can be seen that all three FRP reinforced beams failed in a similar manner. The FRP reinforced beams exhibit linear elastic deformation in the initial part of the load-deflection curve, follows by a pseudo plastic deformation exhibiting the strain hardening characteristic similar to that observed in steel reinforced concrete beams. The ductility indices, as determined by computing the ratio of ultimate to yield strain in the flexural load-deformation curve, of the braided FRP reinforced beams were founded to be greater than 5. This is remarkably similar to that of the steel reinforced concrete beam. Such high ductility has yet to be achieved with the presently available linearly elastic FRP systems!

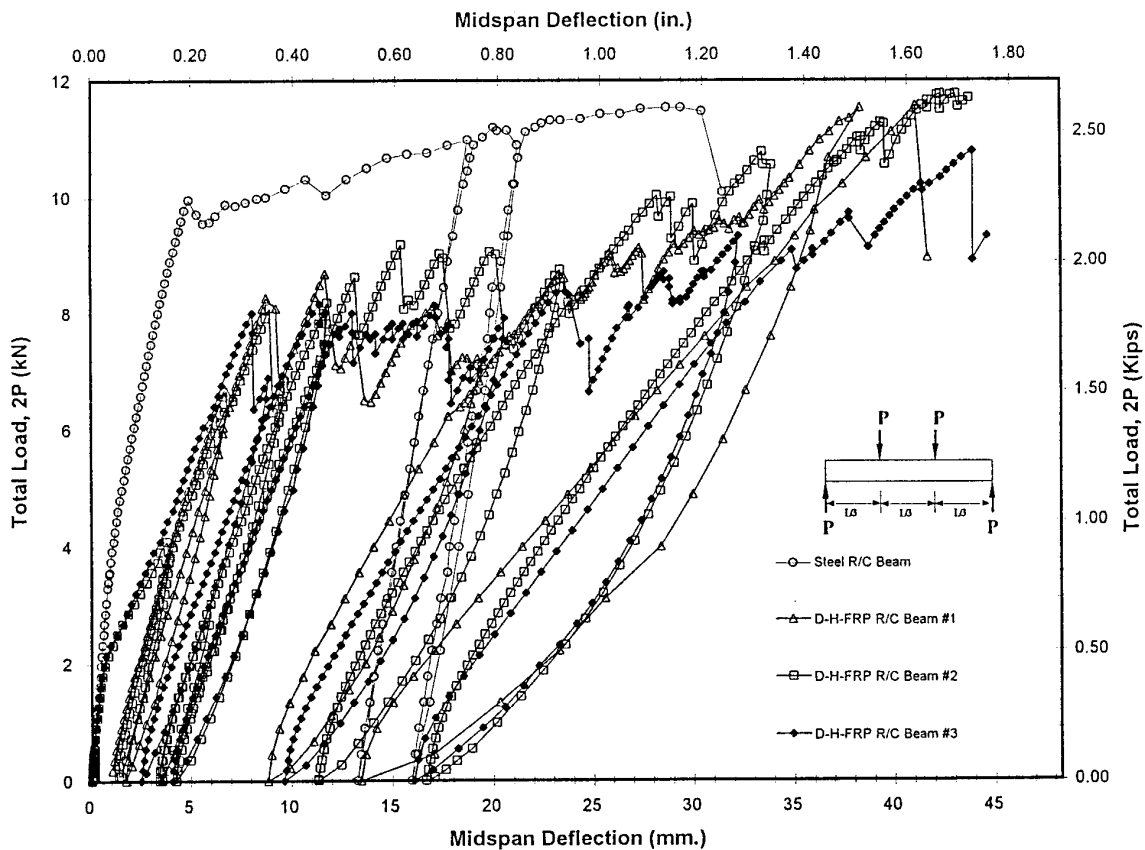


Figure 7. Load Deflection Behavior of Braided Composite Reinforced Concrete Beams

CONCLUSIONS

Guided by a fiber architecture based model (the FGM), a series of experiments were designed and carried out using carbon fiber as core yarn and Kevlar fiber for braiding yarns. An on-line braiding pultrusion process was constructed to provide a continuous process to produce the

hybrid fiber reinforced epoxy matrix rebar. The braided composite rebar specimens of various diameters were tested according to ASTM D638 using a 50mm gage length. It was shown, as predicted by the FGM, that the composite rebar failed in a ductile manner after an initial region of elastic response. The slip-stick, pseudoyield behavior can be attributed to the in situ balancing of elongation of the various fibers/matrix components in the hybrid composite. This preliminary result suggests that the proper selection of higher modulus core fibers coupled with a well balanced elongation of the components in the braided fiber assembly will generate a stress-strain curve for the composite rebar approaching that of the steel rebar. Further experiments on the flexural response of concrete beams reinforced by the braided composite rebar confirmed that metal-like ductility can be engineered using composite rebar. With the availability of a low cost manufacturing process and a well established design tool, the adaptation of braided composite rebar for large scale civil infrastructure applications will be realized when high performance fibers such as carbon and aramids are available at a low cost.

REFERENCES

1. Department of Commerce, Advanced Technology Program: Public Meeting on Manufacturing Composite Structures, April 16-17, 1996.
2. A., Nanni, Editor (1993) . Fiber-Reinforced Plastic (FRP) Reinforcements for Concrete, "*Fiber-Reinforced Plastic (FRP) Reinforcement for Concrete Structures*, Elsevier Science Publishers.
3. F. K. Ko, "Textile Structural Composites for Building Constructions, in *Textile Composites in Building Construction*", Part 3, pp.43-60, edited by Hamelin, P., and Verchery G., Pluralis (1990)
4. F. K. Ko, "Braiding," *Engineered Materials Handbook, Vol. 1: Composites*, ASM International, Metals Park, Ohio, pp. 519-528. (1987).
5. F. K. Ko, "Three Dimensional Fabrics for Composites," *Textile Structural Composites*, Chou, T. W. and Ko, F.K., editors, Elsevier, New York. (1989).
6. J. Averston, and A. Kelley, "Tensile First Cracking Strain and Strength of Hybrid Composites and Laminates," *Phil. Trans.*, London, A294, pp. 519-534. (1980)
7. F. K. Ko, K. Krauland, and F. L. Scardino, "Weft Insertion Warp Knit for Hybrid Composites," *Progress in Science and Engineering of Composites*, ICCM-V, Fourth International Conference on Composites, Japan, pp. 982. (1982).

EXPERIMENTAL AND NUMERICAL EVALUATION OF BOND STRESS OF CONCRETE BEAMS REINFORCED BY GFRP BARS

Luis Calado¹, Carlo A. Castiglioni² and Maria Rosario Agatino²

¹ *Instituto Superior Técnico, Department of Civil Engineering
Av. Rovisco Pais, 1096 Lisboa Codex, Portugal*

² *Politecnico di Milano, Structural Engineering Department
P.za Leonardo da Vinci, 32, 20133 Milano, Italy*

SUMMARY: The paper presents the results of an experimental and numerical research on the behaviour of concrete beams reinforced by GFRP bars. Experimental tests aimed to the assessment of the bond stress between concrete and GFRP bars, by means of Standard Beam-Tests, were performed in co-operation between Instituto Superior Técnico of Lisbon and Politecnico di Milano. Various GFRP bars having different diameters and surface roughness were analysed and their performance compared. Steel re-bars with similar diameters and surface characteristics were also experimentally analysed in order to compare the behaviour and bond stress of GFRP bars with steel re-bars. A numerical model able to represent the bond between GFRP bars and concrete was developed and applied to the experimental tests. Its accuracy is discussed and its performance is compared with other numerical models available in the literature.

KEYWORDS: beam-tests, GFRP bars, concrete beams, experimental tests, bond stress.

INTRODUCTION

Since the thirties, glass has been considered as a potential substitute for steel in reinforcing or prestressing concrete structures. The initial studies noted problems with anchorage, surface protection of bars and bonding glass to concrete. For that reason, it has been a period of about twenty years where research remained inert for the most part. Since the seventies, great advances have been made in this field.

The last few years, the use of composite materials was limited to fields where, due to the small volumes of the material needed, the unit cost was not a significant factor in the selection process. Examples of such applications are the aerospace and defence industries where intricate high performance components have been constructed at high cost. For civil engineering applications, the use of such materials could not be justified. Fortunately, with recent developments in fibers, resin and manufacturing process, the cost of fiber reinforced plastics (FRP) has been reduced to a point where they can compete with conventional materials such as steel [1].

A major advantage of composite materials is their corrosion resistance. However, it must be noted that similar to steel, composites can also be damaged as result of exposure to certain aggressive environments. While GFRP bars have high resistance to acids, they can deteriorate rapidly in an alkaline environment. Concrete, particularly immediately after it is cast, is alkaline. The use of alkaline resistant glass fibers is one approach to solve this problem.

It is clear that in today's competitive global market, the survival and success of any new construction material is greatly dependant on its cost. However, initial cost of the materials cannot be used as the sole factor in making such comparisons. Other expenses associated with

durability, maintenance, transportation and handling on the job site must also be included in these analysis.

General properties of GFRP re-bars

By comparing the properties of GFRP with steel bars (obtained by means of uniaxial tests), it was noticed that GFRP bars reach their ultimate tensile strength without exhibiting any yielding of the material and that, although the tensile strength of GFRP bars is slightly higher than that of steel, it is significantly higher than the yield strength of steel re-bars. Furthermore, unlike steel, the tensile strength of GFRP bars is a function of the bar diameter. In fact, due to shear lag, the fibers located near the centre of the bar cross-section are not subjected to as much stress as those fibers which are near the outer surface of the bar. This phenomenon results in reduced strength and efficiency in larger diameter bars.

The behaviour under fire conditions of concrete members reinforced with GFRP bars shows interesting possibilities of application of GFRP re-bars. Concrete will serve as a barrier to protect the GFRP bars from direct contact with flames. However, as the temperature in the interior of the member increases, the mechanical properties of the GFRP bars may change significantly. Tests [2] have shown that rods of E-glass after 30 minutes of exposure to a temperature of 300° C perform better than prestressing steel; however the strength reduction increases at higher temperature approaching that of steel at nearly 500° C.

Manufacturing techniques of GFRP re-bars

There are several techniques for manufacturing FRP composites. Although due to its fast speed of operation, good quality control and relatively low equipment cost, pultrusion is the method most commonly utilised for manufacturing FRP composites used in construction industry.

Some manufacturers have proprietary techniques where, a set of strands is helical wrapped around the re-bar before the re-bar is cured. The deformations or indentations thus formed on the surface of the bar improve its bond strength to concrete.

In other cases, proprietary techniques are adopted to increase the surface roughness of the pultruded bar by application, during the curing process, of an external “wrapping” having a given surface roughness, which is later eliminated (“peel ply”). This fabrication process has the advantage of guaranteeing the quality control of the process both in terms of bar dimensions and bond strength.

Bond between GFRP re-bars and concrete

Bond between concrete and reinforcing bars is one of the main aspects in the behaviour of both reinforced and prestressed concrete structures. Therefore, the development of an adequate bond is a critical aspect of the structural behaviour also in the case of GFRP re-bars.

Bond strength between bars and concrete depends on many influencing factors such as:

- concrete compressive strength (to resist the concentrated forces generated at the ribs);
- concrete tensile strength (of major importance if failure is caused by splitting);
- roughness conditions of the bars surface;
- cross section shape of the bars (e.g. bond strength is lower for rectangular bars);
- bar diameter (bond strength decreases as the diameter increases);
- clear concrete cover;
- bars spacing;
- bar direction in the cast (bond strength is lower in horizontal bars than in vertical ones);
- bar position in concrete cross section;
- amount of transversal reinforcement.

The major contribution to bond strength between deformed steel bars and concrete comes from the bearing component. As the surface deformations of GFRP reinforcing bars do not possess those characteristics of steel re-bars (high shear strength, high rigidity, deformation geometry) that provide enough lateral confinement through rib bearing, low bearing stresses are developed in the concrete by the action of the reinforcing bar deformation. Adhesion and friction may than be the important bond strength components in GFRP bars.

Due to the lack of industry standards and the numerous proprietary manufacturing techniques that exist, a wide range of products are available in the market. Clearly these products have different bond characteristics. The subject is under investigation by several researchers and in some cases preliminary design guidelines have also been presented [3-4].

The scope of this research is the study of the bond between GFRP re-bars produced by pultrusion with regard to the effect of different surface treatments (carved bars, bars with different surface roughness obtained by means of different peel-ply techniques). A number of beam-tests was performed on GFRP and steel bars having similar diameters, and a comparison of the obtained results is carried out. An analytical study was also performed, comparing the experimental results with those of a number of theoretical models of the bond between GFRP and concrete, which are available in the literature.

EXPERIMENTAL TESTS

Several test methods have been described in the technical literature to study the bond between rods and concrete. The most utilised are pull-out [3] and beam tests [4]. The pull-out test is sometimes viewed with scepticism due to the compressive stresses existing in the concrete near the loaded end of the bar. Although this stress state in the concrete is more of concern in steel-reinforced concrete (where failure of the concrete governs pull-out behaviour) rather than in the case of GFRP reinforced concrete (where pull-out is primarily governed by the GFRP), it must be observed that in the pull-out tests the concrete surrounding the reinforcing bar is under compression, reducing the possibility of cracking and thus increasing bond strength and slip at loaded and free ends.

On the contrary, in beam tests [4] the concrete surrounding the reinforcing bar is under tension, causing cracking at low stresses and hence reducing bond strength despite the confinement provided by the stirrups. It is believed that the results from beam tests are more realistic as they simulate better the real behaviour of flexural members.

For this reason, the present study on the bond strength of GFRP re-bars with concrete has been based on the results of standard beam-tests, according to [4].

Test set-up and loading history

Test beams consist of two rectangular reinforced concrete blocks jointed at the top by a steel pin joint and at the bottom by the reinforcing bar. The beam rests on two roller bearing and is loaded in bending by two equal forces applied symmetrically on either side of the steel joint (Fig. 1). One part of the reinforcement is anchored in each block while the remaining part is isolated from the concrete using plastic sleeves around the reinforcement. Anchorage length l_b depends on the reinforcement diameter ϕ ; embedment length must be equal to 10 times reinforcement bar diameter. According to [4], the load is applied step by step to the test specimen by means of an hydraulic jack so that the stress σ_s in the bar increases at the rate of 40 MPa per step. Each load step has two phases:

- a load increasing phase, nearly 30 seconds long;
- a load stationing phase no longer than 2 min until slip stabilisation is reached.

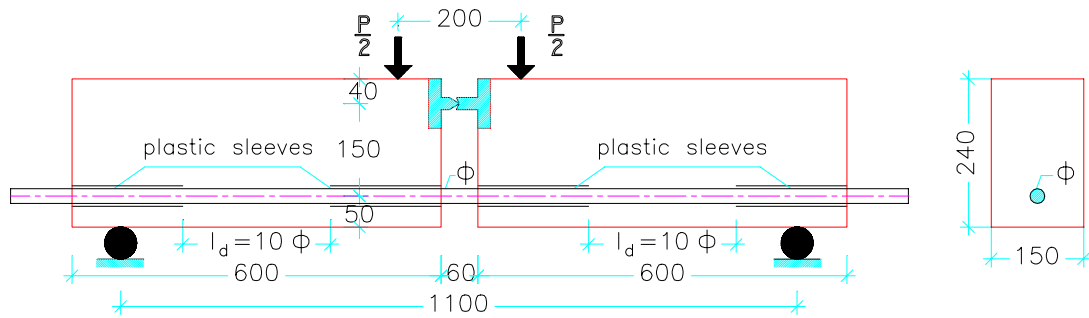


Fig. 1: Test set-up.

During the test, slip at the free ends of the reinforcing bar are measured using LVDTs. The test goes on until maximum bond strength is reached.

Specimens characteristics

The bond characteristics of four types of GFRP re-bars produced by pultrusion having different surface characteristics were experimentally analysed:

- type A: external surface with high roughness obtained by “peel ply” process;
- type B: external surface with low roughness obtained by “peel ply” process;
- type CE and CF: external smooth surface with helicoidal indentations;
- type D: external smooth surface.

Two types of steel re-bars commonly used in concrete structure, with external surface and diameter similar to the GFRP re-bars, were also experimentally analysed:

- type SB and SD: plain smooth bars with different diameters;
- type SC: ribbed bar resulting in high bond action.

The geometrical and mechanical properties of the GFRP and steel re-bars are reported in Tables 1 and 2.

Table 1: Characteristics of GFRP and steel re-bars.

Bar type	Number of bars tested	Type of surface	Diameter ϕ (mm)	Young modulus (GPa)	Ultimate tensile strength (MPa)	Yield tensile strength (MPa)
A	4	high roughness	22.0	32.2	400.1	-
B	4	low roughness	24.0	23.0	229.9	-
CE	1	helicoidal indentations	24.0	20.0	174.4	-
CF	1	helicoidal indentations	24.0	25.0	344.3	-
D	2	smooth	16.0	30.0	423.1	-
SB	2	smooth	25.0	200.0	330.0	330.0
SC	2	ribbed	25.0	200.0	330.0	330.0
SD	2	smooth	16.0	200.0	375.0	370.0

Table 2: Geometrical properties of the machined GFRP re-bars.

Bar type	Diameter ϕ (mm)	Indentation spacing (mm)	Indentation depth (mm)	Indentation width (mm)	Indentation angle
CE	24.0	47.5	1.5	9.0	35°
CF	24.0	195	2.5	15	70°

The tensile equipment available in the laboratory does not have plates to fix bars with a diameter of 24 mm. For that reason, plates to fix bars with a diameter of 30 mm were used. In order to avoid the slip, a greater transversal pressure was applied which damaged partially the cross-section of the bars. For this reason the ultimate stress of GFRP bars with 24 mm diameter is lower when compared to those with diameter 22 and 16 mm.

Test results

In each test slippage of the two ends of the bars was recorded on a plotted curve versus the load applied to the beam. It was observed that slip occurred only at one end, except in the case of smooth bars, type D, in which slip occurred approximately at same time on both ends. The curves of Figs. 2 and 3 describe this evolution for each type of GFRP bars, while in Fig. 4 it is shown a typical failure mode.

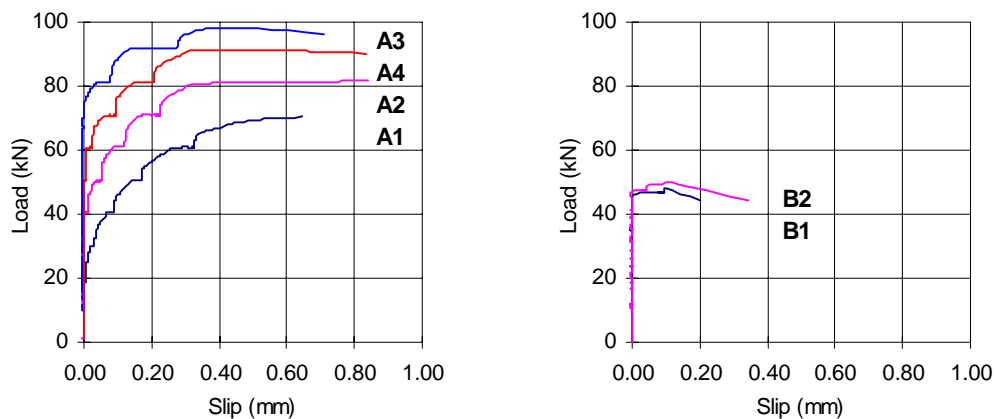


Fig. 2: Load-slippage curves for bars with external surface obtained by “peel ply” process, high (type A) and low (type B) roughness.

The curves show a clear difference in the behaviour of the four types of GFRP re-bars, making evidence that the external surface is the main parameter that governs the behaviour of the beams. Bars with external surface with a roughness obtained by “peel ply” process (type A and B), have a higher load carrying capacity when compared to those whose external surface is smooth independently on the presence of helicoidal indentations with large spacing (type CF and D).

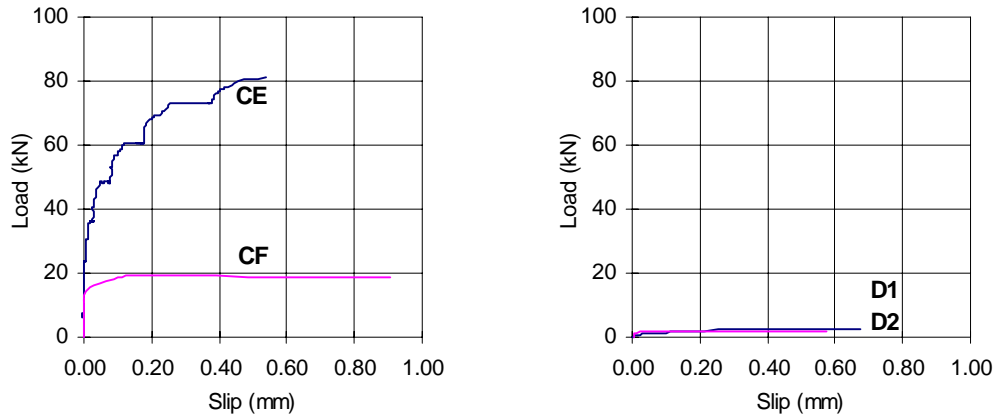


Fig. 3: Load-slippage curves for smooth bars with surface indentation (type C) and smooth bars (type D).

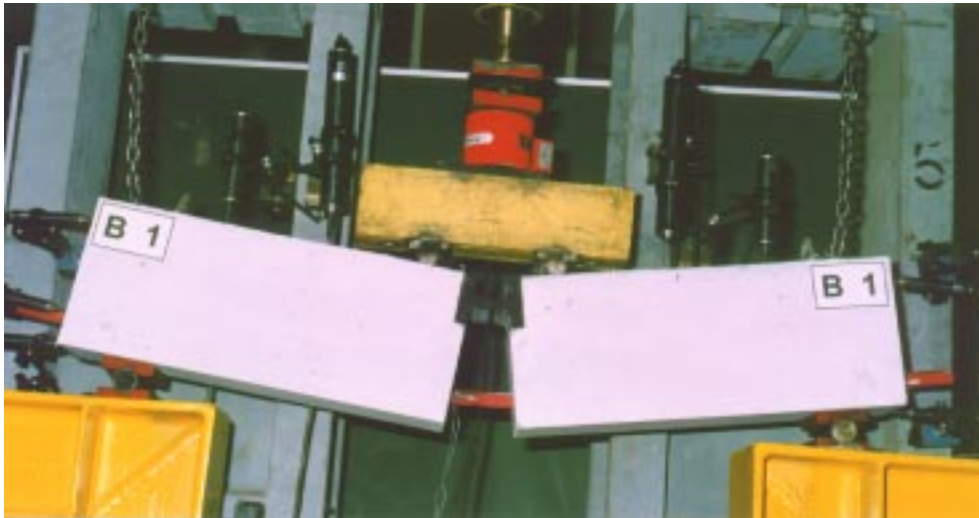


Fig 4 Typical failure mode of a beam-test

Beams with bars having high roughness, type A, showed approximately a load carrying capacity double of those with bars of low roughness, type B, despite the area is 7% smaller. Beams with smooth bars, type D, had approximately a null load carrying capacity. The mechanical indentation improve the behaviour of the bar as the slip starts for higher loads. The decrease of the indentation spacing also improves the behaviour of the bar, in terms of the maximum slip load.

Smooth bars with small spacing of the mechanical indentation exhibit a behaviour similar to bars with external high roughness obtained by “peel ply” process. In these two types of external surface, it was possible to increase the applied load, after the occurrence of the first slip, although the slip have grown. This is due to the mechanical interlock provided by the external surface, which is not possible in smooth bars, bars with low roughness or bars with large spacing of the mechanical indentation, for which the bond is only due to friction.

Only beam-tests with bars of type CE exhibit at high load crack pattern and spacing in concrete beams similar to those of conventionally reinforced beams.

Fig. 5 presents the load-slippage curves for two types of steel re-bars with different external surfaces.

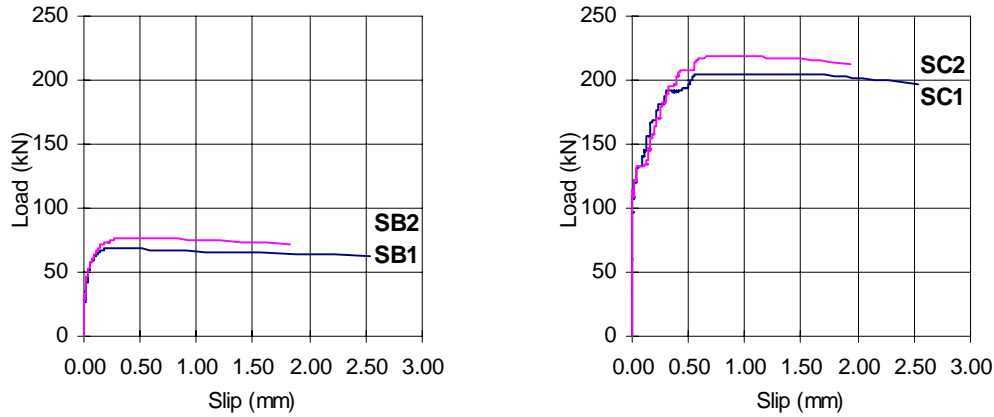


Fig. 5: Load-slippage curves for plain smooth bars (type SB) and ribbed bars resulting in high bond action (type SC).

As well known, for the same diameter the roughness of the external surface increases the load carrying capacity of the beam and the slip at which failure occurs.

RE-ELABORATION OF TEST DATA

The load-slip curve obtained during the test gives the bond stress value for each slip value considered uniformly distributed over the anchorage length $l_b = 10 \phi$. From RILEM recommendations [4], if the total load on the beam is P , the bar tensile stress calculated by pure bending moment is approximately:

$$\sigma_a = 1.25 \cdot \frac{P}{A} \quad (\phi < 16 \text{ mm}) \quad (1)$$

$$\sigma_a = 1.5 \cdot \frac{P}{A} \quad (\phi \geq 16 \text{ mm}) \quad (2)$$

in which A is the cross section area of the reinforcing bar (mm^2). The value of the mean bond strength τ_b over the embedment length is calculated by:

$$\tau_b = \frac{\sigma_a \cdot \pi \cdot \phi^2}{4 \cdot \pi \cdot \phi \cdot 10 \cdot \phi} = \frac{\sigma_a}{40} \quad (3)$$

According to [4], the characteristics bond strength values are:

- τ_m which is the mean value of $\tau_{0.01}$, $\tau_{0.1}$, and τ_1 , corresponding to 0.01, 0.10, and 1.00 mm slippage respectively on each bar end;
- maximum bond strength τ_r , mean value of bond strength values at the ends of the bars, corresponding to 3.00 mm slippage.

If the bar fails before reaching 1.00 mm slippage, bond strength corresponding to the reached maximum load is considered as τ_r , and this τ_r is the third value for τ_m calculation.

Beam tests results re-elaborated according to RILEM [4] are shown in Table 3 which gives, for all types of external surfaces, the mean bond stress at 0.01 mm and 0.10 mm, and the value of maximum bond stress, $\tau_{m\acute{a}x}$, and the corresponding slip at $\tau_{m\acute{a}x}$.

Table 3: Mean bond stress for different types of external surfaces of GFRP and steel bars.

Bar type	$\tau_{0.01 \text{ mm}}$ (MPa)	$\tau_{0.10 \text{ mm}}$ (MPa)	$\tau_{m\acute{a}x}$ (MPa)	slip at $\tau_{m\acute{a}x}$ (mm)
A	5.11	6.63	8.26	0.62
B	4.00	4.40	4.21	0.11
CE	2.59	4.77	6.76	0.54
CF	1.25	1.56	1.61	0.15
D	~ 0.0	0.27	0.53 *	1.00
SB	2.47	4.87	5.56	0.42
SC	8.33	10.51	16.17	0.92
SD	3.91	5.22	5.61	0.22

* - assessed for slip equal to 1.00 mm.

These results show a clear influence of the external surface of the GFRP re-bars - concrete bond. Independently of the diameter, bars with high roughness obtained by “peel ply” process or smooth surface with helicoidal indentations with small spacing exhibit a higher bond stress when compared to those having low roughness or with mechanical indentation with large spacing. Although the bar CF had an external surface with helicoidal indentation, $\tau_{m\acute{a}x}$ is 24% of $\tau_{m\acute{a}x}$ for CE type, which has a small spacing between indentations. For bars of type A and CE, the experimental bond stress clearly demonstrated the perfect bond between GFRP re-bars and the surrounding concrete.

Large variation in the spacing of the indentation results in a large variation in bond stress. For the cases studied (CE and CF) a value of 24% was obtained. Concerning the “peel ply” process a variation of 51% in the bond stress can be found when comparing bars with low and high roughness external surfaces.

Similar beam-tests on plain smooth bars and ribbed bars with helicoidal indentations have given a value equal to 5.59 MPa and 16.17 MPa for the $\tau_{m\acute{a}x}$. Comparing these values to those of similar GFRP re-bars, the ratio of the maximum bond stress for similar external surfaces is 148% for type A, 75% for type B and 42% for type CE.

NUMERICAL MODELS

The development of numerical models that can simulate the bond behaviour between GFRP bars and concrete allows the evaluation of the anchorage length which is necessary for design purposes of structures with this kind of reinforcement. The main difficulty of the generalisation of these models is due to the existence of different surfaces treatments which lead to different bond behaviours. That is why it is not easy to develop a model independent from direct experimental parameters.

Two analytical models for bond stress-slip relationship, developed on purpose for GFRP bars by other authors are presented [5,6] as well as the model adopted by CEB-FIB Model Code 90 [7]. A simple model named Logarithmic, for the assessment of the bond between concrete and the GFRP bars is proposed.

Malvar's model

A modelling of the bond phenomenon in case of GFRP bars was developed by Malvar [5] which carried out an extensive experimental research in fiber glass bars characterised by different shapes of the outer surface. Tests were performed for different values of the confinement pressure and for a fixed tensile strength of the concrete. According to test results, Malvar proposed a refined model of the overall bond behaviour dependent on seven empirical constants to be determined by curve-fitting the experimental $\tau - s$ curves. This model is able to reproduce the entire constitutive bond-slip curve by means of a unique equation. All the empirical parameters are obtained from the experimental data by the least square error method.

Cosenza, Manfredi & Realfonzo's model

An alternative analytical modelling between GFRP reinforcing bars and concrete has been proposed by Cosenza, Manfredi and Realfonzo [6] (C.M.R. model) which describes only the ascending branch of the bond stress-slip curve. According to the authors the parameters needed have to be evaluated from experimental data with the least square error method. Results obtained with this model showed that the bond behaviour is mainly influenced by the shape of the outer surface being not quite dependent from the fiber type.

Bertero, Eligehausen & Popov's model

This model (B.E.P. model) is adopted by CEB-FIB Model Code 90 [7] for the bond between steel re-bars and concrete. This model divides the τ -s relationship in four branches. The ascending branch, in which the ribs penetrate into the mortar matrix, simulates the local crushing and micro-cracking. The horizontal level occurs only for confined concrete, referring to advanced crushing and shearing of the concrete between the ribs. The decreasing branch refers to the reduction of bond resistance due to the occurrence of splitting cracks along the bars. The horizontal part represent a residual bond capacity, which is maintained by virtue of a minimum transverse reinforcement, keeping a certain degree of integrity intact.

Logarithmic model

The experimental results have showed that a logarithmic model is able to simulate the stress-slip relationship of GRFP bars, and can be expressed by the following Eqn:

$$\tau = \tau_m + A \cdot \log(s) \quad (4)$$

where τ_m is the peak bond stress and A is an empirical parameter based on curve-fitting of the experimental data. As the Cosenza model, the logarithmic model only describes the ascending branch of the bond stress-slip curve.

Numerical simulations

All these models were applied to simulate the experimental τ -s obtained during the tests. In Fig. 6 the results for two experimental tests are presented.

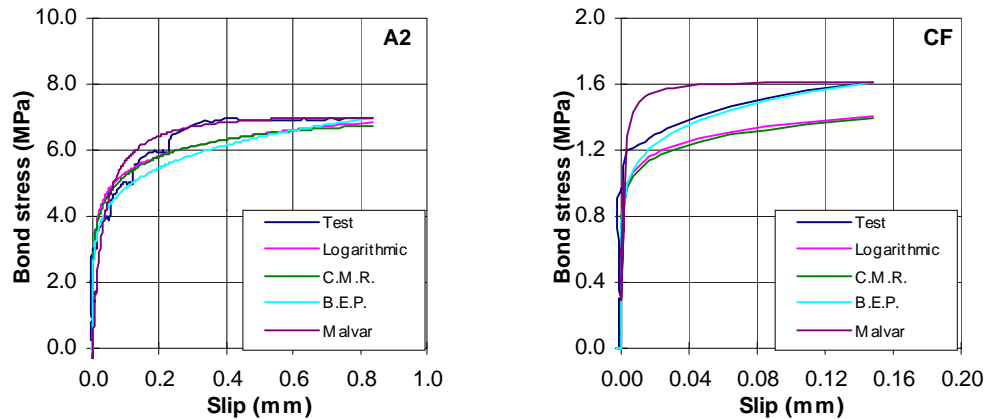


Fig. 6: Comparison between numerical models and experimental tests.

The numerical simulations performed to all tests showed that in general Malvar's model overestimates the stress for all types of GFRP bars, while, on the contrary, the other three models in general underestimate the stress. The models developed by Bertero et al. and Cosenza et al. exhibit approximately the same curve for the τ - s relationship. The logarithmic model, as well as B.E.P. and C.M.R. simulates quite well the experimental τ - s relationship for GFRP bars of the type A, CE and CF, showing a maximum error less than 7%. In the case of bars of type B the logarithmic model showed the worst correlation exhibiting a maximum error equal to 33%.

The initial tangent (for $s = 0$) of B.E.P., C.M.R. and Logarithmic models becomes infinity thus allowing to reproduce quite well the physical evidence of the phenomenon; in fact, no slip was observed during the experimental tests for low values of bond stress (adhesion).

CONCLUSIONS

The results obtained with this experimental research showed a clear influence of the external surface of the GFRP re-bars in the τ - s relationship. Independently of the diameter, bars with high roughness obtained by "peel ply" process exhibit a higher bond stress when compared to those having low roughness or with mechanical indentation with large spacing. Decreasing the space between helicoidal indentation increases the bond between bar and concrete and the behaviour is similar to the bars with high roughness obtained by "peel ply" process.

For the types of GFRP bars under investigation, the model proposed in the CEB-FIB Model Code 90 (B.E.P. model) for steel re-bars is the one that exhibits a lower error between the stress assessed during the tests and the stress numerically simulated.

ACKNOWLEDGEMENTS

The financial support from JINCT, from ERASMUS Program and from M.U.R.S.T. 40% is gratefully acknowledged. The authors would like to thank TOP GLASS S.p.a., Italy, and Betão Liz, Portugal, for their generous contributions respectively on GFRP re-bars and concrete. Grateful acknowledgements are due to Monica Vanzan and Davide Pozzi for the assistance during the tests and the research.

REFERENCES

1. Gustafson, D.P., "Epoxy Update", Civil Engineering, October 1988, pp. 38-41.
2. Eshani, M.R., Saadatmanesh, H., Tao, S., "Design Recommendations for Bond of GFRP Re-bars to Concrete", Journal of Structural Engineering, ASCE, March 1996, pp.247-254.
3. ASTM C234-91a "Standard Test Method for Comparing Concretes on the Basis of the Bond Developed with Reinforcing Steel".
4. RILEM-CEB-FIP - "Test of the Bond Strength of Reinforcement of Concrete: Test by Bending", Recommendation RC.5., 1978.
5. Malvar, L.J., "Bond Stress-Slip Characteristics of FRP Re-bars" TR - 2013 - SHR - Naval Facilities Engineering Service Centre, Port Hueneme, CA, February 1994.
6. Cosenza, E., Manfredi, G. and Realfonzo, R., "Analytical Modelling of Bond between FRP Reinforcing Bars and Concrete" Non-metallic (FRP) Reinforcement for Concrete Structures. Edited by L. Taerwe. RILEM, 1995, pp. 164-171.
7. CEB-FIP Model Code 90. "General models: Bond Stress-Slip Relationship", pp. 82-86.

COMPRESSION FAILURE OF LAMINATED COMPOSITE CYLINDRICAL SHELLS UNDER AXIAL LOADING

M.A. Battley¹, G. R. Dromgoole²

¹ *Industrial Research Limited, PO Box 2225, Auckland, New Zealand*

² *Kestrel Aircraft Company, 1630 Westheimer Drive, Norman, Oklahoma 73069, USA*

SUMMARY: This paper addresses failure characterisation and prediction for moderately thin-walled carbon fibre/epoxy cylinders subjected to compressive axial loads. Specimens of [02/902]_s configuration failed in a local buckling mode, with virtually no prebuckling acoustic activity. In the case of the [90/45/-45/0]_{as} laminates there was moderate acoustic activity at load levels as low as 40% of the final failure load, suggesting that damage was occurring within the laminate well before the final failure in a buckling related mode. The [45/-45/45/-45]_s specimens demonstrated significant acoustic activity from low load levels and failed by material fracture. A finite element analysis based design methodology is presented which considers failure modes such as local buckling, intralamina and interlamina damage. A key feature of the new methodology is that it recognises the significant effect that geometric imperfections have on the localised laminate stress fields, as well as on local buckling behaviour.

KEYWORDS: compression, buckling, failure, cylindrical shells, thin-walled, acoustic emission, finite element, design

INTRODUCTION

Cylindrical shell sections are commonly used as structural members for resisting various loading configurations. In aerospace and marine applications they are often used as compression or torsion resisting spars. The use of fibre reinforced composite materials in the fabrication of such structures provides advantages which include high specific stiffness and specific strength, and good dimensional stability. Calculation of the strength of composite cylindrical shells presents a formidable task, since the failure mode is very dependent on the load distribution, geometry, imperfections, material type and laminate configuration of the structure. Depending on these parameters the mode of failure can occur at a structural level (global buckling), laminate level (local buckling, lamina in-plane fracture, delamination), or at a microstructural level (fibre buckling, kink band formation). The actual failure may also be a combination of modes, often involving interaction of different mechanisms.

The effect of geometric imperfections such as shape and thickness variations on the stability of thin shells is well documented [1]. However in the case of composite materials, localised laminate bending caused by geometric imperfections can also generate high intralamina and interlamina prebuckling stresses, resulting in damage to the laminate which may then initiate other failure modes such as buckling or delamination.

The failure mode of cylindrical shells is primarily governed by the geometry of the structure, particularly the thickness of the shell wall (t) relative to its radius of curvature (r). The compressive strength of thin-walled shells (r/t typically > 100) is normally governed by the stability of the shell wall. The prediction of the buckling load and postbuckling behaviour of such shells is reasonably well understood. Geometrically nonlinear finite element methods can be used to predict the buckling loads with an acceptable level of accuracy [2]. The modes of failure of thick-walled shells (r/t typically < 10) in compression have been identified as primarily kink band formation and delamination, although failure criteria are still in their infancy [3]. The failure of shells in the intermediate range ($10 < r/t < 100$) is not well understood.

This paper addresses failure prediction for moderately thin-walled cylinders ($r/t \approx 60$) subjected to compressive axial loads. For cylinders of such dimension the local buckling load can be of similar magnitude to the compressive strength of the laminate. The failure modes of 8 ply carbon fibre/epoxy cylinders with layup configurations $[0_2/90_2]_s$, $[90/45/-45/0]_{as}$, and $[45/-45/45/-45]_s$ (subscript s designates a symmetric layup, as corresponds to antisymmetric) are characterised experimentally with the aid of acoustic emission monitoring and predicted by a finite element analysis (FEA) based design methodology. The key feature of the new methodology is that it recognises the significant effect that geometric imperfections have on the localised laminate stress fields, as well as on local buckling behaviour.

FAILURE CHARACTERISTICS

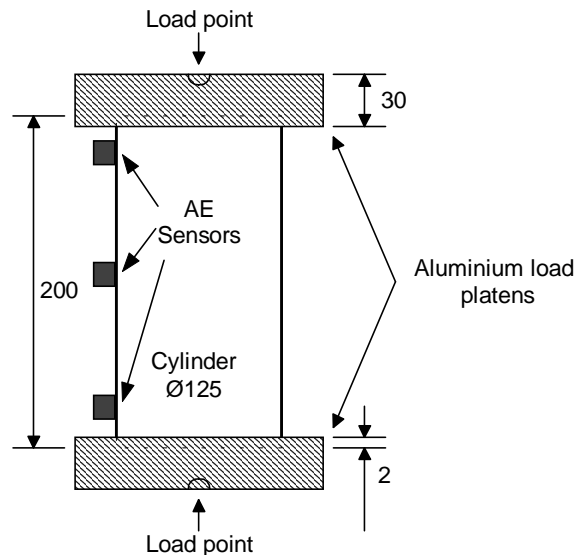
Introduction

The ability to monitor dynamically, providing a response to a discontinuity under an imposed structural stress in real time provides Acoustic Emission monitoring (AE) with a significant advantage over other nondestructive testing methods. Methods such as radiography, dye penetrant and magnetic particle techniques are not capable of continuous monitoring. Eddy current and ultrasonics, although being capable of such continuous monitoring, are not as suitable for defect monitoring because the location and direction of the defect needs to be known. AE is able to monitor relatively large regions of a structure, and with appropriate sensor location and signal processing, can be used to locate the origins of emissions. In theory, AE can be used to identify the failure type from the signal characteristics, however in the case of composite materials the characteristics of different failure modes are still not well defined. Attempts to correlate results with those from other researchers is complicated by the effect that acquisition parameters such as filtering and threshold settings have on the processed AE results. Most AE transducers also have highly nonlinear response curves, meaning that the form of the processed AE signals is very dependent on the type of transducer used. Characterisation of signals based upon spectral response is often avoided because of non-uniform absorption, dispersions, scattering and reflections. Typically the response waveform is defined and characterised by events (acoustic activity) and/or the amplitude of the signal. These two parameters were used for the characterisation of an event in this study.

Experimental Details

Carbon fibre/epoxy composite cylinders were fabricated on a 125mm diameter aluminium mandrel. The mandrel was machined and polished to tolerances of ± 0.01 mm to ensure minimal geometric variation of the laminate. Three different 8 ply layups $[0_2/90_2]_s$, $[90/+45/-$

$45/0]_{AS}$ and $[+45/-45/+45/-45]_S$ were constructed from 150g/m^2 , intermediate modulus, carbon fibre/epoxy pre-impregnate (CYCOM 950-1 IM2C-150g). High strength epoxy resin (Lockfast K2001) was used to bond the samples into 2mm wide and 2mm deep grooves in machined aluminium platens. The laminates were tested with an Instron test machine (model no. 1186, 200kN) at a cross-head displacement rate of 0.5mm/min. Load was applied to the aluminium platens through steel spheres to ensure axial loading. Fig. 1 shows the experimental configuration.



*Fig.1: Experimental configuration
(Dimensions in mm)*

The acoustic emission system used was a Vallens AMS-3, 4 channel acquisition unit with Vallens SE-45 type transducers. These transducers have a sensitivity in the range of 25 to 120kHz and a secondary range of sensitivity from 130kHz to approximately 230kHz. The acoustic emission signal was bandpass filtered with a 30kHz to 1MHz preamplifier and the total system amplification maintained at 34dB allowing processing of the preamplifier input signal up to 99.9dB above 1mV ($\pm 99\text{mV}$ peak). A threshold of 36dB above 1mV ($\pm 63.1\text{mV}$ peak) was set to eliminate any background noise. Rubber bands held the transducers onto the cylinder surface during the tests with petroleum based gel being used as an acoustic coupling medium. The directional acoustic propagation characteristics of composite materials and the multiple propagation paths of a cylindrical geometry greatly complicate planar source location. In this test programme a three sensor linear transducer configuration was used to enable the axial location of events to be determined. This allowed any extraneous noise from sources such as crushing of the specimen ends and machinery related noise to be identified.

Experimental Results

Failure modes

Each of the three laminate configurations demonstrated a different mode of failure. This is graphically shown in Fig. 2, which presents the cumulative acoustic events vs. load level for typical samples of each layup. The $[0_2/90_2]_S$ specimens failed in an asymmetric local buckling type mode, with virtually no prebuckling acoustic activity. In the case of the $[90/45/-$

45/0]_{AS} laminates there was moderate acoustic activity at load levels as low as 40% of the failure load, suggesting that damage was occurring within the laminate well before the final failure which appeared to be a buckling dominated mode. The [45/-45/45/-45]_S laminates demonstrated significant acoustic activity from low load levels with a dramatic increase in the number of events as the load reached approximately 50kN. The final failure was characterised by significant localised damage to the laminate.

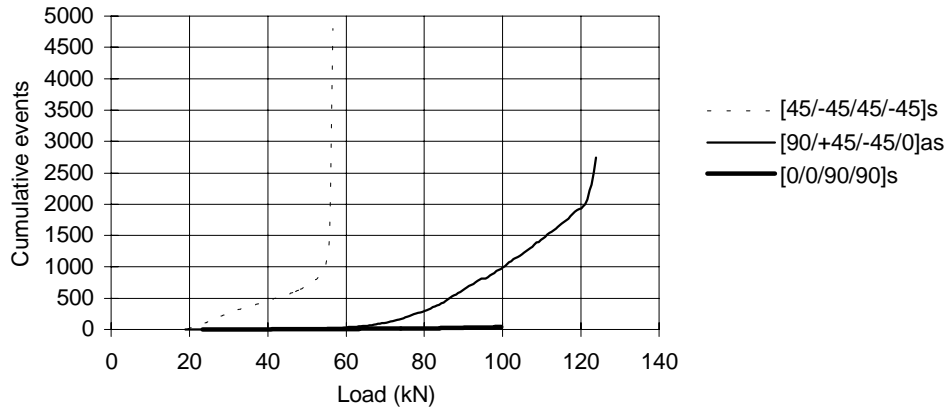


Fig. 2: Cumulative acoustic events vs. applied compressive load

Location of Failures

The distribution of the acoustic emissions for all specimen types indicated concentrations of emissions which corresponded well with the actual failure locations. As shown in Fig. 3, a uniform spread was observed across the remaining portion of the cylinder for the [90/45/-45/0]_{AS} and [45/-45/45/-45]_S laminates, suggesting that the mechanism generating them is related to a global laminate strength parameter rather than a consequence of a single localised imperfection or boundary constraints. Although the final failure of the [45/-45/45/-45]_S laminate (between 12-14 cm) was related to significant local bending caused by the constraining effects of the end platens, Fig. 3 (b) clearly demonstrates that damage occurred throughout the cylinder length. This figure also shows that the large cumulative number of events shown in Fig. 2 for the [45/-45/45/-45]_S case is the result of relatively few events at many positions and times during the test. The few events detected for the [02/902]_S specimens were all located at the position of the final failure.

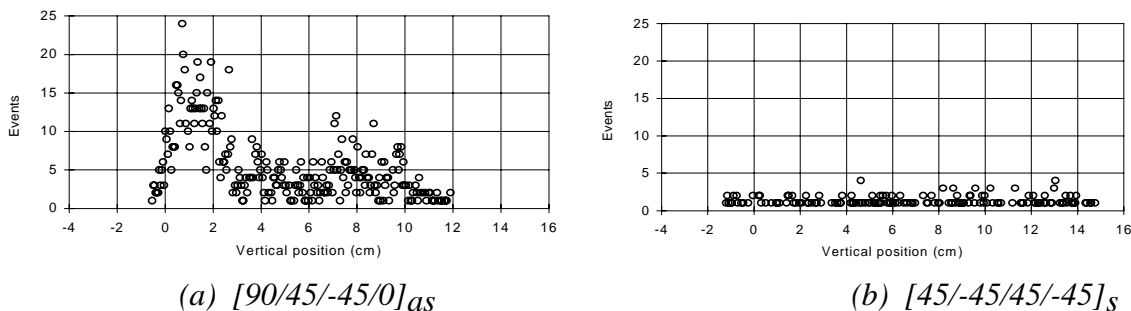


Fig. 3: Acoustic events vs. position
 (The 0 position refers to the top sensor as shown in Fig. 1.
 Sensors 2 and 3 are positioned down the specimen at 6 and 12cm respectively)

Failure Loads

The failure loads of the specimens are presented in Table 1. The mean strength of the $[90/45/-45/0]_{as}$ specimens was approximately 6% higher than that of the $[0_2/90_2]_s$, and the $[45/-45/45/-45]_s$ specimens were as anticipated, significantly weaker than the other two configurations. The failure loads for the $[45/-45/45/-45]_s$ tubes were remarkably consistent with less than 2% difference in load between each specimen. Experimental buckling failure loads, as in the case of the $[90/45/-45/0]_{as}$ and $[0_2/90_2]_s$ specimens, are typically subject to significant variation because of the sensitivity to variations in imperfection size. The consistency of the $[45/-45/45/-45]_s$ specimens may be related to their different failure mode, which is more dependent on material strength parameters than imperfection magnitudes.

Table 1: Failure loads

Laminate	Individual Failure Loads (kN)	Mean Failure Load (kN)
$[90/45/-45/0]_{as}$	124, 113, 128, 128, 114	121
$[0_2/90_2]_s$	117, 100	109
$[45/-45/45/-45]_s$	56, 56, 57	56

Acoustic Event Amplitude

The acoustic emissions from the $[+45/-45/+45/-45]_s$ laminate were identified as predominantly high amplitude events, typically greater than 70dB. In contrast the $[0_2/90_2]_s$ and $[90/+45/-45/0]_{as}$ laminates showed relatively few events greater than 60dB. Fig. 4 shows a typical amplitude vs. load response for a $[90/+45/-45/0]_{as}$ specimen.

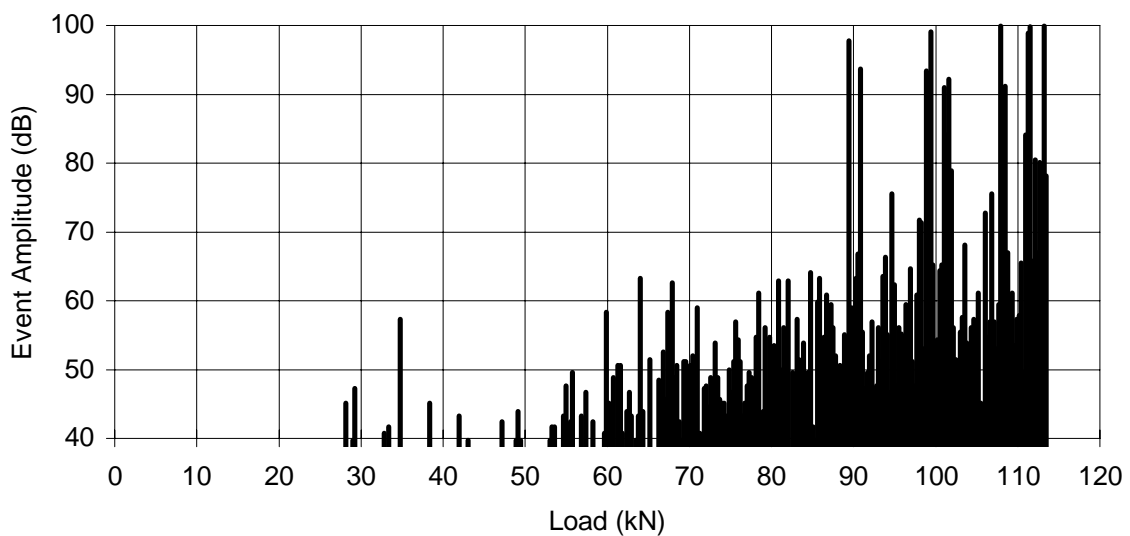


Fig. 4: Amplitude of acoustic events vs. load for $[90/+45/-45/0]_{as}$ specimen (Threshold at 40dB)

FAILURE PREDICTION

Introduction

Buckling failure of thin and medium walled cylindrical shells is often predicted by using a linear eigenvalue buckling analysis. However this type of analysis does not account for the degrading effects of geometric imperfections and consequently normally over estimates the buckling load. A more accurate approach is to perturb a finite element mesh, often by using the first mode eigenvector scaled to an amplitude equivalent to that of a typical imperfection, and conduct a geometrically nonlinear analysis. Arc controlled step incrementation is usually used for such analyses because it has proved effective in negotiating limit points and snap back points associated with nonlinear buckling analyses. However because nonlinear analyses are computationally intensive, they are usually only performed if the design load is similar to the eigenvalue predicted buckling load. If buckling is not of concern for the shell, then linear FEA based stress analysis is often used to predict the failure load of the structure. The danger in using such an approach for thin or medium walled shells is that imperfections or boundary constraints can generate large local bending related stresses, which will not be accurately predicted by a linear analysis. The methodology presented in this paper focuses on the significant effect that geometric imperfections have on the localised stress fields, as well as on the local buckling behaviour. The effect of nonlinear shear stress constitutive behaviour typical of carbon fibre/epoxy composite lamina is also considered.

Methodology

A commercial FEA code (EMRC NISA) was used to model the cylinders with laminated composite quadrilateral shell elements (NKTP 32). A quarter model was constructed, with symmetric boundary conditions imposed at the two longitudinal boundaries. At the load boundary, full constraints were imposed with exception of the load translational direction, to simulate a built-in end as in the experimental tests. The load was applied to the shell as a nodal force at the load boundary through rigid links, simulating a centrally loaded rigid plate. A convergence study confirmed that the mesh of 200 elements (3846 degrees of freedom) was adequately refined to accurately model the buckling load and mode.

Several types of analyses were conducted to assess the accuracy of alternative finite element modeling approaches for the prediction of compressive load carrying ability. A suitable methodology must be able to accurately predict the failure load of the structure, whether it fails by buckling, material fracture, or a combination of both. Analysis alternatives included linear FEA based stress analysis, linear eigenvalue extraction for both perfect and perturbed meshes, geometrically nonlinear stress and buckling analyses, and nonlinear analyses including material nonlinearity in shear.

The most successful approach proved to be a multi-analysis scheme, beginning with a linear eigenvalue analysis to predict a buckling load and mode shape. The initial mesh was then perturbed into a shape based on the first mode eigenvector, and the maximum load for the nonlinear analysis set to the predicted eigenvalue load. In this study the perturbation magnitudes were based on measured geometric properties of the experimental specimens (a maximum amplitude of 10% of the wall thickness), however in the absence of such data it would be necessary to estimate a likely perturbation based on expected production tolerances. Geometrically nonlinear analyses were then performed using arc controlled step incrementation. Experimentation with step control and convergence parameters were usually

required to achieve stable solutions. The predicted stress levels within each ply were then assessed with the FEA software's postprocessor, both to check if material fracture was likely prior to buckling failure, and also to determine the level of intralamina shear stresses. In cases where the predicted shear stress levels were significant (in excess of 30 MPa in this case), nonlinear analyses were performed with nonlinear lamina shear stiffness properties. The stress levels within the laminates were then reassessed.

The accuracy of alternative failure criteria for composite materials remains a topic of considerable debate. This study employed the simple “maximum stress” criterion, which has the advantage of simplicity while appearing to have some degree of correlation with experimental results [4]. The critical stress component for both the $[+45/-45/+45/-45]_s$ and $[90/+45/-45/0]_{as}$ laminates proved to be the intralamina shear of the $\pm 45^\circ$ laminae, while the $[0_2/90_2]_s$ case was predicted to fail in a buckling mode before any stress component became critical. Software limitations prevented the calculation of interlamina stresses from the results of the nonlinear analyses, however these were assessed from linear analyses of perturbed meshes, and by creating quasi-three-dimensional models from beams and shells, as proposed by Nishiwaki et al. [5]. Interlamina stresses did not appear to be critical for these laminates and loading condition.

Results

Deformations

The load vs. deflection curves determined for each laminate from the geometrically nonlinear analyses are shown in Fig. 5. A postbuckling response was predicted for the $[90/45/-45/0]_{as}$ laminate, however numerical difficulties were encountered at the bifurcation point for the other two laminates. All three curves show a well defined nonlinear region, confirming the need for a geometrically nonlinear analysis. The analyses which failed to follow the load deflection behaviour into the stable postbuckling region are a result of the structure approaching zero stiffness at the point of buckling and the governing matrix becoming singular. In practice the analytical postbuckling responses were not realised experimentally because the large strains incurred in the postbuckling region result in laminate failure which is not simulated in the analysis. Fig. 6 shows the deformations of the $[90/45/-45/0]_{as}$ laminate, illustrating the change from pre- to postbuckling deformation mode and the resulting large deformations that are predicted.

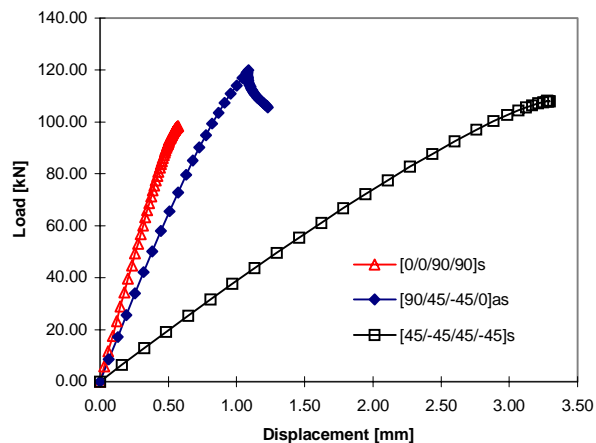
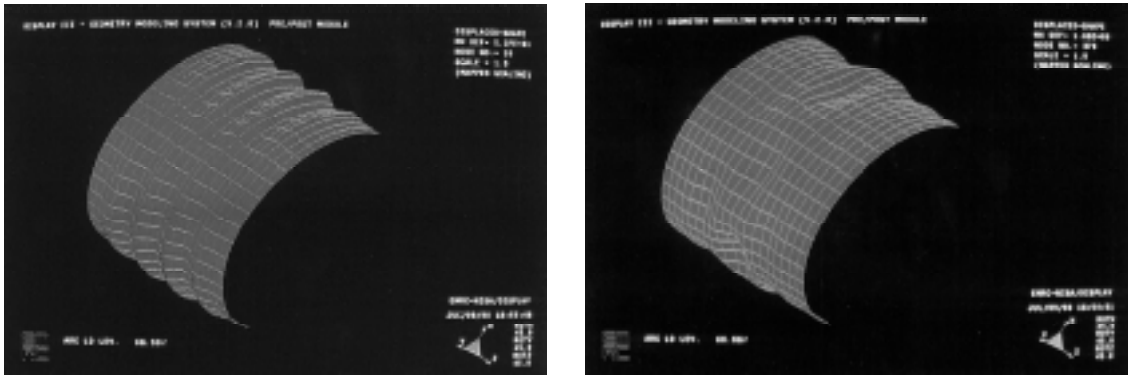


Fig. 5: Nonlinear buckling load deflection responses



(a) Prebuckled

(b) Postbuckled

Fig. 6: Prebuckled and postbuckled deformed shapes for $[90/45/-45/0]_{as}$ laminate

Effect of Material Nonlinearities

The $[90/+45/-45/0]_{as}$ and $[0_2/90_2]_s$ experimental load-deflection curves followed the same basic shape as the FEA predictions. However as shown in Fig. 7, the experimental curve for the $[+45/-45/+45/-45]_s$ case diverges from the geometrically nonlinear predictions at a load of approximately 25 kN. This load corresponds to the onset of acoustic emissions, as shown in Fig. 2, and corresponds to FEA predictions of maximum shear stresses of approximately 30 MPa. As the shear stiffness of these types of materials is typically significantly nonlinear, combined material and geometric nonlinear models were created which used a nonlinear shear stress behaviour for the laminae. The exact shear stiffness characteristics for the material were not available, so generic data was used with the initial modulus scaled to match the previous linear material properties. Numerical difficulties at yield prevented results being obtained from a piecewise nonlinear shear model, however modeling the shear behaviour as bilinear was more successful as shown in Fig. 7. The results should be regarded as only indicative since the material stiffness and yield parameters are estimated, and the bilinear model was unable to model the shear stress behaviour of the material through to final failure. However correlation with the experimental results is greatly improved for the initial part of the experimental curve, demonstrating that the nonlinear shear behaviour of the material is a significant factor in the global response of the cylinders.

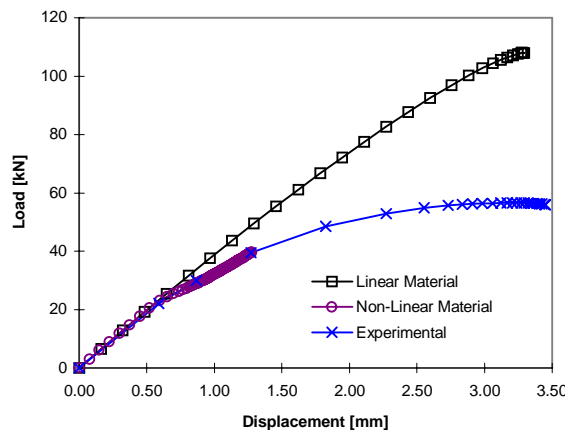
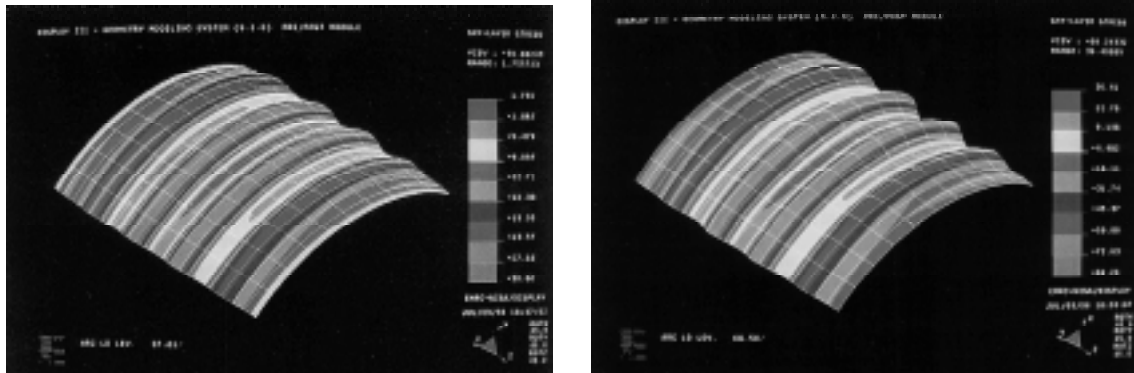


Fig. 7: Effects of shear nonlinearity on buckling load predictions for $[+45/-45/+45/-45]_s$ specimen

Predicted Stress Levels

There was very good correlation between the onset of acoustic emissions and high predicted shear stresses for the $[90/+45/-45/0]_{as}$ laminates. Fig. 8 shows contour plots of the shear stresses within the most highly loaded lamina. At a load of 64.5 kN which corresponds to the onset of acoustic emissions the maximum shear stress is approximately 30 MPa, while at 117 kN which corresponds to the final mixed mode failure of the cylinders the predicted shear stress is approximately 86 MPa. For the $[+45/-45/+45/-45]_s$ case the onset of acoustic emissions also correlates with a predicted shear stress of approximately 30 MPa and the maximum predicted shear stress at failure is approximately 83 MPa.



(a) Layer 7 at 64.5 kN

(b) Layer 7 at 117 kN

Fig. 8: Shear stress contours for $[90/45/-45/0]_{as}$ laminate

Failure Loads

Table 2 summarises the predicted and measured failure loads for each specimen. The linear FEA (LFEA) laminate failure models apply the maximum stress failure criterion to a linear static analysis, and the LFEA buckling results refer to a linear eigenvalue analysis. The main limitation of the linear analyses is that they do not consider the increases in bending stresses and reductions in stability which occur as deflections and rotations of the shell wall increase. The critical failure loads predicted by the nonlinear FEA (NLFEA) for each laminate type are highlighted, and correlate well with the experimental results. In the $[90/45/-45/0]_{as}$ case the predicted load for laminate failure (maximum stress criterion) is almost exactly the same as that for a buckling failure, which supports the experimental observations of a mixed mode failure. The poorest correlation is for the $[0_2/90_2]_s$ specimens, for which the buckling failure load is very sensitive to imperfection magnitude and only limited experimental data was available.

Table 2: Predicted failure loads

Laminate	Laminate Failure		Buckling		Load	Experimental Mode
	LFEA	NLFEA	LFEA	NLFEA		
[90/45/-45/0] _{as}	226	117	171	120	121	Laminate and Buckling
[02/902] _s	318	>98	120	98	109	Buckling
[45/-45/45/-45] _s	62	53	130	108	56	Laminate

CONCLUSIONS

Each of the laminate configurations demonstrated a different mode of failure. The [02/902]_s specimens failed in an asymmetric local buckling mode, with virtually no prebuckling acoustic activity. In the case of the [90/45/-45/0]_{as} laminates there was moderate acoustic activity at load levels as low as 40% of the final failure load, suggesting that damage was occurring within the laminate well before the final failure in a buckling related mode. The [45/-45/45/-45]_s demonstrated significant acoustic activity from low load levels and failed in a material fracture mode.

Nonlinear finite element analyses demonstrated that geometric imperfections and constraint effects result in localised bending deformations which generate high intralamina stresses, particularly as inplane shear within the 45° plies. The nonlinear shear behaviour of the laminae also influences the stress fields within the shells, particularly for the +/-45° laminate. The load at failure of the [02/902]_s specimens correlated well with nonlinear FEA predictions of local buckling.

The onset of acoustic emissions from the [90/45/-45/0]_{as} specimens appears to be related to intralamina shear failures within some of the 45° laminae. The final failure of these specimens occurred at loads close to those predicted by nonlinear FEA buckling analyses suggesting that the prebuckling damage did not significantly degrade the laminate stiffness. The [45/-45/45/-45]_s cylinders failed at a load corresponding to shear failure of the laminae, at a load of approximately 50% of the predicted buckling load. The proposed design methodology accurately predicted the mode and failure load of each of the laminates. The key feature of the methodology is that it recognises the significant effect that geometric imperfections have on the localised laminate stress fields, as well as on local buckling behaviour.

ACKNOWLEDGEMENTS

This research was supported financially by the New Zealand Foundation for Research, Science and Technology under Contract CO 8513. Glen Dromgoole was a graduate student at the Department of Mechanical Engineering, University of Auckland during the course of this work, and their assistance is gratefully acknowledged.

REFERENCES

1. Donnell L. H. and Wan C. C., "Effect of Imperfections on Buckling of Thin Cylinders and Columns Under Axial Compression", *J. of Applied Mechanics*, Vol.17, 1950, pp. 73-83.
2. Bull, J.W., *Finite Element Analysis of Thin-Walled Structures*, Elsevier Applied Science Publishers, 1988
3. Camponeschi, E.T., Jr, "Compression Response of Thick-Section Composite Materials", Report DTRC-SME-90/60, David Taylor Research Center, October 1990
4. Hinton, M.J., Soden, P.D., and Kaddour, A.S., "Strength of Composite Laminates Under Biaxial Loads", *Proceedings Tenth International Conference on Composite Materials*, Whistler, British Columbia, Canada, August 14-18, 1995, Vol. IV, pp. 65-72
5. Nishiwaki T., Yokoyama A., Maekawa Z., Hamada H, "A new numerical modeling for laminated composites", *Composite Structures*, Vol. 32, 1995, pp. 641-647.

APPLIED THEORY OF SANDWICH PANELS ALLOWING FOR LOCAL EFFECTS

V.A. Polyakov

*Institute for Polymer Mechanics of Latvian Academy of Science,
Riga, Latvia LV-1006*

SUMMARY: The model of cylindrical bending was advanced including in its kinematics a normal contractability and transversal shear and offering an analysis of the effect of free end as well as local load on panel stress state. Direct variational method employed in the model with four degrees of freedom made along with the equations of the twelfth order derived possible to lay down the six conditions for generalized forces at the free end correctly. The solution has been derived with the help of the Laplace transform method and represented both for continuous and piecewise constant as well as point load functions in a close form. The analysis of transversal normal stresses for three-point bending has been carried out. The body of estimates for these stresses at the centre, on the supports and at the free panel end resisting analysis by previously known applied models has been established.

KEYWORDS: layered plate, boundary effect, transversal stresses, cylindrical bending, point force, local effect, Dirac's function

INTRODUCTION

The survey of present-day design procedures and experimental data on sandwich panels [1] points to the following circumstances: the refinement of design models due to allowing for transverse shear for deflection in bending is the one of correcting agents in selection of sandwich structure parameters. Refined approaches, where deflection in stack bending is a function of layer location across the thickness take account of local effects and techniques for predicting how a panel will behave in circumstances where it is being fixed. Applied theory for discrete layered model considering deformation of a normal was developed in [2],[3]. Solutions of boundary-value problem according to the approach [3] were carried out to detect the distinctions of elementary loading cases at the end of a semi-infinite layered strip. Substantial effect arising from different layer deflections is obtained in the boundary-value problem for a layered half-space in action on its boundary the point force perpendicular to a layer plain [4]. Change-over from the solution for semi-infinite region to finite one taken up by a layer stack is not trivial and calls for individual consideration using mathematical procedure that fits adequately boundary-value problem.

Deformation Features Caused by Point Forces and at Free Face

The following issue under consideration associated with the justification of the procedure for derivation of sandwich plate bending solution in point force action on its surface. Elementary method of point force representation in the form of expansion into series in terms of boundary-value problem eigenfunctions - that is usually trigonometric series - inherit in it the two limitations: the solutions derived in this fashion are only applicable for uniform boundary conditions and poorly convergent for stresses.

In relation to the local nature of loads in action of point force on a panel or piecewise constant nature of distributed loads we will use the Laplace integral transform. This analytical approach allows one to drop a representation of the load as poorly convergent series and thereby disregard a consideration of the solution convergency.

In the boundary-value problem [5] with the statement of boundary conditions at support section for the same sandwich model, solved by numerical method having five degrees of freedom in finite element, the deflections of both outer layers were prohibited and only non-zero values of lengthwise displacements were allowed (or forbidden). It is possible in theory but, practically, with a transversal compressibility the realization of a device prohibiting the deflections of both outer layers at the panel free face seems to be problematical. In the [2], [6] the widening possibilities in the kinematics of sandwich deformation were described with the help of functions for displacements and internal stresses and were not in every aspect correct. Internal stresses at the surfaces of layers mating in the interaction mechanism of three layers were considered as the external surface loads of elementary layer - a beam or a plate. In doing so the joint deformation of elements (layers) was described by the set of equations from a theory of beams (plates) which was not identical in its notation with the equations of direct or mixed variation principle. The main disagreement with the statement of the problem taken in present work, as it can be revealed, is in the definition of boundary conditions that should be aligned with natural ones for a free face.

Transversal force Q_x at the end face should be defined layer by layer and in its notation the shear stresses in a middle layer as well as the Kirchoff forces for outer layers considered in accordance with direct variational method based on the variations of displacements. There are six boundary force factors at a panel end face, which at not uniform notation of their expressions in the case of fixing in the end face through different structural versions can also be offered. In the event that the point support falls on the end of a panel the transversal force is equal in value to the reaction if it occurs in the end face, otherwise at the point pressure on the outer surface of a lower layer, the transversal force equals zero.

ANALYTICAL DESCRIPTION OF THE MODEL

Cylindrical bending of a panel of asymmetric structure with the load versions shown in Fig. 1a,b is described by the kinematic model of [3],[5] type. Basically, in the model the classical rotation mechanism of a normal according to the Kirchoff - Love in face layers and an uniform transverse shear coupled with a normal reduction throughout the middle layer section thickness are taken. The joint deformation of three layers is thus defined by the four degrees of freedom characterizing the deflections w_t and the longitudinal displacements u_t , $t = 1,2$ of face layers.

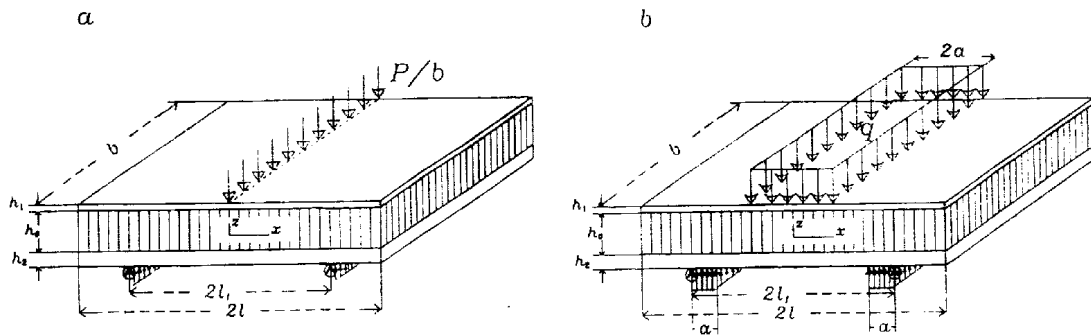


Fig. 1: Dimensional parameters and loading chart of sandwich panel. a - point force; b - piecewise-distributed load

Equations and boundary conditions

Elastic potential of a three-layer system from the model taken is written as:

$$2V = b \int_{-l}^l L(u_t, u'_t, w_t, w'_t, w''_t) dx = b \int_{-l}^l \left\{ B[u_2 - u_1 + (h_0 + h_1)(\chi_0 w_2' + w_1')/2]^2 + C(w_2 - w_1)^2 + \sum_{t=1,2} [D_t (w_t'')^2 + A_t (u_t')^2 - 2q_t w_t] \right\} dx \quad (1)$$

where D_t, A_t are respectively the cylindrical and membrane stiffnesses of face layers, $B = G_{xz}/h_0$, $C = E_z/h_0$ and $q_t(x)$ is the surface load on the outer planes of the layers. The equilibrium equations of the system are the Euler's equations of a variational problem $\delta V = 0$ with the Lagrange's function, which is the integrand in (1). In such a manner the following set of equations of the twelfth order can be derived:

$$\begin{aligned}
\bar{u}_1'' + k_1[\bar{u}_2 - \bar{u}_1 + (\chi_0 \bar{w}_2' + \bar{w}_1')/2] &= 0 \\
\bar{u}_2'' - (\gamma_1 - 1)k_1[\bar{u}_2 - \bar{u}_1 + (\chi_0 \bar{w}_2' + \bar{w}_1')/2] &= 0 \\
\bar{w}_1^{iv} - (6/\mu^2)k_1[\bar{u}_2' - \bar{u}_1' + (\chi_0 \bar{w}_2'' + \bar{w}_1'')/2] - 12k_2(\bar{w}_2 - \bar{w}_1) &= \bar{q}_1 \\
\bar{w}_2^{iv} - (6/\mu^2)\gamma_2\chi_0 k_1[\bar{u}_2' - \bar{u}_1' + (\chi_0 \bar{w}_2'' + \bar{w}_1'')/2] + 12\gamma_2 k_2(\bar{w}_2 - \bar{w}_1) &= \bar{q}_2
\end{aligned} \tag{2}$$

where the right - hand sides for the point forces ,Fig 1a, are given in terms of the Dirac's function $\delta(\xi)$, and for the piecewise distributed load are specified by the unit function $\eta(\xi)$ of a delayed argument:

$$\begin{aligned}
\bar{q}_1 &= 2q_0\delta(\xi), \quad \bar{q}_2 = -\gamma_2 q_0\delta(|\xi| - \xi_1), \quad a = 0, \\
\delta_a(\xi) &= [\eta(|\xi|) - \eta(|\xi| - \xi_a)]/(2\xi_a), \quad a \neq 0
\end{aligned} \tag{3}$$

and the following relative values are introduced:

$$\begin{aligned}
\xi &= x/(h_1 + h_0), \quad u_i = \bar{u}_i/(h_1 + h_0), \quad w_i = \bar{w}_i/(h_1 + h_0), \quad i = 1, 2 \\
k_1 &= m_z/[\mu(1 - \mu)], \quad k_2 = n_z/[\mu^3(1 - \mu)], \quad k_3 = 3\chi_0 m_z/[\mu^3(1 - \mu)] \\
\mu &= h_1/(h_1 + h_0), \quad \chi_0 = (h_2 + h_0)/(h_1 + h_0), \quad \chi = h_2/h_1 \\
\gamma_1 &= 1 + 1/(n_x \chi), \quad \gamma_2 = 1/(n_x \chi^3),
\end{aligned} \tag{4}$$

$$\begin{aligned}
n_x &= (E_x^{(2)}/E_x^{(1)})[(1 - \nu_1^2)/(1 - \nu_2^2)], \quad n_z = (E_z/E_x^{(1)})(1 - \nu_1^2), \\
m_z &= (G_{xz}/E_x^{(1)})(1 - \nu_1^2), \quad q_0 = 6P(1 - \nu_1^2)/[E_x^{(1)}b(h_1 + h_0)\mu^3]
\end{aligned}$$

Boundary conditions at the free panel end $\xi = \xi_1$ are defined as natural at the variation of the functional V . Their notation corresponds the homogeneous expressions of the generalized transversal Kirchhoff's force, the bending moment and the longitudinal load of every face layer:

$$\begin{aligned}
\bar{w}_i'''(\pm\xi_1) - \lambda_i[\bar{w}_1' + \chi_0 \bar{w}_2' + 2(\bar{u}_2 - \bar{u}_1)]_{\pm\xi_1} &= 0 \\
\bar{w}_i'(\pm\xi_1) = u_i'(\pm\xi_1) &= 0, \quad i = 1, 2 \\
\text{where } \lambda_1 &= k_3/\chi_0, \quad \lambda_2 = k_3\gamma_2.
\end{aligned} \tag{5}$$

DECISION FUNCTIONS

Operational solution technique

Solution of the inhomogeneous set of equations (2) with discontinuous functions at its right-hand side was derived through the use of the integral Laplace transform. The followed procedure for symmetric load distribution about the central panel section $\xi = 0$

furnishing the initial values taken $w'_i(0) = u_i(0) = 0$, $i = 1, 2$ has been detailed in [7].

As a result of inverse transformation the set of eigenfunctions normalized at the origin of coordinate axis $\xi = 0$ was derived:

$$p_n(\xi) = \int_0^\xi p_{n+1}(\xi) d\xi, \quad (6)$$

$$p_n(0) = 0, \quad p_5(0) = 1, \quad n = -5, -4, \dots, 3, 4$$

$$p_5(\xi) = (a_1^4/d_1)ch(a_1\xi) + (1 - a_1^4/d_1)ch(\alpha\xi)\cos(\beta\xi) +$$

$$+ (1/d_1)[2\alpha\beta(\alpha^2 - \beta^2) - \rho_0(\alpha^2 - \beta^2) + 2\alpha_1^2\alpha\beta]sh(\alpha\xi)stn(\beta\xi), \quad (7)$$

where

$$d_1 = 3a_1^4 + 2b_2a_1^2 + b_1, \quad \rho_0 = \sqrt{3}(\rho_1 - \rho_2)/(\rho_1 + \rho_2),$$

$$\rho_{1,2} = (\sqrt{\Delta} \mp c_0/2)^{1/3}, \quad \Delta = (c_1/3)^3 + (c_0/2)^2 \quad (8)$$

$$c_1 = b_1 - b_2^2/3, \quad c_0 = (2/27)b_2^3 - (1/3)b_1b_2 + b_0$$

and with $\Delta > 0$ the numbers a_1, α, β are respectively the greatest real root, positive real and imaginary parts of the complex roots of characteristic equation derived for the set (2) on reducing the zero root of the six multiplicity:

$$P_6(t) = t^6 + b_2t^4 + b_1t^2 + b_0 = 0 \quad (9)$$

$$b_0 = -12k_1k_2[(1 + \gamma_2)\gamma_1 + \gamma_2(3/\mu^2)(1 + \chi_0)^2]$$

$$b_1 = 12k_2(1 + \gamma_2), \quad b_2 = -k_1[\gamma_1 + (3/\mu^2)(1 + \gamma_2\chi_0^2)]$$

Solution variants of the (7) type at $\Delta \leq 0$ and also for the degeneration of the coefficients (9) at $k_1 \rightarrow 0$ or $k_2 \rightarrow 0$ have been represented in [7].

The particular solution to the set (2) was represented as the linear combination of the (6) type functions of argument shifted along the axis ξ as to parameters ξ_a, ξ_1, ξ_l :

$$\tilde{p}_n^a(\xi_1, \xi_l) = (1/\xi_a)[p_n(\xi_l) - p_n(\xi_l - \xi_a) + p_n(\xi_l + \xi_a - \xi_1) -$$

$$- p_n(\xi_l - \xi_1)], \quad (10)$$

Therefore the boundary-value problem with the condition (5) have

been reduced to the Cauchy problem i.e. determination at the point $\xi = 0$ the initial displacement values and their derivatives to the third order inclusive.

Transversal normal stresses in three-point bending

For the purpose of specific application of the design formulae derived the transverse stress σ_z in three-point bending of a panel (see Fig.1,a) has been studied. In this event in the (10) the length $a = 0$ and thus the limiting function value \tilde{p}_n is deduced by differentiation with respect to parameter ξ_a .

The following formula for transversal stress in the case of a symmetrical sandwich panel has been derived:

$$\sigma_z(\xi) = - \frac{q_0 E_z}{1-\mu} \left\{ \hat{w}_\Delta \operatorname{ch} \alpha \xi \operatorname{cosa} \xi - \frac{1}{4\alpha^4} \left[(\operatorname{ch} \alpha \xi \operatorname{cosa} \xi)^{\sim} + 4\alpha^2 \alpha_\alpha \operatorname{sh} \alpha \xi \operatorname{stna} \xi \right] \right\} \quad (11)$$

where $(\operatorname{ch} \alpha \xi \operatorname{cosa} \xi)^{\sim}$ equals $(1/\xi_a)(-1 + \operatorname{ch} \alpha \xi \operatorname{cosa} \xi)$ in $0 \leq \xi < \xi_a$, $(1/\xi_a)[\operatorname{ch} \alpha \xi \operatorname{cosa} \xi - \operatorname{ch} \alpha(\xi - \xi_a) \operatorname{cosa}(\xi - \xi_a)]$ in $\xi_a \leq \xi < \xi_1 - \xi_a$, $(1/\xi_a)[-1 + \operatorname{ch} \alpha \xi \operatorname{cosa} \xi - \operatorname{ch} \alpha(\xi - \xi_a) \operatorname{cosa}(\xi - \xi_a) + \operatorname{ch} \alpha(\xi + \xi_a - \xi_1) \operatorname{cosa}(\xi + \xi_a - \xi_1)]$ in $\xi_1 - \xi_a \leq \xi < \xi_1$, and according to (10) in $\xi \geq \xi_1$. The expression (11) is only dependent on the ratio of the Young's moduli E_x/E_z and independent of G_{xz} . In this formula the symmetrical solution part for deflections is only considered as defined as their difference $w_\Delta = w_2(0) - w_1(0)$. For the remaining parameters with $\alpha = \beta = (\sqrt{2}/2)b_1^{1/4}$ the following notation is introduced:

$$s_0(\xi_1) = (1/2\alpha)[\operatorname{ch}(\alpha\xi_1)\operatorname{stn}(\alpha\xi_1) + \operatorname{sh}(\alpha\xi_1)\operatorname{cos}(\alpha\xi_1)]$$

$$s_1''(\xi_1) = \alpha^2 \operatorname{sh}(\alpha\xi_1)\operatorname{stn}(\alpha\xi_1), \quad \hat{w}_\Delta = -w_\Delta/q_0 = \frac{\tilde{s}_0^a(\xi_1, \xi_1) - 2\alpha_\alpha s_0''(\xi_1)}{b_1 s_0(\xi_1)}$$

$$\alpha_\alpha = - \frac{4\alpha}{b_1} \cdot \frac{s_1''(\xi_1)\tilde{s}_0^a(\xi_1, \xi_1) - s_0(\xi_1)\tilde{s}_1''^a(\xi_1, \xi_1)}{\operatorname{sh}(2\alpha\xi) + \operatorname{stn}(2\alpha\xi)} \quad (12)$$

The oscillating variation of stresses σ_z along the panel length caused by the presence of trigonometric functions in (11) is defined by a big gradient in the vicinity of a central section and close to panel support points. The diagram of these

stresses was displayed in the Fig.2 a,b for a relatively short panel from the material of Aluminum/Polyurethane foam type at $h_0 = 10$ mm, $h_1 = 10$ mm, $G_{xz} = 138$ MPa, $E_z = 310$ MPa, $E_x = 40$ GPa.

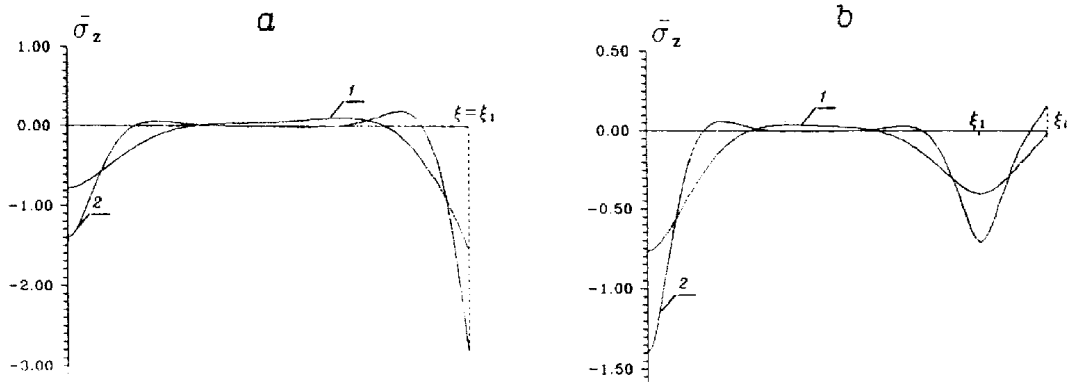


Fig.2: Variation of relative transversal stress $\bar{\sigma}_z = \sigma_z/\sigma_0$ along the panel length: 1 - $E_z = 0.31$ GPa, 2 - $E_z = 3.50$ GPa
 $\sigma_0 = P/bh$, $h = 2h_1 + h_0$. a: $2l_1 = 2l = 5h$, b: $2l_1 = 5h$, $2l = 6h$

Fundamental change in the transfer mechanism of pressure on a middle layer occurred in the displacement of supports a half the panel thickness from the end (Fig.2 b). Given in the last case the stress $\sigma_z(\xi_1)$ is half as many as $\sigma_z(0)$ the inverse value of their ratio in the case of the support coincident with the end (Fig. 2 a) contrary to what might be expected from static considerations (end force $P/2$ less than central force P) was derived. The effect is responsible for the rotation of a layer free face through an acute angle. The mathematical analysis of the expression (11) for $l = l_1$, as distinct from the case $l \gg l_1$, corresponding the condition of the "console" type both for the support section $w_1'(l_1) = w_2'(l_1) = 0$ and for the central one $w_1'(0) = w_2'(0) = 0$, validates the estimates of $\sigma_z(l_1)$ derived.

With distance from supports the stresses σ_z are damped and for the infinite strip of the same sandwich structure at $\xi \gg \xi_1$ become zero. The asymptotic formula for infinite sandwich strip loaded on the section $2l_1$ from the system of three point forces is displayed for $\xi \geq \xi_1$ and any $\xi_1 \geq 0$ in the following form:

$$\sigma_z(\xi) = -q_0 E_z [8\alpha^3(1-\mu)]^{-1} [2\psi(\xi) + \psi(\xi - \xi_1) + \psi(\xi + \xi_1)] \quad (13)$$

where $\psi(\xi) = e^{-\alpha\xi}(\cos\alpha\xi + \sin\alpha\xi)$.

For $0 \leq \xi \leq \xi_1$ the formula (13) interchanging in it the values ξ and ξ_1 should be employed.

A comprehensive idea of a transformation of the stress $\sigma_z(\xi)$ diagram against the panel length and the extent of a span between the supports in three - point bending is shown in Fig. 3a,b in dimensionless coordinates.

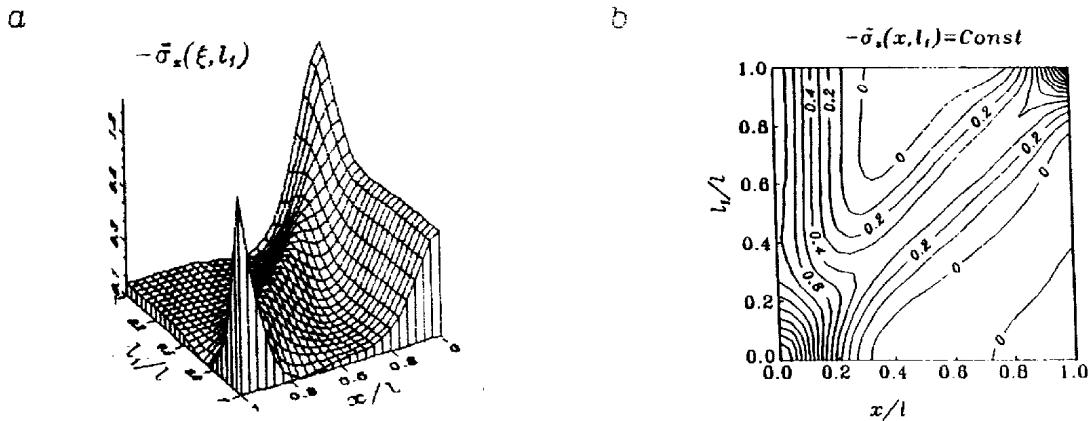


Fig.3: Variation of transversal stress diagrams along the panel length with relative displacement of supports from the centre to the panel end (l_1/l) at $2l=5h$.

a - coordinate lines on the surface, b - stress level lines

Stress at the centre in bilateral pointwise loading with the forces $\pm P$ ($x = l_1 = 0$) proved to be equal in magnitude to the stress at the end with support reaction $P/2$, provided $l = l_1$.

Other cases, that hold the greatest interest correspond to the diagram $\sigma_z(0, l_1)$ represented by coordinate line on the surface at $x = 0$ and the $\sigma_z(x = l_1)$ diagram represented at the surface by the line along its "ridge". These curves as the coordinate l_1 recedes from the centre and the panel end are represented by straight lines, having constant Z - coordinates equal respectively to $1/2$ and $1/4$ of $\sigma_z(0, 0)$. Fairly long coordinate intervals correspond to $\sigma_z > 0$. The positive σ_z values are less than expected by an order of magnitude than the stress at the centre. Their domains are outlined by zero level lines in Fig. 3b.

CONCLUSIONS

By the development of a bending problem for the layered plate of a sandwich type its general solution (7), (10) suitable for the cases of arbitrary piecewise constant and point loads applied symmetrically about central section was derived. The correction

α_α to face layer curvatures, represented in the closed form (12) refines the bending characteristics deduced from simplified applied theories. The analysis of transversal deformation, considered in these theories basically at the expense of a transversal shear, have been extended to the joint consideration of a transversal reduction as the most important factor in local loads. The formulae (11),(13) derived for transversal stress σ_z for three-point panel bending allow one to clarify the interplay of parameters defining the concentration and the value of these stresses in the panels of a finite and infinite length. The analytical solution variant of the bending problem for layered model can be employed both in addition to simplified design methods and for the detailed investigation of the limiting parameter values of the model evaluating its efficiency.

REFERENCES

1. Johnson, A.F. and Sims G.D., "Mechanical properties and design of Sandwich materials", *Composites*, Vol.17, No.4, 1986, pp. 321-328.
2. Frostig Y., "On the Stress Concentration in the Bending of Sandwich Beams with Transversely Flexible Core", *Composite Structures*, Vol.24, 1993, pp. 161-169.
3. Bolotin, V.V. and Novitchkov, Yu.N, *Mechanics of Multilayer Structures*. Mashinostroenie, Moscow, 1980. (in Russian)
4. Bolotin, V.V. and Parcevsky, V.V., "Stresses in layered media of the action of concentrated force", *Mechanics of Solid Bodies*, No.2, 1968, pp. 52-57 (in Russian)
5. Chen, R.S. and Wu, P.C., "Analysis of the Special Finite Element Model for Honeycomb Composites", *Proceedings of the Ninth Int. Conf. on Composite Materials*, Madrid, July 12-16, 1993. Vol.IV: Composites Design, Miravete, A. Ed., pp.392-397.
6. Thomsen, O.T. and Rits, W., "Analysis of Sandwich Plate Theory", *Proceedings Tenth International Conference on Composite Materials*, Whistler, British Columbia, Canada, August 14-18, 1995, Vol. V: Structures, Poursartip, A. and Street, K.N., Eds, pp. 35-42.
7. Polyakov, V.A., "Deformation Features of Sandwich Panels in Cylindrical Bending by Point Forces. 1. Analytical construction", *Mechanics of Composite Materials*, Vol.32, No.5, 1996, pp.588-611.

ACCURATE PREDICTION OF THERMAL DEFORMATION OF SANDWICH PANELS CONSIDERING THE EFFECT OF ADHESIVE

Shigenori Kabashima

*Advanced Technology R&D Center, Mitsubishi Electric Corporation
Miyashimo1-1-57, Sagamihara, Kanagawa, 229 Japan*

SUMMARY: Adhesive has been reported to influence the thermo-mechanical behavior of honeycomb sandwich panels with very thin skins which are widely used for satellite structures. Though high dimensional stability is a great interest in the aerospace field, the effect of adhesive has never been quantitatively investigated. This paper describes the effect of adhesive and the computational modeling of sandwich panels.

First, dimensionally stable sandwich panels with different bonds were fabricated and their coefficients of thermal expansion(CTEs) were evaluated. For this measurement, a high precision measuring system was developed. Second, a finite element model was built by simulating a unit cell of a honeycomb sandwich panel. In this model, the effect of adhesive was taken in to account. Suitable boundary conditions were discussed here, so that repetitive structures of a sandwich panel could be effectively analyzed by the unit cell model. Finally, the calculated CTEs were compared with the experimental result and the thermo-mechanical behavior of sandwich panels was discussed.

KEYWORDS: honeycomb sandwich panel, coefficient of thermal expansion, adhesive, finite element method

INTRODUCTION

Honeycomb sandwich panels with thin PMC(Polymer Matrix Composite) skins have been used to fabricate dimensionally stable satellite structures[1][2]. In the severest cases, CTEs of honeycomb sandwich panels are required to be controlled with the accuracy of 0.1 ppm/K. Recently developed pitch based high modulus graphite fibers have good potentiality to realize this kind of structures. However, this is not a easy task because a methodology to accurately predict thermal deformation of sandwich panels is not established. In actual design of satellite structures, thermo-mechanical behavior of sandwich panels is often calculated by laminate theory assuming that honeycomb core and adhesive are plies of homogeneous materials[3]. However this method does not always produce good results because of complex behavior of constitutional materials; honeycomb core and adhesive. Equivalent properties of honeycomb cores are reported to have dependency on the properties of skin materials[4]. Besides, orthotropic behavior of honeycomb cores are well known. Form of adhesive is also known to impact the thermo-mechanical property of sandwich panels, although this effect have never been quantitatively studied. Finite element method(FEM) is thought to be helpful to study the

thermal deformation of sandwich panels considering the effects of all the constitutional materials[5]. In the present paper, a FEM model schematizing the detailed structure of honeycomb sandwich panels is presented, in which the effect of honeycomb core and adhesive on the thermal deformation is taken into account. In order to make the simulation effective, the models are focused on the structure of a unit cell of honeycomb sandwich panels. Validation of these models is also discussed comparing with experimental tests.

EXPERIMENTAL TEST

In order to evaluate the influence of adhesive, dimensionally stable sandwich panels with different skin/core bonds were fabricated and their CTEs were measured. For this purpose, a high precision CTE measuring system was originally developed.

Test Specimens

Three kinds of sandwich panels were manufactured with materials shown in Table 1; thin PMC skin (high-modulus graphite fiber reinforced epoxy), aluminum honeycomb core and light weight film adhesive. K13A/934 woven fabric prepreg whose thickness is 0.07mm/ply was autoclave cured with (0/90)/(+45) configuration making the stacking sequence of sandwich panel symmetric as a whole. This is a typical configuration of sandwich panels for antenna reflectors. Then the skins and cores were bonded. Table 2 shows the skin/core bonding conditions. The amount of adhesive was controlled by the number of film sheets stacked. The two kinds of adhesive forms are shown in Figure 1. Film adhesive was heated in an oven after placed on honeycomb cores for reticulation.

Table 1 Materials for sandwich panel

part	material
skin	K13A/934 (pitch based graphite fiber/epoxy)
core	Hexcel aluminum honeycomb 3/8in/ 5056/ 0.0007in/9.35mm
adhesive	FM-96U (film adhesive, 0.015psf/ply)

Table 2 Skin/core bonding condition

specimen	adhesive	
	quantity	form
Panel#1	0.015psf	reticulated
Panel#2	0.015psf	as placed
Panel#3	0.030psf	reticulated

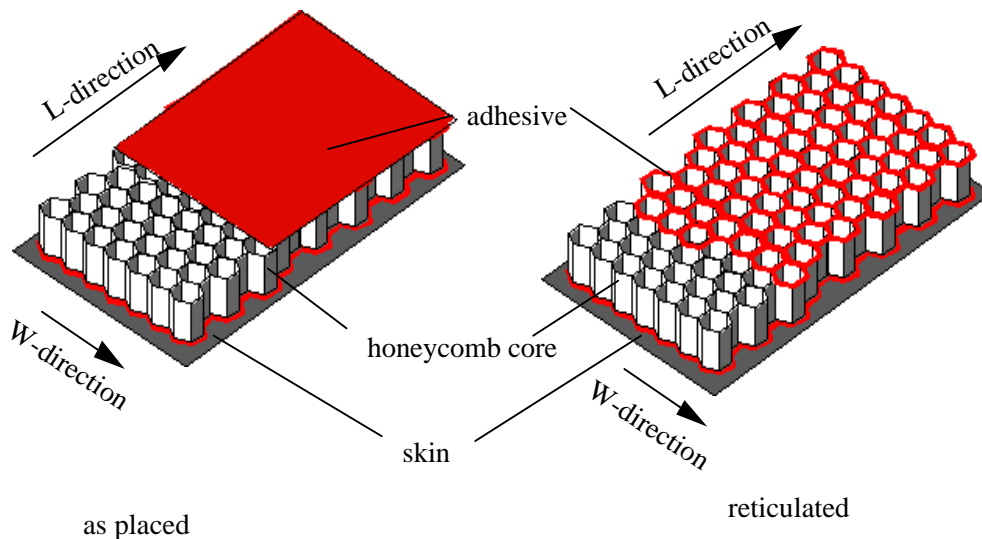


Figure 1 Forms of adhesive

CTE Measurement System

In order to evaluate the thermal deformation of sandwich panels, a high precision CTE measurement system was developed. The system consists of a temperature controlled chamber and an electro-optical displacement detecting system (Figure 2). The chamber is equipped with a pipe-shaped heater and a liquid nitrogen supplier. The maximum size of specimens for this chamber is 300*500*100mm. The temperature in the chamber is controlled between -150 and +150°C with the variation of $\pm 1^\circ\text{C}$ by circulating nitrogen gas. This temperature range meets the requirements of satellite structures. OPT-FOLLOW7100C (YAMAN LTD.) is utilized for displacement detecting system which consists of two electro-optical cameras and amplifiers. The cameras detect optical targets colored with black and white through optical fibers attached with magnification lenses. The deformation of a specimen due to temperature change is measured from the differential displacement of two targets mounted on the specimen. Targets need to be lightened with stable and intense light. Xenon lamps were chosen for the light source so that the specimen would not be heated during the measurement. Relative position of the two magnification lenses and specimen need to be unchanged during the testing. In particular, stability of the distance between the two lenses directly affects the performance of the system. Therefore, zero-expansive glass was used to fix the lenses (Figure 3).

Calibration of the displacement detecting system was carried out by measuring the displacement of a target attached to a micrometer. Then the measuring accuracy of the whole system was examined using zero-expansive glass and low expansive laminate composites as specimens with known CTEs. As the result, this system was found to have accuracy of 0.1 ppm/K and reproducibility of 0.05 ppm/K.

Test Procedure

The CTEs of the specimens between 0 and 50°C were measured. The specimens were dried in a vacuum oven under 80°C for 24 hours prior to testing and placed in the chamber after mounted with optical targets colored with black and white (Figure 4). Specimens were cooled at 0°C for 60 minutes, then heated to 50°C at the rate of 2°C/min and kept for 60 minutes. The average values of CTE between 0 and 50°C were obtained from the measured displacement of

targets caused by the deformation of specimen due to the temperature change. The measurement was carried out both for L-direction and W-direction (Figure 1).

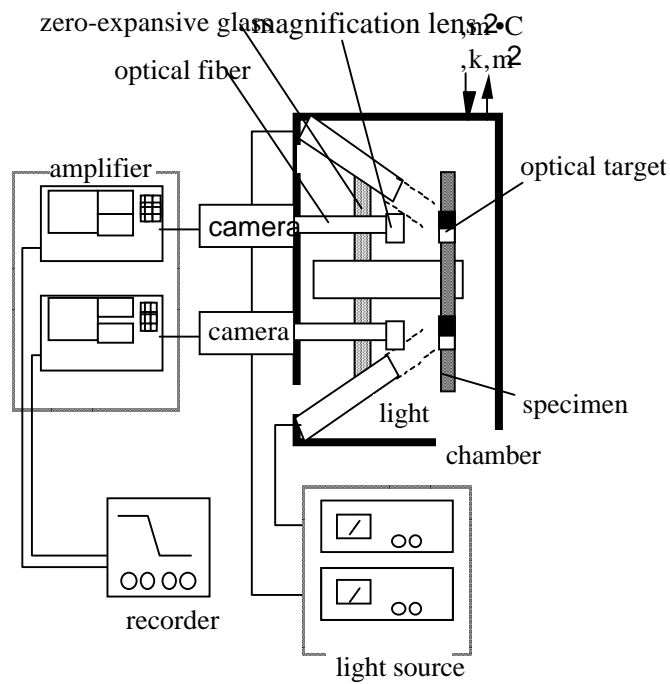


Figure 2 Configuration of CTE measurement system for honeycomb sandwich panels

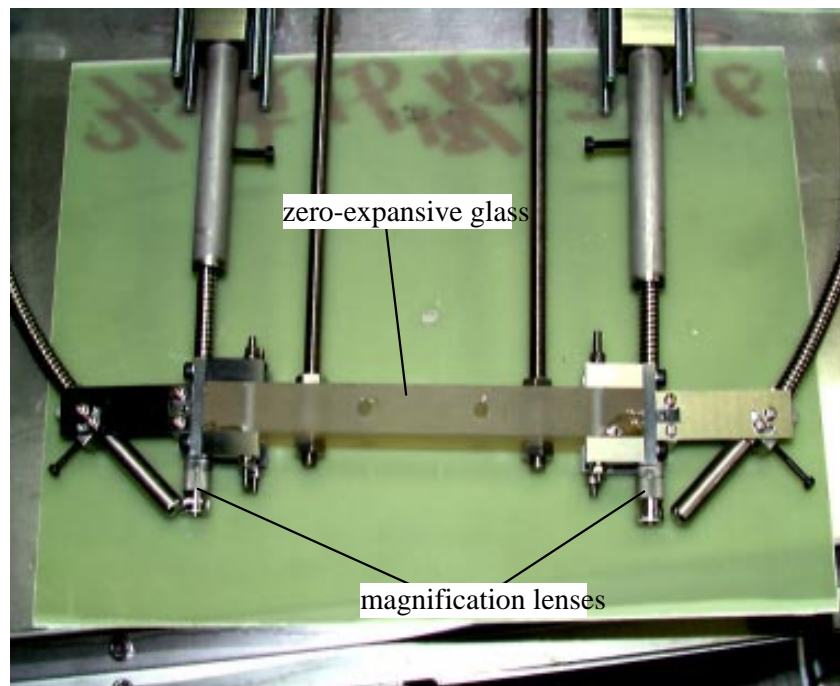


Figure 3 Configuration of magnification

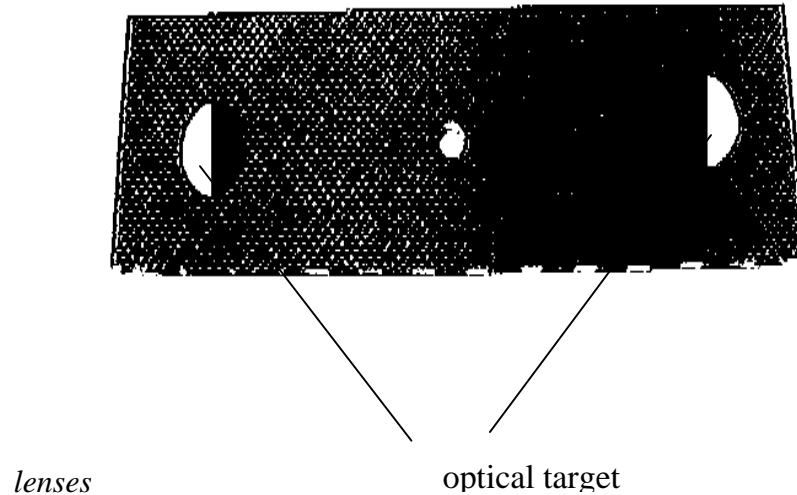


Figure 4 Test specimen with optical targets

NUMERICAL ANALYSIS

In order to study the thermo-mechanical behavior of sandwich panels and develop an effective method to predict the deformation, a FEM model simulating a unit cell of sandwich structure was built.

Unit cell Model

A FEM model simulating the thermo-mechanical behavior of honeycomb sandwich panel was built with the following assumptions;

1. The sandwich panel is plane and large enough compared with the unit cell.
2. The ply configuration of the sandwich panel is symmetrical.
3. The sandwich panel has no temperature variation.

Figure 5 shows the generated model. I-DEAS was utilized as the FEM analysis program. Thin shell element was chosen both for the honeycomb core and the skin because no bending effect was expected in the structure. Effect of adhesive was not considered here. All necessary properties of the skin were experimentally measured. As for the stiffness of honeycomb cell wall, elastic modulus of aluminum is not applicable because core reaction capability is considered to be reduced due to deformed condition of the thin cell wall. Therefore stiffness of the cell wall was calculated from the equivalent compressive modulus of the honeycomb core which was measured by the material supplier, which indicates the reducing proportion from aluminum stiffness. The CTE of the honeycomb cell wall was considered to be equal to that of aluminum.

In general, honeycomb sandwich panels cannot be correctly simulated by a unit cell model because of their repetitive structures. Though models simulating large number of cells are expected to produce good results, that kind of models require a lot of time to be built and calculated. In order to make the simulation effective, a refined unit cell model is desirable. When we considered the assumptions of this problem, it was surmised that every unit cell is symmetrical with its neighboring cells because all the cells are identical in their structure and

condition. Hence this symmetrical condition was introduced as a boundary condition for the unit cell model. When we compared the thermal deformation calculated from this unit cell model with that from a multi-cell model that contains 400 cells, they were found to agree well. Thus this unit cell model was considered to be valid to calculate the CTEs of sandwich panels.

Modeling of Skin/core Adhesive

Next, skin/core adhesive was schematized considering its form. Thin shell element and bar element were used for the as placed and the reticulated adhesive respectively(Figure 6). Thin shell elements schematizing the as placed adhesive were placed to overlap with skin elements. Bar elements schematizing the reticulated adhesive were placed between nodes on the edges of honeycomb cell. The CTE and elastic modulus of the adhesive were measured using a thermo-mechanical analyzer (Shinku-Riko DL-7000Y-RH) and dynamic mechanical analyzer (TA Instruments DMA983), respectively. CTEs of Panel#1, #2, #3 were calculated by giving these models the temperature change of 1°C.

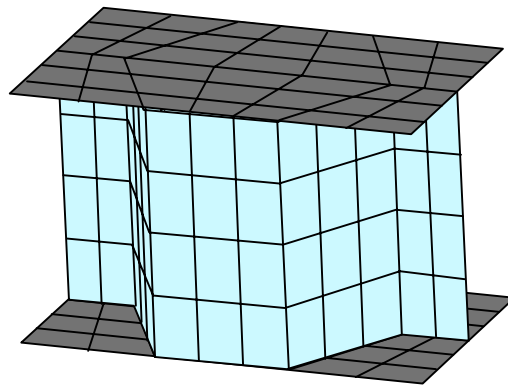


Figure 5 Unit cell model of honeycomb sandwich panel

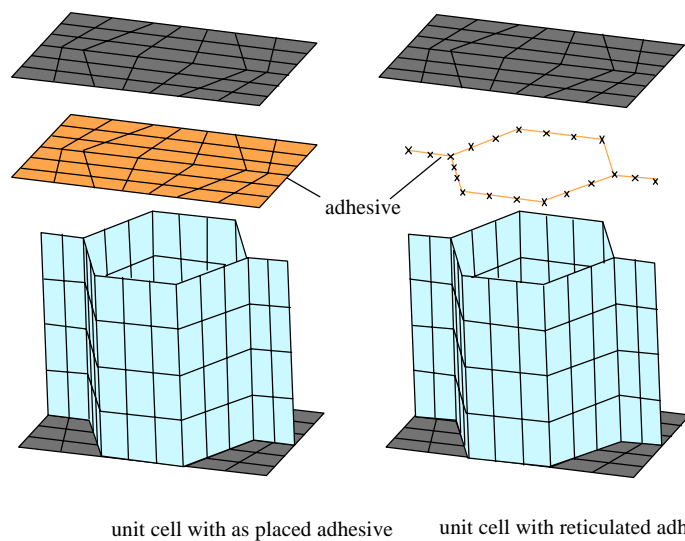


Figure 6 FEM models in which adhesive is schematized

RESULT AND DISCUSSION

Table 4 shows the measured and calculated CTEs of the specimens. The measurement shows that reticulation and reduction of adhesive makes CTEs of sandwich panels lower. Further, this effect of adhesive is correctly calculated. Focusing on the orthotropy of the panels, it was a little underestimated by the simulation; the calculated differences of CTEs between L-direction and W-direction are smaller than measured values. The walls oriented to the L-direction are made of two plies of aluminum foils bonded together and their thickness is doubled. Therefore apparent elastic modulus of these walls is larger than that of other walls. This variation of stiffness of the honeycomb walls is considered to emphasize the orthotropic behavior of the sandwich panel. In total, the prediction and the measurement agreed very well.

Table 3: Measured and calculated CTEs of the specimens

specimen	measured CTE(ppm/K)		calculated CTE(ppm/K)	
	L-direction	W-direction	L-direction	W-direction
Panel #1 (0.015psf, reticulated)	-0.52	-0.66	-0.57	-0.62
Panel #2 (0.015psf, as placed)	-0.29	-0.37	-0.26	-0.30
Panel #3 (0.030psf, reticulated)	-0.25	-0.36	-0.40	-0.44

CONCLUSIONS

By studying the effect of adhesive on the thermo-mechanical behavior of sandwich panels and a FEM model simulating a unit cell of the structure, the following was concluded.

1. Three kinds of sandwich panels with different bonds were fabricated and their CTEs were evaluated. This measurement showed that reticulation and reduction of adhesive make CTEs of sandwich panels lower.
2. In order to evaluate CTEs of sandwich panels, a accurate CTE measuring system was originally developed. This system was proved to have the measuring accuracy of 0.1ppm/K.
3. A FEM model simulating a unit cell of sandwich panels was built considering the effect of adhesive. The CTEs calculated from this model agreed very well with the measured values.

The developed predicting method is very helpful in designing satellite structures.

REFERENCES

1. Kelly J. Dodson et. al., "Thermal stability considerations for space flight optical benches", 34th International SAMPE symposium, pp.1578-1689 (1989).
2. F.Grimalde et. al., "Development of dimensionally stable lightweight composite satellite antenna structures", 34th International SAMPE symposium, pp.1590-1602 (1989).
3. L. Scolamiero, "Modeling of honeycomb for sandwich CTE prediction", ESA SP-321, pp.427-430 (1991).
4. H. Groth, "Thermal stability of sandwich reflectors", *ESA SP-243*, pp.133-139 (1986).
5. C. C. Chemis et.al., "Composite sandwich thermostructural behavior: computational simulation", NASA 0948, pp.370-381(1986).

FREE VIBRATION OF COMPOSITE SHELLS

S. Mirza¹ and N. Li²

¹ *Department of Mechanical Engineering, WPI, Worcester, MA, USA*

² *Department of Mechanical Engineering, University of Ottawa, Ottawa, Canada*

SUMMARY: A comprehensive analytical method is presented here for the vibration of cross-ply laminated shells with general boundary conditions. The approach is based on the combination of the superposition and the state-space techniques. A refined higher-order shear deformation theory is employed. Non-dimensional fundamental frequencies are obtained for shells having two adjacent sides clamped. Results are compared with those generated by the classical and first-order shear deformation theories.

KEYWORDS: vibration, cross-ply laminates, shells, superposition, state space technique, higher order theory, analytical method.

INTRODUCTION

Early analyses of laminated shells were mostly based on classical theory. This theory, although being simple to use, neglects transverse shear deformation. Consequently, it is not suitable for laminated shells in which material exhibits a finite rigidity in transverse shear.

Many theories have been developed to refine the classical theory by incorporating transverse shear effects. Among them is the first-order shear deformation theory [2-5]. In this theory the boundary conditions of zero thickness shear stresses on inner and outer surfaces are not satisfied. To overcome this shortcoming, Reddy and Liu [1] proposed a higher-order theory, to include both transverse shear deformation and zero transverse shear stresses on the surfaces.

Reviewing the published literature shows that most of the solutions are available only for simply supported shells, or those with simply supported edges on opposite sides. In this paper, an attempt is made to extend the CSST method (combination of superposition and state-space techniques), which was developed by the authors for the laminated plates [6], to the laminated cross-ply shells with general boundary conditions.

GOVERNING EQUATIONS

Using the third-order shear deformation theory, the governing equations for the cross-ply laminated shells are expressed as:

$$L_{ij} u_j = 0 \quad i, j = 1, \dots, 5 \quad (1)$$

In the above equation, the parameters u_j denote the displacement components,

$$u_1 = u; \quad u_2 = v; \quad u_3 = w; \quad u_4 = \chi; \quad u_5 = \phi \quad (2)$$

and the terms in the differential operator L_{ij} are given in the appendix A. Also u, v, w are the mid surface displacements in x, y, z directions and χ and ϕ are rotations with respect to mid surface in $\chi - z$ and $y - z$ planes.

The stress resultants can be expressed in terms of the strain components:

$$\begin{aligned}
 N_i &= A_{ij} \epsilon_j + B_{ij} k_j + E_{ij} k_j^1; \quad M_i = B_{ij} \epsilon_j + D_{ij} k_j + k_j^1 \quad i, j = 1, 2, \\
 P_i &= E_{ij} \epsilon_j + F_{ij} k_j + H_{ij} k_j^1 \\
 Q_i &= A_{6-ij} \epsilon_j + D_{6-ij} k_j^1; \quad K_i = D_{6-ij} \epsilon_j + F_{6-ij} k_j^1 \quad i = 1, 2; j = 4,
 \end{aligned} \tag{3}$$

The laminate stiffness parameters A_{ij} , B_{ij} , D_{ij} etc. are defined by eq. (5) and the strain components are given by

$$\begin{aligned}
 \epsilon_1 &= u_{,x} + \frac{w}{R_1}; \quad \epsilon_2 = v_{,y} + \frac{w}{R_2}; \quad \epsilon_6 = u_{,y} + v_{,x}; \quad \epsilon_4 = \varphi + w_{,y}; \\
 \epsilon_5 &= \chi + w_{,x}; \quad k_1 = \chi_{,x}; \quad k_2 = \varphi_{,y}; \quad k_6 = \chi_{,y} + \varphi_{,x}; \\
 k_1^1 &= -c_2(\chi_{,x} + w_{,xx}); \quad k_2^1 = -c_2(\varphi_{,y} + w_{,yy}); \quad k_4^1 = -c_1(\varphi + w_{,y}); \\
 k_5^1 &= c_1(\chi + w_{,x}); \quad k_6^1 = -c_2(\varphi_{,x} + \chi_{,y} + 2w_{,xy})
 \end{aligned} \tag{4}$$

The symbols $w_{,x}$ and $w_{,xx}$ etc. denote the first and the second derivatives of w with respect to x . The laminate stiffnesses are defined as follows.

$$(A_{ij}, B_{ij}, D_{ij}, E_{ij}, F_{ij}, H_{ij}) = \sum_{k=1}^N \int_{h_{k-1}}^{h_k} Q_{ij}^{(k)} (1, z, z^2, z^3, z^4, z^6) dz \quad (i, j = 1, 2, 4, 5, 6) \tag{5}$$

where $Q_{ij}^{(k)}$ are the transformed reduced stiffnesses of the k th lamina, R_1 , R_2 are the principal radii of curvature and k_1 , k_2 , k_6 are middle surface curvatures.

MATHEMATICAL PROCEDURE

Very often, in solving the boundary value problems, we find that it is difficult to satisfy the boundary conditions than to satisfy the governing equations. To this end, superposition technique has been found a useful tool in the boundary-value analysis. The principle of superposition technique is to choose the sub-problems for which accurate solutions are easily obtained, superpose these solutions and impose the combined solution to the original boundary conditions. In the case of a shell with two adjacent boundaries clamped and others simply supported, six components need to be superposed to construct the complete general solution. Each of these components has simple supports except for a bending moment or an in-plane force acting along one edge. For simplicity, only the first component is presented here.

The boundary conditions at $x=0$ and $x=a$ are given by

$$v = w = \varphi = N_1 = P_1 = M_1 = 0 \tag{6}$$

Along the boundary $y=0$, and $y = b$ the conditions are,

$$u = w = \chi = N_2 = P_2 = 0 \tag{7}$$

In addition we observe $M_2=0$ on $y=0$ and $M_2 = M_2^*$ on $y=b$.

$$u = w = \chi = N_2 = P_2 = 0; \quad M_2 = M_2^* \tag{8}$$

Here, a and b are the dimensions of the shell in x and y directions and h is thickness of the shell.

Where the bending moment M_2^* is expanded in a Fourier series:

$$M_2^* = \sum_{m=1}^{\infty} E_m \sin K_m x \tag{9}$$

It is obvious that the general solution for the first component is in the form proposed by Lévy.

$$\begin{pmatrix} u^1(x,y,t) \\ v^1(x,y,t) \\ w^1(x,y,t) \\ \chi^1(x,y,t) \\ \varphi^1(x,y,t) \end{pmatrix} = \sum_{m=1}^{\infty} \begin{pmatrix} U_m^1(y) \cos K_m x \\ V_m^1(y) \sin K_m x \\ W_m^1(y) \sin K_m x \\ X_m^1(y) \cos K_m x \\ Y_m^1(y) \sin K_m x \end{pmatrix} e^{i\omega t} \tag{10}$$

In the above equations $K_m = m \pi/a$ and m identifies the term in the series.

Equation (1) can be rewritten by substituting the assumed displacement solution given by eq.(10). These equations may be modified in the state-space form by defining the following variables.

$$\begin{aligned} Z_1 = U_m^1; Z_2 = U_{m,y}^1; Z_3 = V_m^1; Z_4 = V_{m,y}^1; Z_5 = W_m^1; Z_6 = W_{m,y}^1; \\ Z_7 = W_{m,yy}^1; Z_8 = W_{m,yyy}^1; Z_9 = X_m^1; Z_{10} = X_{m,y}^1; Z_{11} = Y_m^1; Z_{12} = Y_{m,y}^1 \end{aligned} \tag{11}$$

Finally, we obtain

$$\{Z(y)\}_{,y} = [C] \{Z(y)\} \tag{12}$$

which has a solution of the form

$$\{Z(y)\} = [R] \begin{pmatrix} e^{\lambda_1 y} \\ e^{\lambda_2 y} \\ \cdot \\ e^{\lambda_{12} y} \end{pmatrix} \{P\} \tag{13}$$

where $\{P\}$ is a column matrix of unknown constants determined by the associated boundary conditions, λ_i represents the distinct eigenvalues and $[R]$ the matrix of corresponding eigenvectors.

The matrices $[C]$ and $\{Z(y)\}$ are given by equations (14),

$$[C] = \begin{bmatrix} 0 & 1 & 0 & 0 & 0 & 0 & 0 & 0 & 0 & 0 & 0 & 0 \\ C_1 & 0 & 0 & C_2 & C_3 & 0 & C_4 & 0 & C_5 & 0 & 0 & C_6 \\ 0 & 0 & 0 & 1 & 0 & 0 & 0 & 0 & 0 & 0 & 0 & 0 \\ 0 & C_7 & C_8 & 0 & 0 & C_9 & 0 & C_{10} & 0 & C_{11} & C_{12} & 0 \\ 0 & 0 & 0 & 0 & 0 & 1 & 0 & 0 & 0 & 0 & 0 & 0 \\ 0 & 0 & 0 & 0 & 0 & 0 & 1 & 0 & 0 & 0 & 0 & 0 \\ 0 & 0 & 0 & 0 & 0 & 0 & 0 & 1 & 0 & 0 & 0 & 0 \\ C_{13} & 0 & 0 & C_{14} & C_{15} & 0 & C_{16} & 0 & C_{17} & 0 & 0 & C_{18} \\ 0 & 0 & 0 & 0 & 0 & 0 & 0 & 0 & 0 & 1 & 0 & 0 \\ C_{19} & 0 & 0 & C_{20} & C_{21} & 0 & C_{22} & 0 & C_{23} & 0 & 0 & C_{24} \\ 0 & 0 & 0 & 0 & 0 & 0 & 0 & 0 & 0 & 0 & 0 & 1 \\ 0 & C_{25} & C_{26} & 0 & 0 & C_{27} & 0 & C_{28} & 0 & C_{29} & C_{30} & 0 \end{bmatrix}; \{Z\} = \begin{bmatrix} Z_1 \\ Z_2 \\ Z_3 \\ Z_4 \\ Z_5 \\ Z_6 \\ Z_7 \\ Z_8 \\ Z_9 \\ Z_{10} \\ Z_{11} \\ Z_{12} \end{bmatrix} \quad (14)$$

The coefficients C_{ij} are defined in appendix B which are functions of C_1 and C_2 . These constants are given as: $C_1 = 4/h^2$ and $C_2 = 4/(3h^2)$.

The solutions for the rest of the components can also be established by the same procedures as for the first component. Once the solutions for all the components have been obtained, the boundary conditions of the original shell as prescribed by the following equations must be satisfied.

Along the boundary $x=0$: $u = w_{,x} = \chi = 0$; along the boundary $y=0$: $v = w_{,y} = \phi = 0$
 Application of these equation give rise to an eigenvalue system of homogeneous equations $[M]\{\delta\} = 0$.

If k term are employed in the displacement solutions for each of the components, $[M]$ constitutes an eigenvalue matrix of dimensions $k \times k$, while $\{\delta\}$ denotes a column matrix containing unknown Fourier coefficients, such as E_m etc.

Following the same procedure as for the shell with two adjacent edges clamped and others simply supported, the results for shell with other support conditions can be obtained.

COMPUTATIONS AND RESULTS

As a numerical example, the shells are assumed to be composed of the laminate of equal-thickness, equal-density and equal-orthotropicity. The following material properties are considered: $E_1/E_2=40$, $G_{12}/E_2=G_{13}/E_2=0.5$ and $\nu_{12}=0.25$. Non-dimensional frequency ω^* is used to make the solution more general and it is defined as $\omega^* = \omega a^2 / h (\rho/E_2)^{1/2}$. Furthermore E_i and G_{ij} are the modulus of elasticity in i direction and shear modulus in i - j plane and ν_{ij} are Poisson's ratio for transverse strain in j -direction with stress in i -direction. The thickness of the shell is given by h .

These frequencies are generated for a two-layer square cylindrical shell and the typical results are presented in Tables 1, where the length-to-thickness ratio a/h is allowed to vary from 5 to 20 and radius-to length ratio R/a takes the values of 5 and 20 respectively. In addition, in order to compare the results with those produced by classical (CT) and first-order shear deformation theories (FSDT), the frequencies

resulting from the last two theories are also listed in the tables. It is seen that CT theory over-estimates the fundamental frequencies, especially for the shells with large thickness ($a/h > 10$). On the other hand, FSDT and TSDT theories can produce very comparable results in most of the cases. However for the very thick shells, there still exists a discrepancy (in some cases, as high as 10%) in the frequencies predicted by FSDT and TSDT. For the thin shells, the three theories yield fairly close results.

Figure 1 shows the effects of different theories as well as length-to-thickness ratio on the frequencies of two-layer CCSS cylindrical shell panels. It is obvious that CT theory produces an unstable curve for thick shell ($a/h > 10$) in each of the three cases. This simply implies that CT is not suitable for thick laminated shells.

CONCLUSIONS

The authors believe that this paper presents the first comprehensive study for the cross-ply laminated shells by using the combination of superposition and state-space techniques (CSST). The unique advantage of the CSST method lie in the fact that it can easily deal with shells with any support condition. Besides, the solutions obtained by this approach can satisfy the governing equations exactly throughout the domain of the structures, and the boundary condition can be satisfied to any desired degree of accuracy by taking more terms.

It is concluded that the classical theory over estimates the fundamental frequencies, especially for shells with large thickness ($a/h > 10$). On the other hand, FSDT and TSDT theories can produce very comparable results in most of the cases except for very thick shells.

REFERENCES

1. J. N. Reddy and C. Liu, "A higher-order shear deformation theory of laminated elastic shells", *International Journal of Engineering Science*, Vol. 23, No. 3, 319-330, 1985.
2. S. B. Dong and F. K. W. Tso, "On a laminated orthotropic shell theory including transverse shear deformation", *Journal of Applied Mechanics*, Vol. 39, 1091-1096, 1971.
3. J. M. Whitney and C. T. Sun, "A higher order theory for extensional motion of laminated anisotropic shells and plates", *Journal of Sound and Vibration*, Vol. 30, p. 85, 1973.
4. J. M. Whitney and C. T. Sun, "A refined theory for laminated anisotropic cylindrical shells", *Journal of Applied Mechanics*, Vol. 41, 471-476, 1974.
5. J. N. Reddy, "Exact solutions for moderately thick laminated shells", *Journal of Engineering Mechanics*, Vol. 101, No. 5, 795-809, 1984.
6. N. Li and S. Mirza, "Vibration of antisymmetric angle-ply laminated plates including transverse shear deformation", *Mechanics of Composite Materials and Structures*, Vol. 2, 163-175, 1995.

APPENDIX A: Differential Operator L_{ij}

The differential operators L_{ij} used in equation (1) are given as follows:

$$\begin{aligned}
 L_{11} &= A_{11}d_{xx} + A_{66}d_{yy} - \bar{I}_1 d_{tt}; & L_{12} &= (A_{12} + A_{66})d_{xy}; \\
 L_{13} &= \bar{I}_3 d_{xxt} - c_2[E_{11}d_{xxx} + (E_{12} + 2E_{66})d_{xyy}] + (A_{11}/R_1 + A_{12}/R_2)d_x \\
 L_{14} &= (B_{11} - c_2E_{11})d_{xx} + (B_{66} - c_2E_{66})d_{yy} - \bar{I}_2 d_{tt}; \\
 L_{15} &= [B_{12} + B_{66} - c_2(E_{12} + E_{66})]d_{xy}; & L_{22} &= A_{66}d_{xx} + A_{22}d_{yy} - \hat{I}_1 d_{tt}; \\
 L_{23} &= \hat{I}_3 d_{xxt} - c_2[E_{22}d_{yy} + (E_{12} + 2E_{66})d_{xyy}] + (A_{12}/R_1 + A_{22}/R_2)d_y \\
 L_{24} &= L_{Hx}; & L_{25} &= (B_{22} - c_2E_{22})d_{yy} + (B_{66} - E_{66}c_2)d_{xx} - \hat{I}_2 d_{tt} \\
 L_{33} &= [c_1(D_{55} - c_1F_{55}) - (A_{55} - c_1D_{55})]d_{xx} + [c_1(D_{44} - c_1F_{44}) - \\
 & (A_{44} - c_1D_{44})]d_{yy} + c_2^2[H_{11}d_{xxx} + 2(H_{12} + 2H_{66})d_{xyy} + H_{22}d_{yyy}] \\
 & - 2c_2[(E_{11}/R_1 + E_{12}/R_2)d_{xx} + (E_{12}/R_1 + E_{22}/R_2)d_{yy}] + (AxI/R_1^2 + \\
 & 2A_{12}/R_1/R_2 + A_{22}/R_2^2) + I_1 d_{tt} - c_2^2 I_7 (d_{xxt} + d_{yxt}) \\
 L_{34} &= [c_1(D_{55} - c_1F_{55}) - (A_{55} - c_1D_{55})]d_x - c_2\{(F_{11} - c_2H_{11})d_{xxx} + [2F_{66} + \\
 & F_{12} - c_2(H_{12} + 2H_{66})d_{xyy}] + [B_{11}/R_1 + B_{12}/R_2 - c_2(E_{11}/R_1 + E_{12}/R_2)] + \bar{I}_5 d_{xtt}\}; \\
 L_{35} &= [c_1(D_{44} - c_1F_{44}) - (A_{55} - c_1D_{44})]d_y - c_2(F_{22} - c_2H_{22})d_{yyy} - c_2[2F_{66} + \\
 & F_{12} - c_2(2H_{66} + H_{12})]d_{xyy} + [B_{12}/R_1 + B_{22}/R_2 - c_2(E_{12}/R_1 + E_{22}/R_2)] + \hat{I}_5 d_{ytt} \\
 L_{44} &= c_1(D_{55} - c_1F_{55}) - (A_{55} - c_1D_{55}) + (D_{11} - 2c_2F_{11} + c_2^2H_{11})d_{xx} + (D_{66} - \\
 & 2c_2F_{66} + c_2^2H_{66})d_{yy} - \bar{I}_4 d_{tt} \\
 L_{45} &= [D_{12} + D_{66} - 2c_2(F_{12} + F_{66}) + c_2^2(H_{12} + H_{66})]d_{xy} \\
 L_{55} &= c_1(D_{44} - c_1F_{44}) - (A_{44} - c_1D_{44}) + (D_{22} - 2c_2F_{22} + c_2^2H_{22})d_{yy} + (D_{66} - \\
 & 2c_2F_{66} + c_2^2H_{66})d_{xx} - \hat{I}_4 d_{tt}
 \end{aligned}$$

where the inertia coefficients are determined by

$$\begin{aligned}\bar{I}_1 &= I_1 + \frac{2}{R_1} I_2; \quad \bar{I}_2 = I_2 + \frac{I_3}{R_1} - c_2 I_4 - \frac{c_2}{R_1} I_5; \\ \bar{I}_3 &= c_2 I_4 + \frac{c_2}{R_1} I_5; \quad \bar{I}_4 = I_3 - 2c_2 I_5 + c_2^2 I_7; \quad \bar{I}_5 = c_2 I_5 - c_2^2 I_7; \\ I_i &= \sum_{k=1}^N \int_{h_{k-1}}^{h_k} \rho z^{i-1} dz \quad (i=1, 2, 3, 4, 5, 7)\end{aligned}$$

The inertia coefficients \hat{I}_i have the same expression as \bar{I}_i except that R_1 is replaced by R_2 .

APPENDIX B: Coefficient C_i

C_i in equations (11) are given as follows:

$$\begin{aligned}C_1 &= (g_1 g_{34} - g_7 g_{28}) / \phi_1; \quad C_2 = (g_3 g_{34} - g_7 g_{30}) / \phi_1; \quad C_3 = (g_4 g_{34} - g_7 g_{31}) / \phi_1; \\ C_4 &= (g_5 g_{34} - g_7 g_{32}) / \phi_1; \quad C_5 = (g_6 g_{34} - g_7 g_{33}) / \phi_1; \quad C_6 = (g_8 g_{34} - g_7 g_{35}) / \phi_1; \\ C_7 &= (g_9 g_{43} - g_{36} g_{16}) / \phi_2; \quad C_8 = (g_{10} g_{43} - g_{37} g_{16}) / \phi_2; \quad C_9 = (g_{12} g_{43} - g_{39} g_{16}) / \phi_2; \\ C_{10} &= (g_{13} g_{43} - g_{40} g_{16}) / \phi_2; \quad C_{11} = (g_{14} g_{43} - g_{41} g_{16}) / \phi_2; \quad C_{12} = (g_{15} g_{43} - g_{42} g_{16}) / \phi_2; \\ C_{13} &= -(h_1 + h_2 C_7 + h_6 C_{25}) / h_4; \quad C_{14} = -(g_{19} + h_2 C_8 + h_6 C_{26}) / h_4; \\ C_{15} &= -(h_2 C_9 + g_{21} + h_6 C_{27}) / h_4; \quad C_{16} = -(h_2 C_{10} + h_3 + h_6 C_{28}) / h_4; \\ C_{17} &= -(h_2 C_{11} + h_5 + h_6 C_{29}) / h_4; \quad C_{18} = -(h_2 C_{12} + g_{26} + h_6 C_{30}) / h_4; \\ C_{19} &= -(g_{28} + g_{29} C_1) / g_{34}; \quad C_{20} = -(g_{30} + g_{29} C_2) / g_{34}; \quad C_{21} = -(g_{31} + g_{29} C_3) / g_{34}; \\ C_{22} &= -(g_{32} + g_{29} C_4) / g_{34}; \quad C_{23} = -(g_{33} + g_{29} C_5) / g_{34}; \quad C_{24} = -(g_{35} + g_{29} C_6) / g_{34}; \\ C_{25} &= -(g_{36} + g_{38} C_7) / g_{43}; \quad C_{26} = -(g_{37} + g_{38} C_8) / g_{43}; \quad C_{27} = -(g_{39} + g_{38} C_9) / g_{43}; \\ C_{28} &= -(g_{40} + g_{38} C_{10}) / g_{43}; \quad C_{29} = -(g_{41} + g_{38} C_{11}) / g_{43}; \quad C_{30} = -(g_{43} + g_{38} C_{12}) / g_{43}\end{aligned}$$

where ϕ_i ($i=1,2$), h_j ($j=1, \dots, 6$) and g_k ($k=1, \dots, 30$) are functions of material and geometric properties.

$$\begin{aligned}
 \Phi_1 &= g_7 g_{29} - g_2 g_{34}; \quad \Phi_2 = g_{38} g_{16} - g_{11} g_{43}; \\
 h_1 &= g_{18} + g_{20} C_7 + g_{27} C_{25}; \quad h_2 = g_{17} + g_{20} C_8 + g_{27} C_{26}; \quad h_3 = g_{22} + g_{20} C_9 + g_{27} C_{27}; \\
 h_4 &= g_{23} + g_{20} C_{10} + g_{27} C_{28}; \quad h_5 = g_{25} + g_{20} C_{11} + g_{27} C_{29}; \quad h_6 = g_{26} + g_{20} C_{12} + g_{27} C_{30}; \\
 g_1 &= \bar{I}_1 \omega^2 - A_{11} K_m^2; \quad g_2 = A_{66}; \quad g_3 = (A_{12} + A_{66}) K_m; \\
 g_4 &= [c_2 E_{11} K_m^2 + (A_{11}/R_1 + A_{12}/R_2) - \bar{I}_3 \omega^2] \omega^2; \quad g_5 = -c_2 K_m (E_{12} + 2E_{66}); \\
 g_6 &= \bar{I}_2 \omega^2 - (B_{11} - c_2 E_{11}) K_m^2; \quad g_7 = B_{66} - c_2 E_{66}; \quad g_8 = [B_{12} + B_{66} - c_2 (E_{12} + E_{66})] K_m; \\
 g_9 &= -g_3; \quad g_{10} = \hat{I}_1 \omega^2 - A_{66} K_m^2; \quad g_{11} = A_{22}; \quad g_{12} = c_2 (E_{12} + 2E_{66}) K_m^2 + A_{12}/R_1 + A_{22}/R_2 \\
 &\quad - \hat{I}_3 \omega^2; \quad g_{13} = -c_2 E_{22}; \quad g_{14} = -(B_{66} - c_2 E_{66} + B_{12} - E_{12} c_2) K_m; \quad g_{15} = \hat{I}_2 \omega^2 - (B_{66} \\
 &\quad - c_2 E_{66}) K_m^2; \quad g_{16} = B_{22} - c_2 E_{22}; \quad g_{17} = -g_4; \quad g_{18} = -g_5; \quad g_{19} = g_{12}; \quad g_{20} = g_{13}; \\
 g_{21} &= [A_{55} - 2c_1 D_{55} + c_1^2 F_{55}] K_m^2 + c_2^2 H_{11} K_m^4 + 2c_2 (E_{11}/R_1 + E_{12}/R_2) K_m^2 \\
 &\quad + A_{11}/R_1^2 + 2A_{12}/R_1 R_2 + A_{22}/R_2^2 - (I_1 + c_2^2 I_7 K_m^2) \omega^2; \\
 g_{22} &= (D_{44} - c_1 F_{44}) c_1 - (A_{44} - D_{44} c_1) - 2c_2^2 (H_{12} + 2H_{66}) K_m^2 - 2c_2 (E_{12}/R_1 + E_{22}/R_2) \\
 &\quad + c_2^2 I_7 \omega^2; \quad g_{23} = c_2^2 H_{22}; \quad g_{24} = (A_{55} - 2c_1 D_{55} + c_1^2 F_{55}) K_m - c_2 (F_{11} - c_2 H_{11}) K_m^3 - \\
 &\quad [(B_{12} - c_2 E_{11})/R_1 - (B_{12} - c_2 E_{12})/R_2] K_m + \bar{I}_5 K_m^2; \quad g_{25} = c_2 [(2F_{66} + F_{12}) \\
 &\quad - c_2 (H_{12} + 2H_{66})] K_m; \quad g_{26} = c_1 (D_{44} - c_1 F_{44}) - (A_{44} - c_1 D_{44}) + c_2 [2F_{66} + F_{12} - \\
 &\quad c_2 (2H_{66} + H_{12}) K_m^2 + (B_{12} - c_2 E_{12})/R_1 + (B_{22} - c_2 E_{22})/R_2 - \hat{I}_5 \omega^2]; \\
 g_{27} &= -c_2 (F_{22} - c_2 H_{22}); \quad g_{28} = g_6; \quad g_{29} = g_7; \quad g_{30} = -g_{14}; \quad g_{31} = -g_{24}; \quad g_{32} = -g_{25}; \\
 g_{33} &= c_1 (D_{55} - c_1 F_{55}) - (A_{55} - D_{55} c_1) - (D_{11} - 2c_2 F_{11} + H_{11} c_2^2) K_m^2 + \bar{I}_4 \omega^2; \\
 g_{34} &= D_{66} - 2F_{66} c_2 + c_2^2 H_{66}; \quad g_{35} = [D_{12} + D_{66} - 2c_2 (F_{12} + F_{66}) + c_2^2 (H_{12} + H_{66})] K_m; \\
 g_{36} &= -g_8; \quad g_{37} = g_{15}; \quad g_{38} = g_{16}; \quad g_{39} = g_{26}; \quad g_{40} = g_{27}; \quad g_{41} = -g_{35}; \quad g_{42} = c_1 (D_{44} \\
 &\quad - c_1 F_{44}) - (A_{44} - c_1 D_{44}) - (D_{66} - 2c_2 F_{66} + c_2^2 H_{66}) K_m^2 + \hat{I}_4 \omega^2; \quad g_{43} = D_{22} - 2c_2 F_{22} - c_2^2 H_{22}
 \end{aligned}$$

Table 1. Non-dimensional fundamental frequencies ω^* ($=\omega a^2/h(\rho/E_2)^{1/2}$) for cross-ply cylindrical square shells ($0^\circ/90^\circ$)

theories R/a	a/h 5		10		15		20	
	5	20	5	20	5	20	5	20
TDST	9.463	9.468	12.50	12.40	13.72	13.43	14.42	13.88
FDST	8.820	8.815	12.20	12.09	13.56	13.26	14.33	13.79
CT	14.19	13.22	14.43	14.26	14.65	14.41	14.98	14.47

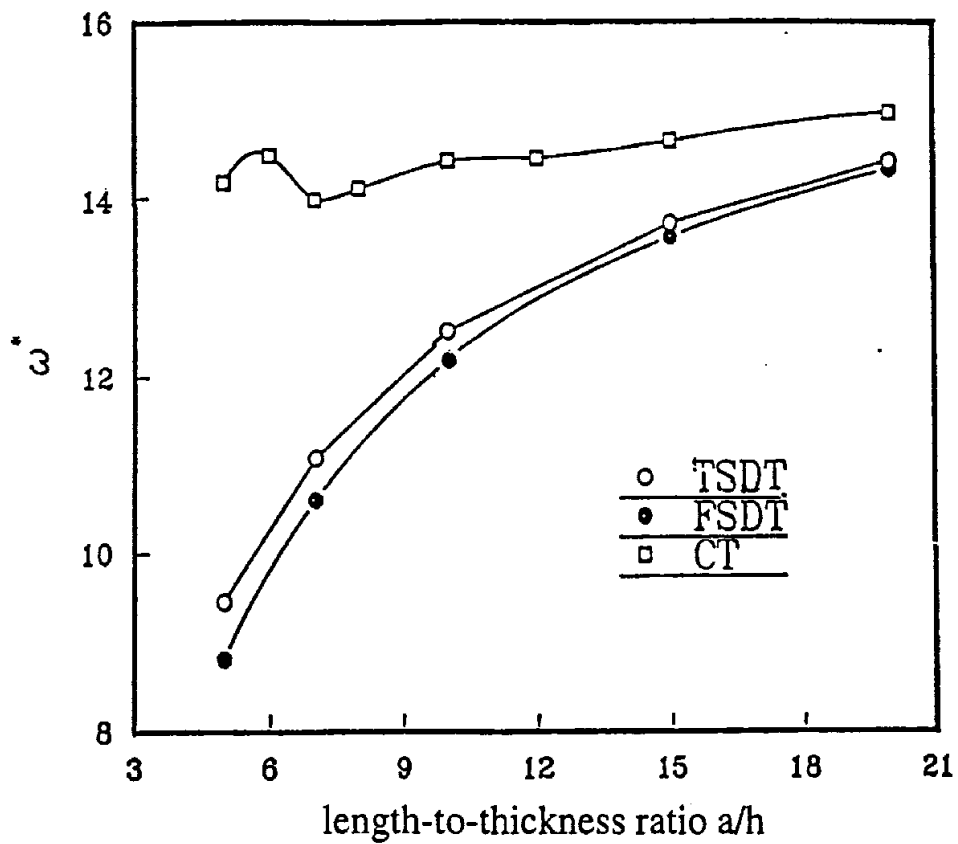


Figure 1: Fundamental frequencies ω^* versus a/h ratio of cross-ply two-layer CCSS shells.

ANALYSIS OF ANISOTROPIC MULTILAYERED PLATES AND SHELLS BASED ON A NEW HIGHER-ORDER THEORY

V. E. Verijenko, S. Adali, P. Y. Tabakov, S. Shaikh

*Department of Mechanical Engineering,
University of Natal, Durban 4001, South Africa*

SUMMARY: A rational higher-order shear deformation theory of anisotropic laminated plates and shallow shells is developed for the solution of static problems subject to both normal and tangential loads. There are three distinctive properties of the proposed theory. First one lies in the fact that it is based on hypotheses which are fully tied to the elastic characteristics of the anisotropic materials of the layers. Secondly, the theory is built on a rational level of difficulty, i.e. it does not add complexity in comparison with known theories of this type. Thirdly, the hypotheses and, correspondingly, all governing relations take into account the influence of the direct application of the tangential loads.

KEYWORDS: rational transverse shear deformation higher-order theory

INTRODUCTION

In this study the transverse shear model and the theory correspondent to it, oriented to solve anisotropic laminated plates and shells, are built on a rational level where the relations remain between the hypotheses for transverse shear stresses and the material characteristics of anisotropic layers.

Using the specific approach for the derivation of hypotheses, all the relations of the stress-strain state of anisotropic laminated shells are obtained. Using the variational approach the system of governing differential equations and corresponding boundary conditions are derived. The possible solutions for this system are studied, and the special cases are formulated which are the cross-ply and angle-ply laminates. For these cases analytical solution exists. Numerical results are given and compared with exact three-dimensional and with some approximate solutions available in the literature. The influence of the lamination upon the accuracy of results and the characteristics of stress-strain state are studied and discussed.

BASIC ASSUMPTIONS

We consider shells with anisotropic layers which have one surface of elastic symmetry. The shell is represented by a curvilinear orthogonal coordinate system x_1Ox_2 which is parallel to the bounding surfaces and surfaces of contact between the layers (Fig. 1). The axes of the curvilinear coordinates $x_i = \text{const}$ ($i = 1, 2$) coincide with the principal lines of curvature and the coordinate $x_3 = z$ defined along the normal to the reference surface x_1Ox_2 which is positioned arbitrarily through the thickness of the shell. No limitations are placed on the thickness, rigidity, number and/or sequence of the layers. The assumptions that the layers are perfectly bonded ensures their deformation as a single unit without delamination. Thus, the structure of the shell through the thickness is arbitrarily irregular and heterogeneous.

It is assumed that the coefficients of the first quadratic form of a surface are close to unity, i.e. $A \approx 1$, and the main curvatures are constant, i.e. $k_{ij} = \text{const}$ ($i, j = 1, 2$). The total thickness of the shell is small in comparison to the radii of the curvatures ($1 + k_{ij} \approx 1$).

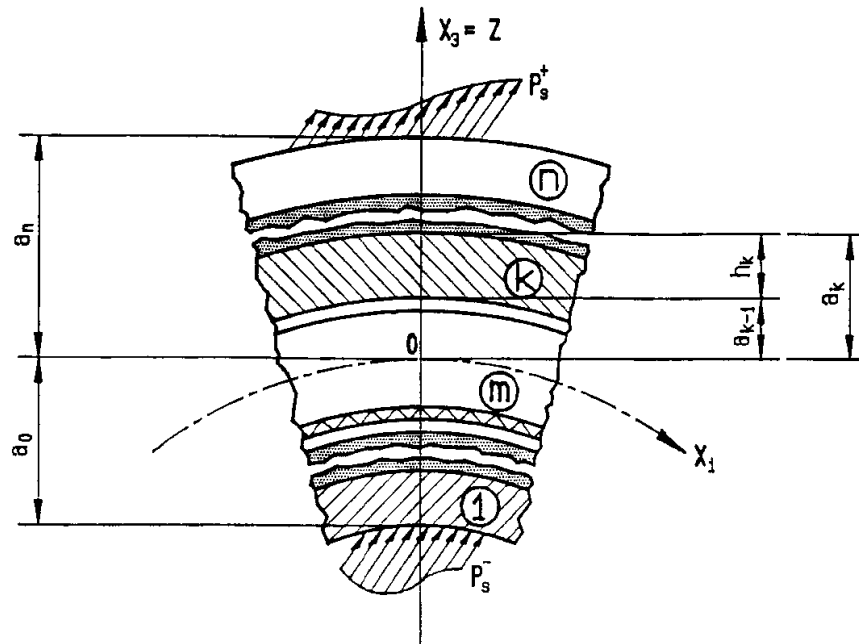


Figure 1. Geometry of a laminated shell.

Loads are applied on the outer and inner surfaces of the laminate so that

$$p_s^\pm(x_i) = p_s^\pm, \quad s = 1, 2, 3 \quad (1)$$

where p_s^+ and p_s^- are loads applied to the outer and inner surfaces, respectively, and the subscript s denotes the corresponding coordinate axis. Consequently, the stress conditions on the external surfaces take the following form

$$\sigma_{s3}^{(1)} = -p_s^- \quad \text{for } z = a_0 \quad (k = 1) \quad (2)$$

$$\sigma_{s3}^{(n)} = +p_s^+ \quad \text{for } z = a_n \quad (k = n) \quad (3)$$

$$s = 1, 2, 3$$

where k denotes the layer number and n is the total number of layers. Since the layers are assumed to be perfectly bonded, the continuity conditions for an arbitrary surface $z = a_{k-1}$ are given by

$$\sigma_{s3}^{(k)} = \sigma_{s3}^{(k-1)} \quad (\text{static}) \quad (4)$$

$$u_s^{(k)} = u_s^{(k-1)} \quad (\text{kinematic}) \quad (5)$$

In the following derivations, summation is assumed over subscripts $i, j = 1, 2$; $s, r = 1, 2, 3$, and p, q, f, g . However no summation is implied over the index $k = 1, 2, \dots, m, \dots, n$. A subscript after a comma denotes differentiation with respect to the variable following the comma and a superscript is expressed in brackets to distinguish it from an exponent.

DERIVATION OF THE NONCLASSICAL THEORY

In deriving a nonclassical higher-order transverse shear theory we assume that transverse shear strains are not equal to zero, that is

$$2e_{i3}^{(k)} \neq 0; \quad i = 1, 2 \quad (6)$$

However, we assume that the transverse normal deformations and transverse normal stresses, as in the classical theory, are equal to zero, i.e.,

$$e_{33}^{(k)} = 0; \quad \sigma_{33}^{(k)} = 0 \quad (7)$$

Thus, the normal displacements are constants through the thickness of the laminated shell and are equal to those displacements on the reference surface

$$u_3^{(k)} = u_3(x_i, 0) = w \quad (8)$$

The tangential displacements can be obtained as follows

$$u_{i,3}^{(k)} = 2e_{i3}^{(k)} - u_{3,i}^{(k)} \quad (9)$$

and after integrating we have

$$u_i^{(k)} = u_i + \int_0^z (2e_{i3}^{(k)} - u_{3,i}^{(k)}) dz \quad (10)$$

We introduce the following distribution functions of the tangential displacements

$$\psi_{ip}^{(k)} = - \int_0^z \Psi_{ip}^{(k)} dz, \quad i = 1, 2; \quad p = 1, 2, \dots, 8 \quad (11)$$

Using these functions the expression for the tangential displacements may be written as

$$\begin{aligned} u_1^{(k)} &= u_1 - (w_{,1}z + \kappa_{11,1}\psi_{11}^{(k)} + \kappa_{22,1}\psi_{12}^{(k)} + \kappa_{11,2}\psi_{13}^{(k)} + \kappa_{22,2}\psi_{14}^{(k)} \\ &\quad + p_1^- \psi_{15}^{(k)} + p_1^+ \psi_{16}^{(k)} + p_2^- \psi_{17}^{(k)} + p_2^+ \psi_{18}^{(k)}) \\ u_2^{(k)} &= u_2 - (w_{,2}z + \kappa_{11,1}\psi_{21}^{(k)} + \kappa_{22,1}\psi_{22}^{(k)} + \kappa_{11,2}\psi_{23}^{(k)} + \kappa_{22,2}\psi_{24}^{(k)} \\ &\quad + p_1^- \psi_{25}^{(k)} + p_1^+ \psi_{26}^{(k)} + p_2^- \psi_{27}^{(k)} + p_2^+ \psi_{28}^{(k)}) \end{aligned} \quad (12)$$

The distribution functions defined in the equation (11) allow us to satisfy the continuity conditions in between the layers for the tangential displacements when the reference surface is positioned arbitrarily through the thickness of the shell.

First two terms in the expression (12) contain unknown functions u_1 , u_2 , w . These items are from the classical theory whereas the rest of items are new. They take into account the influence of the transverse shear strains on the tangential displacements. It is clear that the highest degree of the polynomials, which results from the distribution function (11) written in an explicit form, equals three. Thus, the tangential displacements are nonlinear through the thickness of the shell.

In order to derive relations of the nonclassical theory we retain first two terms in the expressions (12). For the next four terms we introduce new unknown functions of the reference surface using the following irreversible relations

$$[\kappa_{11,1}; \kappa_{22,1}; \kappa_{11,2}; \kappa_{22,2}] \longrightarrow [\chi_1; \chi_2; \chi_3; \chi_4] \quad (13)$$

Additionally, we introduce the following relations for the functions of the given external load

$$[p_1^-; p_1^+; p_2^-; p_2^+] = [\chi_5; \chi_6; \chi_7; \chi_8] \quad (14)$$

Replacing the functions in the relations (12) in accordance with the relationships defined by (13) and (14), the expression for the tangential displacements may be written as

$$u_i^{(k)} = u_i - w_{,i}z - \chi_p \psi_{ip}; \quad i = 1, 2; \quad p = 1, 2, \dots, 8 \quad (15)$$

In this expression summation is assumed over "mute" index p . Items containing this index take into account the influence of the transverse shear deformations as a result of impact of the transverse shear stresses. And, the last four terms ($p = 5, 6, 7, 8$) account for the direct effect of impact of the external load.

Let us now obtain the components of the strain tensor for the k -th layer. Taking into account the kinematic model (8) and (15), the tangential components may be written as

$$\begin{aligned} e_{ij}^{(k)} &= \frac{1}{2}(u_{i,j}^{(k)} + u_{j,i}^{(k)}) + k_{ij}u_3^{(k)} \\ &= \frac{1}{2}\left[(u_{i,j} + u_{j,i}) - (w_{,ij} + w_{,ji})z - (\chi_{p,j}\psi_{jp} + \chi_{p,i}\psi_{ip})\right] + k_{ij}w \\ &\quad i, j = 1, 2; \quad p = 1, 2, \dots, 8 \end{aligned} \quad (16)$$

The transverse shear strains are given by

$$\begin{aligned} 2e_{i3}^{(k)} &= u_{i,3}^{(k)} + u_{3,i}^{(k)} = u_{i,3}^{(k)} + w_{,i} = -(w_{,i} - \chi_p\psi_{ip}^{(k)}) + w_{,i} = \chi_p\psi_{ip}^{(k)} \\ &\quad i = 1, 2; \quad p = 1, 2, \dots, 8 \end{aligned} \quad (17)$$

The strain due to the normal compression is equal to zero as hypothesis

$$e_{33}^{(k)} = 0 \quad (18)$$

The components of the stress tensor can be determined using the strains (16), (17) and (18) and taking relations of the Hooke's law into account as

$$\begin{aligned} \sigma_{11}^{(k)} &= A_{1i}^{(k)}e_{ir}^{(k)} + 2A_{16}^{(k)}e_{12}^{(k)} = A_{1i}^{(k)}(u_{i,r} - w_{,ir}z - \chi_{p,i}\psi_{rp}^{(k)} + k_{ir}w) \\ &\quad + A_{16}^{(k)}\left[(u_{1,2} + u_{2,1}) - 2w_{,12}z - (\chi_{p,2}\psi_{1p}^{(k)} + \chi_{p,1}\psi_{2p}^{(k)}) + 2k_{12}w\right] \\ &\quad \sigma_{22}^{(k)} = \sigma_{11}^{(k)} \\ \sigma_{12}^{(k)} &= A_{i6}^{(k)}e_{ir}^{(k)} + 2A_{66}^{(k)}e_{12}^{(k)} = A_{i6}^{(k)}(u_{i,r} - w_{,ir}z - \chi_{p,i}\psi_{rp}^{(k)} + k_{ir}w) \\ &\quad + A_{66}^{(k)}\left[(u_{1,2} + u_{2,1}) - 2w_{,12}z - (\chi_{p,2}\psi_{1p}^{(k)} + \chi_{p,1}\psi_{2p}^{(k)}) + 2k_{12}w\right] \\ &\quad i = 1, 2; \quad r = i; \quad p = 1, 2, \dots, 8 \end{aligned} \quad (19)$$

$$\begin{aligned} \sigma_{13}^{(k)} &= \chi_p(A_{55}\psi_{1p}^{(k)} + A_{54}\psi_{2p}^{(k)}) \\ \sigma_{23}^{(k)} &= \chi_p(A_{45}\psi_{1p}^{(k)} + A_{44}\psi_{2p}^{(k)}) \\ &\quad p = 1, 2, \dots, 8 \end{aligned} \quad (20)$$

$$\begin{aligned} \sigma_{33}^{(k)} &= A_{3i}^{(k)}e_{ir} + 2A_{66}^{(k)}e_{12}^{(k)} = A_{3i}^{(k)}(u_{i,r} - w_{,ir}z - \chi_{p,i}\psi_{rp}^{(k)} + k_{ir}w) \\ &\quad + A_{66}^{(k)}\left[(u_{1,2} + u_{2,1}) - w_{,12}z - (\chi_{p,2}\psi_{1p}^{(k)} + \chi_{p,1}\psi_{2p}^{(k)}) + 2k_{12}w\right] \\ &\quad i = 1, 2; \quad r = i; \quad p = 1, 2, \dots, 8 \end{aligned} \quad (21)$$

where $A_{11}^{(k)}, A_{22}^{(k)}, \dots, A_{66}^{(k)}$ are stiffness parameters of the k -th layer.

In the subsequent study of the stress-strain state of the shell it is necessary to obtain the set of governing equations and boundary conditions expressed in terms of the unknown functions of the reference surface $u_i, w, \chi_p, (i = 1, 2; p = 1, 2, 3, 4)$. As this takes place, the functions of normal z are assumed as known and they are distribution functions of the stress-strain state components

through the thickness of the multilayered anisotropic shell. These distribution functions are defined in a form which facilitates the satisfaction of the conditions on the external surfaces and the continuity conditions in between the layers when the reference surface is positioned arbitrarily through the thickness of the shell. Clearly, the governing equations are independent of the thicknesses, stiffnesses and other properties of the layers.

An important feature of the proposed nonclassical model of the stress-strain state is the relation of its expressions with physical and mechanical characteristics of the anisotropic shell layers.

VARIATIONAL EQUATION, EQUATIONS OF EQUILIBRIUM AND BOUNDARY CONDITIONS

The equations of equilibrium and the boundary conditions may be determined using the Lagrange's variational principle

$$\delta U - \delta H = 0 \tag{22}$$

where δU is the variation of the potential energy of the deformation and δH is the variation of the work done by the external forces.

For a laminated shell we consider the tangential and normal components of the stress and strain tensors. Then substituting integral characteristics of the stresses and using Ostrogradsky-Gauss theorem we derive the following variational equation

$$\begin{aligned} & \iint_S \left\{ [N_{ij,j} + (p_i^- + p_i^+)]\delta u_i + [M_{ij,ij} - k_{ij}N_{ij} + (p_{i,i}^- a_0 + p_{i,i}^+ a_n + p_3)]\delta w \right. \\ & \left. - [N_{ij}^{(if)} + Q_i^{(if)} + p_i^- \psi_{ij}^{(1)}(a_0) + p_i^+ \psi_{ij}^{(n)}(a_n)]\chi_f \right\} dS \\ & - \int_L \left\{ (N_{hh}\delta u_h + N_{hl}\delta u_l) + [(M_{hh,h} + 2M_{hl,l}) + (p_h^- a_0 + p_h^+ a_n)]\delta w \right. \\ & \left. - M_{hh}\delta w_{,h} - N_{hh}^{(hf)}\delta\chi_f^{(h)} - N_{hl}^{(lf)}\delta\chi_f^{(l)} \right\} dL - [M_{hl}\delta w]_{L_1}^{L_2} = 0 \end{aligned} \tag{23}$$

$i, j = 1, 2; \quad f = 1, 2, 3, 4$

where S is the two-dimensional domain of the shell surface; h and l are normal and tangent to the boundary L of the domain of the shell, respectively.

The variations of independent functions u_i , w , χ_p which determine the displacements in the shell, have arbitrary values everywhere over the domain of the shell excluding the boundary and, consequently, they cannot be equal to zero. Equating the multipliers of the variations in the first integral of the equation (23) to zero, we obtain the system of equations of equilibrium of the shell as

$$\begin{aligned} N_{ij,j} + (p_i^- + p_i^+) &= 0 \\ M_{ij,ij} - k_{ij}N_{ij} + (p_{i,i}^- a_0 + p_{i,i}^+ a_n + p_3) &= 0 \\ N_{ij}^{(if)} + Q_i^{(if)} + [p_i^- \psi_{ij}^{(1)}(a_0) + p_i^+ \psi_{ij}^{(n)}(a_n)] &= 0 \end{aligned} \tag{24}$$

$i, j = 1, 2; \quad f = 1, 2, 3, 4$

There are eight boundary conditions, which is the same as the order of the system of equations (24). A detailed interpretation of the boundary conditions is given in [1,2].

SYSTEM OF GOVERNING EQUATIONS

The system of governing differential equations may be written in the following form

$$[D]\{U\} = [D_X]\{X\} + [F]\{P\} \quad (25)$$

where $[D]$ is the matrix of differential operators over the vector of unknown functions of the reference surface, which is given by

$$\{U\} = \{u_i; w; \chi_p\}^T, \quad i = 1, 2; \quad p = 1, 2, 3, 4 \quad (26)$$

$[D_X]$ is the matrix of differential operators over the vector of known functions defined by (14) and given as

$$\{X\} = \{\chi_p\}^T, \quad p = 5, 6, 7, 8 \quad (27)$$

and $[F]$ is the matrix of differential operators over the vector of given loads which is

$$\{P\} = \{p_i^{\bar{f}}; p_3\}^T \quad (28)$$

Finally, the left part of the equation (25) may be written in the following form

$$[D]\{U\} = \begin{bmatrix} [D_{11}] & [D_{12}] & [D_{13}] & [D_{1p}] \\ [D_{21}] & [D_{22}] & [D_{23}] & [D_{2p}] \\ [D_{31}] & [D_{32}] & [D_{33}] & [D_{3p}] \\ [D_{f1}] & [D_{f2}] & [D_{f3}] & [D_{fp}] \end{bmatrix} \begin{Bmatrix} u_1 \\ u_2 \\ w \\ \chi_p \end{Bmatrix} \quad (29)$$

In order to multiply the matrix by the vector it is necessary to expand it over the index $f = 1, 2, 3, 4$ and make summation over the index $p = 1, 2, 3, 4$. It is noted that submatrices $[D_{f1}]$ and $[D_{f2}]$ can be obtained from submatrices $[D_{1p}]$ and $[D_{2p}]$ by replacing index p with f .

The right hand side of the equation (25) is formed by two terms. The first item has the following form

$$[D_X]\{X\} = - \begin{bmatrix} [D_{1p}] \\ [D_{2p}] \\ [D_{3p}] \\ [D_{fp}] \end{bmatrix} \left\{ \chi_p = \begin{Bmatrix} p_1^- \\ p_1^+ \\ p_2^- \\ p_2^+ \end{Bmatrix} \right\} \quad (30)$$

$f = 1, 2, 3, 4; \quad p = 5, 6, 7, 8.$

The second item is given as follows

$$[F]\{P\} = \begin{bmatrix} -(\dots) & -(\dots) & - & - & - \\ & & -(\dots) & -(\dots) & - \\ a_0(\dots),1 & a_n(\dots),1 & a_0(\dots),2 & a_n(\dots),2 & (\dots) \\ \psi_{1f}^{(1)}(a_0)(\dots) & \psi_{1f}^{(n)}(a_n)(\dots) & \psi_{2f}^{(1)}(a_0)(\dots) & \psi_{2f}^{(n)}(a_n)(\dots) & - \end{bmatrix} \begin{Bmatrix} p_1^- \\ p_1^+ \\ p_2^- \\ p_2^+ \\ p_3 \end{Bmatrix} \quad (31)$$

$f = 1, 2, 3, 4$

The total number of equations in the system (25) is equal to seven. The total order of the equations is equal to 16 and corresponds to the number of boundary conditions which are equal to eight.

ANALYTICAL SOLUTION AND SPECIAL CASES

It is apparent that an analytical solution for the system (25) is only possible for the simplest cases. We will consider the case of a shell with a rectangular plan view. The Navier approach can be used in this case by expanding the applied loads and unknown functions in double Fourier trigonometric series.

We consider two cases of the shell support, for which Fourier series are formed depending upon the boundary conditions. The first case is a hinged movable (free) support, when the edges of the shell can freely move along the normal to the edges. Tangential displacements along the edges are not permitted. This is the case of the hinged movable support of the shell. The boundary conditions are the following

$$\begin{aligned}
 &\text{for } x_1 = 0; a_1 : u_2 = 0; N_{11} = 0; w = 0; M_{11} = 0 \\
 &\quad \chi_3^{(2)} = \chi_4^{(2)} = 0; N_{11}^{(11)} = N_{11}^{(21)} = 0 \\
 &\text{for } x_2 = 0; a_2 : u_1 = 0; N_{22} = 0; w = 0; M_{22} = 0 \\
 &\quad \chi_1^{(1)} = \chi_2^{(2)} = 0; N_{22}^{(23)} = N_{22}^{(24)} = 0
 \end{aligned} \tag{32}$$

The second lines in the conditions (32) model end diaphragms on the corresponded edges, which prevent the transverse shears in the planes of the ends and allow the shear along the normal edges. Various variants of such diaphragms and their modelling using the boundary conditions are given in detail in Ref [1,2].

In order to satisfy the conditions (32) the following expansions in the series are taken

$$\begin{aligned}
 u_1 &= \sum_m \sum_n U_{1mn} C_m S_n; \quad u_2 = \sum_m \sum_n U_{2mn} S_m C_n; \quad w = \sum_m \sum_n W_{mn} S_m S_n \\
 [\chi_1; \chi_2] &= \sum_m \sum_n [X_{1mn}; X_{2mn}] C_m S_n \\
 [\chi_3; \chi_4] &= \sum_m \sum_n [X_{3mn}; X_{4mn}] S_m C_n
 \end{aligned} \tag{33}$$

Correspondingly, expansions for the loads are as follows

$$p_1^{\bar{F}} = \sum_m \sum_n P_{1mn}^{\bar{F}} C_m S_n; \quad p_2^{\bar{F}} = \sum_m \sum_n P_{2mn}^{\bar{F}} S_m C_n; \quad p_3 = \sum_m \sum_n P_{3mn} S_m S_n \tag{34}$$

In equations (33) and (34) the the following notations are used:

$$\begin{aligned}
 \sin \frac{m\pi}{a_1} x_1 &= \sin \lambda_m x_1 = S_m; \quad \cos \frac{m\pi}{a_1} x_1 = \cos \lambda_m x_1 = C_m \\
 \sin \frac{n\pi}{a_2} x_2 &= \sin \gamma_n x_2 = S_n; \quad \cos \frac{n\pi}{a_2} x_2 = \cos \gamma_n x_2 = C_n
 \end{aligned} \tag{35}$$

The second case is a hinged support when the shell edges are not free to move in the directions normal to its contour. Tangential displacements along the edges are possible. This is the case of the hinged immovable support on the boundaries. Here the boundary conditions are as follows

$$\begin{aligned}
 &\text{for } x_1 = 0; a_1 : u_1 = 0; N_{12} = 0; w = 0; M_{11} = 0 \\
 &\quad \chi_3^{(2)} = \chi_4^{(2)} = 0; N_{11}^{(11)} = N_{11}^{(21)} = 0 \\
 &\text{for } x_2 = 0; a_2 : u_2 = 0; N_{21} = 0; w = 0; M_{22} = 0 \\
 &\quad \chi_1^{(1)} = \chi_2^{(1)} = 0; N_{22}^{(23)} = N_{22}^{(24)} = 0
 \end{aligned} \tag{36}$$

In satisfying the conditions (36) we will use the following expressions of the unknown functions in Fourier series

$$u_1 = \sum_m \sum_n U_{1mn} S_m C_n; \quad u_2 = \sum_m \sum_n U_{2mn} C_m S_n; \quad w = \sum_m \sum_n W_{mn} S_m S_n$$

$$\begin{aligned} [\chi_1; \chi_2] &= \sum_m \sum_n [X_{1mn}; X_{2mn}] C_n S_m \\ [\chi_3; \chi_4] &= \sum_m \sum_n [X_{3mn}; X_{4mn}] S_m C_m \end{aligned} \quad (37)$$

Corresponded expansions for the loads are as follows

$$p_1^{\mp} = \sum_m \sum_n P_{1mn}^{\mp} S_m C_n; \quad p_2^{\mp} = \sum_m \sum_n P_{2mn}^{\mp} C_m S_n; \quad p_3 = \sum_m \sum_n P_{3mn} S_m S_n \quad (38)$$

The expressions (33) and (34), (37) and (38) contain amplitudes of unknown functions U_{imn} , W_{mn} , X_{pmn} and the load functions P_{imn}^{\pm} , P_{3mn}^{\pm} .

Expansions of the unknown functions and the functions of loads for each case of the boundary conditions can be substitute into the expressions for submatrices of the system of differential equations (25). The object of such substitution is to obtain the system of algebraic equations for the amplitudes of the unknown functions when the load amplitudes are known. In so doing, the trigonometric multipliers for each equation must be retained. However, one can make sure that none of considered variants of the expansions does not allow to obtain a system of equations which could be free from the trigonometric multipliers. This fact is known, for example, from [3,4].

Therefore, the problem of cancelling terms of one or another of generalized stiffness characteristics and obtaining of the system of equations, which could be solved, must be considered in connection with the structure of the laminated shell, and also, with geometry of its surface. Next we consider some special cases of the structure, for which an analytical solution can be obtained.

There are two significant special cases of the structure of laminated plate or shell in practice. The first case is cross-ply laminated structure formed with layers reinforced at angles 0° and 90° to the orthogonal axes of coordinate x_1 and x_2 . The layers of shell with such a structure are orthotropic. The stiffness parameters $A_{16}^{(k)}$, $A_{26}^{(k)}$, $A_{36}^{(k)}$, $A_{45}^{(k)}$, $A_{54}^{(k)}$ for such layers are equal to zero. Consequently, the distribution functions of the stiffness characteristics will be also reduced to zero.

The second case is angle-ply laminated structure formed with layers reinforced at the same angles but opposite in sign $(-\theta, +\theta)$ to the coordinate axes x_1 and x_2 . The layers of such a shell are anisotropic and all the stiffness parameters remain in the Hooke's law. In this case, of interest is antisymmetric structure through the thickness about the mean surface, that is, each layer with fiber orientation $(-\theta)$ has corresponded layer with respect to the mean surface with fiber orientation $(+\theta)$. For this structure the stiffnesses $A_{16}^{(k)}$, $A_{26}^{(k)}$, $A_{36}^{(k)}$, $A_{45}^{(k)}$, $A_{54}^{(k)}$ of the given layers are opposite in sign (antisymmetric).

NUMERICAL RESULTS

Let us consider the numerical results of the bending problem of plates depending on the fiber orientation in the angle-ply laminates, and with different number of the layers. All the material data used were obtained from [3] for a unidirectional fiber-reinforced composite: $E_L = 174.6 \text{ GPa}$, $E_T = 7 \text{ GPa}$, $G_{LT} = 3.5 \text{ GPa}$, $G_{TT} = 1.4 \text{ GPa}$, $\nu_{LT} = \nu_{TT} = 0.25$, where L and T refer to the fiber direction and transverse direction, respectively.

Three sets of laminates are considered here: 1) two-layer angle ply $(-\theta, +\theta)$ laminates with layers of equal thickness $(h/2)$; 2) four-layer angle ply $(-\theta, +\theta, -\theta, +\theta)$ laminates with layers of equal thickness $(h/4)$; 3) six-layer angle ply $(-\theta, +\theta, -\theta, +\theta, -\theta, +\theta)$ laminates with layers of equal thickness $(h/6)$. Here the angle θ is measured from the positive x_1 -axis. Nondimensionalized deflections and stresses are presented according to the definitions given in [3]: The plates are square ($a_1 = a_2 = a$) and have side-to-thickness ratio $a/h = 10$. The numerical results are

given in Tables 1, 2, 3 and compared with exact three-dimensional solution obtained by [3]; with the values obtained from the first order shear deformation theory (FSDT) proposed by Reddy and based on the hypothesis of straight line; with the classical theory of plates (CTP).

The proposed rational theory of laminates is denoted as RTL. As seen from the tables, the results obtained using RTL are in good agreement with 3D solution. The discrepancy is about 3% for the stresses. FSDT gives deviation up to 15-20%, and CTP has large errors for the deflections: 1.5-2 times, despite the fact that the considered plates are comparatively thin. The results for the case when $\theta = 0$ are given only in Table 1 since for the rest of the cases they remain the same.

CONCLUSIONS

A rational higher-order shear deformation theory of anisotropic laminated plates and shallow shells is developed for the solution of static problems subject to both normal and tangential loads. There are three distinctive properties of the proposed theory. First one lies in the fact that it is based on hypotheses which are fully tied to the elastic characteristics of the anisotropic materials of the layers. Secondly, the theory is built on a rational level of difficulty, i.e. it does not add complexity in comparison with known theories of this type. Thirdly, the hypotheses and, correspondingly, all governing relations take into account the influence of the direct application of the tangential loads.

Summarizing the results presented in this paper, it is noted that the proposed rational shear deformation theory of the anisotropic laminated shells and plates can lead to a substantial improvement of the accuracy in the following and practical problems:

- i) Application of numerical methods for the general theory of the anisotropic laminated shells.
- ii) Investigation of the stress-strain state of the anisotropic laminated and, in particular, angle-ply laminated shells of negative Gauss curvature.
- iii) Optimal design of plates and shells with anisotropic layers for practical application in different engineering branches.

REFERENCES

1. Piskunov, V. G., Verijenko, V. E. and Prisyazhnyouk, V. K. *Calculation of heterogeneous shells and plates using the finite element method.* VEISHA SHKOLA, Kiev, 1987.
2. Piskunov, V. G., Verijenko, V. E., Adali, S. and Summers, E. B. "A higher order theory for the analysis of laminated plates and shells with shear and normal deformation." *International Journal of Engineering Science* **31** (6), 1993, pp. 967-988.
3. Sovaia, M. and Reddy, J. N. "A variational approach to three-dimensional elasticity solutions of laminated composite plates." *Transactions of the ASME*, **59**, 1992, pp. S166-S175.
4. Noor, A. K. and Burton, W. S. "Assessment of computational models for multilayered composite shells." *Appl. Mech. Rev.*, **43**, 1990, pp. 67-97.

Table 1. Maximum deflections and stresses in a laminated square two-layered anisotropic plate ($a = 10h$).

θ	Theory	\bar{w}	$\bar{\sigma}_{11}$	$\bar{\sigma}_{22}$	$\bar{\sigma}_{12}$	$\bar{\sigma}_{13}$	$\bar{\sigma}_{23}$
0	3-D	0.6348	0.5671	0.03567	0.02556	0.4222	0.04644
	RTL	0.6371	0.5701	0.03474	0.02575	0.4225	0.04548
	FSDT	0.6383	0.5248	0.03386	0.02463	0.4315	0.04594
	CTP	0.4313	0.5387	0.02667	0.02128	0.4398	0.03766
15	3-D	0.8027	0.5633	0.08062	0.07498	0.3418	0.08138
	RTL	0.8037	0.5701	0.08029	0.07594	0.3413	0.08058
	FSDT	0.8072	0.5330	0.07594	0.7445	0.3447	0.08160
	CTP	0.6205	0.5436	0.07276	0.07028	0.3493	0.07703
30	3-D	0.8568	0.4204	0.1696	0.1837	0.2699	0.1570
	RTL	0.8493	0.4258	0.1707	0.1874	0.2704	0.1570
	FSDT	0.8584	0.4044	0.1615	0.1799	0.2729	0.1581
	CTP	0.6842	0.4063	0.1614	0.1790	0.2735	0.1575
45	3-D	0.8250	0.2594	0.2594	0.2408	0.2154	0.2154
	RTL	0.8136	0.2625	0.2625	0.2452	0.2155	0.2155
	FSDT	0.8284	0.2498	0.2498	0.2336	0.2174	0.2174
	CTP	0.6547	0.2498	0.2498	0.2336	0.2174	0.2174

Table 2. Maximum deflections and stresses in a laminated square four-layered anisotropic plate ($a = 10h$).

θ	Theory	\bar{w}	$\bar{\sigma}_{11}$	$\bar{\sigma}_{22}$	$\bar{\sigma}_{12}$	$\bar{\sigma}_{13}$	$\bar{\sigma}_{23}$
15	3-D	0.6150	0.4453	0.06153	0.06739	0.4116	0.1074
	RTL	0.6001	0.4381	0.05886	0.07102	0.4149	0.1102
	FSDT	0.5839	0.3977	0.05429	0.06592	0.4228	0.1116
	CTP	0.3999	0.4090	0.05171	0.06158	0.4285	0.1055
30	3-D	0.5619	0.2833	0.1115	0.1331	0.3381	0.1995
	RTL	0.5290	0.2760	0.1068	0.1350	0.3447	0.2037
	FSDT	0.4885	0.2413	0.09346	0.1183	0.3543	0.2092
	CTP	0.3144	0.2431	0.09347	0.1174	0.3550	0.2084
45	3-D	0.5430	0.1749	0.1749	0.1642	0.2684	0.2684
	RTL	0.5063	0.1708	0.1708	0.1627	0.2745	0.2745
	FSDT	0.4549	0.1458	0.1458	0.1388	0.2841	0.2841
	CTP	0.2813	0.1458	0.1458	0.1388	0.2841	0.2841

Table 3. Maximum deflections and stresses in a laminated square six-layered anisotropic plate ($a = 10h$).

θ	Theory	\bar{w}	$\bar{\sigma}_{11}$	$\bar{\sigma}_{22}$	$\bar{\sigma}_{12}$	$\bar{\sigma}_{13}$	$\bar{\sigma}_{23}$
15	3-D	0.5781	0.4295	0.05838	0.06887	0.3696	0.09813
	RTL	0.5717	0.4293	0.05683	0.07257	0.3668	0.09739
	FSDT	0.5589	0.3904	0.05252	0.06738	0.3752	0.09885
	CTP	0.3752	0.4021	0.05003	0.06287	0.3808	0.09320
30	3-D	0.5087	0.2662	0.1037	0.1290	0.2957	0.1749
	RTL	0.4942	0.2685	0.1031	0.1342	0.2916	0.1724
	FSDT	0.4599	0.2362	0.09079	0.1183	0.2989	0.1764
	CTP	0.2858	0.2380	0.09081	0.1174	0.2996	0.1757
45	3-D	0.4890	0.1640	0.1640	0.1548	0.2355	0.2355
	RTL	0.4725	0.1667	0.1667	0.1593	0.2318	0.2318
	FSDT	0.4281	0.1435	0.1435	0.1372	0.2378	0.2378
	CTP	0.2544	0.1435	0.1435	0.1372	0.2378	0.2378

COMPUTATIONAL MODEL FOR DOUBLY CURVED LAMINATED SHELLS BASED ON A REFINED ASYMPTOTIC THEORY

Chih-Ping Wu¹, Jiann-Quo Tarn² and Yang Kai-Lin³

^{1,2,3}*Department of Civil Engineering, National Cheng Kung University, Tainan,
Taiwan 70101, Republic of China.*

SUMMARY: A multilevel computational model based on a refined asymptotic theory is presented. The formulation begins with a Hellinger–Reissner (H–R) functional where the displacements and transverse stresses are taken as the functions subject to variation. Upon introducing a set of appropriate dimensionless scaling and bringing the transverse shear deformations to the stage at the leading-order level, the weak formulation is asymptotically expanded as a series of weak-form equations for various orders. In the multilevel computational model, the transverse stresses and displacements can be interpolated independently. Through successive integration, the transverse stress degrees-of-freedom (DOF) are condensed in the element level. As a result, three midsurface displacement DOF and two rotation DOF for each node in an element are taken as the independent unknowns in the system equations for various orders. The element stiffness matrix for each order level remains unchanged and the forcing vector can be computed from the lower-order solutions. Thus, the solution procedure can be repeated level-by-level in a consistent and hierarchic way. Application of this multilevel computational model to a benchmark problem is demonstrated.

KEYWORDS: refined theory, asymptotic theory, Hellinger–Reissner functional, perturbation, elasticity, laminated shells, thick shells, doubly curved shells

INTRODUCTION

In recent paper [1], a refined asymptotic theory of double curved laminated shells by means of perturbation is proposed. It is an extension of the asymptotic theory [2, 3] developed recently for static and dynamic analyses of the laminated shells where the basic equations for various orders are identical to the system equations of the classical laminated shell theory (CST). By means of bringing the effect of transverse shear deformation to the stage at the leading-order level, the refined asymptotic formulation embraces the first-order shear deformation theory (FSDT) as the first-order approximation. The basic equations for each order level are merely the FSDT equations and remain unchanged. Thus, the accurate solutions can be determined hierarchically

by solving the FSDT equations. Applications to benchmark problems show that the convergent speed of the refined theory is rapid.

As illustrated in recent paper [1], we found there are several significant advantages in the refined asymptotic theory. Thus, the present work aims at developing a multilevel computational model based on the refined asymptotic theory for numerical modeling of the doubly curved laminated shell. The formulation begins with the Hellinger–Reissner (H–R) functional where the transverse stresses and displacements are regarded as the functions subject to variation. After an appropriate non-dimensionalization, bringing the shear deformation effect to the stage at the leading-order level, we asymptotically expand the (H–R) functional as a sequence of functionals for various orders. Upon expressing the field variables in an element in terms of the generalized nodal DOF and then imposing the stationary conditions for the (H–R) functional, we obtain a sequence of the weak-form equations for various orders. Through successive integration, the transverse stress DOF are condensed in the element level and three displacement DOF and two rotation DOF are taken as the nodal unknowns in an element. Accordingly, the element stiffness matrices and forcing vectors for various orders are obtained. It is shown that the element stiffness matrices are merely those of the FSDT finite element model and remain unchanged for various orders, and the forcing vectors can be computed from the lower-order approximations. Thus, the computational model provides a solution procedure which can be repeated by solving the system equations of the FSDT finite element model level-by-level. The accurate results can be yielded.

THEORY

Basic Variational Formulation

Consider an anisotropic, heterogeneous doubly curved shell of thickness $2h$ subjected to lateral loads $q(\alpha, \beta)$ on the top surface $\zeta=h$. The orthogonal curvilinear coordinates are denoted by α, β and ζ . R_α and R_β denote the curvature radii to the middle surface, a_α and a_β are the curvilinear dimensions in α and β directions, respectively.

The current computational model is based on the Hellinger–Reissner (H–R) principle. The H–R variational functional for the problem is

$$\begin{aligned} \Pi_R = & \int_{-h}^h \int_{\Omega} [\sigma_{ij} \varepsilon_{ij}(u_i) - B(\sigma_{ij})] d\Omega d\zeta - \int_{\Omega^+} q^+(\alpha, \beta) u_\zeta(\alpha, \beta, h) d\Omega^+ \\ & - \int_{\Omega^-} q^-(\alpha, \beta) u_\zeta(\alpha, \beta, -h) d\Omega^- - \int_{-h}^h \int_{\Gamma_\sigma} \bar{T}_i u_i d\Gamma d\zeta - \int_{-h}^h \int_{\Gamma_u} T_i (u_i - \bar{u}_i) d\Gamma d\zeta, \end{aligned} \quad (1)$$

where $B(\sigma_{ij})$ denotes the complementary energy density function such that $\varepsilon_{ij} = \partial B(\sigma_{ij}) / \partial \sigma_{ij}$; $\varepsilon_{ij}(u_i)$ is the displacement expressions of strains; Γ_σ and Γ_u denote the portions of the the edge boundary where tractions \bar{T}_i are prescribed and where displacements \bar{u}_i are prescribed; Ω represents the shell domain on the α – β plane at a certain thickness coordinate ζ ; $q^+(\alpha, \beta)$ and $q^-(\alpha, \beta)$ are the transverse loads applied on the top surface Ω^+ ($\zeta=h$) and the bottom

surface Ω^- ($\zeta = -h$) of the shell; $d\Omega^+$, $d\Omega^-$, $d\Omega$ are the differential area element on the surfaces of Ω^+ , Ω^- , Ω , respectively.

The displacements (u_α , u_β , u_ζ) and the transverse stresses ($\sigma_{\alpha\zeta}$, $\sigma_{\beta\zeta}$, σ_ζ) are taken as the primary variables, and are subject to variation in the formulation. By imposing $\delta\Pi_R = 0$, we obtain

$$\begin{aligned}
 \delta\Pi_R = & \int_{-h}^h \int_{\Omega} \left\{ [\sigma_\alpha (\delta u_{\alpha,\alpha} / \gamma_\alpha + \delta u_\zeta / \gamma_\alpha R_\alpha) + \sigma_\beta (\delta u_{\beta,\beta} / \gamma_\beta + \delta u_\zeta / \gamma_\beta R_\beta) + \sigma_\zeta \delta u_{\zeta,\zeta} \right. \\
 & + \sigma_{\alpha\zeta} (\delta u_{\zeta,\alpha} / \gamma_\alpha + \delta u_{\alpha,\zeta} - \delta u_\alpha / \gamma_\alpha R_\alpha) + \sigma_{\beta\zeta} (\delta u_{\zeta,\beta} / \gamma_\beta + \delta u_{\beta,\zeta} - \delta u_\beta / \gamma_\beta R_\beta) \\
 & + \sigma_{\alpha\beta} (\delta u_{\beta,\alpha} / \gamma_\alpha + \delta u_{\alpha,\beta} / \gamma_\beta) + u_{\zeta,\zeta} \delta \sigma_\zeta + (u_{\zeta,\alpha} / \gamma_\alpha + u_{\alpha,\zeta} - u_\alpha / \gamma_\alpha R_\alpha) \delta \sigma_{\alpha\zeta} \\
 & + (u_{\zeta,\beta} / \gamma_\beta + u_{\beta,\zeta} - u_\beta / \gamma_\beta R_\beta) \delta \sigma_{\beta\zeta} + [\tilde{c}_{13} u_{\alpha,\alpha} / \gamma_\alpha + \tilde{c}_{36} u_{\alpha,\beta} / \gamma_\beta + \tilde{c}_{36} u_{\beta,\alpha} / \gamma_\alpha \\
 & + \tilde{c}_{23} u_{\beta,\beta} / \gamma_\beta + \tilde{c}_{13} u_\zeta / \gamma_\alpha R_\alpha + \tilde{c}_{23} u_\zeta / \gamma_\beta R_\beta - \sigma_\zeta / c_{33}] \delta \sigma_\zeta - (s_{55} \sigma_{\alpha\zeta} + s_{45} \sigma_{\beta\zeta}) \delta \sigma_{\alpha\zeta} \\
 & \left. - (s_{45} \sigma_{\alpha\zeta} + s_{44} \sigma_{\beta\zeta}) \delta \sigma_{\beta\zeta} \right\} d\Omega d\zeta - \int_{\Omega^+} q^+ \delta u_\zeta d\Omega^+ - \int_{\Omega^-} q^- \delta u_\zeta d\Omega^- \\
 & - \int_{-h}^h \int_{\Gamma_u} [(u_\alpha - \bar{u}_\alpha) \delta T_\alpha + (u_\beta - \bar{u}_\beta) \delta T_\beta + (u_\zeta - \bar{u}_\zeta) \delta T_\zeta] d\Gamma d\zeta \\
 & - \int_{-h}^h \oint_{\Gamma} (T_\alpha \delta u_\alpha + T_\beta \delta u_\beta + T_\zeta \delta u_\zeta) d\Gamma d\zeta \\
 & = 0.
 \end{aligned} \tag{2}$$

Nondimensionalization

As formulated in earlier papers [1-3], the field variables are made dimensionless by introducing the scaling:

$$x = \frac{\alpha}{R\varepsilon}, \quad y = \frac{\beta}{R\varepsilon}, \quad z = \frac{\zeta}{h}; \quad u = \frac{u_\alpha}{R\varepsilon}, \quad v = \frac{u_\beta}{R\varepsilon}, \quad w = \frac{u_\zeta}{R}; \quad R_x = \frac{R_\alpha}{R}, \quad R_y = \frac{R_\beta}{R}; \tag{3a,b,c}$$

$$\sigma_x = \frac{\sigma_\alpha}{Q}, \quad \sigma_y = \frac{\sigma_\beta}{Q}, \quad \tau_{xy} = \frac{\tau_{\alpha\beta}}{Q}; \quad \tau_{xz} = \frac{\tau_{\alpha\zeta}}{Q\varepsilon}, \quad \tau_{yz} = \frac{\tau_{\beta\zeta}}{Q\varepsilon}, \quad \sigma_z = \frac{\sigma_\zeta}{Q\varepsilon^2}. \tag{3d,e}$$

where $\varepsilon^2 = h/R < 1$ is a small perturbation parameter. R denotes a characteristic length of the shell. Q is a reference elastic modulus.

After introducing Eqn 3 and the essential boundary conditions in Eqn 2, then integrating by parts the terms associated with $\delta u_{,\alpha}$ and $\delta w_{,\zeta}$, we have

$$\begin{aligned}
 \delta \Pi_R = QRh^2 & \left[\int_{-1}^1 \int_{\Omega} \left\{ (\mathbf{L}_1 \mathbf{u} + \mathbf{L}_2 \mathbf{w} + \varepsilon^2 \mathbf{L}_3 \sigma_z)^T \mathbf{D}_1 - \sigma_{z,z}^T - \varepsilon^2 (\mathbf{L}_4 \sigma_s)^T - \varepsilon^4 (\mathbf{L}_5 \sigma_s)^T \right\} \delta \mathbf{u} \right. \\
 & + [(\mathbf{L}_1 \mathbf{u} + \mathbf{L}_2 \mathbf{w})^T \mathbf{D}_2 - \sigma_{z,z} - \varepsilon^2 l_1 \sigma_z - \varepsilon^4 l_2 \sigma_z + \sigma_s^T \mathbf{D} + \varepsilon^2 \sigma_s^T \mathbf{L}_6] \delta \mathbf{w} + [\mathbf{D} \mathbf{w} + \mathbf{u}_{,z} + \varepsilon^2 \mathbf{L}_7 \mathbf{u} + \varepsilon^2 \mathbf{L}_6 \mathbf{w} \\
 & + \varepsilon^4 \mathbf{L}_8 \mathbf{u} - \varepsilon^2 \mathbf{S} \sigma_s - \varepsilon^4 \mathbf{L}_9 \sigma_s]^T \delta \sigma_s + [w_{,z} + \varepsilon^2 l_3 \mathbf{w} + \varepsilon^2 \mathbf{L}_{10} \mathbf{u} - \varepsilon^4 l_4 \sigma_z] \delta \sigma_z \left. \right] dx dy dz \\
 & - \int_{-1}^1 \int_{\Gamma_\sigma} (\bar{\mathbf{P}}^T \delta \mathbf{u} + \bar{P}_z \delta w) d\Gamma dz = 0, \tag{4}
 \end{aligned}$$

where $\mathbf{u} = \{u \ v\}^T$, $\sigma_s = \{\tau_{xz} \ \tau_{yz}\}^T$, $\mathbf{S} = \begin{bmatrix} \tilde{s}_{55} & \tilde{s}_{45} \\ \tilde{s}_{45} & \tilde{s}_{44} \end{bmatrix}$, $l_i, \mathbf{D}_i, \mathbf{L}_i$ are the relevant matrices.

The Refined Asymptotic Approach

The relationship between the dimensionless transverse shear stresses and strains is

$$\sigma_s = \varepsilon^{-2} \mathbf{C}_s \gamma_s, \tag{5}$$

where $\mathbf{C}_s = \begin{bmatrix} \tilde{c}_{55} & \tilde{c}_{45} \\ \tilde{c}_{45} & \tilde{c}_{44} \end{bmatrix}$, $\gamma_s = \begin{bmatrix} \varepsilon_{xz} \\ \varepsilon_{yz} \end{bmatrix}$, $\varepsilon_{xz} = \varepsilon \varepsilon_{\alpha\zeta}$, $\varepsilon_{yz} = \varepsilon \varepsilon_{\beta\zeta}$.

As formulated in the earlier paper [1], we realize that the transverse displacement is not explicitly related to the transverse shear stresses while the in-surface displacements are related to the transverse shear stresses at the ε^2 level. In order to account for the effect of transverse shear deformations at the leading-order level, we introduce the auxiliary variables ψ_x, ψ_y associated with the transverse shear deformations and decompose the transverse shear strains as

$$\gamma_s = \boldsymbol{\Psi} + \varepsilon^2 \mathbf{S} \hat{\boldsymbol{\sigma}}_s, \tag{6}$$

where $\boldsymbol{\Psi} = \{\psi_x \ \psi_y\}^T$, $\hat{\boldsymbol{\sigma}}_s = \{\hat{\sigma}_{xz} \ \hat{\sigma}_{yz}\}$; ψ_x and ψ_y are the average shear rotations at the middle surface, $\hat{\sigma}_{xz}$ and $\hat{\sigma}_{yz}$ thus represent the difference between the actual transverse shear stresses and the approximate ones.

Substituting Eqn 6 into Eqn 5, and multiplying both sides of the resulting equation by $\varepsilon^2 \mathbf{S}$, we have

$$\varepsilon^2 \mathbf{S} \sigma_s = \boldsymbol{\Psi} + \varepsilon^2 \mathbf{S} \hat{\boldsymbol{\sigma}}_s. \tag{7}$$

Asymptotic Expansion

We expand the field variables in powers of ε^2 as given by

$$f(x, y, z; \varepsilon) = f_{(0)}(x, y, z) + \varepsilon^2 f_{(1)}(x, y, z) + \varepsilon^4 f_{(2)}(x, y, z) + \dots \tag{8}$$

After substituting Eqns 6–7 into the Eqn 4, and collecting the equal-power term of ε , we obtain

$$\delta\Pi_R = QRh^2(\delta\Pi_{(0)} + \varepsilon^2 \delta\Pi_{(1)} + \varepsilon^4 \delta\Pi_{(2)} + \dots) = 0. \quad (9)$$

where

$$\begin{aligned} \delta\Pi_{(0)} = & \int_{-1}^1 \int_{\Omega} \left\{ (\mathbf{L}_1 \mathbf{u}_{(0)} + \mathbf{L}_2 \mathbf{w}_{(0)})^T (\mathbf{D}_1 \delta \mathbf{u}_0) - \boldsymbol{\sigma}_{s(0),z}^T \delta \mathbf{u}_0 + (\mathbf{L}_1 \mathbf{u}_{(0)} + \mathbf{L}_2 \mathbf{w}_{(0)})^T (\mathbf{D}_2 \delta \mathbf{w}_0) \right. \\ & - \boldsymbol{\sigma}_{z(0),z}^T \delta \mathbf{w}_0 + \boldsymbol{\sigma}_{s(0)}^T (\mathbf{D} \delta \mathbf{w}_0) + z (\mathbf{L}_1 \mathbf{u}_{(0)} + \mathbf{L}_2 \mathbf{w}_{(0)})^T (\mathbf{D}_1 \delta \boldsymbol{\phi}_0) + (\mathbf{C} \boldsymbol{\psi}_0)^T \delta \boldsymbol{\phi}_0 \\ & \left. + [\mathbf{u}_{(0),z}^T + (\mathbf{D} \mathbf{w}_{(0)})^T - \boldsymbol{\psi}_0^T] \delta \boldsymbol{\sigma}_{s(0)} + \mathbf{w}_{(0),z} \delta \boldsymbol{\sigma}_{z(0)} \right\} dx dy dz \\ & - \int_{-1}^1 \int_{\Gamma} (\mathbf{P}^T \delta \mathbf{u}_0 + P_z \delta \mathbf{w}_0) d\Gamma dz - \int_{-1}^1 \int_{\Gamma} z \mathbf{P}^T \delta \boldsymbol{\phi}_0 d\Gamma dz. \end{aligned} \quad (10)$$

$$\begin{aligned} \delta\Pi_{(k)} = & \int_{-1}^1 \int_{\Omega} \left\{ (\mathbf{L}_1 \mathbf{u}_{(k)} + \mathbf{L}_2 \mathbf{w}_{(k)})^T (\mathbf{D}_1 \delta \mathbf{u}_k) + (\mathbf{L}_3 \boldsymbol{\sigma}_{z(k-1)})^T (\mathbf{D}_1 \delta \mathbf{u}_k) - \boldsymbol{\sigma}_{s(k),z}^T \delta \mathbf{u}_k - (\mathbf{L}_4 \boldsymbol{\sigma}_{s(k-1)})^T \delta \mathbf{u}_k \right. \\ & - (\mathbf{L}_5 \boldsymbol{\sigma}_{s(k-2)})^T \delta \mathbf{u}_k + (\mathbf{L}_1 \mathbf{u}_{(k)} + \mathbf{L}_2 \mathbf{w}_{(k)})^T (\mathbf{D}_2 \delta \mathbf{w}_k) - \boldsymbol{\sigma}_{z(k),z}^T \delta \mathbf{w}_k - (l_1 \boldsymbol{\sigma}_{z(k-1)}) \delta \mathbf{w}_k - (l_2 \boldsymbol{\sigma}_{z(k-2)}) \delta \mathbf{w}_k \\ & + \boldsymbol{\sigma}_{s(k)}^T (\mathbf{D} \delta \mathbf{w}_k) + \boldsymbol{\sigma}_{s(k-1)}^T (\mathbf{L}_6 \delta \mathbf{w}_k) + z (\mathbf{L}_1 \mathbf{u}_{(k)} + \mathbf{L}_2 \mathbf{w}_{(k)})^T (\mathbf{D}_1 \delta \boldsymbol{\phi}_k) + z (\mathbf{L}_3 \boldsymbol{\sigma}_{z(k-1)})^T (\mathbf{D}_1 \delta \boldsymbol{\phi}_k) \\ & + (\mathbf{C} \boldsymbol{\psi}_k)^T \delta \boldsymbol{\phi}_k - z (\mathbf{L}_4 \boldsymbol{\sigma}_{s(k-1)})^T \delta \boldsymbol{\phi}_k - z (\mathbf{L}_5 \boldsymbol{\sigma}_{s(k-2)})^T \delta \boldsymbol{\phi}_k + [\mathbf{u}_{(k),z}^T + (\mathbf{D} \mathbf{w}_{(k)})^T - \boldsymbol{\psi}_k^T] \delta \boldsymbol{\sigma}_{s(k)} \\ & - \mathbf{S} \hat{\boldsymbol{\sigma}}_{s(k-1)} \delta \boldsymbol{\sigma}_{s(k)} + (\mathbf{L}_7 \mathbf{u}_{(k-1)}) \delta \boldsymbol{\sigma}_{s(k)} + (\mathbf{L}_6 \mathbf{w}_{(k-1)}) \delta \boldsymbol{\sigma}_{s(k)} + (\mathbf{L}_8 \mathbf{u}_{(k-2)}) \delta \boldsymbol{\sigma}_{s(k)} - (\mathbf{L}_9 \boldsymbol{\sigma}_{s(k-2)}) \delta \boldsymbol{\sigma}_{s(k)} \\ & \left. + \mathbf{w}_{(k),z} \delta \boldsymbol{\sigma}_{z(k)} + (l_3 \mathbf{w}_{(k-1)}) \delta \boldsymbol{\sigma}_{z(k)} + (\mathbf{L}_{10} \mathbf{u}_{(k-1)}) \delta \boldsymbol{\sigma}_{z(k)} - (l_4 \boldsymbol{\sigma}_{z(k-2)}) \delta \boldsymbol{\sigma}_{z(k)} \right\} dx dy dz \quad (k=1, 2, \dots). \end{aligned} \quad (11)$$

The total rotation $\boldsymbol{\phi} = \boldsymbol{\psi} - \mathbf{D} \mathbf{w}$ and $\mathbf{C} = (R/h) \mathbf{S}^{-1}$.

Multilevel Computational Model

Eqn 9 is an expansion of $\delta\Pi_R$ in terms of even powers of ε . Thus, we have decomposed the H-R functional into functionals of various orders; $\delta\Pi_{(0)}=0$ represents the leading-order approximation to the stationary condition $\delta\Pi_R=0$, $\delta\Pi_{(1)}=0$ provides the ε^2 -order modification, $\delta\Pi_{(2)}=0$ the ε^4 -order modification, and so on.

The Leading-Order Level

The x-y plane of the domain is represented by a finite element mesh and variations of the field variables in an element are expressed in terms of the generalized nodal DOF by

$$\mathbf{u}_{(0)}(x, y, z) = \mathbf{N} \mathbf{u}_{(0)}^e(z), \quad (12)$$

$$\mathbf{w}_{(0)}(x, y, z) = \mathbf{N}_w \mathbf{w}_{(0)}^e(z), \quad (13)$$

$$\boldsymbol{\sigma}_{s(0)}(x, y, z) = \mathbf{N}_s \boldsymbol{\sigma}_{s(0)}^e(z), \quad (14)$$

$$\boldsymbol{\sigma}_{z(0)}(x, y, z) = \mathbf{N}_z \boldsymbol{\sigma}_{z(0)}^e(z), \quad (15)$$

$$\boldsymbol{\psi}_0(x, y) = \mathbf{N} \boldsymbol{\psi}_0^e, \quad (16)$$

where \mathbf{N} , \mathbf{N}_w , \mathbf{N}_s , \mathbf{N}_z denote the interpolation functions of x and y , the generalized nodal DOF $\mathbf{u}_{(0)}^e$, $\mathbf{w}_{(0)}^T$, $\boldsymbol{\sigma}_{s(0)}^e$ and $\boldsymbol{\sigma}_{z(0)}^e$ are functions of z , the shear rotation DOF of the midsurface $\boldsymbol{\Psi}_0^e$ are independent of z . As will be shown, the through-thickness variations of the generalized nodal DOF can be derived analytically by successive integration, and the transverse stress DOF are condensed along the way; only the displacement and rotation DOF enter the system equation at each level.

Substituting Eqns 12–16 into $\delta\Pi_{(0)}$ gives

$$\begin{aligned} \delta\Pi_{(0)} = & \int_{-1}^1 \left\{ \left[\left(\mathbf{u}_{(0)}^e \right)^T \boldsymbol{\Psi}_1 + \left(\mathbf{w}_{(0)}^e \right)^T \boldsymbol{\Psi}_2 - \left(\boldsymbol{\sigma}_{s(0)}^e \right)^T \boldsymbol{\Phi}_1 - \mathbf{P}^T \right] \delta \mathbf{u}_0^e + \left[\left(\mathbf{u}_{(0)}^e \right)^T \boldsymbol{\Psi}_3 + \left(\mathbf{w}_{(0)}^e \right)^T \boldsymbol{\Psi}_4 \right. \right. \\ & \left. \left. - \left(\boldsymbol{\sigma}_{z(0),z}^e \right)^T \boldsymbol{\Phi}_3 + \left(\boldsymbol{\sigma}_{s(0)}^e \right)^T \boldsymbol{\Phi}_2 - \mathbf{P}_w^T \right] \delta \mathbf{w}_0^e + \left[z \left(\mathbf{u}_{(0)}^e \right)^T \boldsymbol{\Psi}_1 + z \left(\mathbf{w}_{(0)}^e \right)^T \boldsymbol{\Psi}_2 + \left(\boldsymbol{\Psi}_0^e \right)^T \boldsymbol{\Psi}_c \right. \right. \\ & \left. \left. - z \mathbf{P}^T \right] \delta \boldsymbol{\phi}_0^e + \left[\left(\mathbf{u}_{(0),z}^e \right)^T \boldsymbol{\Phi}_1 + \left(\mathbf{w}_{(0)}^e \right)^T \boldsymbol{\Phi}_2 - \left(\boldsymbol{\Psi}_0^e \right)^T \boldsymbol{\Phi}_1^T \right] \delta \boldsymbol{\sigma}_{s(0)}^e + \left[\left(\mathbf{w}_{(0),z}^e \right)^T \boldsymbol{\Phi}_3 \right] \delta \boldsymbol{\sigma}_{z(0)}^e \right\}, \quad (17) \end{aligned}$$

where

$$\begin{aligned} \boldsymbol{\Psi}_1 &= \int_{\Omega_e} (\mathbf{L}_1 \mathbf{N})^T (\mathbf{D}_1 \mathbf{N}) dx dy, & \boldsymbol{\Psi}_2 &= \int_{\Omega_e} (\mathbf{L}_2 \mathbf{N}_w)^T (\mathbf{D}_1 \mathbf{N}) dx dy, \\ \boldsymbol{\Psi}_3 &= \int_{\Omega_e} (\mathbf{L}_1 \mathbf{N})^T (\mathbf{D}_2 \mathbf{N}_w) dx dy, & \boldsymbol{\Psi}_4 &= \int_{\Omega_e} (\mathbf{L}_2 \mathbf{N}_w)^T (\mathbf{D}_2 \mathbf{N}_w) dx dy, \\ \boldsymbol{\Psi}_c &= \int_{\Omega_e} \mathbf{N}^T \mathbf{C} \mathbf{N} dx dy, & \boldsymbol{\Phi}_1 &= \int_{\Omega_e} \mathbf{N}_s^T \mathbf{N} dx dy, & \boldsymbol{\Phi}_2 &= \int_{\Omega_e} \mathbf{N}_s^T (\mathbf{D} \mathbf{N}_w) dx dy, \\ \boldsymbol{\Phi}_3 &= \int_{\Omega_e} \mathbf{N}_z^T \mathbf{N}_w dx dy, & \mathbf{P} &= \int_{\Gamma_e} \mathbf{N}^T \bar{\mathbf{P}} d\Gamma, & \mathbf{P}_w &= \int_{\Gamma_e} \mathbf{N}_w^T \bar{\mathbf{P}}_w d\Gamma, \end{aligned}$$

Ω_e denotes the element domain, \mathbf{P} and \mathbf{P}_w appear only when the element boundaries coincide with the edge boundary on which tractions are prescribed.

At the element level, the condition $\delta\Pi_{(0)} = 0$ leads to

$$\delta \boldsymbol{\sigma}_{z(0)}^e: \quad \frac{d}{dz} \mathbf{w}_{(0)}^e = \mathbf{0}, \quad (18)$$

$$\delta \boldsymbol{\sigma}_{s(0)}^e: \quad \frac{d}{dz} \mathbf{u}_{(0)}^e + \boldsymbol{\Phi}_1^{-1} \boldsymbol{\Phi}_2 \mathbf{w}_{(0)}^e - \boldsymbol{\Psi}_0^e = \mathbf{0}, \quad (19)$$

$$\delta \mathbf{u}_{(0)}^e: \quad \boldsymbol{\Psi}_1^T \mathbf{u}_{(0)}^e + \boldsymbol{\Psi}_2^T \mathbf{w}_{(0)}^e - \boldsymbol{\Phi}_1^T \frac{d}{dz} \boldsymbol{\sigma}_{s(0)}^e - \mathbf{P} = \mathbf{0}, \quad (20)$$

$$\delta \mathbf{w}_{(0)}^e: \quad \boldsymbol{\Psi}_3^T \mathbf{u}_{(0)}^e + \boldsymbol{\Psi}_4^T \mathbf{w}_{(0)}^e + \boldsymbol{\Phi}_2^T \boldsymbol{\sigma}_{s(0)}^e - \boldsymbol{\Phi}_3^T \frac{d}{dz} \boldsymbol{\sigma}_{z(0)}^e - \mathbf{P}_w = \mathbf{0}, \quad (21)$$

$$\delta \boldsymbol{\phi}_0^e: \quad \int_{-1}^1 \left(z \boldsymbol{\Psi}_1^T \mathbf{u}_{(0)}^e + z \boldsymbol{\Psi}_2^T \mathbf{w}_{(0)}^e + \boldsymbol{\Psi}_c^T \boldsymbol{\Psi}_0^e \right) dz - \int_{-1}^1 z \mathbf{P} dz = \mathbf{0}. \quad (22)$$

Successive integration of Eqns 18–22 with respect to z yields

$$\mathbf{w}_{(0)}^e = \mathbf{w}_0^e, \quad (23)$$

$$\mathbf{u}_{(0)}^e(z) = \mathbf{u}_0^e + z \boldsymbol{\phi}_0^e, \quad (24)$$

$$\boldsymbol{\sigma}_{s(0)}^e(z) = (\boldsymbol{\Phi}_1^T)^{-1} \int_{-1}^z \left[\boldsymbol{\Psi}_1^T (\mathbf{u}_0^e + \eta \boldsymbol{\phi}_0^e) + \boldsymbol{\Psi}_2^T \mathbf{w}_0^e - \mathbf{P} \right] d\eta, \quad (25)$$

$$\begin{aligned} \boldsymbol{\sigma}_{z(0)}^e(z) = & (\boldsymbol{\Phi}_3^T)^{-1} \left\{ \boldsymbol{\Phi}_2^T (\boldsymbol{\Phi}_1^T)^{-1} \int_{-1}^z (z-\eta) \left[\boldsymbol{\Psi}_1^T (\mathbf{u}_0^e + \eta \boldsymbol{\phi}_0^e) + \boldsymbol{\Psi}_2^T \mathbf{w}_0^e - \mathbf{P} \right] d\eta \right. \\ & \left. + \int_{-1}^z \left[\boldsymbol{\Psi}_3^T (\mathbf{u}_0^e + \eta \boldsymbol{\phi}_0^e) + \boldsymbol{\Psi}_4^T \mathbf{w}_0^e \right] d\eta - \int_{-1}^z \mathbf{P}_w d\eta \right\} - \tilde{q}^-, \end{aligned} \quad (26)$$

$$\int_{-1}^1 \left[z \boldsymbol{\Psi}_1^T (\mathbf{u}_0^e + z \boldsymbol{\phi}_0^e) + z \boldsymbol{\Psi}_2^T \mathbf{w}_0^e + \boldsymbol{\Psi}_c^T (\boldsymbol{\phi}_0^e + \boldsymbol{\Phi}_1^{-1} \boldsymbol{\Phi}_2 \mathbf{w}_0^e) \right] dz - \int_{-1}^1 z \mathbf{P} dz = 0, \quad (27)$$

where \mathbf{w}_0^e , \mathbf{u}_0^e represent the leading-order approximation to the midsurface displacement DOF; $\boldsymbol{\phi}_0^e = \boldsymbol{\Psi}_0^e - \boldsymbol{\Phi}_1^{-1} \boldsymbol{\Phi}_2 \mathbf{w}_0^e$ which represents the total rotation DOF.

After imposition of the lateral boundary conditions on top surface ($z=1$) in Eqns 25–26, then a simplification of the resulting equations, it leads to

$$\begin{bmatrix} \mathbf{K}_{uu} & \mathbf{K}_{uw} & \mathbf{K}_{u\phi} \\ \mathbf{K}_{wu} & \mathbf{K}_{ww} & \mathbf{K}_{w\phi} \\ \mathbf{K}_{\phi u} & \mathbf{K}_{\phi w} & \mathbf{K}_{\phi\phi} \end{bmatrix} \begin{Bmatrix} \mathbf{u}_0^e \\ \mathbf{w}_0^e \\ \boldsymbol{\phi}_0^e \end{Bmatrix} = \begin{Bmatrix} \mathbf{F}_{u0} \\ \mathbf{F}_{w0} \\ \mathbf{F}_{\phi 0} \end{Bmatrix}, \quad (28)$$

where $\mathbf{K}_{uu} = \int_{-1}^1 \boldsymbol{\Psi}_1^T dz$, $\mathbf{K}_{uw} = \int_{-1}^1 \boldsymbol{\Psi}_2^T dz$, $\mathbf{K}_{u\phi} = \int_{-1}^1 z \boldsymbol{\Psi}_1^T dz$, $\mathbf{K}_{wu} = \int_{-1}^1 \boldsymbol{\Psi}_3^T dz$,

$$\mathbf{K}_{ww} = \boldsymbol{\Phi}_2^T (\boldsymbol{\Phi}_1^T)^{-1} \left(\int_{-1}^1 \boldsymbol{\Psi}_c^T dz \right) \boldsymbol{\Phi}_1^{-1} \boldsymbol{\Phi}_2 + \int_{-1}^1 \boldsymbol{\Psi}_4^T dz, \quad \mathbf{K}_{w\phi} = \boldsymbol{\Phi}_2^T (\boldsymbol{\Phi}_1^T)^{-1} \int_{-1}^1 \boldsymbol{\Psi}_c^T dz + \int_{-1}^1 z \boldsymbol{\Psi}_3^T dz,$$

$$\mathbf{K}_{\phi u} = \int_{-1}^1 z \boldsymbol{\Psi}_1^T dz, \quad \mathbf{K}_{\phi w} = \int_{-1}^1 z \boldsymbol{\Psi}_2^T dz + \left(\int_{-1}^1 \boldsymbol{\Psi}_c^T dz \right) \boldsymbol{\Phi}_1^{-1} \boldsymbol{\Phi}_2, \quad \mathbf{K}_{\phi\phi} = \int_{-1}^1 z^2 \boldsymbol{\Psi}_1^T dz + \int_{-1}^1 \boldsymbol{\Psi}_c^T dz,$$

$$\mathbf{F}_{u0} = \int_{-1}^1 \mathbf{P} dz, \quad \mathbf{F}_{w0} = \int_{-1}^1 \mathbf{P}_w dz + \boldsymbol{\Phi}_3^T (\tilde{q}^+ + \tilde{q}^-), \quad \mathbf{F}_{\phi 0} = \int_{-1}^1 z \mathbf{P} dz.$$

After carrying out the integral expressions of $\boldsymbol{\Psi}_1$, $\boldsymbol{\Psi}_2$, $\boldsymbol{\Psi}_3$, we have $\boldsymbol{\Psi}_2^T = \boldsymbol{\Psi}_3$, $\boldsymbol{\Psi}_1^T = \boldsymbol{\Psi}_1$. Thus, the coefficient matrix in Eqn 28 is symmetric and $\mathbf{K}_{wu} = \mathbf{K}_{uw}^T$, $\mathbf{K}_{u\phi} = \mathbf{K}_{\phi u}^T$, $\mathbf{K}_{w\phi} = \mathbf{K}_{\phi w}^T$.

Eqn 28 consists of $5n$ equations in $5n$ unknown DOF for an element with n nodes. The resultant shear and moment in the generalized force vector appear only at the boundary nodes on Γ_σ . After assembling the element matrices into system equations and imposing the prescribed essential at the boundary nodes on Γ_u , we can determine the unknown DOF at the interior nodes and at the boundary nodes on Γ_σ , whereas the generalized force components at the boundary nodes on Γ_σ can also be determined. Afterwards, the leading-order approximation to the displacements and stresses are determined by using Eqns 23–26.

Higher-Order Corrections

After the similar manipulation as done at the ε^0 -order level, the ε^{2k} -order corrections to the midsurface displacements ($\mathbf{w}_k^e, \mathbf{u}_k^e$) and rotations (ϕ_k^e) can be determined from

$$\begin{bmatrix} \mathbf{K}_{uu} & \mathbf{K}_{uw} & \mathbf{K}_{u\phi} \\ \mathbf{K}_{wu} & \mathbf{K}_{ww} & \mathbf{K}_{w\phi} \\ \mathbf{K}_{\phi u} & \mathbf{K}_{\phi w} & \mathbf{K}_{\phi\phi} \end{bmatrix} \begin{Bmatrix} \mathbf{u}_k^e \\ \mathbf{w}_k^e \\ \phi_k^e \end{Bmatrix} = \begin{Bmatrix} \mathbf{F}_{uk} \\ \mathbf{F}_{wk} \\ \mathbf{F}_{\phi k} \end{Bmatrix}, \quad (29)$$

where $\mathbf{F}_{uk} = -\Phi_1^T \mathbf{I}_k(z=1)$, $\mathbf{F}_{wk} = \Phi_2^T \mathbf{I}_k(z=1) - \Phi_3^T \mathbf{J}_k(z=1) - \Phi_2^T \mathbf{K}_k(z=1)$, $\mathbf{F}_{\phi k} = -\Phi_1^T \mathbf{K}_k(z=1)$. For brevity, the detailed expressions of $\mathbf{I}_k, \mathbf{J}_k$ and \mathbf{K}_k are omitted.

It is noted that the coefficient matrix at the higher-order levels is the same as that at the leading-order level, and their nonhomogeneous terms can be computed from the lower-order solutions. Thus, the current computational model provides a solution procedure to yield the three-dimensional solution and this procedure can be repeated in a consistent and hierarchic way.

ILLUSTRATIVE EXAMPLES

A $[0/90/0]$ cross-ply laminated spherical shell with shear-diaphragm supports, subjected to $q(\alpha, \beta) = q_0 \sin\pi\alpha/a_\alpha \sin\pi\beta/a_\beta$ is considered. The geometry parameters and material properties used in the computation are $a_\alpha/a_\beta = 1$; $R_\alpha/R_\beta = 1$; $R_\alpha/a_\alpha = 1$; $2h/a_\alpha = 0.01, 0.03, 0.05, 0.07, 0.09, 0.1$; and $E_l/E_T = 25$; $G_{lT}/E_T = 0.5$; $G_{TT}/E_T = 0.2$; $E_T = 689 \times 10^6 \text{ KN/m}^2$ (10^6 psi); $\nu_{lT} = \nu_{TT} = 0.25$.

Table 1 shows the $\varepsilon^0, \varepsilon^2, \varepsilon^4$ and ε^6 -order solutions of the normalized transverse displacement \bar{w} , $\bar{w} = u_\zeta (2h)^3 E_T 10^3 / q_0 (a_\alpha)^4$, for different ratios of $2h/a_\alpha$. To obtain convergent results, the analysis is carried to ε^2 order in the case of thin shells ($2h/a_\alpha = 0.01$), and to ε^4 order in the case of thick shells ($2h/a_\alpha = 0.1$). Comparisons of the numerical results obtained from a discrete-layer higher-order theory [4], an approximate 3-D elasticity [5], FSDT [6], HSDT [7] and CST [8] are presented. It is found that the ε^0 -order solution of the present asymptotic theory agrees with the FSDT solution. The convergent results are in close agreement with the discrete-layer solution as well as the approximate elasticity solution. Figs. 1-2 consider a $[0/90/0/90/0]_2$ doubly curved shell subjected to a sinusoidal load. The geometry parameters are $a_\alpha/a_\beta = 1$; $R_\alpha/a_\alpha = 1$; $R_\beta/a_\beta = 10$; $2h/a_\alpha = 0.1$. Through-thickness distributions of the transverse shear and normal stresses for the $\varepsilon^0, \varepsilon^2, \varepsilon^4$ orders are presented. As can be seen, the convergent speed of the present asymptotic solution is rapid. The asymptotic solution yields continuous interlaminar stresses through the thickness, and traction boundary conditions at the lateral surfaces are satisfied exactly.

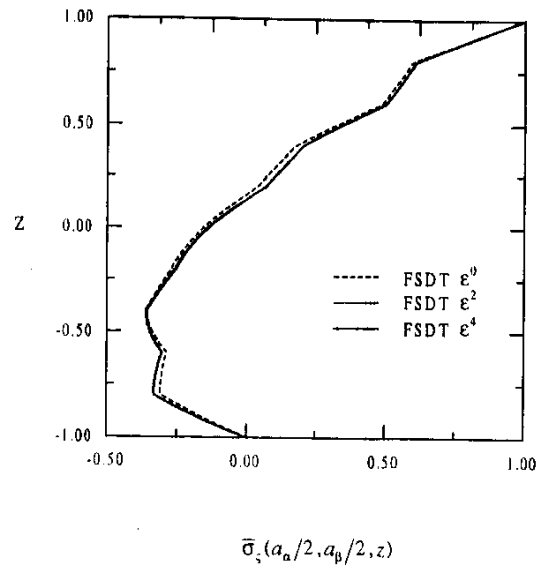
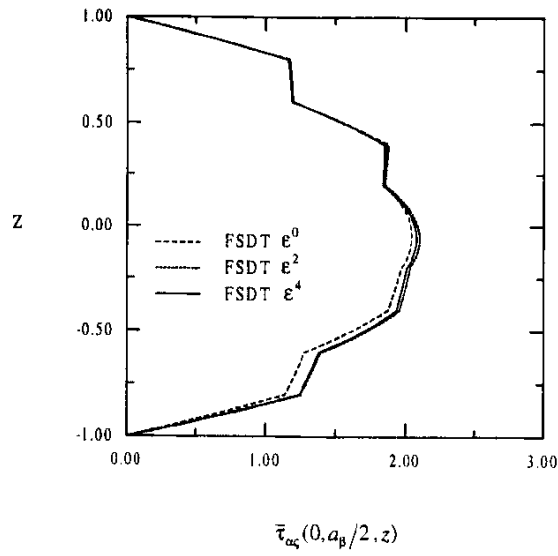


Fig. 1: Distribution of transverse shear stress through thickness of a $[0/90/0/90/0]_2$ doubly curved shell

Fig. 2: Distribution of transverse normal stress through thickness of a $[0/90/0/90/0]_2$ doubly curved shell

Table 1: Center deflection parameter of $[0/90/0]$ spherical shells

$2h/R_\alpha$ ($2h/a_\alpha$)	Present study		Wu and Liu [4] (discrete-layer theory)	Fan and Zhang [5] (approximate elasticity solution)	Reddy [6] (FSDT)		Reddy and Liu [7] (HSDT)	Leissa and Qatu [8] (CST)
					($k_1=07$, $k_2=06$)	($k_1=5/6$, $k_2=5/6$)		
0.01	e^0	0.0535	0.0541	0.0541	0.0536	0.0536	0.0535	0.0535
	e^2	0.0541						
	e^4	0.0541						
	e^6	0.0541						
0.03	e^0	0.4397	0.4624	0.4624	0.4487	0.4480	0.4419	0.4379
	e^2	0.4626						
	e^4	0.4624						
	e^6	0.4624						
0.05	e^0	1.0571	1.1723	1.1724	1.1144	1.1052	1.0730	1.0304
	e^2	1.1726						
	e^4	1.1726						
	e^6	1.1723						
0.07	e^0	1.7686	2.0860	2.0863	1.9435	1.9024	1.8231	1.6427
	e^2	2.0848						
	e^4	2.0870						
	e^6	2.0860						
0.09	e^0	2.5224	3.1659	3.1667	2.8953	2.7870	2.6473	2.1746
	e^2	3.1612						
	e^4	3.1674						
	e^6	3.1659						
0.10	e^0	2.9135	3.7664	3.7676	3.4152	3.2588	3.0856	2.4007
	e^2	3.7595						
	e^4	3.7674						
	e^6	3.7664						

CONCLUSIONS

A multilevel computational model based on a refined asymptotic theory is presented for the bending analysis of doubly curved laminated shells. The formulation begins with a H-R functional. By introducing a set of appropriate scaling, asymptotically expanding the field variables in terms of a small perturbation parameter and applying the stationary condition of the H-R functional, we obtain recursive sets of system equations leading to the FSDT equations for various orders. The accurate solution can be obtained by solving the FSDT-type equations level-by-level.

ACKNOWLEDGMENTS

This work is supported by the National Science Council of Republic of China through Grants NSC 85-2211-E-006-002 and NSC 85-2732-E-006-001.

REFERENCES

1. Wu, C.P., Tarn J.Q. and Chen, P.Y., "A Refined Asymptotic Theory of Doubly Curved Laminated Shells", *J. Engrg. Mech.*, ASCE, 1997 (in press).
2. Wu, C.P., Tarn J.Q. and Chi, S.M., "A Three-Dimensional Analysis of Doubly Curved Laminated Shells", *J. Engrg. Mech.*, ASCE, Vol. 122, No. 5, 1996, pp. 391-401.
3. Wu, C.P., Tarn J.Q. and Chi, S.M., "An Asymptotic Theory for Dynamic Response of Doubly Curved Laminated Shells", *Int. J. Solids Struct.*, Vol. 33, No. 26, 1996, pp. 3813-3841.
4. Wu, C.P. and Liu, C.C., "Stress and Displacement of the Thick Doubly Curved Laminated Shells", *J. Engrg. Mech.*, ASCE, Vol. 120, No. 7, 1994, pp. 1403-1428.
5. Fan, J. and Zhang, J., "Analytical Solution for Thick Doubly Curved Laminated Shells", *J. Engrg. Mech.*, ASCE, Vol. 118, No. 7, 1994, pp. 1338-1356.
6. Reddy, J.N., "Exact Solutions of Moderately Thick Laminated Shells", *J. Engrg. Mech.*, ASCE, Vol. 110, No. 5, 1984, pp. 794-808.
7. Reddy, J.N. and Liu, C.F., "A Higher-Order Shear Deformation Theory of Laminated Elastic Shells", *Int. J. Engrg. Sci.*, Vol. 23, No. 3, 1985, pp. 319-330.
8. Leissa, A.W. and Qatu, M.S., "Equations of Elastic Deformation of Laminated Composite Shallow Shells", *J. Appl. Mech.*, ASME, Vol. 58, No. 1, 1991, pp. 181-188.

PROBLEMS IN MODELLING THE DETAIL GEOMETRY OF A COMPOSITE SHIP STRUCTURE, FLUID AND EXPLOSIVE IN AN UNDERWATER EXPLOSION SCENARIO

John Marco ¹, Jeff Lingard ²

^{1,2}*Defence Science and Technology Organisation, Aeronautical and Maritime Research Laboratory, P.O. Box 4331 Melbourne 3001, Australia*

SUMMARY: Dynamic modelling of three dimensional, underwater explosion scenarios containing the explosive, surrounding fluid and a section of full size surface ship structure presents many difficulties for a finite element(FE) modeller. In order to translate a static engineering drawing into a FE model for dynamic simulation requires a large amount of human and computing resources to address the numerical and practical issues of the problem in hand. For example, critical factors might be the level of detail incorporated into the FE model(ie the total size of the FE model, element material, detail and type), the capacity of the computer system needed to execute the problem, the time it takes to execute the problem, the detail level of predicted data that will be obtained and finally, the time available to do the analysis. This paper will discuss the author's experiences in the procedure used in the incremental development to model and simulate a dynamic, non linear, three dimensional underwater explosion scenario for a surface vessel fabricated from composite materials.

KEYWORDS: LS-DYNA3D, ship, underwater shock, non linear, three dimensional, dynamic

INTRODUCTION

Surface ships built entirely from composite materials are uncommon in the Navy, but some classes have been developed for specific operational roles. These ships, as do all other Naval vessels, need to withstand dynamic loads resulting from normal operational roles as well as, loads received from underwater shock[1-2]. This paper will discuss in general terms the procedures involved in building a finite element model of a composite surface ship. Assumptions used to model the dynamic simulation will be discussed as well as some of the preliminary checks on the structure, loads and boundary conditions.

When undertaking a three dimensional non linear dynamic analysis of a complete surface ship an incremental method needs to be adopted in order to be able to manage such a large task. A few key points need first to be address, namely, the FE model for the ship needs to be broken up into a number of manageable parts which can be examined and tested individually prior to assembling the complete structure, secondly, as enormous amounts of computing time will be consumed, simplifications to the actual geometry and material models need to be introduced initially in order to expedite the model development process to a stage where confidence is

achieved of what has been done. Thirdly, the actual loading scenario of an underwater explosion can be initially modelled through the representation of pressure load curves. When confidence is achieved that the simplifications produce a viable solution, complexity can be added to the simulation scenario through combining the separate parts of the ship to form a single complete ship, simple material models(ie isotropic) can be changed to actual complex material models(ie orthotropic) and the simplified loading scenarios can also be replaced with more accurate loading scenarios.

UNDERWATER EXPLOSION SCENARIO

The scenario examined is a section from a complete surface ship which will be subjected to an underwater explosion(UNDEX) as shown on Figure 1. Only a portion of the complete ship was chosen, as the area of structural interest was the middle section of the model and the pressure loading on the hull was assumed to be approximately a plane wave. Lumped rigid body masses representing all the forward and aft sections of the ship structure were included at either ends of the ship FE model. The scenario examined included an explosive charge positioned below and off to the starboard side of the ship. The charge is midway along the length of the ship. The charge position was chosen such that a far field scenario simulation would arise and therefore an approximate plane wave would load the hull structure, other loads resulting from the bubble pulsation and collapse upon the structure were not considered.

The code used in the study was LS-DYNA3D[3] which is a product of the Livermore Software Technology Corporation, in the USA. The code is capable of analysing the dynamic , non linear response of three dimensional structures under impact, air and underwater blast loading scenarios.

FINITE ELEMENT MODELS

Geometry Models

Data used to constructed the FE model came from production engineering drawings of the vessel, these are considered to be the best source of information for geometry detail, fabrication methods and material properties. Given the size of the ship structure; components like brackets, nuts and bolts were not included, but stiffener beams were included, as they play an integral part in the structure stiffness. A minimum acceptable shape profile for the ship hull and structure was determined, see Figure 2, such that the hull stiffness was preserved without the excessive generation of nodes and elements. Manpower and CPU usage constraints was also other controlling factors. The FE mesh represents the minimum number of nodes and elements used in constructing the model, the final grid mesh density(not shown) will be much finer. The structure consisted of only shell and beam elements, brick elements were not an option due to the relative sizes of element length and width, compared to element thickness, see Table 1 for details.

TABLE 1 Details of FE Parameters

	Structure		Fluid		Explosive	
	#Nodes	#Elements	#Nodes	#Elements	#Nodes	#Elements
Model 1-Pressure Load Curves						
Beams(1D)	3122	1407	n/a	n/a	n/a	n/a
Shells(2D)	12999	9976	n/a	n/a	n/a	n/a
Bricks(3D)	n/a	n/a	33226	34838	n/a	n/a
Model 2-Explosive Model						
Bricks(3D)	n/a	n/a	159515	145651	3587	2160

Explosive

Three possibilities existed for modelling the explosive charge in this sort of simulation,

- (a) include a FE model for the explosive charge,
- (b) simulate the applied loading with a number of pressure-time curves, and
- (c) use an external load prediction boundary element(BE) code(ie Underwater Shock Analysis code) that can be coupled to the FE structural code

Including the explosive charge as a part in the FE model, see Figure 3, provides the most general and complete simulation, however, it does increase the complexity and FE model size of the simulation, especially for a far field scenario analysis. There are features within the FE code that provide capabilities and mechanisms such that, upon initiation of the charge, the explosive begins to expand, thus imparting a load onto the surrounding fluid model which in turn transfers the load onto the structure. In a far field scenario simulation, the number of fluid elements shown in Figure 3 were inadequate to capture and transfer the shock load over the distance between the charge and structure. An enormous number of fluid elements, many more than are represented in the figure, would be required to adequately capture and describe the shock pulse as it travels through the fluid to the structure. Hence, modelling the explosive charge in this far field scenario is not really a practical option, this approach is more relevant to near field scenarios.

The second approach is to represent the incoming shock wave as a series of pressure-time load curves on a much reduced fluid element volume model, see Figure 4. The load curves can be approximated from classical theory, that is, from free field pressure predictions in an infinite fluid medium. This approach allows a much more reduced number of fluid elements to be generated and hence, reduces computational time considerably.

The third alternative is a more sophisticated and accurate approach to the pressure-time load curves. Essentially, a boundary element model is overlaid on either a reduced fluid element model or directly upon the ship structure geometry; upon commencement of the simulation a staggered solution technique approach can be used between the two codes, where by, pressure is supplied initially by the BE code to the FE code, then the structural geometry location is returned by the FE code to the BE code. This alternating of data between the two codes is continuous throughout the simulation in order to calculate the reflected pressure on the surface of the vessel. This is a far more accurate approach, but does involve much more human and

computing effort in understanding and running the code, as well as, the purchase of the BE code.

The pressure-time load curve approach was used for the simulation described in this paper, because of the relative ease and effort required to analysis the response of the model in the allocated time.

Fluid

The reduced fluid model was constructed from solid (ie 3D) elements and its overall shape and density were based upon the direction and number of pressure-time load curves applied to the charge side of the model, see Table 1 for details.

Material Models

The ship structure consisted entirely of composite items except for the stanchions (ie vertical columns) and nuts and bolts which were metal. For the preliminary analysis, the composite material was assumed to be homogenous and isotropic with a linear elastic material response, where as, the metal was assumed to be homogenous and isotropic with an elastic-plastic material model. Material strain hardening effects were not included for either the composite or metal models. The initial approximation of the ship structure material type was chosen simply to reduce modelling effort and computer run time, orthotropic properties will be used at a later stage.

The fluid material model assumed simple viscous behaviour, also, an equation of state model inconjunction with its material model was required, this essentially described the pressure and volume relationships for the fluid

Hull Loading

The technique used to apply load to the hull was identified earlier as arising from a number of predetermined pressure-time load curves. The starboard side of the fluid FE model was intentionally made as a flat inclined surface so that the impinging shock wave would be nominally planar. This surface was then divided into a number of coarse symmetrical regions either side of the centerline defined by the explosive charge location, see Figure 5. Nominally, the distance between the charge and any point on the plane region is about the same, therefore, pressure-time profiles were only calculated for the 10 vertical regions on the starboard side of the fluid FE model. This reduced the number of pressure profiles required to characterise the incident shock load. Figure 6 shows two pressure-time curves for regions 1 and 10 and peak pressures between these two regions only varied by 8%.

Boundary Conditions

The fluid element model was restrained in all three translational degrees of freedom at a number of points and edges as shown in Figure 4. The ship model was not restrained in any translational or rotational movement, but nodes coincident between ship and fluid were merged in the model, thus eliminating the need for a contact surface to be applied and, hence, ensuring proper load transfer between fluid and structure at the interface.

Ship Equipment Masses

Masses for equipment, non structural walls, other items and crew were all accounted for by adding onto existing decks a uniformly distributed static surface load as point masses.

Since only a section of the longitudinal portion of the ship was modelled, bulkheads at either end of the ship section were treated as rigid material walls with their respective masses increased to account for all the forward and aft structure of the ship not modelled for this preliminary investigation. This is a simple technique to employ, however, ship structural responses approaching these rigid walls are inaccurate. Given that the area of interest is the region between the two inner internal bulkheads, this approach is assumed adequate, checks with full scale field trials will determine its accuracy.

SIMULATION CHECKS

Numerous simulation runs were done during the model development phase, this was necessary in order to check various aspects of the FE model, for example, to ensure

- (a) nodes on neighbouring shell parts of the structure merged where required,
- (b) nodes on beams attached to shells merged where required,
- (c) contacting surfaces applied between internal fuel and water tanks and bulkheads, were tied together, as well as, the beams, decks and bulkheads
- (d) coincident nodes between the fluid and hull merged

This checking process prior to final analysis is a critical one and needs to be done rigorously undertaken during model development and not at the completion of the 'detailed' FE model. On going checks are easy to do and although time consuming; they detect modelling errors during development which become impossible to correct for large structures at the end of the modelling phase.

These kinds of checks discussed so far, only resolve 'holes' and, or 'protrusions' that may exist or occur in the model when a load is applied. Checks on the magnitudes of hull, deck and bulkhead response can only be verified from experiments, these types of checks will be not be discussed in the paper.

RESULTS

For the coarse geometry modelled, see Figure 1, the cpu run time on a Silicon Graphics, eight processor, Power Challenge was about 3.5 hours for a simulated real time of 100 milliseconds.

Figure 7 shows plots of the global structural response as a function of time. The ship structure responds in both a lateral and vertical global motion due to the underwater pressure load originating below and off to the starboard side of the ship; essentially no longitudinal motion is experienced. Superimposed on the ship global motion is the local hull, deck and bulkhead deformations, these responses can be seen on the starboard side of the hull structure, as well as on the top deck, even with the coarse element mesh developed so far. With validation of the predicted responses for the coarse mesh, the structure can be modelled to a greater level of detail in order to capture the local motion (ie equipment motion) more accurately. This next level of meshing has not been completed.

CONCLUSIONS

The building of a FE model for a large structure is both complex and time consuming and many issues need to be addressed in relation to the simulation including structure size, FE geometry details, type of loading applied, boundary conditions and material models. Incremental development with checks along the way need to be adopted. To date the authors have completed only the middle section of the surface ship and are progressing with model developments for the forward and aft parts of the ship. An averaged isotropic material is still being used to simulate the composite materials of the ship during when a simulated load is applied to a section of the structure, but this model will be replaced with a more accurate orthotropic material model after all ship parts have been developed and tested and assembled to form a single surface ship structure.

REFERENCES

1. Marco, John, 1996, "Effects Of Stiffeners and Panels Inside A Cylinder When Subjected To An Underwater Shock", ABCA-7 9th Quadripartite Conference, Sydney, May 1996.
2. Marco, John, 1996, "The Dynamic Response of a Surface Ship to an Underwater Explosion", 67th Shock & Vibration Symposium, Monterey, USA, November, 1996.
3. Hallquist, John, et al, April 1994, "LS-DYNA3D User's Manual", Livermore USA.

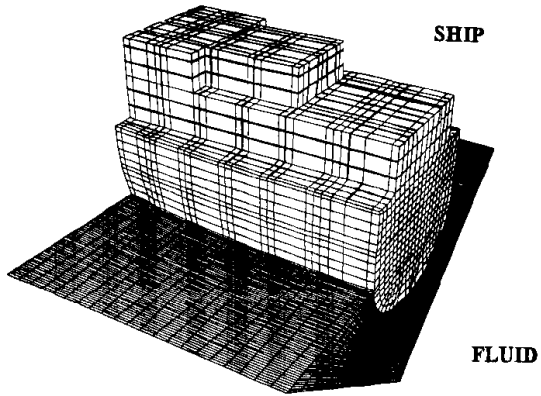
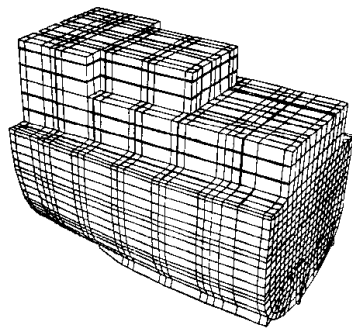


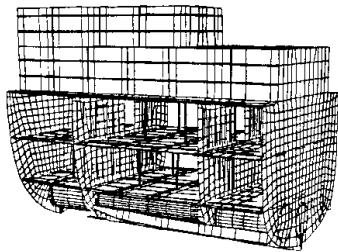
FIGURE 1 UNDERWATER EXPLOSION SCENARIO



FIGURE 2 FE MODEL OF SHIP STRUCTURE



EXTERNAL VIEW



INTERNAL VIEW

SHIP STRUCTURE(NOT SHOWN)

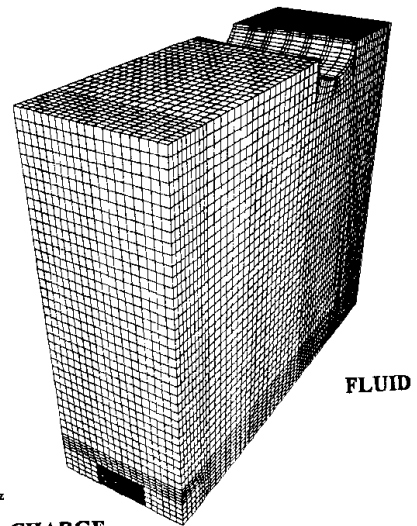


FIGURE 3

CHARGE

FE MODEL OF FLUID AND EXPLOSIVE CHARGE SCENARIO

FIGURE 4 PRESSURE LOAD SURFACE ON FLUID FE MODEL

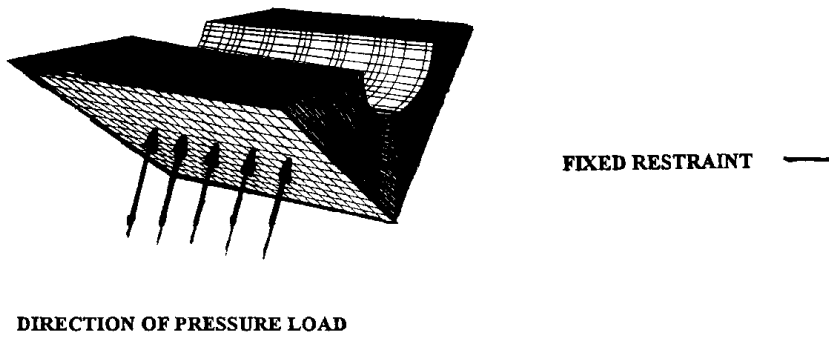


FIGURE 5 PRESSURE LOAD REGIONS ON FLUID FE MODEL

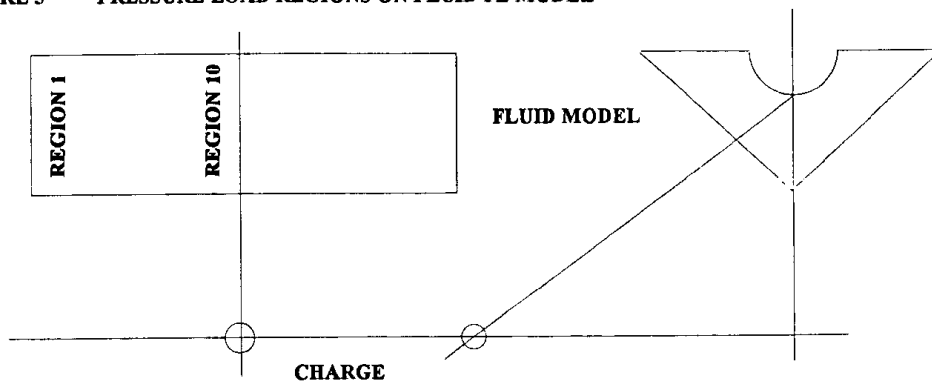


FIGURE 6 PRESSURE - TIME LOAD CURVES

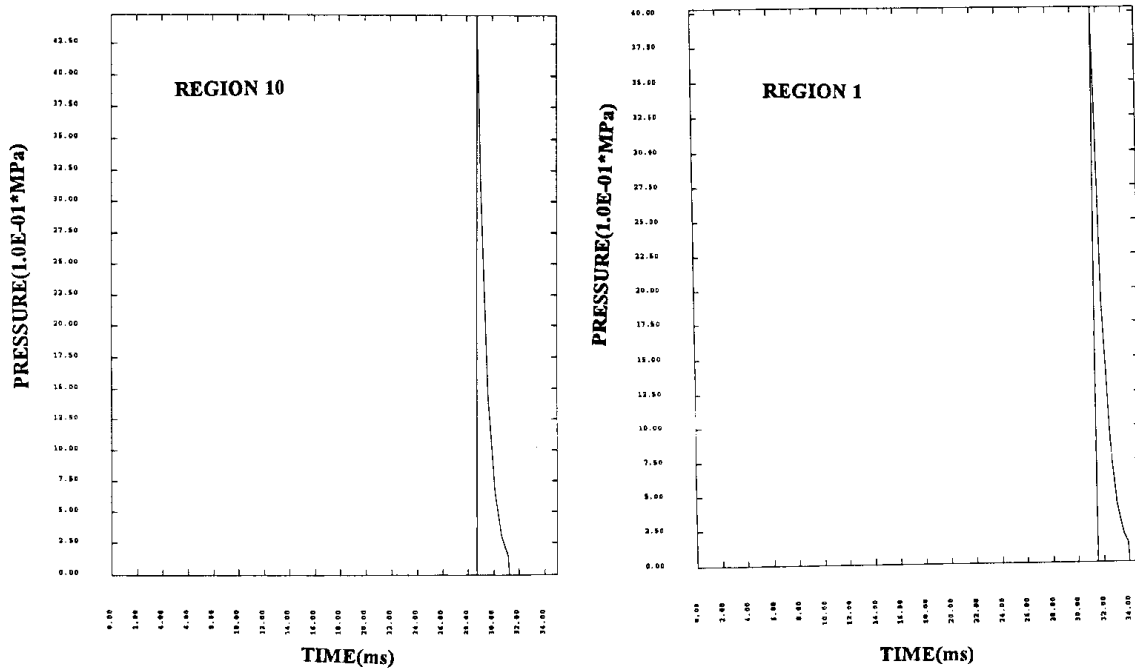
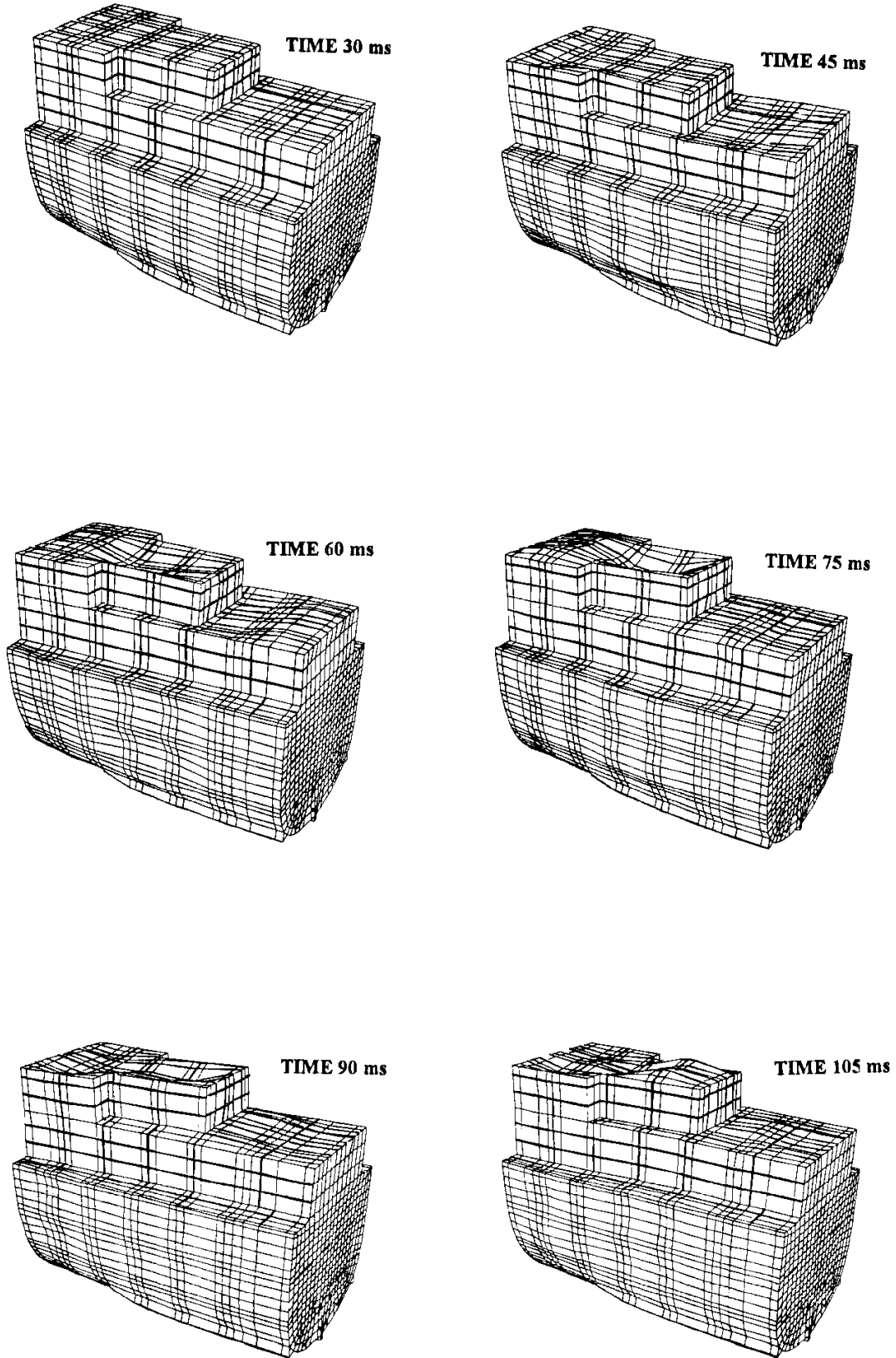


FIGURE 7 TIME SEQUENCE PLOTS OF SHIP STRUCTURE RESPONSE



DISPLACEMENT SCALE FACTOR 25

NON-LINEAR FINITE ELEMENT ANALYSIS OF THIN COMPOSITE STRUCTURES

José Simões Moita¹, Cristóvão M. Mota Soares², Carlos A. Mota Soares²

¹ *Escola Superior de Tecnologia, Universidade do Algarve, 8000 Faro, Portugal*
² *IDMEC - IST, Av. Rovisco Pais, 1096 Lisboa Codex, Portugal*

SUMMARY: A non-conforming three-node triangular finite element with 18 degree of freedom, is used in conjugation with the Kirchhoff theory for the non-linear analysis of thin composite plate-shell structures. The formulation of the geometrically non-linear analysis is based on an updated Lagrangian formulation associated with the Newton-Raphson iterative technique, which incorporates an automatic arc-length control procedure. Several illustrative test cases of thin and multilaminated plate-shell structures are analysed. The results of large displacements analyses are compared with alternative numerical solutions. From the applications a good accuracy has been found. The versatility of the element to model arbitrary thin structures and the simplicity of the formulation makes it a very computational efficient numerical tool.

KEYWORDS: non-linear analysis, finite elements, multilaminated shells

INTRODUCTION

In the recent years, the use of laminated composite materials has increased in a variety of engineering structures, due to their high strength to weight and high stiffness to weight ratios, which can be tailored through the variation of fibre orientation and lamination sequence.

The objective of this paper is to present the formulation, implementation and illustrative applications of a simple versatile finite element model, based on a flat multilaminated triangular element by employing the superposition of in-plane and bending effects to obtain the stiffness matrix. To carry out the large displacement analysis an updated Lagrangian formulation [1,2] has been implemented. This formulation is used in association with the Newton-Raphson incremental-iterative method having an automatic arc-length load control to contemplate general shell analysis [3].

The analytical formulation is based on Kirchhoff plate theory, applied to the geometrical non-linear analysis, considering anisotropy of the structure, with symmetric and asymmetric lay-ups, enabling coupling between membrane and bending and twisting.

The model is developed, through the generalisation of a pioneering non-conforming plate triangular element with 3 degrees of freedom per node, used on linear statics, free vibration and buckling analyses of isotropic and unilayered orthotropic plates [4,5,6]. The present multilaminated plate-shell element has 6 degrees of freedom per node, three displacements and three rotations, which includes an additional degree of freedom to enable the analysis of general structures, as an assembly of flat elements [7]. Related with the present study, but for isotropic shell structures, a comparative study has been carried out by Talbot and Dhatt [8] to

assess flat triangular elements. Recently, Madenci and Barut [9], carried out a brief review on non-linear analysis of multilaminated shell structures. They developed a flat shell triangular element based on the concept of free formulation, using a co-rotational form of the updated Lagrangian formulation. Numerical validation problems of anisotropic plate/shell structures with symmetric and non-symmetric lay-ups are discussed to assess the effect of loading, geometry and material properties.

The performance of the present model is established through validation problems involving large deflections. The present results are compared with alternative numerical solutions [9,11,12].

FORMULATION OF THE THEORY

Displacements and Strains

The classical Kirchhoff Theory is considered. The displacement components (Figure 1) at a generic point in the laminate are assumed to be of the form :

$$\begin{aligned}
 u(x, y, z) &= u_0(x, y) - z \theta_y \\
 v(x, y, z) &= v_0(x, y) + z \theta_x \\
 w(x, y, z) &= w_0(x, y)
 \end{aligned}
 \tag{1}$$

where (u_0, v_0, w_0) are the displacements of the point on the reference plane of the laminate, and $\theta_x = -\frac{\partial w}{\partial y}$ and $\theta_y = \frac{\partial w}{\partial x}$ are the rotations about the x and y axes respectively.

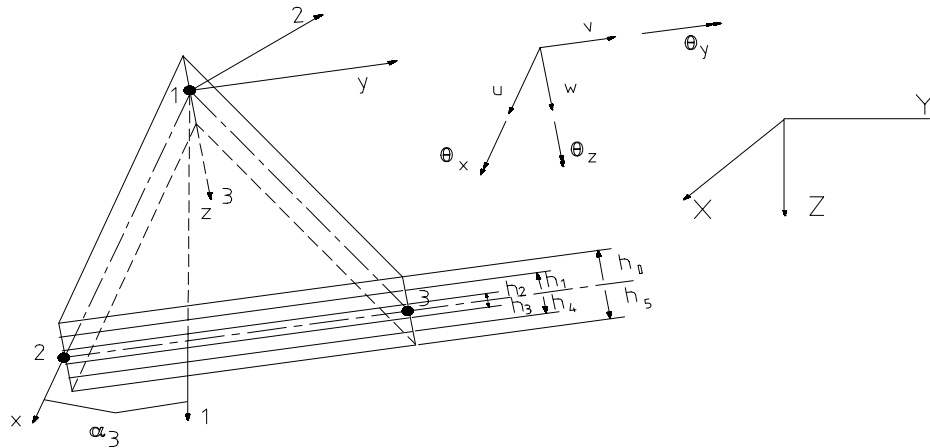


Fig. 1: Element with Local and Global co-ordinate systems

The present theory considers large displacements with small strains. The Green's strains components associated with the displacement in Eqn 1 are given by :

$$\begin{aligned}\varepsilon_{xx} &= \frac{\partial u_0}{\partial x} - z \frac{\partial \theta_y}{\partial x} + \frac{1}{2} \left[\left(\frac{\partial u_0}{\partial x} \right)^2 + \left(\frac{\partial v_0}{\partial x} \right)^2 + \left(\frac{\partial w_0}{\partial x} \right)^2 \right] \\ \varepsilon_{yy} &= \frac{\partial v_0}{\partial y} - z \frac{\partial \theta_x}{\partial y} + \frac{1}{2} \left[\left(\frac{\partial v_0}{\partial y} \right)^2 + \left(\frac{\partial v_0}{\partial y} \right)^2 + \left(\frac{\partial w_0}{\partial y} \right)^2 \right] \\ \varepsilon_{xy} &= \left(\frac{\partial u_0}{\partial y} + \frac{\partial v_0}{\partial x} \right) + z \left(\frac{\partial \theta_y}{\partial y} + \frac{\partial \theta_x}{\partial x} \right) + \left(\frac{\partial u_0}{\partial x} \frac{\partial u_0}{\partial y} + \frac{\partial v_0}{\partial x} \frac{\partial v_0}{\partial y} + \frac{\partial w_0}{\partial x} \frac{\partial w_0}{\partial y} \right)\end{aligned}\quad (2)$$

Laminate Analysis

For the case of a laminate of n layers, schematically shown in Figure1, the stress-strain relations of the laminate are based on the stress-strain relations in each layer, for which principal orthogonal material axes (1,2,3) are defined. A local orthogonal reference system (x, y, z), is applied to the laminate. The constitutive equations, in terms of material axes, for the k th layer can be written as [10] :

$$\sigma_k = Q_k \varepsilon_k \quad \sigma_k = [\sigma_{11} \ \sigma_{22} \ \sigma_{12}]^T \quad \varepsilon_k = [\varepsilon_{11} \ \varepsilon_{22} \ \gamma_{12}]^T \quad (3)$$

Where σ_{11} σ_{22} and σ_{12} are the normal and shearing stresses, ε_{11} ε_{22} and γ_{12} are the normal and distortion strains, and Q_k is the elasticity matrix, whose non - zero elements are given by:

$$Q_{11} = \frac{E_1}{1 - \nu_{12}\nu_{21}} \quad , \quad Q_{22} = \frac{E_2}{1 - \nu_{12}\nu_{21}} \quad , \quad Q_{12} = Q_{21} = \frac{\nu_{12}E_2}{1 - \nu_{12}\nu_{21}} \quad , \quad Q_{33} = G_{12} \quad (4)$$

where E_1 and E_2 are the Young's modulus referred to 1 and 2 material axes respectively, G_{12} the shear modulus, ν_{12} the major Poisson's ratio of k th orthotropic layer, and $\nu_{21} = \nu_{12} (E_2 / E_1)$. Relating the principal material axis 1 to the x axis of the reference system of the laminate, through an angle α_k , the stress-strain relations for the k th orthotropic layer are given by:

$$\bar{\sigma}_k = \bar{Q}_k \bar{\varepsilon} \quad , \quad \bar{\sigma}_k = [\sigma_{xx} \ \sigma_{yy} \ \sigma_{xy}]^T \quad , \quad \bar{\varepsilon} = [\varepsilon_{xx} \ \varepsilon_{yy} \ \gamma_{xy}]^T \quad (5)$$

where

$$\begin{aligned}\bar{Q}_{11} &= Q_{11} \cos^4 \alpha + 2(Q_{12} + 2Q_{33}) \cos^2 \alpha \sin^2 \alpha + Q_{22} \sin^4 \alpha \\ \bar{Q}_{12} &= (Q_{11} + Q_{22} - 4Q_{33}) \cos^2 \alpha \sin^2 \alpha + Q_{12} (\cos^4 \alpha + \sin^4 \alpha) \\ \bar{Q}_{22} &= Q_{11} \sin^4 \alpha + 2(Q_{12} + 2Q_{33}) \cos^2 \alpha \sin^2 \alpha + Q_{22} \cos^4 \alpha \\ \bar{Q}_{33} &= (Q_{11} + Q_{22} - 2Q_{12} - 2Q_{33}) \cos^2 \alpha \sin^2 \alpha + Q_{33} (\sin^4 \alpha + \cos^4 \alpha) \\ \bar{Q}_{13} &= (Q_{11} - Q_{12} - 2Q_{33}) \cos^3 \alpha \sin \alpha + (Q_{12} - Q_{22} + 2Q_{33}) \sin^3 \alpha \cos \alpha \\ \bar{Q}_{23} &= (Q_{11} - Q_{12} - 2Q_{33}) \sin^3 \alpha \cos \alpha + (Q_{12} - Q_{22} + 2Q_{33}) \cos^3 \alpha \sin \alpha\end{aligned}\quad (6)$$

The strains for an arbitrary point of the k th layer given by Eqn. (2) can be written in the form:

$$\begin{aligned} \bar{\boldsymbol{\varepsilon}} &= \boldsymbol{\varepsilon}_0^L + z\boldsymbol{\kappa} + \boldsymbol{\varepsilon}_0^{NL} \quad ; \quad \boldsymbol{\varepsilon}_0^L = \left[\varepsilon_{0_{xx}}^L \quad \varepsilon_{0_{yy}}^L \quad \varepsilon_{0_{xy}}^L \right]^T \\ \boldsymbol{\kappa} &= \left[\kappa_{xx} \quad \kappa_{yy} \quad \kappa_{xy} \right]^T \quad ; \quad \boldsymbol{\varepsilon}_0^{NL} = \left[\varepsilon_{0_{xx}}^{NL} \quad \varepsilon_{0_{yy}}^{NL} \quad \varepsilon_{0_{xy}}^{NL} \right]^T \end{aligned} \quad (7)$$

where $\boldsymbol{\varepsilon}_0^L$ is the linear strain vector of the middle surface, $\boldsymbol{\kappa}$ the vector of curvatures and $\boldsymbol{\varepsilon}_0^{NL}$ the vector of non linear strains. From Eqn 5 and 7 yields:

$$\bar{\boldsymbol{\sigma}}_k = \bar{Q}_k \left(\boldsymbol{\varepsilon}_0^L + \boldsymbol{\varepsilon}_0^{NL} + z \boldsymbol{\kappa} \right) \quad (8)$$

The resultant forces and moments acting on the laminate are obtained by integrating the stresses in each layer through the laminate thickness :

$$\begin{aligned} N &= \left[N_{xx} \quad N_{yy} \quad N_{xy} \right]^T = \int_{-h/2}^{h/2} \left[\sigma_{xx} \quad \sigma_{yy} \quad \sigma_{xy} \right]^T dz = \sum_{K=1}^n \int_{h_{K-1}}^{h_K} \left[\sigma_{xx} \quad \sigma_{yy} \quad \sigma_{xy} \right]^T dz \\ M &= \left[M_{xx} \quad M_{yy} \quad M_{xy} \right]^T = \int_{-h/2}^{h/2} \left[\sigma_{xx} \quad \sigma_{yy} \quad \sigma_{xy} \right]^T z dz = \sum_{K=1}^n \int_{h_{K-1}}^{h_K} \left[\sigma_{xx} \quad \sigma_{yy} \quad \sigma_{xy} \right]^T z dz \end{aligned} \quad (9)$$

where h is the overall thickness of the laminate. After integration one obtains in the condensed form the matrix relation:

$$\begin{bmatrix} N \\ M \end{bmatrix} = \begin{bmatrix} A & B \\ B & D \end{bmatrix} \begin{Bmatrix} \boldsymbol{\varepsilon}_0^L + \boldsymbol{\varepsilon}_0^{NL} \\ \boldsymbol{\kappa} \end{Bmatrix} \quad ; \quad \hat{\boldsymbol{\sigma}} = \hat{D} \bar{\boldsymbol{\varepsilon}} \quad (10)$$

with

$$A_{ij} = \sum_{K=1}^n \bar{Q}_{ij} (h_K - h_{K-1}) \quad ; \quad B_{ij} = \sum_{K=1}^n \bar{Q}_{ij} (h_K^2 - h_{K-1}^2) / 2 \quad ; \quad D_{ij} = \sum_{K=1}^n \bar{Q}_{ij} (h_K^3 - h_{K-1}^3) / 3 \quad (11)$$

where A_{ij}, B_{ij}, D_{ij} are called extensional stiffness, extension-bending/twisting coupling stiffness, and bending stiffness respectively.

FINITE ELEMENT FORMULATION

The present model has been developed for isotropic plate and shell structures by Bazeley et al [4], Zienkiewicz [7] and Mirza et al. [5] among others. More recently Malhotra et al [6] applied it to orthotropic plates. In the present work this element is extended to the geometrically non-linear analysis of general multilayered thin composite plate-shell type structures. As is shown in Figure 1, the element has three nodes and six degrees of freedom per node, the displacements u_i, v_i, w_i and rotations $\theta_{xi}, \theta_{yi}, \theta_{zi}$. It requires the introduction of fictitious stiffness coefficients $K_{\theta z}$, corresponding to rotations θ_z , which does not enter in the formulation in the local coordinate system [7].

The element local displacements u, v, w , are expressed in terms of nodal variables through shape functions given in terms of area co-ordinates L_i :

$$u = \sum_{i=1}^3 L_i u_i \quad ; \quad v = \sum_{i=1}^3 L_i v_i \quad ; \quad w = \sum_{i=1}^3 [{}_1N_i \quad {}_2N_i \quad {}_3N_i] \begin{Bmatrix} w_i \\ \theta_{xi} \\ \theta_{yi} \end{Bmatrix} \quad (12)$$

where

$$\begin{aligned} L_1 &= (a_1 + b_1x + c_1y) / 2A \\ L_2 &= (a_2 + b_2x + c_2y) / 2A \\ L_3 &= (a_3 + b_3x + c_3y) / 2A \end{aligned} \quad (13)$$

$$\begin{aligned} {}_1N_1 &= L_1 + L_1^2 L_2 + L_1^2 L_3 - L_1 L_2^2 - L_1 L_3^2 \\ {}_2N_1 &= b_3 \left(L_1^2 L_2 + \frac{1}{2} L_1 L_2 L_3 \right) - b_2 \left(L_1^2 L_3 + \frac{1}{2} L_1 L_2 L_3 \right) \\ {}_3N_1 &= c_3 \left(L_1^2 L_2 + \frac{1}{2} L_1 L_2 L_3 \right) - c_2 \left(L_1^2 L_3 + \frac{1}{2} L_1 L_2 L_3 \right) \end{aligned} \quad (14)$$

with

$$\begin{aligned} a_1 &= x_2 y_3 - x_3 y_2 & b_1 &= y_2 - y_3 & c_1 &= x_3 - x_2 \\ a_2 &= x_3 y_1 - x_1 y_3 & b_2 &= y_3 - y_1 & c_2 &= x_1 - x_3 \\ a_3 &= x_1 y_2 - x_2 y_1 & b_3 &= y_1 - y_2 & c_3 &= x_2 - x_1 \end{aligned} \quad (15)$$

and A is the area of the element

The shape function ${}_jN_i$ for nodes 2 and 3 are written by a cyclic permutation of suffixes 1- 2- 3. In matrix form, we have :

$$\begin{Bmatrix} u \\ v \\ w \end{Bmatrix} = \sum_{i=1}^3 \begin{bmatrix} L_i & 0 & 0 & 0 & 0 & 0 \\ 0 & L_i & 0 & 0 & 0 & 0 \\ 0 & 0 & {}_1N_i & {}_2N_i & {}_3N_i & 0 \end{bmatrix} \begin{Bmatrix} u_i \\ v_i \\ w_i \\ \theta_{xi} \\ \theta_{yi} \\ \theta_{zi} \end{Bmatrix} \quad (16)$$

$$\{d\} = [N] \{d_e\} \quad (17)$$

UPDATED LAGRANGIAN FORMULATION

An updated lagragian formulation is adopted in conjugation with an incremental-iterative process [1],[2],[3],[8] to obtain the solution by the finite element method. The configuration at the begining of a load step is the reference configuration C^1 , and the actualised configuration C^2 is associated with the current iteration within each load step Since small deformations are assumed, elementary internal forces and bending moments are calculated as in linear analysis , and we have for iteration (i):

$$\hat{\sigma}^{(i)} = \hat{\sigma}^{(i-1)} + \Delta \hat{\sigma} \quad ; \quad \Delta \hat{\sigma} = \hat{D} \Delta \bar{\epsilon} \quad (18)$$

The application of the virtual work principle to an element yields in the incremental large displacement analysis :

$$[K_L^e + K_\sigma^e]^{(i-1)} \{\Delta d_e\}^{(i)} = \{F_{ext}^e\} - \{F_{int}^e\}^{(i-1)} \quad (19)$$

where the linear stiffness matrix K_L^e , the geometrical stiffness matrix K_σ^e , the external load vector F_{ext}^e and internal load vector $F_{int}^{e(i-1)}$, are given by :

$$[K_L^e] = \int_A [B^L]^T [\hat{D}] [B^L] dA \quad ; \quad [K_\sigma^e] = \int_A [G]^T [\tau] [G] dA$$

$$\{F_{ext}^e\} = \int_A [N]^T \{p\} dA + \int_S N^T \{t\} dS + \{P\} \quad ; \quad \{F_{int}^e\}^{(i-1)} = \int_A [B^L] \hat{\sigma}^{(i-1)} dA \quad (20)$$

In these equations $[B^L]$ is the membrane-bending linear strain-displacement matrix, $[G]$ is the non-linear strain-displacement matrix, $[\tau]$ is the matrix of the total updated membrane force components, $\{p\}$, $\{t\}$ and $\{P\}$ are the surface, side distributed in-plane and concentrated load vectors, respectively. The sub-matrices $[G_1]$ and matrix $[\tau]$, are given by :

$$[G_i] = \begin{bmatrix} \frac{\partial L_i}{\partial x} & 0 & 0 & 0 & 0 & 0 \\ \frac{\partial L_i}{\partial y} & 0 & 0 & 0 & 0 & 0 \\ 0 & \frac{\partial L_i}{\partial x} & 0 & 0 & 0 & 0 \\ 0 & \frac{\partial L_i}{\partial y} & 0 & 0 & 0 & 0 \\ 0 & 0 & \frac{\partial_1 N_i}{\partial x} & \frac{\partial_2 N_i}{\partial x} & \frac{\partial_3 N_i}{\partial x} & 0 \\ 0 & 0 & \frac{\partial_1 N_i}{\partial y} & \frac{\partial_2 N_i}{\partial y} & \frac{\partial_3 N_i}{\partial y} & 0 \end{bmatrix} \quad (21)$$

$$[\tau] = \begin{bmatrix} N_{xx} & N_{xy} & 0 & 0 & 0 & 0 \\ N_{xy} & N_{yy} & 0 & 0 & 0 & 0 \\ 0 & 0 & N_{xx} & N_{xy} & 0 & 0 \\ 0 & 0 & N_{xy} & N_{yy} & 0 & 0 \\ 0 & 0 & 0 & 0 & N_{xx} & N_{xy} \\ 0 & 0 & 0 & 0 & N_{xy} & N_{yy} \end{bmatrix} \quad (22)$$

To obtain the strain-displacements matrices, differentiation of the shape functions N_i with respect to Cartesian co-ordinates, needs to be carried out. For example, with respect to x , this is as follows:

$$\frac{\partial N_i}{\partial x} = \frac{\partial L_1}{\partial x} \frac{\partial N_i}{\partial L_1} + \frac{\partial L_2}{\partial x} \frac{\partial N_i}{\partial L_2} + \frac{\partial L_3}{\partial x} \frac{\partial N_i}{\partial L_3} \quad (23)$$

The system of equations of equilibrium are obtained in the usual way, after the local (x,y,z) - global (X,Y,Z) transformations [7] are carried out, yielding :

$$[K_L + K_\sigma]^{(i-1)} \{\Delta q\}^i = \{F_{ext}\} - \{F_{int}\}^{(i-1)} \quad (24)$$

where $\{\Delta q\}$ is the system displacement vector.

For shell analysis the arc-length method [3] is used. The Eqn 24 is then written in the form:

$$[K_L + K_\sigma]^{(i-1)} \{\Delta q\}^i = (\lambda^{(i-1)} + \Delta\lambda^{(i)}) \{F_{ext}^0\} - \{F_{int}\}^{(i-1)} \quad (25)$$

and an additional equation is employed to constrain the length of a load step :

$$\{\Delta q\}^{iT} \{\Delta q\}^i = \Delta l^2 \quad (26)$$

where F_{ext}^0 is a fixed load vector, λ is a load factor, $\Delta\lambda$ is the incremental load factor within the load step, and Δl is the arc-length.

NUMERICAL APPLICATIONS

A simply-supported square (axa) laminated plate with two layers, subjected to a uniform pressure load $p = \lambda p_0$ ($p_0 = 100 \text{ N/m}^2$) is considered, for two different cases of fibre orientation, $[0^\circ/90^\circ]$ and $[45^\circ/-45^\circ]$. The geometry and material properties are : $a = 1.0 \text{ m}$, $h = 0.002 \text{ m}$, $E_1 = 250 \text{ GPa}$, $E_2 = 20 \text{ GPa}$, $G_{12} = 10 \text{ GPa}$, $\nu_{12} = 0.25$. The boundary conditions are:

for cross-ply laminates :

- along $x = 0$: $v_0 = 0$, $w = 0$, $\theta_x = 0$
- along $x = a$: $v_0 = 0$, $w = 0$, $\theta_x = 0$
- along $y = 0$: $u_0 = 0$, $w = 0$, $\theta_y = 0$
- along $y = a$: $u_0 = 0$, $w = 0$, $\theta_y = 0$

for angle-ply laminates :

- along $x = 0$: $u_0 = 0$, $w = 0$, $\theta_x = 0$
- along $x = a$: $u_0 = 0$, $w = 0$, $\theta_x = 0$
- along $y = 0$: $v_0 = 0$, $w = 0$, $\theta_y = 0$
- along $y = a$: $v_0 = 0$, $w = 0$, $\theta_y = 0$

In Figure 2, are shown the results obtained in the present study, using a (8x8) element full plate mesh, and those obtained by Barbero and Reddy [11] that used a higher order displacement model. It can be observed a very closed agreement for both lay-ups.

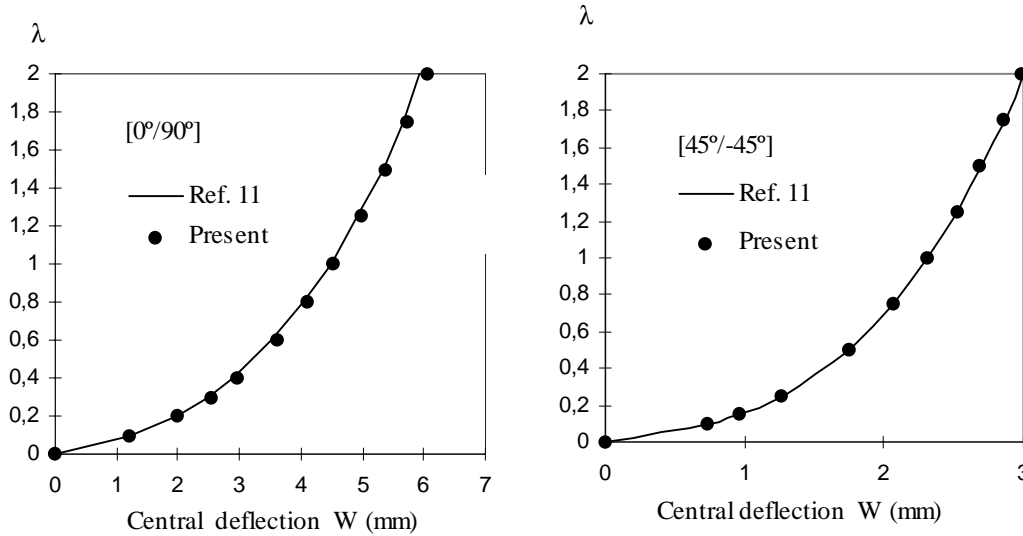


Fig. 2 : Load - Deflection curves for simply - supported plates under transverse load.

A clamped square (axa) laminated plate with a stacking sequence $[\pm 45^\circ / 0^\circ_2 / \pm 45^\circ / 90^\circ_2]_s$, under uniform pressure load $p = p_0 a^2 / E_2 h^2$ is studied. The geometric dimensions and the material properties are : $a = 254 \text{ mm}$, $h = 2.114 \text{ mm}$, $E_1 = 131.0 \text{ GPa}$, $E_2 = 13.03 \text{ GPa}$, $G_{12} = 6.41 \text{ GPa}$, and $\nu_{12} = 0.38$.

The results of the present study obtained with (10x10) full plate mesh, and its comparison with the finite element solution (10x10 full plate mesh) obtained by Madenci and Barut [9] are presented in Figure 3. An excellent agreement is observed between both solutions.

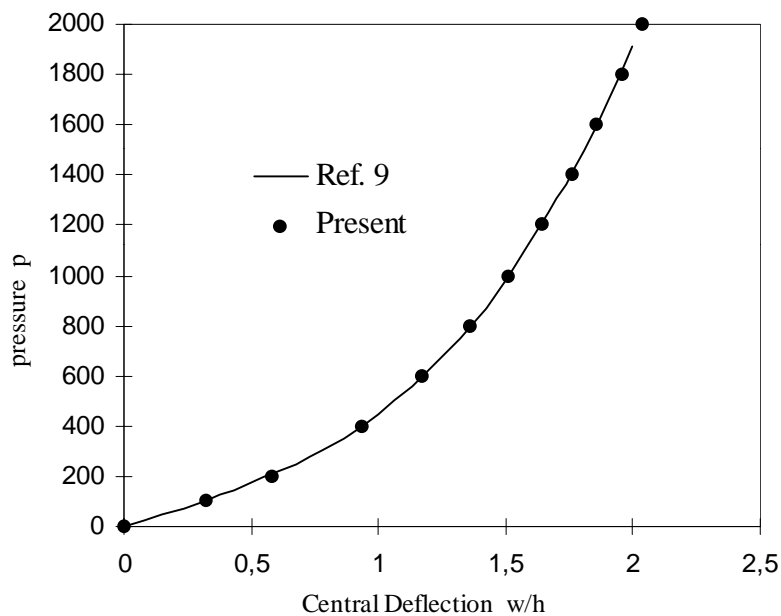


Fig. 3 : Load-Deflection curves for a clamped laminated square plate under uniform pressure

Hinged-free symmetric and antisymmetric cylindrical panels (Figure 4), with lay-ups $[90^\circ/0^\circ/90^\circ]$ and $[-45^\circ/45^\circ]$, respectively, subjected to a point load, are analysed. The geometry and material properties are : $R = 2540$ mm, $L = 508$ mm, $h = 12.6$ mm, $\theta = 0.1$ rad, $E_1 = 3.3$ GPa, $E_2 = 1.1$ GPa, $G_{12} = 0.66$ GPa, and $\nu_{12} = 0.25$. The straight edges are hinged and the curved edges are free. A model discretization with (8x8) elements is used. The non-linear load deflection curves obtained with the present non-conforming CPT triangular element and those obtained by Madenci and Barut [9], are shown in Figure 5. A good agreement is found between both solutions.

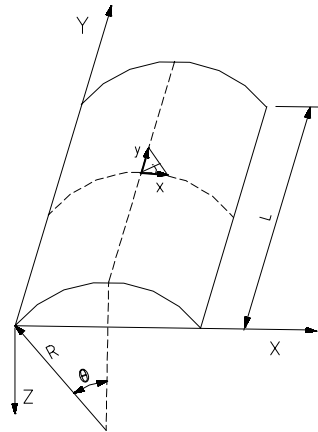


Fig. 4 : Cylindrical shell.

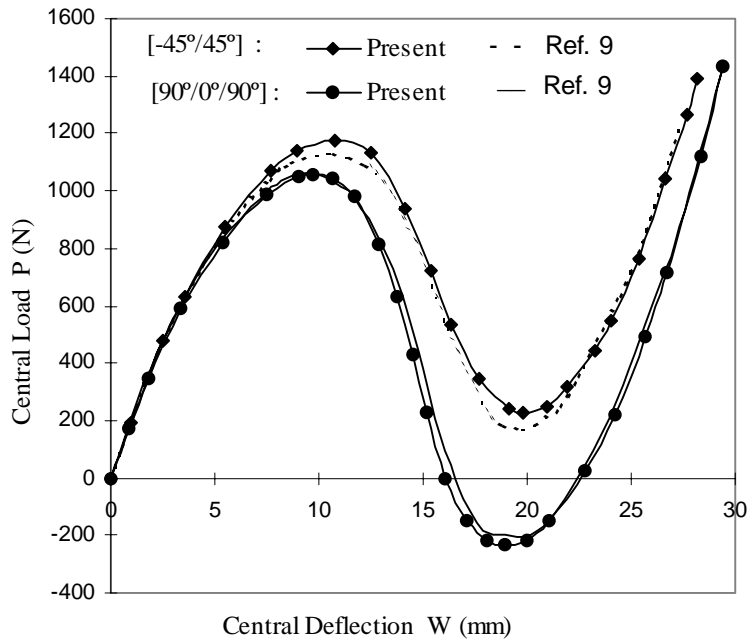


Fig. 5 : Load-Deflection curves of laminated shells under point load.

A nine-layer symmetric cross-ply $[0^\circ/90^\circ/\dots/0^\circ]$ laminated spherical shallow shell (Figure 6), subjected to a normal pressure loading $p = p_0 R^2 / E_2 h^2$, and with the following geometric and material data: $R / a = 10$, $a / h = 1000$, $E_1 / E_2 = 40$, $G_{12} / E_2 = 0.6$, $\nu_{12} = 0.25$, is considered. The shell has simply supported edges which were restricted from moving in the direction of the edge line but were free to move in a direction perpendicular to the edge line. A mesh of (8x8) elements has been used. The solution obtained by using the present CPT triangular flat element is compared, Figure 7, with the solution obtained by Saigal et al [12] that used a 48 degree-of-freedom quadrilateral curved shell element. A very good agreement is found between both solutions.

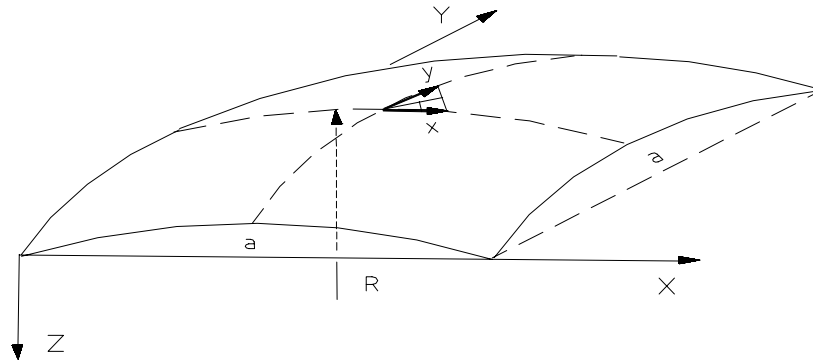


Fig. 6 : Spherical shell

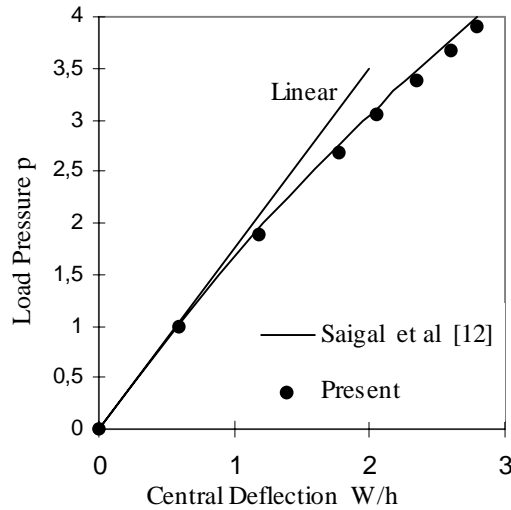


Fig.7 :Load - Deflection curves of a shallow spherical shell under uniform pressure loading

CONCLUSIONS

A non-conforming flat triangular plate/shell element, based on Kirchhoff theory, is developed to carry out the geometrically non-linear analysis of general multilaminated anisotropic thin shell structures. The updated Lagrangian formulation has been implemented. This simple model has proved to be very efficient for predicting the non-linear response of thin multilaminated plate and shell structures. The comparison of the results with alternative numerical solutions shows that the model is accurate and versatile.

ACKNOWLEDGEMENTS

The authors thank the financial support received from H.C.M. Project CHRTX-CT93-0222 , and Fundação Calouste Gulbenkian .

REFERENCES

1. Bathe,K.J.and Bolourchi,S.,“A Geometric and Material Nonlinear Plate and Shell Element”, Computers and Structures, Vol. 11, 1980, pp.23-48.
2. Bathe, K.J. and Ho, L.W., “ A Simple and Efficient Element for Analysis of General Shell Structures”, Computers and Structures , Vol. 13 , 1981, pp. 673-681.
3. Crisfield M. A. , “A Fast Incremental/Iterative Solution Procedure that Handles “Snap -Through”. Computers and Structures , Vol. 13, 1980, pp.55-62.
4. Bazeley, G. P., Cheung, Y. K., Irons, B. M., Zienkiewicz, O. C., “Triangular Elements in Bending -- Conforming and Non-conforming Solutions”, Proc.Conf. Matrix Methods in Struct. Mech., Ed. J. R. Przemienieck , et al., Air Force Inst. of Tech., Wright Patterson A.F. Base, Ohio, Vol. AFFDL-TR-66-80,1966, pp.547-576.
5. Mirza , S. and Bijlani , M. , “Vibrations of Triangular Plates of Variable Thickness”, Computers and Structures, Vol.21,Nº 6, (1985), pp. 1129-1135.
6. Malhotra,S.K., Ganesan, N. and Veluswami, M.A., “Vibrations of Orthotropic Triangular Plates”, Computers and Structures , Vol.12 , 1989, pp.17-26.
7. Zienkiewicz,O.C. , The Finite Element Method in Engineering Sciences, McGraw-Hill, 3rd edn, London, 1977.
8. Talbot, M. and Dhatt, G. , “Three Discrete Kirchhoff Elements for Shell Analysis with Large Geometrical Non-Linearities and bifurcations”, Eng. Comput. ,Vol 4 , 1987, pp.15-22 .
9. Madenci, E. and Barut, A, “A Free-Formulation-Based Flat Shell Element For Nonlinear Analysis of Thin Composite Structures”, International Journal for Numerical Methods in Engineering, Vol. 37, 1994 , pp. 3825-3842.
10. Vinson,J. R. and Sierakowski,R. L.,The Behaviour of Structures Composed of Composite Materials. Martinus Nijhoff Pub., Dordrecht , 1986.
11. Barbero, E.J. and Reddy, J.N. , “Nonlinear Analysis of Composite Laminates Using a Generalized Laminated Plate Theory” , AIAA Journal , Vol. 28 , No.11 , 1990, pp.1987-1984.
12. Saigal , S., Kapania , R.K. and Yang, T.Y., “Geometrically Nonlinear Finite Element Analysis of Imperfect Laminated Shells”, Journal of Composite Materials ,Vol. 20 ,1986, pp. 197-214.

THE BEHAVIORS OF STRENGTHENED CONCRETE GIRDERS WITH GFRP LAMINATES

Dujun Yang and Shijie Wang

*Department of Structure and Bridge Engineering
Congqing Institute of Communications
Congqing City, Sichuan Province, 630074, P.R. China*

SUMMARY: The work described that behaviors of reinforced concrete girders strengthened with GFRP laminates (GFRP/RC girders) that were been investigated by authors. The GFRP/RC girders have more advance properties than reinforced concrete girders. They are distinctly improved such as carrying and crack of reinforced concrete girders. This paper discusses stress-strain curves in composite cross-section, crack controlling and other details.

KEYWORDS: composite, glass fiber reinforce plastic, girder, highway bridge, laminate, reinforced concrete.

INTRODUCTION

The most of existing highway reinforce concrete bridges were built with lower technique specification in China, its total length is about 50% of highway bridges spread all over. As we as known, with the traffic and carrying increasing advanced, many concrete girders of bridges must be rebuilt because of its lower technique specification. It will require more and more money, and a lot of times. Therefore, a lot of effort requirements have been raised to repairing techniques for reinforced concrete girders of highway bridges.

There are many techniques to repair concrete bridge such as prestressed tendon, paste steel plates or welding reinforcing bars at the tensile area of girders. Fiber composites, a kind of new engineering materials, have been used more and more in civil engineering. CFRP composite (carbon fiber reinforce plastic) were used to repair a Swedish prestress concrete highway bridge(1), M.R.Ehsani(2) investigated the possibility of strengthened concrete girders with GFRP laminates (glass fiber reinforced plastic).

According to a government's research contract with the Chongqing Institute of Communications, authors investigated the repairing techniques for reinforced concrete bridges with GFRP laminates in recent years. This paper discusses properties of GFRP/RC girder that are strengthened with GFRP laminates, included the curves of stress-strain in cross-sections, crack control of concrete, contributions of GFRP laminates and other details.

PROPERTIES OF STRESS-STRAIN IN COMPOSITE CROSS-SECTIONS OF GFRP/RC GIRDERS

Reference(3) presented structural details of GFRP/RC girders in which there are author's previously works. GFRP/RC girders are consisted of three materials that are concrete, steel bars, and GFRP laminates. Because of their Young's modules are obviously different, especially modules of GFRP laminates are only 10% of the reinforced bars, so it presents apparently distinguish on the property of stress-strain at the composite cross-section between GFRP/RC girders and RC girders.

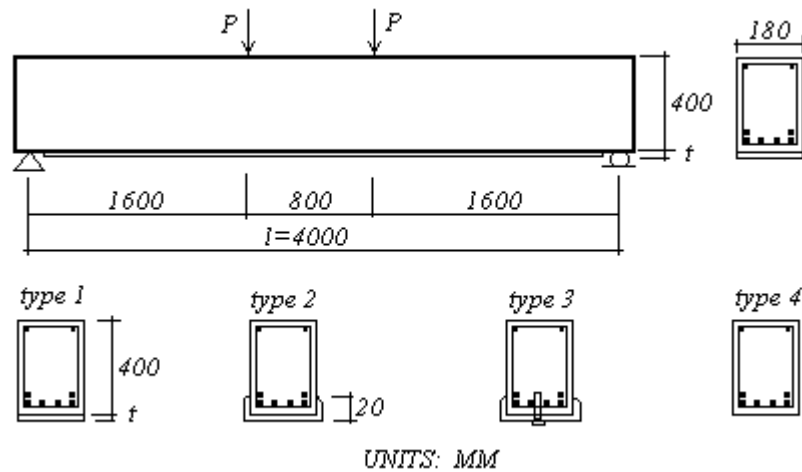


Fig.1 GFRP/RC Tested Girders

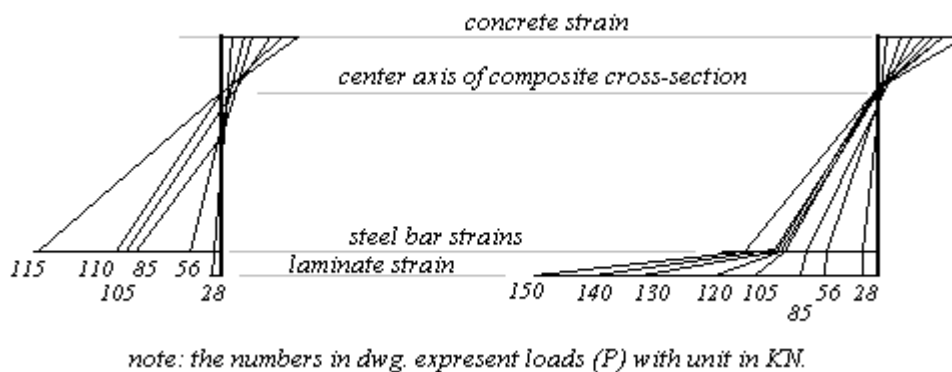


Fig.2 Stress-Strain Curves of GFRP/RC Girders

For investigating regular pattern of its cross-section, 24 vast-scale ($L = 400$ cm) FRP/RC girders were researched which have various thicknesses of laminates and grades of concrete but there were same reinforcing in the cross-section of girders. The dimensions and models of GFRP/RC girders can be shown as Fig.1, and the typical stress-strain curves of composite cross-section are compared between GFRP/RC girders with variously laminates and RC girders (see Fig.2).

From curves in Fig.2, we can see that stress-strain along the height of GFRP/RC girders is nonlinear when limit state. This is not the same as RC girders. Furtherly, we can discover that strains of steel in these girders are not nearly rising with the strain of GFRP laminates when

the steel bars approach its yield limit. At that time, the stresses in composite beams are distributed among concrete, steel bars and GFRP laminates. In other words, the laminates will carry more strain than steel bars.

ANALYSIS OF LIMIT CARRYING BASED ON GFRP/RC GIRDER'S FLEXURE EXPERIMENTS

We can make a simple mode from the nonlinear curve of stress-strain of section for analysis. According to this mode, we can change nonlinear strain curves in a kind of equivalent line relationship, so obtain equations of nature axis and carrying conveniently throughout relationship of the section.

On the other hand, experience equation based on GFRP/RC tested girders can be described as:

$$Y = \frac{M_f}{M_c} = 1427 \exp(-48626 \cdot 10^{-3} \cdot \frac{E_h}{E_f} \cdot \frac{x}{t} \cdot \frac{h-0.5x}{h_o-0.5x}) \quad (x \neq 0) \quad (1)$$

Where:

M_f / M_c --- ratio of limit bending moments between GFRP/RC and reinforced concrete girders;

x --- nurture axis position of the reinforced concrete cross-section;

h --- depth of reinforced concrete girder;

t --- thickness of GFRP laminates used on the GFRP/RC girders;

h_o --- distance between the center of gravity of reinforcing bars and the top surface of reinforced concrete girders.

Values of testing and calculating are identical and present that carrying bending moment of beams strengthen by GFRP laminate is usually higher 15-40% than reinforced concrete girders. The strengthen ratio may be change with parameters such as modules of materials, thickness of GFRP laminates, etc.. When the stress of bar and concrete achieve their limit value, strains of GFRP laminates are only 50% of themselves limit strain. therefore, strengths of laminates have more than needed.

CRACK ANALYSIS OF LIMIT CARRYING BASED ON GFRP/RC GIRDER'S FLEXURE EXPERIMENTS

Cracks Compare in Loading Of Flexure Experiments

Tab.1 gives the comparing of two kinds of beams based on flexure test. From the crack comparing of GFRP/RC girders and reinforced concrete girder, we can find different properties of GFRP/RC beams as following:

- a. distances of any two cracks of GFRP/ RC girders are more short;
- b. the number of cracks increasing and breadth of cracks reducing;
- c. when the strain of tensile bars is approach yield limit, the developing speed of concrete cracks is obviously reducing;

- d. main factor of control concrete cracks is thickness of GFRP laminate, others such as the shape and construction of GFRP laminates are not clearly control cracks developing.

Table 1 Aaverage Width of Concrete Cracks δ_f (mm)

load (KN)	95		105		130	
girder type	δ_f	δ_f/δ_0	δ_f	δ_f/δ_0	δ_f	δ_f/δ_0
RC girders	0.190		0.405	δ_f		
RC girders with 5 mm plates	0.130	31.6	0.133	67.2	0.364	----
RC girders with 5 mm U-shapes plates	0.136	28.4	0.165	59.3	0.333	----
RC girders with 8 mm plates	0.108	43.2	0.127	68.6	0.291	----

From the table it can be seen that cracks width of GFRP/RC girder have been obviously reduced with the thickness of laminates, the crack's widths are only about 50-70 percent of crack's width of reinforced concrete girders. This ratio is approach with the strength ratio of the composite cross-section.

Calculating Equation Of Crack Width Of Gfrp/Rc Girders

The cracks developing of general reinforce concrete girder is a very complex process. When reinforced concrete girders are strengthened by GFRP laminate, the girders become a composite cross-section girder, and its concrete cracks developing will change more complex. Up to now, Chinese highway specification use line equation for calculating crack width of concrete girders. But this equation is approach, and it has very great error when cracks have large width. From Tab.1 we known that GFRP/RC girders can carrying larger loading than RC girders, therefore, calculating equation of GFRP/RC girder's crack width is not simple line relationship.

Let equation of crack width is following relationship

$$\delta_{f \max} = f(\alpha \cdot \beta \cdot \gamma \cdot \delta_{o \max}) \quad (2)$$

in which:

$\alpha = \frac{E_h}{E_f}$, it is relationship of materials properties;

$\beta = \frac{S_g}{S_f}$, it is relationship of constructural dimensions of tensile bars and GFRP laminates.

Its physic quality is a ratio of internal paste forces between bars and laminates with concrete. S_g is the circumference of one bar in the girder; S_f is the paste length of GFRP laminate with concrete at composite cross-section;

$\gamma = \frac{a_g}{t}$, it described the dimensions relation between the center (a_g) of bars gravity and the thickness (t) of GFRP laminate;

$\delta_{o \max} = \theta \cdot \delta_{0 \max}$, it is calculating crack width of reinforced concrete girder. θ is nondimension factor it may be obtained from test;

$\delta_{f\max}$ -- GFRP/RC girder's maxims crack width.

From the our investigating, nondimension factor θ relationship as following

$$\theta = a \times \exp(b \times \delta_{0\max} / d) \tag{3}$$

in the equation, a and b are experience apparatus from testing, d is diameter of tensile bars. If let

$$x = \alpha \times \beta \times \gamma \times \theta \times \delta_{0\max} \tag{4}$$

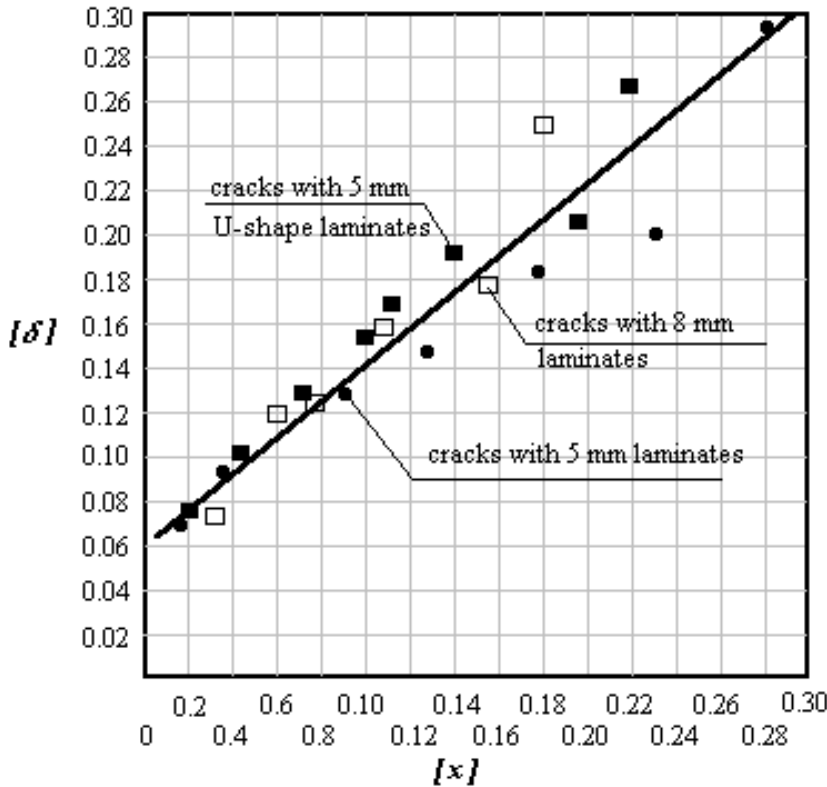


Fig.3 relationship of $\delta_{f\max}$ vs. parameters

according to equation (2), and based on approach line relationship between x and $\delta_{f\max}$ (see Fig.3), we can introduce a simple equation of the maxtural crack width of GFRP/RC girders as:

$$\delta_{f\max} = f(x) = 0.058 + 0.086 \times x \tag{5}$$

APPLICATION OF THE TECHNIQUE ON TWO HIGHWAY BRIDGES

The technique of strengthening concrete girders with GFRP laminates have been successfully employed in the reparation of two highway reinforced concrete bridges. One of them is three spans 3×20 m T-girders that has built been for 28 years when it was been repaired. Another

one is located in main line of nation with five spans (5×17 m), total length 101.33 m and about 25m height of piers across the river, it's frequency of flood water was been designed 50 years. Because of tremendous influences of floodwater and earthquake in 1989, it was been only allowed carrying lower 80 KN of automobiles. And it has been built 27 years, original design bearing standard of the old bridge was only about 150 KN automobiles when it was been repaired.

The bearing standard of 300 KN weight automobiles and 800 KN single trailer for second one was been required if it can be repaired. During repairing engineering, traffic must be held because of it is that in main line of nation.

According to equations from this paper, sum up the effects such as moments, shears, width of concrete of the early old cross-sections, GFRP laminates were been employed strengthening 25 T-girders of the bridge which already serious damaged. The thickness of laminates can be varied from equations' (1)~(5). The laminates were been manufactured in plates of 160 mm width and 1580 mm length. For reducing total costs of the repaired engineering, the GFRP plates were been manufactured varied thickness from 10 mm ~ 12 mm along button axis of the reinforced concrete T-girders based on internal forces of composite sections.

The time of repairing engineering was cost about 30 days, in which, the time of repairing 25 pieces T-girders cost only about 10 nights.

After repairing engineering of the bridge completed, it has been test which has the same bearing standard of repairing. Loading tests present:

- Any strains of every material are lower than allowing strain values, and stresses of bars and concrete reduce in the same load levels than non-repairing.
- The strength of GFRP materials has enough and to spare.
- The crack widths of old girders were usually 0.3 mm ~ 0.36 mm when testing loading was 150 KN, but the maxtural crack of repaired girders was only 0.25 mm at the same loading and large cracks have been reduced. When maxtural design loads have been tested, only appeared one crack of 0.26 mm width which is very approach with calculating value by equation's (2)~(5), the error between testing values and calculated expecting value is lower 10 percent.

CONCLUSION

GFRP laminates can be used to repair existed reinforcement concrete highway bridges. Crack's propagation is controlled, and the carrying capability can be raised according to require. The application is easy, and the construtural period is very short. Moreover, the repairing costs can be reduced about 20% compared to general repairing methods.

The equations for calculating the bending capability and maxtural breadth of cracks are very useful since the effects of primary parameters of materials and construtural dimensions have been taken into account. Calculation values agreed very well with the test data.

This paper described one repairing method of reinforced concrete girders with GFRP laminates. The equations for calculating strength of cross-section and especially maxtural width of concrete cracks with GFRP laminate to repairing concrete girders are given, it may be described the contribution of composite materials for composite girders. At last, paper given two applications used this method.

REFERENCES

1. Meier,U. & Kaiser, H., “Strengthening of Structures with CFRP Laminates”, *Advanced Composites Materials in Civil Engineering Structures*, MT Div/ASCE/Las Vegas, 1991, pp224-232.
2. Ehsani, M.R. & Saadatmanesh, H., “Fibre Composite Plates for Strengthening Bridge Beams”, *Composite Structures*, Vol.15, pp343-355, Elsevier Sicence Ltd., England, 1990.
3. Saadatmanesh, H. & Ehsani, M.R., “Fibre Composite Bar Reinforced Concrete Construction”, *Composite Materials*, Vol.25, 1991, pp188-203.
4. Wang, S.J. & Zhang, R.X., The Study of Fiber Composite Plates for Strengthening Reinforced Bridges, *ICCED-9*, 12-16 July, 1993, Madrid-Spain.

HAZARDS OF LOCAL FAILURE IN BENDING OF COMPOSITE SANDWICH PANELS FROM POINT FORCES

I.G. Zhigun, R.P. Shlitsa and V.V. Khitrov

Institute for Polymer Mechanics, LV- 1006 Riga, Latvia

SUMMARY: Simple design formulae have been given to evaluate the flexural characteristics of a sandwich panel in three-point bending. The model modification has allowed consideration of distinctions in the deflections of face layers and hence the deformation of a normal as well as transverse normal stresses in the middle layer have been deduced. Local curvatures, bending and transversal stresses have been studied depending on the thicknesses of face layers and the transversal properties of a core in shear and compression. Hazard of initial failure from local moment stresses at the central section as well as transversal stresses at the support section and close to the panel end has been revealed. Comparative estimates for bending stresses refining the results of conventional designs have been obtained.

KEYWORDS: sandwich panels, design calculations bending and transversal stresses, loading points, boundary effect.

INTRODUCTION

Layered plates type of sandwich panels among a wide range of structures, offering promising scope for the use of composite materials are of interest for varied structure mechanics problems. The development of the approach considering details of a structure and composite behaviour of these panels will occupy our attention in the bulk of this work. The solutions were above all refined based on Kirohoff-Love and Timoshenko hypotheses, considering transverse shear, anisotropy of layers and their sectionally uniform distribution across stack thickness [1], [2]. Refined approach where the deflection in stack bending is a function of layer location across the thickness takes account of local effects and characteristics of panel edge fixing. Applied theory for discrete layered model considering deformation of a normal was developed in [3]. Values of Cylindrical stiffness (D) and stiffness in transverse shear (K) derived from the sandwich model [2] and obtained based on experimental deflection data will agree. Different situation arises in the assessment of strength properties: design assessment of panel strength in terms of ultimate normal stress of outer layer.

$$\sigma_x^* = E_x \varepsilon_x^*,$$

corresponding to the limitation on bending moment as large as

$$M^* = bh^2 \sigma^* E_f / (6E_\tau),$$

(where, according to symmetric structure sandwich model, its effective modulus in bending

E_f was derived from the formula $E_f = E_o(1 - \mu_V)^3 + E_x[1 - (1 - \mu_V)^3]$ and $\mu_V = 2h_1/h$, $h = h_o + 2h_1$, see dimensional parameters in Fig.1). substantively differed from the value M^* , recorded in experiment.

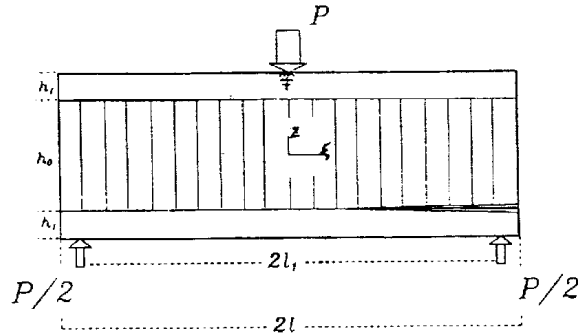


Fig. 1: Schematic of sandwich panel

The reason is attributive to the local bending of an outer layer under point force in three - point bending of sandwich plate. The following issue under consideration associated with justification of the procedure for deduction of the solution for point force action on a panel surface. Employment of the exact solution for a half-plane loaded by point force (kind of Flamman's problem or one of Lechnitsky in case of material orthotropy) is combined with superposition of boundary-value problem solution for the region "cut out" from a half-plane representing a beam or plate. Some results which concern three-point bending of a beam have been derived with the use of superposition technique mentioned in case of the uniform material and the orthotropy of elastic properties [4]. At the present work by virtue of inhomogeneity of elastic properties the cylindrical bending of a sandwich panel from point forces is considered relying on the refined method [5], based on analytical solution for variational problem on a sandwich plate. The bending of a face layer of the Kirchhoff's type and the transversal deformations of a core in shear and compression were validated through their energy estimate.

KEY DESIGN RELATIONSHIPS

In description for the bending of a panel, which dimensions and the scheme of three-point loading are shown in Fig. 1, the kinematic model [5] was adopted allowing for consideration for transversal deformation of a normal as the difference in deflections between face layers. With this point clear, the traditional solution part allowing for transversal shear was supplemented by this deformation factor together with a local bending of face layers and therefore the elastic potential for a layer stack has been deduced. The Euler's equations derived from the variations of four displacements have been solved by the Laplace transform as the most suitable solution technique in discontinues and point loads. Leaving out the details of the procedure described in [5] let us represent here the final solution form for the deflection difference of outer layers and their local curvatures.

Distinction in deflections at the central section

Key impact from point force at the panel centre is governed by the gap of the deflections of face layers in between. The normal stress $\sigma_z(0)$ within the middle layer is also determined by the difference $w_\Delta(0) = w_2(0) - w_1(0)$ accurate to the transversal stiffness coefficient of a panel. The relative value of this difference for the panel of a symmetric structure ($h_1 = h_2$, $E_x^{(1)} = E_x^{(2)}$) is defined by the following expression:

$$w_\Delta = -w_\Delta/q_0 = [\tilde{s}_0(\xi_1, \xi_l) - 2x_\alpha s_0''(\xi_l)]/[b_1 s_0(\xi_l)] \quad (1)$$

where displacements w_i and u_i are dimensionless (related to $h_1 + h_0$), by a prime the operation of derivation with respect to relative variable $\xi = x/(h_1 + h_0)$ is designated and the following functions are introduced:

$$\begin{aligned} s_0(\xi) &= (\text{ch}\alpha\xi \text{sh}\alpha\xi + \text{sh}\alpha\xi \text{ch}\alpha\xi)/2\alpha \\ s_1''(\xi) &= \alpha^2 \text{sh}\alpha\xi \text{sh}\alpha\xi \end{aligned} \quad (2)$$

which can be grouped together at the certain points as:

$$x_\alpha = -\frac{4}{b_1} \cdot \frac{s_1''(\xi_l) \tilde{s}_0(\xi_1, \xi_l) - s_0(\xi_l) \tilde{s}_1''(\xi_1, \xi_l)}{\text{sh}2\alpha\xi_l + \text{sh}2\alpha\xi_l} \quad (3)$$

$$\begin{aligned} \tilde{s}_0(\xi_1, \xi_l) &= s_0'(\xi_l) - s_0'(\xi_l - \xi_1), \\ \tilde{s}_1''(\xi_1, \xi_l) &= s_1''(\xi_l) - s_1''(\xi_l - \xi_1) \end{aligned} \quad (4)$$

For the dimensionless parameters the following notation is taken:

$$\begin{aligned} \mu &= h_1/(h_1 + h_0), \quad \xi_1 = l_1/(h_1 + h_0), \quad \xi_l = l/(h_1 + h_0) \\ k_1 &= m_z/[\mu(1 - \mu)], \quad k_2 = n_z/[\mu^3(1 - \mu)] \\ m_z &= (G_{xz}/E_x)(1 - \nu^2), \quad n_z = (E_z/E_x)(1 - \nu^2) \\ b_1 &= 24k_2, \quad b_2 = -2k_1(1 + 3/\mu^2), \quad \alpha = \sqrt[4]{6k_2}, \quad \alpha_1^2 = -b_2, \\ q_0 &= 6P(1 - \nu^2)/[E_x \mu^3 b(h_1 + h_0)] \end{aligned} \quad (5)$$

where the panel width is denoted by b .

For infinite panel length $l \rightarrow \infty$ from (1) can be derived:

$$\lim_{\xi_l \rightarrow \infty} w_\Delta = [1 + e^{-\alpha\xi_1} (\text{cos}\alpha\xi_1 + \text{sin}\alpha\xi_1)]/4\alpha^3 \quad (6)$$

Mean and local curvatures

Expressions for face layer curvatures at the panel central section can be represented as:

$$w_1''(0) = -q_0 x, \quad w_2''(0) = -q_0(\hat{\xi}_1 - x) \quad (7)$$

where the dimensionless parameter for the doubled value of the mean curvature $\hat{\xi}_1 = -[w_1''(0) + w_2''(0)]/q_0$ is defined as:

$$\hat{\xi}_1 = \frac{\xi_1}{1 + 3/\mu^2} + \frac{sh(a_1 \xi_1) - sh[a_1(\xi_1 - \xi_1)]}{a_1(1 + \mu^2/3) ch(a_1 \xi_1)} \quad (8)$$

and for the curvature parameter of an upper face layer the simple notation can be deduced:

$$x = \hat{\xi}/2 + x_\alpha \quad (9)$$

where x_α is derived from (3).

In such a manner in the bending of a symmetric structure panel the mean curvature (8) depending on the parameter a_1 is variable with a core shear stiffness value according to (5), while independent on transversal stiffness in tension / compression, defining the parameter α . Face layer local curvatures by (9) are the functions of both transversal stiffness factors.

STRESS CONCENTRATION

To estimate the maximum stress in sandwich panel layers in three-point bending the central section $\xi = 0$ is considered wherein $\max \sigma_x$ existing, however in deducing $\max \sigma_z$ the support section $\xi = \xi_1$ is also added to the first one and for $\sigma_z > 0$ - the free face $\xi = \xi_1$. Stresses at these sections seem to be the most hazardous as governing the initial failure of face layers induced by a longitudinal compression (due to σ_x) or delamination (due to σ_z).

Bending stresses at a central section.

Revision of conventional design methods for stress σ_x calls for deduction the moment stresses caused by the local bending of face layers, which are added to average stress. Let us estimate the value of moment stresses and examine the difference between average stresses and bending ones derived from simplified sandwich models based on the Kirchhoff-Love hypothesis for the whole layer stack. The bending stress of a face layer at the extreme points of its section is represented as two components:

$$\sigma_{x,t} = \pm \sigma_{x,t}^M + \sigma_{x,t}^O \dots t = 1,2 \quad (10)$$

of which the first one is a moment stress resulted from a local layer bending:

$$\sigma_{x,t}^M = \mu E_x^{(t)} w_t'' / [2(1 - \nu_t^2)] \quad (11)$$

and the second - an average stress due to the longitudinal layer force $N_{x,t}$

$$\sigma_{x,t}^O = \langle \sigma_{x,t} \rangle = N_{x,t} / h_t = E_x^{(t)} u_t' / (1 - \nu_t^2) \quad (12)$$

At the central panel section in view of (8) the derivative $u_t'(0) = \pm q_0(\mu^2/12)(\xi_1 - \hat{\xi}_1)$ and the (10) will appear as:

$$\sigma_{x,t} = [E_x^{(t)} / (1 - \nu_t^2)] [\pm q_0(\mu^2/12)(\xi_1 - \hat{\xi}_1) \pm (\mu/2)w_t''(0)] \quad (13)$$

where the upper and lower signs of the first summand in the square brackets correspond to $t = 1,2$ respectively and the second - to upper and lower points on the thickness of face layers each.

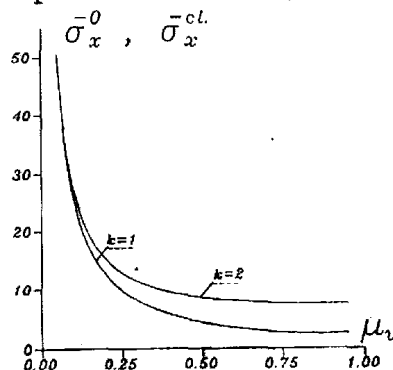


Fig.2: Variation of mean across thickness of outer layer relative bending stress σ_x^O ($k = 1$) and the maximum bending stress by classical theory σ_x^{cl} ($k = 2$) at the centre of the panel with the relative volume of outer layers. $2l_1 = 5h$, $\sigma_x = (\sigma_x/P)bh$

The design values of the first summand in (13) can be related to the bending stress σ_x^{cl} calculated according to the classical Kirchoff-Love hypothesis for the whole stack [2] in view of the longitudinal stiffness of face layers $E_x^{(t)}$ and middle layer E_x^O . As the stiffness of the face layers increases (their relative volume $\mu_v = 2h_1/h$, $h = h_0 + 2h_1$) the disparity between the values σ_x^O and σ_x^{cl} grows up (see Fig.2). However with relatively thin

face layers in the material of HEXCEL/Al type [3], $E_x = 40 \text{ GPa}$, $E_z = 310 \text{ MPa}$, $G_{xz} = 138 \text{ MPa}$, $h_1 = 1 \text{ mm}$, $h_0 = 10 \text{ mm}$ this discrepancy may be neglected. Notice that the longitudinal Young's modulus E_x^0 as well as the transversal one E_z is not involved in the expression for σ_x^0 and, hence, the estimate of maximum bending stress by classical theory can be obtained taking account of the longitudinal Young's modulus E_x of a face layer only. To this must be added, whereas the transversal shear stiffness is ruled out in the σ_x^{cl} design in three-point bending, it appears in the expression for the σ_x^0 evaluation and as G_{xz} increases by an order of magnitude the σ_x^0 value grows up in the range of 35% at $\mu = 0.9$. Substantial correction to the values of average bending stresses σ_x^0 is dependent on transversal stiffness in tension/compression E_z of the middle layer and is governed by the second summand in (13). Referring to Fig. 3 the stress $\sigma_{x,t}$, calculated for the central section by this formula, differs from σ_x^0 in Fig. 2 as high as 1 - 4 times depending on section dimensions. Due to sizable distinctions between the relative curvature values $\alpha_1 = \hat{\xi}/2 + \alpha_\alpha$ and $\alpha_2 = \hat{\xi}/2 - \alpha_\alpha$ a symmetry about x axis in the location of the curves in Fig.3, obtained at $z = \pm h/2$ and $z = \pm h_0/2$ is nonexistent.

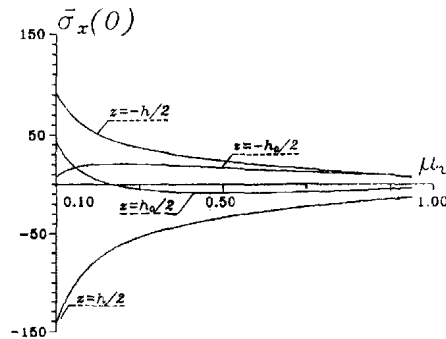


Fig. 3: Bending stresses at the central section along the surfaces of face layers versus their relative volume at $2l_1 = 5h$

Face layer moment stresses dependent on the relative parameter α_α favour the overload of the upper face layer in bending as compared with the lower one. Overload coefficient is dictated by the values of the moment stresses. Taking the form

$$k_m = \frac{w_1''(0)}{w_2''(0)} = \frac{\hat{\xi}/2 + \alpha_\alpha}{\hat{\xi}/2 - \alpha_\alpha} \quad (14)$$

k_m increases infinitely at $\alpha_\alpha \rightarrow \hat{\xi}/2$, i.e. in the special case that

the local bend of the lower face layer is absent: $w_2''(0) = 0$. Each face layer relative thickness (defined by the structural parameter μ_V) for a panel in the material of HEXCEL/Al type corresponds to a definite k_m value shown by the curve $k = 3$ in Fig. 4. At $\mu_V^* = 0.15$ the value $k_m = \infty$.

Table 1: Alternate versions of the transversal characteristics of a panel stiffness.

k	1	2	3	4	5
G_{xz} , GPa	0.00	0.14	0.14	0.14	1.40
E_z , GPa	0.31	3.50	0.31	0.00	0.31

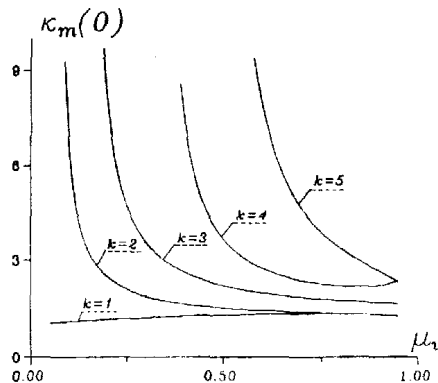


Fig. 4: Overload coefficient k_m of the upper layer by moment stresses at the central section versus relative volume of outer layers at $2l_1 = 5h$

Increase in the shear modulus G_{xz} by an order of magnitude, see Tab. 1 and Fig. 4 at $k = 5$, as well as the decrease by a factor of 10^3 in the Young's modulus $E_z - k = 4$ corresponds to μ_V^* displaced to the right as compared with the case $k = 3$. At $G_{xz} = 0 - k = 1$, as for the infinite E_z value, the denominator in (14) has a nonzero value everywhere at $0 < \mu_V < 1$ and a change in the curvature sign of the lower face layer at the small μ_V is absent. The opposite signs of curvatures in three-point bending theoretically at the arbitrary values of transversal stiffness and layer thickness data are not ruled out, however, in practice it may be found unlikely. In such an event the regularity of an increase in the coefficient k_m as the structural parameter μ_V is reduced, see Fig. 4, can be used as far as a certain limit. The latter can be established from the test data for a panel of varied layer thickness. The elaboration of a theory that follows and the relevant design method of a bending behavior should give due consideration for a strain variation throughout the middle layer thickness, as has

been done in [3] using the numerical realization of the method.

Transversal stresses

In evaluating the transversal stress responsible of failure by debonding mechanism the greatest gap in the classical theory [1], [2] exists for σ_z stress as distinct from τ_{xz} . By the model [5] taken here the normal transversal stress at the panel centre is evaluated from the following expression:

$$\sigma_z(0) = - \frac{q_0 E_z}{1 - \mu} \cdot \frac{1 + e^{-\alpha \xi_1} (\cos \alpha \xi_1 + \sin \alpha \xi_1)}{4\alpha^3} \tag{15}$$

suitable for a span length $l_1 > h$. Notice, that the stress σ_z is unaffected by the shear module G_{xz} , and varies as $(E_z/E_x)^{1/4}$. The effect of a dimensional parameter μ_V on the stress σ_z at the central section is shown in Fig. 5. With a very thin face layer the stress σ_z increases infinitely defined by the multiplicity of a zero - $3/4$, when $\mu_V \rightarrow 0$. In the other limit case, when $\mu_V \rightarrow 1$, this degree is $-1/4$. Minimum σ_z value is taken at $\mu_V = 0.75$.

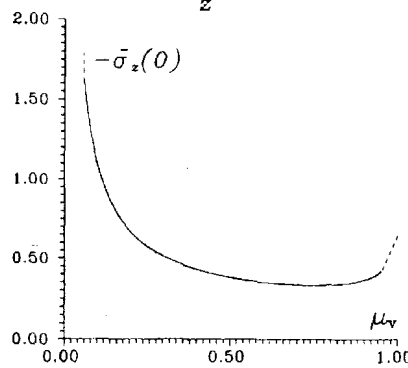


Fig. 5: Effect of the relative volume of outer layers on the transversal stress at the panel centre: $\sigma_z = (\sigma_z/P)bh$

Notice, that for the material structure of HEXEL/Al type the stress $\sigma_z(0) \cong (3/2)(P/bh)$. What this means is the shear stress $\tau_{45^\circ}(0) = (3/4)(P/bh)$ acting at the panel centre $\xi = 0$ over the area inclined at the angle $\pm 45^\circ$ to z - axis equals in magnitude to the maximum shear stress in three-point bending *max* τ_{xz} , calculated by the classical theory. Hence, in this situation the shear mode of failure caused by either normal compressive stress or transverse shear stress is equiprobable. Feasibility of a panel local failure by the debonding mechanism as a result of positive σ_z values depends within certain limits on a panel extent along x - axis, i.e. on a ratio - (panel length / span). The expression for evaluation of σ_z stress at the panel end $\xi = \xi_1$ can be represented in the following form:

$$\sigma_z(\xi_1) = - \frac{q_0 E_z}{1 - \mu} \cdot \frac{1}{2\alpha^3} \exp[-\alpha(\xi_1 - \xi_1)] \cos[\alpha(\xi_1 - \xi_1)] l, \quad (16)$$

suitable for a span length l_1 , satisfying the relationship $\varepsilon \geq \exp(-\alpha \xi_1)$, where ε is an any preassigned small number.

Variation of a relative σ_z value at the panel end is represented in Fig. 6 by the curve 1. Asymptotic formula for σ_z , applicable to the analysis of this stress damping as ξ coordinate recedes from support in case of $l \rightarrow \infty$, is deduced in [5]. In the construction of the curve 2 in Fig. 6 matching the case $l \rightarrow \infty$, the abscissa x/l_1 have been equated to the value l/l_1 for the panel of finite length. Fourfold increase in compressive σ_z stresses at the support of a panel in length $l = l_1$ in reference to the panel of infinite length and still further difference of positive σ_z values allows contention, that for a finite length panel the hazard of failure by debonding mechanism in three-point bending is more probable, than for an infinite length panel.

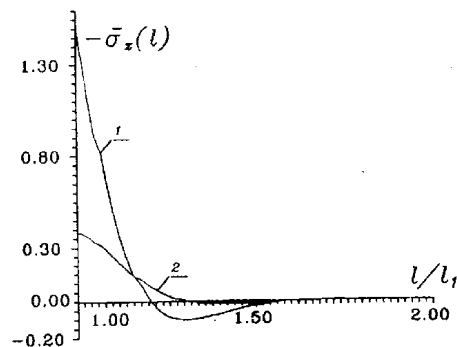


Fig 6: Variation of transversal stress at the panel free face with the relative parameter l/l_1 at $2l_1 = 5h$

In the prediction of initial failure by debonding mechanism the positive σ_z values should obviously be correlated with their negative values at the support and central sections, having regard to the ratio of material strength in tension and compression in the transverse direction.

CONCLUSIONS

By the elaboration of analytical method for sandwich panel design in bending the refined characteristics for face layer curvatures and transversal normal stress have been deduced. The advantage of the derived formulae for stresses lies in analytical estimation of the effect of model parameters on the design characteristic considered. This have been achieved via the separation of the solution into a symmetric and antisymmetric components. The first one defines the transverse deformation of a normal as well as the

transversal σ_z stress and is independent of transverse shear modulus G_{xz} . The local effects of reduction at the panel centre and supports were demonstrated to be comparable with the transverse shear effects resulting in initial failure via delamination. Boundary effect at a free panel face with the specific length of panel sections extending beyond the supports is the next factor aggravating the hazard of delamination due to positive σ_z values.

Expression for the bending stress σ_x was represented as the combination of symmetric and antisymmetric solution parts. Moment stresses of each layer exert primary control over the local bending in point forces. The average σ_x^0 stresses for the panel having relatively thin face layers were demonstrated to be equivalent to the classical bending stresses derived by the Kirchhoff-Love hypothesis for the layer stack as a whole. Revised shear correction to the σ_x^0 has been deduced in term of a mean curvature. Local layer curvatures have been derived in terms of a mean curvature and an additional curvature caused by the transversal reduction. Combination of the transverse stiffness properties in shear and compression entering respectively into these curvatures given section dimensions governs the overload coefficient of the one of face layers in a local bending. The formulae proposed and assessments deduced from them are usable both in a sandwich panel design and in an effort to determine the parameters of a simplified model bounding its scope.

REFERENCES

1. Allen N.G., *Analysis and Design of Structural Sandwich Panels*, Pergamon Press, Oxford, U.K., 1969.
2. Johnson, A.F. and Sims G.D., "Mechanical properties and design of Sandwich materials", *Composites*, Vol.17, No.4, 1986, pp. 321-328.
3. Thomsen, O.T. and Rits, W., "Analysis of Sandwich Plate Theory", *Proceedings Tenth International Conference on Composite Materials*, Whistler, British Columbia, Canada, August 14-18, 1995, Vol. V: Structures, Poursartip, A. and Street, K.N., Eds, pp. 35-42.
4. Tarnopol'sky Yu.M. Zhigun I.G. and Polyakov V.A. "Distribution of Shearing Stresses under Three-Point Flexion in Beams made of Composite Materials", *Polymer Mechanics*, Vol. 13, No. 1, 1977, pp. 52-58, (in Russian).
5. Polyakov, V.A., Zhigun, I.G., Shlitsa, R.P. and Khitrov. V.V., "Deformation Features of Sandwich Panels in Cylindrical Bending by Point Forces. 2. The technique devised", *Mechanics of Composite Materials*, Vol. 33, No. 1, 1997, pp.32-63.

SUBJECT INDEX

ablation	611	c-block	432
acoustic emission	16, 25, 193, 223, 742	certification	119, 357
acoustic fatigue	327	CF/GF hybrid laminate	483
acousto-ultrasonic technique analysis	213	CFRP	395
active element placement	591	CFRP heater	483
active vibration control	454	CFRP laminates	223
actuator	432, 500	clearance	139
adhesive	762	cocuring	687
adhesive bonded joints	129	coefficient of thermal expansion	258, 762
adhesive bonded repairs	374	comb joint	95
adhesive bonding	1	complex relative permittivity	55
adhesive joining	111	composite	819
adhesive joints	95	composite hinge	158
adhesive stresses	347	composite joints	74, 148
adhesively bonded	8	composite material	632
advanced signal process	237	composite material evaluation,	213
aging	102	composite materials design	246
aircraft	279	composite patch	296
aircraft repair	337	composite plates	374
airframes	707	composite repair	317
airworthiness certification	337	composite repairs	119, 357
Al/TiNi composite	510	composite structure design	203
aluminum	279	composite structures	707
analytical method	770	composites	36, 55, 271, 500
anisotropic inclusion method	464	compression	742
asymptotic theory	789	compression after impact (CAI)	185
average stress criterion	395	compressive residual stress	510
axial compression	695	compressive strength	395
		concrete beams	731
β -ray monitoring system	271	cone calorimeter	611
beams	444	constitutive relations	444
beam-tests	731	contact behavior	167
bearing	102	contact-type transducers	213
bending and transversal stresses	826	continuous analysis method	668
bolt	65, 102	continuous fibres	230
bolted	148	crack closure	493
bond stress	731	crack growth	337
bonded composite patches	306	crack patching	279
bonded composite repairs	306	creep	102, 474
bonded joint design	1	creep strength	26
bonded joints	84, 119, 357	critical modulus ratio	528
bonded repair	1, 279, 327, 347	cross-ply laminates	770
bonded repairs	296, 306	cylindrical bending	129, 753
bonding	175	cylindrical shells	742
boron	279		
boron/epoxy composite	337	damage tolerance	74, 203
boundary effect	753	damping control	483
boundary effect.	826	debonding	296, 687
braid fiber architecture	723	delaminated beam-plate	668
braiding	723	delamination	185, 246
buckling	658, 668, 742	density	258
buckling prediction	203	design	742
butted test pieces	55	design calculations	826
bypass	102	design of patches	347
		Dirac's function	753, 761
carbon fibre	36	dislocations	193

distributed sensor/actuator	454	GFRP sheets	16
doubly curved shells	789	girder	819
ductile	723	glass fiber reinforce plastic	819
durability	677	glass/epoxy composite	289
dynamic	799, 807	global/local procedures	707
		Green's functions	193
eigenproblem	648		
elastic wave propagation	213	heat sink strength	500
elastic/viscoelastic	46	heating power	500
elasticity	789	helicopter blades	289
elasticity solution	432	Hellinger-Reissner functional	789
elastomer	500	high load intensity	95
electrode pattern	454	high stress gradients	296
energy absorption	74	higher order theory	770
environmental effects	677	highway bridge	819
Eshelby tensor	464	hole identification	639
experimental testing	357	honeycomb sandwich panel	762
experimental tests	622, 731	hybrid	723
extended Kantorovich method	648		
		impact damage	223, 385
failure	687, 742	IMSC	551
failure criterion	167	indirect measuring methods	237
failure load prediction	395	induced strain	432
failure loads	357	injection molding	175
failure process	16	inserts	148
fastener repair	668	in-situ	230
fatigue	385, 394, 677	integer, discrete, and continuous design variables	591
fatigue behavior	582	intelligent materials and structures	421
fatigue life prediction equation	365	intelligent or smart material	528
fatigue modulus	365	intensity attenuation	271
fatigue resistance	74	interface debonding	571
fatigue strength	26	interfacial bonding strength	510
FEA models	289	interlaminar stress	648
fibre-reinforced thermoplastic	55	interlaminar stresses	444
field repairing	405	internal defects	582
film adhesive	279, 405	internal stresses	230
finite difference theory	632	interphase	237
finite element	658, 742	inverse analysis	639
finite element analysis	8, 95, 444, 707	iteration	648
finite element calculations	246		
finite element method	139, 519, 762	joining	36, 65, 139
finite element modeling	622	joint	26
finite element models	374	joints	102
finite element stress analysis	395		
finite elements	808	laminate	819
fire behaviour	611	laminate plates	658
fire testing	611	laminated shells	789
flush scarf patch repairs	395	laminates	129, 167
foam core	385	large transformations	622
formula optimization	405	laser signal intensity	582
forward analysis	639	layered plate	753
fracture	175	linear elastic	317
fracture toughness	16, 493	linear/non-linear behaviour of adhesives	129
free edge	648	load rate	1
free vibration test	483	loading points	826
FRP	723	local effect	753
		loss tangent	55
g/e bolted joints	148	low-velocity impact	185
GFRP	26	LQR	551
GFRP bars	731	LS-DYNA3D	799

macromechanical analysis	317	rehabilitation of infrastructure	16
magnetolectric coupling effect	464	reinforced composite structures	622
magneto-electro-elastic	464	reinforced concrete	723, 819
marine structures	412	reinforcing effects	16
material behaviour	317	repair	385, 412
material nonlinearities	622	repaired graphite/epoxy laminates	365
mechanical fastening	139	residual strain	279
mechanical joints	84	residual strength	223
microwave and peripheral facilities	55	residual stress	46
microwaves	65	resin content	271
modal sensor and actuator	519	resistance welding	36
modelling	611	ribs	723
Mori-Tanaka theory	464	rivets	167
mortar and concrete beams	16	Ross-Kerwin-Unger analysis	483
multilaminate shells	808	RTM	158
multiple loading modes	639, 640	sandwich beam	385
multi-segment method of integration	129	sandwich composite beam	483
NDT	271	sandwich panels	289, 826
neutron diffraction	230	sandwich structures	412
nitinol	561, 570	scanning acoustic microscopy (SAM)	185
NiTi-reinforcement	230	shape active	230
noise reduction	74	shape control	561
non linear finite element program	540	shape memory alloys	493, 500, 528, 540, 561
non linear	799	shape memory composite	528
non-destructive evaluation	203, 223, 258	shape memory polymer	483
non-linear analysis	808	shape memory recovery	510
nonlinear optimization	639	shear stresses	317
nonlinear piezo-electro-thermo-viscoelasticity	444	shells	770
offshore	611	ship	799
one-sided repair	347	short-circuit plunger	55
on-line monitoring	271	skew	658
optical fibre sensors	421, 571, 582	smart composite structures	582
optimal control	519	smart composites	230, 493
optimization method	591	smart fiber reinforced polymer composites	571
optimum scarf angle	395	smart materials	421, 483
perturbation	789	smart materials and structures	551
phase transformation	230, 493	smart patches	421
photoelasticity	493	smart structures	421, 432, 591
piezoelectric material	519	SMARTCOM	551
piezoelectric polymers	474	S-N curve	582
point force	753	spatial filtering	454
polycarbonate	175	specific heat	258
Polyetherimide	36	state space technique	770
polymer matrix	444	static behaviour	385
post impact evaluation	203	static strength	8, 26
postbuckling	167, 677, 687	steady state fracture	111
postbuckling failure	695, 707	steel	175
practical engineering design	246	stepped circular repair	317
prepreg	271	stiffened carbon/epoxy panels	695
principle of complementary minimum energy	648	stiffened composite plate	687
pultrusion	571, 723	stiffened structures	677
pvdF sensor and actuator design	454	strain concentration	582
random response	327	strain energy release rate	111
rational transverse shear deformation		strain hold	1
higher-order theory	779	strength of bonded joints	1
refined theory	789	strength tests	337
		stress amplitude	258
		stress analysis	119
		stress function	648

stress intensity factor	347, 493	thin films	474
stresses	8	thin-walled	742
stress-induced martensite	510	three dimensional	799
stringer/skin panels	707	time response	500
strip methods	203	time-of-flight analysis	185
structural hierarchy	723	time-temperature superposition principle	26
structural integrity	611	total Lagrangian approach	540
structural stability	632	toughness	405
superposition	770	transversal stresses	753
supervised pattern recognition	237	transverse matrix crack	582
surface temperature	258	tube-in-sleeve	8
		tubular joints	84
temperature effects	337	two-dimensional	500
tensile	175	two-dimensional composite structure	639
tensile and shear strength	571		
testing	707	ultrasonic	237
testing and design	158	ultrasonic C-scan	223
thermal cycle	528	underwater shock	799
thermal expansion coefficient	528	uniaxial	648
thermal residual strain	279	unidirectional materials	84
thermal stresses	95		
thermo-elastic constant	258	vibration	770
thermomechanical loading	111	vibration control	551
thermopiezoelectricity	551	vibration suppression	519
thermoplastic	36, 175	viscoelastic laminated composites	444
thermoplastic adhesive bonding	46	viscoelasticity	474
thermoplastic composites	65		
thermoplastics	158	weight and energy minimization	591
thick shells	789	welding	65

AUTHOR INDEX

ADALI, S.	779	GU, Haozhong	432
ADAMS, R.D.	84, 95	HAARS, Hanno	317
AGATINO, Maria Rosario	731	HAN, K.S.	365
AHMAD, Hafiz	102	HARRIS, Harry G.	723
ALBAT, A.M.	279	HE, Tung-Chien	167
ALESI, H.	707	HILTON, H.H.	444
ALEXIADIS, S.	8	HOLLOWAY, Frank	474
ALLEN, H.G.	385	HONG, Chang-Sun	687
ALTENBACH, Holm	317	HONG, Doo-Hyun	223
AN, Deukman	510	HOU, M.	36, 158
ANASTASOPOULOS, A.	237	HOUSE, J.R.	74
ARMSTRONG, W.D.	230	HSU, Jui-Che	464
BALL, J.A.R.	55	HU, F.Z.	395
BATTLE, M.A.	742	HU, Hsuan-Teh	658
BEN DHIA, A.	622	HUANG, Jin H.	464
BOYKETT, R.	337	HWANG, W.	365
CALADO, Luis	731	HWU, Chyanbin	639
CALLINAN, R.J.	327	IMAI, Tomoya	26
CAMANHO, P.P.	139	INUI, Daisuke	483
CARDON, A.	237	ISHIKAWA, Takashi	258
CASTIGLIONI, Carlo A.	731	JANG, Tae Seong	582
CHAN, W.S.	601	JAUSS, M.	65
CHAO, M.	119	JEONG, T.H.	528
CHATTOPADHYAY, Aditi	432	JOHNSON, W.Steven	102
CHEN, Changqing	519	JONES, R.	119, 357, 707
CHEN, Ru	540	KABASHIMA, Shigenori	762
CHENG, Shou-Hsiung	668	KALAMKAROV, Alexander L.	571
CHIU, W.K.	119, 357	KEDWARD, Keith	203
CHIU, Ya-Hui	464	KELLY, D.	119, 707
CHO, Kyungmox	510	KHITROV, V.V.	826
CHO, Maenghyo	648	KIM, Busob	510
CHO, Youngsu	510	KIM, Ho	582
CHOI, Ildong	510	KIM, Hyonny	203
CHOI, J.W.	365	KIM, Jang-Kyo	185
CLARK, S.D.	385	KIM, Ji Hwan	454
CLARKE, A.B.	84	KIM, Seung-Jo	454
DAVIES, G.A.O.	84, 695	KIMPARA, Isao	16
DAVIES, M.J.	1	KAGEYAMA, Kazuro	16
DE WILDE, W.P.	237	KITIPORNCHAI, S.	213
DEEPAK, B.P.	296	KO, Frank K.	723
DODDS, N.	611	KOKO, Tamunoiyala S.	551
DROMGOOLE, G.R.	742	KONG, Cheol-Won	687
EMMERICH, R.	65	KU, H.S.	55
EYERER, P.	65	KWON, Oh-Yang	223
FRIEND, Clifford M.	374	LEE, D.J.	528
FUKUDA, Takehito	483	LEE, Dong Chun	582
FURUYA, Yasubumi	493	LEE, In-Cheol	677
GALEA, S.C.	148, 306, 327, 357, 421	LEE, Jung Ju	582
GAO, Shang-Lin	185	LEE, Ya-Jung	167
GIBSON, A.G.	611	LI, N.	770
GORDANINEJAD, Faramarz	500	LIANG, Bin	405
GRABOVAC, Ivan	412	LIANG, Yan-Chu	639
GREEN, E. Rhian	193	LIEW, K.M.	213
		LIN, Chien-Chang	668

LINGARD, Jeff	799	SHIEH, Rong C.	591
LIU, Li	271	SHIMAMOTO, A.	493
LIU, Linan	405	SHLITSA, R.P.	826
LIU, Lixun	271	SHYU, Yau	167
LIU, Qingfang	405	SIHN, Sangwook	26
LIU, T.	213	SIORES, E.	55
LORENTZEN, T.	230	SMITH, Malcolm J.	551
LUESCHER, Raoul E.	412	SOMBOONSONG, Win	723
MACDONALD, Douglas O.	571	SONI, Som R.	296
MAI, Y.-W.	36, 158	SOUTIS, C.	395
MARCO, John	799	SPEARING, S. Mark	111
MARTIN, J.	289	SPECHT, S.	695
MATTHEWS, F.L.	139	SPRINGER, K.L.	601
MCNICHOLS, B.	289	STEVEN, G.P.	8, 158
MIYANO, Yasushi	26	STEVENS, K.A.	695
MILESHKIN, N.	707	SUZUKI, Toshio	16
MIRABELLA, L.	148	SUGIMOTO, Sunao	258
MIRZA, S.	770	TABAKOV, P.Y.	779
MOITA, José Simões	808	TAPANES, Edward	421
MORIARTY, Brendan	175	TARN, Jiann-Quo	789
MORTENSEN, Flemming	129	TAYA, Minoru	493
MOTA SOARES, Carlos A.	808	THOMSEN, Ole Thybo	129
MOTA SOARES, Cristóvão M.	808	TSAI, Stephen W.	26
NAKADA, Masayuki	26	THOMSON, Rodney S.	412, 677
NAGAR, Arvind	296	TIRRY, L.	237
NGUYEN, V.M.	707	TONG, L.	8, 158
OCHOA, O.O.	289	TOWSE, A.	95
ODI, Randolph A.	374	TZENG, Wen-Long	658
ORISAMOLU, Irewole R.	551	VAN DER WIJST, M.W.M.	561
OSHAWA, Isamu	16	VAN HEMELRIJCK, D.	237
OSHIMA, Nobuo	483	VERIJENKO, V.E.	779
OZTELCAN, C.	289	VINOGRADOV, Aleksandra M.	474
PARK, H.C.	365	VINSON, Jack R.	444
PARK, Ik-Min	510	WALKER, K.	337
PARK, Keun-Young	454	WANG, C.H.	347
PEIJS, T.	561	WANG, J.	119
PITT, S.	357	WANG, Shijie	819
POLYAKOV, V.A.	753	WISNOM, M.R.	84, 95
POTTER, K.D.	84, 95	WRIGHT, Richard J.	102
RAIZENNE, M.D.	279	WU, Chih-Ping	789
RAMANI, Karthik	46, 175	WU, Weida	500
RASTOGI, Naveen	296	XIAN, X.J.	185
RISPLER, A.R.	158	YANG, Dujun	819
ROMILLY, D.P.	279	YANG, Kai-Lin	789
ROSE, L.R.F.	347	YE, L.	36, 158
RYOU, Jung-Kyu	454	YEN, Jinliang	540
SANCHO, José	246	YI, S.	444
SANDERSON, S.	327	YIN, Yunyu	632
SCHREURS, P.J.G.	561	YOON, Jin-Young	648
SCOTT, Murray L.	677	YAMAGUCHI, Koji	16
SEM, K.	289	YUDONG, Huang	271
SEO, Dae Cheol	582	ZHANG, Zhiqian	271
SHAIKH, C.	779	ZHAO, Wenping	46
SHEN, Yapeng	519, 540	ZHIGUN, I.G.	826
SHENOI, R. A.	385	ZUIDERVAART, J.	561
SHETTY, Sharath P.	111		